Karlsruhe Institute of Technology

Joint project: Retention of radionuclides relevant for final disposal in natural clay rock and saline systems

Final report

by Christian M. Marquardt (Editor)[1]

KIT SCIENTIFIC WORKING PAPERS 112

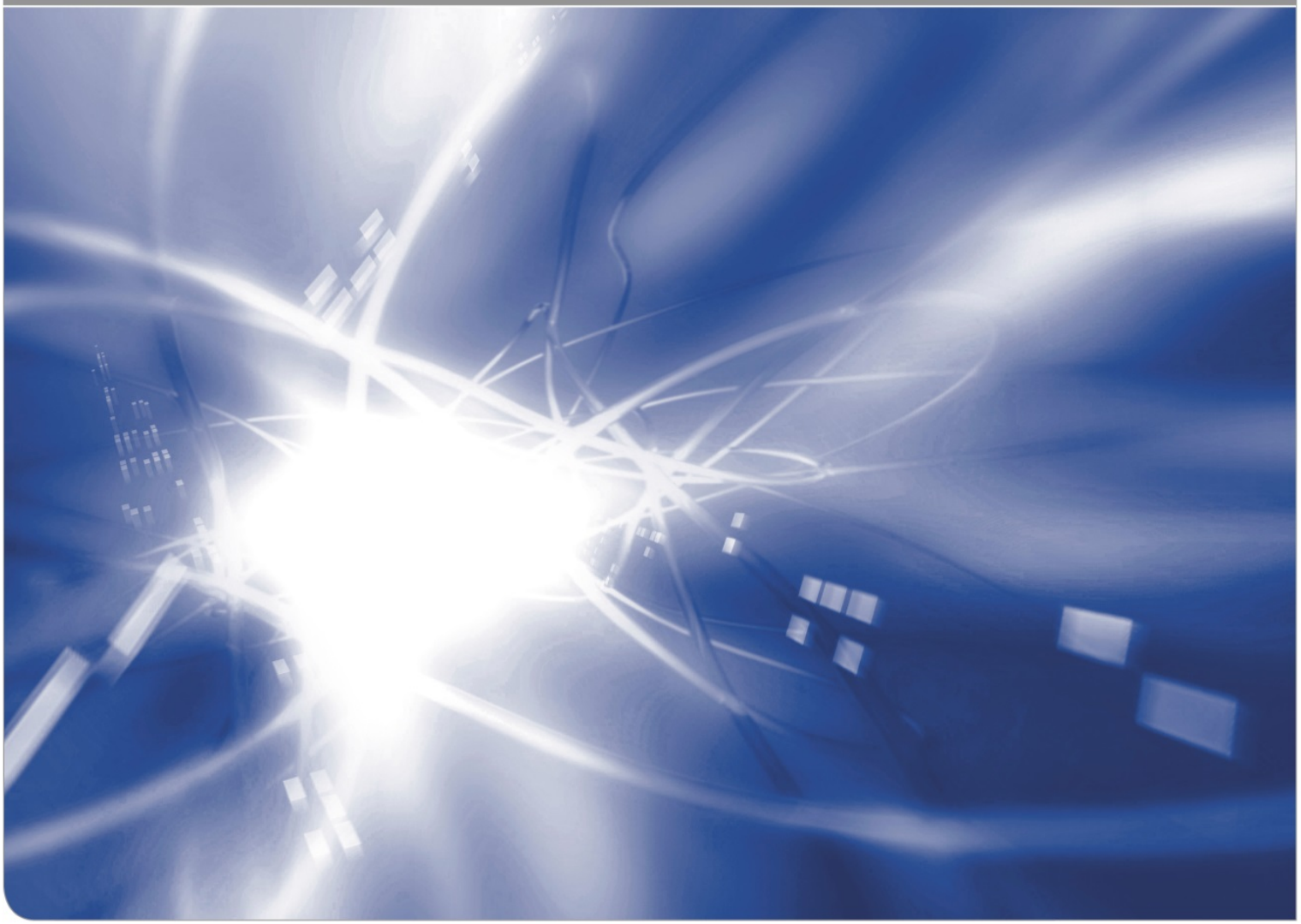

[1]In collaboration with

Helmholtz-Zentrum Dresden-Rossendorf, Institut für Ressourcenökologie

Johannes Gutenberg-Universität Mainz, Institut für Kernchemie

Technische Universität München, Theoretische Chemie

Universität des Saarlandes, Anorganische Festkörperchemie, Anorganische und Analytische Chemie

Karlsruher Institut für Technologie, Institut für Nukleare Entsorgung

Universität Potsdam, Institut für Chemie, Physikalische Chemie

Technische Universität Dresden, Sachgebiet Strahlenschutz und Professur für Radiochemie

Ruprecht-Karls Universität Heidelberg, Physikalisch-Chemisches Institut

Impressum

Karlsruher Institut für Technologie (KIT)
www.kit.edu

2019

ISSN: 2194-1629

Joint project:
Retention of radionuclides relevant for final disposal in natural clay rock and saline systems

by

C.M. Marquardt (Editor)

In collaboration with

Helmholtz-Zentrum Dresden-Rossendorf, Institut für Ressourcenökologie

Johannes Gutenberg-Universität Mainz, Institut für Kernchemie

Technische Universität München, Theoretische Chemie

Universität des Saarlandes, Anorganische Festkörperchemie, Anorganische und Analytische Chemie

Karlsruher Institut für Technologie, Institut für Nukleare Entsorgung

Universität Potsdam, Institut für Chemie, Physikalische Chemie

Technische Universität Dresden, Sachgebiet Strahlenschutz und Professur für Radiochemie

Ruprecht-Karls Universität Heidelberg, Physikalisch-Chemisches Institut

The work described in this report has been financially supported by the German Federal Ministry of Economics and Technology (BMWi). The authors are responsible for the content of their contributions.

BMWi Project No.: 02 E 10971
Partner No. 1: Helmholtz-Zentrum Dresden-Rossendorf,
Institut für Ressourcenökologie
K. Schmeide, K. Fritsch, H. Lippold, M. Poetsch, J. Kulenkampff, J. Lippmann-Pipke, N. Jordan, C. Joseph, H. Moll, A. Cherkouk, M. Bader

BMWi Project No.: 02 E 10981
Partner No. 2: Johannes Gutenberg-Universität Mainz, Institut für Kernchemie
S. Amayri, P.J.B. Börner, U. Kaplan, J.V. Kratz, M. Lübke, T. Reich, R. Scholze, N. Trautmann, C. Willberger

BMWi Project No.: 02 E 11001
Partner No. 3: Technische Universität München, Theoretische Chemie
S. Krüger, A. Kremleva

BMWi Project No.: 02 E 10991
Partner No. 4: Universität des Saarlandes, Anorganische Festkörperchemie,
Anorganische und Analytische Chemie
C. Hein, J. Sander, R. Hahn, R. Kautenburger, H.P. Beck, G. Kickelbick

BMWi Project No.: 02 E 10961
Partner No. 5: Karlsruher Institut für Technologie, Institut für Nukleare Entsorgung
N. Banik, M. Bouby-Laliron, N. Finck, K. Hinz, T. Kupcik, R. Marsac, A. Schnurr, M. Altmaier, C.M. Marquardt, Th. Schäfer

BMWi Project No.: 02 E 11011
Partner No. 6: Universität Potsdam, Institut für Chemie, Physikalische Chemie
K. Brennenstuhl, K. Burek, S. Eidner, M.U. Kumke

BMWi Project No.: 02 E 11021
Partner No. 7: Technische Universität Dresden, Sachgebiet Strahlenschutz
und Professur für Radiochemie
M. Acker, J. Schott, F. Taube, A. Barkleit, M. Müller, S. Taut, T. Stumpf

BMWi Project No.: 02 E 11031
Partner No. 8: Ruprecht-Karls Universität Heidelberg, Physikalisch Chemisches Institut
D. R. Fröhlich, A. Skerencak-Frech, P. Panak

Table of content

List of abbreviations

2 SPNE SC/CE	Two-site protolysis non-electrostatic surface complexation and cation exchange model
α	Rock capacity factor
D_e	Effective diffusion coefficient
$\Delta_r H_{0,m}$	Standard molar reaction enthalpy
$\Delta_r S_{0,m}$	Standard molar reaction entropy
ε(i,k),	binary ion-ion interaction coefficients (SIT)
EXAFS	Extended X-ray absorption fine structure
FA	Fulvic acid
FEM	Finite element method
F-RET	Förster resonance energy transfer
HA	Humic acid
HPLC	High performance liquid chromatography
HTO	Tritiated water
ICP MS	Inductively coupled plasma mass spectrometry
ILET	Interlanthanide energy transfer
IMTC	isothermal micro-titration calorimetry
K_0	Complex stability constants
K_D	Sorption distribution coefficient
Lac	Lactate
LMWOC	Low molecular weight organic compounds
MCCE	Miniaturised clay column experiments
NEA-TDB	Thermochemical database of the Nuclear Energy Agency
NICA-Donnan	Non ideal competitive adsorption-Donnan
NOM	Natural organic matter
OPA	Opalinus clay
Ox	Oxalate
PET	Positron emission tomography
pH	negative common logarithm of the proton activity
pH_c	negative common logarithm of the molar proton concentration
pH_m	negative common logarithm of the molal proton concentration
UV-vis	Ultraviolett to visible (light)
SFG	Sum frequency generation spectroscopy
SEM-EDS	Scanning electron microscopy with energy dispersive spectroscopy
SIT	Specific ion interaction theory
THEREDA	Thermodynamische Referenzdatenbank
TRLFS	Time resolved laser-induced fluorescence spectroscopy
WIPP	Waste isolation pilot plant
XANES	X-ray absorption near edge structure
XRD	X-ray diffraction
XRF	X-ray fluorescence

Introduction

The present report summarizes the progress and the results obtained within the joint research project “Retention of radionuclides relevant for final disposal in natural clay rock and saline systems” which received financial support by BMWi . The work presented here is a continuation of the work within former BMWi projects performed in the years 2003 to 2010 whose results have been published in two scientific reports of the Karlsruhe Institute of Technology (KIT, former Forschungszentrum Karlsruhe (FZK)), Report FZKA-7407 (2008) and KIT Scientific Report 7633 (2012). The project was conducted in the framework of a BMWi program focusing on future research & development studies on the disposal of high-level nuclear waste in deep geological formations: "Schwerpunkte zukünftiger FuE-Arbeiten bei der Endlagerung radioaktiver Abfälle (2007-2010)", updated and extended for the period 2011-2014.

According to the BMWi concept, tasks on problems regarding the final disposal in rock salt, which are not finalized so far, should be completed. Parallel to this work, the scientific and technical knowledge of the final disposal of heat producing radioactive waste in clay stone should be improved as comprehensive as possible. As a result, the scientific and technical basis for a final repository is provided, especially for heat producing radioactive waste. This scientific and technical basis shall continually be matched to the state-of-the-art of science and technology. And last but not least, the work of the project contributes to the preservation of the scientific and technical competence and supports young scientists in the field of radioactive waste management.

Eight partners (see page I) were involved in this joint research project, and they all have contributed to this report. To make the results of the joint project available for a broader international community and to present them as a unit, it was decided to publish the individual final reports of the project partners as a KIT scientific report. The executive summary gives an overview of the covered topics and the obtained results without going into details. More information can be found in the individual reports attached in Annex B, or in many publications listed in Annex A. Especially, the relationships among the different groups and their studies are pointed out. The results are important contributions to the safety assessment of nuclear waste disposal in deep geologic formations, focusing on clay and saline systems.

1 Sorption of radionuclides onto clay minerals

A central topic of the project was to investigate the sorption of actinides and lanthanides on various clay minerals at elevated ionic strengths. The studies comprised pure clay minerals like kaolinite, montmorillonite, and illite as well as the natural clay stone Opalinus clay from the Mont Terri rock laboratory in Switzerland. Many studies of the sorption of metal ions on clay minerals have been performed so far in diluted aqueous solutions. Bradbury and Baeyens developed the 2 Site Protolysis Non-Electrostatic Surface Complexation and Cation Exchange (2SPNE SC/CE) model to describe the sorption behavior of metal ions on clay minerals in low and medium ionic-strength media[1,2].In order to test the applicability of this model to ionic strengths up to 3 M, corresponding experimental data for the sorption of actinides and lanthanides on various clay minerals were collected.

1.1 Sorption on kaolinite, montmorillonite and illite

The sorption experiments have been performed with the following lanthanides and actinides: europium (Eu), uranium (U), neptunium (Np), plutonium (Pu), americium (Am), curium (Cm), and technetium (Tc). The metal concentration was varied from micromolar down to picomolar concentrations. The amount of clay in solution was 2–18 g/L. The background electrolytes NaCl, $NaClO_4$, $CaCl_2$, or $MgCl_2$ used had concentrations of up to 3 M and the pH range covers pH 3 to pH 12. The sorption experiments were either performed under ambient air conditions or under oxygen and carbon dioxide free atmospheres. Qualitatively, the sorption of metal ions is low in the acidic pH range (log K_d ~ 1- 3, K_d in units of L/kg) and increases with pH to almost quantitative sorption. Exceptions are Np(V) and the tetravalent actinides. Np(V) shows only weak sorption with a log K_d value not higher than 3, and the tetravalent actinides are strongly sorbed even at low pH values, which is expressed in high log K_d values > 4.

Eu(III), Cm(III), and U(VI)

The experimental sorption data of Eu(III) and U(VI) onto montmorillonite and illite show a small influence of the salinity (NaCl, $CaCl_2$, $MgCl_2$) on the log K_d values in the neutral to alkaline pH range. For montmorillonite the sorption is 0.5 to 1 log K_d units lower in solutions with $CaCl_2$ or $MgCl_2$ as background electrolyte compared to NaCl solutions. This lowered sorption was not observed for illite. In acidic media the sorption is significantly diminished with increasing NaCl concentration, because the cation exchange reaction is suppressed with increasing Na^+ concentration in solution. This effect is also observed for $CaCl_2$ and $MgCl_2$. Nevertheless, an almost

[1] Bradbury, M.H. and Baeyens, B., A mechanistic description of Ni and Zn sorption of Na-montmorillonite: Part I: Titration and sorption measurements. Journal of Contaminant Hydrology, 1997. 27: p. 199-222.

[2] Bradbury, M.H. and Baeyens, B., A mechanistic description of Ni and Zn sorption of Na-montmorillonite: Part II: Modelling. Journal of Contaminant Hydrology, 1997. 27: p. 223-248.

quantitative sorption (log $K_d \geq 4.5$) occurs for all systems at $pH_c > 8$. However, at a $pH_c > 11$, a significant decrease of the sorption is observed in the presence of dissolved CO_2, which is independent of the background electrolytes. Such high pH values are relevant for ground waters in contact with cement or concrete construction parts.

To get more insight into the sorption process of Cm(III) or Eu(III) ions by the clay mineral kaolinite, TRFLS investigations were performed. Eu(III) adsorbed onto kaolinite showed a complex luminescence decay behavior. Also its luminescence spectrum was altered compared to Eu(III) in aqueous solution, allowing the specific identification of the sorbed species. TRLFS investigations with Cm(III) in saline systems did not show any significant change of the first coordination sphere of the metal ion, indicating that the surface speciation of Cm(III) is not influenced by elevated ionic strength.

The sorption of U(VI) on montmorillonite in absence of CO_2 shows no significant difference between experiments in NaCl and $CaCl_2$: the sorption steadily decreases with the pH, reaching a plateau with log K_d ~5 for NaCl and log K_d ~4.5 for $CaCl_2$ at pH 7 and higher pH values. Investigations in the presence of CO_2 showed a significant influence of CO_2 on the sorption of U(VI) on montmorillonite at pH values greater than 6. In NaCl the sorption decreases from log K_d ~ 4.5 to log K_d ~ 1.5 at pH 9-10; in $CaCl_2$ the sorption curve shows a large bump at pH > 6 from log K_d ~4 to log K_d ~1.8 at pH 7, and finally decreases to a log K_d of about 4.5 at pH 9. The sorption in $MgCl_2$ solution does not decrease at pH > 6 and reaches a plateau with log K_D ~ 3.5. The U(VI) uptake was presumably governed by (co-)precipitation with magnesium and silicon compounds of low solubility.

Redox sensitive actinides: Np(IV, V), Pu(III, IV, V)

The average log K_d values for the sorption of Np(V) on Na-montmorillonite were independent of the NaCl concentration. This independence of the ionic strength of NaCl was also observed at pH 8.5 over a wide range of initial Np(V) concentrations (1×10^{-12} – 1×10^{-4} M, ambient-air conditions, 4 g/L). The pH dependence of the sorption was also studied under ambient-air and CO_2-free conditions (8×10^{-6} M Np(V) in 0.1 M NaCl). While the Np(V) sorption steadily increased with pH in the absence of CO_2, the sorption decreased above pH 9 under ambient-air conditions because of the formation of a Np(V) carbonate complex.

In sorption studies with focus on reducing conditions, log K_D values are clearly higher than those measured for Np(V) sorption onto illite at oxidizing conditions, e.g. under ambient-air conditions. The observation that log K_D increases with decreasing pe (pe = -log activity(e^-); e^- = electron) suggests partial reduction to Np(IV), although measured redox potentials (pe values) suggest the predominance of Np(V) in solution. Reduction to Np(IV) at the illite surface was confirmed by X-ray absorption near-edge structure (XANES) spectroscopy.

Similar to the Np experiments Pu also showed an influence of redox reactions on the sorption. At pH > 7, the sorption of Pu remains very high over time (log K_D ~5), and it is assumed that Pu(IV) is mainly present. The results of the Np and Pu studies, i) Pu(IV)/Pu(III) transitions in presence of illite, ii) Pu(V)/Pu(IV) redox reactions in aqueous kaolinite suspensions, or iii)

Np(V)/Np(IV) transitions in the presence of illite, demonstrate the applicability of the approach – correlation of pe in solution and log K_D as input parameter for surface complexation modelling and assuming that tetravalent actinides are formed at the mineral surface - to describe actinide redox reactions in the presence of mineral surfaces over a wide range of possible redox conditions (i.e. when Pu(III), Pu(IV), and Pu(V) occur).

Geochemical Modeling

All experimental results at high ionic strengths can be modeled quite well with the 2SPNE SC/CE model in combination with the Specific Ion Interaction Theory (SIT) or the Pitzer formalism for ionic strength correction of aqueous species up to 3 M. If redox reactions are expected, good modeling is accomplished by introducing the appropriate redox reactions and pe values corresponding to the experimental conditions. To model metal surface complexation in mixed electrolyte systems, surface complexation constants derived in pure electrolytes can be used. This could be demonstrated in a study of U(VI) sorption onto montmorillonite with a solution containing 2.52 mol kg^{-1} NaCl, 0.12 mol kg^{-1} $CaCl_2$ and 0.048 mol kg^{-1} $MgCl_2$, which resembles the groundwater composition in the Konrad mine, Lower Saxony[3].

Under certain experimental conditions, it is sometimes necessary to introduce ternary complexes to improve the modeling. Ternary Np(V) surface complexes with carbonate had to be included to model the sorption curves in the presence of atmospheric CO_2. In case of U(VI) at elevated Cl^- concentrations, an additional possible surface species ($SO\text{-}UO_2Cl(OH)_2^{2-}$) was introduced to improve the modeling of the experimental data over the whole pH_c and ionic strength range.

[3] Brewitz, W., Eignungsprüfung der Schachtanlage Konrad für die Endlagerung radioaktiver Abfälle. Tech. Rep. GSF-T 136 (1982).

1.2 Sorption on Opalinus clay

This section focuses on sorption studies of actinides and lanthanides on clay powder, prepared from Opalinus clay (OPA) from Mont Terri (Switzerland). The main components of this OPA powder are the clay minerals kaolinite, illite, illite/smectite mixed layers, chlorite, and the minerals quartz and calcite. For Eu(III) sorption experiments, OPA was purified from non-clay minerals yielding an almost pure clay mineral fraction. This batch was named OPA-CF (Opalinus clay – clay fraction). Pure electrolyte solutions (NaCl, $CaCl_2$, $MgCl_2$) and synthetic pore water were used as background electrolytes.

Sorption of Eu(III), Pu(III), Am(III)

The Eu(III) sorption edge (point of 50% sorption) on illite and OPA-CF is for all NaCl concentrations quite similar and the increase of the sorption is nearly the same. The K_d values in the quasi quantitative sorption range with > 99.5 % Eu(III) sorption (log K_d > 5, pH_c> 8) are for OPA somehow lower compared to the very high values for the pure illite system. This is caused by a small amount of carbonate in solution released from the OPA-CF, because of dissolution of calcite as a component of OPA that could not be removed during the purification. The same trend is found in a $CaCl_2$ solution.

Am(III) and the redox sensitive Pu(III) showed an identical sorption behavior in OPA pore water, 0.1 M $MgCl_2$ or 0.1 M $CaCl_2$ solutions, in the pH range of 1 to 10. The sorption edge was reached at pH 5.5 and quantitative sorption was observed at pH > 7. In 0.1 M NaCl solution these values were shifted to pH 4 and pH > 6, respectively.

At pH 5, an elevated ionic strength due to an excess of competing Na^+ ions leads to a decrease in Eu(III) retention on clay and log K_D values decrease from 2.6 (0.01 M NaCl) to 1.9 (5 M NaCl). At lower pH values, outersphere complexation dominates as expressed by the observed ionic strength dependency.

Sorption of Np(V)

A weaker sorption is observed for Np(V) on OPA in NaCl solution. The sorption showed no influence of the ionic strength of NaCl (0.1 and 1.0 M NaCl) over the whole initial Np(V) concentration range ($1 \times 10^{-4} – 1 \times 10^{-12}$ M). The sorption in pore water as well as in the presence of divalent cations like Mg^{2+} or Ca^{2+} is significant lower than in NaCl solutions. This can be explained by the competitive behavior of divalent cations contained in OPA pore water and $MgCl_2$ solutions for sorption sites. Also the Np(V) sorption significantly decreases with increasing $MgCl_2$ concentration.

Sorption of Tc(IV) and Tc(VII)

The sorption of the redox-sensitive Tc on OPA was investigated under various conditions in batch experiments. Under ambient-air conditions $Tc^{VII}O_4^-$ was not sorbed on OPA at pH ≥ 5. In the pH range 3–5, Tc(VII) uptake was also very low with log K_D < 1. Only under Ar atmosphere and reducing conditions the Tc uptake by OPA reached 99% at pH 7.7, because of dissolved Fe(II) and reduction of Tc(VII) to Tc(IV). Thus, Tc(VII) is not or very weakly sorbed on OPA. Spectroscopic investigations by Tc K-edge XANES and EXAFS confirmed that the initial Tc(VII) was reduced to Tc(IV) and was taken up by the clay predominantly as TcO_2.

Desorption experiments

The influencing factors for desorption of the metals from OPA differ considerably from those relevant for the sorption. Over a wide pH range Eu(III) cannot be desorbed from clay and above pH 7 even an increase in salinity has no effect on its remobilization. Contrary to Eu(III), U(VI) can be released into the solution depending on pH and ionic strength. The interpretation of these results is difficult because the experiments were performed under ambient air conditions and the equilibrium state of the solution with atmospheric CO_2 might not have been reached.

Influence of clay organic components on the sorption

The impact of HA-like clay organics on the sorption of actinides at high salinity (NaCl, $CaCl_2$ and $MgCl_2$ up to 4 M) was investigated in radiotracer studies for binary and ternary systems. As chemical analogue components for trivalent actinides, ^{152}Eu(III), ^{160}Tb(III), and ^{14}C-fulvic acid were used. It was found that there is no synergism in the mobilizing effects of humic-like matter and electrolytes at in-situ pH. This is due to the fact that metal-humic complexation is strongly suppressed at increasing ionic strength while adsorption of the organic component is hardly influenced. Its resultant effect on the solid-liquid distribution of the actinide analogues can be approximately predicted by geochemical modeling using a combined K_d approach (Linear Additive Model), based on interaction data determined for the binary subsystems (metal / fulvic acid, metal / OPA, fulvic acid / OPA). This applies to the influence of ionic strength as well as to the transition from demobilizing to mobilizing properties with increasing pH. The effect of electrolytes on fulvate complexation was characterized in detail by luminescence spectroscopy and mechanistic modeling (NICA-Donnan approach). In contrast to fulvic acid, humic acid increases the retention of Eu on OPA at higher ionic strengths, most presumably because of precipitation or rather co-precipitation of Eu together with humic acid. In reference experiments the influence of LMWOC like formic, acetic, propionic, or glycolic acid on the metal-kaolin sorption was investigated. Based on Eu(III) luminescence parameters only at high LMWOC concentrations (> mM) the sorbed species were altered and a mixed LMWOC-surface Eu(III) species was observed.

Influence of temperatures on the sorption

A few experiments have been carried out at elevated temperatures to gain first experiences in this difficult field. First Np(V) sorption experiments showed that temperatures up to 80 °C have

no influence on the sorption of Np(V) on OPA at pH 7.6 in 0.1 or 3.0 M NaCl solutions. In contrast to this finding the sorption of Eu(III) on OPA slightly increases with increasing temperature in the range from 25 °C to 60 °C at 0.01 and 1 M NaCl. Also some desorption experiments have been done at elevated temperatures. An influence of the temperature has not been observed for Eu(III) desorption over a wide range of temperatures. In the ternary system Eu(III)/humic acid/OPA increased temperatures results in enhanced desorption of Eu(III) depending on the pH and ionic strength. U(VI) desorption decreases at elevated temperatures in the binary system U(VI)/OPA – whereas in the ternary U(VI)/HA/OPA system, the effect of temperature is somehow more complex because of the variety of uranium species.

1.3 Quantum mechanical modeling

Sorption of actinides on clay mineral surfaces has also been investigated by quantum chemical simulations. These calculations aim to contribute to the speciation at mineral surfaces, to search for favorable sorption sites, and to develop a mechanistic understanding at the atomic scale.

The Sorption of U(VI) and Np(V) on the reactive edge surfaces of various models of smectites has been investigated. Here, models with neutral and charged mineral layers were compared, taking into account montmorillonitic and beidellitic cation substitutions. These models can be regarded as representing various local structures of a generic smectite.

The first systematic study of U(VI) adsorption at three solvated edge surfaces was carried out. For sites close to a proton accepting AlOH group, besides UO_2^{2+} also its monohydroxide has been determined as adsorbate. For both adsorbates coordination numbers of 5 and 4 have been found. The latter one appears on sterically demanding sites. Type and structure of the sorption complexes are independent of the mineral model and determined mainly by the type of the sorption site. Variation of the mineral layer charge or of the adsorbate coverage leads to small structural changes only. Thus, for various 2:1 clay minerals, the same sorption complexes are expected at specific sites on edge surfaces of same orientation. With a newly developed simulated annealing procedure complex formation energies comparable for sorbed actinides at various sites were calculated for the first time. These improved energies showed that sorption on charged minerals is favored compared to neutral pyrophyllite and that sites with high effective charges, especially those including negatively charged substituted cations, are preferred.

U(VI) and Np(V) sorbed on the (110) edge surface of montmorillonite occupy the same sites preferentially. U(VI) tends to bidentate coordination while Np(V) favors monodentate coordination to the surface. For Np(V) the monohydroxide is less common as adsorbate, in line with its lower hydrolysis constant.

Inspection of Mg^{2+} and Ca^{2+} sorption on montmorillonite reveals that these cations sorb preferentially on different sites than U(VI). As the alkaline earth cations also yield lower surface

complex formation energies, no strong competition with U(VI) sorption is expected, in line with experimental results of this project.

These computational results on actinide sorption on clay mineral edge surfaces suggest the interaction of actinides with smectites to be a local phenomenon, essentially determined by the sorption site. The sorption also depends on the permanent charge of the mineral and the number and strength of sorption sites, which increase with increasing degree of deprotonation of the surfaces. These findings support the concept of a generic thermodynamic model for actinide sorption at clay minerals, as realized in the 2SPN SC/CE model for example. As a variety of sites are available at various edge surfaces, a diversity of sorption complexes of variable strength is expected to be coexisting.

1.4 Conclusion

The sorption of tri-, tetra-, penta-, and hexavalent actinides on pure clay minerals like kaolinite, montmorillonite, and illite can be described quite well with the surface complexation model (2SPNE SC/CE) at low and high ionic strengths. The ionic strength has only minor impact on the sorption for background electrolytes with monovalent ions. For background electrolytes with higher charged ions like the divalent Ca^{2+} and Mg^{2+}, competing sorption and complex reactions can diminish the sorption of actinides. In general, the sorption of tri- tetra-, and hexavalent actinides is strong and log K_D values are larger than 4.5 in NaCl solutions and at pH > 6. Np(V) is sorbed weaker, but has no relevance under anaerobic conditions because of the reduction to Np(IV). Atmospheric CO_2 has a significant impact on the sorption because of formation of strong carbonate complexes. The redox driven sorption of actinides, e.g. Np and Pu, on a natural clay like OPA is not figured out completely, because of the heterogeneous composition of the OPA . Consequently, for site specific assessments in the future studies with a site specific clay rock are mandatory.

2 Diffusion and transport processes

Sorption and diffusion are the main processes that determine the migration of long-lived radionuclides like uranium, neptunium, and plutonium in the far-field of a nuclear waste repository with clay rocks as host rock.

Compacted illite as a pure clay system and Opalinus clay (OPA) from Mont Terri, Switzerland, as reference for a natural clay were used to study the diffusion of U(VI), Np(V), Pu(V), and Eu(III). Eu(III) was used again as chemical analogue for trivalent actinides like Pu(III), Am(III) or Cm(III). In case of U(VI), the influence of a low molecular weight organic compound (citrate) on the diffusion of U(VI) was studied. In the diffusion experiments with Np(V), the influence of the ionic strength of NaCl solutions and of the temperature on the diffusion parameters, i.e. the effective diffusion coefficient D_e and the rock capacity factor α, was investigated. A detailed molecular-level picture of the diffusion of Np(V) and Pu(V) in OPA was obtained using synchrotron-based X-ray micro-beam techniques (µ-XRF, µ-XANES, and µ-XRD).

Since OPA contains 15-30% illite and 5-20% illite/smectite mixed layers, diffusion studies were also conducted with compacted illite, i.e., the diffusion of tritiated water (HTO), Cl^-, and Eu(III) with solutions with various NaCl concentrations as mobile phase.

Finally, the Positron Emission Tomography (PET) was developed for and applied to the visualization of transport phenomena of corresponding tracers in intact and fractured clay rocks.

2.1 Diffusion in compacted illite

HTO, Cl^-, Eu(III) and fulvic acid in illite

For HTO, effective diffusion coefficients D_e and values of the rock capacity factor α (or the porosity ε, respectively) are similar in 0.1 and 0.5 M NaCl, indicating that an increase of background electrolyte concentration has no effect on the geometrical properties (tortuosity or constrictivity) of the compacted clay mineral. However, an increase in ionic strength affected the transport parameters in case of $^{36}Cl^-$, where D_e and α are observed to be higher in 0.5 M NaCl than in 0.1 M solutions. The lower D_e value for Cl^- compared to HTO can be related to a reduced accessible pore space for anionic tracers (anion accessible porosity ε_{acc}), as anions are repelled in the vicinity of the negatively charged clay surfaces. On the other hand, the increase in D_e at higher ionic strength can be linked to an enhanced electrostatic shielding of this negative surface charge, increasing the fraction of anion accessible pore space.

The Eu(III) diffusion experiment showed a steady decrease of the initial Eu concentration to almost zero after 1500 h. In the reservoir after the illite core, no Eu was measured. This result indicates a complete Eu uptake by the Na-illite mineral.

As an analogue for clay organic polyelectrolytes, the diffusive properties of tritiated fulvic acid (^{3}H-FA) in compacted Na-illite were investigated. During the experimental run time the activity in the low concentration reservoir after the illite core increased gradually, with a steady state (constant flux) being observed after ~70 d. From the boundary conditions of the experiment the averaged diffusion coefficient D_e is determined to be about 1.6×10^{-11} m^2/s for 0.1 M as well as 1.0 M NaCl. The diffusion coefficient is comparable to D_e values determined for negatively charged tracers like $^{36}Cl^-$.

2.2 Diffusion in OPA

Diffusion of U(VI) in Opalinus clay in the absence and presence of citric acid

The influence of citrate as a surrogate for clay organics on the diffusion of U(VI) in OPA was studied under anaerobic conditions using OPA pore water as background electrolyte. The diffusion parameters obtained for the HTO through-diffusion and the U(VI) in-diffusion in the absence of citric acid were in agreement with literature data (Joseph et al., 2013). In the presence of citric acid the U(VI) diffusion was significantly retarded, which was attributed to a change in speciation. Probably, part of U(VI) was reduced to U(IV) directly on the clay surface within the three months the diffusion experiment was conducted. Citric acid diffused slightly faster through OPA than small humic acid colloids studied previously[4]. The study shows that the chemical system has to be investigated in more detail to clarify the occurring reactions. In particular, the U-citric acid species formed under these environmentally relevant conditions needs to be described spectroscopically, thermodynamically, structurally, and including all available information from literature.

Diffusion of Np(V) in Opalinus clay in dependence of salinity and temperature

To study the influence of salinity on the diffusion of Np(V) at 24 ± 2 °C, 1 M and 3 M NaCl solutions at pH 7.6 were used as mobile phases and compared to experiments with OPA pore water (pH 7.6, I = 0.4 M). Analogous diffusion experiments were performed with HTO and $^{22}Na^+$ for comparison with known literature data. The diffusion experiments showed that for 1 M NaCl the effective diffusion coefficient for Np(V) of $D_e = 6.9 \times 10^{-12}$ m^2/s is the same as in OPA pore water and decreases to 2.4×10^{-12} m^2/s for 3 M NaCl. The K_d values for the sorption of Np(V) as derived from the determined α did not show any dependence of the ionic strength in the range of 1 M to-3 M NaCl. This observation agrees with the results of the corresponding batch sorption experiments (see Section 1.2).

[4] Joseph, C., Van Loon, L.R., Jakob, A., Steudtner, R., Schmeide, K., Sachs, S., Bernhard, G.: Diffusion of U(VI) in Opalinus Clay: Influence of temperature and humic acid. Geochim. Cosmochim. Acta 109, 74-89 (2013).

The diffusion of Np(V) in OPA with OPA pore water and 1 M NaCl as mobile phases was studied in the temperature range from (24 ± 2) °C to (60 ± 2) °C. The observed increase of D_e with temperature can be described by the Stokes-Einstein equation with activation energies of (21 ± 2) kJ/mol and (18 ± 2) kJ/mol in OPA pore water and 1 M NaCl, respectively. The K_d values derived from α did not show any temperature dependence, again in agreement with the corresponding batch experiments (s. Section 1.2).

Speciation of Np and Pu after diffusion in Opalinus clay

The diffusion of Np(V) in OPA was studied in dependence of the composition of the mobile phase, i.e., OPA pore water (pH 7.6) and 1 M NaCl (pH 8.1). The diffusion profiles of Np in OPA measured by µ-XRF show a pronounced dependence on the mobile phase and the diffusion time. Np L_3-edge µ-XANES measurements reveal that significant parts (up to ca. 25%) of the initial Np(V) is reduced to Np(IV) during diffusion. Higher degrees of Np reduction, i.e., up to 88% Np(IV), were observed in the vicinity of iron enrichments in the clay, which could be identified in some cases as pyrite using µ-XRD.

The capability of OPA to induce redox reactions could be observed also in case of Pu(V) diffusion with OPA pore water (pH 7.6) as mobile phase. Along its diffusion path Pu(V) is increasingly reduced to Pu(III) and Pu(IV). At the interface between the clay and the Pu(V)-containing pore solution, approximately 30% Pu(III), 50% Pu(IV), and 20% Pu(V) were detected by Pu L_3-edge µ-XANES spectroscopy. After the diffusion of Pu(V) by 200 µm into the clay, Pu(V) was completely reduced to approximately 30% Pu(III) and 70% Pu(IV). It should be noted that this reduction leads to a significantly higher retention of Pu by OPA due to stronger sorption of Pu(III, IV) compared to Pu(V).

2.3 Miniaturized clay column experiments (MCCE)

Online hyphenation of miniaturized clay column experiments (MCCE) with ICP-MS allows for the visualization of sorption and desorption processes of Eu and U on OPA dynamically. Small amounts of heavy metals (Eu, U) in aqueous solution are repeatedly injected on self-packed clay columns in a modified HPLC (high performance liquid chromatography) setup. Owing to ICP-MS detection the metal retention on the compacted clay columns can be monitored and recorded without effort. During a series of repeated injections (each time 5 µL of a 2 mM solution of europium perchlorate) over a column containing 1% OPA and 99% sea sand (SiO_2) three different stages can be distinguished: At first, the injected amount of Eu(III) is sorbed completely on the solid phase and no Eu(III) can be detected at the column outlet. Subsequently, the gradual breakthrough of Eu(III) with increasing eluted concentrations is observed. Thirdly, the saturation level is reached where no further increase in the eluted amounts of Eu(III) is recorded at the column outlet during further injections. As a verification for the successful sorption process Eu(III) retained on OPA can be subsequently displaced by repeated injections of Al(III) leading to typical desaturation behavior. Aside from that, in additional

MCCE the mobilizing influence of lactate representing the class of LMWOC in natural clay can be reproduced.

2.4 Spatiotemporal observation of diffusion processes with PET for determination of heterogeneous effects

The objective of this study was to establish PET as a reliable measurement method for the quantitative determination of heterogeneous diffusion coefficients in clays and for general tracer transport studies in barrier rocks. The main focus was the improvement of quantification, both by improving image quality and the parameter determination method. Two issues of the image reconstruction procedure were identified and successfully addressed: normalization and scattering. Monte-Carlo simulations of the physical processes, from radioactive decay of the tracer nuclide to detection in the detectors, were conducted in order to estimate and quantify these effects. These studies resulted in an improved image reconstruction procedure that yields tracer concentrations quantitatively, as well as an error estimate.

PET experiments with ^{22}Na and ^{124}I were conducted on OPA samples as test cases for the method and in order to better understand experimental artefacts by sample alteration and damage. Spatiotemporal data sets of the tracer concentration were computed. From these datasets diffusion coefficients were computed by inverse FEM-modeling. These diffusion coefficients are in accordance with literature results derived from through-diffusion experiments in diffusion cells. Indications for deviations from transversal-isotropic behavior on a minor level were found, which could be due to preferential diffusion pathways along silty layers or fractured zones.

2.5 Conclusions

Progress has been made in the understanding of the diffusion behavior of HTO, Na^+, Np(V), U(VI) in OPA and HTO, Na^+, Cl^-, and FA in compacted illite. For these cations and anions and HTO the diffusion parameters ε, α, and D_e were determined. However, the diffusion of actinides in presence of organic compounds like citric acid is not fully understood and has to be studied in the future.

Temperature effects were observed for the diffusion of HTO, Na^+, and Np(V) between 24° C and 60° C, which are expressed in increased D_e values at elevated temperature. The observations are in agreement with the literature.

Additional tools for transport studies have been developed like MCCE and PET, which can be used for specific investigations of the transport of radionuclides in relevant media in future studies.

3 Interaction of radionuclides with clay organic compounds

3.1 Low molecular weight organic compounds (LMWOC)

A major topic within this project is the interaction of actinides with small organic ligands either originating from the pore waters of potential host rock formations or being formed through degradation of higher molecular weight organic compounds. The main focus has been on the complexation reactions of U(VI), Np(V), Am(III), and Cm(III) and their analogues Eu(III), Nd(III)) with various monocarboxylic (formate, acetate, propionate, lactate) and dicarboxylic acids (oxalate, malonate) using either spectroscopic techniques (TRLFS, EXAFS, UV-vis) or isothermal micro-titration calorimetry (IMTC). The extensive study of the dependency of these complexation reactions on ionic strength and temperature has resulted in a large set of thermodynamic constants including temperature dependent standard state stability constants log $K^0(T)$, ion-ion interaction coefficients ε(i,k), standard reaction enthalpies $\Delta_r H^0_m$ and entropies $\Delta_r S^0_m$. These thermodynamic investigations are complemented by molecular-level structural information for Am(III) complexes with selected ligands obtained by EXAFS spectroscopy.

With a few exceptions (e.g. formation of $[CmOx]^+$ and NpO_2Lac) all investigated complexation reactions show an endothermic behavior. Therefore, the impact of LMWOC type ligands on the aqueous speciation of the studied actinides and analogues lanthanides generally increases with increasing temperature. However, the changes of the different standard state stability constants are generally small in the temperature range of up to 90 °C. In this temperature interval, the maximum change of log $K^0(T)$ for individual complexation steps is ~ 1. For dicarboxylic acids or lactate, featuring an additional hydroxyl group, the changes with temperature are smaller compared to simple monocarboxylic ligands and the endothermic behavior is less pronounced. These noticable differences are explained by the different coordination modes of these ligands towards the metal ions. Whereas monocarboxylates like acetate bind in an end-on fashion through the single carboxylic function, dicarboxylates form chelate complexes through both functional groups. Using EXAFS spectroscopy, the same behavior was observed for the interaction of Am(III) with lactate forming a 5-membered chelate ring through the carboxylic and the α-hydroxo group.

With respect to the long-term safety assessment of a nuclear waste repository in deep geological formations containing LMWOC the results demonstrate that the impact of these organic ligands will slightly increase due to the heat generation resulting from the radioactive decay of the short-lived radionuclides in the waste material. The present studies have significantly extended the thermodynamic database which is mandatory for long-term predictions relying on decisions which interaction processes are relevant and which are negligible. However, the expected concentrations of most of these ligands are considerably lower than those of strong complexing inorganic ligands in the aquifer (especially carbonate) which will definitely impact

the aqueous actinide speciation to a higher degree. Furthermore, the expertise regarding the determination of thermodynamic constants and the handling of the different required tools has been improved and manifested among the partners of this project which facilitates the work on thermodynamic topics within future projects.

3.2 Polyelectrolytes

Regarding polyelectrolytes in natural aquatic systems, humic substances, which are divided into fulvic and humic acids as well as insoluble humics, are of particular interest. The interaction of humic substances with different actinides and lanthanides has been studied extensively in the past. Therefore, the focus within this project is on more specific questions, like the temperature dependency and the existence of dynamic equilibria.

The effect of temperature has been examined by investigating the complexation of Eu(III) and Cm(III) with three fulvic acids (FA) of different origin in the temperature range between 20° and 80 °C. The impact of FA (or HA) on the aqueous speciation of Eu(III) and Cm(III) increases with increasing temperature. The endothermic behavior observed for these complexation reactions points out that these fulvic acids do not form chelates with trivalent metals, as this would be reflected by an exothermic complexation behavior. Therefore, the interaction with Eu(III) and Cm(III) is predominantly related to a simple coordination by carboxylic functions of the macromolecules. It is also notable that only one complex species is observed for all Ln(III)/An(III) pointing out a highly specific interaction between the macromolecule and the trivalent metals. No significant differences are observed for fulvic acids of different origin.

Applying ultrafiltration followed by ICP-MS analysis conditional complex formation constants of Eu(III) and U(VI) have been determined in 0.1 or 1 M NaCl solution using various humic acids and a NOM extract from the Suwannee River water (SNOM). As a result, the significant influence of both origin and composition on the complexation of the metal ions has been proven. The SNOM complex formation affinity is markedly lower than that of humic acids. Humic acids of different origins show different complex formation constants. The reason for these differences seems to be the varying structural composition of the humic acids depending on their origin.

Fluorescence quenching experiments were carried out to investigate the complexation of Eu(III) with humic/fulvic acids (HA/FA) of different origins and a synthetic polymer varying the ionic strength ((0.5 mol/kg to 3.0 mol/kg NaCl) and temperature (20 °C – 50 °C). For the conditional stability constants ($\log \beta'(T)$) for the complexation with different HA/FA no distinct trends were found regarding the temperature and ionic strength dependencies. As the heterogeneity of HA/FA might play an important role, model polymers (poly(vinyl benzoic acid)) were synthesized. They show strong similarities in their photo physical characteristics with HA/FA.

In complementary experiments, the luminescence of Eu(III) was measured via indirect excitation using the NOM as sensitizer. In this case only Eu(III) complexed by HA/FA was detected

and, based on its luminescence characteristics, contributions from strong and weak binding sites to the complexation were determined as well as the effect of competing metal ions such as Mg(II).

Due to the coordination of metal ions, the overall negative charge of a polyelectrolyte molecule decreases, which reduces intermolecular repulsion and hence, favors coiling of the polyelectrolyte molecules. This behavior was monitored applying inter-lanthanide luminescence energy transfer (ILET), which highly depends on the distance between donor and acceptor Ln(III) ions, to different HA/FA and model polymer samples with Eu(III) and Nd(III) as donor-acceptor pair. In this case donor-acceptor pair distances in the Ångstrom range become accessible.

Additionally, extensive experimental studies on the dynamics of the metal-humate complexation equilibrium have been executed focusing on the complexation of Tb(III) with two different humic acids. The application of an isotopic exchange approach using stable ^{159}Tb and short-lived ^{160}Tb showed the existence of a dynamic equilibrium for the first time. This is a prerequisite for the applicability of thermodynamic constants in speciation and transport modeling. However, reaction rates decrease considerably when the metal concentrations are lowered to levels relevant to contaminant metals, and stabilization processes come into action. The time frames of equilibration and stabilization were investigated. Due to the slow equilibration process of humic complexes with trace amounts of metals, these species will not be in equilibrium with dissolved reactants or mineral surfaces if the conditions change on a time scale shorter than a year. These findings are important in case of relatively fast transport processes rather than nearly stagnant systems as present in migration scenarios related to a final repository.

3.3 Microorganisms

Microorganisms are known to occur in subterranean environments and might affect the speciation and hence the mobility of the actinides in aqueous systems relevant for a nuclear waste repository scenario in deep geological formations.

The interaction of Pu – solution of mainly Pu(VI) (~70%) and Pu(IV)-polymers (~20%) - with two different bacteria (*Sporomusa* sp. and *Paenibacillus* sp.) isolated from OPA samples was investigated at anaerobic conditions as a function of the pH value and the initial Pu concentration. In some cases Na-pyruvate was added as a potential electron donor. Generally, the removal of Pu from the solution increases with increasing pH. Sorption experiments showed that *Sporomusa* sp. cells are more effective in removing Pu from the solution than *Paenibacillus sp.* cells. This effect is even more pronounced at longer contact times. Furthermore, the results show that with increasing Na-pyruvate concentration less Pu is bound to the biomass. Hence the cells display a higher affinity for Pu in the absence of an electron donor.

Additionally, experiments on the speciation of Eu(III) and Cm(III) in suspensions of the halophilic archaeon *Halobacterium noricense* were carried out. This microorganism requires high salt concentrations, thus TRLFS measurements were performed in 3 M NaCl solution under anaerobic conditions. The sorption of Eu(III) on the cells increased with increasing pH. The combination of spectroscopic techniques and iterative transformation factor analysis suggests the existence of three species for Eu(III) and Cm(III): The metal aquo ion, a species resulting from the interaction of Eu(III)/Cm(III) with the functional groups of the microorganism, and a species resulting from interactions with dissolved species (e.g. released cell metabolites).

Investigations of the biosorption of U(VI) by *Halobacterium noricense* as a function of incubation time, initial U(VI) concentration and pH show a higher affinity for U(VI) compared to Eu(III).

3.4 Quantum mechanical modeling

Quantum chemical modeling of actinide carboxyl complexes has been undertaken to characterize structures and thermochemical properties of species resulting from the interaction of actinides with the soluble fraction of clay organic matter. Mono- and dicarboxylate complexes of U(VI), Np(V), and Am(III) have been compared for formate and acetate. Preferred coordination modes of the carboxyl ligands are in agreement with EXAFS results, except for Np(V) acetate, which yields monodentate coordination. Calculated energy differences between the coordination modes are often small, suggesting the coexistence of isomers. This aspect, not considered until now, is of interest for an accurate thermochemistry. Complexation energies increase with the effective charge of the actinides, U(VI) ≥ Am(III) > Np(V), and the pK_a of the carboxylic acid, as expected for mainly ionic complexes. Comparison with measured complexation constants suggests that data for Am(III) formate might be too high, as they violate the charge trend. Structures are in general in good agreement with EXAFS results. In contrast to current interpretations, the commonly measured average equatorial An-O distances are found to be insensitive to the coordination mode of carboxyl ligands. As shown earlier, this quantity depends mainly on the coordination number of the complexes. Thus, the only geometry parameter discriminating the coordination mode of carboxylates is the actinide-carbon distance. These results are corroborated by calculations on U(VI) and Np(V) lactate complexes. Calculated energies and structures suggest chelate coordination for U(VI) monolactate, in agreement with experiment, while there is a tendency for bidentate coordination for Np(V). For U(VI) monolactate, various coordination modes are nearly degenerate. Reported complexation constants for Np(V) lactate exceeding those for acetate are not supported by our calculations, in line with the lower pK_a of lactic acid. These computational results show that actinide carboxylate complexes may exist as several isomers, especially for U(VI). This finding and some deviations of measured complexation constants from simple chemical trends suggest to regard available complexation constants as effective. To improve the accuracy and transferability of these thermochemical data, further efforts to characterize isomers and coordination numbers

of actinide carboxylates, especially by means of vibrational modes, are regarded as worthwhile.

3.5 Conclusions

It has been shown that due to the high variety of clay organic compounds the investigation of interaction processes with actinides and lanthanides is a challenging task. Due to the dependence on several system parameters (e.g. pH, ionic strength, temperature, etc.), the characterization of the related complexation reactions requires various analytical techniques (TRLFS, UV-Vis, CE-ICP-MS, IMTC, ultrafiltration, etc.). In general, complexation reactions with monocarboxylic ligands and most natural organic matter show endothermic behavior. Furthermore, it has been proven that dynamic equilibria exist for the interaction with organic macromolecules which also points out that the relevance of certain geochemical processes strongly depends on how fast system conditions might change in the waste repository. The characterization of the interaction between heavy metals and microorganisms is even more complicated. However, it has been shown that different complex/sorption species of bacteria with Eu(III)/Cm(III) are formed.

In order to resolve the molecular structure of actinide complexes with different organic ligands, the combination of EXAFS spectroscopy with iterative transformation factor analysis has proven to be a powerful tool. However, for weak organic ligands predictions from quantum chemical calculations are essential to generate a sound overall picture regarding actinide speciation.

4 Interaction of radionuclides with borate

Borate species can be present in nuclear waste repositories as component of the emplaced waste and as component of ingressing brine in rock-salt formations. For instance, large boron concentrations up to 0.16 M were reported for brines of the WIPP site (Waste Isolation Pilot Plant, New Mexico, USA). This has to be expected in other salt-based repositories, like in Germany, too. So far, the influence of An-borate on the actinide speciation and solubility is investigated very insufficiently. Thus, a systematic study of An-borate interaction under a large variation of geochemical parameters (pH, ionic strength of NaCl, $MgCl_2$, $CaCl_2$, [B], organic content) is essential to estimate the potential of borate species concerning the actinide mobilization. In the current thermodynamic data bases NEA-TDB and THEREDA no thermodynamic data for any An-borate complex or solid compound are summarized. In this joint research project the interaction of borate with An(III, IV, V, VI) and Ln(III) was investigated in diluted to concentrated saline solutions with a combination of solubility experiments, spectroscopic methods (*e.g.* TRLFS, UV-Vis, ^{11}B-NMR), quantum mechanical modeling and solid phase characterization (*e.g.* XRD, XPS, XANES/EXAFS) in order to gain a better understanding of the An-borate system.

4.1 Speciation of the borate system

The aqueous boron speciation is very complex and several species can exist in solutions, e.g. $B(OH)_3(aq)$, $B(OH)_4^-$, $B_3O_3(OH)_4^-$, $B_4O_5(OH)_4^{2-}$, $B_5O_6(OH)_4^-$, $B_3O_3(OH)_5^{2-}$; depending on pH values and boron concentrations. Reliable thermodynamic data, which allow the calculation of boron species distribution, are very scarce. In $CaCl_2$ and $MgCl_2$ media the divalent alkaline earth metal ions influence the (poly)borate speciation significantly due to formation of Ca^{2+}- and Mg^{2+}-borate complexes (*e.g.* $CaB(OH)_4^+$ and $MgB(OH)_4^+$ species at pH > 7). Up to now no complete thermodynamic model for a borate speciation in $CaCl_2$ and $MgCl_2$ solution including possible Mg/Ca polyborate species is available. Thus, the simple thermodynamic data set of polyborate formation of Ingri and coworkers (Acta Chem. Scand. 16439–448 (1962), Acta Chem. Scand. 11, 1034–1058 (1957)) was applied for modeling the An(III)/Ln(III) complexation studies.

4.2 Interaction of An(III)/Ln(III) and U(VI) with borate

The complex formation of borate with trivalent Eu(III)/Am(III) and Cm(III) was studied in diluted to concentrated NaCl, $MgCl_2$ and $CaCl_2$ solutions at slightly acidic pH ($5 < pH_m < 6$) and at $pH_m = 8$. In the slightly acidic pH range the An(III)/Ln(III) hydrolysis and the reaction with carbonate is negligible. At both investigated pH values a complexation of An(III)/Ln(III) by borate is only detectable at higher borate concentration ($[B]_{total} > 0.1$ M) where a considerable amount of polyborate species is present in solutions. TRLFS investigations indicate that one Eu(III)/Am(III)/Cm(III) (poly)borate species (1:1 complex) and two Cm(III) borate species (with

unknown exact complex stoichiometry) exist in NaCl solution at pH_m = 6 and in NaCl/$MgCl_2$ solution at pH_m = 8, respectively. The complexation of Eu(III)/Am(III) with polyborate was studied at pH_m = 6 in NaCl solutions up to 3 m. Under the assumption, that all polyborate species have a similar complexation behavior the sum of the equilibrium concentration of all polyborate species was used for the calculation of the formation constants, which were extrapolated to standard state conditions using the SIT approach. Generally, the Ln(III)/An(III) polyborate complexation is weak (*e.g.* log β_1^0 = 3.12 ± 0.21 for the 1:1 Eu(III) polyborate complex in NaCl media) compared with the strong hydrolysis.

Despite the proven formation of An(III)/Ln(III) borate complexes no significant increase in solubility for $Nd(OH)_3$(am) was observed in the presence of $[B]_{total} \leq 0.4$ M near neutral pH_m conditions in all salt systems. Conversely, a clear drop in the Nd(III) solubility of 2–3 orders of magnitude occurs at $6 \leq pH_m \leq 9$. This can be attributed to a Nd(III) borate coating or formation of a new Nd(III) borate solid phase. This phase was confirmed by XPS and SEM-EDS techniques. Similar observations were made in the Pu(III)-borate system under analogues experimental conditions. A solid phase formation within days to weeks is also observed in the aqueous Eu(III) (poly)borate system at pH_m = 6 depending on medium, ionic strength and $[B]_{total}$. Unfortunately, detailed information about structure and composition of these Ln(III) borate solids were not deducible within this project.

Quantum chemical investigations of borate complexes focusing on species relevant at low borate concentrations, where only the species $B(OH)_4^-$ and $B(OH)_3$ are expected, were carried out. The calculations show, as expected, that a complexation of Am(III) and U(VI) by $B(OH)_3$ does not occur. The calculated $B(OH)_4^-$ complexes of Am(III) and U(VI) are thermodynamically stable and their complexation strength is comparable to the corresponding acetate species. Besides the Lewis anion form $B(OH)_4^-$ also the Brønsted anion $B(OH)_2O^-$ of borate may be present as a ligand in actinide complexes. However, this species has not been found experimentally as free species in solution until now. Besides the pure monoborate complexes also ternary hydroxoborate species are calculated to be stable. These results show that borate complexation, even at low borate concentrations, might be more complex than experimentally detectable until now.

4.3 Solubility of An(IV,V,VI) in presence of borate

The solubility of Th(IV), Pu(IV), Np(V) and U(VI) was studied in diluted to concentrated NaCl and $MgCl_2$ solutions with various boron concentrations at $6.5 \leq pH_m \leq 11$.

Borate has a minor impact on the solubility of Th(IV). Only in concentrated NaCl and $MgCl_2$ solutions at pH_m = 9, a slight increase of the Th(IV) solubility was found at high boron concentrations. Thus, a minor effect of borate on Th(IV) speciation cannot be excluded. Similar observations were made for Pu(IV). Because of the very strong hydrolysis of tetravalent actinides, the An(IV) borate interaction is even weaker compared to Ln(III)/An(III), An(V), and An(VI).

The speciation of Np(V) is clearly affected by the presence of borate in diluted to concentrated NaCl and $MgCl_2$ solutions at pH_m = 8 and 9 and $[B]_{total} \geq 0.04$ M. UV-Vis/NIR studies indicate the formation of a single Np(V) borate complex (in $MgCl_2$ solution), suggesting $B(OH)_4^-$ as most probable complexing borate species. A determination of a complexation constant was not feasible. Similar to the Nd(III) borate system no significant increase of the solubility of NpO_2OH(am, fresh) is observed in the presence of $[B]_{total} \leq 0.4$ M. However, a clear drop in the solubility occurs associated with a formation of the previously unreported Np(V) borate solid phase that was confirmed by XRD, XPS, SEM-EDS, and EXAFS analysis.

Borate increases the solubility of U(VI) in NaCl solutions with $pH_m \geq 9$ and (in lesser extent) in $MgCl_2$ solutions with pH_m = 7.5 because of the formation of U(VI) borate aqueous complexes. In contrast to An(III)/Ln(III) and Np(V), no solubility decrease caused by a solid phase transformation is observed in the U(VI) system in the presence of borate over the investigated timescale of 380 days. This observation is explained by the significantly lower solubility, i.e. higher stability, of $Na_2U_2O_7 \cdot H_2O$(cr) compared to $Nd(OH)_3$(am) and NpO_2OH(am,fresh) at pH_m = 7 – 8, which makes the transformation into a hypothetical U(VI)-borate solid phase unlikely.

4.4 Interaction of Eu(III) with organoborate

The knowledge of the An-$B(OH)_4^-$ complexation constant is mandatory for the quantitative description of the An-borate system. Attempts of direct measurements were not successful because of the small $B(OH)_4^-$ amounts at neutral pH and the strong An hydrolysis in the alkaline region. Therefore, a structurally similar organoborate, which exists in the neutral region, was used as model ligand for $B(OH)_4^-$. The reaction of boric acid with lactate and salicylate leads to the formation of cyclic organic borate species with a fourfold coordinated boron center resembling the one in mono-borate $B(OH)_4^-$. Therefore, salicylate- and lactateborate as borate model ligands were chosen. Their complexation of Eu(III) was investigated by TRLFS and ^{11}B-NMR spectroscopy. The complexation is weak and comparable to the Eu(III) polyborate system with a complexation constant log $\beta^0_{EuBOrganic}$ for a 1:1 complex between 2.6 and 3.2. Quantum chemical investigations indicated a weaker complexation for the preferred monodentate coordination of these organoborateester ligands, compared to monoborate. Thus, while structural differences between the modeled borate ester complexes and monoborate complexes are small, their lower complexation ability limits their application as models for borate complexes. These results suggest that borate ester formation should reduce actinide complexation by borates and thus their solubility in borate containing solutions.

4.5 Conclusions

For the first time a multitude of comprehensive experimental complexation and solubility studies were performed on actinide-borate systems in diluted to concentrated salt solutions.

These experimental studies were supported and complemented by quantum mechanical calculations. Actinide borate complexes were detected for Am(III)/(Cm(III)/Eu(III), Np(V) and U(VI). The An(III)/Ln(III) borate complex is weak as the experimentally derived complexation constants and quantum mechanical calculations show. Borate has a minor impact of the solubility and thus on the mobilization of actinides. On the contrary, the formation of solid An-borate phases indicate a hitherto unknown actinide retention mechanism in a nuclear repository for highly mobile actinides. A first thermodynamic description and model of the Np(V) interactions in the presence of borate in NaCl and $MgCl_2$ systems has been proposed in this project.

5 Analytical instrumentation and developments

5.1 Spectroscopic methods

An **optical compartment (cell)** for measurements at high pressure (max. 35 bar) and/or high temperature (max. 200 °C) conditions in combination with different spectroscopic techniques (laser spectroscopy, UV-Vis absorption spectroscopy, XANES, EXAFS) was developed. Depending on the spectroscopic technique the cell can be equipped with two to four optical windows (quartz for optical measurements, beryllium for EXAFS experiments) and fiber optics.

The speciation of lanthanide ions, especially of Eu(III) as an optical probe, was further developed for measurements at ultralow temperatures (**fluorescence line narrowing spectroscopy**, $T \sim 5$ K). Due to the elimination of contributions from inhomogeneous line broadening, the analysis of Stark splitting patterns allows a speciation even of complex systems such as borates.

For the analysis of metal ions immobilized on mineral surfaces **inter-lanthanide energy transfer** (ILET) was evaluated using different lanthanide ions as donor-acceptor couples (FRET pair). From the alteration in the luminescence properties of the different lanthanide ions the average distance between lanthanide ions on a mineral surface on the sub-nanometer scale became accessible.

To expand the toolbox of available techniques to study interactions of metal ions with (in)organic ligands vibrational spectroscopic methods (**Raman microscopy** and **sum frequency generation** (**SFG) spectroscopy**) were further explored. Here, intercalation compounds made of potassium acetate and kaolinite were investigated. Due to intercalation, the vibrational frequency of the inner surface hydroxyls decreases. The spatially resolved probing of specifically prepared kaolinite samples showed a different extend of intercalation. This demonstrated the potential of Raman microscopy for chemical imaging. In addition, experiments were carried out with SFG spectroscopy, which gave similar results with respect to the changes in the vibrational spectrum comparing unmodified and intercalated kaolinite samples.

5.2 Other analytical methods

The **isothermal micro-titration calorimetry** provides enthalpies and equilibrium constants simultaneously. From this the complete thermodynamic dataset (log K'_{n}, $\Delta_{\mathrm{r}}\mathrm{G}'_{\mathrm{m}}$, $\Delta_{\mathrm{r}}\mathrm{H}'_{\mathrm{m}}$, $\Delta_{\mathrm{r}}\mathrm{S}'_{\mathrm{m}}$) can be obtained by direct measurements. A micro-titration calorimetry device (ITC_{200}, Malvern Instruments) with a small sample volume (0.2 mL) was established. Complete thermodynamic datasets of complexation reactions of the trivalent lanthanides (Eu(III), Nd(III)) with selected

LMWOC (lactate, oxalate, malonate) were obtained as function of ionic strength by using this micro-titration calorimeter. It turned out that preferably 1:1 (and under favorable prerequisites 1:2) complexes with complexation constants log K_n^0 of approximately 2.5 and above can be examined very well with this ITC setup. The necessary minimum concentrations of the reactants are in the sub-millimolar range.

In order to efficiently analyze highly saline solutions after batch experiments with ICP-MS a new method for element trace analysis was developed **(transient measurement for ICP-MS)**. The new method allowed for direct measurement of undiluted batch samples using an ICP-MS setup modified with regards to sample introduction (online dilution with make-up solution) and signal evaluation (time resolved transient measurement). This transient method enabled the direct quantification of metal concentrations in samples with up to 5 M NaCl without any pre-treatment or matrix removal steps. Altogether, the transient method is now applied as a matter of routine.

The coupling of **capillary electrophoresis (CE) with inductively coupled plasma mass spectrometry (ICP-MS)** is an effective and highly sensitive method that enables the determination of the speciation of metal ions under environmentally relevant concentrations. CE-ICP-MS was used to determine the electrophoretic mobilities of different actinide species (e.g., Eu(III), Am(III), Th(IV), Np(V), and U(VI)) and furthermore, to investigate the speciation of Pu. The order of elution for the different Pu oxidation states is first Pu(III) with the highest mobility, followed by Pu(VI), Pu(V), and finally Pu(IV) with the lowest electrophoretic mobility. However, first CE-ICP-MS measurements of Pu(III) sorption on OPA indicated the need for further investigations. As a general tendency the order of elution for the various oxidation states of the actinides seemed to be $\mu_e(\mathrm{An(III)}) > \mu_e(\mathrm{An(VI)}) > \mu_e(\mathrm{An(V)}) > \mu_e(\mathrm{An(IV)})$. Although the complete series can only be confirmed by the values for Pu, as it is the only element showing all four oxidation states during CE-ICP-MS measurements, the values for the electrophoretic mobilities of Np and U fitted nicely in this order. The CE-ICP-MS setup achieved a separation of different species within twenty minutes with limits of detection of approximately 1×10^{-9} mol·L^{-1}.

Quantum chemical method development and validation focused on the challenging problem of modeling surface solvation. A newly developed efficient computational scheme for explicit surface solvation provides considerably improved energies of adsorbates by equilibration of the solvent structure. Validation of a recently published polarizable continuum model yields useful results but needs a careful design of model systems to be of comparable quality.

5.3 Conclusions

The challenge of the project was to perform speciation at higher ionic strengths, elevated temperatures and at metal ion concentrations as low as possible. Some progress could be rendered to improve the measurement of such samples. Spectroscopic measurements, UV-Vis and XAFS, of aqueous samples is now possible at temperatures up to 200 °C. The oxidation

state of actinides can be specified at concentrations lower than 10^{-10} mol/L, sometimes down to 10^{-12} mol/L by coupling CE to sector field ICP-MS. The application of Raman spectroscopy, sum frequency spectroscopy, and ICP-MS at higher ionic strengths were progressed to apply them to specific questions. Last but not least the computational tools were improved to properly model surface solvation.

Annex A: Publications generated from the project

2017

Banik, N. l., Marsac, R., Lützenkirchen, J., Marquardt, C. M. Dardenne, K., Rothe, J. et al. (2017): Neptunium sorption and redox speciation at the illite surface under highly saline conditions. *Geochim. Cosmochim. Acta* 215, 421–431.

Fröhlich D., Kremleva A., Rossberg A., Skerencak-Frech A., Koke C., Krüger S., Rösch N., Panak P.J. (2017): Combined EXAFS spectroscopic and quantum chemical study on the complex formation of Am(III) with formate. *Inorg. Chem*. 56 (12), 6820 – 6829.

Lippmann-Pipke, J., Gerasch, R., Schikora, J., Kulenkampff, J. (2017): Benchmarking PET for geoscientific applications: 3D quantitative diffusion coefficient estimation in clay rock. *Comput. Geosci.* 101, 21 - 27.

Lippold, H., Eidner, S., Kumke, M.U., Lippmann-Pipke, J. (2017): Dynamics of metal-humate complexation equilibria as revealed by isotope exchange studies – a matter of concentration and time. *Geochim. Cosmochim. Acta*. 197, 62 – 70.

Marsac, R., Banik, N. l., Lützenkirchen, J., Diascorn, A., Bender, K., Marquardt, C. M., Geckeis, H. (2017): Sorption and redox speciation of plutonium at the illite surface under highly saline conditions. *J. Colloid Interface Sci*. 485, 59–64.

Moll, H.; Cherkouk, A.; Bok, F.; Bernhard, G. (2017): Plutonium interaction studies with the Mont Terri Opalinus Clay isolate Sporomusa sp. MT-2.99. *Environ. Sci. Pollut. Res.* 24 (15), 13497 – 13508.

Schönberg, P., Mokry, C., Runke, J., Schönenbach, D., Stöbener, N., Thörle-Pospiech, P., Trautmann, N., Reich, T. (2017): Application of resonance ionization mass spectrometry for ultratrace analysis of technetium. *Anal. Chem.* 89, 9077-9082.

2016

Banik, N.l., Marsac, R., Luetzenkirchen, J., Diascorn, A., Bender, K., Marquardt, C.M., Geckeis, H. (2016): Sorption and redox speciation of plutonium at the illite surface. *Environ. Sci. Technol.* 50 (4), 2092–2098.

Kremleva, A., Krüger, S. (2016): Comparative Computational Study of Np(V) and U(VI) Adsorption on the (110) Edge Suface of Montmorillonite. *Clay Clay Min.* 64, 438-451.

Kremleva, A., Krüger, S., Rösch, N. (2016): Toward a Reliable Energetics of Adsorption at Solvated Mineral Surfaces: A Computational Study of Uranyl(VI) on 2:1 Clay Minerals. *J. Phys. Chem.* C 120, 324-335.

Kremleva, A., Krüger, S., Rösch, N. (2016): Uranyl Adsorption at Clay Minerals, in *High Performance Computing in Science and Engineerin*g 2016, Wagner, S., Bode, A., Brüchle, H., Brehm, M. (Eds.). Bayer. Akad. Wissenschaften, 2016, p. 177-179.

Kulenkampff, J., Gründig, M., Lippman-Pipke, J., Zakhnini, A. (2016): Quantitative experimental monitoring of molecular diffusion in clay with positron emission tomography. *Solid Earth* 7, 1207-1215 (2016).

Kulenkampff, J., Gründig, M., Zakhnini, A., Lippmann-Pipke, J. (2016): Geoscientific process monitoring with positron emission tomography (GeoPET). *Solid Earth* 7, 1217-1231.

Poetsch, M., Lippold, H. (2016): Effects of ionic strength and fulvic acid on adsorption of Tb(III) and Eu(III) onto clay. *J. Contam. Hydrol*. 192, 146-151.

Reich, T., Amayri, S., Börner, P.J.B., Drebert, J., Fröhlich, D.R., Grolimund, D., Kaplan, U. (2016): Speciation of neptunium during sorption and diffusion in natural clay. *J. Phys. Conf. Ser*. 712, 012081 (1-4).

2015

Fröhlich, D. R., Skerencak-Frech, A., Bauer, N., Rossberg, A., Panak, P. J. (2015): The pH dependence of Am(III) complexation with acetate: An EXAFS study, *J. Synchro. Rad*., 22, 99-104.

Fröhlich, D.R., Skerencak-Frech, A., Kaplan, U., Koke, C., Rossberg, A., Panak, P.J. (2015): An EXAFS spectroscopic study of Am(III) complexation with lactate, *J. Synchro Rad*., 22, 1469-1474.

Fröhlich, D. R., Skerencak-Frech, A., Panak, P. J. (2015): Complex formation of Cm(III) with formate studied by time-resolved laser fluorescence spectroscopy, *Appl. Geochem.,* 61, 312-317.

Krawczyk-Bärsch, E., Lütke, L., Moll, H., Bok, F., Steudtner, R., Rossberg, A. (2015): A spectroscopic study on U(VI) biomineralization in cultivated Pseudomonas fluorescens biofilms isolated from granitic aquifers. *Environ. Sci. Pollut. Res.* 22, 4555-4565.

Kremleva, A., Krüger, S., Rösch, N. (2015) : Uranyl Adsorption on Solvated Edge Surfaces of 2:1 Smectites. A Density Functional Study. *Phys. Chem. Chem. Phys*. 17, 13757-13768.

Kulenkampff, J., Gründig, M., Zakhnini, A., Gerasch, R., Lippmann-Pipke, J. (2015): Process tomography of diffusion, using PET, to evaluate anisotropy and heterogeneity. *Clay Miner.* 50, 369-375.

Marsac, R., Banik, N.L., Luetzenkirchen, J., Buda, R.A., Kratz, J.V., Marquardt, C.M. (2015): Modeling plutonium sorption to kaolinite: Accounting for redox equilibria and the stability of surface species. *Chem. Geol.* 400, 1–10.

Marsac, R., Banik, N.l., Luetzenkirchen, J., Marquardt, C.M., Dardenne, K., Schild, D., Rothe, J., Diascorn, A., Kupcik, T., Schaefer, T., Geckeis, H. (2015): Neptunium redox speciation at the illite surface. *Geochim. Cosmochim. Acta* 152, 39–51.

Moll, H., Lütke, L., Cherkouk, A. (2015): Bacterial diversity in clay and actinide interactions with bacterial isolates in relation to nuclear waste disposal. In: *Radionuclides in the Environment - Influence of chemical speciation and plant uptake on radionuclide migration*. (Editoren: C. Walther, D. K. Gupta) Heidelberg, Springer Verlag.

Schott, J., Kretzschmar, J., Tsushima, S., Acker, M. Eidner, S., Barkleit, A., Taut, S. Brendler, V., Stumpf, T. (2015): The interaction of Eu(III) with organoborates – a further approach to understand the complexation in the An/Ln(III) – borate system. *Dalton Trans.* 44, 11095-11108.

Schnurr, A., Marsac, R., Rabung, T., Luetzenkirchen, J., Geckeis, H. (2015): Sorption of Cm(III) and Eu(III) onto clay minerals under saline conditions: Batch adsorption, laser-fluorescence spectroscopy and modeling. *Geochim. Cosmochim. Acta* 151, 192–202.

Skerencak-Frech A., Maiwald M., Trumm, M., Fröhlich D.R., Panak P.J., (2015): The complexation of Cm(III) with oxalate in aqueous solution at T = 20-90 °C: A combined TRLFS and quantum chemical study, *Inorg. Chem*., 54, 1860-1868.

Vasiliev, A.N., Banik, N.L., Marsac, R., Froehlich, D.R., Rothe, J., Kalmykov, S.N., Marquardt, C.M. (2015): Np(V) complexation with propionate in 0.5-4 M NaCl solutions at 20-85 degrees C. *Dalton Trans.* 44 (8), 3837–3844.

Xiong, Q., Joseph, C., Schmeide, K., Jivkov, A.P. (2015): Measurement and modelling of reactive transport in geological barriers for nuclear waste containment. *Phys. Chem. Chem. Phys.* 17, 30577-30589.

2014

Barkleit, A., Kretzschmar, J., Tsushima, S., Acker, M. (2014): Americium(III) and europium(III) complex formation with lactate at elevated temperatures studied by spectroscopy and quantum chemical calculations. *Dalton Trans.* 43(29), 11221-11232

Fröhlich, D. R., Skerencak-Frech, A., Gast, M., Panak, P. J. (2014): Fulvic acid complexation of Eu(III) and Cm(III) at elevated temperatures studied by time-resolved laser fluorescence spectroscopy, *Dalton Trans.* 43, 15593-15601.

Fröhlich, D. R., Skerencak-Frech, A., Panak, P. J. (2014): A spectroscopic study on the formation of Cm(III) acetate complexes at elevated temperatures, *Dalton Trans.* 43, 3958-3965.

Harzmann, S., Braun, F., Zakhnini, A., Weber, W.A., Pietrzyk, U., Mix, M. (2014): Implementation of Cascade Gamma and Positron Range Corrections for I-124 Small Animal PET. IEEE *Trans. Nucl. Sci.* 61, 142-153.

Hein C., Sander J.M., Kautenburger R. (2014): Speciation via Hyphenation–Metal Speciation in Geological and Environmental Samples by CE-ICP-MS. *J. Anal. Bioanal. Tech.* 5, 225.

Kautenburger R. (2014): A new timescale dimension for migration experiments in clay: proof of principle for the application of miniaturized clay column experiments (MCCE). *J. Radioanal. Nucl. Chem.* 300, 255-262

Kautenburger R., Hein C., Sander J.M., Beck H.P. (2014): Influence of metal loading and humic acid functional groups on the complexation behavior of trivalent lanthanides analyzed by CE-ICP-MS. *Anal. Chim. Acta* 816, 50-59.

Lippold, H., Lippmann-Pipke, J. (2014): New insights into the dynamics of adsorption equilibria of humic matter as revealed by radiotracer studies. *Geochim. Cosmochim. Acta* 133, 362-371.

Marsac, R., Banik, N.l., Marquardt, C.M., Kratz, J.V. (2014): Stabilization of polynuclear plutonium(IV) species by humic acid. *Geochim. Cosmochim. Acta* 131, 290–300.

Moll, H., Lütke, L., Bachvarova, V., Cherkouk, A., Selenska-Pobell, S., Bernhard, G. (2014): Interactions of the Mont Terri Opalinus Clay isolate Sporomusa sp. MT-2.99 with curium(III) and europium(III). *Geomicrobiol. J.* 31, 682-696.

Schmeide, K., Gürtler, S., Müller, K., Steudtner, R., Joseph, C., Bok, F., Brendler, V. (2014): Interaction of U(VI) with Äspö diorite: A batch and in situ ATR FT-IR sorption study. *Appl. Geochem.* 49, 116-125.

Skerencak-Frech, A., Fröhlich, D.R., Rothe, J., Dardenne, K., Panak, P.J. (2014): A combined TRLFS and EXAFS study on the complexation of trivalent actinides with chloride at T = 25 - 200°C, *Inorg. Chem.* 53, 1062-1069.

Schott, J., Kretzschmar, J., Acker, M., Eidner, S., Kumke, M. U., Drobot, B., Barkleit, A., Taut, S., Brendler, V., Stumpf, T. (2014): Formation of a Eu(III) borate solid species from a weak Eu(III) borate complex in aqueous solution. *Dalton Trans.* 43(30), 11516-11528.

2013

Barkleit, A., Acker, M., Bernhard, G. (2013): Europium(III) complexation with salicylic acid at elevated temperatures. *Inorg. Chim. Acta* 394, 535-541.

Demetriou, A., Pashalidis, I., Nicolaides, A.V., M.U. Kumke, M.U. (2013): Surface mechanism of the boron adsorption on alumina in aqueous solutions, *Desalin. Water Treat.* 51(31-33), 6130-6136 (2013).

Fröhlich, D. R., Skerencak-Frech, A., Morkos, M.-L. K., Panak, P. J. (2013). A spectroscopic study of Cm(III) complexation with propionate in saline solutions at variable temperatures, New J. Chem. 37, 1520-1528.

Joseph, C., Van Loon, L.R., Jakob, A., Steudtner, R., Schmeide, K., Sachs, S., Bernhard, G. (2013): Diffusion of U(VI) in Opalinus Clay: Influence of temperature and humic acid. *Geochim. Cosmochim. Acta* 109, 74-89.

Joseph, C., Stockmann, M., Schmeide, K., Sachs, S., Brendler, V., Bernhard, G. (2013): Sorption of U(VI) onto Opalinus Clay: Effects of pH and humic acid. *Appl. Geochem.* 36, 104-117.

Kremleva, A., Krüger, S., Rösch, N. (2013): Assigning EXAFS Results for Uranyl Adsorption on Minerals via Formal Charges of Bonding Oxygen Centers. *Surf. Sci.* 615, 21-25.

Pietrzyk, U., Zakhnini, A., Axer, M., Sauerzapf, S., Benoit, D., Gaens, M. (2013): EduGATE - basic examples for educative purpose using the GATE simulation platform. *Z. Med. Phys.* 23, 65-70.

Raditzky, B., Sachs, S., Schmeide, K., Barkleit, A., Geipel, G., Bernhard, G. (2013): Spectroscopic study of americium(III) complexes with nitrogen containing organic model ligands. *Polyhedron* 65, 244-251.

Skerencak, A., Höhne, S., Hofmann, S., Marquardt, C.M., Panak, P.J. (2013): Spectroscopic Studies on the Thermodynamics of the Complexation of Trivalent Curium with Propionate in the Temperature Range from 20 to 90°C, *J. Solution Chem.,* 42, 1-17.

Skerencak, A., Panak, P.J., Fanghänel, T. (2013): Complexation and thermodynamics of Cm(III) at high temperatures: The formation of [Cm(SO4)n](3-2n) (n = 1, 2, 3) complexes at T = 25 to 200 °C, *Dalton Trans.,* 42, 542-549.

Zakhnini, A., Kulenkampff, J., Sauerzapf, S., Pietrzyk, U., Lippmann-Pipke, J. (2013): Monte Carlo simulations of GeoPET experiments: 3D images of tracer distributions (18F, 124I and 58Co) in Opalinus Clay, anhydrite and quartz. *Comput. Geosci.* 57, 183-196.

2012

Kremleva, A., Martorell, B., Krüger, S., Rösch, N. (2012): Uranyl Adsorption on Solvated Edge Surfaces of Pyrophyllite: A DFT Model Study. *Phys. Chem. Chem. Phys.* 14, 5815-5823.

Kremleva, A., Zhang, Y., Shor, A.M., Krüger, S., Joseph, C., Raditzky, B., Schmeide, K., Sachs, S., Bernhard, G., Rösch, N. (2012): Uranyl(VI) complexation by sulfonate ligands: A relativistic density functional and time-resolved laser-induced fluorescence spectroscopy study. *Eur. J. Inorg. Chem*. 22, 3636-3644.

Lippold, H., Eidner, S., Kumke, M.U., Lippmann-Pipke, J. (2012): Diffusion, degradation or on-site stabilisation – identifying causes of kinetic processes involved in metal-humate complexation. *Appl. Geochem.* 27, 250-256.

Möser C., Beck H.P., Kautenburger R. (2012): Complexation of Europium and Uranium by Humic Acids Analysed by Capillary Electrophoresis - Inductively Coupled Plasma Mass Spectrometry. *Electrophoresis* 33, 1482-1487.

Primus, P.-A., Kumke, M.U. (2012): Flash Photolysis Study of Complexes between Salicylic Acid and Lanthanide Ions in Water, *J. Phys. Chem. A* 116(4), 1176-1182 (2012).

Schäfer, Th., Huber, F., Seher, H., Missana, T., U. Alonso, U., Kumke, M.U., Eidner, S., Claret, F., Enzmann, F. (2012): Nanoparticles and their influence on radionuclide mobility in deep geological formations, *Appl. Geochem.* 27, 390-403 (2012).

Schmeide, K., Sachs, S., Bernhard, G. (2012): Np(V) reduction by humic acid: Contribution of reduced sulfur functionalities to the redox behavior of humic acid. *Sci. Total Environ.* 419, 116-123.

Stöbener, N., Amayri, S., Gehl, A., Kaplan, U., Malecha, K., Reich, T. (2012): Sensitive redox speciation of neptunium by CE-ICP-MS. *Anal. Bioanal. Chem.* 404, 2143-2150.

2011

Kautenburger R. (2011): Batch is bad? Leaching of Opalinus clay samples and ICP-MS determination of extracted elements. *J. Anal. At. Spectrom.* 26, 2089-2092.

Steudtner, R., Müller, K., Schmeide, K., Sachs, S., Bernhard, G. (2011): Binary and ternary uranium(VI) humate complexes studied by attenuated total reflection Fourier-transform infrared spectroscopy. *Dalton Trans.* 40, 11920-11925.

Antoniou, S., Pashalidis, I., Gessner, A., Kumke, M.U. (2011): The effect of humic acid on the formation and solubility of secondary solid phases ($Nd(OH)CO_3$ and $Sm(OH)CO_3$), *Radiochim. Acta* 99(4), 217-223 (2011).

Antoniou, S., Pashalidis, I., Gessner, A., Kumke, M.U. (2011): Spectroscopic investigations on the effect of humic acid on the formation and solubility of secondary solid phases of $Ln_2(CO_3)_3$, *J. Rare Earth* 29, 516-521 (2011).

Annex B: Final reports of the project

Nr. 1: BMWi Project No.: 02 E 10971
Partner No. 1: Helmholtz-Zentrum Dresden-Rossendorf, Institut für Ressourcenökologie. K. Schmeide, K. Fritsch, H. Lippold, M. Poetsch, J. Kulenkampff, J. Lippmann-Pipke, N. Jordan, C. Joseph, H. Moll, A. Cherkouk, M. Bader

Nr. 2: BMWi Project No.: 02 E 10981
Partner No. 2: Johannes Gutenberg-Universität Mainz, Institut für Kernchemie, S. Amayri, P.J.B. Börner, U. Kaplan, J.V. Kratz, M. Lübke, T. Reich, R. Scholze, N. Trautmann, C. Willberger

Nr. 3: BMWi Project No.: 02 E 11001
Partner No. 3: Technische Universität München, Theoretische Chemie, S. Krüger, A. Kremleva

Nr. 4: BMWi Project No.: 02 E 10991
Partner No. 4: Universität des Saarlandes, Anorganische Festkörperchemie, Anorganische und Analytische Chemie, C. Hein, J. Sander, R. Hahn, R. Kautenburger, H.P. Beck, G. Kickelbick

Nr. 5: BMWi Project No.: 02 E 10961
Partner No. 5: Karlsruher Institut für Technologie, Institut für Nukleare Entsorgung, N. Banik, M. Bouby-Laliron, N. Finck, K. Hinz, T. Kupcik, R. Marsac, A. Schnurr, M. Altmaier, C.M. Marquardt, Th. Schäfer

Nr. 6: BMWi Project No.: 02 E 11011
Partner No. 6: Universität Potsdam, Institut für Chemie, Physikalische Chemie, K. Brennenstuhl, K. Burek, S. Eidner, M.U. Kumke

Nr. 7: BMWi Project No.: 02 E 11021
Partner No. 7: Technische Universität Dresden, Sachgebiet Strahlenschutz und Professur für Radiochemie, M. Acker, J. Schott, F. Taube, A. Barkleit, M. Müller, S. Taut, T. Stumpf

Nr. 8: BMWi Project No.: 02 E 11031
Partner No. 8: Ruprecht-Karls Universität Heidelberg, Physikalisch Chemisches Institut, D. R. Fröhlich, A. Skerencak-Frech, P. Panak

Final Report

BMWi Project No.: 02 E 10971

Joint project: Retention of radionuclides relevant for final disposal in natural clay rock and saline systems

Subproject 2: Geochemical behavior and transport of radionuclides in saline systems in the presence of repository-relevant organics

Katja Schmeide, Katharina Fritsch, Holger Lippold, Maria Poetsch, Johannes Kulenkampff, Johanna Lippmann-Pipke, Norbert Jordan, Claudia Joseph[1], Henry Moll, Andrea Cherkouk, Miriam Bader

Helmholtz-Zentrum Dresden-Rossendorf, Institute of Resource Ecology,
Bautzner Landstr. 400, 01328 Dresden, Germany

[1] Present address: Glenn T. Seaborg Institute, Physical & Life Sciences Directorate, Lawrence Livermore National Laboratory, L-231, P.O. Box 808, Livermore, CA 94550, USA

Bundesministerium für Wirtschaft und Energie

Das diesem Bericht zugrunde liegende Vorhaben wurde mit Mitteln des Bundesministeriums für Wirtschaft und Energie unter dem Förderkennzeichen 02 E 10971 gefördert. Die Verantwortung für den Inhalt dieser Veröffentlichung liegt bei den Autoren.

Vorhaben:

VERBUNDPROJEKT: Rückhaltung endlagerrelevanter Radionuklide im natürlichen Tongestein und in salinaren Systemen

Teilprojekt 2: Geochemisches Verhalten und Transport von Radionukliden in salinaren Systemen in Gegenwart endlagerrelevanter Organika

Laufzeit des Vorhabens: 01.07.2011 bis 30.06.2015

Projektleiter: Dr. Katja Schmeide

Institut für Ressourcenökologie, Helmholtz-Zentrum Dresden-Rossendorf

Contents

Summary

The objective of this project was to study the influence of increased salinities on interaction processes in the system radionuclide – organics – clay – aquifer. For this purpose, complexation, redox, sorption, and diffusion studies were performed under variation of the ionic strength (up to 4 mol kg^{-1}) and the background electrolyte (NaCl, $CaCl_2$, $MgCl_2$).

The complexation of U(VI) by propionate was studied in dependence on ionic strength (up to 4 mol kg^{-1} $NaClO_4$) by combining time-resolved laser-induced fluorescence spectroscopy (TRLFS), attenuated total reflection Fourier-transform infrared (ATR FT-IR) spectroscopy, and density functional theory (DFT) calculations. U(VI)/propionate complexes with a 1:1, 1:2, and 1:3 stoichiometry were identified. The stability constants were found to vary with ionic strength, whereby the ionic strength influence depended on the charge of the respective complexes. The conditional stability constants, determined for $UO_2(Prop)^+$, $UO_2(Prop)_2^0$ and $UO_2(Prop)_3^-$ complexes at specific ionic strengths, were extrapolated to zero ionic strength.

Microbes, as another source of organics in clay, can change the speciation of released radionuclides. The interaction of bacteria, isolated from Mont Terri Opalinus Clay core samples (Moll et al., 2013), namely *Sporomusa* sp. MT-2.99 and *Paenibacillus* sp. MT-2.2 cells, with Pu was studied in aqueous solution under anaerobic conditions. In a previous project (Moll et al., 2013), only the Pu interaction with *Sporomusa* sp. MT-2.99 cells at pH 6.1 in 0.1 M $NaClO_4$ without adding an electron donor was investigated. Now, these experiments were extended in order to get a more comprehensive overview of the interaction potential of both bacterial isolates towards Pu. The experiments can be divided into experiments without an electron donor where biosorption is favored and experiments with added Na-pyruvate as an electron donor stimulating also bioreduction processes. Additionally, the knowledge to explore actinide/lanthanide interaction processes with bacteria isolated from clay on a molecular level could be extended to microbes occurring in salt rock, another potential host rock for nuclear waste disposal. Within this project, first experiments were performed to study the interactions of the halophilic archaeon *Halobacterium noricense* DSM-15987 with U(VI), Eu(III), and Cm(III) in 3 M NaCl solutions.

Another objective of the project was to further improve process understanding concerning the mobility of radionuclides in systems containing humic matter. Attention was focused on reversibility of elementary processes and their interaction. For humate complexation of multivalent metals, the existence of a dynamic equilibrium was proven in isotope exchange studies for the first time. This is a prerequisite for the applicability of thermodynamic constants in speciation and transport modeling. However, reaction rates decrease considerably as metal concentrations are lowered to levels relevant to contaminant metals, and stabilization processes come into action. The time frames of equilibration and stabilization were investigated. Humic complexes with trace amounts of metals will not be in equilibrium with dissolved reactants or mineral surfaces if conditions change on a time scale shorter than a year. Thus, humic-bound metals are to be regarded as fixed in case of relatively fast transport processes, but not in nearly stagnant systems as present in migration scenarios related to a final repository.

The influence of high salinity (NaCl, $CaCl_2$ and $MgCl_2$ up to 4 M) on the mobilizing potential of humic-like clay organics towards actinides was investigated in radiotracer studies for binary and ternary systems of the (analogue) components [^{152}Eu]Eu(III), [^{160}Tb]Tb(III), [^{14}C]fulvic acid and Opalinus Clay at adequate concentration levels for different pH values. High ionic strengths do not lead to immobilization of fulvic acid by flocculation. Generally, however, possible mobilizing effects cannot be enhanced under highly saline conditions because metal-fulvate complexation is strongly suppressed especially by multivalent electrolytes, whereas the adsorption behavior of the organic component is largely unaffected. Its resultant effect on solid-liquid distribution of the actinide analogues can be derived and predicted from interaction data determined for the binary subsystems, in part quantitatively. This applies to the influence of ionic strength as well as the transition from demobilizing to mobilizing properties with increasing pH already in the neutral range. The effect of electrolytes on fulvate complexation was characterized in detail by luminescence spectroscopy and mechanistic modeling (NICA-Donnan approach).

The sorption of Tc(VII)/Tc(IV) onto the iron(II)-containing minerals magnetite ($Fe^{II}Fe^{III}_2O_4$) and siderite ($Fe^{II}CO_3$), occurring ubiquitously in nature and as corrosion products of carbon steel canisters used for storing radioactive waste, was studied by means of batch sorption experiments as well as ATR FT-IR and X-ray absorption spectroscopy (XAS). The strong Tc retention onto these minerals could be attributed to surface-mediated reduction of Tc(VII) to Tc(IV). It can be concluded that both minerals contribute effectively to the retention of Tc under repository conditions. An influence of ionic strength (0.1 or 1 M) was not observed.

The influence of ionic strength, background electrolyte, pH value and CO_2 absence or presence on U(VI) sorption onto montmorillonite, as model clay, was studied. As background electrolyte, pure NaCl, $CaCl_2$ or $MgCl_2$ electrolytes were used with ionic strengths up to 3 mol kg^{-1} (NaCl) or up to 9 mol kg^{-1} ($CaCl_2$, $MgCl_2$). The U(VI) sorption onto montmorillonite in NaCl and $CaCl_2$ was found to depend strongly on pH value and CO_2 presence. In $CaCl_2$, the U(VI) sorption onto montmorillonite is 0.5 to 1 log K_d units lower than in NaCl. In $MgCl_2$, the U(VI) uptake is governed by (co-)precipitation with magnesium and silicon compounds of low solubility. The influence of ionic strength on U(VI) sorption was found to be small in the investigated ionic strength range. Surface complexation modeling for the interaction of U(VI) with montmorillonite was performed applying the two-site protolysis non-electrostatic surface complexation and cation exchange (2SPNE SC/CE) model (Bradbury and Baeyens, 1997, 1999, 2002). Surface complexation constants could successfully be determined for the NaCl and $CaCl_2$ system for all ionic strengths studied. That means the 2SPNE SC/CE model can be applied to high ionic strengths. The surface complexation constants, generated at different ionic strengths, were extrapolated to zero ionic strength. The U(VI) sorption onto montmorillonite was also studied in a mixed electrolyte which consists of 2.52 mol kg^{-1} NaCl, 0.12 mol kg^{-1} $CaCl_2$ and 0.048 mol kg^{-1} $MgCl_2$ (similar to the groundwater composition in the Konrad mine, Lower Saxony (Brewitz, 1982)). It was found that surface complexation constants derived in pure electrolytes can be used to model surface complexation in mixed electrolytes.

The influence of citrate on U(VI) diffusion in Opalinus Clay was studied using Opalinus Clay pore water as background electrolyte. The diffusion parameter values obtained for the HTO through-diffusion and the U(VI) in-diffusion in the absence of citric acid were in agreement with literature data. In the presence of citric acid the U(VI) diffusion was significantly retarded, which was attributed to a change in speciation. Probably, U(VI) was reduced to U(IV) within the three months the diffusion experiment was conducted. Citric acid diffused slightly faster through OPA than small humic acid colloids, studied previously. The study shows that the chemical system has to be investigated in more detail to clarify the occurring reactions. In particular, the U(VI)-citric acid species formed under these environmentally relevant conditions needs to be described spectroscopically, thermodynamically, and structurally.

PET could be established as a reliable measurement method for quantitative determination of heterogeneous diffusion coefficients in clays and for general tracer transport studies in barrier rocks. The main focus was the improvement of quantification, both by improving image quality and the parameter determination method. Two issues of the image reconstruction procedure were identified and successfully addressed: normalization and scattering. Monte-Carlo simulations of the physical processes, from radioactive decay of the tracer nuclide to detection in the detectors, were conducted in order to estimate and quantify these effects. These studies resulted in an improved image reconstruction procedure that yields tracer concentrations quantitatively, as well as an error estimate.

PET-experiments were conducted on Opalinus Clay samples as test cases for the method and in order to better understand experimental artefacts by sample alteration and damage. Spatiotemporal data sets of the tracer concentration were computed. From these datasets diffusion coefficients were computed by inverse FEM-modeling. These diffusion coefficients are in accordance with literature results derived with through-diffusion experiments in diffusion cells. Indications for deviations from transversal-isotropic behavior on a minor level were found, which could be due to preferential diffusion pathways along silty layers or fractured zones.

Furthermore, PET-imaging was applied to better understand processes in the excavation damage zone. Here, the effect of waterglass impregnations on flow properties and pathways was investigated. The success of injection into void structures depends on a number of factors: the reaction kinetics of the injected waterglass with salt and brines, the nature of the fractures, and the injection velocity. Previously, this rather complex process could not be observed directly, and only the final results could be tested with destructive methods. Now, an improved description of this process was achieved, by which full spatial resolution over the whole time-frame becomes accessible. In these experiments the sealing success was not significant, because the waterglass congealed predominantly at the surface, and only a small portion significantly penetrated into the material.

Zusammenfassung

Ziel dieses Projektes war es den Einfluss erhöhter Salinitäten auf die Wechselwirkungsprozesse im System Radionuklid – Organika – Ton – Aquifer zu untersuchen. Deshalb wurden Komplexierungs-, Redox-, Sorptions- und Diffusionsstudien unter Variation der Ionenstärke (bis 4 mol kg^{-1}) und des Hintergrundelektrolyten (NaCl, $CaCl_2$, $MgCl_2$) durchgeführt.

Die Komplexierung von U(VI) durch Propionat wurde in Abhängigkeit von der Ionenstärke (bis 4 mol kg^{-1} $NaClO_4$) mittels TRLFS, ATR FT-IR Spektroskopie, und DFT-Rechnungen untersucht. Es wurden U(VI)/Propionat-Komplexe mit einer 1:1-, 1:2-, und 1:3-Stöchiometrie identifiziert. Ein Einfluss der Ionenstärke auf die Stabilitätskonstanten wurde nachgewiesen, wobei der Ionenstärkeeinfluss von der Ladung der entsprechenden Komplexe abhängig ist. Die konditionellen Stabilitätskonstanten, welche für $UO_2(Prop)^+$, $UO_2(Prop)_2^0$ und $UO_2(Prop)_3^-$ bei spezifischen Ionenstärken bestimmt wurden, wurden auf Ionenstärke 0 extrapoliert.

Bakterien, eine weitere Quelle für Organika im Ton, können die Speziation freigesetzter Radionuklide beeinflussen. Die Wechselwirkung von Bakterien, welche aus Mont Terri Opalinuston-Bohrkernen isoliert wurden (Moll et al., 2013), namentlich *Sporomusa* sp. MT-2.99 und *Paenibacillus* sp. MT-2.2, gegenüber Pu wurde in wässriger Lösung unter anaeroben Bedingungen untersucht. In einem früheren Projekt (Moll et al., 2013) wurde die Pu-Wechselwirkung mit *Sporomusa* sp. MT-2.99 Zellen bei einem pH-Wert von 6.1 ohne Zugabe eines Elektronendonors untersucht. Auf Basis dieser ersten Experimente wurde in diesem Projekt die Studie fortgeführt, um einen umfassenderen Überblick zu erhalten wie die beiden bakteriellen Isolate die Speziation des Pu beeinflussen können. Die durchgeführten Experimente können in solche ohne Elektronendonor, wo Biosorption dominiert, und solche mit Elektronendonor, wo auch Bioreduktionsprozesse stimuliert werden, aufgeteilt werden. Außerdem, konnten die gewonnenen Erkenntnisse hinsichtlich der komplexen Wechselwirkungsmechanismen der Actiniden/Lanthaniden mit isolierten Ton-Bakterien innerhalb dieses Projektes auf Salz-Mikroben ausgeweitet werden, da Salzgestein eine weitere potentielle Wirtsformation für die sichere Lagerung von nuklearem Abfall darstellt. Innerhalb dieses Projektes wurden erste Experimente zu den Wechselwirkungen des halophilen Archaeon *Halobacterium noricense* DSM-15987 mit U(VI), Eu(III) und Cm(III) in 3 M NaCl durchgeführt.

Ein weiteres Anliegen des Projektes war auch die Verbesserung des Prozessverständnisses hinsichtlich der Mobilität von Radionukliden in huminstoffhaltigen Systemen. Das betrifft insbesondere die Reversibilität und das Zusammenwirken der maßgeblichen Elementarprozesse. Für die Humatkomplexbildung mehrwertiger Metalle konnte die Existenz eines dynamischen Gleichgewichts in Isotopenaustauschstudien erstmals nachgewiesen werden. Dies ist Voraussetzung für die Verwendbarkeit thermodynamischer Konstanten in Speziations- und Transportmodellen. Liegt die Metallkonzentration im Spurenbereich, ist die Dissoziationsgeschwindigkeit allerdings sehr gering und unterliegt kinetischen Stabilisierungsprozessen. Die zugehörigen Zeiträume wurden für verschiedene Huminstoffe erfasst. Metall-Huminstoffkomplexe befinden sich demnach nicht im Gleichgewicht mit gelösten Reaktanden oder Mineraloberflächen, wenn sich Bedingungen in Zeitmaßstäben von weniger als einem Jahr verändern. In relativ schnellen Transportprozessen sind huminstoffgebundene Metalle

daher als fixiert zu betrachten, nicht aber in nahezu stagnierenden Fließsystemen, wie sie in endlagerbezogenen Ausbreitungsszenarien vorliegen.

Die Auswirkung hoher Salinitäten (NaCl, $CaCl_2$ und $MgCl_2$ bis 4 M) auf das Mobilisierungsvermögen von huminstoffartigen Tonorganika gegenüber Actiniden wurde in Radiotracerstudien an binären und ternären Systemen aus den (Analog-)Bestandteilen [^{152}Eu]Eu(III), [^{160}Tb]Tb(III), [^{14}C]Fulvinsäure und Opalinuston unter adäquaten Konzentrationsverhältissen bei verschiedenen pH-Werten untersucht. Hohe Ionenstärken bewirken keine Immobilisierung von Fulvinsäuren durch Ausflockung, können aber deren potentiell mobilisierende Wirkung prinzipiell nicht verstärken, denn während die Metall-Fulvatkomplexbildung vor allem durch mehrwertige Elektrolyte stark unterdrückt wird, bleibt das Adsorptionsverhalten der organischen Komponente weitgehend unverändert. Ihr resultierender Einfluss auf die Fest-Flüssig-Verteilung der Actinid-Analoga lässt sich nach einem kombinierten K_d-Modell z.T. quantitativ aus der Ionenstärkeabhängigkeit der Wechselwirkungen in den binären Randsystemen ableiten und entsprechend prognostizieren, ebenso der Übergang von demobilisierenden zu mobilisierenden Eigenschaften bei pH-Wert-Erhöhung bereits im neutralen Bereich. Der Elektrolyteffekt auf die Fulvatkomplexbildung wurde mittels Lumineszenzspektroskopie und mechanistischer Modellierung (NICA-Donnan-Ansatz) näher charakterisiert.

Die Sorption von Tc(VII)/Tc(IV) an den Fe(II)-haltigen Mineralen Magnetit ($Fe^{II}Fe^{III}_2O_4$) und Siderit ($Fe^{II}CO_3$), welche sowohl in der Natur als auch als Korrosionsprodukte der zur Lagerung des radioaktiven Abfalls genutzten Stahlbehälter vorkommen, wurde mittels Batch-Sorptionsexperimenten sowie unter Anwendung von ATR FT-IR und Röntgenabsorptionsspektroskopie (XAS) untersucht. Die starke Tc-Sorption an diesen Mineralen kann auf die oberflächeninduzierte Reduktion von Tc(VII) zu Tc(IV) zurückgeführt werden. Die Ergebnisse zeigen, dass beide Minerale effektiv zur Tc-Immobilisierung unter Endlagerbedingungen beitragen können. Ein Einfluss der Ionenstärke (0.1 oder 1 M) wurde nicht beobachtet.

Der Einfluss von Ionenstärke, Hintergrundelektrolyt, pH-Wert und CO_2-Abwesenheit bzw. Gegenwart auf die U(VI)-Sorption an Montmorillonit wurde untersucht. Als Hintergrundelektrolyt wurden NaCl-, $CaCl_2$- bzw. $MgCl_2$-Lösungen mit Ionenstärken bis zu 3 mol kg^{-1} (NaCl) bzw. bis zu 9 mol kg^{-1} ($CaCl_2$, $MgCl_2$) verwendet. Die U(VI)-Sorption an Montmorillonit in NaCl und $CaCl_2$ wird stark vom pH-Wert und der Gegenwart von CO_2 beeinflusst. In $CaCl_2$ ist die U(VI)-Sorption an Montmorillonit 0.5 bis 1 Größenordnung niedriger als in NaCl. In $MgCl_2$ wird die U(VI)-Konzentration in der überstehenden Lösung hauptsächlich durch gemeinsame Ausfällung mit Magnesium- und Siliziumverbindungen niedriger Löslichkeit gesteuert. Der Ionenstärkeeinfluss auf die U(VI)-Sorption ist im untersuchten Ionenstärke-Bereich klein. Die Modellierung der Oberflächensorption für die U(VI)/Montmorillonit-Wechselwirkung erfolgte unter Anwendung des “two-site protolysis non-electrostatic surface complexation and cation exchange (2SPNE SC/CE)“-Modells (Bradbury und Baeyens, 1997, 1999, 2002). Oberflächenkomplexierungskonstanten wurden für das NaCl- und das $CaCl_2$-System für alle untersuchten Ionenstärken ermittelt. Das zeigt, dass das 2SPNE SC/CE-Modell für die bei hohen Ionenstärken erhaltenen Sorptionsergebnisse angewendet werden kann. Die für unterschiedliche Ionenstärken erhaltenen Oberflächenkomplexierungskonstanten wurden auf Ionenstärke 0 extrapoliert. Die U(VI)-Sorption an Montmorillonit wurde auch in einem gemischten

Elektrolyten, bestehend aus 2.52 mol kg^{-1} NaCl, 0.12 mol kg^{-1} $CaCl_2$ und 0.048 mol kg^{-1} $MgCl_2$ (vergleichbar zur Grundwasserzusammensetzung im Schacht Konrad, Niedersachsen (Brewitz, 1982)) untersucht. Es zeigte sich, dass die Oberflächenkomplexierung in gemischten Elektrolyten mit den im NaCl- bzw. $CaCl_2$-System bestimmten Oberflächenkomplexierungskonstanten modelliert werden kann.

Der Einfluss von Citrat auf die U(VI)-Diffusion in Opalinuston wurde in Gegenwart von Opalinuston-Porenwasser untersucht. Die Diffusionsparameter, welche für die HTO- und die U(VI)-Diffusion in Abwesenheit von Citronensäure erhalten wurden, stimmten mit Literaturdaten überein. In Gegenwart von Citronensäure, wurde die U(VI)-Diffusion signifikant verzögert, was auf eine Änderung der Speziation hinweist. Wahrscheinlich wird U(VI) während des 3-monatigen Diffusionsexperimentes zu U(IV) reduziert. Citronensäure diffundierte etwas schneller durch Opalinuston als kleine Huminsäure-Kolloide, die in einem früheren Experiment untersucht wurden. Das Diffusionsexperiment zeigt, dass das vorliegende chemische System detaillierter untersucht werden muss, um die ablaufenden Reaktionen besser zu verstehen. Insbesondere muss die sich unter diesen Bedingungen bildende U(VI)-Citratspezies spektroskopisch, thermodynamisch und strukturell beschrieben werden.

Der Nutzen von PET als verlässliche Messmethode für die quantitative Bestimmung von Diffusionskoeffizienten in Ton und generell für Untersuchungen von Tracertransport in Barrieregestein wurde nachgewiesen. Die Verbesserung der quantitativen Auswertung bildete einen Schwerpunkt des Projektes, sowohl bezüglich der Verbesserung der Abbildungsqualität als auch der Ableitung von Parametern. Normalisierung und Streukorrektur wurden als bedeutende Ursachen für unzulängliche Abbildungsqualität gefunden und Abhilfen geschaffen. Hierzu wurden Monte-Carlo Simulationen der PET durchgeführt, die alle für die Bildgebung relevanten physikalischen Prozesse berücksichtigen, vom radioaktiven Zerfall des Traceratoms bis zur Detektion. Das Ergebnis der Untersuchungen ist eine verbesserte Rekonstruktionsprozedur, mit der sich die Tracerkonzentration quantitativ auswerten lässt und mit der auch Fehlerabschätzungen möglich sind.

PET-Experimente wurden als Testmessungen für die Auswertemethode durchgeführt und um das Verständnis experimenteller Artefakte durch Alteration und Beschädigung der Proben zu beurteilen. Räumlich-zeitliche Verteilungen der Tracerkonzentration wurden gemessen. Daraus wurden mit Hilfe inverser FEM-Modellierung Diffusionskoeffizienten berechnet. Die Ergebnisse sind im Einklang mit Literaturergebnissen, die mit Hilfe von „through-diffusion“-Experimenten in Diffusionszellen gewonnen wurden. Darüber hinaus wurden Hinweise auf Abweichungen vom einfachen transversal-isotropen Verhalten gefunden. Diese Abweichungen sind gering; sie könnten sich durch materialbedingte präferentielle Pfade für die Diffusion ergeben, die durch feine Silt-Schichten oder durch Mikrorisse verursacht werden.

Weitere PET-Untersuchungen dienten dem besseren Verständnis von Prozessen in der Auflockerungszone. Hierbei wurde der Einfluss von Wasserglas-Injektionen auf Transportparameter und -wege untersucht. Der Vergütungserfolg hängt von mehreren Faktoren ab: Der Reaktionskinetik des Wasserglases in Kontakt mit Salzgestein und Porenlösungen, den Ei-

genschaften des Risssystems und der Injektionsrate. Bisher konnte dieser komplexe Prozess nur mittels destruktiver Methoden am Endergebnis untersucht werden. Nun gelang es, ihn im zeitlichen Verlauf räumlich aufgelöst darzustellen. Der Vergütungseffekt in diesen Experimenten war allerdings nicht sehr deutlich, sondern das Wasserglas erstarrte überwiegend als Film auf der Probenoberfläche und nur ein geringer Anteil drang in die Probe ein.

1 Introduction and objectives

The long-term disposal of high-level nuclear waste in deep geological formations is discussed worldwide as main strategy for nuclear waste management. In addition to salt and crystalline rock, clay rock has been proposed as potential host rock for nuclear waste repositories (Nagra, 2002). Moreover, clay in form of bentonite is considered as backfill material in a variety of nuclear repository types. Advantages of clay rock as barrier against radionuclide migration are related to its swelling properties, low hydraulic permeability and crack-healing features as well as to the large surface areas of clay minerals leading to a high retention efficiency toward radionuclides (Nagra, 2002; Hoth et al., 2007). However, clay rock and clay minerals are sensitive to high temperatures, show anisotropic behavior and, compared to salt, greater efforts in geotechnical engineering are necessary to stabilize the tunneling in the rock (Hoth et al., 2007).

Clay rock is closely associated with natural organic matter that can be released from the clay under certain conditions. In the pore waters of Callovo-Oxfordian argillite (France) and Opalinus Clay formations, which represent potential host rocks for the disposal of radioactive waste, low molecular weight organic acids such as acetate, propionate, lactate, and formate (up to 1865×10^{-6} M, 127×10^{-6} M, 9×10^{-6} M, and 2×10^{-6} M, respectively) were detected that account for 88 % and 36 % of the total dissolved organic carbon (DOC) in the pore waters of the two host rock formations (Courdouan, 2007a,b). Moreover, fulvic and humic acid-like substances, organic polyelectrolyte molecules, were identified in alkaline extracts of previously acidified rock materials (Claret et al., 2003; Schäfer et al., 2003). In addition, further organic material is often contained in the radioactive waste itself such as citrate and EDTA, used as decontaminants (Hummel, 2008; Suzuki et al., 2010), as well as resins, cellulose, halogenated/non-halogenated polymers (PVC, PE, PP). Their degradation by radiolysis and hydrolysis under repository conditions results in the formation of further organic degradation products. Generally, organic substances, occurring as dissolved species or as colloids in pore waters as well as attached to solids, can affect the mobility of radionuclides in the environment.

Thus, for the assessment and reduction of risks related to the disposal of nuclear waste a detailed knowledge of all interaction processes in the system radionuclide – organics – clay – aquifer is necessary.

While ground and pore waters of South German clay deposits have ionic strengths below 0.5 M, the North German clay deposits are characterized by highly saline ground and pore waters with ionic strengths up to 4 M (Brewitz, 1982). So far, most of the studies with regard to radionuclide complexation by organics or radionuclide retention by clays were performed at low ionic strengths. Consequently, it has to be investigated whether literature data to complexation, sorption, diffusion, and redox chemistry of radionuclides obtained for low ionic strength systems can be used for the prediction of the geochemical behavior of radionuclides in systems with higher salinity. Therefore, the effect of high salt concentrations on interaction processes in the system radionuclide – organics – clay – aquifer is studied in the present work.

With regard to long-term safety assessment of nuclear waste repositories, actinides (mainly uranium, neptunium, plutonium, americium, and curium) are of particular interest, because of their high radio- and chemotoxicity and their very long half-lives. Furthermore, fission products, such as technetium-99 and selenium-79, are elements of concern for the safe storage of high-level nuclear waste, because of their long half-lives and their high mobility under aerobic conditions. Lanthanides, e.g. europium and terbium, are often used as analogues for trivalent actinides.

Exemplary for low molecular weight organic acids, the complexation of U(VI) by propionate is studied as a function of ionic strength (up to 4 mol kg^{-1} $NaClO_4$) by combining time-resolved laser-induced fluorescence spectroscopy (TRLFS), attenuated total reflection Fourier-transform infrared (ATR FT-IR) spectroscopy, and density functional theory (DFT) calculations. The complex stability constants will improve the thermodynamic database.

The sorption and diffusion studies within this project are focusing on model clay minerals (mainly montmorillonite, in some cases illite) as well as on the natural clay rock Opalinus Clay from the Mont Terri rock laboratory (Switzerland). Opalinus Clay is currently internationally investigated as one potential host rock for high-level nuclear waste disposal in Switzerland (Thury and Bossart, 1999; Nagra, 2002).

In order to quantify the influence of ionic strength and background electrolyte on U(VI) sorption onto montmorillonite, U(VI) sorption is studied applying both pure NaCl, $CaCl_2$ or $MgCl_2$ electrolytes with ionic strengths up to 3 mol kg^{-1} (NaCl) or up to 9 mol kg^{-1} ($CaCl_2$, $MgCl_2$) as well as a mixed electrolyte which consists of 2.52 mol kg^{-1} NaCl, 0.12 mol kg^{-1} $CaCl_2$ and 0.048 mol kg^{-1} $MgCl_2$ (similar to the groundwater composition in the Konrad mine, Lower Saxony (Brewitz, 1982)). Surface complexation modeling for the interaction of U(VI) with montmorillonite is performed to determine surface complexation constants. In this context, it will be checked whether the two-site protolysis non-electrostatic surface complexation and cation exchange (2SPNE SC/CE) model, developed by Bradbury and Baeyens (1997, 1999, 2002), can be applied for sorption results obtained at high ionic strengths. The surface complexes are verified by means of TRLFS and ATR FT-IR spectroscopy.

The migration of radionuclides in clay rock is governed by molecular diffusion. This process can be studied by diffusion experiments, whereby diffusion and distribution coefficients (D_e and K_d) are determined. In continuation of diffusion studies performed in the previous project, where U(VI) diffusion in compacted Opalinus Clay was studied in the absence and presence of humic acid at 25 and 60°C (Joseph et al., 2013b), the objective of the present study is to evaluate the influence of citrate, a further representative of low molecular weight organic acids, on U(VI) diffusion in Opalinus Clay. Furthermore, the influence of increased ionic strengths on U(VI) diffusion in compacted montmorillonite is studied applying NaCl solution as well as a mixed electrolyte (similar to Konrad groundwater, see above), both having an ionic strength of about 3 mol kg^{-1}.

Microorganisms that are indigenous in potential host rocks, foreseen for nuclear waste disposal, are able to influence the speciation and therefore the mobility of actinides and their re-

tardation both by direct and indirect pathways (e.g., Lloyd and Gadd, 2011; Swanson et al., 2012; Lütke et al., 2013; Wouters et al., 2013; Moll et al., 2014). Recently, from Mont Terri Opalinus Clay indigenous bacteria were isolated and their interactions with U, Eu and Cm were investigated (Lütke et al., 2013; Moll et al., 2014). Some investigations (Panak and Nitsche, 2001; Neu et al., 2005; Moll et al., 2006; Renshaw et al., 2009; Ohnuki et al., 2009) documented the manifold impact of bacteria on the speciation of Pu. Plutonium can coexist in different oxidation states under environmental conditions which makes interaction studies in biological systems challenging. Therefore, the interactions of the bacterial isolates from Opalinus Clay are investigated in more detail.

In salt rock in addition to bacteria and fungi, archaea are dominating the indigenous microbial community (McGenity et al., 2000; Stan-Lotter and Fendrihan, 2015) as shown in the Waste Isolation Pilot Plant in Carlsbad, New Mexico, USA (Swanson et al., 2012). To date, only a few studies have evaluated the interactions of halophilic microorganisms with U (Francis et al., 2000, 2004) and other actinides (Gillow et al., 2000; Ozaki et al., 2004; Ams et al., 2013) at high ionic strength. Recently, an extremely halophilic archaeon namely *Halobacterium* (*Hbt*.) sp., putatively *noricense* (WIPP strain) was isolated from the WIPP site (Swanson et al., 2012). Its closest phylogenetic relative *Halobacterium noricense* DSM-15987 was originally isolated from a salt mine in Austria (Gruber et al., 2004). Within this project, first experiments are performed to study the interactions of the halophilic archaeon *Halobacterium noricense* DSM-15987 with U(VI), Eu(III), and Cm(III).

Another objective is to obtain an improved understanding of the equilibrium characteristics of metal-humate complexation, particularly with regard to possible stabilization processes and their consequences in respect of reversibility. Complexation with dissolved humic matter can be crucial in controlling the mobility of toxic or radioactive metals. For speciation and transport modeling, a dynamic equilibrium process is commonly assumed, where association and dissociation run permanently. This is, however, questionable in view of reported observations of a growing resistance to dissociation over time (Cacheris and Choppin, 1987; Choppin and Clark, 1991; Rao et al., 1994; Artinger et al., 1998; King et al., 2001; Geckeis et al., 2002). If, in the end, humic-bound metals are to be regarded as "fixed", this will entail completely different predictions of their migration behavior than in the case of a dynamic partitioning process. So far, the existence of a dynamic equilibrium has never been proven. In this project, the isotope exchange principle is employed to gain direct insight into the dynamics of the complexation equilibrium, including kinetic stabilization phenomena.

Different from small ligands, the mobilizing potential of humic or humic-like substances is not only determined by complex stability (and inertness), but also by colloidal stability. Fulvic acids, which are to some extent comparable to high-molecular-weight clay organics, are stable towards flocculation at low ionic strength, but this is possibly not the case at very high electrolyte contents close to saturation. Colloid-borne mobilization of radionuclides could be excluded a priori if flocculation prevents any migration in the fluid phase. For this reason, colloidal stability of fulvic acids in highly saline systems with NaCl, $CaCl_2$ and $MgCl_2$ is systematically investigated at different pH values.

In the absence of flocculation, humic-like clay organics must be regarded as possible carriers. High salinity as well as natural organic matter are known to facilitate migration of multivalent metals, but little is known on their combined influence. Both synergistic and antagonistic effects are conceivable. In general, interaction of metal ions with negatively charged binding sites on mineral surfaces or humic colloids is counteracted at high electrolyte contents. Depending on the type of cation, this may be caused both by charge screening effects and direct competition. Regarding adsorption of humic substances, the influence of high ionic strength is not known. Thus, the behavior of metals in highly saline systems with humic matter is hardly predictable.

Basically, both mobilizing and retarding effects are possible, which is mainly dependent on the pH value (cf. (Lippold et al., 2005) and references therein). The influence of pH and ionic strength on the solid-liquid distribution of a metal in such “ternary” systems (consisting of metal, solid surface and humic colloids) should be explainable by combining the interactions in the constituent binary subsystems (metal adsorption, metal-humic complexation, adsorption of the humic substance). This is a prerequisite for modeling humic-bound transport. However, the applicability of this “linear additive model” is uncertain for several reasons (Lippold et al., 2009).

In this project, complexation of Tb(III) and Eu(III) (as analogues of trivalent actinides) with fulvic acid and their adsorption onto Opalinus Clay are investigated for binary and ternary systems at different pH values in the presence of NaCl, $CaCl_2$, and $MgCl_2$ as a function of ionic strength up to saturation. ^{160}Tb, ^{152}Eu, and ^{14}C-labeled fulvic acid are used as radioactive tracers, allowing studies at very low concentrations to be in accordance with probable conditions in the far-field of a nuclear waste repository. In order to specify the influence of the electrolyte constituents on fulvate complexation, a mechanistic model (NICA-Donnan) is applied. The complexes are characterized by means of TRLFS. The linear additive model is tested for suitability in reconstructing the ternary systems from the corresponding binary systems.

Most geological materials are heterogeneous and highly structured on all scales, starting from the surface structure of each grain, up to the geometry of layers on the field scale. The scaling to the macroscopic scale of processes which are identified and well understood on the molecular scale, like sorption and transport, is a challenging question. An effective volume which depends on the process has to be considered, which specifies the portion of the volume and the particular pathways where the process takes effect. Particularly, effects of preferential pathways and preferential transport direction (anisotropy) were found to be present in Opalinus Clay (e.g. Van Loon et al. 2004; Keller et al., 2011).

Diffusion properties are commonly determined in diffusion cells and on small-sized samples that are considered homogeneous. Directional measurements on a large number of samples could yield information on anisotropy and inhomogeneity on the particular size scale of the sample and are missing deviations on a larger scale, which could be caused by a system of micro-fractures, fine layering, or other structures. Such deviations could become effective as preferential transport zones and therefore delimit the barrier function of the material.

In previous projects, positron emission tomography (PET) was established as an experimental method for process observation that is capable to bridge the scale from processes on the molecular scale to the macroscopic scale. It had been shown that the method was applicable for qualitative imaging. For example, it was possible to visualize the anisotropy of diffusion processes in Opalinus Clay, but the quantitative results were questionable. This was due to the lack of correction methods for samples with high density, because common correction methods are designed for biological tissue. Recently, new data correction methods have become available, which are applicable for geological materials and greatly improve quantitative usability of the PET images.

An intrinsic property of the excavation damage zone is preferential transport behavior due to fracturing caused by pressure release. One option to improve these degradations of the geological barrier is impregnation of waterglass. The success of effective injection into void structures depends on a number of factors: the reaction kinetics of the injected waterglass with salt and brines, the nature of the fractures, and the injection velocity. This rather complex process could not be observed directly, only the final results could be tested with destructive methods. The low contrast between waterglass and water, as well as the experimental conditions, complicate the application of the common µCT-method. In contrast, PET is proposed as appropriate method for observation of such geochemical processes.

A further objective of the project was the evaluation of the retention capacity of iron(II)-containing mineral phases occurring ubiquitously in nature as well as corrosion products of carbon steel canisters used for storing radioactive waste. For instance, magnetite, green rust, mackinawite, or siderite can form during corrosion of large quantities of steel that are planned to be installed throughout a deep geological disposal facility. Siderite forms in anoxic environments rich in carbonates. Such iron(II)-containing mineral phases are expected to be one of the key surfaces of interest for controlling radionuclide behavior under disposal conditions. In this project, the Tc(VII)/Tc(IV) sorption by the iron(II)-containing minerals magnetite ($Fe^{II}Fe^{III}{}_2O_4$) and siderite ($Fe^{II}CO_3$) is studied under anoxic conditions by means of batch sorption experiments as well as ATR FT-IR and X-ray absorption spectroscopy. For comparison, Tc retention on iron(III) minerals hematite (α-Fe_2O_3) and maghemite (γ-Fe_2O_3) is studied.

This research project, funded by the Bundesministerium für Wirtschaft und Energie (BMWi), was performed in collaboration with the R&D projects of the Karlsruher Institut für Technologie (Institut für Nukleare Entsorgung), Johannes Gutenberg-Universität Mainz (Institut für Kernchemie), Technische Universität Dresden (Sachgebiet Strahlenschutz), Technische Universität München (Fachgebiet Theoretische Chemie), Universität Heidelberg (Physikalisch-Chemisches Institut), Universität Potsdam (Institut für Chemie/Physikalische Chemie) and Universität des Saarlandes (Anorganische Festkörperchemie).

2 Complexation of U(VI) by propionate at different ionic strengths in $NaClO_4$

2.1 Literature review

So far, the interaction between U(VI) and propionate at high ionic strength has been scarcely studied in the literature.

Miyake and Nürnberg (1967) and Kirishima et al. (2007) studied this interaction both in 1 M $NaClO_4$, at 20°C and 25°C, respectively. By means of UV-vis spectroscopy, Miyake and Nürnberg (1967) determined the formation of 4 species, namely $UO_2(Prop)^+$, $UO_2(Prop)_2^0$, $UO_2(Prop)_3^-$ and $UO_2(Prop)_4^{2-}$. They postulated a monodentate coordination of the propionate ligand to the uranyl moiety. Kirishima et al. (2007) investigated the complexation of U(VI) by propionic acid by potentiometric and microcalorimetric titration. The formation of $UO_2(Prop)^+$ and $UO_2(Prop)_2^0$ was deduced.

Table 1: Summary of the complexation constants for the U(VI)/propionate system reported in the literature.

	log β (I = 1 M $NaClO_4$)	
Species	Miyake and Nürnberg (1967)	Kirishima et al. (2007)
$UO_2^{2+} + Prop^- \rightleftharpoons UO_2(Prop)^+$	2.53 ± 1.11	2.50 ± 0.01
$UO_2^{2+} + 2\ Prop^- \rightleftharpoons UO_2(Prop)_2^0$	4.68	4.79
$UO_2^{2+} + 3\ Prop^- \rightleftharpoons UO_2(Prop)_3^-$	6.49	
$UO_2^{2+} + 4\ Prop^- \rightleftharpoons UO_2(Prop)_4^{2-}$	8.25	

By combining density functional theory (DFT) calculations, ultraviolet−visible (UV−vis), extended X-ray absorption fine-structure (EXAFS), and attenuated total reflection Fourier-transform infrared (ATR FT-IR) spectroscopy, Lucks et al. (2012) revisited the aqueous speciation of the U(VI)-acetate system. Complexes with the 1:1, 1:2 and 1:3 U:acetate stoichiometry were identified. The U(VI)-acetate complexes exhibited exclusively a bidentate coordination. Since acetic acid and propionic acid only differ by a $–CH_2$ group, a strong analogy on the behavior of both ligands towards U(VI) is to be expected.

2.2 Sample preparation

Sodium propionate from Acros (99.0-100.5 %) and sodium perchlorate monohydrate (p.a.) (Merck Millipore) were used. The concentration of U(VI) was set to 5×10^{-4} mol kg^{-1}. Three molalities (0.75, 2.0 and 4.0 mol kg^{-1}) were studied, imposed by $NaClO_4$. The concentration of propionate was increased from 0.005 mol kg^{-1} to 0.25 mol kg^{-1}. All experiments were performed at 20°C. Samples were analyzed by time-resolved laser-induced fluorescence spec-

troscopy (TRLFS) and the data deconvolution performed using Parallel Factor Analysis PARAFAC (Bro, 1997; Drobot et al., 2015). To get insights on the number of species, additional IR absorption spectroscopy measurements were performed on a Bruker Vertex 80/v instrument using an ATR diamond cell ([U(VI)] = 5×10^{-3} mol kg^{-1}, 0.1 mol kg^{-1} propionate, pH from 0.98 to 5.03). Since perchlorate exhibits a broad peak in the IR spectrum from 1120 to 928 cm^{-1}, these experiments were performed without background electrolyte. Speciation should not be impacted since no coordination between U(VI) and perchloric acid up to 11.5 mol L^{-1} was evidenced by Semon et al. (2001).

2.3 pH measurements at high salinity

At ionic strength higher than 0.1 mol kg^{-1}, the pH measured in solutions (pH_{exp}) is an operational apparent value (Altmaier et al., 2003; Altmaier et al., 2008; Fanghänel et al., 1996; Felmy et al., 1991). It can be related to the molal H^+ concentration as follows:

$$-\log m_{H+} = pH_{exp} + A \quad (2.1)$$

Indeed, the liquid junction potential, which depends on the electrolyte concentration, differs for saline solutions and dilute buffer solutions (used for the calibration of the pH electrode). This variation as well as the individual activity coefficient γ_{H+} are included in the term A, which depends exclusively on the concentration and composition of the solutions (Altmaier et al., 2003; Altmaier et al., 2008; Fanghänel et al., 1996; Felmy et al., 1991).

The following relation was used (Petrov et al., 2011):

$$A(NaClO_4) = -0.0152 + 0.27\ x + 0.0046\ x^2 \quad (2.2)$$

where A is in mol L^{-1}, and x is the concentration of $NaClO_4$, also in mol L^{-1} units.

After conversion to molal units, the pH_{exp}, given in Table 2, were used:

Table 2: Experimental pH_{exp} used.

I (mol kg^{-1})	pH_{exp}	$-\log m_{H+}$
0.75	3.70	3.89
2	3.39	3.89
4	2.94	3.89

Combination pH electrodes (SenTix® MIC from VWR) were used for pH measurements. In order to avoid precipitation of $KClO_4$ in the diaphragm of the electrode, the original junction electrolyte 3 M KCl was replaced by a 3 M NaCl solution. The electrodes were calibrated using standard buffer solutions (WTW).

2.4 DFT calculations and ATR FT-IR spectroscopy

Density Functional Theory (DFT) calculations were performed in an aqueous phase using the Gaussian 09 program employing the density functional theory by using a conductor like polarizable continuum model. Structure optimizations were performed for 1:1, 1:2, and 1:3 complex of uranyl propionate at B3LYP level followed by vibrational frequency analysis at the same level to confirm the absence of imaginary frequencies. The energy-consistent small-core effective core potential and the corresponding basis set suggested by Küchle et al. (1994) were used for uranium. The most diffuse basis functions on uranium with the exponent 0.005 (all s, p, d, and f type functions) were omitted. For carbon, oxygen and hydrogen, the valence triple-z plus polarization basis was used. The spin-orbit effects and basis set superposition error corrections were neglected.

The DFT calculations were performed considering a bidentate coordination of the propionate to the uranium(VI) moiety. The three complexes are represented in Fig. 1.

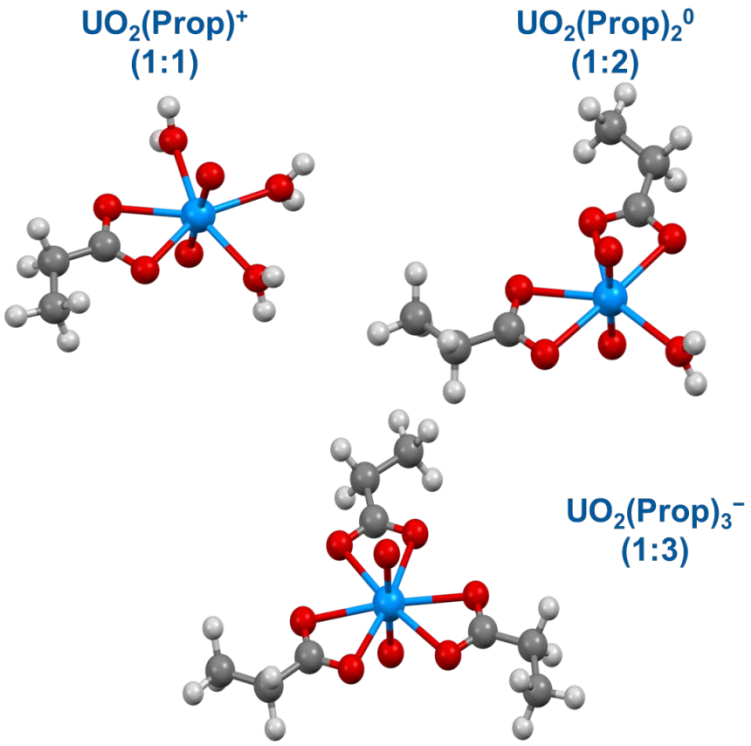

Fig. 1: Proposed structures of the 1:1, 1:2, and 1:3 U(VI) propionate complexes (blue: uranium; red: oxygen; gray: carbon; light gray: hydrogen).

The DFT calculated IR spectra for the $UO_2(Prop)^+$, $UO_2(Prop)_2^0$ and $UO_2(Prop)_3^-$ complexes are shown in Fig. 2a. As it can be seen in Fig. 2a, a large red shift from 986 to 912 cm^{-1} of the asymmetric stretching mode $\nu_3(UO_2)$ of the uranyl moiety upon complexation with propionate is predicted. As already shown by Lucks et al. (2012), this red shift upon complexation is due to the weakening of the axial(ax) $U-O_{ax}$ bond because of the σ and/or π contribution from the propionate ligands. The spectral feature predicted by DFT at around 893 cm^{-1} arises from the *ν*(CC) mode of the propionate ligand.

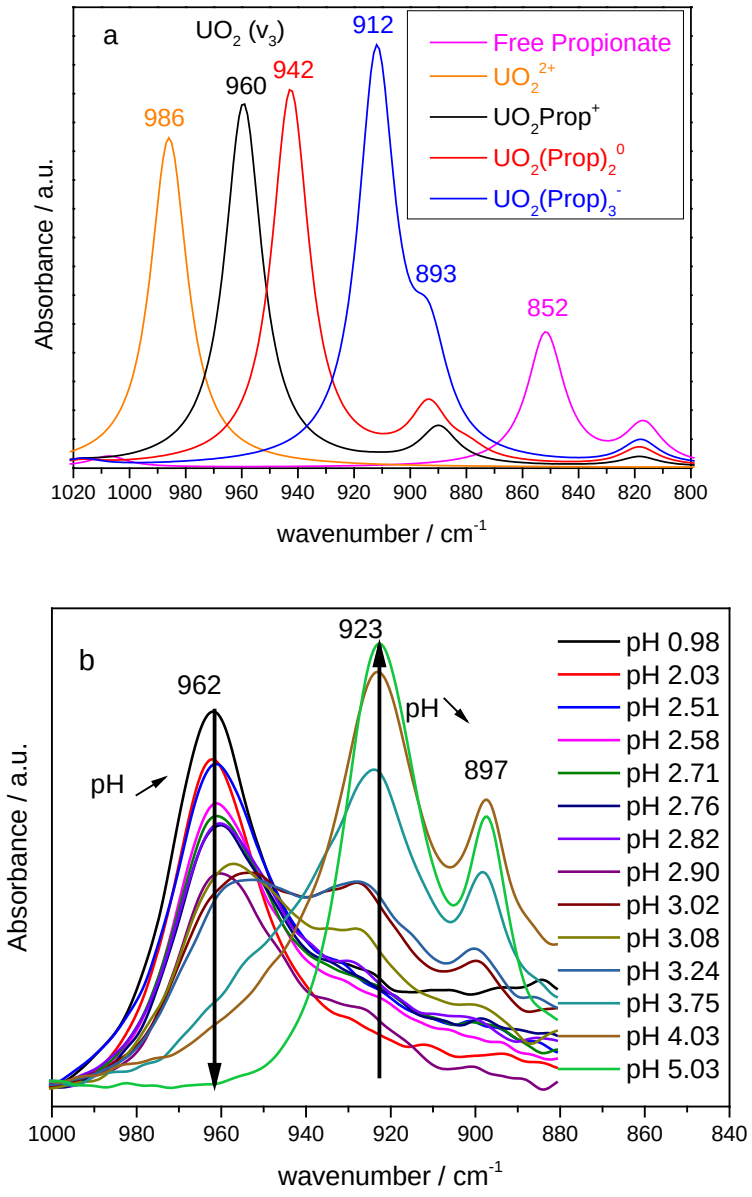

Fig. 2: Comparison of (a) DFT calculated band positions of the asymmetric stretching mode of the uranyl moiety and (b) experimentally observed values in the U(VI) propionate system ([U(VI)] = 5×10^{-3} mol kg^{-1}, 0.1 mol kg^{-1} propionate, pH from 0.98 to 5.03).

Fig. 2b represents the experimental IR spectra of the aqueous U(VI) propionate solutions recorded at pH values ranging from pH 0.98 to pH 5.03 in the spectral range of the $\nu_3(UO_2)$ mode. In agreement with DFT, a large frequency shift from 962 to 923 cm^{-1} is observed upon increasing pH, due to the increasing proportion of U(VI)/propionate complexes. A similar shift as similar frequencies was already observed by Lucks et al. (2012) for the U(VI) acetate system. The contribution of hydrolyzed U(VI) complexes can be neglected due to the excess of ligand. While the peak maxima observed at 962 and 923 cm^{-1} appear to correspond to two pure species, the presence of two additional species showing band maxima at 948 and 933 cm^{-1} are observed (Fig. 2b). The spectral feature at 897 cm^{-1}, also predicted by DFT, exhibits an increasing intensity with increasing number of propionate ligands coordinated to the U(VI).

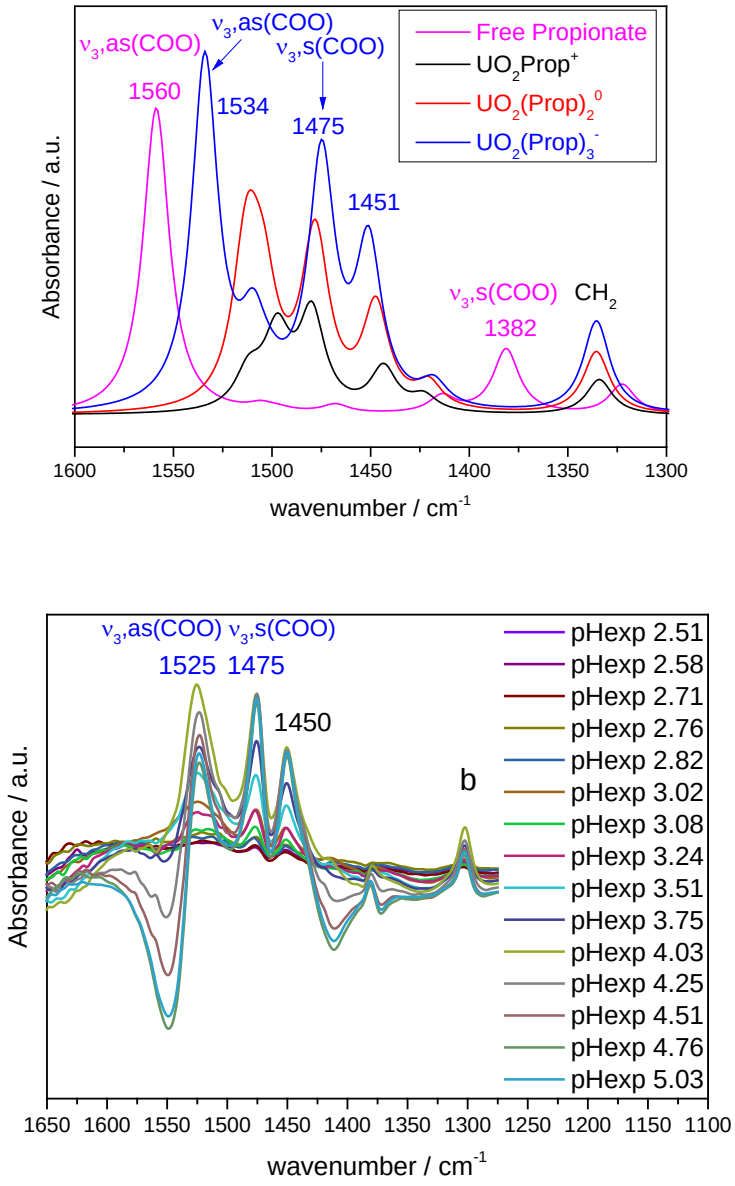

Fig. 3: Comparison of (a) DFT calculated band positions of the carboxylate region and (b) experimentally observed values in the U(VI) propionate system ([U(VI)] = 5×10^{-3} mol kg^{-1}, 0.1 mol kg^{-1} propionate, pH from 2.51 to 5.03).

In the DFT calculated spectra, the bidentately coordinated U(VI) propionate complexes exhibit the antisymmetric and symmetric stretching modes of the carboxyl groups, $\nu_{3,as}$(COO) and $\nu_{3,s}$(COO), at 1534-1520 cm^{-1} and 1475 cm^{-1}, respectively (Fig. 3a). The spectral splitting of these bands ($\Delta\nu$), lying from 37 to 59 cm^{-1}, allows a discrimination of bidentate and monodentate coordination of the carboxyl group (Kahikana et al., 1987; Deacon and Philipps, 1980). According to Kahikana et al. (1987), a splitting lower than 100 cm^{-1} is characteristic to a bidentate coordination, while a monodentate coordination exhibits a spectral splitting larger than 150 cm^{-1}. The band predicted at 1451 cm^{-1} has contributions of both the symmetric stretching modes of the carboxyl groups as well as the $-CH_2$ group. The experimental vibrational modes of the carboxyl group of the propionate ligand after complexation with U(VI) are shown in Fig. 3b. The $\nu_{3,as}$(COO) mode at 1525 cm^{-1} and the $\nu_{3,s}$(COO) mode at 1475 cm^{-1}

are present throughout the whole pH range exhibited. The band splitting $\Delta\nu$ is 50 cm^{-1}, in perfect agreement with DFT predictions. This confirms the bidentate coordination of the carboxylic groups and rules out a monodentate one. Note that the frequency of the band at 1450 cm^{-1} perfectly matches the DFT calculations.

2.5 TRLFS spectroscopy and PARAFAC deconvolution

TRLFS measurements were performed using a Nd:YAG laser, at λ = 266 nm and a laser energy of 0.3 mJ. Samples were placed in a quartz cuvette. An average of 50 accumulations was collected and the baseline correction was performed with the software LabSpec 5 (Horiba). A 70 ns step size for 50 spectra was used. All measurements were done at 20°C using a controlled Peltier element (TC125 Temperature Control, Quantum Northwest). The static fluorescence spectra recorded after the initial delay of 70 µs at I = 0.75 mol kg^{-1} $NaClO_4$ are exemplarily shown in Fig. 4.

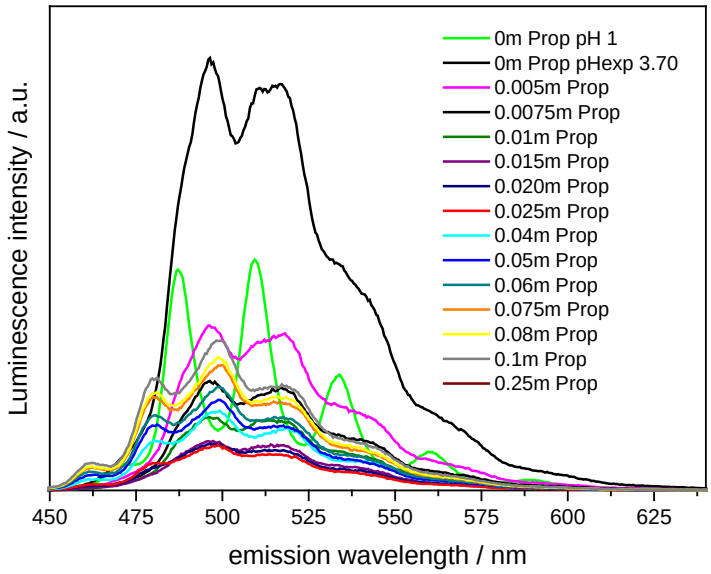

Fig. 4: Static TRLFS spectra of the U(VI) propionate system ([U(VI)] = 5×10^{-4} mol kg^{-1}, 0 to 0.25 mol kg^{-1} propionate, 0.75 mol kg^{-1} $NaClO_4$).

PARAFAC, coupled to a Newton-Raphson algorithm, was used to extract speciation information from the fluorescence data (Fig. 5). The extracted emission spectra of the five single components are shown in Fig. 5.

The 1st component corresponds to the uranyl UO_2^{2+} aquo ion, with peak maximum at 471, 486, 508, 532, 559 and 589 nm, in agreement with the literature (Drobot et al., 2015). The second can be attributed to the 1st hydrolyzed species of U(VI), i.e. UO_2OH^+, with peak maximum at 480, 496, 517, 541, 567 and 595 nm (Drobot et al., 2015). The three other components correspond then to the 1:1, 1:2 and 1:3 complexes. These five components can describe the fluorescence data observed in Fig. 4.

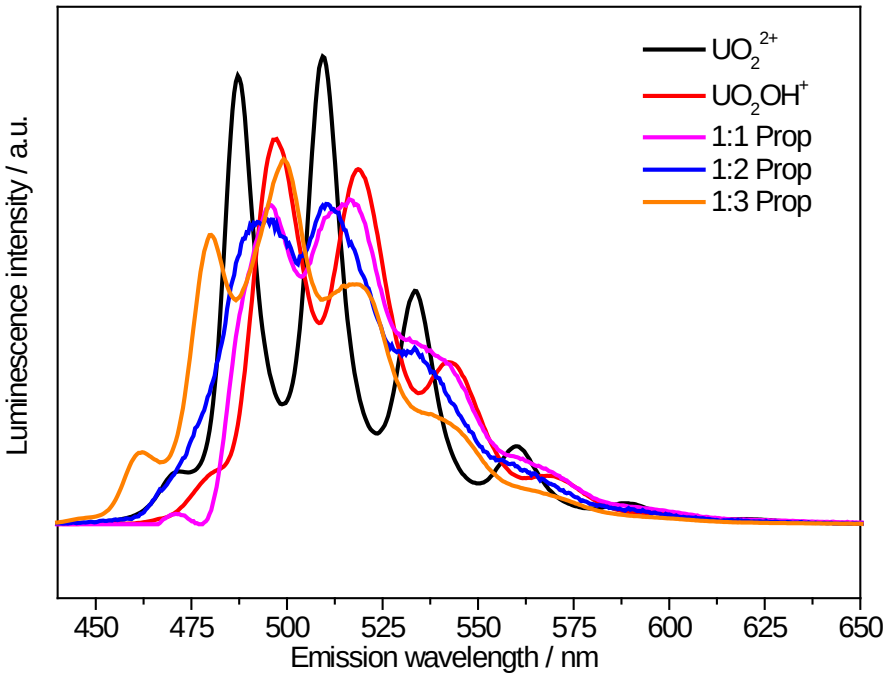

Fig. 5: Extracted emission spectra for 5 components of the U(VI) propionate system ([U(VI)] = 5×10^{-4} mol kg^{-1}, 0 to 0.25 mol kg^{-1} propionate, 0.75 mol kg^{-1} $NaClO_4$).

From the PARAFAC deconvolution of the fluorescence data, the following species distribution was obtained (Fig. 6).

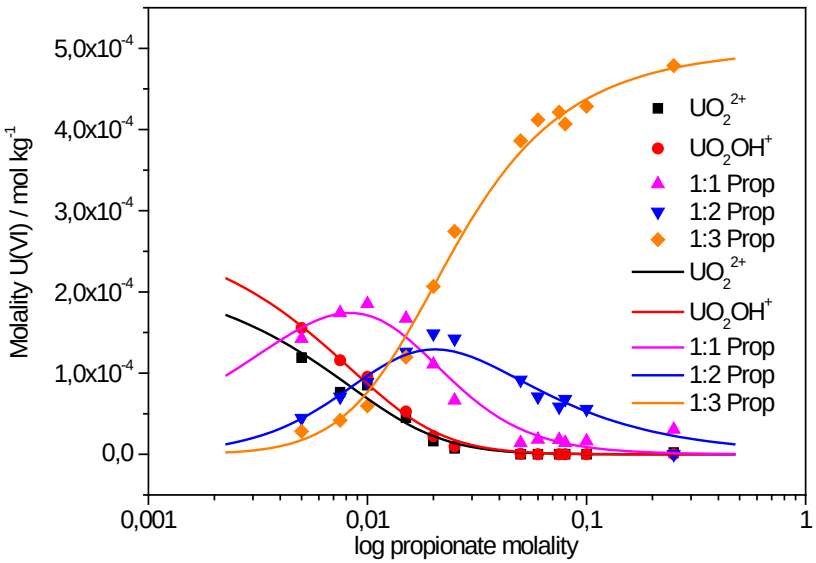

Fig. 6: Species distribution based on luminescence spectroscopy and PARAFAC deconvolution ([U(VI)] = 5×10^{-4} mol kg^{-1}, 0 to 0.25 mol kg^{-1} propionate, 0.75 mol kg^{-1} $NaClO_4$).

2.6 Determination of the complexation constants

The reactions leading to the formation of the three complexes and their equilibrium constants can be defined as follows:

$UO_2^{2+} + Prop^- \rightleftharpoons UO_2(Prop)^+$ (2.3)

$$\beta_1 = \frac{[UO_2Prop^+]}{[UO_2^{2+}][Prop^-]}$$

$UO_2^{2+} + 2\ Prop^- \rightleftharpoons UO_2(Prop)_2^0$ (2.4)

$$\beta_2 = \frac{[UO_2(Prop)_2]^0}{[UO_2^{2+}][Prop^-]^2}$$

$UO_2^{2+} + 3\ Prop^- \rightleftharpoons UO_2(Prop)_3^-$ (2.5)

$$\beta_3 = \frac{[UO_2(Prop)_3]^-}{[UO_2^{2+}][Prop^-]^3}$$

For each ionic strength, the speciation can be verified by slope analysis, by plotting log ($[UO_2(Prop)_n^{[2-n]+}]/[UO_2(Prop)_{n-1}^{[2-(n-1)]+}]$) as a function of log $[Prop^-]_{eq}$ (example for I = 0.75 mol kg^{-1} in Fig. 7).

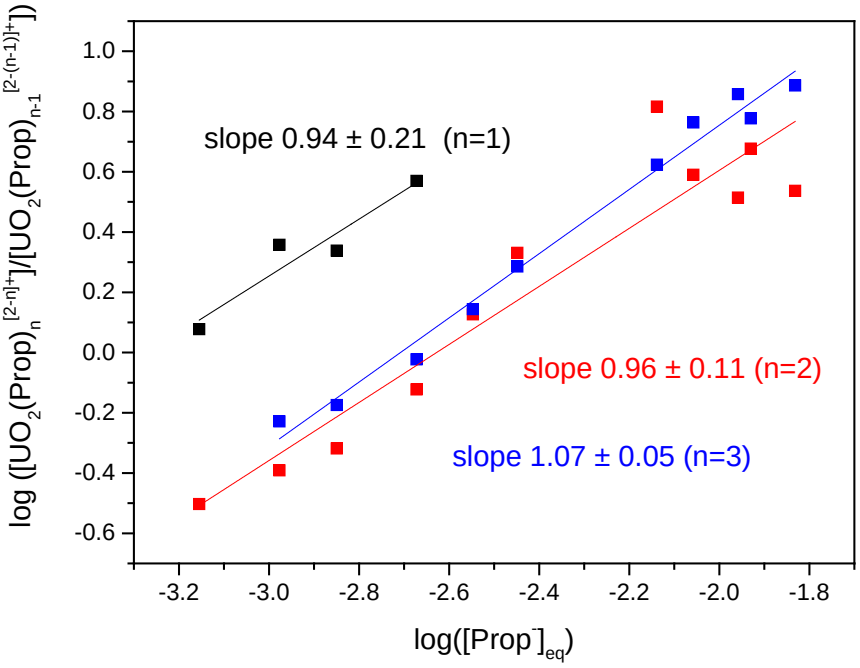

Fig. 7: Slope analyses for the stepwise formation of $UO_2(Prop)_n^{[2-n]+}$ complexes a n = 1, 2, 3 at 20°C and I = 0.75 mol kg^{-1} $NaClO_4$.

The slope of the linear correlations confirms the formation of the $UO_2(Prop)^+$, $UO_2(Prop)_2^0$ and $UO_2(Prop)_3^-$ complexes and their distribution as a function of the propionate concentration.

Based on the slope analysis, the following complexation constants were obtained (Table 3).

Table 3: Overall thermodynamic stability constants log β of the three U(VI)-propionate complexes at variable ionic strengths.

I (mol kg^{-1})	log β_1	log β_2	log β_3
0.75	3.30	5.93	8.67
2	2.89	5.69	8.80
4	2.51	5.76	7.85

The differences of the ionic strength dependencies of the log β values are connected with the charge of the complexes. For log β_1, all of the involved species (UO_2^{2+}, $Prop^-$, $UO_2(Prop)^+$) are charged. For log β_2, the $UO_2(Prop)_2^0$ complex has no charge. For log β_3, the complex is negatively charged $UO_2(Prop)_3^-$. Since $UO_2(Prop)_2^0$ is non-charged, the variation of its activity coefficient should be less pronounced than for a charged complex, i.e. $UO_2(Prop)^+$ and $UO_2(Prop)_3^-$. This is in good agreement with the data given in Table 3. Both the stability constants for the $UO_2(Prop)^+$ complex and the $UO_2(Prop)_3^-$ complexes change more with I than the $UO_2(Prop)_2^0$ complex. The differences in the two charged complexes are most likely related to the different interactions with the background electrolyte ($UO_2(Prop)^+$ interacts with ClO_4^-, $UO_2(Prop)_3^-$ interacts with Na^+) and to the different geometries of the complexes.

2.7 Extrapolation to zero ionic strength

The conditional stability constants, i.e. determined at specific ionic strength, can be extrapolated to zero ionic strength based on the Specific Interaction Theory (SIT) (Lemire et al., 2013). The relation between the conditional stability constant and the stability constant at zero ionic strength is given by the following equation:

$$\log_{10} {}^*\beta - \Delta z^2 D - n \log a(H_2O) = \log_{10} \beta^\circ - \Delta\varepsilon I \qquad (2.6)$$

$\log_{10} {}^*\beta$: conditional stability constant (at specific I)

$D = \frac{A\sqrt{I}}{1+Ba_j\sqrt{I}}$: the Debye-Hückel term

(A and B_{aj} are Debye-Hückel parameters taken from Lemire et al. (2013))

n = 0 for the 1:1, 1:2 and 1:3 complexes

$\log_{10} \beta^\circ$: stability constant at zero ionic strength

For the three reactions considered, Δε and Δz^2 are defined as follows:

$UO_2^{2+} + Prop^- \rightleftharpoons UO_2(Prop)^+$ (2.7)

$\Delta\varepsilon = \varepsilon(UO_2(Prop)^+;ClO_4^-) - \varepsilon(UO_2^{2+};ClO_4^-) - \varepsilon(Na^+;Prop^-)$; $\Delta z^2 = -4$

$UO_2^{2+} + 2\ Prop^- \rightleftharpoons UO_2(Prop)_2^0$ (2.8)

$\Delta\varepsilon = \varepsilon(UO_2(Prop)_2^0;ClO_4^-) - \varepsilon(UO_2^{2+};ClO_4^-) - 2\varepsilon(Na^+;Prop^-)$; $\Delta z^2 = -6$

$UO_2^{2+} + 3\ Prop^- \rightleftharpoons UO_2(Prop)_3^-$ (2.9)

$\Delta\varepsilon = \varepsilon(Na^+;UO_2(Prop)_3^-) - \varepsilon(UO_2^{2+};ClO_4^-) - 3\varepsilon(Na^+;Prop^-)$; $\Delta z^2 = -6$

$\varepsilon(UO_2^{2+};ClO_4^-) = 0.46$ (kg mol^{-1}) was taken from Lemire et al. (2013). No interaction coefficient is available for $\varepsilon(Na^+;Prop^-)$. Since ε(i,j) depends mostly on the charge of the ion (Skerencak et al., 2013), we used the analogy with $\varepsilon(Na^+;Acetat^-) = 0.08$ (kg mol^{-1}).

By plotting $\log_{10} {}^*\beta - \Delta z^2 D$ vs. the ionic strength, the slope and the intercept with the y-axis at $I = 0$ give $-\Delta\varepsilon$ and $\log_{10} \beta°$, respectively. The linear SIT regression plots for the experimental log β_1, log β_2 and log β_3 values are shown in Fig. 8.

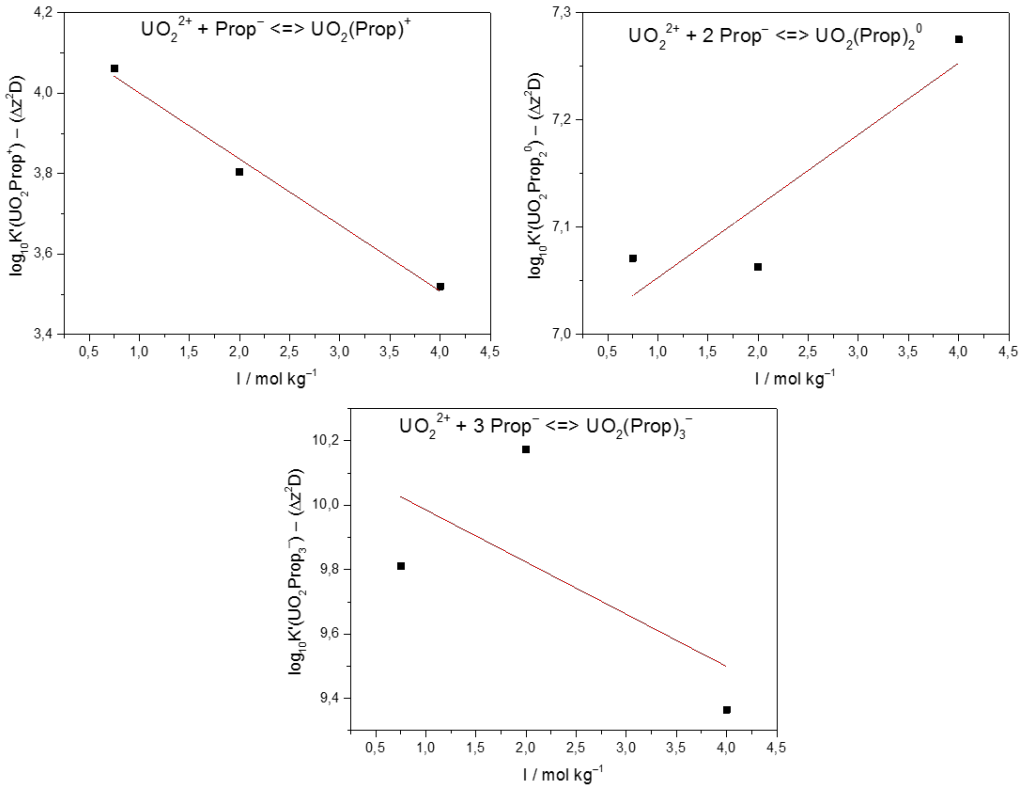

Fig. 8: Linear SIT regression plots for the first, second and third complexation constant of the U(VI) propionate system at 20°C.

The results, $\log_{10} \beta°$ and the different interaction coefficients ε(i,j) are shown in Table 4.

Table 4: Overall thermodynamic stability constants log β at I = 0 and the determined ε(i,j).

log $\beta_1°$	log $\beta_2°$	log $\beta_3°$
4.17	6.99	10.15
$\varepsilon(UO_2(Prop)^+;ClO_4^-)$	$\varepsilon(UO_2(Prop)_2^0;ClO_4^-)$	$\varepsilon(Na^+; UO_2(Prop)_3^-)$
0.70	0.55	0.86

Due to the lack of published data, our results cannot be directly compared. However, complexation constants at I = 0 are available for the U(VI)/acetate system. Sladkov (2013, 2014) found log $\beta_1°$ = 2.94 ± 0.08 (25°C) and log $\beta_2°$ = 5.50 ± 0.15 (25°C). Moskvin (1969) published log $\beta_3°$ = 7.25 (temperature not indicated). By comparing these data with our results from Table 4, it seems that the propionate ligand has a stronger affinity than acetate towards U(VI).

3 Interaction of radionuclides with microorganisms

One potential source of actinides (An) in the environment could be the accidental release from nuclear waste disposal sites. Microorganisms indigenous in potential host rocks are able to influence the speciation and therefore the mobility of An and their retardation both by direct and indirect pathways. They can as well affect the conditions in a geologic repository (e.g., by gas generation or canister corrosion). Currently salt, clay and granite are considered as potential host rocks for a nuclear waste disposal in Germany. Microorganisms are indigenous present in such subterranean environments and it was demonstrated that they can affect the speciation and hence the mobility of actinides (e.g., Lloyd and Gadd, 2011; Swanson et al., 2012; Lütke et al., 2013; Wouters et al., 2013; Moll et al., 2014). The Opalinus Clay layer of the Mont Terri Underground Rock Laboratory (Switzerland) is one potential host rock tested for nuclear waste disposal (Thury and Bossart, 1999). Recently, indigenous bacteria were isolated from Mont Terri Opalinus Clay and its interactions with uranium, europium and curium were investigated (Lütke et al., 2013; Moll et al., 2014). A couple of investigations (Panak and Nitsche, 2001; Neu et al., 2005; Moll et al., 2006; Renshaw et al., 2009; Ohnuki et al., 2009) documented the manifold impact of bacteria on the speciation of plutonium. Plutonium can coexist in different oxidation states under environmental conditions which makes interaction studies in biological systems challenging. Therefore, the interactions of the bacterial isolates from Mont Terri Opalinus Clay were investigated more in detail (cf. 3.1).

In salt rock, another potential host rock for nuclear waste disposal, in addition to bacteria and fungi, archaea are dominating the indigenous microbial community (McGenity et al., 2000; Stan-Lotter and Fendrihan, 2015) as shown in the Waste Isolation Pilot Plant in Carlsbad, New Mexico, USA (Swanson et al., 2012). To date, only a few studies have evaluated the interactions of halophilic microorganisms with uranium (Francis et al., 2000 and 2004) and other actinides (Gillow et al., 2000; Ozaki et al., 2004; Ams et al., 2013) at high ionic strength. Recently, an extremely halophilic archaeon namely *Halobacterium* (*Hbt*.) sp., putatively *noricense* (WIPP strain) was isolated from the WIPP site (Swanson et al., 2012). Its closest phylogenetic relative *Halobacterium noricense* DSM-15987 was originally isolated from a salt mine in Austria (Gruber et al., 2004). Within this project, first experiments were performed to study the adsorption of uranium(VI), europium(III), and curium(III) on the halophilic archaeon *Halobacterium noricense* DSM-15987 (cf. 3.2).

3.1 Interaction of Pu with bacterial isolates from Mont Terri Opalinus Clay

In this study, the unknown interactions between bacteria, isolated from Mont Terri Opalinus Clay core samples, namely *Sporomusa* sp. MT-2.99 and *Paenibacillus* sp. MT-2.2 cells and Pu were explored in aqueous solution under anaerobic conditions.

The Pu interaction experiments performed are the continuation of our first study with the Mont Terri Opalinus Clay bacterial isolates within the BMWi-project 02E10618 “Mikrobielle Diversität im Tongestein (Opalinus-Ton) und Wechselwirkung dominanter Mikroorganismen

mit Actiniden" (Moll et al., 2013). In Moll et al. (2013) we could only investigate the Pu interaction with *Sporomusa* sp. MT-2.99 cells at one pH value of 6.1 in 0.1 M $NaClO_4$ without adding an electron donor. These first experiments could be extended in order to get a more comprehensive overview of the interaction potential of our bacterial isolates namely *Sporomusa* sp. MT-2.99 and *Paenibacillus* sp. MT-2.2 towards Pu. The experiments can be divided in experiments without an electron donor where biosorption is favored and in experiments adding Na-pyruvate as an electron donor stimulating also bioreduction processes.

Experimental: Pu biosorption, solvent extraction

Sporomusa sp. MT-2.99 and *Paenibacillus* sp. MT-2.2 cells were cultured anaerobically in R2A medium at 30°C. Cells were harvested in the mid-exponential growth phase, washed and suspended in 0.9 % NaCl solution containing 10^{-4} M Na-pyruvate. The details of strain isolation, cultivation and characterization are summarized in (Moll et al., 2013).

The starting compound to obtain the ^{242}Pu stock solution was a green-brown powder of PuO_2 (AEA technology QSA GmbH) with the following composition: 0.009 % of Pu-238, 0.008 % Pu-239, 0.020 % Pu-240, 0.017 % Pu-241, 99.945 % Pu-242, and 0.001 % Pu-244. The problem is that this substance is chemically highly inert and dissolves extremely slowly in acids (Keller, 1971). We performed an oxidative dissolution of $^{242}PuO_2$ in HNO_3 in the presence of $AgNO_3$ and $K_2S_2O_8$. Finally, the ^{242}Pu(VI) stock solution in 3 M $HClO_4$ was prepared by electrolysis. Because of the low absorption coefficients of Pu(IV), Pu(V), and Pu(IV)-polymers (Keller, 1971; Wilson et al., 2005; Ockenden and Welch, 1956) and the low concentration of Pu in the solutions, the quantification of the different Pu oxidation states was performed by solvent extraction as described in (Moll et al., 2006). The extractions were performed rapidly and in parallel. All plutonium concentrations were measured by liquid scintillation counting (LSC) using a LS counter, Wallac system 1414 (Perkin Elmer). For this, defined sample volumes (50 to 300 µL) were mixed with 5 mL of Ultima Gold scintillation cocktail. The solvent extraction experiments demonstrated that the acidic Pu stock solution still contained, besides 70 % Pu(VI), 21 % Pu(IV)-polymers due to the synthesis procedure.

The pH was measured using an InLab Solids electrode (Mettler-Toledo, Giessen, Germany) calibrated with standard buffers and a pH meter (Microprocessor pH Meter pH 537, WTW, Weinheim, Germany). The pH was adjusted with a precision of 0.05 units. The pH adjustments were made with $HClO_4$ or NaOH both from Merck, Germany. The redox potential in blanks and cell suspensions was measured using a combination redox electrode (BlueLine 31 Rx from Schott, Germany) by applying the single point calibration using a redox buffer.

The adsorption of Pu onto the reaction vessel as source of error was investigated. Therefore after the Pu interaction experiments the reaction tubes were rinsed 3 times with Milli-Q water and then incubated for 2 days with 1 M $HClO_4$ to desorb Pu. Solutions where then analyzed with LSC regarding [Pu]. The determined loss of Pu was accounted for the calculation of, for instance, the amount of Pu bound per g dry biomass.

The Pu-bacteria interaction experiments were performed at [dry biomass] of 0.33 ± 0.01 $g_{dry\ weight}$/L and pH values of 3, 4, 6.1 and 7 under N_2 atmosphere at 25°C in 0.1 M $NaClO_4$ solution. $[^{242}Pu]_{initial}$ was varied between 0.2 and 110 mg/L. For the *Paenibacillus*-system selected pH values (4 and 6) were investigated. In the *Sporomusa*-system, Na-pyruvate as one potential electron donor was added in two concentrations (0.1 and 10 mM) at pH 6.1. At pH 4 only one Na-pyruvate concentration (10 mM) was added. For *Paenibacillus* sp. cells the influence of 10 mM Na-pyruvate on the time-dependent Pu oxidation state distribution was investigated at pH 6.1. The ^{242}Pu present in blank (no cells added), supernatant, and washed biomass suspension at pH 0 was analyzed using solvent extraction, and LSC as described in (Moll et al., 2006). Samples were taken after defined time steps. The separation of cells from the supernatant solution was performed by centrifugation (6000*g*).

Accumulation of plutonium (^{242}Pu) by *Sporomusa* sp. and *Paenibacillus* sp. as a function of pH and the initial Pu concentration under anaerobic conditions – no electron donor

The decrease of Pu concentration in the supernatant after contact with the cells of both strains is shown in Fig. 9.

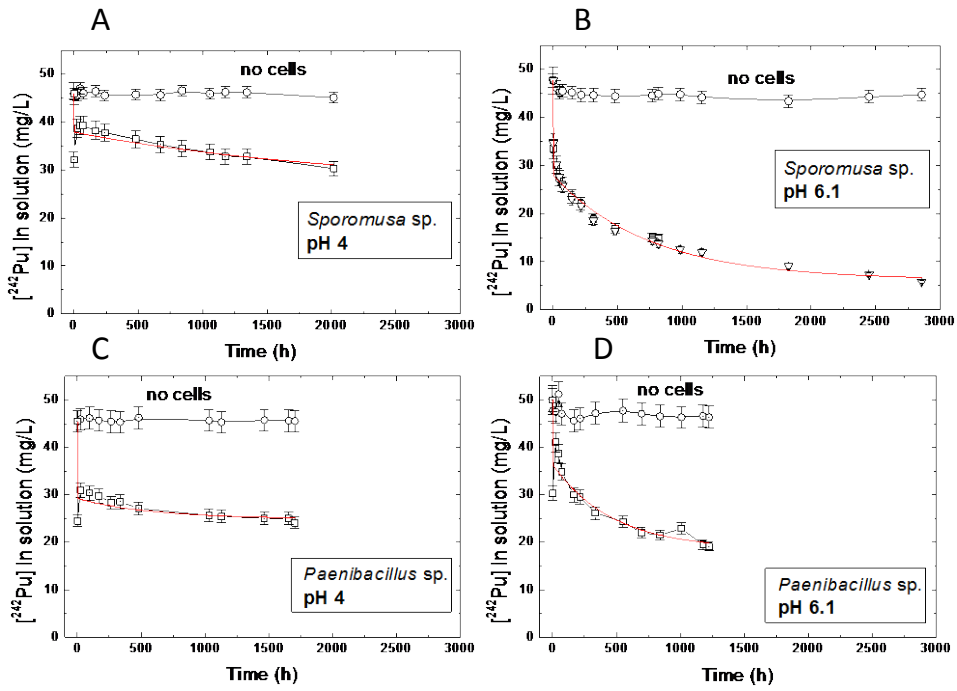

Fig. 9: Decrease of $[^{242}Pu]$ in solution at $[^{242}Pu]_{initial}$: 46 mg/L in 0.1 M $NaClO_4$ at pH 4 and 6.1 after contact with 0.33 $g_{dry\ weight}$/L of (A, B) *Sporomusa* sp. MT-2.99 and (C, D) *Paenibacillus* sp. MT-2.2. The red line represents the best fit of the experimental data.

In general, more Pu was removed at pH 6.1 compared with the results measured at pH 4.0. The time-dependent behavior of Pu in the supernatants was bi-exponential fitted ($y = y_0 + A_1\, e^{-(x/t1)} + A_2\, e^{-(x/t2)}$). The kinetic fits showed that the overall process consists of at least two parts: a fast process having a time frame of ~ 0.5 h (e.g., biosorption) and a much

slower process with a time frame of ~ 1000 h. We observed an increased amount of Pu at contact times > 300 h. This could be interpreted by a larger Pu binding capacity of the dead biomass. It seems that *Paenibacillus* has a slightly different strategy to avoid the stress caused by Pu. After 2 h of contact time (cf. Fig. 9 C, D) the cells released 40 % of this bound Pu. At incubation times ≥ 24 h an exponential decrease of the Pu concentration in solution was detected. This behavior was observed in all experiments performed as a function of the initial Pu concentration. A similar effect (but less pronounced) was observed in the *Sporomusa* sp. experiments at pH 4 at the two highest initial Pu concentrations (46 and 111 mg/L, Fig. 9 A).

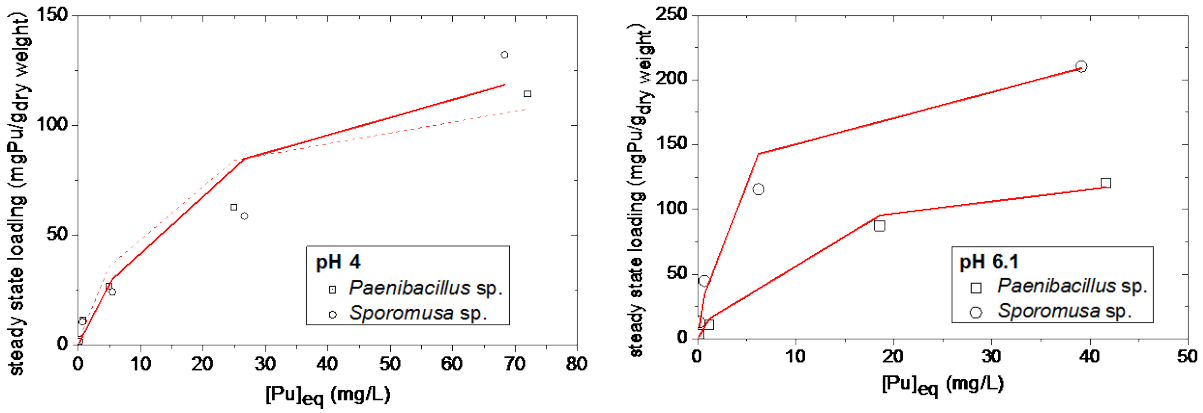

Fig. 10: Langmuir isotherms obtained in the *Sporomusa* sp. and the *Paenibacillus* sp. system at pH 4 and 6.1.

The biosorption of Pu on both strains was evaluated using the Langmuir absorption isotherm model. The application of the Langmuir-isotherm model in order to describe the biosorption of heavy metals in biological systems (e.g., biosorption of heavy metals on algae) was reported for instance in (Klimmek, 2003). The Langmuir constant b describes the affinity of the adsorbed metal to the bacterial surface (Kümmel and Worch, 1990; Atkins, 1998).

Table 5: Langmuir absorption isotherm data.

Strain	pH	a_m (mgPu/g)	b (L/mg)	R^2
Sporomusa sp.	4.0	160±46	0.043±0.011	0.730
	6.1	230±14	0.268±0.08	0.989
Paenibacillus sp.	4.0	130±21	0.081±0.04	0.892
	6.1	140±21	0.108±0.04	0.934

As depicted in Fig. 10 and Table 5 the Langmuir model could describe the experimental data with both strains and at both pH values with a reasonable quality. The sorption experiments showed that *Sporomusa* sp. cells are more effective in removing Pu from the surrounding solution. This effect is more pronounced at longer contact times. *Paenibacillus* sp. cells are accumulating less Pu. At pH 6.1 the maximal Pu loading on *Sporomusa* sp. cells was calculated to be 230 mgPu/g compared to 140 mgPu/g for *Paenibacillus* sp. cells. Panak and

Nitsche (2001) reported that aerobic soil bacteria accumulated ca. 45 mgPu/$g_{dry\ weight}$. This shows that *Sporomusa* sp. and also *Paenibacillus* sp. accumulated relatively high amounts of Pu.

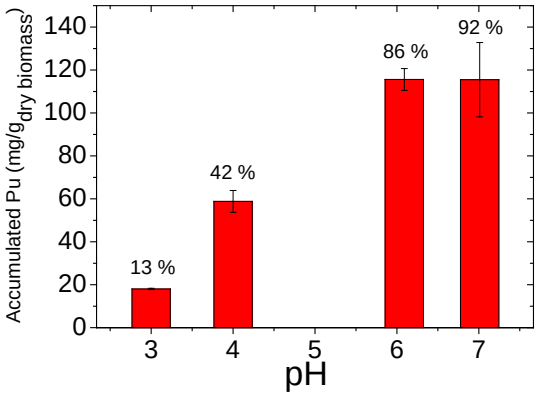

Fig. 11: Biosorption of Pu on *Sporomusa* sp. MT-2.99 at $[^{242}Pu]_{initial}$: 45 mg/L in 0.1 M $NaClO_4$ as a function of pH under steady state conditions.

Sporomusa sp. cells display a strong pH-dependent affinity for Pu (cf. Fig. 11). At pH 3, only 13 % of the initial Pu was accumulated whereas at pH 7, 90 % were associated with the biomass. The pH induced effect on the amount of biosorbed Pu was lower for *Paenibacillus* sp. cells.

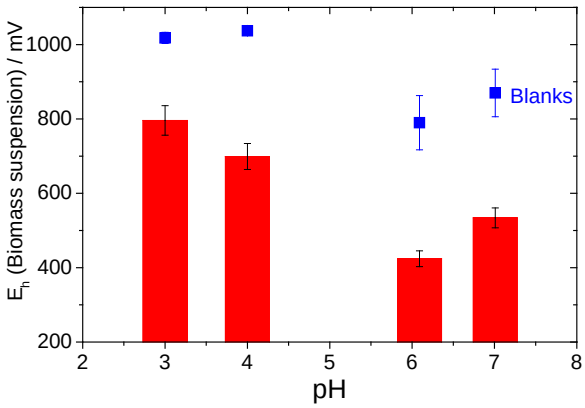

Fig. 12: Redox potentials in the *Sporomusa* sp. MT-2.99 system at $[^{242}Pu]_{initial}$: 45 mg/L in 0.1 M $NaClO_4$ as a function of pH under steady state conditions.

In the *Sporomusa* sp. system, the redox potential measurements indicated that the cells generated reducing conditions (cf. Fig. 12). The cell induced effect on the redox potential was highest at pH 6.1. Hence, the ability of the cells to decrease the redox potential seems to depend on the pH. At pH 6.1, in the blank sample at $t \geq 312$ h a redox potential of 790 ± 73 mV was measured. In the cell suspensions immediately a constant value of 331 ± 25 mV was reached. *Paenibacillus* sp. cells were less effective in minimizing the redox potential.

Desorption studies with 1 M $HClO_4$ showed that there was an incomplete Pu removal from the biomass. For both strains at $[Pu]_{initial}$ between 15 and 110 mg/L and independently of pH only 60 to 30 % of the Pu was released indicating irreversibly bound Pu.

Time-dependent Pu oxidation state distributions

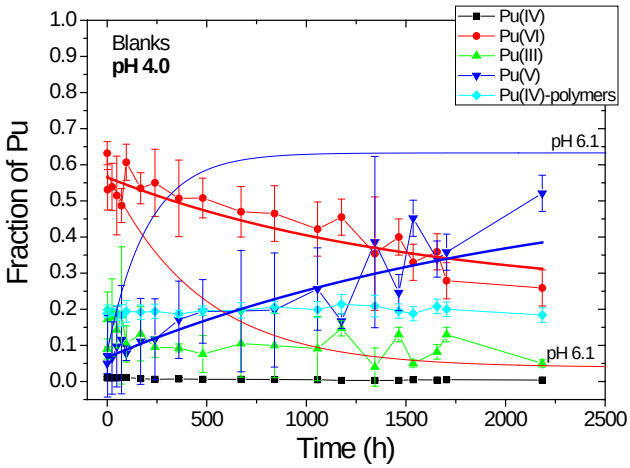

Fig. 13: ^{242}Pu oxidation state distributions in the blank samples determined by solvent extraction as a function of the incubation time ($[^{242}Pu]_{initial}$: 104±11 mg/L, 0.1 M $NaClO_4$, pH 4).

The blanks. The values depicted in Fig. 13 were averaged from three individual experimental runs. The relatively large errors of Pu(VI) and Pu(V) concentrations are the results of the averaging of the individual values from the different experimental runs. The error of the method is at largest 5 %. It reflects the temporally fluctuations of the abiotic reduction of Pu(VI) to Pu(V). In the beginning the dominating Pu species are Pu(VI), 58 ± 7 %, Pu(IV)-polymers, 19 ± 1 % and Pu(III), 13 ± 6 % (cf. Fig. 13). The time-dependent behavior of Pu(VI) and Pu(V) was mono-exponential fitted ($y = y_0 + A_1\, e^{-(x/t1)}$). By comparing the data at pH 6.1 with those at pH 4 one can conclude that the Pu redox chemistry is more reproducible at pH 4. The scattering of the data and hence the time-dependent decrease of Pu(VI) and the increase of Pu(V) is much less pronounced. The decrease of Pu(VI) at pH 6.1 is 3.2 times faster than at pH 4. The increase of Pu(V) at pH 6.1 is 3.3 times faster than at pH 4. It follows that a more acidic pH stabilizes Pu(VI). The Pu(IV)-polymer amount is with 19.6 ± 0.8 % constant within the investigated time range.

A significant change of the Pu oxidation state distributions was observed in the supernatants of both strains as shown in Fig. 14. At both pH values and for both strains a fast decrease of Pu(VI) combined with a fast increase of Pu(V) was observed. For a better comparison of the overall results the fitted Pu(VI) and Pu(V) concentrations measured at pH 6.1 were included in Fig. 14. At pH 6.1 in the *Sporomusa* sp. system the formation of Pu(V) in the supernatant is 48 times faster than in blank samples. The decrease of Pu(VI) in the supernatant is 28 times faster than in the blanks.

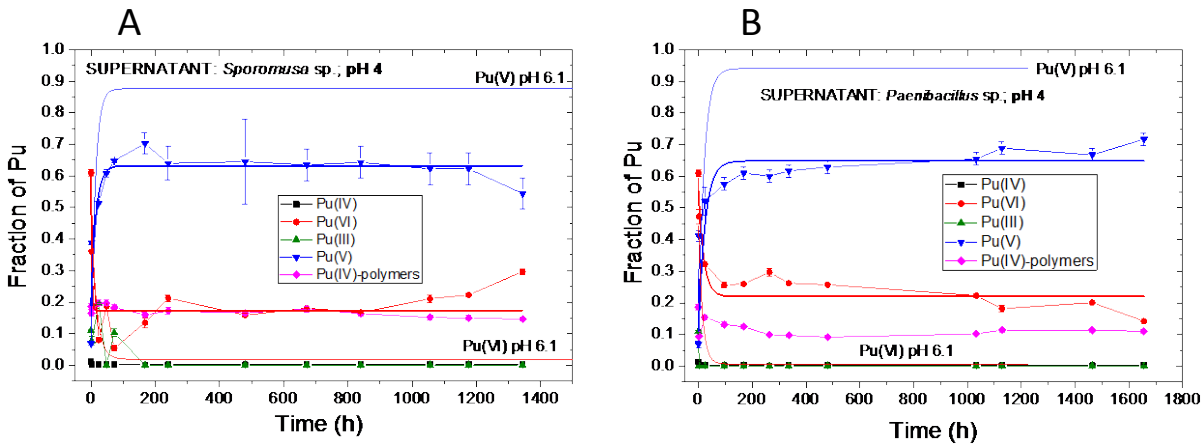

Fig. 14: ^{242}Pu oxidation state distributions in the supernatants after separation of the cells determined by solvent extraction as a function of time A) *Sporomusa* sp. and B) *Paenibacillus* sp. ([^{242}Pu]$_{initial}$: 111±2 mg/L, [dry biomass] 0.34 g/L, 0.1 M $NaClO_4$, pH 4).

At pH 6.1 in the *Paenibacillus* sp. system the formation of Pu(V) in the supernatant is only 30 times faster than in blank samples. The decrease of Pu(VI) in the supernatant is 31 times faster than in the blanks. The equilibrium concentration of Pu(V) in the supernatants of both strains is with ca. 90 % higher than in the blanks where 76 % were found. The difference between both strains is that in the *Sporomusa* sp. system the enrichment of Pu(V) in the supernatant was faster. At pH 4 in the *Sporomusa* sp. system the formation of Pu(V) in the supernatant is 144 times faster than in blank samples. The decrease of Pu(VI) in the supernatant is 626 times faster than in the blanks. The difference between both strains at pH 4 again is that in the *Sporomusa* sp. system the enrichment of Pu(V) (2 times) and the decrease of Pu(VI) (8 times) was faster compared to the *Paenibacillus* sp. system. The observed bioreduction process of Pu(VI) to Pu(V) by cells of *Sporomusa* sp. and *Paenibacillus* sp. is not yet fully understood. After the interaction the majority of the Pu(V) was detected in solution. We assume that this happens due to the comparable weak complexing properties of the PuO_2^+ ion which is related with a release from the cell envelope. Similar observations were made in the past (Panak and Nitsche, 2001; Moll et al., 2006; Moll et al., 2013). The formed Pu(V) is relatively stable after removing the cells from solution. At pH 6.1 for both strains the equilibrium concentration of the Pu(IV)-polymers was 6 % compared with 12.5 % found in the blanks. This suggests a pronounced biosorption of Pu(VI)-polymers on the biomass. At pH 4 similar results were observed for *Paenibacillus* sp. where 11 % Pu(IV)-polymers were measured in the supernatant compared with 20 % in the blanks. The average Pu(IV)-polymer concentration in the *Sporomusa* sp. supernatants was with 17 % higher showing a lower tendency to interact with cells.

Both strains showed no differences in the Pu-oxidation state distribution of the Pu associated on the biomass at pH 6.1 (cf. Fig. 15). The summary of all extraction data observed in the electron-donor free experiments with *Sporomusa* sp. and *Paenibacillus* sp. showed scattered concentration data of the individual plutonium oxidation states. However, a few trends can be seen.

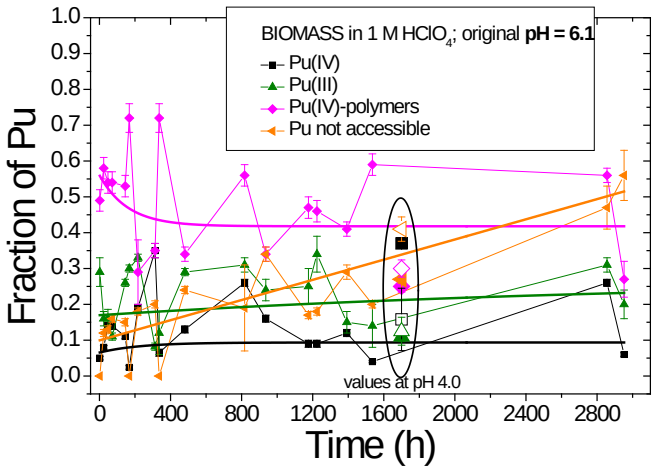

Fig. 15: ^{242}Pu oxidation state distributions in the biomass (*Sporomusa* sp. and P*aenibacillus* sp.) by solvent extraction over the time ([^{242}Pu]$_{initial}$: 15 to 110 mg/L, [dry biomass] 0.34 g/L, 0.1 M $NaClO_4$, pH 6.1 and 4).

The major oxidation state identified were Pu(IV)-polymers with an average amount of 42 %. The scattered data of Pu(IV)-polymers could be fitted to a mono-exponential decay function ($y = y_0 + A_1\ e^{-(x/t1)}$). The Pu(III) average amount of 27 % is clearly higher than found in the blanks and supernatant. There is a linear increase of Pu which was not accessible by the extraction technique. This plutonium could be masked for instance by an uptake in dead biomass. This amount of Pu can be also correlated with the amount of irreversibly bond Pu (*Sporomusa* sp.: 40-60 %; *Paenibacillus* sp.: ca. 30 %). The scattered values of Pu(IV) could be fitted to an exponential growth function ($y = y_0 + A_1\ e^{(x/t1)}$) giving an average concentration of 9 ± 2 %. This value is significantly higher compared to the findings in the blanks and supernatants of ca. 1 %. In general lower amounts of Pu(IV)-polymers, 34 %, were found at pH 4. This corresponds with higher concentrations of Pu(IV) (*Sporomusa* sp. are more effective in forming Pu(IV), 31 %, than *Paenibacillus* sp., 16 %). The other Pu oxidation states correspond well with the dependencies detected at pH 6.1.

Interaction of plutonium (^{242}Pu) with *Sporomusa* sp. and *Paenibacillus* sp. in the presence of an electron donor – 10 mM Na-pyruvate

The decrease of Pu concentration in the supernatant after contact with the cells of both strains applying 10 mM Na-pyruvate is shown in Fig. 16.

Sporomusa sp. system. At pH 4 the time-dependent behavior of Pu in the supernatants was bi-exponential fitted ($y = y_0 + A_1\ e^{-(x/t1)} + A_2\ e^{-(x/t2)}$) (cf. Fig. 16 A). The kinetic fits showed that the overall process consists of at least two parts: a fast process having a time frame of ~ 0.1 h (e.g., biosorption) and a much slower process with a time frame of ~ 120 h. We observed faster processes compared with the results at pH 6.1. At pH 6.1 the time-dependent decrease of Pu could be best fitted applying a mono-exponential decay law (cf. Fig. 16 B). This indicates one dominating step having a time frame of 8.3 h.

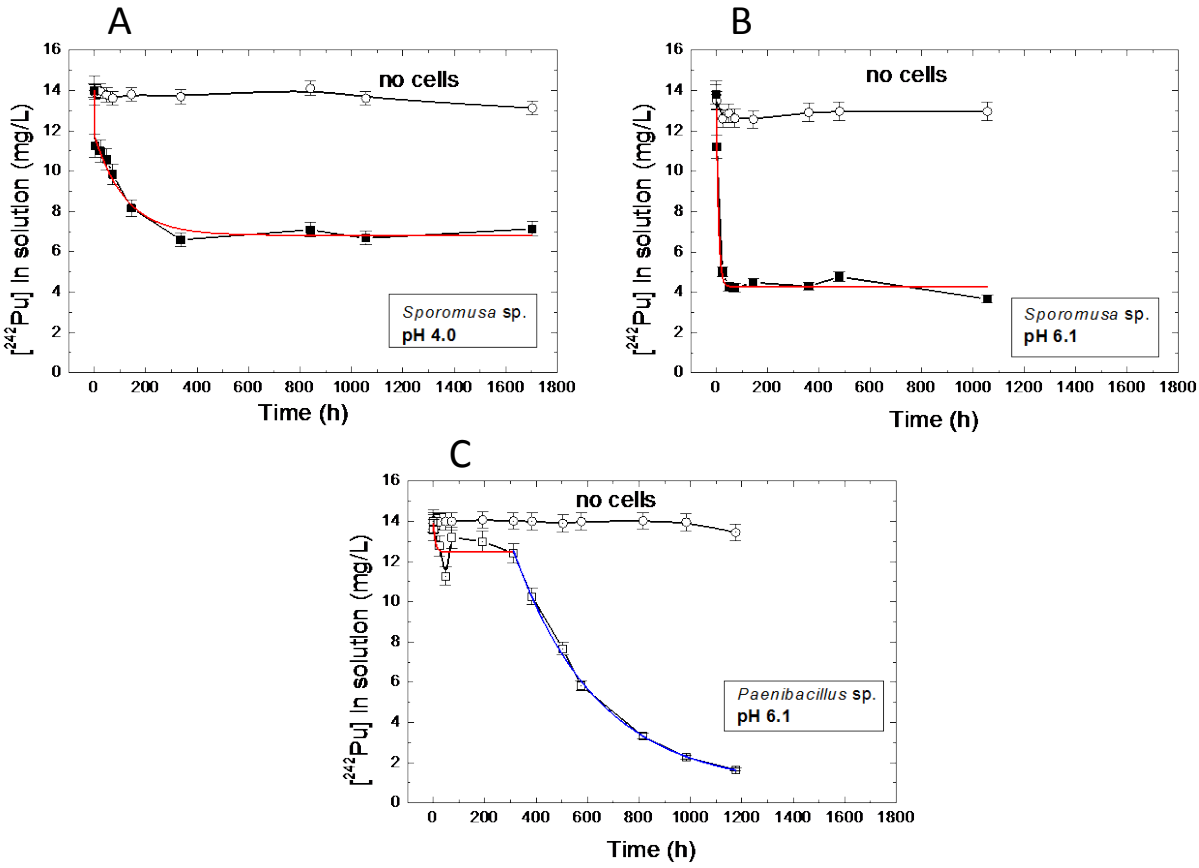

Fig. 16: Decrease of the [^{242}Pu] in solution at [^{242}Pu]$_{initial}$: 14 mg/L in 0.1 M $NaClO_4$ at pH 4 and 6.1 after contact with 0.34 g/L of (A, B) *Sporomusa* sp. MT-2.99 and (C) at pH 6.1 after contact with 0.22 g/L *Paenibacillus* sp. MT-2.2. The red and blue line represents the best fit of the experimental data.

Paenibacillus sp. system. The time-dependent decrease of the plutonium concentration in solution could only be fitted by dividing the time frame into two ranges and applying a mono-exponential law. Here the lack phase was longer compared to the 0.1 M $NaClO_4$ system (cf. Fig. 9 D). A continuous decrease of the plutonium in the cell surrounding solutions was observed first after 312 h of incubation. This underlines the finding in the 0.1 M $NaClO_4$ system except that the time frame is clearly longer than observed there with 24 h.

For *Sporomusa* sp. a comparison of the accumulated Pu in dependence of pH and Na-pyruvate concentration was done. The accumulated amount of Pu was calculated based on the fit of the Pu concentrations in solution. The results showed that with increasing Na-pyruvate concentration less Pu is associated on the biomass. Hence the cells displayed a higher affinity for Pu in the absence of an electron donor.

In the *Sporomusa* sp. system in contrast to the electron donor free experiments, we could measure that more than 80 % of the plutonium was released from the cells over the investigated time range at 10 mM Na-pyruvate at pH 6.1 (cf. Fig. 17).

Table 6: Pu loadings on *Sporomusa* sp. biomass at $[Pu]_{initial}$ = 14 mg/L.

Strain	pH	[Na-pyruvate] (mM)	Pu loading ($mgPu/g_{dry\ weight}$)
Sporomusa sp.	4.0	no	24.4
	4.0	10	20.5
	6.1	no	44.6
	6.1	0.1	41.9
	6.1	10	26.4

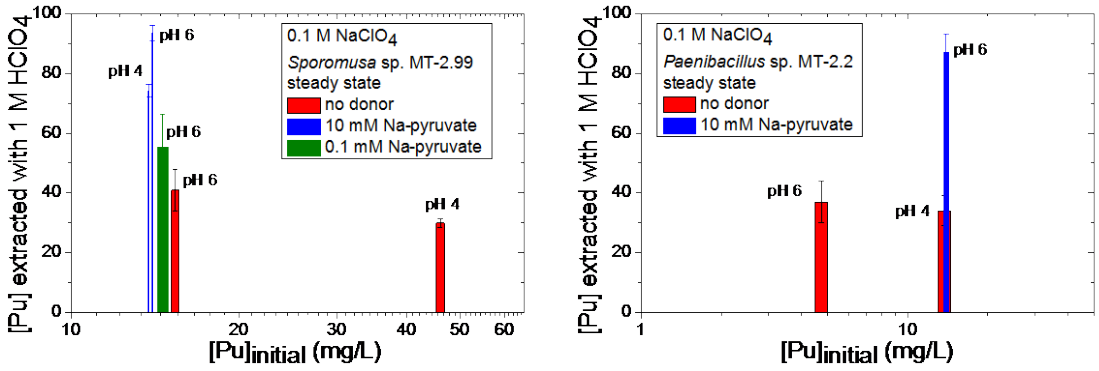

Fig. 17: Percentage of the cell bound Pu extracted from the biomass with 1 M $HClO_4$.

At pH 4.0 the value drops down to 74 %. However, this might indicate a dominant complexation/fixation of plutonium on functional groups located at the cell surface in the presence of 10 mM Na-pyruvate. Also for *Paenibacillus* sp. the majority (more than 80 %) of the plutonium could be dissolved from the cells pointing to a dominant surface complexation onto functionalities of the bacterial cell surface. In the case of *Sporomusa* sp. desorption experiments were performed as a function of the pyruvate concentration. The average amounts of extractable Pu from the cells at an initial Pu concentration of 14 mg/L were: 41 ± 7 % no donor, 55 ± 11 % 0.1 mM pyruvate, and 93 ± 3 % 10 mM pyruvate at pH 6. In the absence of an electron donor at pH 4 the average amount of extractable Pu from the biomass was in the same region (ca. 35 %) as observed for pH 6 for both strains. In the presence of 10 mM Na-pyruvate for both strains and independent of pH always more than 70 % of the Pu could be extracted from the biomass. It seems that increased concentrations of pyruvate increase also the contribution of a reversible surface complexation of Pu on the bacterial cell surface.

Between 2 and 144 h we measured lower redox potentials in the cell suspensions compared to the blanks at pH 4 (cf. Fig. 18). After 336 h similar redox potentials in blank and cell suspensions were measured. The average redox potential in blank solutions (144 to 1704 h) was 471 ± 18 mV. In the cell suspensions immediately a constant value of 477 ± 7 mV was reached. In the blank sample the redox potential drops slowly from 490 mV to 200 mV after 144 h of contact time and was than with 180 ± 18 mV nearly constant. In the cell suspensions immediately a drop in the redox potential to 284 mV was detected. Very quickly a constant value (24 to 1056 h) of 190 ± 10 mV was reached. After 360 h similar redox potentials

were measured in the blank and the cell suspensions. Both the pH and the Na-pyruvate are influencing the redox potential.

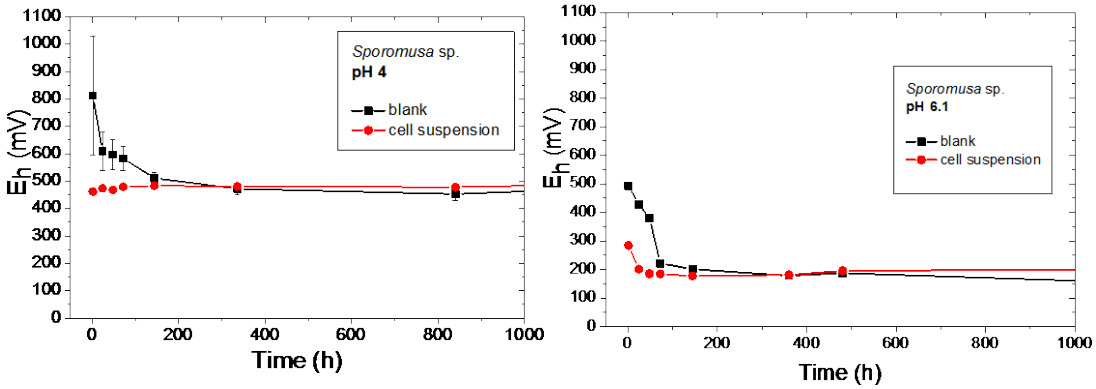

Fig. 18: Time-dependent redox potentials measured in the *Sporomusa* sp. system in the presence of 10 mM Na-pyruvate at pH 4 and pH 6.1 ($[Pu]_{initial}$ = 14 mg/L, 0.1 M $NaClO_4$).

Paenibacillus sp. cells are less effective in decreasing the redox potential in the presence of 10 mM Na-pyruvate (data not shown). To conclude, the cell induced effect on the redox potential is smaller in the presence of 10 mM Na-pyruvate.

Time-dependent Pu oxidation state distributions

Compared to the pyruvate-free system (cf. Fig. 13) a complicated Pu redox-chemistry was observed due to the reducing properties of pyruvate as depicted in Fig. 19.

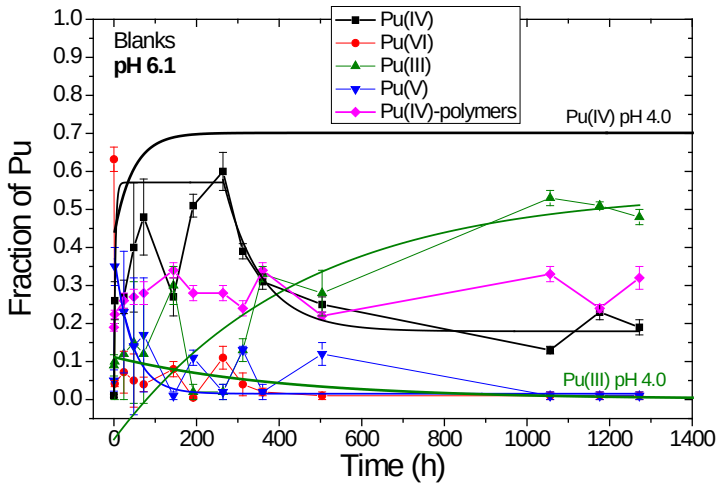

Fig. 19: ^{242}Pu oxidation state distributions in the blank samples determined by solvent extraction as a function of the incubation time ($[^{242}Pu]_{initial}$: 13.8±0.5 mg/L, 0.1 M $NaClO_4$, 10 mM Na-pyruvate, pH 6.1).

At pH 6.1 and 4 a fast abiotic reduction of Pu(VI) was observed. At pH 6.1 within the first 1.2 h the amount of Pu(VI) decreased from 61 to about 4 %. Whereas after 2 h almost no Pu(VI) could be detected at pH 4. At both pH values simultaneously Pu(V) and Pu(IV) increased to about 31 % (22 % at pH 4) and 22 % (45 % at pH 4), respectively. Due to the pH

of 6.1, we observed also an increase of Pu(IV)-polymers from 19 % in the beginning to about 34 % at the end of the experiment. This could be explained by a transfer of the formed Pu(IV) into Pu(IV)-polymers. At pH 4 the Pu(IV)-polymer fraction remained constant at 27.0 ± 2.9 %. Pu(V) was abiotically reduced to Pu(IV) due to the presence of pyruvate. Later on (t ≥ 144 h) we observed an increase of Pu(III) in combination with an decrease of Pu(IV) at pH 6.1. This might indicate a further reduction of Pu(IV) forming Pu(III). Hence to model the Pu(IV) behavior at pH 6 the data were split into two time ranges. First there was an exponential growth of Pu(IV) followed by an exponential decrease. In contrast at pH 4, there was an exponential growth of the Pu(IV) fraction with a steady state concentration of 70 % (major difference between both pH values). A further difference was the behavior of Pu(III). At pH 6.1 an exponential growth with an equilibrium concentration of 55 % was calculated. Whereas at pH 4 for Pu(III) an exponential decay with very low (0.1 %) equilibrium concentrations were found.

At the beginning at pH 6.1, the major oxidation states (complexed with pyruvate) interacting with the biomass are Pu(V) with 31 %, Pu(IV) with 22 %, and Pu(IV)-polymers with 23 %. At the beginning at pH 4, the major oxidation states (complexed with pyruvate) interacting with the biomass are Pu(IV) with 39 %, Pu(V) with 20 %, and Pu(IV)-polymers with 24 %.

Differences between the time-dependent Pu oxidation state distributions in the supernatant at pH 6.1 between both strains were detected (cf. Fig. 20).

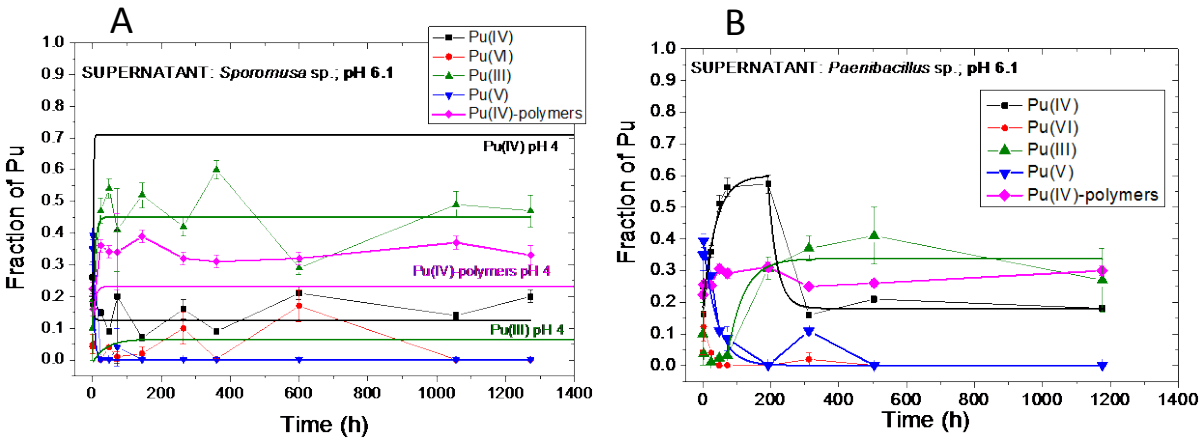

Fig. 20: ^{242}Pu oxidation state distributions in the supernatants after separation of the cells determined by solvent extraction as a function of time A) *Sporomusa* sp.: [dry biomass] 0.34 g/L at pH 4 and 6.1 and B) *Paenibacillus* sp.: [dry biomass] 0.22 g/L at pH 6.1 ($[^{242}Pu]_{initial}$: 14 mg/L, 0.1 M $NaClO_4$, 10 mM Na-pyruvate).

In the *Paenibacillus* experiment for the individual Pu oxidation states in the supernatants similar trends were observed as in the blanks. One reason could be the lower reducing properties of *Paenibacillus* sp. as indicated by the redox potential measurements compared to the *Sporomusa* sp. findings. At pH 6.1 the time-dependent behavior of Pu(III), Pu(IV), and Pu(V) was calculated with mono-exponential growth or decay functions except for Pu(IV) in the *Paenibacillus* experiment. The Pu(IV) data were split into two time ranges. First there was an mono-exponential growth followed by an exponential decrease of Pu(IV). At pH 6.1 in the

Sporomusa sp. system the formation of Pu(III) as the major oxidation state in the supernatant is 68 times faster than in blank samples. The decrease of Pu(IV) in the supernatant is 9 times faster than in the blanks. The decrease of Pu(V) is 35 times faster than in the blank samples. Under steady state conditions similar concentrations of Pu(III) (~50 %), Pu(IV) (~15 %), and Pu(V) (~1 %) were measured in blanks and the *Sporomusa* sp. supernatants. As a difference in the *Paenibacillus* sp. experiment slower processes than in the *Sporomusa* sp. supernatants were measured. At pH 6.1 Pu(III) was major Pu oxidation state in the blanks (55 %), the *Sporomusa* sp. supernatants (45 %), and the *Paenibacillus* sp. supernatants (34 %). At pH 4 in the *Sporomusa* sp. system a clear enrichment of Pu(IV) was observed. The main differences (influence of the cells) compared to the blanks are a faster increase of Pu(IV) (33 times), a slight increase of Pu(III) and slightly lower concentration of Pu(IV)-polymers (23.2 %). The equilibrium concentration of Pu(III) was with 6.5 % higher as in the blank (0.1 %).

The Pu oxidation state distributions of the Pu associated on the biomass under addition of 10 mM Na-pyruvate are summarized in Fig. 21.

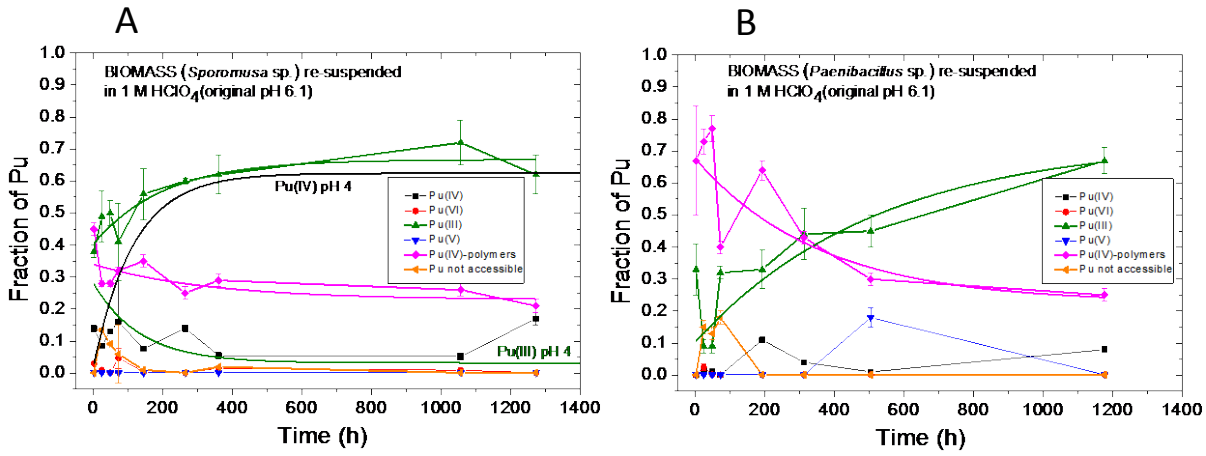

Fig. 21: ^{242}Pu oxidation state distributions in the biomass (*Sporomusa* sp. 0.34 g/L and P*aenibacillus* sp. 0.22 g/L) by solvent extraction over the time ($[^{242}Pu]_{initial}$: 14 mg/L, 0.1 M $NaClO_4$, 10 mM Na-pyruvate, pH 6.1 and 4 (only for *Sporomusa* sp.).

At pH 6.1 there was a clear enrichment of Pu(III) in the biomass in the presence of 10 mM Na-pyruvate (Fig. 21). Pu(IV)-polymers associated on biomass dominated in 0.1 M $NaClO_4$ (Fig. 15). The formation of Pu(III) was in the *Sporomusa* sp. system three times faster than in the *Paenibacillus* sp. system. In both cases similar steady state concentrations of 70 ± 4 % were observed. This amount is three times higher than in the electron donor free system. In the presence of Na-pyruvate, the Pu(IV)-polymer concentration in the biomass yielded lower steady state concentrations than in the electron donor free experiments. Therefore, we assume a transfer of Pu(IV)-polymers into Pu(III) promoted by pyruvate and surface functional groups of the cell surface. From the pyruvate concentration-dependent experiments one can conclude that 0.011 g/L pyruvate has a similar influence on the Pu redox chemistry as 0.33 g/L *Sporomusa* sp. MT-2.99 cells. For *Sporomusa* sp. the time-dependent behavior of the fractions Pu(V), Pu(VI), Pu not accessible, and Pu(IV)-polymers is comparable at both pH

values. The decrease of the Pu(IV)-polymer amount is approximately 4 times faster at pH 6.1 compared to pH 4. The equilibrium amount is with 23.5 % equal for both pH values. The main difference (as also observed in the blank and the supernatants) is an enrichment of Pu(IV) on the biomass at pH 4. Whereas at pH 6.1 Pu(III) was enriched.

Summary of the plutonium (^{242}Pu) interaction studies with *Sporomusa* sp. and *Paenibacillus* sp.

In this study, the interaction of Pu with two bacterial isolates, *Sporomusa* sp. and *Paenibacillus* sp., from Mont Terri Opalinus Clay was investigated in 0.1 M $NaClO_4$ as a function of the initial Pu concentration, the pH, and with and without adding Na-pyruvate as one potential electron donor. The decrease of the Pu concentration in the supernatants was bi-exponential fitted. The calculations showed that the overall process consists of at least two parts: a fast process having a time frame of ~ 0.5 h (e.g., biosorption) and a much slower process with a time frame of ~ 1000 h. In the electron donor containing system faster kinetics especially for the *Sporomusa* sp. were found. It seems that *Paenibacillus* has a slightly different strategy to avoid the stress caused by Pu. After 2 h of contact time the cells released 40 % of this bound Pu. At contact times ≥ 24 h an exponential decrease of the Pu concentration in solution was detected. This phase of the release of biosorbed Pu from the cells was prolonged in the presence of 10 mM Na-pyruvate. At pH 6.1 in the presence of 10 mM Na-pyruvate in the *Sporomusa* sp. system a mono-exponential decrease of Pu was found in the supernatant. The isolates displayed a strong pH-dependent affinity for Pu. Using the Langmuir model the maximal Pu loading at pH 6.1 on *Sporomusa* sp. and *Paenibacillus* sp., 230±14 and 140±21 mgPu/$g_{dry\ biomass}$, respectively, were calculated. This shows that *Sporomusa* sp. is more efficient in removing Pu from the surrounding solution. The maximal loadings are high compared to literature values (e.g., Panak and Nitsche, 2001). Desorption studies with 1 M $HClO_4$ showed that in the electron donor free samples only 60 to 40 % of the Pu was released indicating irreversibly bound Pu. In the presence of 10 mM Na-pyruvate more than 80 % of the Pu was released indicating a higher amount of reversible sorption reaction of Pu onto the cell surface. The redox potential measurements indicated that the cells generated reducing conditions. *Paenibacillus* sp. cells were less effective in minimizing the redox potential. The cell induced effect on the redox potential is smaller in the presence of 10 mM Na-pyruvate. In the pure $NaClO_4$ solutions a strong enrichment of Pu(V) in the supernatants was discovered. In the *Sporomusa* sp. system the formation of Pu(V) was 48 times faster than in blanks. In the *Paenibacillus* sp. system the enrichment of Pu(V) and the subsequent decrease of Pu(VI) was slower but still faster than in blanks. The Pu(V) was surprisingly stable in the bacterial suspensions. At pH 4 the enrichment of Pu(V) was less strong and also higher remaining Pu(VI) concentrations in the supernatants were measured. This might indicate a lower reducing impact of the cells at pH 4. No differences between both strains were observed regarding the Pu oxidation state distributions in the acidified biomass suspensions if no electron donor was previously added. The major Pu oxidation state was Pu(IV)-polymers with an average amount of 42 %. A change of the Pu oxidation state distributions in blanks, supernatants, and acidified biomass suspensions was observed in the presence of 10 mM Na-pyruvate. Also the pH influenced the Pu oxidation state distributions. At pH 6.1 for *Sporomusa* sp. an enrichment of Pu(III) was detected in the supernatant. This process was 68 times faster than in blanks. As a difference between both strains slower processes (Pu(III)

increase, Pu(IV)- and Pu(V) decrease) were measured in the *Paenibacillus* sp. system. At pH 6.1 Pu(III) was major Pu oxidation state in the blanks (55 %), the *Sporomusa* sp. supernatants (45 %), and the *Paenibacillus* sp. supernatants (34 %). At pH 4 in the *Sporomusa* sp. system a clear enrichment of Pu(IV) was observed. In contrast to the experiments in pure $NaClO_4$ solution, in the presence of 10 mM Na-pyruvate an enrichment of Pu(III) at pH 6.1 and of Pu(IV) at pH 4 was observed in the acidified biomass suspensions. This might indicate bio-reduction processes taking place. At pH 6.1 again the observed processes (decrease of Pu(IV)-polymers and increase of Pu(III)) were faster in the presence of *Sporomusa* sp. cells compared with *Paenibacillus* sp. cells. Hence, at a fixed concentration of Na-pyruvate of 10 mM the cell induced impact on the Pu oxidation state distributions depends on pH. To conclude, a moderate to strong impact of *Sporomusa* sp. and *Paenibacillus* sp. cells on the Pu speciation was observed. Differences in the Pu interaction process of both strains for instance depend on the presence or absence of an electron donor were detected.

3.2 Eu(III), Cm(III), and U(VI) interaction with the halophilic archaeon *Halobacterium noricense* (DSM-15987)

3.2.1 General remarks

Cultivation of Halobacterium noricense DSM-15987

The archaeon *Halobacterium noricense* DSM-15987 was ordered from the Leibniz Institute DSMZ-German Collection of Microorganisms and Cell cultures and cultivated in DSM-Medium 372 at 30°C. The strain was originally isolated from a salt mine in Austria (Gruber et al., 2004). The cells were grown up to exponential growth phase (OD_{600} of 0.5) for 4 days and harvested by centrifugation at 10.000 g for 10 min. To study the interactions of *Hbt. noricense* DSM-15987 with lanthanides and actinides, the cell pellet was washed three times and resuspended in 3 M NaCl solution. The biomass of the cell stock suspension was determined by measuring the OD_{600} which was then converted to the dry biomass.

Correction of the pH value at high ionic strength

Due to the high ionic strength the measured pH value corresponds not to the real hydrogen ion activity. For the microbiological studies the method described by (Ams et al., 2013) was used to correct the hydrogen ion concentration:

$$pC_{H+} = \text{pH measured} + K \quad (3.1)$$

There is a linear relationship between the ionic strength I and K, so that K can be calculated with the following equation.

$$K = (0.1868 \times I) - 0.073 \quad (3.2)$$

For a 3 M NaCl solution the measured pH value has to be corrected by the factor of 0.49.

3.2.2 Eu(III)/Cm(III)

The Eu(III)/Cm(III) experiments performed in the present project were planned as preliminary investigations to get a first insight on possible speciation changes of Eu(III)/Cm(III) in suspensions of the halophilic archaeon *Halobacterium noricense*. This organism requires high salt concentrations. Hence the speciation experiments using time-resolved laser-induced fluorescence spectroscopy (TRLFS) were performed in 3 M NaCl. Experiments were conducted at a fixed metal ([Eu] 30 µM, [Cm] 0.3 µM) and biomass concentration of 0.5 g/L as a function of pC_{H+}. The results will be compared with those measured in the presence of the bacterium *Sporomusa* sp. from Mont Terri Opalinus Clay (Moll et al., 2013; Moll et al., 2014). The investigations on the interaction of *Hbt. noricense* with Eu(III)/Cm(III) will be complemented by the HZDR Young Investigator Group MicroSalt.

In the past many spectroscopic investigations have demonstrated that the characteristic luminescence emission band of Cm^{3+} at 593.7 ± 0.1 nm is sensitive to changes in its first coordination sphere. The corresponding luminescence spectrum of Eu^{3+} is characterized by emission bands at 585-600 nm and 610-625 nm representing the magnetic dipole transition $^5D_0 \rightarrow {}^7F_1$ and the hypersensitive transition $^5D_0 \rightarrow {}^7F_2$, respectively (e.g., Plancque et al., 2003; Bünzli and Piguet, 2005; Heller et al., 2012). In contrast to curium, changes in the first coordination sphere of europium leads rather to a change in the intensity of the hypersensitive transition $^5D_0 \rightarrow {}^7F_2$ than in a wavelength shift of the emission maxima. Hence, this technique can be successfully used as a direct speciation method to explore Cm^{3+} and Eu^{3+} complex formation in the µM concentration range (e.g., Collins et al., 2011). Available experimental data until 2006 on the speciation of Cm(III) investigated by TRLFS were compiled by Edelstein et al. (2006). Compared to processes involving inorganic and organic ligands, little is known about the direct speciation of Cm(III) with halophilic microorganisms (e.g., Ozaki et al., 2004). Hitherto there is no literature source available on the Cm(III)/Eu(III) interaction with a *Halobacterium noricense* strain, whereof a phylogenetic closely related strain was isolated from the Waste Isolation Pilot Plant in Carlsbad, New Mexico, USA (Swanson et al., 2012).

Experimental: Preparation of Cm(III)/Eu(III) microbe solutions, TRLFS: experimental setup and evaluation of spectra

The cultivation of *Halobacterium noricense* DSM-15987 was already explained under 3.2.1.

A stock solution of the long-lived curium isotope ^{248}Cm (half-life: 3.4×10^5 years) was used. This solution had the following composition: 97.3 % ^{248}Cm, 2.6 % ^{246}Cm, 0.04 % ^{245}Cm, 0.02 % ^{247}Cm, and 0.009 % ^{244}Cm in 1.0 M $HClO_4$. $EuCl_3 \bullet 6H_2O$ (99.999 %) was purchased from Sigma. An Eu(III) stock solution, 0.01 M, was prepared by dissolving $EuCl_3$ in water. The exact concentration was determined by ICP-MS (Elan 6000, Perkin Elmer). The experiments were performed in a glove box under a N_2 atmosphere at 25°C. As a background electrolyte, analytical grade 3 M NaCl (Sigma-Aldrich, Germany) was used. To prevent the carbonate complexation of Cm(III) and Eu(III), carbonate-free water and NaOH solutions were used. The pH was measured using an InLab Solids combination pH puncture electrode (Mettler-Toledo, Giessen, Germany) calibrated with standard buffers. The pH was changed by

adding analytical grade NaOH or HCl with an accuracy of ± 0.05 units. The measured pH was corrected for 3 M NaCl by the factor 0.49 to get the real hydrogen ion activity pC_{H+} (cf. 3.2.1). For the Eu(III) measurements appropriate amounts of the concentrated cell suspension were centrifuged and the pellet was re-suspended in the corresponding blank solution with the required pC_{H+} containing 30 µM Eu in 3 M NaCl. Two series of experiments were performed at 30 µM Eu^{3+} and at [dry biomass] 0.5 g/L to explore its interaction behavior with *Hbt. noricense*, while varying the pC_{H+} between 4.0 and 8.0. In one run cells and supernatants were separated by centrifugation and analyzed for [Eu] by ICP-MS. Three series of experiments were performed at 0.3 µM Cm^{3+} and at [dry biomass] 0.5 g/L to explore its interaction behavior with *Hbt. noricense*, while varying the pC_{H+} between 4.0 and 8.0. All TRLFS spectra were measured after an equilibration time of 1 h. The pC_{H+}-dependent TRLFS spectra of the Cm(III)/Eu(III) containing *Hbt. noricense* suspensions will be discussed.

The time-resolved luminescence spectra were recorded using a unique pulsed flash lamp pumped Nd:YAG-OPO laser system (Powerlite Precision II 9020 laser equipped with a Green PANTHER EX OPO from Continuum, Santa Clara, CA, USA). The laser pulse energy, which was between 1.5 and 3.5 mJ was monitored using a photodiode. The luminescence spectra were detected using an optical multi-channel analyzer-system, consisting of an Oriel MS 257 monochromator and spectrograph with a 300 or 1200 line mm^{-1} grating and an Andor iStar ICCD camera (Lot-Oriel Group, Darmstadt, Germany). The Cm(III)/Eu(III) single luminescence emission spectra were recorded in the 570-650 nm (1200 line mm^{-1} grating with 0.2 nm resolution) range. The time-dependent luminescence spectra were detected in the 500-700 nm (300 line mm^{-1} grating) range. A constant time window of 1 ms length was applied, and due to the high absorption of the F-band usually observed in Cm^{3+} excitation spectra an excitation wavelength of 396 nm was used. For Eu(III) an excitation wavelength of 394 nm was used. The TRLFS setup has been described in detail elsewhere (Moll et al., 2008; Moll et al., 2014).

The spectra were base-line corrected; energy corrected and normalized using the OriginPro 8.6G (OriginLab Corporation, USA) code. The lifetime of luminescent species was obtained also with this software. In the case of Eu(III) normalization was applied only to the peak area of the $^5D_0 \rightarrow {}^7F_1$ band because the luminescence of this transition is a magnetic dipole and therefore not influenced by the chemical environment of the metal ion. In the case of Eu(III) the relative peak intensity ratio ($R_{E/M}$) was defined as:

$$R_{E/M} = I\,(^5D_0 \rightarrow {}^7F_2) \,/\, I\,(^5D_0 \rightarrow {}^7F_1) \qquad (3.3)$$

where I ($^5D_0 \rightarrow {}^7F_2$) and I ($^5D_0 \rightarrow {}^7F_1$) were calculated from the peak areas. The number of coordinated water molecules was calculated using the empirical equations given by Kimura et al. (1994; 1996; 1998):

$$nH_2O \pm 0.5 = 0.65 \times 1/\tau - 0.88 \text{ for Cm(III)} \qquad (3.4)$$

$$nH_2O \pm 0.5 = 1.07 \times 1/\tau - 0.62 \text{ for Eu(III)} \qquad (3.5)$$

where τ is the measured luminescence lifetime in ms. Luminescence data were analyzed with the factor analysis technique iterative transformation factor analysis (ITFA) to determine the number of acting species and their pH speciation. Applying factor analysis, the number of acting complexes can be estimated and the spectral mixtures can be decomposed into spectra of the acting complexes and their pH speciation. The application of ITFA to analyze spectroscopic date is summarized in (e.g., Rossberg et al., 2003; Lucks et al., 2012).

The *Hbt. noricense* Eu(III) system – TRLFS

Fig. 22 summarizes the amount of Eu(III) associated on the cells based on the ICP-MS analyses of the supernatants after separating the cells. We could detect a slightly pH-dependent biosorption of Eu(III) on *Hbt. noricense* cells. The affinity of *Hbt. noricense* cells to accumulate Eu(III) is relatively low after an incubation time of 1 h. There was an increase in Eu(III) sorption moving from pC_{H+} 4.1, 10 % sorbed to pC_{H+} 7.98, 40 % sorbed. The halophilic archaeon *Hbt. noricense* removed much less Eu(III) from the surrounding solution compared for instance with the Mont Terri Clay isolate *Sporomusa* sp. where independently of pH always ≥ 90 % of the Eu(III) was associated on the biomass (Moll et al., 2014).

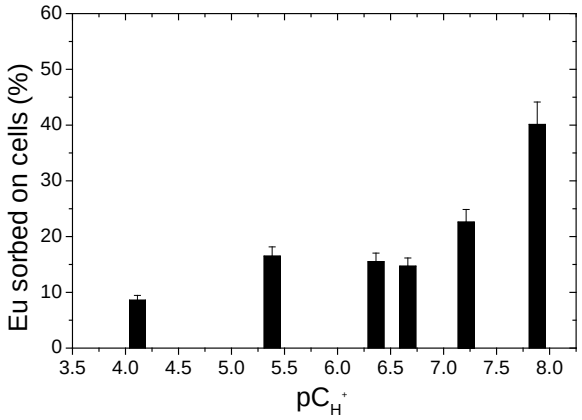

Fig. 22: Eu(III) association on *Halobacterium noricense* DSM-15987 after an incubation time of 1 h as a function of pC_{H+} ([Eu] 30 µM, [dry biomass] 0.5 g/L, 3 M NaCl).

Higher Eu(III) loadings were observed by increasing the incubation time to 48 h where than 55 %, 74 %, and 61 % of the Eu(III) was sorbed on the cells at pC_{H+} 4.5, 5.5 and 6.2, respectively. Ozaki et al. (2004) observed faster kinetics in their experiments between Eu(III) and for instance the halophilic archaeon *Halobacterium salinarum*. Already after 20 min of incubation time maximal loadings between 25 and 75 % were observed moving from pC_{H+} 3.7 to 5.7. As described later on for U(VI) also during the Eu(III) interaction experiments indications were found for an agglomeration of the cells especially at low and high pH in the presence of Eu(III) (stress response).

The luminescence spectrum of Eu^{3+} displays the changes upon cell addition and pC_{H+} change which points to complexation reactions of Eu(III) in *Hbt. noricense* suspensions (cf. Fig. 23 A).

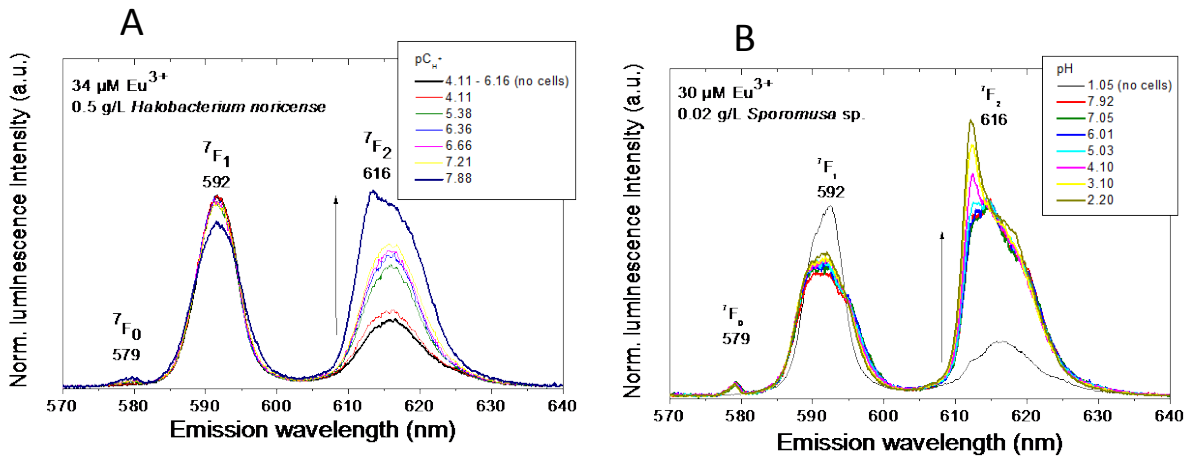

Fig. 23: Luminescence emission spectra of 32±3 µM Eu(III) as a function of pH/pC_{H+} after 1 h of contact time in (A) 3 M NaCl with 0.5 g/L *Hbt. noricense* DSM-15987 and in (B) 0.1 M $NaClO_4$ with 0.02 g/L *Sporomusa* sp. MT-2.99.

The intensity of the hypersensitive $^5D_0 \rightarrow {}^7F_2$ transition at about 616 nm increases (with increasing pH/pC_{H+}), the symmetry-forbidden $^5D_0 \rightarrow {}^7F_0$ transition at around 579 nm appears, and the luminescence decay changes to bi-exponential with prolonged lifetimes (cf. Table 7). The luminescence spectrum of the Eu^{3+} aqua ion is characterized by emission bands at 585-600 nm (magnetic dipole transition $^5D_0 \rightarrow {}^7F_1$) and 610-625 nm (hypersensitive transition $^5D_0 \rightarrow {}^7F_2$). The intensity ratio according to Eq. (3.3) of 0.54 and the measured lifetime of 112 ± 5 µs corresponding to 9 water molecules in its first coordination sphere are in agreement with the literature (e.g., Horrocks and Sudnick, 1979; Kimura et al., 1994; Kim et al., 1994; Moulin et al., 1999; Plancque et al., 2003; Heller et al., 2012; Barkleit et al., 2013). Even when it is proposed that the $^7F_1$ peak should not be influenced by complexation, we observed in cell suspensions slight variations in intensity combined with a broadening of this transition. The interaction of Eu^{3+} with *Hbt. noricense* cells is primarily pronounced in the $^7F_2$ peak. Based on the TRLFS spectra depicted in Fig. 23 we can conclude more intensive interactions of Eu(III) with *Sporomusa* sp. cells compared to the *Hbt. noricense* system. The changes in the $^7F_2$ transition are more pronounced (cf. Fig. 23 B). One main difference is also that *Sporomusa* sp. cells interact strongly with Eu(III) already at the acidic pH of 2.2.

Table 7: Spectroscopic properties of the identified Eu(III) species.

	Eu^{3+} (aq)	*Hbt. noricense* species 1	*Hbt. noricense* species 2
Emission (nm)			
$^7F_0$	-	579.7 (1.75)	578.9 (2.49)
$^7F_1$	591.2 (5.56)[a]	591.5 (5.56)	592.0 (8.28)
$^7F_2$	616.2 (9.18)	616.0 (7.69)	612.7 (3.48) 617.2 (9.54)
$R_{E/M}$[b]	0.54	1.21	1.96
Lifetime (µs)	112 ± 5	190 ± 42 **430 ± 52**	**190 ± 42** 430 ± 52

[a] Values in parentheses are full width at half-maximum; [b] Intensity ratio of the $^7F_2$ (electric dipole transition) over the $^7F_1$ (magnetic dipole transition) luminescence band.

In the *Hbt. noricense* system at $pC_{H+} \leq 5.4$ there are only weak changes visible in the TRLFS spectra coming from interactions between Eu(III) and *Hbt. noricense* (cf. Fig. 23 A). This might indicate that *Sporomusa* sp. can better cope with lower pH values than *Hbt. noricense*. Ozaki et al. (2004) reported strong Eu(III) interactions with *Hbt. Salinarum* at pH 3 (corresponds to pC_{H+} 3.7). Hence, *Hbt. salinarum* behaves differently at lower pH/pC_{H+}. The pC_{H+}-dependent effects in the TRLFS spectra are in agreement with the lifetime measurements. In all cell suspensions a bi-exponential luminescence decay behavior was measured. Within pC_{H+} 3.9 and 6.4 the short lifetime of ca. 108 µs can be assigned with the Eu^{3+} ion. Whereas the long lifetime of 430 µs measured at all pH values indicates a Eu(III) species either complexed with cell exudates or directly on functional groups of the cell envelope. From pC_{H+} 6.7 to 8.1 the shorter lifetime increased to an average value of 190 µs. This indicates a second distinct chemical environment contributing to the speciation of Eu(III) in the cell suspensions. These lifetimes correspond to 2.0 and 5.0, respectively, remaining water molecules in the Eu(III) first coordination sphere. By comparing our lifetime and later discussed speciation results with literature data on bacterial Eu^{3+} interaction studies (cf. Moll et al., 2013; Moll et al., 2014 and references therein), the longer lifetime can be assigned to Eu^{3+}–*Hbt. noricense* species 1, whereas the shorter lifetime corresponds to Eu^{3+}–*Hbt. noricense* species 2. That cell exudates from the halophilic archaeon could have an affinity for Eu(III) was reported in (Ozaki et al., 2004). From the relatively low amount of bound Eu(III) (cf. Fig. 22) and the measured effects by TRLFS (cf. Fig. 23 A) it is likely that *Hbt. noricense* cells secreted exudates. Based on the experimental findings presented it is not possible to distinguish between cell bound and ligand bound Eu(III).

Fig. 24 shows the Coordination-Environment diagram (CE diagram) for Eu(III) in *Hbt. noricense* suspensions. The CE diagram was constructed as described by Ozaki et al. (2002). The interpretation on the basis of the CE diagram implies that Eu(III) interacts with the coordination site characterized by the long lifetime in an inner-spherical complex (to compare with: phosphoryl sites: Eu^{3+}–*Sporomusa* sp. species 1).

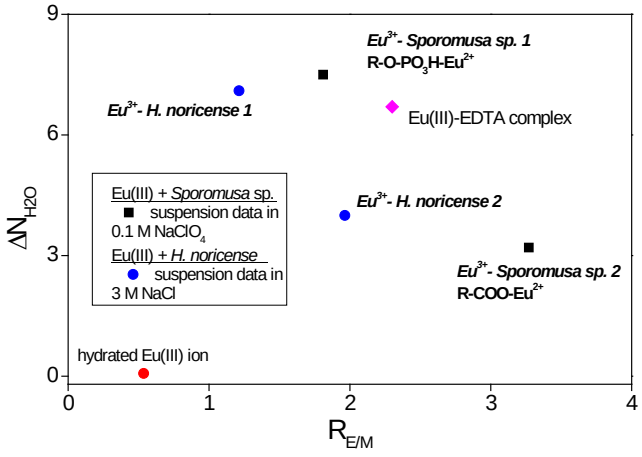

Fig. 24: CE diagram of Eu(III) in *Halobacterium noricense* DSM-15987 suspensions in comparison to the Eu(III)-*Sporomusa* sp. system (Moll et al., 2013; Moll et al., 2014).

The interaction with the coordination site characterized by the short lifetime combines both outer-spherical and inner-spherical properties (to compare with: carboxyl sites: Eu^{3+}–*Sporomusa* sp. species 2). Eu(III) associated on microbial phosphoryl sites are characterized by long luminescence lifetimes between 515 and 730 µs, whereas Eu(III) coordinated to carboxyl sites displayed luminescence lifetimes in the range of 98 to 255 µs (results summary in Moll et al., 2013 and 2014). The experimental results in comparison to the literature would suggest for Eu^{3+}–*Hbt. noricense* species 1 a coordination to phosphoryl sites and for Eu^{3+}–*Hbt. noricense* species 2 a coordination to carboxyl sites.

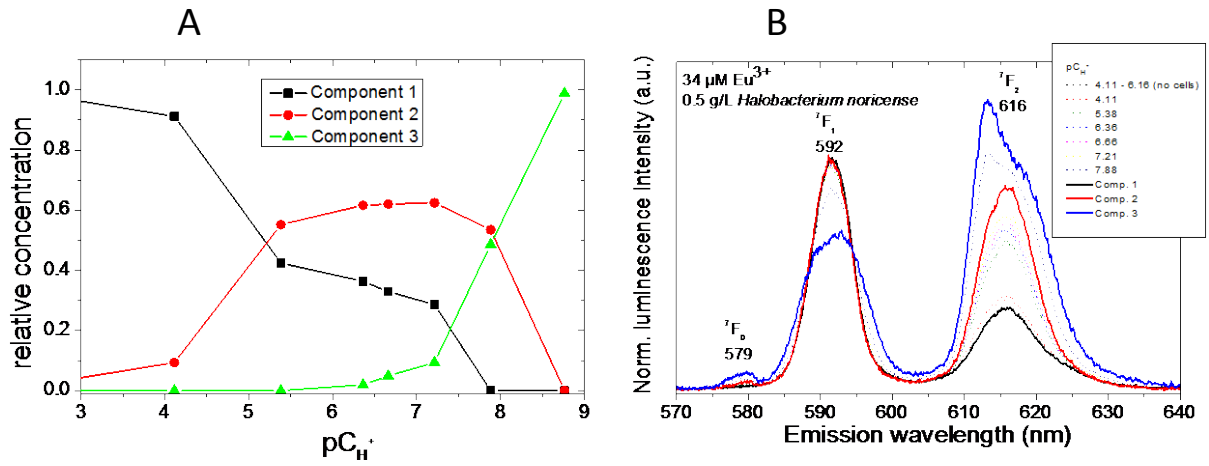

Fig. 25: ITFA results gained from the TRLFS spectra of the Eu(III)-*Hbt. noricense* system taken after 1 h of incubation time (Fig. 23 A). A: iterative target test (ITT) calculated species distribution of the components and B: ITFA extracted TRLFS component spectra (solid lines) and experimental data (dotted lines).

For a comprehensive evaluation of the spectral data set recorded throughout the whole pC_{H+} range, ITFA was applied to study the correlations between the observed changes in the luminescence spectra. As a first step, the principal component analysis (PCA) of the TRLFS spectra was performed. The eigenvalues which are a measure of the importance of a component rapidly drops down after the first 3 components. This inspection points out that the system contains three distinct components. As a second step, the VARIMAX rotation provided model-independent factor loadings which correlate with the assumption of three components and also with the later on calculated species distribution with ITT (cf. Fig. 25 A). For the ITT some relative concentrations or at least their minima and maxima in the spectral mixtures were used as constraints. The minima and maxima of the relative concentrations are supplied by the VARIMAX rotation. Component 1 can be assigned with the Eu^{3+} aquo ion. A significant influence of *Hbt. noricense* species on the Eu(III) speciation started at $pC_{H+} \geq 5.1$ and much later in pH units as observed in the Eu(III)-*Sporomusa* sp. system. Component 2 can be interpreted by interactions of Eu(III) with carboxyl groups, but phosphoryl groups may also participate. The influence of component 3 increased at $pC_{H+} \geq 7.1$. Component 3 could indicate interactions with a dissolved species what is in accordance with the percentage sorption data. A detailed characterization of aqueous Eu^{3+}–*Hbt. noricense* species based on the changes of the intrinsic luminescence of Eu^{3+} has not been reported before.

The *Hbt. noricense* Cm(III) system – TRLFS

The presented results allow a first insight in the pC_{H+}-dependent speciation of Cm(III) in cell suspensions of the halophilic archaeon *Hbt. noricense*.

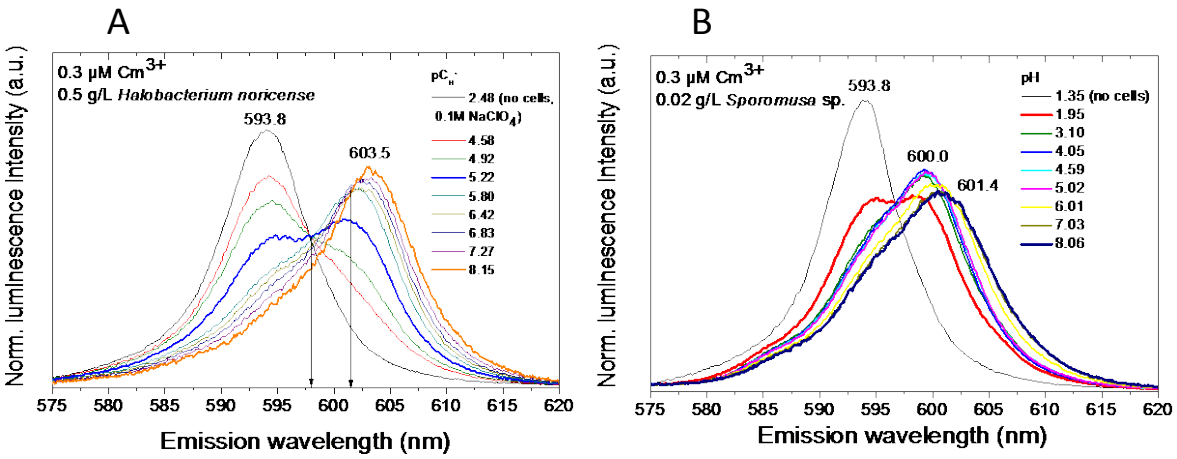

Fig. 26: Luminescence emission spectra of 0.3 µM Cm(III) as a function of pH/pC_{H+} taken after 1 h of incubation time in (A) 3 M NaCl with 0.5 g/L *Halobacterium noricense* DSM-15987 and in (B) 0.1 M $NaClO_4$ with 0.02 g/L *Sporomusa* sp. MT-2.99.

In agreement with our observations in the Eu(III)-*Hbt. noricense* system, a significant change in the luminescence spectra was first visible at $pC_{H+} \geq 5.1$ (cf. Fig. 26 A). *Sporomusa* sp. cells influenced strongly the luminescence spectra already at a low pH of 2 (Fig. 26 B). A stronger affinity of Cm(III) to the archaeon *Hbt. salinarum* was observed already at pC_{H+} 3.7 (Ozaki et al., 2004). This shows that both archaea behave different in the presence of Cm(III). For *Hbt. noricense* TRLFS investigations at pC_{H+} 3 are extremely difficult due to a fast agglomeration of cells. With increasing pH/pC_{H+} the intensity of the emission maximum at 593.8 nm (Cm^{3+}) decreases and simultaneously a second emission maximum increases at 602 nm (Cm(III)-*Hbt. noricense* 1). Within the investigated pC_{H+} range there is a continuous red shift of the emission maxima up to 603.5 nm indicating the occurrence of a second complex (Cm(III)-*Hbt. noricense* 2). There are two isosbestic points at 598 and 601.5 nm visible in Fig. 26 A underlining the assumption of two complex Cm(III) species besides the Cm^{3+} aquo ion in *Hbt. noricense* suspensions. The interaction of Cm(III) with *Hbt. noricense* cells and/or cell exudates resulted in more red shifted emission spectra compared to the *Sporomusa* sp. system (cf. Fig. 26).

In 3 M NaCl we observed with 70.3 µs a slightly longer lifetime for the Cm^{3+} aquo ion than 68 ± 4 µs reported in the literature for 0.1 M $NaClO_4$ systems (Edelstein et al., 2006). This could be explained by a reduced quenching caused by the O-H vibration due to the higher Cl^- concentration. Again in all cell suspensions a bi-exponential luminescence decay behavior was measured. The occurrence of two lifetimes suggests that two distinct chemical environments contribute to the total speciation of Cm(III) in the presence of the biomass. In the cell suspensions the short lifetime of 77 ± 6 µs shows the influence of the Cm^{3+} ion between pC_{H+} 4.1 and 5.1. However, the increase of 7 µs in comparison to the pure Cm^{3+} ion might

indicate the beginning influence of Cm(III)-*Hbt. noricense* species. The second longer lifetime of 328 ± 44 µs was measured over the whole pC_{H+} range and can be attributed to Cm(III)-*Hbt. noricense* 1. At pC_{H+} ≥ 5.1 the short lifetime increases to 129 ± 27 µs and can be assigned to Cm(III)-*Hbt. noricense* 2. These lifetimes correspond to 1.1 and 4.0, respectively, remaining water molecules in the Cm(III) first coordination sphere. By comparing our lifetime and later discussed speciation results with literature data on bacterial Cm^{3+} interaction studies (cf. Moll et al., 2013; Moll et al., 2014 and references therein), the longer lifetime can be assigned to Cm^{3+}–*Hbt. noricense* species 1, whereas the shorter lifetime corresponds to Cm^{3+}–*Hbt. noricense* species 2. Cm(III) associated on microbial phosphoryl sites are characterized by long luminescence lifetimes between 250 and 477 µs, whereas Cm(III) coordinated to carboxyl sites displayed shorter luminescence lifetimes in the range of 108 to 230 µs (results summary in Moll et al., 2013 and 2014). The experimental results in comparison to the literature would suggest for Cm^{3+}–*Hbt. noricense* species 1 a coordination to functional groups of the cell envelope (e.g. phosphoryl sites and carboxyl sites). Cm^{3+}–*Hbt. noricense* species 2 could be assigned to a solution species providing carboxyl sites (e.g. cell exudates). That cell exudates from halophilic archaea could have an affinity also for Cm(III) was reported in (Ozaki et al., 2004). Based on the experimental findings presented it is not possible to distinguish between cell bound and ligand bound Cm(III).

As described for the Eu(III) data, ITFA was applied to study the correlations between the observed changes in the luminescence spectra measured in the corresponding Cm(III) system. Again the PCA calculations of the TRLFS spectra pointed out that the system contains three distinct components. The VARIMAX rotation provided model-independent factor loadings which correlate with the assumption of three components and also with the later on calculated species distribution with ITT (cf. Fig. 27 A). For the ITT some relative concentrations or at least their minima and maxima in the spectral mixtures were used as constraints. The minima and maxima of the relative concentrations are supplied by the VARIMAX rotation.

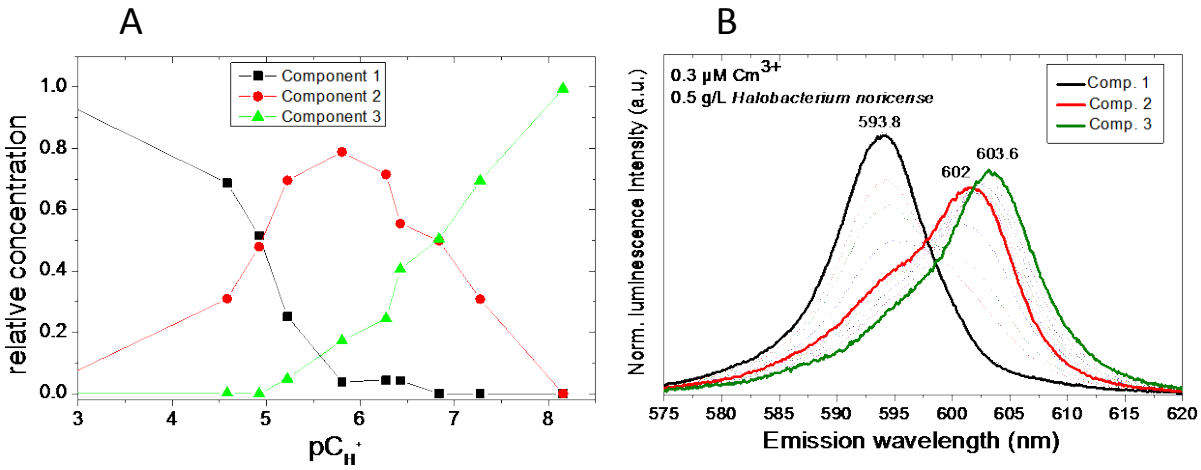

Fig. 27: ITFA results gained from the TRLFS spectra of the Cm(III)-*Hbt. noricense* DSM-15987 system (Fig. 26 A). A: iterative target test (ITT) calculated species distribution of the components and B: ITFA extracted TRLFS component spectra (solid lines) and experimental data (dotted lines).

Component 1 can be assigned with the Cm^{3+} aquo ion. A significant influence of *Hbt. noricense* species on the Cm speciation started at $pC_{H+} \geq 5.1$ and much later in pH units as observed in the Cm(III)-*Sporomusa* sp. system (cf. Fig. 26 B). Component 2 can be interpreted by interactions of Cm with functional groups of the cell envelope (Cm(III)-*Hbt. noricense* 1). The influence of component 3 increased at $pC_{H+} \geq 6.6$. Component 3 could indicate Cm(III) interactions with for instance carboxyl groups of released cell exudates (Cm(III)-*Hbt. noricense* 2). A detailed characterization of aqueous Cm^{3+}–*Hbt. noricense* species based on the changes of the intrinsic luminescence of Cm^{3+} has not been reported before.

The first TRLFS speciation analyses of Eu(III) and Cm(III) in *Hbt. noricense* suspensions revealed consistent results. Further investigations will focus on different aspects such as the kinetics, the analyses of supernatants and re-suspended cells in addition to the suspensions, and experiments as a function of biomass and Eu(III) concentration and will be performed by HZDR Young Investigator Group MicroSalt.

3.2.3 U(VI)

U(VI) biosorption by *Hbt*. *noricense* DSM-15987 was investigated in dependence on incubation time, initial U(VI) concentration and pC_{H+}. U(VI) sorption behavior over time was studied at 110 µM U(VI), pC_{H+} 6 over a time period of 0.5 up to 90 h. The U(VI) binding in dependence on initial U(VI) concentration (10-120 µM) was investigated at pC_{H+} 4 and 6. For all U(VI) experiments a stock solution of 80 mM in 0.1 M HCl was used. U(VI) accumulation experiments were carried out in 3 M NaCl (Carl Roth, Germany). The pC_{H+} adjustments were made with HCl or NaOH. The pC_{H+} was measured using an InLab Solids electrode (Mettler-Toledo, Giessen, Germany) calibrated with standard buffers and a pH meter (InoLab720, WTW, Weinheim, Germany). The pC_{H+} was adjusted with a precision of 0.05 units. For all these investigations the dry biomass was set to 0.5 $g_{dry\ weight}$/L. After contact of the cells with U(VI) for a certain time, the cells were separated by centrifugation 10000*g* for 10 min and Live/Dead staining was undertaken according to manufacturer's instructions (LIVE/DEAD® Bac Light™ Bacterial Viability Kit L7012, Molecular Probes). The supernatant was analyzed with Inductively Coupled Plasma Mass Spectrometry (ICP-MS) (Elan900, Perkin Elmer, Waltham, MA, USA) to determine how much uranium was bound to the cells. In selected samples the formed uranium-cell complexes were analyzed with time-resolved laser-induced fluorescence spectroscopy (TRLFS). For analysis a quadrupled (266 nm) Nd:YAG laser (Minilite, Continuum, San Jose, USA) with 0.3 mJ per 4 ns pulse were used and the slot was maximal opened (2238 mm). The measurements were performed at room temperature. Prior to the TRLFS measurement, the U(VI)-loaded cells were washed with 3 M NaCl at the appropriate pC_{H+} to remove loosely bound U(VI). In addition to the U(VI)-loaded cells also the corresponding supernatants were measured with TRLFS.

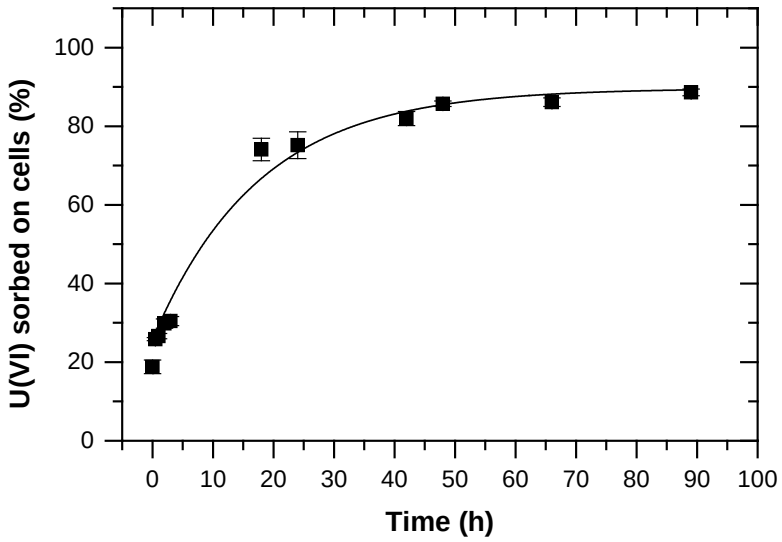

Fig. 28: Kinetic of U(VI) sorption on cells of *Hbt. noricense* (pC_{H+} 6, [U(VI)] = 110 µM, 0.5 $g_{dry\ weight}$/L, triplicate).

First insights into the interactions of *Hbt*. *noricense* with U(VI) can be gained by studying its time-dependent behavior. The sorption of U(VI) on *Hbt*. *noricense* cells during an incubation time of 0.5 up to 90 h is shown in Fig. 28 and can be described by a two-step process. At the beginning only a small part of the initial U(VI) (~35 %) is rapidly sorbed by the cells. The second slower step last up to 48 h, whereas finally 90 % of added uranium was bioassociated.

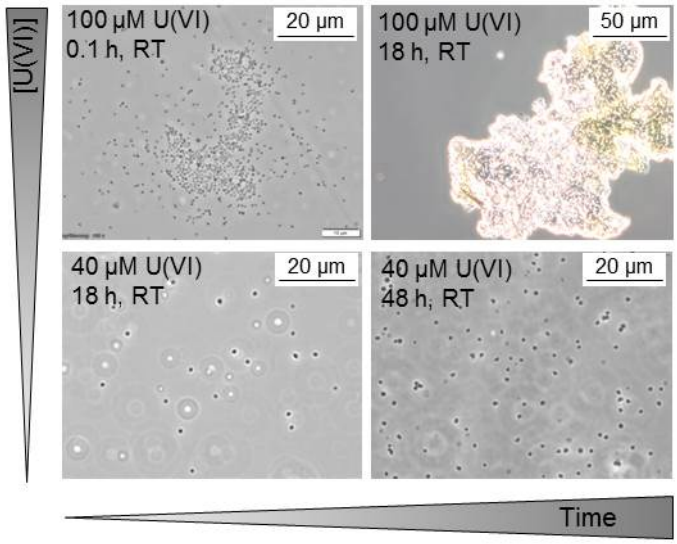

Fig. 29: Agglomeration of *Hbt. noricense* cells with increasing time and uranium concentration.

Another interesting observation is that with increasing incubation time as well as uranium concentration an agglomeration of the cells occurred (Fig. 29). A staining of cells with Bac Light™ Bacterial Viability Kit demonstrated that agglomerated cells were mostly alive whereas single cells were dead. A conclusion could be that this agglomeration process is a kind of

stress response to protect the cells themselves against environmental challenges. The formation of biofilms by other haloarchaea was just recently shown (Fröls et al., 2012).

The biosorption of U(VI) by *Hbt*. *noricense* cells depending on different initial U(VI) concentrations and two different pC_{H+} values (4 and 6) in 3 M NaCl after 48 h incubation time is shown in Fig. 30.

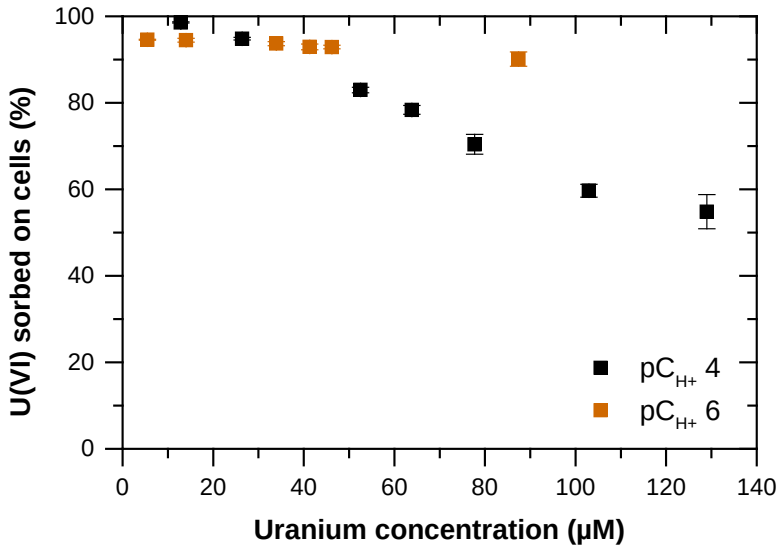

Fig. 30: Biosorption of uranium on cells of *Hbt. noricense* in dependence on pC_{H+} and U(VI) concentration (48 h incubation time, triplicate).

Hbt. noricense cells associate independent of the initial U(VI) concentration approximately 90 % of the added U(VI) at pC_{H+} 6, whereas the percentage sorption at pC_{H+} 4 decreases.

Furthermore, the supernatant and the washed cell suspension of selected samples were analyzed with TRLFS to characterize the binding of uranium to the cells. Despite the high quenching effect of chloride to uranium fluorescence a luminescence signal could be detected. One hypothesis of this phenomenon is the high quantum yield of some formed complexes. As shown in Fig. 31, uranium luminescence could be detected even at 3 M NaCl and binding kinetics could be documented over time. The further characterization of formed uranium-cell complexes will be performed by attenuated total reflection Fourier-transform infrared spectroscopy (ATR FT-IR) and also by microscopic investigations.

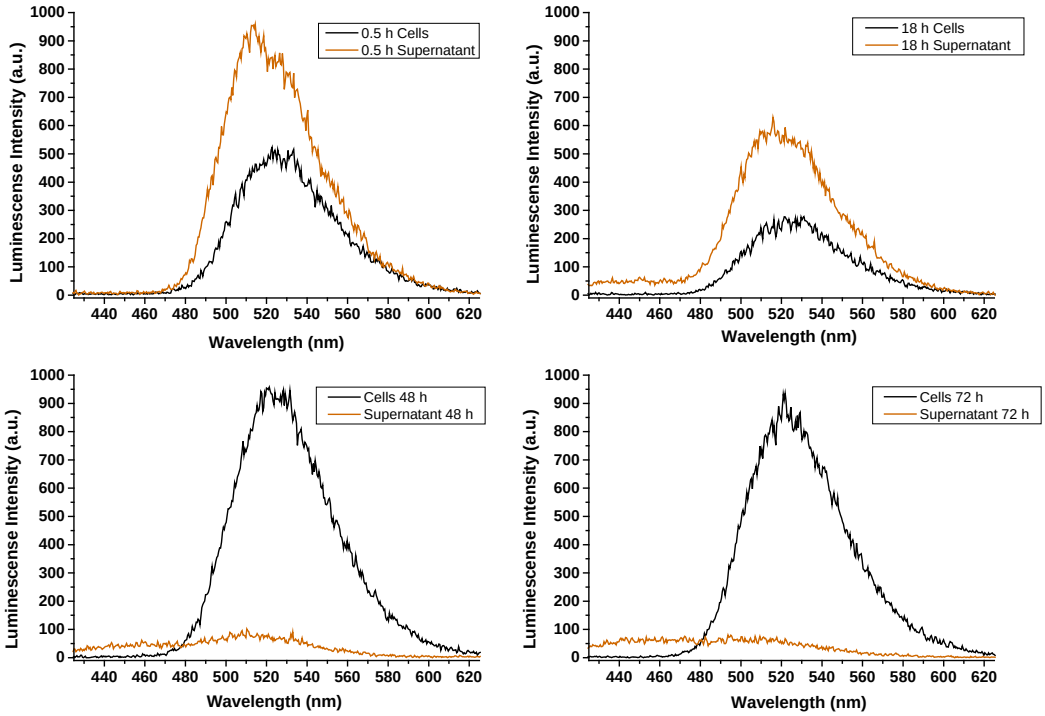

Fig. 31: By tracking the sorption process with TRLFS, increasing uranium intensity is detectable in the samples from the cell pellets (black), whereas the intensity decreases in the samples from the supernatant. After 48 h almost no uranium is detectable in the supernatant, everything is bioassociated.

The interactions of *Halobacterium noricense* DSM-15987 with uranium will be further investigated within the HZDR Young Investigator Group MicroSalt.

4 Dynamics of metal-humate complexation equilibria

4.1 Experimental

Materials. Non-radioactive chemicals and humic acid were purchased from Sigma-Aldrich (Germany). Another humic acid was isolated from surface water collected on the raised bog "Kleiner Kranichsee" (near Carlsfeld, Germany). Separation was carried out according to the recommendations of the International Humic Substances Society. Both humic materials were purified by repeated precipitation and redissolution with 0.1 M HCl and 0.1 M NaOH / 0.01 M NaF, respectively, followed by dialysis and lyophilization. [^{160}Tb]$TbCl_3$ (specific activity: ~ 1 GBq per mg Tb) was supplied by Radioisotope Centre Polatom (Poland).

Isotope exchange experiments. Stock solutions of 0.1 M $NaClO_4$ and of humic acid, $Tb(NO_3)_3$ as well as [^{160}Tb]$TbCl_3$ in 0.1 M $NaClO_4$, all adjusted to a pH of 4.0, were dispensed into 5 mL centrifuge tubes at variable amounts, giving a total volume of 4 mL. The component to be added finally after a pre-equilibration step was introduced in a small volume of 20 µL, keeping the concentrations of the other components virtually unchanged. Concentrations of humic acid and [^{160}Tb]Tb were fixed at 0.5 g L^{-1} and 1 nM, respectively. The solutions were rotated end-over-end during the equilibration steps. Wall adsorption was ascertained to be insignificant.

In a first series of experiments (illustrated in Fig. 32), humic acid was contacted with Tb (natural stable isotope ^{159}Tb) at a range of concentrations (0.3 mM - 2.4 mM), covering a binding isotherm up to the state of saturation. The systems were completed by adding a small amount of [^{160}Tb]Tb, either instantaneously or subsequently after different time periods of pre-equilibration.

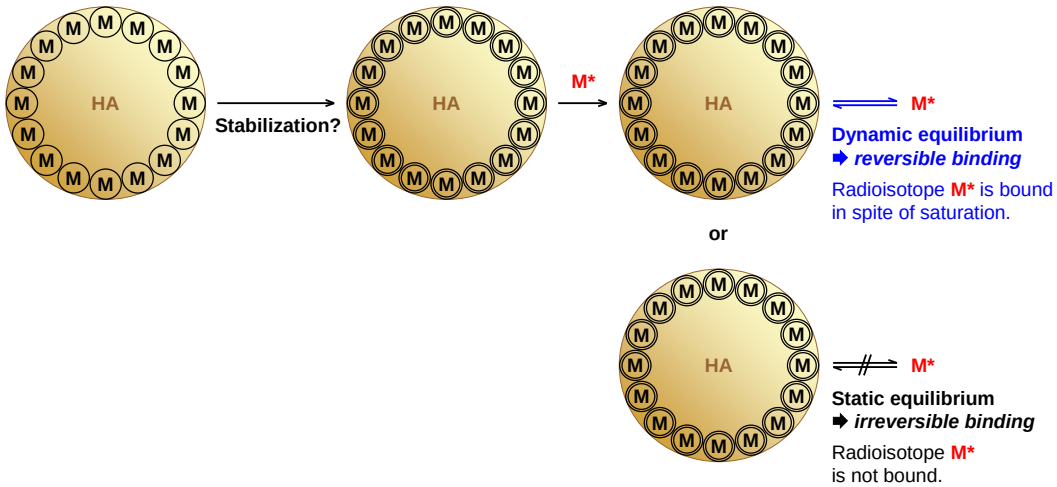

Fig. 32: Isotope exchange experiments for probing the equilibrium characteristics of metal-humate complexation (HA: humic acid, M: metal, M*: radioisotope), starting from the state of saturation.

Owing to the high metal loads, flocculation of humic colloids generates a solid-liquid system where adsorbed amounts of Tb can be determined by radiometric analysis of the supernatant

after centrifugation, presuming that ^{160}Tb represents total Tb. Flocculation was verified to be nearly complete by UV-vis spectrometry, using a Lambda 45 spectrophotometer (Perkin Elmer, USA). Concentrations of ^{160}Tb were determined by means of a gamma counter 1480 Wallac Wizard 3" (Perkin Elmer, USA).

In a modified procedure (Fig. 33), [^{160}Tb]Tb was introduced first, followed by saturation with non-radioactive ^{159}Tb after pre-equilibration for different periods of time. A fixed concentration within the plateau region of the binding isotherm (2 mM ^{159}Tb) was chosen in these experiments, and data were quantified referring to [^{160}Tb]Tb instead of total Tb. Humic-bound amounts of [^{160}Tb]Tb in the absence of ^{159}Tb were determined by ultrafiltration with Vivaspin 2 kDa centrifuge filters (Sartorius, Germany).

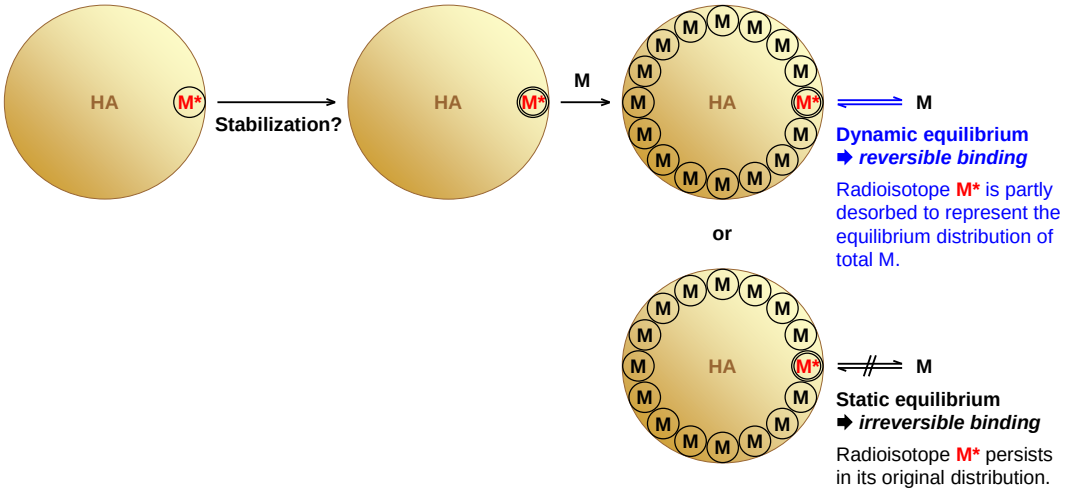

Fig. 33: Isotope exchange experiments in a reverse procedure, starting from a very low metal load with the radioisotope M*.

4.2 Results and discussion

Fig. 34 shows isotherms for binding of Tb to humic acid, obtained with ^{160}Tb as a radiotracer. The square symbols show the results of conventional experiments where the tracer was simultaneously added together with the bulk of non-radioactive Tb. At equilibrium concentrations higher than 1 mM, a plateau level is reached, indicating that more binding sites are not available under the given conditions. In a static equilibrium, where binding is simply "adhesion", all sites will be blocked in this state of saturation.

However, if the radiotracer is subsequently introduced after Tb and humic acid have already been pre-equilibrated (triangle symbols), coincident isotherms are obtained. The radioactive probe represents the solid-liquid distribution of total Tb, even though it encounters the state of maximum occupancy. It is thus evident that there is a permanent exchange between dissolved and humic-bound Tb; the tracer is involved a dynamic equilibrium. In additional tests, complete equilibration was also observed when reducing the time of contact with the radiotracer to 15 min instead of 1 day. This indication of a rapid isotope exchange is consistent with a spectroscopic study on Cm-humate complexation (Freyer et al., 2009).

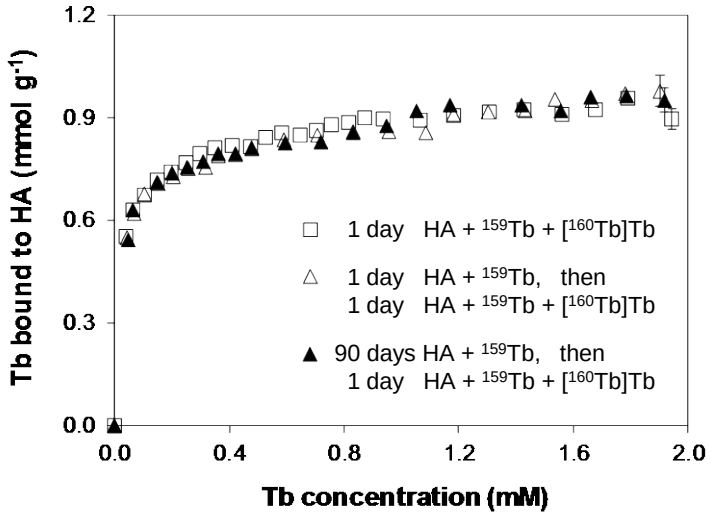

Fig. 34: Isotherms of adsorption of Tb(III) onto flocculated humic acid, obtained with ^{160}Tb(III) as a radiotracer, which was added simultaneously or subsequently after different times of pre-equilibration with non-radioactive ^{159}Tb(III) (1 nM [^{160}Tb]Tb, 0.5 g L^{-1} HA Aldrich, 0.1 M $NaClO_4$, pH 4.0).

Notably, there are no indications of stabilization processes, even after extended periods of pre-equilibration (90 days). Reported observations of increasing complex inertness refer to a similar or a shorter time frame. Metal loads were, however, far below saturation in these studies. An influence of concentration is conceivable since humic molecules comprise a multitude of binding sites with a broad affinity distribution (Tipping, 2002).

For this reason, the experimental approach was modified in that the sequence of introducing the isotopes was reversed: At first, humic acid was contacted with [^{160}Tb]Tb at a very low concentration. Subsequently, the large excess of ^{159}Tb was added at a concentration in the range of saturation. For representing the solid-liquid distribution of total Tb in a dynamic equilibrium, the radioisotope was expected to be partly desorbed since the bound fraction of total Tb is lower in the plateau region of the binding isotherm.

Fig. 35 shows the results of these experiments, conducted with two different humic materials. The upper equilibrium lines show their initial loads with [^{160}Tb]Tb prior to adding ^{159}Tb. The lower equilibrium lines show the amounts of bound [^{160}Tb]Tb representing the bound fraction of total Tb (virtually, ^{159}Tb) in the case of simultaneous addition. If the non-radioactive isotope is introduced later, desorption of the radiotracer is in fact initiated, striving towards the equilibrium state – however, at much lower rates compared to the equilibration process in the reverse procedure. Moreover, the rates proved to be dependent on the time of pre-equilibration with [^{160}Tb]Tb. Equilibrium is closely approached after 1 month of exchange for the shortest pre-equilibration times, whereas bound amounts are still far away from equilibrium after 3 months if more time is admitted for pre-equilibration. Evidently, desorption of the radiotracer is increasingly hindered. The existence of kinetic stabilization phenomena was thus substantiated. However, it appears that they are confined to the most reactive sites, occupied by the radiotracer.

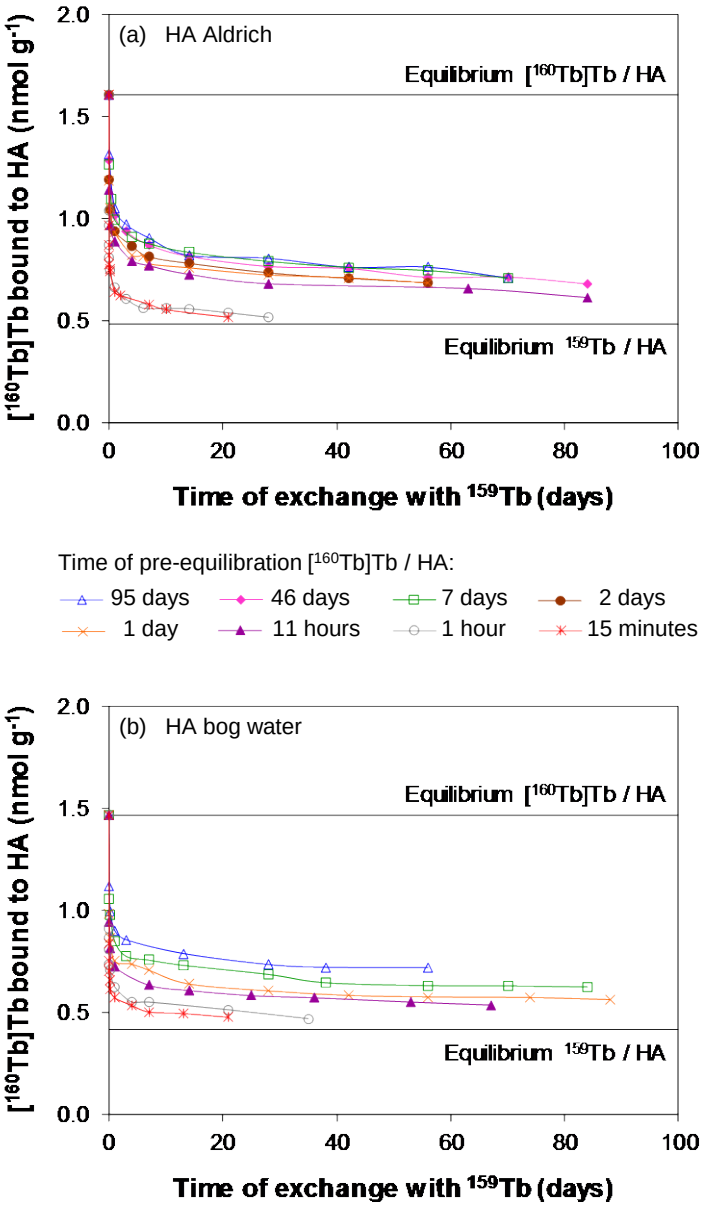

Fig. 35: Amount of [^{160}Tb]Tb(III) bound to humic acids after saturating with non-radioactive ^{159}Tb(III), shown as a function of exchange time for different times of pre-equilibration (1 nM [^{160}Tb]Tb, 2 mM ^{159}Tb, 0.5 g L^{-1} HA, 0.1 M $NaClO_4$, pH 4.0).

The time-dependent progress of this stabilization is shown in Fig. 36, where adsorbed amounts after a fixed time of exchange (1 h) are plotted as a function of pre-equilibration time. Changes are most pronounced in the first days, followed by a very minor trend over an extended time period. A similar time dependence was also reported for inertization effects in respect of complex dissociation (Cacheris and Choppin, 1987; Choppin and Clark, 1991; Rao et al., 1994; Lippold et al., 2012).

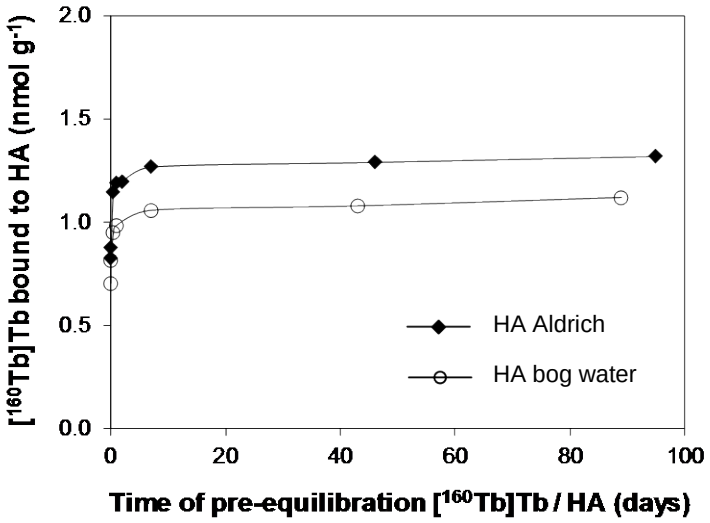

Fig. 36: Amount of [^{160}Tb]Tb(III) bound to humic acids after 1 h of exchange with ^{159}Tb(III), shown as a function of pre-equilibration time (conditions as in Fig. 35).

Aiming at an elucidation of the chemical background of this stabilization process, an attempt was made to detect structural changes in the microenvironment of the metal by means of time-resolved laser fluorescence spectroscopy, using Eu(III) as a (more sensitive) probe. However, significant time-dependent spectral changes could not be detected, probably because higher metal concentrations had to be applied to obtain sufficient fluorescence intensity.

For short pre-equilibration times, the kinetics of exchange (Fig. 35) is superimposed by the kinetics of stabilization (Fig. 36), resulting in a prolongation of the process. This interference can be neglected for longer times of pre-equilibration, and a kinetic analysis of the exchange process itself is possible. It can be shown that isotope exchange always follows first-order kinetics, regardless of the mechanism of the exchange reaction (Duffield and Calvin, 1946). For the system under study, the rate of approach to equilibrium is given by Eq. (4.1)

$$-\frac{\mathrm{d}c_{\mathrm{ads}}}{\mathrm{d}t} = k\left(c_{\mathrm{ads}} - c_{\mathrm{ads}}^{\mathrm{eq}}\right), \qquad (4.1)$$

where k is the rate constant, c_{ads} is the concentration of humic-bound [^{160}Tb]Tb at time t after saturation, and $c_{\mathrm{ads}}^{\mathrm{eq}}$ is its concentration at equilibrium. Integration yields Eq. (4.2) for the time course of isotope exchange

$$c_{\mathrm{ads}} = \left(c_{\mathrm{ads}}^{0} - c_{\mathrm{ads}}^{\mathrm{eq}}\right) e^{-kt} + c_{\mathrm{ads}}^{\mathrm{eq}}, \qquad (4.2)$$

where c_{ads}^{0} is the initial concentration of humic-bound [^{160}Tb]Tb. Fitting this monoexponential equation to the data was not successful, due to the very steep decrease for short times of exchange. In Eq. (4.3), the total amount of [^{160}Tb]Tb is split into a fast exchanging and a slowly exchanging component, characterized by the rate constants k_1 and k_2, respectively, with x denoting the fraction of the fast exchanging component.

$$c_{ads} = x \left(c_{ads}^{0} - c_{ads}^{eq}\right) e^{-k_1 t} + \left(1-x\right) \left(c_{ads}^{0} - c_{ads}^{eq}\right) e^{-k_2 t} + c_{ads}^{eq} \qquad (4.3)$$

Using this equation, the progress of exchange can be well described, as shown for an exemplary dataset in Fig. 37. Obviously, the very small fraction of sites occupied by [^{160}Tb]Tb (~ 1/10^6) is still heterogeneous with respect to exchange kinetics. Extrapolating the fit indicates that it takes about 2 years for a stabilized complex to arrive at equilibrium.

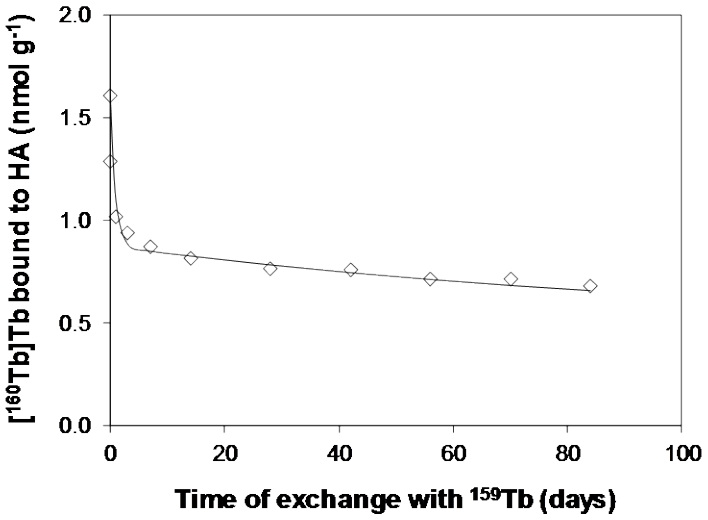

Fig. 37: Kinetic analysis of isotope exchange by fitting Eq. (4.3) (symbols: data set for HA Aldrich after 46 days of pre-equilibration, solid line: fitted curve calculated with the parameters k_1 = 1.20 d^{-1}, k_2 = 0.01 d^{-1}, x = 0.65).

Stabilization and slow kinetics as observed for the radiotracer will certainly affect humic-bound contaminant metals in geochemical systems since their concentrations are similarly low. A humic complex, loaded with trace amounts of metals and "aged" for some time, will not be in equilibrium with its aqueous surroundings if conditions change relatively fast, e.g., in case of rapid movement. To decide how to treat humic-bound metals in speciation and transport modeling, two aspects of the present findings are important: (I) The stabilization process does not continue endlessly but is virtually completed after a fairly short time period (Fig. 36). (II) Reversibility is not affected (Fig. 35). Whether humic-bound metals take part in interaction processes is a question of the time frame under consideration. Equilibration times of several years are still very short compared to the time scale to be covered in safety assessments for nuclear waste repositories. Nearly stagnant systems are to be considered, where steady equilibria may be assumed in spite of very slow kinetics. Under these conditions, metal exchange between humic carriers and mineral surfaces cannot be neglected in predictive transport calculations, and equilibrium constants are fully applicable.

5 Influence of higher salinities on the mobilization potential of high-molecular-weight organics towards Tb(III) and Eu(III)

5.1 Dispersion stability of fulvic acid in highly saline solutions (Na^+, Mg^{2+}, Ca^{2+})

Dissolved humic substances are dispersions of colloidal particles that are stabilized towards precipitation (flocculation) due to their negative surface charge. This stabilization is counteracted by cationic solutes. On the one hand, the dielectric properties of the aqueous medium are altered. On the other hand, the surface charge can be compensated by cation binding to acidic groups. The latter kind of destabilization applies to multivalent metal ions as well as protons. In contrast, monovalent metal ions are not directly bound to humic ligands. High-molecular-weight clay organics are, in some respect, comparable to fulvic acids. Different from humic acids, fulvic acids do not flocculate on protonation owing to their higher charge density. Ionic strengths of highly saline solutions, however, exceed the proton concentration even of concentrated acids. So far, nothing was known on colloidal stability of fulvic acids at salt concentrations close to saturation, as encountered in pore waters of Lower Cretaceous clay in Northern Germany. If flocculation occurs, humic-bound migration of radionuclides can be excluded. Specifying the conditions of such immobilization was the objective of this work package.

Two organic materials were chosen for these investigations: Suwannee River fulvic acid St. II standard material (International Humic Substances Society) and a fulvic acid isolated from surface water collected on the raised bog “Kleiner Kranichsee” (near Carlsfeld, Germany). Dispersion stability was examined on addition of NaCl, $MgCl_2$ and $CaCl_2$ as main electrolyte constituents of clay pore waters. Since co-operative effects by protonation are to be taken into account, investigations were performed at two different pH values; pH 5 and pH 7. The pH adjustment for stock solutions of the salts was carried out at a low salt concentration before the bulk amount was added to give the final concentration. Systems of 40 mg L^{-1} fulvic acid and variable amounts of NaCl, $MgCl_2$ and $CaCl_2$ (up to 4.9 M) were prepared in clear glass vials and were left to stand in the dark for 3 months. Flocculation was then evaluated by visual inspection.

No precipitation of fulvic acid was observed in any of these systems. It may be concluded that fulvic acid-like clay organics are not prone to flocculation even at very high salinities. Thus, the possibility of a mobilization of radionuclides by complexation with such material cannot be excluded and needs to be investigated for the special conditions of high electrolyte contents.

5.2 Effects of ionic strength and presence of fulvic acid on the adsorption of Tb^{3+} and Eu^{3+} onto Opalinus Clay

5.2.1 Experimental

5.2.1.1 Materials

^{160}Tb (half-life 72.3 d) was produced at the TRIGA Mark II reactor at the University of Mainz (Germany) and was used in the form of a stock solution of 10^{-4} M [^{160}Tb]terbium in 0.1 M $NaClO_4$. ^{152}Eu was purchased as a [^{152}Eu]$EuCl_3$ stock solution in 0.1 M HCl from Radioisotope Centre Polatom (Poland).

An Opalinus Clay sample (BHE-241) from the Mont Terri rock laboratory (Switzerland) was used as a 4.8 $g \cdot L^{-1}$ suspension. Characteristics of this material are given in Marquardt (2011) and Nagra (2002).

The fulvic acid was isolated from surface water collected on the moor *Kleiner Kranichsee* (near Carlsfeld, Germany). Purification was carried out according to the recommendations of the International Humic Substances Society (Aiken, 1985). The average molecular weight was determined to be 38 kDa by size exclusion chromatography, the total acidity was found to be 8.46 $meq \cdot g^{-1}$ by potentiometric titration.

All other chemicals were of analytical grade and used without further pretreatment. Solutions were prepared using ultrapure Milli-Q water. All experiments were carried out at ambient conditions.

5.2.1.2 Adsorption experiments

Variable amounts of NaCl, $CaCl_2$ or $MgCl_2$ in the range of 0 - 4 $mol \cdot L^{-1}$ were added to the clay suspension. The pH was adjusted to 5 or 7 by using HCl. Stock solutions of [^{160}Tb]terbium (for pH 5) or [^{152}Eu]europium (for pH 7) were added to yield a concentration of 10^{-6} M (42 $Bq \cdot mL^{-1}$ ^{160}Tb, 930 $Bq \cdot mL^{-1}$ ^{152}Eu). Fulvic acid solutions, adjusted to pH 5 or 7, were added to the clay suspension resulting in a concentration of 40 $mg \cdot L^{-1}$. After reaching equilibrium (24 h), the remaining [^{160}Tb]terbium or [^{152}Eu]europium concentration in the supernatant was determined after centrifugation (45 min at 7000 rpm), using a gamma counter WIZARD 3" (Perkin-Elmer, USA).

For measuring the adsorption of fulvic acid onto clay, ^{14}C-radiolabeled fulvic acid was prepared by azo-coupling with [^{14}C]aniline (Mansel and Kupsch, 2007). A detailed description of the procedure is given elsewhere (Lippold and Lippmann-Pipke, 2014). The [^{14}C]fulvic acid (40 $mg \cdot L^{-1}$; 150 $Bq \cdot mL^{-1}$) was added to the 4.8 $g \cdot L^{-1}$ clay suspension with variable amounts of NaCl, $CaCl_2$ or $MgCl_2$ (0 - 4 $mol \cdot L^{-1}$) at pH 5 and pH 7. After equilibration for 24 h and centrifugation, the remaining concentration of [^{14}C]fulvic acid was determined by liquid scintilla-

tion counting on a Tri-Carb 3110TR (Perkin-Elmer, USA), using Ultima Gold scintillation cocktail (Perkin-Elmer, USA).

5.2.1.3 Complexation experiments

Solutions of 40 mg·L^{-1} fulvic acid, 10^{-6} M [^{160}Tb]terbium (pH 5) or [^{152}Eu]europium (pH 7) and variable amounts of NaCl, $CaCl_2$ or $MgCl_2$ in a range of 0 - 4 mol·L^{-1} were shaken for an hour and then centrifuged (7000 rpm) with "Vivaspin 2" 2 kDa ultrafilters (Sartorius, Germany). The remaining [^{160}Tb]terbium or [^{152}Eu]europium concentration in the filtrate (non-complexed fraction) was determined with a gamma counter WIZARD 3" (Perkin-Elmer, USA).

5.2.2 Modeling adsorption in ternary systems

In order to predict the effect of ionic strength on the interactions in the ternary system of clay / metal / fulvic acid on the basis of the adsorption and complexation data in the constituent binary systems, a combined K_d approach was applied.

The solid-liquid distribution coefficient for metal adsorption $K_d^{M/S}$ (L·g^{-1}) is given by Eq. (5.1)

$$K_d^{M/S} = \frac{\Gamma_M}{c_M} \tag{5.1}$$

with Γ (mol·g^{-1}) denoting the amount of adsorbed metal M and *c* (mol·L^{-1}) denoting the concentration of free metal in solution.

Accordingly, the distribution coefficient for adsorption of fulvic acid $K_d^{FA/S}$ (L·g^{-1}) is equal to

$$K_d^{FA/S} = \frac{\Gamma_{FA}}{c_{FA}} \tag{5.2}$$

For simplicity, metal-fulvate complexation is likewise given as a distribution coefficient $K_d^{M/FA}$ (L·g^{-1}), calculated according to Eq. (5.3)

$$K_d^{M/FA} = \frac{c_{M-FA}}{c_M\, c_{FA}} \tag{5.3}$$

where $c_{M\text{-}FA}$ is the concentration of metal bound to fulvic acid.

According to the linear additive model, these distribution coefficients are independent of each other, and Eqs. (5.1) - (5.3) can be combined to Eq. (5.4) where K_d^{LAM} (L·g^{-1}) is the solid-liquid distribution coefficient of the metal (free and as fulvate complex) in the ternary system:

$$K_d^{LAM} = \frac{K_d^{M/S} + K_d^{FA/S}\, K_d^{M/FA}}{1 + K_d^{M/FA}} \tag{5.4}$$

5.2.3 Results

Fig. 38 shows the adsorption of Tb(III) (pH 5) and Eu(III) (pH 7) onto Opalinus Clay, represented as logarithmical solid-liquid distribution coefficient $K_d^{M/S}$ as a function of ionic strength. With increasing ionic strength *I* (up to almost saturated solutions, *I* = 4 M for NaCl, *I* = 12 M for $CaCl_2$ and $MgCl_2$), K_d values strongly decrease, most pronounced for the bivalent cations. At a pH of 5, metal adsorption is stronger suppressed than at pH 7, which is explained by the lower adsorption capacity of clay resulting from protonation.

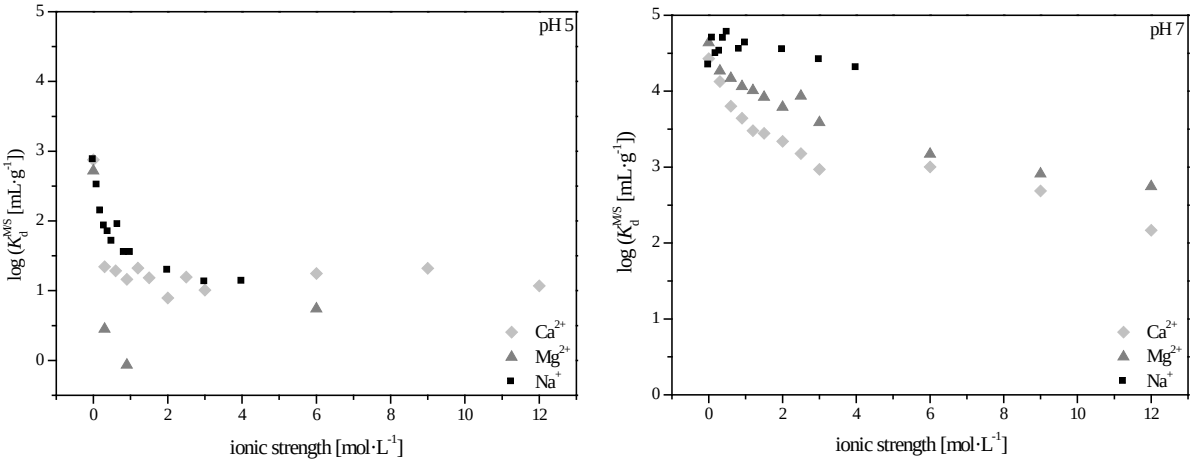

Fig. 38: Adsorption of Tb(III) (pH 5) and Eu(III) (pH 7) onto Opalinus Clay in the presence of NaCl, $CaCl_2$ and $MgCl_2$.

In Fig. 39, adsorption of fulvic acid at pH 5 and 7 in the presence of NaCl, $CaCl_2$ and $MgCl_2$ is shown as a function of ionic strength. Adsorbed amounts are relatively insensitive to increasing ionic strength. Adsorption of fulvic acid is slightly higher at pH 5 since repulsion by negative charge on fulvic acid and clay surface is reduced by protonation (Lippold and Lippmann-Pipke, 2009).

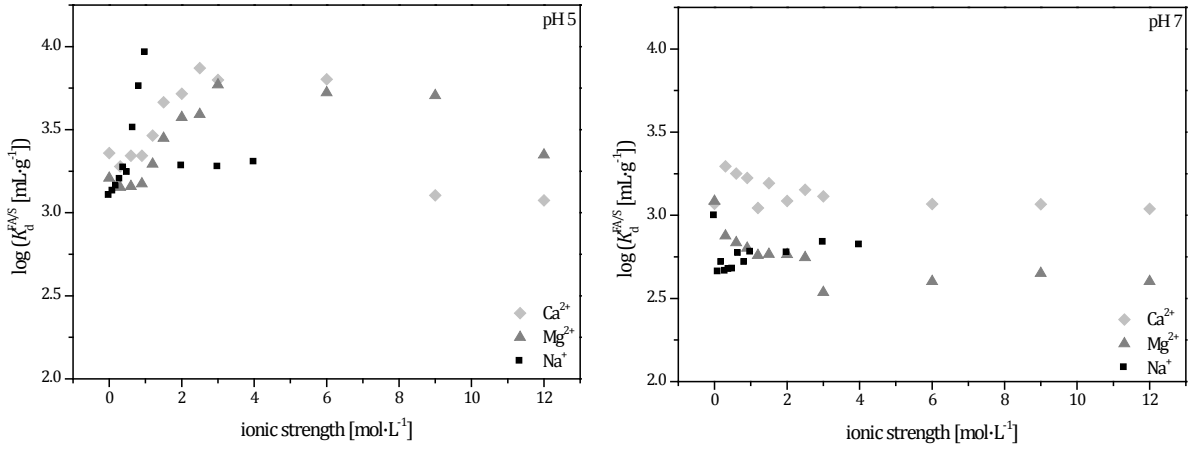

Fig. 39: Adsorption of fulvic acid onto Opalinus Clay at pH 5 and 7 in the presence of NaCl, $CaCl_2$ and $MgCl_2$.

The dependence of Tb(III)- or Eu(III)-fulvate complexation on ionic strength is shown in Fig. 40. For better comparison, these data are likewise given as distribution coefficients $K_d^{M/FA}$, considering the fulvic acid colloids as a pseudo solid phase. Complexation of Tb(III) and Eu(III) is strongly suppressed with increasing ionic strength and is significantly lower at pH 5 than at pH 7. The pH dependence is caused by the protonation of fulvic acid which leads to blocking of ligands (Lippold et al., 2005).

Again, the influence of ionic strength is higher for the bivalent cations Ca^{2+} and Mg^{2+}. Both show strong interference on complexation, which is explained by competition or shielding effects. More detailed investigations by mechanistic modeling to differentiate between these two influences are described in chapter 5.4.

To verify the accuracy of the separation of free and fulvic-bound metal via ultrafiltration, possible sources of experimental errors were taken into consideration. (I) The membrane of the ultrafilters may be transmissible for small fulvic acid molecules, pretending lower complexed fractions. (II) Tb or Eu may be adsorbed at the membrane, pretending higher complexed fractions. (III) A possible perturbation of the complexation equilibrium due to the up-concentration of fulvic acid during the filtration process may lead to changes in the results. Issues (I) and (II) proved to be insignificant in preliminary tests. Complexation was also investigated by time-resolved laser fluorescence spectroscopy (TRLFS) as an alternative method (cf. chapter 5.3.). Very similar results were obtained, showing that issue (III) is not important as well. The TRLFS studies have also shown that formation of chloro complexes for Tb(III) and Eu(III) at high ionic strength is negligible.

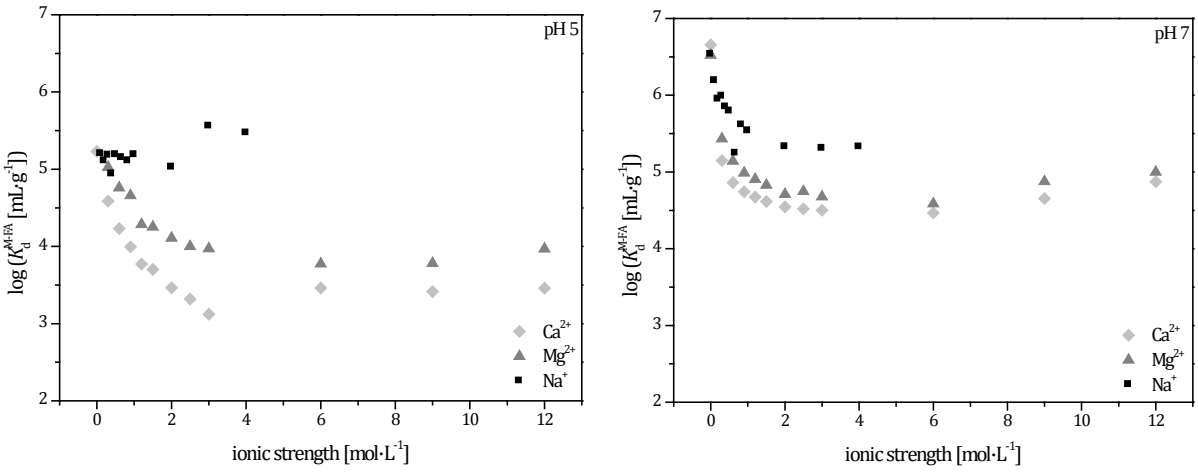

Fig. 40: Complexation of Tb(III) or Eu(III) with fulvic acid as a function of ionic strength at pH 5 and 7 in the presence of NaCl, $CaCl_2$ and $MgCl_2$.

Fig. 41 shows the adsorption of Tb(III) and Eu(III) on Opalinus Clay in the presence and absence of fulvic acid as a function of ionic strength for NaCl, $CaCl_2$ and $MgCl_2$. At pH 5, the presence of fulvic acid leads to increased adsorption of Tb(III) in general. In the case of $MgCl_2$, high ionic strength suppresses adsorption of Tb(III) on clay almost completely, whereas the ternary system with fulvic acid shows significant adsorption. Mineral-bound fulvic acid increases adsorption of metal ions at acidic conditions. With increasing ionic

strength, complexation is suppressed and leads to lower adsorbed amounts. At pH 7, the effect of fulvic acid is reversed: Metal adsorption is decreased compared to the system without fulvic acid. Obviously, this changeover is a consequence of the pH-dependent adsorption behavior of the organic carrier (cf. Fig. 39).

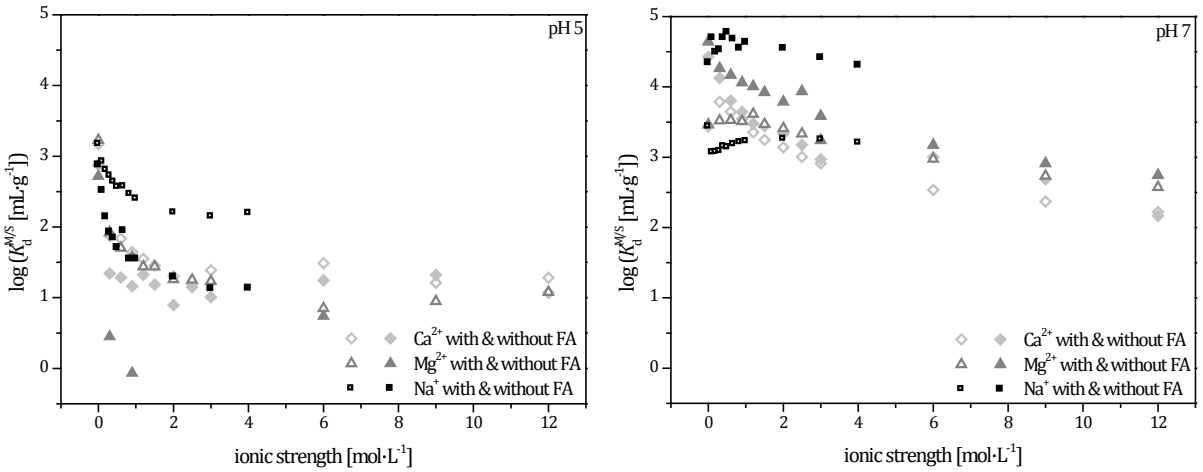

Fig. 41: Adsorption of Tb(III) (pH 5) and Eu(III) (pH 7) on Opalinus Clay in the presence (empty symbols) and absence (full symbols) of fulvic acid as a function of ionic strength for NaCl, $CaCl_2$ and $MgCl_2$ as electrolytes.

Fig. 42 shows the measured distribution coefficients for the co-adsorption of metal and metal-fulvate complex together with the corresponding K_d^{LAM} values calculated according to Eq. (5.4).

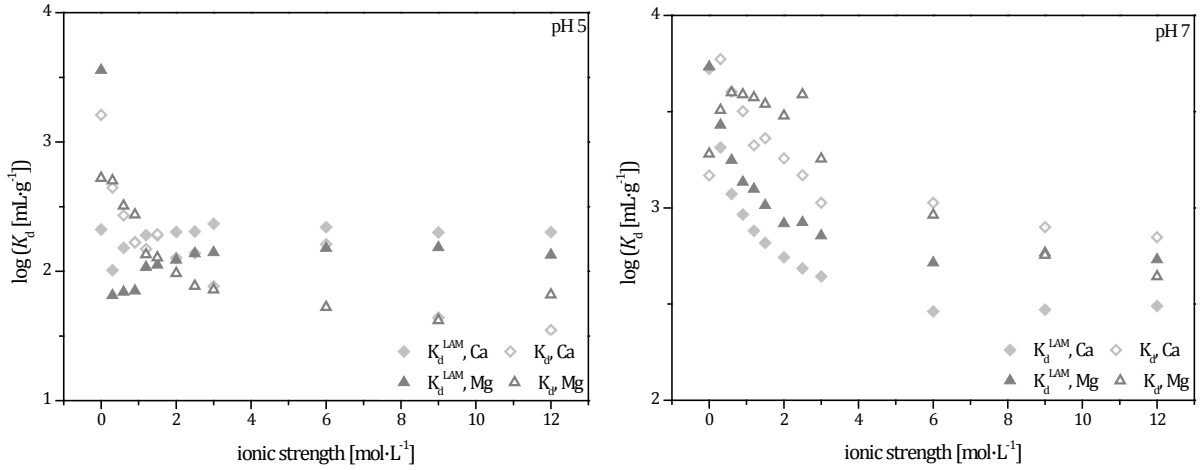

Fig. 42: Adsorption of Tb(III) (pH 5) and Eu(III) (pH 7) on Opalinus Clay in the presence of fulvic acid as a function of ionic strength for $CaCl_2$ and $MgCl_2$ as electrolytes. The full symbols show the calculated values according to the linear additive model (Eq. (5.4)).

The model reproduces the measured data for the bivalent cations quite well, especially for pH 7. Nonetheless, the prediction by the linear additive model leads to slightly lower (in case of pH 5) or higher (for pH 7) K_d values for the solid-liquid distribution ratio in the ternary system. Nonetheless, the predicted (i.e., not fitted!) modeled data show a similar trend as the

measured values. Overall, the additivity concept proved to be suitable for estimations on the effect of humic material on metal adsorption at variable solution conditions.

In summary, this study has shown that a mobilization of metals caused by humic matter is not enhanced by high ionic strength. On the contrary, a mitigating effect was evidenced, based on the fact that complexation is suppressed while adsorption of humic matter is hardly influenced. At low pH, adsorption of metals on a clay surface is increased by fulvic acid due to the formation of surface complexes of the type S-FA-M. Their presence has been proven by the applicability of the linear additive model. This approach is a simple method to reconstruct adsorption data, proving or disproving the additivity of the binary equilibria in the ternary system. It was found to be suitable for predicting trends in the co-adsorption of metals and fulvic acid in dependence on ionic strength, in part nearly quantitatively.

A main reason of deviations is that selectivities in complexation and adsorption within the polydisperse system of fulvic acid molecules are not taken into account. For instance, preferred adsorption of molecules with high metal loads would entail an underestimation by the model, since it operates with an averaged metal load, determined for the humic substance as a whole. Furthermore, a certain amount of ternary surface complexes of the kind S-M-FA may be present, which is not considered in this approach.

5.3 TRLFS studies of Eu-fulvate complexes at high ionic strength

5.3.1 Experimental

Multiple series of experiments were made to investigate the influence of high ionic strength on the complexation of fulvic acid with Eu^{3+} in detail. Variable amounts of NaCl, $CaCl_2$, $MgCl_2$, $AlCl_3$ or $GdCl_3$ (0 - 2 mol·L^{-1}) were added to solutions of 40 mg·L^{-1} fulvic acid and 10^{-5} M Eu. The pH of the solutions was adjusted to 5. Time-resolved luminescence spectra were recorded using a pulsed flash lamp pumped Nd:YAG-OPO laser system (Powerlite Precision II 9020 laser equipped with a green PANTHER EX OPO from Continuum, Santa Clara, USA). The laser pulse energy, which was between 1.2 and 1.9 mJ, was monitored using a photodiode. Luminescence spectra were detected using an optical multi-channel analyzer-system, consisting of an Oriel MS 257 monochromator and spectrograph with a 300 or 1200 lines·mm^{-1} grating and an Andor iStar ICCD camera (Lot-Oriel Group, Darmstadt, Germany) (cf. Moll et al., 2014). The Eu(III) single luminescence emission spectra were recorded in a range of 570 - 640 nm (1200 lines·mm^{-1} grating) at an excitation wavelength of 394 nm. The time-dependent luminescence spectra were detected in the same range of wavelengths with a 300 lines·mm^{-1} grating. The spectra were base-line corrected, energy corrected and normalized using MATLAB R2015a (MathWorks GmbH, USA) and Origin 8.5 (OriginLab Corporation, USA).

The F1 and F2 bands were observed because these transitions are influenced by the chemical environment of the metal ion. The relative peak intensity ratios (F1:F2) were calculated

from the peak areas. The number of coordinated water molecules *n* was calculated using an empirical equation proposed by Kimura et al. (1996)

$$n(H_2O) = \frac{1.07}{\tau(Eu)} - 0.62 \qquad (5.5)$$

where τ is the measured luminescence lifetime (ms).

5.3.2 Results

As the emission spectra in Fig. 43 show, complexation of Eu with fulvic acid is highly suppressed at higher ionic strength. With increasing Ca^{2+} concentration, the F1 and F2 bands progressively converge to the spectrum of the Eu^{3+} aquo ion (black in Fig. 43).

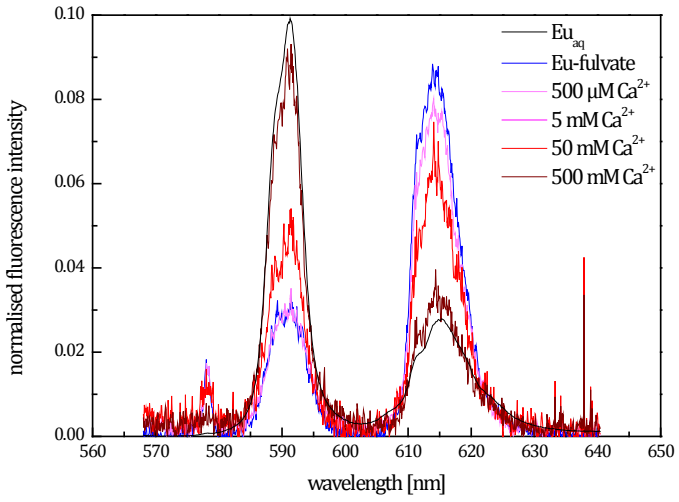

Fig. 43: Emission spectra of Eu-fulvate with different concentrations of $CaCl_2$. The spectrum in black represents the Eu^{3+} aquo ion, the spectrum in blue represents the Eu-fulvate complex without a background electrolyte.

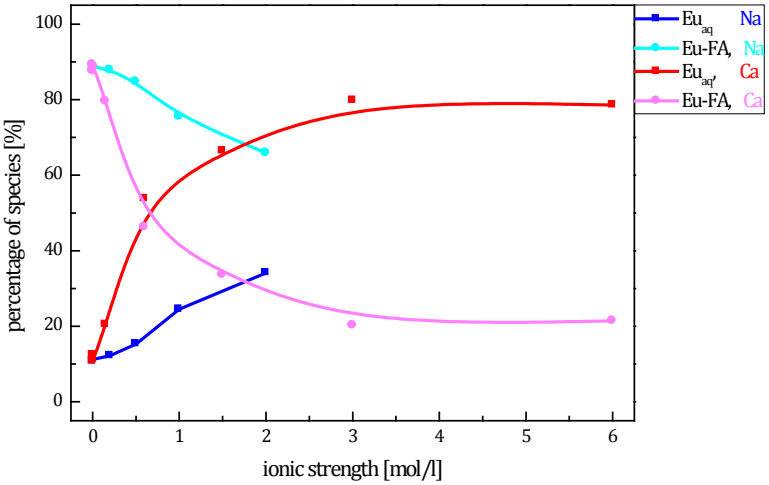

Fig. 44: Percentage of Eu species in solution as a function of ionic strength for Na^+ and Ca^{2+}. Light colors: fulvate species, dark colors: aquo species.

On the basis of this dependence, the species distribution of Eu can be calculated. Fig. 44 shows the percentages of Eu aquo and Eu-fulvate species depending on ionic strength.

As batch studies have shown before (Fig. 40), the percentage of Eu-fulvate decreases with increasing ionic strength. The TRLFS studies indicate that displaced Eu is present in the form of aquo species. By means of Eq. (5.5), it was found that at a concentration of 2 M NaCl or 50 mM $CaCl_2$, Eu is completely coordinated with water molecules and forms a $Eu(H_2O)_9$ complex.

At a fixed electrolyte concentration, different cations show very different spectral effects, as can be seen in Fig. 45. It is obvious that the influence of Na on complexation of Eu with fulvic acid is least. Even in the presence of 500 mM Na (Fig. 45, right), the spectrum is changed only slightly. The trivalent cations Al and Gd cause the most pronounced spectral changes. Already at a low electrolyte concentration of 500 µM, (Fig. 45, left), the spectra are close to that of the $Eu(H_2O)_9$ complex. This shows that the electrolyte cations differ greatly in their competing effects towards Eu. Binding sites are blocked by trivalent metals much more efficiently than by mono- and divalent cations.

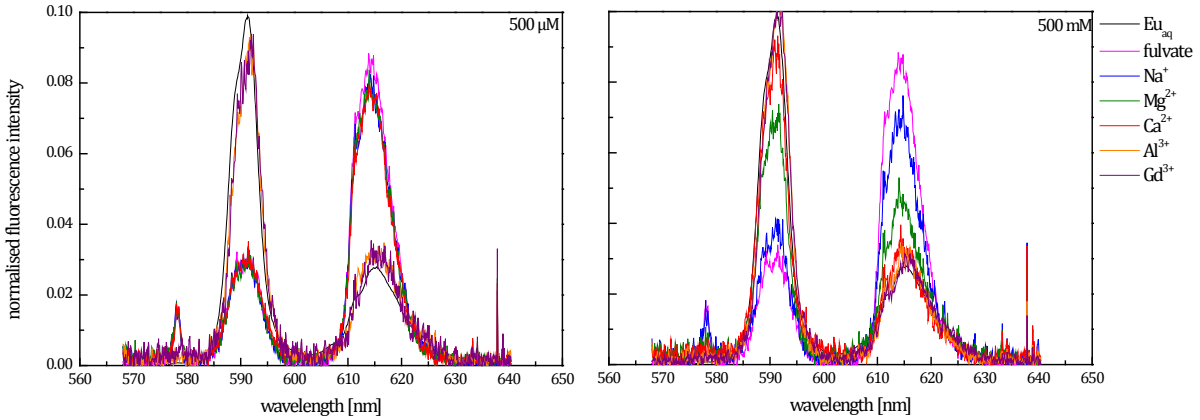

Fig. 45: Emission spectra of Eu-fulvate with 500 µM (left) and 500 mM (right) of Na^+, Mg^{2+}, Ca^{2+}, Al^{3+} or Gd^{3+}. The spectrum in black represents the Eu^{3+} aquo ion, the spectrum in magenta represents the Eu-fulvate complex without a background electrolyte.

The influence of the type of electrolyte anion was investigated as well and is shown in Fig. 46. The investigated counterions ClO_4^-, NO_3^- and Cl^- do not show a significant difference in their influence on the complexation of Eu with fulvic acid. The spectra are nearly identical for a defined concentration (1 mM and 200 mM). It is known that ClO_4^- ions, owing to their size, do not form complexes with Eu. Thus, it may be concluded that chloro complexes are not formed as well.

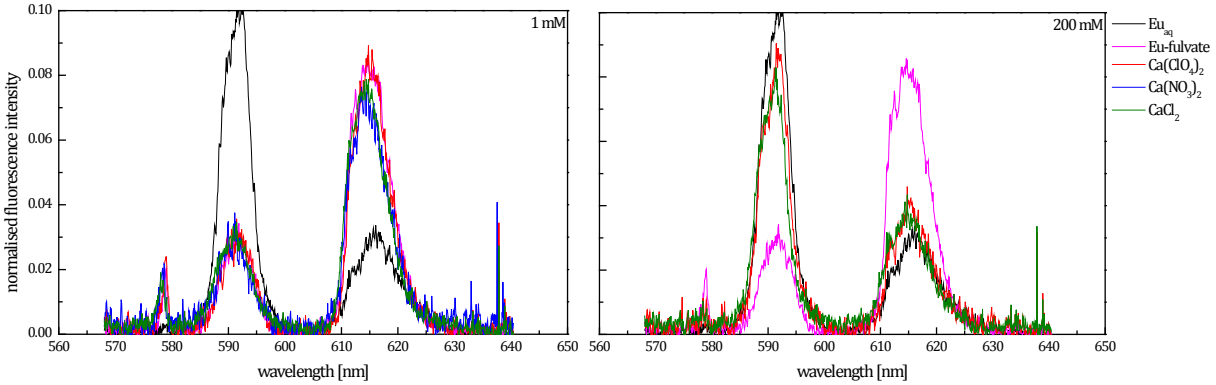

Fig. 46: Emission spectra of Eu-fulvate with 1 mM (left) and 200 mM (right) of ClO_4^-, NO_3^- or Cl^-. The spectrum in black represents the Eu^{3+} aquo ion, the spectrum in magenta represents the Eu-fulvate complex without a background electrolyte.

5.4 Modeling metal binding to fulvic acid

5.4.1 NICA-Donnan model

The NICA-Donnan model (Kinniburgh et al., 1996) describes cation binding to humic substances by specific interactions with functional groups as well as non-specific Coulomb interactions.

The NICA (non-ideal competitive adsorption) model (Koopal et al., 1994; Benedetti et al., 1995) is based on a continuous distribution of site affinities for protons and metal ions. The bimodal form for carboxylic and phenolic binding sites (type I and II, respectively) is given by Eq. (5.6)

$$Q_i = Q_{i,max}\,\theta_i = Q^{I}_{i,max}\,\theta^{I}_i + Q^{II}_{i,max}\,\theta^{II}_i = Q^{I}_{i,max}\,\frac{(\tilde{K}^{I}_i c_i)^{n^{I}_i}}{\sum_i (\tilde{K}^{I}_i c_i)^{n^{I}_i}}\,\frac{\{\sum_i (\tilde{K}^{I}_i c_i)^{n^{I}_i}\}^{p^{I}}}{1+\{\sum_i (\tilde{K}^{I}_i c_i)^{n^{I}_i}\}^{p^{I}}} + Q^{II}_{i,max}\,\frac{(\tilde{K}^{II}_i c_i)^{n^{II}_i}}{\sum_i (\tilde{K}^{II}_i c_i)^{n^{II}_i}}\,\frac{\{\sum_i (\tilde{K}^{II}_i c_i)^{n^{II}_i}\}^{p^{II}}}{1+\{\sum_i (\tilde{K}^{II}_i c_i)^{n^{II}_i}\}^{p^{II}}} \quad (5.6)$$

where Q describes the amount of a component i bound to the humic substance, Q_{max} is the number of binding sites, Θ is the degree of coverage, c is the concentration, $\widetilde{K_i}$ is the median equilibrium constant, p represents the width of the affinity distribution, and n is a parameter accounting for non-ideality with respect to component i.

Electrostatic effects are considered by using concentrations near binding sites rather than concentrations in the bulk solution. The up-concentration by the electric field is described by the Donnan model, assuming a gel-like phase with a uniform electric potential Ψ_D. Specific binding (Q_i) is calculated by Eq. (5.6), using enhanced concentrations c^D, which are given by Eq. (5.7):

$$c^{D}_{i} = c_i \exp(-z_i e \Psi_D / k T) \quad (5.7)$$

In this equation, c^D is the concentration of component i in the Donnan phase, z is the charge number of the ion, e is the elementary charge, k is the Boltzmann constant, and T is the absolute temperature.

Up-concentrated ions within the Donnan phase (in excess of the bulk concentration) are included in the total amount bound to the humic substance (non-specific binding):

$$Q^{D}_{i} = V_D (c^{D}_{i} - c_i) + Q_i \quad (5.8)$$

Q^D is the amount of component i enriched within the Donnan volume V_D by specific and non-specific binding. The Donnan volume is dependent on the ionic strength I. The following empirical relation holds:

$$\log V_D = B \log I - B - 1 \quad (5.9)$$

The parameter B is specific to the type of humic substance.

5.4.2 Results of modeling

NICA-Donnan parameters for binding of Eu, Na, Ca and Mg to a generalized fulvic acid were taken from (Milne et al., 2003). Measured data were modeled by fitting the parameters $\widetilde{K_i}$ and n in Eq. (5.6) for Tb and Eu by means of the speciation software ECOSAT 4.8 (Keizer and Van Riemsdijk, 2005) coupled with the parameter optimization program FIT. Results and adjusted parameters are shown in Fig. 47 and Table 8.

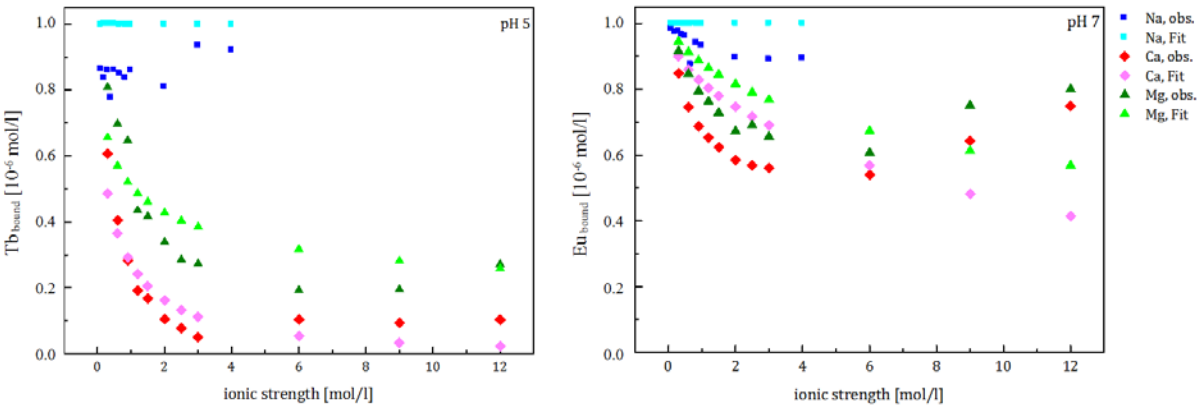

Fig. 47: Amount of Tb and Eu bound to fulvic acid at pH 5 and pH 7, respectively, plotted against ionic strength for NaCl, $CaCl_2$ and $MgCl_2$. Dark colors: experimental data, light colors: calculated data obtained with the NICA-Donnan model.

Table 8: NICA-Donnan parameters adjusted for Tb and Eu. All other parameters in Eqs. (5.6) - (5.9) were taken from Milne et al. (2003).

	log $\widetilde{K}^{I}$	log $\widetilde{K}^{II}$	n^{I}	n^{II}
Eu only (Milne et al., 2003)	-1.92	5.87	0.47	0.45
Eu with Na, pH 7	-1.91	5.87	0.50	0.49
Eu with Ca, pH 7	-1.92	5.87	3.07	4.17
Eu with Mg, pH 7	-1.61	5.29	0.44	0.93
Tb with Na, pH 5	-1.92	5.86	0.51	0.41
Tb with Ca, pH 5	-1.92	4.62	2.92	2.12
Tb with Mg, pH 5	-2.40	5.87	0.83	0.05

In general, the adjusted values for the equilibrium constants $\widetilde{K}^{I}$ and $\widetilde{K}^{II}$ show only moderate deviations from the generic parameters given by Milne et al. (2003), which were used as starting values for Eu as well as for Tb. From the fact that non-specific electrolyte effects at high ionic strengths are not yet considered adequately in these calculations, it may be inferred that the influence of the electrolyte cations is dominated by direct competition rather than shielding. This is, however, a tentative conclusion. More detailed studies including SIT and Pitzer parameters are pending.

6 Tc(VII)/Tc(IV) retention by iron(II)-containing minerals

Technetium-99 is a *β*-emitting fission product of uranium-235 and plutonium-239 with a long half-life (2.1×10^5 years) and a high content in radioactive waste (6 % of all fission products consist of Tc-99).

Under oxic conditions, Tc is present as pertechnetate (TcO_4^-, Tc(VII)), which is a highly soluble, aqueous species that is known not to sorb significantly on minerals or sediments. However, under anaerobic conditions and in the presence of a reducing agent, Tc(VII) is reduced to Tc(IV). Thereby, the Tc solubility decreases drastically due to precipitation of respective hydrolysis products of Tc(IV) (Peretyazhko et al., 2008, 2012; Kobayashi et al., 2013).

Iron(II)-containing minerals occur ubiquitously in nature and as corrosion products of carbon steel canisters used for storing radioactive waste. Iron(II)-minerals are characterized by redox reactivity and a high sorption capacity. Thus, they can control the environmental fate of radionuclides, for instance, Tc.

The objective of this study was to improve the understanding of Tc(VII)/Tc(IV) retention by iron(II)-containing minerals such as magnetite ($Fe^{II}Fe^{III}{}_2O_4$) and siderite ($Fe^{II}CO_3$). For this, batch sorption experiments were performed at room temperature under anoxic conditions and exclusion of CO_2 (glove box with N_2 atmosphere, O_2 <5 ppm), as function of pH, ionic strength of the background electrolyte (NaCl), contact time, and solid-to-liquid (S/L) ratio. In addition, ATR FT-IR and XAS spectroscopy were applied. For comparison, Tc retention on iron(III)-containing minerals hematite (α-Fe_2O_3) and maghemite (γ-Fe_2O_3) was studied.

6.1 Experimental

Materials

The mineral phases magnetite and siderite were prepared under inert gas conditions (glovebox, N_2 atmosphere, <10 ppm O_2) with degassed Milli-Q water.

Magnetite: 60 mL of a 6 M NH_4OH (p.a., Merck) solution was slowly added to 50 mL solution of 0.4 M $FeCl_2 \times 4H_2O$ (ReagentPlus 99 %, Sigma Aldrich) and 0.8 M $FeCl_3 \times 6H_2O$ (p.a., Merck) under vigorous stirring. Immediately a black precipitate was formed. The stirring of the solution was continued for 12 h. Then, the solid was separated by centrifugation (0.5 h, 4600*g*). Two batches of magnetite were synthesized. One part of the synthesized magnetite was washed two times with water and then, two times with 0.01 M NaCl (p.a., Merck). This material was stored as suspension in 0.01 M NaCl. The other part was washed four times with water and then, freeze-dried whereby a magnetite powder was obtained. The phase-purity and structure of the synthesized magnetite powder was characterized by X-ray diffraction (XRD) (mod. Bruker-AXS Diffractometer D8 with curved PG-secondary monochromator) and moreover, the specific surface area was determined applying the Brunauer-Emmet-Teller (BET) equation (mod. SA 3100, Beckman Coulter, Fullerton, USA).

Siderite: 100 mL of 0.8 M Na_2CO_3 (p.a., VWR) solution was slowly added (within 8 h by peristaltic pump) to 100 mL of 0.4 M $FeCl_2 \times 4H_2O$ (ReagentPlus 99 %, Sigma Aldrich) solution under vigorous stirring and purging with N_2. The formed pale solid was separated by centrifugation (0.5 h, 4600*g*) and washed with water. Then, the purified solid was washed three times with 0.1 M NaCl (p.a., Merck) and finally, equilibrated in 0.1 M NaCl. A detailed characterization of the siderite was not possible because of its pronounced oxidation-sensitivity. However, the characteristic light-grey color of the siderite suspended in solution, without any color change over time, is an indication of the chemical (redox) stability of the siderite batch.

Hematite, maghemite: The minerals hematite (>99 %, US Research Nanomaterials) and maghemite (>99 %, Alfa Aesar) were applied as obtained.

Batch sorption experiments

Calculated amounts of the minerals hematite and maghemite or calculated volumes of the magnetite and siderite stock suspensions (36.2 g/L and 54 g/L, respectively) were given in 15 mL centrifuge tubes (PP, Cellstar, Greiner Bio-One GmbH, Frickenhausen, Germany). After that, 10 mL of the background electrolyte (0.1 M or 1 M NaCl solution, which were prepared by dissolution of NaCl (p.a., Merck) in degassed Milli-Q water) were added. The pH values of the sample suspensions were measured applying a pH meter (mod. inoLab pH 720, WTW, Weilheim, Germany) with a SenTix® Mic pH microelectrode (WTW), calibrated using standard buffer solutions (WTW; pH= 4.006, 6.865, 9.180). If necessary, the pH values were adjusted by addition of small amounts of diluted HCl or NaOH (p.a., Merck; carbonate-free) solutions.
After pre-equilibration, the sorption experiment was started by adding an aliquot (5.55 µL) of the $^{99}TcO_4^-$ stock solution (1.81×10^{-2} M $^{99}TcO_4^-$; 1.125 MBq/mL) resulting in a Tc concentration of 1×10^{-5} M. Blank suspensions of the minerals in the background electrolytes without TcO_4^- were prepared and processed under the same conditions.
During pre-equilibration and sorption, the samples were continuously shaken on a horizontal shaker (mod. IKA Vibrax VXR basic). The pH values were measured/adjusted daily.
After the sorption experiments, the final pH values of the samples were determined. Moreover, for the experimental series with magnetite and siderite performed in 1 M NaCl background electrolyte as a function of pH, redox potentials (E_h) were monitored at selected pH values using a combined Pt/Ag/AgCl redox electrode (Schott, Mainz, Germany), calibrated using a standard redox buffer solution (WTW) at pH 7. The values were recorded after at least 1 h. The E_h values given in the paper correspond to the minima of the E_h evolution during the measurements and are corrected for the standard hydrogen potential (SHE).
With the exception of the siderite samples, the solid and liquid phases were separated by centrifugation (6800*g* for 2 h). To prevent the transport of the extremely oxidation-sensitive siderite samples to the centrifuge, standing outside the inert gas box, the siderite suspensions were filtered (0.2 µm, polyethersulfone, VWR International, Darmstadt, Germany) inside the glove box to separate the mineral from the sample solution.
The final Tc concentration in the supernatants was determined by liquid scintillation counting (LSC; mod. TriCarb 3100 TR, Perkin Elmer, Freiburg, Germany) using 1 mL supernatant and 15 mL Ultima Gold™ (Perkin Elmer) as scintillation cocktail.
A compilation of the various sorption series is given in Table 9. All sorption experiments were performed in duplicate.

Table 9: Summary of batch sorption experiments.

Mineral	Solid/solution ratio [g/L]	Contact time	pH value	Ionic strength [mol/L]
Hematite	1	18 d	4	0.1
Maghemite	1	18 d	4	0.1
Magnetite	0.1 – 1.5	2 d	4	0.1
	0.2	1 - 165 h	4	0.1
	0.2	2 d	4 - 12	0.1
	0.2	2 d	4 - 12	1
Siderite	0.2 - 0.5	0.5 - 150 h	8	0.1
	0.2	2 d	8 - 12	0.1
	0.2	2 d	8 - 12	1

ATR FT-IR spectroscopic sorption study

The Tc sorption onto hematite, maghemite and magnetite was studied by means of *in situ* ATR FT-IR spectroscopy. Although all sample preparation steps were performed in a glove box under N_2 atmosphere, the Tc sorption onto siderite could not be studied since a complete exclusion of oxygen during the FT-IR measurements was obviously not possible which led to a partial oxidation of iron(II) in the siderite mineral.

Infrared spectra were measured from 1000 to 800 cm^{-1} on a Bruker Vertex 70/v vacuum spectrometer, equipped with a Mercury Cadmium Telluride (MCT) detector. Spectral resolution was 4 cm^{-1} and spectra were averaged over 256 scans. A horizontal diamond crystal with nine internal reflections (DURA SamplIR II, Smiths Inc.) was used. The measurements were performed in D_2O to prevent an overlapping of the TcO_4^- band at about 900 cm^{-1} with the pronounced absorption band of H_2O at 1000 cm^{-1}.

For the *in situ* ATR FT-IR experiments a mineral film was prepared directly as stationary phase on the surface of the ATR diamond crystal. Then, the mineral film was conditioned by flushing with 0.1 M NaCl solution for 45 min using a flow cell (V = 200 µL) at a rate of 200 µL/min. Subsequently, the sorption reactions were induced by rinsing the stationary phase with the sample solution ($[TcO_4^-] = 5\times10^{-4}$ M; 0.1 M NaCl) for 60 min. Finally, the loaded mineral phase was flushed again with 0.1 M NaCl solution (45 min) in order to gain more information on the reversibility of the sorbed species.

XAS sample preparation and measurements

The XAS samples were prepared and processed analogous to the samples of the batch sorption experiments under N_2 atmosphere. 300 mg magnetite mineral and 5.55 mL siderite suspension, respectively, were added in 50 mL centrifuge tubes (PP). The volume was filled up to 40 mL with 0.1 M NaCl electrolyte and calculated amounts of the Tc stock solution. The solid-to-liquid ratio was 7.5 g/L. The Tc content, the pH values as well as the contact times were varied as specified in Table 10.

Table 10: Summary of XAS samples.

Sample	Mineral	Tc content [Bq/sample]	Solid/solution ratio [g/L]	Ionic strength [mol/L]	Contact time [d]	pH
Tc15-14	Magnetite	1265379	7.5	0.1	5	7.18
Tc15-15	Magnetite	631405	7.5	0.1	5	7.14
Tc15-16	Magnetite	159545	7.5	0.1	2	11.87
Tc15-17	Magnetite	633180	7.5	0.1	1	5.31
Tc15-18	Magnetite	183825	7.5	3.0	2	11.80
Tc15-19	Magnetite	631763	7.5	0.1	2	5.33
Tc15-20	Siderite	1263875	7.5	0.1	2	7.75
Tc15-21	Siderite	630847	7.5	0.1	2	7.82
Tc15-22	Siderite	1258953	7.5	0.1	2	11.83
Tc15-23	Siderite	633116	7.5	0.1	2	11.91

(The XAS data of Tc15-16 and Tc15-18 could finally not be evaluated since the surface loading was not high enough.)

After equilibration, the samples were centrifuged and the supernatants were removed. The remaining minerals were transferred as wet pastes into double confined sample holders (SH01C). Subsequently, the samples were shock frozen in liquid N_2. After that, the samples were transported to the Rossendorf Beamline at the European Synchrotron Radiation Facility (ESRF) in Grenoble, France. During the XAS measurements, the samples were kept at 15 K in a closed-cycle He cryostat. The spectra were acquired in fluorescence mode at the Tc *K*-edge (21044 eV). Energy of the Si(111) double-crystal monochromator was calibrated using a Mo foil (edge energy 20000 eV).

6.2 Results and discussion

6.2.1 Characterization of magnetite

Phase-purity and structure of the synthesized magnetite was checked by X-ray diffraction (XRD). The diffractograms recorded for the magnetite charges 1 and 2 are very similar (cf. Fig. 48). Only the diffractogram obtained for charge 1 shows a very slight 2θ-shift. Nevertheless, the reflexes correspond very well to the reflexes of a synthetic magnetite reference shown in red. This verifies a high phase-purity and a highly ordered crystal lattice of the synthesized magnetite charges.

The specific surface areas of the magnetite charges 1 and 2 were determined with 84.2 m^2/g and 86.3 m^2/g, respectively (cf. Table 11). This again shows, that the two magnetite charges are very similar. Thus, the comparability of the sorption series performed with the two charges is ensured.

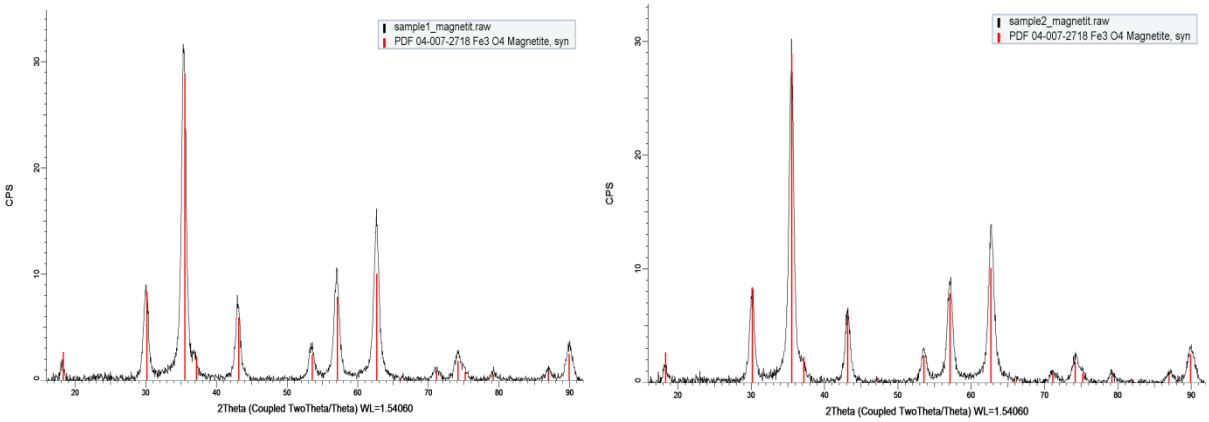

Fig. 48: Diffractograms of magnetite charges 1 and 2.

Table 11: Specific surface areas (BET) of magnetite charges 1 and 2.

	Charge 1 BET [m^2/g]	Charge 2 BET [m^2/g]
	85.1	86.3
	83.2	86.0
	84.2	86.6
Mean value	**84.2**	**86.3**

6.2.2 Batch sorption experiments

The objective of these experiments was the quantification of the retention behavior of various iron mineral phases towards pertechnetate.

Tc retention by hematite and maghemite

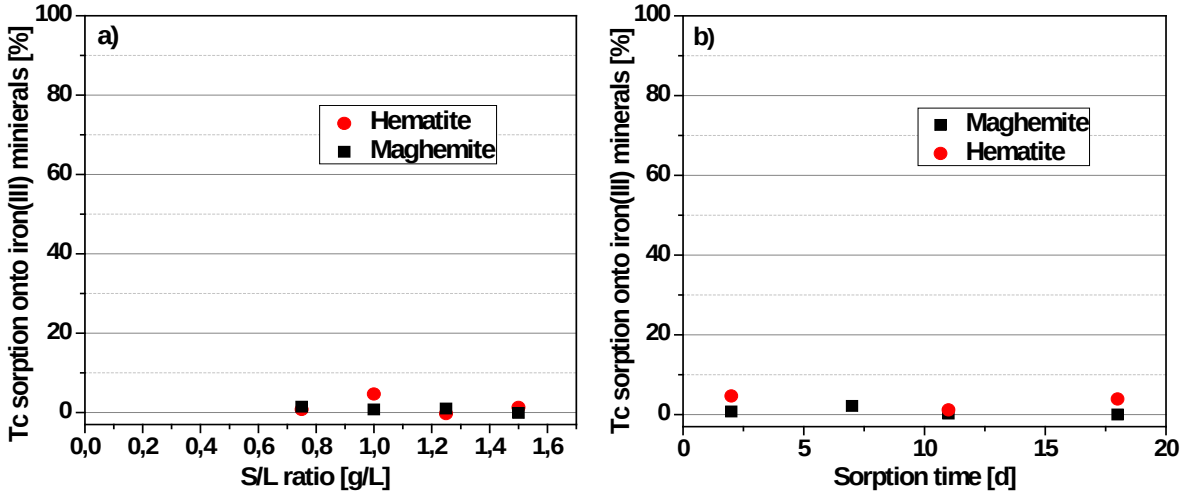

Fig. 49: Tc retention onto hematite and maghemite as function of a) S/L ratio ($[Tc(VII)]_{init}$ = 1×10^{-5} M, pH 4, 0.1 M NaCl, 2 d contact time) and b) contact time ($[Tc(VII)]_{init}$ = 1×10^{-5} M, pH 4, 0.1 M NaCl, S/L ratio: 1 g/L).

Fig. 49 shows that, independent of the S/L ratio, there is no Tc retention on the iron(III) oxides hematite and maghemite after 2 d contact time. Also for contact times of up to 18 d, shown for the samples with an S/L ratio of 1 g/L, no significant sorption of Tc, added as TcO_4^-, can be observed. These results correspond to the results of Peretyazkho et al. (2008).

Tc retention by magnetite and siderite

The iron(II) containing minerals magnetite and siderite show a retention behavior toward Tc completely different from that of maghemite and hematite. After addition of TcO_4^- to the siderite suspension equilibrated at pH 8.6, the Tc retention occurs almost instantly and completely, even at the small S/L ratio of 0.2 g/L (cf. Fig. 50). The Tc retention onto magnetite at pH 4 (Fig. 50), occurs slower and a maximum Tc retention of only 80 % is observed in this experiment.

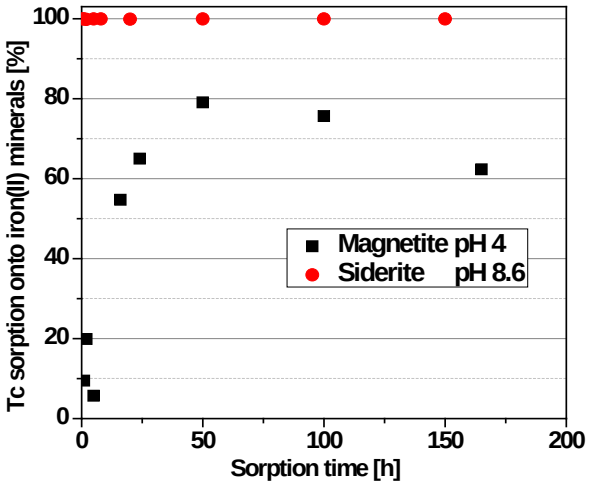

Fig. 50: Tc retention onto magnetite (pH 4) and siderite (pH 8.6) as function of contact time ($[Tc(VII)]_{init}$ = 1×10^{-5} M, S/L = 0.2 g/L, 0.1 M NaCl, N_2).

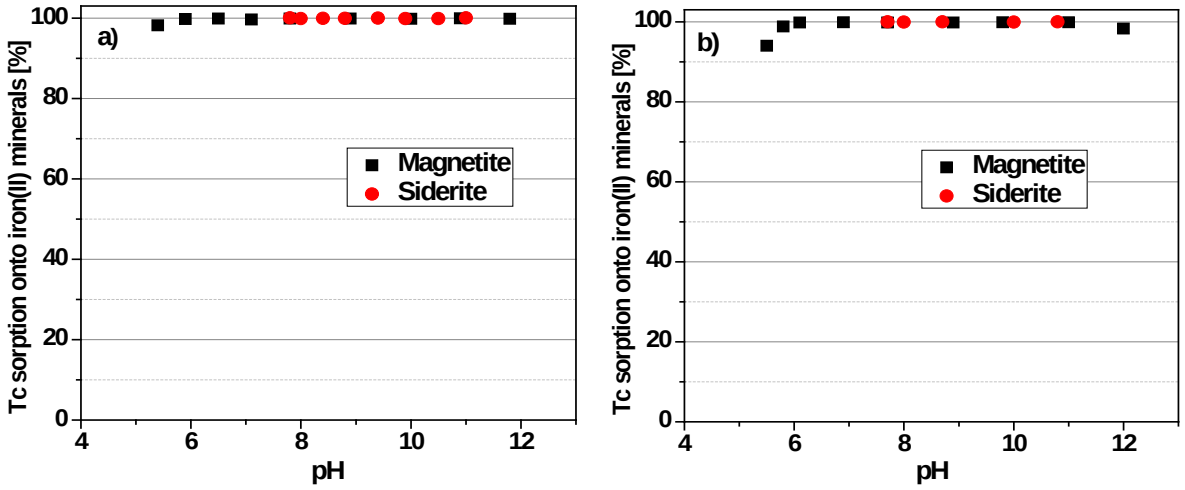

Fig. 51: Tc retention onto magnetite and siderite as function of pH value in a) 0.1 M NaCl and b) 1 M NaCl ($[Tc(VII]_{init}$ = 1×10^{-5} M, S/L = 0.2 g/L, N_2, 2 d contact time).

Fig. 51 shows the Tc retention onto magnetite and siderite as a function of pH value and ionic strength. In the case of siderite, independent of pH value and ionic strength, the Tc retention is almost complete. Magnetite also shows a very high Tc retention, only at pH values lower than 6 a slight decrease is observed. These results support results found by Kobayashi et al. (2013).

From the strong difference observed for the retention behavior of iron(II) and iron(III) minerals towards TcO_4^- it can be concluded that the immobilization of Tc in the case of iron(II) minerals is due to a reduction of Tc(VII) to Tc(IV). In order to estimate the potential for Tc reduction, redox potentials were measured in selected samples.

6.2.3 Redox potentials

Fig. 52 shows the E_h-pH diagram for Tc in aqueous solution, calculated for conditions applied in the sorption experiments (10 µM Tc, 1 M NaCl, 25°C). The calculation was performed with the geochemical speciation code „Geochemist's Workbench" (version 10.0.5) using the default data base „thermo.dat" (LLNL database). Here, the extended Debye-Hückel equation was applied, although only valid for low ionic strengths. However, the application of more adequate equations (SIT, Pitzer) was not possible due to the lack of thermodynamic data for technetium.

In Fig. 52, redox potentials of selected Tc/magnetite samples, monitored at the end of the sorption experiments, are shown as blue squares. They are near the borderline between Tc(VII) and Tc(IV). This means TcO_4^- can be reduced by magnetite. The redox potentials of Tc/siderite samples are even lower (cf. Fig. 53). This confirms the results of batch experiments where the Tc retention by siderite was found to be faster compared to magnetite.

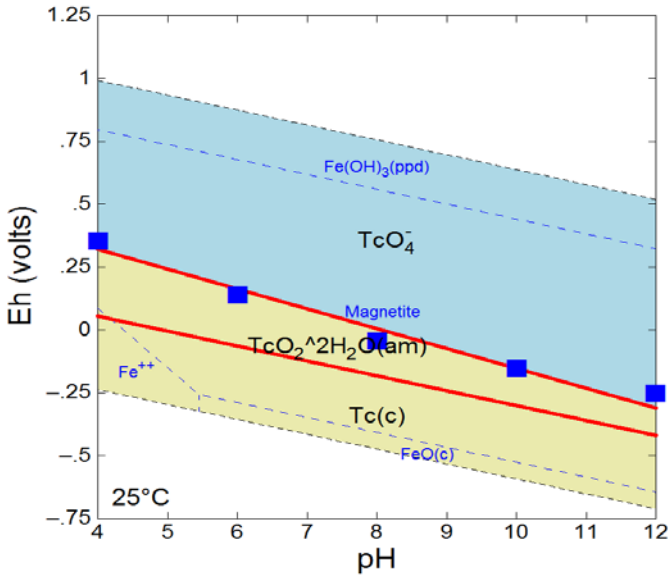

Fig. 52: Eh-pH diagram for Tc in 1 M NaCl (10 µM Tc, 25°C) calculated applying the extended Debye-Hückel equation. Redox potentials of selected Tc/magnetite samples monitored at the end of the sorption experiments are shown as blue squares.

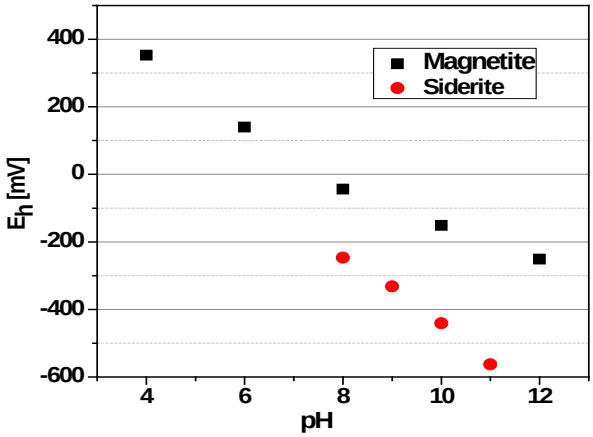

Fig. 53: Redox potentials of selected Tc/magnetite and Tc/siderite samples (1 M NaCl, 25°C).

For the identification of Tc species in aqueous solution as well as on the mineral phase *in situ* ATR FT-IR spectroscopy and X-ray absorption spectroscopy are applied.

6.2.4 ATR FT-IR spectroscopy

The IR spectrum of a pertechnetate reference sample shows that the absorption band of the pertechnetate ion in solution is found at about 908 cm^{-1} (Fig. 54).

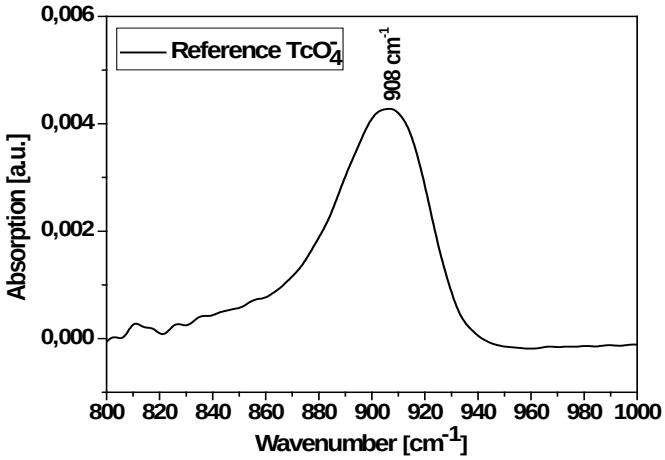

Fig. 54: Reference IR spectrum of pertechnetate ([Tc(VII] = 5×10^{-4} M, 0.1 M NaCl, 25°C).

The FT-IR spectra recorded during Tc(VII) sorption on magnetite, hematite and maghemite do not change with time, thus, for simplicity the spectra recorded after a contact time of 15 min are shown in Fig. 55. The Tc bands observed in these spectra are similar to the band of the aqueous TcO_4^- reference. No shifts are observed and no differences between iron(II) and iron(III) minerals are observed. This means, that during IR experiments only the aquatic, hardly sorbed TcO_4^- was observed. In the time frame of the *in situ* IR experiment, the signal of the Tc(VII) ion did not disappear indicating that the reduction to Tc(IV) occurs on a longer time scale.

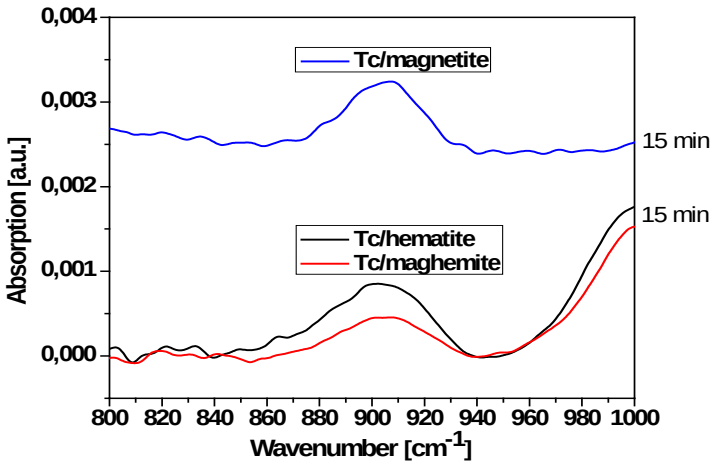

Fig. 55: *in situ* ATR FT-IR spectra of Tc(VII) sorption on magnetite, hematite and maghemite after a contact time of 15 min.

6.2.5 X-ray absorption spectroscopy

A first evaluation of the XAS data obtained for Tc/magnetite and Tc/siderite samples led to XANES spectra shown in Fig. 56 and Fig. 57. The XANES spectra, obtained for magnetite and siderite, are similar (absorption edge 21058 eV, no pre-edge) to each other, but differ from the XANES spectrum of TcO_4^-. This verifies that the immobilization of Tc onto these minerals is due to surface-mediated reduction of Tc(VII) to Tc(IV).

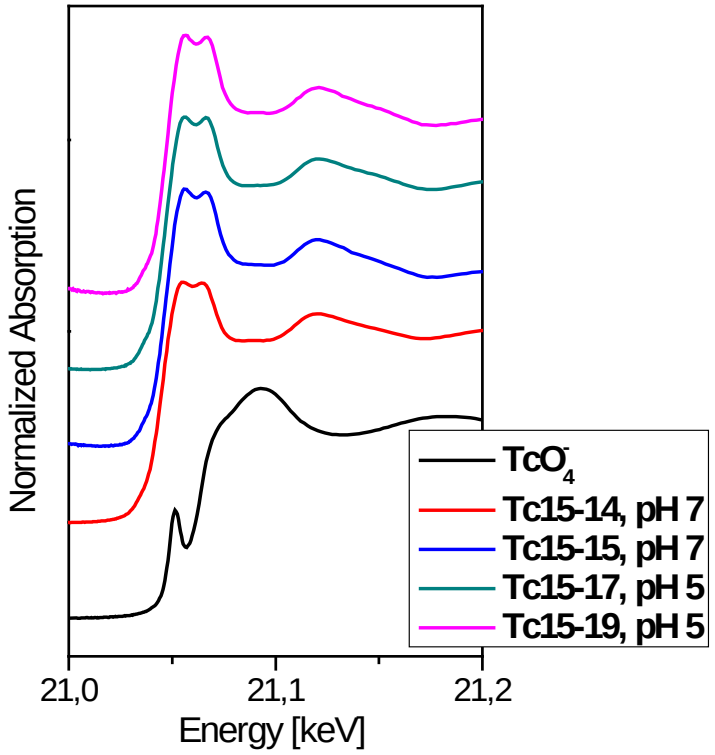

Fig. 56: Tc *K*-edge XANES spectra of Tc(VII) reacted with magnetite in comparison to a TcO_4^- reference spectrum (sample characteristics are given in Table 10).

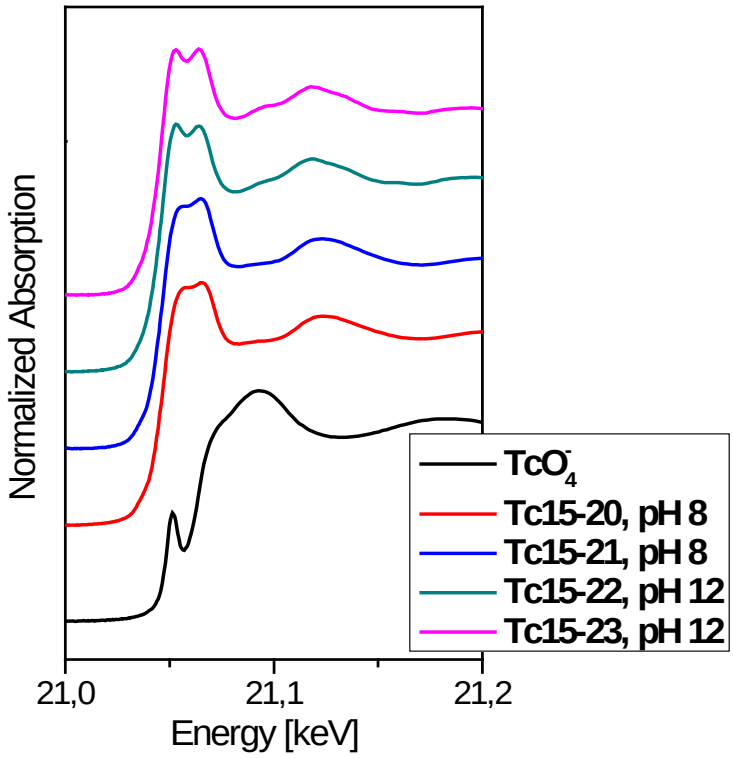

Fig. 57: Tc *K*-edge XANES spectra of Tc(VII) reacted with siderite in comparison to a TcO_4^- reference spectrum (sample characteristics are given in Table 10).

It can be concluded that both iron(II) minerals, occurring ubiquitously in nature and as corrosion products of carbon steel canisters used for storing radioactive waste, contribute effectively to the retention of Tc under repository conditions. This was found for a large pH range. An influence of ionic strength (0.1 or 1 M) was not observed.

7 U(VI) sorption on montmorillonite at high ionic strengths

In Germany, there are potentially two types of clay deposits that are eligible for high-level nuclear waste disposal: The Opalinus Clay of South Germany and Cretaceous clay sediments in North Germany. The latter exhibit ionic strengths of up to 4 mol L^{-1} in the groundwaters found in the relevant depths (Brewitz, 1982). Therefore, research into nuclear waste disposal in North German clays has to take these high ionic strengths into account.

For the safety case of a nuclear waste repository, thermodynamic data are needed that describe the interaction between radionuclide and host rock. Many studies have focused on the interaction between actinides with clay minerals or clay rock at low ionic strengths (Akcay and Kurtulmuş, 1995; Bradbury and Baeyens, 2002, 2005; Catalano and Brown, 2005; Chakraborty et al., 2010; Chisholm-Brause et al., 2001; Joseph et al., 2011, 2013a; Křepelová et al., 2006, 2007; Marques Fernandes et al., 2012; Meleshyn et al., 2009; Pabalan and Turner, 1996; Schmeide and Bernhard, 2010). Data and research for the behavior of radionuclides under the conditions found in North German clay is however still scarce.

Both ionic strength and pH have an influence on radionuclide speciation and sorption processes. In this chapter, this influence is investigated for U(VI) in detail, as spent fuel elements contain more than 90 % uranium. Furthermore, surface complexation modeling for the interaction of U(VI) with montmorillonite at high ionic strengths is presented. Surface complexation constants have been generated at high ionic strengths and these values have been extrapolated to zero ionic strength with the Specific Interaction of Ions Theory (SIT). The applicability of surface complexation constants generated in pure electrolytes to surface complexation in mixed electrolytes is shown.

7.1 Experimental

A Na-montmorillonite (SWy-2; Crook County, Wyoming, USA) was used as model clay mineral in this study. It was purified according to Poinssot et al. (1999) and Bradbury and Baeyens (2009). This purification consisted of sieving the clay to obtain the < 63 µm fraction, transforming the clay into its Na-form, a size separation to enrich the < 5 µm fraction, an acidification step to eliminate carbonates and hydroxides of low solubility and lastly a dialysis against Milli-Q water (until a residual conductivity of < 10 S cm^{-1} was achieved) and a freeze-drying step. The purified clay was then analyzed by X-ray diffraction (XRD) and, after digestion, inductively coupled plasma mass spectrometry (ICP-MS, ELAN 9000, Perkin Elmer, Waltham, MA) to obtain the phase composition and the elemental composition, respectively. Furthermore, N_2-BET (mod. Coulter SA 3100, Beckman Coulter, Fullerton, USA) and cation exchange capacity (CEC, $BaCl_2$ method according to Bain and Smith (1987)) measurements were performed. These methods yielded a specific surface area A_{sp} = (41.1 ± 0.8) m^2 g^{-1} and CEC of 85.0 $mmol_c$ $(100\ g)^{-1}$.

A U(VI) stock solution (5×10^{-4} mol L^{-1} $^{238}UO_2Cl_2$ in 0.01 mol L^{-1} HCl) was used for all experiments, with the exception of the determination of cation exchange and the U(VI) sorption isotherm in NaCl, for which a ^{233}U solution was employed (1.5×10^{-4} mol L^{-1} $^{233}UO_2Cl_2$ in 0.001 mol L^{-1} HCl). To prepare the background electrolyte, NaCl (p.a., > 99.5 %, Roth, Karlsruhe, Germany), $CaCl_2 \times 2\ H_2O$ (p.a., Merck) or $MgCl_2 \times 6\ H_2O$ (p.a., Merck) was dissolved in Milli-Q water (18 MΩ; mod. Milli-RO/Milli-Q-System, Millipore, Schwalbach, Germany). The pH values were adjusted with diluted HCl (Roth) and NaOH (p.a., Merck, Darmstadt, Germany). For experiments in absence of CO_2, NaOH prepared from carefully rinsed NaOH pellets (p.a., Roth) was used. The pH values were measured with laboratory pH meters (inoLab pH 720, WTW, Weilheim, Germany and pMX 3000/pH coupled with Multiplex 3000/pMX, WTW) with SenTix®Mic pH microelectrodes (WTW), calibrated with standard buffers at pH 1.679, 4.006, 6.865 (WTW) and 9.18 (Hanna Instruments, Woonsocket, Rhode Island, USA).

At high ionic strengths, the usage of pH as the negative decadic logarithm of the hydrogen ion activity is not feasible due to the strong dependency of activity on ionic strength. Instead, pH_c is used, the negative decadic logarithm of the molal hydrogen concentration. For practical measurement, a correction function that correlates the value displayed by the pH meter (pH_{exp}) with the pH_c is needed. This correction function can be approximated by a quadratic function. In this study, the approximation found by Altmaier et al. (2003, 2008) was used.

$$A_m = -0.0988 + 0.1715\ c_{m,NaCl} + 0.0013\ c_{m,NaCl}^2 \quad (7.1)$$

$$A_m = -0.1176 + 0.4308\ c_{m,CaCl_2} + 0.0096\ c_{m,CaCl_2}^2 \quad (7.2)$$

7.1.1 Batch sorption experiments

For the batch sorption experiments, 40 mg each of the purified montmorillonite were weighed into 15 mL PP centrifuge tubes (Cellstar, Greiner Bio-One GmbH, Frickenhausen, Germany). To the clay, calculated amounts of NaCl or $CaCl_2$ and/or $MgCl_2$ were weighed. Depending on the sample series, either the pure electrolytes were used or a mixed electrolyte consisting of 2.52 mol kg^{-1} NaCl, 0.12 mol kg^{-1} $CaCl_2$ and 0.048 mol kg^{-1} $MgCl_2$.

For the experiments under ambient conditions (p_{CO2} = $1\times10^{-3.5}$ atm), 8.5 g of Milli-Q water were added. For samples above pH_c 7, calculated amounts of 1 mol L^{-1} $NaHCO_3$ (Merck) were added to achieve near-instant equilibrium with atmospheric CO_2. The samples were shaken continuously in an overhead shaker (mod. Reax 20, Heidolph, Schwabach, Germany). The samples were pre-equilibrated for 10 days (NaCl, $MgCl_2$), 4.5 weeks ($CaCl_2$) or 5 weeks (mixed electrolyte), during which pH_c was adjusted frequently until pH_c stability was reached. Then, Milli-Q water was added so that the samples contained 10 g of water each. After an additional pH_c adjustment, an aliquot of U(VI) stock solution was added to achieve the predetermined initial UO_2^{2+} concentration. For the batch sorption experiments in dependence on pH_c, this initial U(VI) was 1×10^{-6} mol kg^{-1}, while for the sorption isotherms the initial U(VI) concentration ranged from 1×10^{-5} mol kg^{-1} to 1×10^{-8} mol kg^{-1}. After four to seven days, during which the pH_c was continually adjusted, sorption was complete.

Samples that were to be equilibrated under CO_2-free conditions were transferred into a N_2-glove box, where 8.5 g of degassed Milli-Q water were added. The samples were loaded into an airproof shaking vessel and transferred to an overhead shaker. Pre-equilibration lasted 4.5 weeks with frequent pH adjustments until pH stability was reached, after which the samples were filled up to contain 10 g of water. After an additional pH adjustment, U(VI) stock solution was added to achieve the predetermined initial U(VI) concentration. Sorption was complete after one week, with frequent pH adjustments during this week.

When sorption was complete, the samples were centrifuged (Avanti J-20XP, Beckman Coulter, Brea, CA, 30 min, 4500 g) and then filtered (PES syringe filter, 0.2 µm, vwr, Radnor, PA) into new centrifuge tubes. Photon correlation spectroscopy (BI90, Brookhaven Instruments, Holtsville, NY) showed that this treatment was sufficient to remove colloids. Subsequently, the solution was acidified to 1 % HNO_3 and analyzed by ICP-MS. Alternatively, liquid scintillation chromatography (LSC, Wallac 1414WIN Spectral Low-Level α/β, Perkin Elmer) was used for several sample series. For LSC measurements, a scintillation cocktail suitable for high ionic strengths was used, namely Optiphase HiSafe 3 (Perkin Elmer). Analysis for Na and Ca was done by flame atomic absorption spectroscopy (F-AAS, AAS-4100, Perkin Elmer) to control the final ionic strength of the samples.

Under these conditions, batch sorption experiments in dependence on pH_c and ionic strength were performed (maximum pH_c and ionic strength range: pH_c 4 to 10, I = 0.1 to 9 mol kg^{-1}), as well as leaching experiments. Furthermore, the cation exchange coefficient for U(VI) in NaCl and $CaCl_2$ was determined at pH_c 2 at various ionic strengths. In the mixed electrolyte, the ionic strength was fixed and the experiments were conducted at pH_c 5.3, 6.5 and 8.5, with one sample series at pH_c 6.5 and 60°C.

Table 12 gives an overview of conditions of batch sorption experiments conducted for this study.

Table 12: Overview of conditions of batch sorption experiments conducted for this study.

Background electrolyte	Type of experiment	I / mol kg^{-1}	$c_{m,U(VI),ini}$ / mol kg^{-1}	Atmosphere	pH_c	Sorption time / d	Equilibration time / weeks
NaCl	I/pH_c dependence	0.3 / 1 / 3	1×10^{-6}	N_2	5–9	7	4.5
		0.1 / 0.3 / 1 / 2 / 3		CO_2	4–9	5	1.5
	Cation exchange	0.3 / 1 / 3			2	4	1
	Sorption kinetic	2			5.3	0.5 h – 7d	1.5
	Sorption isotherm	2	1×10^{-5} to 1×10^{-8}	N_2	5.3	7	4.5
$CaCl_2$	I/pH_c dependence	0.3 / 1 / 3	1×10^{-6}	N_2	5–9	7	4.5
		0.3 / 1 / 3 / 9		CO_2	4–9	5	4.5
		0.3 / 1 / 3 / 6 / 9			4–10	7	1.5
	Cation exchange (1st series)	0.3 / 1 / 3			2	4	1
	Cation exchange (2nd series)						
	Sorption isotherm	2	1×10^{-5} to 1×10^{-8}	N_2	5.3	7	4.5
$MgCl_2$	I/pH_c dependence	3 / 6 / 9	1×10^{-6}	CO_2	4–9	5	1.5
Mixed electrolyte	Isotherms (23°C)	3	1×10^{-5} to 1×10^{-7}	N_2	5.3 / 6.5 / 8.5	7	5
	Isotherm (60°C)						
	pH dependency		1×10^{-6}				
	Mineral batch comparison				6.5		17.5

7.1.2 IR and TRLFS spectroscopy

To investigate sorption on a molecular level, *in situ* attenuated total reflection Fourier-transform infrared spectroscopy (ATR FT-IR) and time-resolved laser-induced fluorescence spectroscopy (TRLFS) experiments were performed.

The IR measurements are based on the principle of reaction-induced difference spectroscopy. IR single beam spectra of a mineral film (stationary phase) are continuously recorded while it is rinsed by a flushing blank solution for equilibration and subsequent actinide solution for induced sorption (mobile phase). Since the acquisition time of each spectrum is about 30 seconds, the progress of the sorption process can be monitored with a time resolution in the sub-minute time range. This procedure allows the detection of spectral features showing very small absorption changes. A montmorillonite film was deposited on the ATR crystal from a suspension which was pre-equilibrated in a dilute NaCl solution for a week ($^{S}/_{L}$ = 2.5 g L^{-1}). To this end, the suspension was pipetted with intermittent drying steps until a film thickness of about 1 mg cm^{-2} was reached. In the first step of the online monitoring of the surface reaction, the conditioning of the mineral surface was performed. The montmorillonite film was equilibrated with an inactive solution that otherwise shares the same properties as the active solution in the sorption step. In this case, the solution had a corrected pH of 6.8 and an ionic strength of 3 M and 0.3 M respectively. To increase the signal-noise ratio, D_2O was used instead of H_2O. The experiment was performed under exclusion of CO_2 in a N_2 atmosphere. The velocity of the solution that is pumped through the used flow cell was 0.2 mL min^{-1}. For the sorption step, the inactive solution is replaced with a solution containing 2×10^{-5} M U(VI). The concentration of 2×10^{-5} M U(VI) ensures that a decent signal-noise ratio can be achieved while operating at a concentration where U(VI) speciation in solution is still reasonably similar to solutions with 1×10^{-6} M U(VI). Difference spectra of the sorption reaction are calculated from single beam spectra at the end of the conditioning stage and at distinct time intervals during the sorption stage. When the sorption step is deemed complete, the mineral is once again contacted with inactive solution in a flushing step to determine whether a surface complex is flushed out.

The TRLFS experiments were performed under cryogenic conditions at 153 K. The samples were prepared as described in section 7.1.1. To determine the U(VI) speciation in solution, the samples were prepared without mineral and after pH stability was reached after U(VI) was added to the solution, an aliquot of solution was filled in a plastic cuvette and frozen at 255 K. Directly before the measurement, the samples were cooled further down with liquid nitrogen. They were then placed in a sample holder that was placed inside a cryogenic cooling system (KGW Isotherm, Karlsruhe, Germany). Laser pulses with a wavelength of 266 nm and an average energy of 3 mJ (Minilite high-energy solid-state laser; Continuum, Santa Clara, CA) were used for the excitation of the samples. The spectra were recorded in the wavelength range of 371 to 670 nm with an iHR550 spectrograph (HORIBA Jobin Yvon, Edison, NJ) and an ICCD camera (HORIBA Jobin Yvon), using delay times of up to 9.5 ms.

7.1.3 Surface complexation modeling

Surface complexation modeling was performed using the two-site protolysis non-electrostatic surface complexation and cation exchange (2SPNE SC/CE) model. Aqueous geochemistry modeling was performed with PHREEQC v3.1.2 (Parkhurst and Appelo, 2013), which was coupled with the model-independent parameter estimation program PEST v13.0 (Doherty and Hunt, 2010). The database employed was the NEA thermodynamic database (Guillaumont et al., 2003) to which the complexation constants for $Ca_2UO_2(CO_3)_3(aq)$ and $CaUO_2(CO_3)_3^{2-}$ were added (Bernhard et al., 2001; Dong and Brooks, 2006). Due to the high ionic strengths in the experiments, the Specific Interaction of Ions Theory was applied (Guggenheim and Turgeon, 1955).

The 2SPNE SC/CE model describes the interaction of aqueous metal ions with the surface of a mineral (for a detailed description of the model see Bradbury and Baeyens (1997, 1999, 2002). It is a non-electrostatic model and therefore does not take any electrostatic interactions on the surface into account. The 2SPNE SC/CE model takes cation exchange and reactions between ions and surface groups into account. Cation exchange reactions

$$z_B\, A - clay + z_A\, B^{z_B+} \leftrightarrow z_A\, B - clay + z_B\, A^{z_A+} \tag{7.3}$$

and inner-sphere surface reactions of the general form

$$\equiv SOH + Me^+ \leftrightarrow \equiv SOMe \quad + H^+ \tag{7.4}$$

are defined in this model.

For the cation exchange reaction, the Gaines-Thomas convention was used to model cation exchange (Gaines and Thomas, 1953). This convention uses the equivalent fraction N_i of the exchangeable cation – which is the amount of sorbed cation expressed in equivalents divided by the cation exchange capacity – to express the activity of the exchange species. This leads to the following equation for the selectivity coefficient:

$${}^{B}_{A}K_c = \frac{N_B^{z_A}}{N_A^{z_B}} \times \frac{c_A^{z_B}}{c_B^{z_A}} \tag{7.5}$$

The 2SPNE SC/CE model uses several types of surface sites: Two weak sites W1 and W2 and one type of strong surface sites S. The model describes metal binding to the S and W1 sites. The weak sites are more abundant than the strong surface sites, but they have a much lower affinity towards metal cations than the strong surface sites. For trace metal sorption this means that the cations will only bind to the weak sites once the strong sites are beginning to get saturated.

The cation exchange and surface complexation reactions are combined to describe the experimental results. Furthermore, site capacities and surface site protolysis constants are fed

into the model. As non-adjustable parameters, the values for the site capacities and surface site protolysis constants that were derived by Bradbury and Baeyens are used in this work.

At high ionic strength, the Specific Interaction of Ions Theory (SIT) is commonly employed to correct the ion activity:

$$\log k^0 = \log k - \sum_i \nu_i Z_i^2 \frac{A\sqrt{I_m}}{1+1.5\sqrt{I_m}} + \sum_k \varepsilon(i,k) m_k \quad (7.6)$$

This can be linearized to

$$\log k - \Delta Z^2 D = \log k^0 - m\Delta\varepsilon \quad (7.7)$$

with A = 0.5100 $kg^{0.5}$ $mol^{-0.5}$. Values for ε are tabulated and can be found in Grenthe et al. (1992).

The workflow to obtain the thermodynamic parameters was as follows: Cation exchange, which was determined in a separate experiment, is modeled in a first step and then kept constant for the rest of the calculations. Then, all data points from experiments in dependence on pH were included in the model. In this work, they were included as equilibrium concentrations of U(VI). These equilibrium concentrations span three orders of magnitude, which is why they were weighted to normalize them to a value of 1. For the background electrolyte concentration, the experimentally determined values for each data point were used. For each background electrolyte and ionic strength, a separate set of log k values is calculated in an iterative process. The surface complexation constants are then extrapolated to zero ionic strength, which yields log k^0 for each surface reaction.

7.2 NaCl and $CaCl_2$ systems

7.2.1 U(VI) speciation in NaCl and $CaCl_2$

The calculated U(VI) speciation in NaCl and $CaCl_2$ solutions with an ionic strength of 3 mol kg^{-1} is shown in Fig. 58 and Fig. 59. According to these calculations, the uranyl cation and uranyl chlorides are the dominant species up to pH_c 5.5. In absence of CO_2 in both electrolytes, U(VI) forms various uranyl hydroxide species above pH_c 5.5. In presence of CO_2 in NaCl, uranyl hydroxides have a much lower influence on U(VI) speciation and uranyl carbonates dominate the speciation in the circumneutral and alkaline pH_c range. While in NaCl, $(UO_2)_2(CO_3)(OH)_3^-$ and $UO_2(CO_3)_3^{4-}$ dominate the range between pH_c 6.5 and 8.5, U(VI) in $CaCl_2$ forms the $Ca_2UO_2(CO_3)_3(aq)$ complex. Furthermore, due to the formation of $CaCO_3$ precipitates, with increasing pH the carbonate content in solution becomes small enough that uranyl hydroxides become once again the dominant U(VI) species by pH_c 8.5.

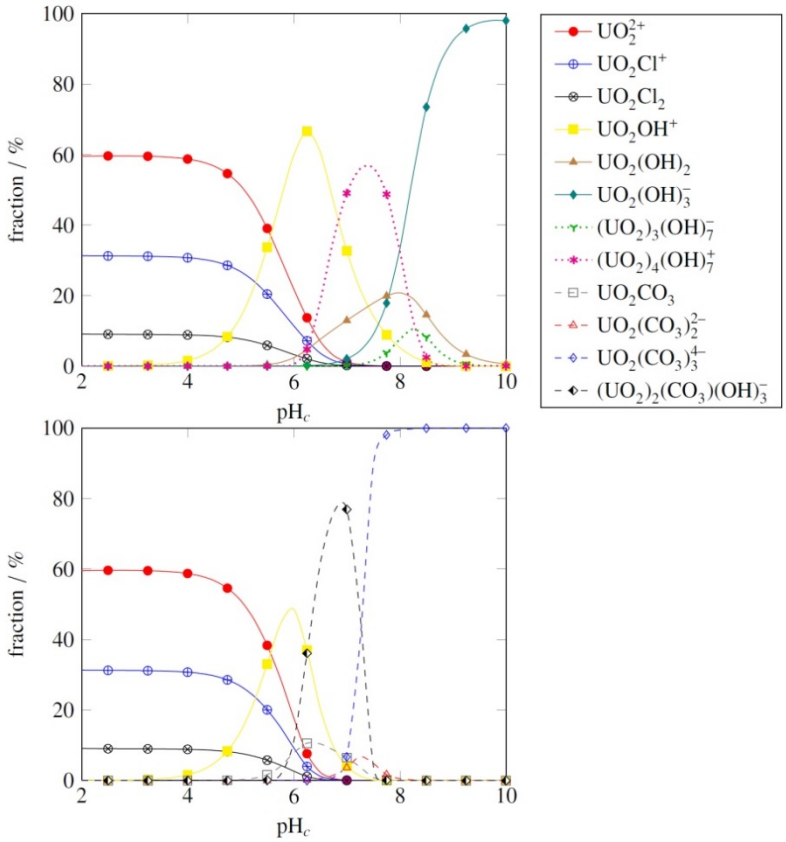

Fig. 58: Calculated U(VI) speciation in 3 mol kg^{-1} NaCl in absence (upper picture) and presence (lower picture) of CO_2 ($c_{U(VI)}$ = 1×10^{-6} mol kg^{-1}).

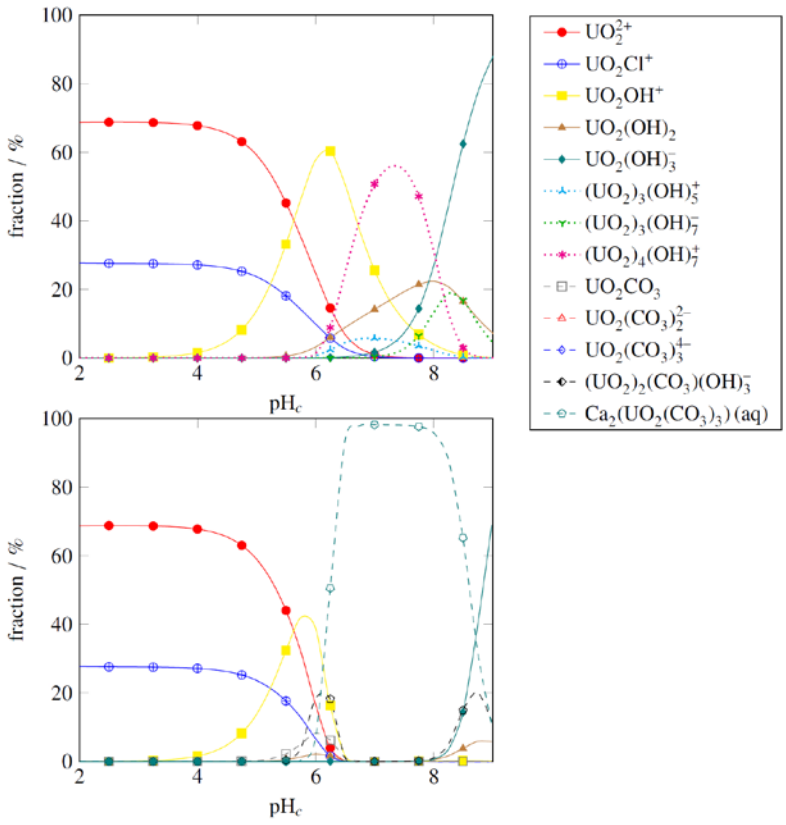

Fig. 59: Calculated U(VI) speciation in 1 mol kg^{-1} $CaCl_2$ in absence (upper picture) and presence (lower picture) of CO_2 ($c_{U(VI)}$ = 1×10^{-6} mol kg^{-1}).

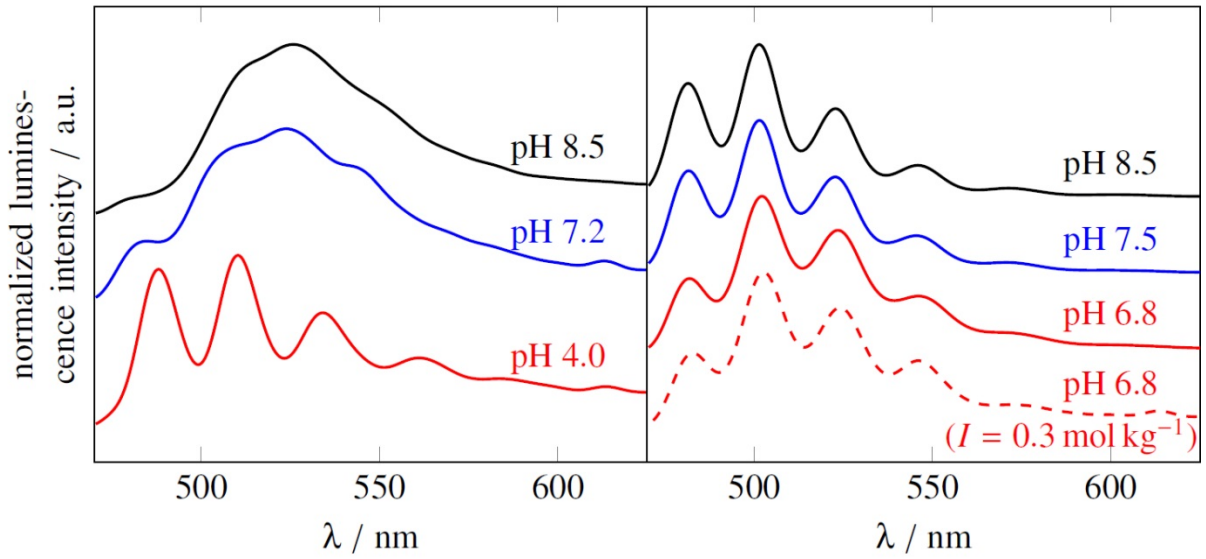

Fig. 60: TRLFS spectra of U(VI) ($c_{m,U(VI)}$ = 1×10^{-6} mol kg^{-1}) in 3 mol kg^{-1} NaCl in depedence on pH. Left picture: absence of CO_2, right picture: presence of CO_2.

Table 13: Luminescence properties of the spectra measured in absence of CO_2.

pH	Aqueous species	Emission bands / nm (±0.5 nm)				τ / µs	T / K
4.0	UO_2^{2+}	487.6	509.8	533.4	561.2	292 ± 53	153
7.2	$(UO_2)_3(OH)_7^-$ or $(UO_2)_4(OH)_7^+$	502.4	523.7	545.5	---	368 ± 48	153
8.5	$(UO_2)_3(OH)_7^-$ or $(UO_2)_4(OH)_7^+$	510.3	525.6	552.9	---	96 ± 11	153

Table 14: Luminescence properties of the spectra measured in presence of CO_2.

Sample	Aqueous species	Emission bands / nm (±0.5 nm)				τ / µs	T / K
6.8 (0.3 m)	UO_2CO_3	481.6	502.4	524.6	546.4	486 ± 107	153
6.8	⇩	481.1	502.0	523.7	547.8	603 ± 32	153
7.5		481.1	501.5	523.2	546.4	731 ± 11	153
8.5	$UO_2(CO_3)_3^{4-}$	481.1	501.5	523.2	546.4	801 ± 11	153

Cryogenic TRLFS measurements (cf. Fig. 60, Table 13, Table 14) in 3 mol kg^{-1} NaCl show that at pH_c 4, the free uranyl cation is indeed the dominant U(VI) species. In absence of CO_2, spectra at pH_c 7.2 and 8.5 were interpreted to indicate the presence of $(UO_2)_3(OH)_7^-$ or $(UO_2)_4(OH)_7^+$, which is in reasonably good agreement with the calculated speciation. Measurements at higher pH values were not successful. In presence of CO_2, UO_2CO_3 is the dominant species at pH_c 6.8 in a sample prepared at I = 0.3 mol kg^{-1}. At pH_c 6.8 and 7.5 in

3 mol kg^{-1} NaCl, a mixture of UO_2CO_3 and $UO_2(CO_3)_3^{4-}$ can be found, with $UO_2(CO_3)_3^{4-}$ becoming the sole U(VI) species in evidence at pH_c 8.5, as evidenced by the increase in lifetime with increasing pH_c. No evidence for $(UO_2)_2(CO_3)(OH)_3^-$ could be found in this experiment.

7.2.2 Sorption kinetics

To verify that the chosen sorption time of 5 to 7 days is sufficiently long, an experiment into the U(VI) sorption kinetic was conducted at pH_c 5.3 and 2 mol kg^{-1} NaCl. Sorption has reached >95 % after half an hour and within 4 hours, sorption was stable (Fig. 61).

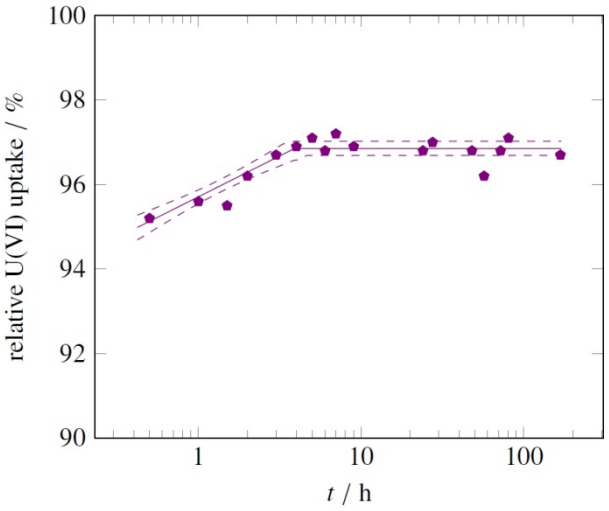

Fig. 61: U(VI) sorption kinetic in NaCl.

7.2.3 Cation exchange

In both NaCl and $CaCl_2$, cation exchange was determined at pH_c 2 to ensure that UO_2^{2+}, which is susceptible to ionic strength, was the only U(VI) species in solution (cf. Fig. 62).

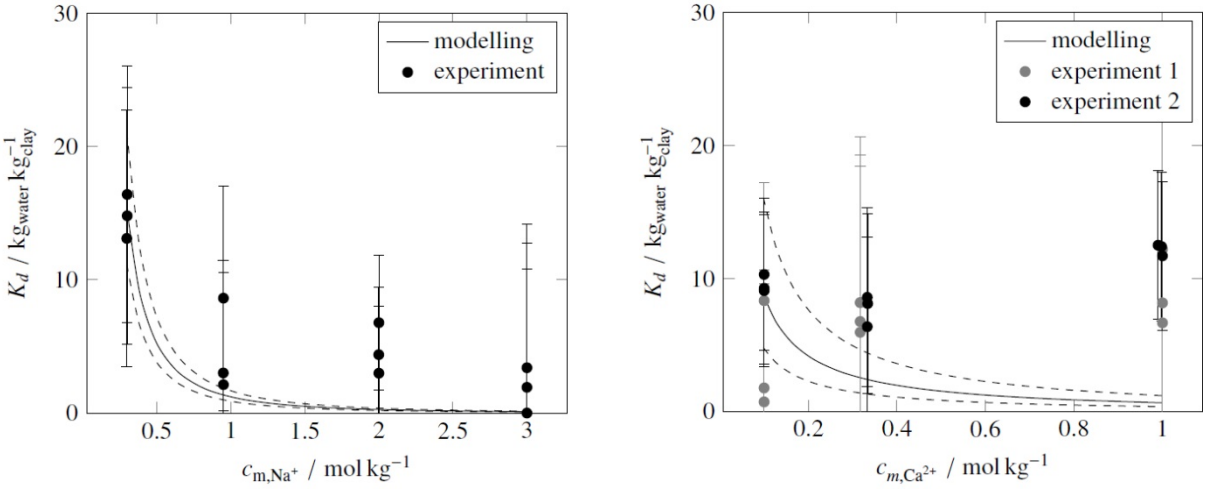

Fig. 62: Cation exchange of U(VI) in NaCl and $CaCl_2$ in dependence on ionic strength.

In NaCl, a logarithmic cation exchange coefficient for the exchange of UO_2^{2+} against Na^+ of 0.55 ± 0.14 was determined, which is within the expected range for divalent cations. In $CaCl_2$, the logarithmic coefficient for the exchange of UO_2^{2+} against Ca^{2+} was found to be 0.33 ± 0.23, which is higher than expected for an exchange of one divalent cation exchange against another divalent cation. However, a second experiment confirmed this value.

Due to measurement constraints, the selectivity coefficients have broad error margins, but at high ionic strengths cation exchange does not exert a great influence, therefore the selectivity coefficients were deemed usable.

7.2.4 Sorption in dependence on pH value and ionic strength

U(VI) sorption on montmorillonite shows a marked dependence on pH and CO_2 presence (cf. Fig. 63 and Fig. 64). In absence of CO_2, the sorption curves in NaCl and $CaCl_2$ look similar, with U(VI) sorption in $CaCl_2$ being 0.5 to 1 log K_d units lower than in NaCl. The maximum U(VI) uptake in NaCl is >99.5 %, while in $CaCl_2$ it is >98.5 %.

In both systems, a small influence of ionic strength below pH_c 5 can be observed, which is caused by the ionic strength dependence of cation exchange. In NaCl, the U(VI) uptake is significantly higher for I > 1 mol kg^{-1} than for lower ionic strengths at the sorption maximum both in absence and presence of CO_2. At pH_c 9 and 10 however, no difference in U(VI) sorption can be observed for the different ionic strengths. Larger error margins in the sorption values in the $CaCl_2$ do not make a similar conclusion possible.

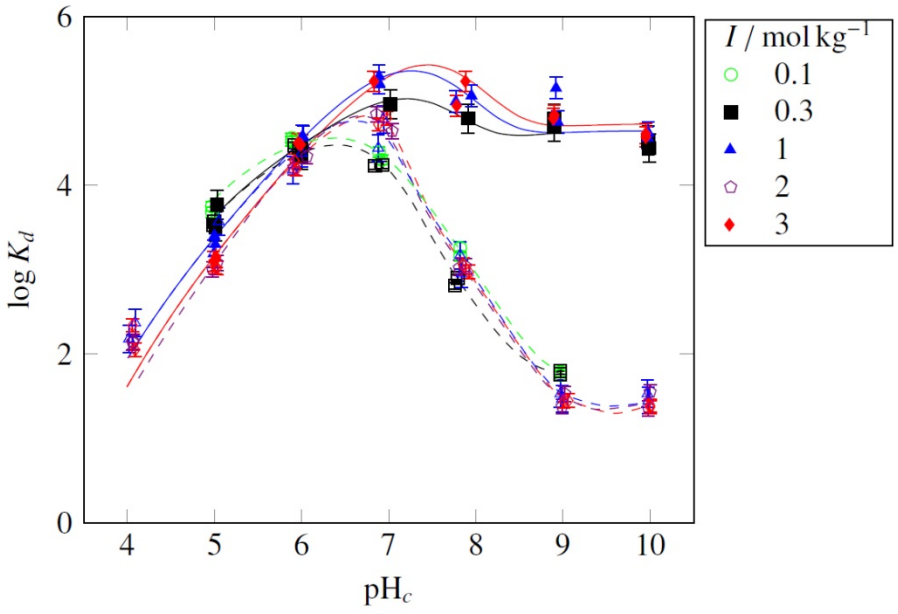

Fig. 63: U(VI) sorption in NaCl in dependence on pH and ionic strength in absence (closed symbols) and presence (open symbols) of CO_2.

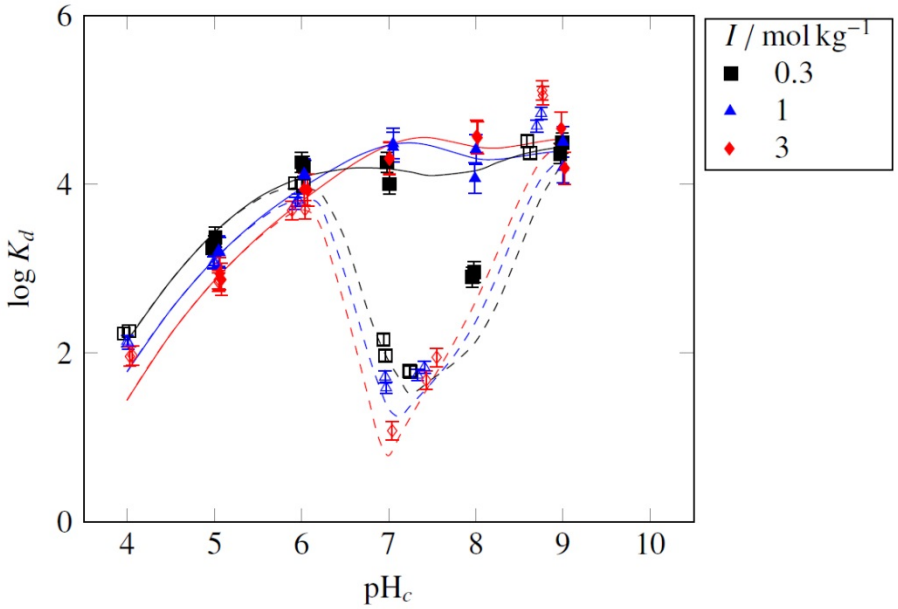

Fig. 64: U(VI) sorption in $CaCl_2$ in dependence on pH and ionic strength in absence (closed symbols) and presence (open symbols) of CO_2. (Data points at pH_c 8 at I = 0.3 mol kg^{-1} were excluded from the fit due to carbonate content in the sample. Carbonate concentration could not be determined experimentally but was modeled to 2.1×10^{-5} mol kg^{-1}.)

Additionally to the experiments in dependence on pH, U(VI) sorption isotherms at pH_c 5.3 and at an ionic strength of 2 mol kg^{-1} have been produced (cf. Fig. 65). These have been fitted with the linearized Freundlich equation.

$$\log a_{eq} = n_F \times \log c_{m,eq} + \log k_F \qquad (7.8)$$

The U(VI) sorption isotherm in NaCl was fitted to log k_F = 1.51 ± 0.14 and n_F = 0.709 ± 0.018, while the U(VI) sorption isotherm in $CaCl_2$ was fitted to log k_F = 1.56 ± 0.13 and n_F = 0.748 ± 0.017.

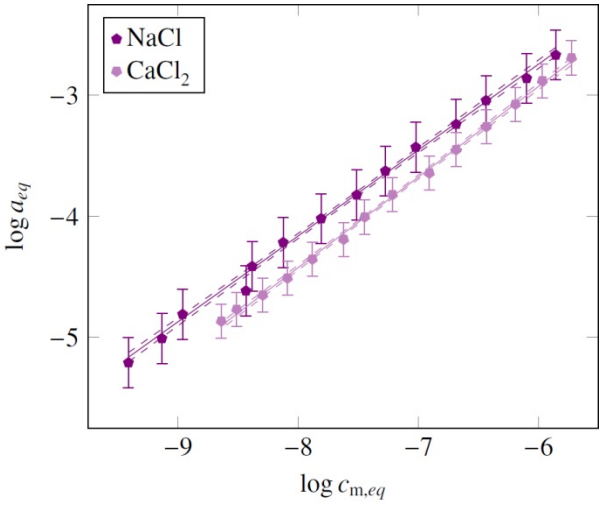

Fig. 65: U(VI) sorption isotherm at I = 2 mol kg^{-1} and pH 5.3.

In the U(VI) sorption experiments in dependence on pH and ionic strength in pure $MgCl_2$, U(VI) uptake was governed by (co-)precipitation with magnesium and silicon compounds of low solubility. The apparent log K_d values in this system averaged at 3.5 ± 1 for pH_c 5.5 to 9 (cf. Fig. 66).

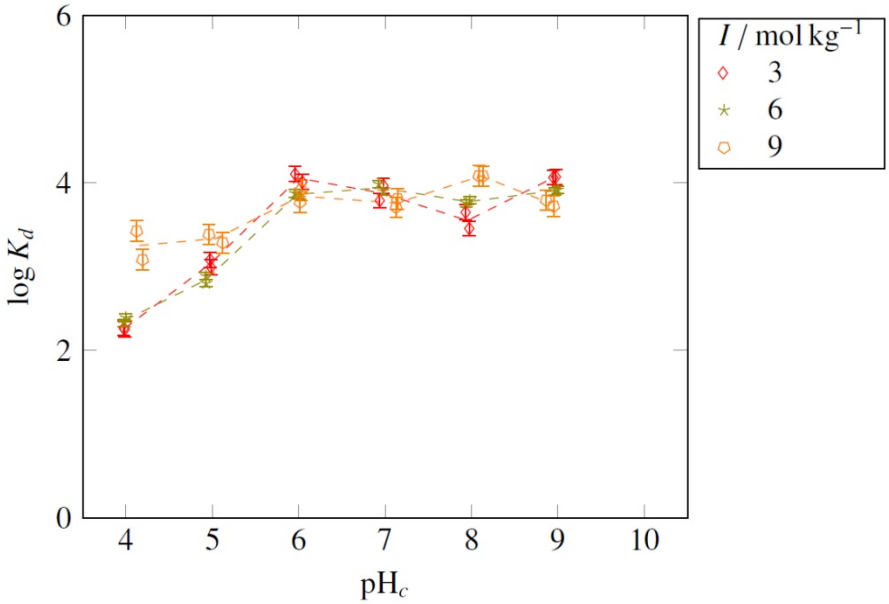

Fig. 66: U(VI) sorption on montmorillonite in $MgCl_2$ in presence of CO_2. Points connected for clarity.

TRLFS spectra of sorption samples showed a signal noise ratio that prevented interpretation.

7.2.5 ATR FT-IR measurements

Fig. 67 (left) illustrates the course of an ATR FT-IR *in situ* sorption experiment at a total U(VI) concentration of 20 µM at an ionic strength of 3 M NaCl and pH 6.8 in D_2O in N_2 atmosphere. The spectrum referred to as “Conditioning” reflects the equilibrium state of the montmorillonite mineral film after flushing it with the blank solution for 60 minutes (Fig. 67, left, lower red trace). Small absorption changes are observed in the spectral region from 1150 to 1000 cm^{-1} most likely attributed to vibrational modes of the mineral. The bands possibly result from a slight instability of the clay film, presumably due to out-flushing of some few clay platelets. The pattern is observed similarly during the whole experiment. The transmission spectra taken from the dried film before and after the experiment (not shown) confirms only very small deviations in band intensities, indicating that wash-out must be insignificant low.

The ATR FT-IR difference spectra calculated from the spectra recorded at the end of the conditioning step and after 5, 10, 15, 30, 60 and 120 minutes of the induction of U(VI) sorption are denoted as “Sorption” spectra in Fig. 67 (left, middle black traces). Clearly, a broad positive band is observed around 900 cm^{-1}, corresponding to the ν_3 antisymmetric stretching mode of the uranyl cation. The time-resolved spectra are characterized by an increasing band amplitude reflecting U(VI) accumulation on the mineral’s surface with ongoing sorption time. The free uranyl cation in solution shows an absorption band of the ν_3 mode at 961 cm^{-1}

(Quilès and Burneau, 2000). Upon complexation in solution, e.g. with inorganic ions or at mineral-water interfaces, the v_3 mode shifts to lower wavenumbers because of a decrease of the U=O force constant. Under the conditions chosen for this experiment, $(UO_2)_3(OH)_5^+$ is predicted to be the dominant uranyl species in solution (see section 7.2.1), characterized by an absorption band at 923 cm^{-1} (Quilès and Burneau, 2000). At a reduced total U(VI) concentration of 20 µM recently the formation of a monomeric species was proposed with a very similar spectral response of v_3 at 922 cm^{-1} (Müller, 2008). During the U(VI) sorption process onto montmorillonite, a very broad band of v_3 emerges with a maximum at 910 cm^{-1} and a distinct shoulder at 900 cm^{-1} possibly indicating the presence of more than one surface species. The shift of more than 10 cm^{-1} in comparison to the predicted species in solution points to the formation of an inner-sphere uranyl species on the montmorillonite surface. The *in situ* vibrational data of U(VI) sorbed onto other oxides of Al and Ti serves as references showing similar shifts of the v_3 mode under identical U(VI) concentrations (Müller et al., 2012, 2013). A coordination of the actinyl ion by physisorption (electrostatic attraction) is not expected to shift the absorption frequency to such an extent (Lefèvre, 2004).

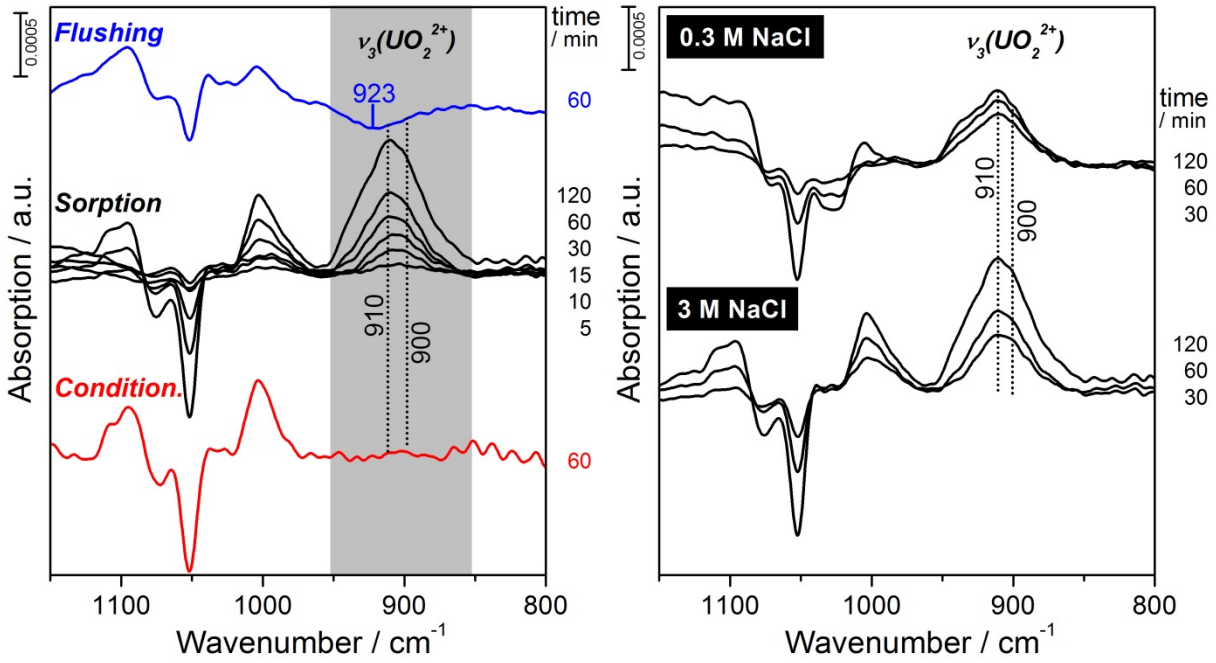

Fig. 67: ATR FT-IR study of U(VI) sorption on montmorillonite at the sorption maximum in absence of CO_2 in D_2O ($c_{U(VI)}$ = 2×10^{-5} mol kg^{-1}, pH 6.8). Left picture: *in situ* spectra in 3 M NaCl. Right picture: comparison of U(VI) uptake in 0.3 and 3 M NaCl.

Subsequent to sorption, “Flushing” of the montmorillonite film with blank solution was performed in order to potentially provide information on surface species, which can be easily removed. The difference spectrum, shown in Fig. 67 (left, upper blue trace) was calculated from the spectra recorded at the end of the sorption step and after 60 minutes of flushing. No further changes in the spectra are observed after prolonged flushing. The absence of a negative band of v_3 around 910 cm^{-1} indicates that none of the sorbed species are easily removed by flushing the mineral with the blank solution and therefore strengthens the assumption of the formation of an inner-sphere sorption complex. The tentatively labeled very small nega-

tive band located at 923 cm^{-1} can be explained by flushing of remaining aqueous complexes from the pores of the mineral film.

In order to check the impact of ionic strength on the U(VI) sorption complex the experiment was repeated using 0.3 M NaCl in solutions of conditioning and sorption. A comparison of the calculated ATR FT-IR difference spectra of the sorption stage is shown in Fig. 67 (right). The spectral signal seems to be identical, indicating the formation of equal sorption complexes. However, the intensity of the v_3 related band at 910 cm^{-1} is found to be slightly higher at increased ionic strength, confirming the findings from batch sorption studies.

Experiments in 3 M NaCl in presence of CO_2 and in 1 M $CaCl_2$ showed a signal-noise ratio that prevented meaningful interpretation of the spectra.

7.2.6 Surface complexation modeling

The 2SPNE SC/CE model uses up to 10 parameters to describe U(VI) sorption on clays - cation exchange, 4 surface complexes on strong sorption sites in absence of CO_2, 2 surface complexes on weak sorption sites in absence of CO_2 and, in presence of CO_2, three further sorption complexes that contain carbonate, one of which is bound at a weak sorption site (Marques Fernandez et al., 2012). To render the calculations for the surface complexation model more robust, a reduction of the numbers of parameters was attempted in this work.

Exemplary for the total ionic strength range studied, the modeling of the U(VI) sorption on montmorillonite is shown for 3 mol kg^{-1} NaCl and $CaCl_2$ in Fig. 68 and Fig. 69, respectively. At pH_c 4, innersphere sorption is already the dominant sorption mechanism in both systems. The $\equiv S^SOUO_2^+$ surface complex (k1 in Fig. 68 and Fig. 69) is the predominant sorption complex until pH_c 5.5. In absence of CO_2, the sorption maximum around pH_c 7, $\equiv S^SOUO_2OH$ (k2) contributes most to the overall U(VI) uptake in both systems. Above pH_c 8, sorption is determined by the $\equiv S^SOUO_2(OH)_3^{2-}$ (k3) surface complex. In contrast to Bradbury and Baeyens (2005), neither $\equiv S^SOUO_2(OH)_2^-$ nor any U(VI) surface complexes on weak sites could be fitted to the experimental data, as these would have greatly increased the error margins of the fit or rendered the parameter estimation calculations unstable.

In presence of CO_2, marked differences between the NaCl and $CaCl_2$ systems are apparent. In the NaCl system, U(VI) speciation above pH_c 6.5 is dominated by uranyl carbonate complexes. Therefore, U(VI) sorption in NaCl in presence of CO_2 decreases above pH_c 7. $\equiv S^SOUO_2(CO_3)_2^{3-}$ (k4) is the predominant U(VI) sorption complex in the alkaline pH range until pH_c 9. To be able to describe U(VI) sorption until pH_c 10, the $\equiv S^SOUO_2(CO_3)_3^{5-}$ surface complex (k5) was added to the model, as proposed by Bachmaf and Merkel (2011). This addition widens the error margins of the overall sorption curve; this could be rectified by the inclusion of experimental data points above pH_c 10. In contrast to Marques Fernandes et al. (2012), no changes to the uranyl carbonate complexation constants in Guillaumont et al. (2003) was necessary to achieve a better fit between experimental data and model for U(VI) in presence of CO_2. Similar to the modeling performed in absence of CO_2, no surface complexes on weak surface sites were included in the calculations.

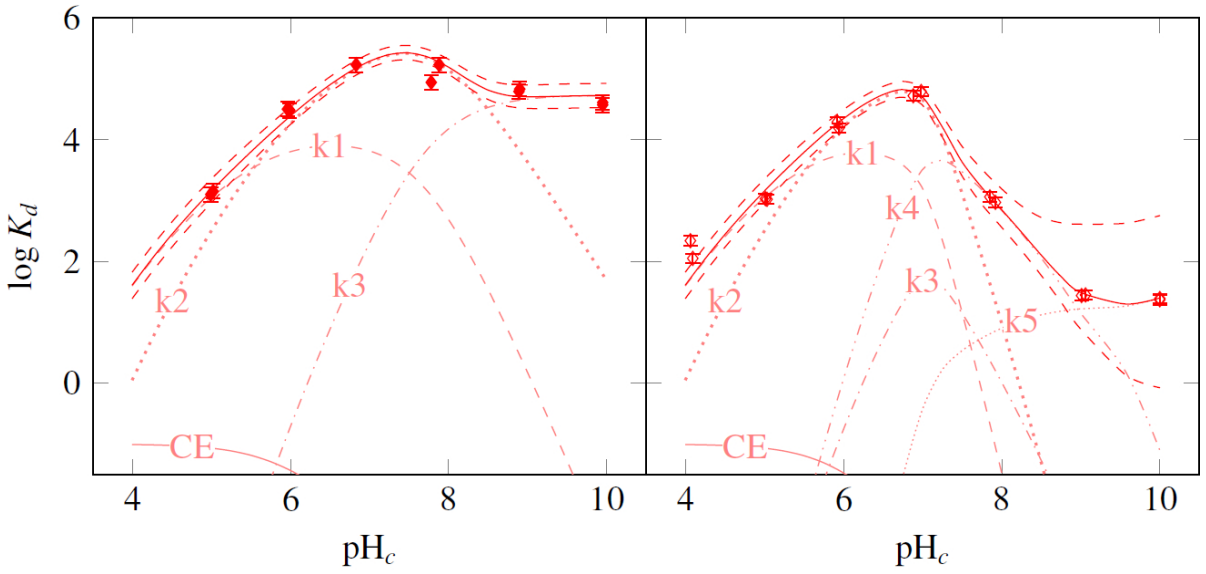

Fig. 68: U(VI) sorption in 3 mol kg^{-1} NaCl in absence (left) and presence (right) of CO_2 with contribution of U(VI) surface complexes to overall sorption.

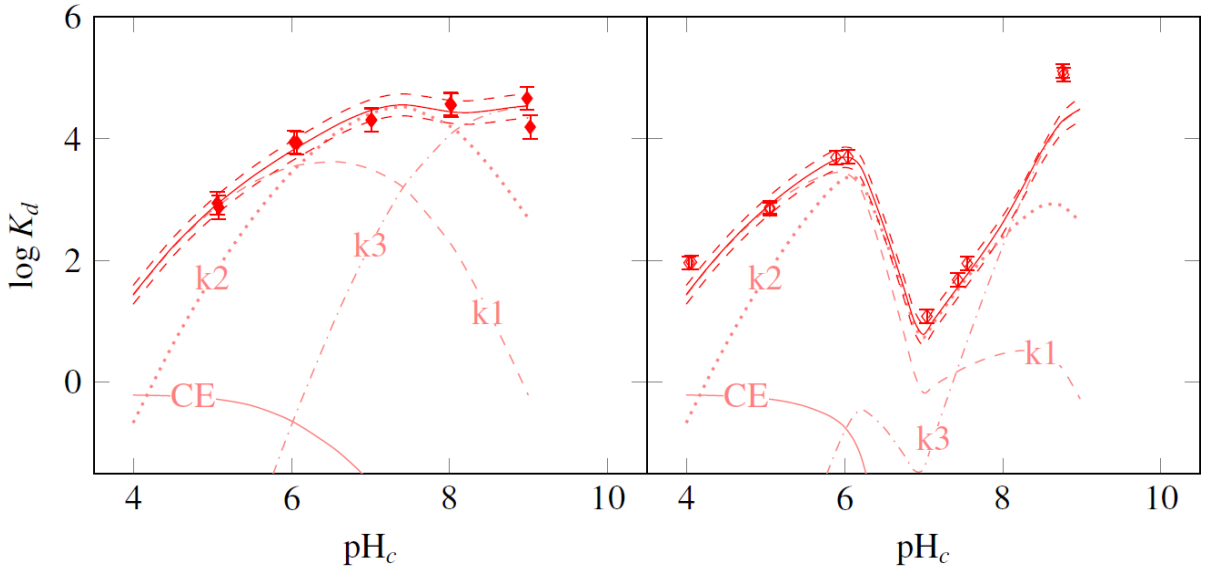

Fig. 69: U(VI) sorption in 3 mol kg^{-1} $CaCl_2$ in absence (left) and presence (right) of CO_2 with contribution of U(VI) surface complexes to overall sorption.

In the $CaCl_2$ system, a steep decrease in sorption can be observed above pH$_c$ 6. The $Ca_2UO_2(CO_3)_3$(aq) complex dominates the U(VI) speciation from pH$_c$ 6.5 to 8.5, which greatly reduces U(VI) sorption as compared to the NaCl system. Above pH$_c$ 7 however, a decrease in carbonate content in solution due to $CaCO_3$ precipitation is responsible for the dominance of uranyl hydroxides in solution at this point. Therefore, after a sorption minimum at pH$_c$ 7, U(VI) uptake increases again. At ionic strengths of 0.3 and 1 mol kg^{-1}, $\equiv S^SOUO_2(CO_3)_2^{3-}$ contributes to the overall U(VI) uptake, while at an ionic strength of 3 mol kg^{-1} no uranyl carbonate complex could be modeled to the experimental data. Data points at pH$_c$ 9 were excluded from the modeling, as they show an increased sorption as compared to the sorption

curves in $CaCl_2$ in absence of CO_2. Due to the high salt content in the samples, no experimental determination of a reason for this behavior was possible, however it is likely that either coprecipitation with $CaCO_3$ or the formation of U(VI) precipitates play a role.

In fact, in $CaCl_2$ a dependence on pre-equilibration time could be observed. A sample series with a pre-equilibration time of 1.5 weeks had a U(VI) uptake that in the acidic pH range was one order or magnitude higher than for the sample series that was pre-equilibrated for 4.5 weeks. Furthermore, the sample series with the shorter pre-equilibration time showed a marked difference in U(VI) uptake between the different ionic strengths in the alkaline pH range, with U(VI) uptake increasing with ionic strength (see Fig. 70). In NaCl however, sample series could be replicated regardless of differences in contact time between clay and electrolyte. Furthermore, there are no interaction parameters between uranyl carbonates and Ca^{2+} tabulated. Modeling of U(VI) interaction with montmorillonite in $CaCl_2$ in presence of CO_2 is therefore less accurate than in NaCl because of the assumption that these interactions are small enough to be ignored for the calculation.

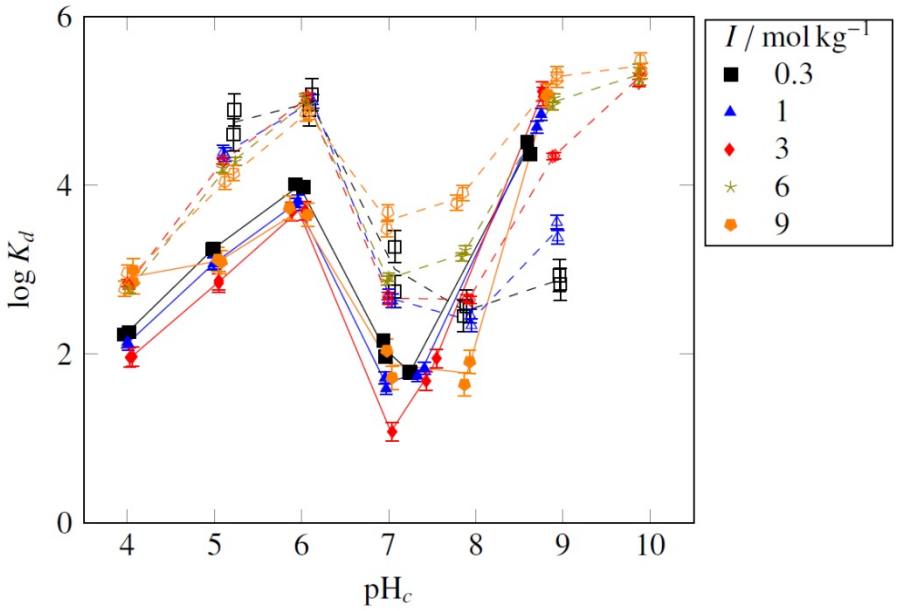

Fig. 70: U(VI) sorption in $CaCl_2$ in presence of CO_2. Open symbols: Pre-equilibration time 1.5 weeks, closed symbols: 4.5 weeks. Points connected for clarity.

7.2.7 Extrapolation to zero ionic strength

The batch sorption experiments, performed in NaCl and $CaCl_2$, yielded surface complexation constants in dependence on ionic strength (Fig. 71). These were extrapolated to zero ionic strength with the SIT approach. For the extrapolation to zero ionic strength, the log *k* values derived in the ionic strength-dependent surface complexation calculations are plotted against ionic strength. Except for log k^0, all parameters are known.

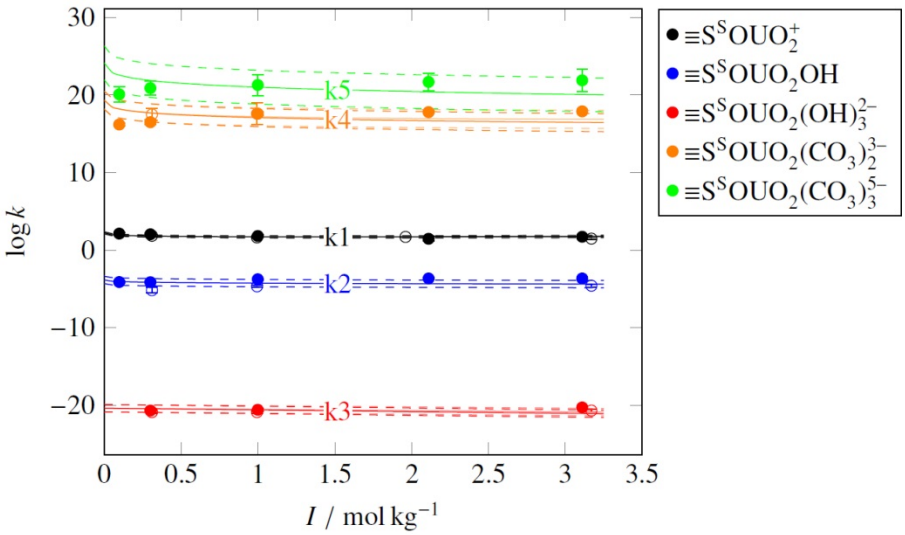

Fig. 71: Extrapolation of surface complexation constants in NaCl and $CaCl_2$ to I = 0. Closed symbols: log k in NaCl, open symbols: log k in $CaCl_2$.

The surface complexation constants for NaCl and $CaCl_2$ were at first extrapolated separately, however statistical analysis showed that with 95 % confidence they belong to the same population. Therefore, they were extrapolated to a single log k^0, valid for U(VI) sorption in both NaCl and $CaCl_2$. Table 15 shows the resulting values for log k^0 for each surface complex.

Table 15: Surface complexation constants in NaCl and $CaCl_2$ at I = 0.

	Surface complex	log k^0
k1	$\equiv S^SOUO_2^+$	2.24 ± 0.13
k2	$\equiv S^SOUO_2OH$	-3.84 ± 0.47
k3	$\equiv S^SOUO_2(OH)_3^{2-}$	-20.4 ± 0.5
k4	$\equiv S^SOUO_2(CO_3)_2^{3-}$	19.4 ± 1.2
k5	$\equiv S^SOUO_2(CO_3)_3^{5-}$	24.2 ± 2.2

7.3 Mixed electrolyte

To investigate the interactions of U(VI) with montmorillonite in an electrolyte that is closer to the composition of natural groundwater, a mixed electrolyte was employed. This electrolyte consists of 2.52 mol kg^{-1} NaCl, 0.12 mol kg^{-1} $CaCl_2$ and 0.048 mol kg^{-1} $MgCl_2$. The composition of this electrolyte was derived from the groundwater composition in the Konrad mine in Lower Saxony in a depth of 480 m, for which measurements that were taken over the space of twenty years can be found in Brewitz (1982).

7.3.1 U(VI) speciation in mixed electrolyte

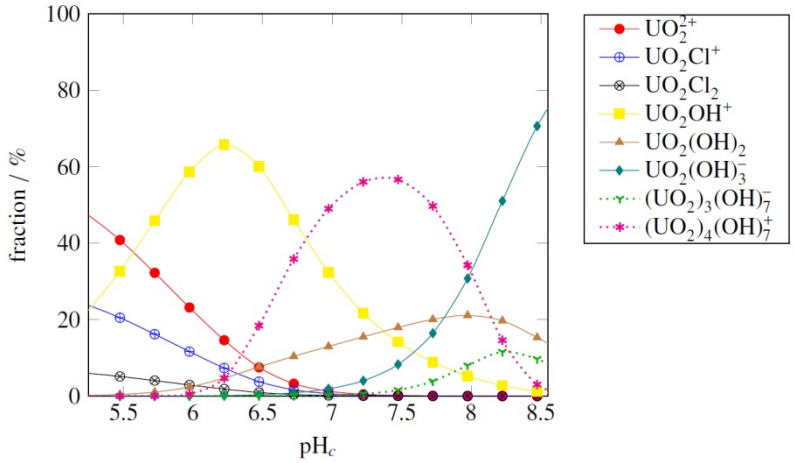

Fig. 72: Calculated U(VI) speciation in mixed electrolyte in absence of CO_2 ($c_{U(VI)}$ = 1×10^{-6} mol kg^{-1}).

As shown in Fig. 72, U(VI) speciation in the mixed electrolyte at pH_c 5.3 is dominated by the free uranyl cation with a contribution of almost 50 %. Additionally, UO_2OH^+ and UO_2Cl^+ each contribute with slightly over 20 % to the U(VI) speciation. At pH_c 6.5, half the U(VI) is found in form of UO_2OH^+, with $(UO_2)_4(OH)_7^+$ contributing just under 20 % to the U(VI) speciation. At pH_c 8.5, the largest fraction of U(VI) with about 75 % is found in the $UO_2(OH)_3^-$ complex.

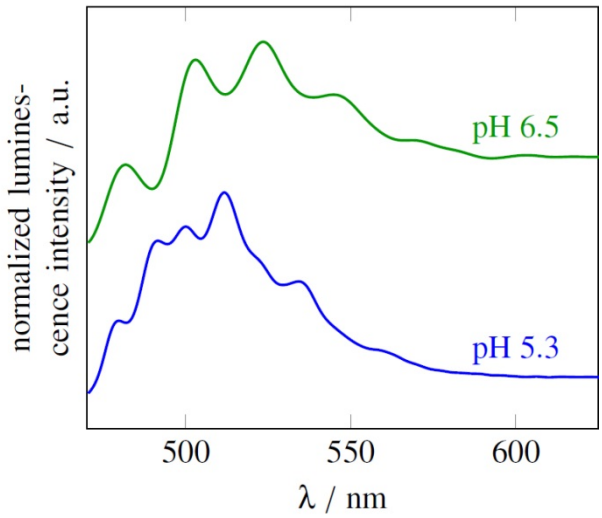

Fig. 73: TRLFS spectra of U(VI) ($c_{m,U(VI)}$ = 1×10^{-6} mol kg^{-1}) in mixed electrolyte in depedence on pH in absence of CO_2.

TRLFS measurements in the mixed electrolyte at $c_{m,U(VI)}$ = 1×10^{-6} mol kg^{-1} show that at pH_c 5.3 there is evidence for the formation of uranyl chloro species in solution (Fig. 73, Table 16). At pH_c 6.5, uranyl hydroxide is the dominant U(VI) complex, in good accordance with the calculated U(VI) speciation in solution. Measurements at pH_c 8.5 were not successful.

Table 16: Luminescence properties of the spectra measured in mixed electrolyte.

pH	Species	Emission bands / nm (±0.5 nm)				τ / µs	T / K
5.3	UO_2Cl_x species	489.9	500.0	511.7	535.7	338 ± 12	153
6.5	UO_2OH^+	---	501.5	523.2	547.3	43 ± 19	153

7.3.2 Sorption in dependence on U(VI) concentration and pH value

Three U(VI) sorption isotherms at 23°C and at pH_c 5.3, 6.5 and 8.5 have been determined as well as one isotherm at a temperature of 60°C at pH_c 6.5. Additionally, one series of U(VI) sorption samples at pH_c 5.3, 6.5 and 8.5 with $c_{m,U(VI),ini}$ = 1×10^{-6} mol kg^{-1} and furthermore, one experiment that compared U(VI) uptake on different clay minerals under the same experimental conditions. All experiments in the mixed electrolyte were performed in absence of CO_2.

The sorption isotherms were fitted with the linearized Freundlich isotherm (see Fig. 74 and Table 17).

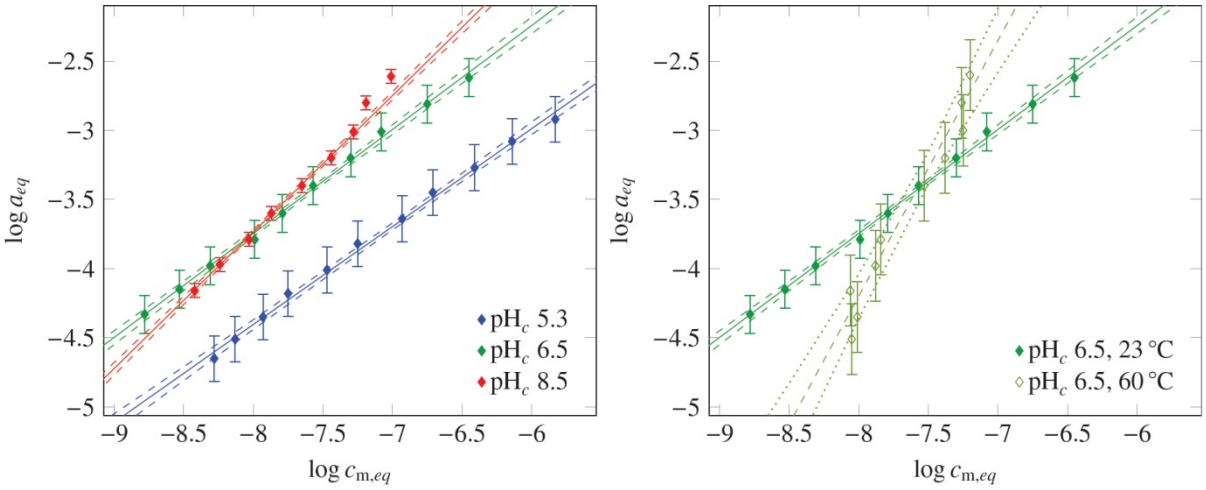

Fig. 74: U(VI) sorption isotherms in mixed electrolyte in absence of CO_2.

Table 17: Freundlich coefficients of U(VI) sorption isotherms in mixed electrolytes.

Isotherm	log k_F	n_F
pH_c 5.3, 25°C	1.26 ± 0.23	0.708 ± 0.031
pH_c 6.5, 25°C	2.27 ± 0.25	0.752 ± 0.032
pH_c 8.5, 25°C	4.16 ± 0.25	0.987 ± 0.031
pH_c 6.5, 60°C	10.6 ± 2.4	1.85 ± 0.31

The U(VI) uptake at pH_c 5.3 is slightly lower but shows otherwise the same characteristics as the isotherm in pure NaCl. U(VI) sorption at pH_c 6.5 and 8.5 is considerably higher. For the two highest initial U(VI) concentrations, 1×10^{-5} mol kg^{-1} and 6.3×10^{-6} mol kg^{-1}, at pH_c 8.5, a U(VI) uptake that lies above the level predicted by the Freundlich isotherm is observed. Thermodynamic calculations show that it is likely that U(VI) precipitates begin to form at this point. The comparison between U(VI) uptake at 60°C and 23°C shows a strong contrast. The slope of the sorption isotherm is much steeper at 60°C. At an initial U(VI) concentration of 1.6×10^{-6} mol kg^{-1}, data points in both sample series show a practically identical log K_d value, however, above and below this concentration, the amount of U(VI) sorbed at the different temperatures quickly diverges. This means that at U(VI) equilibrium concentrations in solution below 2.6×10^{-8} mol kg^{-1}, sorption is considerably higher at 25°C than at 60°C, while above this equilibrium concentration, U(VI) uptake at 60°C is increased over U(VI) uptake at 25°C.

A comparison between U(VI) sorption on different clay minerals as well as a comparison of U(VI) sorption on montmorillonite in different experimental setups at pH_c 6.5 shows no significant differences between the samples (see Fig. 75).

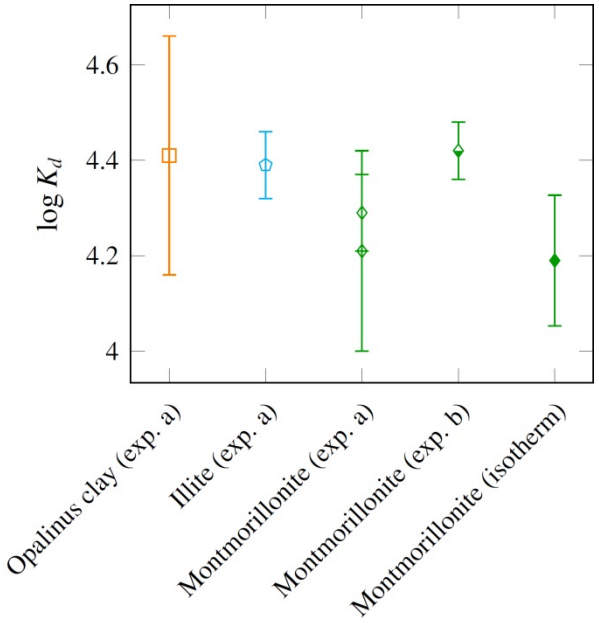

Fig. 75: Comparison of U(VI) sorption on different minerals in mixed electrolyte at 23°C and pH_c 6.5 in absence of CO_2. Experiment (a): 4 months equilibration time, experiment (b) and isotherm: 6 weeks pre-equilibration time.

The sample series with Opalinus Clay, illite and two different batches of montmorillonite, termed experiment (a) in Fig. 75, was pre-equilibrated for 4 months. It has to be noted that for pH adjustments of the Opalinus Clay samples, much greater amounts of acid than for the other samples were necessary to achieve pH_c 6.5 and small amounts of gas bubbles formed in the electrolyte solution. This points towards a dissolution of a part of the calcite content of the Opalinus Clay. Experiment (b) used the same conditions as the U(VI) sorption isotherm, however the isotherm experiments were conducted by a another operator. Differences be-

tween the results in the experiments which used montmorillonite as mineral can be attributed to differences in electrolyte concentration brought on by crystallization of salts and evaporation of water during the pH adjustments.

7.3.3 Surface complexation modeling

For surface complexation modeling in the mixed electrolytes, two approaches were used: The direct fit of surface complexation constants on the experimental data and the calculation of sorption curves with the data that were derived in the pure electrolytes as described in sections 7.2.6 and 7.2.7. For the latter approach, the log k^0 values were used to calculate theoretical surface complexation constants that correspond to the composition and ionic strength of the mixed electrolyte.

The first approach of a direct fit to generate surface complexation constants for the mixed electrolyte system gave the surface complexation constants in the middle column in Table 18.

Table 18: Surface complexation constants for modeling U(VI) sorption isotherms in the mixed electrolyte.

Surface complex	log *k* (fit)	log *k* (calculated)
$\equiv S^S OUO_2^+$	1.70 ± 0.06	1.75 ± 0.13
$\equiv S^S OUO_2OH$	-4.48 ± 0.10	-4.37 ± 0.47
$\equiv S^S OUO_2(OH)_3^{2-}$	-20.8 ± 0.1	-21.0 ± 0.5

According to the surface complexation calculations, at pH_c 5.3 $\equiv S^S OUO_2^+$ is the dominant complex with a fraction of 92 %. $\equiv S^S OUO_2OH$ accounts for 8 % of the U(VI) uptake, while $\equiv S^S OUO_2(OH)_3^{2-}$ plays no role at this pH value. At pH_c 6.5, 55 % of U(VI) is found in the form of $\equiv S^S OUO_2OH$, while $\equiv S^S OUO_2^+$ binds 45 % of the uranium present. At pH_c 8.5, most uranium is found in the $\equiv S^S OUO_2(OH)_3^{2-}$ complex (65 %), with $\equiv S^S OUO_2OH$ making up the remaining 35 %.

This approach generates a fit for the data that is very precise. However, as mentioned in the discussion of the Freundlich fit, it is likely that the formation of precipitates plays a role in the uptake of uranium from the solution. The sample series at pH_c 8.5 has a silicon content in solution of on average 3×10^{-5} mol kg^{-1}, while the average silicon content in a leaching series in a NaCl solution of the same ionic strength lies about one order of magnitude higher. The surface complexation modeling as presented in Fig. 76 was done without the inclusion of any precipitates including U(VI) as it is likely that after one week of U(VI) being in contact with the clay and the solution the system is not yet in thermodynamic equilibrium with any U(VI) precipitates.

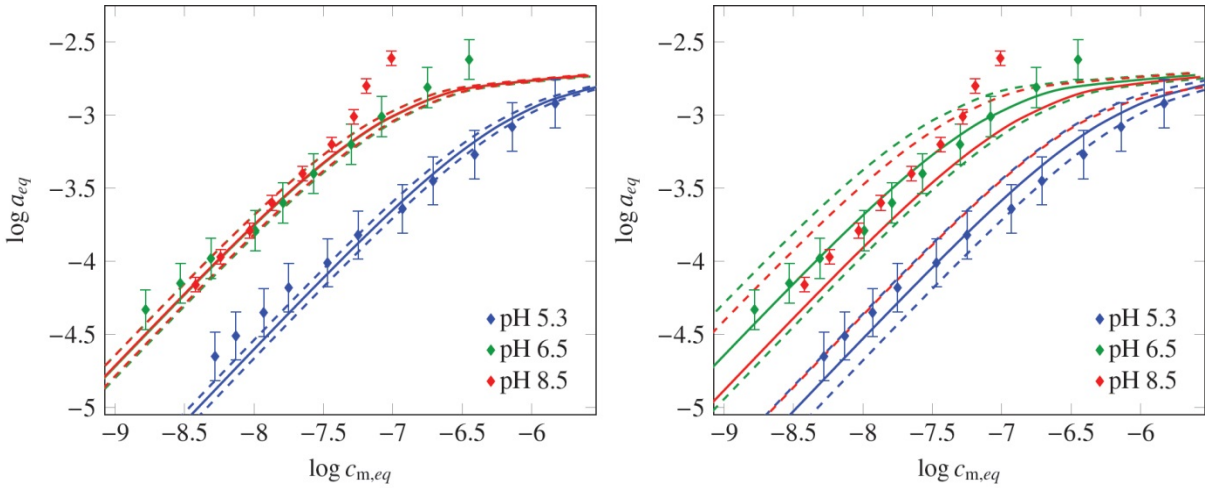

Fig. 76: Surface complexation modeling of U(VI) sorption isotherms in mixed electrolyte (absence of CO_2). Left picture: Fit on isotherm data. Right picture: Use of surface complexation constants generated in pure electrolytes and calculated to composition and ionic strength of the mixed electrolyte.

To check the applicability of the surface complexation constants derived in section 7.2 to mixtures of different electrolytes, the log k^0 values derived in section 7.2.7 were used to calculate log k values for the composition and ionic strength of the mixed electrolyte (see third column Table 18). These were then used to calculate U(VI) sorption isotherms, as pictured in Fig. 76 (right picture). The calculated sorption isotherms for pH_c 5.3 and 6.5 are accurate though they are less precise than the direct fit of the experimental data. For pH_c 5.3, the error margins of the sorption isotherm calculated from the parameters derived in the pure electrolytes are about the same size as the experimental error margins. The error margins of the sorption isotherm at pH_c 6.5 are twice the size of the experimental error. At pH_c 8.5, the discrepancy between the error margins of the calculation and the experiment is even larger and furthermore, while all experimental data lie within the error margin of the calculated isotherm, the calculated sorption isotherm slightly underestimates the actual U(VI) uptake. Nevertheless, this comparison shows that it is in fact possible to use surface complexation constants derived in single electrolytes to describe U(VI) sorption in a mixed electrolyte.

Fig. 77 plots the results of several sample series with different operators and/or experimental setups in dependence on pH_c. Due to crystallization and evaporation processes, the samples from different series showed differences in ionic strength at the conclusion of the experiments, which causes differences in U(VI) uptake. Therefore, the calculated sorption curve that was derived from the isotherm data can only be expected to fit the data from this experiment over the whole pH range. The sorption curve that was calculated from the fit in pure electrolyte was calculated for the average solution composition of all data points presented in this figure, and due to its wider error margins manages to describe all data points.

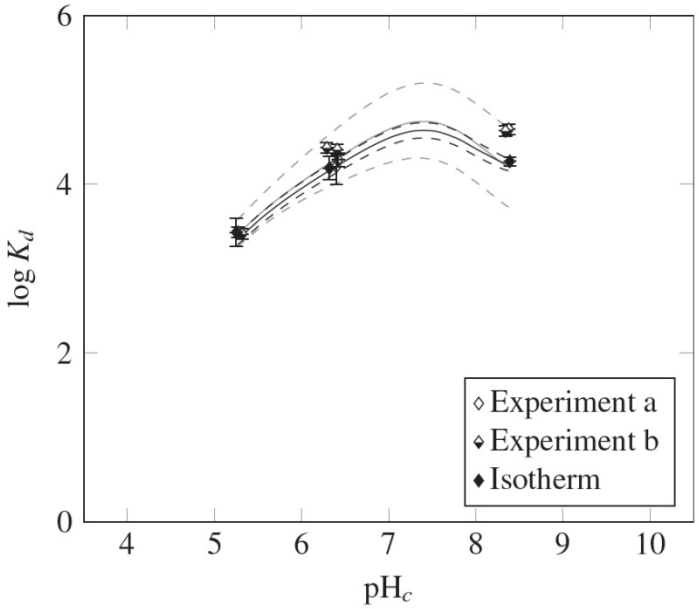

Fig. 77: Comparison of results of different U(VI) sorption experiments on montmorillonite in mixed electrolyte at $c_{U(VI)}$ = 1×10^{-6} mol kg^{-1}. Experiment (a): 4 months equilibration time, experiment (b) and isotherm: 6 weeks pre-equilibration time. Solid line: Fit on isotherm data. Shaded line: Use of surface complexation constants generated in pure electrolyte and calculated to average ionic strength and composition of the mixed electrolyte after the end of the experiments.

7.4 Conclusions

It can be concluded that at environmentally relevant pH values, ionic strength does not exert an adverse influence in the conditions investigated. In absence of CO_2, U(VI) uptake is consistently above 95 % for pH_c > 6 in all investigated systems. In presence of CO_2, a reduction of U(VI) uptake occurs in the alkaline pH range, and in presence of calcium ions, U(VI) will be mobilized due to formation of the $Ca_2UO_2(CO_3)_3$(aq) complex. Whether an elevated temperature leads to an increase or a decrease of U(VI) uptake depends on the U(VI) concentration in solution, with a higher uptake promoted by higher U(VI) concentrations.

The 2SPNE SC/CE model was successfully applied to high ionic strengths. A decrease in the number of parameters led to a more robust surface complexation calculation. The surface complexation constants that were generated at different ionic strengths were extrapolated for a common log k^0 for both the NaCl and $CaCl_2$ systems. These values were then successfully used to calculate sorption isotherms in a mixed electrolyte that consists of the main ions found in groundwaters in North Germany.

8 Diffusion of U(VI) in Opalinus Clay in the absence and presence of citric acid

Uranium represents the main mass fraction of spent nuclear fuel planned to be stored in high-level nuclear waste repositories in deep geologic formations. It represents a serious radiotoxic and chemotoxic hazard (Bleise et al., 2003). Current performance assessment models predict the waste container rupture and release of radionuclides after 10^5 years (Jové Colón et al., 2014). Under present repository conditions, the initial stored immobile U(IV)O_2 will be partly oxidized to more mobile U(VI) species (Thoenen, 2014).

After passing barriers such as the waste container and the backfill material, U(VI) will interact with the repository host rock. Opalinus Clay (OPA) is one representative clay host rock internationally investigated (Nagra, 2002). Due to its high density and low porosity the migration of waste-released radionuclides, such as uranium, through this clay rock, is governed by molecular diffusion. Wu et al. (2009) investigated the diffusion and sorption of Np(V) in/onto OPA and Bauer et al. (2006) the Pu diffusion in OPA. Recently, the U(VI) diffusion in OPA and the influence of humic acid and elevated temperature on it was reported by Joseph et al. (2013b). No significant effect of humic acid and a temperature of 60°C on the diffusion parameter values of the dominating aqueous U(VI) species, $Ca_2UO_2(CO_3)_3(aq)$, was found. However, a change of U(VI) speciation was observed at elevated temperature resulting in the partly formation of particles. For the Np(V) diffusion in OPA only a slight influence of humic acid was detected by Fröhlich et al. (2013).

Notably, the nuclear waste contains a substantial amount of organic compounds (IAEA, 2004). One low molecular weight representative used for decontamination is citric acid. In the past, its complexation behavior with U(IV) and U(VI) was thoroughly studied in inert background electrolytes as summarized in Hummel et al. (2005). Under repository conditions, water with much more complex composition will be present (e.g., OPA pore water). This can significantly influence the uranium speciation. Recent studies were focused on the investigation of the U(VI) complexation with citric acid in the presence of calcium ions (Steudtner et al., 2012). At pH 6, the formation of a new species, $Ca(UO_2)_2(cit)_2(aq)$, is described. Furthermore, Steudtner (2010) investigated the uranium / citric acid system in the absence and presence of light under aerobic and anaerobic conditions. He showed that the system acts very light-sensitive, citric acid is able to reduce U(VI) to U(IV).

The influence of citric acid on the U(VI) sorption onto OPA was studied by Schmeide and Joseph (2012) among other organic ligands. Due to the formation of U(VI)-citric acid complexes in solution the U(VI) sorption to OPA decreases with increasing citric acid concentration. The sorption and diffusion of organic acids, in particular, EDTA, isosaccharinate, phthalate, and oxalic acid, with Callovo-Oxfordian Clay was investigated by Dagnelie et al. (2014). They obtained diffusion coefficients which are lower than values for tritiated water (HTO) diffusion but in the same order of magnitude as anions (Cl^-, I^-, SO_4^{2-}). The organic acids showed a higher affinity towards the clay rock than usual anions. Diffusion studies with small organic compounds were performed by Wu et al. (2015). They observed that EDTA, oxalic acid and hydrazine have no influence on ^{125}I diffusion in bentonite. Staunton et al. (1990) studied the

Np(V) sorption and diffusion with montmorillonite, kaolinite, and illite as a function of background electrolyte and organic ligand (EDTA, citrate, and humic acid). They found that the diffusion coefficients are higher in Na-conditioned clays than in Ca-conditioned clays. The addition of small organic ligands, such as EDTA and citrate, leads to a decrease of the diffusion coefficient in the case of montmorillonite but an increase in the case of kaolinite.

In the present work, the diffusion of HTO, ^{233}U(VI), and citric acid in OPA was investigated under anaerobic conditions under exclusion of light. HTO diffusion experiments were used to determine values for the transport porosity (ε) in the clay samples. The U(VI) diffusion was studied in the absence and presence of citric acid for a duration of three months. To study the U(VI) speciation in solution as a function of time UV-vis spectroscopy was applied. The outcome of this work will be published in Joseph and Schmeide (in preparation).

8.1 Materials and methods

8.1.1 Materials

OPA bore cores from the Mont Terri underground rock laboratory in Switzerland were taken by the Federal Institute for Geosciences and Natural Resources (BGR) and stored under argon atmosphere. The preparation of the OPA bore core samples for the diffusion experiments (length: 11 mm, diameter: 25.5 mm) was performed at the Karlsruhe Institute of Technology – Institute for Nuclear Waste Disposal (KIT–INE). Thereby, only the inner part of the bore core was used for sample preparation. The mineralogy of OPA can be found elsewhere (Nagra, 2002).

Synthetic OPA pore water (pH 7.6 (Pearson, 1998); cf. Table 19) was prepared in Milli-Q water (18 MΩ; mod. Milli-RO/Milli-Q-System, Millipore, Schwalbach, Germany) and used as background electrolyte in all diffusion experiments. Its true ionic strength (I_t) of 0.36 M was calculated using the speciation code EQ3/6 (Wolery, 1992).

Table 19: Composition of OPA pore water according to Pearson (1998).

Ion	M
Na^+	2.4×10^{-1}
K^+	1.6×10^{-3}
Mg^{2+}	1.7×10^{-2}
Ca^{2+}	2.6×10^{-2}
Sr^{2+}	5.1×10^{-4}
Cl^-	3.0×10^{-1}
SO_4^{2-}	1.4×10^{-2}
CO_3^{2-}/HCO_3^-	4.8×10^{-4}
I_t [a]	0.36

To avoid bacterial growth during the diffusion experiment, 1×10^{-3} M NaN_3 (extra pure, Merck, Darmstadt, Germany) was added to the pore water.

A $^{233}U(VI)$ stock solution was used for the diffusion experiments. For that, a solution of $^{233}UO_2(NO_3)_2$ was acquired (Eckert & Ziegler, Valencia, CA, USA) and dried up. After adding the threefold molar quantity of 0.01 M $NaHCO_3$ (p.a., Merck) to form $^{233}UO_2(CO_3)_3^{4-}$ as precursor, a surplus of 0.1 M HCl (p.a., Merck) was added and $^{233}UO_2Cl_2$ was formed. The specific activity of the $^{233}U(VI)$ stock solution determined with liquid scintillation counting (LSC; mod. TriCarb 3100 TR, Perkin Elmer, Freiburg, Germany) using Ultima Gold (Perkin Elmer) as scintillation cocktail amounted to 13.4 kBq/mL (1.7×10^{-4} M $^{233}UO_2Cl_2$). For UV-vis spectroscopy a $^{238}U(VI)$ stock solution was used (0.1 M $^{238}UO_2Cl_2$). For the studies with citric acid, a mixture of unlabeled and ^{14}C-labeled citric acid (9.43×10^{-4} M; 1.85×10^{6} Bq) was prepared. For this, the unlabeled and ^{14}C-labeled citric acid were dissolved in Milli-Q water and mixed in the ratio 21000 : 1. Subsequently, the pH of the mixture was adjusted to pH 5 using 2 M NaOH (*p.a.*, Roth, Karlsruhe, Germany) which resulted in a citric acid stock solution of 0.17 M (29 kBq/mL). The solution was stored under exclusion of light.

8.1.2 Experimental set-up

The details of the diffusion cells applied in the experiments can be found in literature (Van Loon et al., 2003a). Two identical diffusion cells were conditioned at room temperature under inert gas atmosphere (N_2). Each OPA bore core sample was placed in the cells between two stainless steel filter plates (length: 1.55 mm, diameter: 25.5 mm, ε: 0.3, bulk density: 5000 kg/m^3; 316L, pore diameter: 0.01 mm; MOTT industrial division, Farmington, USA). The confining pressure on each sample was 5 MPa. The experimental set-up used for the experiments is presented in Fig. 78.

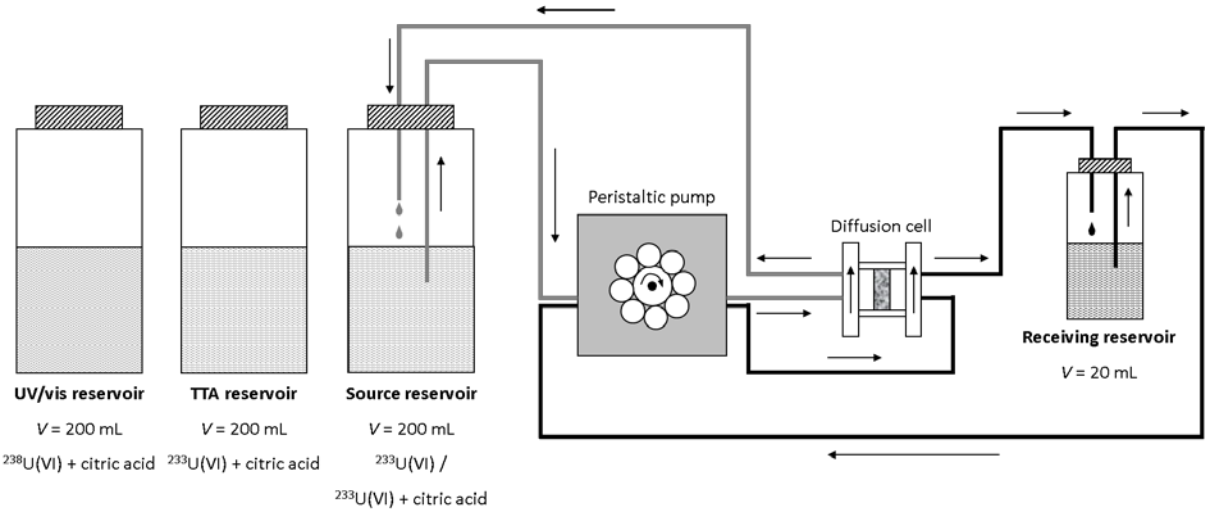

Fig. 78: Experimental set-up used to investigate the U(VI) diffusion in the absence and presence of citric acid (based on (Van Loon et al., 2003a)).

During the studies, care was taken to exclude light from the experiment. Each diffusion cell was coupled with a peristaltic pump (mod. Ecoline, Ismatec, IDEX Health & Science, Glattbrugg, Switzerland) and a source and receiving reservoir filled with 200 mL and 20 mL synthetic OPA pore water, respectively. 250 mL and 25 mL PTFE bottles (vwr collection, Darmstadt, Germany) served as reservoirs. As connection between reservoirs and cells dark-colored tubing was used (pump tubing: Fluran® F-5500-A, Saint-Gobain, Courbevoie, France; reservoir tubing: PTFE-EX, Bohlender GmbH, Grünsfeld, Germany).

The solutions circulated through the end plates of the cells in order to saturate the clay samples. The saturation time was three weeks. After this time the pressure was constant indicating that the samples were hydrostatically in equilibrium. Subsequently, the solutions were replaced by fresh ones, whereby the source reservoir contained the tracer.

At first, HTO through- and out-diffusion experiments were performed as described by Van Loon et al. (2003a) in order to determine values for the porosity (ε) of the clay samples (c_0(HTO) = 1000 Bq/mL). Subsequently, the ^{233}U(VI) in-diffusion in the absence (Cell 1) and presence of citric acid (Cell 2) was studied (c(^{233}U(VI)) = 1×10^{-6} M, c(citric acid) = 1×10^{-3} M). The pH value in the reservoirs was not adjusted, but monitored using a laboratory pH meter (mod. inoLab pH 720, WTW, Weilheim, Germany), equipped with a SenTix Mic pH microelectrode (WTW), and calibrated using standard buffers pH 7 and 9 (WTW).

Since the mixture of U(VI) and citric acid represents a light-sensitive redox system, two additional separate reservoirs, each containing 200 mL OPA pore water, were prepared to monitor possible redox reactions during the experiment. One reservoir contained 1×10^{-6} M ^{233}U(VI) and 1×10^{-3} M citric acid. Here, with respect to a possible reduction of U(VI) to U(IV) in distinct time steps an aliquot of the solution was taken and analyzed by solvent extraction using thenoyltrifluoroacetone (TTA; *p.a.*, Fluka/Sigma–Aldrich, Steinheim, Germany) according to Bertrand and Choppin (1982). The second reservoir contained 1×10^{-4} M ^{238}U(VI) and 1×10^{-3} M citric acid. Aliquots of this solution were regularly analyzed by UV-vis spectroscopy (mod. Cary 500, Varian Inc., Palo Alto, CA, USA; mod. Lambda 900, Perkin Elmer). To distinguish between the different reservoirs used in this study, the following designations were used: Cell 1, Cell 2, TTA, and UV-vis.

The redox potential of all four 200 mL reservoirs was regularly measured using a BlueLine 31 RX redox electrode (SI Analytics GmbH, Mainz, Germany). Additionally, the reservoir solutions were investigated for colloids and for the size of the colloidal particles by photon correlation spectroscopy (PCS; mod. BI-90, Brookhaven Instruments, USA). A detailed description of the instruments and the procedure is given in Dreissig et al. (2011).

After 3 months, the diffusion experiments were stopped and the clay samples were extruded from the cells. Using the abrasive peeling technique (Van Loon and Eikenberg, 2005), U(VI) and citric acid diffusion profiles were determined. The peeled layers were extracted with 1 M HNO_3 (*p.a.*, Roth). This method was already applied in former experiments (Joseph et al., 2013b; Sachs et al., 2007). The tracer concentrations in the extracts were determined by LSC.

The reservoir solutions tracered with $^{233}U(VI)$, $^{238}U(VI)$, and citric acid were analyzed for Na, K, Sr, Ba, Al, Si, Mn, and U by inductively coupled plasma – mass spectrometry (ICP-MS; mod. ELAN 9000, Perkin Elmer, Boston, USA), for Mg and Ca by atomic absorption spectroscopy (AAS; mod. AAS-4100, Perkin Elmer), and for SO_4^{2-} and Cl^- by ion chromatography (IC; mod. IC separation center 733, Metrohm, Herisau, Switzerland). The total inorganic carbon content (TIC) was determined using the multi N/C 2100 analyzer (Analytik Jena, Jena, Germany) as difference of the total carbon (TC) and the total organic carbon (TOC). Based on the TIC results, the CO_3^{2-}/HCO_3^- concentration in the reservoirs were re-adjusted to the value given in Table 19 before the start of the experiment. Fe and P were determined, too, but were always below the ICP-MS detection limit.

8.1.3 Theoretical background

All diffusing species were assumed to migrate via molecular diffusion through OPA. The theoretical background of molecular diffusion has been described previously, e.g., by Crank (1975) and Van Loon et al. (2003b). For the determination of the diffusion parameters, a one-dimensional model composed of source reservoir, filter, OPA bore core sample, filter, and receiving reservoir was applied as described by Jakob et al. (2009). The OPA sample and the filters were considered as homogeneous each with a single value for the transport porosity.

The diffusion process through a porous medium is defined by Fick's first law:

$$J = -D_e \cdot \frac{\partial c}{\partial x} \tag{8.1}$$

where J [mol/(m^2·s)] is the diffusive flux of a solute, c [mol/m^3] represents the decay corrected tracer concentration in the mobile phase, and x [m] is the spatial coordinate. The change of concentration with time, t [s], is expressed by Fick's second law:

$$\frac{\partial c}{\partial t} = D_a \cdot \frac{\partial^2 c}{\partial x^2} \tag{8.2}$$

Thereby, D_a [m^2/s] denotes the apparent diffusion coefficient. Both diffusion coefficients are linked by the rock capacity factor α [–] according to:

$$D_a = \frac{D_e}{\alpha} \tag{8.3}$$

The rock capacity factor is defined as:

$$\alpha = \varepsilon_{eff} + \rho \cdot K_d \tag{8.4}$$

where ρ [kg/m^3] is the dry bulk density and K_d [m^3/kg] the sorption distribution coefficient. For non-sorbing tracers such as HTO with K_d = 0, it is assumed that α is equal to ε_{eff}. In contrast to D_e, D_a considers the tracer sorption to the clay.

For HTO, D_e and α were determined by modeling the through-diffusion flux of HTO monitored in the receiving reservoir as a function of time. For ^{233}U(VI) and citric acid, the values for the diffusion parameters (D_e, α, ε, K_d) were determined by fitting the experimental tracer distribution profiles in the clay.

The clay samples as well as the filters were initially free of tracer. For all diffusing tracers investigated the model boundary condition for the source reservoir concentration was as follows:

$$c(x = 0, t > 0) = f_0(t) \quad (8.5)$$

For the boundary conditions of the receiving reservoir two possible descriptions were applied:

$$c(x = L, t > 0) = f_L(t) \text{ and} \quad (8.6)$$

$$c(x = L, t > 0) = 0, \quad (8.7)$$

whereby L [m] describes the thickness of the system filter/clay/filter. Condition (8.6) was only applied for tracers detected in the receiving reservoir, that means, HTO. For ^{233}U(VI) and citric acid, where no tracer breakthrough could be observed, condition (8.7) was applied. According to (Jakob et al., 2009) continuity regarding tracer flow [mol/s] at the interfaces of filters and clay was considered in the model.

All experimental results were evaluated using the commercial software COMSOL Multiphysics® 4.2a (COMSOL, 2011).

The experimental uncertainties of the values of the diffusive HTO flux and the accumulated diffused HTO activity in the receiving reservoir solution resulted from the uncertainty of the parameters required to calculate these values (cf. Van Loon and Soler (2004)). To analyze the HTO through-diffusion, the COMSOL Optimization Module was applied. A least square fit was performed using the Levenberg-Marquardt algorithm to determine best fit values for the diffusion parameters. The uncertainty of D_e and ε was estimated by fitting the upper and the lower boundaries covered by the uncertainties of the experimental fluxes.

In the case of ^{233}U(VI) and citric acid diffusion profiles, the experimental uncertainty of the diffusion depth was given by the average of the individual distance measurement at four points of the clay sample. The uncertainties of the D_e and K_d values were estimated by fitting the upper and lower boundaries of the diffusion profile. Both D_e and K_d were varied in such a way that 90 % of the experimental values were covered by the envelope curves.

8.1.4 Filter diffusion parameters

For fitting the clay diffusion parameters, the diffusion characteristics of the adjacent stainless steel filter plates for HTO, U(VI), and citric acid had to be included in the model, because they could have influenced the retardation and migration of the tracer. In the case of HTO,

the filter K_d value was assumed to be 0. The corresponding filter D_e value, D_f, was 2.3×10^{-10} m^2/s (Glaus et al., 2008).

In contrast to HTO, for $^{233}U(VI)$ and citric acid an interaction of the tracers with the filters was assumed. The respective filter K_d values were obtained by extraction experiments. Subsequently after the clay diffusion experiment $^{233}U(VI)$ and citric acid were extracted from the filter plates by 1 M HNO_3. After shaking for 7 days, the extracts were analyzed by LSC. The resulting K_d values were $K_d(U(VI)) = 7.91\times10^{-4}$ m^3/kg in the absence of citric acid and $K_d(U(VI)) = 1\times10^{-3}$ m^3/kg in the presence of citric acid, and $K_d(\text{citric acid}) = 9\times10^{-5}$ m^3/kg. Values for D_f of U(VI) and citric acid were taken from the literature. D_f of $Ca_2UO_2(CO_3)_3(aq)$, the dominating U(VI) species in OPA pore water (Joseph et al., 2011), was taken from (Joseph et al., 2013b) and amounted to 3.5×10^{-11} m^2/s. If the diffusion coefficient of a diffusing species in bulk water, D_w [m^2/s], is known, D_f can be estimated by $D_f = D_w/10$ (Glaus et al., 2008). For citric acid at pH 4, D_w values around 0.7×10^{-9} m^2/s were reported (Laguerie et al., 1976; Liu et al., 2004). Therefore, a D_f value of 7×10^{-11} m^2/s was used.

8.2 Results and discussion

8.2.1 HTO diffusion in Opalinus Clay

The results obtained by fitting the experimentally determined diffusive flux of HTO in the respective receiving reservoir solution are presented in Table 20. As shown, the data are in reasonably good agreement with literature values. Small differences can be attributed to the different OPA bore cores used in the experiment.

Table 20: Diffusion parameters determined by HTO diffusion experiments through OPA.

	Cell 1	Cell 2	(Van Loon and Soler, 2004)
c_0 / Bq/mL	986 ± 3	990 ± 107	1217 ± 83
D_e / × 10^{-11} m^2/s	1.67 ± 0.12	1.33 ± 0.11	1.21 ± 0.08
ε / –	0.10 ± 0.01	0.10 ± 0.005	0.09 ± 0.02

The obtained ε values were included in the COMSOL model used for fitting the U(VI) and citric acid diffusion depth profiles.

8.2.2 Aqueous U(VI) and citric acid speciation

To interpret the obtained diffusion profiles of U(VI) and citric acid in OPA, the diffusing species have to be known. As discussed previously (Joseph et al., 2011), the U(VI) speciation in OPA pore water is dominated by the neutral $Ca_2UO_2(CO_3)_3(aq)$ complex to almost 100 %. In respective diffusion experiments, this species was assumed to be the main diffusing species in the system (Joseph et al., 2013b).

In the present study, the U(VI) speciation in the absence and presence of citric acid as well as the citric acid speciation in the presence of U(VI) in the source reservoir solutions were calculated using the speciation code EQ3/6 (Wolery, 1992) considering the thermodynamic data compiled in Guillaumont et al. (2003), Bernhard et al. (2001), Lee et al. (2015), Hummel et al. (2005), and Steudtner et al. (2012). In the model, the present cation and anion concentration of the dissolved salts as well as the concentration of U(VI) and citric acid, the pH, and the redox potential in the source reservoir solutions were included. The conditions and the resulting species distributions in the beginning of the experiment are summarized in Table 21 for the solutions of the reservoirs Cell 1, Cell 2, TTA, and UV-vis.

Table 21: Conditions present in the solutions of reservoirs Cell 1, Cell 2, TTA, and UV-vis at the *beginning* of the diffusion experiment as well as the corresponding U(VI) speciation in the solution.

	Cell 1	Cell 2	TTA	UV-vis
c(U(VI)) / M	9.85×10^{-7}	9.84×10^{-7}	9.98×10^{-7}	1.08×10^{-4} [a]
c(citric acid) / M	-	9.92×10^{-4}	1.01×10^{-3}	9.99×10^{-4}
Na / M [a]	2.31×10^{-1}	2.37×10^{-1}	2.37×10^{-1}	2.30×10^{-1}
K / M [a]	1.98×10^{-3}	2.21×10^{-3}	2.49×10^{-3}	2.23×10^{-3}
Mg / M [b]	1.65×10^{-2}	1.65×10^{-2}	1.67×10^{-2}	1.61×10^{-2}
Ca / M [b]	2.62×10^{-2}	2.59×10^{-2}	2.57×10^{-2}	2.57×10^{-2}
Sr / M [a]	4.96×10^{-4}	4.91×10^{-4}	4.88×10^{-4}	4.85×10^{-4}
Ba / M [a]	6.68×10^{-8}	1.25×10^{-7}	8.59×10^{-8}	7.04×10^{-8}
Al / M [a]	8.78×10^{-7}	9.01×10^{-7}	7.78×10^{-7}	3.74×10^{-7}
Si / M [a]	3.63×10^{-6}	6.41×10^{-6}	5.95×10^{-6}	4.49×10^{-6}
Mn / M [a]	3.49×10^{-8}	3.28×10^{-8}	2.86×10^{-8}	3.24×10^{-8}
Cl^- / M [c]	2.85×10^{-1}	2.93×10^{-1}	2.96×10^{-1}	2.85×10^{-1}
SO_4^{2-} / M [c]	1.37×10^{-2}	1.42×10^{-2}	1.38×10^{-2}	1.37×10^{-2}
CO_3^{2-}/HCO_3^- / M [d]	4.80×10^{-4}	5.20×10^{-4}	4.60×10^{-4}	4.77×10^{-4}
pH	8.46	8.47	8.46	8.39
E_h / mV	390	340	275	270
U(VI) speciation (aqueous species accounting for 99 % or more)				
$Ca_2UO_2(CO_3)_3(aq)$	97.91	97.77	97.72	96.28
$UO_2(CO_3)_3^{4-}$	0.66	0.77	0.79	0.75
$MgUO_2(CO_3)_3^{2-}$	0.63	0.67	0.69	0.65
$(UO_2)_2CO_3(OH)_3^-$				1.4
Citric acid speciation (aqueous species accounting for 99 % or more)				
$Ca(cit)^-$	-	60.41	59.92	60.60
$Mg(cit)^-$	-	37.10	37.58	36.91
Cit^{3-}	-	2.48	2.49	2.48

[a] ICP-MS (error: ±10 %), [b] AAS (error: ±2 %), [c] IC (error: 3-10 %), [d] TC-TOC (error: ±3 %)

The diffusion experiments were conducted for 3 months. At the end of the experiment the conditions in the source reservoir solutions were measured again and the speciation was calculated (cf. Table 22).

Table 22: Conditions present in the solutions of reservoirs Cell 1, Cell 2, TTA, and UV-vis at the *end* of the diffusion experiment as well as the corresponding U(VI) speciation in the solution.

	Cell 1	Cell 2	TTA	UV-vis
c(U(VI)) / M	9.00×10^{-7}	8.61×10^{-7}	1.03×10^{-6}	5.80×10^{-5} [a]
c(citric acid) / M	-	9.19×10^{-4}	9.66×10^{-4}	8.84×10^{-4}
Na / M [a]	2.52×10^{-1}	2.57×10^{-1}	2.57×10^{-1}	2.50×10^{-1}
K / M [a]	2.46×10^{-3}	4.25×10^{-3}	3.48×10^{-3}	2.84×10^{-3}
Mg / M [b]	1.80×10^{-2}	1.78×10^{-2}	1.78×10^{-2}	1.74×10^{-2}
Ca / M [b]	2.82×10^{-2}	2.82×10^{-2}	2.82×10^{-2}	2.82×10^{-2}
Sr / M [a]	5.07×10^{-4}	5.14×10^{-4}	5.15×10^{-4}	5.04×10^{-4}
Ba / M [a]	1.38×10^{-7}	1.66×10^{-7}	1.22×10^{-7}	8.16×10^{-8}
Al / M [a]	1.03×10^{-6}	2.04×10^{-6}	1.03×10^{-6}	6.86×10^{-7}
Si / M [a]	2.32×10^{-5}	2.62×10^{-5}	1.13×10^{-5}	5.98×10^{-6}
Mn / M [a]	1.65×10^{-6}	7.55×10^{-7}	1.18×10^{-7}	1.29×10^{-7}
Cl^- / M [c]	2.91×10^{-1}	3.10×10^{-1}	2.99×10^{-1}	2.88×10^{-1}
SO_4^{2-} / M [c]	1.49×10^{-2}	1.41×10^{-2}	1.31×10^{-2}	1.25×10^{-2}
CO_3^{2-}/HCO_3^- / M [d]	2.62×10^{-4}	3.23×10^{-4}	3.62×10^{-4}	4.70×10^{-4}
pH	8.81	9.09	9.06	8.92
E_h / mV	250	210	230	140
U(VI) speciation (aqueous species accounting for 99 % or more)				
$Ca_2UO_2(CO_3)_3(aq)$	98.02	97.93	97.98	98.03
$UO_2(CO_3)_3^{4-}$	0.63	0.69	0.66	0.63
$MgUO_2(CO_3)_3^{2-}$	0.60	0.62	0.61	0.59
Citric acid speciation (aqueous species accounting for 99 % or more)				
$Ca(cit)^-$	-	60.66	60.62	61.05
$Mg(cit)^-$	-	36.98	37.07	36.68
Cit^{3-}	-	2.36	2.30	2.27

[a] ICP-MS (error: ±10 %), [b] AAS (error: ±2 %), [c] IC (error: 3-10 %), [d] TC-TOC (error: ±3 %)

The comparison of the speciation in the beginning and at the end of the experiment showed that, based on the currently available data for U(VI) and citric acid, the $Ca_2UO_2(CO_3)_3(aq)$ complex should be the main diffusing U(VI) species in the absence and presence of citric acid. In the case of citric acid, $Ca(cit)^-$ was calculated to dominate the speciation in solution.

The decrease of the U(VI) and citric acid concentration in the solution of Cell 1 and Cell 2 was due to the diffusion of species into the clay. In the TTA reservoir solution no significant change in U(VI) and citric acid concentration was observed. In contrast, the U(VI) and citric acid concentration in the UV-vis reservoir solution decreased by about 50 % and by about

10 %, respectively, during the experiment. Since no diffusion cell was connected to this reservoir solution a U(VI) precipitation with citric acid involvement can be assumed.

Compared to the three reservoirs with low U(VI) concentration, the UV-vis reservoir showed the largest variance in redox potential (cf. Fig. 79). Based on these observations it can be assumed that instead of a U(VI) precipitation a reduction to U(IV) with subsequent precipitation occurs in the reservoir, probably caused by the citric acid. Perhaps, the about two orders of magnitude higher U(VI) concentration was more sensitive towards reduction than the lower U(VI) concentration in the reservoirs Cell 1, Cell 2, and TTA. However, the precipitation was not entire; the majority of uranium was still in solution (cf. Table 22).

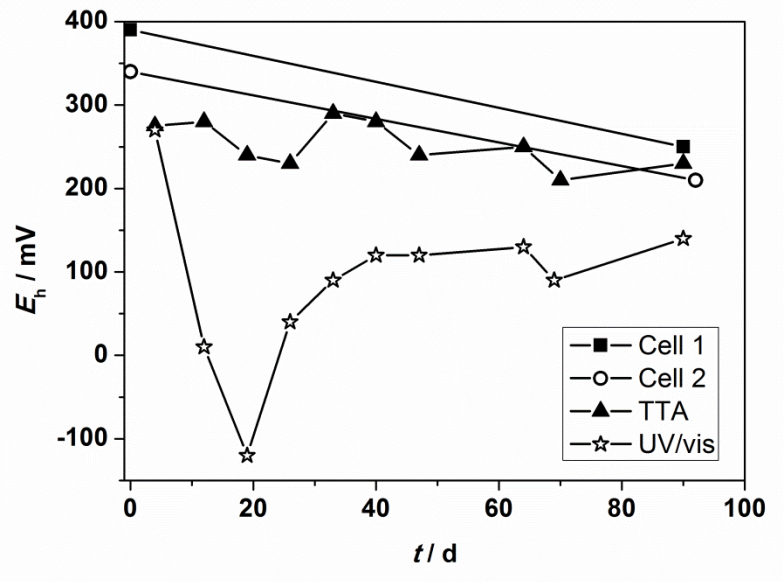

Fig. 79**:** Redox potential as a function of time determined in the solutions of reservoir Cell 1, Cell 2, TTA, and UV-vis. Lines were drawn for visual reasons.

In addition to redox potential measurements, the redox state of uranium was determined by TTA solvent extraction using aliquots of the reservoir solutions of Cell 1, Cell 2, and TTA. No reduction of U(VI) to U(IV) was detected in all samples taken within the three months. This supported the results of the redox potential measurement, that uranium was stable in the hexavalent oxidation state in these solutions.

The solution of the UV-vis reservoir was regularly analyzed by UV-vis spectroscopy. The spectra are presented in Fig. 80.

In the beginning of the experiment the spectrum of the solution was similar to the spectrum of the $(UO_2)_3(cit)_3(OH)_3^{8-}$ complex (Steudtner et al., 2012). This observation indicated the presence of a U(VI)-citric acid species in the beginning of the experiment which was in contrast to the results of the speciation calculation (cf. Table 21). It seems that based on the current knowledge of U(VI)-citric acid species the present experimental speciation is not described correctly. Species containing U(VI) and citric acid which may form under the investigated environmentally relevant conditions are not reported yet. Felipe-Sotelo et al. (2015) investigated

to solubility of U(IV)/U(VI) in the presence of citric acid at higher pH values in saturated $Ca(OH)_2$ solution. They observe a 3-4 orders of magnitude higher solubility of uranium than in the absence of citric acid. Thermodynamic modeling underestimates the solubility since thermodynamic constants of these conditions are missing. They assume that soluble metal-citrate-OH complexes stabilized by Ca^{2+} are formed.

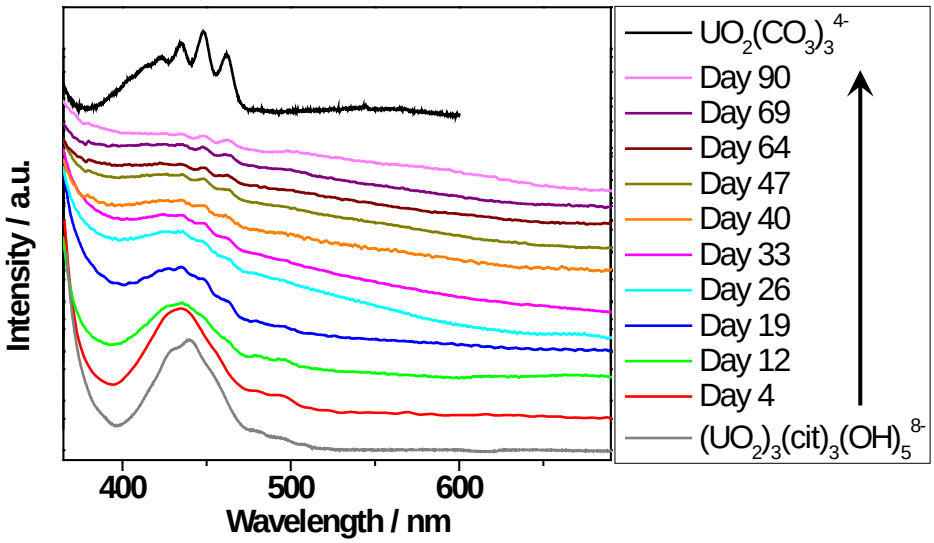

Fig. 80: UV-vis spectra of the UV-vis reservoir solution as a function of time. Spectra of $UO_2(CO_3)_3^{4-}$ and $(UO_2)_3(cit)_3(OH)_5^{8-}$ provided by Steudtner et al. (2012).

The UV-vis spectra changed within 12 and 19 days which was in agreement with the largest variation in redox potential (cf. Fig. 79) and can be attributed to the assumed partly reduction of U(VI) to U(IV). At the end of the experiment the UV-vis spectrum showed a slightly smaller intensity which can be due to the lower U(VI) concentration in solution and/or a change of the extinction coefficient associated to a change in speciation. The shape of the spectrum was similar to the spectrum of $UO_2(CO_3)_3^{4-}$. That indicates that after the reaction of the U(VI)-citric acid species with possible U(IV) precipitation, the remaining U(VI) seems to form a carbonates species, probably $Ca_2UO_2(CO_3)_3(aq)$, which would be in agreement with the U(VI) speciation calculated.

PCS measurements showed the absence of colloids in the solutions of the reservoirs TTA and UV-vis. Contrary, colloids were detected in the source reservoir solution of Cell 1 and Cell 2. Probably, mineral particles were released from the clay during the diffusion experiment.

8.2.3 Influence of citric acid on the diffusion of U(VI) in Opalinus Clay

At the end of the diffusion experiment, depth profiles of $^{233}U(VI)$ in OPA in the absence and presence of citric acid were determined (cf. Fig. 81). Within the three months neither $^{233}U(VI)$ nor citric acid were detected in the receiving reservoir solution.

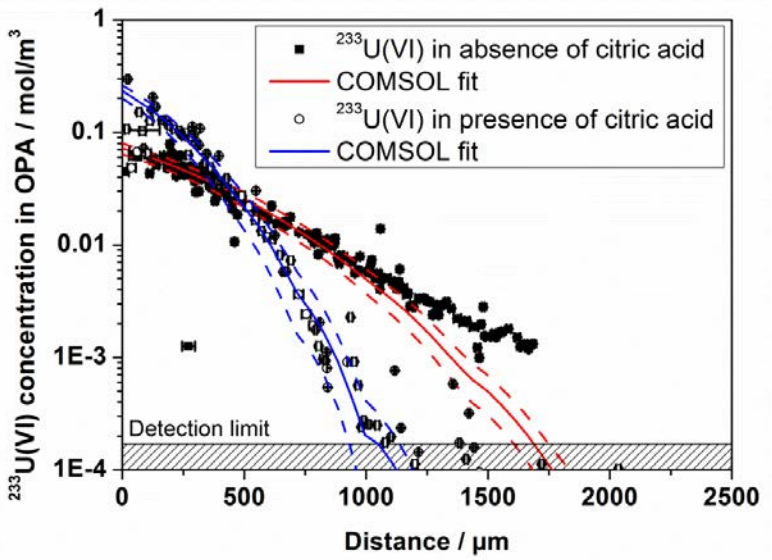

Fig. 81: Concentration profiles of ^{233}U(VI) in the absence (filled symbols) and presence (open symbols) of citric acid.

The comparison of the profiles shows that in the presence of citric acid more ^{233}U(VI) was detected at the boundary of the clay sample pointing to a much stronger sorption of ^{233}U(VI) on the clay. In addition, ^{233}U(VI) diffusion was less deep in the clay (about 1 mm) than in the absence of citric acid (about 1.75 mm). These observations indicate the presence of different diffusing species in the absence and presence of citric acid. Furthermore, the data of the ^{233}U(VI) profile in the presence of citric acid scatter close to the OPA boundary. A small fraction of a different U(VI) species could have been formed, perhaps reaction products. As discussed in section 8.2.2, although it was observed only in the UV-vis reservoir solution a reaction of the main diffusing species in the solution of Cell 2 during the three-month experiment cannot be excluded. Another reason for this data scattering could be the preparation method. The observed behavior of the profiles is contrary to the results of the speciation calculations (Table 21 and Table 22) where in the absence as well as presence of citric acid $Ca_2UO_2(CO_3)_3$(aq) was identified as dominant U(VI) species in solution and assumed to be the main diffusing species in the diffusion experiment. It seems, that in addition to the U(VI) speciation of the UV-vis reservoir solution also the U(VI) speciation in the solutions of the reservoirs Cell 2 and TTA are incorrect. Based on the diffusion results there should be another species diffuse through the clay than $Ca_2UO_2(CO_3)_3$(aq). This discrepancy represents a further example of missing thermodynamic data of U(VI)-citric acid species for the present conditions.

Under consideration of the boundary conditions, the experimental profile data were fitted with COMSOL by variation of D_e and K_d. The diffusion parameter values obtained for ^{233}U(VI) in the absence and presence of citric acid are summarized in Table 23. In the model, the transport porosity of U(VI) and citric acid equaled ε(HTO), although it appears likely that ε(U(VI) and ε(citric acid) are smaller than for HTO. Given their relatively large size, the dominant U(VI) and citric acid species may not have access to the interlayers of the smectite fraction of OPA. However, Joseph et al. (2013b) have been discussed previously that the choice

of ε_{eff} has no significant impact on the modeled U(VI) diffusion parameters, since the U(VI) sorption onto the clay is dominating (cf. Eq. (8.4): $\rho \cdot K_d >> \varepsilon_{eff}$).

Table 23: Parameter values for the ^{233}U(VI) diffusion in OPA in the absence and presence citric acid.

	Cell 1: ^{233}U(VI) in the absence of citric acid	^{233}U(VI) [b]	Cell 2: ^{233}U(VI) in the presence of citric acid
t / d	90	89	91
ρ / kg/m^3	2364	2424	2357
ε / – [a]	0.10 ± 0.01	0.16 ± 0.01	0.10 ± 0.005
K_d / m^3/kg	0.038 ± 0.005	0.025 ± 0.003	0.15 ± 0.03
α / –	90 ± 12	61 ± 7	354 ± 70
D_e / × 10^{-12} m^2/s	1.9 ± 0.4	1.9 ± 0.4	2.3 ± 0.8
D_a / × 10^{-14} m^2/s	2.1 ± 0.2	3.1 ± 0.3	0.65 ± 0.1

[a] Determined by HTO through-diffusion.

[b] Determined by diffusion experiments (Joseph et al., 2013b).

The comparison of the results from Cell 1 with literature data (Joseph et al., 2013b) shows that the literature D_e value determined under similar conditions could be confirmed by this experiment. This indicates that the same diffusing U(VI) species was present in both diffusion experiments, probably $Ca_2UO_2(CO_3)_3$(aq). However, in the present study the determined K_d value was slightly larger than the reported value which can be attributed to differences in the clay batch used in the diffusion cells. This batch had also a smaller porosity than the literature sample which can have an effect on K_d.

As discussed, in the presence of citric acid a U(VI)-citric acid species may be formed in solution which seemed to be the main diffusing species in Cell 2. Based on the modeling results, this species sorbed stronger onto OPA than $Ca_2UO_2(CO_3)_3$(aq). The K_d increased by one order of magnitude. This is in contrast to previous findings where the influence of citric acid on the U(VI) sorption to OPA was investigated by batch sorption experiments (Schmeide and Joseph, 2012). There, a significant decrease of the K_d value of U(VI) was observed with increasing citric acid concentration. At a citric acid concentration of 1×10^{-3} M the K_d value decreased from about 0.025 m^3/kg to about 0.0045 m^3/kg. This was explained by the formation of very stable aqueous U(VI)-citric acid complexes with probable smaller sorption affinity towards OPA than the $Ca_2UO_2(CO_3)_3$(aq) complex. A reduction of U(VI) to U(IV) was not detected in the batch sorption experiments. These contradictory observations point to the presence of different uranium species in the batch sorption and diffusion experiments. Although it was not found in the source reservoir solution by solvent extraction U(VI) could have been reduced to U(IV) directly on the clay surface. A similar behavior was observed for the Np(V) / OPA system (Wu et al., 2009). Without the probable catalyzing effect of citric acid, a one order of magnitude higher K_d value was obtained by Np(V) diffusion experiments than by Np(V) batch sorption experiments. It was assumed that Np(V) was partly reduced to Np(IV) in OPA. It can be assumed that the formation of $Ca_2UO_2(CO_3)_3$(aq) stabilized U(VI) against reduction by OPA, but as the U(VI) species changed due to the influence of citric acid, U(VI) may have become more vulnerable for reduction.

Under consideration of the uncertainties the D_e value of the species formed in the presence of citric acid was comparable to the D_e value of $Ca_2UO_2(CO_3)_3(aq)$. The combination of similar D_e and increased K_d led to an one order of magnitude decreased D_a value for the assumed U(VI)-citric acid species compared to the D_a value of U(VI) in the absence of citric acid. That means, the formed uranium species was stronger retarded by OPA than $Ca_2UO_2(CO_3)_3(aq)$. Citric acid had a significant influence on the retention of U(VI) in OPA.

8.2.4 Diffusion of citric acid in Opalinus Clay

In addition to the profiles of U(VI), the diffusion profile of citric acid in the OPA sample of Cell 2 was studied. The experimental and model profile data are presented in Fig. 82.

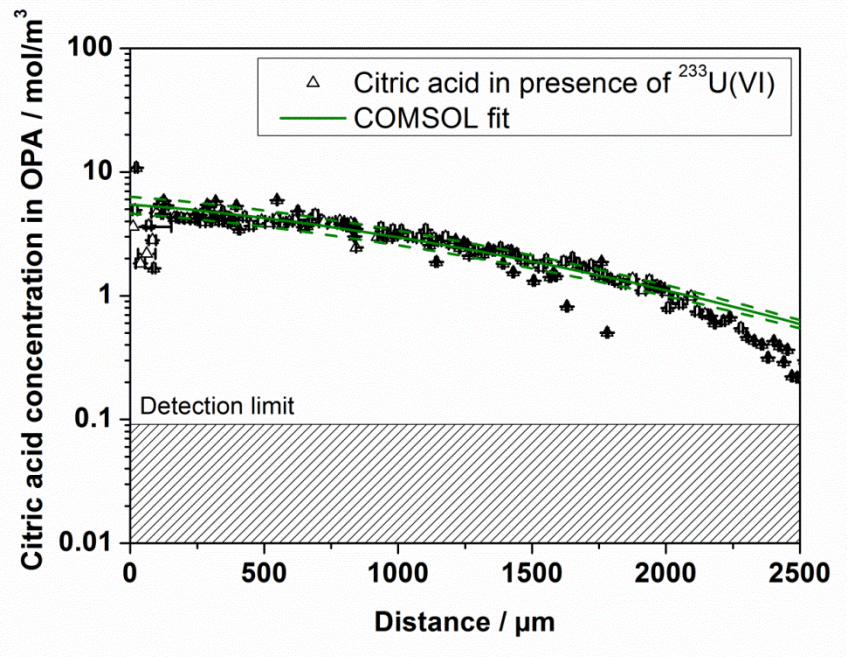

Fig. 82: Concentration profile of citric acid in the presence of $^{233}U(VI)$.

In the main part of the OPA sample only one profile can be seen assuming that there was only one main citric acid species diffusing through the clay. Based on the species distribution shown in Table 21 and Table 22, this could be $Ca(cit)^-$. A small fraction of citric acid should be associated to $^{233}U(VI)$ which diffused only about 1 mm deep into the clay (cf. Fig. 81). However, since the concentration of $Ca(cit)^-$ is about three orders of magnitude higher than any U(VI)-citric acid complex which may have formed, the $Ca(cit)^-$ profile superimposes any other profile. As seen in the U(VI) profile in the presence of citric acid at the boundary of the OPA sample the data scattering was quite large. Since this was observed for different species in Cell 2 in different concentration ranges the scattering could be attributed to the preparation method. However, citric acid is a strong complexation agent which also complexes ions from the mineral itself, in that way it can dissolve the clay and can alter the mineral surface with time (Huang and Keller, 1971). Although over the course of the diffusion experiment the concentration of clay released ions did not significantly increase in the source reservoir solutions (cf. Table 21 and Table 22) an alteration of the OPA surface within the first

100 µm of the OPA sample cannot be excluded due to the contact with citric acid. This would lead to a weaker sorption of the diffusing species at the boundary of the clay sample and would explain the data scattering at this diffusion depth.

The diffusion parameter values for citric acid obtained by COMSOL modeling are summarized in Table 24. For comparison literature data for the humic acid diffusion through OPA in the presence of U(VI) (Joseph et al., 2013b) are shown, too.

Table 24: Parameter values for the citric acid and humic acid diffusion in OPA in the presence ^{233}U(VI).

	Cell 2: Citric acid in the presence of ^{233}U(VI)	Small humic acid colloids [b]
t / d	91	87
ρ / kg/m^3	2357	2392
ε / – [a]	0.10 ± 0.005	0.15 ± 0.01
K_d / m^3/kg	0.0025 ± 0.0004	0.002 ± 0.0005
α / –	6 ± 1	5 ± 1.2
D_e / × 10^{-13} m^2/s	9 ± 1	4 ± 2.5
D_a / × 10^{-14} m^2/s	15 ± 1	8 ± 3

[a] Determined by HTO through-diffusion.

[b] Determined by diffusion experiments (Joseph et al., 2013b).

Citric acid sorbed relatively weakly onto OPA. The K_d value was about one and two orders of magnitude smaller than the K_d value of $Ca_2UO_2(CO_3)_3$(aq) and the sorbed U(VI)-citric acid species (cf. Table 23), respectively, but comparable to the sorption strength of small humic acids. Probably, the negative charge of the main diffusing species, Ca(cit)$^-$, led to electrostatic repulsion from the negatively charged clay surface. The D_e value of the main diffusing citric acid species was smaller than the D_e value of the respective diffusing U(VI) species in Cell 1 and 2, but was slightly higher than the D_e value for small humic acid colloids. Both competing effects, sorption and migration, led to an increased D_a value for the predominantly diffusing citric acid species compared to the D_a values of U(VI) in the absence and presence of citric acid and of small humic acid colloids. Dagnelie et al. (2014) obtained one order of magnitude higher D_a values for the diffusion of EDTA ($D_a = 3.5\times10^{-12}$ m^2/s) and oxalic acid ($D_a = 1.9\times10^{-12}$ m^2/s) through Callovo-Oxfordian Clay.

In contrast to small humic acid colloids, citric acid was not detected in the receiving reservoir of Cell 2 within three months of diffusion. Since humic acid colloids have no distinct size but a molecular size distribution, probably, smaller colloids than the main fraction of small humic acid colloids diffused through the OPA sample. However, in the case of citric acid, modeling based on the fitted diffusion parameters showed that a detectable amount of citric acid in the receiving reservoir solution can be expected after 250 days of diffusion time.

8.2.5 Conclusions

In this study the HTO and U(VI) diffusion through OPA was conducted using OPA pore water as background electrolyte. The U(VI) diffusion experiments were conducted in the absence and presence of citric acid.

The diffusion parameter values obtained for the HTO through-diffusion and the U(VI) in-diffusion in the absence of citric acid were in agreement with literature data. In the presence of citric acid the U(VI) diffusion was significantly retarded, which was attributed to a change in speciation. Probably, U(VI) was reduced to U(IV) within the three months the diffusion experiment was conducted.

Citric acid diffused slightly faster through OPA than small humic acid colloids. Based on modeling results it should be detectable in the receiving reservoir solution after about 250 days.

Speciation calculations using currently available uranium and citric acid thermodynamic data gave contrary results to the experimental observations. Instead of the calculated dominance of the $Ca_2UO_2(CO_3)_3(aq)$ complex in solution in the presence of citric acid, the respective diffusion profile ([U(VI)] : [citric acid] = 1 : 1000) and UV-vis spectra ([U(VI)] : [citric acid] = 1 : 10) revealed the significant influence of citric acid on U(VI). In both cases a citric acid mediated partly reduction of U(VI) to U(IV) was assumed. The study shows that the chemical system has to be investigated in more detail to clarify the occurring reactions. In particular, the U(VI)-citric acid species formed under these environmentally relevant conditions needs to be described spectroscopically, thermodynamically, and structurally.

9 Diffusion of U(VI) in montmorillonite at high ionic strengths

The migration behavior of radionuclides in clay rock is governed by molecular diffusion. Diffusion experiments can be used to determine the parameters of these migration processes. Most studies today focus on radionuclide diffusion in clay rock or compacted clay minerals at low ionic strengths (Glaus et al., 2007, 2010; González Sánchez et al., 2008; Jakob et al., 2009; Joseph et al., 2013b; Van Loon et al., 2003; Wu et al., 2014). In this study, diffusion experiments were conducted in both a mixed electrolyte (see section 7.1.1) as well as a NaCl solution of the same ionic strength. The mineral used in these studies was purified compacted montmorillonite. In a first step, HTO was diffused as a conservative tracer, which allows the determination of the rock capacity factor α, while in a second step, a U(VI) solution is contacted with the clay.

SWy-2 montmorillonite was purified according to Poinssot et al. (1999) and Bradbury and Baeyens (2009). In contrast to the procedure described in section 7.1, the step in which the <5 µm fraction is enriched was omitted. This was done to ensure a consistency of the dried clay that allows the clay to be ground easily. The ground clay was then pressed at Karlsruher Institut für Technologie, Institut für Nukleare Entsorgung (KIT-INE) into a clay tablet of 10.7 mm length and a diameter of 25.4 mm. This was then placed in a Teflon cell of compact design in which the reservoirs for the solutions that are contacted with the clay are in direct contact with the filters (Titanium, 25.4 x 0.75 mm, 0.5 µm nominal pore size, Mott Corporation, Farmington, CT, USA) placed on each side of the clay plug. Each reservoir has a volume of 100 mL. The diffusion cells were placed on two magnetic stirring plates (Color squid, IKA®-Werke GmbH & CO. KG, Staufen, Germany), one under each reservoir, so that the solutions in the reservoirs could be agitated by stirring discs (PTFE, 6x9 mm, Cowie Technologies, Middlesbrough, UK). For diffusion, a HTO solution ($c_{m,HTO}$ = 1 kBq mL^{-1}) and a ^{233}U(VI) solution ($c_{m,U(VI)}$ = 1×10^{-6} mol kg^{-1}) were used, the latter prepared as described in section 7.1.1. The mixed electrolyte (see section 7.1.1) and a NaCl solution of I = 3.02 mol kg^{-1}, i.e. identical ionic strength to the mixed electrolyte, were used as pore waters. The experimental procedure followed Van Loon et al. (2003), however, due to the design of the diffusion cells, the solutions were not exchanged, but remained in the reservoir for the duration of each part of the diffusion experiment.

The clay mineral was equilibrated in the inactive electrolyte solutions for 5.4 months. During this time, the pH_c was adjusted to 6.5. When pH stability over several days was reached, the electrolyte solutions in the reservoir were analyzed and exchanged against new solutions. Photon correlation spectroscopy showed that no colloidal particles could be found in the reservoirs. Crystallization of salts on the walls of the diffusion cells reduced the electrolyte concentration. In the diffusion experiment in NaCl, a calcium content of 3.7×10^{-3} mol kg^{-1} was present.

The HTO in-diffusion took place over 29 days. During this time, samples were collected daily in triplicate and analyzed by LSC (300 µL sample diluted with 2.7 mL Milli-Q water, dispersed in 20 mL Ultima Gold LLT). To keep the amount of solution constant, 900 µL of the appropri-

ate solution were added to the electrolyte solution reservoirs after sampling. Preliminary analysis of the data gave a rock capacity factor α of 0.39 (NaCl) and 0.76 (mixed electrolyte) respectively, and an effective diffusion coefficient D_e of 1.3×10^{-9} m² s^{-1} in NaCl and 9.8×10^{-10} m² s^{-1} in the mixed electrolyte. For the out-diffusion, the electrolyte solutions in the reservoirs were exchanged against inactive solutions and the sample frequency was reduced to twice a week. After the HTO out-diffusion, the U(VI) diffusion experiment was started. The solution was sampled once a week and analyzed by LSC (300 µL sample diluted with 2.7 mL Milli-Q water, dispersed in 20 ml Ultima Gold LLT). At the time of writing, U(VI) diffusion was still on-going.

10 Spatiotemporal observation of diffusion processes with PET for determination of heterogeneous effects on the core scale

10.1 Aim

The general aim of the work package was to establish PET (Positron Emission Tomography) as a reliable measuring method for quantitative determination of heterogeneous diffusion coefficients in clays. In the preceding project the suitability for imaging diffusive tracer transport was shown, however, open questions remained with respect to quantification and thus interpretation of the results. In particular, extremely high diffusion coefficients were estimated from the measurements. Therefore, the main focus was improvement of quantification, both by improving image quality and parameter determination method. Further experiments were conducted in order to understand experimental artefacts by sample alteration and damage.

10.2 Improvement of the PET-imaging procedure

The ClearPET-scanner, which is utilized in our institute, is a high-resolution scanner which is originally designed for biomedical research on small animals (Roldan et al., 2007). Over the period of the project, our concern was the higher impact of material density than that of biological tissue, which causes blurring and artefacts of the images. We had to improve the imaging algorithms in order to acquire high-quality quantitative images for parameter derivation and as reference for heterogeneous geochemical modeling.

Two issues of the image reconstruction procedure were identified and successfully addressed: normalization and scattering. This work on image improvement was largely based upon Monte-Carlo simulations of the physical processes, from radioactive decay of the tracer nuclide to detection in the detectors. Normalization is a calibration procedure which considers space-dependent inhomogeneities of sensitivity matrix, which is caused by the individual efficiencies of the detectors and their geometrical configuration. We found a strong impact of gaps between the detector cassettes, although the gantry is rotating in order to improve image homogeneity. The image deteriorating effect of these gaps is amplified by scattering and attenuation of radiation, because these cause events at locations that are not duly considered by the iterative image reconstruction procedure (Zakhnini et al., 2013).

10.2.1 Image reconstruction procedure and normalization

The original supplied image reconstruction software (STIR1.4-alpha) was updated to the recent version 3.0 which has more options for optimizing the normalization scheme (Thielemans et al., 2012). Normalization and attenuation correction where now applied directly on the original projection data. The normalization data are from the measurement on a homogeneously filled cylindrical phantom. It was found that gaps in the normalization projection (projection bins filled with zero), which are caused by the gaps between the detector cassettes,

have significant effect on image quality (Loukiala et al., 2010). Therefore, we fill the gaps with values from the projection of a synthetic unity image with the same geometry as the cylinder phantom used for the normalization measurement. Calibration of these inserted values with the minimum value of the non-empty bins of the measured normalization yielded the best suppression of ring artefacts. Star artefacts, which have been observed frequently with the first reconstruction procedure, could be eliminated completely by reducing the number of subsets from 10 to 2 in the OSEM – algorithm, at the cost of more cpu-time.

With these optimizations of the reconstruction algorithm image quality was largely improved. Reconstruction of measurements on phantoms with low density generally brought satisfactory results.

10.2.2 Scatter correction

In dense material we still experienced blurring of the images and again ring artefacts, which therefore were assigned to scattering effects. We therefore conducted Monte-Carlo simulations with OpenGATE (Jan et al., 2004) in order to identify scatter effects, quantify the scatter fraction and the impact of “false” coincidences (coincidences of nuclear gamma radiation, not from positron annihilation). These simulations yield projections of all detected coincidences, with the history of each event being known, in particular the number of Compton scattering events and the energy loss. It was found that the scatter fraction could be reduced to some extent by energy filtering (reducing the detection energy window from 250 – 750 keV to 400 – 650 keV), and that multiple scatter with a deviation of about 20° is dominating. We were able to correct measurements of simple source geometries with the help of these simulated scatter projections, which could be rated in comparison with images produced only from non-scattered events. However, the computation time of these simulations exceeds the measuring time by far.

The recent version of the reconstruction software (since STIR 2.1) supplies a simpler and faster approach, approximating the scatter deviation of the coincidences with a simplified Klein-Nishina equation (single scatter simulation SSS). Input data are the distribution of mass attenuation coefficients, as measure of the scatter cross section and an estimate of the source, which could be an uncorrected image. The result is unscaled and has to be calibrated in order to produce the due scatter fraction; we therefore still rely on an estimate of the scatter fraction which can be produced with one single Monte-Carlo simulation of a rough model. The scatter calibration was implemented as iterative procedure. In spite of the simplifications of the SSS it yields acceptable results for correction of the measured projections. The processing time of the SSS, which originally took 12 h for one projection, was optimized to about 40 min by simplification of the geometry.

The new reconstruction procedure was implemented as Python script which allows batch reconstruction and high flexibility for further improvements.

10.2.3 Error estimation, resolution, and detection threshold

There are fundamental differences between the well-known X-ray CT imaging modality and PET. CT responds to the material density. CT-data are commonly processed in order to produce structural images, segmenting the grey-level images into two or multiple domains with different density. Therefore, the most significant characteristics are spatial resolution and homogeneity of the mapping, in order to facilitate segmentation.

In contrast, PET responds to (tracer) concentration, which is the intensive thermodynamic parameter that is crucial in geochemical modeling. Concentration is a continuous value, referred to a finite test volume which is defined by the spatial resolution of the measuring method. Here, spatial resolution is the parameter of the response function which controls the smoothing of the image. More meaningful characteristics of PET images than spatial resolution are quantification errors and the detection threshold.

A rigorous error analysis of the PET imaging procedure is an intricate task (cf. e.g. Prekeges, 2013). The analysis starts on the detector level. Although the total number of recorded events is large (e.g. 10^7), the occupations of the detector positions (bins) are small numbers, responding to the Binomial distribution. The reconstruction procedure is a complicated surjective mapping method from the projection space of measurements to the image space, which requires additional parameters (normalization, attenuation correction, scatter correction) that are also subject to errors. Currently, the error propagation analysis of this complex procedure is not feasible, because we would have to analyze the system matrix with a size of several TBytes.

Instead, we estimate the error from the number of counts N that are projected to one voxel. This number is large; therefore we can consider the Poisson distribution with a relative error $\sigma = {}^{1}/_{\sqrt{N}}$. It is typically in the order of $\pm$10 % or less. However, we also have to consider systematic errors that are caused by deficiencies of the reconstruction algorithm and the parameter values. These are identifiable as imaging artefacts occurring in zones where the sensitivity – magnitude of the response function of the mapping from the projections to the image – is low. Eventually, these artefacts include zeros (e.g. from scatter-overcorrection) or errors in the order of a factor 2.

In summary, the error depends on the number of counts per voxel and is typically in the order of 10 %. In zones with lower sensitivity it eventually diverges and produces ring artefacts.

Apart from the relative error we have to consider a detection threshold of activity below which the source is not reliably detected. This threshold depends on the background level, detector properties and the reconstruction procedure. The background coincidence count rate, as deduced from blank measurements, is in the order of 500 cps. However, scattered events from strong sources can also be considered as background, in so far as they are not considered by the scatter correction procedure. A general threshold is caused by the number of events required to reconstruct one voxel. This threshold was determined with the help of Monte-

Carlo simulations of ^{22}Na-point sources in Opalinus Clay to be as low as 10 Bq, corresponding to a total of 50 counts in 18 min.

10.3 Measurements

In total we prepared and conducted PET-observations of diffusion processes on 12 Opalinus samples, most of them with ^{124}I as tracer. We tested the integrity of the samples during the experiment on blocks with a volume of 30 cm^3 which were cast in epoxy and which were prepared from fresh Opalinus cores. The upper surface was exposed to synthetic [^{124}I]-OPA-water according to Pearson (2003). Over an observation period of 4 weeks we observed significant swelling (up to 10 %), loss of integrity, and fast tracer transport into the sample. Thus, we have to consider alteration effects by unconfined swelling. This situation is not representative for conditions in the undisturbed host rock remote from the excavation damage zone (EDZ).

In order to observe diffusion on a larger scale and to reduce the alteration effect observed on small blocks we prepared horizontal drill cores (diameter 100 mm, length 80 mm) of Opalinus Clay from Mont Terri, which also were cast in epoxy. Perpendicular to the bedding, a blind hole (diameter 5 mm, length 50 mm) was drilled into the core to infill synthetic Opalinus pore water. After an equilibration period, which included observations with ^{124}I-labeled OPA-water, equilibration, the hole was filled with synthetic OPA-water, now labeled with ^{22}Na. Then it was closed with a screw, establishing a physically sealed source. The sample was stored at 20°C.

As example, we report the measurements on one sample (BLT 137/3): Beginning daily, with increasing time lag, we produced a sequence of 20 PET-images over a period of 150 days until the tracer was roughly equally distributed over the core (Fig. 83) (t = 0, 3, 6, 10, 13, 16, 20, 22, 27, 31, 35, 41, 48, 55, 69, 93, 112, 127, 143, 161 days). Because of the large amplitude range the images were scaled frame-wise. Fig. 84 shows the evolution of the maximum value, which is the reference, and the 90 % and 99.9 %-quantile. Fig. 85 shows slices in the direction of the major anisotropy axes. A gas bubble becomes visible, which at frame 1 had moved from its initial position at the bottom of the hole. The maximum projection in vertical direction is plotted as height-map at the bottom of each frame. It indicates that the diffusing tracer reaches the sample surface after 31 days at frame 10. Then, the tracer distribution homogenizes over the sample; therefore, the quantiles stabilize (Fig. 84) and the anisotropy of the distribution decreases until frame 18, which shows almost homogeneous tracer distribution.

Fig. 86 is an enlargement of the maximum projection. The shape of this distribution appears as roughly 10 mm thick rectangular block, rather than as an anisotropy ellipsoid, notwithstanding remaining indications for circular artefacts. This type of shape could be interpreted as an indication for diffusion along fine layering, rather than homogenous transversal anisotropic behavior. However, these findings should be assured by additional investigations (e.g. µCT, radiography and analysis of thin sections, as well as model simulations) and after further improvement of image quality.

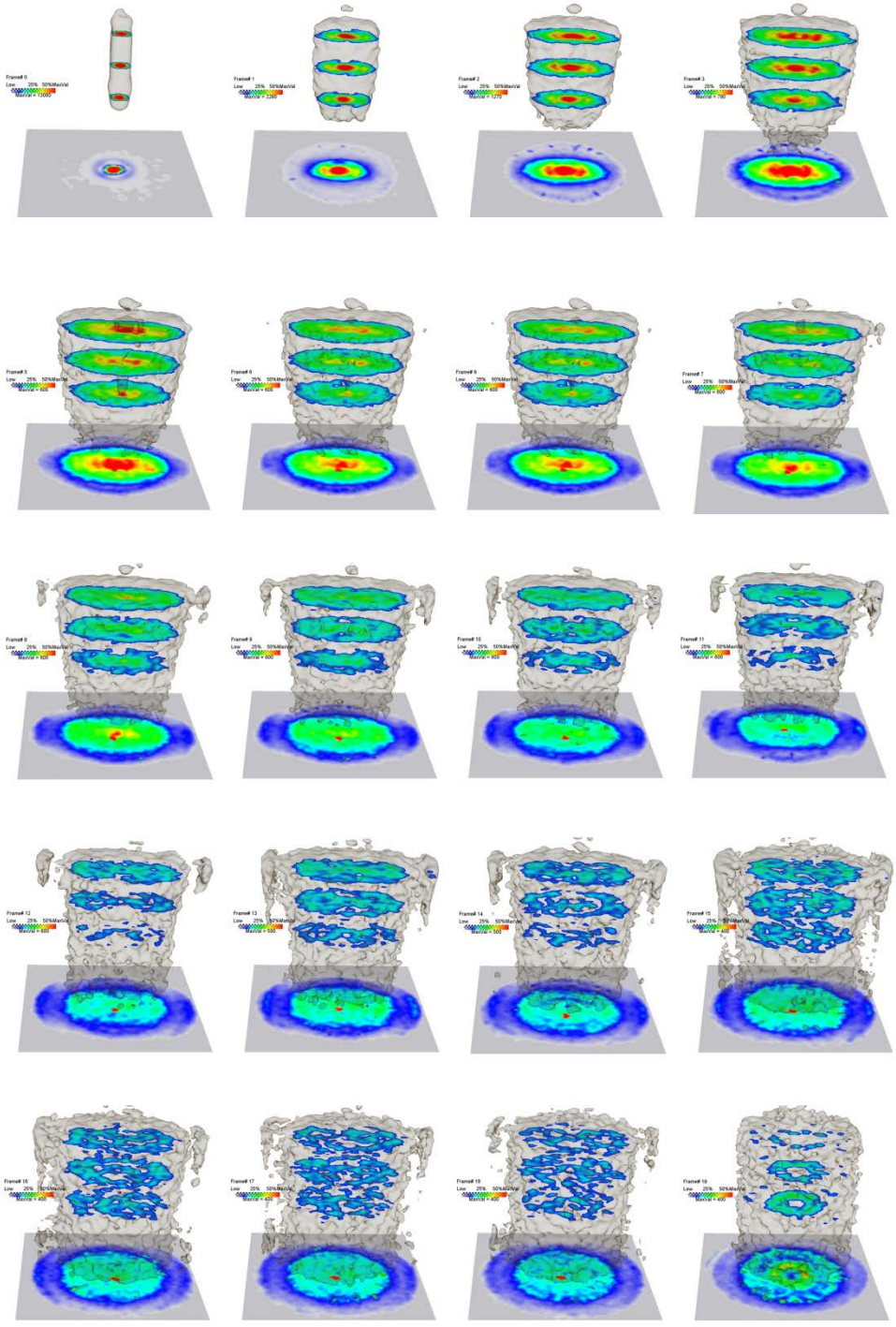

Fig. 83: 20 PET-frames of ^{22}Na-diffusion in a OPA-drill core (diameter: 100 mm, length 80 mm). At the bottom of each image: axial (vertical) maximum projection. Above: 3 horizontal slices through the source region; iso-surface of maximum/10, the scaling of the color scales is frame-wise, the maximum value of the color scale is half maximum total amplitude for each (amplitude distribution cf. Fig. 84).

Prior to the investigations with ^{22}Na we tested ^{124}I as PET-tracer (Fig. 87). In principle, its decay time (4.176 d) allows observations periods up to 1 month, sufficient for parameter derivations according to the procedure outlined below. However, the images are noisy, because of other “parasitic” γ-radiation (“false coincidences”), and the decreasing countrate causes an increasing error with time. Therefore, application of ^{124}I merely is a qualitative test method, rather than suited for quantitative estimations.

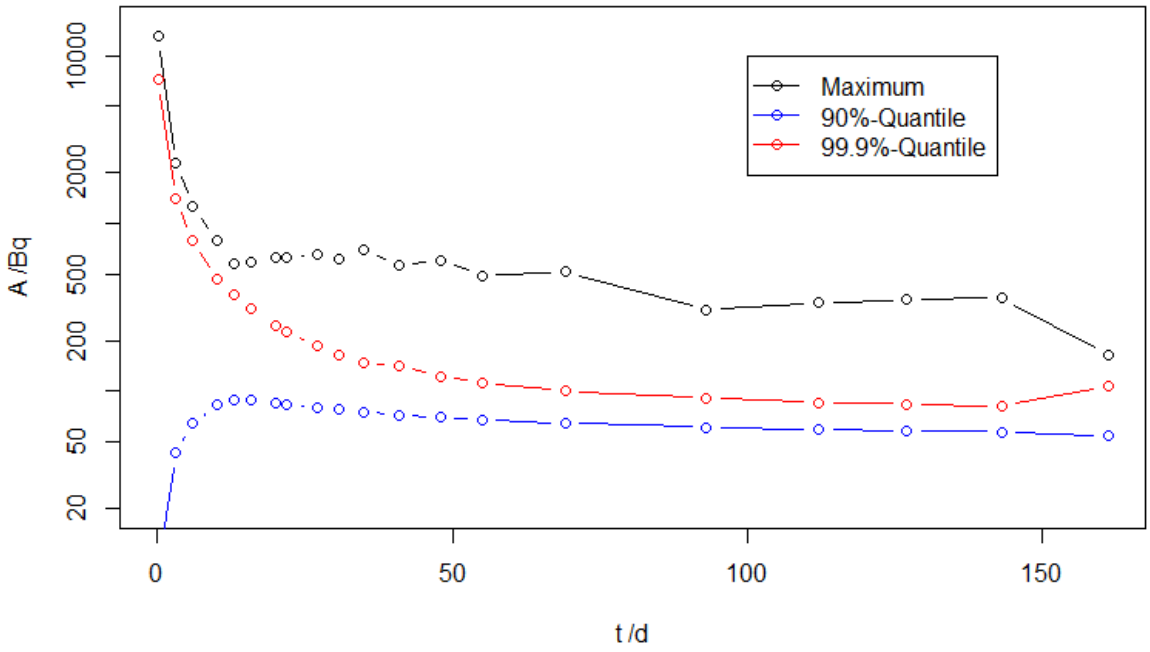

Fig. 84: Maximum, 99.9 %- and 90 %-quantiles of the amplitude vs. frame time. The color scale in Fig. 83 refers to the maximum.

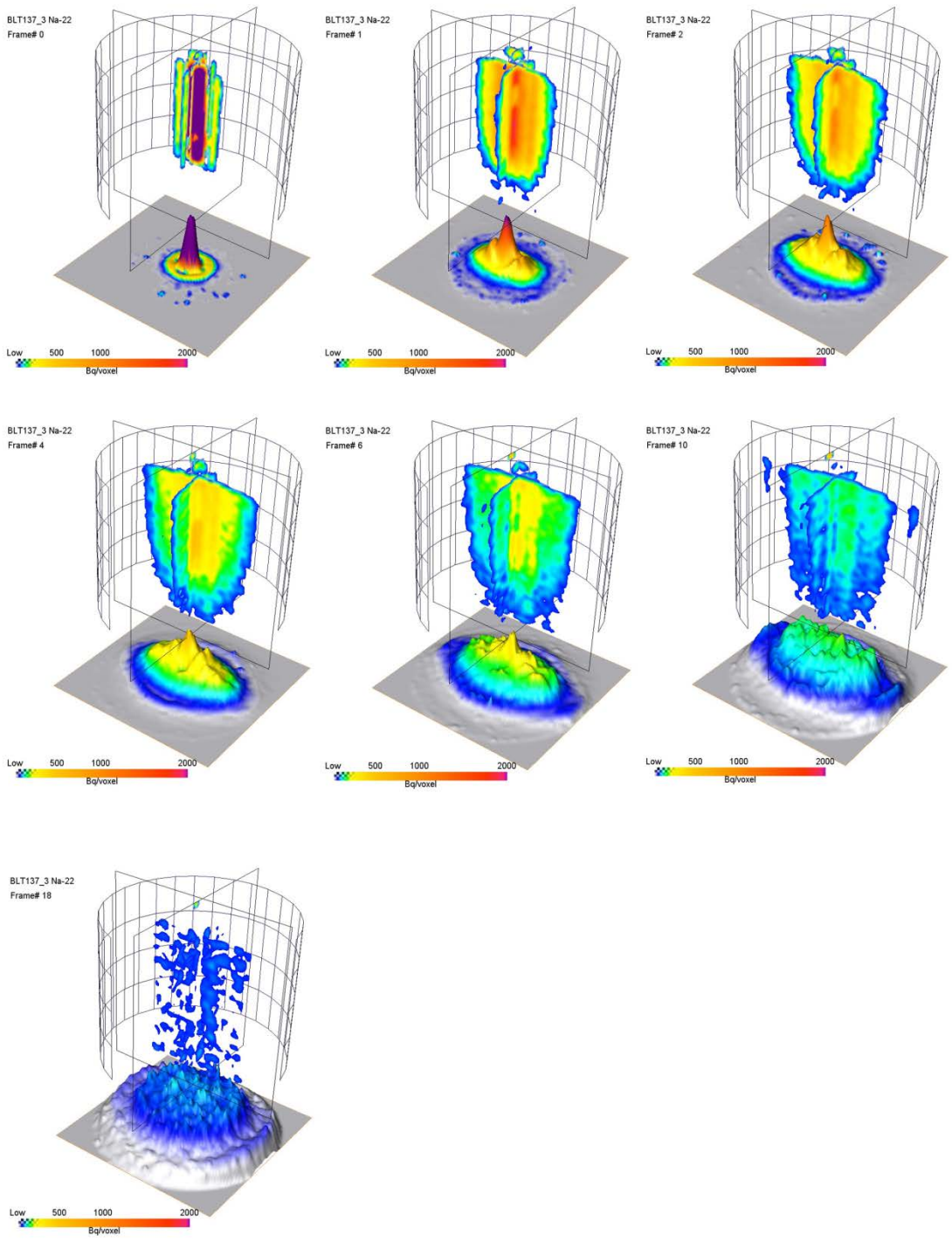

Fig. 85: Vertical slice representation of frames 0, 1, 2, 4, 6, 10, 18. At the bottom: axial projection of the maximum amplitude as height-map.

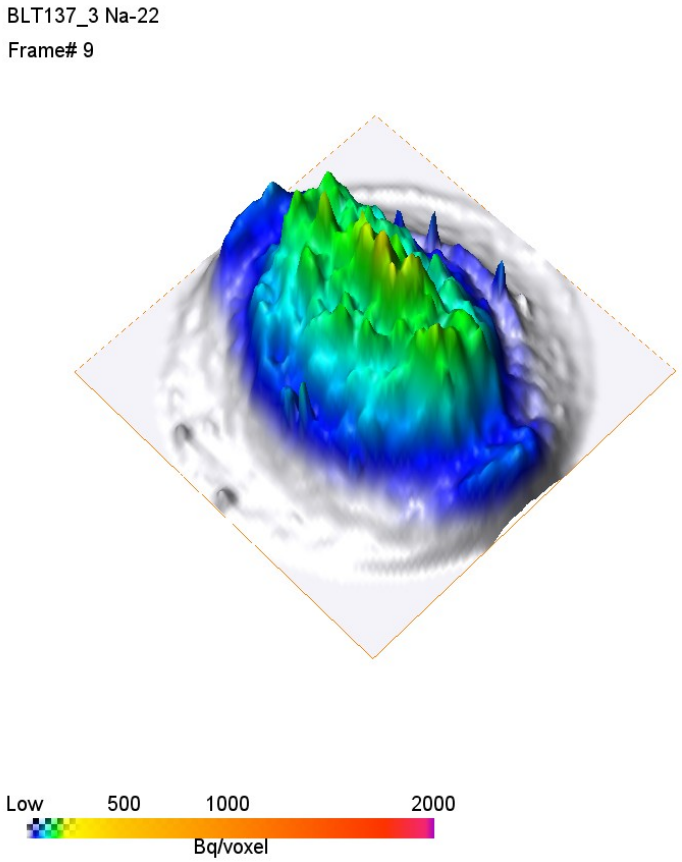

Fig. 86: Axial maximum projection of frame 9 (27 days).

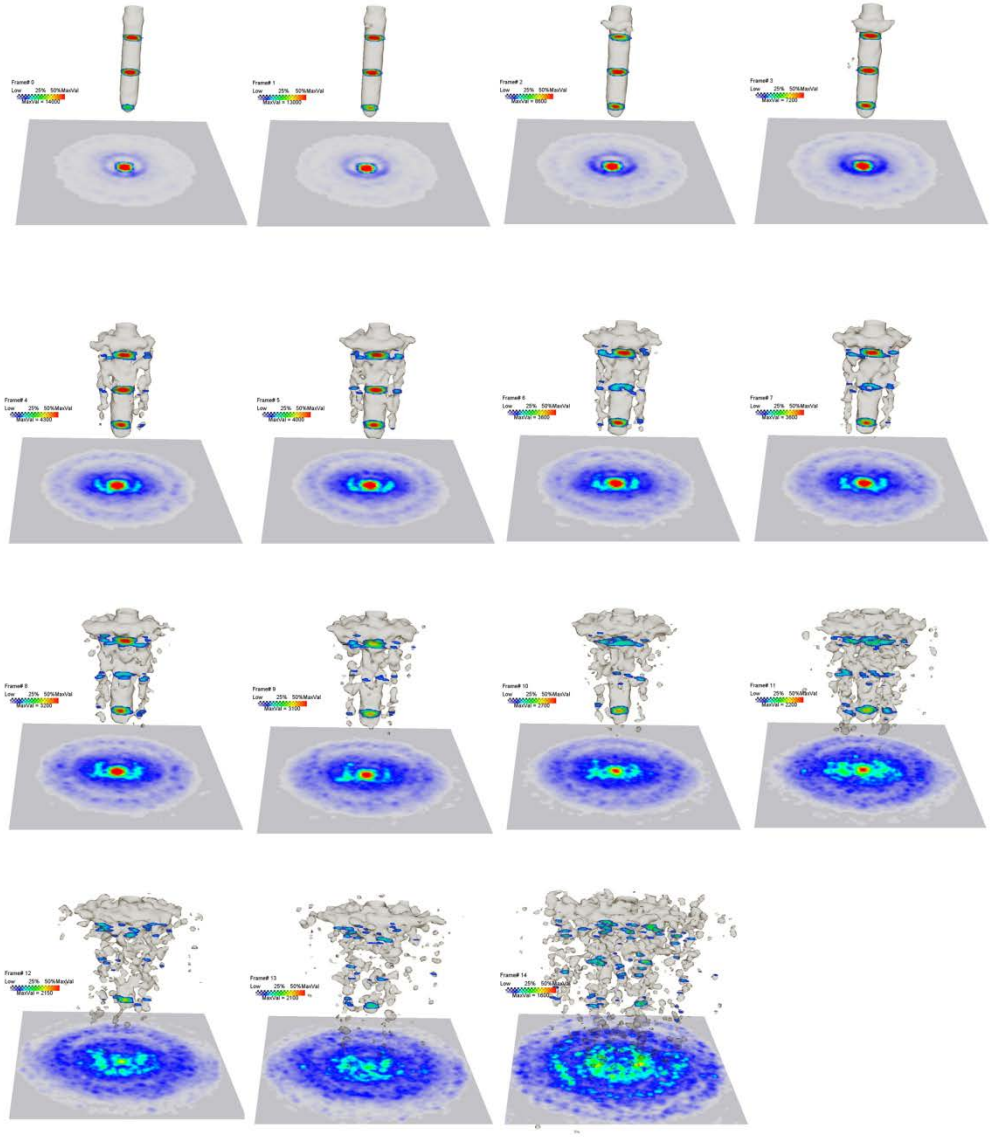

Fig. 87: 15 PET-frames of ^{124}I-diffusion in the same OPA-drill core. At the bottom of each image: axial (vertical) maximum projection. Above: 3 horizontal slices through the source region; iso-surface of maximum/10, the scaling of the color scales is frame-wise, the maximum value of the color scale is half maximum total amplitude for each (amplitude distribution cf. Fig. 88).

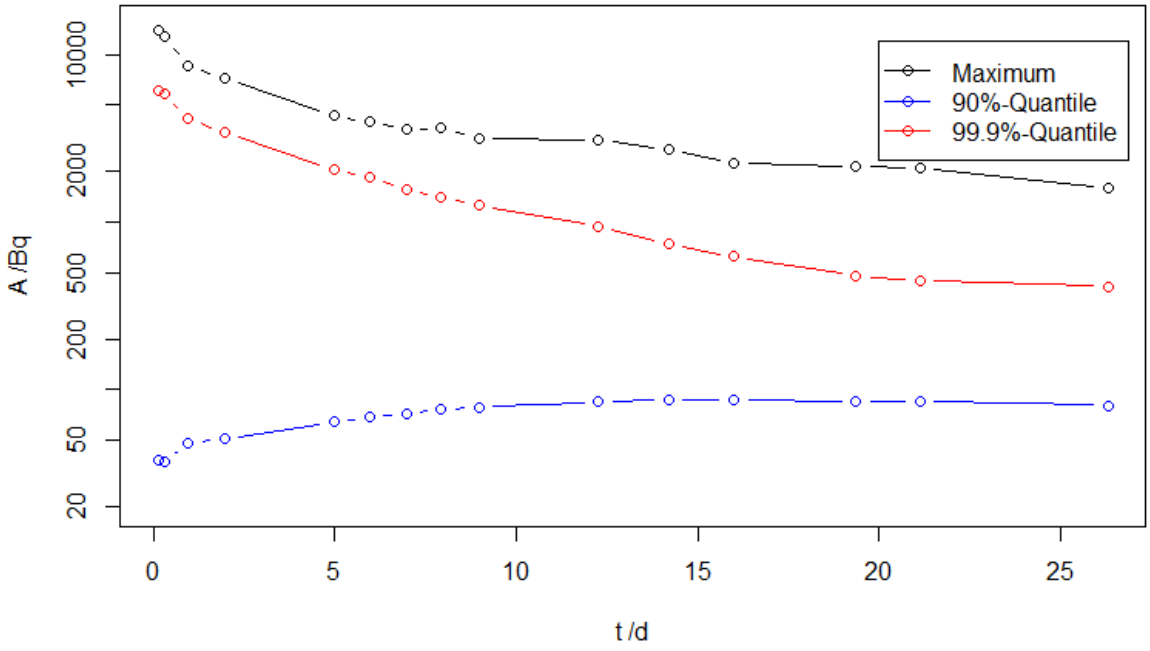

Fig. 88: Maximum, 99.9 %- and 90 %-quantiles of the amplitude of Fig. 87 vs. time.

10.4 Parameter derivation

Earlier, we developed a method for parameter derivation and attempted to derive these parameters from PET-data that were not scatter corrected (Schikora, 2012). We then derived rather high diffusion coefficients that were deviating from literature values (e.g. Van Loon et al., 2004). Therefore, we considered additional fast transport processes, which could be caused by suction and swelling effects. After a scatter correction technique became available, we conducted a similar procedure on corrected PET-data (Gerasch, 2015). First results are published in Kulenkampff et al. (2015).

Here we only consider the initial period, until the tracer propagation reached the surface of the sample. We aligned COMSOL multiphysics simulations of anisotropic diffusion in clay to our PET-observations and were able to clearly differentiate and evaluate likely explicit sample features and transport processes. From our non-invasive, spatio-temporal PET observations of the diffusion process in a real clay sample two 2D sets c_i(x,z) and c_i(y,z), are extracted and provided to the Optimization Module for the parameter estimation for Dxx=Dzz and Dyy. A sensitivity analysis quantifies the effects on uncertainties regarding porosity n, initial concentration c_0 and spatial resolution.

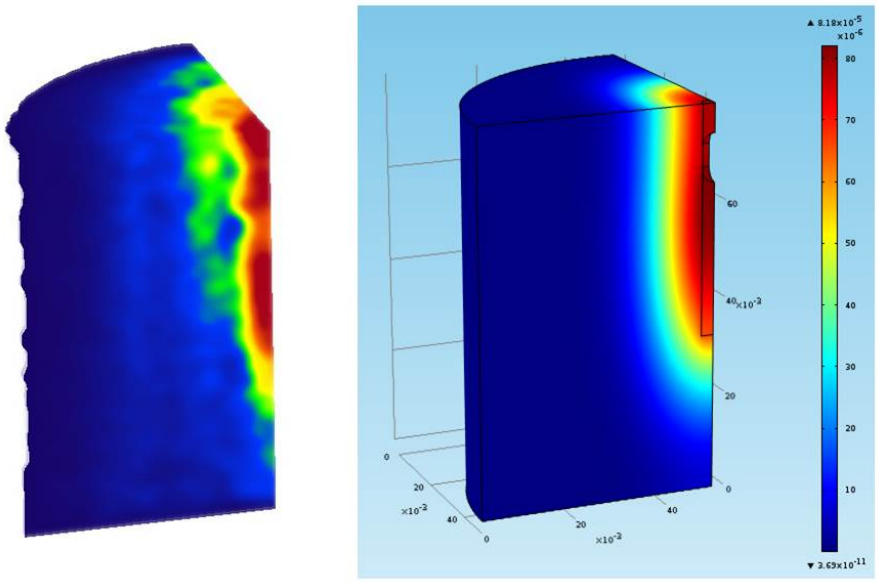

Fig. 89: Result of the optimum fit of the PET - tracer distribution (left) with a COMSOL Multiphysics FEM model (right) (scaled in molar concentrations).

The 4D simulation results nicely match quantitatively with our 4D experimental results obtained in GeoPET experiments. Fig. 89 shows a comparison of the experimental data with the simulated values. This method yielded the apparent diffusion coefficients in the principal directions, $D_{a,xx}$ = 1.1e-10 m^2/s and $D_{a,yy}$ = 3.4e 11 m^2/s, which are in accordance with results from through-diffusion experiments parallel and perpendicular to the bedding (Van Loon et al., 2004).

This method shall be improved in future to consider complete 3D+t-data sets instead of sequential optimization of data subsets from single frames. Also, it should consider more complex geochemical models, which is possible with PHREEQC-COMSOL-coupling, than simply including a constant K_d.

10.5 Conclusions

With the new image reconstruction algorithm and the improved parameter determination procedure it is now possible to yield reliable diffusion parameters from PET-measurements. The method is ready for application as rather rapid test procedure of diffusion properties on the scale of drill cores. Further improvements are possible and will reduce instrumental deficiencies that cause systematic – yet recognizable – errors.

A number of experimental requirements have been identified: Longer living PET-nuclides, like ^{22}Na should be preferred, rather than ^{124}I, because the observation period should be one month, and the detectability of the tracer decreases caused by radioactive decay, which is

negligible with ^{22}Na, and diffusional spreading. In order to reduce preparation damage and overburden release effects the sample should prepared immediately after retrieval and kept at simulated overburden conditions as far as possible. These requirements are compatible with PET-experiments. In the present studies, which were designed to develop and improve the method, such complications were not considered. Therefore, alteration effects are likely.

Smaller sample sizes could speed up the testing procedure. However, we experienced significant alterations of the samples on smaller samples. Also, then heterogeneous effects on the larger scale would be neglected which are detectable with PET imaging on larger scale samples. Heterogeneous effects on the larger scale, caused by e.g. more sandy layers and lenses, could significantly moderate the transport behavior, because they could cause preferential diffusional transport along localized zones and therefore affect both transport velocity and retention in an unfavorable way for the barrier function. We found indications for such effects, although they could not yet be quantified and they could also be due to experimental conditions, e.g. fracturing through swelling or stress release.

The derived diffusion parameters are not exclusively valid for available PET-nuclides. Following Appello et al. (2010), we can principally derive spatially resolved material parameters, like formation factors, which then can be considered for diffusion modeling of other types of ions. Then, only interaction parameters of the tracer, in particular Na^+-ions, and the other ions have to be determined in batch experiments.

11 Observation of reactive transport in fractured barrier rock

11.1 Aim

Mining operations and drilling inevitably produce an EDZ, which is caused by pressure release, build-up of differential stress, loss of formation water and air entry. One option to improve these degradations of the geological barrier is impregnation of waterglass (Bollingerfer et al., 2011). The success of effective injection into void structures depends on a number of factors: the reaction kinetics of the injected waterglass with salt and brines, the nature of the fractures, and the injection velocity. This rather complex process was not yet observed directly, but only the final results had been tested with destructive methods.

We developed a method to observe the waterglass injection process into salt rock and quantify the resulting modification of transport pathways with PET (Bittner, 2014). The results can be combined with numerical process simulation based on CT-imaging, allowing to improve fundamental process understanding and to verify the underlying assumptions and model codes.

11.2 Method

We are using a sylvinite core from Staßfurt of the type Z2KSTh. It is a cylindrical sample with a diameter of 100 mm and a length of 150 mm. Before our injection studies, the core had undergone a geomechanical triaxial test, which caused cone shaped internal fractures with a total porosity of 6 % and a slightly convex cylinder surface, which are clearly visible in the µCT-image (Fig. 90). The core itself was cast into a PMMA-cylinder with epoxy resin. PVC-end caps were adapted with a small dead volume of about 1.5 ml. The fluid was injected and ejected through central ports in the end caps.

Saturated sodium chloride solution with sediment was applied as injection test fluid and waterglass (sodium silicate, $Na_2SiO_3 + H_2O$) was used as impregnation agent. Sodium silicate in contact with salt solutions and evaporite minerals results in a fast formation of solids. The chemical and mineralogical composition of these solids depends on the concentration and type of salts. Waterglass also polymerizes at a reduction of the pH value, this can be done by simple dilution with water, or in contact with salt. Therefore, the sealing efficiency, i.e. depth of penetration and distribution, is a result of both injection rate and reaction kinetics.

We studied the impact of the fast reaction kinetics on small columns filled with granular salt, which were treated with waterglass and brine. The propagation of the fluids was observed with PET. Depending on flow rate, grain size, and pore fill we achieved a penetration depth of the waterglass of 1 to 10 mm before the injection pressure increased abruptly.

The injection study with PET-observation consists of five steps:

1) A saturated NaCl-solution labeled with [^{18}F]KF with an activity of 100 MBq was injected with a flowrate of 0.25 ml/min in order to visualize the effective flow paths of the brine and to quantifying the permeability of the core. The pressure was 0.3 bars, according to a permeability of 9e-15 m^2.

2) [^{18}F]KF-waterglass solution was injected into the wet core with a flowrate of 0.5 ml/min and shut-off pressure of 2.6 bars.

3) Again, [^{18}F]KF-saturated NaCl-solution was injected to allow for direct comparison with the initial brine flow experiment, flow rate: 0.25 ml/min, pressure: 0.6 bars, permeability 2e-15 m^2.

4) Second [^{18}F]KF-waterglass injection with higher flow rate (5 ml/min) and higher final injection pressure (5 bars), to improve the sealing result, after drying the sample with dry pressured air.

5) The final test with [^{18}F]KF-saturated NaCl-solution showed no significant change of the solution flow compared to step 3.

Exemplary images of these five phases are shown in Fig. 90.

11.3 Conclusions

The initial suite of PET-images showed two major transport zones, one central branch, and one branch along the contact of the fracture with the epoxy cast. The penetration of the waterglass followed these zones, but did not exceed a penetration depth of ca. 10 mm. The major part congealed as film on the sample surface and inhibited further penetration.

In this feasibility study we demonstrated the capabilities of process observations with PET for the study of injection methods for improving the barrier function of geological material. We did not intend to apply higher pressures or flow rates and therefore, in particular, no conclusions on the efficiency of waterglass injections for improvements of the geological barrier in salt rocks are drawn. Experiments with practically more relevant higher injection rates and endpoint pressures of around 50 bars would have implied significantly higher costs for pressure vessels and a high pressure injection system. However, the present study proves the capabilities of the method and its potential for observing and better understanding such coupled hydraulic-chemical processes.

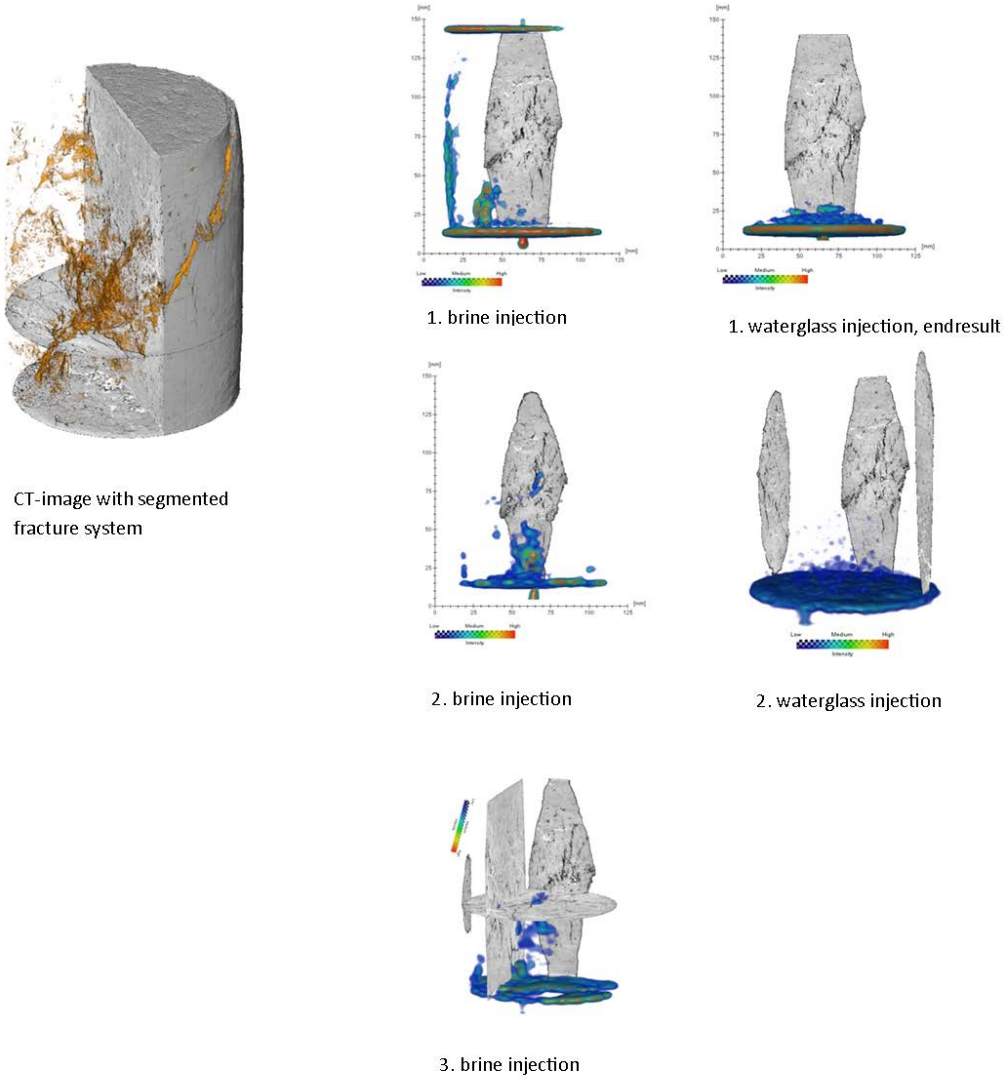

Fig. 90: µCT-image of the fracture system and exemplary images of the waterglass injection tests: Initial brine injection shows flow mainly along the outer edge of one fracture and through the sample, 1st waterglass injection penetrates up to ca. 15 mm and seals the surface, 2nd brine injection shows some sealing effect mainly of large voids, 2nd waterglass injection did not penetrate the volume and causes no improvement of the sealing effect, as can be seen in the 3rd brine injection.

12 References

Aiken, G.R.: Isolation and concentration techniques for aquatic humic substances, in: Humic substances in soil, sediment and water: Geochemistry and isolation (Aiken, G.R., MacKnight, D.M., Wershaw, R.L., MacCarthy, P., eds.). Wiley-Interscience, New York, pp. 363-385 (1985).

Akcay, H., Kurtulmuş, F.: Study of uranium sorption and desorption on some turkish clays. J. Radioanal. Nucl. Chem. 200 (6), 529-544 (1995).

Altmaier, M., Metz, V., Neck, V., Muller, R., Fanghänel, T.: Solid-liquid equilibria of $Mg(OH)_2$(cr) and $Mg_2(OH)_3Cl_x4H_2O$(cr) in the system Mg-Na-H-OH-Cl-H_2O at 25°C . Geochim. Cosmochim. Acta 67, 3595-3601 (2003).

Altmaier, M., Neck, V., Fanghänel, T.: Solubility of Zr(IV), Th(IV) and Pu(IV) hydrous oxides in $CaCl_2$ solutions and the formation of ternary Ca-M(IV)-OH complexes. Radiochim. Acta 96, 541-550 (2008).

Ams, D.A., Swanson, J.S., Szymanowski, J.E.S., Fein, J.B., Richmann, M., Reed, D.T.: The effect of high ionic strength on neptunium (V) adsorption to a halophilic bacterium. Geochim. Cosmochim. Acta 110, 45-57 (2013).

Appelo, C.A.J., Van Loon, L.R., Wersin, P.: Multicomponent diffusion of a suite of tracers (HTO, Cl, Br, I, Na, Sr, Cs) in a single sample of Opalinus Clay. Geochim. Cosmochim. Acta 74(4), 1201-1219 (2010).

Artinger, R., Kienzler, B., Schüßler, W., Kim, J.I.: Effects of humic substances on the ^{241}Am migration in a sandy aquifer: column experiments with Gorleben groundwater/sediment systems. J. Contam. Hydrol. 35, 261-275 (1998).

Atkins, P.W.: Physical Chemistry. Oxford University Press: Oxford (1998).

Bachmaf, S., Merkel, B.J.: Sorption of uranium(VI) at the clay mineral–water interface. Environ. Earth Sci. 63 (5), 925-934 (2011).

Bain, D.C., Smith, B.F.L.: Chemical analysis. In: Wilson, M.J. (Ed.), A Handbook of determinative methods in clay mineralogy. Blackie, New York, USA (1987).

Barkleit, A., Acker, M., Bernhard, G.: Europium(III) complexation with salicylic acid at elevated temperatures. Inorg. Chim. Acta 394, 535-541 (2013).

Bauer, A., Fiehn, B., Marquardt, C.M., Klein, M., Römer, J., Schäfer, T., Görtzen, A., Kienzler, B.: Results on the Pu Diffusion in the Opalinus Clay. 6th EC FP - FUNMIG IP. Stockholm. 2nd Annual Workshop Proceedings, pp. 231-237 (2006).

Benedetti, M.F., Milne, C.J., Kinniburgh, D.G., Van Riemsdijk, W.H., Koopal, L.K.: Metal ion binding to humic substances: Application of the non-ideal competitive adsorption model. Environ. Sci. Technol. 29, 446-457 (1995).

Bernhard, G., Geipel, G., Reich, T., Brendler, V., Amayri, S., Nitsche, H.: Uranyl(VI) carbonate complex formation: Validation of the $Ca_2UO_2(CO_3)_3$(aq.) species. Radiochim. Acta 89, 511-518 (2001).

Bertrand, P.A., Choppin, G.R.: Separation of actinides in different oxidation states by solvent extraction. Radiochim. Acta 31, 135-137 (1982).

Bittner, L.: Prozessbeobachtung von Vergütungsmaßnahmen im Salzgestein mittels Positronen Emissions Tomographie (GeoPET). Diploma thesis, Hochschule Zittau/Görlitz, Zittau (2014).

Bleise, A., Danesi, P.R., Burkart, W.: Properties, use and health effects of depleted uranium (DU): a general overview. J. Environ. Radioact. 64, 93-112 (2003).

Bollingerfehr, W., von Borstel, L.E., Engelhardt, H.-J., Müller, C., Schmidt, H.: Vergütung der Auflockerungszone im Salinar (VerA), Abschlussbericht FKZ 02E10649, DBE Technology GmbH (2011).

Bradbury, M.H., Baeyens, B.: A mechanistic description of Ni and Zn sorption on Na-montmorillonite. Part II: modelling. J. Contam. Hydrol. 27 (3), 223-248 (1997).

Bradbury, M.H., Baeyens, B.: Modelling the sorption of Zn and Ni on Ca-montmorillonite. Geochim. Cosmochim. Acta 63 (3), 325-336 (1999).

Bradbury, M.H., Baeyens, B.: Sorption of Eu on Na-and Ca-montmorillonites: experimental investigations and modelling with cation exchange and surface complexation. Geochim. Cosmochim. Acta 66 (13), 2325-2334 (2002).

Bradbury, M.H., Baeyens, B.: Modelling the sorption of Mn(II), Co(II), Ni(II), Zn(II), Cd(II), Eu(III), Am(III), Sn(IV), Th(IV), Np(V) and U(VI) on montmorillonite: Linear free energy relationships and estimates of surface binding constants for some selected heavy metals and actinides. Geochim. Cosmochim. Acta 69 (4), 875-892 (2005).

Bradbury, M.H., Baeyens, B.: Sorption modelling on illite. Part I: Titration measurements and the sorption of Ni, Co, Eu and Sn. Geochim. Cosmochim. Acta 73 (4), 990-1003 (2009).

Brewitz, W.: Eignungsprüfung der Schachtanlage Konrad für die Endlagerung radioaktiver Abfälle. GSF-T 136 (1982).

Bro, R.: PARAFAC: Tutorial and applications. Chemom. Intell. Lab. Syst. 38, 149-171 (1997).

Bünzli, J.-C., Piguet C.: Taking advantage of luminescent lanthanide ions. Chem. Soc. Rev. 34, 1048-1077 (2005).

Cacheris, W.P., Choppin, G.R.: Dissociation kinetics of thorium-humate complex. Radiochim. Acta 42, 185-190 (1987).

Catalano, J.G., Brown, G.E.: Uranyl adsorption onto montmorillonite: Evaluation of binding sites and carbonate complexation. Geochim. Cosmochim. Acta 69 (12), 2995-3005 (2005).

Chakraborty, S., Favre, F., Banerjee, D., Scheinost, A.C., Mullet, M., Ehrhardt, J.-J., Brendle, J., Vidal, L., Charlet, L.: U(VI) sorption and reduction by Fe(II) sorbed on montmorillonite. Environ. Sci. Technol. 44 (10), 3779-3785 (2010).

Chisholm-Brause, C.J., Berg, J.M., Matzner, R.A., Morris, D.E.: Uranium(VI) sorption complexes on montmorillonite as a function of solution chemistry. J. Colloid Interface Sci. 233 (1), 38-49 (2001).

Choppin, G.R., Clark, S.B.: The kinetic interactions of metal ions with humic acids. Mar. Chem. 36, 27-38 (1991).

Claret, F., Schäfer, T., Bauer, A., Buckau, G.: Generation of humic and fulvic acid from Callovo-Oxfordian clay under high alkaline conditions. Sci. Total Environ. 317, 189-200 (2003).

Collins, R.N., Saito, T., Aoyagi, N., Payne, T.E., Kimura, T., Waite, D.T.: Applications of time-resolved laser fluorescence spectroscopy to the environmental biogeochemistry of actinides. J. Environ. Qual. 40, 731-741 (2011).

COMSOL: COMSOL Multiphysics® 4.2a. Finite element analysis, solver and simulation software package for various physics and engineering applications. COMSOL, Inc., Burlington. http://www.comsol.com (2011).

Courdouan, A., Christl, I., Meylan, S., Wersin, P., Kretzschmar, R.: Isolation and characterization of dissolved organic matter from the Callovo-Oxfordian formation. Appl. Geochem. 22, 1537-1548 (2007a).

Courdouan, A., Christl, I., Meylan, S., Wersin, P., Kretzschmar, R.: Characterization of dissolved organic matter in anoxic rock extracts and in situ pore water of the opalinus clay. Appl. Geochem. 22, 2926-2939 (2007b).

Crank, J.: The mathematics of diffusion. Oxford University Press Inc., New York (1975).

Dagnelie, R.V.H., Descostes, M., Pointeau, I., Klein, J., Grenut, B., Radwan, J., Lebeau, D., Georgin, D., Giffaut, E.: Sorption and diffusion of organic acids through clayrock: Comparison with inorganic anions. J. Hydrol. 511, 619-627 (2014).

Deacon, G.B., Phillips, R.J.: Relationships between the carbon-oxygen stretching frequencies of carboxylato complexes and the type of carboxylate coordination. Coord. Chem. Rev. 33(3), 227-250 (1980).

Doherty, J.E., Hunt, R.J.: Approaches to highly parameterized inversion—a guide to using PEST for groundwater-model calibration. Scientific Investigations Report 2010–5169, US Geological Survey (2010).

Dong, W., Brooks, S.C.: Determination of the formation constants of ternary complexes of uranyl and carbonate with alkaline earth metals (Mg^{2+}, Ca^{2+}, Sr^{2+}, and Ba^{2+}) using anion exchange method. Environ. Sci. Technol. 40 (15), 4689-4695 (2006).

Dreissig, I., Weiss, S., Hennig, C., Bernhard, G., Zänker H.: Formation of uranium(IV)-silica colloids at near-neutral pH. Geochim. Cosmochim. Acta 75, 352-367 (2011).

Drobot, B., Steudtner, R., Raff, J., Geipel, G., Brendler, V., Tsushima, S.: Combining luminescence spectroscopy, parallel factor analysis and quantum chemistry to reveal metal speciation–a case study of uranyl(VI) hydrolysis. Chem. Sci. 6(2), 964-972 (2015).

Duffield, R.B., Calvin, M.: The stability of chelate compounds. III. Exchange reactions of copper chelate compounds. J. Am. Chem. Soc. 68, 557-561 (1946).

Edelstein, N.M., Klenze, R., Fanghänel, Th., Hubert, S.: Optical properties of Cm(III) in crystals and solutions and their application to Cm(III) speciation. Coord. Chem. Rev. 250, 948-973 (2006).

Fanghänel, T., Neck V., Kim J.I.: The ion product of H_2O, dissociation constants of H_2CO_3 and Pitzer parameters in the system $Na^+/H^+/OH^-/HCO_3^-/CO_3^{2-}/ClO_4^-/H_2O$ at 25°C. J. Sol. Chem. 25, 327-343 (1996).

Felipe-Sotelo, M., Edgar, M., Beattie, T., Warwick, P., Evans, N.D.M., Read, D.: Effect of anthropogenic organic complexants on the solubility of Ni, Th, U(IV) and U(VI). J. Hazard. Mater. 300, 553-560 (2015).

Felmy, A.R., Rai D., Mason M.J.: The solubility of hydrous thorium(IV) oxide in chloride media: Development of an aqueous ion-interaction model. Radiochim. Acta 55, 177-185 (1991).

Francis, A.J., Dodge, C.J., Gillow, J.B. and Papenguth, H.W.: Biotransformation of uranium compounds in high ionic strength brine by a halophilic bacterium under denitrifying conditions. Environ. Sci. Technol. 34, 2311-2317 (2000).

Francis, A.J., Gillow, J.B., Dodge, C.J., Harris, R., Beveridge, T.J., Papenguth, H.W.: Uranium association with halophilic and non-halophilic bacteria and archaea. Radiochim. Acta 92, 481-488 (2004).

Freundlich, H.: Ueber Kolloidfällung und Adsorption. Ztschr. F. Chem. u. Indus. Kolloide 1, 321-331 (1907).

Freyer, M., Walther, C., Stumpf, T., Buckau, G., Fanghänel, T.: Formation of Cm humate complexes in aqueous solution at pH_c 3 to 5.5: The role of fast interchange. Radiochim. Acta 97, 547-558 (2009).

Fröhlich, D.R., Amayri, S., Drebert, J., Reich, T.: Influence of humic acid on neptunium(V) sorption and diffusion in Opalinus Clay. Radiochim. Acta 101, 553-560 (2013).

Fröls, S., Dyall-Smith, M., Pfeifer, F.: Biofilm formation by haloarchaea. Environ. Microbiol. 14, 3159-3174 (2012).

Gaines Jr., G.L., Thomas, H.C.: Adsorption studies on clay minerals. ii. A formulation of the thermodynamics of exchange adsorption. J. Chem. Phys. 21 (4), 714-718 (1953).

Geckeis, H., Rabung, T., Ngo Manh, T., Kim, J.I., Beck, H.P.: Humic colloid-borne natural polyvalent metal ions: dissociation experiment. Environ. Sci. Technol. 36, 2946-2952 (2002).

Gerasch, R.: Simulation und Parameterschätzung von ^{22}Na Diffusion in einem Opalinus-Bohrkern mittels COMSOL Multiphysics und GeoPET-Datenabgleich. Diploma thesis, Brandenburgische Technische Universität Cottbus-Senftenberg, Senftenberg (2015).

Gillow, J.B., Francis, A.J., Papenguth, H.W.: The role of subterranean microbes in facilitating actinide migration at the Grimsel Test Site and Waste Isolation Pilot Plant. Radiochim. Acta 88, 769-774 (2001).

Glaus, M.A., Baeyens, B., Bradbury, M.H., Jakob, A., Van Loon, L.R., Yaroshchuk, A.E.: Diffusion of ^{22}Na and ^{85}Sr in montmorillonite: Evidence of interlayer diffusion being the dominant pathway at high compaction. Environ. Sci. Technol. 41, 478-485 (2007).

Glaus, M.A., Frick, S., Rossé, R., Van Loon, L.R.: Comparative study of tracer diffusion of HTO, $^{22}Na^{+}$ and $^{36}Cl^{-}$ in compacted kaolinite, illite and montmorillonite. Geochim. Cosmochim. Acta 74, 1999-2010 (2010).

Glaus, M.A., Rossé, R., Van Loon L.R., Yaroshchuk, A.E.: Tracer diffusion in sintered stainless steel filters: measurement of effective diffusion coefficients and implications for diffusion studies with compacted clays. Clays Clay Miner. 56, 677-685 (2008).

González Sánchez, F., Van Loon, L.R., Gimmi, T., Jakob, A., Glaus, M.A., Diamond, L.W.: Self-diffusion of water and its dependence on temperature and ionic strength in highly compacted montmorillonite, illite and kaolinite. Appl. Geochem. 23, 3840-3851 (2008).

Grenthe, I., Fuger, J., Konings, R.J.M., Lemire, R.J., Muller, A.B., Nguyen-Trung, C., Wanner, H.: Chemical Thermodynamics of Uranium. Nuclear Energy Agency (1992).

Gruber, C., Legat, A., Pfaffenhuemer, M., Radax, C., Weidler, G., Busse, H.-J., Stan-Lotter, H.: *Halobacterium noricense* sp. nov., an archaeal isolate from a bore core of an alpine Permian salt deposit, classification of *Halobacterium* sp. NRC-1 as a strain of *H. salinarum* and emended description of *H. salinarum*. Extremophiles 8, 431-439 (2004).

Guggenheim, E.A., Turgeon, J.C.: Specific interaction of ions. Trans. Faraday Soc. 51 (0), 747-761 (1955).

Guillaumont, R., Fanghänel, T., Neck, V., Fuger, J., Palmer, D.A., Grenthe, I., Rand, M.H.: Update on the Chemical Thermodynamics of Uranium, Neptunium, Plutonium, Americium and Technetium (OECD/NEA, ed.). Elsevier, Amsterdam (2003).

Heller, A., Barkleit, A., Foerstendorf, H., Tsushima, S., Heim, K., Bernhard, G.: Curium(III) citrate speciation in biological systems: An europium(III) assisted spectroscopic and quantum chemical study. Dalton Trans. 41, 13969-13983 (2012).

Horrocks, W.D., Sudnick, D.R.: Lanthanide ion probes of structure in biology - Laser-induced luminescence decay constants provide a direct measure of the number of metal-coordinated water-molecules. J. Am. Chem. Soc. 101(2), 334-340 (1979).

Hoth, P., Wirth, H., Reinhold, K., Bräuer, V., Krull, P., Feldrappe, H.: Endlagerung radioaktiver Abfälle in tiefen geologischen Formationen Deutschlands – Untersuchung und Bewertung von Tongesteinsformationen. Bundesanstalt für Geowissenschaften und Rohstoffe (BGR), Berlin/Hannover (2007).

Huang, W.H., Keller, W.D.: Dissolution of clay minerals in dilute organic acids at room temperature. Am. Mineral. 56, 1082-1095 (1971).

Hummel, W., Anderegg, G., Rao, L., Puigdomènech, I., Tochiyama, O.: Chemical Thermodynamics of Compounds and Complexes of U, Np, Pu, Am, Tc, Se, Ni and Zr with Selected Organic Ligands. Elsevier, Amsterdam (2005).

Hummel, W.: Radioactive contaminants in the subsurface: The influence of complexing ligands on trace metal speciation. Chem. Monthly 139, 459-480 (2008).

IAEA: Predisposal management of organic radioactive waste. Technical Reports Series No. 427, IAEA, Vienna (2004).

Jakob, A., Pfingsten, W., Van Loon, L.R.: Effects of sorption competition on caesium diffusion through compacted argillaceous rock. Geochim. Cosmochim. Acta 73, 2441-2456 (2009).

Jan, S., Santin, G., Strul, D., Staelens, S., Assie, K., Autret, D., Avner, S.: GATE: a simulation toolkit for PET and SPECT. Physics in Medicine and Biology 49(19), 4543-4561 (2004).

Joseph, C., Schmeide, K., Sachs, S., Brendler, V., Geipel, G., Bernhard, G.: Sorption of uranium(VI) onto Opalinus Clay in the absence and presence of humic acid in Opalinus Clay pore water. Chem. Geol. 284, 240-250 (2011).

Joseph, C., Schmeide, K.: Influence of citric acid on U(VI) diffusion in Opalinus Clay (in preparation).

Joseph, C., Stockmann, M., Schmeide, K., Sachs, S., Brendler, V., Bernhard, G.: Sorption of U(VI) onto Opalinus Clay: Effects of pH and humic acid. Appl. Geochem. 36, 104-117 (2013a).

Joseph, C., Van Loon, L.R., Jakob, A., Steudtner, R., Schmeide, K., Sachs, S., Bernhard, G.: Diffusion of U(VI) in Opalinus Clay: Influence of temperature and humic acid. Geochim. Cosmochim. Acta 109, 74-89 (2013b).

Jové Colón, C.F., Weck, P.F., Sassani, D.H., Zheng, L., Rutqvist, J., Steefel, C., Kim, K., Nakagawa, S., Houseworth, J., Birkholzer, J., Caporuscio, F.A., Cheshire, M., Rearick, M.S., McCarney, M.K., Zavarin, M., Benedicto, A., Kersting, A.B., Sutton, M., Jerden, J., Frey, K.E., Copple, J.M., Ebert, W.: Fuel Cycle Research and Development: Evaluation of Used Fuel Disposition in Clay-Bearing Rock (FCRD-UFD-2014-000056). SAND2014-18303 R, Sandia National Laboratories, Albuquerque, New Mexico (2014).

Kakihana, M., Nagumo, T., Okamoto, M., Kakihana, H.: Coordination structures for uranyl carboxylate complexes in aqueous solution studied by IR and ^{13}C NMR spectra. J. Phys. Chem. 91(24), 6128-6136 (1987).

Keizer, M.G., Van Riemsdijk, W.H.: ECOSAT – a computer program for the calculation of speciation and transport in soil-water systems (version 4.8). User manual, Wageningen University (2005).

Keller, C.: The Chemistry of the Transuranium Elements, Volume 3, Verlag Chemie GmbH, Weinheim, Germany (1971).

Kim, J.I., Klenze, R., Wimmer, H., Runde, W., Hauser, W.: A study of the carbonate complexation of Cm-III and Eu-III by time-resolved laser fluorescence spectroscopy. J. Alloys Compd. 213-214, 333-340 (1994).

Kimura, T., Choppin G.R.: Luminescence study on determination of the hydration number of Cm(III). J. Alloys Compd. 213-214, 313-317 (1994).

Kimura, T., Choppin, G.R., Kato, Y., Yoshida, Z.: Determination of the hydration number of Cm(III) in various aqueous solutions. Radiochim. Acta 72, 61-64 (1996).

Kimura, T., Kato, Y.: Luminescence study on hydration states of lanthanide(III)–polyaminopolycarboxylate complexes in aqueous solution. J. Alloys Compd. 277, 806-810 (1998).

King, S.J., Warwick, P., Hall, A., Bryan, N.D.: The dissociation kinetics of dissolved metal–humate complexes. Phys. Chem. Chem. Phys. 3, 2080-2085 (2001).

Kinniburgh, D.G., Milne, C.J., Benedetti, M.F., Pinheiro, J.P., Filius, J., Koopal, L.K., Van Riemsdijk, W.H.: Metal ion binding by humic acid: Application of the NICA-donnan model. Environ. Sci. Technol. 30, 1687-1698 (1996).

Kirishima, A., Onishi, Y., Sato, N., Tochiyama, O.: Determination of the thermodynamic quantities of uranium(VI)-carboxylate complexes by microcalorimetry. J. Chem. Thermodynamics 39, 1432-1438 (2007).

Klimmek, S.: Charakterisierung der Biosorption von Schwermetallen an Algen. PhD thesis, Technische Universität Berlin, Berlin (2003).

Kobayashi, T., Scheinost, A.C., Fellhauer, D., Gaona, X., Altmaier, M.: Redox behavior of Tc(VII)/Tc(IV) under various reducing conditions in 0.1 M NaCl solutions. Radiochim. Acta 101, 323-332 (2013).

Koopal, L.K., Van Riemsdijk, W.H., de Wit, J.C.M., Benedetti, M.F.: Analytical isotherm equations for multicomponent adsorption to heterogeneous surfaces. J. Colloid Interf. Sci. 166, 51-60 (1994).

Křepelová, A., Brendler, V., Sachs, S., Baumann, N., Bernhard, G.: U(VI)-kaolinite surface complexation in absence and presence of humic acid studied by TRLFS. Environ. Sci. Technol. 41 (17), 6142-6147 (2007).

Křepelová, A., Sachs, S., Bernhard, G.: Uranium(VI) sorption onto kaolinite in the presence and absence of humic acid. Radiochim. Acta 94 (12), 825-833 (2006).

Küchle, W., Dolg, M., Stoll, H., Preuss, H.: Energy-adjusted pseudopotentials for the actinides. Parameter sets and test calculations for thorium and thorium monoxide. J. Chem. Phys. 100, 7535-7542 (1994).

Kulenkampff, J., Gründig, M., Zakhnini, A., Gerasch, R., Lippmann-Pipke J.: Process tomography of diffusion with PET for evaluating anisotropy and heterogeneity. Clay Minerals, in press (2015).

Kümmel, R., Worch, E.: Adsorption aus wässrigen Lösungen. Dt. Verl. für Grundstoffindustrie: Leipzig (1990).

Laguerie, C., Aubry, M., Couderc, J.P.: Some physiochemical data on monohydrate citric acid solutions in water - Solubility, density, viscosity, diffusivity, pH of standard solution, and refractive index. J. Chem. Eng. Data 21, 85-87 (1976).

Lee, J.-Y., Gaona, X., Vespa, M., Dardenne, K., Rothe, J., Rabung, T., Altmaier, M., Yun, J.-I.: Formation and structural analysis of ternary Mg-UO_2-CO_3 complexes using TRLFS and EXAFS. 15th International Conference on the Chemistry and Migration Behaviour of Actinides and Fission Products in the Geosphere, Santa Fe, New Mexico, 303-304 (2015).

Lefèvre, G.: *In situ* Fourier-transform infrared spectroscopy studies of inorganic ions adsorption on metal oxides and hydroxides. Adv. Colloid Interface Sci. 107, 109-123 (2004).

Lemire, R.J., Berner, U., Musikas, C., Palmer, D.A., Taylor, P., Tochiyama, O.: Chemical Thermodynamics of Iron Vol. 13a, Part, OECD, NEA-TDB, North Holland, Amsterdam (2013).

Lippold, H., Müller, N., Kupsch, H.: Effect of humic acid on the pH-dependent adsorption of terbium(III) onto geological materials. Appl. Geochem. 20, 1209-1217 (2005).

Lippold, H., Lippmann-Pipke, J.: Effect of humic matter on metal adsorption onto clay materials: Testing the linear additive model. J. Contam. Hydrol. 109, 40-48 (2009).

Lippold, H., Eidner, S., Kumke, M.U., Lippmann-Pipke, J.: Diffusion, degradation or on-site stabilisation – identifying causes of kinetic processes involved in metal-humate complexation. Appl. Geochem. 27, 250-256 (2012).

Lippold, H., Lippmann-Pipke, J.: New insights into the dynamics of adsorption equilibria of humic matter as revealed by radiotracer studies. Geochim. Cosmochim. Acta 133, 362-371 (2014).

Liu, J.G., Luo, G.S., Pan, S., Wang, J.D.: Diffusion coefficients of carboxylic acids in mixed solvents of water and 1-butanol. Chem. Engineering Processing 43, 43-47 (2004).

Lloyd, J.R., Gadd, G.M.: The Geomicrobiology of Radionuclides. Geomicrobiol. J. 28, 383-386 (2011).

Loukiala, A., Tuna, U., Beer, S., Jahnke, S., Ruotsalainen, U.: Gap-filling methods for 3D PlanTIS data. Physics in Medicine and Biology 55(20), 6125-6139 (2010).

Lucks, C., Rossberg, A., Tsushima, S., Foerstendorf, H., Scheinost, A.C., Bernhard, G.: Aqueous uranium(VI) complexes with acetic and succinic acid: speciation and structure revisited. Inorg. Chem. 51, 12288-12300 (2012).

Lütke, L., Moll, H., Bachvarova, V., Selenska-Pobell, S., Bernhard, G.: The U(VI) speciation influenced by a novel *Paenibacillus* isolate from Mont Terri Opalinus clay. Dalton Trans. 42, 6979-6988 (2013).

Mansel, A., Kupsch, H.: Radiolabelling of humic substances with ^{14}C by azo coupling [^{14}C]phenyldiazonium ions. Appl. Rad. Isot. 65, 793-797 (2007).

Marquardt, C. (ed.): Beiträge zum geochemischen Langzeitsicherheitsnachweis eines Endlagers für radioaktive Abfälle. Wechselwirkung und Transport von Actiniden im natürlichen Tongestein unter Berücksichtigung von Huminstoffen und Tonorganika. Abschlussbericht, KIT (2011).

Marques Fernandes, M., Baeyens, B., Dähn, R., Scheinost, A.C., Bradbury, M.H.: U(VI) sorption on montmorillonite in the absence and presence of carbonate: A macroscopic and microscopic study. Geochim. Cosmochim. Acta 93, 262-277 (2012).

McGenity, T.J., Gemmell, R.T., Grant, W.D., Stan-Lotter, H.: Origins of halophilic microorganisms in ancient salt deposits. Environ. Microbiol. 2, 243-250 (2000).

Meleshyn, A., Azeroual, M., Reeck, T., Houben, G., Riebe, B., Bunnenberg, C.: Influence of (calcium-)uranyl-carbonate complexation on U(VI) sorption on Ca- and Na-bentonites. Environ. Sci. Technol. 43 (13), 4896-4901 (2009).

Milne, C.J., Kinniburgh, D.G., van Riemsdijk, W.H., Tipping, E.: Generic NICA-donnan model parameters for metal ion binding by humic substances. Environ. Sci. Technol. 37, 958-971 (2003).

Miyake, C., Nürnberg, H.W.: Co-ordination compounds of actinides. -I-The determination of the stability constants of uranyl complexes with anions of carboxylic acids. J. Inorg. Nucl. Chem. 29, 2411-2429 (1967).

Moll, H., Merroun, M.L., Hennig, Ch., Rossberg, A., Selenska-Pobell, S., Bernhard, G.: The interaction of *Desulfovibrio äspöensis* DSM 10631^T with plutonium. Radiochim. Acta 94, 815-824 (2006).

Moll, H., Johnsson, A., Schäfer, M., Pedersen, K., Budzikiewicz, H., Bernhard, G.: Curium(III) complexation with pyoverdins secreted by a groundwater strain of *Pseudomonas fluorescens*. Biometals 21, 219-228 (2008).

Moll, H., Lütke, L., Bachvarova, V., Steudner, R., Geißler, A., Krawczyk-Bärsch, E., Selenska-Pobell, S., Bernhard, G.: Microbial diversity in Opalinus Clay and interaction of dominant microbial strains with actinides. Wiss.-Techn. Berichte, HZDR-036, Helmholtz-Zentrum Dresden-Rossendorf, Dresden (2013) and Ref. therein.

Moll, H., Lütke, L., Bachvarova, V., Cherkouk, A., Selenska-Pobell, S., Bernhard, G.: Interactions of the Mont Terri Opalinus Clay isolate *Sporomusa* sp. MT-2.99 with curium(III) and europium(III). Geomicrobiol. J. 31, 682-696 (2014).

Moskvin, A.I.: Complex formation of the actinides with anions of acids in aqueous solutions. Radiokhimiya 11, 458-460 (1969).

Moulin, C., Wei, J., Van Iseghem, P., Laszak, I., Plancque, G., Moulin, V.: Europium complexes investigations in natural waters by time-resolved laser-induced fluorescence. Anal. Chim. Acta 296, 253-261 (1999).

Müller, K., Brendler, V., Foerstendorf, H.: Aqueous uranium(VI) hydrolysis species characterized by attenuated total reflection Fourier-transform infrared spectroscopy. Inorg. Chem. 47, 10127-10134 (2008).

Müller, K., Foerstendorf, H., Meusel, T., Brendler, V., Lefève, G., Comarmond, M.J., Payne, T.E.: Sorption of U(VI) at the TiO_2-water interface: an *in situ* vibrational spectroscopic study. Geochim. Cosmochim. Acta 76, 191-205 (2012).

Müller, K., Foerstendorf, H., Brendler, V., Rossberg, A., Stolze, K., Gröschel, A.: The surface reactions of U(VI) on γ-Al_2O_3 - *In situ* spectroscopic evaluation of the transition from sorption complexation to surface precipitation. Chem. Geol. 357, 75-84 (2013).

Nagra: Projekt Opalinuston. Synthese der geowissenschaftlichen Untersuchungsergebnisse. Entsorgungsnachweis für abgebrannte Brennelemente, verglaste hochaktive sowie langlebige mittelaktive Abfälle. Technischer Bericht 02-03, Nagra (2002).

Neu, M.P., Icopini, G.A., Boukhalfa, H.: Plutonium speciation affected by environmental bacteria. Radiochim. Acta 93, 705-714 (2005).

Ockenden, D.W., Welch, G.A.: The preparation and properties of some plutonium compounds. Part V. Colloidal quadrivalent plutonium. J. Chem. Soc., 3358-3363 (1956).

Ohnuki, T., Yoshida, T., Ozaki, T., Kozai, N., Sakamoto, F., Nankawa, T., Suzuki, J., Francis, A.J.: Modeling of the interaction of Pu(VI) with the mixture of microorganism and clay. J. Nucl. Sci. Technol. 46, 55-59 (2009).

Ozaki, T., Arisaka, M., Kimura, T., Francis, A.J., Yoshida, Z.: Empirical method for prediction of the coordination environment of Eu(III) by time-resolved laser-induced fluorescence spectroscopy. Anal. Bioanal. Chem. 374, 1101-1104 (2002).

Ozaki, T., Gillow, J.B., Kimura, T., Ohnuki, T., Yoshida, Z., Francis, A.J.: Sorption behavior of europium(III) and curium(III) on the cell surface of microorganisms. Radiochim. Acta 92, 741-748 (2004).

Pabalan, R.T., Turner, D.R.: Uranium(6+) sorption on montmorillonite: Experimental and surface complexation modeling study. Aquat. Geochem. 2 (3), 203-226 (1997).

Panak, P.J., Nitsche, H.: Interaction of aerobic soil bacteria with plutonium(VI). Radiochim. Acta 89, 499-504 (2001).

Parkhurst, D.L., Appelo, C.A.J.: Description of input and examples for PHREEQC version 3 - a computer program for speciation, batch-reaction, onedimensional transport, and inverse geochemical calculations. In: Book 6. U.S. Geological Survey Techniques and Methods, Ch. A43, p. 497 (2013).

Pearson, F.J.: Opalinus Clay experimental water: A1Type, Version 980318. PSI Internal report TM-44-98-07, Paul Scherrer Institut, Villigen PSI (1998).

Pearson, F., Bath, A., Boisson, J.-Y., Fernández, A.M., Gäbler, H.-E., Gaucher, E., Gautschi, A., Griffault, L., Hernán, P., Waber, H.N.: Mont Terri Project – Geochemistry of Water in the Opalinus Clay Formation at the Mont Terri Rock Laboratory. Reports of the Federal Office for Water and Geology (FOWG), Geology Series. F., 5: 321, (2003).

Peretyazhko, T., Zachara, J.M., Heald, S.M., Jeon, B.H., Kukkadapu, R.K., Liu, C., Moore, D., Resch, C.T.: Heterogeneous reduction of Tc(VII) by Fe(II) at the solid-water interphase. Geochim. Cosmochim. Acta 72, 1521-1539 (2008).

Peretyazhko, T.S., Zachara, J.M., Kukkadapu, R.K., Heald, S.M., Kutnyakov, I.V., et al.: Pertechnetate (TcO_4^-) reduction by reactive ferrous iron forms in naturally anoxic, redox transition zone sediments from the Hanford Site, USA. Geochim. Cosmochim. Acta 92, 48-66 (2012).

Petrov, V., Gaona, X, Fellhauer, D., Dardenne, K., Kalmykov, S., Altmaier, M.: Contribution to Migration Conference, Beijing (China) (2011).

Plancque, G., Moulin V., Toulhoat, P., Moulin C.: Europium speciation by time-resolved laser-induced fluorescence. Anal. Chim. Acta 478, 11-22 (2003).

Poinssot, C., Baeyens, B., Bradbury, M.H.: Experimental studies of Cs, Sr, Ni, and Eu sorption on Na-illite and the modelling of Cs sorption. NTB-99-04 (1999).

Prekeges, J.: Positron-Emission-Tomography. In: Nuclear Medicine Instrumentation, 195-252. Jones & Bartlett, Burlington (2013).

Quilès, F., Burneau, A.: Infrared and Raman spectra of uranyl(VI) oxo-hydroxo complexes in acid aqueous solutions: a chemometric study. Vib. Spectrosc. 23, 231-241 (2000).

Rao, L., Choppin, G.R., Clark, S.B.: A study of metal-humate interactions using cation exchange. Radiochim. Acta 66, 141-147 (1994).

Renshaw, J.C., Law, N., Geissler, A., Livens, F.R., Lloyd, J.R.: Impact of the Fe(III)-reducing bacteria *Geobacter sulfurreducens* and *Shewanella oneidensis* on the speciation of plutonium. Biogeochem. 94, 191-196 (2009).

Roldan, P.S., Chereul, E., Dietzel, O., Magnier, L., Pautrot, C., et al.: Raytest ClearPET(TM), a new generation small animal PET scanner. Nuclear Instruments and Methods in Physics Research Section A: Accelerators, Spectrometers, Detectors and Associated Equipment 571(1-2), 498-501 (2007).

Rossberg, A., Reich, T., Bernhard, G.: Complexation of uranium(VI) with protocatechuic acid – application of iterative transformation factor analysis to EXAFS spectroscopy. Anal. Bioanal. Chem. 376, 631-638 (2003).

Sachs, S., Křepelová, A., Schmeide, K., Koban, A., Günther, A., Mibus, J., Brendler, V., Geipel, G., Bernhard, G.: Joint Project: Migration of actinides in the system clay, humic substance, aquifer - Migration behavior of actinides (uranium, neptunium) in clays: Characterization and quantification of the influence of humic substances. Wissenschaftlich-Technische Berichte, FZD-460, Forschungszentrum Dresden-Rossendorf, Dresden (2007).

Schäfer, T., Claret, F., Bauer, A., Griffault, L., Ferrage, E., Lanson, B.: Natural organic matter (NOM)-clay association and impact on Callovo-Oxfordian clay stability in high alkaline solution: Spectromicroscopic evidence. J. Phys. IV 104, 413-416 (2003).

Schikora, J.: Simulation of diffusion-adsorption processes in natural geological media by means of COMSOL Multiphysics. Faculty of Mechanical Science and Engineering. Diploma thesis, Technische Universität Dresden, Dresden (2012).

Schmeide, K., Bernhard, G.: Sorption of Np(V) and Np(IV) onto kaolinite: Effects of pH, ionic strength, carbonate and humic acid. Appl. Geochem. 25 (8), 1238-1247 (2010).

Schmeide, K., Gürtler, S., Müller, K., Steudtner, R., Joseph, C., Bok, F., Brendler, V.: Interaction of U(VI) with Äspö diorite: A batch and *in situ* ATR FT-IR sorption study. Appl. Geochem. 49, 116-125 (2014).

Schmeide, K., Joseph, C.: Influence of organic ligands on U(VI) sorption onto Opalinus Clay between 10 and 50°C. Annual Report 2011, HZDR-013, Helmholtz-Zentrum Dresden-Rossendorf, Dresden, 41 (2012).

Schnurr, A., Marsac, R., Rabung, T., Lützenkirchen, J., Geckeis, H.: Sorption of Cm(III) and Eu(III) onto clay minerals under saline conditions: Batch adsorption, laser-fluorescence spectroscopy and modeling. Geochim. Cosmochim. Acta 151, 192-202 (2015).

Sémon, L., Boehme, C., Billard, I., Hennig, C., Lützenkirchen, K., Reich, T., Rossberg, A., Rossini, I., Wipff, G.: Do perchlorate and triflate anions bind to the uranyl cation in an acidic aqueous medium? A combined EXAFS and quantum mechanical investigation. Chem. Phys. Chem. 2, 591-598 (2001).

Skerencak, A., Höhne, S., Hofmann, S., Marquardt, C.M., Panak, P.J.: Spectroscopic studies on the thermodynamics of the complexation of trivalent curium with propionate in the temperature range from 20 to 90°C. J. Solution Chem. 42, 1-17 (2013).

Sladkov, V.: Uranyl complexation with acetate studied by means of affinity capillary electrophoresis. J. Chromatography A 1289, 133-138 (2013).

Sladkov, V.: Interaction of uranyl with acetate in aqueous solutions at variable temperatures. J. Chem. Thermodynamics 71, 148-154 (2014).

Spranger, F.: Immobilisierung von Tc(VII)/Tc(IV) an Eisenphasen. Bachelorarbeit, Technische Universität Dresden (2015).

Stan-Lotter, H., Fendrihan, H.: Halophilic Archaea: Life with desiccation, radiation and oligotrophy over geological times. Life 5, 1487-1496 (2015).

Staunton, S., Clay, P.G., Rees, L.V.C.: Diffusion of neptunium(V) in clays. Radiochim. Acta 49, 147-153 (1990).

Steudtner, R.: Zur Wechselwirkung von Uran mit den Bioliganden Citronensäure und Glucose. PhD thesis, Technische Universität Dresden, Dresden (2010).

Steudtner, R., Müller, K., Jäckel, E., Meyer, R., Schmeide, K., Günther A.: Uranium chemistry in citric acid solution. 4th EuCheMS Chemistry Congress, Prague (2012).

Suzuki, Y., Tanaka, K., Kozai, N., Ohnuki, T.: Effects of citrate, NTA, and EDTA on the reduction of U(VI) by Shewanella putrefaciens. Geomicrobiology J. 27, 245-250 (2010).

Swanson, J.S., Reed, D.T., Ams, D.A., Norden, D., Simmons, K.A.: Status report on the microbial characterization of halite and groundwater samples from the WIPP, Los Alamos National Laboratory, p. 1 (2012).

Thielemans, K., Tsoumpas, C., Mustafovic, S., Beisel, T., Aguiar, P., Dikaios, N., Jacobson, M.: STIR: software for tomographic image reconstruction release 2. Physics in Medicine and Biology 57(4), 867-883 (2012).

Thoenen, T.: Speciation calculations supporting the sorption data bases for argillaceous rocks and bentonite for the provisional safety analyses for SGT-E2. Arbeitsbericht NAB 12-52, Nagra, Wettingen (2014).

Thury, M., Bossart, P.: The Mont Terri Rock Laboratory, a new international research project in a Mesozoic shale formation, in Switzerland. Eng. Geol. 52, 347-359 (1999).

Tipping, E.: Cation binding by humic substances. Cambridge Environmental Chemistry Series, Vol. 12; Cambridge University Press: Cambridge, 2002.

Van Loon, L.R., Eikenberg, J.: A high-resolution abrasive method for determining diffusion profiles of sorbing radionuclides in dense argillaceous rocks. Appl. Radiat. Isot. 63, 11-21 (2005).

Van Loon, L.R., Soler, J.M., Bradbury, M.H.: Diffusion of HTO, $^{36}Cl^-$ and $^{125}I^-$ in Opalinus Clay samples from Mont Terri - Effect of confining pressure. J. Contam. Hydrol. 61, 73-83 (2003a).

Van Loon, L.R., Soler, J.M., Jakob, A., Bradbury, M.H.: Effect of confining pressure on the diffusion of HTO, $^{36}Cl^-$ and $^{125}I^-$ in a layered argillaceous rock (Opalinus Clay): diffusion perpendicular to the fabric. Appl. Geochem. 18, 1653-1662 (2003b).

Van Loon, L.R., Soler, J.M., Müller, W., Bradbury, M.H.: Anisotropic diffusion in layered argillaceous rocks: A case study with Opalinus Clay. Environ. Sci. Technol. 38(21), 5721-5728 (2004).

Van Loon, L.R., Soler, J.M.: Diffusion of HTO, $^{36}Cl^-$, $^{125}I^-$, and $^{22}Na^+$ in Opalinus Clay: Effect of Confining Pressure, Sample Orientation, Sample Depth and Temperature. PSI-Bericht 04-03, Paul Scherrer Institute, Villigen PSI (2004).

Wilson, R.E., Hu, Y.-J., Nitsche, H.: Detection and quantification of Pu(III, IV, V, and VI) using a 1.0-meter liquid core wave guide, Radiochim. Acta 93, 203-206 (2005).

Wolery, T.J.: EQ3/6, A software package for the geochemical modeling of aqueous systems, UCRL-MA-110662 Part I. Lawrence Livermore National Laboratory, Livermore (1992).

Wouters, K., Moors, H., Boven, P., Leys, N.: Evidence and characteristics of a diverse and metabolically active microbial community in deep subsurface clay borehole water. FEMS Microb. Ecol. 86, 458-473 (2013).

Wu, T., Amayri, S., Drebert, J., Van Loon, L.R., Reich, T.: Neptunium(V) sorption and diffusion in Opalinus Clay. Environ. Sci. Technol. 43, 6567-6571 (2009).

Wu, T., Wang, H., Zheng, Q., Li, J.Y.: Effect of organic matter on ^{125}I diffusion in bentonite. J. Radioanal. Nucl. Chem. 303, 255-260 (2015).

Wu, T., Wang, H., Zheng, Q., Zhao, Y. L., Van Loon, L. R.: Diffusion behavior of Se(IV) and Re(VII) in GMZ bentonite. Appl. Clay Sci. 101, 136-140 (2014).

Zakhnini, A., Kulenkampff, J., Sauerzapf, S., Pietrzyk, U., Lippmann-Pipke, J.: Monte Carlo simulations of GeoPET experiments: 3D images of tracer distributions (^{18}F, ^{124}I and ^{58}Co) in Opalinus Clay, anhydrite and quartz. Computers & Geosciences 57, 183-196 (2013).

13 Publications of the Helmholtz-Zentrum Dresden-Rossendorf (HZDR)

The following peer-reviewed publications, oral presentations and posters were published or presented at conferences in the 2011 to 2015 funding period to the actual project (02 E 10971) as well as to preceding projects financially supported from the BMWi (02 E 10156, 02 E 10176, 02 E 10618).

Publications (peer-reviewed):

Lippold, H., Lippmann-Pipke, J.: Dynamics of metal-humate complexation equilibria as revealed by isotope exchange studies – a matter of concentration and time. Geochim. Cosmochim. Acta (under review).

Poetsch, M., Lippold, H.: Effects of ionic strength and fulvic acid on the adsorption of Tb^{3+} and Eu^{3+} onto clay. J. Contam. Hydrol. (under review).

Kulenkampff, J., Gründig, M., Zakhnini, A., Lippmann-Pipke, J.: Process tomography of diffusion with PET for evaluating anisotropy and heterogeneity. Clay Minerals (in press).

Xiong, Q., Joseph, C., Schmeide, K., Jivkov, A.P.: Measurement and modelling of reactive transport in geological barriers for nuclear waste containment. Phys. Chem. Chem. Phys. 17, 30577-30589 (2015).

Moll, H., Lütke, L., Cherkouk, A.: Bacterial diversity in clay and actinide interactions with bacterial isolates in relation to nuclear waste disposal. In: Radionuclides in the Environment - Influence of chemical speciation and plant uptake on radionuclide migration. (Editoren: C. Walther, D.K. Gupta) Heidelberg, Springer Verlag (2015).

Krawczyk-Bärsch, E., Lütke, L., Moll, H., Bok, F., Steudtner, R., Rossberg, A.: A spectroscopic study on U(VI) biomineralization in cultivated Pseudomonas fluorescens biofilms isolated from granitic aquifers. Environ. Sci. Pollut. Res. 22, 4555-4565 (2015).

Moll, H., Lütke, L., Bachvarova, V., Cherkouk, A., Selenska-Pobell, S., Bernhard, G.: Interactions of the Mont Terri Opalinus Clay isolate Sporomusa sp. MT-2.99 with curium(III) and europium(III). Geomicrobiol. J. 31, 682-696 (2014).

Schmeide, K., Gürtler, S., Müller, K., Steudtner, R., Joseph, C., Bok, F., Brendler, V.: Interaction of U(VI) with Äspö diorite: A batch and *in situ* ATR FT-IR sorption study. Appl. Geochem. 49, 116-125 (2014).

Harzmann, S., Braun, F., Zakhnini, A., Weber, W.A., Pietrzyk, U., Mix, M.: Implementation of Cascade Gamma and Positron Range Corrections for I-124 Small Animal PET. IEEE Trans. Nucl. Sci. 61, 142-153 (2014).

Lippold, H., Lippmann-Pipke, J.: New insights into the dynamics of adsorption equilibria of humic matter as revealed by radiotracer studies. Geochim. Cosmochim. Acta 133, 362-371 (2014).

Zakhnini, A., Kulenkampff, J., Sauerzapf, S., Pietrzyk, U., Lippmann-Pipke, J.: Monte Carlo simulations of GeoPET experiments: 3D images of tracer distributions (^{18}F, ^{124}I and ^{58}Co) in Opalinus Clay, anhydrite and quartz. Computers & Geosciences 57, 183-196 (2013).

Joseph, C., Stockmann, M., Schmeide, K., Sachs, S., Brendler, V., Bernhard, G.: Sorption of U(VI) onto Opalinus Clay: Effects of pH and humic acid. Appl. Geochem. 36, 104-117 (2013).

Joseph, C., Van Loon, L.R., Jakob, A., Steudtner, R., Schmeide, K., Sachs, S., Bernhard, G.: Diffusion of U(VI) in Opalinus Clay: Influence of temperature and humic acid. Geochim. Cosmochim. Acta 109, 74-89 (2013).

Pietrzyk, U., Zakhnini, A., Axer, M., Sauerzapf, S., Benoit, D., Gaens, M.: EduGATE - basic examples for educative purpose using the GATE simulation platform. Zeitschrift für Medizinische Physik 23, 65-70 (2013).

Raditzky, B., Sachs, S., Schmeide, K., Barkleit, A., Geipel, G., Bernhard, G.: Spectroscopic study of americium(III) complexes with nitrogen containing organic model ligands. Polyhedron 65, 244-251 (2013).

Schmeide, K., Sachs, S., Bernhard, G.: Np(V) reduction by humic acid: Contribution of reduced sulfur functionalities to the redox behavior of humic acid. Sci. Total Environ. 419, 116-123 (2012).

Kremleva, A., Zhang, Y., Shor, A.M., Krüger, S., Joseph, C., Raditzky, B., Schmeide, K., Sachs, S., Bernhard, G., Rösch, N.: Uranyl(VI) complexation by sulfonate ligands: A relativistic density functional and time-resolved laser-induced fluorescence spectroscopy study. Eur. J. Inorg. Chem. 2012, 3636-3644 (2012).

Lippold, H., Eidner, S., Kumke, M.U., Lippmann-Pipke, J.: Diffusion, degradation or on-site stabilisation – identifying causes of kinetic processes involved in metal-humate complexation. Appl. Geochem. 27, 250-256 (2012).

Steudtner, R., Müller, K., Schmeide, K., Sachs, S., Bernhard, G.: Binary and ternary uranium(VI) humate complexes studied by attenuated total reflection Fourier-transform infrared spectroscopy. Dalton Trans. 40, 11920-11925 (2011).

PhD theses, diploma theses, bachelor theses:

Spranger, F.: Immobilisierung von Tc(VII)/Tc(IV) an Eisenphasen. Bachelor thesis, Technische Universität Dresden (2015).

Gerasch, R.: Simulation und Parameterschätzung von ^{22}Na-Diffusion in einem Opalinuston-Bohrkern mittels COMSOL Multiphysics und GeoPET-Datenabgleich. Master thesis, Brandenburgische Technische Universität Cottbus-Senftenberg (2015).

Bittner, L.: Prozessbeobachtung von Vergütungsmaßnahmen im Salzgestein mittels Positronen Emissions Tomographie (GeoPET). Diploma thesis, Hochschule Zittau/Görlitz (2014).

Joseph, C.: The ternary system U(VI) / humic acid / Opalinus Clay. PhD thesis, Technische Universität Dresden (2013).

Zehlike, L.: Durchführung von Sorptions- und Desorptionsversuchen von U(VI) an Montmorillonit. Bachelor thesis, Technische Universität Dresden (2013).

Schikora, J.: Simulation von Diffusions-Adsorptionsprozessen in natürlichem Gesteins-material mit COMSOL Multiphysics. Diploma thesis, Technische Universität Dresden (2012).

Oral presentations on conferences:

Fritsch, K., Schmeide, K.: U(VI) retention by montmorillonite at high salinities: Surface complexation modeling. International Workshop ABC-Salt (IV) - Actinide Brine Chemistry in a Salt-Based Repository. 14.-15.04.2015, Heidelberg, Germany.

Fritsch, K., Schmeide, K.: Montmorillonite as barrier material for uranium(VI) at high ionic strengths. 7th Mid-European Clay Conference, 16.-19.09.2014, Dresden, Germany.

Kulenkampff, J., Gründig, M., Zakhnini, A., Lippmann-Pipke, J.: Process tomography of diffusion with PET for evaluating anisotropy and heterogeneity. 7th Mid-European Clay Conference, 16.-19.09.2014, Dresden, Germany.

Gerasch, R., Kulenkampff, J., Lippmann-Pipke, J.: Parameter estimation of anisotropic diffusion in clay with COMSOL Multiphysics. COMSOL Conference 2014, 17.-19.09.2014, Cambridge, United Kingdom.

Moll, H., Lütke, L., Cherkouk, A., Bernhard, G.: Pu interaction with bacterial isolates from Mont Terri Opalinus Clay. Plutonium Futures - The Science 2014, 07.-12.09.2014, Las Vegas, USA.

Schmeide, K., Joseph, C., Brendler, V.: Uranium(VI) retention in clay and crystalline rock: How and why does it differ. 8th European Summer School on Separation Chemistry and Conditioning as well as Supramolecular, Intermolecular, Interaggregate Interactions, 07.-09.07.2014, Gustav-Stresemann-Institut, Bonn/Bad Godesberg, Germany.

Moll, H., Cherkouk, A.: Microorganisms and their impact on radionuclide speciation. 8th European Summer School on Separation Chemistry and Conditioning as well as Supramolecular, Intermolecular, Interaggregate Interactions, 07.-09.07.2014, Gustav-Stresemann-Institut, Bonn/Bad Godesberg, Germany.

Moll, H., Lütke, L., Cherkouk, A., Bernhard, G.: Actinide/Lanthanide interaction studies with a typical bacterial isolate from Mont Terri Opalinus Clay a potential host rock for nuclear waste disposal. IGD-TP Geodisposal 2014 Conference, 24.-26.06.2014, Manchester, United Kingdom.

Poetsch, M., Claus, M., Lippold, H.: Effect of ionic strength on the mobility of radionuclides in the presence of natural organic matter: Testing the Linear Additive Model. Goldschmidt Conference 2014, 08.-13.06.2014, Sacramento, USA.

Schmeide, K., Joseph, C., Fritsch, K.: Uranium(VI) and neptunium(V) retention by clay minerals and natural clay rock – Influence of clay organics, temperature and pore water salinity. 51st Annual Meeting of the Clay Minerals Society, 17.-21.05.2014, College Station, Texas, USA.

Schmeide, K., Joseph, C., Brendler, V.: U(VI) retention by potential host rocks: Comparison of clay and crystalline rock. RadChem 2014 - 17th Radiochemical Conference, 11.-16.05.2014, Mariánské Lázně, Czech Republic.

Moll, H., Lütke, L., Cherkouk, A., Bernhard, G.: Pu interaction studies with a typical bacterial isolate from Mont Terri Opalinus Clay. TD-246 Joint BN, GD, HT, MA Mont Terri Meeting, 10.-11.02.2014, St. Ursanne, Switzerland.

Bittner, L., Kulenkampff, J., Gründig, M., Lippmann-Pipke, J., Enzmann, F.: Direct observation of waterglass impregnation of fractured salt rock with positron emission tomography. International Conference on the Performance of Engineered Barriers: Backfill, Plugs & Seals, 06.-07.02.2014, Hannover, Germany.

Moll, H., Lütke, L., Cherkouk, A., Selenska-Pobell, S., Bernhard, G., Brendler, V.: Microbial influences on radionuclide behaviour – an example of less-understood problems and how to solve them. IGD-TP 4th Exchange Forum (EF4), 29.-30.10.2013, Prague, Czech Republic.

Wolf, M., Enzmann, F., Kulenkampff, J., Lippmann-Pipke, J.: 3D analysis of fluid flow in fissured salt rock. Migration'13 - 14th International Conference on the Chemistry and Migration Behaviour of Actinides and Fission Products in the Geosphere, 08.-13.09.2013, Brighton, United Kingdom.

Kulenkampff, J., Gründig, M., Korn, N., Zakhnini, A., Barth, T., Lippmann-Pipke, J.: Application of high-resolution positron-emission-tomography for quantitative spatiotemporal process monitoring in dense material. 7th World Congress on Industrial Process Tomography, 02.-05.09.2013, Krakow, Poland.

Fritsch, K., Schmeide, K.: Uranium(VI) sorption on montmorillonite in high ionic strength media. International Workshop ABC-Salt (III) - Actinide Brine Chemistry in a Salt-Based Repository. 15.-17.04.2013, Santa Fe, USA.

Kulenkampff, J., Gründig, M., Zakhnini, A., Lippmann-Pipke, J.: PET-Prozesstomographie von Transportvorgängen in Bohrkernen zur Verbesserung des Prozessverständnisses und zur Verifikation von Modellcodes. 73. Jahrestagung der Deutschen Geophysikalischen Gesellschaft, 04.-07.03.2013, Leipzig, Germany.

Joseph, C., van Loon, L. R., Jakob, A., Steudtner, R., Schmeide, K., Sachs, S., Bernhard, G.: Do elevated temperatures and organic matter influence the U(VI) diffusion through argillaceous rock? 5th International Meeting on "Clays in Natural and Engineered Barriers for Radioactive Waste Confinement", 22.-25.10.2012, Montpellier, France.

Kulenkampff, J., Gründig, M., Schikora, J., Zakhnini, A., Lippmann-Pipke, J.: Long-term spatiotemporal monitoring of diffusion processes in Opalinus drill cores with GeoPET and parameterization with COMSOL Multiphysics. 5th International Meeting on "Clays in Natural and Engineered Barriers for Radioactive Waste Confinement", 22.-25.10.2012, Montpellier, France.

Sauerzapf, S., Zakhnini, A., Weber, W., Pietrzyk, U., Mix, M.: Analyse und Optimierung einer Positronenreichweitenkorrektur innerhalb der iterativen Rekonstruktion für die Kleintierbildgebung. 43. Jahrestagung der Deutschen Gesellschaft für Medizinische Physik, 26.-29.09.2012, Jena, Germany.

Steudtner, R., Müller, K., Jäckel, E., Meyer, R., Schmeide, K., Günther, A.: Uranium chemistry in citric acid solution. 4th EuCheMS Chemistry Congress, 26.-30.08.2012, Prague, Czech Republic.

Lippold, H., Lippmann-Pipke, J.: Radiotracer studies on the kinetics and equilibrium characteristics of adsorption of humic matter. Goldschmidt 2012, 24.-29.06.2012, Montreal, Canada.

Zakhnini, A., Kulenkampff, J., Lippmann-Pipke, J., Pietrzyk, U.: GATE-based simulation in GeoSciences. OpenGATE collaboration meeting, 03.-04.05.2012, Athens, Greece.

Lippmann-Pipke, J., Kulenkampff, J., Gründig, M., Richter, M.: Matching 4D porous media fluid flow GeoPET data with COMSOL Multiphysics simulation results. COMSOL Multiphysics Konferenz, 26.-28.10.2011, Stuttgart/Ludwigburg, Germany.

Joseph, C., Van Loon, L.R., Jakob, A., Schmeide, K., Sachs, S., Bernhard, G.: Effect of temperature and humic acid on the U(VI) diffusion in compacted Opalinus Clay. 6th International Conference Uranium Mining and Hydrogeology (UMH VI), 18.-22.09.2011, Freiberg, Germany.

Posters presented at conferences:

Moll, H., Cherkouk, A., Bernhard, G.: Interaction of anaerobic Mont Terri Opalinus Clay bacteria with plutonium(VI). Migration'15 - 15th International Conference on the Chemistry and Migration Behaviour of Actinides and Fission Products in the Geosphere, 13.-18.09.2015, Santa Fe, USA.

Lippold, H., Lippmann-Pipke, J.: Complexation of f-elements with humic carriers – how dynamic is the equilibrium? Migration'15 - 15th International Conference on the Chemistry and Migration Behaviour of Actinides and Fission Products in the Geosphere, 13.-18.09.2015, Santa Fe, USA.

Kulenkampff, J., Gründig, M., Zakhnini, A., Schikora, J., Gerasch, R., Lippmann-Pipke, J.: Visualization of heterogeneous diffusion processes with PET aligned with 3D FE simulation results. 7th International Symposium on Process Tomography, 01.-03.09.2015, Dresden, Germany.

Kulenkampff, J., Gründig, M., Lippmann-Pipke, J.: High-resolution Positron-Emission-Tomography for ultrasensitive spatio-temporal monitoring of tracer transport in porous media. 7th International Conference on Porous Media, 18.-21.05.2015, Padova, Italy.

Lippmann-Pipke, J., Kulenkampff, J., Lippold, H., Stuhlfauth, C., Gerasch, R., Gründig, M.: Benchmarking of reactive transport visualisation (PET) by numerical modelling with COMSOL Multiphysics and PhreeqC. 7th International Conference on Porous Media, 18.-21.05.2015, Padova, Italy.

Bader, M., Drobot, B., Müller, K., Stumpf, T., Cherkouk, A.: Biosorption of uranium on the cells of the halophilic archaea Halobacterium noricense DSM 15987 under highly saline conditions. International Workshop ABC-Salt (IV) - Actinide Brine Chemistry in a Salt-Based Repository. 14.-15.04.2015, Heidelberg, Germany.

Fritsch, K., Schmeide, K.: Uranium retention by montmorillonite at high ionic strengths. Clays in natural and engineered barriers for radioactive waste confinement, 23.-26.03.2015, Brussels, Belgium.

Lippmann-Pipke, J., Stuhlfauth, C., Lippold, H., Kulenkampff, J., Enzmann, F.: Aligning 1D and 2D axial symmetric transport simulations with observations: consequences for the reactive transport. International Symposium of the German Priority Programme SPP 1315 Biogeochemical Interfaces in Soil - Towards a Comprehensive and Mechanistic Understanding of Soil Functions, 06.-08.10.2014, Leipzig, Germany.

Fritsch, K., Schmeide, K.: Influence of ionic strength on U(VI) sorption onto montmorillonite at high salinities. 8th European Summer School on Separation Chemistry and Conditioning as well as Supramolecular, Intermolecular, Interaggregate Interactions, 07.-09.07.2014, Gustav-Stresemann-Institut, Bonn/Bad Godesberg, Germany.

Cherkouk, A., Lütke, L., Moll, H., Bachvarova, V., Selenska-Pobell, S., Bernhard, G.: Microorganisms in potential host rocks for geological disposal of nuclear waste and their interactions with uranium. IGD-TP Geodisposal 2014 Conference, 24.-26.06.2014, Manchester, United Kingdom.

Fritsch, K., Schmeide, K.: Effect of high ionic strengths on U(VI) retention in montmorillonite. RadChem 2014 - 17th Radiochemical Conference, 11.-16.05.2014, Mariánské Lázně, Czech Republic.

Fritsch, K., Schmeide, K., Bernhard, G.: Investigation of the mobility of uranium(VI) in argillaceous rock at higher salinity. Migration'13 - 14th International Conference on the Chemistry and Migration Behaviour of Actinides and Fission Products in the Geosphere, 08.-13.09.2013, Brighton, United Kingdom.

Lippold, H., Lippmann-Pipke, J.: Radiotracer exchange studies on the reversibility of interaction processes related to humic-bound metal transport. Migration'13 – 14th International Conference on the Chemistry and Migration Behaviour of Actinides and Fission Products in the Geosphere, 08.-13.09.2013, Brighton, United Kingdom.

Moll, H., Lütke, L., Bachvarova, V., Geissler, A., Selenska-Pobell, S., Bernhard, G.: Bacterial diversity in Mont Terri Opalinus Clay and the influence of the bacterial Sporomusa sp. isolate on plutonium speciation. Migration'13 - 14th International Conference on the Chemistry and Migration Behaviour of Actinides and Fission Products in the Geosphere, 08.-13.09.2013, Brighton, United Kingdom.

Schikora, J., Kulenkampff, J., Gründig, M., Lippmann-Pipke, J.: Modelling and simulation of 4D GeoPET measurements with COMSOL Multiphysics 4.2a. EGU General Assembly 2012, 22.-27.04.2012, Vienna, Austria.

Schmeide, K., Steudtner, R., Bernhard, G.: Formation of U(VI) lactate and citrate complexes and their sorption onto Opalinus Clay between 10 and 60°C. Workshop "HiTAC – High Temperature Aqueous Chemistry", 09.11.2011, Karlsruhe, Germany.

Kulenkampff, J., Enzmann, F., Gründig, M., Wolf, M., Lippold, H., Lippmann-Pipke, J.: Direct observation of preferential transport pathways in salt rocks by means of GeoPET. International Workshop ABC-Salt (II) - Actinide Brine Chemistry in a Salt-Based Repository. 07.-08.11.2011, Karlsruhe, Germany.

Zakhnini, A., Kulenkampff, J., Sauerzapf, S., Lippmann-Pipke, J., Pietrzyk, U.: Monte Carlo simulations of a ClearPET: Scatter and attenuation of gamma rays in various rock formations. 2011 IEEE Nuclear Science Symposium and Medical Imaging Conference, 23.-29.10.2011, Valencia, Spain.

Schmeide, K., Joseph, C., Steudtner, R., Bernhard, G.: Influence of organic ligands and temperature on U(VI) sorption and diffusion in the system Opalinus Clay/Opalinus Clay pore water. Migration'11 - 13th International Conference on the Chemistry and Migration Behavior of Actinides and Fission Products in the Geosphere, 18.-23.09.2011, Beijing, China.

Schmeide, K., Joseph, C., Bernhard, G.: Sorption and diffusion of U(VI) in the system Opalinus Clay/pore water in the absence and presence of organic ligands. NEA ClayClub Workshop "Clays under Nano- to Microscopic Resolution", 06.-08.09.2011, Karlsruhe, Germany.

Steudtner, R., Schmeide, K., Bernhard, G.: U(VI) complexation with lactate and citrate in dependence on temperature (7-65°C). Goldschmidt 2011, 14.-19.08.2011, Prague, Czech Republic.

List of figures

List of tables

Acknowledgements

The authors thank the Federal Ministry for Economic Affairs and Energy (BMWi) and the Project Management Agency Karlsruhe (PTKA-WTE) for financial support (no. 02 E 10971).

We also thank Karsten Heim, Dr. Harald Foerstendorf and Dr. Katharina Müller for FT-IR measurements and for their help in spectra interpretation, Stephan Weiss, Christa Müller, Heidrun Neubert and Henry Lösch for technical support during UV-Vis and PCS measurements, Dr. Vinzenz Brendler for helpful discussions concerning SIT theory and surface complexation modelling as well as Prof. Dr. Satoru Tsushima for DFT calculations and Dr. Frank Bok for calculation of the E_h-pH diagram.

For support during TRLFS measurements and for discussion of laser spectroscopic results we thank Dr. Robin Steudtner, Björn Drobot, Dr. Nina Huittinen and Dr. Sascha Eidner (Universität Potsdam); Björn Drobot is especially thanked for PARAFAC deconvolution of the data. For scientific discussions on complexation studies we thank Dr. Andrej Skerencak-Frech (Universität Heidelberg) and Dr. Remi Marsac (Karlsruher Institut für Technologie). Dr. Xavier Gaona (Karlsruher Institut für Technologie) is acknowledged for his advice concerning pH measurements at high ionic strength.

For support during XAS measurements we thank Dr. Janeth Lozano-Rodriguez, Dr. Kristina Kvashnina, Dr. Natalia Shcherbina (Forschungszentrum Jülich) and Dr. Natallia Torapava (MAX IV Laboratory). For support in preparation of XAS samples we thank Felix Spranger, Carola Franzen and Stephan Weiss.

Furthermore, we thank Aline Ritter, Sabrina Gurlit, Stefanie Schubert, and Carola Eckardt for ICP-MS analyses, ion chromatography, TIC measurements, and BET determinations, Kathrin Nebe for the help during LSC measurements and Andrea Scholz for XRD measurements.

The authors thank the Bundesanstalt für Geowissenschaften und Rohstoffe (BGR) for providing clay samples, Velina Bachvarova and Dr. Sonja Selenska-Pobell for isolation of the strains and Monika Dudek for anaerobic cultivation of the bacterial isolates from Mont Terri Opalinus Clay. Moreover, the authors are thankful to Tomas Kupcik and Dr. Christian Marquardt (both from Karlsruher Institut für Technologie) for preparing clay tablets for diffusion experiments as well as to Christa Müller, Heidrun Neubert, Sylvia Gürtler, Nadine Lense, Stefanie Schubert, and Lisa Zehlike for technical support in the laboratory. Dr. Susanne Sachs is thanked for help in preparing the Pu-242 stock solution.

For support during PET measurements we thank Marion Gründig, Lars Bittner and Stefan Gruhne.

Technical support by Prof. Dr. Norbert Trautmann, Dr. Klaus Eberhardt and Beatrix Praast (Johannes Gutenberg-Universität Mainz) for the production of Tb-160 in the TRIGA Mark II reactor is gratefully acknowledged.

The authors are indebted for the use of the Cm-248 to the U.S. Department of Energy, Office of Basic Energy Sciences, through the transplutonium element production facilities at Oak Ridge National Laboratory which was made available as part of a collaboration between HZDR and the Lawrence Berkeley National Laboratory (LBNL).

Finally, we would like to thank all other colleagues who contributed to the success of the project.

Retention of radionuclides in natural clay rocks under saline conditions
- Interaction of Np, Pu, and Tc with a natural clay rock at higher salinities -

S. Amayri, P. J. B. Börner, V. Häußler, U. Kaplan, M. Lübke, T. Reich, R. Scholze, N. Trautmann, C. Willberger

Institut für Kernchemie, Universität Mainz

Final Report

Contract number
02 E 10981

Institut für Kernchemie
Johannes Gutenberg-Universität Mainz
Fritz-Straßmann-Weg 2
55128 Mainz
Germany

Table of content

Kurzzusammenfassung

Das Ziel dieses Projektes war die Untersuchung des geochemischen Verhaltens von Actiniden, hauptsächlich von Neptunium (Np) und Plutonium (Pu), und des Spaltproduktes Technetium (Tc) in Lösungen höherer Ionenstärke, wie sie für Endlagersysteme in Tonformationen in Norddeutschland relevant sind. Dazu wurden Sorptions- und Diffusionsversuche mit Np, Pu und Tc durchgeführt, wobei Opalinuston (OPA) aus Mont Terri, Schweiz, als Referenz für ein natürliches Tongestein verwendet wurde. Als salinare Lösungen kamen NaCl, $MgCl_2$ und $CaCl_2$ mit einer Ionenstärke von bis zu 3 M zum Einsatz. Die Ergebnisse wurden mit den für synthetisches Opalinuston-Porenwasser (OPA-PW) erhaltenen Daten verglichen, das eine Ionenstärke von 0,4 M besitzt.

Bei den Sorptionsuntersuchungen mit Np(V) und Montmorillonit wurde über einen Konzentrationsbereich von 10^{-4} – 10^{-12} M Np(V) und einem pH-Bereich von 2,5 – 10 beobachtet, dass die Salinität der NaCl-Lösungen im Bereich von 0,1 – 3 M keinen signifikanten Einfluss auf die Sorption von Np(V) an diesem Tonmineral hat. Die erhaltenen Daten konnten mit Hilfe des Sorptionsmodells 2 SPNE SC/CE (2 Site Protolysis Non Electrostatic Surface Complexation and Cation Exchange) und der Specific Ion Interaction Theory (SIT) über den gesamten Ionenstärkebereich beschrieben werden.

Bei der Sorption von Np(V) an OPA war in NaCl-Lösungen (0,1 – 2,8 M) ebenfalls keine Abhängigkeit von der Ionenstärke festzustellen. Jedoch zeigten Batch-Experimente zur Sorption von Np(V) in $MgCl_2$-Lösungen eine Abnahme der Np-Sorption mit zunehmender Ionenstärke. Insgesamt ist die Sorption von Np(V) bei gleicher Ionenstärke in der zweiwertigen Erdalkalielektrolytlösung geringer als in NaCl und ähnlich wie in OPA-PW. In NaCl-Lösungen ist die Sorption von Np(V) an OPA zwischen 20 und 80 °C von der Temperatur unabhängig. Für Pu(III) wurde das Sorptionsverhalten an OPA im pH-Bereich von 2 – 10 in NaCl-, $MgCl_2$-, $CaCl_2$-Lösungen und OPA-PW studiert. Eine Abhängigkeit der Pu(III)-Sorption von der Art des Elektrolyten und der Ionenstärke wurde nur im pH-Bereich 4.0 – 5.5 beobachtet, bei dem Ionenaustausch als Sorptionsmechanismus dominiert.

Detailliert wurde die Diffusion von Np(V) in OPA mit NaCl als mobile Phase bei verschiedenen Temperaturen studiert und die entsprechenden Diffusionsparameter bestimmt. Bei Erhöhung der Ionenstärke von 1 M NaCl auf 3 M beobachtet man eine Verlangsamung

der Diffusion von Np(V). Im Temperaturbereich von 24 – 60 °C verdoppelt sich der Koeffizient D_e für die Diffusion von Np(V) in OPA mit 1 M NaCl als mobile Phase. Untersuchungen mittels µ-XRF und Np L_{III}-Kante µ-XANES zeigten, dass Np(V) entlang seines Diffusionspfades im OPA zunehmend zu Np(IV) reduziert wird. Zu einem ähnlichen Ergebnis kamen auch die ortsaufgelösten Synchrotronstrahlungsmessungen zur Diffusion von Pu(V) in OPA. Je weiter Pu(V) in den Ton hinein diffundiert um so mehr wird es zu Pu(III) und Pu(IV) reduziert. Um mit Hilfe der CE-ICP-MS die Speziation von Pu in Lösungen bei Sorptionsexperimenten zu bestimmen, wurden systematische Messungen der elektrophoretischen Mobilität μ_e der Actiniden Th, U, Np, Pu und Am in verschiedenen Oxidationszuständen durchgeführt.

Für Tc wurden die Sorption und Diffusion in OPA eingehend studiert. Obwohl Tc(VII) als TcO_4^--Anion im neutralen pH-Bereich bei Batch-Experimenten an Luft nicht am Ton sorbiert wird, zeigten Tc K-Kante µ-XANES Untersuchungen, dass Tc(VII) unter anaeroben Bedingungen durch OPA teilweise zu Tc(IV) reduziert wird. Diese Reduktion von Tc(VII) zu Tc(IV) ist wahrscheinlich der Grund, warum bei der Diffusion von Tc(VII) auch nach 182 Tagen noch kein Durchbruch von Tc durch den OPA-Bohrkern (11 mm Dicke) beobachtet wurde. Hingegen erreichte bei dem Versuch an Luft die Diffusion von Tc(VII) bereits nach 60 Tagen einen stationären Zustand.

Die erhaltenen Daten verbessern die thermodynamische Datenbasis für die Wechselwirkung von Actiniden und Technetium mit Tongestein bei höheren Salinitäten und dienen als Eingangsparameter für die Langzeitsicherheitsanalyse eines nuklearen Endlagers.

Abstract

The goal of this work was to study the geochemical behavior of the actinides, in particular neptunium (Np) and plutonium (Pu), and the fission product technetium (Tc) in solutions of higher salinity. These conditions are especially relevant for deposits in argillaceous rock formations in Northern Germany. Therefore, sorption and diffusion experiments of Np, Pu, and Tc were performed using Opalinus Clay (OPA) from Mont Terri, Switzerland, as a reference for natural clay. NaCl, $MgCl_2$, and $CaCl_2$ solutions were used as background electrolytes or mobile phases with ionic strengths up to 3 M. The obtained results were compared to previous ones using synthetic OPA porewater (PW) of 0.4 M ionic strength.

The sorption of Np(V) on montmorillonite showed over a Np concentration range of 10^{-4} to 10^{-12} M and pH range of 2.5–10 no dependency on the ionic strength in 0.1–3.0 M NaCl solutions. It was possible to model the obtained results using the 2 SPNE SC/CE (2 Site Protolysis Non Electrostatic Surface Complexation and Cation Exchange) model and the Specific Ion Interaction Theory (SIT) over the whole ionic strength range.

The sorption of Np(V) on OPA in NaCl solutions showed no dependence on ionic strength. In case of $MgCl_2$ solutions the sorption decreased with increasing ionic strength. In general, the sorption of Np(V) at the same ionic strength of divalent electrolytes is smaller than in NaCl solutions and comparable to OPA PW. No influence of the temperature (20–80 °C) was found on the sorption of Np(V) on OPA in NaCl solutions. The sorption behavior of Pu(III) on OPA was investigated in solutions of NaCl, $MgCl_2$, $CaCl_2$, and OPA PW. An influence of the ionic strength could be observed in the pH range of 4.0–5.5 due to the dominating effect of the cation exchange mechanism.

The effect of temperature on the Np(V) diffusion in OPA with NaCl as mobile phase was studied and the respective diffusion parameters were determined. With increasing ionic strength from 1 M to 3 M NaCl a slower diffusion was observed. In contrast to this, the diffusion coefficient D_e increased by a factor of two in the temperature range between 24 °C and 60 °C.

Spatially resolved investigations using µ-XRF and Np L_{III}-edge µ-XANES showed a progressive reduction of Np(V) to Np(IV) along its diffusion pathway. Similar results were

obtained for the diffusion of Pu(V) in OPA using synchrotron based techniques. Pu(V) was reduced mainly to Pu(III) and Pu(IV). To study the speciation of Pu in solution after sorption experiments, CE-ICP-MS measurements were performed and the electrophoretic mobility (μ_e) was determined for the actinides Th, U, Np, Pu, and Am in different oxidation states from III to VI.

Additionally, the sorption and diffusion of Tc was studied intensively. Tc(VII), present as pertechnetate (TcO_4^-), did not sorb at neutral pH under ambient-air conditions on OPA, although µ-XANES measurements at the Tc K edge showed under anaerobic conditions partial reduction to Tc(IV). This reduction might be the reason why no break-through (11 mm bore core length) was observed after 182 days under anaerobic conditions. In contrast to that, a steady state of the flux of Tc was reached within 60 days for experiments under aerobic conditions.

The results of this study improve the thermodynamic database for the uptake of actinides and technetium by clay rocks at higher salinity and serve as input parameters for the performance assessment of a future nuclear waste repository.

Introduction

Germany considers argillaceous rock formations as a potential host rock for a deep geological repository for high-level long-lived radioactive waste. Beside Opalinus Clay (OPA) deposits in Southern Germany, Jurassic argillaceous rock formations in Northern Germany are discussed as potential host rock. Groundwaters, which are in contact with these Jurassic and Triassic clay formations are known as formation waters containing Na-Ca-Mg-Cl brine solutions with salinities close to saturation. The salt concentration in groundwaters such as Gorleben or pit Conrad [1] are significantly higher (up to 4 mol/L) compared to OPA pore water (0.4 mol/L) [2]. The high salinity of these waters may influence the speciation of radionuclides and their sorption in the near field or transport in the far field of the repository. Due to the heat released from high-level nuclear waste, the surrounding of the waste containers will warm up significantly. Concepts for the disposal of nuclear waste in clay formations proceed on the restriction that the temperature at the contact surface of the containers has to stay below 100 °C [3]. An increase in temperature might change the physical and chemical properties of the clay and influence the sorption and migration of the radionuclides. While most studies on the migration behavior of radionuclides are performed at room temperature, less is known about their sorption and diffusion behaviors at elevated temperatures.

Neptunium (Np) and plutonium (Pu) are the primary actinides of fundamental concern for long-term storage of nuclear waste due to their long half-lives ($t_{1/2}$ = 2.14 × 10^6 a for ^{237}Np and

2.41 × 10^4 a for ^{239}Pu) and radiotoxicity [4]. Both radioelements are redox-sensitive with two or more stable oxidation states under environmentally relevant conditions. This fact requires specialized techniques to determine the oxidation state after the uptake on clay, which can be provided by synchrotron based measurements (µ-XANES, EXAFS). Furthermore, µ-XRF measurements can be used to determine the spatial distribution of the investigated radionuclides. The K_d value, as one of the most important parameters to evaluate the migration behavior of radionuclides in argillaceous rocks, can be determined by both sorption and diffusion experiments. Although diffusion experiments are more complex to perform and take a longer time, they may be more representative for simulating the transport of radionuclides in the environment, nevertheless some studies showed a good agreement

between these two methods [5-8]. For safety assessments it is important to develop a robust sorption and diffusion model based on the determined experimental data.

1 Sorption of Np on montmorillonite under saline conditions

1.1 Experimental procedure of batch studies

To investigate the sorption behavior of Np we used batch sorption experiments. The general procedure is described below and did not vary if not stated otherwise. The clay mineral montmorillonite (STx-1), obtained from the Source Clay Repository (Clay Minerals Society, USA) had to be purified and transformed into the Na-form prior use as described in the literature [9]. All solutions and background electrolytes were prepared as described in the Appendix. In experiments with high Np concentration we used ^{237}Np, spiked with ^{239}Np for lower detection times. In experiments at low Np concentration ($\leq 10^{-10}$ M) we used exclusively ^{239}Np. The preparation and purification of both stock solutions – ^{237}Np and ^{239}Np – is described in the Appendix.

Batch sorption experiments under anaerobic conditions were performed in an argon glove-box (Ar $\geq$ 99.99%, $c_{O_2} < 0.1$ ppm) to exclude oxidation processes by O_2 and to eliminate carbonate complexation by dissolved CO_2. Aerobic batch experiments were carried out under ambient air conditions, with addition of $NaHCO_3$ / Na_2CO_3 solutions for pH > 7 to equilibrate the suspensions with atmospheric CO_2 ($p_{CO_2} = 10^{-3.5}$ atm). To obtain solid-to-liquid ratios of 2–18 g/L for Na-STx-1, a suspension of the desired S/L ratio and background electrolyte was pipetted into 10 mL polycarbonate vials (Beckman Coulter, USA) and left for preconditioning on an end-over-end rotator (SB 3, Stuart Scientific, UK) for 72 h. To avoid shifts of the pH during batch experiments, buffer solutions were added to the samples as suggested by Bradbury and Baeyens [10]. The used buffers are given in Table 1 and were chosen because of their weak complexation affinity towards metals [11]. The final buffer concentration in the samples was 5×10^{-3} M. Any pH adjustments were carried out using freshly prepared solutions of NaOH and HCl ranging from 0.01 M to 5 M. After adjusting the pH to the desired value, aliquots of

the stock solution of $^{237}Np/^{239}Np$ were added. Under high saline conditions one has to take into account the influence of the ionic strength on the pH. Therefore, an additional value has to be added to the experimental pH to correct for effects deriving from high ionic strengths. Detailed information are given in the Appendix.

Table 1: List of used buffers in batch sorption experiments.

Buffer	**pK_a**	**pH range**
AA (acetic acid)	4.76	4.5–5.5
MES (2-(N-morpholino)ethanesulfonic acid	6.15	6.0–7.0
MOPS (3-(N-morpholino)propanesulfonic acid)	7.20	7.5–8.0
TRIS (Tris(hydroxymethyl)aminomethane	8.06	8.5–9.0
CHES (2-(cyclohexylamino)ethanesulfonic acid)	9.55	9.5–10.0

After the addition of the radionuclide of interest, the pH was readjusted (ΔpH = ± 0.05) and the samples were filled up to 8 mL for the 10 mL sample tubes. During the contact time of 72 h the pH was regularly controlled and readjusted if necessary. Prior to the separation process the pH was measured to determine the final value. To separate the solid and liquid phases, the samples were centrifuged at first at 5000 rpm for 5 minutes with a Sigma 3K30 centrifuge (Sigma Laborzentrifugen, Germany) to allow the majority of the solid phase to gather at the bottom of the tube. A complete separation was achieved at 30,000 rpm for 1 h with an Avanti J-30I (Beckman Coulter, USA). For quantification of the supernatant solution aliquots of 0.5 mL or 1.0 mL were taken for γ-ray spectroscopy measurements. For liquid scintillation counting (LSC) measurements 1 mL of the supernatant was added to 10 mL scintillation cocktail (Ultima Gold^{TM} XR, PerkinElmer LAS GmbH, Germany) and quantified with a Hidex 300 SL (Hidex, Finland). Eh measurements were performed after phase separation.

The percentage sorption derives from the following equation:

$$\text{Sorption}\% = \left(1 - \frac{[\text{An}]_{\text{eq}}}{[\text{An}]_0}\right) \cdot 100\%. \quad (1)$$

Another form of presenting the sorption independent of the solid-to-liquid ratio is the distribution coefficient K_d defined by following equation:

$$K_d = \frac{V}{m} \cdot \left(\frac{[An]_0 - [An]_{eq}}{[An]_{eq}} \right), \quad (2)$$

where $[An]_{eq}$ (mol/L) is the radionuclide concentration in equilibrium (concentration in the supernatant), $[An]_0$ (mol/L) is the initial concentration of the radionuclide, V (m^3) is the sample volume and m (kg) is the mass of sorbent.

1.2 Sorption of Np on montmorillonite

We studied the influence of pH, ionic strength, Np(V) concentration, and background electrolyte under aerobic and anaerobic conditions on the sorption of Np(V) on pure mineral phases such as montmorillonite. The general procedure is described in section 1.1 and was not varied as long as stated otherwise. As mentioned within the general procedure, the purchased clay was purified and transformed into the homo-ionic Na-form. It is from now on quoted as Na-STx-1, which indicates the homo-ionic Na-form (prefix “Na-“) and the clay batch type (suffix “STx-1”).

The influence of the solid-to-liquid ratio (2–18 g/L) on the Np(V) sorption in different background electrolyte concentrations (0.1, 1.0, and 3.0 M NaCl) is shown in Figure 1. As one can see, the log K_d values are constant within the uncertainties over a solid-to-liquid ratio of

2–18 g/L. Average log K_d values were 1.7, 1.5, and 1.6 for 0.1 M, 1.0 M, and 3.0 M NaCl solutions, respectively. Taking the respective errors into account, there is no significant influence of the ionic strength on the sorption of Np(V). Nagasaki et al. reported for Np(V) sorption on illite, shale, and MX-80 in SR-270-PW log K_d values independent of the ionic strength in a range of 0.1 to 4.6 M of a Na-Ca-Cl brine solution [12]. The study of Li et al. on the sorption of Np(V) on Na-bentonite showed for pH 8.5 no influence of the NaCl concentration [13]. The same was observed by Kasar et al., who investigated the retention of

Np(V) by a smectite-rich clay in dependence of the ionic srength (0.1–1.0 M NaCl) [14], which is in very good agreement with our experiments.

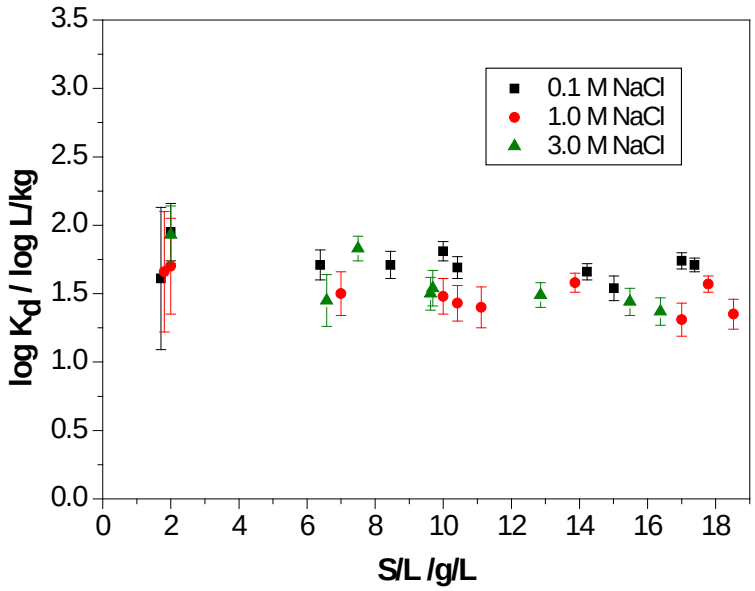

Figure 1: log K_d of Np(V) (8×10^{-6} M) against the S/L ratio of Na-STx-1 at pH 8 under aerobic conditions in 0.1 M NaCl (black squares), 1.0 M NaCl (red dots), and 3.0 M NaCl (green triangles) solutions.

As the Np concentration can vary over a wide range within a repository, Np(V) concentration depending experiments were performed. The initial Np(V) concentration was varied between 1×10^{-4} M and environmentally relevant concentrations of 1×10^{-12} M at pH 8.5 in various NaCl solutions as background electrolyte (0.1–3.0 M) at 4 g/L Na-STx-1.

As in the previous study, no dependence of the Np(V) uptake by Na-STx-1 on the NaCl concentration can be observed (Figure 2, left). Only slight differences within the respective errors are apparent. Due to the higher pH in this isotherm experiment (pH 8.5), the log K_d values are slightly higher as in the previous batch experiment at pH 8.0. This observation is not surprising because of the pH dependent sorption of Np(V), where with increasing pH the uptake increases as well. Until a concentration of 1×10^{-7} M the uptake is constant and does not show any influence of the Np(V) concentration, which changes at higher concentrations. It seems as if a maximum uptake boundary is reached at 1×10^{-7} M, from which on the strong binding sites are saturated and complexation on weak sorption sites has to be taken into account. Starting from an average log K_d value of 2.5 for the concentration range of 1×10^{-12} M to 1×10^{-7} M, the log K_d decreases to 1.7 for 1×10^{-4} M Np(V).

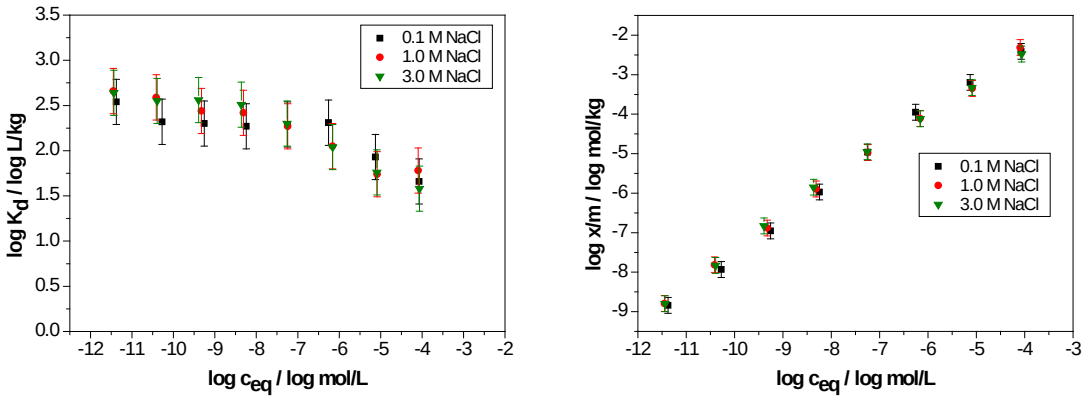

Figure 2: Np(V) sorption isotherm at pH 8.5 on 4 g/L Na-STx-1 under anaerobic conditions in 0.1 M NaCl (black squares), 1.0 M NaCl (red dots), and 3.0 M NaCl (green triangles) solutions.

The data of the sorption isotherm in Figure 2 (right figure) can be described by two linear regressions crossing at a c_{eq} value of about 10^{-7} M. This finding is congruent with the previously made observation that the log K_d values decrease with increasing Np(V) concentration.

Since the sorption mechanisms are strongly depending on the speciation of the surface and the radionuclide, which vary with pH, we investigated the sorption of Np(V) on Na-STx-1 over a wide range of pH (2.5–10.0) under aerobic and anaerobic conditions. Figure 3 shows the results of the pH dependent sorption of Np(V) (8×10^{-6} M) on Na-STx-1 in 0.1 M NaCl solution under aerobic and anaerobic conditions. In the acidic range the cation exchange on permanently negatively charged sites predominates the sorption mechanism. Since NpO_2^+, which is the main species in the acidic pH range, is quite large because of the transitional bound oxygen atoms and has a small effective charge (2.3) compared to tri-, tetra-, and hexavalent actinides (3, 4, and 3.3, respectively) [15], the tendency for an exchange reaction is quite low and thus comparable to the Na^+ cation [16]. With rising deprotonation of the surface hydroxyl groups, surface complexation becomes increasingly important. The first complexation starts at approximately pH 6.5 and seems to reach a local maximum at pH 7 to 8 with a log K_d value of 1.5. No differences can be observed between the sorption edges under aerobic and anaerobic conditions to that point. The first gaps appear at pH values ≥ 8.5 and become significant at pH ≥ 9.5. Whereas the sorption in the anaerobic samples increases furthermore, the sorption in the aerobic samples decreases due to Np(V) complexation with carbonate.

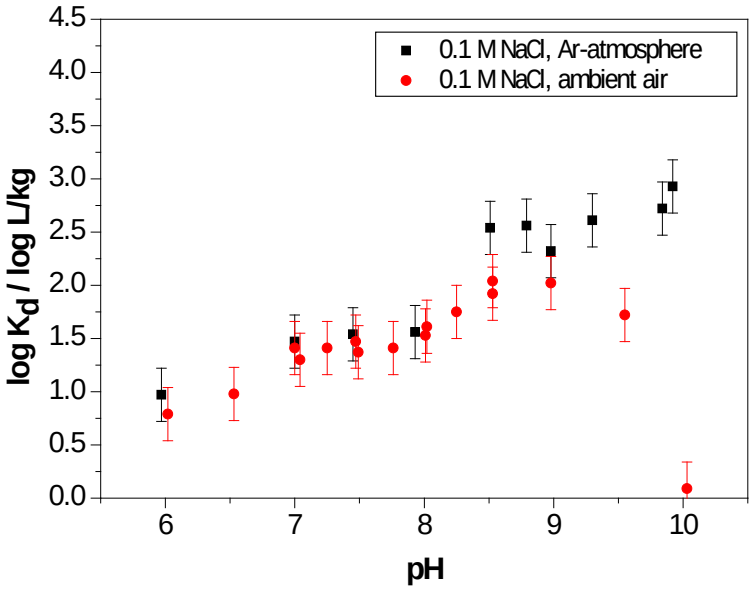

Figure 3: log K_d of Np(V) (8×10^{-6} M) against the pH on Na-STx-1 in 0.1 M NaCl solution under ambient air condition (red dots) and Ar atmosphere (black squares).

The maximum sorption is reached for the aerobic samples at pH 9 with a log K_d value of 2.0. Under CO_2-free conditions the sorption increases continuously with a log K_d value of 3.0 at pH 10. This difference in the sorption curves under aerobic and anaerobic conditions is known from the literature [17-19].

Figure 4 presents the sorption curves of Np(V) (3.5×10^{-12} M) on Na-STx-1 in 0.1 M and 1.0 M NaCl solution under aerobic conditions. As one can see the ionic strength does not have any significant influence on the sorption of Np(V) on Na-STx-1 in the pH range of 5–9. The maximum in sorption is attained at pH 8 with a log K_d value of 2.3. As described above the decrease in sorption after this point derives from carbonate complexation. The overall higher sorption values at the environmentally relevant concentration range (3.5×10^{-12} M) agrees with the results shown in Figure 2.

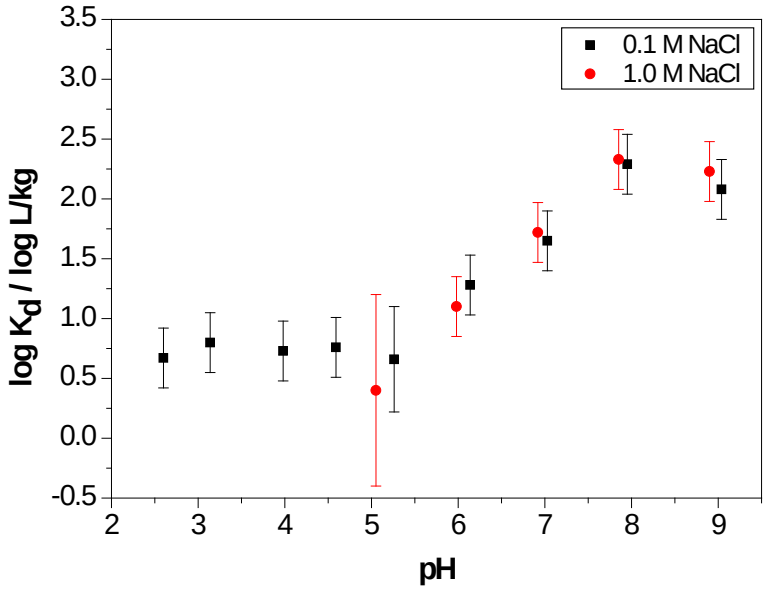

Figure 4: log K_d against the pH of Np(V) (3.5×10^{-12} M) on Na-STx-1 in 0.1 M NaCl (black squares) and 1.0 M NaCl (red dots) solutions under ambient air conditions.

1.3 Modeling the sorption of Np under saline conditions

An important point in the assessment of a deep geological waste repository is the prediction of species distribution and migration of radionuclides. Therefore, predictive models have to be developed which on the one hand calculate the migration and sorption behavior correctly, and on the other hand are as simple as possible without neglecting important parameters. The model should be robust against system changes so that they are applicable over a wide range of conditions as these can change within a repository and its far-field. One of these models is the

2 Site Protolysis Non Electrostatic Surface Complexation and Cation Exchange model (2 SPNE SC/CE) developed by Bradbury and Baeyens [9, 20]. It provides good results for low and medium ionic strengths and is due to its simplicity applicable over a wide range of conditions [16, 21, 22]. Table 2 summarizes the non-adjustable parameters which are specific for Na-montmorillonite and were determined by modeling titration experiments [20]. Since we focused on modeling data under saline conditions, we had to take into account the decreasing activities due to high ionic strength. Therefore, we used the Specific Ion

Interaction Theory (SIT). As thermodynamic database served the default database of MinteQ v3.0 [23].

Table 2: Summary of clay specific parameters [20].

		log $K_{protolysis}$	
Site	**Site density**	$SOH + H^+ \rightarrow SOH_2^+$	$SOH \rightarrow SO^- + H^+$
^{s}SOH	2×10^{-3} mol/kg	4.5	-7.9
^{w1}SOH	4×10^{-2} mol/kg	4.5	-7.9
^{w2}SOH	4×10^{-2} mol/kg	6.0	-10.5
CEC	0.870 eq/kg		

Most of the studies mentioned above were conducted in $NaClO_4$ as background electrolyte, and due to the very weak complexation of perchlorate anions (ClO_4^-) it is a suitable medium to study the sorption behavior of radionuclides without interference of the background electrolyte.

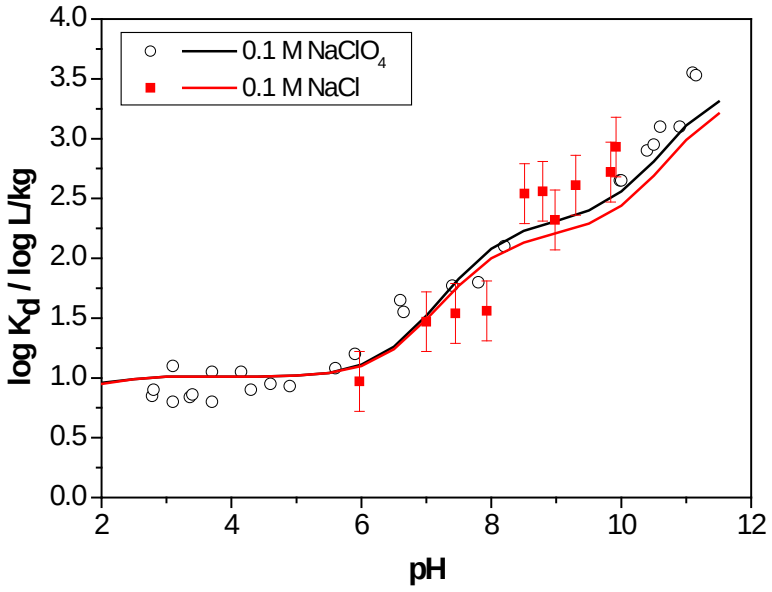

Figure 5: Differences in the 2SPNE SC/CE model between 0.1 M NaCl (data from Figure 3, red squares, 8 µM Np(V)) and 0.1 M $NaClO_4$ (data from [22], black circles, 1.1 µM Np(V)) as background electrolytes for the Np(V) (sorption on Na-montmorillonite. K_{sel} = 1.1, log K_1 = -2.8, log K_2 = -12.8 [22].

Figure 5 shows the predicted differences in the sorption of Np(V) on Na-montmorillonite between 0.1 M NaCl (red line) and 0.1 M $NaClO_4$ (black line) solutions as background

electrolyte. While the experimental data shows no difference, the model predicts slight deviations in the upper pH range, which result from different starting concentrations. The initial Np(V) concentration in the literature data was 1.1×10^{-6} M and in our experiments 8.0×10^{-6} M. Table 3 shows the used input reaction and the respective values of the logarithmic equilibrium constants (log K_1 and log K_2) in the case of surface-complexation reactions and the equilibrium constant (K_{sel}) in the case of ion-exchange reactions.

Table 3: Used equilibrium reactions for model input and its respective nomenclature [22].

Reaction	**Nomenclature**	**Value**
$NaX + NpO_2^+ \rightarrow NpO_2X + Na^+$	K_{sel}	1.1
$NpO_2^+ + SOH \rightarrow SONpO_2 + H^+$	log K_1	-2.8
$NpO_2^+ + SOH + H_2O \rightarrow SONpO_2(OH)^- + 2H^+$	log K_2	-12.8

As described in section 1.2, the ionic strength does not have any significant influence on the Np(V) uptake. These results were tested by the model for increasing NaCl concentrations up to 1 M including and excluding ambient air conditions ($p_{CO_2} = 10^{-3.5}$atm) as shown in Figure 6.

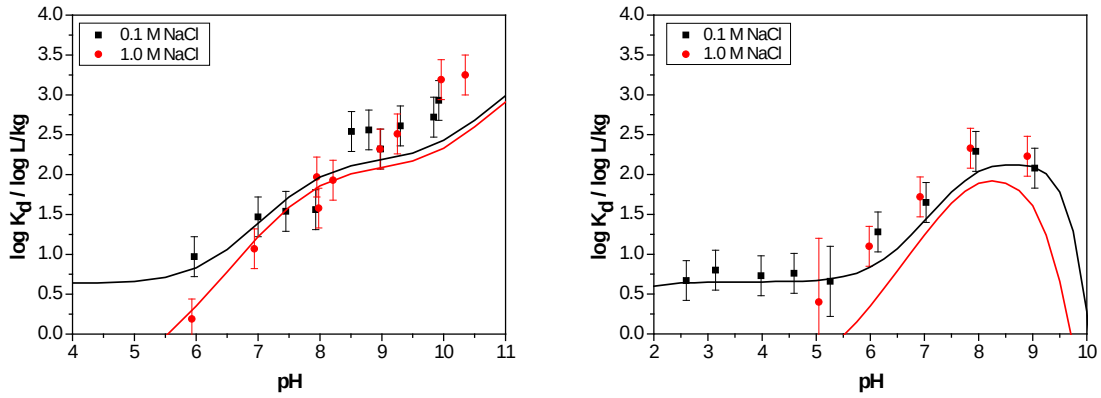

Figure 6: 2 SPNE SC/CE model for Np(V) sorption on Na-montmorillonite in 0.1 M NaCl (black line) and 1.0 M NaCl (red line) solutions under Ar atmosphere (left, [Np(V)] = 8 µM) and ambient air (right, [Np(V)] = 3.5 pM) with K_{sel} = 1.1, log K_1 = -2.8, log K_2 = -12.8, log K_3 = 1.9.

A major influence can be seen in the acidic range, where the sorption decreases with increasing NaCl concentration due to the cation-exchange mechanism, which is the main contributor to sorption in this pH range. The other gap arises from the dissolved CO_2 as aquatic CO_3^{2-}, which forms very stable and negatively charged complexes with Np(V). These

negative complexes are repelled by the negatively charged surface due to electrostatic repulsion, which makes it very difficult to form surface complexes. Therefore, the uptake of Np(V) lowers under aerobic conditions at pH > 8, which is described correctly by the model. The decrease in sorption is stronger for higher NaCl concentrations because of the increased carbonate content in solution due to equilibrium shifts. This means that with increasing Na^+ concentration the dissolution capacity of atmospheric CO_2 in the background electrolyte increases.

Testing the 2 SPNE SC/CE model on our experimental data of Figure 4 – shown in Figure 7 – revealed, that the predicted decrease of the model did not describe the data satisfactorily (dotted line). Therefore, an additional surface-complexation reaction was included.

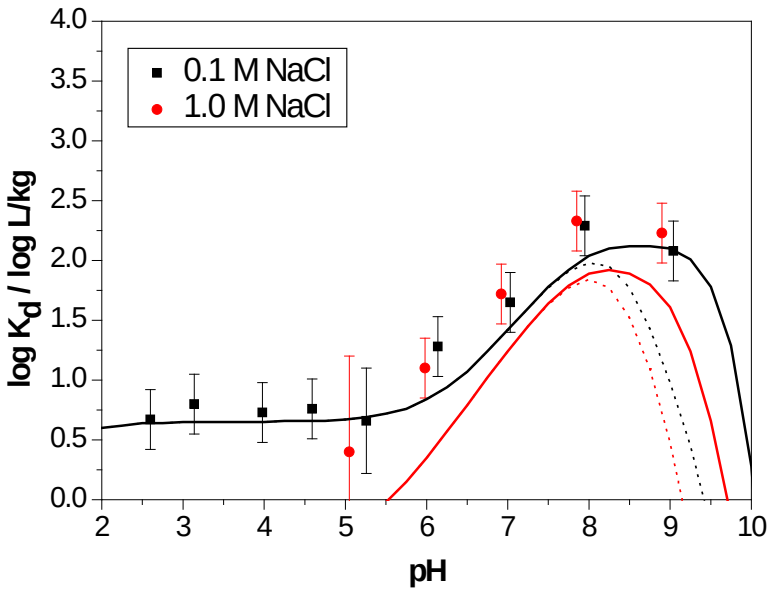

Figure 7: log K_d against the pH of Np(V) (3.5×10^{-12} M) on 17 g/L Na-STx-1 in 0.1 M NaCl (black squares) and 1.0 M NaCl (red dots) solution under aerobic conditions. Solid lines represent the predicted sorption by the 2 SPNE SC/CE model with K_{sel} = 1.1, log K_1 = 2.8, log K_2 = 12.8, log K_3 = 1.9 and the dotted lines represent the model without log K_3.

This species was "$SONpO_2(CO_3)^{2-}$" with a log K_3 value of 1.9 as assumed in the literature [24]. The contribution of this species lies in the upper pH range between pH 8 and 10 and prevents that the sorption curve falls off too rapidly. For the 0.1 M NaCl solution the experimental data is described quite well by the model while in the 1.0 M NaCl solution the deviation becomes more pronounced. Unfortunately, no data for the 1.0 M NaCl solution is available in the lower pH range. To verify that the used parameter set is applicable over a

wide range of concentration, the measured sorption isotherm of Figure 2 was modeled as shown in Figure 8.

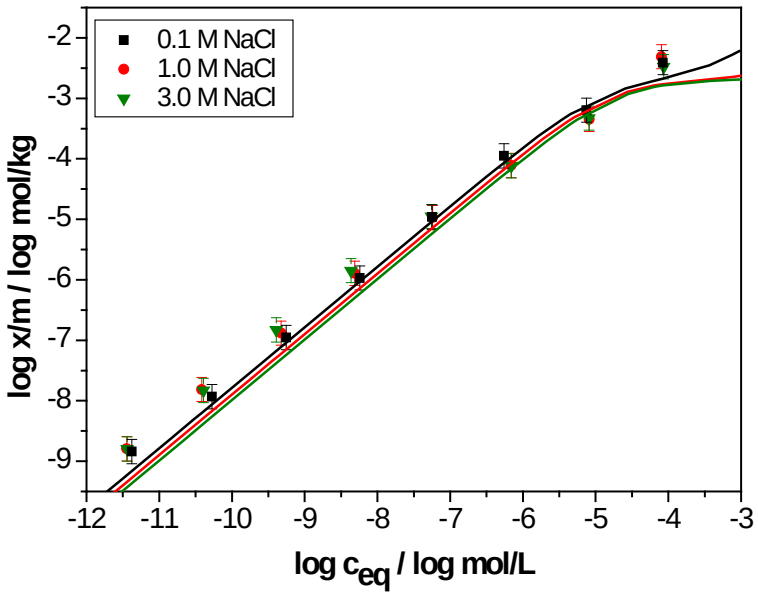

Figure 8: Sorption isotherm of Np(V) on Na-montmorillonite at pH 8.5 in NaCl solutions under Ar atmosphere. The solid lines represent the predicted sorption by the 2 SPNE SC/CE model with K_{sel} = 1.1, log K_1 = -2.8, log K_2 = -12.8, log K_3 = 1.9.

The high-concentration part of the isotherm is described very well and only small deviations between the experimental data and the predicted curve occur in the low-concentration range at about 1×10^{-8} M and below.

It can be concluded that the 2SPNE SC/CE model can be used to describe the sorption under saline conditions up to ≤ 3 M and Ar atmosphere. For ambient air conditions the model is applicable for 0.1 M NaCl concentration, but small differences between the experiment and the model do exist in 1.0 M NaCl solution as shown in Figure 7.

2 Sorption of Np and Pu on Opalinus Clay under saline conditions

This section focuses on the investigation of Np and Pu uptake by Opalinus Clay (OPA) depending on various parameters such as pH, ionic strength, type of background electrolyte, radionuclide concentration, clay concentration, and temperature. Batch experiments with Np(V) and Pu(II) were performed similar as described in section 1.1. Opalinus clay powder (Mont Terri, Switzerland) with grain sizes < 63 µm was stored respective to its use under ambient air for aerobic experiments (BHE 24/1) or in an Ar glove-box for anaerobic experiments (BHE 24/2). The dry powder was weighed-in into 10 mL polycarbonate tubes (Beckman Coulter, USA) and filled with the desired background electrolyte. After a preconditioning period of 3 days on an end-over-end rotator (SB 3, Stuart Scientific, UK) it was proceeded as described in section 1.1.

It is assumed that in a deep geological repository containing OPA as host rock material reducing conditions will be present [25] and hence we used Pu in the trivalent oxidation state in our studies. All batch experiments with Pu(III) were replicated with Am(III) to ensure that no oxidation of Pu to the tetravalent or higher states has taken place. Furthermore, the redox potential of the supernatant solution was measured and compared with pe-pH diagrams showing the areas of dominating oxidation states. The Pu(III) experiments were carried out in an argon-glove box under exclusion of O_2 and CO_2, whereas the Am(III) experiments were performed under ambient air conditions, but without addition of carbonate solutions for equilibration with ambient air CO_2.

2.1 Sorption of Np on Opalinus Clay

Figure 9 shows the log K_d values for the Np(V) sorption on OPA (15 g/L) at pH 7.6 for varying NaCl concentrations under aerobic conditions. The highest Np(V) concentration was chosen so that Np precipitations were suppressed. The log K_d values of Np(V) are constant in the low concentration range up to 10^{-9} M. This accounts for the abundance of strong sites in relation to Np(V), so that the sorption solely depends on the grade of complexation of Np(V)

in solution. As the Np(V) concentration rises the strong site capacities of the clay minerals get gradually exhausted and the log K_d value decreases. These results are comparable to those gained in the previous section for Np(V) sorption on Na-montmorillonite and to literature data [17]. The second effect studied in these experiments was the influence of the NaCl concentration. The NaCl concentration varied between 0.1 and 2.8 M. One can see that there is no significant influence of the ionic strength on the sorption of Np(V) on OPA. This is also consistent with results of section 1.2.

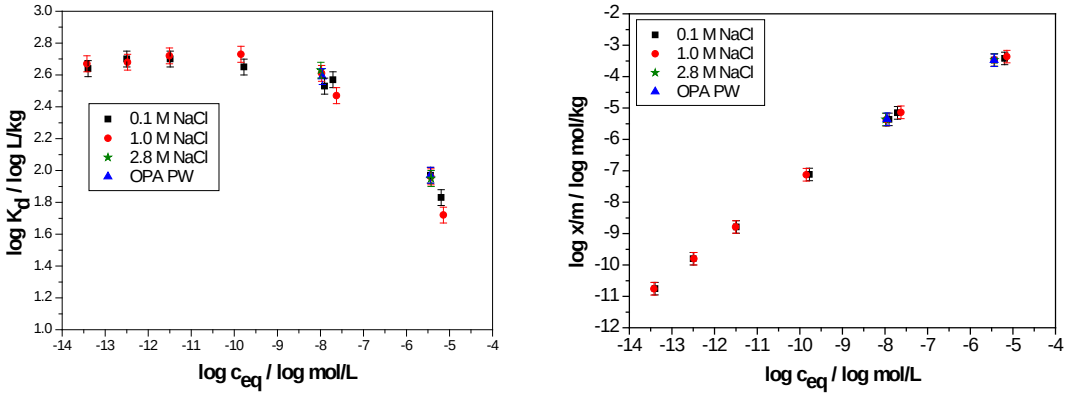

Figure 9: log K_d and log *x/m* for the sorption of Np(V) as a functions of the equilibrium Np(V) concentrations (c_{eq}) on OPA at pH 7.6 under aerobic conditions for 0.1–2.8 M NaCl solutions and OPA PW.

The clay pore waters of Northern Germany contain besides high NaCl concentrations elevated concentrations of divalent cations such as Ca^{2+} and Mg^{2+}. The competitive effect of divalent cations in the background electrolyte on the Np(V) sorption has already been reported in the literature to be much more pronounced than for the monovalent cations [26]. However, this study was prepared in diluted solutions and not in saline. For the investigation of the effect of divalent cations on the sorption of Np(V) on OPA in high saline solutions, batch experiments were performed at pH 7.6 under aerobic conditions with Np(V) concentrations of 8×10^{-6} M in solutions of ionic strengths of 0.1 M and 3.0 M $MgCl_2$ (c = 0.033 M and 1.0 M, respectively) over a pH range of 3.5–8.5. The maximum pH is limited by the precipitation of $Mg(OH)_2$ in the alkaline region. The concentration of 0.1 M is exactly the same as in [26], so that the results of the sorption experiment in diluted solution can be validated. Supplementary samples were prepared under anaerobic conditions without differing results as presented in Figure 10. The results show a significant influence of the concentration of the divalent cation Mg^{2+}. The rise of the Np(V) sorption on OPA begins for both ionic strengths after pH 5.5 and increases to 80% in 0.1 M and approximately 50% in 3.0 M $MgCl_2$ solution. Furthermore, the

results are matching those in [26] and account for a log K_d of 1.8 ± 0.1 at pH 7.8 in solution with I = 0.1 M $MgCl_2$ and in this study for 1.7 ± 0.1 at the slightly lower pH of 7.7. In contrast to these values, the log K_d in I = 3.0 M $MgCl_2$ solution reaches only a value of 1.3 ± 0.1 at pH 7.6.

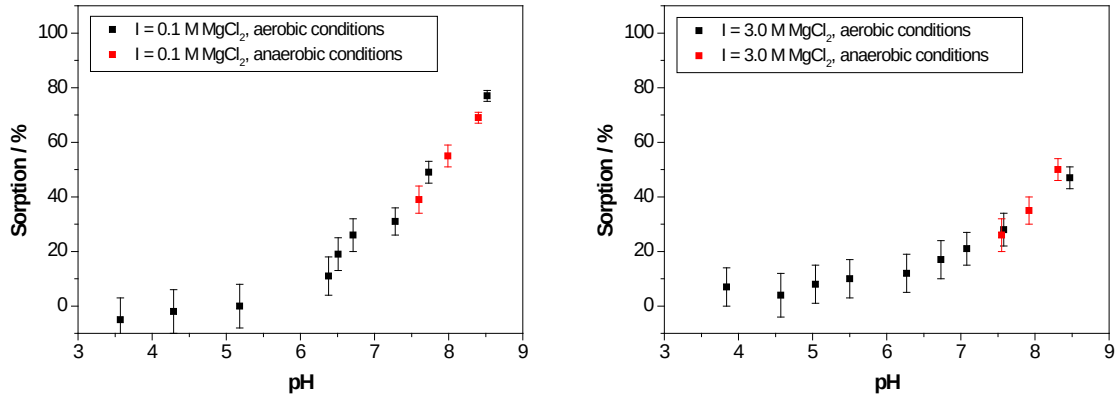

Figure 10: Left figure: Sorption of Np(V) (8×10^{-6} M) on 20 g/L OPA in I = 0.1 M $MgCl_2$ solution. Right figure: Sorption of Np(V) (8×10^{-6} M) on 20 g/L OPA in I = 3.0 M $MgCl_2$ solution.

Figure 11 compares the high salinity sorption experiment results on OPA at pH 7.6 with the Np(V) sorption in synthetic OPA porewater [26] with ionic strength of 0.4 M (all under aerobic conditions and with 8 µM Np(V)).

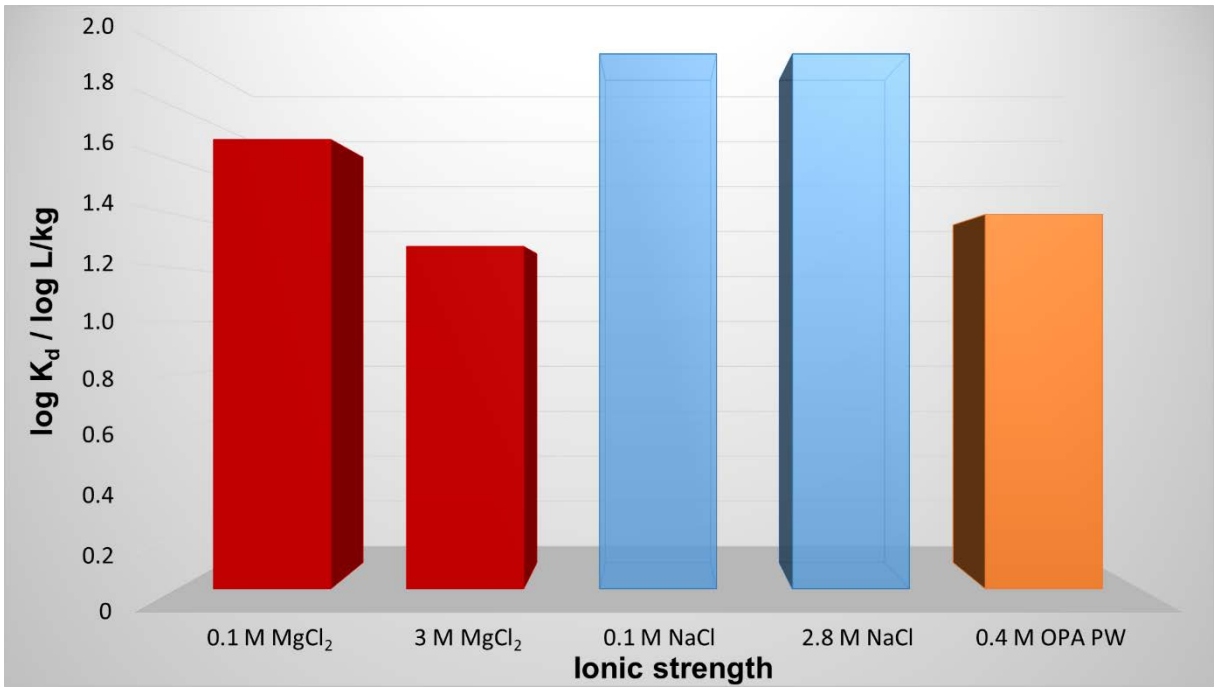

Figure 11: Influence of the background electrolyte and its ionic strength on the sorption of Np(V) (8×10^{-6} M) on OPA at pH 7.6 under aerobic conditions.

As mentioned above, one can see the decrease of the Np(V) sorption in high saline $MgCl_2$ solutions, while the sorption in 0.1 and 2.8 M NaCl solutions is higher and remains constant. For OPA PW as background electrolyte, the sorption values are lying in between. This means they are slightly higher as in 3 M $MgCl_2$, but lower than in 0.1 M $MgCl_2$. These findings can be explained by the competitive behavior of the divalent cations Mg^{2+} and Ca^{2+}. In the case of $MgCl_2$ as background electrolyte, Mg^{2+} blocks strong surface binding sites so that these are not available for the Np uptake. This mechanism is concentration depending and therefore the Np sorption decreases with increasing Mg^{2+} concentration. In OPA PW Mg^{2+} as well as Ca^{2+} ions are present with a combined ionic strength of I = 0.12 M (c = 0.04 M). This explains the medium sorption value of Np(V) with OPA PW as background electrolyte.

Another influence on the sorption behavior could arise from the elevated temperatures appearing in the near field of a long-term geological repository for high-level radioactive waste (HLW). A sorption experiment with Np(V) on OPA in synthetic OPA PW was done by Fröhlich et al. for temperatures between 40 and 80 °C showing an increase of sorption by approximately one order of magnitude in the log K_d [26]. Therefore, the sorption of Np(V) was studied in 0.1 M and 3.0 M NaCl solutions at 80 °C. The results are shown in Figure 12.

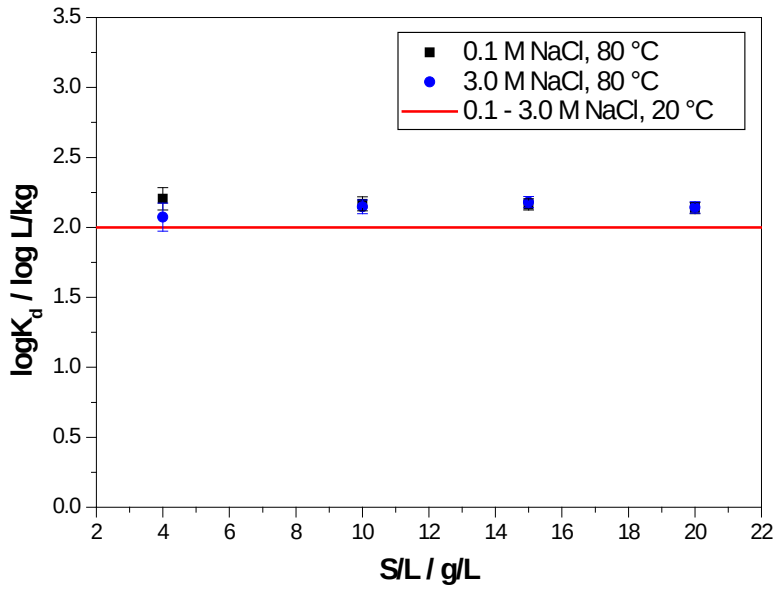

Figure 12: Influence of the temperature (80 °C) on the Np(V) (8×10^{-6} M) sorption on OPA in dependency of the clay (4–20 g/L) and NaCl concentrations (0.1 and 3.0 M) at pH 7.6. The red line represents the log K_d value, of similar sorption experiments performed at room temperature.

The elevated temperature does not seem to have an impact on the Np(V) uptake on OPA neither in diluted nor in saline NaCl solutions compared to the uptake at 20 °C. The difference between both temperatures is only 0.1 log units, which ranges within the typical errors of batch experiments and is therefore negligible. These results are supported by studies made by Li et al., who found no influence of the temperature (15–80 °C) on the sorption of Np(V) (4×10^{-7} M) on Na-bentonite (10 g/L) in 0.1 M NaCl solution [13]. On the other hand, this is in contradiction to previously made studies which illustrated a significant influence of the temperature on the Np(V) sorption on OPA in OPA PW [26] and on hematite, montmorillonite, and silica in Yucca mountain on-site well water [27].

In [26] the sorption increased from log K_d values of 1.4 at room temperature to 2.8 at 80 °C, which is similar to results gained in [27], where the log K_d increased by one order of magnitude for the Np(V) sorption on montmorillonite. The authors explained the observed behavior by an endothermic sorption of NpO_2^+ and a possibly higher deprotonation of the surface due to a shifted point of zero net proton charge (pH_{pznpc}). The main difference between these experiments ([26] and [27]) and our own as well as [13], is the background electrolyte which is in the first cases pore water and well water, containing a complex matrix of electrolytes. On the other hand, a simple matrix consisting of NaCl was used by Li et al. [13] and in our experiments. As Ca^{2+} and Mg^{2+} are present in the pore and well water, precipitations of $MgCO_3$ and $CaCO_3$, which have exothermic enthalpies of solution [28], might occur. Based on the contradicting findings and literature data, the influence of the temperature on the Np(V) sorption demands further investigations.

2.2 Sorption of Pu on Opalinus Clay

The first batch experiment focused on the influence of the pH and redox stability of Pu(III) during the sorption experiment. pH dependent sorption curves were measured for Pu(III) (4×10^{-7} M) at anaerobic and for Am(III) (4×10^{-7} M) at aerobic conditions with 2 g/L OPA

in 0.1 M NaCl solution as background electrolyte. The results are shown on the left in Figure 13. The perfectly matching curves support the assumption that during the experiment Pu(III) was not oxidized to Pu(IV) at least up to pH 6. As one can see, there is a strong influence of the pH on the sorption, with 50% sorption (sorption edge) at pH 4 and a complete Pu uptake above

pH 6. The right side of Figure 13 presents similar batch experiments with Pu(III) (4×10^{-7} M) and Am(III) (2×10^{-7} M) and 2 g/L OPA in OPA PW. Compared to the sorption experiments in 0.1 M NaCl solution, the strong pH dependence remains the same, but the point of 50% sorption as well as the point of quantitative uptake are shifted to higher pH values of 5.5 and 7, respectively. Buda et al. investigated the sorption of Pu(III) (1×10^{-6} to 1×10^{-8} M) as well as Am(III) (8×10^{-9} M) on 4 g/L kaolinite in 0.1 M $NaClO_4$ under aerobic and anaerobic conditions [29]. The sorption curves on kaolinite are slightly different in the point of 50% and 100% sorption, which are shifted to higher pH values (pH 5 and 9, respectively). This difference could arise from the higher pH_{pznpc} of kaolinite compared to illite and montmorillonite [30], which are assumed to be the main sorbing clay minerals in OPA.

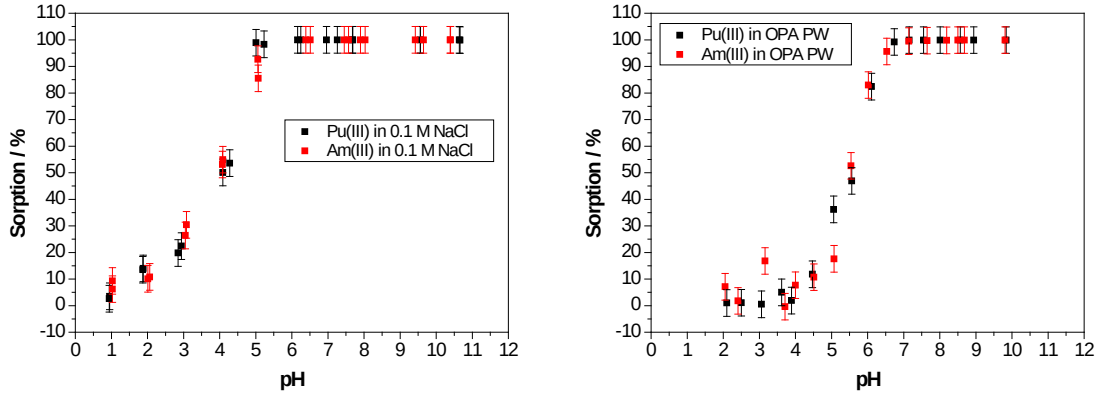

Figure 13: Left figure: Sorption of Pu(III) (4×10^{-7} M) and Am(III) (4×10^{-7} M) on 2 g/L OPA in 0.1 M NaCl solution. Right figure: Sorption of Pu(III) (4×10^{-7} M) and Am(III) (2×10^{-7} M) on 2 g/L OPA in OPA PW.

The different sorption behavior of these two background electrolytes can be assigned to the influence of the divalent cations present in OPA PW. As mentioned previously for Np(V) in section 2.1, divalent cations compete for strong sorption sites as well as cation exchange sites. To investigate the possible influence of divalent cations, the sorption of Pu(III) (2×10^{-7} M and 4×10^{-7} M) and Am(III) (5×10^{-7} M and 4×10^{-7} M) on OPA (2 g/L) in 0.1 M $CaCl_2$ and

0.1 M $MgCl_2$ solution was studied as shown in Figure 14 on the left and right, respectively. The experimental conditions were the same as for the studies in NaCl solution and OPA PW. The sorption curves of Pu(III) and Am(III) match again very well for both background electrolytes, except for the sorption value of Pu(III) at pH 5.5. In both solutions this particular pH shows sorption of about 99% rather than 50% as expected from the Am(III) sorption curve. This behavior is not seen in NaCl solutions due to the fact that the point of quantitative sorption is already reached at pH 5.5. Furthermore, the sorption edge in the divalent cationic background electrolytes is steeper and the point of 50% sorption is at higher pH values (pH 5.5). These findings are very similar to those obtained in OPA PW and indicate that the amount of divalent cations in the OPA PW is playing a major role.

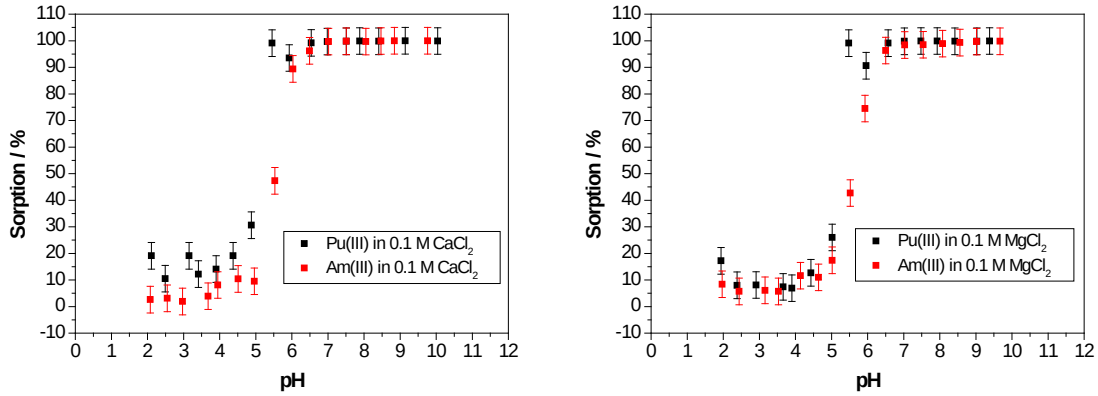

Figure 14: Left figure: Sorption of Pu(III) (2×10^{-7} M) and Am(III) (5×10^{-7} M) on 2 g/L OPA in 0.1 M $CaCl_2$. Right figure: Sorption of Pu(III) (4×10^{-7} M) and Am(III) (4×10^{-7} M) on 2 g/L OPA in 0.1 M $MgCl_2$.

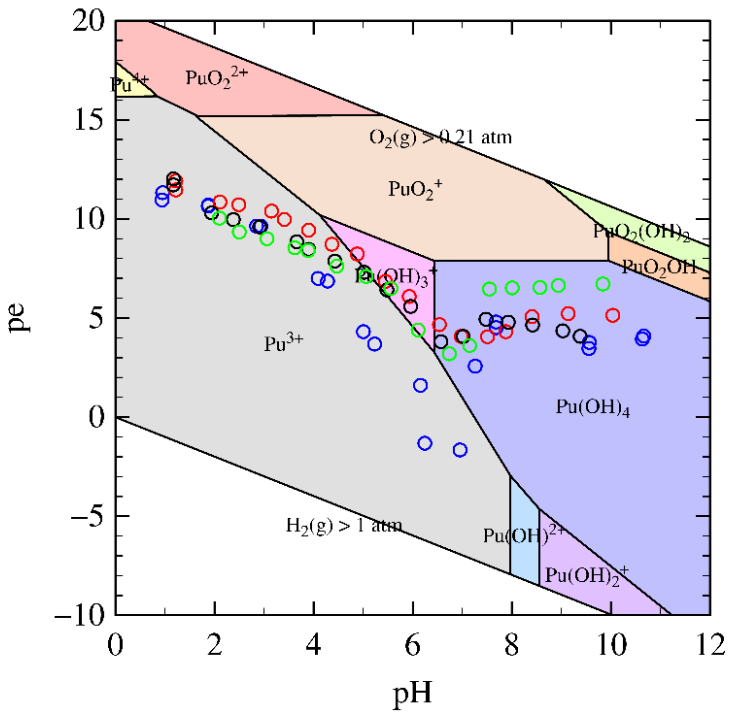

Figure 15: Calculated pe-pH diagram for Pu(III) (4×10^{-7} M) in 0.1 M NaCl solution under anaerobic conditions using PhreePlot v1.0 [31] and the thermodynamic database of the PSI [32]. The circles represent the experimental data for the sorption experiments in 0.1 M NaCl (blue), 0.1 M $CaCl_2$ (red), 0.1 M $MgCl_2$ (black), and
OPA PW (green).

The measured Eh values indicate that Pu(III) is the main species at lower pH as shown in Figure 15. The circles represent the experimental redox potentials (SHE) which were measured in the supernatant after phase separation. The data shows, that the solutions' redox potentials range in the Pu(III) predominance area until pH 6 and raise beyond this point up to around 5–7 pe and stay at this level while the pH increases further on. Therefore the possibly predominant oxidation state at pH values higher than 6 is Pu(IV). Additional studies on the speciation of Pu in these batch experiments using CE-ICP-MS can be found in section 4.2.3.

To investigate the influence of higher salinities on the sorption of Pu(III) such as 2 M NaCl solutions, which could be present in pore waters in Northern Germany [33], we studied the dependence of the sorption on the NaCl concentration. At pH 7.6 the sorption exceeded 99.5% which made it difficult to study influences on the sorption behavior at different NaCl concentrations. Therefore, we took the point of 50% uptake at pH 4. Solutions of 0.01 M, 0.1 M, 1.0 M, and 2.0 M NaCl were prepared at pH 4 with a solid-to-liquid ratio of 2 g/L OPA and Am(III) concentrations of 4×10^{-7} M. The results are presented in Figure 16.

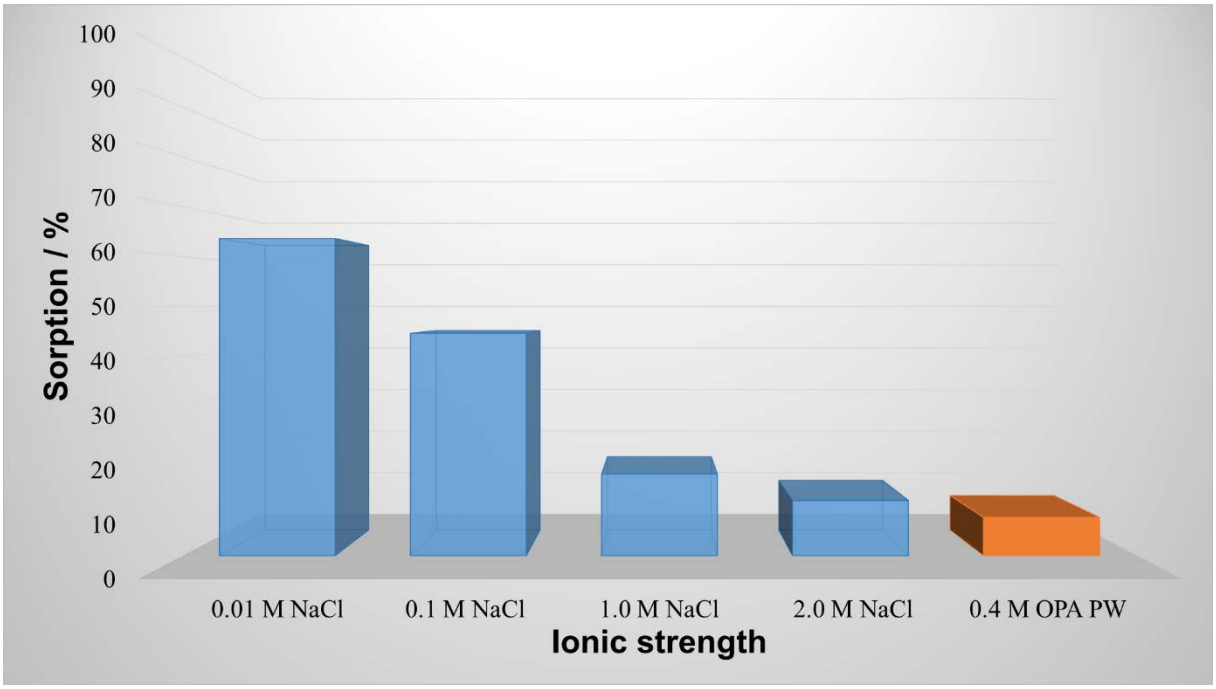

Figure 16: Influence of the ionic strength of NaCl solutions and OPA PW on the sorption of Am(III) (4×10^{-7} M) onto 2 g/L OPA at pH 4 under aerobic conditions.

Due to the fact that Am(III) could be handled under ambient air and does not undergo redox reactions, the studies of the impact of the ionic strength were not performed with Pu(III) but with Am(III). In diluted NaCl solutions (0.01 M) the sorption is about 65% and decreases with increasing salt concentrations to 45% in 0.1 M NaCl, 16% in 1 M NaCl, and 10% in 2 M NaCl solutions. At such low pH values the main sorption process is cation exchange at permanently negatively charged sites. By introducing more Na^+ cations into the system, the competition reaction with the radionuclide is enhanced, leading to a decrease in sorption at higher NaCl concentrations. Since the cation exchange process becomes less important at higher pH values (>7) and the sorption is dominated by surface complexation, the effect of increasing ionic strength in a NaCl medium will become less pronounced at pH $\geq$ 7, as observed for the sorption of Np(V) on OPA (Figure 11). The influence of divalent cations (Ca^{2+}) is shown in Figure 17. Since the sorption curves of $MgCl_2$ and $CaCl_2$ did not show any differences, ionic strength depending sorption experiments were performed only with Ca^{2+} as representative for the divalent ions. The pH was adjusted to 5.5 to be in the 50% sorption region and the concentrations of Am(III) and OPA accounted for 4×10^{-7} M and 2 g/L, respectively. As observed for NaCl solutions, the highest uptake (85%) takes place at the lowest ionic strength (0.03 M). The following decrease of sorption with increasing $CaCl_2$ concentration is stronger than in NaCl solutions, whereby one has to take into account that the

ionic strength is increasing much stronger with the concentration in $CaCl_2$ mediums than in NaCl mediums. This leads to sorption values of 40%, 12%, and 5% for the 0.3 M, 3.0 M, and 6.0 M solutions (which accounts for $c(CaCl_2)$ = 0.1 M, 1.0 M, and 2.0 M), respectively.

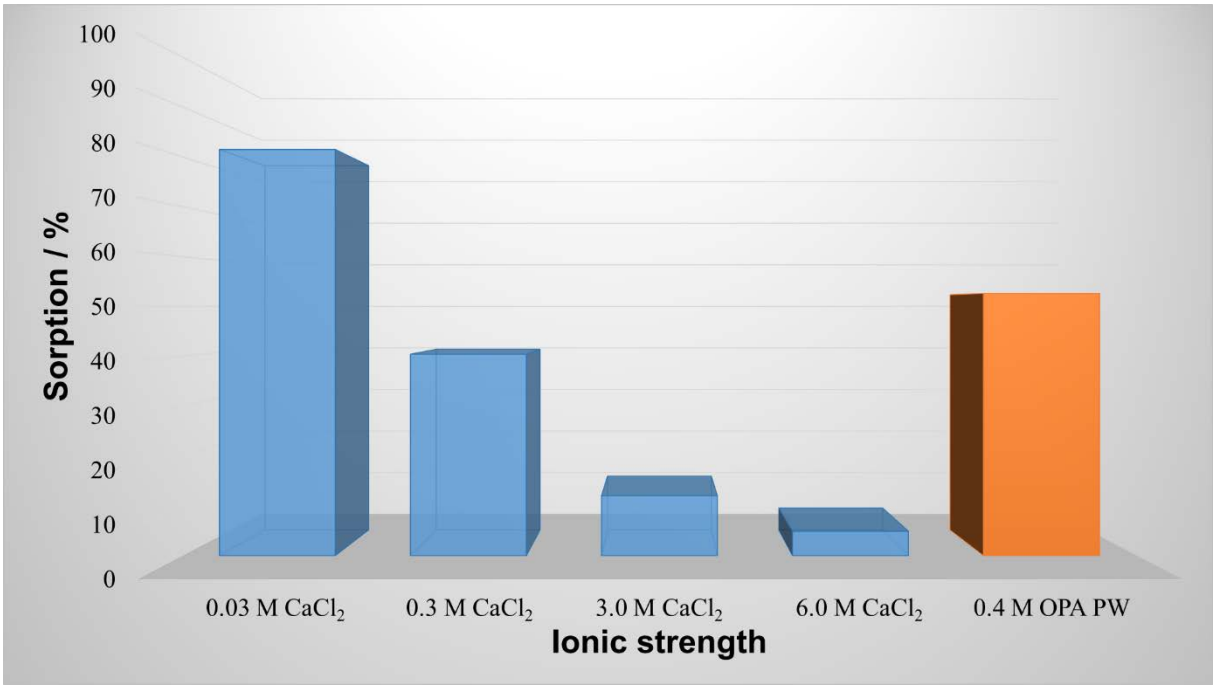

Figure 17: Influence of the ionic strength of $CaCl_2$ solutions and OPA PW on the sorption of Am(III) (4×10^{-7} M) onto 2 g/L OPA at pH 5.5 under aerobic conditions.

To clarify whether the sorption of Pu(III) on OPA is reversible or not, we performed a two-step desorption experiment with four different samples at varying pH (2, 4, 6, and 8) after a Pu(III) batch sorption experiment. Subsequent to the removal of the supernatant after phase separation of the batch sorption experiment, the solid was resuspended in fresh background electrolyte solutions of the respective pH values. The contact time of Pu loaded clay with background electrolyte without Pu was 3 days, the same time as for the sorption experiments. Thereafter, another phase separation was carried out and aliquots of the supernatant were measured to determine the Pu concentration. In a second desorption step we contacted the solid phase, after complete removal of the supernatant of desorption step one, for 3 days with 0.01 M HCl to yield a background electrolyte of pH 2 which should be acidic enough to desorb nearly all Pu without dissolving the clay mineral.

Because of the very strong sorption of Pu(IV) on clay minerals [34], the desorption should show deviations between the log K_d values of the sorption and the desorption experiments, if oxidation from Pu(III) to Pu(IV) had taken place.

Table 4: log K_d values of the sorption and desorption experiment of Pu(III) ($c_0 = 4 \times 10^{-7}$ mol/L) in 0.1 M NaCl solution.

	Sorption		Desorption		Acidic desorption	
Sample	**pH**	**log K_d / log L/kg***	**pH**	**log K_d / log L/kg***	**pH**	**log K_d / log L/kg***
Pu-1	2.1	1.9	2.1	2.3	2.0	2.6
Pu-2	4.0	2.5	4.2	3.2	1.9	2.2
Pu-3	6.3	4.9	6.3	5.2	1.9	2.3
Pu-4	8.0	5.0	8.7	4.8	2.0	2.3

***** uncertainty in the log K_d values account for ± 0.25 log units

The results in Table 4 show that the K_d values from the desorption experiments are slightly higher than the values from the sorption experiments at the same pH. This leads to the conclusion that the sorption of Pu(III) on OPA is not completely reversible. Furthermore, this finding suggests the partial formation of Pu(IV) which is a very strongly sorbing species that cannot be totally removed even in strong acidic media (pH 2), similar to Np(IV) [35]. The obtained log K_d values of all samples at pH 2 in both desorption steps show good agreement (log K_d ~2.3).

3 Diffusion of Np in Opalinus Clay under saline conditions

Our goal in this study was to investigate the transport behavior of Np in solutions of higher ionic strength at both room and high temperature (60 °C), as they are relevant for repository systems in clay formations in Northern Germany, and to compare the obtained results with previous results of diffusion experiments in synthetic OPA PW at room temperature (24 °C) under the same conditions [36].

Owing to the small hydraulic conductivity (10^{-14} to 10^{-13} m/s [37]) of OPA, it is expected that the transport of radionuclides released from a repository will be dominated by diffusion processes. Due to little diffusion data available for Np and to extend our previous results of Np(V) diffusion in OPA [36], the diffusion of Np(V) was investigated as a function of ionic strength in NaCl solutions ($I \leq 3$ M) at pH 7.6 and in dependence of the temperature (24 °C and 60 °C) in 1 M NaCl solution.

The experimental setup and all details of the diffusion experiments (through-, out-, and in-diffusions) and the performed procedures are described below. The theoretical background and data processing of through-, out-, and in-diffusions have been described elsewhere [36-38].

3.1 General procedure of diffusion experiments

For diffusion experiments with Np, cylinders of about 25 mm diameter and 11 mm thickness were prepared from the aerobic OPA bore core (BLT 14), sandwiched between two stainless steel filter plates and mounted in a stainless steel diffusion cell (Figure 18). The direction of transport (diffusion) was perpendicular to the bedding for experiments using the abrasive peeling method and parallel for speciation investigations. The average dry density of the intact OPA was about 2400 kg/m³. As mobile phases synthetic OPA PW, 1 M NaCl, and 3 M NaCl solutions were used. All diffusion experiments with Np(V) were carried out under ambient air (aerobic conditions) and the temperature was between 24 ± 2 °C (room temperature) and 60 ± 2 °C. The experimental setup can be seen in Figure 18 and follows the procedure of the through-diffusion experiments by Van Loon et al. [39]. Detailed information about our diffusion setup can be found also in [36].

To achieve an equilibrium between the OPA sample and the mobile phase, the sample was contacted from both sides with the respective solution for at least 5 weeks.

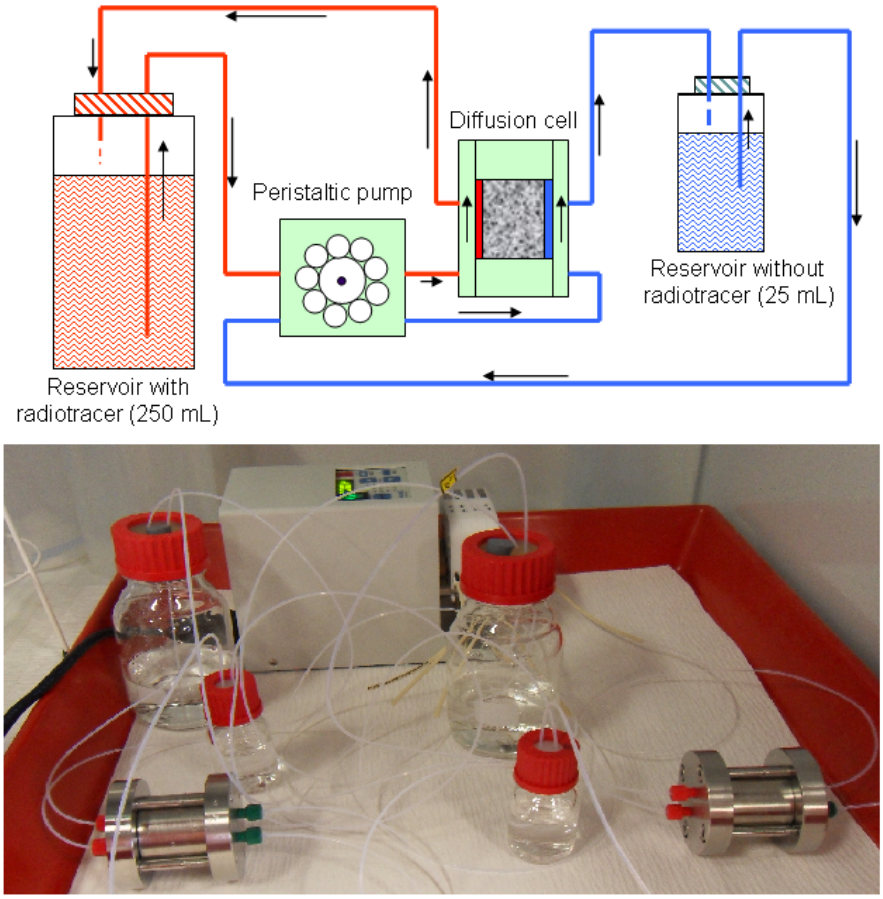

Figure 18: Schematic sketch (adapted from [39]) and a photography of the experimental setup for diffusion experiments in our laboratory.

To determine the porosity of the used OPA sample and to exclude possible cracks which would make the sample unsuitable, HTO and $^{22}Na^{+}$ diffusion experiments were conducted. The related effective diffusion coefficient (D_e), accessible porosity of the clay (ε) and the rock capacity factor (α) were calculated using the equation given by Van Loon et al. [38]. The distribution coefficient (K_d) of $^{22}Na^{+}$ was calculated from the rock capacity factor under the assumption that the diffusion-accessible porosity of $^{22}Na^{+}$ is the same as for HTO.

$$\alpha = \varepsilon + \rho \cdot K_d, \qquad (3)$$

where α is the rock capacity factor, ε the diffusion-accessible porosity, ρ the bulk dry density in kg/m^3 and K_d the distribution coefficient in m^3/kg (or L/kg). The diffusion parameters (D_e, ε, α) were obtained by fitting the results of the experimental data of the transient and steady state phases to an analytical solution of the accumulated activity. The quality of the derived D_e and α values was tested by using them as input parameters in the equation for the flux.

$$J(L,t) = \frac{1}{S} \cdot \frac{\partial A}{\partial t}, \quad (4)$$

where J(L,t) is the flux at the low-concentration boundary ($x = L$) at diffusion time t, A (Bq/m^3) the radionuclide activity in solution, t (s) the diffusion time and S (m^2) the cross section area of the sample. If the diffusion parameters for HTO and $^{22}Na^+$ were in good agreement with known values from the literature [39], the integrity of the OPA sample was assumed.

After these through-diffusion experiments were finished, the out-diffusion was started by replacing both reservoirs with fresh vials containing the respective mobile phase without any radiotracer. The vials were changed daily until no activity was detectable in the reservoirs. The out-diffused amount of HTO/$^{22}Na^+$ was measured by LSC. Once the out-diffusion was finished, we spiked the 210 mL vial with ^{237}Np(V) and started the in-diffusion experiment for 40 to 76 days. Samples of 0.5 mL were taken on regularly time basis from the 210 mL vial to measure the decrease in activity, which indicates the amount of the Np that diffused into the OPA sample. Close to the end of the Np diffusion experiment, the high-concentration reservoir was exchanged by a smaller vial (20 mL) containing the same concentration of Np(V), and in addition $^{22}Na^+$. Around 20 hours after exchanging the high-concentration reservoir, the diffusion was terminated, the OPA sample removed from the diffusion cell and attached to a sample holder for abrasive peeling with P220 abrasive paper as described elsewhere [36, 40]. The peeled OPA layers were measured by γ-ray spectroscopy to determine the ^{237}Np (at 29.37 keV and 86.48 keV) and $^{22}Na^+$ (at 1274.5 keV) concentrations. Diffusion experiments at elevated temperatures were carried out in an incubator (INE-200 heating incubator, Memmert GmbH, Germany) with temperature fluctuations of less than ± 2 °C. The data analysis for through-, out- and in-diffusion experiments was done with an in-house developed computer code as described in detail elsewhere [36, 37].

3.2 Influence of the background electrolyte on the diffusion of HTO, $^{22}Na^+$, and Np(V)

To study the influence of the background electrolyte and ionic strength on the diffusion of Np(V) in OPA, NaCl solutions with ionic strengths of 1.0 M and 3.0 M were used as background electrolyte. The obtained results were compared with previous diffusion studies using OPA pore water as mobile phase. Therefore, three cylinders of intact OPA were prepared from the OPA bore core BLT 14 and used in the diffusion experiments as described in section 3.1. To characterize the used OPA bore cores, through-diffusion experiments with HTO and $^{22}Na^{+}$ were performed. All experimental details and obtained diffusion parameters (D_e, ε, and α) for HTO and $^{22}Na^{+}$ are summarized in Table 5 and Table 6.

Table 5: Experimental details of cells 1 and 2 prepared under ambient air in NaCl solutions (1 M and 3 M) at pH 7.6.

Cell	Temp. / °C	Mobile phase	ø / mm	*l* / mm	ρ / kg/m³
1	24	1 M NaCl	25.48	11.00	2346
2	24	3 M NaCl	25.42	10.90	2363
3*	60	1 M NaCl	25.40	11.00	2377
4*	60	OPA PW	25.45	11.00	2353

* Cells used to study the influence of temperature in section 3.3

Table 6: Diffusion parameters (D_e, ε) for HTO (c_0 = 1.3 × 10^9 Bq/m^3) and (D_e, α, and K_d) for $^{22}Na^{+}$ (c_0 = 5.5 × 10^9 Bq/m^3) in OPA obtained by through-diffusion experiments under ambient air in NaCl solutions (1 M and 3 M) at pH 7.6 and 24 °C.

	HTO		$^{22}Na^{+}$		
	ε	D_e / 10^{-11} m^2/s	α	D_e / 10^{-11} m^2/s	K_d / L/kg
1 M NaCl (cell 1)	0.18 ± 0.01	1.9 ± 0.1	0.35 ± 0.02	1.6 ± 0.1	0.10 ± 0.01
3 M NaCl (cell 2)	0.18 ± 0.01	1.6 ± 0.1	0.20 ± 0.01	0.9 ± 0.1	0.01 ± 0.01
OPA PW [36]	0.15 ± 0.01	1.5 ± 0.1	0.50 ± 0.02	1.9 ± 0.1	0.15 ± 0.03

As shown in Table 6 the investigated OPA bore cores have a similar porosity, which agrees well with known values of Mont Terri OPA [25]. No ionic strength effect was observed for the diffusion of HTO in OPA, as it is apparent from the obtained D_e values for 1 M and 3 M NaCl solutions. In the case of $^{22}Na^{+}$ the D_e value decreases with increasing salt concentration from 1.6 ± 0.1 × 10^{-11} m^2/s in 1 M NaCl to 1.0 ± 0.1 × 10^{-11} m^2/s in 3 M NaCl solution. Our results are in good agreement with published data by Glaus et al., who studied the diffusion of

HTO and $^{22}Na^{+}$ in compacted kaolinite, Na-illite, and Na-montmorillonite as a function of the salt concentration (0.1–1.0 M $NaClO_4$) [41, 42]. Glaus et al. assumed that the $^{22}Na^{+}$ diffusion in montmorillonite and illite, which are the main phases contained in OPA, occurs – in case of high salinities – preferentially in the interlayer or diffuse double layers in these clays.

After the complete out-diffusion of HTO and $^{22}Na^{+}$, in-diffusion experiments with 8 µM Np(V) were started. To assess the reliability of the diffusion technique and the determination of the diffusion parameter of Np in intact OPA, we performed in-diffusion experiment with $^{22}Na^{+}$ as a control. The obtained diffusion parameters D_e and K_d of $^{22}Na^{+}$ obtained by in-diffusion were compared with those from through-diffusion experiments and show good agreement, indicating that both methods can be used to study the diffusion behavior of radionuclides in the clay. Np was given a period of 63 and 67 d to diffuse into the clay for cells 1 and 2, respectively. About 50 thin layers from the primary side of the clay were removed by the abrasive peeling method. The ^{237}Np and $^{22}Na^{+}$ activities in each layer were measured via γ-ray spectroscopy.

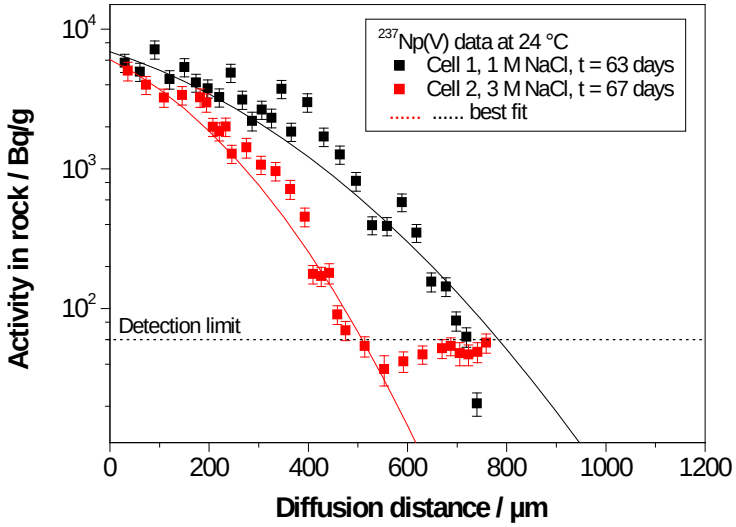

Figure 19: Diffusion profiles of 8 × 10^{-6} M $^{237}Np(V)$ in OPA of cells 1 and 2 in NaCl solutions (1 M and 3 M) at pH 7.6 under ambient air at 24 °C together with the fit curves.

The obtained diffusion profiles were evaluated using the equations given in [36] which are based on the model of Yaroshchuk et al., including a correction for the retardation effect of Np by the stainless steel filters [43]. Figure 19 shows the diffusion profiles of Np(V) in OPA of cells 1 and 2 in NaCl solutions (1 M and 3 M) at pH 7.6 under ambient air at 24 °C together with the fit curves.

The concentration profiles of ^{237}Np(V) in the clay show that the diffusion distance for ^{237}Np(V) is influenced by the ionic strength as described before for $^{22}Na^{+}$. The penetration depth of Np in 1 M NaCl solution at 24 °C was 740 µm and thus significantly further than in 3 M NaCl solution with 550 µm. Despite the decrease of the penetration depth, no differences in either shape of the curves or the quality of the fit were observed. The results of the fitting represented by D_e, α, and K_d are summarized in Table 7.

Table 7: Diffusion parameters (D_e, α, and K_d) for ^{237}Np and $^{22}Na^{+}$ in OPA determined by in-diffusion experiments of cells 1 and 2 in NaCl solutions (1 M and 3 M) at pH 7.6 under ambient air at 24 °C.

	^{237}Np			**$^{22}Na^{+}$**		
	α	**D_e / 10^{-12} m^2/s**	**log K_d / log L/kg**	**α**	**D_e / 10^{-11} m^2/s**	**K_d / L/kg**
1 M NaCl	742 ± 9	6.9 ± 1.2	2.5 ± 0.1	0.46 ± 0.01	1.6 ± 0.1	0.12 ± 0.01
3 M NaCl	455 ± 7	2.4 ± 1.0	2.3 ± 0.1	0.19 ± 0.002	1.0 ± 0.1	-
OPA PW [36]	243 ± 4	6.9 ± 1.1	2.0 ± 0.1	0.44 ± 0.03	1.8 ± 0.2	0.14 ± 0.01

As can be seen in Table 7, the D_e value of Np(V) increases by a factor of two with increasing ionic strength. The log K_d values for Np(V) are independent of the ionic strength within the uncertainties. This result agrees with our batch experiments, which did not show any influence of the ionic strength (1–3 M) on the Np(V) sorption on OPA in NaCl solutions (section 2.1). The determined log K_d values from diffusion experiments in NaCl solutions are slightly higher than those in OPA PW (2.00 ± 0.04 L/kg), which indicates somewhat higher retardation of Np in NaCl solutions. The diffusion parameters for $^{22}Na^{+}$ determined by in- and through-diffusion are in good agreement (Table 6 and Table 7).

3.3 Influence of the temperature on the diffusion of HTO, Na^{+}, and Np

To investigate the diffusion of Np(V) in OPA at 60 °C in 1 M NaCl and synthetic OPA PW (pH = 7.6, I = 0.4 M), two cylinders of intact OPA were prepared and installed in stainless steel diffusion cells so that the direction of transport (diffusion) was perpendicular to the bedding. The diffusion experiments were performed as described before. Both clays were

characterized after 5 weeks of preconditioning with the background electrolyte by through-diffusions of HTO and $^{22}Na^{+}$. The resulting diffusion parameters (D_e, ε, and α) for HTO and $^{22}Na^{+}$ are summarized in Table 8.

Table 8: Diffusion parameters (D_e, ε) for HTO and (D_e, α, and K_d) for $^{22}Na^{+}$ in OPA obtained by through-diffusion experiments at 60 °C in 1 M NaCl (cell 3) and OPA PW (cell 4) as background electrolyte at pH 7.6 under ambient air.

	HTO		**$^{22}Na^{+}$**		
	ε	D_e / 10^{-11} m^2/s	α	D_e / 10^{-11} m^2/s	K_d / L/kg
1 M NaCl, 60 °C	0.21 ± 0.01	4.1 ± 0.2	0.37 ± 0.01	4.4 ± 0.1	0.07 ± 0.01
1 M NaCl, 24 °C	0.18 ± 0.01	1.9 ± 0.1	0.35 ± 0.02	1.6 ± 0.1	0.10 ± 0.01
OPA PW, 60 °C	0.16 ± 0.01	3.4 ± 0.2	0.42 ± 0.01	3.0 ± 0.1	0.11 ± 0.01
OPA PW, 24 °C [36]	0.15 ± 0.01	1.5 ± 0.1	0.50 ± 0.02	1.9 ± 0.1	0.15 ± 0.03

As it is well known that molecular diffusion is temperature dependent, the dependence of diffusion coefficient on temperature can de described by the Arrhenius activation energy (eq. 5) [44].

$$D = A \cdot e^{\frac{-E_A}{R \cdot T}} , \quad (5)$$

where D (m^2/s) is the diffusion coefficient, A (m^2/s) Arrhenius parameter, E_A (kJ/mol) the activation energy, R (8.314 J/mol·K) gas constant, and T (K) absolute temperature. The activation energy of the self-diffusion of HTO in OPA was ~20 kJ/mol [37]. The diffusion coefficient of HTO in OPA at 65 °C was ~3.7 × 10^{-11} m^2/s. This is a factor of ~2.5 higher than the value measured at room temperature (25 °C, 1.4 × 10^{-11} m^2/s).

Our diffusion results in dependence of temperature show, as expected, that the D_e value increases with increasing temperature and agrees well with Appelo et al. [45]. In the case of D_e for HTO and $^{22}Na^{+}$ in 1 M NaCl solution, an increase by a factor of 2.2 and 2.8 with the temperature is observed, respectively, while ε and α remain similar for both radiotracers. In

OPA PW the obtained D_e value for HTO increases by a factor of 2.3 when rising the temperature to 60 °C. The diffusion of $^{22}Na^+$ is also significantly affected by the temperature with an increasing D_e by a factor of about 1.6 with increasing temperature. The determined activation energies for the diffusion of HTO were 18.7 kJ/mol and 17.6 kJ/mol in OPA PW and 1 M NaCl, respectively. These values agree with the activation energy determined by Van Loon et al. for HTO in OPA PW (20 kJ/mol) [37]. The calculated K_d values of $^{22}Na^+$ at both temperatures were constant within the experimental errors, indicating temperature independency.

After the complete out-diffusion of HTO and $^{22}Na^+$, the in-diffusion experiments with 8 µM Np(V) were started. The contact times with Np were 67 and 40 d for OPA PW and 1 M NaCl solution as background electrolytes, respectively. About 20 h before the end of the experiments, $^{22}Na^+$ was added to the reservoirs containing Np to determine the diffusion and distribution coefficients for $^{22}Na^+$ as well. Figure 20 shows the diffusion profiles of Np(V) at room temperature and 60 °C in 1 M NaCl together with the best fit curves.

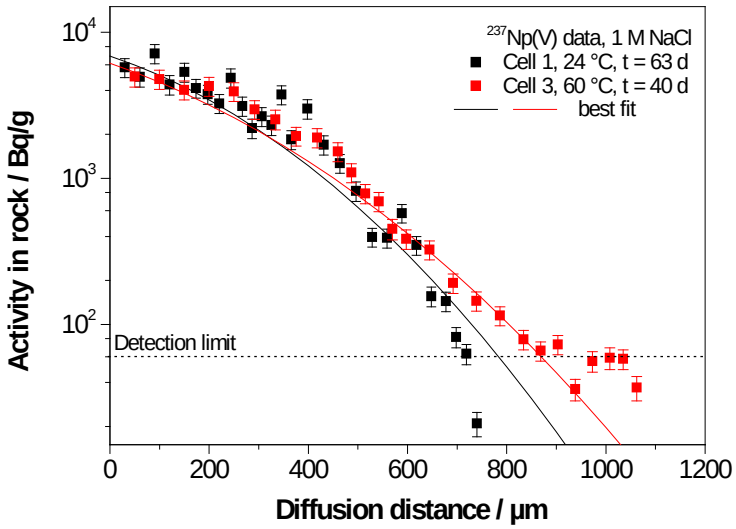

Figure 20: Diffusion profiles of 8 × 10^{-6} M ^{237}Np(V) in OPA (cells 1 and 3) at 24 °C and 60 °C in 1 M NaCl at pH 7.6 under aerobic conditions together with the fit curves.

As one can see, the diffusion depth of Np increases from 740 µm at 24 °C to 900 µm at 60 °C, whereas the diffusion time of cell 3 is about 33% lower than in cell 1. This much faster diffusion is reflected by the more than twice as high D_e value for Np at 60 °C in 1 M NaCl, while the K_d stays the same (Table 9).

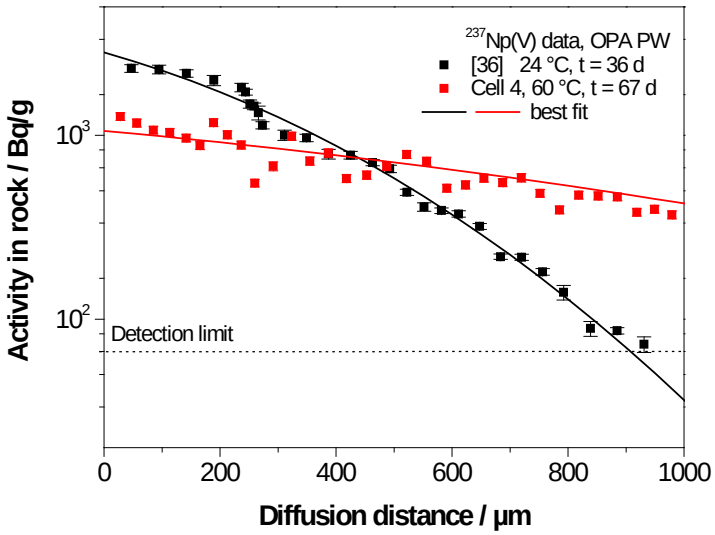

Figure 21: Diffusion profiles of 8 × 10^{-6} M ^{237}Np(V) in OPA at 24 °C [36] and 60 °C in OPA PW at pH 7.6 (cell 4) under aerobic conditions together with the fit curves.

As can be seen in Figure 21 the concentration profile of ^{237}Np(V) in the clay shows faster diffusion at higher temperature. The diffusion distance for Np(V) at 60 °C exceeds 1 mm in 67 d and the curve is very flat due to the rapid diffusion. The parameters used to fit the experimental data are summarized in Table 9. For the diffusion of Np(V) in OPA PW a small decrease of the log K_d value with temperature was observed. In case of 1 M NaCl, the log K_d values for Np(V) did not show any temperature dependence. This agrees with the results from the corresponding batch experiment (section 2.1).

Table 9: Diffusion parameters (D_e, α, and K_d) for ^{237}Np and $^{22}Na^+$ in OPA (cell 1, 3, and 4) obtained by in-diffusion experiments at 60 °C and 24 °C in 1 M NaCl and OPA PW at pH 7.6 under ambient air.

Cell	^{237}Np(V)			$^{22}Na^+$		
	α	D_e / 10^{-12} m^2/s	log K_d / L/kg	α	D_e / 10^{-11} m^2/s	K_d / L/kg
1 M NaCl, 60 °C	834 ± 8	17.5 ± 1.8	2.5 ± 0.1	0.43 ± 0.004	1.8 ± 0.2	0.10 ± 0.01
1 M NaCl, 24 °C	742 ± 9	6.9 ± 1.2	2.5 ± 0.1	0.46 ± 0.010	1.6 ± 0.1	0.12 ± 0.01
OPA PW, 60 °C	66 ± 2	15.0 ± 1.6	1.5 ± 0.1	0.39 ± 0.004	3.1 ± 0.3	0.09 ± 0.07
OPA PW, 24 °C [36]	243 ± 4	6.9 ± 1.1	2.0 ± 0.1	0.44 ± 0.03	1.8 ± 0.2	0.14 ± 0.01

* Values obtained by batch experiments

4 Speciation of Np and Pu after interaction with Opalinus Clay

4.1 Speciation of Np and Pu after diffusion using synchrotron based techniques

The samples of Np and Pu were measured at the Swiss Light Source (SLS) at the Paul Scherrer Institute (PSI) in Switzerland. The facility and specific parameters of the measurements are summarized in the Appendix.

4.1.1 Experimental

Sample preparation for XAS measurements

The used setup for the Np diffusion experiments is described in section 3.1. The bore cores were conditioned with OPA pore water (pH 7.6) and 1 M NaCl as mobile phases and were contacted with 8 µM Np(V). After the termination of the diffusion process, each bore core was cleaved along the axis of diffusion.

In contrast to the described procedure in section 3.1, the diffusion experiment with Pu was performed in a diffusion cell without stainless steel filters to avoid sorption of Pu on the filters and the bore core was embedded in epoxy resin. The diffusion experiments were performed under ambient-air conditions with synthetic OPA pore water (pH 7.6) as mobile phase. This pore water was prepared as described by Pearson et al. [2], with the exception that no Sr was added to avoid spectroscopic interferences with Pu in the measurements later on. The total concentration of Pu(V) in the primary reservoir (110 mL volume) was 2×10^{-5} M. The cross section of the clay that was in contact with the pore water was $10 \times 13\ mm^2$ in size. The thickness of the sample, i.e., the length of the diffusion path was 10 mm. After 26 d the diffusion experiment was stopped. Two clay samples were prepared for speciation investigations: Sample Pu-1 represents the $10 \times 13\ mm^2$ surface that had been in direct contact with the Pu(V) solution for 26 d. To follow the diffusion path of Pu inside the clay, sample Pu-2 was prepared by cleaving the clay stone along its bedding.

4.1.2 Speciation of Np after diffusion in Opalinus Clay

The primary intension of the following study was to get information for the migration modeling in argillaceous rock by the combination of the synchrotron-based microscopic methods µ-XRF, µ-XRD and µ-XANES applied on a time series of Np diffusion profiles, revealing the Np diffusion pattern simultaneously with the local Np speciation in a chemical image. The data were collected from three samples at the microXAS beamline at the SLS (PSI, Switzerland) using the experimental setup and data analysis tools as described in the Appendix. Details on the specific samples are given in Table 10.

Table 10: Description of the diffusion samples, contacted with 8×10^{-6} M Np(V) and diffusion parallel to the bedding.

Sample	**Np-1**	**Np-2**	**Np-3**
Background electrolyte	OPA PW (I = 0.4 M)	1 M NaCl	OPA PW (I = 0.4 M)
pH	7.6	8.1	7.6
Diffusion time / days	61	61	83
Porosity	0.11	0.13	0.14

The diffusion of 8×10^{-6} M Np(V) in OPA was investigated in dependency of time (61 d and 82 d) and salinity (OPA pore water without Sr^{2+} at pH 7.6 and 1 M NaCl solution at pH 8.1 equilibrated over $CaCO_{3(s)}$ to prevent dissolutions of the OPA). The three samples and their untreated, smooth surfaces can be seen in Figure 22. The black arrows start at the interface on the left which has been contacted with Np and point in the direction of diffusion.

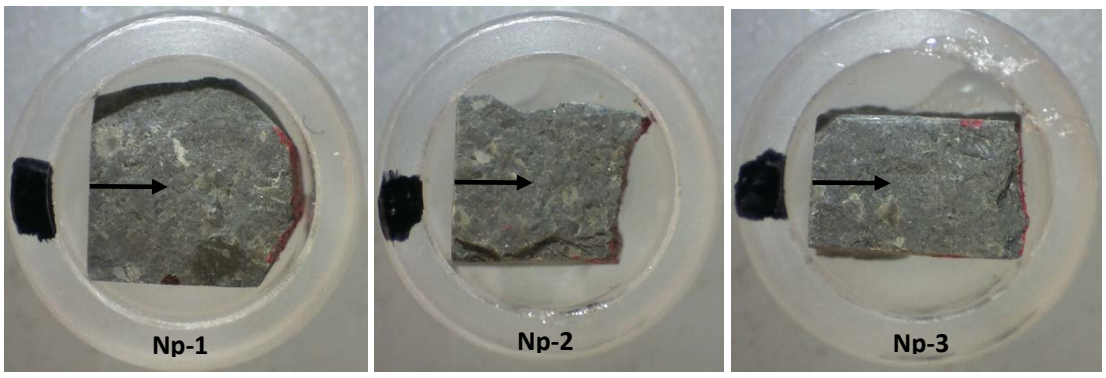

Figure 22: The samples are mounted on the beamline sample holders. The arrows point in the direction of diffusion.

As described in the Appendix several fluorescence lines of elements contained in OPA were simultaneously measured, from which Ca, Fe, S, and Si are shown in Figure 23 to display the heterogeneity of the prepared samples.

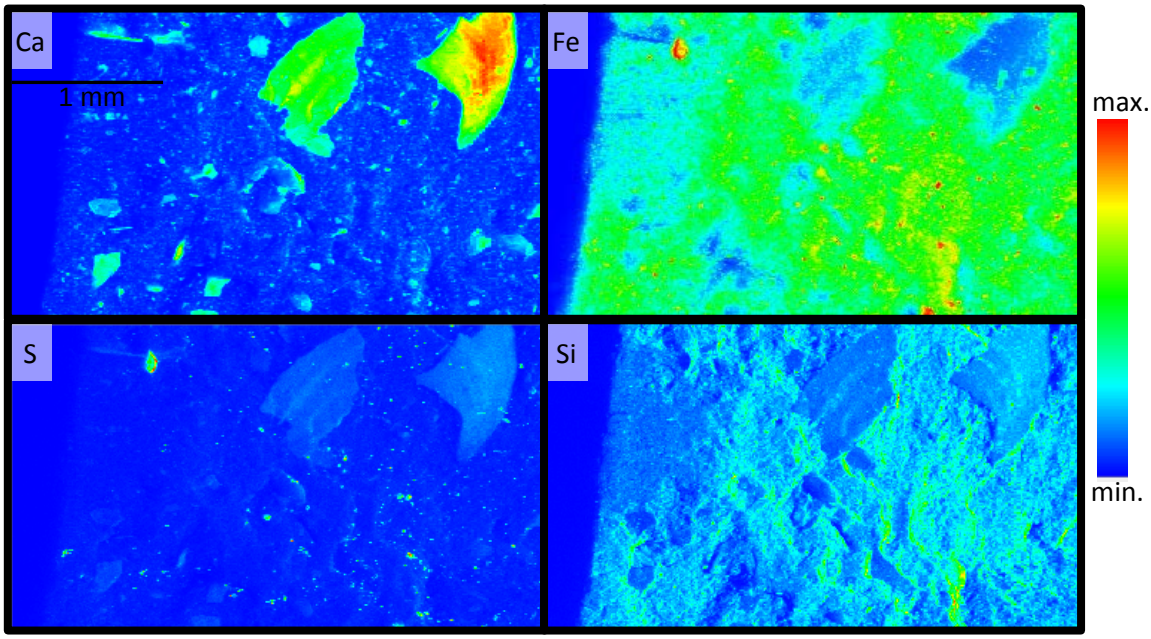

Figure 23: µ-XRF mappings of Ca, Fe, S, and Si of sample Np-3 with a mapping size of 3.5 × 2.0 mm^2 and an excitation energy of 17620 eV.

An exemplary µ-XRF mapping of a Np diffusion profile calculated from the contrast-edge method is shown in Figure 24 for sample Np-3 (83 d diffusion). As one can see, the average diffusion profile on the right side of the figure reaches background level at approximately 2.4 mm.

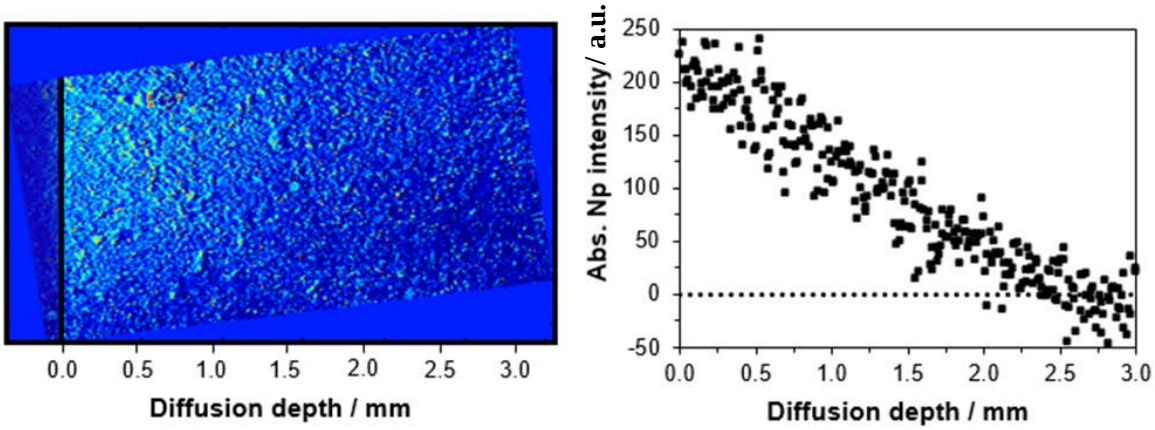

Figure 24: On the left can be seen the Np diffusion profile of sample Np-3 calculated by the edge-contrast method with the corresponding averaged diffusion profile on the right side.

If one compares the three diffusion profiles in Figure 25, one can see that the green profile of Np-2 varies widely from the others. It shows with 0.7 mm diffusion depth in 62 d compared to 1.5 mm (Np-1, 62 d, black) and 2.4 mm (Np-3, 83 d, red) the shortest diffusion depth and the highest absolute Np intensity at the interface. This can be explained by two different effects. Even though the synthetic OPA pore water (I = 0.4 M) has a lower ionic strength, it contains besides Na^+ also divalent cations such as Mg^{2+} and Ca^{2+}. These divalent cations are sorbing stronger at the clay surface than the NpO_2^+ and compete for surface sites. Our related batch experiments have also shown that higher NaCl concentrations have only a negligible influence on the sorption of Np(V) on OPA, as described in section 2.1. The second effect, which also amplifies the first one, is the influence of the slightly shifted pH for the sample Np-3 with pH 8.1 compared to pH 7.6 of the others, so that more Np(V) from the reservoir can sorb on the stronger deprotonated clay surface. The time depending diffusion experiment shows an increased diffusion depth with 2.4 mm after 83 d compared to 1.5 mm after 62 d.

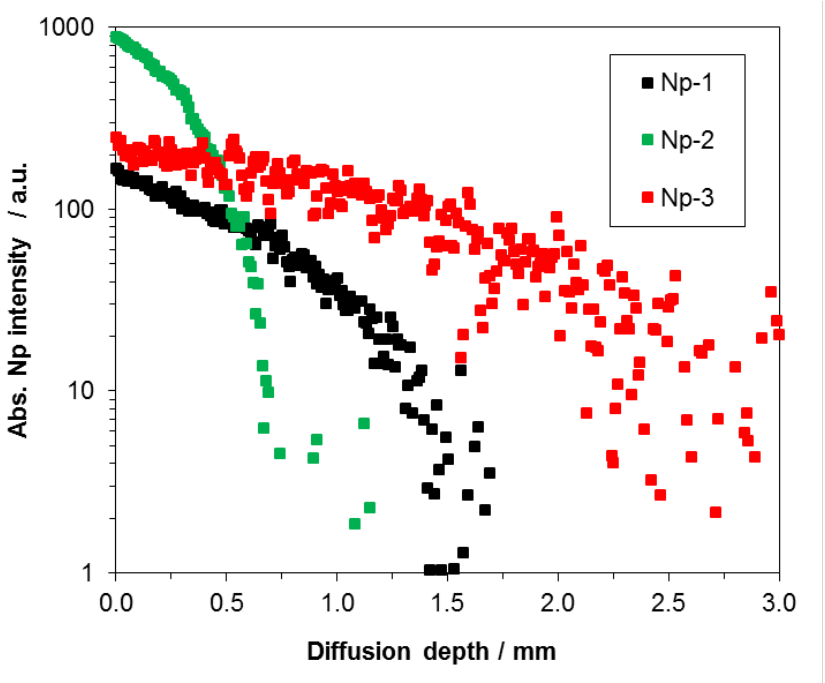

Figure 25: Diffusion profiles of the samples Np-1, -2, and -3 in absolute intensities.

The successive reduction of Np(V) by the inner redox potential of the OPA can be seen in the normalized Np L_{III}-edge µ-XANES spectra in Figure 26. The Np(IV) ratios have been calculated by linear combination fitting (LCF) with the program ATHENA using Np(V) and Np(IV) reference spectra from aqueous solution [46]. Due to the low Np concentration 10–20 scans were combined for each µ-XANES spectrum. At the interface of the clay, no Np(IV) was determined, which can be explained by the fact that Np(V) was initially used in the

experiment. This means that only the specific redox potential inside the OPA was capable to initialize the reduction. 30 µm behind the interface (A1) 12% and at 525 µm (A2) 26% Np(IV) was found. The µ-XANES spectrum in spot B was measured near a pyrite hot spot of sample Np-3 and shows almost 77% of Np(IV), which underlines the relevance of redox active minerals contained in OPA. Figure 27 includes all µ-XANES spectra of samples Np-1 and Np-3 included into the diagram of absolute Np intensities, showing which part of the absolute Np intensity comes from the Np(IV) species. This data presentation reveals the reduction and progression of Np(V) more than the separate presentation of the Np(IV) ratios and diffusion profiles as both are related to each other. Furthermore the change of the absolute fraction of Np(IV) becomes more visible. For the sample Np-1 several µ-XANES spectra were taken at the first 150 µm, indicating a stepwise increase of the Np(IV) ratio in this area. This may suggest a small redox potential gradient behind the interface as the *Eh* of the background electrolyte and the OPA are not in equilibrium.

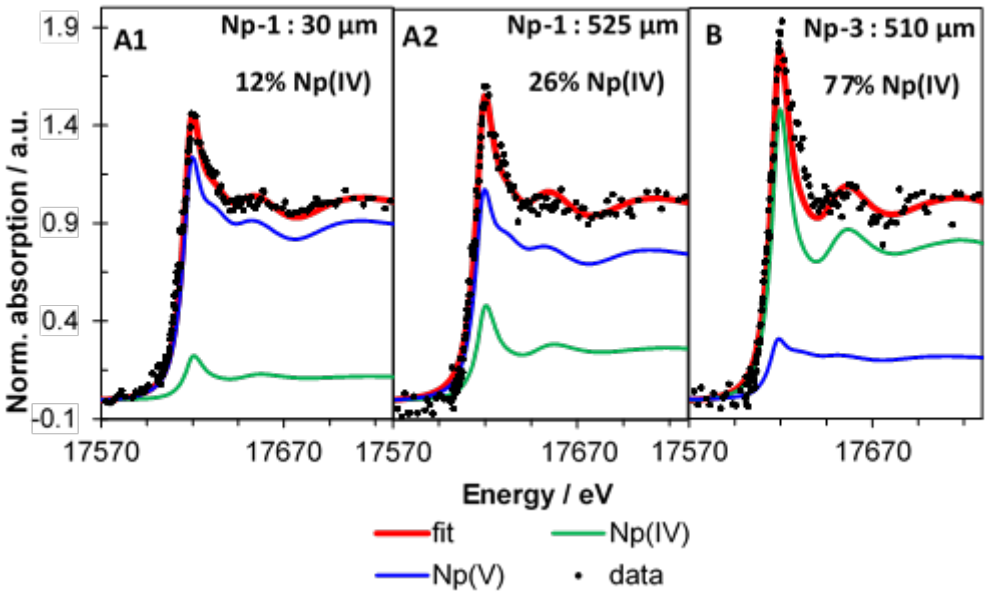

Figure 26: Normalized Np L_{III}-edge µ-XANES spectra at different spots.

All results of the µ-XANES measurements are shown in Table 11. Note that spots at equal distance can differ regarding the width of the sample.

Table 11: Np(IV) ratios from LCF for Np-1,-2, and -3 in dependency of the diffusion distance**.** The average error was 5%.

Np-1		Np-2		Np-3	
Diffusion depth / µm	**Np(IV) ratio**	**Diffusion depth / µm**	**Np(IV) ratio**	**Diffusion depth / µm**	**Np(IV) ratio**
25	0%	300	15%	26	0%
30	12%	311	45%	226	28%
75	13%	495	45%	476	77%
78	12%			999	25%
105	22%			1310	39%
117	21%				
144	23%				
175	75%				
425	83%				
525	26%				
675	45%				
925	61%				

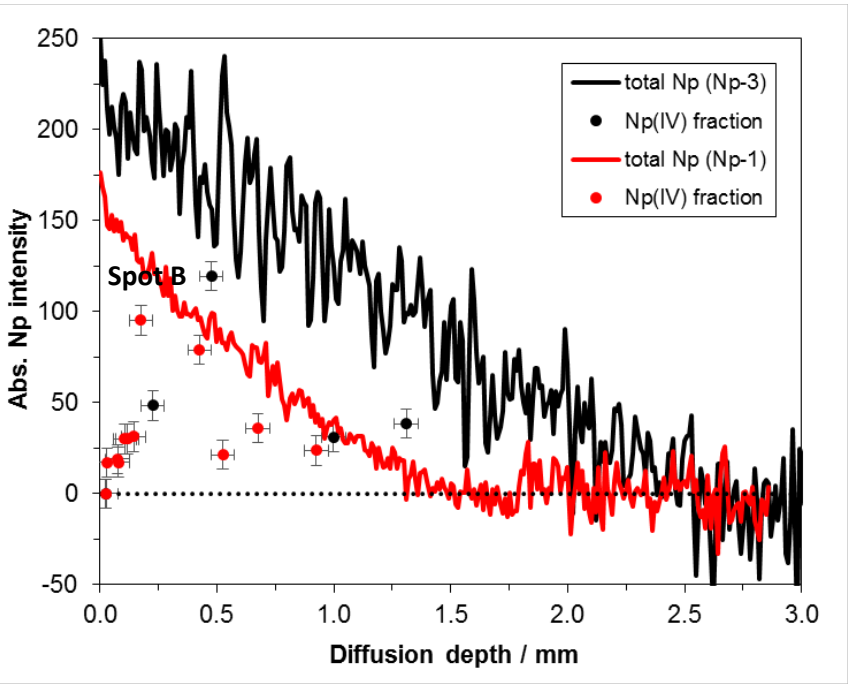

Figure 27: Diffusion profiles of samples Np-1 and Np-3 with the respective Np(IV) contribution to the absolute Np intensities.

For the certain identification of the Fe phase at spot B a maximum resolution µ-XRF mapping and an additional µ-XRD mapping were done, which give proof of the presence of pyrite, as

can be seen in Figure 28. However, on the pyrite particle itself was found less Np, but some Np hot spots were found beside it.

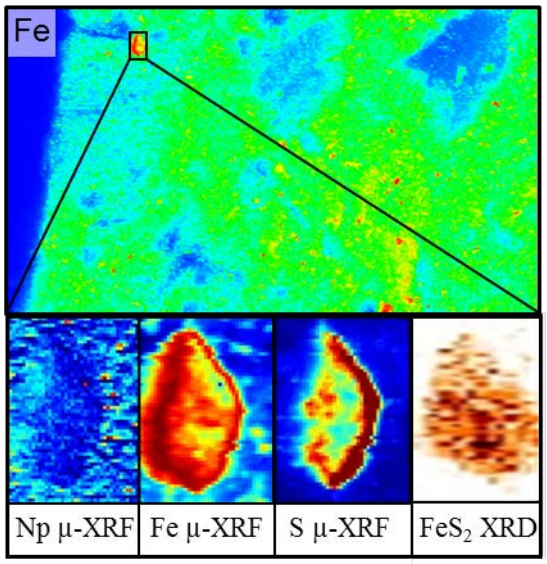

Figure 28: The Fe µ-XRF mapping of sample Np-3 on the top has been investigated further with an additional high-resolution µ-XRF mapping (120 × 170 µm^2; step size and a beam size of 5 µm) and a µ-XRD mapping (right). The µ-XRD mapping (X-ray energy 17.62 keV) has been calculated by taking the reflexes around the ROI at 2Θ = 24.5° which can be seen in Figure 29.

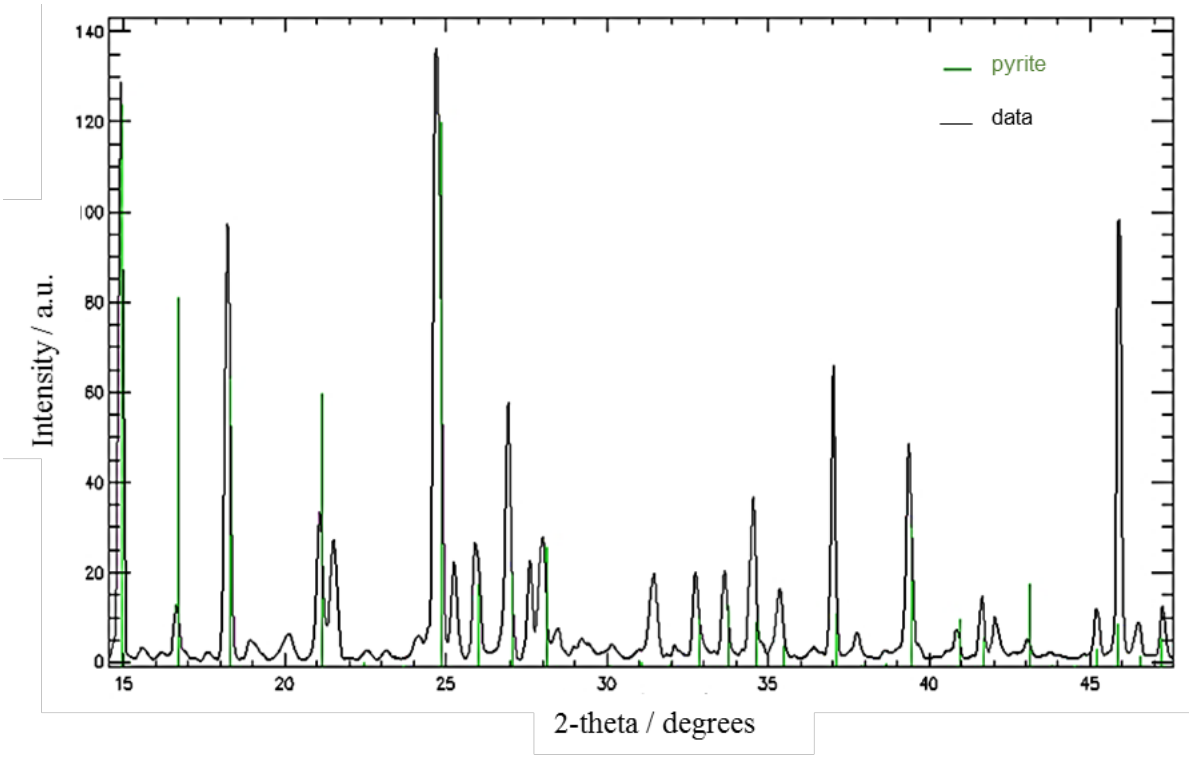

Figure 29: Diffractogram taken from the µ-XRD mapping shown in Figure 28. The green lines represent the reference reflexes of pyrite (PDF 03-065-1211).

In summary, we found a strong effect of the background electrolyte on the diffusion of Np(V). The time depending diffusion experiment in combination with the µ-XANES data might give the chance for a better modelling of the coupled transport reaction process of the diffusion of Np(V) in OPA.

4.1.3 Speciation of Pu after diffusion in Opalinus Clay

Sorption and diffusion are important processes determining the transport of radioactive contaminants in argillaceous rocks. The migration behavior of the redox-sensitive element Pu is governed by its oxidation state, which depends on pH, redox potential, ligand concentration etc. In this study the interaction of mobile Pu(V) with OPA during sorption and diffusion was investigated, and the Pu speciation was determined by synchrotron-based µ-XRF and µ-XAFS.

As described in Section 4.1.1, two clay samples were prepared for speciation investigations: Sample Pu-1 represents the $10 \times 13\ mm^2$ surface that had been in direct contact with 2×10^{-5} M Pu(V) in OPA pore water (pH 7.6) during the diffusion experiment for 26 days. To follow the diffusion path of Pu inside the clay, sample Pu-2 was prepared by cleaving the clay stone along its bedding.

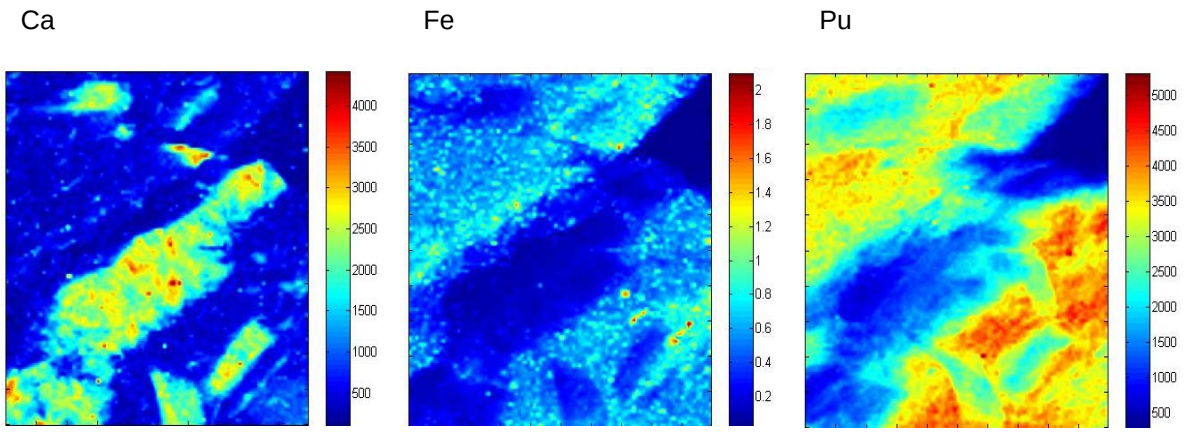

Figure 30: µ-XRF mappings of Ca, Fe, and Pu (from left to right) of sample Pu-1: $1 \times 1\ mm^2$, step size: 10 µm, excitation energy at 18067 eV.

Figure 30 shows the µ-XRF mappings ($1 \times 1\ mm^2$) of the elements Ca, Fe, and Pu of sample Pu-1, i.e., the clay surface where Pu could be sorbed due to the contact with the Pu(V) pore

water solution. All three elements show a heterogeneous spatial distribution. Areas with higher Ca concentration – indicating calcite occurrences – have lower Fe concentration and vice versa. As can be seen in Figure 30, Pu prefers to accumulate in areas with higher Fe than Ca concentrations. Figure 31 shows a Pu L_{III}-edge XANES spectrum that is representative for the Pu spectra measured in areas with higher Fe and Pu concentrations. This XANES spectrum was fitted with a linear combination of $Pu(III)_{(aq)}$, $Pu(IV)_{(aq)}$, and $Pu(V)_{(aq)}$ reference spectra (courtesy of Ch. Den Auwer, CEA, Marcoule, France). The measured Pu XANES spectrum could be modeled with 30 ± 2% Pu(III), 50 ± 3% Pu(IV), and 20 ± 2% Pu(V).

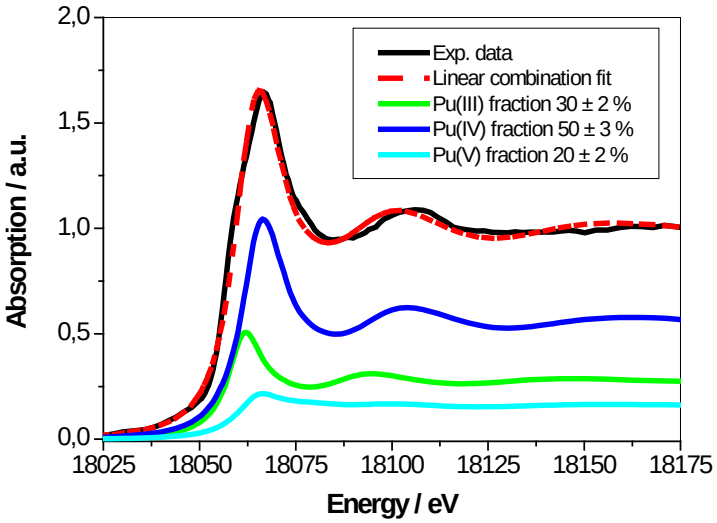

Figure 31: Pu L_{III}-edge µ-XANES spectrum at the clay-water interface (sample Pu-1).

This result shows that at least part of the dissolved Pu(V) has been reduced during the contact with the clay surface over a period of 26 d. From batch sorption experiments it is known that at pH 7.6 the sorption on OPA is strongest for Pu(III) and Pu(IV) and significantly less for Pu(V) [47]. This explains why Pu(IV) and Pu(III) are the dominating species at the clay surface, although Pu(V) is the dominating aqueous species in the OPA pore water at pH 7.6.

To follow the diffusion of Pu inside the clay rock, sample Pu-2 was studied by µ-XRF and Pu L_{III}-edge XAFS spectroscopy. The µ-XRF mappings (1×1 mm^2) of the elements Ca and Fe show again the natural heterogeneity of the clay (Figure 32). The µ-XRF mapping of Pu (Figure ***32***) shows that Pu diffused approximately 350 µm into OPA within 26 days. Pu L_{III}-edge XANES spectra were measured along a 300 µm long diffusion path in steps of 50 µm. The corresponding Pu XANES spectra were fitted with a linear combination of the

$Pu(III)_{(aq)}$, $Pu(IV)_{(aq)}$, and $Pu(V)_{(aq)}$ reference spectra. The fit results are summarized in Table 12.

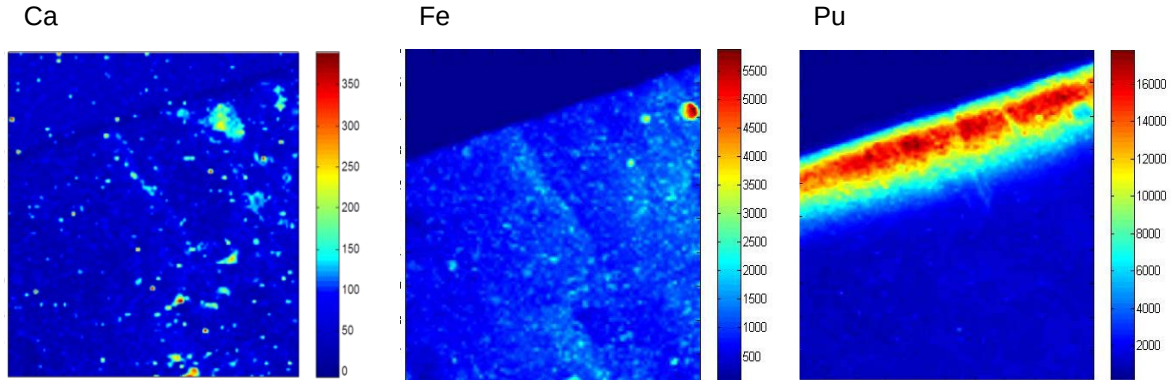

Figure 32: µ-XRF mappings of Ca, Fe, and Pu (from left to right) of sample Pu-2: 1 × 1 mm^2, step size: 10 µm, excitation energy at 18067 eV.

At the beginning of the diffusion path, the speciation of Pu consists of 27 ± 2% Pu(III), 43 ± 2% Pu(IV), and 30 ± 2% Pu(V). As expected, this Pu species distribution is similar to that observed at the clay surface (sample Pu-1). As one can see in Table 12, the relative amount of Pu(V) decreases and the relative amount of Pu(IV) increases with increasing diffusion length. The amount of Pu(III) is constant (22–32%) across the entire diffusion path from 0 to 300 µm. It can be concluded that the properties of OPA, e.g., the presence of Fe(II)-containing minerals (pyrite, siderite), cause a progressive reduction of Pu(V) during its diffusion and the retention of the reduced species as Pu(IV).

Table 12: Fractions of Pu(III), Pu(IV), and Pu(V) in percent derived from Pu L_{III}-edge XANES measurements at different diffusion distances (sample Pu-2).

Distance / µm	Pu(III)	Pu(IV)	Pu(V)
0	27 ± 2	43 ± 2	30 ± 2
50	22 ± 2	47 ± 3	31 ± 3
100	24 ± 2	48 ± 3	28 ± 3
150	22 ± 2	53 ± 3	25 ± 3
200	25 ± 2	66 ± 3	9 ± 4
250	32 ± 3	68 ± 4	0
300	30 ± 3	70 ± 5	0

The speciation of Pu was probed at another spot at a diffusion distance of 200 µm by Pu L_{III}-edge XANES and EXAFS spectroscopy (Figure 33 and Figure 34). The Pu XANES spectrums shown in Figure 33 could be modeled with 33 ± 2% Pu(III) and 67 ± 2% Pu(IV), confirming Pu(IV) as the dominating species inside the clay rock. The average Pu-O distance measured by EXAFS equals 2.34 ± 0.02 Å. For comparison, the Pu-O bond distances for Pu(III) and Pu(IV) are 2.48–2.51 Å [48, 49] and 2.39 Å [49], respectively. It can be concluded that both XANES and EXAFS measurements confirm that Pu(IV) is the main species at diffusion distances ≥ 200 µm.

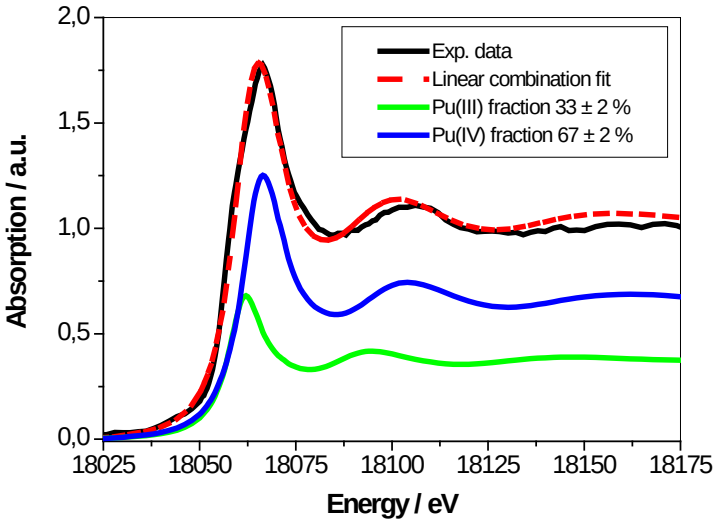

Figure 33: Pu L_{III} edge µ-XANES spectrum at 200 µm diffusion depth (sample Pu-2).

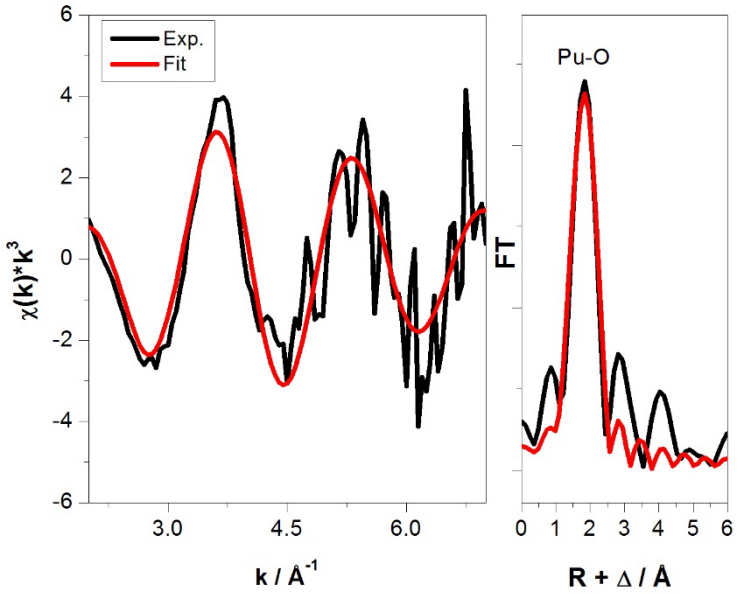

Figure 34: Pu L_{III}-edge µ-EXAFS spectrum (left) and corresponding Fourier transform magnitude (right) at 200 µm diffusion depth (sample Pu-2).

In summary, the spatially-resolved microprobe studies of Pu(V) diffusion in Opalinus Clay show for the first time that the speciation of Pu changes along its diffusion path due to progressive reduction. At the beginning of the diffusion path, i.e., at the interface between the clay and the Pu(V) containing pore water, the species distribution is approximately 30% Pu(III), 50% Pu(IV), and 20% Pu(V). Already after a short diffusion length of ca. 200 µm, Pu(V) is completely reduced to approximately 70% Pu(IV) and 30% Pu(III). One can expect that Pu is highly immobile in Opalinus Clay due to redox reactions of Pu inside the clay rock, the stronger retention of Pu(III) and Pu(IV) on clay surfaces compared to Pu(V), and the low solubility of Pu(IV).

4.2 Speciation of actinides with CE-ICP-MS

The determination of the speciation of actinides under environmental conditions in a deep geological repository needs an effective and highly sensitive analytical method which can be achieved by coupling capillary electrophoresis (CE) with inductively coupled plasma mass spectrometry (ICP-MS). With this setup, separation of different species can be achieved within 20 minutes with limits of detection of approximately 1×10^{-9} M [50].

CE-ICP-MS was used to determine the electrophoretic mobilities of different actinide species and furthermore, to investigate the species in the supernatant solution from batch experiments with Pu(III).

4.2.1 General procedures of CE-ICP-MS and sample preparation

The principle of separating different species in capillary electrophoresis is the differing velocity of migration of the ions in solution in an applied electric field. The velocity of a specific ion in turn depends on the applied electric field strength E and its electrophoretic mobility μ_e, which is a characteristic feature of the ion in a given medium and depends on the electric charge q of the ion and on its ionic radius r. As can be seen in equation (6), μ_e rises, which means that the ion moves faster, with a smaller radius and a higher charge.

$$\mu_e = \frac{q}{6\pi\eta r}. \tag{6}$$

To compare the results of different measurements or different CE-ICP-MS systems, one has to refer the migration times of the investigated ions to the velocity of the so called electroosmotic flow (EOF). The EOF describes the flow of the whole liquid inside the capillary in the electric field and overlies the migration of the ions, but does not lead to an additional separation. Because small, neutral species only migrate with the EOF, such molecules can be used to determine the EOF migration time t_{EOF} and are called EOF marker.

The electrophoretic mobility of the different species μ_i can then be calculated from the determined migration time of an ion t_i via equation (7) taking into account different capillary lengths l_K and the applied high voltage U, as well as the influence of the EOF.

$$\mu_i = \frac{l_K^2}{U}\left(\frac{1}{t_i} - \frac{1}{t_{EOF}}\right). \tag{7}$$

CE-ICP-MS setup

In our measurements we used an Agilent 7100 CE (Agilent Technologies, USA), equipped with fused silica capillaries (Polymicro Technologies, USA) with an inner diameter of 50 µm. As background electrolyte 1 M acetic acid was used. The samples were transferred to the

capillary via hydrodynamic injection, then the sample vials were replaced by a vial containing the background electrolyte and a high voltage of 25 kV was applied to start the separation.

After separation in the capillary the sample reaches the coupling device, consisting of a T-piece, leading the capillary as well as the make-up electrolyte supply into the nebulizer. The electric circuit between the two capillary ends is closed via the make-up electrolyte passing a tube shaped Pt-electrode. The electrolyte itself is introduced by a syringe pump (PicoPlus, Harvard Apparatus, USA) and consists of a 1.25% HNO_3 solution with 10% ethanol and 5 ppb ^{89}Y, ^{103}Rh, ^{140}Ce, and ^{209}Bi as internal standards. The nebulizer then generates an aerosol from the eluate, the make-up electrolyte and the nebulizer gas. This aerosol is introduced into a Scott-type spray chamber (AHF Analysentechnik, Germany) which removes bigger droplets. From the spray chamber, the aerosol is directly transferred to the ICP-MS system via an Ar-gas flow. To preserve the high resolution and separation capability of the CE, the transportation of the sample from the nebulizer tip into the ICP-MS system has to be efficient and fast.

Figure 35 shows the used setup for the coupling of the CE with the ICP-MS system (Agilent 7500 ce (Agilent Technologies, USA)) using a Mira Mist CE nebulizer (Burgener Research, Canada).

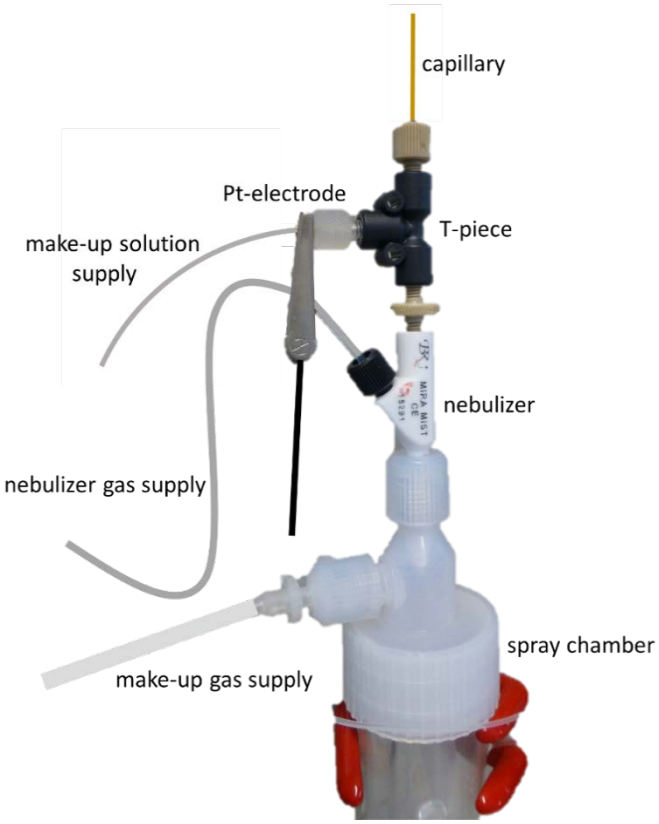

Figure 35: Coupling system between CE and ICP-MS.

The ICP-MS system itself is used as a highly sensitive detector for the arriving aerosol and is capable of simultaneous multi-element detection.

Sample preparation

CE-ICP-MS measurements were performed for Eu(III), Th(IV), U(IV/VI), Np(IV/V/VI), Pu(III/IV/V/VI), and Am(III) in 1 M HCl and 1 M $HClO_4$ solutions. Stock solutions of ^{153}Eu(III), ^{232}Th(IV), and ^{238}U(VI) were prepared from ICP-MS standard solutions, whereas the ^{238}U(IV) solution was gained by dissolving ^{238}U wires in 1 M HCl. The ^{237}Np(V) stock solution was prepared as described in the literature [19]. The ^{237}Np(IV) solution was prepared from the ^{237}Np(V) solution by chemical reduction with hydroxyl ammonium hydrochloride. The ^{237}Np(VI) solution as well as the ^{239}Pu(VI) solution were prepared from existing Np and Pu stock solutions by repeated evaporation with 1 M $HClO_4$ with a small amount of NaF to prevent colloid formation. Based on these, the tri-, tetra and pentavalent state solutions could be obtained by electrolytic reduction and oxidation. The ^{241}Am(III) was prepared from an existing ^{241}Am(III) solution by evaporation and dissolution in the required background electrolyte.

Because some of the prepared oxidation states were not stable under the used conditions, they had to be stabilized during sample preparation and CE-ICP-MS measurement. NaClO was added to the Np(VI) samples to ensure an oxidizing environment whereas the Pu(III) samples were supplemented with hydroxyl ammonium hydrochloride to generate a reducing environment. Both additives could stabilize the reactive oxidation states without inducing further complexation reactions [51].

The purity of the different oxidation states produced was controlled by UV-vis measurements. The concentrations of the prepared solutions were measured by liquid scintillation counting for Pu and by γ-ray spectroscopy for U, Np, and Am. The ICP-MS standard solutions were prepared with a concentration of $c = 5 \times 10^{-5}$ M. Already existing stock solutions were diluted to the same concentration, whereas stock solutions of less than 5×10^{-5} M were used in the available concentration.

Prior to their use in the CE-ICP-MS measurements, the solutions were filtered through 0.2 µm syringe filters (Nalgene, USA) to prevent clogging of the capillary. The samples for the CE-ICP-MS measurement itself were prepared by mixing 2 µL of the analyte solution with 198 µL 1 M acetic acid and 1 µL 2-bromopropane (EOF marker) in conical micro-inserts of borosilicate glass (Carl Roth AG, Switzerland). Therefore, the final sample concentration accounted to $c = 5 \times 10^{-7}$ M. The micro-inserts were placed in polyethylene vials and closed with polyethylene olefin snap caps (both Agilent Technologies, USA) to fit into the CE system.

The capillaries were preconditioned prior use by flushing them several times with MilliQ-water, 0.1 M NaOH solution, 0.1 M HCl, and 1 M acetic acid. Before each measurement, the capillary was flushed for 15 minutes with freshly prepared background electrolyte, which was 1 M acetic acid. The parameters used in the measurements are listed in Table 13.

Table 13: Parameters for the CE-ICP-MS system.

Capillary electrophoresis	
CE system	Agilent 7100 CE (Agilent Technologies)
CE voltage	25 kV
CE current	10–30 µA
CE capillary	fused-silica capillaries, inner diameter: 50 µm, length: 76 cm
sample introduction	hydrodynamic, 8 s with 100 mbar
CE background electrolyte	1 M acetic acid, pH 2.4
Coupling device	
nebulizer	Mira Mist CE
spray chamber	Scott-typ
make-up electrolyte	1.25% HNO_3 and 10% ethanol, 5 ppb Rh, Y, Bi, and Ce as internal standard, flow rate: 5 $\frac{\mu L}{min}$
carrier gas	Ar, flow rate: 0.86–1.15 $\frac{L}{min}$
make-up gas	Ar, flow rate: 0.28–0.77 $\frac{L}{min}$
ICP-MS	
ICP-MS system	Agilent 7500 ce (Agilent Technologies)
plasma power	1550 W
detection mode	time-resolved analysis
dwell time	100 ms

4.2.2 Mobility measurements of actinides in oxidation states III-VI

As described in section 4.2.1 a number of measurements was performed to determine the migration times of the different redox states of the elements mentioned above and to calculate their electrophoretic mobilities μ_e via equation (7). First, the mobilities of some redox-stable species were determined to ensure a clear assignment of the signals in the electropherograms to the different oxidation states of redox-sensitive elements such as Pu. The measured redox-stable species were Eu(III), Th(IV), Np(V), and U(VI).

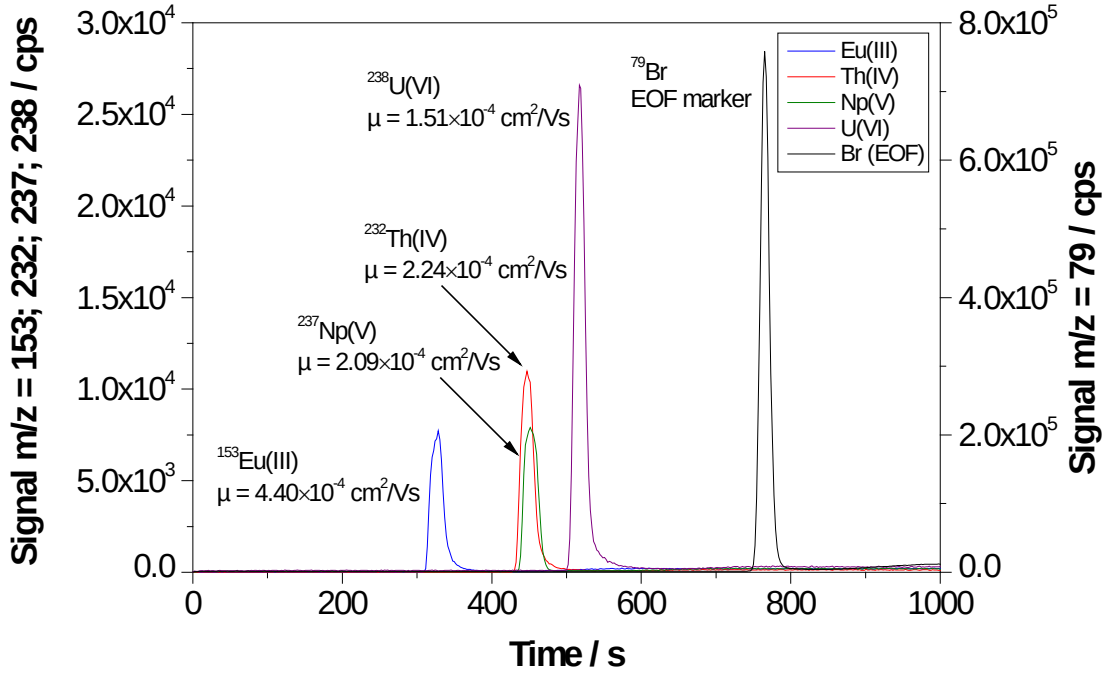

Figure 36: Electropherogram of the redox stable analogues with their electrophoretic mobilities in 1 M HCl.

Figure 36 shows an electropherogram of a sample containing the four redox analogues Eu(III), Th(IV), Np(V), and U(VI) (each 5×10^{-7} M) with their electrophoretic mobilities and the EOF signal in 1 M HCl.

To investigate the influence of a weak-complexing agent in comparison to a non-complexing agent on the electrophoretic mobility, such measurements were performed in 1 M HCl as well as in 1 M $HClO_4$. The average determined mobilities in both media for a series of measurements of the redox-stable species, including Am(III) are listed in Table 14.

Table 14: Electrophoretic mobilities of the redox-stable species in 1 M HCl and 1 M $HClO_4$.

Medium	Mobilities / $10^{-4}\,\frac{cm^2}{Vs}$				
	Eu(III)	Am(III)	Th(IV)	Np(V)	U(VI)
1 M $HClO_4$	4.27 ± 0.20	3.86 ± 0.10	2.18 ± 0.04	2.03 ± 0.08	1.48 ± 0.04
1 M HCl	4.40 ± 0.33	3.92 ± 0.03	2.24 ± 0.11	2.09 ± 0.14	1.51 ± 0.09

As one can see, the electrophoretic mobilities show the same values within their errors, seem independent from the medium under the used conditions. This can be explained by the fact that the stock solutions, no matter if in hydrochloric or perchloric medium, are diluted 1:100

in acetic acid during sample preparation, making acetic acid the only complexing agent influencing the electrophoretic mobility.

Furthermore, Figure 36 and Table 14 show that the retention times increase from Eu(III) over Am(III), Th(IV), and Np(V) to U(VI). This order does, in first sight, not match the expected order, indicating that the ion with the highest charge and the smallest radius shows the highest mobility.

To explain the determined order of elution, the exact speciation of the analytes has to be considered rather than just size and charge of the isolated ion. This means, that Np(V) and U(VI) exist in aqueous solution as neptunyl (NpO_2^+) and uranyl cation (UO_2^{2+}), respectively, lowering their effective charge, whereas Eu(III) and Th(IV) appear as the free ions Eu^{3+} and Th^{4+}. Additionally, one has to take into account the complexation behavior of the different ions. In this case the complexation with acetic acid causes a shielding of the surrounded cation and results in a lower effective charge being exposed to the applied electric field. Therefore, UO_2^{2+} seems to show a higher degree of complexation resulting in a compensation of its higher charge in comparison to the NpO_2^+ cation and hence a lower mobility. The same explanation can be transferred to the Eu^{3+}/Th^{4+} couple, a higher degree of complexation with acetic acid leads to a shielding of the charge of Th^{4+} and results in a lower electrophoretic mobility in comparison to Eu^{3+}.

Another point is the influence of the ionic radius: the smaller the ion, the faster its migration. Table 14 shows the electrophoretic mobilities of Eu(III), being a lanthanide, and Am(III), standing below Eu in the actinide series and consequently showing a higher ionic radius. Just as expected, the ion with the smaller ionic radius shows the higher electrophoretic mobility.

After the completion of measurements with redox-stable species, the different Pu oxidation states were under investigation, which were produced electrochemically in 1 M $HClO_4$. However, CE-ICP-MS measurements showed, that Pu(III) as well as Pu(V) were not stable during the measurements resulting in electropherograms showing signals of Pu(IV) and Pu(VI) caused by disproportionation and oxidation reactions. For the Pu(III) samples a stabilization was achieved by adding hydroxyl ammonium chloride, whereas Pu(V) could not be stabilized at all in 1 M $HClO_4$. Therefore, a Pu(VI) solution was allowed to stand in OPA pore water (pH 7.6) for several days resulting in a Pu(V) solution stable enough for CE-ICP-MS measurements. The composition of the pore water is described in the literature [2].

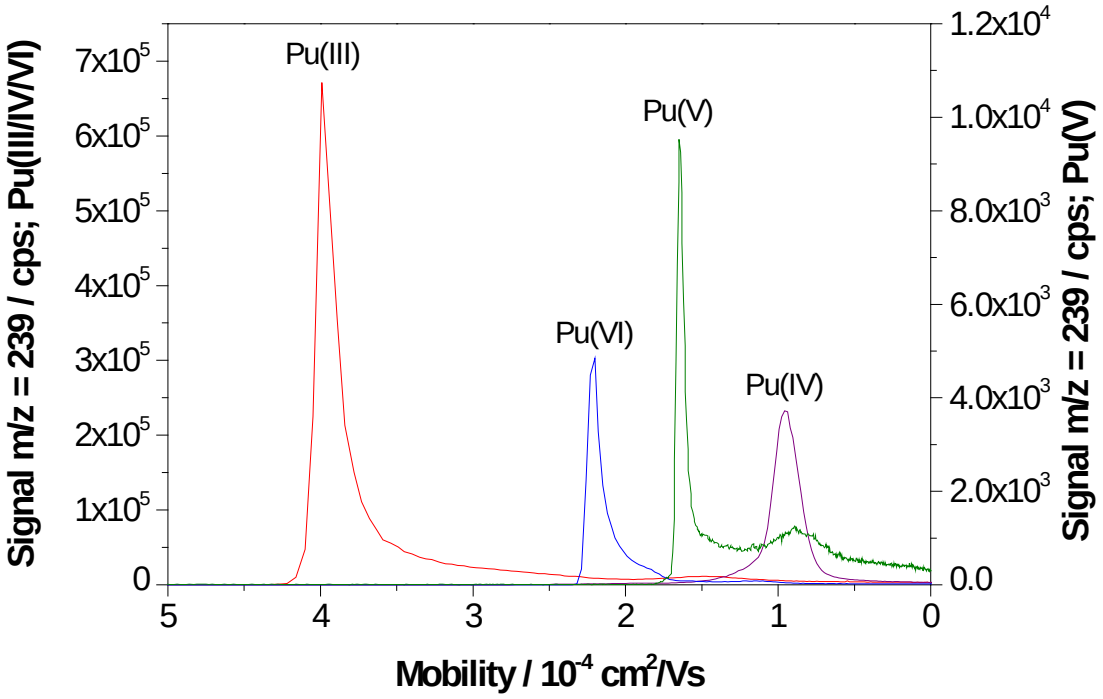

Figure 37: Electrophoretic mobilities of different Pu oxidation states in 1 M $HClO_4$ and OPA pore water.

In Figure 37 the data of different CE-ICP-MS measurements are plotted, showing the ICP-MS signals on the mass 239 as a function of the electrophoretic mobility which in turn was calculated from the determined migration times via equation (7). The figure shows that for the oxidation states +III, +IV, and +VI sharp single peaks were received, whereas the sample prepared in OPA pore water shows one clear peak with a mobility assigned to Pu(V) and one other but smaller peak with the mobility of Pu(IV). Even though we already changed the medium for the determination of the Pu(V) mobility, it was not possible to completely avoid further redox reactions.

The order of elution for the different Pu oxidation states is (Figure 37): First Pu(III) with the highest mobility, followed by Pu(VI), Pu(V), and finally Pu(IV) with the lowest electrophoretic mobility. In comparison to their redox stable analogues the +III oxidation state shows the highest mobility as well and the +V oxidation state is the third one in the order of elution, but the +IV and the +VI states are reversed. For Pu the +IV oxidation state is the one with the lowest mobility while Th(IV) shows a mobility even faster than the one of Np(V). This could be explained by the higher complexation constant for Pu(IV) with acetate ions [52] in comparison to Th(IV) [53], resulting in a better shielding of the charge of Pu(IV) and consequently leading to its lower electrophoretic mobility.

The determined electrophoretic mobilities of the different Pu oxidation states are listed in Table 15. Additionally, a number of literature data is shown in this table. As can be seen, the determined electrophoretic mobilities correspond well with literature data from [54] and [55]. While Graser et al. recently published values for the electrophoretic mobilities of the different Pu oxidation states, the measurements of Kuczewski et al. were performed without any EOF marker, as a result of which the concerning publication only showed migration times instead of mobilities. To gain the mobilities, we tried to calculate the retention time of a theoretical EOF marker by reading out the retention time of a Np(V) sample and count back to the EOF retention time by using the known electrophoretic mobility of Np(V). Assuming a constant retention time of the EOF for all measurements, the electrophoretic mobilities of all investigated species could be calculated. Considering the inaccurate reading of the retention times from the published electropherograms and the assumption of a constant EOF retention time, the values agree well with these from [55] and the present work.

Table 15: Electrophoretic mobilities of the Pu oxidation states and comparison with literature data.

Medium	Mobility / $10^{-4}\,\frac{\mathrm{cm}^2}{\mathrm{Vs}}$			
	Pu(III)	**Pu(IV)**	**Pu(V)**	**Pu(VI)**
1 M $HClO_4$	3.97 ± 0.04)	0.98 ± 0.07		2.22 ± 0.06
OPA pore water			1.65	
Literature	**Pu(III)**	**Pu(IV)**	**Pu(V)**	**Pu(VI)**
[54] *	3.85	0.82	1.69	2.10
[55]	4.0 ± 0.07	1.2 ± 0.08	1.6 ± 0.06	2.4 ± 0.08
[56] **			1.93 ± 0.12	
[57, 58] **			2.360–2.405	

* calculated from the electropherograms shown in the publication
** different pH-values and ionic strengths

The values for the electrophoretic mobility of Pu(V) from [56], [57], and [58], however, show the necessity of performing measurements under the same conditions such as pH value or ionic strength to get comparable data. In the present work, the pH value of the samples was 2.4 and the ionic strength I = 1.0 mol/L, whereas Topin et al. used variable pH values and lower ionic strengths, what apparently resulted in deviations of the electrophoretic mobilities.

After the determination of the different Pu mobilities, more oxidation states of Np and U were under investigation. All determined electrophoretic mobilities including those of Np(IV),

Np(VI), and U(IV) are listed in Table 16. The table shows that the order of elution for the oxidation states of one actinide seems to be always the same as given in (8).

$$\mu_e\big(An(III)\big) > \mu_e\big(An(VI)\big) > \mu_e\big(An(V)\big) > \mu_e\big(An(IV)\big)\,. \qquad (8)$$

The complete order can only be confirmed by the values for Pu, being the only element showing all four oxidation states during CE-ICP-MS measurements. However, the values for the electrophoretic mobilities of Np and U also fit in this order.

Table 16: Electrophoretic mobilities of Eu and the investigated actinides with their different oxidation states.

Element	Electrophoretic mobilities of the different oxidation states / $10^{-4}\,\frac{cm^2}{Vs}$			
	+III	**+IV**	**+V**	**+VI**
Eu	4.27	-	-	-
Th	-	2.18	-	-
U	-	0.34*	-	1.48
Np	-	1.42	2.03	2.60*
Pu	3.97	0.98	1.65	2.22
Am	3.86	-	-	-

*U(IV) and Np (VI) samples were prepared by mixing 2 µL analyte solution with 198 µL 1 M HCl and 1 M $HClO_4$, respectively, instead of acetic acid. BGE remains the same (1 M acetic acid).

In summary, a number of electrophoretic mobilities of different oxidation states of the actinides could be determined using CE-ICP-MS. The results provide a good basis for the identification of different species of the actinides in further investigations as for example in batch experiments.

4.2.3 Applicability of CE-ICP-MS to samples from batch experiments

After the determination of the mobilities of different actinide redox species, it was attempted to apply CE-ICP-MS on batch samples for the identification of the redox species in solution. Especially for the redox-sensitive element Pu, this would be an easy method to monitor the redox processes occurring in batch experiments.

In preparation for the measurements with the redox-sensitive Pu(III), the experiment was performed with samples containing redox-stable Eu(III), to test the applicability of CE-ICP-MS measurements on solutions from batch experiments.

Both batch series were prepared in 0.1 M NaCl solution under anaerobic conditions and with concentrations of $c = 5.0 \times 10^{-7}$ mol/L for Eu(III) and Pu(III). Each series contained four batch samples with pH 2, 4, 6, and 8. A detailed description of the procedure of the batch experiments is given in section 1.1.

For the following CE-ICP-MS measurements 200 µL of the supernatant solution of the Eu(III) and Pu(III) batch samples – after phase separation – were transferred into the CE sample vials and 1 µL 2-bromopropane was added as EOF marker. The settings for the measurements were just like the ones used before. Solutions for the background electrolyte and the flushing of the capillary were the same as described in section 4.2.1.

While the Eu and Pu concentrations in the supernatant solution of the samples with pH 6 and 8 were too low for CE-ICP-MS measurements due to high sorption of both elements on OPA under these conditions, the samples at pH 2 and 4 showed clear signals in the electropherograms.

For the first series with Eu(III) the calculated electrophoretic mobilities were $\mu_e = 3.8 \times 10^{-4}$ cm^2/Vs for the samples at pH 2 and 4. Using the results from section 4.2.2, this value can be assigned to the Eu(III) species. Thus, this first experiment showed that direct speciation from batch experiment solutions by CE-ICP-MS is in general possible.

On the basis of the results of the Eu series, the batch experiment with Pu(III) and the subsequent CE-ICP-MS measurements of the samples with pH 2 and 4 were performed.

The associated, calculated electrophoretic mobilities were $\mu_e = 0.9 \times 10^{-4}$ cm^2/Vs and $\mu_e = 0.8 \times 10^{-4}$ cm^2/Vs for the Pu samples at pH 2 and 4, respectively. Depending on the pH, the *Eh*, and the sorption values, this signal should originate from a Pu(III) species. Comparison with the determined electrophoretic mobilities of the different Pu species in section 4.2.2 however suggests that the peaks originate from a Pu(IV) species. This result is not necessarily evidence for the presence of Pu(IV) in the batch sample solution. As already shown in section 4.2.2, it is necessary to stabilize Pu(III) during the CE-ICP-MS measurement by adding a reducing agent. This clearly is not suitable when it comes to measurements directly after batch sorption experiments to determine the solution species in the supernatant without influencing the redox equilibrium under investigation.

These results suggest that, in general, direct determination of redox species in batch sample solutions by CE-ICP-MS measurements should be possible, but further investigations are necessary.

5 Sorption and speciation of Tc after interaction with Opalinus Clay

The radioactive isotope technetium (^{99}Tc) is a long-lived ($t_{1/2}$ = 2 × 14·10^5 a) and redox-sensitive fission product of ^{235}U and ^{239}Pu (yield ~6.13%) and contributes significantly to the radiotoxicity of spent nuclear fuel after storage times of more than thousand years [59]. In case of a leakage or corrosion of steel canisters in a repository, the geochemistry of Tc is determined by its oxidation state +IV and +VII. Under oxidizing conditions the speciation of Tc is dominated by the soluble pertechnetate anion (TcO_4^-), and under anoxic conditions by the sparingly soluble $TcO_2 \cdot nH_2O$ [60, 61]. The very mobile and almost non-sorbing TcO_4^- dominates the speciation of Tc over a wide range of pH and Eh and is considered as the most hazardous species. Accordingly, a detailed knowledge of the geochemical behavior of ^{99}Tc, including the different interaction processes with the surrounding host rock and the aquifer regulating the Tc retention (e.g., sorption, diffusion, solubility, complexation with (in)organic ligands), is indispensable for an accurate long-term safety assessment of a repository.

The aim of our study was to investigate the interaction of Tc with OPA as a reference material for natural clay by sorption and diffusion experiments under different experimental conditions such as pH, aerobic/anaerobic conditions and the influence of dissolved Fe(II). The influence of these parameters on the uptake or diffusion of Tc in OPA is quantified by the distribution coefficients (K_d) and diffusion parameters (D_e, ε, and α). Our batch and diffusion experiments were completed by synchrotron based X-ray absorption spectroscopy techniques to determine the speciation and structural parameters of Tc sorbed on OPA.

5.1 Sorption of Tc on Opalinus Clay

The sorption behavior of TcO_4^- on OPA was investigated in batch experiments using the same procedure as described in section 1.1 by varying different parameters such as pH (3–10), TcO_4^-concentration (4, 13 µM), solid-to-liquid-ratio (S/L = 15, 100 g/L), and contact time (7, 17 d) under aerobic conditions in synthetic OPA pore water as background electrolyte. Batch experiments were carried out with well characterized aerobic (BHE 24/1) dry powder of OPA [17]. Although the natural OPA pore water has a pH of 7.6 (I = 0.4 M), deviations from this value are possible in the near field of a repository. In order to determine the influence of pH on the sorption of TcO_4^-, batch experiments were carried out in the pH range of 3 to 10. In the first experiment, the clay suspensions (15 g/L) were contacted with 4 µM TcO_4^- for 3 d. Since low sorption values were obtained at pH 3 (K_d = 9.0 ± 1.0 L/kg), pH 4 (K_d = 3.8 ± 0.4 L/kg),

and no sorption was observed above pH 5, the experiment was repeated with a higher amount of OPA (100 g/L) contacted with a 13 µM TcO_4^- solution for 17 d. In this case the same trend was observed and the sorption decreased with increasing pH value (at pH 3: K_d = 3.6 ± 0.2 L/kg and at pH 4: K_d = 1.3 ± 0.1 L/kg). Again, no uptake was observed between pH 5–10. In both batch experiments the redox potential in the OPA pore water ranged between 570 mV (SHE) at pH 3 and 350 mV at pH 5, which is clearly in the stability field of TcO_4^- (Figure 38).

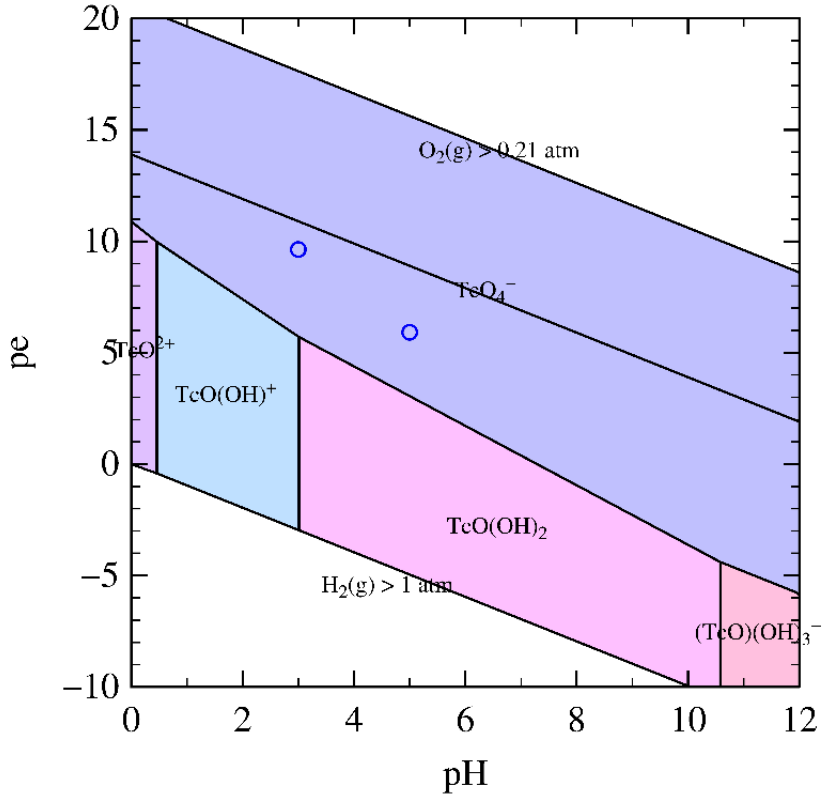

Figure 38: Calculated pe-pH diagram of 13 µM TcO_4^- in OPA pore water using PhreePlot v1.0 [31].

The same sorption behavior of Tc was found by Vinšová et al. [61], who showed that the sorption of TcO_4^- on natural bentonite clay decreases under aerobic conditions in the pH range of 2–5 (27–20%). At a pH value of 6 the sorption was below 10%. However, the retention of TcO_4^- on bentonite was overall very low (K_d ~1 L/kg). Also Palmer and Meyer [62] studied the sorption of Tc on several naturally occurring minerals. They found that sorption is very low under oxic conditions and that the K_d values are usually below 5 L/kg. The sorption behavior of anions on mineral surfaces can be explained as follows: at low pH values, the silanol and aluminol groups are protonated. Due to the positive charge on the mineral surface, the anions can adsorb there. With increasing pH and the resulting deprotonation and

formation of negative charge on the mineral surface, an electrostatic repulsion between the anions and the mineral surface arises and results in low sorption.

Influence of Fe(II) on the sorption of TcO_4^- on OPA under anaerobic conditions

Since the retention of 13 µM TcO_4^- on OPA in OPA pore water at pH ~7.8 under anaerobic conditions (glove box, $O_2 \leq 15$ ppm, *Eh* = 200 mV) was almost neglectable (sorption ≤ 7%) and independent of the OPA concentration (S/L = 2–20 g/L) and contact time (4–14 d), several additives, e.g., $FeCl_2$ and FeS were added to the OPA suspensions in order to investigate the influence of dissolved Fe(II). The chemical and mineralogical composition of OPA is complex [17] and minor Fe(II)-components such as pyrite and siderite contained in OPA may have some reducing properties, which can be employed to change the chemical properties of redox-sensitive radionuclides. This reducing effect of dissolved Fe(II) is known, from Vinšová et al. and Law et al. who showed that TcO_4^- sorbed on bentonite [61] and sediments [63] was reduced to Tc(IV).

Mackinawite (FeS, 0.5 g) was added to anaerobic OPA powder (BHE 24/2) suspended in 8 mL OPA pore water and contacted for two weeks. Assuming that about 4% of Fe(II) dissolves from the total amount of FeS, the concentration of dissolved Fe(II) in solution accounted for 2.4×10^{-4} M [64]. After this period of time, TcO_4^- was added to the mixture and contacted for three weeks. The presence of 0.24 mM dissolved Fe(II) in the solution decreased the redox potential from 200 mV to -80 mV and increased the uptake of 8 µM Tc to 99% for S/L ratios of 10–20 g/L at pH 7.7.

To investigate the second additive, 1 mM $FeCl_2$ was added to OPA suspensions in OPA pore water at pH 7.5. After the addition of 5 µM TcO_4^- the measured redox potential in all solutions was nearly constant at about -100 mV over the contact time of 5 d. It is important to note that the redox potential of the samples with 1 mM Fe(II) was already negative at the beginning of the experiment. The results show that even without OPA no Tc was detectable in the solution. Again the higher uptake of Tc on OPA in both experiments with dissolved FeS and $FeCl_2$ in all suspensions indicates that TcO_4^- was completely reduced to Tc(IV) and the precipitation of Tc is most probably. The calculated equilibrium concentration of Tc of 10^{-9} to 10^{-8} M agrees very well with the solubility limit of TcO_2 [65, 66] and thus supports the suggestion of a precipitation of TcO_2. The results of the influence of 1 mM Fe(II) are in good agreement with previously published works. The reduction of TcO_4^- and formation of

precipitates by Fe(II) addition has been reported in several studies such as by Kobayashi et al. [67] and Zachara et al. [68].

5.2 Diffusion of Tc in Opalinus Clay

Up to now there are few diffusion data available for Tc diffusion in OPA, and our study focused on the effect of oxygen (aerobic/anaerobic conditions) on the in-diffusion of $^{99}TcO_4^-$ using OPA pore water (pH = 7.6) as mobile phase. A detailed description of the experimental setup and data processing for the diffusion experiments can be found in section 3.1. Two stainless steel diffusion cells – for experiments under aerobic and anaerobic conditions (argon glove box) – were used to study the diffusion of TcO_4^- in OPA and to determine the diffusion parameters (D_e, α, and ε), which are needed for transport modeling. In the aerobic experiment stainless steel filters were used and for the anaerobic bore core polyethylene filters were used. The direction of diffusion was perpendicular to the bedding in both experiments.

As already explained in section 3.1, the OPA bore cores (BLT 14) were characterized via through-diffusion experiments using tritiated water (HTO) and $^{22}Na^+$. If the determined porosity of the used bore cores were in the known range of OPA, in-diffusion of TcO_4^- was started. The obtained diffusion parameters (D_e, ε, and α) for HTO and $^{22}Na^+$ are presented in Table 17.

Table 17: Experimental details of cell 1 and 2 together with the obtained diffusion parameters D_e, ε, and α for HTO and $^{22}Na^+$ in OPA by through-diffusion experiments.

Cell	**ø / mm**	**l / mm**	**ρ / kg/m³**	**O_2**	**HTO ($c_0 = 1.1 \times 10^{-9}$ mol/L)**		**$^{22}Na^+$ ($c_0 = 1.1 \times 10^{-9}$ mol/L)**	
					ε	**D_e / 10^{-11} m²/s**	**α**	**D_e / 10^{-11} m²/s**
1	25.44	11.08	2354	yes	0.17 ± 0.01	1.6 ± 0.1	0.56 ± 0.03	1.7 ± 0.01
2	25.55	10.97	2354	no	0.20 ± 0.01	1.8 ± 0.1	0.64 ± 0.03	1.7 ± 0.1
[36]	25.40	11.00	2420	yes	0.15 ± 0.01	1.5 ± 0.1	0.50 ± 0.02	1.9 ± 0.1

As shown in Table 17, the OPA bore cores of cell 1 and 2 have similar porosities, which are representative for OPA from Mont Terri [36, 39]. Furthermore, the D_e values of HTO and $^{22}Na^+$ for both cells are in the same range as values known from the literature [36, 39].

The in-diffusion experiment of TcO_4^- was started after the through- and out-diffusion of HTO and $^{22}Na^+$ had been completed. The high-concentration reservoir was filled with 220 mL artificial pore water (pH 7.6), spiked with ~8 µM $^{99}TcO_4^-$. The diffusion time was 153 d (cell 1) and 182 d (cell 2). During this time, the *Eh* (SHE) in the high-concentration reservoir was equal to approximately 430 mV (cell 1) under aerobic conditions and 80 mV (cell 2) under anaerobic conditions. Figure 39 shows the flux (left) and the accumulated activity (right) as a function of diffusion time of TcO_4^- in OPA. In the case of diffusion under aerobic conditions (black dots), the flux increased with diffusion time at the transient phase and reached steady state after 60 d. The accumulated activity increased also with time, becoming a linear function of time as the steady state was reached. Breakthrough of TcO_4^- was observed after one month.

Under anaerobic conditions (blue circles) no Tc was found on the secondary side within diffusion times of 182 d. This suggests a complete retardation of the TcO_4^- in the OPA bore core. The obtained diffusion parameters (D_e, α, and K_d) for TcO_4^- are summarized in Table 18.

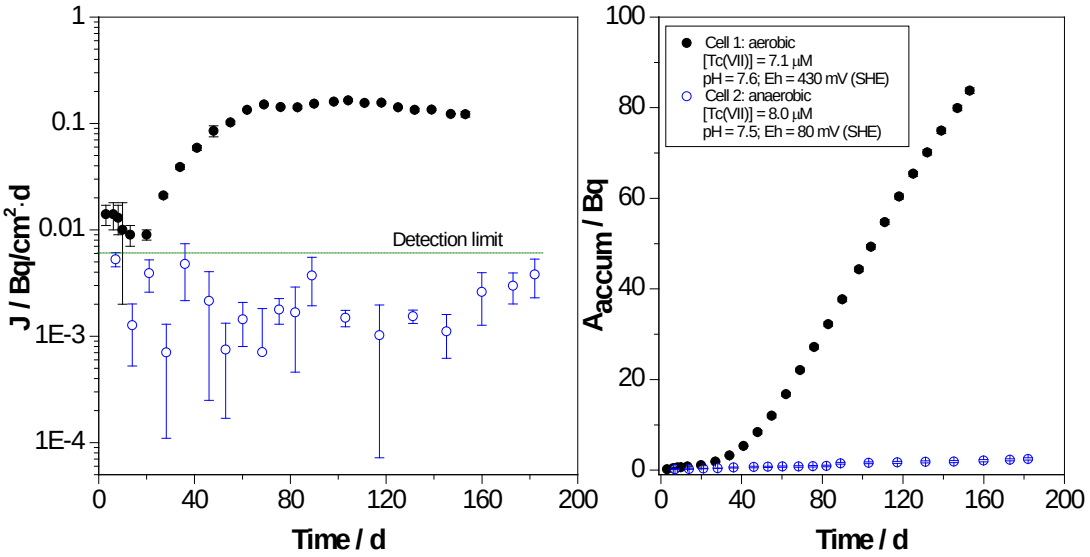

Figure 39: The flux (left) and accumulated activity (right) as a function of diffusion time of TcO_4^- under aerobic (cell 1) and anaerobic (cell 2) conditions.

Table 18: Experimental details of cell 1 and 2 and the obtained diffusion parameters D_e and α for Tc in OPA determined by in-diffusion experiments in comparison with literature data.

Cell	Clay	c_0	D_e / 10^{-13} m^2/s	α
1	OPA	$^{99}TcO_4^-$ / 7.1 µM	4.06 ± 0.02	0.07 ± 0.004
2	OPA	$^{99}TcO_4^-$ / 8.0 µM	-	-
[39]	OPA*	$^{125}I^-$ / 34 pM	45.70 ± 2.90	0.10 ± 0.01
[69]	GMZ bentonite	$^{99}TcO_4^-$ / 39 µM	35 ± 2 to 280 ± 20	0.06 ± 0.01 to 0.19 ± 0.01
[70]	GMZ bentonite *	$^{99}TcO_4^-$ / 39 µM	42 ± 2	0.06 ± 0.01
[70]	GMZ bentonite *	ReO_4^{2-} / 8.9 mM	530 ± 20	0.29 ± 0.02

* Diffusion experiments were carried out at temperature range 10 ± 3 °C under ambient conditions.

As can be seen in Table 18 the values of D_e and α for TcO_4^- are smaller than the values for HTO (D_e = (1.6 ± 0.1) × 10^{-11} m^2/s, α = 0.17 ± 0.01). This can be explained by the anion exclusion effect caused by the permanent negative charge on the clay surface and the ionic strength of pore water [39, 45, 71, 72], and confirms the non-sorption of TcO_4^- on OPA in neutral pH range under aerobic conditions. Our determined diffusion coefficient (D_e) is smaller by a factor of 10 to 100 than those available in the literature for TcO_4^- and its analogues ReO_4^- and I^- in other clay minerals such as bentonite [39, 69, 70]. Up to now there is no explanation for this result and more experiments are required.

To explain the complete retardation of TcO_4^- in the anaerobic cell further experiments and spectroscopic investigations on the speciation of Tc in the bore core are required.

5.3 Speciation of Tc after interaction with Opalinus Clay

As already mentioned, sorption and diffusion experiments provide useful constants such as K_d values and diffusion parameters, which are necessary for transport modeling. But they cannot provide an understanding on a molecular scale of the involved mechanisms. Therefore, synchrotron-based techniques such as µ-XRF, µ-XANES, and µ-XRD were used to determine the chemical speciation of Tc after uptake on OPA. These spatially resolved investigations were complemented by X-ray absorption fine structure measurements (XANES and EXAFS)

of powder samples from batch experiments to determine the speciation and the structural parameters of the near-neighbor environment of sorbed Tc.

µ-XRF, µ-XANES, and µ-XRD measurements of Tc on thin section and diffusion sample

For the spatially resolved molecular-level investigations two kinds of samples were prepared: thin sections and parts from the OPA bore cores. Thin sections of OPA (BAE 25/10) on high-purity quartz glass object slides were prepared at the Max-Planck-Institut für Chemie, Mainz, as described in the Appendix. The thin sections had a dimension of 25 × 23 mm^2 and a thickness of about 50 µm. The top surface area of OPA which was brought into contact with the solution was about 16 mm^2. After preconditioning, the OPA thin section was contacted with background electrolyte (8 mL MilliQ-water) in an argon glove box (anaerobic conditions) at pH 9.5 using a homemade sorption cell (Figure 40). A 35 µM TcO_4^- solution was added and contacted with the thin section for two weeks. The amount of Tc sorbed on the thin section accounted for 16% (Tc loading of 0.29 µg/mm^2) and the redox potential in the samples was 275 mV (SHE).

Figure 40: OPA thin section and sorption cell used for spatially resolved synchrotron radiation investigations: a: OPA thin section, b: parts of sorption cell, c: assembled sorption cell.

The diffusion sample was prepared by the same experimental procedure used for the in-diffusion experiment of Np(V) as described in the Appendix. An intact OPA bore core (BLT 14) embedded into epoxy resin and mounted in a filter free PEEK diffusion cell (Figure ***41***) was contacted with 7 µM TcO_4^- for 28 d under ambient air conditions using OPA pore water (pH = 7.6) as mobile phase. The measured redox potential was about 370 mV. The clay in the cell was installed in a manner that the diffusion proceeded parallel to the bedding. At the end of the experiment, the bore core was removed from the cell, dried and cut into small pieces (Figure 41). One piece was used to study the Tc speciation after diffusion in OPA.

µ-XRF mappings were measured to determine the elemental distributions of Tc and its potential correlation with other elements contained in OPA such as Fe and Ca. Regions of high Tc concentrations were subsequently investigated by µ-XANES to determine the oxidation state of Tc. Further, µ-XRD was employed to gain knowledge of reactive crystalline mineral phases in the vicinity of Tc enrichments.

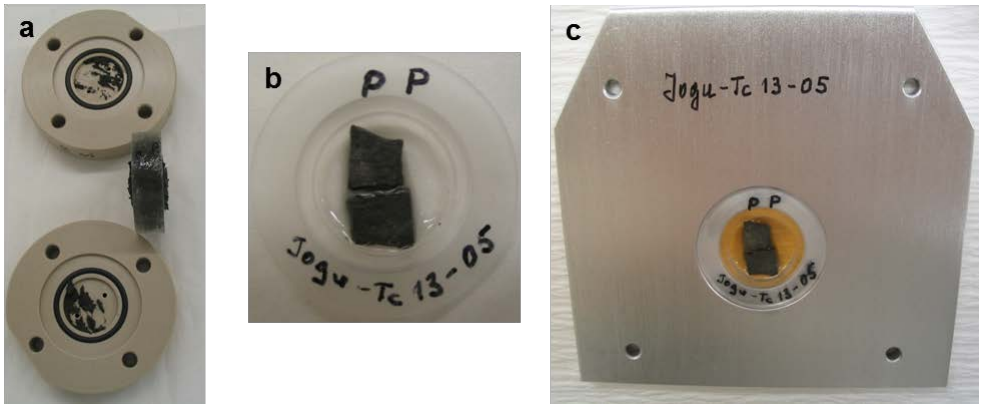

Figure 41: Preparation of diffusion samples for spectroscopic studies at the Diamond Light Source; a) diffusion cell and OPA bore core embedded in epoxy resin; b) split OPA bore core in the sample holder, c) diffusion sample mounted on an aluminum sample holder.

These speciation investigations of the OPA thin section and diffusion sample by µ-XRF, µ-XANES, and µ-XRD were performed at the I18 beamline at the Diamond Light Source (DLS, Harwell Science and Innovation Campus, UK) [73], with settings described in the Appendix. Figure 42 shows a 1 × 1 mm^2 overview mapping of Tc, Fe, and Ca of the thin section sample recorded at 21100 eV.

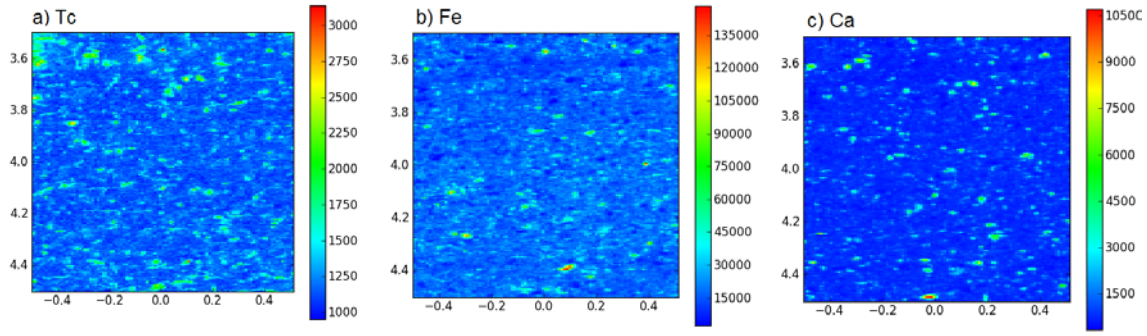

Figure 42: µ-XRF overview mapping (1 × 1 mm^2, step size 20 × 10 μm^2 (h × v), *E* = 21100 eV) of (a) Tc, (b) Fe, and (c) Ca of the thin section sample.

As can be seen in Figure 42 the spatial distributions of Tc, Fe, and Ca in the thin section sample were measured with good quality and show a widely homogeneous distribution with minor enrichments (“hot spots”). No clear visual correlation between these elements was observed. This was also confirmed by scatter plots using the Excel function CORREL. The calculated correlation coefficients were 0.03 for Tc/Fe and 0.32 for Tc/Ca. Due to the high energy used for the µ-XRF analysis, it was not possible to measure lighter elements such as Al and Si contained in OPA simultaneously with Tc and Fe. For further investigations three regions of the overview mapping were selected and remapped with a higher resolution (Figure 43).

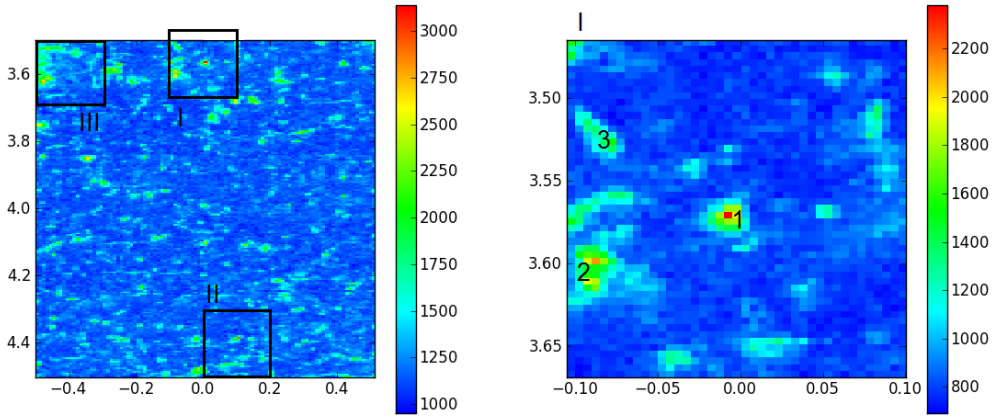

Figure 43: Left: µ-XRF overview mapping (1 × 1 mm^2, step size 20 × 10 $µm^2$ (h × v), *E* = 21100 eV) of Tc of the thin section sample. Right: Remapping (200 × 200 $µm^2$, step size 5 × 2.5 $µm^2$ (h × v), *E* = 21100 eV) of location I marked in the overview mapping.

From region No. I three points of local Tc enrichments were selected for further µ-XANES investigations (Figure 43, right). A maximum of two absorption spectra were recorded per point to determine the speciation. The resulting normalized spectra are shown in Figure 44 together with the reference data of TcO_2 and NH_4TcO_4. The measured µ-XANES spectra of spot 1–3 show similar near-edge structure (sorption edge at 21054 eV) and agree well with the reference spectrum for TcO_2 [74]. Furthermore, none of the spectra show the characteristic pre-edge peak of the NH_4TcO_4 spectrum at 21023 eV [75]. The results of the LCF show a quantitative reduction of TcO_4^- in the local enrichments to TcO_2 (96–100%). Both, the shape of the absorption spectra as well as the position of the absorption edge [74-77] support the result of the LCF.

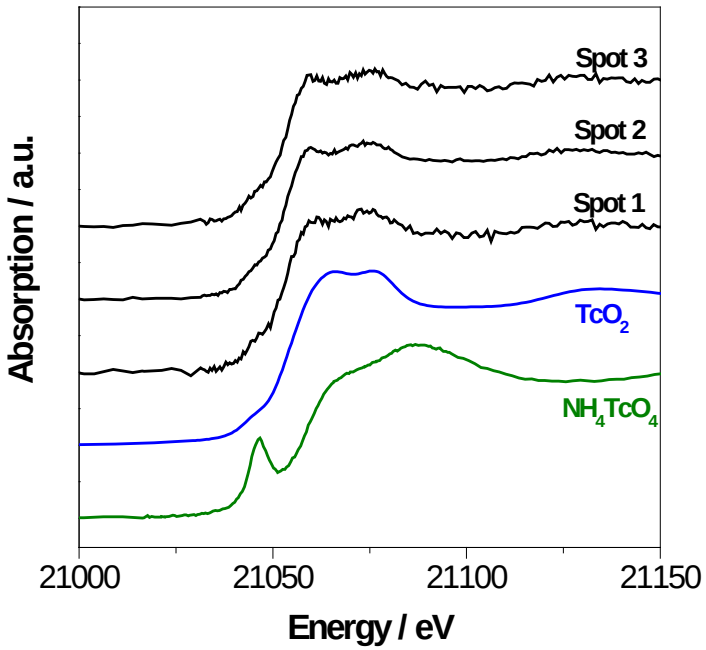

Figure 44: Normalized Tc K-edge XANES spectra measured on spots 1 to 3 marked in Figure 43 (right) with the reference spectra of TcO_2 and NH_4TcO_4.

For this reduction at least one redox-active couple (such as Fe^{2+}/Fe^{3+}) contained in OPA must be responsible. Therefore, several selected areas around the Tc hot spots which had been examined by µ-XANES were analyzed by µ-XRD. Using the XRDUA software [78] the collected reflection of the selected area were compared with the XRD data of different mineral phases contained in OPA such as pyrite, siderite, illite, and calcite (data not shown). Unfortunately, broad peaks of the XRD patterns were obtained which did not allow an unambiguous assignment of one of the possible mineral phases. Our present results are consistent with many spectroscopic investigations, indicating a reduction of TcO_4^- while interacting with clay minerals. For example Bishop et al. studied the Tc sorption on clay minerals such as montmorillonite and illite [79]. They showed that TcO_4^- was reduced to insoluble Tc(IV) by Fe(II) contained in the clays. Jaisi et al. confirmed the reduction of TcO_4^- to TcO_2 by Fe(II) associated with the clay mineral nontronite [80].

In case of the diffusion sample only the surface that was contacted with 7 µM Tc solution for about one month under ambient air condition was investigated. The total Tc concentration in the bore core was below the detection limit for µ-XRF measurements.

XAFS measurements of Tc uptake by Opalinus Clay

XAFS investigations (XANES and EXAFS) were performed at the MARS beamline at the Synchrotron Soleil in France [81] on different powder samples from batch sorption experiments (authorized sample holder is shown in Figure 45). From XANES and EXAFS measurements the main species of Tc taken up by OPA can be determined and enable to distinguish between surface complexes and precipitations.

The sorption of TcO_4^- on OPA was investigated by XAFS as a function of the OPA concentration and contact time in the presence of dissolved Fe(II) under anaerobic conditions in OPA pore water as background electrolyte at pH ~7.6. Details of the measured samples can be found in Table 19.

Table 19: Summary of the OPA samples prepared at 12 µM TcO_4^- under anaerobic conditions at pH 7.6 in presence of 0.1 mM $FeCl_2$ for EXAFS measurements.

Sample	Contact time	Tc loading / ppm	[OPA] / g/L	*Eh* / mV	Tc sorption / %
Tc-1	1 h	160	3.5	-59	49 ± 4
Tc-2	1 d	187	3.5	-51	57 ± 3
Tc-3	1 d	34	8.0	-46	22 ± 6
Tc-4	5 d	223	3.5	63	68 ± 2
Tc-5	5 d	23	8.0	81	14 ± 6

As shown in Table 19 the samples with S/L ratios of 3.5 g/L do not show the expected complete uptake of Tc, and the lowest sorption of Tc was found in the samples with 8 g/L. With increasing contact time the Tc concentration decreased in solution. Since all redox potentials are in the stability range of Tc(IV) and below, precipitation or quantitative sorption of Tc on the OPA surface was expected. One possible explanation for our results is a slower kinetics due to a higher Tc concentration in solution. Peretyazhko et al. showed that an increase of Tc concentration decreases the kinetics of reduction significantly [82].

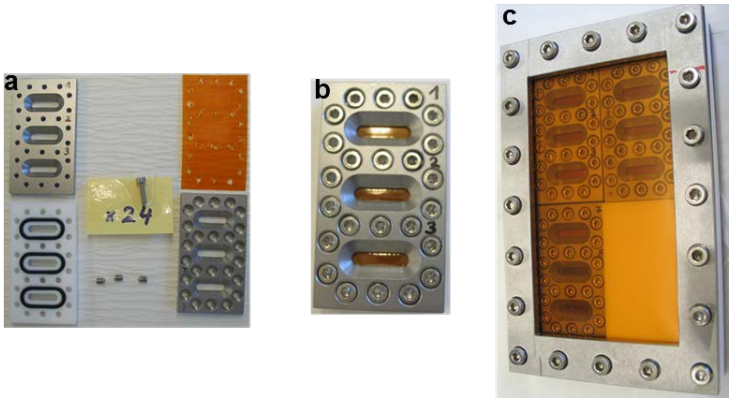

Figure 45: a) Components of the XAFS sample holder; b) assembled sample holder; c) sample array.

Tc K-edge XANES spectra of the samples Tc-1 to Tc-5 together with reference spectra of NH_4TcO_4 and TcO_2 taken from [74] are shown in Figure 46. All spectra are very similar and show the characteristic pre-edge peak at 21044 eV of the TcO_4^-. The quantification of the amounts of TcO_4^- and Tc(IV) in the samples was carried out using LCF. As an example for all samples Figure 47 presents the reproduction of the absorption spectrum of the sample Tc-4.

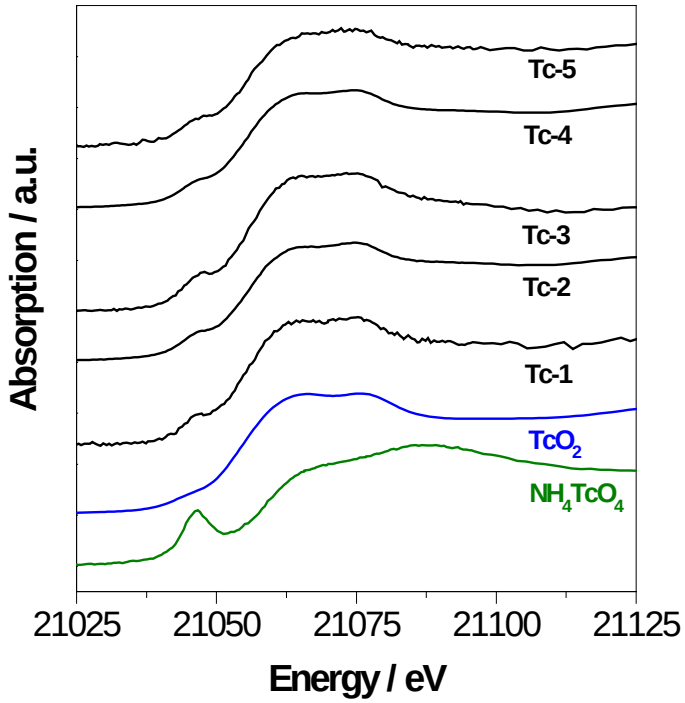

Figure 46: Normalized Tc K-edge XANES spectra of samples Tc-1 to Tc-5 together with reference spectra of NH_4TcO_4 and TcO_2 (taken from [74]).

The result of the LCF shows that in all spectra Tc(IV) is the dominant species and TcO_4^- is the minor species. This is also in good agreement with the previous results obtained by spatially resolved investigations of OPA thin sections. The position of the absorption edge (21056 eV) agrees well with previously published values for Tc(IV) [67, 74, 76], and thus confirms the results of the LCF. The small amounts of TcO_4^- in the samples can be explained by possible oxidation of reduced Tc during the transport or derive from small residues of the supernatant after phase separation.

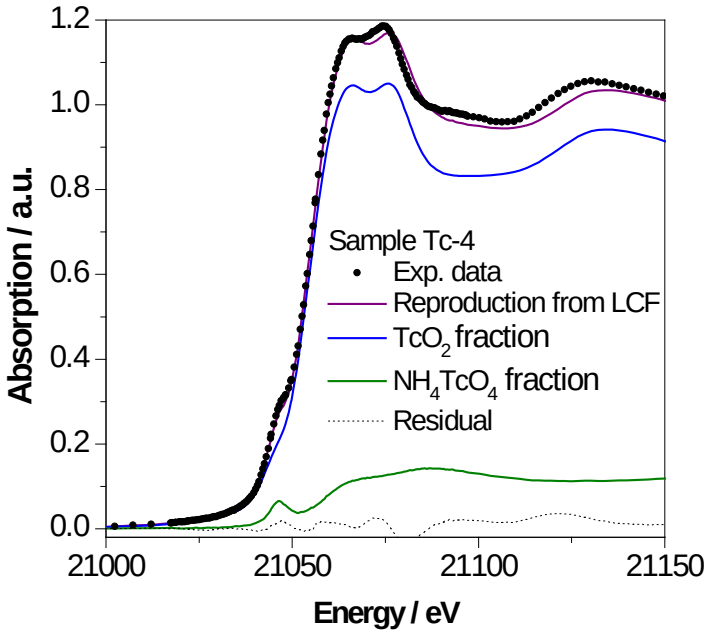

Figure 47: Normalized Tc K-edge XANES spectrum of sample Tc-4 together with reproductions from LCF using reference spectra of NH_4TcO_4 and TcO_2 (taken from [74]).

Table 20: Results of the LCF of the XANES spectra of samples Tc-1 to Tc-5.

Sample	Species / %	
	Tc(IV)	TcO_4^-
Tc-1	93 ± 2	7 ± 2
Tc-2	86 ± 1	14 ± 1
Tc-3	83 ± 1	17 ± 1
Tc-4	88 ± 1	12 ± 1
Tc-5	80 ± 1	20 ± 1

Figure 48 presents the Tc K-edge k^3-weighted EXAFS spectra together with the related Fourier transform magnitudes (FT) of samples Tc-2 and Tc-4. Due to low Tc loading in the samples Tc-3 (34 ppm) and Tc-5 (23 ppm), no EXAFS spectra were measured. Unfortunately, the sample Tc-1 (160 ppm) showed a poor signal-to-noise ratio and was therefore excluded.

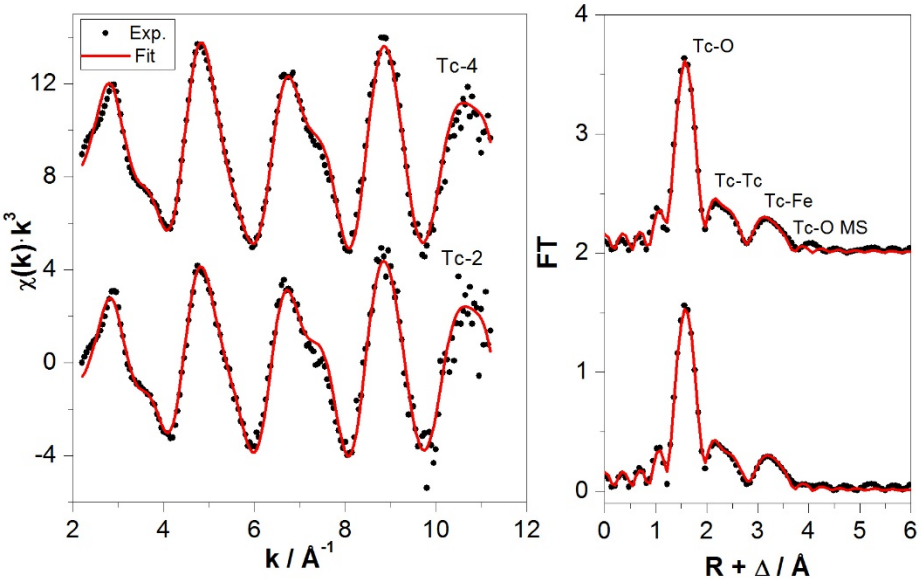

Figure 48: Raw Tc K-edge k^3-weighted EXAFS spectra together with the related Fourier transform magnitudes (FT) of samples Tc-2 and Tc-4.

As can be seen in Figure 48 both samples show very similar EXAFS patterns with minor differences. That means that the contact time and difference in the *Eh* values have no influence on the local structure of the Tc uptake on the clay surface.

The EXAFS spectra were analyzed using the software packages Athena [46] and EXAFSPAK [83]. Backscattering phase and amplitude functions required for data fitting were calculated with FEFF 8.20 [84] using crystal structures of TcO_2 [85]. For modeling possible interactions of Tc with Fe, McKale wave theory included in EXAFSPAK was used. In both samples the structural parameters derived from the best EXAFS fits show five coordination shells summarized in Table 21. The structure shows three O atoms at 2.0 Å, one Tc atom at 2.5 Å, one Tc atom at 3.2 Å, one Fe atom at 3.6 Å, and a Tc-O-Tc-O multiple scattering interaction at 4.1 Å.

Table 21: EXAFS structural parameters of samples Tc-2 and Tc-4 determined by EXAFS measurements.

Sample	Shell	N	R (Å)	σ^2 (Å^2)	ΔE_0 (eV)	Red. error
Tc-2	O	2.7 (1)	2.023 (27)	0.0009 (4)	5.7 (2)	0.30
	Tc	1.1 (1)	2.537 (10)	0.0116 (12)		
	Tc	1.1 (1)	3.274 (7)	0.0043 (8)		
	Fe	1.1. (1)	3.607 (19)	0.0030 (9)	5.4 (7)	
	MS	1.8 (4)	4.170 (22)	0.0012 (38)	5.7 (2)	
Tc-4	O	3.2 (1)	2.021 (2)	0.0019 (3)	5.1 (1)	0.16
	Tc	1.5 (4)	2.539 (7)	0.0130 (19)		
	Tc	1.1(1)	3.260 (5)	0.0046 (5)		
	Fe	1.1 (1)	3.592 (6)	0.0039 (7)	5.0 (6)	
	MS	1.6 (3)	4.138 (17)	0.0023 (29)	5.1 (1)	
TcO_2 [74]	O	6	1.94–2.08	-	-	-
	Tc	1	2.48			
	Tc	1	3.08			
	Tc	4	3.65			
TcO_2 [85]	O	6	1.86–2.14	-	-	-
	Tc	1	2.52			
	Tc	1	3.07			
	O	1	3.25			
	O	4	3.37–3.38			
	MS	4	3.92			

N coordination number, *R* distances, σ^2 Debye-Waller factors, E_0 energy, MS multiple scattering (Tc-O-Tc-O). The number in parentheses are the uncertainty of the values (In general, coordination numbers have an error of 25% and bond distances have an error of 0.5% when compared to data from crystallography).

The obtained EXAFS parameters, compared with the literature values for TcO_2 [74, 85], show a good agreement between the respective coordination shells, although small deviations in the number of neighboring atoms or distances occur. The lower coordination number of the first Tc-O shell may indicate a chain structure of Tc(IV) as described by Lukens et al. for TcO_2 as a radiolytic reduction product of TcO_4^- in highly alkaline solution [86]. To improve the obtained fit, the EXAFS data of the samples were fitted with a mixture of TcO_4^- and Tc(IV) as determined by LCF of the XANES spectra. However, no improvement of the fit was obtained.

Furthermore, two atoms of Si/Al neighbor at 3.8 Å (instead of the Tc-Fe interaction at 3.6 Å) were considered but did not improve the fit significantly by reducing the obtained error. As a conclusion TcO_4^- is reduced to TcO_2 by Fe(II) and forms an inner-sphere complex on the OPA surface and / or precipitates as TcO_2 cluster on the OPA surface. EXAFS measurements show again that Tc(IV) is the dominant species on the clay surface after uptake process and confirm the obtained results by µ-XANES measurements of thin sections.

6 Appendix

Chemicals: All chemicals used were at least of analytical grade or higher and obtained from different distributors (Alfa-Aeser, Fluka, Merk, Carl Roth, Sigma-Aldrich, Riedel-de Haën, Fisher Scientific, High-Purity Standards, Accu Trace™, CPI International). Experiments under anaerobic condition were carried out in a glove box (Unilab, MBraun, Germany) under Ar atmosphere (> 99.99% purity) with oxygen concentrations below 0.1 ppm. Millipore water (18.2 MΩ, Synergy™ Millipore water system, Millipore GmbH, Germany) was used to prepare the solutions of background electrolytes (i.e., OPA pore water, NaCl, $CaCl_2$, $MgCl_2$). All solutions used for experiments in the absence of CO_2 were prepared with CO_2-free, boiled Millipore water.

All solutions used for CE-ICP-MS or potentiometric reductions were filtered through a 0.2 µm syringefilter Mini Tip with PVDF-membrane (Nalgene, USA).

Opalinus Clay (OPA): The Opalinus Clay used in this work came from the Mont Terri Rock Laboratory, Switzerland. Thin sections and cylinders for diffusion studies were prepared out of intact OPA bore cores (BLT 14, different depths) and OPA powder for batch experiments was prepared from crushed and grinded bore cores and stored either under aerobic (BHE 24/1, depth 3.30–3.56 m) or anaerobic (BHE 24/2, depth 3.56–3.89 m) conditions.

The cation exchange capacity (CEC) of the aerobic powder (BHE 24/1) equals to 10 ± 4 meq/kg and the specific surface area (SSA) determined using the N_2 BET method equals to 41.3 ± 0.5 m²/g [87]. The mineral composition and trace element concentration was measured by X-ray fluorescence analysis and published by Fröhlich et al. [17]. More detailed information about the main physicochemical characteristics of the Mont Terri Opalinus Clay can be found in the NAGRA technical report 02-03 [25]**.** All OPA powders and cylinders were prepared at the Karlsruhe Institute of Technology – Institute for Nuclear Waste Disposal (KIT-INE).

Stock solutions:

Neptunium: Stock solutions of ^{237}Np(V) and ^{239}Np(V) were prepared by the same procedure as described in detail elsewhere [19]. The oxidation state of ^{237}Np stock solution was verified by UV-Vis absorption spectroscopy with the characteristic absorption band of Np(V) at 980.4 nm. The concentration of ^{237}Np and ^{239}Np were determined by γ-ray spectroscopy using

the γ-lines at 29.37 keV and 86.48 keV for ^{237}Np and 103.37 keV and 106.12 keV for ^{239}Np. The resulting stock solutions had a pH value of about 1.5 and a concentration of 8×10^{-3} M ^{237}Np(V) and 8×10^{-9} M ^{239}Np(V). For the sorption experiments, the pH of the Np stock solution was adjusted to ~ 4.0 using 5 M NaOH.

Plutonium: A 3.0×10^{-3} M ^{239}Pu(VI) stock solution was obtained after purification from its decay products and ^{241}Am using anion exchange chromatography. Pu was eluted with 0.5 M HCl and fumed several times with 1 M $HClO_4$ (not to complete dryness). The trivalent, tetravalent, and pentavalent oxidation states of Pu were obtained from the purified Pu(VI) stock solution by potentiostatic electrolysis in 1 M $HClO_4$. The oxidation state purity was verified by UV-Vis spectroscopy using the characteristic absorption bands at 601 nm for Pu(III), 470 nm for Pu(IV), 569 nm Pu(V), and 830 nm for Pu(VI) [88, 89]. The concentration of the ^{239}Pu stock solutions was determined by liquid scintillation counting (LSC). The resulting stock solutions had a concentration of 4×10^{-4} M Pu(III), 6×10^{-4} M Pu(IV), 5×10^{-4} M Pu(V), and 3×10^{-3} M Pu(VI).

Americium: A stock solution of ^{241}Am(III) was prepared by evaporating an Am solution in HCl obtained from home isotopic depot until dryness and redissolving the residue in 1 M $HClO_4$. The concentration of the resulting 3×10^{-5} M ^{241}Am(III) solution was checked by γ-ray spectroscopy using the specific γ-line at 59.5 keV.

Technetium: ^{99}Tc stock solution was purchased from Eckert and Ziegler with a concentration of 1.2×10^{-2} mol/L.

Analytical techniques:

α-spectroscopy: This spectroscopic technique was used to confirm the purity of the used α emitting radionuclide solutions of ^{237}Np, ^{239}Pu, and ^{241}Am. The detector was a silicon surface barrier detector (ORTEC, USA) with an active area of 450 mm², a detector resolution of < 25 keV at 5.5 MeV and an efficiency of about 15%. The samples were prepared by depositing a small volume of 10–30 µL on a titanium or tantalum foil and evaporating this to dryness.

γ-ray spectroscopy: The concentration and purity of ^{22}Na, ^{237}Np, ^{239}Np, and ^{241}Am was analyzed with a coaxial semiconductor γ-detector of high purity germanium (HPGe GMX-12180-S, ORTEC, USA) combined with a Canberra Inspector 2000 (model IN2K, Canberra Industries, Inc., USA) and the data were processed with the computer program

Genie 2000 gamma acquisition and analysis software (V. 3.0, Apr 05, 2004; Canberra Industries, Inc., USA). The calibration of the detector was done with a multi-element standard reference solution QCY48 (No.: R6/50/38, Amersham plc, UK). All samples were measured until an error level of about 3% was reached at a confidence level of 2σ.

UV-Vis spectroscopy: UV-Vis absorption spectra were recorded for Pu and Np using a high-resolution UV-Vis spectrometer (Tidas 100, J&M Analytik AG, Germany). The solutions were stored in 1.5 mL semi-microcuvettes (Brand GmbH, Germany) and checked for the purity of the produced oxidation states.

Liquid scintillation counting (LSC): ^{239}Pu, HTO and $^{22}Na^{+}$ concentrations were determined using LSC (Hidex, Finland) by adding 1–2 mL of sample solution to 10 mL LSC-cocktail (Ultima Gold^{TM} XR, PerkinElmer LAS GmbH, Germany). The samples were measured until a 2σ error of 2% was attained.

pH and Eh measurements: The pH of solutions was measured using a pH meter (Cond pH 720, WTW GmbH, Germany) equipped with a pH electrode (blue line 16 pH, Schott, Germany) and a temperature sensor (TFK 150, WTW, Germany). The electrode was regularly calibrated with certificated buffer solutions of pH 4.01, 6.87, and 9.18 (Schott, Germany). Temperature depending experiments were performed with a heated aluminum block in which the sample tubes of 50 mL volume were placed. The solutions within the tubes were stirred with small stirring bars. The temperature in the samples was checked by measuring simultaneously a blank sample containing MilliQ-water. While the pH can be detected directly at low ionic strengths (< 0.1 M), one has to correct the measured pH value at higher ionic strengths (> 0.1 M) because of deviations in the activities of the ions between the electrode´s electrolyte solution and the sample solution. The correction parameter (A-value) is calculated by measuring solutions at distinct pH values in the absence and presence of salt of a defined amount.

$$pH = pH_{exp} + A\,,$$

where pH is the real pH value of the solution, pH_{exp} is the measured pH value and A the correction parameter.

Redox potential measurements were performed by connecting a redox electrode (blue line 31 RX, reference system: Ag/AgCl, Germany) to the pH meter which was checked with a

standard solution of known potential (240 mV, HI 7021 ORP solution, HANNA instruments, USA).

Measurements of Np and Pu at the Swiss Light Source: Spatially resolved synchrotron radiation measurements µ-XRF, µ-XANES, and µ-XRD of Pu and Np samples were performed at the microXAS beamline at the Swiss Light Source, Paul Scherrer Institute (PSI), Switzerland [90] using a Kirkpatrick-Baez mirror micro focusing system and a double-crystal monochromator with three different crystal pairs (Si (111), Si (311) and Ge (111)). In this experiment, a pair of Si(111) crystals was used. The ring current during the measurement was about 400 mA. X-ray fluorescence was measured using a Ketek single-element Si-detector. Detailed information about these spatially resolved studies can be found in [26]. µ-XRF mappings of elements (Si, S, K, Ca, Ti, Mn, Fe, Zn, Rb, Sr) which are contained in OPA, were collected at an excitation energy above the L_{III}-edge. Overview mappings were taken at a step size of 20–10 µm, fine mappings were performed in 5–1 µm steps. All measurements were done with a beam size (h × w) of ≈ 1–2 × 2–5 μm^2. A Zr foil (17998 eV) was used for energy calibration. As Sr has a high abundance in OPA (>200 µg/g OPA), the Np Lα fluorescence (E(Lα) = 13.95 keV) is covered by the Sr Kα fluorescence (E(Kα) = 14.16 keV). Therefore, the Np µ-XRF mappings can be calculated by an application of two different methods. The first one is the edge-contrast method. This means a subtraction of fast on-the-fly µ-XRF mappings of Sr with an excitation energy of 17550 eV from those using 17620 eV, which is above the Np L_{III}-edge of 17610 eV. The other applied method uses the ratio of the counts of the Np Lα ROI to those of the Sr Kα ROI both at the excitation energy of 17620 eV from the same on-the-fly µ-XRF image. This second method provides Np profiles with less noise from spatial jitter of the measuring assembly and higher quality than the edge-contrast method. Yet, this data evaluation depends more on a homogeneous distribution of Sr which can be different due to the OPA heterogeneity. According to that, a second scan was always taken below the Np L_{III}-edge for the subtraction method. Usage of both methods provided an enhanced reliability and was used as a verification of the collected data. However, the further data analysis is limited on the contrast-edge mode. All XRF mappings for Np or Pu were analyzed using a PSI intern MATLAB code. Np or Pu hot spots were studied by L_{III}-edge µ-XANES in fluorescence mode. Deadtime corrections for the measured XANES spectra were performed using an in-house java applet code. Background and energy correction of the spectra were performed with the software package Athena [46]. The XANES spectra were analyzed using a LCF code of the software package Athena [46] and reference spectra of

Np(IV) and Np(V) and in case of Pu from Pu(III), Pu(IV), and Pu(V) from aqueous solution. LCF allows to determine the relative amount of different oxidation states in the sample from XANES spectrum. The µ-XRD measurements were performed using the above mentioned beam size and a Pilatus 100K detector. Experimental parameters such as sample-detector distance, detector plane orientation, etc., were refined by measuring different reference powders or foils (i.e. Al_2O_3, SiO_2, Si-Zr). The analysis of the diffraction patterns was performed with the program XRDUA [78].

Measurements of Tc at Soleil and Diamond Light Source: For X-ray absorption fine structure measurements (XAFS), the sorption samples were centrifuged at 108,000 g for 1 h after a contact time of 1 h to 5 d to separate the solid and liquid phases. The solid residues were dried under Ar atmosphere (Ar glove box > 99.99%) for a few days, grinded and loaded into a sample holder with Kapton windows (authorized design by Soleil synchrotron facility). The transport of the samples was performed in an anaerobic transport container purged with argon and equipped with a seal ring. Tc K-edge absorption spectra (21044 eV) were collected in fluorescence mode at the Mars beamline [81] at the Synchrotron Soleil in France using a 13 element HPGe solid-state detector. A Si(111) and Si (220) double-crystal monochromator was used for tuning the energy of the incident X-ray beam. One sample containing pure 95 µM NH_4TcO_4 was used for both energy calibration and as reference for the linear combination analysis. In order to reduce the dead time of the detector, the fluorescent radiation has been attenuated by means of a 1 mm thick aluminum foil. The beam used was also slightly defocused (0.5 × 2.2 mm) to prevent photo-induced redox reactions in the samples. The beam current was constant at about 430 mA. The EXAFS analysis was performed with the software packages Athena [46] and EXAFSPAK [83]. Backscattering phase and amplitude functions required for data fitting were calculated with FEFF 8.20 [84] using crystal structures of NH_4TCO_4 [91], TcO_2 [85] and TcS_2 [92]. For modeling possible interactions of Tc with Fe, McKale wave theory included in EXAFSPAK was used. The shift in threshold energy, ΔE_0, was allowed to vary as a global parameter in the fits.

Spatially resolved synchrotron radiation measurements µ-XRF, µ-XANES, and µ-XRD of Tc samples were performed at the I18 beamline at the Diamond Light Source (DLS, Harwell Science and Innovation Campus) UK [73]. For these investigations, several OPA samples were prepared as follows: (i) ^{99}Tc(VII) was sorbed on OPA thin sections under anaerobic conditions (Ar glove box) at pH 9.5 using a sorption cell (homemade) with a contact time of 15 d, (ii) small pieces of OPA were taken from an in-diffusion experiment with Tc(VII),

which lasted for about one month. Thin sections were prepared on glass slides from OPA batches (BLT 14). The preparation of these samples was performed at the Max-Planck-Institut für Chemie in Mainz. The thickness of the thin sections was approximately 50 µm and the contacted area always smaller than 1 cm².

µ-XRF, µ-XANES and µ-XRD measurements of all Tc samples were performed as mentioned above at I18 beamline at DLS, using a Si(111) monochromator. The incident X-ray beam was focused to ~ 4 × 7 μm^2 using Kirkpatrick-Baez (KB) focusing mirrors. The ring current during the measurement was about 300 mA. The fluorescence data were collected using a high rate fluorescence 9 element solid state detector system optimised for energies above 5 keV. µ-XRF mappings of elements of interest (i.e. Ca, Fe, Sr, As, Tc) were collected at an excitation energy above the Tc K-edge (21.1 keV). Overview mappings (1 × 1 mm^2 for thin sections and up to 9 × 3 mm^2 for diffusion samples) were taken at a step size of 20–10 µm horizontal and 10–5 µm vertical, fine mappings (50 × 50 μm^2) were performed in 5–2.5 µm steps. All measurements were done with a beam size (h × w) of ≈ 3.9 × 6.7 µm. A Mo foil (20 keV) was used for energy calibration. XRF maps were analyzed using the PyMca program [93]. Tc hot spots were studied by Tc K-edge µ-XANES in fluorescence mode. Background and energy correction of the spectra were performed with the software package Athena [46]. The XANES spectra were analyzed using linear combination fitting analysis (LCF) [46] and reference spectra of NH_4TcO_4 and TcO_2. LCF allows to determine the relative amount of different Tc oxidation states in the sample from XANES spectrum. The µ-XRD measurements were performed using the above mentioned beam size and a CCD detector, which has been calibrated using X-ray diffraction patterns of silicon. The analysis of the diffraction patterns was performed with the program XRDUA [78].

7 Bibliography

1. Brewitz, W., *Eignungsprüfung der Schachtanlage Konrad für die Endlagerung radioaktiver Abfälle: Abschlussbericht (GSF - T 136)*. 1982: GSF.
2. Pearson, F.J., *Opalinus Clay experimental water: A1 type*, in *PSI Internal Report TM-44-98-07,*1998, Paul Scherrer Institut: Villigen/Switzerland.
3. Brasser, T., et al., *Endlagerung wärmeentwickelnder radioaktiver Abfälle in Deutschland*, in *GRS-247,*2008.
4. Gompper, K., *Zur Abtrennung langlebiger Radionuklide*. Radioaktivität und Kernenergie. 2001, Karlsruhe: Forschungszentrum Karlsruhe.
5. Bradbury, M.H. and B. Baeyens, *A comparison of apparent diffusion coefficients measured in compacted Kunigel V1 bentonite with those calculated from batch sorption measurements and D_e (HTO) data: A case study for Cs(I), Ni(II), Sm(III), Am(III), Zr(IV) and Np(V)*, in *PSI Bericht 03-02,*2003.
6. Wang, X.K., et al., *Diffusion and sorption of U(VI) in compacted bentonite studied by a capillary method.* Radiochimica Acta, 2005. **93**: p. 273-278.
7. Van Loon, L.R., B. Baeyens, and M.H. Bradbury, *Diffusion and retention of sodium and strontium in Opalinus clay: Comparison of sorption data from diffusion and batch sorption measurements, and geochemical calculations.* Applied Geochemistry, 2005. **20**(12): p. 2351-2363.
8. Joseph, C., et al., *Diffusion of U(VI) in Opalinus Clay: Influence of temperature and humic acid.* Geochimica et Cosmochimica Acta, 2013. **109**: p. 74-89.
9. Bradbury, M.H. and B. Baeyens, *A mechanistic description of Ni and Zn sorption on Na-montmorillonite: Part I: Titration and sorption measurements.* Journal of Contaminant Hydrology, 1997. **27**: p. 199-222.
10. Bradbury, M.H. and B. Baeyens, *Sorption modelling on illite Part I: Titration measurements and the sorption of Ni, Co, Eu and Sn.* Geochimica et Cosmochimica Acta, 2009. **73**(4): p. 990-1003.
11. Perin, D.D. and B. Dempsey, *Buffers for pH and metal ion control*. 1974, New York: John Wiley & Sons, Inc.
12. Nagasaki, S., T. Saito, and T.T. Yang, *Sorption behavior of Np(V) on illite, shale and MX-80 in high ionic strength solutions.* Journal of Radioanalytical and Nuclear Chemistry, 2015.
13. Li, P., et al., *Effects of pH, ionic strength and humic acid on the sorption of neptunium(V) to Na-bentonite.* Journal of Molecular Liquids, 2015. **206**: p. 285-292.
14. Kasar, S., et al., *Retention behaviour of Cs(I), Sr(II), Tc(VII) and Np(V) on smectite-rich clay.* Journal of Radioanalytical and Nuclear Chemistry, 2014. **300**(1): p. 71-75.
15. Choppin, G.R., *Utility of oxidation state analogs in the study of plutonium behavior.* Radiochimica Acta, 1999. **85**: p. 89-95.
16. Bradbury, M.H. and B. Baeyens, *Modelling sorption data for the actinides Am(III), Np(V) and Pa(V) on montmorillonite.* Radiochimica Acta, 2006. **94**: p. 619-625.

17. Fröhlich, D.R., et al., *Sorption of neptunium(V) on Opalinus Clay under aerobic/anaerobic conditions.* Radiochimica Acta, 2011. **99**(2): p. 71-77.
18. Schmeide, K. and G. Bernhard, *Sorption of Np(V) and Np(IV) onto kaolinite: Effects of pH, ionic strength, carbonate and humic acid.* Applied Geochemistry, 2010. **25**(8): p. 1238-1247.
19. Amayri, S., A. Jermolajev, and T. Reich, *Neptunium(V) sorption on kaolinite.* Radiochimica Acta, 2011. **99**(6): p. 349-357.
20. Bradbury, M.H. and B. Baeyens, *A mechanistic description of Ni and Zn sorption on Na-montmorillonite: Part II: modelling.* Journal of Contaminant Hydrology, 1997. **27**: p. 223-248.
21. Bradbury, M.H. and B. Baeyens, *Sorption of Eu on Na- and Ca-montmorillonites: Experimental investigations and modelling with cation exchange and surface complexation.* Geochimica et Cosmochimica Acta, 2002. **66**(13): p. 2325-2334.
22. Bradbury, M.H. and B. Baeyens, *Modelling the sorption of Mn(II), Co(II), Ni(II), Zn(II), Cd(II), Eu(III), Am(III), Sn(IV), Th(IV), Np(V) and U(VI) on montmorillonite: Linear free energy relationships and estimates of surface binding constants for some selected heavy metals and actinides.* Geochimica et Cosmochimica Acta, 2005. **69**(4): p. 875-892.
23. Gustafsson, J., *Visual MINTEQ v 3.0.* Swedish Royal Institute of Technology (KTH), 2004.
24. Wendt, S., *Sorption and Direct Speciation of Neptunium(V) on Aluminium Oxide and Montmorillonite*, in *Institut für Kernchemie, Dissertation*2009, Johannes Gutenberg-Universität Mainz: Mainz.
25. Nagra, *Projekt Opalinuston - Synthese der geowissenschaftlichen Untersuchungsergebnisse*, in *Technical Report 02-03,*2002, Nagra: Wettingen, Switzerland.
26. Fröhlich, D.R., et al., *Influence of temperature and background electrolyte on the sorption of neptunium(V) on Opalinus Clay.* Applied Clay Science, 2012. **69**: p. 43-49.
27. Runde, W., et al., *Solubility and sorption of redox-sensitive radionuclides (Np, Pu) in J-13 water from the Yucca Mountain site: comparison between experiment and theory.* Applied Geochemistry, 2002. **17**(6): p. 837-853.
28. Plummer, L.N. and E. Busenberg, *The solubilities of calcite, aragonite and vaterite in CO_2-H_2O solutions between 0 and 90 °C, and an evaluation of the aqueous model for the system $CaCO_3$-CO_2-H_2O.* Geochimica et Cosmochimica Acta, 1982. **46**(6): p. 1011-1040.
29. Buda, R., et al., *Studies of the ternary systems humic substances – kaolinite – Pu(III) and Pu(IV).* Radiochimica Acta, 2008. **96**(9-11).
30. Stumm, W. and J.J. Morgan, *An introduction emphasizing chemical equilibria in natural waters*. 1971, New York: Wiley-Interscience.
31. Kinniburgh, D. and D. Cooper, *PhreePlot - Creating graphical output with PHREEQC*, 2010. p. www.phreeplot.org.
32. Thoenen, T., et al., *The PSI/Nagra Chemical Thermodynamic Database 12/07*, in *PSI Bericht 14-04,*2014.
33. Kienzler, B., et al., *Sicherheitstechnische Einzelfragen*, in *Geochemische begründete Eingangsparameter für Kritikalitätsanalysen,*2003, FZK-INE: Karlsruhe.
34. Lujanienė, G., et al., *Study of Pu(IV) and Am(III) sorption to clay minerals: laboratory experiments and modeling.* Proceedings Radiochimica Acta, 2011. **1**: p. 237-244.
35. Sabodina, M.N., et al., *Behavior of Cs, Np(V), Pu(IV), and U(VI) in pore water of bentonite.* Radiochemistry, 2006. **48**(5): p. 488-492.
36. Wu, T., et al., *Neptunium(V) sorption and diffusion in Opalinus Clay.* Environmental Science & Technology, 2009. **43**: p. 6567-6571.
37. Van Loon, L.R. and J.M. Soler, *Diffusion of HTO, $^{36}Cl^-$, $^{125}I^-$ and $^{22}Na^+$ in Opalinus Clay: Effect of confining pressure, sample orientation, sample depth and temperature*, in *PSI Bericht Nr. 04-03,*2004, PSI: Villingen, Switzerland.
38. Van Loon, L.R., et al., *Effect of confining pressure on the diffusion of HTO, $^{36}Cl^-$ and $^{125}I^-$ in a layered argillaceous rock (Opalinus Clay): diffusion perpendicular to the fabric.* Applied Geochemistry, 2003. **18**: p. 1653-1662.

39. Van Loon, L.R., J.M. Soler, and M.H. Bradbury, *Diffusion of HTO, $^{36}Cl^-$ and $^{125}I^-$ in Opalinus Clay samples from Mont Terri: Effect of confining pressure*. Journal of Contaminant Hydrology, 2003. **61**(1-4): p. 73-83.
40. Van Loon, L.R. and J. Eikenberg, *A high-resolution abrasive method for determining diffusion profiles of sorbing radionuclides in dense argillaceous rocks.* Applied Radiation and Isotopes, 2005. **63**(1): p. 11-21.
41. Glaus, M.A., et al., *Diffusion of ^{22}Na and ^{85}Sr in Montmorillonite: Evidence of interlayer diffusion being the dominant pathway at high compaction.* Environmental Science & Technology, 2007. **41**: p. 478-485.
42. Glaus, M.A., et al., *Comparative study of tracer diffusion of HTO, $^{22}Na^+$ and $^{36}Cl^-$ in compacted kaolinite, illite and montmorillonite.* Geochimica et Cosmochimica Acta, 2010. **74**(7): p. 1999-2010.
43. Yaroshchuk, A.E. and L.R. Van Loon, *Improved interpretation of in-diffusion measurements with confined swelling clays.* Journal of Contaminant Hydrology, 2008. **97**(1-2): p. 67-74.
44. Eisenberg, D.S. and W. Kauzmann, *The structure and properties of water*. Vol. 123. 1969: Clarendon Press Oxford.
45. Appelo, C.A.J., L.R. Van Loon, and P. Wersin, *Multicomponent diffusion of a suite of tracers (HTO, Cl, Br, I, Na, Sr, Cs) in a single sample of Opalinus Clay.* Geochimica et Cosmochimica Acta, 2010. **74**(4): p. 1201-1219.
46. Ravel, B. and M. Newville, *ATHENA, ARTEMIS, HEPHAESTUS: data analysis for X-ray absorption spectroscopy using IFEFFIT.* Journal of Synchrotron Radiation, 2005. **12**(Pt 4): p. 537-41.
47. Amayri, S., et al., *Distribution coefficients for the sorption of Th, U, Np, Pu, and Am on Opalinus Clay.* Radiochimica Acta, 2016. **104**(1).
48. Allen, P.G., et al., *Investigation of aquo and chloro complexes of UO_2^{2+}, NpO_2^+, Np^{4+}, and Pu^{3+} by X-ray absorption fine structure spectroscopy.* Inorganic Chemistry, 1997. **36**: p. 4676-4683.
49. Conradson, S.D., et al., *Higher order speciation effects on plutonium L_3 X-ray absorption near edge spectra.* Inorganic Chemistry, 2004. **43**: p. 116-131.
50. Stobener, N., et al., *Sensitive redox speciation of neptunium by CE-ICP-MS.* Analytical and Bioanalytical Chemistry, 2012. **404**(8): p. 2143-50.
51. Gaona, X., et al., *Np(V/VI) redox chemistry in cementitious systems: XAFS investigations on the speciation under anoxic and oxidizing conditions.* Applied Geochemistry, 2013. **28**: p. 109-118.
52. Schwabe, K. and D. Nebel, *Potentiometric studies on plutonium. I. Investigation of the complex formation between PuIV and PuIII and acetate ions.* Z. Phys. Chem. (Leipzig), 1962. **220**(Copyright (C) 2016 American Chemical Society (ACS). All Rights Reserved.): p. 339-54.
53. Richard, L., M. Grivé, and L. Druo, *Andra-TDB7 Task 3 – Organics*, 2011, Amphos 21.
54. Kuczewski, B.M., Ch. M.; Seibert, A.; Geckeis, H.; Kratz, J.V.; Trautmann, N., *Separation of Plutonium and Neptunium Species by Capillary Electrophoresis-Inductively Coupled Plasma-Mass Spectrometry and Application to Natural Groundwater Samples.* Analytical Chemistry, 2003. **75**: p. 6769-6774.
55. Graser, C.H., et al., *Sensitive redox speciation of iron, neptunium, and plutonium by capillary electrophoresis hyphenated to inductively coupled plasma sector field mass spectrometry.* Anal Chem, 2015. **87**(19): p. 9786-94.
56. Topin, S., J. Aupiais, and P. Moisy, *Direct determination of plutonium(V) and neptunium(V) complexation by carbonate ligand with CE-ICP-sector field MS.* Electrophoresis, 2009. **30**(10): p. 1747-55.
57. Topin, S., J. Aupiais, and N. Baglan, *Determination of the stability constants of nitrate complexes of Np(V) and Pu(V) using CE-ICP-MS.* Radiochimica Acta, 2010. **98**(2): p. 71-75.

58. Topin, S., et al., *Trace Metal Speciation by Capillary Electrophoresis Hyphenated to Inductively Coupled Plasma Mass Spectrometry: Sulfate and Chloride Complexes of Np(V) and Pu(V).* Analytical Chemistry, 2009. **81**: p. 5354–5363.
59. Benedict, M., T.H. Pigford, and H.W. Levi, *Nuclear chemical engineering*. 1981, New York: McGraw-Hill Book Company.
60. Lieser, K.H. and C. Bauscher, *Technetium in the hydrosphere and in the geosphere.* Radiochimica Acta, 1987. **42**: p. 205-213.
61. Vinšová, H., P. Večerník, and V. Jedináková-Křížová, *Sorption characteristics of ^{99}Tc onto bentonite material with different additives under anaerobic conditions.* Radiochimica Acta, 2006. **94**(8/2006).
62. Palmer, D.A. and R.E. Meyer, *Adsorption of technetium on selected inorganic ion-exchange materials and on a range of naturally occuring minerlas under oxic conditions.* Journal of Inorganic & Analytical Chemistry 1981. **43**(11): p. 2979-2984.
63. Law, G.T.W., et al., *Role of nitrate in conditioning aquifer sediments for technetium bioreduction.* Environmental Science and Technology, 2010. **44**: p. 150-155.
64. Lübke, M., *Sorption von Neptunium(V) an Mackinawit (FeS)*, in *Institut für Kernchemie, Diplomarbeit*2011, Johannes Gutenberg-Universität Mainz: Mainz.
65. Icenhower, J., et al., *The biogeochemistry of technetium: Areview of the behavior of an artificial element in the natural environment.* American Journal of Science, 2010. **310**: p. 721-752.
66. Meyer, R.E., et al., *Solubilities of Tc(VII) oxides.* Radiochimica Acta, 1991. **55**: p. 11-18.
67. Kobayashi, T., et al., *Redox behavior of Tc(VII)/Tc(IV) under various reducing conditions in 0.1 M NaCl solutions.* Radiochimica Acta, 2013. **101**(5): p. 323-332.
68. Zachara, J.M., et al., *Reduction of pertechnetate [Tc(VII)] by aqueous Fe(II) and the nature of solid phase redox products.* Geochimica et Cosmochimica Acta, 2007. **71**(9): p. 2137-2157.
69. Li, J.Y., et al., *Pertechnetate diffusion in GMZ bentonite.* Journal of Radioanalytical and Nuclear Chemistry, 2012. **293**(3): p. 763-767.
70. Wu, T., et al., *Effect of EDTA on the diffusion behavior of $^{99}TcO_4^-$ and ReO_4^- in GMZ bentonite.* Journal of Radioanalytical and Nuclear Chemistry, 2013. **299**(3): p. 2037-2041.
71. Glaus, M.A., et al., *Consistent interpretation of the results of through-, out-diffusion and tracer profile analysis for trace anion diffusion in compacted montmorillonite.* Journal of Contaminant Hydrology, 2011. **123**(1-2): p. 1-10.
72. Van Loon, L.R., M.A. Glaus, and W. Müller, *Anion exclusion effects in compacted bentonites: Towards a better understanding of anion diffusion.* Applied Geochemistry, 2007. **22**(11): p. 2536-2552.
73. Mosselmans, J.F., et al., *I18--the microfocus spectroscopy beamline at the Diamond Light Source.* Journal Synchrotron Radiation, 2009. **16**(Pt 6): p. 818-24.
74. Almahamid, I., et al., *Electronic and structural investigations of technetium compounds by X-ray absorption spectroscopy.* Inorganic Chemistry, 1995. **34**: p. 193-198.
75. Allen, P.G., et al., *Technetium speciation in cement waste forms determined by X-ray absorption fine structure spectroscopy.* Radiochimica Acta, 1997. **76**: p. 77-86.
76. Liu, Y., J. Terry, and S.S. Jurisson, *Pertechnetate immobilization in aqueous media with hydrogen sulfide under anaerobic and aerobic environments.* Radiochimica Acta, 2007. **95**(12).
77. Maes, A., et al., *Evidence for the interaction of technetium colloids with humic substances by X-ray absorption spectroscopy.* Environmental Science and Technology, 2004. **38**: p. 2044-2051.
78. De Nolf, W., F. Vanmeert, and K. Janssens, *XRDUA: crystalline phase distribution maps by two-dimensional scanning and tomographic (micro) X-ray powder diffraction.* Journal of Applied Crystallography, 2014. **47**(3): p. 1107-1117.

79. Bishop, M.E., et al., *Bioreduction of Fe-bearing clay minerals and their reactivity toward pertechnetate (Tc-99).* Geochimica et Cosmochimica Acta, 2011. **75**(18): p. 5229-5246.
80. Jaisi, D.P., et al., *Reduction and long-term immobilization of technetium by Fe(II) associated with clay mineral nontronite.* Chemical Geology, 2009. **264**(1-4): p. 127-138.
81. Llorens, I., et al., *X-ray absorption spectroscopy investigations on radioactive matter using MARS beamline at SOLEIL synchrotron.* Radiochimica Acta, 2014. **102**(11): p. 957-972.
82. Peretyazhko, T.S., et al., *Pertechnetate (TcO4−) reduction by reactive ferrous iron forms in naturally anoxic, redox transition zone sediments from the Hanford Site, USA.* Geochimica et Cosmochimica Acta, 2012. **92**: p. 48-66.
83. George, G. and S. George, *EXAFSPAK*, SSRL, 2000.
84. Ankudinov, A.L., et al., *Parallel calculation of electron multiple scattering using Lanczos algorithms.* Physical Review B, 2002. **65**(10).
85. Rogers, D.B., et al., *Crystal chemistry of metal dioxides with rutile-related structures.* Inorganic Chemistry, 1969. **8**(4): p. 841-849.
86. Lukens, W.W., et al., *Products of pertechnetate radiolysis in high alkaline solution: Structure of TcO_2xH_2O.* Environmental Science and Technology, 2002. **36**: p. 1124-1129.
87. Joseph, C., et al., *Sorption of uranium(VI) onto Opalinus Clay in the absence and presence of humic acid in Opalinus Clay pore water.* Chemical Geology, 2011. **284**(3-4): p. 240-250.
88. Cohen, D., *Electrochemical studies of plutonium ions in perchloric acid solution*.* Journal of Inorganic and Nuclear Chemistry, 1961. **18**: p. 207-210.
89. Cohen, D., *The absorption spectra of plutonium in perchloric acid solutions*.* Journal of Inorganic and Nuclear Chemistry, 1961. **18**: p. 211-218.
90. Borca, C.N., et al., *The microXAS beamline at the swiss light source: Towards nano-scale imaging.* Journal of Physics: Conference Series, 2009. **186**: p. 012003.
91. Faggiani, R., C.J.L. Lock, and J. Pocé, *The structure of ammonium pertechnetate at 295, 208 and 141 K.* Acta Crystallographica, 1980. **B36**: p. 231-233.
92. Lamfers, H.-J., et al., *The crystal structure of some rhenium and technetium dichalcogenides.* Journal of Alloys and Compounds, 1996. **241**: p. 34-39.
93. Solé, V.A., et al., *A multiplatform code for the analysis of energy-dispersive X-ray fluorescence spectra.* Spectrochimica Acta Part B: Atomic Spectroscopy, 2007. **62**(1): p. 63-68.

Acknowledgment

This work was financed by the German Federal Ministry for Economic Affairs and Energy (BMWi) under contract No. 02E10981, Talisman, and Actinet-I3 under contract No. 323300 and 232631, respectively. We acknowledge the Soleil synchrotron facility (SOLEIL), Diamond Light Source (DLS), and Swiss Light Source (SLS) for provision of synchrotron beam time. We are grateful to P. Solari from SOLEIL for the experimental support during the XAFS measurements at MARS beamline. For support during the µ-XAS experiments we thank F. Mosselmans from the I18 beamline at DLS as well as D. Grolimund and V. A. Samson from the MicroXAS Beamline at SLS, Paul Scherrer Institute (PSI). Further we thank Dr. Ch. Marquardt from the Institute for Nuclear Waste Disposal, Karlsruher Institut für Technologie (KIT), for providing the OPA samples. M. Biegler from the Max-Planck-Institut für Chemie in Mainz is acknowledged for preparation of the OPA thin sections.

We would like to thank all colleagues who contributed to the success of this work.

Quantum Mechanical Modeling of Sorption of Actinides on Mineral Surfaces and Complexation with Clay Organics Under Conditions of Deep Geological Repositories

Abschlussbericht für das Teilprojekt
„Quantenmechanische Modellierung zur Sorption von Actiniden an Mineraloberflächen und Komplexierung mit Tonorganika unter Endlagerbedingungen“

im Rahmen des Verbundprojektes
„Rückhaltung endlagerrelevanter Radionuklide im natürlichem Tongestein und in salinaren Systemen“

Förderkennzeichen 02E11001

Projektlaufzeit Juli 2011 bis August 2015

Sven Krüger, Alena Kremleva
Department Chemie, Technische Universität München
85747 Garching

Contents

1 Introduction

Distribution and transport of actinides in the environment is a central topic of safety considerations and environmental protection regarding radioactive waste and its safe long-term storage. Uranium plays here a central role as the common fuel in nuclear power plants. Other actinides with long half-lives appear as fission products. Essential for understanding and prediction of the fate of released or stored actinide containing materials is a thorough knowledge of the involved actinide chemistry as an important prerequisite for modeling distribution and transport of these elements. This necessary chemistry knowledge first involves the identification of pertinent actinide compounds under pertinent conditions, where mainly complexes in solution and at surfaces as well as bulk and colloidal solid phases are of interest. The equilibrium thermodynamics of all these compounds has to be determined to account for the equilibria of their chemical transformations. Finally also kinetic considerations are necessary to discern common and improbable reaction pathways as well as fast and slow reactions with corresponding short and long time scales to reach equilibrium. While for actinide complexes in aqueous solution speciation and basic thermodynamic data are available at acidic pH conditions and at room temperature for many well characterized species [blue books, data bank, review altmaier], this is the case to a lower extent only at basic pH and at higher temperature [altmaier review]. The surface chemistry of actinides interacting at mineral surfaces is by far less developed [geckeis review]. Here the knowledge on adsorbed species and on pertinent adsorption sites is until now rather limited and available thermodynamical models, although incorporating the available insight from various experiments, are essentially empirical [Bradbury, bayens]. A thorough knowledge on species and processes at the atomic level is essential to gain a sufficient mechanistic understanding of the actinide chemistry allowing reliable and transferable predictions and modeling at various pertinent conditions, also beyond the range experimentally already considered. It was the goal of this consortium to contribute to such a mechanistic understanding of actinide chemistry pertinent to conditions of long term storage of nuclear waste in a deep geological repository, focusing on actinide adsorption on natural clay rocks and actinide chemistry under salinar conditions.

Quantum chemical modeling of actinide chemistry has been the central topic of this particular project in the consortium. The computational approach applying rather accurate quantum chemical methods is complementary to experiment providing a different view and access to systems and their properties, which are sometimes hard to study experimentally. Experimental studies of actinide complexes or adsorption systems are commonly facing complex systems composed of several species which complicates the identification and characterization of single species, as they often can not be isolated and sometimes not even studied under conditions where they are predominant. Here the quantum chemical approach is helpful, as well defined species are treated and many of their properties can be determined.

Thus combination of experimental and computational results has been shown also for actinide chemistry to complement each other favorably [churakov? Sulfonate, tsushima, vallet/grenthe].

Some of its issues of the present project are based on previous work carried out in the framework of the previous consortium “Wechselwirkung und Transport von Actiniden im natürlichen Tongestein unter Berücksichtigung von Huminstoffen und Tonorganika”, where actinide adsorption at the neutral clay minerals kaolinite and pyrophyllite as well as the interaction of actinide ions with humic substances have been the main topics. Building on this experience actinide adsorption on smectites, a more complex class of charged clay minerals of wide importance, has been studied in some detail for the first time in this project. The interaction of actinide ions with carboxylic acids, previously studied as model systems for the interaction with corresponding chemical groups in humic substances, is now studied with the new focus on those acids which form the low molecular weight fraction of clay organic matter. In the field of actinide complexation in aqueous solution aspects of complexation in solutions of finite ionic strength and the complexation by borate have been considered. These latter two topics, despite their importance in environmental chemistry and related aspects of deep geological repositories, have until now only very rarely been studied applying quantum chemical methods.

Actinide adsorption on minerals has widely been studied experimentally, applying batch and column experiments as well as spectroscopic methods [1-3]. Macroscopic experiments show that the adsorption depends on the charge of the actinide ion, yielding adsorption at lower pH for higher charged species. Adsorption is further affected by the presence of organic matter or other metal ions [40-44,4]. Spectroscopic methods like EXAFS, TRLFS, and vibrational spectroscopy allow a microscopic view on adsorbed actinide species. Inner- and outer-sphere complexes as well as mono- and polynuclear adsorbates have been identified; all these complexes may even coexist [5,6]. Preferred mineral surface orientations and their structures in contact with aqueous solution are known only in a few cases. Therefore, a microscopic picture of actinide adsorption at mineral surfaces is currently a topic of intense research as such knowledge is a prerequisite for a thorough thermodynamic modeling. In this project we contributed the first systematic studies of actinide adsorption on clay minerals by density functional calculations of periodic slab models [7,8].

[9-11], [12,13]. [14,15].[16].[17],[18-23]. [24-26]. EXAFS[27,28] FT-IR [29] TRLFS [30,31][32-34].[35-37],[38,39]. [40-44] [45-47].[48].[49,50]. [5152].

2 Project Tasks and Prerequisites

3 Development of the state of the art

4 Results

4.1 Actinide Complexes

4.1.1 Am(III) in aqueous solution

The Am(III) aqua ion

The Am(III) aqua ion has been studied as an important reference for various complexes as well as a test case for the performance of the method applied. Interestingly there seem to be until now no accurate quantum chemical calculations for this species, which dominates the Am(III) speciation for pH < 5-8 []. An earlier DFT study employing pseudopotentials only gas phase geometries were determined and energies were corrected for solvation effects in single point fashion [53]. This study suggests a coordination number (CN) of 8 for the Am^{3+} aqua complex, while experimental results suggest values between 7 and 10 []. By analogy to the lanthanides, which show the same oxidation state, CN = 9 is expected [54,55, Buch].

Our calculated results for Am(III) aqua complexes with 6-10 aqua ligands surrounded by a PCM medium are collected in Table 1. The energies of addition of an aqua ligand are slightly exothermic for CN =6, endothermic for CN = 9 and close to zero for CN = 7 and 8. These results are compatible with CN = 7-9, suggesting even the coexistence of several coordination numbers. Measured average Am-O distances of 245-248 pm [56,57] fit better to CN = 7 and 8 than to CN = 9. Thus, in agreement with our energy results, the calculated geometries favor the lower part of the experimentally determined interval of 7-10 for the CN of Am(III).

Table 1: Gibbs free energy of aqua ligand addition (kJ/mol) and average bond distances (pm) to aqua ligands and of the Am(III) aqua ion in water compared to experimental data.

		n	ΔG	Am-O
Calc.		6	-8	244
		7	+2	245
		8	-0	247
		9	+20	251
		10		257
Exp.	a	7.4		247
	b	7.6		248
	d	9.6		245
	c	10.1		247

[a] Stumpf Environm. Science Tech 2006, [b] Ref. 57Stumpf Radiochim 2004, [c] Ref. 56U Heidelberg, [d] Allen eta al Inorg. Chem 2000.

Suggestion of tricapped trigonal pyramidal structure of Am(III)$(H2O)_9$, compatible with our results? For this species we confirm the tricapped trigonal pyramidal structure of approximate D3h symmetry to be more stable than a capped tetragonal antiprism.

Am(III) hydroxide

The first hydroxide species of Am(III), $Am(OH)^{2+}$, is present in solution in appreciable amounts between pH 5-9 []. To the best of our knowledge, this species has been characterized until now neither spectroscopically [???] nor computationally. As the competition between the hydroxide and the aqua ligands suggests a lower CN than for the aqua ion, we modeled Am monohydroxide complexes, including their first solvation shell explicitly, for CN = 4-8 (Table 2). Two structures for each coordination number have been generated by abstracting different protons of the corresponding aqua complex with the same coordination number. The Gibbs

Table 2: Gibbs free energy of aqua ligand addition (kJ/mol) and geometry (distances in pm) of Am(III) monohydroxide in water compared to experimental data.

n	ΔG	$Am\text{-}O_H$	$Am\text{-}O_W$	$Am\text{-}O_{av}$
4	+8	210	249	241
5	+1	213	250	244
6	+6	213	254	248
7	+20	213	258	252
8		218	259	255

free energies of addition of an aqua ligand as shown in Table 2 allow only to tentatively exclude the species with CN = 9 and 8. For lower CN small energies of water addition have been calculated, which show no clear trend. Thus, a tendency of lowering of the CN due to bond competition is visible in our results, but a more careful search for isomers for the lower CNs is necessary to determine a reasonable estimate of the coordination number. The structure of the complexes $Am(OH)^{2+}$ is characterized by a short Am-OH bond of 210-213 pm length and bonds to aqua ligands which are about 10-13 pm longer than in the aqua complexes. Averaging over all Am-O bonds yields distances of 248-255 pm for CN = 6-8 (Table X), which are by 4-8 pm longer than the corresponding values of the aqua ligands with the same CN (Table Y). Thus, the onset of hydrolysis should be visable in EXAFS experiments at pH values above 5 due to a slightly increase of the average Am-O distance.

Table 3. Complexation energies ΔG (in kJ/mol) of U(VI), Np(V) and Am(III) of mono- and diformate complexes and mono- and bidentate coordinations modes of formiate.

	U(VI)		Np(V)		Am(III)	
Complex	CN	ΔG	CN	ΔG	CN	ΔG
mono	5	-88	5	-32	8/9	-78/-75
bi	5	-81	5	-33	8/9	-72/-70
mono-mono, trans	5	-157	5	-93	8/9	-127/-128
mono-bi, trans	5	-161	5	-86	8/9	-133/-130
bi-bi	5/6	-136/-145	4/5	-81/-77	8/9	-136/-146

4.1.2 Complexation with carboxylic acids

Complexation of actinide ions with small carboxylic acids has been inspected as these reactive acids form a part of the soluble organic content of clays, which has been shown e.g. for the relevant formations of Callovo-Oxfordian [58] and Opalinus clay [59]. Acetic acid is the most common one. Formic acid, propionic acid and lactic acids have been found in smaller concentrations [58,59]. As these acids are well known to form complexes with actinides, which contribute to the overall solubility of these elements, we systematically studied complexes for U(VI), Np(V) and Am(III), covering a set of important oxidation states. Our study concentrates on mono- and dicarboxylate complexes, as these species are the more important ones at sour to weakly basic pH conditions and at the low ligand concentrations found in clay formations [58, 59, more]. Available complexation constants in the literature refer to these complexes as single species with sometimes unknown coordination number and structure []. The question of possible coexisting isomers has not yet been investigated experimentally. With our computational studies we thus contribute to a more detailed knowledge about simple actinide carboxylate complexes, which is a necessary prerequisite for a thorough understanding and prediction of their thermodynamic properties under various conditions.

Comparing the complexation of a set of similar ligands like small aliphatic carboxylic acids, one expects in general a similar species and thermodynamic properties for various actinide oxidation states, modulated essentially by the charge of the metal ions. The complexation strength, as characterized by complexation energies ΔG, should follow the general trend $AnO_2^+ < An^{3+} \leq AnO_2^{2+}$ according to the charges of these actinide ions [60] and assuming a predominantly ionic bonding.

Formiate and Acetate

We calculated model complexes of formiate and acetate, assuming for U(VI) and Np(V) the common equatorial coordination number 5 [] and inspected coordination numbers of 8 and 9

Table 4. Complexation energies ΔG (in kJ/mol) of U(VI), Np(V) and Am(III) of mono- and diacetate complexes and mono- and bidentate coordinations modes of acetate.

	U(VI)		Np(V)		Am(III)	
Complex	CN	ΔG	CN	ΔG	CN	ΔG
mono	5	-98	5	-51	8/9	-90/-82
bi	5	-99	5	-45	8/9	-105/-86
mono-mono, trans	5	-178	5	-99	8/9	-143/-143
mono-bi, trans	5	-176	5	-99	8/9	-150/-137
bi-bi	5/6	-166/-176	5/6	-95/-71	8/9	-160/-156

for Am(III), which are probable ones according to our calculations as well as experimental results and the comparison with lanthanide ions (see Section 2.1.1) []. Mono- and bidentate coordination modes are compared for the carboxylate ligands in mono- and dicarboxylate complexes (Fig. X)

Tables 3 and 4 #unite# collect the complexation Gibbs free energies according to the reaction equations

$$[An(H_2O)_n]^{x+} + RCOO^- \rightarrow [AnRCOO(H_2O)_{n-m}]^{(x-1)+} + m\ H_2O$$

$$[An(H_2O)_n]^{x+} + 2\ RCOO^- \rightarrow [An(RCOO)_2(H_2O)_{n-m}]^{(x-2)+} + m\ H_2O$$

for mono- and dicarboxylate complexes, respectively, with R = H for formiate and R = CH_3 for acetate. An represents uranyl(VI), neptunyl(V) and Am(III) ions with charges x = 2, 1, and 3, respectively. n is the number of aqua ligands of the actinide ions, 5 for the actinyls and 8 or 9 for Am(III), and m designates the number of aqua ligands replaced by carboxylates, where a monodentate coordinated ligand contributes 1 and a bidentate coordinated one 2.

The complexation energies for formate follow the effective charges of the actinide ions. The largest energies are calculated for U(VI), slightly lower ones for Am(III) and considerably lower ones for Np(V) (Table 1), for both, mono- and dicarboxylate complexes. U(VI) monoformate shows a slight preference for monodentate ligand binding, confirming earlier calculations and an EXAFS experiment of the project partner Helmholtz-Zentrum Dresden-Rossendorf [61]. The same trend is calculated for Am(III), independent of the coordination number, while mono- and bidentate coordinated formate complexes of Np(V) are degenerate. These trends do not hold always for the dicarboxylates. For U(VI) diformate isomers with one or two monodentately coordinated ligands are preferred compared to a species with two bidentate ligands, even if one takes into account that the small bite angle of the carboxyl group allows an increase of the coordination number of this complex from 5 to 6 (Table 1). For Np(V) we find a preference for monodentate formate binding, while for Am(III) there is a weak tendency to bidentate coordination.

Table 5. Complexation constants $\log\beta_n$ of U(VI), Np(V) and Am(III) formiate and acetate complexes with one and two ligands from various experiments.[a]

	U		Np		Am	
Complex	$\log\beta_1$	$\log\beta_2$	$\log\beta_1$	$\log\beta_2$	$\log\beta_1$	$\log\beta_2$
formate	1.6-1.9	2.6-3.1	-	-	2.54[d]	4.02[d]
acetate	2.4-2.9	4.1-5.5	1-1.9	1.6-3.1	1.8-2.4	3.2-3.8

Acetate complexes yield in general a little higher complexation energies than formate complexes (Table 4). This trend is in line with the higher proton binding of acetic acid (pK_a = 4.8) compared to formic acid with a pK_a of 3.8. Again, comparison of U(VI), Am(III) and Np(V) complexes shows that the complexation energies follow the effective charges of the actinide ions, being highest for U(VI), slightly lower for Am(III) and considerably lower for Np(V). The results collected in Table 4 show for U(VI) monoacetate that mono- and bidentate complexes are energetically degenerate. Also for the diacetate, all combinations of mono and bidentate ligand coordination yield about the same stability. EXAFS experiments have been interpreted to show bidentate coordination for U(VI) acetate [62-64] and are supported by IR measurements [64], which have been complemented by density functional calculations. Hints for monodentate acetate coordination in fresh probes [63], which convert with time to bidentate coordination, support our finding, that complexes with these two coordination modes are close in energy. For the U(VI)-diacetate a change of the coordination number from 5 to 6 is favorable, due to the small bite angle of the carboxyl group. For Np(V) there is a more clear trend to monodentate coordination, for mono- as well as diacetate (Table 4), in disagreement with the results of an EXAFS experiment (see also below) [65]. Am(III), on the other hand, shows a clear preference for bidentate acetate binding, independent of the coordination number and in agreement with a recent EXAFS experiment of the project partner Universität Heidelberg [56]. According to our results, acetate tends more to bidentate coordination than formate.

Comparison of calculated and experimental complexation energies is hampered by an overestimation of calculated reaction energies, which is most probable due to the comparison of results achieved by a polarizable continuum model for species of varying charge []. Nevertheless, calculated relative complexation energies for formate and acetate as well as all three actinide ions treated should be well comparable with trends found experimentally, as this error should cancel out. To compare our results we collected ranges of experimentally determined stability constants $\log\beta_1$ and $\log\beta_2$ in Table 5. Only results for actinide formate and acetate complexes in perchlorate solutions of low ionicity have been taken into account. The results for acetate follow the effective charge of the actinide ions, yielding results for $NpO_2^+ < Am^{3+} < UO_2^{2+}$ in good agreement with our calculated results (Table 3). Only for Am(III) monoacetate with CN = 8 we obtain a complexation energy which slightly exceeds the one of U(VI) monoacetate, while the experimental results yield a lower one. This

experimental trend for monoacetate is reproduced by our results for CN = 9. For formate, in line with the calculated results, lower complexation constants compared to acetate have been measured for U(VI) (Table 5). While our calculations yield also lower complexation energies for Am(III) formate, the experimental values for Am formate complexes are comparable to the highest values measured for acetate. These complexation constants are also higher than for U(VI) formates, in contrast to the calculated results for Am formate complexes. For these reasons we regard the complexation constants for Am formate to be too high.

Structures

For the discussion of calculated geometries of An carboxylate complexes in relation to experimental results, a corresponding view on the performance of DF calculations for the aqua complexes of the actinide ions is helpful as a guideline. A direct comparison to experiment shows for the actinide aqua complexes that GGA calculations, as ususal [], tend to slightly overestimate bond lengths compared to EXAFS results. For the uranyl(VI) aqua complex with the established CN of 5 the uranyl bond length of 179 pm (Table 6) is calculated, slightly larger than the experimental values of 176-178 pm [37,63,64]. The calculated average equatorial bond length U-O_{av} of the aqua ligands of 245 pm (Table 6) exceeds the experimental results of 240-241pm [37,63,64] by about 4 pm. The neptunyl(V) aqua complex with five aqua ligands shows an actinyl bond length of 183 pm, in good agreement with the varying experimental determinations of 182-185 pm [37,65,66,67]. On the other hand, Np-O_{av} of 255 pm again overestimates the EXAFS results of 249-252 pm [37,65,68,69] by a few pm. Although our calculated average Am-O_w distances fit better to experiment for CN = 7 and 8 than for CN = 9 and also considering of dehydration energies supports a slightly lower CN (see Section 4.1.1), the common overestimation of An-O_W distances in other calculations suggests CN = 8 and 9 as most reasonable coordination number for Am(III).

Structures of actinide mono- and diformate complexes are compared for U(VI), Np(V), and Am(III) in Table 6. The actinyl bond lengths of U(VI) and Np(V) complexes increase due to complexation slightly, by about 1 pm per ligand. This effect is a little stronger for U(VI) than

Table 6. Geometric parameters of U(VI), Np(V), and Am(III) formate (Fo) complexes (pm): Actinyl bond length An-O_{ax}, bond to carboxyl oxygen An-$O_{C,}$ averaged bond to aqua ligands An-O_{aq}, average over An-O bond to all ligands An-O_{av}, distance to carboxyl C An-C.

Complex		CN	An-O_{ax}	An-O_C	An-O_W	An-O_{av}	An-C
U(VI) aqua		5	179.1		245	245	
U(VI)Fo	mono	5	180.2	231	247	244	340
	bi	5	179.9	244	243	244	282
U(VI)Fo_2	mono-mono, trans	5	181.2	236	248	243	342
	mono-bi, trans	5	181.1	232/247	244	243	343/284
	bi-bi	5	180.4	245	248	246	283
		6	180.7	249	251	250	287
U(VI)Fo_3	mono-mono-mono	5	182.1	237	247	241	346
	bi-bi-bi	6	181.6	250		250	287
Np(V) aqua		5	183.3		255	255	
Np(V)Fo	mono	5	183.5	250	260	258	346
	bi	5	183.8	254	258	256	289
Np(V)Fo_2	mono-mono, trans	5	185.0	251	255	252	351
	mono-bi, trans	5	184.7	251/255	254	254	350/290
	bi-bi	5	184.8	257	256	256	292
	bi-bi	4	184.4	254		254	289
Am(III) aqua		8			247	247	
		9			251	251	
Am(III)Fo	mono	8		238	252	250	339
	mono	9		243	254	252	344
	bi	8		249	253	252	285
	bi	9		250	252	252	286
Am(III)Fo_2	mono-mono, trans	8		246	252	250	346
	mono-mono, trans	9		246	255	253	344
	mono-bi, trans	8		251/245	254	252	345/288
	mono-bi, trans	9		251/248	256	254	348/287
	bi-bi, trans	8		251	250	251	287
	bi-bi, trans	9		252	254	253	288

for Np(V), in line with the higher complexation energies for U(VI). Actinide-carboxyl bonds An-O_C are shorter for mono- than for bidentate carboxyl coordination as the essentially ionic attraction between these two species is distributed over two coordinative bonds in case of bidentate coordination. An-O_C bonds of monodentate coordinated ligands are shorter than the

bonds of aqua ligands, An-O_W, while the An-O_C bond lengths of bidentate coordinated formate are rather similar to An-O_W (Table 6). Average An-O_{av} distances, as often measured by EXAFS, vary by a few pm at most, showing no clear trend in dependence of the number of formate ligands. The known trend of An-O_{av} to increase with the CN [] and to be independent of the coordination mode, is confirmed for the U(VI) and Np(V) species, where different CN have been inspected (Table 6). For Am(III) species with CN = 8 and 9 this effect is small, up to 4 pm at most. Thus, An-O distances do not provide easily detectable signatures to discriminate the formate coordination mode. The only geometrical feature which clearly reflects the ligand coordination mode is the An-C distance.

In a combined IR and computational study [61], based on vibrational frequencies, the coordination of formate to U(VI) was identified to be preferentially monodentate. EXAFS results of the same study yield a U-O_{ax} bond length of 177 pm and an equatorial U-O distance of 239-241 pm, showing a weak tendency to decrease with increasing pH. These values are in good agreement with our results (Table 6) for the energetically preferred monodentate coordination of formate. If only monodentate formate coordination is considered, we also found a weak trend of decreasing An-O_{av} from 245 pm for the U(VI) aqua ion to 244 pm for monoformate, to 243 pm for diformate and finally to 241 pm for the triformate complex. As such a trend is not observed for the other actinides inspected (Table 6), this agreement with experiment has to be taken with caution. To the best of our knowledge, no structural information is available for Np(V) formate complexes in the literature. In the course of this project, our project partner University of Heidelberg planned an EXAFS experiment on Am(III) formate, which will be carried out with our support in the end of 2016.

Calculated structures of actinide acetate complexes yield a rather similar picture as for formate (Table 7). Actinyl bond lengths increase by about 1 pm per coordinated acetate ligand. An-O_C bond lengths are considerably shorter than An-O_W bonds for monodentate coordination and similar to An-O_W for bidentate coordination. This tendency is more pronounced for U(VI) than for Np(V) (Table 7) Average equatorial An-O bond lengths An-O_{av} can be regarded as independent of the ligand coordination mode. They increase with the coordination number. Again, this trend is nicely seen even for the small change from CN = 8 to CN = 9 for Am(III) (Table 7). An-C distances of 280-290 pm for monodentate coordinated ligands and of 340-350 pm for bidentate coordinated ligands (Table 7) are the only trustworthy geometrical feature to discriminate the coordination modes experimentally, as for formate. Structural differences between formate and acetate complexes are small. In line with the higher ligand binding energy of acetate (Tables 3 and 4), the actinyl bonds of acetate complexes are by 0.2 to 1 pm longer and the An-O_C bonds by 1-4 pm shorter than for formate complexes (Tables 6 and 7).

A direct comparison to experiment shows for the actinide aqua complexes that the GGA calculations tend to slightly overestimate bond lengths compared to EXAFS results. For the uranyl(VI) aqua complex with the established CN of 5 the uranyl bond length of 179 pm (Table 6) is calculated, slightly larger than the experimental values of 176-178 pm [37,63,64]. The calculated average equatorial bond length U-O_{av} of the aqua ligands of 245 pm (Table 6) exceeds the experimental results of 240-241pm [37,63,64] by 4 pm. The neptunyl(V) aqua complex with five aqua ligands shows an acintyl bond length of 183 pm, in good agreement with the experimental determinations of 182-185 pm [37,65,70,71]. On the other hand, Np-

Table 7. Geometric parameters of U(VI), Np(V), and Am(III) acetate (Ac) complexes (pm): Actinyl bond length An-O_{ax}, bond to carboxyl oxygen An-$O_{C,}$ averaged bond to aqua ligands An-O_{aq}, average over An-O bond to all ligands An-O_{av}, distance to carboxyl C An-C.

Complex		CN	An-O_{ax}	An-O_C	An-O_W	An-O_{av}	An-C
U(VI) aqua		5	179.1		245	245	
U(VI)Ac	mono	5	180.5	229	247	243	341
	bi	5	180.2	242	246	244	283
U(VI)Ac_2	mono-mono, trans	5	181.6	232	250	243	342
	mono-bi, trans	5	181.4	233/246	245	243	338/286
	bi-bi	5	181.1	243	249	244	283
		6	181.4	247	253	249	287
U(VI)Ac_3	mono-bi-bi	5	182.4	225/246		242	342/285
	bi-bi-bi	6	182.2	248		248	288
Np(V) aqua		5	183.3		255	255	
Np(V)Ac	mono	5	183.7	251	256	255	345
	bi	5	184.4	253	256	255	291
Np(V)Ac_2	mono-mono, trans	5	185.2	250	254	252	352
	mono-bi, trans	5	185.2	247/255	254	253	347/292
	bi-bi	5	185.4	254	257	254	291
	bi-bi	6	185.4	258	261	259	295
Am(III) aqua		8			247	247	
		9			251	251	
Am(III)Ac	mono	8		236	250	248	343
	mono	9		242	253	252	343
	bi	8		245	253	251	284
	bi	9		249	256	254	288
Am(III)Ac_2	mono-mono, trans	8		241	254	251	342
	mono-mono, trans	9		248	256	254	349
	mono-bi, trans	8		245/249	253	251	349/286
	mono-bi, trans	9		245/251	257	255	352/287
	bi-bi, trans	8		249	251	250	287
	bi-bi, trans	9		250	256	254	289

O_{eq} of 255 pm again overestimates the EXAFS results of 249-252 pm [37,65,72,73] by a few

pm. Although our calculated average Am-O_w distances fit better to experiment for CN = 7 and 8 than for CN = 9 and also consideration of dehydration energies support a slightly lower coordination (see Section 4.1.1), the common overestimation of An-O_W distances in our calculations suggests CN = 8 and 9 as most reasonable coordination number for Am(III).

According to various experiments the coordination of acetate to U(VI) is regarded as bidentate, which is best confirmed by measured short U-C distances of about 290 pm in EXAFS experiments [62-64] and the splitting of symmetric and asymmetric vibrational modes of the carboxyl group of acetate [64,74], as determined in IR experiments. Thus, we preferentially compare our calculated geometries of species with bidentate coordination to EXAFS results. Calculated U-O_{ax} bond lengths of 179-182 pm for complexes with 0-3 acetate ligands are as usual somewhat longer than the corresponding EXAFS results of 176-179 pm [62-64]. Only in one of these experiments the expected increase of the uranyl bond lengths with increasing number of acetate ligands is obtained [64], in agreement with our computational results.

Details

For Np(V) acetate only a single EXAFS experiment carried out by our project partner Helmholtz-Zentrum Dresden Rossendorf is available [65]. At low pH the bond length of the neptunyl aqua complex has been determined to 183 pm, in very good agreement to our result of 183 pm. With increasing pH the Np-O_{ax} bond length increases due to coordination of acetate ligands to 185 pm for a solution with about 50% contribution of the triacetate species. Also this increase parallels nicely the calculated results, which show an increase of Np-O_{ax} of 2 pm for the diacetate complex. An-O_{av} is measured independent of the pH to amount to 251 pm, thus a little shorter than the calculated results of 256 and 257 pm for the bidentate coordinated mono- and diacetate complexes (Table 7) This confirms with our general result of the independence of An-O_{av} from the number of acetate ligands []. In contrast to our complexation energies (see above), bidentate acetate coordination is inferred from the EXAFS results by fitting a weak feature as a Np-C distance of 290-293 pm [65], which is in very good agreement with our computational result of 291 pm for bidentate complexes (Table 7). Taking into account the weakness of this EXAFS feature compared to Np(VI) [65], the calculated weak preference of Np(V) acetate complexes for monodentate coordination, as well as the very small calculated geometry differences for An-O_{ax} and An-O_{av} between mono- and bidentate coordinated complexes (Table 7), a contribution of both complexation modes seems most plausible. Further investigations, favorably by vibrational spectroscopy, are necessary to clarify this issue.

The structure of Am(III) acetate complexes has recently been inspected by our project partner Universität Heidelberg by means of EXAFS [56]. Spectra measured from pH = 1 to pH = 6 reflect the formation of Am acetate species with up to three ligands. For pH = 6 still Am diacetate is the dominating species according to speciation calculations [56]. Average Am-O

bond lengths of 247 pm increasing to 249 pm going along with a CN of 10 have been measured. These bond lengths are as usual a little shorter than our calculated ones of 250 to 254 pm for the preferred bidentate acetate coordination for CN = 8 and 9. Compared to the Am aqua ion we calculated an increase of Am-O_{av} of about 3 pm due to acetate coordination, which is in line with the increase of 2 pm comparing the EXAF spectra at low and higher pH [56]. Bidentate acetate coordination is identified in the measurements by resolving an Am-C distance of 278-284 pm, which is in reasonable agreement with the calculated values for bidentate ligand coordination of 284-289 pm. Am-C distant value. For all geometry parameters we obtained a tendency to increase with increasing CN, thus there is a marginally better agreement with experiment for CN = 8 (Table 7). Overall, relative energies and EXAFS results agree on bidentate acetate coordination to Am(III) and also the geometry parameters of the complexes coincide satisfactorily. The only uncertainty left is the preferred coordination number of Am(III) acetate complexes. Our model assumption of CN = 8 or 9 is in agreement with the experimental result of 10±2 and an increase of CN in the model calculations would worsen the agreement of geometry parameters with experiment.

An-O_{av} should only reflect coordination number when interpreted.

Lactate

Lactate complexes have been studied as lactic acid forms a common small organic ligand present in clay organic matter. This ligand is also of interest as exemplary case of the α-hydroxy carboxylic acid, which offer more complexation modes to metal ions than aliphatic monocarboxylic acids. Besides mono- and bidentate coordination to the carboxyl group also chelate complexation involving in addition the hydroxyl group are possible (Figure X). Open questions are the mode of complexation as well as a possible deprotonation of the hydroxyl group due to complexation, as suggested by a recent work of the project partner Helmholtz-Zentrum Dresden-Rossendorf on Am(III) and Eu(III) lactate [75], in contrast to earlier work. We concentrate our calculations on U(VI) and Np(V) monolactate as the most relevant complexes at low concentrations and considered also some structural models of U(VI) dilactate.

Calculated complexation energies of U(VI) monolactate for various ligand coordination modes show that monodentate, bidentate, and chelate coordination are essentially degenerate with a weak tendency to twofold coordination of the ligand. In agreement with the lower pK_a of lactic acid of 3.9 compared to acetic acid (pK_a = 4.8), the complexation energies of about 65 kJ/mol are lower than for acetate, where about 100 kJ/mol have been obtained. On the other hand, measured complexation constants $\log\beta_1$ of lactate of 2.4-3.4 are comparable with the ones obtained for acetate, $\log\beta_1$ = 2.4-2.9 [76]. This apparent disagreement might be explained by three energetically degenerate isomers of U(VI) lactate compared to two for acetate, which increases the effective complexation constant of lacate. A possible

deprotonation of the OH group of the chelate U(VI) monolactate complexes requires 62 kJ/mol and thus is improbable at acidic conditions. This finding is in contrast to a recent NMR and IR study, supported by calculations of vibrational frequencies, on Eu(III) monolactate [75], but agrees with an earlier suggestion based on TRLFS [77]. Taking into account that the effective charge of Eu(III) ion should be comparable or even marginally smaller than than for U(VI) [60], a depronation of the hydroxyl group of monolacate complexes is regarded as improbable.

Qualitatively similar results are obtained for the complexation energies of Np(V) monolactate. The energies for various complexation modes of about 20-30 kJ/mol are again considerably below the values obtained for acetate of about 50 kJ/mol, in line with the lower pK_a of lactic acid compared to acetic acid (see above). In contrast to U(VI) there is a weak preference of about 10 kJ/mol for bidentate coordination for Np(V) (Table 8). Reported complexation constants $\log\beta_1$ for Np(V) lactate of 1.4-2.0 tend to be larger than for acetate ($\log\beta_1$ = 0.7-2.0) [76], which was recently confirmed buy our project partner INE Karlsruhe. Here this contradiction can not be resolved by a differing number of isomers for lactate and acetate, as the calculated complexation energies for various isomers differ more than for U(VI) (Tables 4 and 8). Thus, the qualitative disagreement between the complexation energies for lactate and acetate for Np(V) as well as for U(VI) needs further consideration. Due to the lower charge of neptunyl(V) compared to uranyl(VI) the deprotonation of the hydroxyl group of the monolactate complexes is even more improbable for Np(V) (Table 8).

Structural parameters of U(VI) and Np(V) monolactate complexes, supporting our energy results, are collected in Table 9. Actinyl bond lengths of 180 pm for U(VI) and 184 pm for Np(V) are by 1 pm longer than for the corresponding aqua complexes, as for other carboxylates (Table 7). Only for the twofold deprotonated ligand, an increase by about 3 pm is calculated, in line with the stronger interaction due to the higher charge of the ligand. The weak variation of the actinyl bond lengths for singly deprotonated lactate supports the near energetic degeneracy of various coordination modes. Monolactate provides a nice example showing that the commonly measured average equatorial An-O distance An-O_{eq} is essentially independent of the coordination mode, which is valid even for the twofold deprotonated lactate ligand (Table 9). Thus, as for other carboxylates, An-C is the only commonly measured geometry parameter appropriate for differentiation of coordination modes. It is short, about 280 pm and 290 pm for U(VI) and Np(V), respectively, for bidentate coordination, and 330 pm or longer for the other coordination modes (Table 9). Comparison with the only available EXAFS results for U(VI) lactate [78] shows the typical overestimation of U-O_{ax} in our calculations. U-O_{av} with 239 pm is measured a little shorter than for acetate (see above) in agreement with our calculated values of about 243 pm, which are also slightly shorter than for acetate (about 246 pm, Table 7). Comparison of the measured U-C distance of 352 pm with our results excludes definitely bidentate coordination and is best comparable with chelate coordination, which yields an U-C of 342 pm. This result can be compared

tentatively also to an EXAFS experiment of our project partner Universität Heidelberg on Am(III) lacate [79], where independent of the pH Am-C of 341-343 pm and the second nearest Am-C distance Am-C_d of 432-436 pm heave been measured. Although the radius of Am(III) is by about 25 pm larger than for U(VI) [Shannon], we demonstrated for acetate, that An-C distances for both actinide ions are comparable (Table 7). Thus, due to An-C bidentate coordination can may also be excluded for Am(III), although the measured An-C_d fits to the lower values calculated (Table 9). Taking into account the relatively large uncertainty of this latter large distance as well as the relative similar distances calculated for various coordination modes (Table 9), a differentiation of coordination modes based on An-C_d seems to be not trustworthy.

Table 8: Gibbs free energy of lactate complexation (kJ/mol) for various coordination modes[a] of U(VI) and Np(V) with an equatorial coordination number of 5.

Species		U(VI)	Np(V)
AnLac	m	-63	-17
	b	-65	-28
	c	-67	-18
	cd	-5	+112
$AnLac_2$	m-m, cis	-120	
	m-b, trans	-126	
	m-c trans	-123	
	b-b	-110	
	b-c	-102	
	c-c	-114	

a) Coordination modes: m = monodentate, b = bidentate, c = chelate, cd = chelate, deprotonated

Complexes of U(VI) and Np(V) with lactate have been considered

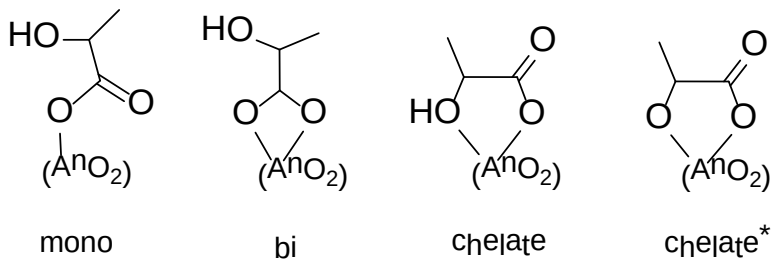

Figure X: Complexation modes lactate to acintyl ions: Monodentate (mono), bidentate (bi), chelate and chelate with deprotonated hydroxyl group (chelate*)

Table 9: Geometry of U(VI) and Np(V) lactate complexes (pm) for various coordination modes[a] with an equatorial coordination number of 5.

Species		An-O_{ax}	An-O_C	An-O_W	An-O_{eq}	An-C	An-C_d
UO_2Lac	m	180	231	246	243	337	467
	b	180	244	244	244	283	435
	c	180	238	246	243	342	454
	cd	183	228	253	243	327	431
Exp.[b]		177			239	352	
NpO_2Lac	m	184	245	256	254	343	476
	b	184	256	256	256	293	445
	c	184	250	258	255	345	482
	cd	186	241	263	254	327	395

a) Coordination modes: m = monodentate, b = bidentate, c = chelate, cd = chelate, deprotonated. b) Ref. 78.

4.1.3 Acetate in saline media: Ternary acetato chlorides

The formation of and the equilibria between complexes are affected in saline media due to modified solvent properties as well as due to direct interactions with dissolved ions of the salt compared to a pure water solvent environment. At the macroscopic scale these effects are accounted for in a cumulative way by activity coefficients (Ref. Fanghänel, Stumm), which are determined by the purely electrostatic Debeye-Hückel model at very low salt concentrations and by more sophisticated empirical models (SIT, Pitzer) at higher concentrations. The basic phenomena at the microscopic level may be divided into effects due to changes of the solvent properties and direct interactions with salt ions. The first group essentially includes the stabilization of charged complexes in the field of counter ions of the

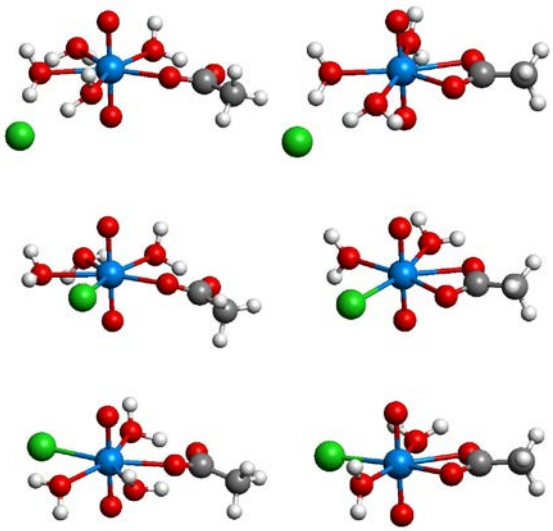

Figur X1. Structures of ternary uranyl(VI) acetatochloride complexes: a) chloride outer sphere b) chloride inner sphere cis c) chloride inner sphere trans. Left and right columns show complexes with acetate mono- and bidentate coordination, respectively.

saline medium and the lowering of the dielectric constant of aqueous solutions with increasing ionicity as a result of the lower orientational polarizability of water molecules in the solvation shell of salt ions.

Table X. Calculated geometry parameters of ternary uranyl monoacetate monochlorate complexes $UO_2CH_3COOCl(H_2O)_n$ with CN = 5 with mono- and bidentate acetate and outer sphere as well as inner sphere cis and trans chloride coordination as well as energies of chloride coordination according Eq. Y Selected average distances in pm, reaction energies ΔG in kJ/mol.

Complex[a]		U-O_{ax}	U–Cl	U–O_{ac}	U–O_{aq}	U–O_{eq}	U–C_{ac}	ΔG
acetate	monodentate	180.5		228.9	247.0	243.4	340.5	
	bidentate	180.2		242.1	244.5	243.5	282.6	
	exp.[18]	177				241		
acetatochloride								
	mono outer sph[b]	180.7	442.2	229.0	247.4	243.8	340.4	-66
	bi outer sph.[b]	180.4	445.9	242.3	244.3	243.5	282.7	-65
	mono cis	181.1	270.2	230.6	251.1	246.0	338.2	-60
	mono trans	181.0	271.3	236.6	248.6	245.6	341.2	-66
	bi cis	180.9	268.5	244.2	247.2	245.7	284.2	-65
	bi trans	180.9	269.5	243.8	246.9	245.4	283.9	-72

[a] *mono*– and *bi*– refers to the coordination fashion of the acetate ligand; *cis*– and *trans*– indicates the positioning of the chloro ligand relative to acetate. [b] outer sphere positioning of the chlorine atom.

For the complexation of metal ions by anionic ligands typically a slight decrease of the complexaton constant at very low ionicity followed by an increase with increasing ionicity is observed (examples). The first effect arises due to the stabilization of the reactant ions by counter ions of the solution, as described by the Debeye-Hückel model (ref). The latter one stems from the decreasing solvation energy of the reactants due to the lowering of the dielectric constant of the saline medium with increasing salt concentration.

In this project we inspected two effects of salinity on the complexation equilibra of actinide complexes, the lowering of the dielectric constant as well as the possibility of direct interaction with the salt ions, which may lead to new equilibria and species in the system. As an exemplary and well studied system of relevance in this cooperative project we have chosen the complexation of uranium(VI) with acetate in a NaCl solution.

To inspect the possible formation of ternary acetatochloride complexes we chose model monoacetate complexes $UO_2CH_3COO(H_2O)_n$ with CN = 5 and mono- (n = 4) and bidentate (n = 3) acetate coordination and exchange an aqua ligand by a chloride ion to form an inner sphere chlorate complex. For comparison also outer sphere coordination of the chloride ion to the aqua ligands of the acetate complexes is considered. The complexation energies of chloride coordination according

$$UO_2CH_3COO(H_2O)_n^+ + Cl^- \rightarrow UO_2CH_3COOCl(H_2O)_{n-1} + H_2O \qquad (Y)$$

are rather similar for various types of acetatochloride complexes (Table X). Chloride binds in outer sphere fashion to a monoacetate complexes with about 65 kJ/mol. Inner sphere complexes with chloride in transposition are marginally more stable for bidentate acetate coordination (72 kJ/mol) and comparable for monodentate acetate coordination (Table X). Thus, our model calculations show that the formation of ternary acetatochloride complexes seems to be thermodynamically possible, even when we consider that our absolute values of reaction energies are overestimated. This complexation has to be regarded as weak, as isomers with inner and outer sphere chloride complexation are energetically close. Interestingly, the equilibrium between isomers with mono- and bidentate acetate coordination is shifted towards bidentate coordination due an inner sphere chloride ligand. The energy difference between bi- and monodentate isomers amounts to 1 kJ/mol in favor of bidentate coordination for monoacetate and increases to 6 kJ/mol for the ternary complexes with chloride in the trans position (Table X).

To inspect the long range effect of the decreasing dielectric constant ε of salt solutions of increasing ionicity, we compared complexation energies calculated with ε = 78.4 for a pure water solvent to results obtained with ε = 60, corresponding to a 2 M NaCl solution [80]. In line with experimental observations [], the increased salt concentration increases the energies

Table X1. ΔG (in kJ/mol) of coordination of acetate and chloride to a uranyl(VI) monoacetate complex with bidentate acetate coordination.

Complex[a]		CN = 5	CN = 6
acetate	mono-mono	-79	
	mono-bi	-77	-60
	bi-bi	-67	-77
choride			
	outer sph	-65	
	inner sph. cis	-65	
	inner sph. trans	-72	

of anionic ligand coordination to cationic complexes. For the formation of monoacetate and monochloride complexes of uranyl, where charge of the complex lowers from +2 to +1 an increase of 8 kJ/mol is calculated. For the reaction of uranyl monoacetate to acetatochloride or diacetate, where the charge of the complex changes from + 1 to 0, we determine an increase of only 2 kJ/mol. These effects are understandable as a lowering of the polarizability of the solvent leads to a decreasing solvation energy of charged complexes.

In Table X we compare geometry parameters of ternary uranyl acetatochloride complexes to uranyl monoacetate. The effect of outer sphere coordination of chloride is marginal, as expected, and not exceeding 0.4 pm for any parameter. Due to inner sphere coordination the axial uranyl bond U-O_{ax} is elongated by 0.5 to 0.7 pm due to the stronger donating capability of chloride compared to an aqua ligand. #charges# The U-Cl bond in the

monodentate acetate complex of about 270 pm is by nearly 2 pm longer than in the bidentate isomer, inline with the lower water exchange reaction energies of this species. Both U-O bonds to acetate as well as to aqua ligands elongate slightly due to the bond competition with the chloride ion. As a result the average equatorial U-O distance U-O_{eq} increases by about 2 pm for the inner sphere complexes. Comparably small changes are calculated for the U-C distance (Table X). Thus, inner sphere chloride coordination yields only small effects in the geometry of the complexes compared to monoacetate, which make a direct identification by EXAFS very challenging, taking also into account that several isomers might coexist.

To shed some more light on the question if ternary uranyl(VI) acetatochloride might exist, we compare calculated model reaction energies of the formation of acetatochloride and diacetate taking bidentate monoacetate as reactant (Table X1). A second acetate ligand is bound by up to about 80 kJ/mol to monoacetate and all variants of mono- and bidentate acetate coordination are calculated to be essentially degenerate if one allows also six-fold coordination in the case of only bidentate acetate coordination. These energies are a little larger than for chloride coordination, which amounts to 72 kJ/mol in the most favorable isomer with bidentate acetate coordination and chloride in trans position. Thus, while thermodynamically possible, the formation of ternary acetatochloride complexes has only to be considered in chloride solutions at low acetate concentrations comparable to the uranium concentrations. These conditions can be fulfilled in saline pore waters with rather low organic content.

4.1.4 Borate and Boratester complexes

With respect to chemical processes relevant for final geological repositories for highly radioactive waste borates are relevant as they are introduced to repositories as part of the nuclear inventory and by borosilicate glasses used to immobilize and dispose hazardous waste. In addition, borate is a minor component of sea salt and thus present in salty ground waters, as they are found e.g. in deep clay formations of northern Germany []. Thus borates may contribute to actinide complexation, thus influencing their mobility. At the beginning of the project no studies on actinide borate complexes were available and also the complexation of the lanthanide analogues has been studied only rarely []. Thus, the goal of this project task was the computational inspection of the complexation abilities of borate and related ions at low concentration conditions in comparison to well characterized ligands. Besides the borate ins itself also borate esters have been considered as these products of the reaction of borate with clay organic matter may also relevant and have been experimentally studied by the project partner Dresden.

Comparison of Ligands and Model Complexes

To support the interpretation of our results on borate and borate ester complexes we inspected pertinent properties of these ligands in comparison to perchlorate as a known non-complexing ligand and acetate as a commonly studied ligand of intermediate complexation strength. As

Table Y1: Comparison of electronic structure of borat and borat ester anions with perchlorate and acetate ions.

	ClO_4^-	BOH_4^-	CH_3COO^-	$lacB(OH)_2^-$	$salB(OH)_2^-$
HOMO /eV	-6.39	-5.27	-4.64	-5.44	-5.34
O 1s / eV	-511.33	-509.32	-508.90	-509.89	-510.01
O 1s / eV compl	-512.23	-510.14	-509.88	-510.56	-510.67
Na 1s / eV	-1035.07	-1034.03	-1034.15	-1034.86	-1034.31
Charge O / au	-0.43	-0.57	-0.53	-0.52	-0.50
Charge Na / au	+0.76	+0.72	+0.68	+0.75	+0.76

mainly the ability to form coordination complexes as a donor ligand are of interest here, we test the donor ability by model complexes with sodium, Na^+L^- without including explicit aqua ligands of the cation.

The HOMO energy of borate and borate esters of -5.3 to -5.4 eV lies between the corresponding values for acetate of -4.6 eV and perchlorate of -6.4 eV (Table X). Thus, it is to be expected that borates and their esters are weaker donor ligands than acetate, but considerably stronger than perchlorate. This trend is confirmed by the energy of the oxygen 1s levels, which serve as a local probe of the electrostatic potential []. Also here borate and borate esters show values between acetate and perchlorate. Mullikan charges, on the other hand, of coordinating oxygen atoms of borate of -0.57 *e* are slightly higher than for acetate (-0.53 *e*), while borate esters yield a marginally lower values (-0.52 *e* for lactatoborate and -0.50 *e* for salicilatoborate). All these negative charges are higher than for perchlorate, which yields a value of -0.43 *e*.

Borate Complexes

Boric acid $B(OH)_3$ in aqueous solutions is known to form a variety of borate multinuclear species with increasing pH provided the borate concentration exceeds 25 mM [81]. At lower concentration only the monoborate anion $B(OH)_4^-$ is formed at a pH above 7. In this first computational study on actinide borate complexes in aqueous solution we concentrate on monoborate complexes of the form $AnB(OH)_4^x$ which should be most relevant at low borate concentrations and medium pH. Although there are no direct hints in the literature, boric acid may form besides the Lewis anion $B(OH)_4^-$ also a Brønstedt anion $BO(OH)_2^-$ by release of a

Table Y3: Gibbs free energies (in kJ/mol) of complexation of boric acid with U(VI) and Am(III) for coordination numbers (CN) of 8 and 9.

	ΔG^0(U)	ΔG^0(Am)	
CN	5	8	9
outersph.	+20	+20	+14
mono	+44	+31	+42

water molecule. #gas phase# With increasing pH hydrolysis competes with actinide complexation. Thus, we also inspect the possible formation of ternary hydroxoborates for U(VI), as its hydrolysis starts already at pH = 3.

We started our investigation of actinide-borate complexes by inspection of a possible complexation of boric acid $B(OH)_3$ with U(VI) or Am(III) aqua ions. These species coexist as dominant species in the acidic pH regime. Not unexpectedly, outer and monodentate inner sphere coordination of the neutral and unpolar boric acid ligand shows endothermic Gibbs free energies (Table Y3). These energies are more endothermic for inner sphere coordination, where boric acid replaces an aqua ligand, than for outer sphere coordination. Thus, the unpolar boric acid species binds as expected weaker than an aqua ligand. These results show

Table Y2: Gibbs free energies (in kJ/mol) of complexation of U(VI) and Am(III) with monoborate

	ΔG^0(U)	ΔG^0(Am)	
CN	5	8	9
outersph.	–	-78	-76
mono	-146	-112	-108
bi	-81	-105	-95
tri	-73	–	–

that complexation of actinides at lower pH by boric acid does not occur.

Uranyl(VI) borate complexes have been modeled with mono-, bi, and tridentate coordination of the borate ligand in the equatorial plane of uranyl (Figure A). For comparison also outer sphere coordination of borate was inspected, but no complex of this type could be stabilized. Instead, deprotonation of an aqua ligand of uranyl was observed and the proton coordinated to borate, yielding an outer sphere complex of uranyl monohydroxide with boric acid. This result does not come as a surprise as the deprotonation constant of the uranyl aqua complex of about 4.5 [] is considerably lower than the pKa of boric acid of 9.2, thus favoring proton transfer from the uranyl aqua complex to borate instead of complexation of the borate ligand. Inner sphere uranyl(VI) borate complexes with mono- bi-, and tridentate coordination of the borate ligand show a decreasing Gibbs free energy of formation with increasing number of borate-uranyl bonds. Thus, monodentate coordination of borate, replacing an aqua ligand, yields the most favorable complex. The replacement of a second aqua ligand in the complex and the formation of a second coordinative bond of borate is unfavorable.

Geometry parameters of the uranyl monoborate complexes show a slightly increasing average uranyl bond U-O_{ax} by less than 1 pm with increasing number of contacts to borate oxygens, reflecting a growing charge donation (Table X). In line with the decreasing Gibbs free energy of complex formation, the bond lengths U-O_B between U and oxygens of borate

increases from 233 pm for the monodentate species to 256 pm for the tridentate one. These bond lengths are comparable to the ones to aqua ligands for the bidentate species and tend to be longer for the tridentate complex. In line with the increasing coordination number of the borate ligand to uranyl, the distances U-B decrease considerably, from 365 pm for the monodentate complex to 283 pm for the tridentate one. The average equatorial U-O bond lengths U-O_{eq} depends, as commonly observed [], essentially on the coordination number of the complex. It amounts to 244 pm for the five-coordinated mono- and bidentate species and increases to 250 pm for the six-coordinate tridentate species (Table X). Thus, this quantity, which is commonly measured by EXAFS, is not helpful for identifying the structure of uranyl monoborate complexes. For this aim U-B as well as the relatively short U-O_B bond of the preferred monodentate complex are suitable. ##

As An(III) ions carry an effective charge comparable to actinyl(VI) species []. Thus we expect Am(III) monoborate complexes to exhibit a similar energy of complexation than for U(VI). In contrast to U(VI) we were able to optimize outer sphere complexes of Am(III) with the borate ion. This finding is explained by the higher complexation constant of the monohydroxide of Am(III) of 6.x [] of compared to 4.5 [] for uranyl(VI), which is still lower than the pK_a of boric acid, but sufficiently close to allow an at least metastable minimum at the potential energy surface. In our model calculations, the outer sphere Am(III) borate species are by about 77 kJ/mol more stable than the well separated ions (Table X) due to electrostatic attraction. Inner sphere borate complexes yield as expected higher complexation energies of -95 to -112 kJ/mol and thus are calculated to be less stable than the most stable U(VI) monoborate isomer (-146 kJ/mol). As for U(VI), monodentate borate coordination is preferred (Table X), although bidentate isomers are energetically close. Also the energy differences between eight- and nine-coordinated species are small, 4 and 10 kJ/mol for the mono- and the bidentate isomer, respectively, with a slight preference for CN = 8. Thus, our model calculations suggest the existence of Am(III) monoborate complexes in solution with a preferred CN of 8 and most probably the existence of isomers and species with neighboring coordination numbers.

Geometry for Am(III) complexes

As accurate absolute energies of complexation are hard to calculate, we compared our energies for Am(III) monoborate complexes to those of monoacetate and monoperchlorate complexes (Table). This allows to confirm the thermodynamic stability of borate complexes by relating the energies of complexation to those of well known species. The complexation energy of Am(III) borate in monodentate coordination of -112 kJ/mol slightly exceeds the one for the most stable bidentate coordinated acetate species of -105 kJ/mol. For monoperchlorate we obtain vanishing or slightly positive Gibbs free energies of complexation. This result qualitatively confirms the expectation that perchlorate does not complexate and supports the qualitative reliability of our approach. Thus, monoborate complexes of U(VI) and Am(III) are

thermodynamically stable and their complexation energy should be a little larger than for acetate.

We also considered the possible existence of the Brønsted anion $B(OH)_2O^-$ of the boric acid in solution. This species has until now only been found in the gas phase [82] and but not in solution. It has also been suggested as possible adsorbed species []. We inspected the energies of the model equilibrium reaction

$$B(OH)_4^- \leftrightarrow B(OH)_2O^-{*}H_2O \leftrightarrow B(OH)_2O^- + H_2O$$

Table X. Geometry of uranyl(VI) monoborate complexes with mono-, bi-, and tridentate borate coordination. Distances in pm.

Complex[a]	CN	U-O_{ax}	U–O_B	U-B	U–O_{aq}	U–O_{eq}
mono	5	180.2	233	365	247	244
bi	5	180.5	246	302	243	244
tri	6	180.9	256	283	244	250

of water dissociation from the Lewis anion to form the Brønsted anion via an intermediate explicit aqua complex. Interestingly, this simple model yields the aqua complex of the

Table X. Geometry of americium(III) monoborate complexes with outer sphere, inner sphere monodentate, and inner sphere bidentate borate coordination. Distances in pm.

Complex[a]	CN	Am–O_B	Am-B	Am–O_{aq}	Am–O_{av}
outer	8		457	249	248
	9		469	251	251
inner mono	8	240	364	250	249
	9	244	368	254	253
inner bi	8	243	309	251	249
	9	246	311	253	252

Brønsted anion as the most stable species. In contrast to a mass spectrometry experiment in the gas phase [82], the Lewis anion is calculated to be about 50 kJ/mol more stable than the Brønsted anion. This difference decreases to about 10 kJ mol in solution, showing that the Brønsted anion might be thermodynamically accessible in complexes.

Table X. Comparison of the geometry of uranyl(VI) monoborate complexes with monodentate ligand coordination of the Lewis anion ligand $B(OH)_4^-$ and the Brønstedt anion ligand $B(OH)_2O^-$in equatorial and axial orientation. Distances in pm.

Complex[a]	CN	U-O_{ax}	U–O_B	U-B	U–O_{aq}	U–O_{eq}
$B(OH)_4^-$	5	180.2	233	365	247	244
$B(OH)_2O^-$ eq.	5	181.2	219	341	250	244
$B(OH)_2O^-$ ax.	6	181.9	217	331	251	244

Hydroxoborate Complexe
Borate Ester Complexes

Table Y4: Comparison of Am(III) complexation with borate, acetate, and perchlorate

	mono	bi
borate	-112	-105
acetate	-90	-105
perchlorate	0	+20

Table Y5: Gibbs free energies (kJ/mol) of water dissociation of the Lewis borate anion in gas phase and solution according scheme 1

	Method	ΔG1	ΔG2	ΔG_{tot}
gas	BP	-33	81	49
	M06L	-18	76	58
solution	BP	-20	27	8
	M06L	-7	23	16

4.2 Adsorption of actinides on clay minerals

4.2.1 Surfaces of charged clay minerals

Mineral models

In the present project we investigated 2:1 type phyllosilicates. They contain layers of an Al octahedral (O) sheet sandwiched between two Si tetrahedral (T) sheets, T-O-T [83] 1-2. The layers may contain charged substitutions (Si4+ by Al3+ or Al3+ by Mg2+, Fe2+, etc.) and solvated counter ions, e.g. Na+, K+, Ca2+, etc. between the layers, respectively. We inspect model clay minerals with the stoichiometric formula Nal(Si8-nAln)(Al4-mMgm)O20(OH)4, where l corresponds to the charge per formula unit (f.u. = half unit cell), n and m are the number of substitutions in tetrahedral and octahedral sheets per f.u., respectively. The two types of substitutions studied are the tetrahedral substitution of Si4+ by Al3+, corresponding to l = 0.5, n = 0.5, m = 0, called further on beidellitic type of model clay mineral. Beidellite is the end-member of smectites with mainly tetrahedral charge 2. The other substitution studied is Al3+ exchanged by Mg2+, with l = 0.5, n = 0, m = 0.5, which we

refer to as montmorillonitic type. As a reference we use the neutral pyrophyllite structure, l = 0, n = 0, m = 0, with a water monolayer between the layers. Such model can also represent a smectite with low charge. For all the clay mineral models a monoclinic lattice was chosen as it is the most common.

Table 1. Lattice parameters for three models of 2:1 clay minerals. The stoichiometric formula of all models is $Na_l(Si_{8-n}Al_n)(Al_{4-m}Mg_m)O_{20}(OH)_4$, lattice vectors are given in pm, angles in degrees. Unit cells are monoclinic.

clay	*a*	*b*	*c*	*B*
pyro	1047.7	903.0	1309.2	99.2
beid	1047.6	903.7	1323.4	99.1
montm	1050.8	905.2	1330.6	97.2

The optimized bulk structures are shown in Fig. 1 and the optimized lattice parameters are given in Table 1. The lattice parameters of all three models almost do not differ except for the c vector that defines the distance between the layers. The neutral model exhibits the shortest c vector of 1309 pm, as it accommodates only water between the layers. Beidellitic and montmorillonitic models exhibit longer c vectors, 1323 and 1330 pm, respectively, due to presence of Na+ counterions. These bulk models were used to create the edge surface models.

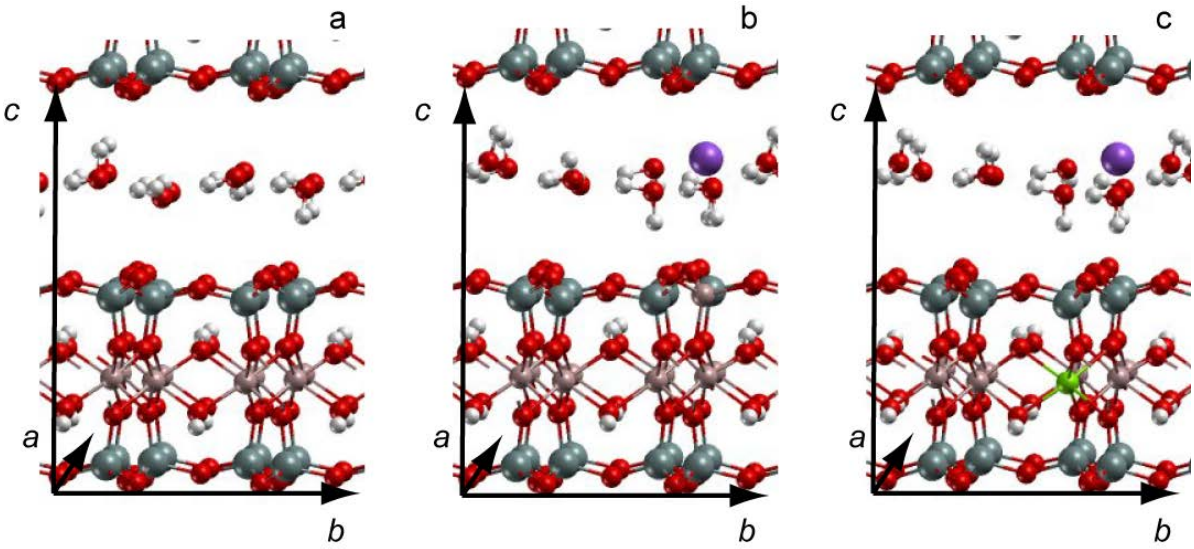

Figure 1. Optimized bulk structures of three models: (a) neutral pyrophyllite type with water interlayer, (b) beidellytic type with substitution in tetrahedral layer, Na^+ counterion and interlayer water, (c) montmorillonitis type with substitution in octahedral layer, Na^+ counterion and interlayer water. Color coding: red are O, grey – Si, brown – Al, green – Mg, violet – Na, white – H.

Surfaces

Crystal growth theory predicts (100), (010), (±110), and (±130) edge surfaces for 2:1 clay minerals 3-5. White and Zelazny derived (110) and (010) edge surfaces using periodic bond chain (PBC) theory 6. Kuwahara studied dissolution of smectites by means of in-situ AFM and detected dissolution on (010) and (110) surfaces 7. Thus, mainly (010) and (110) surfaces are predicted for smectites, in addition (100) and (130) might exist. Structures of all four of them were studied computationally for pyrophyllite 8. Each surface of pyrophyllite exhibits a single preferred termination 8. We assume that the charged clay minerals exhibit edge surfaces with the same structure as pyrophyllite even when substitutions and interlayer counterions are present.

During this project we studied three edge surfaces, (010), (110), and (100). Their structures are shown in Fig. 2. We cut the bulk beidellitic and montmorillonitic models in such a way, that the defect is always in the second outermost cation position from the surface. This position of the defect we define as “inner”. The models of edge surfaces with charged substitutions directly on the surface are created from the “inner” models by simply moving the defect up while the counter ion Na+ stays at the same place. This position of the substitution we call a surface substitution.

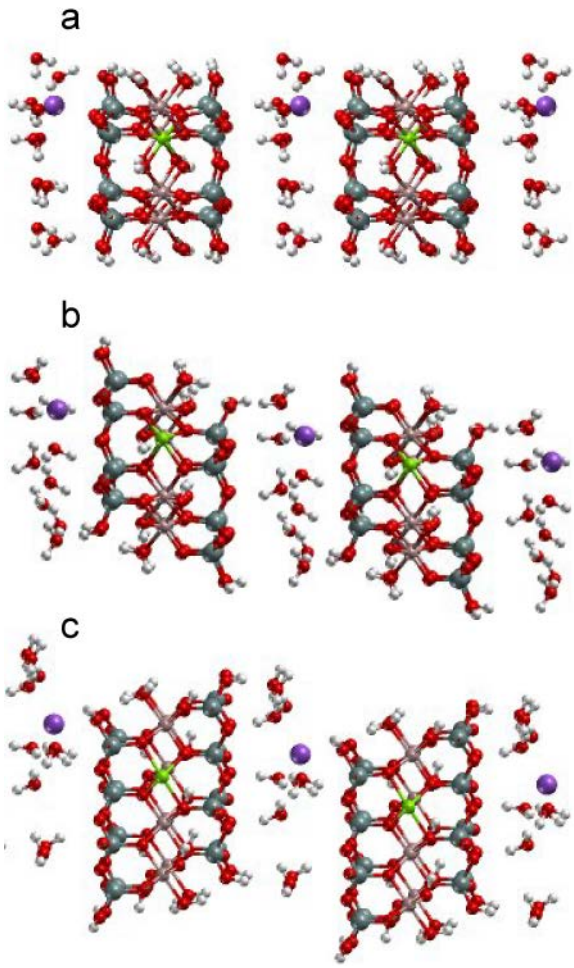

Figure 2. Three types of edge surfaces studied in the present work on the example of montmorillonite “inner defect” model: (a) (010), (b) (110), c (100). The unit cell contains

only one layer of clay minerals and one layer of water. The figure shows at least 2 unit cells in c direction to give an idea how the layers are stacked.

Fig. 2 shows bare surfaces, for these models surface energies were estimated:

$E = (E_{surf} - E_{bulk} - 10*E_{H2O})/2A$

Esurf – total energy of the surface, Ebulk – total energy of the bulk structure, EH2O – total energy of a single water molecule, we took 10 H2O as we need this amount to saturate the surface, A – surface area in Å2. Table 2 shows the surface energies corrected in addition by solvation correction for 10 water molecules, estimated at 0.3 eV for each. The (110) surface seems to be the most stable for pyrophyllite and montmorillonite models. Beidellitic model exhibits (110) and (100) of similar stability. Our results for pyrophyllite are in good comparison with the earlier results of Churakov.

Table 2. Surface energies of bare edge surfaces of 2:1 clay mineral models, in meV/Å^2.

Mineral	(010)	(100)	(110)
pyro	7.49	1.57	0.36
pyro[a]	5.4	1.9	1.6
beid	10.85	8.66	8.94
Beid-s1[b]	10.10	7.21	11.68
Beid-s2[c]	12.02	9.43	8.30
mont	8.80	6.91	3.33
Mont-s	9.69	8.94	4.08

[a] results from Churakov; [b] upper Si is substituted; [c] lower Si is substituted.

The edge surfaces exhibit the following surface groups: SiOH, AlOH2+1/2, AlOH-1/2, AlSiO-1/2, Al2OH. The formal partial charges of oxygens involved are derived from Pauling bond valence theory 9. The AlOH2+1/2 is present on all surfaces. AlOH-1/2 exists only on (010), while the other two, (110) and (100) exhibit the mixed oxygen center Om connected to Al and Si atoms, AlSiO-1/2. Al2OH groups are usually placed rather deep, so we do not consider these groups for adsorption, therefore they are not discussed further. For easier perception we write down all the partial charges of all possible surface groups in Table 3.

Surface solvation must be taken into account, as it was proven to play a crucial role for the edge surface of kaolinite. Therefore, all the calculations were performed with water layer covering the edge surfaces. In most cases surface solvation does not change surface groups. There are only a few exceptions. In case of beidellitic model with the surface substitution s1 – upper Si is substituted by Al, proton from the neighboring AlOH2 surface group moves to the AlOAl center (that was Om before). In case of (010) surface when surface solvation is

accounted for, the proton can move from AlOH2 surface group to protonate the neighboring AlOH group, then the solvated surface does not exhibit such an ordered sequence of AlOH and AlOH2 groups.

Table 3. Types of surface groups and the corresponding formal charges (*e*) of oxygen centers of edge surfaces of 2:1 clay mineral models. For montmorillonite (mont) and beidellite (beid) only the additional groups due to surface substitution are listed.

Surface	Mineral	Groups	Charge
(010), (110), (100)	all	SiOH; SiO	0; -1
		$AlOH_2$; AlOH; AlO	1/2; -1/2; -3/2
	mont	$MgOH_2$; MgOH; MgO	1/3; -2/3; -5/3
	beid	AlOH; AlO	-1/4; -5/4
(110), (100)	all	AlO_m	-1/2
	mont	MgO_m	-2/3
	beid	AlO_{Al}	-3/4

4.2.2 U(VI) adsorption

Adsorption sites

We studied bidentate inner-sphere adsorption of uranyl as in experiments this type of adsorption was postulated 10-11. To avoid a charged unit cell, the surface is always doubly deprotonated. Two oxygen centers of the surface were chosen as adsorption site if they are closer than 340 pm. We studied three types of adsorption sites: aluminol, mixed sites, and silanol sites. Aluminol (silanol) sites are those that include only aluminol (silanol) groups. The mixed sites include an aluminol group and a neighboring silanol group, AlO(H)-SiO(H). If the substitution is not on the surface ("inner" variant), then the available adsorption sites are the same. The adsorption site is regarded as different only for surface substitutions, which leads to more negative surface oxygen charges.

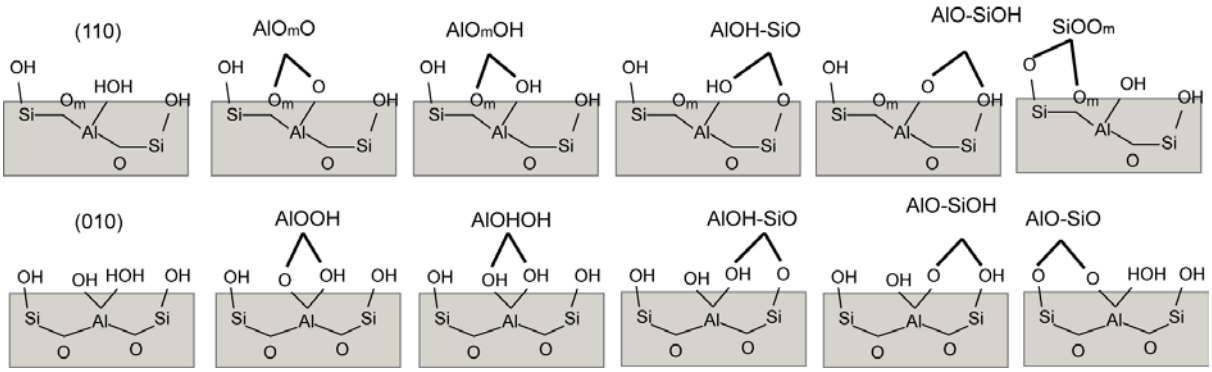

Figure 3. Unsubstituted adsorption sites on various edge surfaces of 2:1 smectites.

Adsorption on (010) and (110) edge surfaces was studied in details. Their adsorption sites are shown in Fig. 3. The (100) surface considered as less probable exhibits sites similar to the ones at the (110) surface, and in addition long-bridge sites that are not available neither on (010), nor on (110) smectite surfaces. Therefore, we inspected three sites on this surface, two characteristic only for this surface, AlOH-AlOH and SiO-SiO, and one is the site present on each surface – mixed AlOH-SiO. Fig. 4 shows the sites inspected.

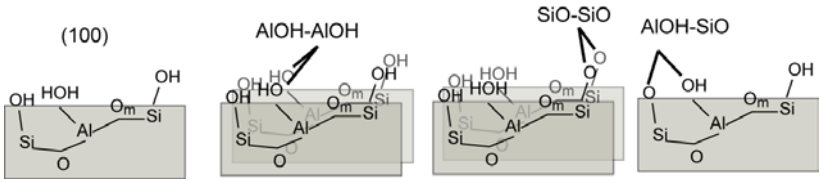

Figure 4. Unsubstituted adsorption sites on (100) edge surfaces of 2:1 smectites.

Adsorbed species

The initial structures of the adsorption complexes were constructed in such a way that the uranyl moiety exhibits two contacts to the surface and coordinates three aqua ligands in the first solvation shell, thus exhibiting the most common uranyl coordination number (CN) of 5.12 In many cases this geometry was preserved during structure optimization and the surface complex converged to five-fold coordinated uranyl adsorbed in bidentate fashion. In addition, we observed hydrolysis on the surface and change of coordination number from 5 to 4. Uranyl monohydroxide as adsorbate resulted from deprotonation one of the aqua ligands, the proton adsorbs at a neighboring surface AlOH-1/2 group to form AlOH2+1/2. It was shown that AlOH-1/2 is a very good proton acceptor.13-15 The pKa value of a uranyl(VI) aqua complex in solution is about 4.5, while the intrinsic pKa of the AlOH2+1/2 surface group was estimated at 5.5 and higher (depends on the surface).16 Thus, a uranyl ion is inclined to deprotonate if there is an AlOH-1/2 surface group nearby. For some sites we modeled hydrolyzed and non-hydrolyzed adsorbed uranyl at the same sites.

Table 4. Various sites for bidentate uranyl adsorption on edge surfaces of 2:1 clay mineral surfaces. The sites are divided into three types, aluminol, mixed, and silanol sites. For each site the adsorbed species and its coordination number are given.

(010)			(110)			(100)		
Site	Adsorbate	CN	Site	Adsorbate	CN	Site	Adsorbate	CN
Aluminol								
AlOOH	UO_2^{2+}	5	AlO_mO^a	UO_2^{2+}	5	AlOH-AlOH	UO_2^{2+}	4
AlOHOH	UO_2^{2+}	5	AlO_mOH	UO_2OH^+	5			
	UO_2OH^+	5						
Mixed								
AlOH-SiO	UO_2OH^+	5, 4	AlOH-SiO	UO_2^{2+}	5, 4	AlOH-SiO	UO_2^{2+}	5

AlO-SiOH	UO_2^{2+}	4	AlO-SiOH	UO_2^{2+}	5, 4		
SiO-AlO	UO_2^{2+}	4					
Silanol							
			$SiOO_m$	UO_2OH^+	5	SiO-SiO	UO_2^{2+} 4

The change of CN is due to the release of an aqua ligand of the first coordination shell of uranyl to the "solution" during structure optimization. This commonly occurred for sites where the two Os centers coordinating to uranyl are more than 300 pm apart. Adsorption sites with a rather long O_s-O_s distance are mixed AlO(H)-SiO(H) sites and long bridge sites on (100) surfaces, SiO-SiO and AlOH-AlOH. Ins ome cases we could optimize complexes with CN 4 and 5 at the same sites. Note that the coordination number may change for both uranyl and uranyl monohydroxide adsorbates.

Comparison of exemplary complexes

In most cases the optimized adsorption species are the same for the same type of site of various model minerals and substitutions. Also the characteristic structural parameters for the complexes adsorbed on the same sites vary only in narrow ranges independent of the specific mineral model. Thus, most structures of uranyl adsorption complexes seem to be essentially determined by the type of surface groups of the site, and this holds for all the complexes studied. The cation substitution affects adsorption complex stronger than the variation of the mineral, however. Comparison of substituted sites to those of other mineral models yields a considerable shortening of the U-Os bonds and therefore a shortening of the U-Al/Mg distances.

As the main structural parameters are quite similar for complexes at the same site, we can reasonably discuss in the following averages over minerals instead of individual values. Complexes at substituted sites need to be separately discussed as their geometric parameters tend to lie outside the range of variation determined for unsubstituted sites.

Adsorption at unsubstituted sites

Table 5 shows averages of structural parameters together with their mean absolute deviations (MAD) for all adsorption complexes studied on various 2:1 smectite models. For the montmorillonitic model with inner substitution we optimized adsorption complexes on AlOmO site with CN 5 and 4 with the latter one being by 21 kJ mol-1 more favorable.

Table 5. Averaged structural parameters[a] of uranyl adsorption complexes on various sites of (010) and (110) edge surfaces of 2:1 smectites. For comparison computational data for the solvated uranyl ion, as well as experimental data for montmorillonite are given. In parentheses the MAD is noted for calculated data and the coordination number for experimental ones.

Site	CN	U-O_t	U-O_s	U-O_s	U-OH	U-O_w	U-O_{eq}	U-Al[c]	U-Si[c]	ΔE_{form} (MAD)
$UO_2(H_2O)_{20}^{2+}$	5	183					240			
(010)										
AlOOH	5	186 (1)	203 (0)	241 (2)		260 (5)	245 (1)	323 (1)		165 (19)
AlOHOH	5	182 (0)	227 (1)	237 (1)		251 (4)	244 (1)	344 (1)		184 (39)
	5	184 (0)	238 (2)	240 (1)	219 (2)	258 (3)	243 (1)	348 (1)		144 (34)
AlO-SiO	4	187 (1)	205 (1)	224 (1)		246 (5)	230 (1)		337 (3)	151 (15)
AlOH-SiO	4	185 (1)	239 (4)	220 (2)	218 (3)	248 (3)	231 (2)		345 (3)	168 (26)
	5	184 (1)	245 (3)	228 (3)	221 (4)	260 (8)	243 (1)		353 (6)	151 (9)
AlO-SiOH	4	186 (0)	199 (0)	249 (5)		245 (4)	235 (0)		361 (4)	164 (28)
(110)										
AlO_mO	5	185 (1)	256 (6)	202 (1)		257 (5)	246 (1)	328 (1)		207 (23)
	4[b]	185	235	202		261	240	329		212
AlO_mOH	5	182 (1)	259 (6)	233 (2)	226 (1)	251 (9)	244 (1)	351 (1)		164 (42)
$SiOO_m$	5	182 (0)	230 (3)	257 (4)	225 (2)	261 (7)	247 (0)		310 (2)	170 (31)
AlOH-SiO	4	183 (0)	227 (2)	217 (2)		245 (6)	233 (2)		359 (1)	127 (35)
	5	183 (1)	229 (3)	218 (1)		259 (9)	245 (1)		362 (1)	121 (20)
AlO-SiOH	4	185 (0)	199 (1)	246 (2)		247 (3)	235 (1)		376 (8)	144 (33)
	5	186 (1)	200 (1)	255 (3)		255 (6)	244 (2)		381 (6)	145 (34)
(100)										
AlOH-AlOH	4	182(1)	227(7)	234(7)			234(1)			
SiO-SiO	4	186(1)	215(3)	221(3)			230(1)			
AlOH-SiO	5	183(1)	231(8)	219(6)			244(2)		367(7)	
Exp.	pH									
mont[17]	8	180(2.2)	230(3.1)			248(2.9)	239(6.0)	309(0.9)		328(0.9)
11	6.6	179(2.3)	229(2.1)			247(2.1)	238(4.2)			331(0.6)
[18]	6.4	178(2.0)					236(6.2)			343(0.6)
	7	180(2.0)	232(2.8)			248(2.1)	234(5.0)			342(0.2)
	5	177(2.0)	230(3.0)			248(2.7)	239(5.7)			
UO_2^{2+}	4	176(2)					241(5)			

[a] Average terminal uranyl bond length U-O_t, bond lengths U-O_s to surface oxygen centers, U-OH bond length to OH ligands, bond lengths U-O_w to aqua ligands, average equatorial U-O bond length U-O_{eq}, U-Al and U-Si distances to the nearest surface Al and Si centers. [b] Only for montmorillonitic model. [c] Only the relevant U-Al/Si distances for comparison with experiment, shorter than 370 pm or the shortest one are noted.

In most cases, the MAD values are rather small (Table 5). The larger MAD values of the U-Ow bonds, by up to 9 pm, reflect the strong variation of individual results between 231 pm and 282 pm (Table 5). The rather low mean absolute deviations of the geometry parameters of the site averages compared to their overall variation confirm that the geometry of the adsorption complexes does not depend on the smectite type as long as the site cation is not substituted.

The uranyl bonds of complexes at sites involving an AlO-3/2 surface group are longer, 185–187 pm, than for other adsorption complexes due to rather strong bonds U-Os between uranyl and the AlO-3/2 group. Correspondingly, these U-Os bonds are also the shortest calculated, 199–205 pm (Table 5). At all other sites inspected, shorter U-Ot bonds of 182–185 pm are calculated.

The average equatorial bonds U-Oeq are calculated shorter, 230–235 pm, for four-coordinated and longer, 243–247 pm, for five-coordinated species due to bond competition (Table 4). The average U-Oeq does not depend on the mineral model or adsorption site, but only on the coordination number of uranyl.

The U-Os distance correlates with the formal charges of the surface centers O_s involved.19 Fig. 5 shows the corresponding results for the various smectite models. The U-O_s values exceeding the general trend at q = -0.5 e are the bonds to Om centers of the (110) surface. Although the formal charge of O_m is -1/2 e, the U-Om bonds are rather long, 256–259 pm, compared to typical values of 230–240 pm for AlOH-1/2 groups with the same formal O_s charge (Table 5). As shown by ab initio molecular dynamics simulations, Om is a weak proton acceptor.14 Thus, the Om center is expected to be less reactive compared to other O_s centers of similar formal charge and therefore exhibits weaker and longer bonds to uranyl.

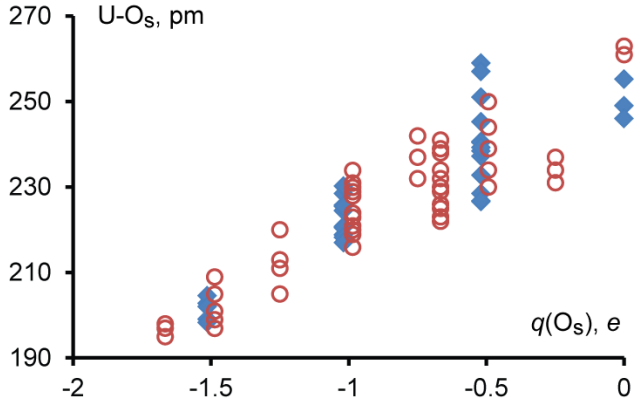

Figure 5. Calculated equatorial U-O_s bond lengths to surface oxygen centers of adsorption complexes of uranyl (VI) on pyrophyllitic, beidellitic, and montmorillonitic 2:1 clay mineral surfaces as a function of the formal charges *q* of surface oxygen centers O_s. Filled diamonds mark bonds of unsubstituted sites. Open circles represent the corresponding bonds for complexes at substituted sites. In case of overlaying symbols they are slightly shifted horizontally for easier discrimination.

U-Al/Si distances also depend in an essential way on the type of site. The shortest U-Al/Si distance, 310 pm, is calculated for the silanol site of the (110) surface (Table 4). U-Al distances of uranyl adsorption on AlOOH sites of (010) surfaces and AlO_mO sites of (110) surfaces are similar, 323 pm and 328 pm, respectively. For adsorption complexes on AlOHOH sites on (010) surfaces and AlO_mOH sites on (110) surfaces, U-Al distances increase to 344 pm and 351 pm, respectively. The U-Si distance when uranyl is adsorbed on deprotonatated silanol group vary between 337 and 362 pm. In all other cases the U-Al/Si distances are longer.

Adsorption at substituted sites

Surface substitutions modify the adsorption sites by increasing the formal charge of the Os centers, see Table 3. In consequence, some of the U-Os bonds shorten considerably. Due to the larger formal charge of Os of these sites, the U-Os bonds to the substituted AlO-5/4 surface group shortens to 205–211 pm, compared to the averages of 217–228 pm for the SiO-1 group (Table 5). Nevertheless, the U-Os distances follow the same correlation as for unsubstituted sites (Fig. 5). The coefficient R^2 for separate linear trends of unsubstituted and substituted sites are 0.81 and 0.84, respectively. Also the slopes of the trend lines are very similar, 34.9 pm/e and 34.2 pm/e. Thus, the effect of site cation substitution on the rather ionic U-Os bonds can be easily rationalized by the change of the formal charge of the surface oxygen centers.

Effects of the surface substitution on the structural parameters U-Ot and U-Oeq are rather small. U-Ot mainly elongates by 1–2 pm due to substitution at the surface, as a result of the stronger interaction with the more negative site. The U-Oeq values change by up to 4 pm as consequence of surface substitutions. As for unsubstituted sites, U-Oeq depends on the CN of the adsorbed uranyl.

Effects of the site substitutions on the U-Al/Si/Mg distances vary with the site. For the aluminol sites changes the U-Al/Mg distance only slightly, by 4 pm at most. For the mixed sites the effects of the site substitution are opposite for beidellitic and montmorillonitic models. When uranyl is adsorbed on MgO(H)-SiO(H) sites of montmorillonite, the U-Si distances elongate due to substitution. As an effect of the increased O_s charge, the distance U-O_s to the substituted MgO(H) surface group shortens compared to the aluminol group AlO(H). To balance this shortening, the second bond to the surface, U-O_s to SiO(H), elongates, which also entails an elongation of U-Si. For the beidellitic type of substitution at the mixed adsorption sites, the substitution induced U-Al distances shorten compared to U-Si due to the considerable shortening of the U-O_s bonds to the aluminol groups which replace the silanol groups. The montmorillonitic substitution increases the U-Si distances by 6–16 pm, while the beidellitic substitution shortens the U-Al distances that replace U-Si by 5–13 pm.

Thus, the main effect of cationic substitutions at the adsorption sites is a shortening of the U-O_s bonds to O_s centers bound to substituted cations. Concomitant structural changes are an elongation of U-O_t and a shortening of corresponding the U-Al/Si/Mg distances.

Energies of adsorption

We estimated the relative stabilities of the various adsorption complexes via their formation energies, according to

$$\Delta E_{form}: \text{S-(OH)}_2 + UO_2(H_2O)_5^{2+} \rightarrow \text{S-O}_2UO_2(H_2O)_3 + 2\ H_3O^+ \qquad (1)$$

where S denotes the mineral surface. ΔE_{form} measures the exchange of two surface protons by the adsorption of uranyl.

The formation energies of various adsorption complexes on the same surface vary by ~100 kJ mol^{-1}. The systems under study exhibit many soft degrees of freedom, especially in the water overlayer and due to bending modes of surface groups. Thus, the total energies of these systems are rather sensitive to structural details. Thus, formation energies yield only a rough guide line and have to be interpreted with due care. Therefore, we resort to energies for sites that are averaged over various minerals (Table 5), similar to our approach to geometry parameters.

First of all, formation energies are all positive, as they include the twofold deprotonation of the adsorption site. The average values vary between 144 kJ mol^{-1} and 184 kJ mol^{-1} for the sites on the (010) surfaces; for the more open (110) surface the energy values fall into the interval from 121 kJ mol^{-1} to 212 kJ mol^{-1}. Thus, both surfaces provide sites of similar complex formation energies.

To classify sites one may refer to the intrinsic pK_a values of various OH groups on the (010) and (110) surfaces of 2:1 clay minerals that were recently estimated.[13, 15] SiOH and $AlOH_2^{+1/2}$ were shown to be the most acidic surface groups on (010) surfaces, both with pK_a values of about 7. The pKa of a $AlOH^{-1/2}$ surface group was estimated at 22.38 The acidity of the substituted surface groups $MgOH_2^{+1/3}$ and $AlOH^{-1/4}$ were obtained higher by at least 3 pK_a units than those of the corresponding aluminol and silanol surface groups.[15] Thus, unsubstituted sites with SiO^- and $AlOH^{-1/2}$ groups are more likely on the (010) surface. Similarly, $AlOH_2^{+1/2}$ surface groups on (110) surfaces exhibit the lowest pK_a, ~5.5, while silanol groups show an acidity constant of ~7.[13, 15] Thus, SiOH and $AlOH_2^{+1/2}$ groups will most probably deprotonate first, while $AlO^{-3/2}$ surface groups are expected to be much less likely. For the (100) no acidity constants were calculated, but based on the similarities of the surface groups we assume, that first appear AlOH-AlOH site, than AlOH-SiO, and then SiO-SiO site.

Comparison to experiment

Montmorillonite is the most commonly studied 2:1 clay mineral in experiments on uranyl adsorption.[10-11, 17-18] To the best of our knowledge there are no experimental studies on U(VI) adsorption on pyrophyllite or beidellite. Thus, we compare our results with data of

various EXAFS studies[10-11, 17-18, 20] on montmorillonite that have been carried out in N_2 or Ar atmosphere to avoid complexes with carbonate (Table 5).

Because of the GGA artefacts we compare adsorption complexes of uranyl with uranyl optimized at the same level of theory, but with the second solvation shell included into the QM model; for the latter, we calculated U-O_t bonds of 183 pm and an U-O_{eq} value of 240 pm (Table 5). In experiment the elongation of U-O_t bonds due to adsorption is 1–4 pm.[10-11, 17] We calculated a strong elongation of 2–4 pm when uranyl is bound to an $AlO^{-3/2}$ surface group. All adsorption complexes on sites involving a fully deprotonated $AlO^{-3/2}$ surface group exhibit very short U-O_s bonds, 199–205 pm (Table 5). Such short U-O distances, if frequently appearing, would be easily resolved in EXAFS spectra, which is not the case. Thus, complexes adsorbed on sites with $AlO^{-3/2}$ surface groups are rare or not be present at all. For all other complexes the effect of adsorption on U-O_t bonds of uranyl agrees well with experiment. To reproduce computationally the experimental shortening of average equatorial distances U-O_{eq} due to adsorption, a mixture of complexes with CN = 4 and 5 has to be assumed, with CN = 4 prevailing.

As two equatorial U-O distances have been fitted in some EXAFS experiments[10-11, 17, 20] we may compare also various calculated equatorial bond lengths, besides the average U-O_{eq}. U-O bonds to OH ligands, SiO^-, and $AlOH^{-1/2}$ surface groups are compatible with the EXAFS result of ~230 pm which is the shorter of the two equatorial U-O distances measured.[10-11, 17] U-O bonds to SiOH groups, O_m, aqua ligands agree well with the longer experimentally resolved distance of ~250 pm (Table 5).

Useful structure parameters for discriminating sites are the distances between U and the surface cations, Al, Si, or Mg. Experimentally these rather long distances, measured by various groups at ~310 pm and from 330 to 345 pm, [18 11, 20 17] are not easy to interpret. Taking into account that (*i*) U-Al/Si distances do not represent chemical bonds, (*ii*) the distances U-Al/Si are in a region of multiple scattering, (*iii*) U-Al/Si distances are experimentally not always observed, the uncertainty of these distances may be quite large. The shortest distance from uranium to a cation, ~310 pm, was calculated for uranyl adsorption at silanol $SiOO_m$ sites on (110) surfaces (Table 5) or its substituted analogue $AlO_{Al}O$. This value is in agreement with the experimental result of 309 pm.[17] The measured distances around 330 pm can be interpreted as U-Al distances for uranyl adsorbed at aluminol sites AlO_mO or AlOOH (Table 5). Note that these sites were estimated as less probable in view of their high deprotonation energy and also due to rather short U-O bonds to the $AlO^{-3/2}$ group. According to the present model results, distances between U and surface cations of 340–350 pm correspond to U-Al for adsorption on AlOHOH sites of the (010) surface or AlO_mOH of the (110) surface or to U-Si for adsorption on mixed AlOH-SiO sites of (010) surfaces.

In summary, the best agreement with experiment exhibit calculated data for complexes adsorbed on sites that involve $AlOH^{-1/2}$, O_m, and/or SiO(H) surface groups. Coexistence of

adsorption complexes with CN = 5 and 4 is suggested with a prevalence for CN 4 to be in agreement with experimental U-O_{eq} values. The experimentally observed U-Al/Si distances are reproduced rather well for uranyl(VI) adsorbed on edge sharing Si tetrahedral (SiO_mO) and Al octahedral sites (AlO(H)OH, AlO_mO). Besides that, U-Si distances calculated for adsorption complexes at mixed sites with deprotonated SiO^- groups (AlOH-SiO) are close to experimental findings.

Effect of coverage

For the most probable sites found in the earlier section we tested the effect of the unit cell size on adsorption. As the adsorption complexes do not depend on the smectite model, we chose montmorillonitic surface with deep defect as exemplary. On the (010) surface AlOHOH and AlOH-SiO sites were tested, while on the (110) surface AlO_mOH, $SiOO_m$, and AlOH-SiO sites were investigated. Fig. 2 shows the unit cells for the two test systems – adsorption complexes of uranyl(VI) on aluminol sites of the (010) and (110) montmorillonite surfaces.

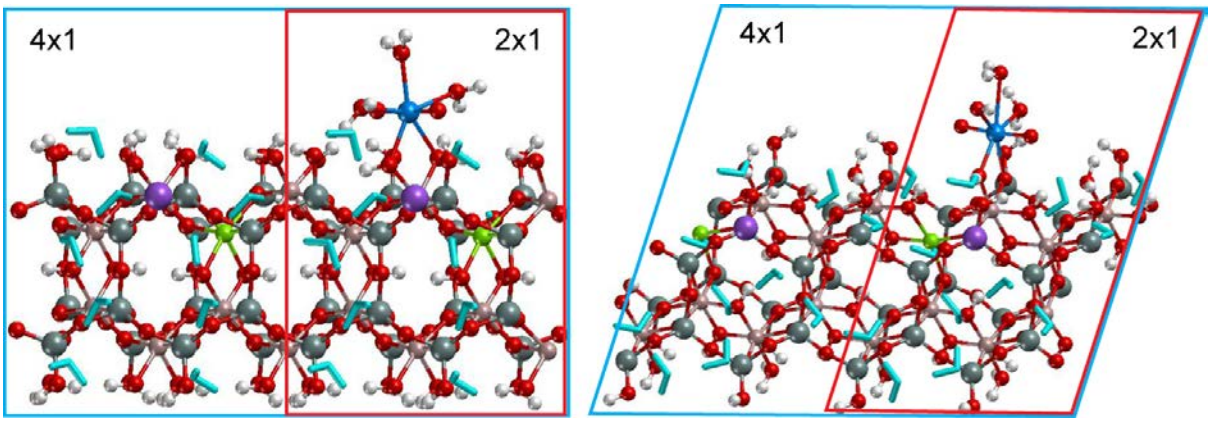

Figure 2. Exemplery adsorption complexes on AlOHOH site of (010) montmorillonite (left) and AlO_mOH site of (110) montmorillonite (right) model with deep defect. Red box shows 2x1 unit cell, blue box shows 4x1 unit cell. Interlayer water is shown by blue sticks, the water molecules from solvation layer are deleted for simplicity.

Structural parameters together with formation energies are given in Table 2. The corresponding data for the adsorption complexes in (2x1) unit cell are given for comparison. The main structural parameters of the same adsorption complexes in (2x1) and (4x1) unit cells are rather similar. The largest difference for the adsorption on (010) surface is observed for the AlOH-SiO site. First of all, in the bigger unit cell both UO_2^{2+} and UO_2OH^+ as adsorbates were successfully optimized, while in the smaller unit cell optimization yields only uranyl monohydroxide as adsorbate. Energetically, UO_2^{2+} adsorption on the AlOH-SiO site of (010) montmorillonite in (4x1) unit cell was found 30 kJ mol^{-1} more favorable, compared to the corresponding complex with uranyl monohydroxide.

Formation energies calculated for the (4x1) and (2x1) unit cells of the (010) montmorillonite are similar, they differ by ±30 kJ mol-1. Interestingly, for the (110) surface

adsorption in (4x1) unit cell is 60–100 kJ mol^{-1} more favorable, than in the smaller (2x1) unit cell.

Table 2. Structural and energetical parameters of uranyl(VI) adsorption on montmorillonitic (010) model surfaces with deep substitution for (2x1) and (4x1) unit cells. The layer charge is 0.25 e per fu.

Site	Adsorbate	Cell	U-O_t	U-O_s	U-OH	U-O_{eq}	U-Al/Si	E_{form}
(010)								
AlOHOH	UO_2^{2+}	2x1	182	227/237		241	346	128
		4x1	185	228/239		242	345	144
	UO_2OH^+	2x1	185	234/242	217	240	349	101
		4x1	185	237/237	217	241	348	95
AlOH-SiO	UO_2OH^+	2x1	183	251/227	227	246	364	167
		4x1	183	246/237	220	244	358	138
	UO_2^{2+}	4x1	182	235/230		244	364	108
(110)								
AlO_mOH	UO_2OH^+	2x1	181	247/232	226	247	352	213
		4x1	181	247/231	228	246	352	98
$SiOO_m$	UO_2OH^+	2x1	182	225/261	229	248	311	221
		4x1	184	223/252	230	245	306	160
AlOH-SiO	UO_2^{2+}	2x1	183	225/219		245	359	160
		4x1	184	224/216		247	362	68

Variation of layer charge

In order to test how the charge of the layer affects the adsorption we created models with the q = 0.5 *e* per fu. For that we substituted one more Al by Mg and introduced the second Na counterion in the interlayer region. Fig. X shows the exemplary slab models with q = 0.5 *e*.

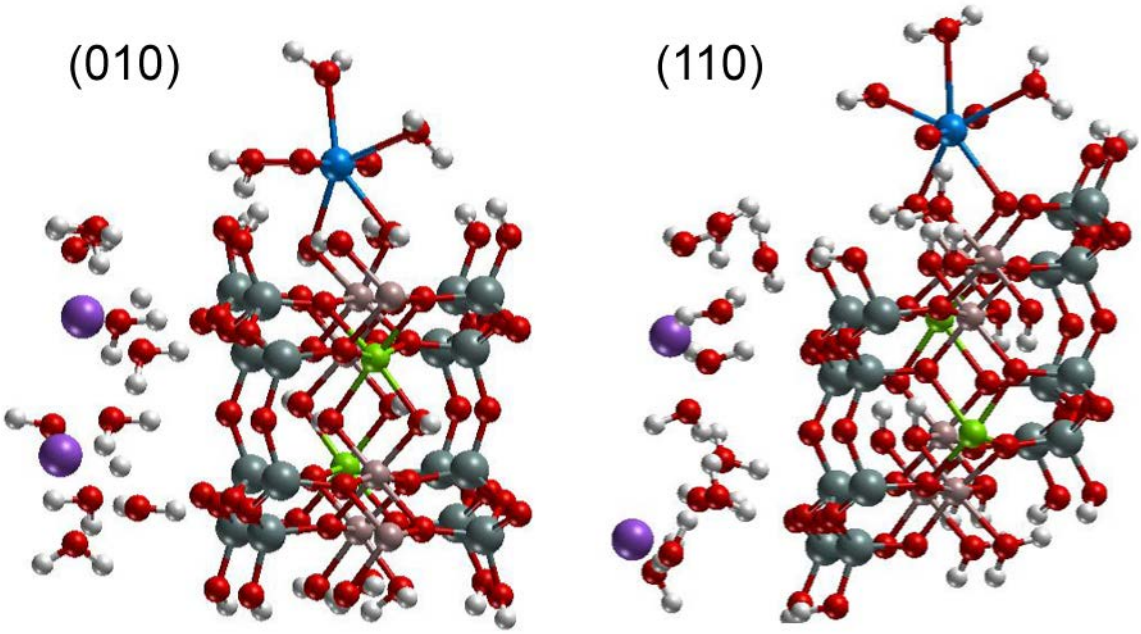

Figure 3. Adsorption complexes of uranyl on the aluminol sites of (010) and (110) montmorillonitic models with deep substitutions and charge of the layer q = 0.5 *e* per fu. Solvation layer is not shown for simplicity.

We tested the effect of the charge on the more likely sites of the (010) and (110) montmorillonite surfaces with deep substitutions. Table X lists the main structural parameters and formation energies for the optimized complexes.

For adsorption complexes on the same sites both structural parameters and formation energies are almost identical and do not depend on the layer charge of the surface. The disturbance due to the increased layer charge is minimal because the initial structures for q = 0.5 *e* were created from the optimized complexes with q = 0.25 *e*. Therefore, the perturbation was mainly created at the opposite side of the slab. That produced minimal changes in the adsorption complexes and solvation layer structure, but shows only the effect of the increased layer charge. As one can see, the layer charge does not affect the adsorption if substitutions are located deep in the slab.

Table 2. Structural and energetical parameters of uranyl(VI) adsorption on montmorillonitic (010) model surfaces with deep substitution for (2x1) and (4x1) unit cells. The layer charge is 0.25 e per fu.

Site	Adsorbate	q	U-O_t	U-O_s	U-OH	U-O_{eq}	U-Al/Si	E_{form}
(010)								
AlOHOH	UO_2^{2+}	0.25	182	227/237		241	346	128
		0.5	182	228/244		241	346	82
	UO_2OH^+	0.25	185	234/242	217	240	349	101
		0.5	185	235/242	217	240	348	108
AlOH-SiO	UO_2OH^+	0.25	183	251/227	227	246	364	167
		0.5	184	252/218	227	243	357	124
(110)								
AlO_mOH	UO_2OH^+	0.25	181	247/232	226	247	352	213
		0.5	181	246/232	226	247	349	212
$SiOO_m$	UO_2OH^+	0.25	182	225/261	229	248	311	221
		0.5	182	228/258	229	248	309	218
AlOH-SiO	UO_2^{2+}	0.25	183	225/219		245	359	160
		0.5	183	226/217		245	360	161

As an example of the mixed substitution, beidellitic surface substitution was added to the montmorillonite model of (010) surface and uranyl adsorption on exemplary sites of the (010) montmorillonitic model. Additional beidellitic substitution was introduced by substituting on surface Si atom by Al. Created charge was neutralized by proton adsorbed on the surface. Fig. X shows the optimized adsorption complexes with various positions of substitutions. Table X gives structural parameters together with formation energies.

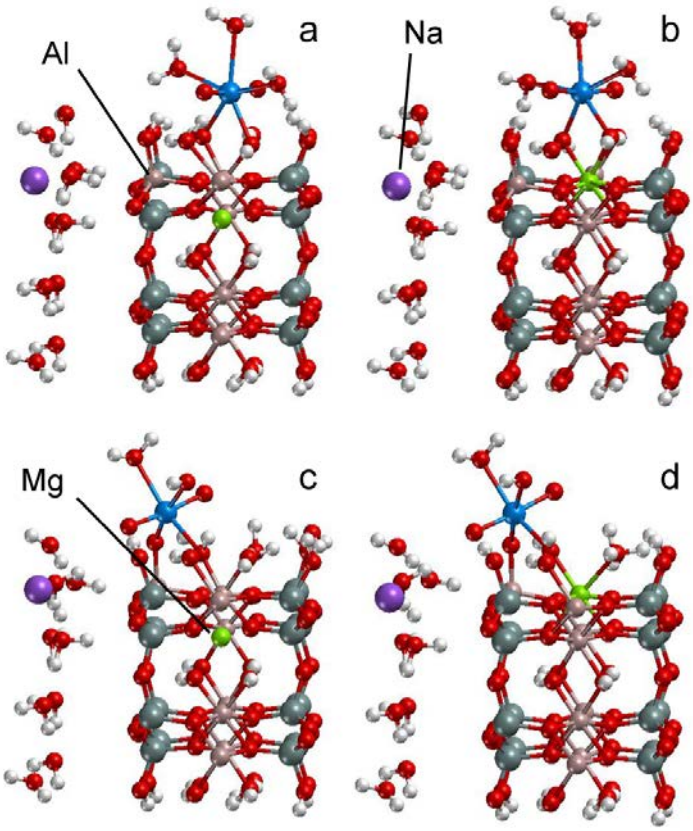

Figure 1. Exemplary adsorption complexes of uranyl on the montmorillonitic models of (010) surfaces with additional beidellitic substitution. Adsorption on (a) AlOHOH site, surface with deep substitution; (b) MgOHOH site, surface substitution; (c) AlOH-AlO site, deep substitution; (d) MgOH-AlO site, surface substitution. Water molecules from the solvation layer are omitted for simplicity.

Table 1. Structural and energetical parameters of uranyl(VI) adsorption on montmorillonitic (010) model surfaces with additional beidellitic substitution, q (in e) is the charge of the layer per fu.

Site	Adsorbate	q	U-O_t	U-O_s	U-OH	U-O_{eq}	U-Al/Si	E_{form}
Deep subst								
AlOHOH	UO_2^{2+}/5	0.25	182	227/237		241	346	128
		0.5	183	224/229		242	343	97
	UO_2OH^+/5	0.25	185	234/242	217	240	349	101
		0.5	185	230/239	217	241	348	99
AlOH-SiO	UO_2OH^+/5	0.25	183	251/227	227	246	364	167
AlOH-AlO		0.5	185	261/218	232	245	362	127
	UO_2OH^+/4	0.25	186	235/217	224	230	351	139
AlOH-AlO		0.5	187	237/210	226	230	354	140
Surf subst								
MgOHOH	UO_2^{2+}/5	0.25	183	222/230		242	344	182
		0.5	184	222/227		242	345	106
	UO_2OH^+/5	0.25	186	230/234	219	240	347	175
		0.5	186	226/233	219	240	348	129
MgOH-SiO	UO_2OH^+/5	0.25	183	239/234	226	245	369	180
MgOH-AlO		0.5	184	252/219	234	244	369	146
	UO_2OH^+/4	0.25	186	226/220	224	229	357	165
MgOH-AlO		0.5	187	233/214	223	230	356	107

4.2.3 Np(V) adsorption

So far one of the most studied actinides is U(VI) [10-11, 17, 21, 24-36] forming the main constituent of radioactive waste. In this work we present the first computational study of the adsorption of Np(V) on a mineral surface. Among other various radionuclides present in typical nuclear waste, Np is of a special interest. Due to the long half-life time of Np^{237} of 2.14×10^6 years it will be the major contributor to the radiotoxicity after a storage time of about 10^6 years [37]. Compared to U(VI) the knowledge about Np(V) sorption properties is limited. There are some experiments on adsorption on iron oxides [38], kaolinite [39-43], gibbsite [44-45], montmorillonite [46-47], silica [48], and alumina [48-49]. The experimental methods include batch experiments [38-41, 46-49], Fourier-transform infrared spectroscopy, FTIR [44-45], extended X-ray absorption fine structure, EXAFS [38, 42-44].

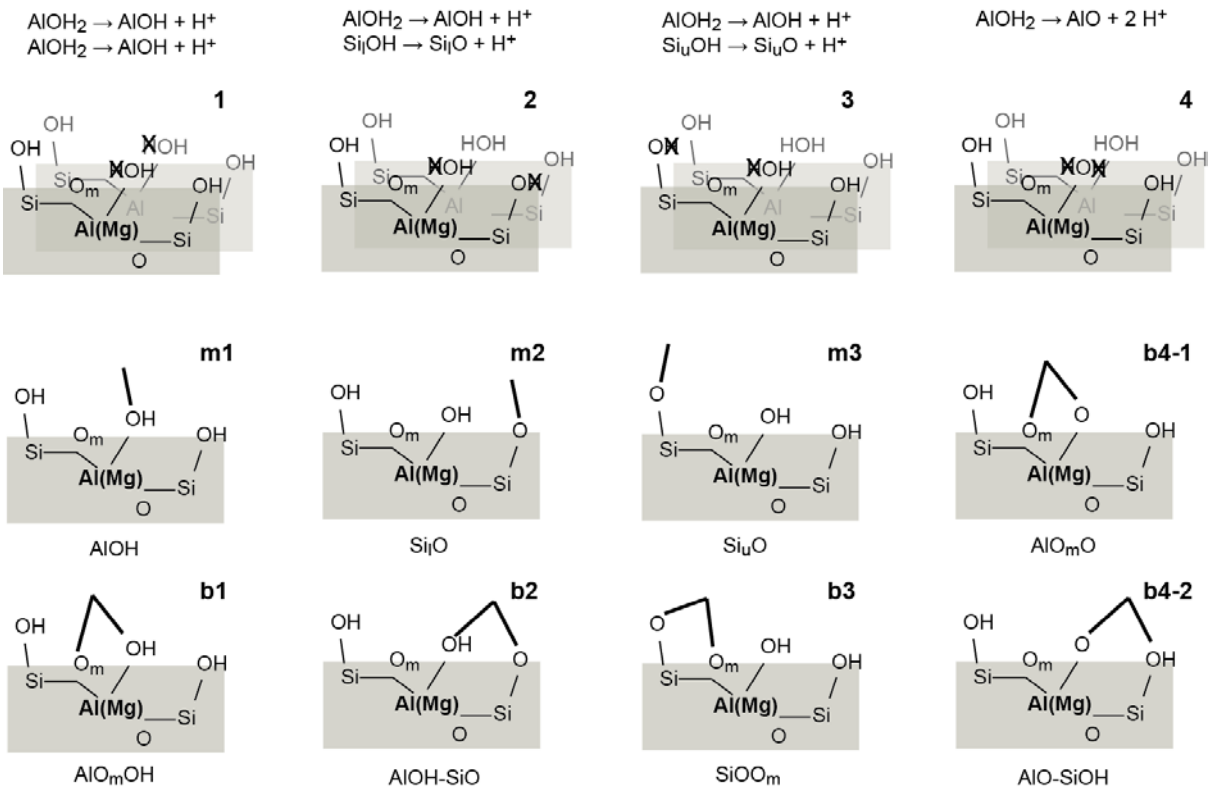

Figure 2. Schematic representation of deprotonated surface groups and adsorption sites studied in the present work. The first row shows the surface groups that are deprotonated according to deprotonation schemes **1** to **4**. (**1**) Two $AlOH_2$ groups deprotonated; (**2**) upper SiOH and $AlOH_2$ groups deprotonated; (**3**) lower SiOH and $AlOH_2$ groups deprotonated; (**4**) two protons from $AlOH_2$ group removed. The second and third rows show the corresponding adsorption sites. **m** = monodentate, **b** = bidentate.

Table 1. Adsorbed species, coordination numbers (CN) and relative energies E_{rel} (in kJ mol^{-1}) for bidentate and monodentate adsorption of UO_2^{2+} and NpO_2^+ at various sites on (110) edge surfaces of montmorillonite. For site designations see Fig. 2.

Site		Adsorbate	CN	E_{rel}
Unsubst.				
AlOH	**m1**	NpO_2OH	4	41
AlO_mOH	**b1**	NpO_2^+	4/5	86/98
Si_lO	**m2**	NpO_2OH	4/5	0/61
AlOH-SiO	**b2**	NpO_2^+	4/5	15/24
Si_uO	**m3**	NpO_2OH	4	36
$SiOO_m$	**b3**	NpO_2^+	4/5	80/85
AlO_mO	**b4-1**	-		
AlO-SiOH	**b4-2**	NpO_2^+	4	127
Subst.				
MgOH	**m1**	NpO_2OH	4	22
MgO_mOH	**b1**	NpO_2OH/NpO_2^+ [a]	4/5	71/97
Si_lO	**m2**	NpO_2OH	4/5	0/81
MgOH-SiO	**b2**	NpO_2^+	4	26
Si_uO	**m3**	NpO_2^+ [b]	4	52
$SiOO_{Mg}$	**b3**	NpO_2^+	4	59
MgO_mO	**b4-1**	-		
MgO-SiOH	**b4-2**	NpO_2^+	4	143

[a] four-coordinated NpO_2OH and five-coordinated NpO_2^+. [b] NpO_2OH as adsorbate was equilibrated with the relative energy of 60 kJ mol^{-1}.

Table 3. Structural parameters (in pm)[a] and relative energies E_{rel} (in kJ mol^{-1}) of neptunyl(V) monodentate and bidentate adsorption complexes for various sites at the unsubstituted and substituted (110) edge surfaces of montmorillonite. For comparison computational data for the solvated neptunyl ion modeled as $NpO_2^+(H_2O)_{64}$ with CN = 4 and 5 and experimental data with CN in parentheses are given. For site designations see Fig. 2.

Site		CN	Np-O_t	Np-O_s	Np-O_s	Np-OH	Np-O_w	Np-O_{eq}	Np-Al	Np-Si	E_{rel}
$NpO_2^+(H_2O)_{64}$		4	185					244			
$NpO_2^+(H_2O)_{64}$		5	185					253			
Unsubst.											
AlOH	**m1**	4	188	232		231	247	239	401		41
AlO_mOH	**b1**	4	184	246	238		242	242	347	351	86
Si_uO	**m2**	4	187	220		235	247	237		377	36
$SiOO_m$	**b2**	4	187	232	258		241	243	420	306	80
Si_lO	**m3**	4	186	230		236	246	240		366	0
AlOH-SiO	**b3**	4	184	240	231		246	241	392	359	15
		5	185	234	231		265	252	395	362	24
AlO-SiOH	**b4-2**	4	188	203	252		256	242	368	385	127
Subst.									Np-Mg		
MgOH	**m1**	4	189	228		230	249	239			22
MgO_mOH	**b1**	4	187	239	233	235	237	236	340	373	71
Si_uO	**m2**	4	186	218			248	241		379	52
$SiOO_{Mg}$	**b2**	4	185	232	245		250	244		300	59
Si_lO	**m3**	4	186	233		221	256	242		366	0
MgOH-SiO	**b3**	4	185	229	232		247	239		366	26
MgO-SiOH	**b4-2**	4	190	197	250		251	237	370	385	143
Exp.	Ref.	pH	Np-O_t					Np-O_{eq}			
NpO_2^+	*b*		182(2)					249(3.6)			
kaolinite	*c*	8	185(2)					245(4)			
	c	9	186(2)					250(4)			
	c	10	187(2)					247(4)			

[a] Average terminal neptunyl bond length Np-O_t, bond lengths Np-O_s to surface oxygen centers, Np-OH bond length to OH ligands, bond length Np-O_w to aqua ligands, average equatorial Np-O bond lengths Np-O_{eq}, Np-Al/Mg and Np-Si distances to the nearest surface Al/Mg and Si centers. [b] [50]. [c] [42].

4.2.4 Adsorption of salt cations

4.3 Methodic topics

4.3.1 Low temperature simulated annealing

In the previous sections comparing structural parameters to experiment, we were able to identify favorable adsorption complexes.[21] However, this identification is only tentative in

view of uncertainties in the calculated energies. More reliable energies of adsorption complexes should be achievable by a carefully equilibrated water overlayer.

We suggest a low-temperature partial equilibration (LTPE) procedure for arriving at the structures of various adsorption complexes and for calculating the corresponding adsorption energies. Compared to a costly full FPMD treatment, this procedure is efficient enough to allow a systematic study of various adsorption complexes at several sites of mineral surfaces. As a case study, we examine the adsorption of uranyl UO_2^{2+} on (110) edge surfaces of three 2:1 model clay minerals.

We used the optimized adsorption complexes discussed in Section XX as initial structures for the LTPE procedure. As a result of that we confirm most of the adsorption species with a few exceptions. Substituted sites commonly showed changes of the adsorbed species compared to the results of simple optimization. The adsorption complexes on aluminol sites generated by substitution, AlOH-AlO and AlO-AlOH, both converged to four-coordinated uranyl. For the montmorillonitic model with a Mg substitution on the surface, the complexes on MgO_mO and MgO_mOH sites also converged to CN = 4. Thus, CN 4 is more common for adsorption on the substituted sites of 2:1 model smectites.

To show the effect of LTPE on the formation energies, we compare two sets of data: (*i*) E_{form} from our earlier static DFT calculations (Fig. 7a) and (*ii*) as calculated here via the equilibration protocol (Fig. 7b). In contrast to the almost randomly distributed formation energies of the first set (Fig. 7a), the E_{form} values calculated after pre-equilibration exhibit clear trends (Fig. 7b).

The formation energies of the same complexes at the same unsubstituted adsorption sites of beidellitic and montmorillonitic models are rather close; they differ by 10 kJ mol^{-1} on average. Adsorption on substituted sites is more favorable compared to the corresponding unsubstituted sites with the single exception (Fig. 7b). Interestingly, the adsorption on the AlOH-SiO site is most favorable for all surface models (Fig. 7b).

In order to rationalize this finding we estimated adsorption energies of uranyl on deprotonated (110) model surfaces of 2:1 smectites. The adsorption energy E_{ads} of a uranyl aqua complex on a deprotonated surface site is the reaction energy of the process

$$\text{Surface-}(O^-)_2 + UO_2(H_2O)_5^{2+} \rightarrow \text{Surface-}(O)_2UO_2(H_2O)_3 + 2\ H_2O \qquad (2)$$

As Eq. (2) implies a charged unit cell, it cannot be used directly. Instead, we determine the adsorption energy of uranyl at various sites as the difference

$$E_{ads} = E_{form} - E_{depr} \qquad (3)$$

where the site deprotonation energy E_{depr} is defined as the energy change of the reaction

$$\text{Surface-}(OH)_2 + 2\ H_2O \rightarrow \text{Surface-}(O^-)_2 + 2\ H_3O^+ \qquad (4)$$

To determine adsorption energies, (Eq. 3), we first need to estimate the site deprotonation energies E_{depr}, Eq. (4). We circumvent the problem of charged surface systems in Eq. (4) by evaluating *model* site deprotonation energies. For details see Ref. XXX. Adsorption energies are given in Table 6.

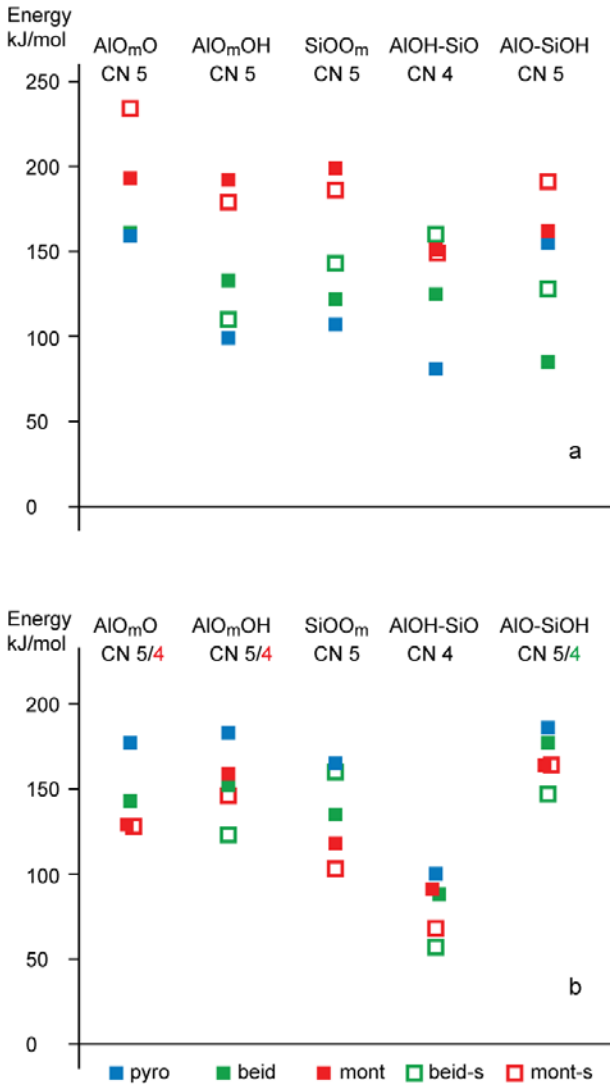

Figure 7. Formation energies, estimated from Eq. (1). Results (a) for the directly optimized structures and (b) for equilibrated systems.

The $_{adsorption}$ energies E_{ads} given in Table 6 at analogous sites of beidellite and montmorillonite with subsurface substitutions are rather similar. The corresponding E_{ads} values for pyrophyllite are significantly higher (Table 6), indicating a weaker binding on this neutral substrate. For all mineral models, substituted sites are calculated more favorable than their unsubstituted analogues (Table 6).

The binding of a uranyl ion to a clay mineral surface can be expected to have a notable ionic character. Thus, the adsorption energy is expected to correlate with the charge of the adsorption site. We inspected the correlation between adsorption energies and charges of the adsorption sites. We employed a specifically designed scheme of effective charges that,

instead of formal valences and bond strength values as in the Pauling scheme, combines Bader charges[22] of the oxygen centers with an empirical measure, borrowed from the bond-valence method,[23] of the strengths of the involved bonds of the oxygen centers. These novel effective charges of the oxygen centers (Table 6) allow one to differentiate groups that are characterized by identical Pauling charges.

Table 6. Estimated adsorption energies E_{ads} (kJ mol^{-1}) as well as effective charges[a] (e) of oxygen centers at various adsorption sites on (110) edge surfaces of 2:1 model smectites.

Model	Site	E_{ads}	q_1	q_2	q_{tot}	Site	E_{ads}	q_1	q_2	q_{tot}
Pyro	AlO_mO	69	-0.07	-0.61	-0.68					
Beid		-17	-0.16	-0.74	-0.90					
Mont		-45	-0.16	-0.67	-0.83	MgO_mO	-75	-0.14	-0.87	-1.01
Pyro	AlO_mOH	121	-0.14	-0.13	-0.27					
Beid		90	-0.14	-0.19	-0.33	AlOOH(o)	34	-0.19	-0.24	-0.43
Mont		81	-0.15	-0.26	-0.41	MgO_mOH	69	-0.21	-0.37	-0.58
Pyro	$SiOO_m$	74	-0.44	-0.04	-0.48					
Beid		18	-0.40	-0.08	-0.48	AlOO(t)	2	-0.55	-0.13	-0.68
Mont		12	-0.38	-0.11	-0.49	$SiOO_m$	-20	-0.44	-0.12	-0.56
Pyro	AlOH-SiO	29	-0.22	-0.41	-0.63					
Beid		13	-0.27	-0.37	-0.64	AlOH-AlO	-54	-0.25	-0.55	-0.80
Mont		29	-0.37	-0.41	-0.78	MgOH-SiO	-49	-0.43	-0.38	-0.81
Pyro	AlO-SiOH	78	-0.61	0.14	-0.47					
Beid		17	-0.62	0.10	-0.52	AlO-AlOH	19	-0.66	-0.08	-0.74
Mont		-10	-0.60	0.08	-0.52	MgO-SiOH	-34	-0.63	0.08	-0.55

[a] q_1 is the charge of the first surface group of the site, q_2 the charge of the second group, in the order indicated by the site label as given in column 2. For example, for the site AlOH-SiO q_1 is the charge of OH of the AlOH group, q_2 is the charge of the O center of the SiO group of the site. $q_{tot} = q_1 + q_2$.

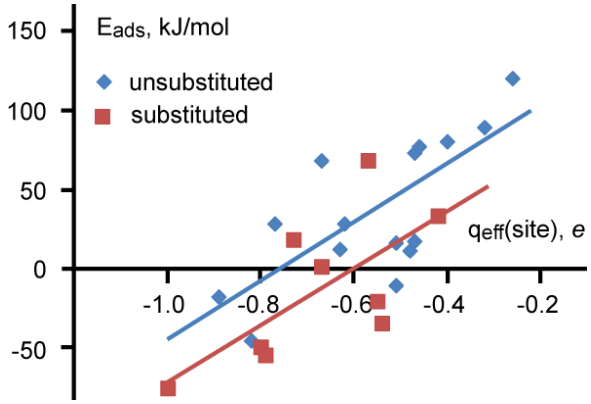

Figure 8. Adsorption energies as a function of the effective charges of the corresponding adsorption sites. All complexes $R^2 = 0.56$ ($y = 208.55\ x + 145.57$); unsubstituted sites $R^2 = 0.53$ ($y = 187.92\ x + 142.88$); substituted sites $R^2 = 0.46$ ($y = 180.1\ x + 111.27$).

Fig. 8 illustrates the weak correlation with $R^2 = 0.56$ between the site charges and the corresponding adsorption energies. The weak correlation may in part be due to the approximate nature of estimating site deprotonation energies. Other factors could be covalent contributions to the uranyl surface bonds. The trend lines in Fig. 6 show that adsorption on substituted sites is ~30 kJ mol^{-1} more favorable compared to adsorption at unsubstituted sites, concomitant with the more negative charges of the former sites.

Two factors, easy deprotonation and a strong negative charge of the resulting adsorption site, lead to the most favorable adsorption complexes on (110) smectite surfaces. The AlO_mOH and AlOH-SiO sites and their substituted analogues exhibit the lowest deprotonation energies of all surface models. However, the effective charges of the AlOH-SiO sites are ~0.3 *e* more negative than those of the AlO_mOH sites. This difference allows one to rationalize the energy preference for adsorption at AlOH-SiO sites (Fig. 7b).

4.3.2 Surface solvation by PCM

5 Summary

6 Publikations resulting from this project

References

[1] E. A. Jenne (Ed.), Adsorption of Metals by Geomedia: Variables, Mechanisms and Model Applications, Academic Press, United Kingdom, 1998.

[2] M. Barnett, D. Kent (Eds.), Adsorption of Metals by Geomedia II: Variables, Mechanisms, and Model Applications, Elsevier, USA, 2008.

[3] H. Geckeis, T. Rabung, J. Cont. Hydrol. 102 (2008) 187.

[4] K. Choi, J. W. Park, Geoscience J. 9 (2005) 53.

[5] S. S. Lee, P. Fenter, C. Park, N. C. Sturchio, K. L. Nagy, Langmuir 26 (2010) 16647.

[6] P. Fenter, S. S. Lee, C. Park, L. Soderholm, R. E. Wilson, O. Schwindt, Geochim. Cosmochim. Acta 74 (2010) 6984.

[7]

[8] A. Kremleva, S. Krüger, N. Rösch, Radiochim. Acta 98 (2010) 635.

[9] J. J. Katz, G. T. Seaborg, L.R. Morss (Eds.), The Chemistry of the Actinide Elements, 2. ed., Chapman and Hall, New York, 1986.

[10] L. R. Morss, N. M. Edelstein, J. Fuger (Eds.), Actinide and Transactinide Elements, 3. ed., Springer, Dordrecht, 2006.

[11] Z. Szabo, T. Toraishi, V. Vallet, I. Grenthe, Coord. Chem. Rev. 250 (2006) 784.

[12] Ref. 2, vol. 4, chap. 22.

[13] D. L. Clark, D. E. Hobart, M. P. Neu, Chem. Rev. 95 (1995) 25.

[14] K. H. Lieser, Radiochim. Acta 70/71 (1995) 355.

[15] R. J. Silva, H. Nitsche, Radiochim. Acta 70/71 (1995) 377.

[16] Ref. 2, vol. 4, chap. 23.

[17] F. J. Stevenson, Humus Chemistry, 2. ed., Wiley, New York, 1994.

[18] K. L. Nash, J. M. Cleveland, T. F. Rees, J. Environ. Radioact. 7 (1988) 131.

[19] G. R. Choppin, Radiochim. Acta 44/45 (1988) 23.

[20] M. A. Denecke, S. Pompe, T. Reich, H. Moll, M. Bubner, K. H. Heise, R. Nicolai, H. Nitsche, Radiochim. Acta 79 (1997) 151.

[21] S. Sachs, K. Schmeide, T. Reich, V. Brendler, K. H. Heise, G. Bernhard, Radiochim. Acta 93 (2005) 17.

[22] K. Schmeide, T. Reich, S. Sachs, V. Brendler, K. H. Heise, G. Bernhard, Radiochim. Acta 93 (2005) 187.

[23] M. A. Denecke, T. Reich, S. Pompe, M. Bubner, K. H. Heise, H. Nitsche, P. G. Allen, J. J. Bucher, N. M. Edelstein, D. K. Shuh, J. Phys. IV 7 C2 (1997) 637.

[24] S. Pompe, K. Schmeide, M. Bubner, G. Geipel, K. H. Heise, G. Bernhard, H. Nitsche, Radiochim. Acta 88 (2000) 553.

[25] K. Schmeide, S. Sachs, M. Bubner, T. Reich, K. H. Heise, G. Bernhard, Inorg. Chim. Acta 351 (2003) 133.

[26] S. Sachs, G. Bernhard, Radiochim. Acta 93 (2005) 141.

[27] S. Pompe, M. Bubner, M. A. Denecke, T. Reich, A. Brachmann, G. Geipel, R. Nicolai, K. H. Heise, H. Nitsche, Radiochim. Acta 74 (1996) 135.

[28] M. A. Denecke, Coord. Chem. Rev. 250 (2006) 730.

[29] R. Steudtner, K. Müller, K. Schmeide, S. Sachs, G. Bernhard, Dalton Trans. 40 (2011) 11920.

[30] R. N. Collins, T. Saito, N. Aoyagi, T. E. Payne, T. Kimura, T. D. Waite, J. Env. Qual. 40 (2011) 731.

[31] S. Pompe, A. Brachmann, M. Bubner, G. Geipel, K. H. Heise, G. Bernhard, H. Nitsche, Radiochim. Acta 82 (1998) 89.

[32] V. Vallet, Z. Szabó, I. Grenthe, Dalton Trans. (2004) 3799.

[33] V. Vallet, P. Macak, U. Wahlgren, I. Grenthe, Theor. Chem. Acc. 115 (2006) 145.

[34] Ref. 2, vol. 3, chap. 17.

[35] H. Moll, G. Geipel, T. Reich, G. Bernhard, T. Fanghänel, I. Grenthe, Radiochim. Acta 91 (2003) 11.

[36] J. Jiang, L. Rao, P. Di Bernardo, P. L. Zanonato, A. Bismondo, J. Chem. Soc., Dalton Trans. 8(2002) 1832.

[37] P. G. Allen, J. J. Bucher, D. K. Shuh, N. M. Edelstein, T. Reich, Inorg. Chem. 36 (1997) 4676.

[38] T. Schäfer, R. Michel, F. Claret, Journal of Physics: Conf. Series 186 (2009) 012095.

[39] T. Schäfer, R. Michel, F. Claret, T. Beetz, R. Wirick, C. Jacobsen, J. Electron Spec. Rel. Phenomena 170 (2009) 49.

[40] P. Benes, K. Kratzer, S. Vlckova, E. Sebestova, Radiochim. Acta 82 (1998) 367.

[41] A. Krepelova, S. Sachs, G. Bernhard, Radiochim. Acta 94 (2006) 825.

[42] R. Kautenburger, H. P. Beck, ChemSusChem 1 (2008) 295.

[43] C. Joseph, K. Schmeide, S. Sachs, V. Brendler, G. Geipel, G. Bernhard, Chem. Geol. 284 (2011) 240.

[44] M. H. Lee, E. C. Jung, K. Song, Y. H. Han, H. S. Shin, J. Radioanal. Nuc. Chem. 287 (2011) 639.

[45] E. A. Jenne (Ed.), Adsorption of Metals by Geomedia: Variables, Mechanisms and Model Applications, Academic Press, United Kingdom, 1998.

[46] M. Barnett, D. Kent (Eds.), Adsorption of Metals by Geomedia II: Variables, Mechanisms, and Model Applications, Elsevier, USA, 2008.

[47] H. Geckeis, T. Rabung, J. Cont. Hydrol. 102 (2008) 187.

[48] K. Choi, J. W. Park, Geoscience J. 9 (2005) 53.

[49] S. S. Lee, P. Fenter, C. Park, N. C. Sturchio, K. L. Nagy, Langmuir 26 (2010) 16647.

[50] P. Fenter, S. S. Lee, C. Park, L. Soderholm, R. E. Wilson, O. Schwindt, Geochim. Cosmochim. Acta 74 (2010) 6984.

51

[52] A. Kremleva, S. Krüger, N. Rösch, Radiochim. Acta 98 (2010) 635.

[53] J. Wiebke, A. Moritz, X. Cao, M. Dolg, Phys. Chem. Chem. Phys. 9 (2007) 459.

[54] M. Duvail, F. Martelli, P. Vitorge, R. Spezia, J. Chem. Phys. 135 (2011) 044503.

[55] P. D´Angelo, R. Speza, Chem. Eur. J. 18 (2012) 11162.

[56] D. R. Fröhlich, A. Skerencak-Frech, N. Bauer, A. Rossberg, P. J. Panak, J. Synchrotron Rad. 22 (2015) 99.

[57] T. Stumpf, C. Hennig, A. Bauer, M. A. Denecke, T. Fanghänel, Radiochim. Acta 92 (2004) 133.

[58] A. Courdouan, I. Christl, S. Meylan, P. Wersin, R. Kretzschmar, Appl. Geochem. 22 (2007) 1537

[59] A. Courdouan, I. Christl, S. Meylan, P. Wersin, R. Kretzschmar, Appl. Geochem. 22 (2007) 2926

[60] G. R. Choppin, L. F. Rao, Radiochim. Acta 37 (1984) 143.

[61] C. Lucks, A. Rossberg, S. Tsushima, H. Foerstendorf, K. Fahmz, G. Bernhard, Dalton Trans. 42 (2013) 13584.

[62] J. Jiang, L. Rao, P. Di Bernardo, P. L. Zanonato, A. Bismondo, J. Chem. Soc., Dalton Trans. (2002) 1832

[63] E. H. Bailey, J. F. W. Mosselmans, P. F. Schofield, Geochim. Cosmochim. Acta 68 (2004) 1711.

[64] C. Lucks, A. Rossberg, S. Tsushima, H. Foerstendorf A. Scheinost, G. Bernhard, Inorg. Chem. 51 (2012) 12288.

[65] K. Takao, S. Takao, A. C. Scheinost, G. Bernhard, C. Hennig, Inorg. Chem. 48 (2009) 8803.

[66] T. Reich, G. Bernahrd, G. Geipel, H. funke, C. Hennig, A. Rossberg, W. Matz, N. Schell, H. Nitsche, Radiochim. Acta 88 (2000) 633.

[67] J.-M. Combes, C. J. Chisholm-Brause, G. E. Brown, G. A. Parks, S. D. Conradson, P. G. Eller, I. R. Triay, D. E. Hobart, A. Meijer, Environ. Sci. Tech. 26 (1992) 376.

[68] T. Reich, G. Bernahrd, G. Geipel, H. funke, C. Hennig, A. Rossberg, W. Matz, N. Schell, H. Nitsche, Radiochim. Acta 88 (2000) 633.

[69] J.-M. Combes, C. J. Chisholm-Brause, G. E. Brown, G. A. Parks, S. D. Conradson, P. G. Eller, I. R. Triay, D. E. Hobart, A. Meijer, Environ. Sci. Tech. 26 (1992) 376.

[70] T. Reich, G. Bernahrd, G. Geipel, H. funke, C. Hennig, A. Rossberg, W. Matz, N. Schell, H. Nitsche, Radiochim. Acta 88 (2000) 633.

[71] J.-M. Combes, C. J. Chisholm-Brause, G. E. Brown, G. A. Parks, S. D. Conradson, P. G. Eller, I. R. Triay, D. E. Hobart, A. Meijer, Environ. Sci. Tech. 26 (1992) 376.

[72] T. Reich, G. Bernahrd, G. Geipel, H. funke, C. Hennig, A. Rossberg, W. Matz, N. Schell, H. Nitsche, Radiochim. Acta 88 (2000) 633.

[73] J.-M. Combes, C. J. Chisholm-Brause, G. E. Brown, G. A. Parks, S. D. Conradson, P. G. Eller, I. R. Triay, D. E. Hobart, A. Meijer, Environ. Sci. Tech. 26 (1992) 376.

[74] M. Kakihana, T. Nagumo, M. Okamoto, H. Kakihana, J. Phys. Chem. 91 (1987) 6128.

[75] A. Barkleit, J. Kretschmar, S. Tsushima, M. Acker, Dalton Trans. 43 (2014) 11221.

[76] R. Moore, M. Borkowski, M. Bronikowski, J. Chen, O. Pokrovsky, Y. Xia and G. Choppin, J.Sol. Chem., 28 (1999) 521.

[77] G. X. Tian, L. R. Martin, L. F. Rao, Inorg. Chem. 49 (2010) 10598.

[78] C. Lucks, PhD Thesis, Institut für Resourcenökologie, Helmholtz-Zentrum Dresden-Rossendorf, 2013.

[79] D. R. Fröhlich, A. Skerencak-Frech, U. Kaplan, C. Koke, A. Rossberg, P. J. Panaka, J. Synchrotron Rad. 22 (2015) 1469.

[80] R. Buchner, G. T. Hefter, P. M. May, J. Phys. Chem. A 103 (1998) 1.

[81] R L. Bassett. Geochim. Cosmochim. Acta 44 (1980) 1151.

[82] M. Attinà, F. Cacace, G. Occhiucci, A. Ricci, Inorg. Chem. 31 (1992) 3114.

[83] F. Wolters, G. Lagaly, G. Kahr, R. Nueesch, K. A. Emmerich, Clays and Clay Minerals 57 (2009) 115.

Joint project

Retardation of radionuclides relevant to waste disposal in clay stone and saline systems

Project 4 (Saarland University)

Interaction and transport of radionuclides (uranium) and their chemical analogues (europium) in geological host rock formations

Verbundprojekt

Rückhaltung endlagerrelevanter Radionuklide im natürlichen Tongestein und in salinaren Systemen

Teilprojekt 4: Universität des Saarlandes

Untersuchung von Sorptionsprozessen von Radionukliden (Uran) und deren Stellvertreter (Europium) in endlagerrelevanten geologischen Formationen

BMWi Project No.: 02E10991

01.07.2011 – 30.09.2015

Final report[1]
2016

Christina Hein, Jonas Sander, Ramona Hahn, Ralf Kautenburger*, Horst P. Beck, Guido Kickelbick

Anorganische Festkörperchemie,
Anorganische und Analytische Chemie,
Universität des Saarlandes, Campus Dudweiler,

66125 Saarbrücken

*Corresponding author: PD Dr. Ralf Kautenburger
(r.kautenburger@mx.uni-saarland.de; 0681 302 2171)

[1] Das diesem Bericht zugrunde liegende Vorhaben wurde mit Mitteln des Bundesministeriums für Wirtschaft und Technologie (BMWi) unter dem Förderkennzeichen 02E10991 gefördert. Die Verantwortung für den Inhalt dieser Veröffentlichung liegt bei den Autoren.

ABSTRACT

The development of a high level nuclear waste (HLW) disposal in deep geological formations is a very important task for the future. The long term safety assessment for more than hundred thousand years needs a full knowledge of all processes of interaction between the radioactive waste and the surrounding formations. This work contributes to this understanding. The interaction between lanthanides (europium as chemical analogue of the actinide americium) as well as uranium as principal component of the radioactive waste and the host rock Opalinus clay under the influence of organic substances (NOM) has been analysed and discussed. Special attention is given to the influence of porewater with high salinity up to 5 M NaCl as well as higher temperatures up to 60°C. Initially, the complex ternary system was split into three binary basic systems, and finally the ternary system consisting of metal, clay and NOM was analyzed.

All binary systems will be influenced by geological parameters like pH, high ionic strength, competing cations and temperature. The sorption / desorption of the analyzed metals onto/from the Opalinus clay is analyzed via inductively coupled plasma mass spectrometry (ICP-MS). For the investigation of the complexation behavior of these metals with NOM from different origins we used ultrafiltration and capillary electrophoresis coupled with inductively coupled plasma mass spectrometry (CE-ICP-MS). Under most conditions the chosen model NOM affected the sorption of the lanthanides onto Opalinus clay favorably due to precipitation of metal-NOM complexes especially in the presence of high ionic strength.

For the sorption experiments in matrices containing up to 5 M NaCl a new time resolved method with online dilution was developed. With this transient method the batch experiments at higher ionic strength ranging from 1 to 5 M NaCl can be measured directly without the need for any further sample clean up or pretreatment steps.

The results of the ternary system are in good agreement with the results of the complexation studies. The presence of NOM especially in form of HA shows a strong influence on the europium sorption due to the strong complexation ability with HA. At pH ≥ 6 the HA complexes the europium and forms negatively charged europium-humate-complexes which remain in solution resulting in higher europium mobility. With increasing ionic strength and the presence of higher Ca concentrations the complex formation is reduced and the influence of the HA on Eu retention onto clay decreases. In contrast to the Eu results, the uranium mobility in the ternary system is only slightly affected by the presence of NOM. The influence of higher amounts of Na and Ca on the U mobility in the ternary system is also relatively low.

Miniaturized clay column experiments (MCCE) with online ICP-MS coupling allow for the visualization of sorption and desorption processes of europium and uranium on clay dynamically. At first, the complete amount of europium injected onto the clay column is sorbed and no europium can be detected at the column outlet. During the breakthrough stage the eluted amount of europium rises incrementally with each further injection until the saturation stage (plateau) is reached where no further increase of the eluted amount of europium is recorded. Europium sorbed on the clay can be displaced by injections of aluminum in a desaturating manner thus verifying the previous europium sorption on the clay.

As new speciation tool B NMR for the speciation of metal borate complexes was tested. Beginning with first and preliminary results on B NMR as speciation technique originating from our group B NMR spectroscopy has found its way into the joint research project.

KURZZUSAMMENFASSUNG

Die Entwicklung von Lagerstätten für hochradioaktive Abfällen in tiefen geologischen Formationen ist eine wichtige Herausforderung bzw. Aufgabe für die Zukunft. Um einen belastbaren Langzeitsicherheitsnachweis für mehrere hunderttausend Jahre zu gewährleisten, müssen möglichst alle Prozesse der Wechselwirkung zwischen den eingelagerten Stoffen und der umgebenden Formation verstanden und eingeschätzt werden. Diese Arbeit leistet ihren Beitrag zu diesem Verständnis, indem sie Wechselwirkungen zwischen dem Lanthanoid Europium (Chemisches Analogon zum Actinoid Americium sowie Uran als Hauptbestandteil des radioaktiven Inventars im Wirtsgestein Opalinuston unter dem Einfluss von Organik darstellt und interpretiert. Die Wechselwirkungen des komplexen Systems aus Tonorganik, Opalinuston und Metallionen wurden zunächst in den drei binären Systemen und schließlich im ternären System analysiert.

Durch geochemische Parameter (pH, Ionenstärke, Konkurrenzkationen) können diese stark beeinflusst werden. Die Quantifizierung der Metalle und ihrer Sorption / Desorption am Ton erfolgten mit Hilfe der Massenspektrometrie mit induktiv gekoppeltem Plasma (ICP-MS). Wechselwirkungen zwischen den Metallen und Organik unterschiedlicher Herkunft wurden mittels Ultrafiltration bzw. über eine Kopplung aus Kapillarelektrophorese und ICP-MS untersucht. Unter den gewählten Bedingungen fördert die Modellorganik Huminsäure den Rückhalt der Metalle neben Sorption zusätzlich durch Ausfällung besonders in Gegenwart hoher Ionenstärke.

Für die Sorptionsexperimente bei Ionenstärken bis zu 5 M NaCl musste eine neue ICP-MS Messmethode entwickelt werden. Durch Umprogrammieren des Autosamplers und einer transienten Aufnahme des Messsignals können Proben bis 5 Mol/L Salzgehalt gemessen werden, ohne vorher aufwändige Probenvorbereitungsschritte zum Entfernen der Salze oder Aufkonzentrieren der Analyten durchführen zu müssen. Die erhaltenen Ergebnisse aus dem ternären System sind in guter Übereinstimmung mit den vorherigen Resultaten aus den binären Systemen. Zusammenfassend kann gesagt werden, dass die Anwesenheit natürlicher hochmolekularer Tonorganik sich eher vorteilhaft auf die Rückhaltung von Uran und Europium auswirkt, speziell bei zusätzlicher Anwesenheit hoher Ionenstärke, wodurch die Bildung negativer mobiler Metall-Humate besonders bei höheren pH-Werten vermieden wird.

Dynamische Sorptions- / Desorptionsexperimente mit miniaturisierten Tonsäulen (MCCE) in online-Kopplung mit ICP-MS-Detektion visualisieren anschaulich den Verlauf von Ad- und Desorptionsprozessen von Europium und Uran an Opalinuston. So werden zunächst die injizierten Europiummengen vollständig am Ton sorbiert. Im weiteren Verlauf kann der allmähliche Durchbruch des Europiums mit steigenden eluierten Mengen bis zur Sättigung der

Säule nachvollzogen werden. Sorbiertes Europium kann als Nachweis der stattgefundenen Sorption anschließend mit Aluminiumionen wieder von der Säule desorbiert werden.

Nach ersten einführenden Arbeiten zur Eignung der B NMR Spektroskopie für die Untersuchung der Borat-Speziation und -Komplexierung hat die NMR Spektroskopie in Zusammenarbeit mit anderen Projektpartnern als neue Methode Eingang in den Werkzeugkasten des Verbundprojekts gefunden.

AUSFÜHRLICHE ZUSAMMENFASSUNG

Für den Langzeitsicherheitsnachweis eines nuklearen Endlagers für Wärme entwickelnde, radioaktive Abfälle ist die Kenntnis der Wechselwirkung und des Transportes von langlebigen Radionukliden zum einen innerhalb der technischen, geotechnischen und geologischen Barrieren, zum anderen aber auch in der Umwelt von entscheidender Bedeutung. Dabei spielen die Actiniden aufgrund ihrer Radiotoxizität eine wichtige Rolle. Ihr Migrationsverhalten in potentiellen Wirtsformationen für ein Endlager und mögliche Transportprozesse nach einer Freisetzung aus dem Endlager in den Aquifer müssen bekannt sein, um die Eignung der verschiedenen Wirtsgesteine (Salz, Ton oder Granit) vergleichen zu können und um die erforderliche Langzeitsicherheit zu gewährleisten. Diese Erkenntnisse sind zwingend erforderlich, um letztlich eine Wirtsformation vor dem Hintergrund der günstigsten geologischen Gesamtsituation für ein Endlager auswählen zu können.

Im letzten Jahrzehnt wurden in Deutschland für das Wirtsgestein Ton vor allem Untersuchungen an Opalinuston (Schweiz) oder Callovo-Oxfordian-Ton (Frankreich) durchgeführt. Die untersuchungswürdigen Regionen in Deutschland sind neben einem kleinen Bereich in Süddeutschland, welcher tatsächlich aus Opalinuston besteht, vor allem in Norddeutschland zu finden. Der dortige Tonstein setzt sich jedoch vor allem aus Unterkreidetonlagerstätten zusammen. Die dort vorkommenden Grund- und Porenwässer stehen im direkten Kontakt mit den ebenfalls in Norddeutschland vorkommenden Salzlagerstätten, weshalb bei den Wässern ein erhöhter Salzgehalt zu beobachten ist. Gegenüber dem Opalinuston ($\leq 0{,}5$ mol L^{-1}) sind in den norddeutschen Wässern Salzkonzentration bis zu 5 mol L^{-1} (entspricht ca. 300 g L^{-1} Natriumchlorid) zu erwarten, wobei neben der Hauptkomponente NaCl auch $MgCl_2$ und $CaCl_2$ in den Wässern zu finden sind.

Für die experimentellen Untersuchungen wurden die Elemente Uran und Europium gewählt. Als Hauptkomponente in Brennstäben aus Kernkraftanlagen spielt Uran eine übergeordnete Rolle bei der Zusammensetzung der endzulagernden, radioaktiven Abfälle. Europium wurde für die Untersuchungen gewählt, da es einfacher zu untersuchen ist als sein radioaktives Homologes Americium, das als minores Aktinid innerhalb der Transuranabfälle anzutreffen ist. Um die Speziation von Radionukliden und ihre Sorption im Nahfeld bei einem möglichen Wasserzutritt in Gegenwart eines korrodierenden Endlagerbehälters richtig zu beschreiben, müssen insbesondere die hohen Salinitäten berücksichtigt werden. Zudem sind erhöhte Temperaturen, wie sie durch die Nachzerfallswärme-Wärmeabgabe der Abfälle vorkommen, noch verstärkt zu untersuchen, da auf diesem Gebiet bisher kaum Untersuchungen durchgeführt worden sind. Auch der Einfluss von unterschiedlichen natürlich vorkommenden Organika soll untersucht werden. Dabei sind Huminstoffe sowie auch andere im Tongestein

enthaltene organische Stoffe („*natural organic matter*“, NOM) zu berücksichtigen, die bei Sorptions- bzw. Desorptionprozessen der Radionuklide im Tonstein auf Grund der starken Komplexbildungstendenz und beim kolloidgetragenen Transport eine wichtige Rolle spielen. Wichtig sind dabei auch der Einfluss der Art der Organik und ihre Genese, da diese einen starken Einfluss auf die Zusammensetzung der Organik und damit ihre Eigenschaften nehmen kann. Aus den durchgeführten Komplexbildungs- und Sorptionsuntersuchungen sollen Komplexbildungskonstanten (log β) und Sorptionskoeffizienten (log K_d) berechnet werden und damit vorhandene Datenbanken ergänzt werden.

Zunächst wurde für die Batch-Untersuchungen mit hohen Ionenstärken eine neue ICP-MS (Massenspektrometrie mit induktiv gekoppeltem Plasma) Methodik für die Elementspurenanalytik entwickelt, da die ICP-MS selbst mit HMI („*high matrix introduction*“ System) ausgestattet, nur für Messungen bis zu Salzgehalten von maximal 3% geeignet ist. Darüber hinaus kann eine erhöhte Salzbelastung zu starken Ablagerungen an den Konen und dem Linsensystem sowie zu einer Verschmutzung des Quadrupol-Massenfilters führen, was die Lebenserwartung und Messgenauigkeit des ICP-MS deutlich verkürzt. Hohe Verdünnungen der Proben zur Verringerung der Salzgehalte sind im unteren Konzentrationsbereich der Analyte bei den Sorptionsuntersuchungen (< 1 µg L^{-1}) auf Grund der hohen Metallsorption am Ton bzw. aufgrund von Ausfällung nicht möglich. Daher musste eine alternative Methodik entwickelt werden, welche durch Modifizierung der ICP-MS Hard- und Software auf einer Online-Verdünnung mit reduzierter Probenzufuhr beruht. Als Ergebnis wird mit Hilfe der peristaltischen Pumpe parallel zur Probe eine Makeup-Lösung in den Zerstäuber geleitet. Durch die Variation der Schlauchdurchmesser kann der Grad der Verdünnung optimal eingestellt werden. Zudem erfolgt die Probenzufuhr nicht mehr für mehrere Minuten sondern nur noch für 10 Sekunden pro Messung. Dies führt dazu, dass als Signal ein Peak erhalten wird, dessen Fläche zur Konzentration proportional ist. Mittels einer Kalibrierung kann das Signal quantifiziert werden. Mit Hilfe dieser transienten ICP-MS Methode können Proben mit einer Matrixkonzentration bis zu 5 M NaCl untersucht werden. Dies ermöglicht die Analyse der Batch-Versuche, ohne dass aufwändige Probenvorbereitungsschritte zur Erniedrigung des Salzgehaltes der Probe bzw. Aufkonzentrierung der Analyten (Europium bzw. Uran) notwendig sind.

In den Sorptionsuntersuchungen wurde zunächst das binäre System aus Metall und Opalinuston untersucht. Dabei wurden Sorptions- und Desorptionsversuche von Europium und Uran unter dem Einfluss unterschiedlicher geochemischer Parameter wie pH-Wert, Ionenstärke, Temperatur und divalenten Konkurrenzkationen (Calcium) durchgeführt. Im ternären System wurde zusätzlich der Einfluss von NOM (beispielsweise Huminsäuren unterschiedlicher Herkunft) auf die Rückhaltung der Metalle untersucht. Die Untersuchungen mit Europium haben jedoch gezeigt, dass sich die Ergebnisse im binären und ternären System

kaum voneinander unterscheiden. Jedoch sind bei pH 5 deutlich größere Einflüsse als bei pH 7 zu beobachten.

Bei pH 5 führt eine erhöhte Ionenstärke zu einer Verringerung der Metall-Rückhaltung am Ton, wobei die log K_d-Werte von 2,6 (0,01 M NaCl) auf 1,9 (5 M NaCl) abnehmen. Dieses Resultat ist vor allem auf die Konkurrenz zu Europium durch die im Überschuss vorhandenen Na^+-Ionen zurück zu führen. Durch die Gegenwart von Huminsäure wird die Rückhaltung von Europium am Opalinuston etwas erhöht, vermutlich weil das Europium mit der Huminsäure ausfällt bzw. mitgefällt wird. Bei erhöhter Ionenstärke herrscht aber auch an den Bindungsstellen der Huminsäure eine Konkurrenz zwischen Na^+ und Eu^{3+} so dass der Einfluss der Huminsäure mit steigender Ionenstärke wieder abnimmt (log K_d-Werte nehmen bei Zunahme der NaCl Ionenstärke von 0,01 auf 5 M von 3,1 auf 2,0 ab). Der Einfluss von divalenten Konkurrenzkationen (Ca^{2+}) ist sowohl im binären als auch im ternären System mit einer vergleichsweise stärkeren Erhöhung der Ionenstärke an monovalenten Kationen (Na^+) zu vergleichen. Die zusätzliche Anwesenheit von Ca^{2+} (0,05 M Ca^{2+}) führt in beiden Systemen zu einer erhöhten Mobilität der Europium-Ionen, weshalb die log K_d-Werte von 2,6 auf 2,3 (0,01 M NaCl, pH 5) und von 2,1 auf 1,8 (1 M NaCl, pH 5) abnehmen. In Gegenwart von Huminsäure nehmen die log K_d-Werte von 3,0 (0,01 M NaCl, pH 5) auf 2,5 (0,01 M NaCl + 0,05 M Ca^{2+}, pH 5) bzw. von 2,3 (1 M NaCl, pH 5) auf 2,1 (1 M NaCl + 0,05 M Ca^{2+}, pH 5) ab. Durch die Erhöhung der Temperatur von 25 auf 60°C bei den Sorptionsversuchen wird die Rückhaltung der Europium-Ionen am Opalinuston bei allen untersuchten Ionenstärken erhöht.

Durch eine Erhöhung des pH-Wertes von 5 auf 7 nimmt unter allen getesteten Bedingungen die Rückhaltung von Europium am Opalinuston zu. Dies ist damit zu erklären, dass bei pH 5 die vorherrschende Sorption teilweise durch die Protonenkonkurrenz vermindert wird, während bei pH 7 neben der Sorption noch zusätzlich eine Ausfällung des Europium beobachtet werden kann. Bei einer Ionenstärke von 0,01 M NaCl nehmen die Sorptionskoeffizienten log K_d für Europium signifikant von 2,6 (pH 5) auf 4,2 (pH 7) zu. Ein relevanter Einfluss der anderen untersuchten geochemischen Parameter (mono- oder bivalente Konkurrenzkationen, organische Komplexliganden) auf die Europium Rückhaltung ist bei pH 7 nicht nachweisbar. Dabei spielt es keine Rolle, ob die Untersuchungen im binären oder im ternären System durchgeführt wurden. Allein eine Temperaturerhöhung auf 60°C führt wiederum, wie schon bei pH 5, zu einer leichten Erhöhung der Europiumrückhaltung (Zunahme der log K_d-Werte von 4,2 auf 4,6).

Für Uran lassen sich solche konkreten Aussagen nicht oder nur sehr schwer treffen, was auf die komplexe Speziation des Urans über einen weiten pH-Bereich zurück zu führen ist. Bei Uran lassen sich zwischen pH 5 und 7 kaum Unterschiede in der Rückhaltung erkennen, beide log K_d-Werte liegen bei etwa 3,7 (0,01 M NaCl). Eine Zugabe von Huminsäure

beeinflusst die Rückhaltung nur bei pH 7, indem Uran etwas mehr in Lösung gehalten wird und somit die Mobilität ansteigt. Durch eine Erhöhung der Ionenstärke auf 1 M NaCl nimmt die Rückhaltung des Uranylkations ähnlich wie beim Europium deutlich ab. Die log K_d-Werte nehmen bei pH 5 von 3,7 auf 3,2 und bei pH 7 von 3,6 auf 3,3 ab. Im ternären System reduziert die erhöhte Ionenstärke den Einfluss der organischen Komplexliganden (Huminsäure). Bei 1 M NaCl wird die negative Ladung der Huminsäure durch Natrium neutralisiert, so dass die Komplexbildung von Uran gehemmt ist. Die Rückhaltung gleicht sich der im binären System an. Der Einfluss der divalenten Konkurrenzkationen wird stark durch die Uran-Speziation beschrieben. Bei pH 5 ist der Einfluss recht gering und vermutlich nur über die Konkurrenz von Calcium zu Uran zu erklären. Bei pH 7 ermöglicht die Bildung des neutralen in Lösung befindlichen Ca-Uranyl-Carbonato-Komplexes eine Erklärung, da dieser nicht am Opalinuston sorbiert und so die Uran-Mobilität erhöht. Die log K_d-Werte nehmen von 3,6 auf 3,0 ab. Ein größerer Einfluss der Huminsäure als Komplexligand für Uranyl ist im ternären System nicht zu beobachten. Die Temperaturerhöhung zeigt ähnliche Auswirkungen auf das Uran wie auf das Europium. Die Mobilität des Urans wird durch eine Erhöhung auf 60°C merklich verringert.

Die Desorptionsuntersuchungen der Metalle vom Opalinuston zeigen im Vergleich zur Sorption deutlich andere relevante Einflussfaktoren. Europium lässt sich über einen weiten pH-Bereich kaum vom Ton wieder desorbieren und auch eine Erhöhung der Ionenstärke zeigt bei pH-Werten ≥7 keinen merklichen Einfluss auf eine mögliche Remobilisierung. Nur bei vergleichsweise geringen pH-Werten (pH 3 und 5) führt eine höhere Ionenstärke auch zu einer erhöhten Mobilität. Durch Huminsäure wird bei höheren pH-Werten die Remobilisierung erhöht, da die Huminsäure das Europium komplexieren und als negative Spezies in Lösung halten kann. Bei den immer wieder erfolgenden Gleichgewichtsschritten der Desorptionen werden immer weniger Konkurrenzkationen aus dem Ton herausgelöst, welche den Einfluss der Huminsäure aufheben könnten. Die Anwesenheit hoher Ionenstärke reduziert den Einfluss der Huminsäure auf die Mobilität von Europium, da normalerweise die bei diesen pH-Werten deprotonierte und damit negativ geladene Huminsäure durch die hohe Konzentration an Na^+ ebenso wie die Tonoberfläche neutralisiert werden kann. Ein Temperatureinfluss ist über einen weiten pH-Bereich nicht zu beobachten und im ternären System führt die erhöhte Temperatur zu einem verringerten Einfluss der Huminsäure. Vermutlich wird durch die Temperatur die Tonauflösung weiter vorangetrieben, weshalb in jedem folgenden Gleichgewichtsschritt neue und damit auch höhervalente Kationen aus dem Ton heraus gelöst werden können. Diese können die Huminsäure neutralisieren und so ihren negativen Einfluss durch Bildung von mobilen Metall-Humat-Komplexen auf die Metallrückhaltung hemmen.

Im Gegensatz zum Europium zeigen bei Uran die Experimente mit höher Ionenstärken bei keinem der untersuchten pH-Werte relevante Einflüsse auf die Remobilisierung des Urans

vom Opalinuston und bei höherer Temperatur wird eine Remobilisierung des Urans sogar verringert. Die Huminsäure im ternären System kann das sorbierte Uran durch Komplexbildung jedoch wieder in Lösung bringen, jedoch wird auch hier durch erhöhte Ionenstärken der Einfluss der Huminsäure auf die Remobilisierung des Urans stark verringert.

Eine andere entwickelte Methodik, welche den Verlauf von Ad- und Desorptionsprozessen von Europium und Uran an Opalinuston sehr gut visualisiert, sind dynamische Sorptions-/Desorptionsexperimente mit miniaturisierten Tonsäulen (MSE), vor allem in online-Kopplung mit ICP-MS Detektion. Bei diesen Experimenten werden selbst gepackte miniaturisierte Tonsäulen in einer modifizierten Flüssigchromatographie-Apparatur wiederholt mit kleinen Mengen wässriger Lösungen, die endlagerrelevante Metallionen enthalten, beaufschlagt. Durch die MSE-ICP-MS-Kopplung kann die Rückhaltung der Metalle im kompakten Tongestein im Verlauf des gesamten Experimentes online beobachtet und registriert werden. Während einer Serie von aufeinanderfolgenden Injektionen von Europium (jeweils 5 µL einer 2 mM Europiumperchlorat-Lösung) über eine Säule mit 1 m-% Opalinuston und 99 m-% Seesand können drei verschiedene Abschnitte beobachtet werden. Zunächst werden die injizierten Europiummengen vollständig am Ton sorbiert und am Säulenausgang kann kein Europium detektiert werden. In der anschließenden Phase wird durch weitere Injektionen der allmähliche Durchbruch des Europiums mit steigenden eluierten Mengen bis zur Sättigung der Säule beobachtet. Das detektierte Europium-Signal erreicht schließlich ein Plateau auf Sättigungsniveau, von dem aus auch bei weiteren Injektionen keine höheren Europium-Konzentrationen am Säulenausgang detektiert werden können. Im Ton zurückgehaltenes Europium kann als Nachweis der stattgefundenen Sorption anschließend mit wiederholten Injektionen einer Aluminiumlösung wieder von der Säule verdrängt werden, wobei der Konzentrationsverlauf des einen Entsättigungsphänomens entspricht. Außerdem kann anhand von Miniatursäulen-Experimenten der mobilisierende Einfluss von Laktat als Stellvertreter von Tonorganik mit geringer Molmasse auf die Sorption von Europium am Ton nachvollzogen werden. Zusammenfassend kann aus den durchgeführten Experimenten eine aufsteigende Sorptionsaffinität der untersuchten (endlagerrelevanten) Metalle an Opalinuston von Europium über Uran zu Aluminium abgeleitet werden.

Zur Bestimmung von Komplexbildungskonstanten (log β-Werte) der Metalle mit natürlich im Ton vorkommender Organik sollte eine Kopplung aus Kapillarelektrophorese und ICP-MS verwendet werden, leider war bei hohen Ionenstärken die Trennung der unterschiedlichen Metall-Organik-Spezies nicht mehr möglich. Aus diesem Grund wurden verschiedene alternative Methoden wie Dialyse und Ultrafiltration hinsichtlich ihrer Eignung zur Bestimmung von Komplexbildungskonstanten untersucht. Mit Hilfe der Ultrafiltration konnten Komplexbildungskonstanten für Europium und Uran in 0,1 und 1 M NaCl Lösung bestimmt werden. Als Organik wurden verschiedene Huminsäuren und NOM-Extrakte mit

unterschiedlichsten Entstehungsorten und Zusammensetzungen eingesetzt, um zu zeigen, dass der Entstehungsort der Organik einen großen Einfluss auf die Metall-Komplexierungsfähigkeit der Organik haben kann. Die bestimmten log β-Werte für Uran (6,0 mit AHA bei 0,1 M NaCl) sind etwas niedriger als die für Europium (6,4 mit AHA bei 0,1 M), was vermutlich an der etwas komplexeren (sterisch sperrigeren) Struktur des Uranylkations liegt und so eine schwächere Komplexierung nach sich zieht. Wird die Ionenstärke erhöht, wird die Komplexierung von Europium geschwächt (Abnahme von log β auf 5,5), während die Komplexstabilität von Uran kaum beeinflusst wird. Eine Zunahme zweiwertiger Konkurrenzkationen im Versuchsansatz führt bei Europium ähnlich wie die erhöhte Ionenstärke an NaCl zu einer Abnahme der Komplexstabilität, während die Uranyl-Humat-Komplexierung ebenfalls annähernd unbeeindruckt von der in Lösung anwesenden Calcium-Konzentration bleibt. An Hand beider Analyte (Eu und U) ist der Einfluss unterschiedlicher Organik sehr gut zu erkennen. Die Komplexierung mit NOM ist deutlich schwächer im Vergleich zu den untersuchten Huminsäuren, wobei die unterschiedliche Herkunft der Huminsäuren ebenfalls zu einer Veränderung der Komplexstabilität führt. Offensichtlich liegt der Grund dieses differenzierten Komplexbildungsverhaltens an der veränderten Zusammensetzung bzw. Struktur der Huminsäuren, die je nach Herkunftsort mehr oder weniger stark variieren kann.

Zusammenfassend kann aus den hier erhaltenen Ergebnissen gefolgert werden, dass möglichst alle Prozesse der Wechselwirkung zwischen den eingelagerten Stoffen und der umgebenden Formation eines konkreten Endlagerstandortes verstanden und eingeschätzt werden müssen, um einen belastbaren Langzeitsicherheitsnachweis für mehrere hunderttausend Jahre zu gewährleisten. Diese Forschungsarbeit leistet ihren Beitrag zu diesem Verständnis, indem sie die zum Teil komplexen Wechselwirkungen zwischen dem Lanthanoid Europium (Chemisches Analogon zum Actinoid Americium) sowie Uran als Hauptbestandteil des radioaktiven Inventars im Wirtsgestein Opalinuston unter dem Einfluss von natürlicher Organik darstellt und interpretiert. Mit der Erweiterung des vorhandenen Werkzeugkastens durch die im Laufe des Forschungsprojektes entwickelten Methoden und den damit erhaltenen Resultaten sind grundlegende Voraussetzungen geschaffen worden, sich ein modellhaftes Bild von den Vorgängen im komplexen System „Natürliches Tongestein – Aquifer“ zu erarbeiten. Die entwickelten analytischen Werkzeuge bilden die Voraussetzung, um auch zukünftig Ergebnisse zum Prozessverständnis der Radionuklid-Migration unter verschiedensten Randbedingungen liefern zu können. So können beispielsweise zahlreiche Tools des immer weiter anwachsenden Werkzeugkastens zur Eignungsuntersuchung verschiedener natürlicher Wirtsgesteine aber auch im Rahmen der Langzeitsicherheitsanalyse der geotechnischen Barriere eines potentiellen Endlagers eingesetzt werden.

TABLE OF CONTENTS

LIST OF SYMBOLS

A	Electrode surface
AHA	Aldrich humic acid
aha-pb	aldrich humic Acid with Blocked groups
β	Conditional stability constant (log β)
c	Concentration
CE	Capillary electrophoresis
CEC	Cation exchange capacity
CE-ICP-MS	Capillary electrophoresis- inductively coupled plasma-mass spectrometry
HPLC	High performance liquid chromatography
HPLC-DAD	High performance liquid chromatography with diode array detection
D	Diffusion coefficient
DOC	Dissolved organic carbon
DP	Differential-pulse
EHA	Elliott soil HA
Eq.	Equation
Eu	Europium (III)
Fig.	Figure
g	Standard acceleration due to Earth's gravity (9.81m/s^2)
Gd	Gadolinium (III)
GoHy573	Gorleben 573-HA
GoHy851	Gorleben 851-HA
HA	Humic acid
I	Ionic strength
ID	Inner diameter
ICP	Inductively coupled plasma
ICP-MS	Inductively coupled plasma-mass spectrometry
IHA	Iodinated humic acid
IHSS	International Humic Substances Society
K	Stability constant (log K)
K‘	Electrochemical constant
K_c	Equilibrium constant
kPa	kilo Pascal
L	Loading in % (compared to the maximum complexation)
LC	Loading capacity
LHA	Leonardite HA
log β	Conditional complex stability constant
M	Molar
Me^{z+}	Metal ion
MQ	MilliQ(-Water)
MCCE	Miniaturized clay column experiments
MICN	Metal ion charge neutralization model
NOM	Natural organic matter
OA-HA	Farmland HA from Hannover

OD	Outer diameter
OPA	Opalinus clay
PEC	Proton exchange capacity
ppb	Parts per billion
ppm	Parts per million
ppt	Parts per trillion
PW	Synthetic porewater
Q-ICP-MS	Inductively coupled plasma - quadrupol-mass spectrometry
s	Rate of potential scan
SNOM	Suwannee river NOM
SP	$NaClO_4$
SS-HA	Swamp soil HA from “*Kleiner Kranichsee*“
SW-HA	Swamp water HA from “*Kleiner Kranichsee*“
Tab.	Table
TOC	Total organic carbon
U	Atomic units
U	Uranium (VI), uranyl cation
UF	Ultrafiltration
V	Volt
WHA	Waskish-peat HA

1 Introduction

For the long-term safety assessment of a high level nuclear waste (HLW) disposal detailed knowledge of interactions and transport behavior of long-lived radionuclides within the technical, geo-technical, and geological barrier as well as in the total environment has a crucial relevance. In this context the actinides uranium, neptunium, plutonium, americium and curium play an important role. The process of migration of actinides in a potential host rock formation after their release from the waste container into the aquifer has to be known to assess possible host formations like clay, salt and granite for their suitability as host rock and to provide the necessary information needed for the required safety case. In contrast to other countries, Germany has not yet decided in favor of a host rock and hence, a site for final disposal of high-level radioactive waste has not been chosen to date. Thus, site specific investigations were not possible concerning a potential German site in the frame of a national research project. Instead, the present project has focused on fundamental investigations as well as design and development of analytical tools to obtain site-independent results. The findings of other studies that can be applied to compare the suitability of different potential host rocks on the one hand and provide important insights of a safety analysis of any disposal site on the other hand are a valuable contribution to assess our own study [e.g. Bradbury & Baeyens 2003, Altmann 2008, Kautenburger 2010, 2012, 2014a].

The aim of the joint project was to elucidate the geochemical behavior (e.g. sorption/desorption processes in natural claystone (Opalinus clay) as well as the complexing behavior with organic or inorganic ligands) of the actinide uranium and of the lanthanide used as chemical analogue of trivalent actinides americium and curium. Special attention in this research project is given to the influence of groundwater and clay porewater with high salinity. The use of porewater with high salinity up to 5 M (NaCl) aims at validating results from another project [Kautenburger et al. 2011a] studying other potential disposal site conditions that are typical for regions in northern or northwest Germany [Brewitz 1982, Herbert & Schwandt 2007]. It is also known, that beside rock salt (NaCl) also anhydrite ($CaSO_4$) and polyhalite ($K_2Ca_2Mg(SO_4)_4{\cdot}2H_2O$) are present in the geological layers relevant for a repository in northern or northwest Germany. Therefore, porewater in this region can also contain relevant concentrations of magnesium and calcium species. Under the aspect of safety analysis of a future disposal site these higher valent cations are of higher relevance due to their sorption behavior to clay stone competing with uranium and europium. This competitive behavior of Ca and Mg ions is therefore a further objective of this study. Due to the fact that elevated temperatures are expected in a HLW-disposal as a consequence of the heat producing radioactive decay, selected experiments were additionally done as a function

of higher temperatures up to 60°C [Tertre et al. 2005, 2006, Möser et al. 2011, Kautenburger et al. 2011a].

Natural organic matter (NOM) like humic substances plays an important role for the aquatic chemistry in the aquifer system. Humic material contains a large and heterogeneous group of macromolecules of different molecular weight and charge density with complex and difficultly identifiable structure [Stevenson 1994, Sutton 2005]. They can influence the migration and retardation behavior of the actinides by their complexing, redox and colloidal properties. In addition the organic components of the natural clay rock – low and high molecular weight compounds - might show similar interactions with actinides. Therefore, another objective of the project was to study the complexation behavior of the mentioned metal ions with natural organic matter (NOM) like humic acid (HA) or lactate/propionate and formate as clay organic compounds [Courdouan et al. 2007a, 2007b] and to evaluate the corresponding complexation constants. Such complex stability constants are required for geochemical modelling of metal-ion behavior in the environment after assembling them in a thermodynamic database [Marquardt 2008, 2012]. Among the different complexation models to describe the metal ion complexation by humic substances the metal ion charge neutralization (MICN) model [Kim & Czerwinski 1996] as well as a conservative “single site model” [Kautenburger et al. 2014] was used in this project to determine complex stability constants of the used metals and NOM.

Typically used analytical tools and methods for the determination of sorption coefficients K_d or complexation constants $\log \beta$ consist of batch experiments alone (e.g. sorption / desorption experiments in the binary system Me - OPA) or in a combination with different chemical separation techniques, e.g. centrifugation, extraction methods, ion exchange, ultrafiltration or precipitation with sensitive detection methods such as nuclear spectroscopy, soft X-ray spectromicroscopy (EXAFS, NEXAFS, XANES, XRD) or mass spectrometry [Röllin & Eklund 2000, Wrobel et al. 2003, Plaschke et al. 2004, Kim et al. 2005, Fröhlich et al. 2012, 2015, Kremleva et al. 2013, Denecke 2015]. Some of these methods are either not able to separate and quantify different metal or metal-organic species or they cannot prevent that kinetically unstable complexes may be modified during chemical separation. For quantitative elemental speciation analysis some separation techniques like high performance liquid chromatography (HPLC), ion- (IC), gas chromatography (GC) or capillary electrophoresis (CE) have been used in combination with element-selective detectors like inductively coupled plasma (ICP), optical emission (OES) and mass spectrometry (MS) or atomic absorption spectroscopy (AAS) [Harrison & Rapsomanikis 1989, Olesik et al. 1995, Michalke 1999, Prange & Schaumlöffel 1999, Cornelis et al. 2005, Kautenburger et al. 2006, Möser et al. 2012, Hein et al. 2014].

In the present study different speciation methods are used. For complexation experiments between the metal ions and NOM like HA capillary electrophoresis hyphenated with inductively coupled plasma-mass spectrometry (CE-ICP-MS) is used as a promising alternative to existing speciation methods at low metal ion concentrations [Schaumlöffel et al. 2002, Kuczewski et al. 2003, Pröfrock et al. 2005, Timerbaev 2009, Timerbaev & Timerbaev 2013, Kautenburger et al. 2007, 2009, 2014]. Additionally, ultrafiltration experiments [Mizera et al. 2005, Melin & Rautenbach 2007, Kautenburger et al. 2007, Pourret et al. 2007, Lohrengel 2012, Hahn 2014] are performed to determine complex stability constants especially for samples containing high ionic strengths. For the speciation of borate and metal-borate complexes nuclear magnetic resonance (^{10}B and ^{11}B NMR) seems to be a powerful tool [Ronconi & Sadler 2008, Rollion-Bard et al. 2011], for which reason this method was also tested for its applicability.

Using such analytical tools the complexation behavior of NOM with different molecular weight and structure and from various origins is analyzed. Hereby its influence on the mobility (performing sorption and desorption experiments) of the lanthanide europium and the actinide uranium is investigated. In first steps we analyze the different binary systems, and finally investigations in the ternary system consisting of these heavy metals, NOM and Opalinus clay (OPA) are performed under varying experimental conditions close to nature [Kautenburger & Beck 2008, 2010]. The influence of geochemical parameters like pH-value, temperature, ionic strength or different competing metal cations on the metal mobility in the absence (binary system) or presence of NOM (ternary system) is investigated. In addition to the above described batch and speciation methods miniaturized clay column experiments (MCCE) [Kautenburger et al. 2011b, Kautenburger 2014b] with compacted clay as a link between highly standardized but unnatural batch studies and near-natural but time-consuming diffusion experiments are performed. By the use of MCCE hyphenated with ICP-MS the influence of different geochemical parameters on the metal mobility in compacted Opalinus clay is analyzed by a kind of short-time dynamic sorption-desorption processes.

2 Experimental

2.1 Materials

2.1.1 Chemicals and standards

All standards and chemicals (see also Table 1) were of p.a. quality or better (e.g. emsure or suprapure) and were obtained from Merck (Darmstadt, Germany). Milli-Q deionized water (18.2 MΩ cm) was used to prepare all solutions. The single element standards CertiPUR® of Sc, Cs, Eu, U and Ho (1 g L^{-1}) were also obtained from Merck. Sc and Ho were diluted 1 : 100 in Milli-Q water and used as spike and internal standard solution for all experiments. For adjusting the pH value perchloric acid (70%, p.a.), hydrochloric acid (35%, suprapure) and NaOH (p.a.) from Merck (Darmstadt, Germany) were applied. Argon 5.0 (99.999%, Praxair Deutschland GmbH, Düsseldorf, Germany) was used as plasma gas for ICP-MS measurements. For sample preparation solutions of sodium chloride (Merck, emsure) with an ionic strength of 0.01, 1, 3 or 5 M were used. Additionally, to the sodium chloride solution different concentrations (0.5, 5 and 50 mM) of $CaCl_2$ were added. The CE electrolyte buffer was a solution of 100 mM acetic acid and 10 mM Na-acetate. Before use all solutions for CE analysis were filtered (0.45 µm syringe filter, Minisart, Sartorius, Germany). For the miniaturized clay column experiments (MCCE) 1-bromopropane, sodium bromide and iodide (Merck, p.a.) were used as inert marker. For ICP-MS measurement 3.33 mL of the sample were diluted with 6.36 mL Milli-Q water. Additionally, 300 µL of conc. HNO_3 (65%, suprapure) were added to adjust a pH value <1 and prevent wall adsorption onto the tube and vial walls. Finally 10 µL of a 10 mg L^{-1} solution of Ho were added as internal standard to compensate variations of the instrument sensitivity.

2.1.1 Natural organic matter (NOM)

Most NOM used in the experiments are commercially available humic acids (HA). One humic acid is available from Aldrich (St. Louis, USA; AHA sodium salt), has lignite as origin and was purified as described in the literature [Kim et al. 1990]. The other humic acids are available from the International Humic Substances Society (IHSS, St. Paul, USA) or from different sites in Germany. These other humic acids have partly similar origins. The Leonardite humic acid (LHA) originated similar to the AHA from lignite. The swamp water (SW-HA) and swamp soil (SS-HA) humic acids from "*Kleiner Kranichsee"* and the Waskish-peat humic acid (WHA) have peat bog as source. The Elliott soil humic acid (EHA) is an extract of fertile prairie soils of Illinois and the Suwannee River natural organic matter (SNOM) is obtained out of the Blackwater River with a DOC content of more than 25 mg L^{-1}. Additionally to the commercially available humic acids, humic acids from Gorleben site (boreholes 851 / 573)

and a farmland humic acid from Hannover (OA-HA) were used. For use 1 g L^{-1} solutions of all humic acids were prepared. 10 mg of humic acid were dissolved in 2 mL of 0.1 M NaCl for 24 h. After this time the solution was restocked to 10 mL.

2.1.2 Opalinus clay, kaolinite and sea sand

The clay mineral used in this study was Opalinus clay (OPA) which was obtained from a drill core in Benken (Switzerland). The core sample was stored in containers with 0.5 bar Ar overpressure. The aerobe homogenate of the clay was obtained by milling the clay to a fine-grained powder with a particle size smaller than 500 µm. The ungrounded Opalinus clay represents a well characterized clay [NAGRA 2002] with a cation exchange capacity (CEC) ranging from 9 to 12 meq/100 g, the porosity of the sample was 10.8% [Lauber et. al. 2000].

The milled clay used in our study was characterized by XRD phase analysis (Siemens D5000, OED) followed by data interpretation with the TOPAS software (version 2.1, Bruker AXS, Delft, The Netherlands).

For the MCCE kaolinite and sea sand were used as stationary phases in the column beside OPA. Due to the strong swelling behavior of the OPA it is not possible to fill 100% Opalinus clay into the column. The OPA was mixed with parts of sea sand. Contrary to the Opalinus clay kaolinite can be used in the HPLC column as reference mineral without relevant swelling characteristics. The sea sand (purified) is commercially available from Merck KGaA (Darmstadt, Germany). The kaolinite is the clay KGa-1b from Georgia, USA sold by the Clay Minerals Society (Chantilly, USA).

2.2 Instrumentation

2.2.1 Mass spectrometry with inductively coupled plasma (ICP-MS)

An Agilent 7500cx ICP-MS (Santa Clara, USA) with ORS collision cell (see Figure 1) was used for the isotope measurements. The helium collision mode is used for reliable, predictable removal of unknown matrix interferences.

ICP-MS measurements of real samples with higher ionic strength are a general problem. Measurements of samples with high salt content, like sea water, are generally possible only with a high matrix introduction system (HMI) for the 7500 and 7700 series.

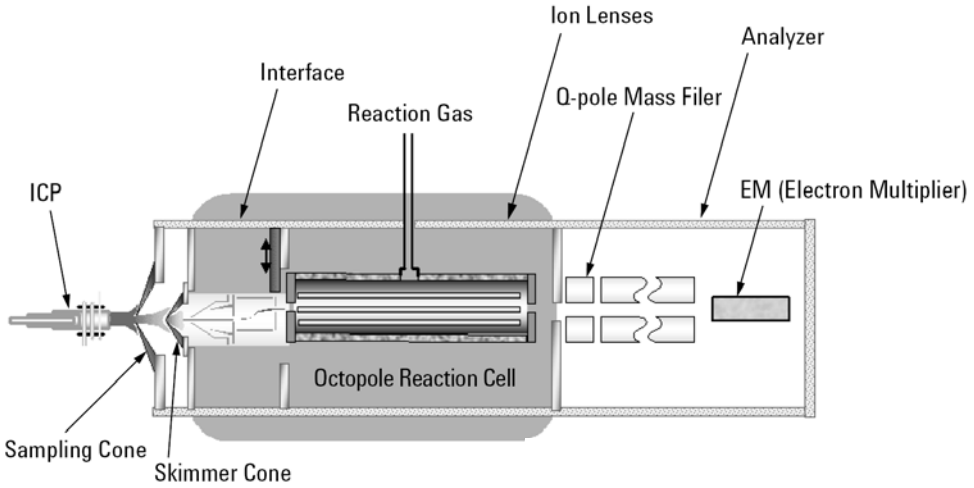

Figure 1: Diagram of the Agilent 7500cx ICP-MS with octopole collision/reaction (ORS) cell [Agilent 2008]

The HMI is an online dilution system of the sample aerosol before sample ionization in the plasma torch. The maximum of the total dissolved solids (TDS) should be at 3%, which increases the matrix tolerance about ten times.

Detailed analytical conditions are given in Table 1. The measurements are performed in spectrum acquisition mode (multi tune) as default ICP-MS method. We used ^{165}Ho as internal standard in all experiments to correct for instrumental instability. All measured isotope counts are therefore corrected by the ^{165}Ho abundance. All samples are measured by ICP-MS in triplicate (RSD values are in the range of 0.3 and 3.9%).

Table 1: Operating parameters of the ICP-MS in spectrum mode

ICP-MS	**Agilent 7500cx**
RF-power	1550 W
Cooling / auxiliary gas	15.0 / 1.05 L min^{-1}
Dwell times / Repetition	100 ms per mass / 3 times
Samples	
Eu-, Gd-, U-ICP-standards	CertiPUR® (Merck), diluted in Milli-Q
Analyzed isotopes	^{81}Br, ^{127}I, ^{133}Cs, ^{153}Eu, ^{158}Gd, ^{165}Ho, ^{238}U
Humic acid (HA)	Purified AHA (Aldrich H1,675-2), miscellaneous HA from IHSS and Gorleben site
Ion strength in all samples:	0.01, 1, 3 and 5 M NaCl, 0.01 M $NaClO_4$
pH values	3, 5, 7, 10

2.2.1.1 Transient ICP-MS method for samples with high salinity

In this work we used samples with more than 5 M ionic strength. A 1 M solution shows a TDS of nearly 6% which is already too much for the HMI. For the new Agilent 7900 ICP-MS an ultra-high matrix introduction system (UHMI) is available which tolerates 25% of TDS, nearly 10 times higher than the previous generation HMI. Unfortunately, an upgrade of older Agilent ICP-MS instruments with this new system is not possible. As an alternative to the dilution procedure described above a matrix separation step during the sample preparation might lead to success. But preliminary test show problems with uranium as analyte element. Additionally, for every analyte an optimization step is necessary. Therefore, a method of analysis for high saline samples up to 5 M NaCl has been developed using the existing ICP-MS instrumentation by reprogramming the autosampler for short injection steps and measuring the resulting transient signals. The ICP Mass Hunter workstation software (vers. B01.01, Agilent) allows the user to select different acquisition modes for measurements. For the transient method the time resolved analysis mode was necessary whereby the data processing is based on peak area.

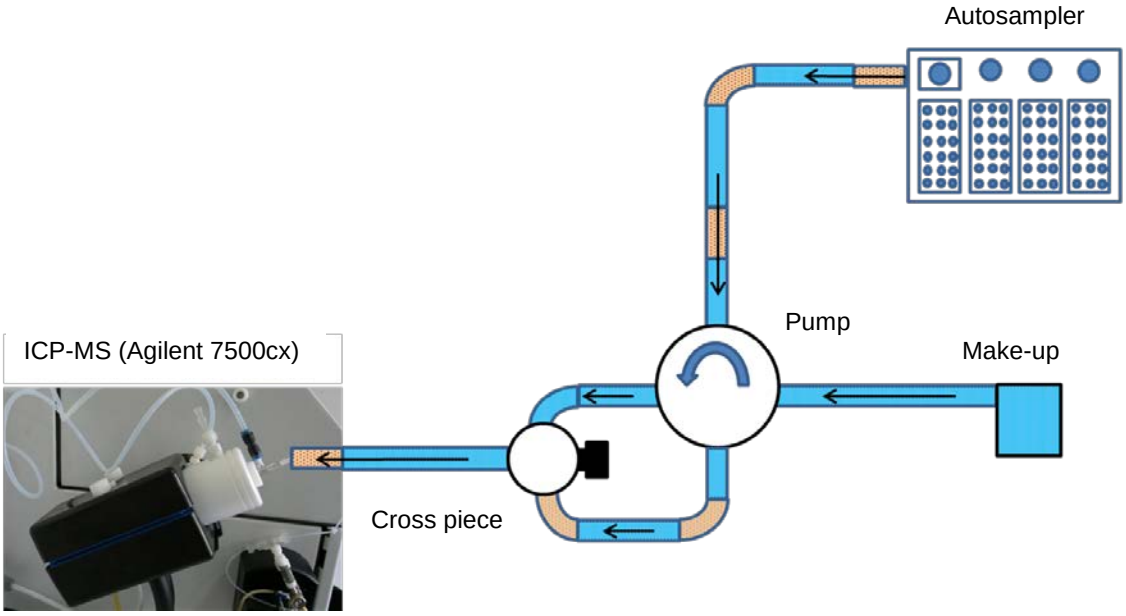

Figure 2 : Setup of the modified ICP-MS for transient measurements

The autosampler was controlled with the software HyperTerminal (Microsoft Corporation, Redmond, USA). For the transient measurements it was necessary to reprogram the autosampler with a new time dependent sequence. The limit of the autosampler memory is 1,000 bytes making a continuous measurement of only six samples possible. The time for sample uptake was fixed to 10 seconds and after optimization the cleaning time period of 90 seconds was used to wash out all elements quantitatively.

Beside the variation of the software, the ICP-MS components were slightly modified. An additional tube leads to an online dilution of the sample volume. The transient ICP-MS setup is shown in Figure 2.

The peristaltic pump rotates with 0.1 rounds per second (rps) and has a radius of 2 cm corresponding to a perimeter of 12.6 cm. With a sample tubing with inside diameter of 0.57 mm nearly 30 µL of the sample was injected in 10 seconds. In order to calculate the relative standard deviations between repeated measurements every sample was measured three times. A total sample volume of 90 µL was injected into the ICP-MS during these three injections. The modified parameters are given in Table 2.

In contrast, during a measurement using the ICP-MS default method (spectrum acquisition mode) where the sample was continuously injected for minutes through the higher inside diameter of the sample tubing, together with a longer sample uptake, several stabilization processes and repeated measurements a total between 1 and 2 mL of the sample was injected for triplicate measurements. Thereby a more than 10- to 20-fold reduction of the injected sample volume was implemented for the transient method as compared to the default method.

Table 2: Operating parameters of the ICP-MS (7500cx series, Agilent) with time resolved analysis mode and the programmed autosampler ASX 500

ICP-MS Parameter	**7500cx series (Agilent)**
RF-power	1550 W
Cooling / auxiliary gas	15.0 / 1.05 L min^{-1}
Pump rotation	0.1 rps
Analyzed Isotopes	^{153}Eu, ^{165}Ho, ^{238}U
Dwell times / Scans / Repetition	100 ms per mass / 1 / 3 times
Total analysis / scan time	800 s
Sample uptake parameters	**ASX 500**
Amounts of samples	6 per run
Sample uptake	10 s
Washing time	90 s

The integration over time of the resulting peaks was performed manually and graphically using the Agilent Mass Hunter software. The integration starts with the increase of the signal and ends with the return to the baseline. Under ideal conditions the peak shows a plateau

with the width of the injection time and the integration is trivial (Figure 3, left). Under real conditions the peak is unsteady and peak integration is more ambitious (Figure 3, right).

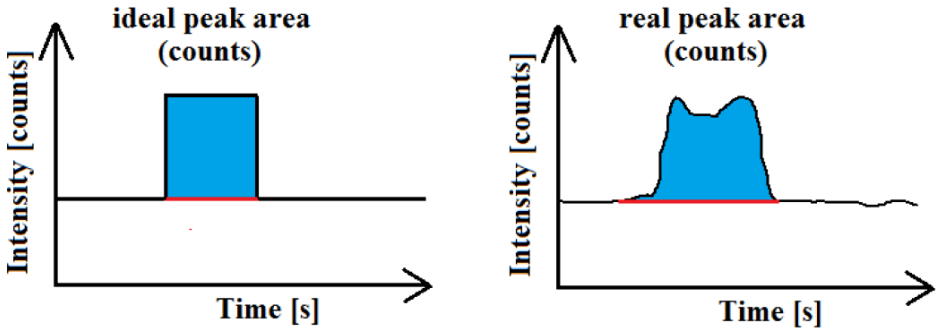

Figure 3: Graphical integration of the peak area

The determined peak area equates to the signal and shows the total amount of counts. If necessary the intensity axis is enlarged in order to integrate small peaks more precisely in the presence of larger peaks. The obtained peak area of the analyte is normalized with the peak area of the internal standard of the same injection and proportional to the analyte concentration.

2.2.2 Capillary electrophoresis (CE)

Electrophoresis is the migration of charged molecules or ions in a solution under the influence of an electric field. In the case of Capillary Electrophoresis (CE) the sample migrates in thin fused-silica capillaries (50-100 cm in length) with inner diameters ranging from 25 to 100 µm filled with an appropriate CE electrolyte [Jandik & Bonn 1993]. The influence of the electrical field on an ion causes a constant migration rate for every ion within the CE buffer. Cations with different electrophoretic mobility (different charge, radius or molar mass) are separated from each other and from neutral or anionic molecules or ions as shown in Figure 4.

Electro-osmotic flow (EOF) is the result of electroneutrality constraints which cause the formation of a charge double layer at the walls of the CE capillary. The walls of a fused silica capillary contain silanol groups which ionize in contact with a high pH electrolyte solution This dissociation produces a negatively charged wall. A layer of counter ions (e.g. metal ions) is then formed at the wall to preserve electroneutrality.

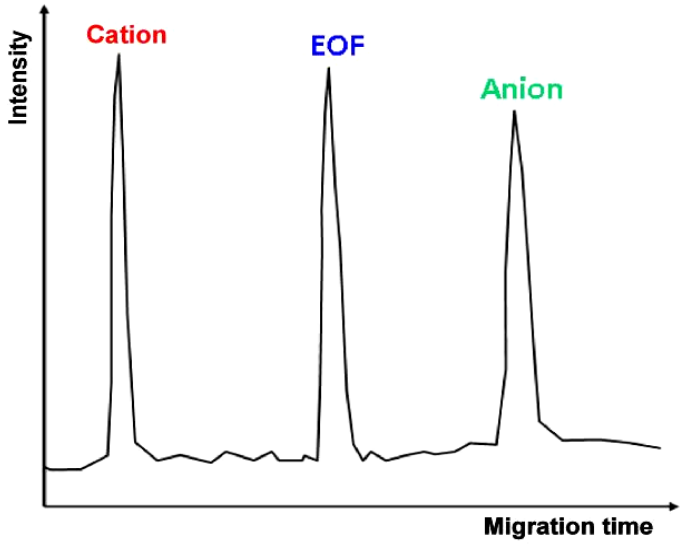

Figure 4: Principal migration of differently charged ions in capillary-electrophoresis

When an electric field is applied these counter ions and their associated solvating water molecules migrate towards the cathode. This movement of ions and their associated water molecules results in a flow of solution towards the detector which is called electroosmotic flow (EOF). At low pH the silanol groups are not ionized and therefore the flow rate is much reduced or even zero at very low pH values. The influence of the electric field on an ion causes a constant migration rate ν for every ion within the solution in the range of about 25-110 µm/s.

The interaction between frictional force (Stokes) and electrical ones is given by the relation

$$\nu = \frac{z \cdot E \cdot F}{6 \cdot \pi \cdot \eta \cdot r \cdot N_A}$$

ν	Electrophoretic migration velocity
z	Net charge of the analyte
N_A	Avogadro constant
r	Stokes radius
E	Electrical field
F	Faraday constant
η	Viscosity of the medium

The principal build-up of a CE is shown in Figure 5. The capillary fits into two buffer vials, and the high voltage is applied through the capillary. A detector and the data acquisition are placed at one end of the capillary.

Figure 5: Principal build-up of a capillary-electrophoresis system

The idea of using capillary electrophoresis for the determination for complex stability constants for metals is not really new (especially in protein chemistry), but the direct separation of metal ions from their complexes is rarely used and - so far - even less in the case of humic acid complexes. The CE experiments were carried out with a Beckmann P/ACE MDQ (Beckmann Instruments, USA). CZE separations were carried out in an uncoated fused silica 80 cm capillary (Polymicro Technologies, USA) with 75 µm of inner diameter.

The samples were injected hydrodynamically at 200 kPa s (10 kPa for 20 s) which corresponds to a sample volume of 220 nL. In order to precondition the capillary before each run the capillary was rinsed with HCl (4.5 M) for 30 s at 140 kPa, with NaOH (0.5 M) for 30 s at 140 kPa, with Milli-Q deionized water for 20 s at 140 kPa and additionally with CE electrolyte buffer for 30 s at 140 kPa. To prevent buffer depletion and to reduce background levels of lanthanides and uranium the buffer was changed completely every 10^{th} run. The separations were performed under optimized conditions at 30 kV and 20 kPa at 25°C.

2.2.3 Hyphenation of CE and ICP-MS

Capillary electrophoresis (CE, Beckman Coulter P/ACE MDQ) was hyphenated by a homemade interface to inductively coupled plasma mass spectrometry (ICP-MS, Agilent 7500cx) to obtain a high sensitivity for the determination of the rare earth element species of europium and uranium with AHA [Kautenburger et al. 2006]. To couple CE to ICP-MS a fused-silica CE-capillary was fitted into a MicroMist 50 µl nebulizer with a Cinnabar cyclonic spray chamber (chilled to 4°C) in the external homemade interface (Figure 6).

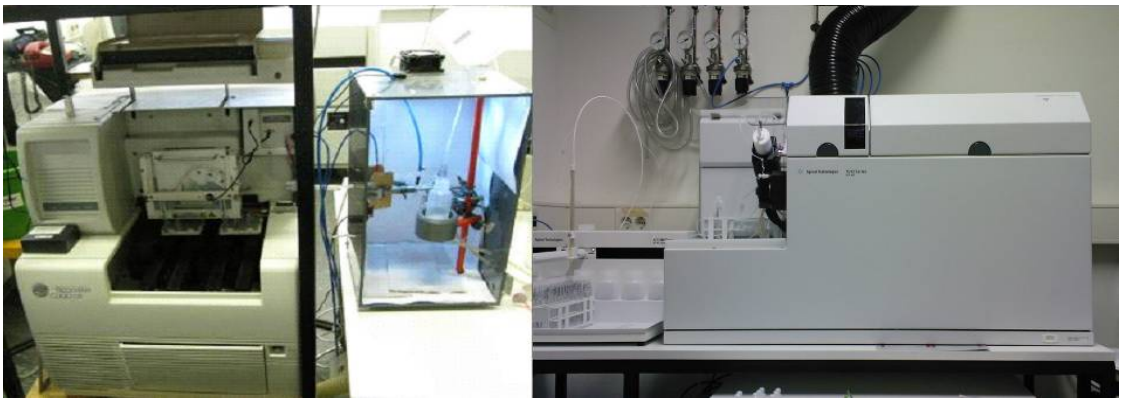

Figure 6: Hyphenation of CE and ICP-MS by the homemade interface

A make-up fluid including 4 ppb Ho as an internal standard was combined with the flow from the capillary within the interface to obtain a fluid throughput high enough to maintain a continuous nebulisation. Detailed analytical conditions are given in Table 3.

Table 3: Operating parameters of the CE with homemade interface

CE	**Beckman Coulter P/ACE® MDQ**
Capillary	fused silica (Polymicro Technologies)
Capillary dimensions / Temperature	74 µm ID, 362 mm OD, 80 cm length / 25°C
CE electrolyte buffer	100 mM acetic acid, 10 mM Na-acetate, pH 3.7
Internal Standard (IS) CE buffer	200 ppb Cs
DC-voltage / current	+ 30 kV / 16–18 µA
Interface	**homemade**
Spray-chamber	Cinnabar cyclonic, chilled at 4°C, 20 mL volume
Nebulizer	MicroMist 50 µL, Type AR35-1-FM005E, 2.8 bar
Make-up fluid	2% HNO_3, 24 nmol L^{-1} (4 ppb) Ho (IS), 112 µL min^{-1}

In the optimized CE-ICP-MS-system we used a DC-voltage of 30 kV, and additionally a pressure of 3 psi was applied as the best separation conditions for the non AHA complexed and AHA complexed metal ions. The comparison of the complexation of Eu and U with non-iodinated and iodinated AHA revealed no detectable differences [Kautenburger et al. 2006]. The CE-ICP-MS method developed was checked by analyzing different standard solutions in a previous project.

2.2.4 High performance liquid chromatography (HPLC) and hyphenation to ICP-MS

High performance liquid chromatography or high pressure liquid chromatography (HPLC) is a well-established analytical method for separating and identifying a mixture of substances. It makes use of a liquid eluent that is pumped through a column containing a stationary phase applying high pressure. This pressure is generated using special HPLC pumps and can reach up to 400 bar. A defined volume of liquid sample is injected in this continuous eluent flow. The separation of two or more compounds present in the mixture is caused by their different affinity to either the liquid or the solid phase. This leads to a characteristic distribution between the liquid and the stationary phase. Depending on the applied stationary phase, the nature and polarity of the eluent, temperature, pH value, etc. various separation mechanisms exist such as size discrimination, separation due to different charge, polarity or solubility. The different tendency of a compound to stay more time in one of the two phases (eluent or stationary phase) is described using the distribution coefficient within the Nernst Distribution Law. Two or more compounds with sufficiently different distribution coefficients can be separated from each other. After the separation step a suitable detection is necessary. Typically applied detection methods are UV-vis diode array detection, refraction index measurement or detection of fluorescence after excitation.

Figure 7: Hyphenation of HPLC with ICP-MS for MCCE setup

In this project an Agilent 1100/1200 LC system (Agilent, Waldbronn, Germany) was used for the miniaturized column experiments. The liquid chromatography (LC) system consists of a LC pump which can deliver constant flow rates between 0.5 µL and 2 mL per minute between 1 and 400 bar. The samples are injected by an autosampler with a sample volume between 0.1 and 100 µL, larger volumes can be added continuously as a second eluent

solution. The column (guard column cartridge, Upchurch Scientific, 20 mm x 3.5 mm ID) can be filled with 100% OPA as stationary phase (sorbent) or using a variable mixture with purified see sand (total weight of 250-290 mg). The temperature of the OPA-column can be controlled exactly between 15 and 80°C in a column compartment. After separation in this clay column the different sample species can be detected via a diode array detector or additionally by hyphenation with ICP-MS to detect the UV/Vis-inactive species. As mobile phase (eluent) different combinations of solutions can be mixed by a binary capillary LC pump.

In our experiments usually ultrapure water (Milli-Q) is used as mobile phase. Iodide or bromide was used as mobility (retention time) reference to check the repeatability of each experiment by adding 0.1 mM NaI or NaBr into all samples to correct the differences of the retention time in different experiments as well as in the different clay columns used.

For the hyphenation of HPLC and ICP-MS (online coupling of the two instruments as shown in Figure 7) the setup has been modified in order to obtain better sensitivity and faster response. This has been done by both minimizing the dead volume of the system and exchanging the standard nebulizer and the spray chamber of the ICP-MS system. The outlet of the HPLC column can be directly connected to the ICP-MS nebulizer inlet thus bypassing the HPLC detectors (such as the diode array).

2.2.7 Nuclear magnetic resonance (NMR) spectroscopy

Nuclear magnetic resonance (NMR) spectroscopy is a spectroscopic method to examine the electronic environment of atoms and their interaction with neighboring atoms of different kind thus allowing to elucidate unknown structures. The underlying physical process is the absorption measurement of electromagnetic radiation in the range of radio frequency (approx. 4 to 900 MHz) leading to magnetic resonance of the stimulated atomic nuclei. A typical NMR measuring set-up is shown in Figure 8.

In the present study NMR spectroscopy of liquid samples has been applied whereas solid state NMR spectroscopy is widely used for characterization of solid samples. The liquid sample, usually in the range of 100 µL to 1 mL, is placed in a strong and constant external magnetic field. This magnetic field causes a splitting up of the nuclei energy levels. Through the irradiation of a radio frequency pulse a small amount of the nuclei is excited from the lower to the higher energy level. Consequently, their subsequent relaxation to the ground state leads to the emission of radio frequency radiation. This is congruent with the classical understanding of absorption spectroscopical methods (excitement to and relaxation from an energetically higher state accompanied by the quantification of the energy absorbed during this process).

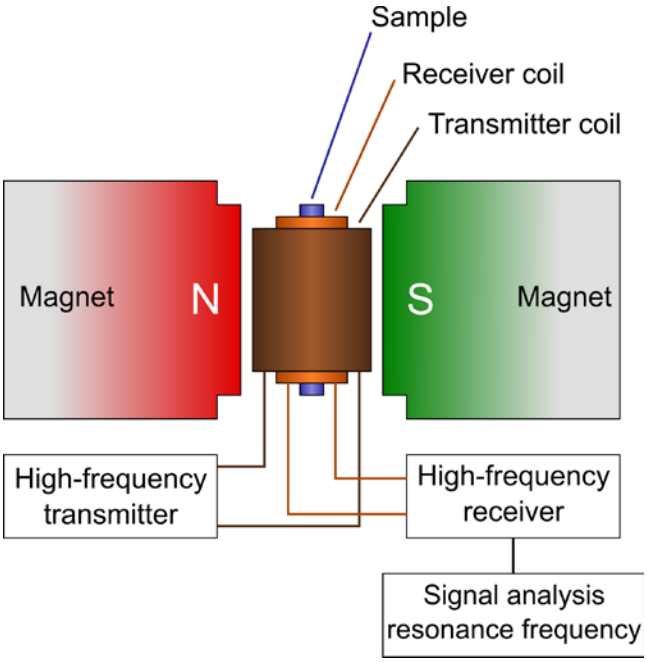

Figure 8: Schematic view of a NMR spectrometer [modified from Oguenther 2011]

The quantum mechanical approach to NMR spectroscopy makes use of the atomic spin that can be (though not correctly) interpreted as rotation of the nuclei around their own axis. This approach shall not be described further in this report.

In the context of the joint research project presented in this report the different borate compounds (ionic compounds with boron oxygen bonds) are of interest due to their presence in a possible final disposal site. The properties of the two naturally occurring boron isotopes ^{10}B and ^{11}B regarding NMR spectroscopy are given in Table 4. Typical chemical shifts δ in B NMR are situated between δ = 100 und δ = -120. As a consequence of the quadrupolar momentum of their nuclei and their heteronuclear nature broad signals are detected with signal widths usually greater than 10 Hz.

Table 4: Properties of the two naturally occurring boron isotopes regarding NMR spectroscopy

Isotope	**^{10}B**	**^{11}B**
Natural abundance [%]	19.9	80.1
Relative sensitivity	0.02	0.17
Nuclear spin	3	3/2
Quadrupolar nuclei	yes	yes

Common NMR sample tubes are made of borosilicate glasses. Their boron content leads to a significant background during B NMR experiments. In order to avoid the boron background NMR sample tubes made of pure quartz glass (Wilmad® Quartz NMR tubes, diameter 5 mm, length 7 inch, Z562262-1 Eq MW 11321, Batch MKBH7851) have been used that do not contain a detectable amount of boron.

It is generally accepted that NMR spectroscopy offers excellent reproducibility and allows quantification without the need for analytical standards. However, sensitivity can be an issue.

2.2.6 Ultrafiltration (UF)

The determination of log ß values is based on the entire separation of free and complexed metal ions. For the separation of different species the method of ultrafiltration was used followed by inductively coupled plasma mass spectrometry to measure the free metal ion concentration. The driving force for the separation process by ultrafiltration is a transmembrane pressure differential. The small hydrated ions are able to pass through the membrane with the liquid flow whereas the bulky complex composed of metal ion and HA is retained. The concentration of free, uncomplexed metal ions is measured by ICP-MS assuming that the remaining metal formed a metal-HA-complex.

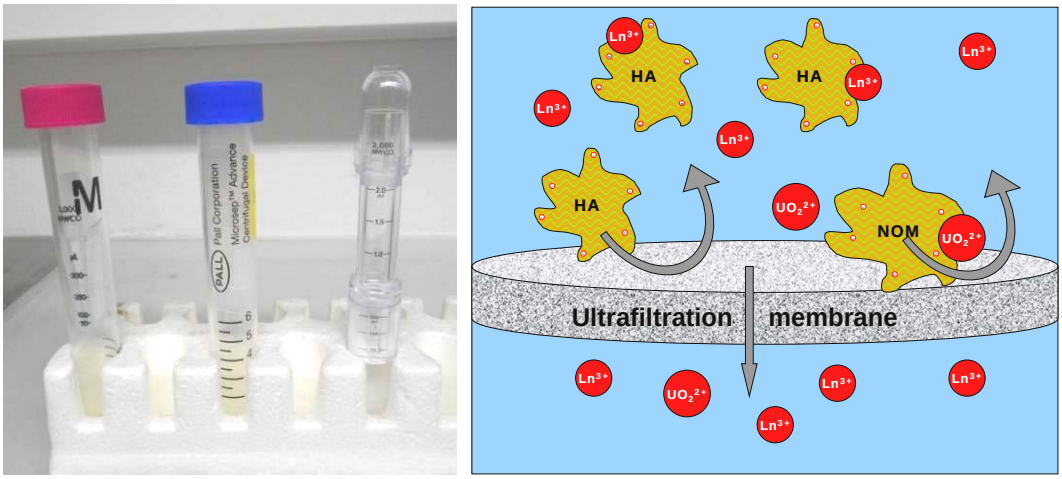

Figure 9: Used UF systems (left hand side): Amicon® Ultra 4 mL filter, MicrosepTM Advance Centrifugal Devices 3K Omega Filter, Vivaspin 2 Filter (from left to right), and principle of ultrafiltration (right hand side).

As best UF-material Amicon® Ultra 4 Centrifugal Filter Devices with a molecular weight cut-off of 3 kDa from Merck Millipore were used. A copolymer build by styrene and butadiene is used as filter device. The membrane consists of a low binding regenerated Ultracel®-cellulose. Phase separation takes place by centrifugation with a force effect of 7500 g for 40 minutes using the 5804 R centrifuge from Eppendorf.

2.3 Methods

2.3.1 Batch experiments

In this study all experiments using the batch technique (sorption, desorption experiments) were performed under ambient atmosphere ($pCO_2 = 10^{-3.5}$ bar) and room temperature (23±2°C).

Figure 10 shows the procedure of the batch experiments schematically. The experiments were performed in centrifuge tubes (SuperClear 15 mL, VWR International GmbH, Darmstadt, Germany) which have low metal sorption properties (step 1).

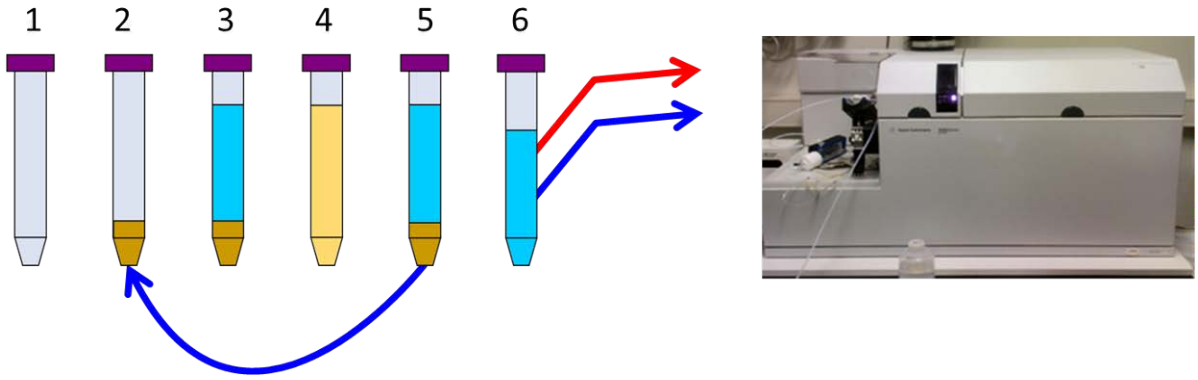

Figure 10: Schematic procedure of the batch experiments

In all experiments with clay an equivalent amount of 4 g L^{-1} OPA was used (each experiment was made by weighing 40 mg OPA into a tube filled up with the adequate solution to a final volume of 10 mL (step 2)). In addition 9.8 mL of background solution 200 µL of 1 M $HClO_4$ / HCl were added to facilitate the adjustment of the pH values in the next steps. After preconditioning the clay (40 mg) with the corresponding background solution for 72 h the remaining components were added (appropriate volumes of the 1 mg L^{-1} or 100 mg L^{-1} metal standard stock solutions or additionally, in the ternary system, NOM concentrations of 25 mg L^{-1}), and the pH was adjusted by addition of dilute $HClO_4$, HCl or NaOH (suprapure, Merck, Darmstadt, Germany) (step 3). The samples were mixed for at least 72 h in a heating thermomixer of Ditabis AG (HLC MHL 23, Pforzheim, Germany) with all components present to reach a stable equilibrium (step 4). Afterwards the tubes were centrifuged at 12800 g (10000 rpm) for 10 minutes (step 5). Samples were taken from the supernatant solutions. Diluted and acidified solutions (pH value was adjusted to pH<1 with HNO_3 suprapure) were prepared to determine the metal content in the solution by ICP-MS (step 6).

As the total metal concentration (before clay contact) is known and the non-adsorbed metal is measured it is possible to calculate the amount of adsorbed and precipitated metal. All

batch experiments containing clay were performed in this way. Filtering (e.g. ultrafiltration) as well as centrifugation of the samples was not performed due to some drawbacks (for example low metal recovery rates due to filter adsorption and disturbed sorption/desorption equilibrium) which were found out in a previous study [Kautenburger & Beck 2007].

2.3.1.1 Sorption experiments

The sorption experiments were performed with U(VI) and Eu (III). The ion strength was varied from 10 mM $NaClO_4$ to 0.01, 1, 3 and 5 M NaCl, and additionally different concentrations of Ca (0.05, 0.5, 5 M) were added as competing cation. Sorption isotherms were determined by increasing the metal concentration from 0.1 µg L^{-1} (equivalent to 0.42 nmol L^{-1} U(VI) and 0.66 nmol L^{-1} Eu, respectively) to 10 mg L^{-1} (equivalent to 42.0 µmol L^{-1} U(VI) and 65.8 µmol L^{-1} Eu, respectively) at pH 5 (pH 5.0±0.05) or pH 7.0 (pH 7.0±0.05). The pH-edges were determined at pH values ranging from 2 to 12 (pH±0.05) with a metal concentration of 300 µg L^{-1}. The correct pH value was adjusted by use of ultra-pure solutions (1 M or 100 mM) of $HClO_4$, HCl and NaOH.

2.3.1.2 Desorption experiments

The performed desorption experiments are based on the corresponding sorption experiments and simulate metal mobilization in the course of repeated equilibrations with fresh metal-free solution. In these test series samples (centrifuged OPA with sorbed metals at the given experimental conditions without discarded supernatant solution) from the corresponding sorption experiments were used. The carryover volume in the desorption experiments was less than 50 µL (coming up to 0.5% of a total volume of 10 mL). Assuming that a fictive desorption step leads to 50% desorption of metal ions (we have never measured such high desorption in one equilibrium step), the maximal error would be less than 1%, and this bias is comparable for all desorption steps and not relevant. The solution (10 mL at the specific experimental condition) for all desorption experiments varied from 0.01 M $NaClO_4$, 0.01, 1, 3 and 5 M NaCl, and additionally different concentrations of Ca (0.05, 0.5 and 5 M) were added to the centrifuged clay samples as competing cation. Thereafter the pH of the desorption solutions was adjusted. The samples were shaken for 72 h respectively to attain desorption equilibrium (in further experiments no significant kinetic effects were observed after 48 hours). This procedure was repeated three times for every sample, for special samples the procedure was repeated 5 times. After each desorption step the tubes with the samples were centrifuged at 12800 g for 10 minutes. A subsample of 3.33 mL was taken from the supernatant solution, and prepared for ICP-MS measurement. The desorbed metals in the samples were analyzed by ICP-MS.

2.3.1 Complexation studies

For the complexation studies via CE-ICP-MS and UF we used a concentration of 0.5 mg·L^{-1} Eu (3.3 µmol L^{-1}) or U (2.1 µmol L^{-1}) and 25 mg L^{-1} humic acids in a final volume of 10 mL solution of 0.01, 0.1 or 1 M NaCl. Additionally, 0.5 and 5 mM $CaCl_2$ were added. The pH values were adjusted with 1 M NaOH and 1 M $HClO_4$ to pH 5. Before filtration the samples were equilibrated for 48 h at 25 °C.

To prove permeability of metal ions through the ultrafiltration membrane and to verify recovery rates of uncomplexed Eu^{3+} and UO_2^{2+} experiments with pure metal ion solutions without HA were performed first.

Different types of HA were added to calculate complex stability constants log β. With CE-ICP-MS all above described humic acids were used. For experiments with UF Aldrich-HA (AHA), Elliot soil-HA (EHA), Gorleben 573-HA (GoHy573), Gorleben 851-HA (GoHy851) and Suwannee River-NOM (SNOM) were used because of the strong difference in their complexation behavior.

2.3.3 Miniaturized clay column experiments (MCCE)

In order to fill the columns with clay or clay sea sand mixtures two different approaches have been examined, namely wet packing of a clay slurry or suspension and dry packing. The wet packing of the column cartridge proved to be difficult due to the small inside diameter of the column and the increased viscosity of the clay slurries. Attempts to facilitate the filling of the clay suspension by either carefully applying a vacuum at the column exit or exerting pressure on the slurry during the filling process using a syringe were not successful. Moreover, a funnel screw-mounted on the column inlet lead to trapped air inside the column that had to be iteratively eluted by mounting the column to the HPLC and repeatedly adding more slurry afterwards.

Moreover, the accurate determination of the amount of stationary phase filled into the column by differential weighing is more error-prone in the case of wet packing due to water absorption of the swellable clay minerals prior to the packing process and the resulting change in volume (and density).

For the stated reasons preference was given to the dry packing procedure to fill the column with clay or mixtures of clay with see sand. The procedure has been adopted from literature [Klawiter et al. 1982, Meyer 2009] and adapted to the applied materials.

It is necessary to mention that particles with a diameter smaller than 20 µm cannot be dry packed due to their aggregation tendency [Meyer 2009]. Such an aggregation is not

expected when taking into account the considerable polydispersity of the examined clay and the irregular shapes of the particles and in the case of the mixtures of clay with sea sand also due to the presence of the sand particles.

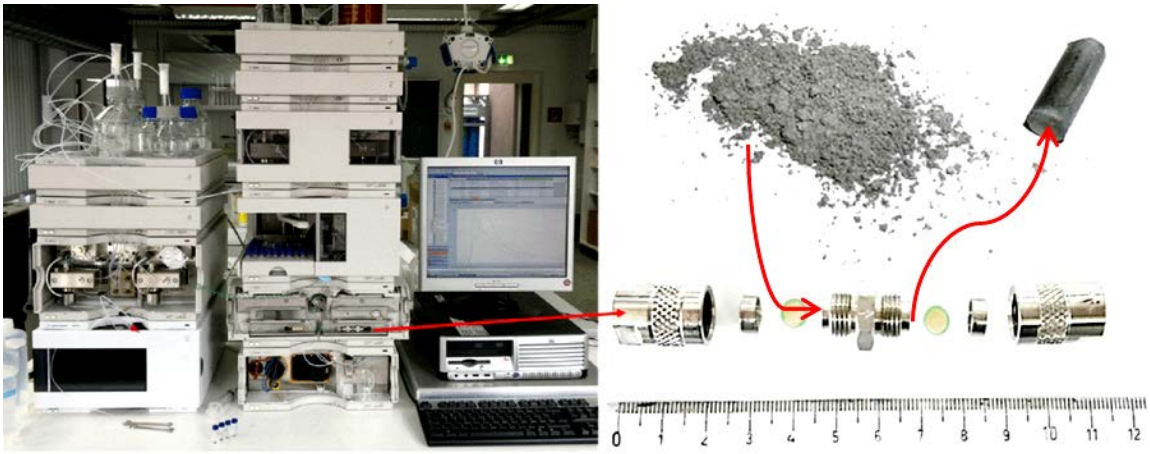

Figure 11: MCCE setup and clay before and after a typical MCCE experiment

2.3.3.1 Injection of discrete sample amounts

The elution chromatography mode is the most prevalently applied mode in the field of chromatography. A defined volume of the sample is injected onto the packed chromatographic column and detected after the column using a suitable detection method.

In the context of MCCE small amounts of dissolved metals relevant for final disposal (uranium, europium) are injected together with the reference tracer and their migration times are determined.

3 Results and discussion

3.1 Optimization of the transient ICP-MS measurement

To check the proof of principle for the transient method calibration measurements with europium and uranium were performed. Typically, all signals of Eu and U are normalized with a normalization factor which is calculated from the Ho signal and the factor 100,000. The normalization compensates the device fluctuation, the changed filling levels of the sample vials during the measurement and additionally the influence of the salinity.

For each metal two calibration curves were measured, a first one for low metal concentrations in the range from 0.1 to 1 µg L^{-1} (0.1, 0.3, 0.5, 0.8, 1 µg L^{-1}) and a second one for higher concentrations (1, 5, 10, 50 and 100 µg L^{-1}). All calibration curves for both metals show a good linearity and a direct proportional relation between metal concentration and peak area. Using for example solutions of 1 M NaCl ionic strength the linear function of the calibration curve for low Eu concentrations is y = 5953.4x + 33.8 and for low U concentrations it is y = 7991.6x – 49.2. The linear functions for high metal concentrations are for Eu y = 6153.8x + 415.7 and for U y = 7612.2x + 1256.7. The coefficients of determination (R^2) are 0.9998 (U) and 0.9995 (Eu) for higher metal concentrations and 0.9992 (U) and 0.9990 (Eu) for lower metal concentrations. All values are close to 1.0000 and confirm the linear relation between concentration and peak area.

It is necessary to compare the congruency of the default method (spectrum acquisition mode) with the transient method (time resolved acquisition mode) to find out if the transient method provides consistent results. In the first experiment samples with 0.01, 1 and 5 M sodium chloride and known concentrations of uranium and europium (0.8, 3, 8, 15, 30 and 80 µg L^{-1}) were prepared. These samples were measured in spectrum and time resolved mode. For the transient ICP-MS measurement all samples are diluted 1:3. Due to the high salinity the samples with 1 and 5 M NaCl need a higher dilution of 1:100.

In Figure 12 the results of this comparison are shown. For the samples with lower metal concentrations (0.8 and 3 µg L^{-1}) a 1: 100 dilution is too high. As consequence the measured metal amount is just above the detection limit. Additionally, the higher salt matrix content negatively influences the metal recoveries. The recoveries differ strongly from the spiked concentrations. In the case of europium the recovery is lower compared to uranium. However, the mentioned very low concentration range is an important range for the metal concentrations measured after the sorption experiments, and a lower dilution of the samples is not possible due to the high ionic strength.

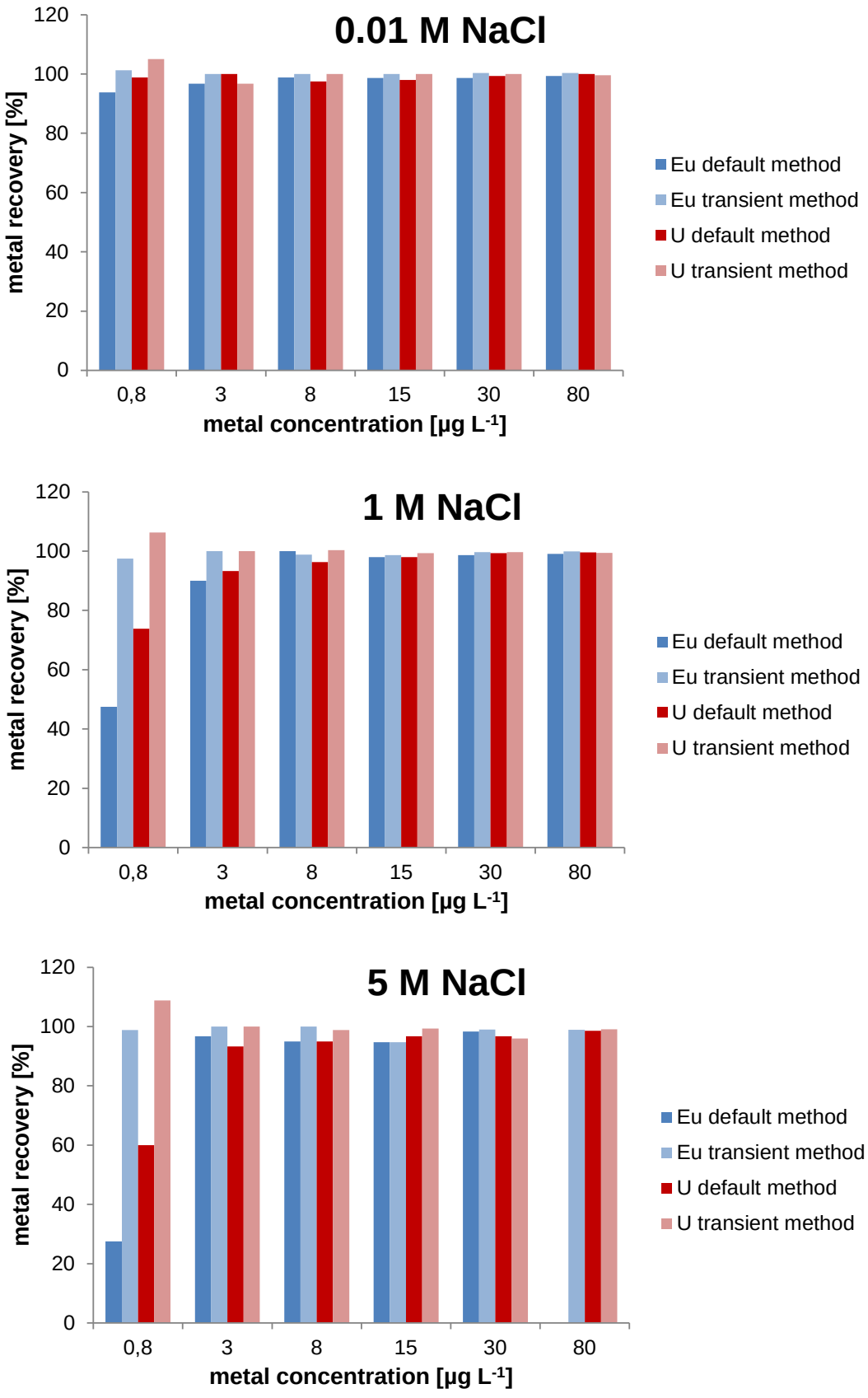

Figure 12: Comparison of the europium and uranium recoveries [%] in 0.01, 1 and 5 M NaCl sample matrix determined by the default and transient ICP-MS method (n=5)

Additionally, the recovery rates show that the transient measurement delivers suitable results and are suitable for the measurement of samples with high matrix content. To check the comparability of the transient and default ICP-MS method experiments with samples at realistic conditions are performed. Real samples to determine pH edges of uranium and europium in 0.01 M $NaClO_4$ solution were analyzed with both methods. The results are shown in Figure 13. For Eu and U only small differences between default and transient method are visible but the differences are smaller than the deviations of the measurement. Additionally, greater differences are observable at higher analyte concentrations in solution.

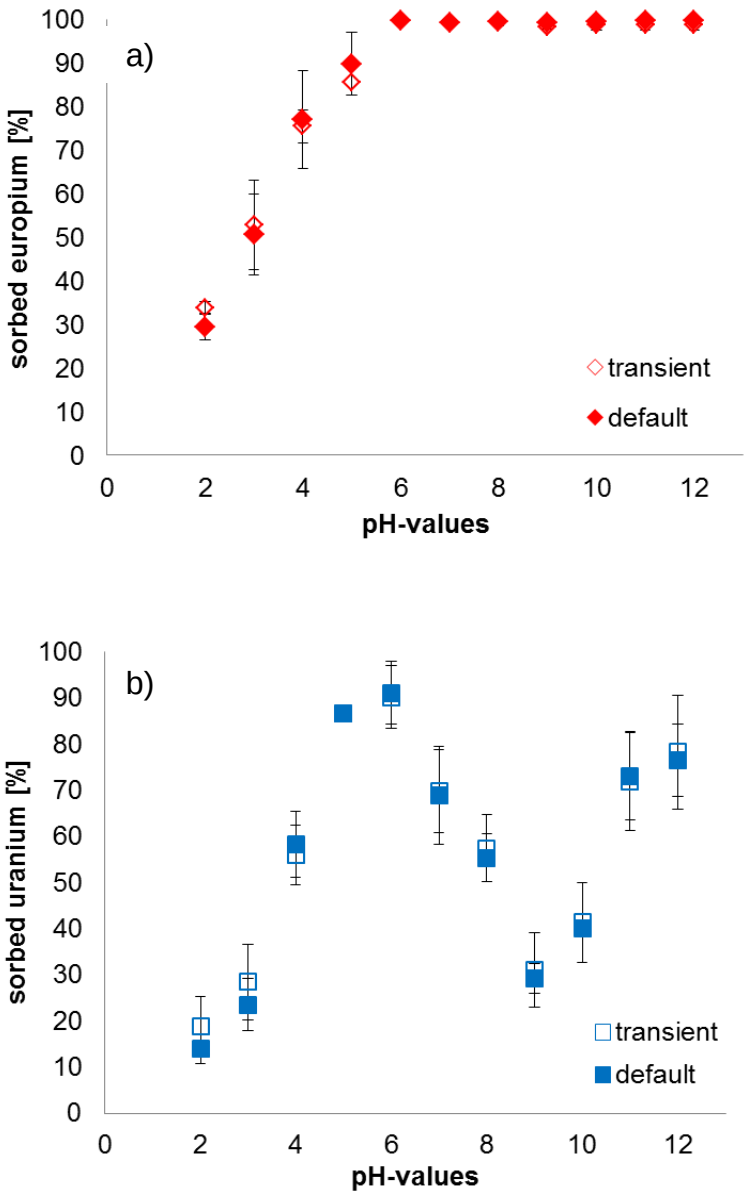

Figure 13: pH edges of europium (a) and uranium (b) onto Opalinus clay in 10 mM sodium chloride solution with default and transient ICP-MS measurements (n=5)

3.3 Analysis of the binary system metal-NOM

3.3.1 CE-ICP-MS

In previous projects the separation of uncomplexed Eu species from those complexed with AHA was optimized with the hyphenation of CE and ICP-MS [Kautenburger et al. 2011a]. The advantage of this speciation technique is the simultaneous measurement of both free metal and metal humate complex in one analysis step. In this project the transferability of the method to uranium is tested. In Figure 14 the typical electropherograms of Eu (a) and U (b) in the presence of AHA are presented. Both show similar features with 3 different metal species complexed or uncomplexed by AHA after the CE-ICP-MS run. The first signal (peak 1) represents the uncomplexed metal before CE separation. This "free" Eu^{3+}or UO_2^{2+} ion was complexed by the acetate (Ac) in the electrolyte buffer during the CE-separation and migrates as $EuAc^{2+}$ / $(UO_2)Ac^{+}$ towards the CE cathode. The second signal observed (peak 2) represents metal complexed on weak binding sites of AHA before the CE-separation step. However, the high voltage power of the CE system enhances the dissociation of Eu^{3+} and UO_2^{2+} out of the AHA-complex during CE separation. The samples were prepared and injected in an acetate free solution (10 mM $NaClO_4$ is used for the experiments). During the CE separation Eu^{3+} / UO_2^{2+} are "extracted" out of the AHA complex through the applied DC voltage. For a short time the uncomplexed from peak 2 extracted metals migrate inside the sample zone (10 mM $NaClO_4$) faster than the $EuAc^{2+}$ / $(UO_2)Ac^{+}$ (peak 1) until it moves also out of the sample zone into the surrounding CE buffer zone which contains acetate in higher concentrations. As a result, the free metal (Eu^{3+} / UO_2^{2+}) is also complexed by the acetate and migrates as second peak towards the cathode. The last signal (peak 3) represents metal complexed at strong binding sites before CE separation.

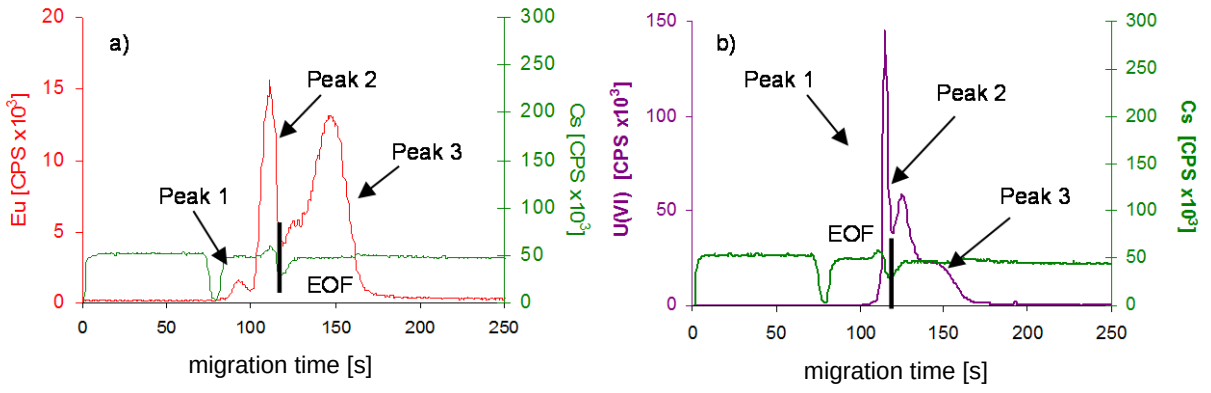

Figure 14: Electropherogram of Eu (a) and U (b) complexed with AHA in 0.01 M NaCl

During the CE run the metal-AHA-complex normally migrates as negatively charged complex towards the anode ($\mu_{e-} > \mu_{eo}$) but due to the applied pressure of 3 psi versus cathode the complex is forced to migrate towards the cathode.

Eu and U differ by different migration times of peak 1 and 2 due to the different charges of Eu^{3+} and UO_2^{2+}. Due to its greater size and lower charge UO_2^{2+} migrates slower to the cathode than the threefold positively charged Eu^{3+} ion. In addition the uranium peak 1 is higher than the Eu peak and peak 2 is notable smaller than that of Eu. A possible explanation is the fact that complexes with twofold charged cations are less stable in comparison to threefold positive charged cation. Furthermore, a steric hindrance of UO_2^{2+} in the process of formation of a complex with AHA is possible.

3.3.1.1 Results of europium complexation with 0.01 M salinity and different NOM

Depending on the repository site different types of natural organic matter (NOM) can occur. Several humic acids were used to simulate effects of different sites. The recoveries of all Eu or Eu-HA species after CE-ICP-MS determination are higher than 90% with exception of the farmland HA from Hannover (OA-HA) where precipitation of the HA could be observed (see Table 5). The proton exchange capacity (PEC) is necessary to calculate the log β values. This PEC is not available for all humic acids, and therefore not all log β values could be calculated correctly. The log β values for the used HAs are in the range between 6.1 and 6.6, the results for the SNOM are significantly lower due to the higher amount of lower molecular compounds.

Table 5: Recovery and calculated log β values of Eu with different NOM in 0.01 M NaCl

Humic acids	Eu recovery [%]	log β values
AHA	96.5	6.1
EHA	95.0	6.5
PHA	97.9	6.6
LHA	98.9	6.4
WHA	90.3	7.0
SNOM	93.3	4.6
SW-HA	97.2	6.7
SS-HA	98.0	6.4
GoHy851	94.4	6.7
GoHy573	96.6	7.0
OA-HA	*58.5**	*4.7*

*Precipitation was observed

The large differences of the Eu signals in the electropherograms show strong distinctions in the complexation behavior due to the various origins, and therefore due the different structure and molecular composition of the humic acids. In Figure 15 the electropherograms for the speciation of Eu with the commercially available humic acids are shown. Among these the Elliott soil HA (b) diagram reveals the strongest variations, the most conspicuous one is the lack of peaks 1 and 2 which shows a very strong complexation of europium by this humic acid. Additionally, the assumption that humic acids with similar origins show similar graphs forms is proven by the comparison of AHA (a) and LHA (d) which are both from lignite residues.

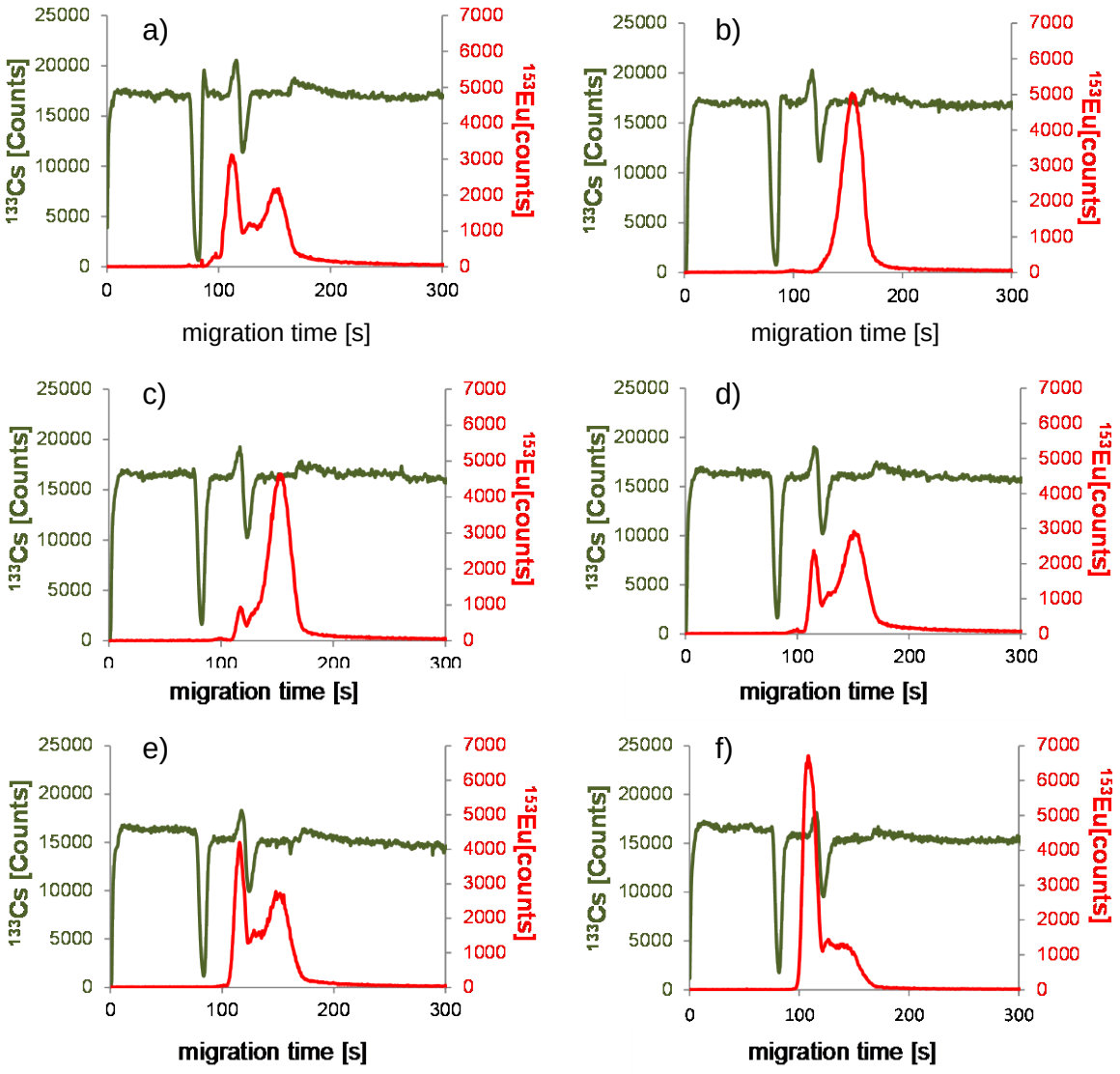

Figure 15: Electropherogram of Eu with 25 mg L-1 NOM; a) Aldrich-HA; b) Elliott-soil-HA; c) Pahokee peat-HA; d) Leonardite-HA; e) Waskish-HA; f) Suwannee-River-NOM

Unfortunately this statement is not in line with all humic acids. In most cases small variations in the origin of a humic acid has a strong effect on the complexation behavior like the two humic acids from "*Kleiner Kranichsee*" in Figure 16 which are from swamp water (a) and swamp soil (b). PHA and WHA have similar origins, but the Eu-signals in the electropherograms are very different, too. As opposed to this, the Suwannee River NOM and the humic acid from farmland by Hannover show really similar electropherograms but the reasons are different. SNOM contains mainly low molecular compounds which form labile complexes with metals like europium. The farmland HA (OA-HA) shows a considerably lower recovery (< 60%) of Eu, and only the first peak is well visible. A great part of the europium is precipitated with the humic acids during the equilibration time, and this was clearly visible in the sample tube.

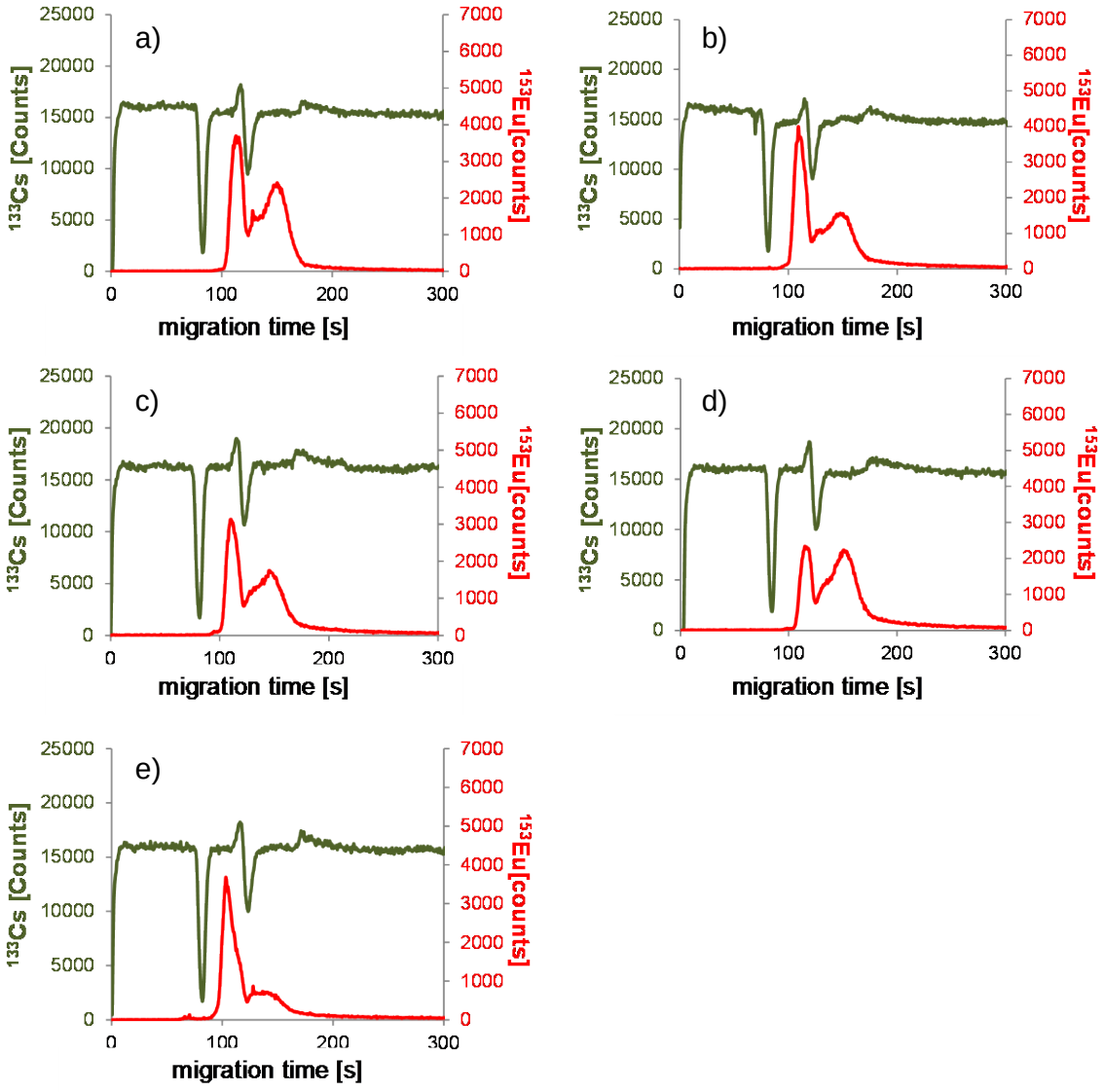

Figure 16: Electropherograms of Eu with 25 mg L^{-1} NOM of samples from "*Kleiner Kranichsee*" (a) swamp water; b) swamp soil); Gorleben bore holes (c) No 851; d) No 573); farmland by Hannover (e)

3.3.1.2 Results of uranium complexation with 0.01 M salinity and different NOM

The recoveries of uranium are partly different compared to the europium results. The range of the recoveries is clearly lower ranging from 75 to 90% with the exception of the farmland HA from Hannover. Strong precipitations are visible and therefore the recovery of uranium is only about 54% as shown in Table 6. Uranium precipitates with the HA similar to europium. The calculated log β values are slightly lower than those of europium. This could be explained by steric hindrances during the uranyl complexation.

Table 6: Recovery and calculated log β values of uranyl with different humic acids in 0.01 M NaCl

Humic acids	U recovery [%]	log β values
AHA	78.0	5.5
EHA	87.8	6.1
PHA	88.4	5.7
LHA	78.1	5.2
WHA	89.7	5.2
SNOM	87.6	4.5
SW-HA	79.6	6.4
SS-HA	70.2	5.5
GoHY851	75.3	6.1
GoHy573	75.2	6.2
OA-HA	*54.2**	*5.2*

*Precipitation was observed

In Figure 17 and the electropherograms of uranyl with different humic acids are shown. The influence of the different humic acids on uranium speciation is similar to that on europium, but the uranium signals in the electropherograms show different peak distributions. In most cases peak 3 is smaller than peak 2 or has entirely vanished. This indicates the different complexation behavior of uranium in comparison to europium. The uranium prefers especially the weak binding sites of the humic acids or it precipitated in a higher amount together with the HA as the recovery rates show. The increase of peak 1 shows that there is more uncomplexed uranium than europium, and this confirms the theory of the steric hindrance in the uranyl complexation.

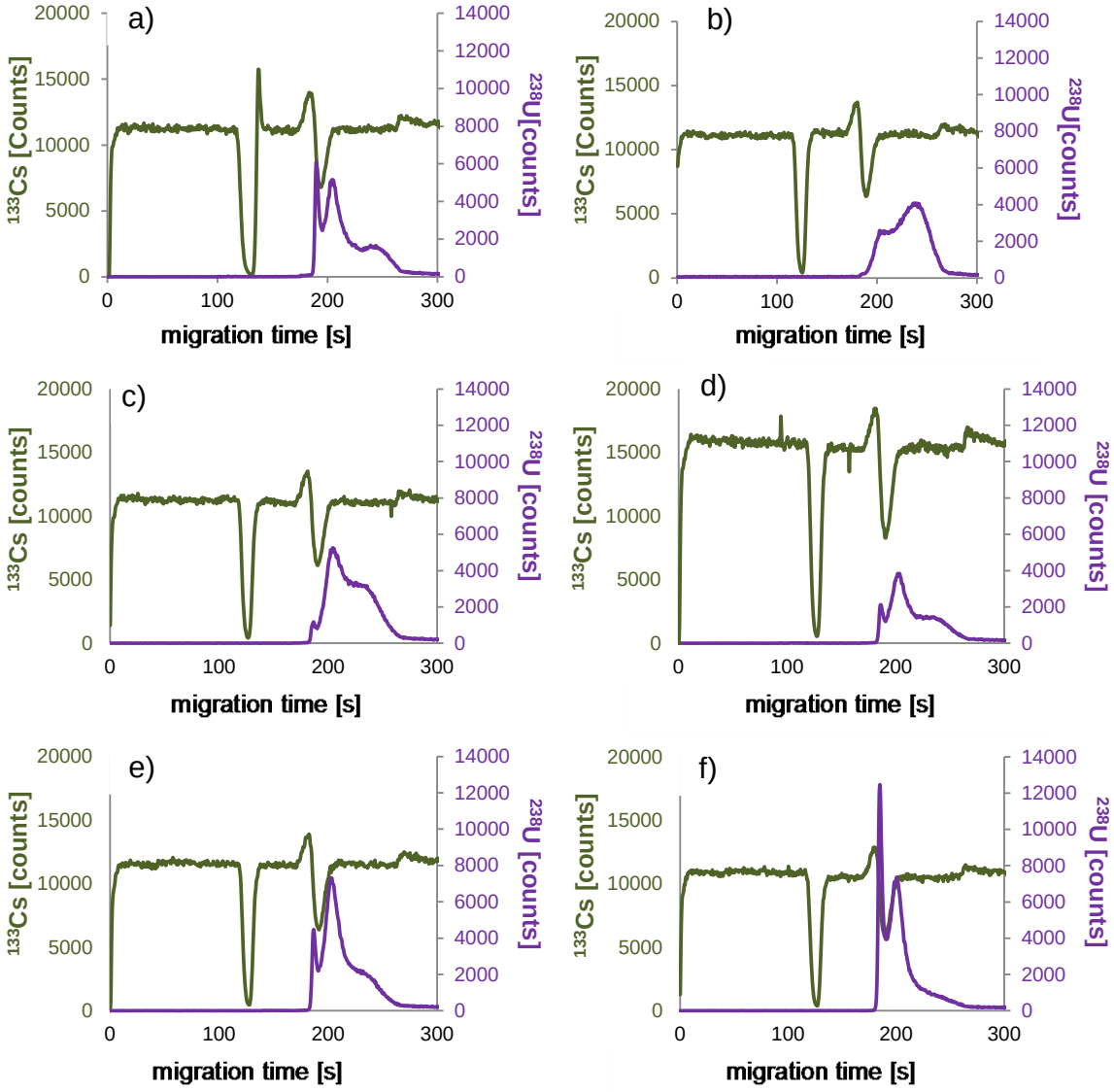

Figure 17: Electropherogram of UO22+ with 25 mg L-1 NOM: a) Aldrich-HA; b) Elliott-soil-HA; c) Pahokee peat-HA; d) Leonardite-HA; e) Waskish-peat-HA; f) Suwannee-river-NOM

The results with EHA and SNOM are very similar in the case of europium. In Figure 17 b) with EHA the uranium peak 1 has nearly vanished, and only complexed species are visible. This shows for both uranium and europium that EHA is the humic acid with the strongest complexation behavior. In contrast to this the Suwannee River NOM has more weak binding sites due to its low molecular weight compounds. Peak 3 is hardly detectable and Peak 1 has increases strongly. The differences in the log β values between europium and uranium with SNOM are not as high as with the humic acids. With low molecular compounds there is no steric hindrance, and therefore U and Eu complexation is in a similar range.

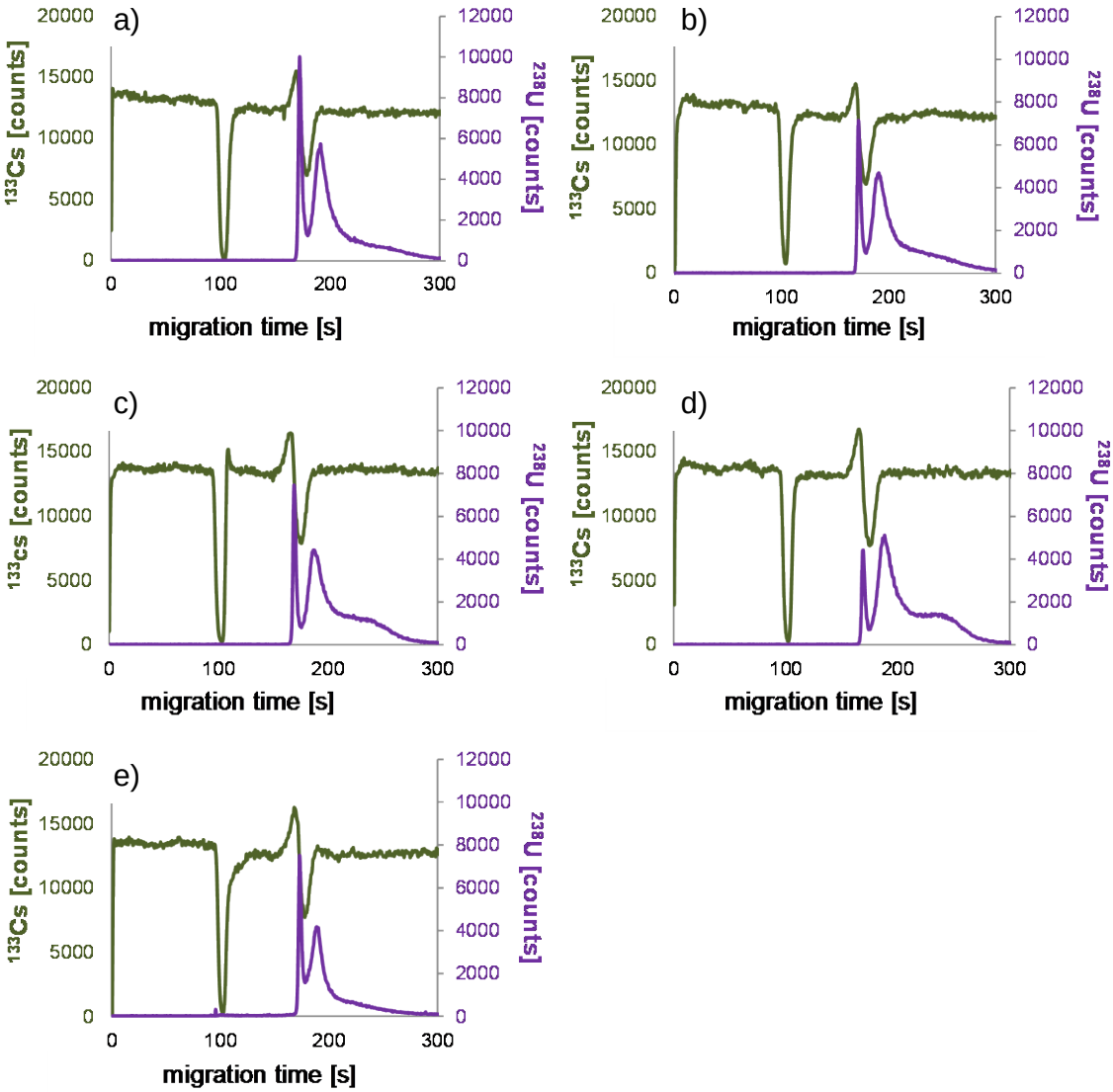

Figure 18: Electropherograms of UO_2^{2+} with 25 mg L^{-1} NOM of samples from "*Kleiner Kranichsee*" (a) swamp water; b) swamp soil); Gorleben bore holes (c) No 851; d) No 573); farmland by Hannover (e)

The farmland HA (OA-HA; Figure 18 e) shows a similar speciation behavior with uranyl like SNOM, but it has a clearly lower recovery of uranium due to precipitation very much like in the case of Eu.

3.3.2 Ultrafiltration (UF)

The hyphenation of CE and ICP-MS allows only the determination of log β values at low ionic strength. An increase of salinity prevents the separation of the different peaks under the used conditions, and therefore a reproducible calculation of the log β values is not possible. For estimation of log β values at high ionic strength another method - such as ultrafiltration (UF) - has to be applied.

3.3.2.1 Results of europium-NOM complexation

Depending on the ionic strength in the sample solution the recovery of dissolved $Eu^{3+}_{(aq)}$ ions in the filtrate ranged between 97 to 100% (Table 7). The permeability of free metal ions through the filter membrane is thereby ensured.

Table 7: Eu-recovery (initial concentration: 0.5 mg L^{-1} Eu) in the filtrate in the presence of different ionic strengths at pH 5

Conditions	Eu recovery [%]
0.1 M NaCl	97.4
+ 0.5 mM Ca^{2+}	98.6
+ 50 mM Ca^{2+}	98.4
1 M NaCl	100.0

With increasing ionic strength log β values for the Eu^{3+}-complexation decrease. Table 8 shows the calculated log β values for the Eu^{3+}-complexation.

Table 8: Calculated log β values for Eu^{3+} complexation

Conditions	AHA	EHA	SNOM	GoHy851
0.1 M NaCl	6.4	6.8	4.5	6.0
+ 0.5 mM Ca^{2+}	5.9	6.7	4.5	5.9
+ 5 mM Ca^{2+}	5.9	6.5	4.4	5.7
1 M NaCl	5.5	6.4	4.1	5.1

The stability of the formed Eu-NOM complexes rises in the following order (Figure 19, left hand side):

SNOM < GoHy851 < AHA < EHA

The lowest complex stability constants are determined for SNOM which represents the weakest binding ligand. The calculated log β values are in a range of 4.1 to 4.5. In contrast to this result, EHA which contains the strongest binding sides shows the highest log β values, ranging from 6.4 to 6.8.

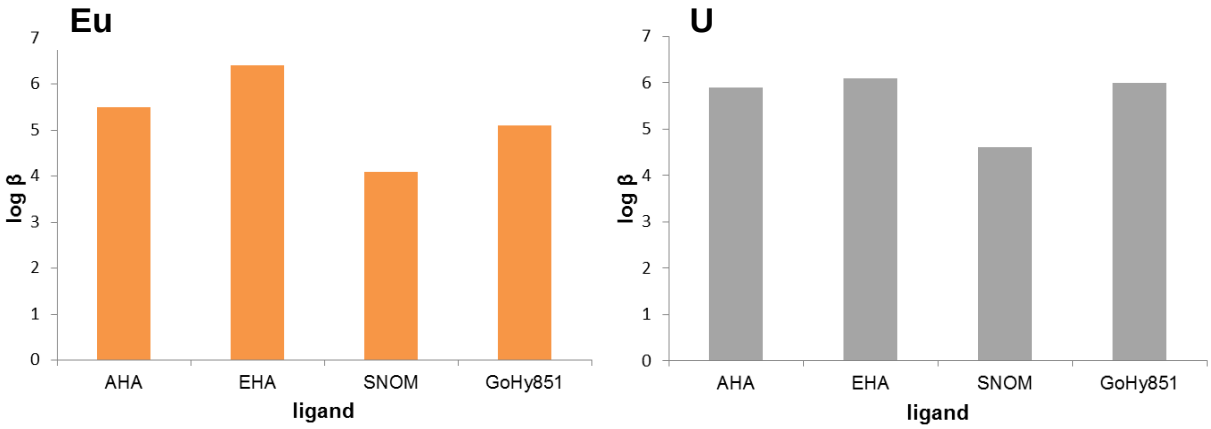

Figure 19: Log β values for the complexation of Eu (left side) compared to uranium (right side) with different NOM in a 1 M NaCl solution

3.3.2.2 Results for uranyl-NOM complexation:

In comparison to Eu^{3+} the recovery UO_2^{2+} is lower (Table 9). Depending on the ionic strength in the solution the recovery of dissolved uranyl in the filtrate ranged between 81 to 93%.

Table 9: U-recovery (initial concentration: 0.5 mg L^{-1} U) in the filtrate in the presence of different ionic strengths at pH 5

Conditions	U recovery [%]
0.1 M NaCl	81.1
+ 0.5 mM Ca^{2+}	90.6
+ 50 mM Ca^{2+}	90.0
1 M NaCl	93.4

The uranyl complexation is not relevantly influenced by an increasing ionic strength. The calculated log β values are given in Table 10.

Table 10: Calculated log β values for the UO_2^{2+} complexation

Conditions	AHA	EHA	SNOM	GoHy851
0.1 M NaCl	6.0	6.1	4.7	5.9
+ 0.5 mM Ca^{2+}	5.7	6.1	4.7	6.0
+ 5 mM Ca^{2+}	5.9	6.1	4.7	6.2
1 M NaCl	5.9	6.1	4.6	6.0

The stability of the formed U(VI)-NOM complexes rises in the following order (Figure 19, right hand side):

SNOM < AHA < GoHy851 < EHA

As for the europium complexation the complex stability constants for the uranyl complexation with SNOM are the lowest ranging from 4.6 to 4.7, while the log β values between 6.1 and 6.2 are the highest when using EHA as ligand for U.

3.3.2.3 Comparison between europium and uranyl

Differences in the complexation of Eu and U exist regarding the strength of the complexing ligands. Using strongly complexing ligands such as EHA, the europium humate formation shows higher log β values (log $\beta_{Eu\text{-}EHA}$: 6.4-6.8) in comparison with the uranyl complexation (log $\beta_{U\text{-}EHA}$: 6.1). Minor differences between Eu^{3+} and UO_2^{2+} humate formation are given by complexation with weakly binding ligands such as SNOM (Figure 20).

A significant influence of the ionic strength on the complex stability can only be observed for the Eu-NOM complexes (Figure 20) where the log β values decrease about 0.5-1.0 log unit at higher ionic strength (see Table 8).

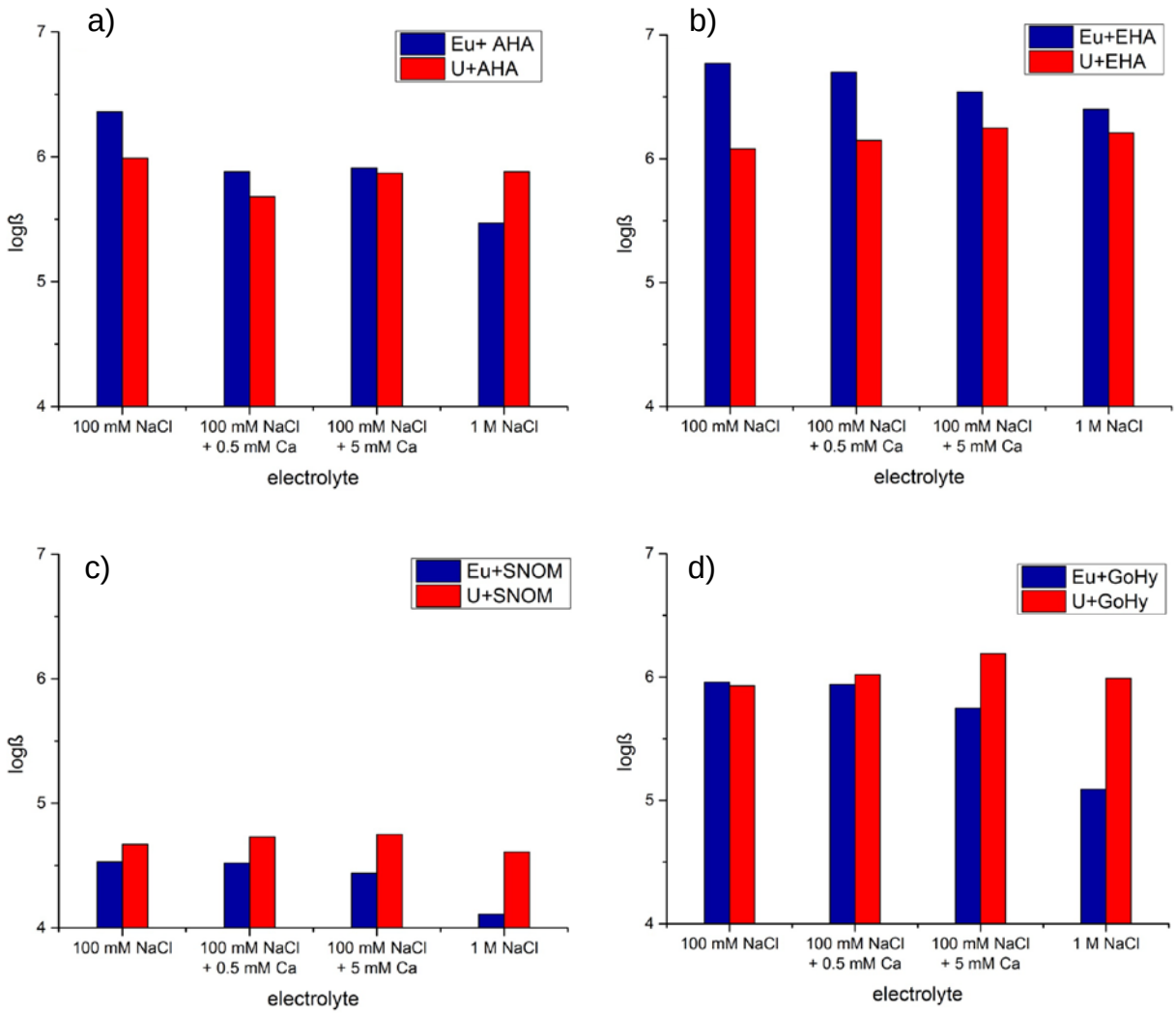

Figure 20: Influence of ionic strength of the log β values for the complexation of Eu^{3+} (blue) and UO_2^{2+} (red) with a) AHA, b) EHA, c) SNOM, d) GoHy851

3.4 Analysis of the binary system metal – clay

Clay sorption experiments with radioactive metals and clay are very important for a better understanding of reaction mechanisms between radioactive compounds and Opalinus clay. In this working package we investigated the sorption and desorption behavior of the trivalent lanthanide Eu as homologue of the actinide Am which is in large amounts in addition to Pu and Np in nuclear waste and nuclear materials inventories stored in various sites around the world. Additionally, U(VI) as major component of HLW was studied, too.

Standardized laboratory batch experiments are performed in the binary system consisting of these heavy metals (Eu, U) and the natural Opalinus clay under conditions close to nature. The Batch technique is “state of the art” to compare a variety of results from different studies in contrast to diffusion experiments, where due to extremely long migration times of higher valent metal ions through the complete clay column only comparatively few experimental data can be acquired. Therefore, the best way would be a combination of batch and column experiments, and this will be the next step to report in our research project.

The K_d values of the metals giving a measure for their interaction with this clay have been determined. Many parameters could influence the interaction of metal and clay like metal concentration, pH value, temperature, ionic strength and competing metal ions (calcium) for which reason their influence on the sorption und desorption was investigated.

3.4.1 Sorption experiments of europium on Opalinus clay (OPA)

The sorption experiments were performed in 0.01, 1 or 5 M sodium chloride solution. After preconditioning the clay for 72 h with the respective solution europium concentrations from 1 µg L^{-1} to 10 mg L^{-1} were added. The pH value was adjusted to pH 5 and 7, respectively. The equilibrium time for the sorption step was again 72 h. The solid/liquid ratio between clay and solution was 4 g L^{-1}. One aim of the experiments is to check the influence of different parameters like pH value (5 and 7), ionic strength (0.01, 1 and 5 M NaCl), temperature (25 and 60°C) and competing cations (0.5 and 5 mM Ca^{2+}) on the sorption of Eu or U onto OPA.

3.4.1.1 Influence of ionic strength on the sorption isotherms of Eu at pH 5 and 7

In Figure 21 the sorption isotherms of europium at increasing salinities (0.01 to 5 M NaCl) at pH 5 are shown. The chosen fitting is the Freundlich isotherm due to its good linearity over a wide concentration range. With increasing ionic strength the mobility of the europium decreases strongly especially between 0.01 and 1.0 M NaCl.

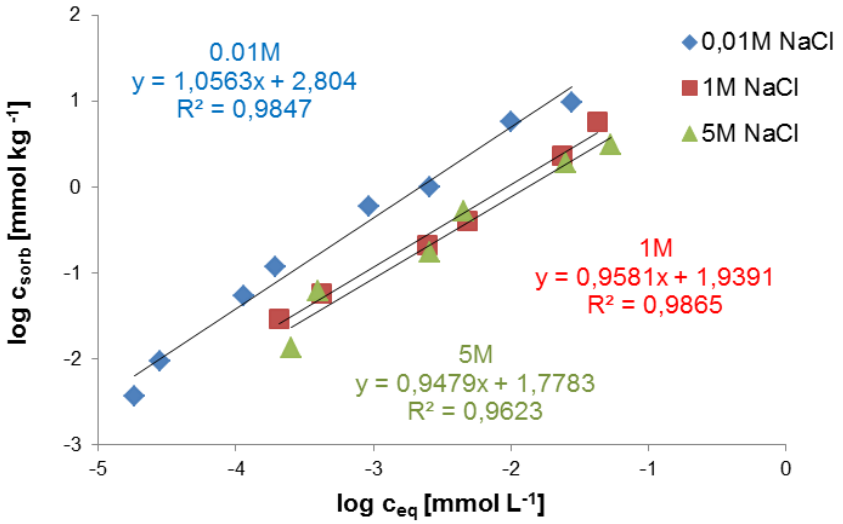

Figure 21: Freundlich sorption isotherms of Eu ($6.6 \cdot 10^{-3}$ to 65.8 µmol L^{-1}) with increasing salinity (0.01, 1 and 5 M NaCl) at pH 5

The slope of all isotherms is nearly 1.0 and therefore the log K_d values could be estimated from the y-intercept of the regression line. For 0.01, 1 and 5 M the log K_d values decrease with increasing salinity from 2.8 over 1.9 to 1.8 (determined from the regression equations in Figure 21). For every europium concentration a log K_d value could be calculated. A plot of the log K_d values with the log c_{eq} values similar to the Freundlich sorption isotherms is given in Figure 22 a). The obtained log K_d values are similar to the log K_d values from the Freundlich isotherms. From 0.01 M NaCl and a related log K_d value of 2.6 the values decrease to 1.9 (Table 11).

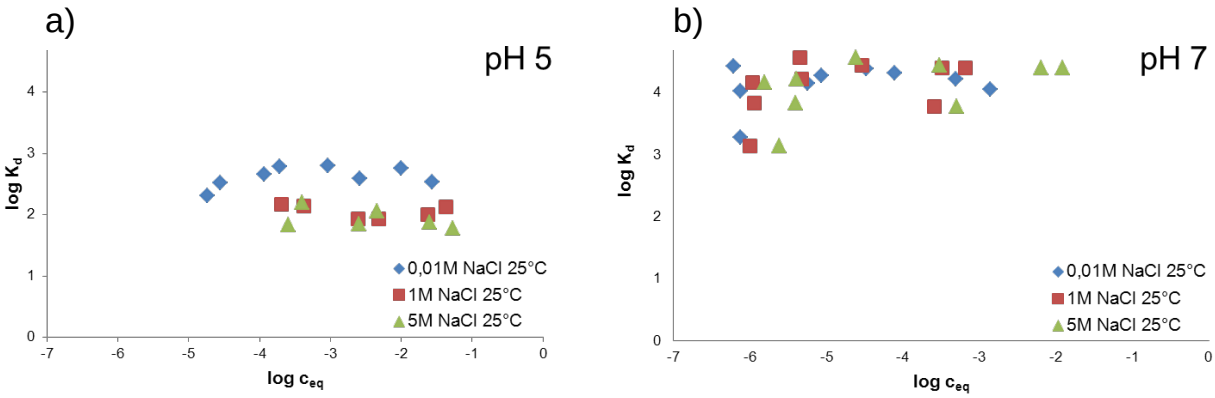

Figure 22: Log K_d values for europium at pH 5 / 7 and 0.01, 1 and 5 M NaCl ionic strength

In Figure 22 b) the plots of the log K_d values of europium with different ionic strengths at pH 7 are shown. The sorption at pH 7 is clearly higher than at pH 5 and the influence of ionic strength is not as strong as with pH 5. There is hardly an influence of different salinities. The

calculated log K_d values are very similar and change from 4.2 to 4.1 with increasing ionic strength. For a better comparison the log K_d values for europium at pH 5 / 7 and with 0.01, 1 and 5 M NaCl as ionic strength are given in Table 11.

Table 11: Log Kd values for Eu at different salinities (0.01, 1 and 5 M NaCl) at pH 5 and 7

pH value	log K_d values 0.01 M NaCl	log K_d values 1 M NaCl	log K_d values 5 M NaCl
5	2.6±0.1	2.1±0.1	1.9±0.2
7	4.2±0.1	4.2±0.4	4.1±0.4

3.4.1.2 Influence of temperature on the sorption isotherms of Eu

The experiments at pH 5 and 60°C are only performed with an ionic strength of 0.01 and 1 M NaCl. In a 5 M NaCl solution the adjustment of pH values to pH 5 is partly complicated and protracted. During the adjusting time the water evaporates out of the vessels and the NaCl salt recrystallizes. Additionally, the europium concentrates in the solution and no reproducible results can be obtained.

In Figure 23 the Freundlich sorption isotherms of Eu at 25 and 60°C are shown. As for the experiments at 25°C a strong salinity effect is observed at a temperature of 60°C. The increasing ionic strength leads to an increasing mobility of Eu. Additionally, the Eu mobility over all analyzed ionic strengths increases also with increasing temperature. There are some explanations for this effect.

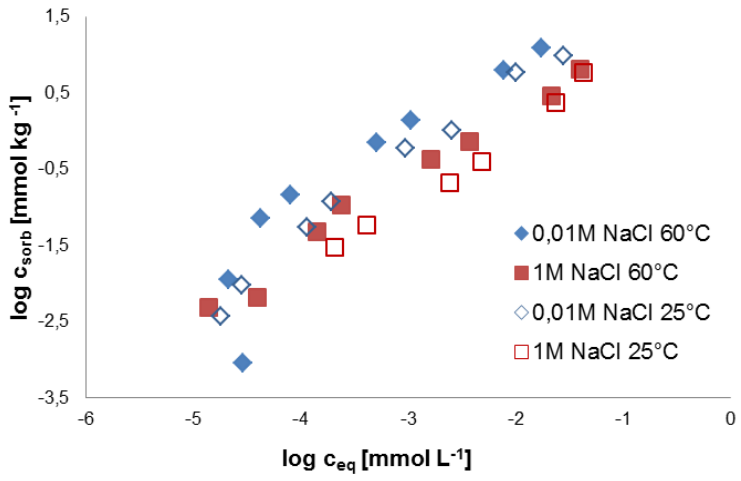

Figure 23: Freundlich sorption isotherms of Eu ($6.6 \cdot 10^{-3}$ to 65.8 µmol L^{-1}) with increasing salinity (0.01, 1 and 5 M NaCl) at pH5 and 60°C

Metal sorption could be assumed as an endothermic reaction and with increasing temperature the sorption would therefore increase. Alternatively or in addition the surface structure of the clay is changed by the heat treatment and its area would increase, and together with this effect some mineral cations could dissociate and open up exchange sites for other metal cations. In the end more europium cations could adsorb onto the clay surface.

The calculated log K_d values are 2.8 for 0.01 M and 2.4 for 1 M NaCl and are clearly higher than for 25°C. The log K_d values for 60°C at pH 5 and 7 are given in Table 12.

At pH 7 high salinities of 5 M NaCl are analyzed, too. The adjustment of the pH values was clearly easier than at pH 5. An influence of the temperature is likewise visible with all used salinities. Because a high sorption is already observed at 25°C a strong increasing of the immobilization is hardly possible. Therefore an influence of the ionic strength on the immobilization is not visible.

Table 12: Log K_d values of Eu for different salinities (0.01, 1 and 5 M NaCl) at 60°C and pH 5 / 7

pH value	log K_d values 0.01 M NaCl	log K_d values 1 M NaCl	log K_d values 5 M NaCl
5	2.8±0.2	2.4±0.2	---
7	4.6±0.5	4.6±0.5	4.5±0.5

3.4.1.3 Influence of divalent competing cations on the sorption isotherms of Eu

With an ionic strength of 0.01 M NaCl the increasing concentration of divalent competing cations (calcium) shows only a small influence on the retention of europium, at least for the used calcium concentrations up to 50 mM.

For pH 5 (Figure 24 a)) the influence is clearly higher than for pH 7 (Figure 24 b)). The mobility of europium increases with the added concentration of competing cations. For pH 7 no or only a small influence on the Eu retention is observed.

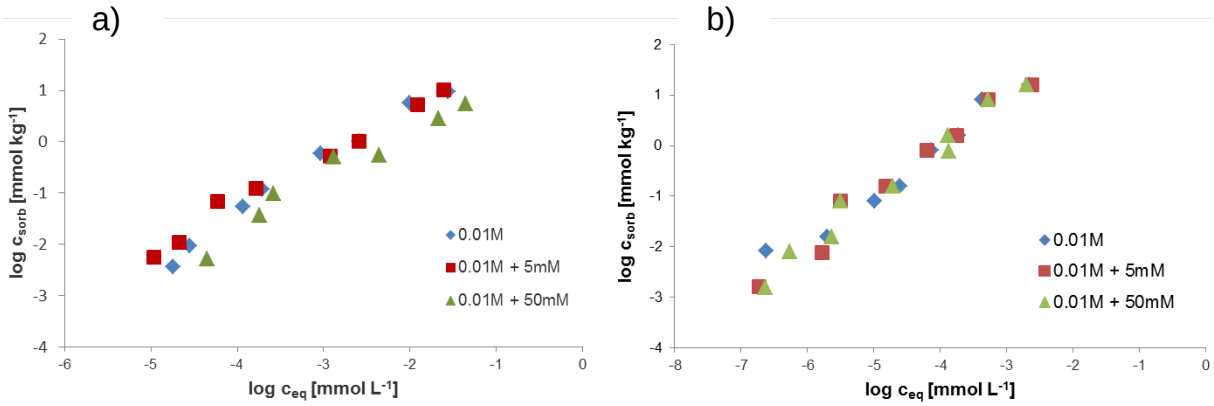

Figure 24: Freundlich sorption isotherms of Eu ($6.6 \cdot 10^{-3}$ to 65.8 µmol L^{-1}) with 0.01 M NaCl and different concentrations of competing cations (0, 5 and 50 mM Ca) at pH 5 (a) and pH 7 (b)

Furthermore, the log K_d values shown in Table 13 also reflect the relatively low influence of the competing cations. For pH 5 a decrease of the log K_d values is observed due to the competition of the calcium cations. At pH 7 no significant influence of the different Ca concentrations used is seen. In this pH range the retention of the europium cations is mainly caused by precipitation of the europium and not by sorption.

Table 13: Log K_d values of Eu for different concentrations of competing cations (0, 5 and 50 mM) with 0.01 M NaCl at pH 5 and 7

Salinity	log K_d at pH 5	log K_d at pH 7
0.01 M NaCl + 0 mM Ca^{2+}	2.6±0.2	4.2±0.6
0.01 M NaCl + 5 mM Ca^{2+}	2.6±0.2	4.0±0.2
0.01 M NaCl + 50 mM Ca^{2+}	2.3±0.2	4.0 ±0.2

In Figure 25 the Freundlich sorption isotherms for europium at an ionic strength of 1 M NaCl are shown. The influence of the competing cations is clearly lower in comparison to 0.01 M NaCl. Neither at pH 5 nor at pH 7 could any competing effect of Ca on the retention of Eu in clay be seen. The influence of the high ionic strength is obviously higher than the influence of the added competing cations at the used concentrations.

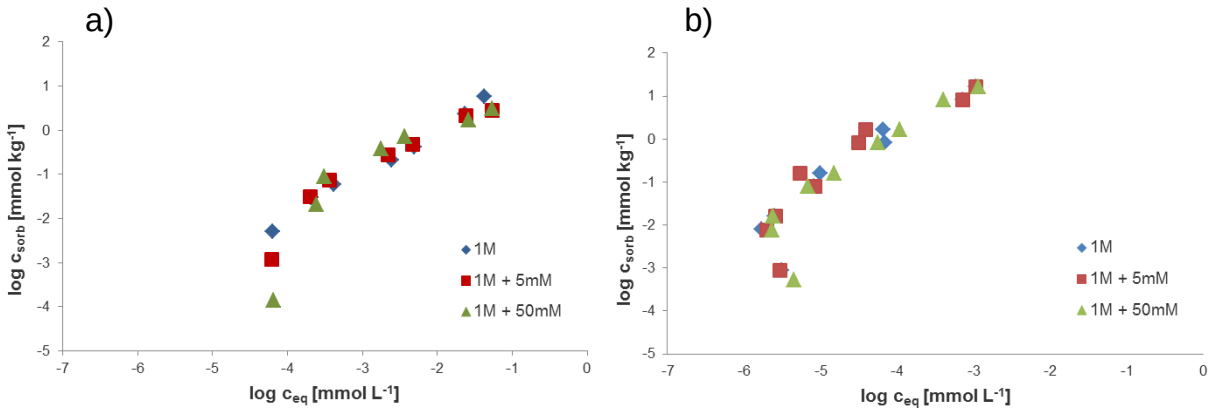

Figure 25: Freundlich sorption isotherms of Eu ($6.6 \cdot 10^{-3}$ to 65.8 µmol L^{-1}) with 1 M NaCl and different concentrations of competing cations (0, 5 and 50 mM Ca) at pH 5 (a) and pH 7 (b)

Table 14 shows the log K_d values of Eu for 1 M NaCl, here too no significant changes with an increasing concentration of competing cations can be observed.

Table 14: Log K_d values of europium for different concentrations of competing cations (0, 5 and 50 mM) with 1 M NaCl at pH 5 and 7

Salinity	log K_d at pH 5	log K_d at pH 7
1 M NaCl + 0 mM Ca^{2+}	2.1±0.2	4.2±0.2
1 M NaCl + 5 mM Ca^{2+}	1.9±0.2	4.1±0.2
1 M NaCl + 50 mM Ca^{2+}	1.8±0.2	4.1±0.2

3.4.2 Sorption experiments of uranium with Opalinus clay

The experiments were performed in 0.01 and 1 M sodium chloride solution. After preconditioning for 72 h uranium concentrations from 1 µg L^{-1} to 10 mg L^{-1} are added. The pH values were adjusted to pH 5 and 7. The equilibration time was 72 h. The solid/liquid ratio between clay and solution was 4 g L^{-1}. One aim of the experiments is to check the influence of different parameters like pH value (5 and 7), ionic strength (0.01 and 1 M NaCl) and competing cations (5 and 50 mM Ca^{2+}).

3.4.2.1 Influence of ionic strength on the sorption isotherms of U at pH 5 and 7

Similar to europium the immobilization of uranium on clay is strongly influenced by the ionic strength. The sorption isotherms of uranium with different ionic strengths at pH 5 and 7 are shown in Figure 26. At both pH values the increasing salinity causes a lower uranium immobilization, at pH 5 this effect is stronger in comparison to pH 7.

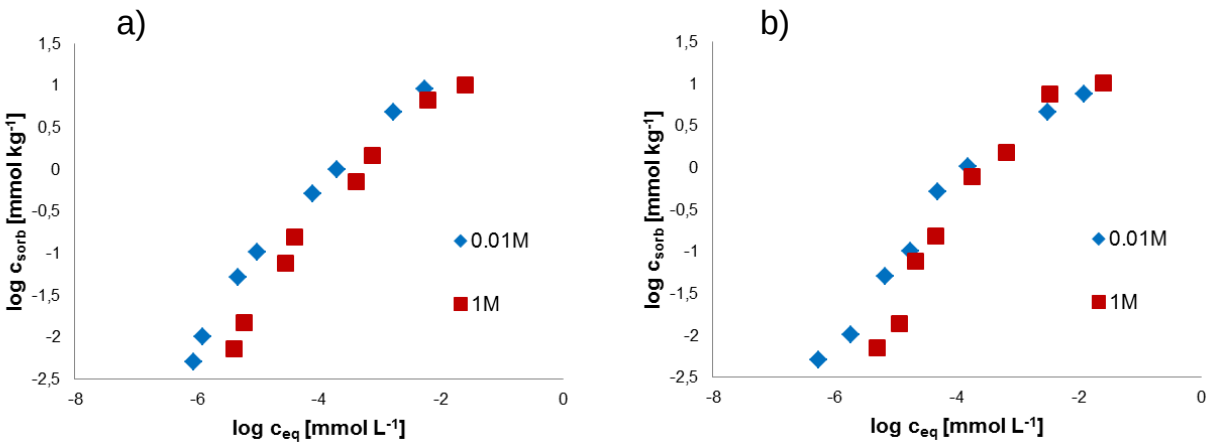

Figure 26: Freundlich sorption isotherms of uranium ($4.2 \cdot 10^{-3}$ to 42.0 µmol L^{-1}) at increasing salinity (0.01 and 1 M NaCl) at pH 5 (a) and pH 7 (b)

Table 15 confirms these results, too. The log K_d values show that the mobilization of U increases with increasing salinity. Additionally, it is clearly shown that the influence of the pH value is lower compared to europium. This is caused by the different speciation of europium and uranium.

At pH 5 the log K_d values of europium are significantly lower and at pH 7 higher in comparison to uranium due to the precipitation of europium carbonates at neutral pH values. That's the reason why the immobilization of uranium is more influenced by ionic strength. For uranium the sorption capability is favored over precipitation.

Table 15: Log K_d values of uranium for different salinities (0.01 and 1 M NaCl) by pH 5 and 7

pH value	log K_d values 0.01 M NaCl	log K_d values 1 M NaCl
5	3.7±0.3	3.2±0.3
7	3.6±0.4	3.3±0.4

3.4.2.2 Influence of divalent competing cations on the sorption isotherms of U

For 0.01 M sodium chloride and pH 5 no or only a small effect of the added calcium concentration on U sorption onto OPA was seen (Figure 27).

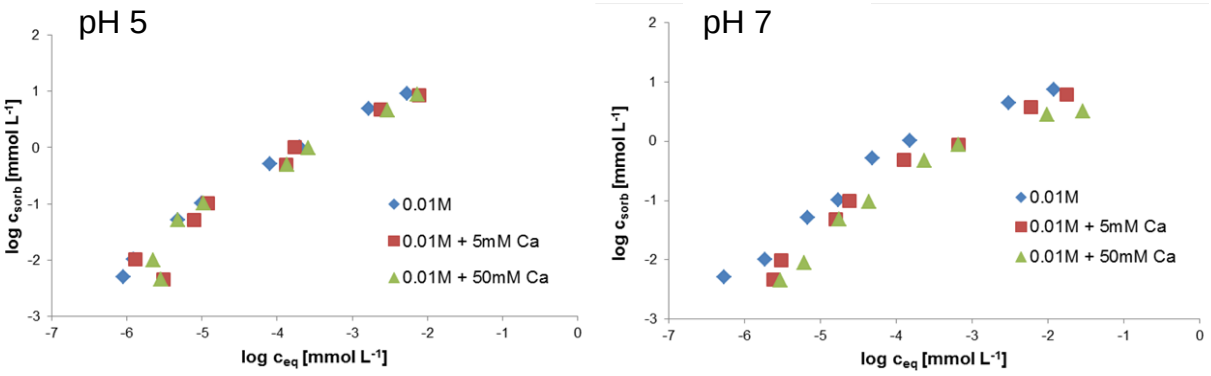

Figure 27: Freundlich sorption isotherms of U ($4.2 \cdot 10^{-3}$ to 42.0 µmol L^{-1}) with 0.01 M NaCl and different concentrations of competing cations (0, 5 and 50 mM Ca) at pH 5 (left hand side) and pH 7 (right hand side)

When looking at the log K_d values in Table 16 a notable influence of competing cations can be observed for pH 7 but also concerning the uranium sorption isotherms for OPA. For pH 5 Ca and U do not use the same sorption sites, and therefore Ca has no influence on the uranium speciation at this pH value.

At pH 7 Ca strongly influences U speciation. Especially, the formation of the neutral calcium-uranyl carbonato complex (which does not sorb onto the clay) leads to a higher amount of uranium in solution.

Table 16: Log K_d values of uranium for 0.01 M NaCl and different concentrations of competing cations (0, 5 and 50 mM Ca^{2+}) at pH 5 and 7

Salinity	log K_d at pH 5	log K_d at pH7
0.01 M NaCl + 0 mM Ca^{2+}	3.7±0.3	3.6±0.4
0.01 M NaCl + 5 mM Ca^{2+}	3.6±0.4	3.3±0.4
0.01 M NaCl + 50 mM Ca^{2+}	3.5±0.4	3.0±0.5

The log K_d values in Table 16 confirm the results mentioned above. At pH 5 only a small but insignificant decrease of U sorption is observable, however, at pH 7 a clear decrease of the log K_d values with an increasing Ca concentration is seen.

At an ionic strength of 1 M NaCl (Figure 28) the results are different in comparison to 0.01 M. Neither at pH 5 nor at pH 7 is an influence on the uranium sorption isotherms visible, but with 50 mM Ca at pH 7 a small decrease of the U sorption is seen.

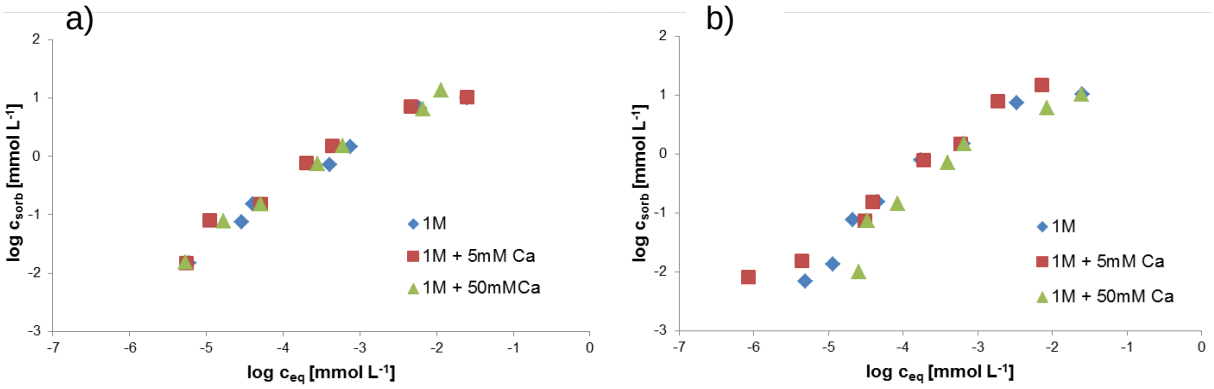

Figure 28: Freundlich sorption isotherms of U ($4.2 \cdot 10^{-3}$ o 42.0 µmol L^{-1}) with 1 M NaCl and different concentrations of competing cations (0, 5 and 50 mM Ca) at pH 5 (a) and pH 7 (b)

The log K_d values in Table 17 reflect the same results. Although a low reduction of the mobility in presence of Ca is visible at pH 5 no clear trend is visible at pH 7.

Table 17: Log K_d values of uranium for 1 M NaCl and different concentrations of competing cations (0, 5 and 50 mM Ca^{2+}) at pH 5 and 7

Salinity	log K_d at pH 5	log K_d at pH7
1 M NaCl + 0 mM Ca^{2+}	3.2±0.3	3.3±0.4
1 M NaCl + 5 mM Ca^{2+}	3.4±0.4	3.5±0.2
1 M NaCl + 50 mM Ca^{2+}	3.4±0.2	3.0±0.4

3.4.3 Desorption experiments

Knowledge of the remobilization process of the metals is important to estimate the retention capability of Opalinus clay with respect to europium and uranium.

In a first step a concentration of uranium ($4.2 \cdot 10^{-7}$ mol L^{-1}) or europium ($1.9 \cdot 10^{-6}$ mol L^{-1}) was sorbed onto the Opalinus clay (OPA) for the desorption experiments. The remobilization of the metal ions from OPA was checked with three subsequent desorption steps. The equilibration time was 72 h, and the concentration of remobilized metal in the supernatant was analyzed by ICP-MS.

In order to evaluate of the retention capability the desorbed metal concentration of every step was subtracted from the initially total sorbed metal concentration. As with the sorption experiments the influence of ionic strength, competing cations, pH values and temperature was analyzed.

3.4.3.1 Influence of ionic strength on the desorption of Eu from OPA at different pH values

The influence of pH values on the desorption of Eu was analyzed during the last project period. As a result, no remobilization at pH values higher than 7 could be observed due to a precipitation of europium with carbonate. At pH values equal or lower than pH 5 a lower sorption and a very low remobilization could be determined (Figure 29 a).

No significant influence on the Eu sorption as well as on the remobilization from clay could be determined with increasing ionic strength at pH $\geq$ 7 (shown in Figure 29 b) + c)). At pH 5 and 3 the ionic strength has a strong influence on the Eu sorption. Apart from the high amount of protons present at pH 3 and 5 the high concentration of Na^+ from the salt (NaCl) in the solution increases the remobilization of the europium cations from the clay.

In conclusion a high ionic strength in combination with a low pH value leads to a remarkable remobilization cations already sorbed onto clay.

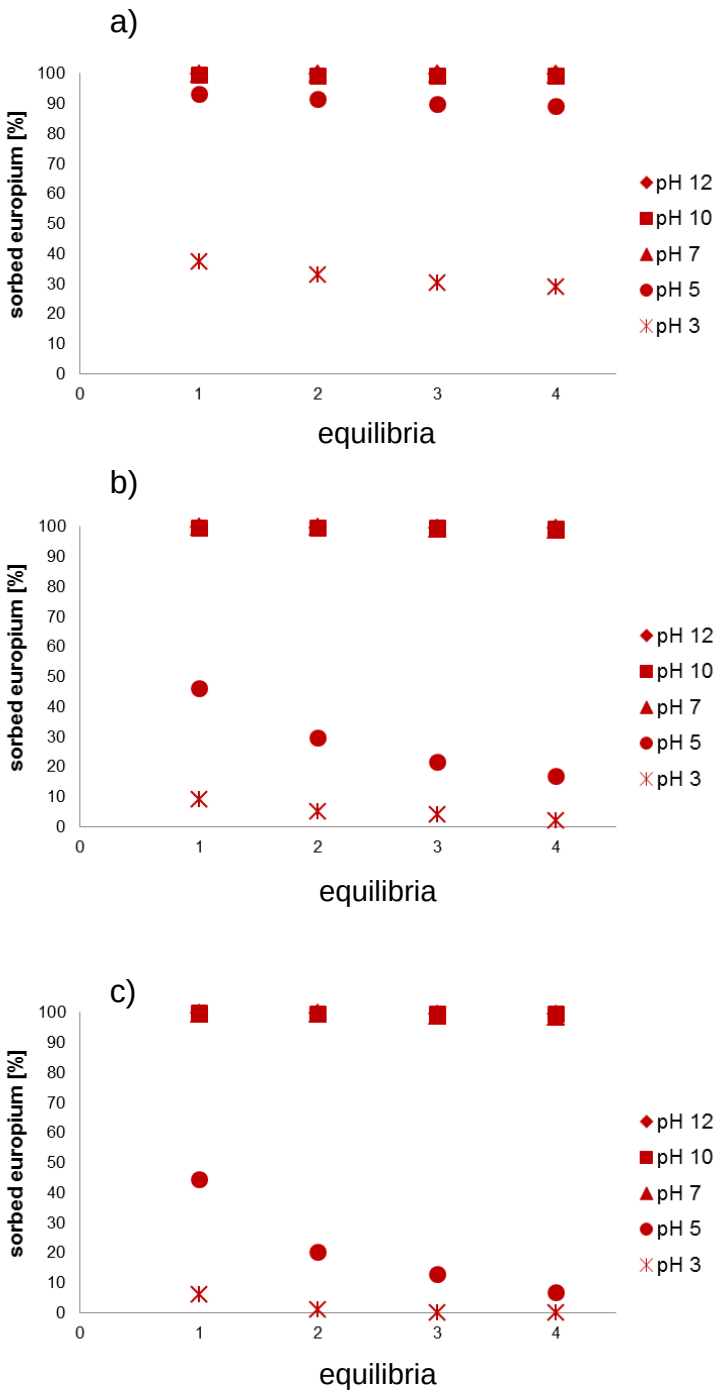

Figure 29: Desorption of Eu at different pH values (12, 10, 7, 5, 3) with different ionic strengths a) 0.01 M, b) 1 M, c) 3 M NaCl

3.4.3.2 Influence of ionic strength on the desorption of U from OPA at different pH values

The remobilization of uranium from OPA in comparison to europium is totally different. The lowest U sorption was observed at pH 3 and 10 whereas desorption of uranium at pH 5 and

also pH 12 shows a very similar behavior (Figure 30). The U sorption is the highest in the neutral pH-range. A clear remobilization of U from OPA at all pH values can be observed. The increasing ionic strength shows only an influence in the first step where uranium is sorbed onto OPA. The desorption behavior of uranium at high ionic strengths is similar to the lowest ionic strength of 10 mM NaCl, and no relevant differences are observable.

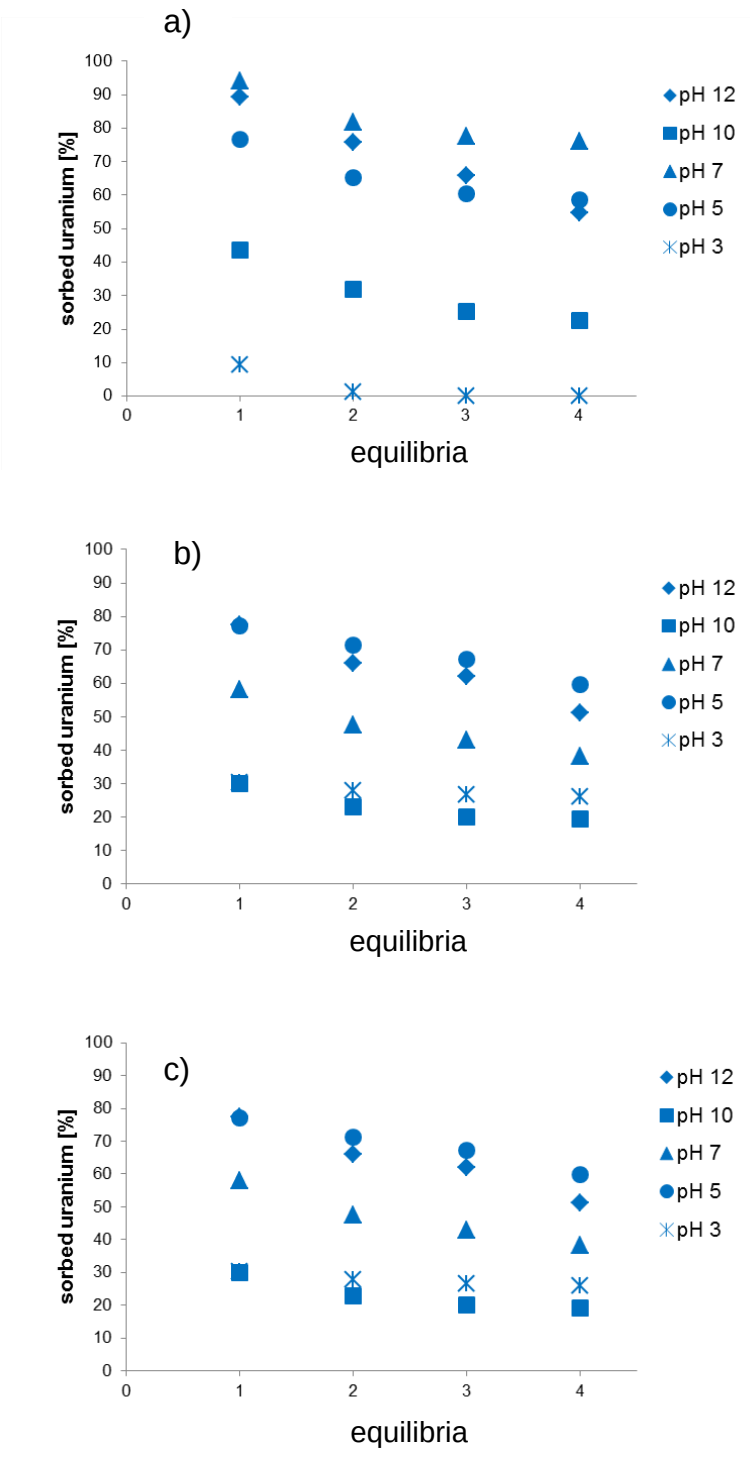

Figure 30: Desorption of U at different pH values (12, 10, 7, 5, 3) and different ionic strengths a) 0.01 M, b) 1 M, c) 3 M NaCl

3.4.3.3 Influence of temperature on the desorption of Eu from OPA at different pH values

In this chapter the influence of higher temperature on sorption and desorption of europium is discussed. As shown in Figure 31 a clearly higher retention but also a stronger remobilization is seen at 60°C and 0.01 M NaCl over all tested pH values compared to the results for Eu at 25°C (0.01 M NaCl). At higher ionic strength an increasing retention is observable over all pH values, but the remobilization at pH 5 and 3 is not stronger than at 25°C.

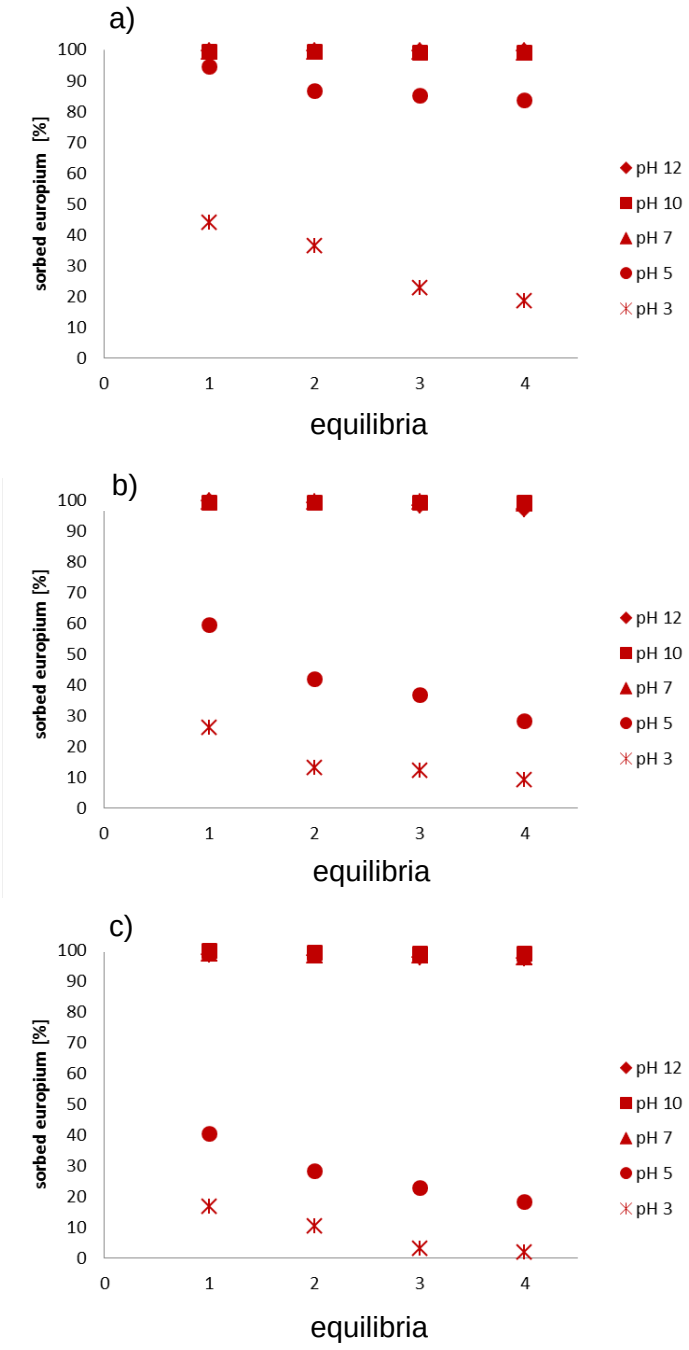

Figure 31: Desorption of Eu at different pH values (12, 10, 7, 5, 3) with different ionic strengths a) 0.01 M, b) 1 M, c) 3 M NaCl at 60°C

3.4.3.4 Influence of temperature on the desorption of U from OPA at different pH values

The temperature effect for uranium is similar to the results for Eu desorption at 60°C (Figure 32). With higher temperature (60°C) the retention of uranium increases strongly over all analyzed pH values.

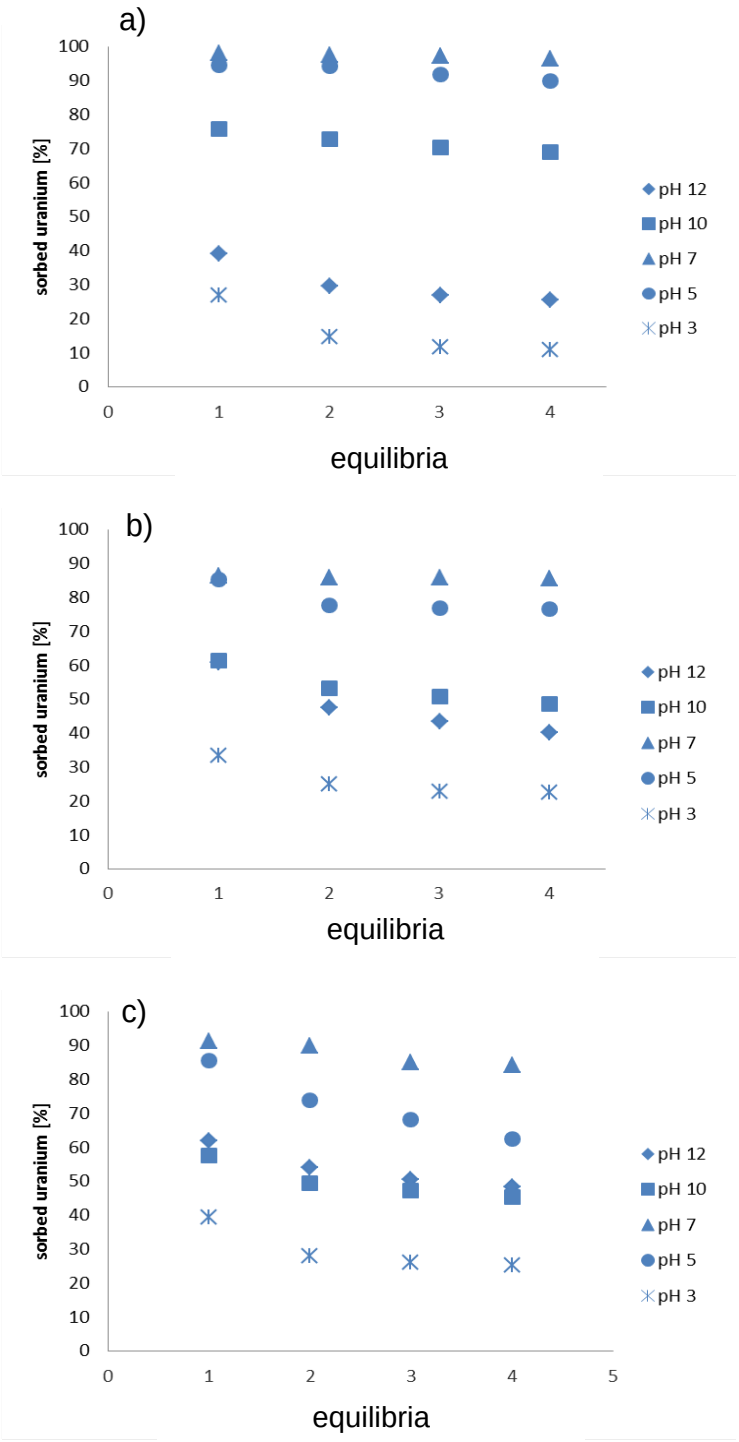

Figure 32: Desorption of U at different pH values (12, 10, 7, 5, 3) at different ionic strengths a) 0.01 M, b) 1 M, c) 3 M NaCl at 60°C

Additionally, no relevant remobilization at pH 10, 7 and 5 is observable with the exception of pH 12 where the sorption and the remobilization increase significantly at 60°C. With increasing ionic strength the influence is similar whereby retention increases with increasing temperature, excepting also for pH 12. Additionally, the ionic strength leads to a stronger remobilization at 60°C in contrast to the results at room temperature (25°C). As possible explanation a stronger dissolution of clay at higher temperatures can be assumed where sorbed cations redissolve.

3.4.3 pH edges

The previous results show the strong influence of pH on metal sorption and remobilization. Additionally, the influence of temperature can be observed. For this reason both influences have to be analyzed simultaneously. To analyze the effects on the pH edges of europium and uranium concentrations of 100 µg L^{-1} of europium ($0.65 \cdot 10^{-6}$ mol L^{-1}) and uranium ($4.2 \cdot 10^{-7}$ mol L^{-1}) were used, respectively. The equilibration time for all experiments in this working package was 72 h. In addition to the pH influence we checked the influence of the ionic strength. For all experiments on pH edges we used an ionic strength of 0.01, 1 and 3 M NaCl.

3.4.3.1 Influence of ionic strength and temperature on the pH edges of Eu

The pH edges of Eu at different ionic strengths at 25 and 60°C are shown in Figure 33.

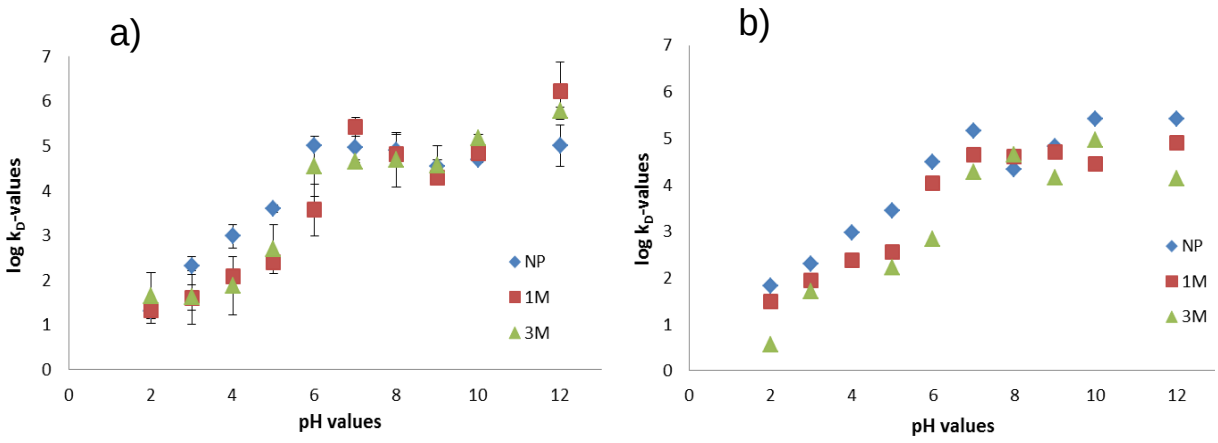

Figure 33: pH edges of europium at different ionic strengths (0.01, 1 and 3 M NaCl) at different temperatures (a) 25°C, b) 60°C)

With increasing pH the log K_d values also increase until a maximum log K_d of 5 is reached in the range between pH 6 and 12. The negative influence of the ionic strength on the Eu sorption is seen at both temperatures, especially at lower pH values (pH ≤ 6). With

increasing ionic strength the retention decreases clearly. At 1 M NaCl the 100-fold amount of ions are retained compared to 0.01 M NaCl so that the differences between 0.01 and 1 M are clearly higher than the difference between 1 and 3 M where only a 3-fold amount of ions is retained. A significant influence of temperature on Eu sorption cannot be observed. Perhaps a slight increase of the Eu retention onto OPA can be seen at increasing temperature.

3.4.3.2 Influence of ionic strength and temperature on the pH edges of U

The pH edges of uranium show a behavior which is clearly different from the pH edges of europium (Figure 34). For uranium the retention increases with increasing pH values till pH 6, after that the mobility of the metal increases with higher pH until pH 10.

In presence of calcium the uranyl cation forms a neutral calcium carbonate complex ($Ca_2(UO_2)(CO_3)_{3\,(aq)}$) at pH values higher than 6 which does not sorb onto the clay [Bernhard et al. 2001, Meleshyn et al. 2009]. At acidic pH values the mobility of the uranium is higher due to the higher proton concentration in solution. At alkaline pH values the mobility is strongly dependent on the formed carbonate complexes whereas precipitation presumably plays a major part.

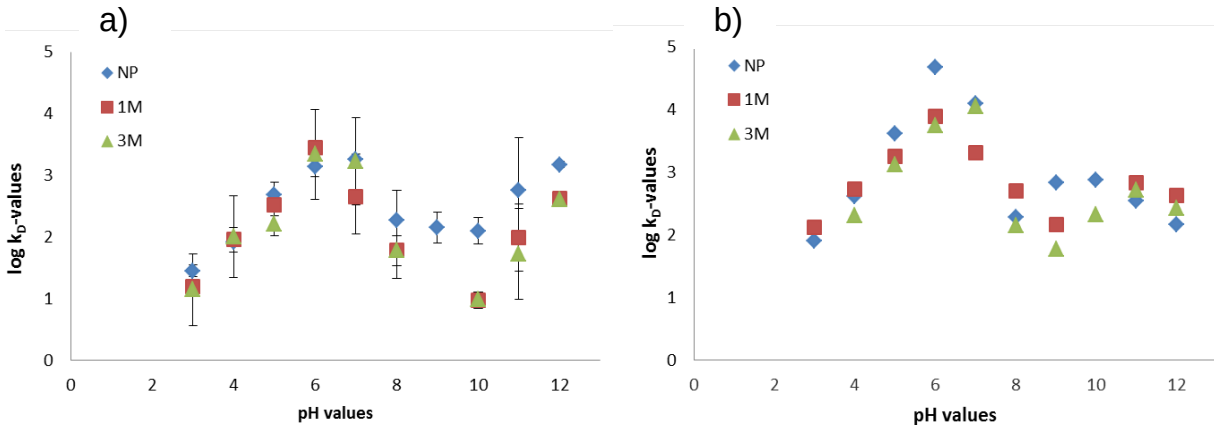

Figure 34: pH edges of uranium with different ionic strength (0.01, 1 and 3 M NaCl) at different temperatures (a) 25°C, b) 60°C)

At room temperature (25°C) an increasing mobility of the uranium with increasing ionic strength is observable only at pH>7. The log K_d values for uranium (see Figure 34) are clearly lower in comparison to europium, and they are in the range from 2.0 to 3.5 (0.01 M NaCl) and from 1.0 and 3.5 for 1 and 3 M NaCl. At 60°C the influence of ionic strength is lower than at 25°C but at higher temperature the U sorption onto OPA increases over the whole analyzed pH range.

3.5 Analysis of the ternary system metal - NOM - OPA

In the previous chapter the results of the binary system metal-OPA were presented. But beside pH value, temperature and ionic strength natural organic matter (NOM) could also have a relevant influence on the mobility of metals in clay formations which is object of this working package.

3.5.1 Sorption experiments of Eu in the presence of NOM

The experiments were performed in 0.01, 1 or 5 M NaCl solution. After preconditioning for 72 h europium concentrations ranging from 1 µg L^{-1} to 10 mg L^{-1} together with 25 mg L^{-1} of NOM were added. The pH values were adjusted to pH 5 and 7. The equilibration time was 72 h. Similarly to the previous experiments in the binary systems the influence of different geochemical parameters like pH, ionic strength, competing cations on metal sorption onto clay was analyzed in the presence of NOM from different origins.

3.5.1.1 Influence of ionic strength on the sorption isotherms of Eu at pH 5 and 7

In this chapter the influence of NOM on the sorption of europium onto Opalinus clay at different ionic strengths at pH 5 and 7 is described. For these experiments Aldrich humic acid (AHA) was used as model NOM. The sorption isotherms are shown in Figure 35. For pH 5 the Eu sorption increases at all ionic strengths in the presence of AHA with the exception of the 5 M NaCl solution. In this case no differences can be observed between the binary and ternary system. The log K_d values in Table 18 confirm the graphical interpretation, with AHA the log K_d values increase for all ionic strengths. This can be explained by the precipitation of the AHA in the acidic pH range due to the high proton concentration. A coprecipitation of the europium with AHA is therefore possible.

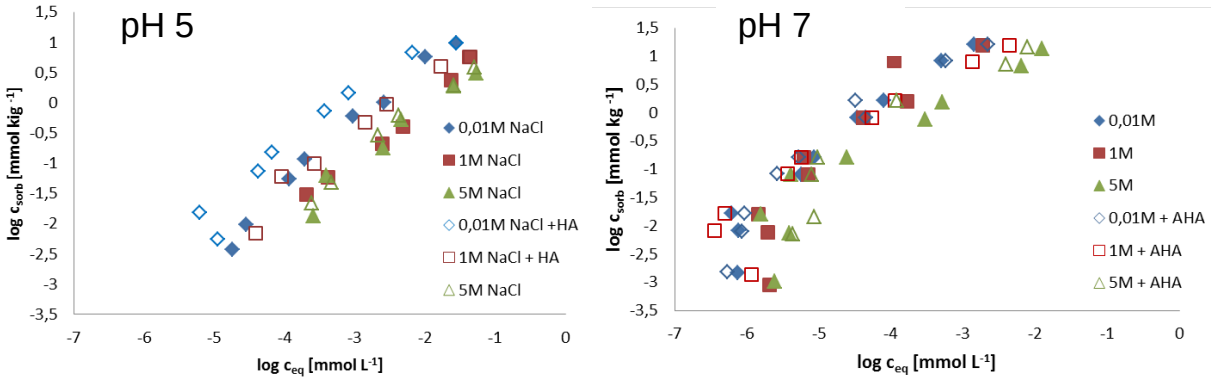

Figure 35: Freundlich sorption isotherms of Eu ($6.6 \cdot 10^{-3}$ to 65.8 µmol L^{-1}) at increasing salinity (0.01, 1 and 5 M NaCl) at pH 5 and 7 in the absence or presence of 25 mg L^{-1} AHA

With increasing ionic strength the influence of the humic acid decreases due to the high concentration and a possible neutralization of AHA with the Na^+ cations present. Therefore, a coprecipitation of europium is prevented due to the high excess of Na in the solution. At pH 7 the influence of the humic acid is different. Relevant influences of the AHA are not visible either graphically or in the log K_d values themselves. Additionally, in the binary as well as in the ternary system the log K_d values for Eu are in the same order of magnitude (Table 18).

Table 18: Log K_d values of europium for different salinities (0.01, 1 and 5 M NaCl) at pH 5 / 7 in the ternary system with Aldrich humic acid

pH value	log K_d values 0.01 M NaCl	log K_d values 1 M NaCl	log K_d values 5 M NaCl
5	3.1±0.3	2.5±0.2	2.0±0.1
7	4.3±0.2	4.2±0.3	4.0±0.4

3.5.1.2 Influence of different NOM on the sorption isotherms of Eu

Depending on the origin of the NOM (HA from different sites) the structure and composition changes, so every HA shows different properties and the complexation behavior is changed too. In Figure 36 the sorption isotherms of Eu with different HA in 0.01 M NaCl are shown. A weak increase of Eu sorption onto OPA in the presence of HA is observable at pH 5.

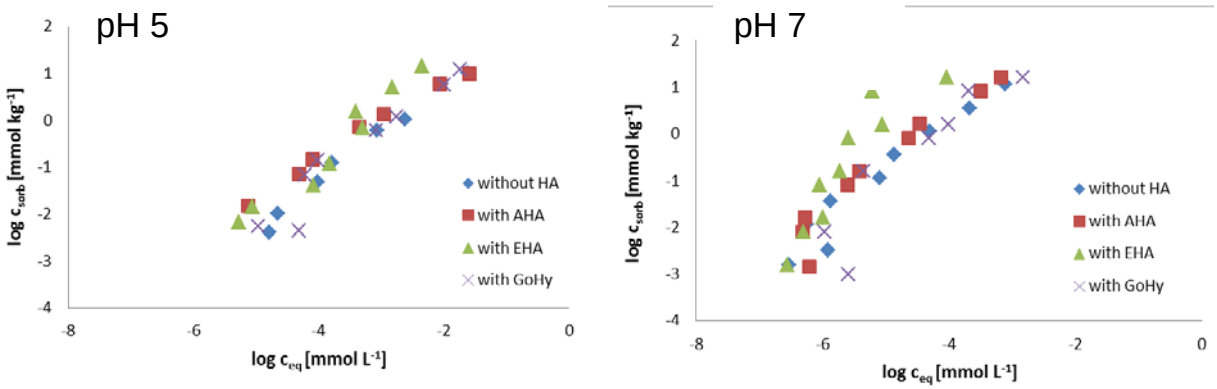

Figure 36: Freundlich sorption isotherms of Eu ($6.6 \cdot 10^{-3}$ to 65.8 µmol L^{-1}) at 0.01 M NaCl at pH 5 and 7 in the presence of 25 mg L^{-1} NOM (AHA, EHA, GoHy851)

Additionally, different effects on the Eu sorption caused by the humic acids from different sites are visible. The presence of Elliot soil HA (EHA) and Aldrich humic acid (AHA) shows the strongest increase on the Eu sorption but compared to the binary system the Eu retention is higher already with Gorleben HA 851 (GoHy851).

At pH 7 these retention effects were reinforced. In the complexation studies EHA shows the strongest complexation behavior, and therefore the positive influence on the retention should be the highest. GoHy851 has the lowest complexation behavior and shows the lowest influence on the sorption. An expected increase of the mobility due to complexation is not visible supposedly due to the presence of other competing cations which were dissolved from the clay. In Figure 37 the sorption isotherms at 1 M NaCl ionic strength are given. At pH 5 and 7 the influence of the different HA on Eu sorption decreases with increasing ionic strengths (1 M shown here in Figure 37 compared to 0.01 M as seen in Figure 36).

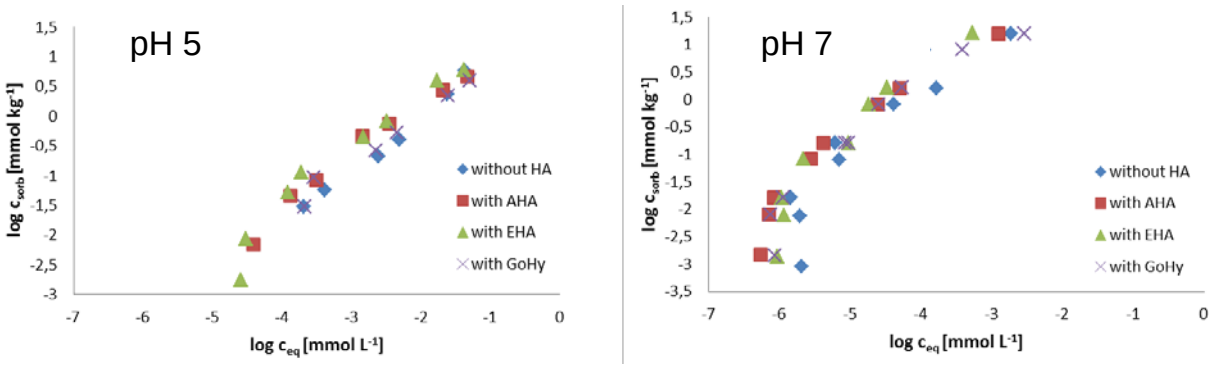

Figure 37: Freundlich sorption isotherms of Eu ($6.6 \cdot 10^{-3}$ to 65.8 µmol L^{-1}) with 1 M ionic strength (NaCl) at pH5 (a) and 7 (b) with different kinds of 25 mg L^{-1} humic acid (Aldrich HA, Elliot soil HA, Gorleben HA 851)

The binary and ternary systems show similar isotherms but a look at the log K_d values cannot confirm this trend. In contrast to these results, the influence of the ionic strength on the mobilization is clearly observable considering the log K_d values shown in Table 19. With increasing salinity the mobilization of europium increases too. At an ionic strength of 5 M NaCl no relevant differences in the sorption behavior of Eu onto OPA between the analyzed binary and ternary system on the one hand and the HA from different sites on the other hand can be determined.

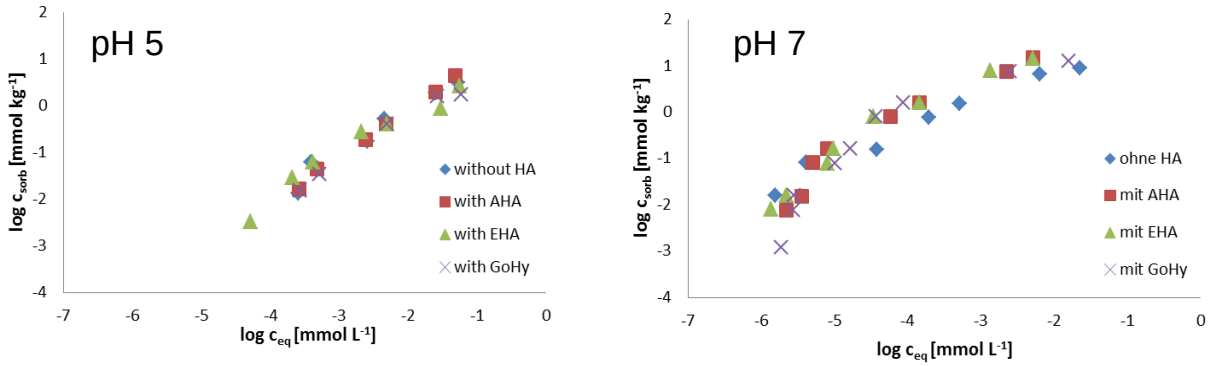

Figure 38: Freundlich sorption isotherms of Eu ($6.6 \cdot 10^{-3}$ to 65.8 µmol L^{-1}) with 5 M ionic strength (NaCl) at pH 5 (a) and 7 (b) with different kinds of 25 mg L^{-1} humic acid (Aldrich HA, Elliot soil HA, Gorleben HA 851)

These findings can be confirmed by the log K_d values for Eu and OPA in both analyzed systems (Table 20). Only small differences between the different humic acids at pH 5 and 7 are visible. However, in the binary and ternary system the mobility of the europium increases with increased ionic strength.

Table 20: Log K_d values of europium for different salinities (0.01, 1 and 5 M NaCl) and pH 5 / 7 in the ternary system with different kinds of humic acid

Conditions	log K_d binary system	log K_d with AHA	log K_d with EHA	log K_d with GoHy851
0.01 M NaCl pH 5	2.6±0.1	3.0±0.3	3.0±0.3	2.7±0.4
1 M NaCl pH 5	2.0±0.1	2.3±0.2	2.5±0.2	2.1±0.2
5 M NaCl pH 5	1.9±0.2	1.9±0.1	1.9±0.3	1.8±0.4
0.01 M NaCl pH 7	4.2±0.1	4.4±0.2	4.6±0.7	4.1±0.4
1 M NaCl pH 7	4.2±0.4	4.2±0.3	4.4±0.2	4.2±0.3
5 M NaCl pH 7	4.0±0.4	4.1±0.4	4.1±0.4	4.1±0.5

3.5.1.3 Influence of Ca as divalent competing cation on the sorption isotherms of Eu

Calcium salts are part of the real porewater in the northern Germany clay stones alongside with sodium chloride. Ca could compete directly with europium and could therefore influence its retention on the clay, and Ca^{2+} could probably change the complexation behavior of the humic acids.

In Figure 39 sorption isotherms of europium in the ternary system with 0.01 M NaCl are shown. At pH 5 Ca has a strong influence as competing cation on the mobility of europium in the ternary system. With increasing Ca concentration the Eu mobility increases too. Presumably, the humic acid is precipitated by the increased Ca concentration and the europium is displaced from the HA and stays in solution.

Another explanation is the competing effect of the Ca ions on the europium sorption onto the clay and the exchange of Eu by Ca at the clay binding sites. The competing effect of Ca correlates with the used Ca concentration especially at pH 5.

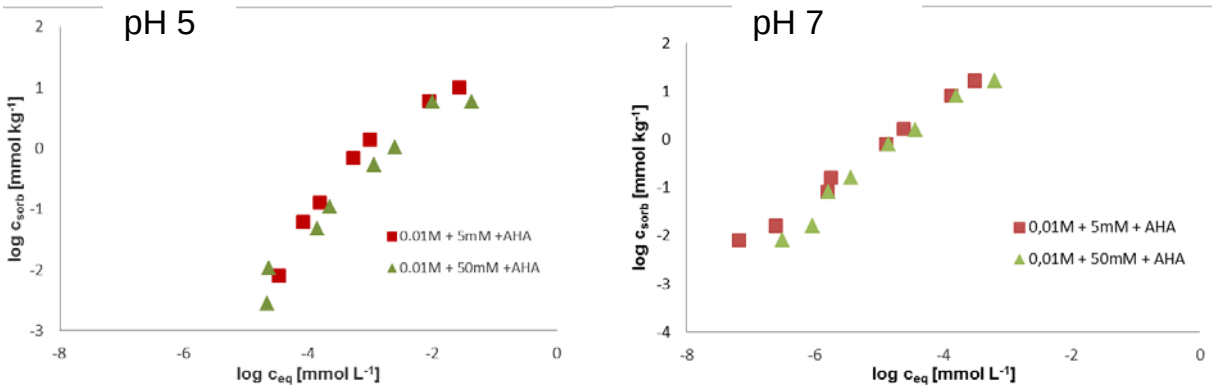

Figure 39: Freundlich sorption isotherms of europium in the presence of 25 mg L-1 AHA at 0.01 M NaCl at pH 5 and 7

At pH 7, in comparison to pH 5, the observable Ca influence is clearly lower due to the lower HA influence on the mobilization at this pH value. Figure 40 shows similar results where a higher ionic strength of 1 M NaCl used. At pH 7 no or only a weak competing effect of calcium with Eu sorption is visible.

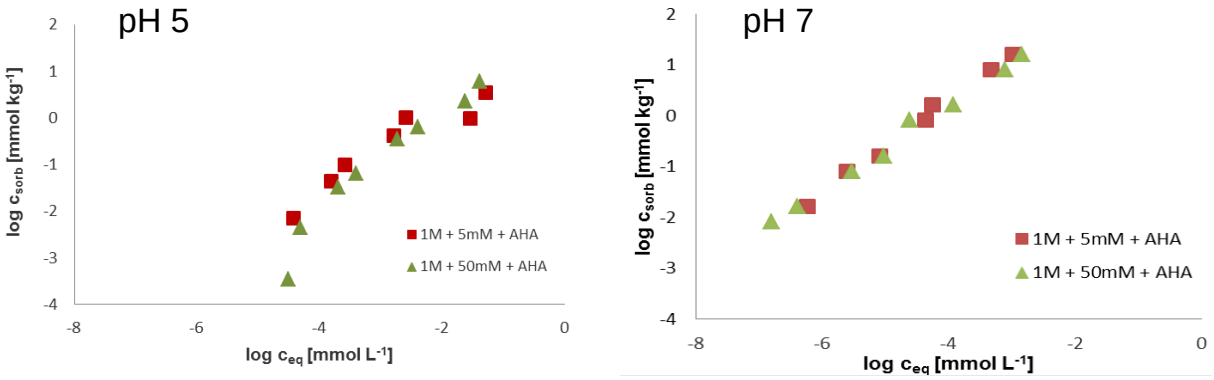

Figure 40: Freundlich sorption isotherms of europium in the presence of 25 mg L^{-1} AHA at 1 M NaCl at pH 5 and 7

Comparing log K_d at both pH values (Table 21) in the presence of additionally added bivalent calcium a high influence of the ionic strength (resulting in a lower Eu retention) at acidic pH values (pH 5) can be observed. At a neutral pH value (pH 7) it is mainly the presence of HA which decreases the mobilization of the europium. All other parameters like ionic strength and competing cations show no relevant influence on the retention at pH 7.

Table 21: Comparison of the log K_d values of Eu in the binary and ternary system with AHA under different conditions (ionic strength, Ca concentration, pH value)

Conditions	log K_d binary 0.01 M NaCl	log K_d ternary 0.01 M NaCl	log K_d binary 1 M NaCl	log K_d ternary 1 M NaCl
+ 5 mM Ca^{2+} pH 5	2.7±0.2	2.9±0.3	1.9±0.3	2.2±0.4
+ 50 mM Ca^{2+} pH 5	2.3±0.2	2.5±0.3	1.8±0.3	2.1±0.1
+ 5 mM Ca^{2} pH 7	4.0±0.2	4.7±0.4	4.1±0.4	4.5±0.5
+ 50 mM Ca^{2} pH 7	4.0±0.2	4.4±0.5	4.1±0.3	4.3±0.3

3.5.2 Sorption experiments of U in the presence of NOM

The sorption experiments with uranium were performed at identical conditions as the experiments with europium.

3.5.2.1 Influence of ionic strength on the sorption isotherms of U at pH 5 and 7

In this chapter we describe the influence of humic acids on the sorption of uranium onto Opalinus clay with different ionic strengths at pH 5 and 7. In Figure 41 the sorption isotherms of uranium onto Opalinus clay are shown.

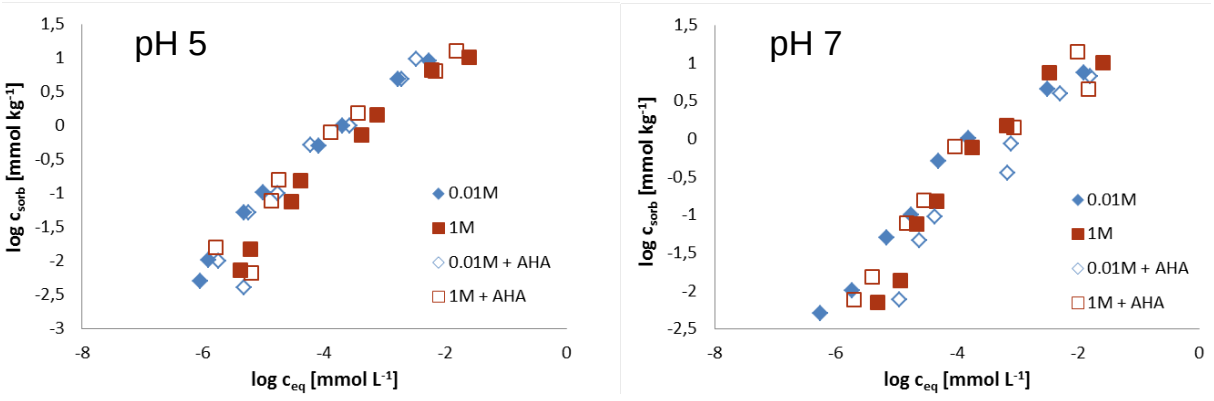

Figure 41: Freundlich sorption isotherms of U (6.6·10^{-3} to 65.8 µmol L^{-1}) with increasing salinity (0.01, 1 and 5 M NaCl) at pH 5 and 7 with and without 25 mg L^{-1} Aldrich humic acid

All processes of sorption or precipitation are more complex for uranium in comparison with europium due to the different speciation of the uranyl ion in solution and its lower charge. In contrast to the results for europium at pH 7, uranium shows a higher mobility at pH 7 compared to pH 5 due to formation of the neutral carbonate complex with calcium ($Ca_2(UO_2)(CO_3)_{3\,(aq)}$).

In the presence of AHA this effect is observable, too. At pH 7 and low ionic strength (0.01 M NaCl) the U mobility increases in the presence of AHA, which is deprotonated and negatively charged under these conditions. As a consequence, the AHA complexes the uranyl cation and forms a soluble negatively charged uranyl-AHA complex. At 1 M NaCl however, the humic acid is neutralized by Na^+ and no AHA effect (complexation of uranyl) is visible.

3.5.2.2 Influence of competing cations on the sorption isotherms of U at pH 5 and 7

In this chapter we analyze the influence of divalent Ca as competing cation. At low ionic strength and pH 5 (Figure 42 on the left hand side) the Ca concentration has no influence on the uranium sorption onto the clay whereas at pH 7 the U sorption onto OPA decreases at higher ionic strength of Ca (Figure 42, right hand side). This effect is similar to the findings for the binary system.

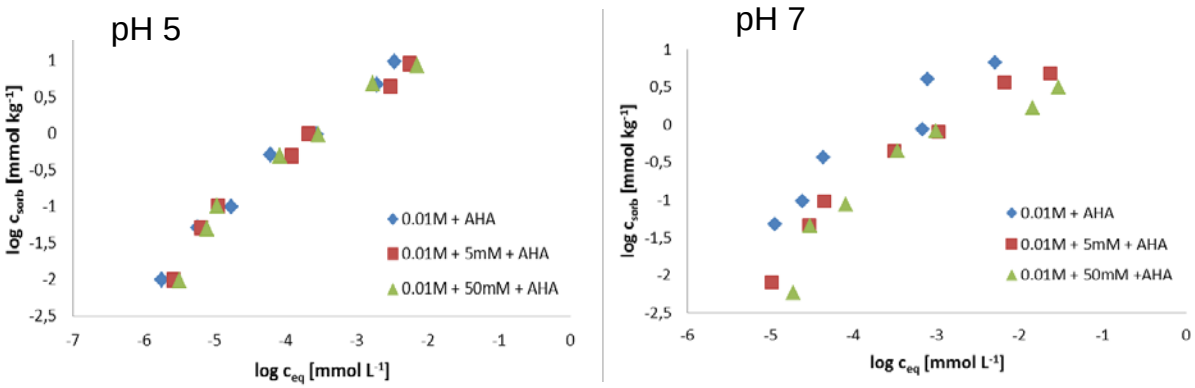

Figure 42: Freundlich sorption isotherms of uranium with 25 mg L^{-1} Aldrich humic acid in 0.01 M NaCl with different Ca concentrations at pH 5 (a) and pH7 (b)

3.5.3 Desorption experiments

In this chapter, the influence of Aldrich humic acid on the remobilization of sorbed or precipitated metals from Opalinus clay (OPA) is described. In every equilibration step 25 mg L^{-1} AHA were added additionally.

3.5.3.1 Influence of ionic strength on the desorption of Eu from OPA at different pH values in the ternary system (Eu-OPA-AHA)

The influence of ionic strength on the remobilization of Eu in the ternary system is shown in Figure 43.

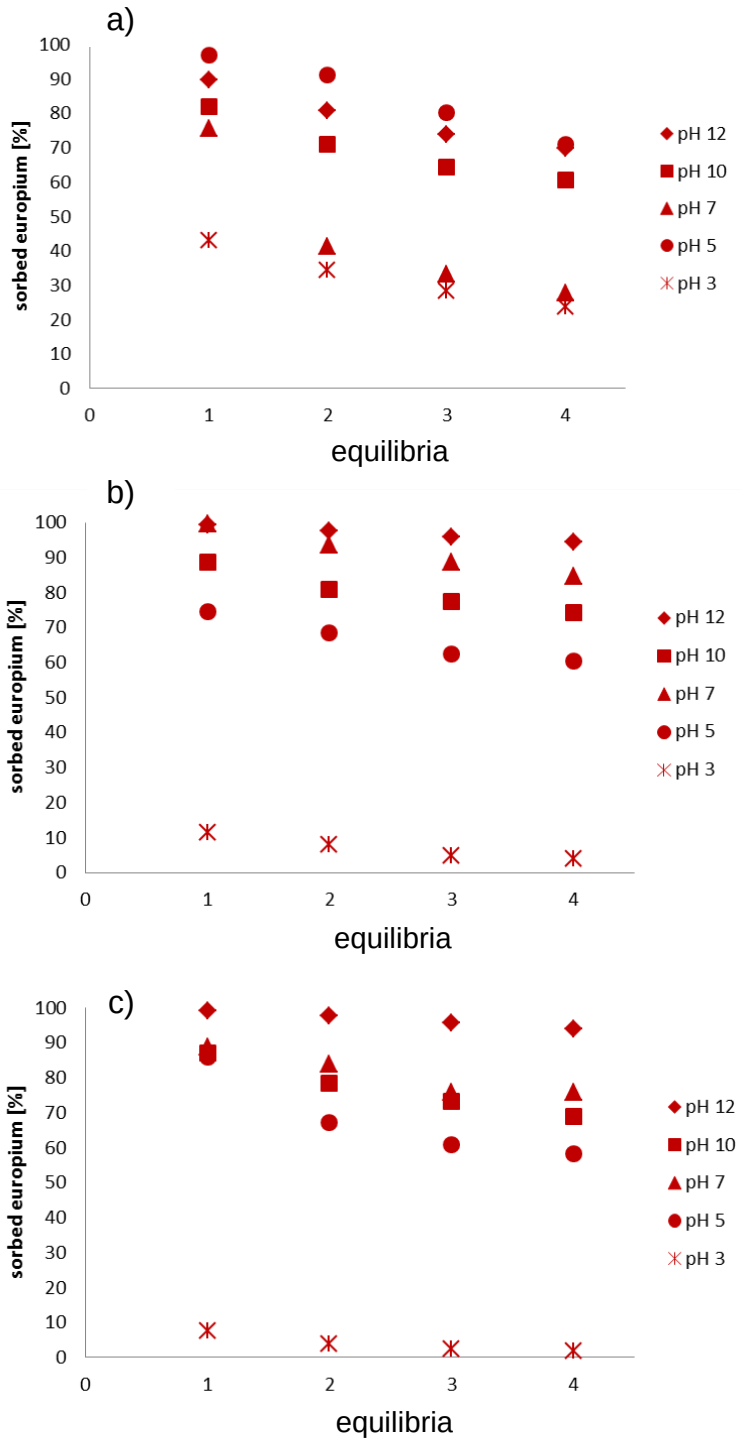

Figure 43: Desorption of Eu at different pH values (12, 10, 7, 5, 3) and ionic strengths a) 0.01 M, b) 1 M, c) 3 M NaCl in the presence of AHA at 25°C

In the presence of AHA an increasing desorption at pH 12, 10 and 7 can be observed in comparison to the binary system (Eu-OPA). The effect is highest in 0.01 M NaCl due to the small amount of sodium cations which are not sufficient to neutralize the HA. Eu stays in solution as negatively charged humate complex. At pH 5 and 3 the HA has only a small influence on the remobilization compared to the desorption results in the binary system (shown in Figure 29).

The humic acid precipitated nearly quantitative with the available protons and therefore a complexation with europium is no longer possible. Due to higher proton concentrations at pH 3 the availability of dissolved humic acid is lower compared to pH 5 and its influence decreases too.

3.5.3.2 Influence of the temperature on the desorption of Eu from Opalinus clay at different pH values and increasing salinity in the ternary system with AHA

During the sorption experiments the temperature showed a positive influence in most cases which means that the retention of the metals increases, and therefore - as shown Figure 31 in for the binary system – a remobilization at 60°C was nearly impossible. In the ternary system the desorption experiments show an opposed effect (Figure 44). At pH 12, 10 and 7 the remobilization is strongly increased in the presence of humic acid. As opposed to this the differences between the binary and ternary system are very small at pH 5 and 3.

The ionic strength shows a relevant effect in the sorption step (decreasing Eu sorption at high ionic strength in the first equilibrium) and a less significant influence in the metal remobilization determined in the desorption experiments (equilibrium steps 2-4). AHA is neutralized by Na^+ and complexation of europium is presumably not possible. The europium is sorbed or precipitated onto the clay like in the binary system.

In comparison to the ternary system at 25°C increasing temperature induced an increased Eu retention onto OPA. The remobilization of Eu from OPA decreases at higher temperature or shows only little influence similar to the binary system. Possibly more competing cations were dissolved from the clay at higher temperatures which neutralize the humic acid and prevent a complexation of the metal with AHA.

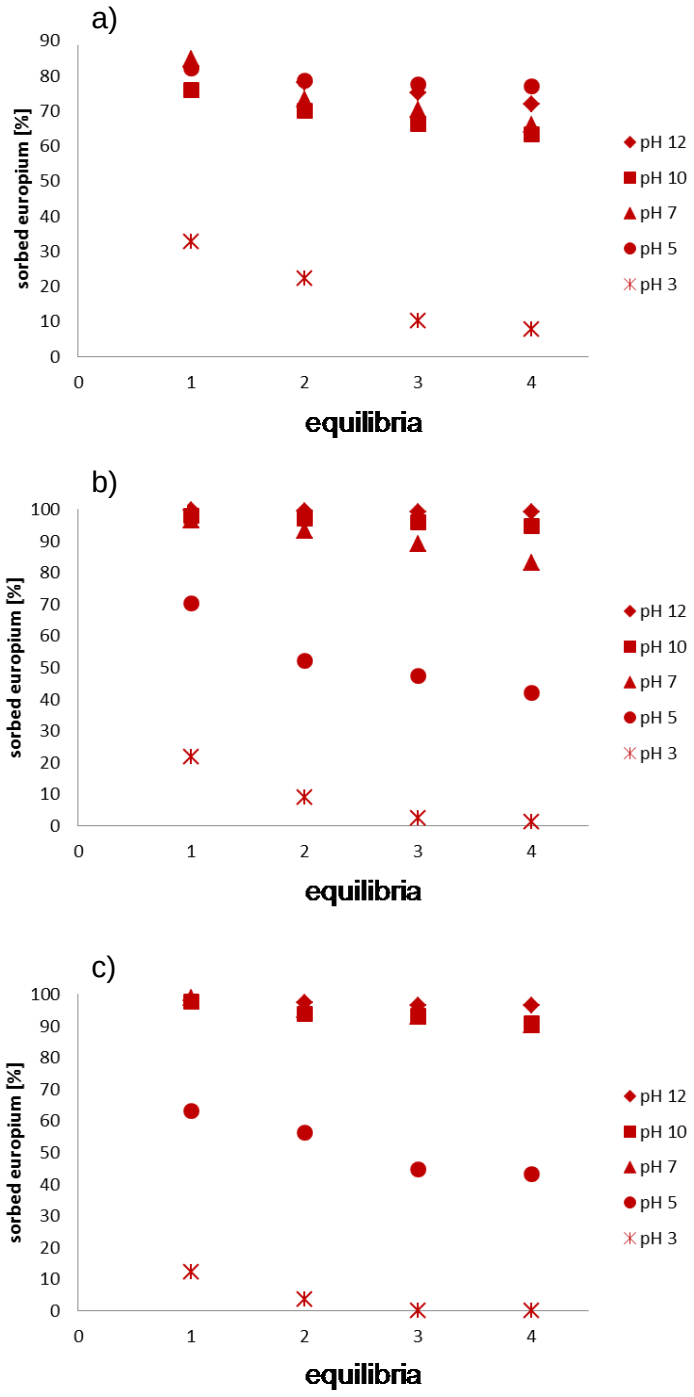

Figure 44: Desorption of Eu at different pH values (12, 10, 7, 5, 3) with different ionic strengths a) 0.01 M, b) 1 M, c) 3 M NaCl and Aldrich HA at 60°C

3.5.3.3 Influence of ionic strength on the desorption of U from Opalinus clay with different pH values in the ternary system with AHA

The results for uranium are more complex compared to the results for europium. The uranium results in the ternary system at 25°C are given in Figure 45. At low ionic strength the U sorption or precipitation decreases in the presence of AHA and the remobilization from the

clay in the different desorption steps increases too. With increasing ionic strength the remobilization is extenuated, and at 3 M NaCl the remobilization is smaller than in the binary system. The humic acid complexes the uranium and keeps it dissolved over a large pH range.

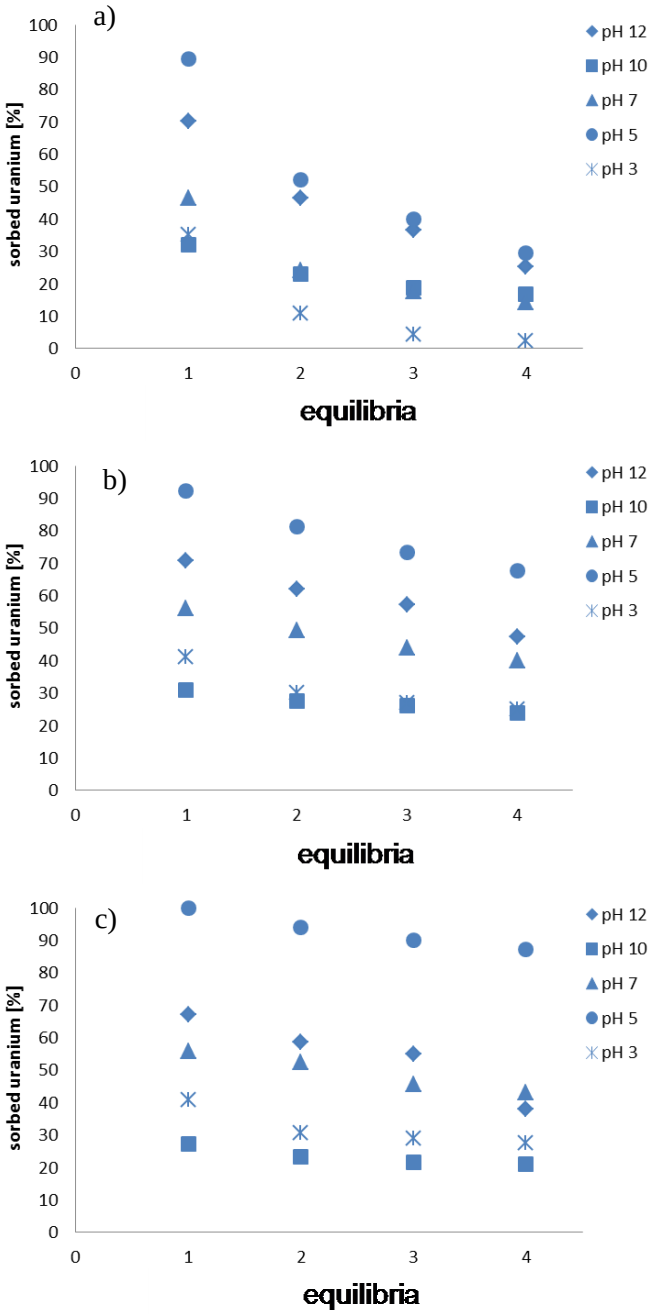

Figure 45: Desorption of U at different pH values (12, 10, 7, 5, 3) with different ionic strengths a) 0.01 M, b) 1 M, c) 3 M NaCl and Aldrich HA at 25°C

Increasing salinity leads to similar but more complex remobilization effects than with europium due to the different uranyl species formed at the different pH values. Altogether, a decreasing mobility of uranium species at higher ionic strength can be observed.

3.5.3.4 Influence of the temperature on the desorption of U from Opalinus clay with different pH values in the ternary system with AHA

The results of desorption experiments of uranium in the ternary system at 60°C are given in Figure 46. Similar to the results at 25°C the humic acid shows a high influence on the retention of uranium at 60°C.

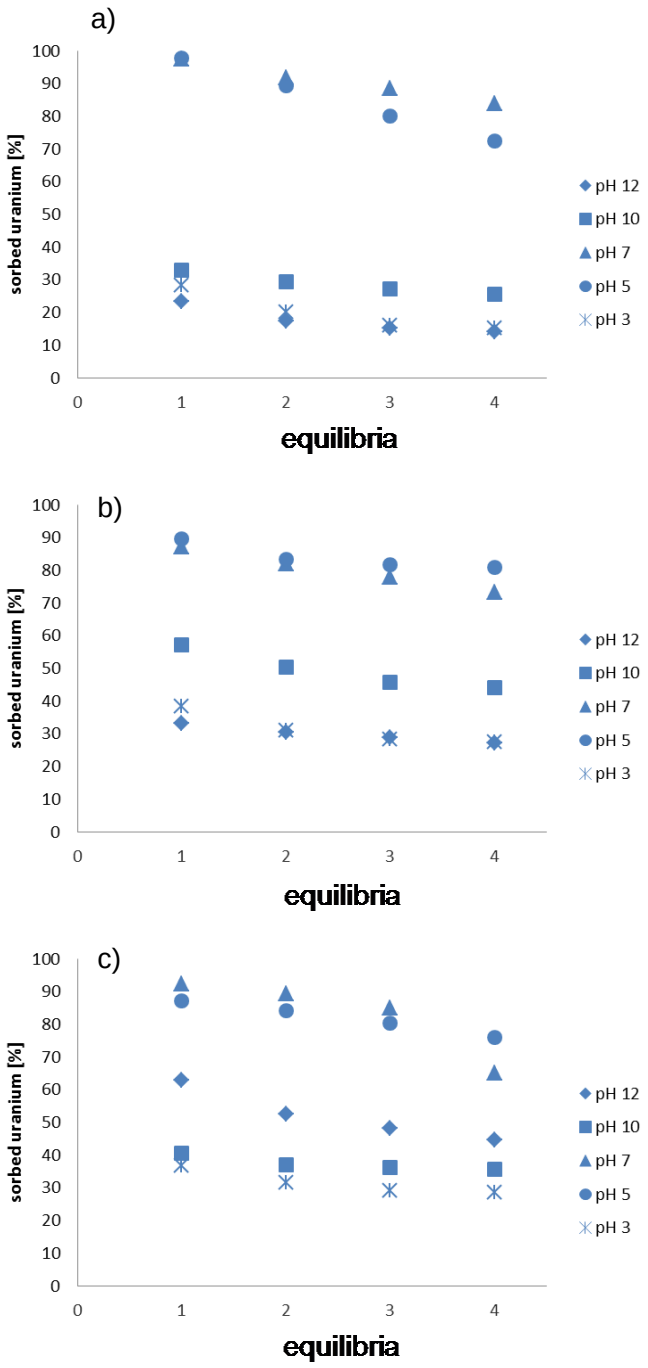

Figure 46: Desorption of U at different pH values (12, 10, 7, 5, 3) with different ionic strengths a) 0.01 M, b) 1 M, c) 3 M NaCl and Aldrich HA at 60°C

Therefore the pH values 12, 10 and 3 are most affected and the increase of temperature reduces the higher remobilization which is caused by the HA. At low ionic strength the humic acid increases the mobility at these pH values. Additionally, a steady remobilization is observable. Similar to 25°C the influence of HA decreases with increasing ionic strength presumably to the neutralization of the humic acid by sodium cations.

3.5.4 pH edges

In this chapter the influence of humic acid on the pH edges of europium and uranium is discussed. The experimental conditions are comparable to the experiments in the binary system.

3.5.4.1 Influence of ionic strength and temperature on the pH edges of Eu in the ternary system

Figure 47 shows the results of the pH edges in the ternary system with increasing ionic strength at 25 and 60°C. The influence of ionic strength is similar to the results in the binary system. At both temperatures the ionic strength increases the mobility of europium in the acidic pH range and at higher pH values no influence of higher salinity is observed.

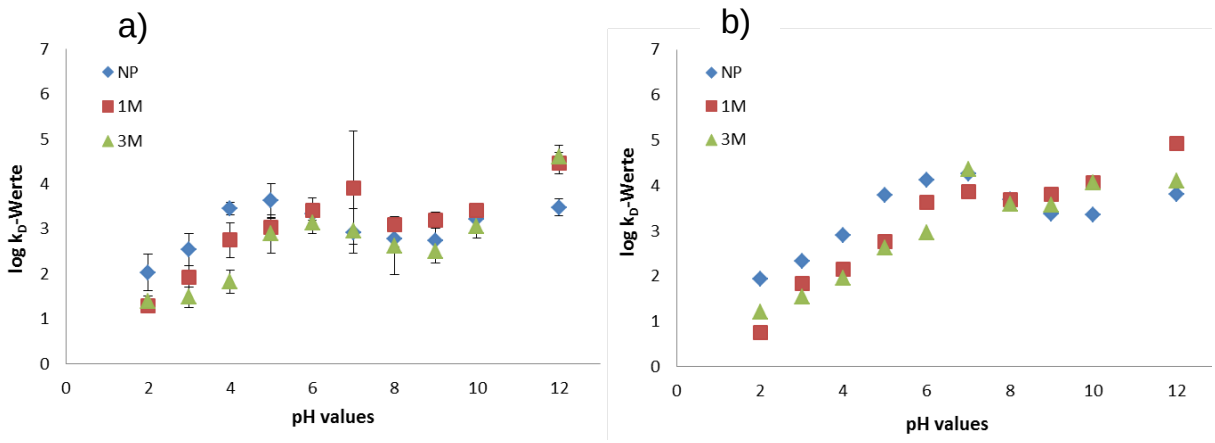

Figure 47: pH edges of europium in 0.01, 1 and 3 M NaCl in the presence of 25 mg L^{-1} AHA at 25°C (a) and 60°C (b)

Additionally, the influence of AHA in comparison to the binary system is insignificant at low pH values (pH < 6). At pH values ≥ 6 we notice a decrease of the log K_d values of more than one log-unit from 5 to less than 4. In the ternary system the influence of higher temperature leads to an increased Eu sorption compared to the binary system.

The influence of AHA at 60°C is not relevant in contrast to 25°C. At 25°C and pH ≥ 6 the log K_d values are in the range between 2.4 and 4.3 depending on pH while the values at 60°C are considerably higher ranging from 3.5 to 4.8.

3.5.4.2 Influence of ionic strength and temperature on the pH edges of U in the ternary system

The pH edges of uranium in the ternary system with Aldrich humic acid at 25 and 60°C are shown in Figure 50. In both cases no relevant influence of the ionic strength can be observed. At higher temperature (60°C) an increased uranium sorption onto clay can be determined under all conditions used. Overall no significant influence of ionic strength can be seen in the ternary system. At 60°C a decrease of uranium sorption induced by the high ionic strength can be observed only in the pH range between 4 and 8.

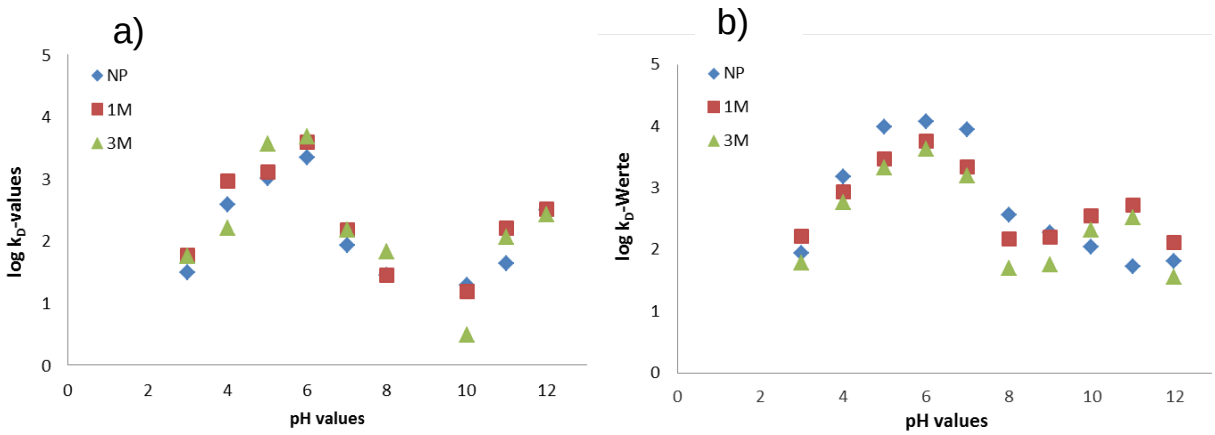

Figure 48: pH edges of uranium in 0.01, 1 and 3 M NaCl with 25 mg L^{-1} Aldrich humic acid at 25°C (a) and 60°C (b)

3.6 Column experiments (MCCE)

3.6.1 Optimization of HPLC-ICP-MS-hyphenation

First experiments to couple the miniaturized clay column experiments (MCCE) with ICP-MS detection were performed applying both instruments (HPLC and ICP-MS) in their standard configuration. Furthermore, the addition of make-up fluid (5% HNO_3, additional peristaltic pump) between the HPLC and the ICP-MS using a T-connector was evaluated.

However, both ways turned out to be unsatisfactory in terms of either reproducibility or sensitivity and entailed significant memory effects arising from the glass nebulizer and the rather large spray chamber of the ICP-MS.

As a consequence, material with lower carryover was chosen, and both the nebulizer and the spray chamber have been substituted by PFA (Perfluoroalkoxy alkane) material during the MCCE experiments. Moreover, the type of the spray chamber was changed from Scott to cyclonic thus minimizing the inner surface of the spray chamber resulting in reduced memory effects.

3.6.2 System with inert flow path

Owing to the use of PFA material and the application of a PTFE transfer capillary between HPLC and ICP-MS memory effects are no longer measurable (commercially available connector capillary marked with a red tag, corresponding to 20 µL min^{-1} naturally aspirated, 1 L argon gas per minute).

The inert flow path of the coupled system (HPLC-ICP-MS) during the MCCE from autosampler or gradient generation to ICP-MS detection can be proven by installing a zero dead volume connector instead of the column and analyzing the development of the signals in time resulting from injections or gradients.

3.6.3 Injection of discrete sample amounts

A typical single injection of europium (5 µL of 2 mM europium perchlorate) over a column made from pure kaolinite is shown in Figure 49. It shows that no detectable amount of europium can be eluted from the column even after a long waiting period after the injection. Initially, europium is thus sorbed quantitatively on the clay column. The same observation can be made when examining columns containing 1 m-% Opalinus clay and 99 m-% sea sand.

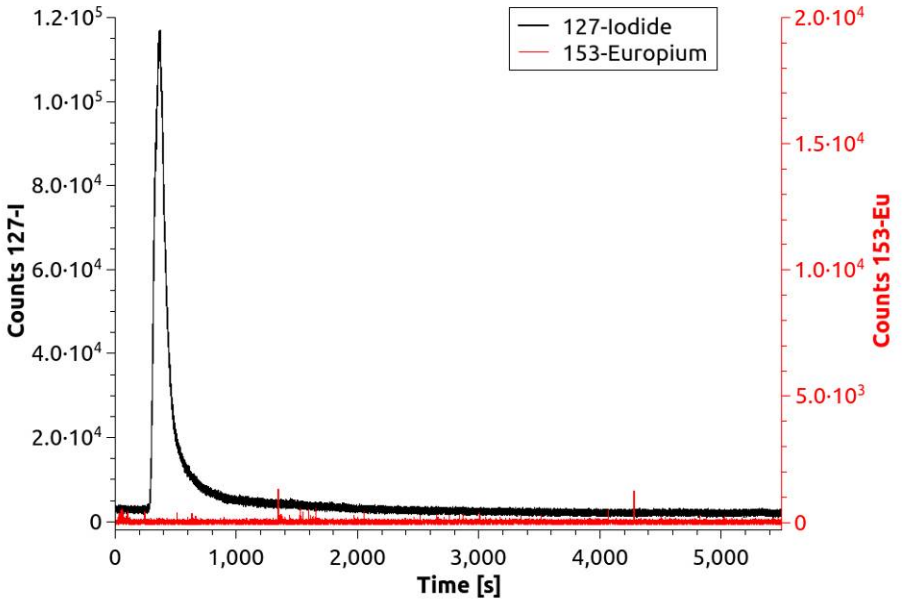

Figure 49: Single injection of 90 ng europium together with 12 ng iodide in 2 µL ultrapure water (corresponding to 45 ppm Eu and 6 ppm I) over a column made of 200 mg pure Kaolinite at a flow of 40 µL min^{-1} Milli-Q ultrapure water

When europium is repeatedly injected (5 µL of 2mM europium perchlorate) over a column containing 1 m-% Opalinus clay no europium can be detected after the first 20 injections (Figure 50). Not before the 21st injection does europium breaks through the column to be registered at the column outlet by ICP-MS online detection. During the following 13 injections the level of the measured europium signal rises with each injection. The europium signals of the last five injections remain at a comparable level.

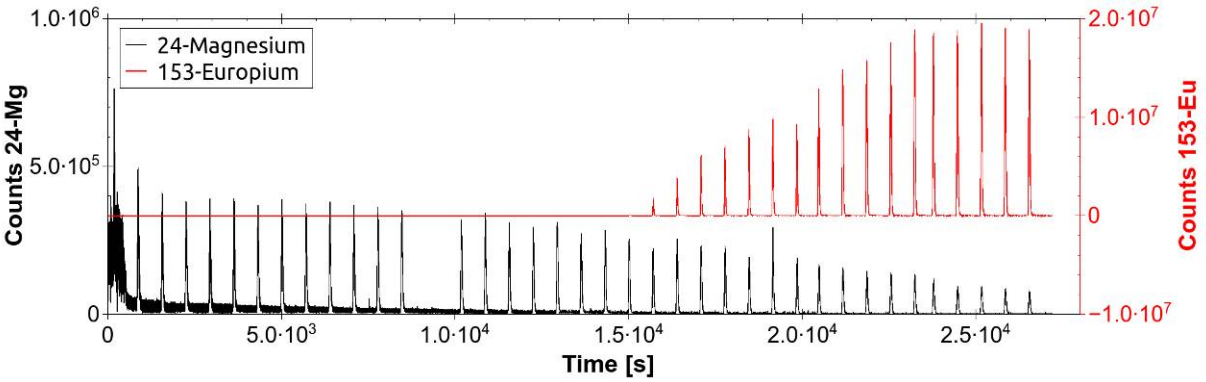

Figure 50: Repeated injection of 5 µL of a 2 mM europium perchlorate solution over a 1 m-% OPA column. Europium breakthrough takes place with the 21st injection. ^{24}Mg is eluted from the column and serves as injection marker

The signal of magnesium (Figure 50) serves merely to visualize the occurred injections since in this series of experiments no reference marker has been added in order to exclude any

possible interferences caused by its addition. It is noteworthy that the magnesium signal drops with the increasing number of injections gradually at first and stronger upon europium breakthrough. This is interpreted as bleeding and leaching of the column filling.

Europium injected onto the column is sorbed quantitatively at first. In the range of the signal rise only a certain fraction of europium is sorbed onto the clay decreasing with each further injection. During the period of saturation either no further amount of europium is sorbed and the injected europium passes the column straightaway or the injected europium is sorbed and the same amount of europium is desorbed from the column in terms of a dynamic equilibrium. These two possibilities cannot be differentiated by means of the experimental data.

Applying the MCCE-ICP-MS hyphenation with repeated injections of small sample volumes over columns filled with 1 m-% OPA an 99 m-% sea sand the following descriptive observations have been made:

When comparing MCCE performed with portions of diluted europium perchlorate solution (5 µL 2 mM) injected over the clay column as described above with MCCE of europium injected together with 20 mM ^{13}C marked sodium lactate the latter shows an earlier breakthrough of europium. In the absence of sodium lactate the breakthrough occurs after 21 injections whereas in the presence of a 10-fold excess of sodium lactate the europium breakthrough already occurs during the 19th injection. In addition, the sorption of europium is slowed down or retarded in the presence of sodium lactate and a prolonged breakthrough stage is observed where the europium signal rises from injection to injection. This mobilizing effect of lactate on europium sorption on OPA and the resulting lower europium sorption capacity of OPA is consistent with earlier results from the joint research project obtained with batch experiments. During these experiments no significant uranium signal was observed which means that uranium naturally occurring in clay cannot be displaced by the amounts and concentrations of the injected europium.

It is to note that prior to any aluminum injection during the online MCCE with OPA no significant aluminum background can be detected in the column eluate. This means that no significant amount of aluminum is eluted from the column.

In order to visualize the sorption of aluminum and the concurring displacement of previously sorbed europium by aluminum the following series of experiments has been performed. A MCCE column (1 m-% OPA) that has been saturated for 150 min with europium beforehand underwent continuous injections of a 2 mM aluminum nitrate solution.

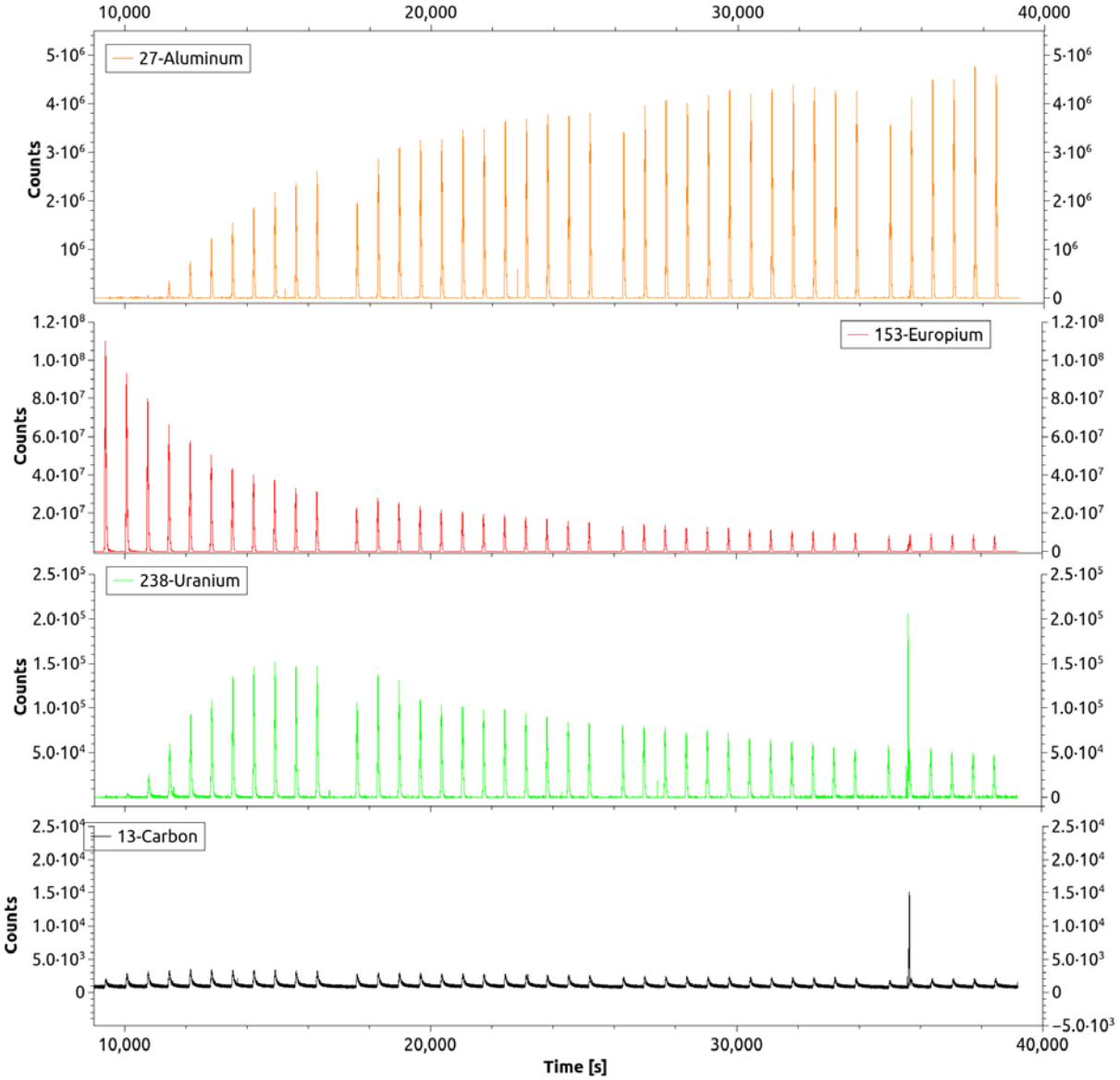

Figure 51: Online MCCE of a clay column (1 m-% OPA, 99 m-% sea sand) previously saturated with europium (0 – 9,000 s, not shown). The graph shows 41 consecutive injections (four sequences with 11, 12, 12, and 6 injections) of 5 µL of a 2 mM aluminum nitrate solution (9,000 – 39,000 s)

Based on the measurement given in the graph depicted in Figure 51 we may reason that aluminum is sorbed onto OPA. During the first injections this sorption proceeds quantitatively. Beginning with the 3rd injection aluminum breaks through the column gradually, i.e. aluminum is no longer sorbed quantitatively but passes the column partly.

Regarding the europium signal in Figure 51 it becomes clear that the europium is stepwise[2] displaced and desorbed from the column with each injection of aluminum. Thus, a displacement effect is taking place that diminishes until the aluminum signal reaches its saturation. It can therefore be assumed that trivalent aluminum displaces divalent europium sorbed onto OPA in terms of a competitive effect.

Unexpectedly, the incremental desorption of naturally occurring uranium was observed throughout the MCCE depicted in Figure 51. Since the column was at no time exposed to a sample or eluent containing uranium the desorbed uranium must be of natural origin. Moreover, this uranium desorption is starts and rises delayed in time while the europium desorption is already within the decreasing stage.

Compared to the preceding injections (approx. 60000 counts ^{13}C, not shown) virtually no further desorption of organic constituents is detected. The strong response of both the ^{13}C and the ^{238}U signal during the fifth to the last injection in Figure 51 are remarkable. It is highly probable that this signal is caused by a species composed of naturally occurring uranium and NOM that is displaced by the injected aluminum but coelutes together with the desorbed aluminum.

During the following injections shown in Figure 52 the concentration of the injected aluminum was increased ten times to 20 mM. Immediately, the detected aluminum signal rises for the first and all following injections by a factor of ten (to $5 \cdot 10^6$ counts) in comparison with the signal of the 2 mM aluminum solution. This means that the column is already completely saturated with aluminum and any further amount of injected aluminum passes the column directly, i.e. does not lead to a higher aluminum sorption on the stationary phase.

Likewise, the europium signal rises by a factor of ten at first (from $4.5 \cdot 10^6$, the last peak from the displacement by 2 mM aluminum solution in Figure 51, to $4.5 \cdot 10^7$, the first peak in Figure 52). However subsequently it decreases in terms of a desorption. Alike, the desorption of uranium can be significantly increased for a short time. The europium signal decreases faster than the uranium signal. This is caused either by the difference in concentration of europium and uranium sorbed onto the column or by a stronger bonding affinity of uranium towards clay when compared to europium.

To summarize, we can again deduce from the experiments shown above and other MCCE that a certain difference in sorption affinity exists for the examined metals (relevant for final disposal) Eu, U, (and Al): Eu < U < Al.

[2] An injection of ultrapure water does not have the same result. The desorption of europium is therefore not caused by the potential pressure pulse during the injection or the switching of the HPLC valve.

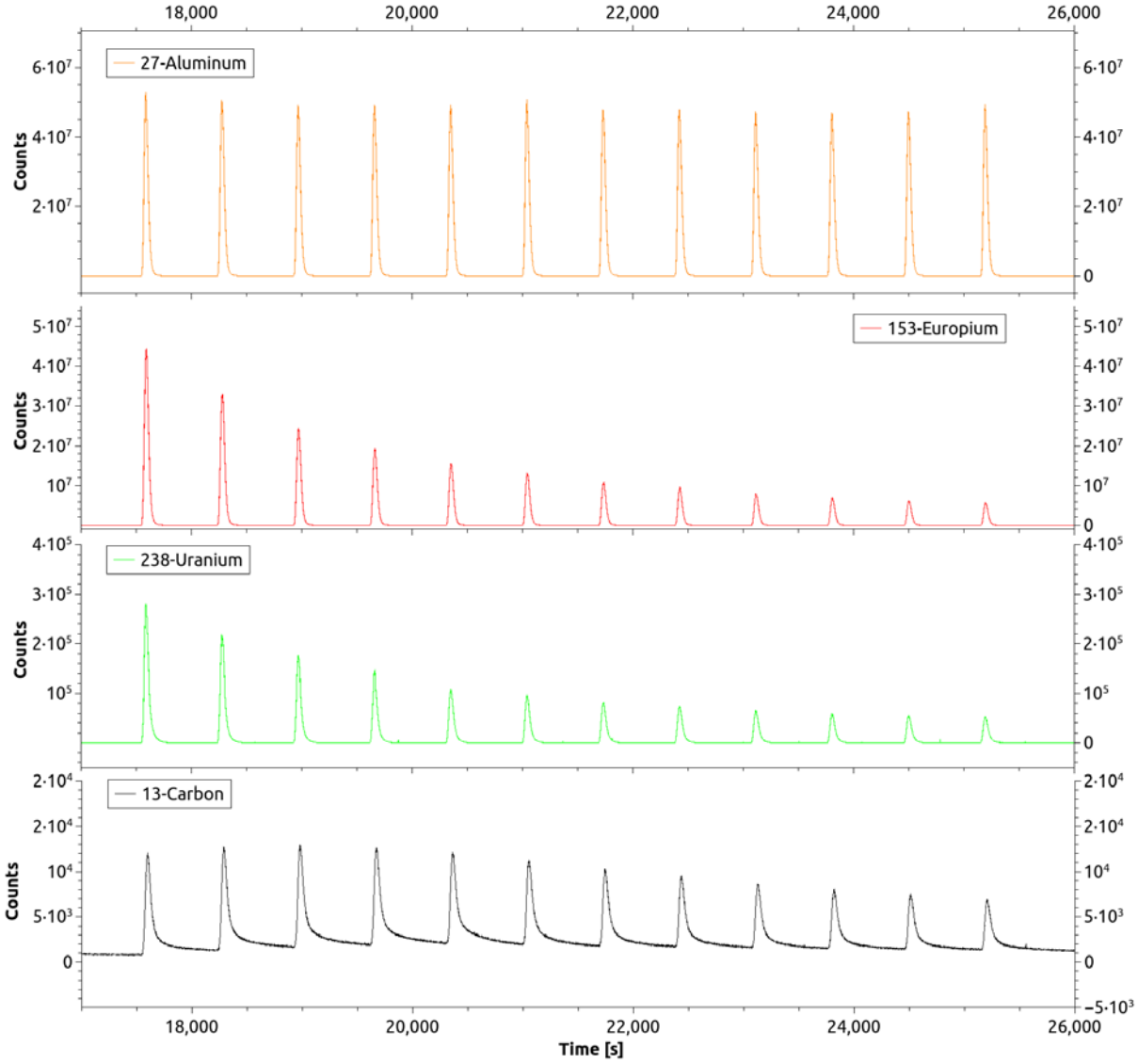

Figure 52: Online MCCE continued from Figure 51: Twelve repeated injections of 5 µL of a 20 mM Al solution (17,000 – 26,000 s)

3.7 B NMR as speciation technique

The distribution of different existing borate species in aqueous solution depends on the pH value [Borkowski et al. 2010]. Once it is changed the distribution of the different borate species in solution changes accordingly as seen in Figure 53.

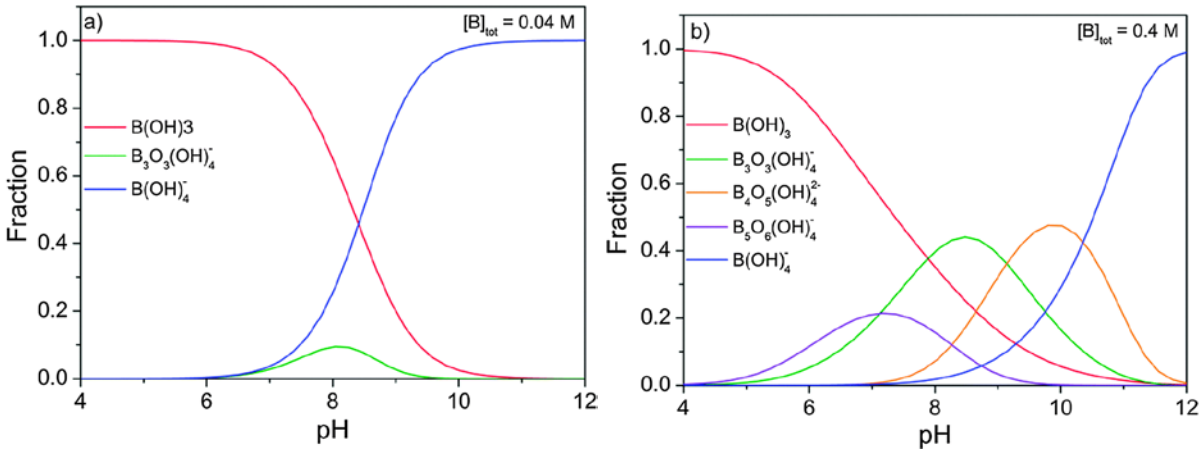

Figure 53: Fraction diagram of aqueous boron species calculated for 4 ≤ pH ≤ 12 at I = 0 for (a) $[B]_{tot}$ = 0.04 M, and (b) $[B]_{tot}$ = 0.4 M [Hinz et al. 2015]

The ^{11}B NMR spectrum of a boric acid sample at pH 8.5 is shown in Figure 54. The three signals at approx. 17, 13, and 1 ppm can be attributed to different borate species present in solution at the adjusted pH value of 8.5.

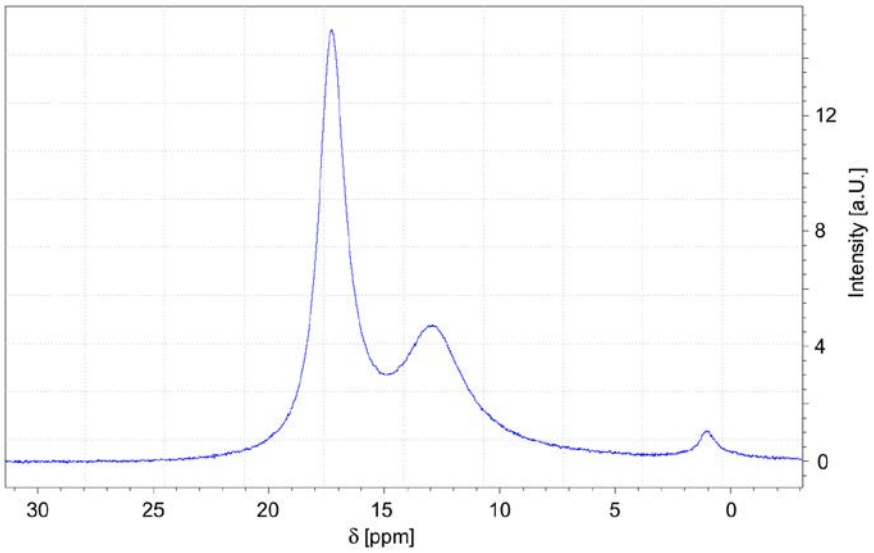

Figure 54: ^{11}B NMR spectrum boric acid c($B(OH)_3$) ≈ 0.4 M at pH 8.5 (attribution of the three signals to the respective species: left: $B(OH)_3$, middle: $B_3O_5(OH)_4^-$, right: $B_5O_6(OH)_4^-$) together with $B(OH)_4^-$

These species are $B(OH)_3$ at 17 ppm, $B_3O_3(OH)_4^-$ at 13 ppm and $B_5O_6(OH)_4^-$ together with $B(OH)_4^-$ at 1ppm. This is in accordance with literature on NMR studies [Salentine 1983] and species distribution diagrams obtained with the temperature jump rate method [Anderson et al.] as well as with newer results from our project partners. According to [Salentine 1983] the $B_4O_5(OH)_4^{2-}$ species which is certainly present at pH 8.5 is not visible in the NMR spectrum most likely due to a broad NMR signal.

An overlay of the ^{11}B NMR spectra of boric acid at different pH values is shown in Figure 55. The species attribution of the spectrum at pH 8.5 has already been given above. At a pH value of 14 only $B(OH)_4^-$ is present in solution and therefore a single signal at 1.5 ppm can be observed. At pH 10.6 the signal broadens and shifts to 2.5 ppm which is both caused by the emergence of one of the $B_3O_3(OH)_x^{n-}$ borate species postulated by Anderson et al. still under the constraint of the non-NMR detectable $B_4O_5(OH)_4^{2-}$ species [Anderson et al. 1964]. The emergence of additional species becomes more obvious at pH 10.3 when two signals are visible at about 12 and 5.5 ppm.

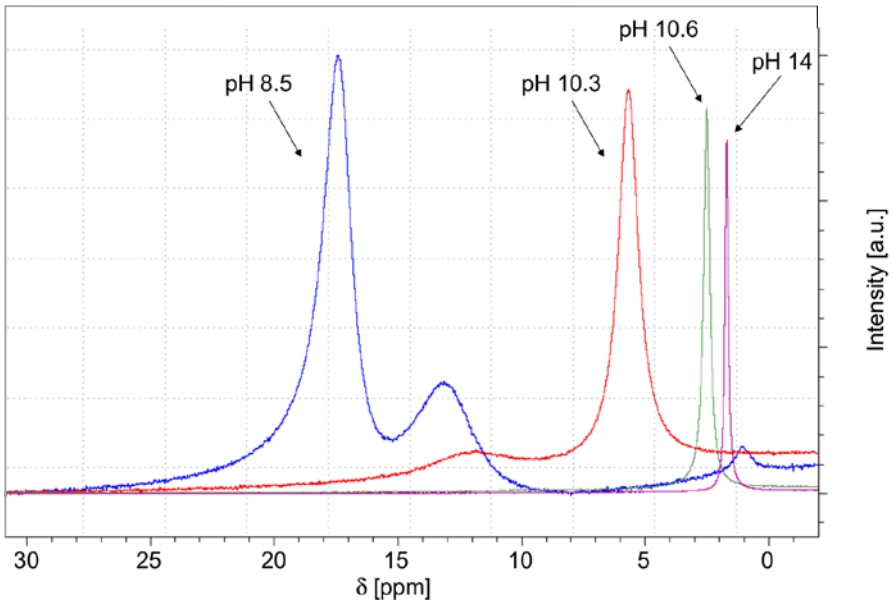

Figure 55: ^{11}B NMR spectra (not normalized) of boric acid c($B(OH)_3$ approx 0.4 M at pH values ranging from 8.5 to 14 (pH values adjusted with 1 M NaOH)

The impact of an europium addition to the boric acid solution at three different pH values is shown in Figure 56. In all cases the addition of europium leads to a shift towards lower field (higher δ) and in the case of pH 8.5 and 10.6 the borate species distribution has been changed.

Whether the above described experimental findings are based on complex formation between europium and borate species or are only the consequences of a lanthanide induced shift (or even a superposition of both effects) has not been further investigated in our group.

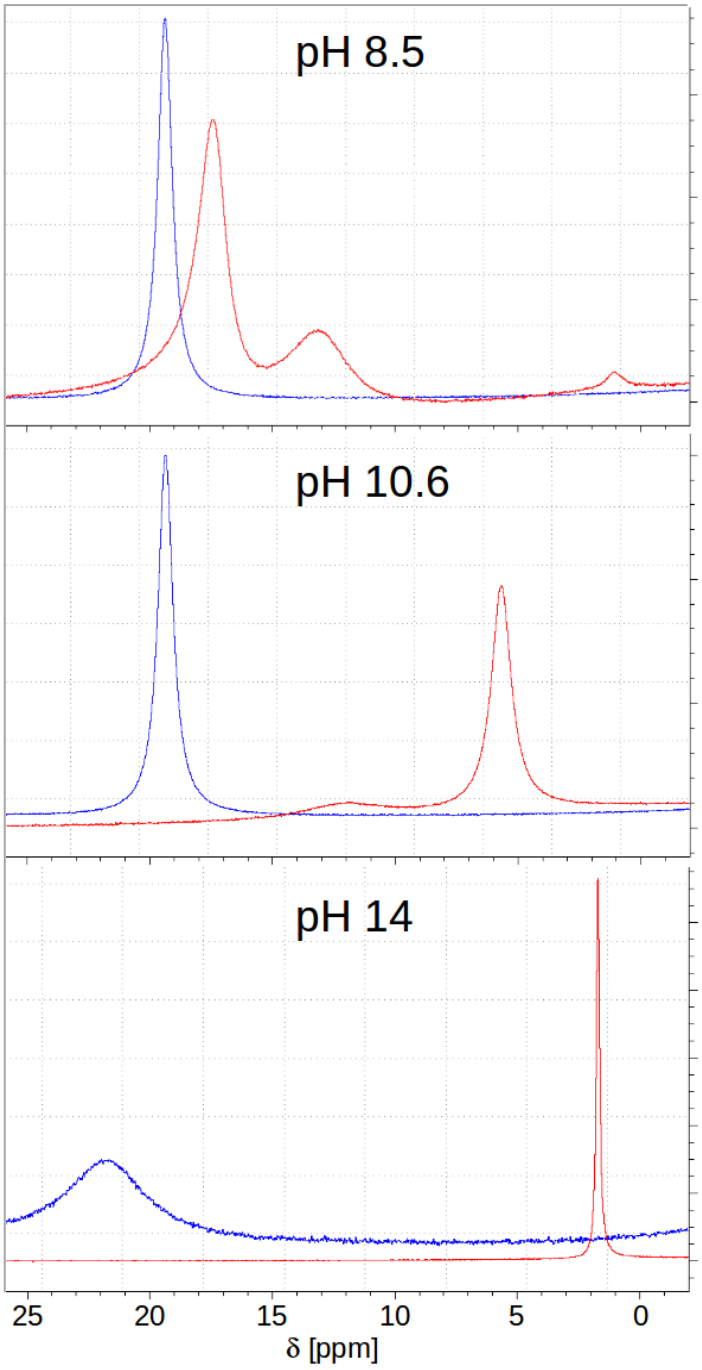

Figure 56: The influence on the ^{11}B NMR spectra of europium perchlorate added to the boric acid solution at different pH values (red without addition and blue after addition of europium)

4 Conclusion and outlook

Objective of the research project was to analyze the geochemical behavior of the actinide uranium and the lanthanide europium as chemical homologue of trivalent actinides like americium in natural claystone (Opalinus clay) as potential host rock for a future HLW disposal. Special attention was given to the influence of groundwater and clay porewater with high salinity. Additionally, the metal mobility in clay in the presence of natural organic matter (NOM) was analyzed. Therefore, the complex ternary system consisting of metal ions, clay and NOM was initially divided into the binary systems which were analyzed separately. Finally, the interaction and transport behavior of the metals in the ternary system was elucidated to acquire more knowledge of the system in the context of the long-term safety assessment for a potential repository.

For complexation experiments of metal ions with natural NOM like humic acids (HA) a hyphenation of capillary electrophoresis (CE) and inductively coupled plasma mass spectrometry (ICP-MS) which was realized in previous experiments was used for the determination of complex stability constants (log β). With this CE-ICP-MS hyphenation the influence of NOM from different origins on the complexation of Eu and U at an ionic strength of 0.01 M NaCl was analyzed. Depending on the nature of HA the log β values for Eu vary between 6.1 and 7.0. These differences are also seen in the speciation patterns shown in the electropherograms. Some HA have a higher amount of strong binding sites for the metal ions. For the analyzed natural organic matter from Suwannee river (SNOM) clearly lower complexation stability constant (log β = 4.6) due to the higher amount of smaller organic compounds are determined. Uranium is less complexed by humic acid than europium. The log β values for the different humic acids vary between 5.2 and 6.4. For SNOM they are in the same order of magnitude as Eu (log β = 4.5).

With increasing ionic strength the CE-ICP-MS method is limited. For experiments at ionic strengths up to 1 M NaCl ultrafiltration (UF) is applied as alternative method. At low ionic strength (< 0.1 M) UF shows similar results for the determination of log β values as the CE-ICP-MS method. Increasing ionic strength (1 M NaCl) reduces the complexation strength of NOM resulting in log β values in the range of 5.1 – 6.4 for Eu and 5.9 – 6.1 for uranyl. The presence of calcium (up to 50 mM) as competing cation leads to log β values in the same order of magnitude. Presumably europium and calcium show a direct competition whereby the presence of calcium ions reduces the europium complexation due to a competitive complexation with NOM. The presence of sodium at high concentrations leads to a neutralization of the humic acid and prevents the europium complexation with NOM.

In the case of uranium the results are different. Higher amounts of Ca (50 mM) in the solution increase the complex stability of uranium humate. A possible explanation is given by the different uranium speciation with the result that uranium and calcium are not in direct competition to each other when forming Me-HA complexes. Perhaps the calcium uranyl species forms a more stable complex with HA than the divalent uranyl cation alone. Additionally, a higher ionic strength shows no relevant influence on the complexation between uranyl and HA.

For sorption experiments in the binary system consisting of metal and clay a highly sensitive method for trace element analysis in matrices containing up to 5 M NaCl was required. A main focus of the project was to determine the influence of high salinity on the metal mobility in clay as host rock. Due to the high salinity these samples cannot be measured with the default ICP-MS method that only tolerates salt concentrations up to 1%. Due to the very low metal concentrations remaining in solution after the sorption step a dilution of the samples was not possible without falling below the metal detection limit. Therefore the development of a new method for liquid samples containing high salt concentrations was crucial.

For this reason a new time resolved method with online dilution was developed that makes use of transient signal integration over time for concentration calculations. While only introducing the sample for ten seconds into the plasma, the transient method shows improved figures of merit compared to the default ICP-MS method. With this transient method the batch experiments for sorption at higher ionic strength ranging from 1 to 5 M NaCl can be measured directly without the need for any further clean up or pretreatment steps.

In the binary system Eu – clay a dependency on temperature, ionic strength and competing cations is clearly evident. The mobilization of europium was increased by higher ionic strength and increasing calcium concentration especially at pH 5. At pH ≥ 7 the retention of europium onto clay is higher compared to pH ≤ 6, and therefore it is not susceptible to the presence of competing cations. The remobilization of the metal ions sorbed onto clay was increased by rising ionic strength especially at acidic pH values. High temperature (60°C) together with acidic pH values lead to higher sorption of europium at all ionic strengths. However, in the following desorption steps the remobilization rates of europium were higher compared to 25°C.

The results of uranium in the binary system (U – OPA) are obviously different compared to the results of europium. High ionic strength reduces the U retention onto clay but the Ca concentration shows only an influence at pH 7. With increasing Ca concentration the mobility of uranium is increased due to formation of the neutral calcium uranyl carbonato complex.

The remobilization of uranium from clay analyzed by the use of desorption experiments differs from the results of europium. Probably due to a completely different speciation behavior mainly influenced by the pH value as well as the Ca presence the remobilization of uranium from OPA shows no predictable or clear trend at increasing ionic strength or different temperatures.

The results of the ternary system are in a good agreement with the results of the complexation studies. The presence of NOM especially in form of HA shows a strong influence on the europium sorption due to the strong complexation ability with HA. At pH values higher than 6 the HA complexes the europium and forms negatively charged europium humate complexes which remain in solution resulting in higher europium mobility. With increasing ionic strength and the presence of higher Ca concentrations the complex formation is reduced and the influence of the HA on Eu retention onto clay decreases. In contrast to the Eu results, the uranium mobility in the ternary system is only slightly affected by the presence of NOM. The influence of higher amounts of Na and Ca on the U mobility in the ternary system is also relatively low.

In the former joint research project miniaturized clay column experiments (MCCE) had been introduced to analyze sorption and desorption processes on clay dynamically. During the current project the instrumentation and methodology of the MCCE has been optimized for increased performance, and online coupling of MCCE with ICP-MS has been realized. On applying the MCCE-ICP-MS hyphenation comprehensible results have been obtained. During a series of repeated injections of europium over a column of 1 m-% OPA and 99 m-% sea sand three different stages can be observed: At first, the complete amount of europium injected is sorbed and no europium can be detected at the column outlet. During the breakthrough stage the eluted amount of europium rises with each further injection until the saturation stage (plateau) is reached where no further increase of the eluted amount of europium is recorded. Additionally, the mobilizing influence of lactate as an example for a small molecular weight clay organic component onto the sorption of europium on clay has been reproduced applying the dynamic sorption / desorption experiments as implemented within the MCCE.

As new speciation tool B NMR was tested for the speciation of metal borate complexes. Beginning with first and preliminary results on B NMR as speciation technique originating from our and other project groups B NMR spectroscopy has found its way into the joint research project where it has proven to be a beneficial tool for borate speciation analysis.

As outlook for further experiments in the context of long-term safety assessment for a future HLW disposal the presence of cementitious material like concrete for construction or

bentonite as backfilling material in a repository for high nuclear waste should be considered. Concrete leaching could show a strong influence on the formation water and the resulting pH value which would be changed into the hyperalkaline region. Experiments with changed formation water and high alkaline pH could be performed in prospective projects. The influence of these parameters on the mobility of europium, uranium and other relevant radionuclides in presence of clay as host rock could be of major interest for a reliable long-term safety assessment.

5 Publications resulting from the project

Hahn R. (2014) Untersuchungen zur Metall-Komplexierung von Europium und Uran mit organischen Komplexliganden mittels Dialyse und Ultrafiltration. Masterarbeit, Naturwissenschaftlich-Technische Fakultät III, Universität des Saarlandes, Saarbrücken.

Hein C., Sander J.M., Kautenburger R., Kickelbick G. (2015) Sorption Experiments With High Salinity - Application Of Time Resolved ICP-MS Measurements Clay. European Winter Conference on Plasma Spectrochemistry, Münster (Poster).

Hein C., Sander J.M., Kautenburger R., Beck H.P., Kickelbick G. (2013) ICP-MS measurement of samples with high salinity – sample clean up or transient measurement. Migration Conference, Brighton, Great Britain (Poster).

Hein C., Sander J.M., Kautenburger R. (2014) Speciation via Hyphenation–Metal Speciation in Geological and Environmental Samples by CE-ICP-MS. Journal of Analytical & Bioanalytical Techniques 5, 225.

Kautenburger R., Hein C., Sander J. M., Beck H. P., Kickelbick G. (2015) Metal Speciation and Mobility in Clay - From ICP-MS Batch and CE-ICP-MS Speciation to Miniaturised Clay Column Experiments (MCCE) Using LC-ICP-MS. European Winter Conference on Plasma Spectrochemistry, Münster (Vortrag).

Kautenburger R. (2011) Batch is bad? Leaching of Opalinus clay samples and ICP-MS determination of extracted elements. Journal of Analytical Atomic Spectrometry 26, 2089-2092.

Kautenburger R. (2011) Untersuchungen zur Metall-Mobilität in nativen Tonformationen - Speziation von Europium, Gadolinium und Uran mit natürlich vorkommender Organik (NOM). Chemiedozententagung, Universität Mainz (Vortrag).

Kautenburger R. (2012) Geochemische Analytik im Rahmen der Endlagerforschung – Neue Endstation Ton? Antrittsvorlesung an der Naturwissenschaftlich-Technische Fakultät III – Chemie, Pharmazie, Bio- und Werkstoffwissenschaften der Universität des Saarlandes, 06.07.2012, Universität des Saarlandes (Vortrag).

Kautenburger R. (2012) Geochemische Analytik: Endlager für radioaktiven Müll gesucht. Analytica PRO 2012, 59-60.

Kautenburger, R. (2012) Metal Mobility in Clay Formations – From Batch Experiments to New Column Setup with Compacted Clay. Chemiedozententagung 2012, Universität Freiburg (Vortrag).

Kautenburger R. (2012) Neue Zeitskala für Migrationsexperimente - Miniatur-Säulenexperimente als Bindeglied zwischen Batch- und Diffusionsversuchen. Gesellschaft für Reaktorsicherheit (GRS), Braunschweig, 03.05.2012 (Vortrag).

Kautenburger R. (2014) A new timescale dimension for migration experiments in clay: proof of principle for the application of miniaturized clay column experiments (MCCE). Journal of Radioanalytical and Nuclear Chemistry 300, 255-262

Kautenburger R. (2014) Hochradioaktive Abfälle - Analytische Tools zur Suche nach einem geeigneten Endlager. GIT Labor-Fachzeitschrift 58, 38-41.

Kautenburger R., Hein C., Sander J.M., Beck H.P. (2013) Metal Mobility in Clay - From Batch Experiments to Miniaturised Column Experiments with Compacted Clay. European Winter Conference on Plasma Spectrochemistry, Krakow, Poland (Poster).

Kautenburger R., Hein C., Sander J.M., Beck H.P. (2014) Influence of metal loading and humic acid functional groups on the complexation behavior of trivalent lanthanides analyzed by CE-ICP-MS. Analytica Chimica Acta 816, 50-59.

Kautenburger R., Hein C., Sander J.M., Beck H.P., Kickelbick G. (2013) Analysing metal speciation and mobility in clay – from ICP-MS batch experiments to a new approach of miniaturized clay column experiments (MCCE) using LC-ICP-MS. Migration Conference, Brighton, Great Britain (Poster).

Kautenburger R., Möser C., Sander J.M., Beck H.P. (2012) Geochemische Analytik im Rahmen der Endlagerforschung. 23. ICPMS Anwendertreffen und 10. Symposium Massenspektrometrische Verfahren Elementspurenanalyse, Tulln an der Donau, Österreich (Poster).

Möser C., Beck H.P., Kautenburger R. (2012) Complexation of Europium and Uranium by Humic Acids Analysed by Capillary Electrophoresis - Inductively Coupled Plasma Mass Spectrometry. Electrophoresis 33, 1482-1487.

Möser C., Sander J., Kautenburger R., Beck H.P. (2012) ICP-MS Messungen von hoch salinaren Lösungen – Proben Clean-up oder transiente Messung? 23. ICPMS Anwendertreffen und 10. Symposium Massenspektrometrische Verfahren Elementspurenanalyse, Tulln an der Donau (Vortrag).

Sander J.M., Hein C., Kautenburger R., Kickelbick G., Beck H.P. (2015) Fast miniaturised column experiments as linker between batch and diffusion experiments for host rock characterisation of final disposal sites in clay. European Winter Conference on Plasma Spectrochemistry, Münster (Poster).

Sander J., Möser C., Kautenburger R., Beck H.P. (2012) Hochdurchsatz-Methoden im Rahmen der Endlagerforschung. 23. ICPMS Anwendertreffen und 10. Symposium Massenspektrometrische Verfahren Elementspurenanalyse, Tulln an der Donau (Vortrag).

Sander J.M., Hein C., Kautenburger R., Beck H.P. (2013) Transient ICP-MS measurements in highly saline solutions. European Winter Conference on Plasma Spectrochemistry, Krakow, Poland (Poster).

Sander J.M., Hein C., Kautenburger R., Beck H.P., Kickelbick G. (2013) Batch experiments made easy - automation of ICP-MS batch experiments. Migration Conference, Brighton, Great Britain (Poster).

Wiehn T. (2014) Untersuchungen zum Sorptionsverhalten von Huminsäure, Europium und Uran an Opalinuston“. Bachelorarbeit, Naturwissenschaftlich-Technische Fakultät III, Universität des Saarlandes, Saarbrücken.

6 References

Agilent (2008) *Agilent 7500 Series ICP-MS Hardware Manual*. Manual Part Number G3270-90106, Edition Rev. A, September 2008.

Altmann S. (2008) 'Geo'chemical research: a key building block for nuclear waste disposal safety cases. Journal of Contaminant Hydrology 102, 174–179.

Anderson J.L., Eyring E.M., Whittaker M.P. (1964) Temperature Jump Rate Studies of Polyborate Formation in Aqueous Boric Acid. The Journal of Physical Chemistry 68, 1128-1132.

Bernhard G., Geipel G., Reich T., Brendler V., Amayri S., Nitsche, H. (2001) Uranyl(VI) carbonate complex formation: Validation of the $Ca_2UO_2(CO_3)_3$(aq.) species. Radiochimica Acta 89, 511–518.

Borkowski M., Richmann M., Reed D.T., Xiong Y. (2010) Complexation of Nd(III) with tetraborate ion and its effect on actinide(III) solubility in WIPP brine. Radiochimica Acta 98, 577–582.

Bradbury M.H., Baeyens B. (2003) *Far field sorption data bases for performance assessment of a high-level radioactive waste repository in an undisturbed Opalinus clay host rock*. PSI Bericht Nr. 03-08, Nagra NTB 02-19, Villigen.

Brewitz W. (1982) *Eignungsprüfung der Schachtanlage Konrad für die Endlagerung radioaktiver Abfälle*: Abschlussbericht (GSF-T136), GSF, Neuherberg.

Cornelis R., Caruso J., Crews H., Heumann K. (2005) *Handbook of Elemental Speciation II - Species in the Environment, Food, Medicine and Occupational Health.* John Wiley & Sons, Ltd, Chichester, UK.

Courdouan A., Christl I., Meylan S., Wersin P. Kretzschmar R. (2007). Isolation and characterization of dissolved organic matter from the Callovo-Oxfordian formation. Applied Geochemistry 22, 1537-1548.

Courdouan A., Christl I., Rabung T., Wersin P., Kretzschmar R. (2008). Proton and trivalent metal cation binding by dissolved organic matter in the opalinus clay and the callovo-oxfordian formation. Environmental Science and Technology 42, 5985-5991.

Denecke M.A. (2015) Actinide speciation using synchrotron-based methods. Journal of Radioanalytical and Nuclear Chemistry 303, 1339-1343.

Fröhlich D.R., Amayri S., Drebert J., Grolimund D., Huth J., Kaplan U., Krause J., Reich T. (2012) Speciation of Np(V) uptake byOpalinus Clay using synchrotron microbeam techniques. Analytical and Bioanalytical Chemistry 404, 2151-2162.

Fröhlich D.R., Skerencak-Frech A., Kaplan U., Koke C., Rossberg A., Panak P.J. (2015) An EXAFS spectroscopic study of Am(III) complexation with lactate. Journal of Synchrotron Radiation 22, 1469-1474.

Hahn R. (2014) Untersuchungen zur Metall-Komplexierung von Europium und Uran mit organischen Komplexliganden mittels Dialyse und Ultrafiltration. Masterarbeit, Naturwissenschaftlich-Technische Fakultät III, Universität des Saarlandes, Saarbrücken.

Harrison R.M., Rapsomanikis S. (1989) *Environmental Analysis Using Chromatography Interfaced with Atomic Spectroscopy*. John Wiley & Sons, New York.

Hein C., Sander J.M, Kautenburger R. (2014) Speciation via Hyphenation–Metal Speciation in Geological and Environmental Samples by CE-ICP-MS. Journal of Analytical & Bioanalytical Techniques 5, 225

Herbert H.-J., Schwandt A. (2007) *Salzlösungszuflüsse im Salzbergbau Mitteldeutschlands. Erfassung und Bewertung der chemischen und physikalischen Analyseergebnisse*. GRS-226.

Hinz K., Altmaier M., Gaona X., Rabung T., Schild D., Richmann M., Reed D.T., Alekseev E.V., Geckeis H. (2015) Interaction of Nd(III) and Cm(III) with borate in dilute to concentrated alkaline NaCl, $MgCl_2$ and $CaCl_2$ solutions: solubility and TRLFS studies. New Journal of Chemistry 39, 849–859.

Jandik P., Bonn G. (1993) *Capillary Electrophoresis of Small Molecules and Ions*. VCH Verlagsgesellschaft, Weinheim.

Kautenburger R., Beck H.P. (2007) Complexation studies with lanthanides and humic acids analysed by ultrafiltration and capillary electrophoresis - inductively coupled plasma mass spectrometry. Journal of Chromatography A 1159, 75-80.

Kautenburger R., Beck H.P. (2008) Waste disposal in clay formations: Influence of humic acid on the migration of heavy metal pollutants. ChemSusChem 1, 295-297.

Kautenburger R., Möser C., Beck H.P. (2010) Influence of Lanthanide Concentration and the Presence of Competing Metal Ions on Europium and Gadolinium Speciation with Humic Acid Analyzed by CE-ICP-MS. In: *Advances in Natural Organic Matter and Humic Substances Research 2008-2010* (Eds: J.A. González-Pérez, F.J. González-Vila & G. Almendros). Proceedings IHSS 15 (Vol. 1), 251-254.

Kautenburger R., Nowotka K., Beck H.P. (2006) Online analysis of europium and gadolinium species complexed or uncomplexed with humic acid by capillary electrophoresis–inductively coupled plasma mass spectrometry. Analytical and Bioanalytical Chemistry 384, 1416-1422.

Kautenburger R., Beck H.P. (2010) Influence of geochemical parameters on the sorption and desorption behaviour of europium and gadolinium onto kaolinite. Journal of Environmental Monitoring 12, 1295-1301.

Kautenburger R. (2009) Influence of metal concentration and the presence of competing cations on lanthanide speciation with humic acid analysed by CE-ICP-MS. Journal of Analytical Atomic Spectrometry 24, 934-938.

Kautenburger R. (2010) Endstation Tonstein? Nachrichten aus der Chemie 58, 751-756.

Kautenburger R. (2011) Batch is bad? Leaching of Opalinus clay samples and ICP-MS determination of extracted elements. Journal of Analytical Atomic Spectrometry 26, 2089-2092.

Kautenburger R. (2012) Geochemische Analytik: Endlager für radioaktiven Müll gesucht. Analytica PRO 2012, 59-60.

Kautenburger R. (2014a) Hochradioaktive Abfälle - Analytische Tools zur Suche nach einem geeigneten Endlager. GIT Labor-Fachzeitschrift 58, 38-41.

Kautenburger R. (2014b) A new timescale dimension for migration experiments in clay: proof of principle for the application of miniaturized clay column experiments (MCCE). Journal of Radioanalytical and Nuclear Chemistry 300, 255-262

Kautenburger R., Hein C., Sander J.M., Beck H.P. (2014) Influence of metal loading and humic acid functional groups on the complexation behavior of trivalent lanthanides analyzed by CE‑ICP-MS. Analytica Chimica Acta 816, 50-59.

Kautenburger R., Möser C., Beck H.P. (2011a) Lanthanide Migration in Natural Clay Formations - From Mineral Suspensions to Compact Clays. BMWi Project No.: 02 E 10196, Final report. Technische Informationsbibliothek (TIB), Hannover.

Kautenburger R., Möser C., Beck H.P. (2011b) Metal mobility in clay formations – From batch experiments with mineral suspensions to column setup with compacted clay. Mineralogical Magazine 75, 1157.

Kim H.J., Baek K., Kim B.K., Yang, J.W. (2005) Humic substance-enhanced ultrafiltration for removal of kobalt. Journal of Hazardous Materials 122, 31-36.

Kim J.I., Buckau G., Li G.H., Duschner H., Psarros N. (1990) Characterization of humic and fulvic acids from Gorleben groundwater. Fresenius Journal of Analytical Chemistry 338, 245-252.

Kim J.I., Czerwinski K.R. (1996) Complexation of Metal Ions with Humic Acid: Metal Ion Charge Neutralization Model. Radiochimica Acta 73, 5-10.

Klawiter J., Kaminski M., Kowalczyk J.S. (1982) Investigation of the relationship between packing methods and efficiency of preparative columns. II. Characteristics of the slurry method of packing chromatographic columns. Journal of Chromatography A 243, 207-224.

Kremleva A., Krüger S., Rösch N. (2013) Assigning EXAFS results for uranyl adsorption on minerals via formal charges of bonding oxygen centers. Surface Science, 615, 21-25.

Kuczewski B., Marquardt C.M., Seibert A., Geckeis H., Kratz J.V., Trautmann N. (2003) Separation of plutonium and neptunium species by capillary electrophoresis-inductively coupled plasma-mass spectrometry and application to natural groundwater samples. Analytical Chemistry 75, 6769-6774.

Lauber M., Baeyens B., Bradbury M.H. (2000) *Sorption of Cs, Sr, Ni, Eu, Th, Sn and Se on Mont Terri Opalinus Clay: physico-chemical characterisation and sorption measurements*. PSI Bericht Nr. 00-10 Villigen, and Nagra NTB 00-11, Wettingen.

Lohrengel B. (2012) *Einführung in die thermischen Trennverfahren*. Oldenbourg Wissenschaftsverlag, München.

Marquardt C.M. (Ed.) (2012) *Interaction and Transport of Actinides in Natural Clay Rock with Consideration of Humic Substances and Clay Organic Compounds*. KIT Scientific Reports 7633, KIT Scientific Publishing, Karlsruhe.

Marquardt C.M. (Ed.) (2008) *Migration of actinides in the system Clay, Humic substances, Aquifer.* Wissenschaftliche Berichte, FZKA 7407, FZ Karlsruhe, Karlsruhe.

Meleshyn A., Azeroual M., Reeck T., Houben G., Riebe B., Bunnenberg C. (2009) Influence of (Calcium−)Uranyl−Carbonate Complexation on U(VI) Sorption on Ca- and Na-Bentonites. Environmental Science and Technology 43, 4896-4901.

Melin T., Rautenbach R. (2007) *Membranverfahren*, Springer-Verlag, Berlin-Heidelberg.

Meyer V.R. (2009) *Praxis der Hochleistungs-Flüssigchromatographie*. Wiley-VCH, Weinheim.

Michalke B. (1999) Potential and limitations of capillary electrophoresis inductively coupled plasma mass spectrometry. Journal of Analytical Atomic Spectrometry 14, 1297-1302.

Mizera J., Mizerová G., Benes P. (2005) Radiotracer study of europium interaction with humic acid using electrophoresis, ultrafiltration, and dialysis. Journal of Radioanalytical and Nuclear Chemistry 263, 75-80.

Möser C., Beck H.P., Kautenburger R. (2012) Complexation of Europium and Uranium by Humic Acids Analysed by Capillary Electrophoresis - Inductively Coupled Plasma Mass Spectrometry. Electrophoresis 33, 1482-1487.

Möser C., Kautenburger R., Beck H.P. (2011) Migration of Europium and Uranium in Opalinus Clay Influenced by pH and Temperature. Mineralogical Magazine 75, 1504.

Möser C., Kautenburger R., Beck H.P. (2011) Migration of Europium and Uranium in Opalinus Clay Influenced by pH and Temperature. Mineralogical Magazine 75, 1504.

NAGRA (2002) *Projekt Opalinuston Synthese der geowissenschaftlichen Untersuchungsergebnisse Entsorgungsnachweis für abgebrannte Brennelemente, verglaste hochaktive sowie langlebige mittelaktive Abfälle*. Technischer Bericht NTB 02-03, NAGRA, Wettingen.

Oguenther (2011) https://commons.wikimedia.org/wiki/File:NMR-Spektrometer.svg, access: 21 January 2016.

Olesik J.W., Kinzer J.A., Olesik S.V. (1995) Capillary Electrophoresis Inductively Coupled Plasma Spectrometry for Rapid Elemental Speciation. Analytical Chemistry 67, 1-12.

Plaschke M., Rothe J., Denecke M., Fanghänel T. (2004) Soft X-ray spectromicroscopy of humic acid europium (III) complexation by comparison to model substances. Journal of electron spectroscopy and related phenomena 135, 53-62.

Pourret O., Davranche M., Gruau G., Dia A. (2007) Competition between humic acid and carbonates for rare earth elements complexation Journal of Colloid and Interface Science 305, 25-31.

Prange A., Schaumlöffel D. (1999) A new interface for combining electrophoresis with inductively coupled plasma mass spectrometry. Fresenius Journal of Analytical Chemistry 364, 452-456.

Pröfrock D., Leonhard P., Ruck W., Prange A. (2005) Development and characterisation of a new interface for coupling capillary LC with collision-cell ICP-MS and its application for phosphorylation profiling of tryptic protein digests. Analytical and Bioanalytical Chemistry 381, 194-204.

Röllin S., Eklund U.B. (2000) Determination of U(IV) and U(VI) by ion chromatography-inductively coupled plasma mass spectrometry and its application to kinetic studies. Journal of Chromatography A 884, 131-141.

Rollion-Bard C., Blamart D., Trebosc J., Tricot G., Mussi A., Cuif J.-P. (2011) Boron isotopes as pH proxy: A new look at boron speciation in deep-sea corals using ^{11}B MAS NMR and EELS. Geochimica et Cosmochimica Acta 75, 1003-1012.

Ronconi L., Sadler P.J. (2008) Applications of heteronuclear NMR spectroscopy in biological and medicinal inorganic chemistry. Coordination Chemistry Reviews 252, 2239-2277.

Salentine C.G. (1983) High-field boron-11 NMR of alkali borates. Aqueous polyborate equilibria. Inorganic Chemistry 22, 3920-3924.

Schaumlöffel D., Prange A., Marx G., Heumann K.G., Brätter P. (2002) Characterization and quantification of metallothionein isoforms by capillary electrophoresis-inductively coupled plasma-isotope-dilution mass spectrometry., Analytical and Bioanalytical Chemistry 372, 155-163.

Stevenson F.J. (1994) *Humus Chemistry*, Wiley-VCH, New York.

Sutton R., Sposito G. (2005) Molecular structure in soil humic substances: the new view. Environmental Science and Technology 39, 9009-9015.

Tertre E., Berger G., Simoni E., Castet S., Giffaut E., Loubet M., Catalette H. (2006) Europium retention onto clay minerals from 25 to 150 °C: Experimental measurements, spectroscopic features and sorption modelling. Geochimica et Cosmochimica Acta 70, 4563-4578.

Tertre E., Berger G., Castet S., Loubet M., Giffaut E. (2005) Experimental sorption of Ni^{2+}, Cs^{+} and $Ln^{(3+)}$ onto a montmorillonite up to 150 degrees C. Geochimica et Cosmochimica Acta 2005 69, 4937-4948.

Timerbaev A.R. (2009) Inorganic species analysis by CE – An overview for 2007–2008. Electrophoresis 31, 192–204.

Timerbaev A.R., Timerbaev R.M. (2013) Recent progress of capillary electrophoresis in studying the speciation of actinides TrAC - Trends in Analytical Chemistry 51, 44-50.

Wrobel K., Sadi B.B., Wrobel K., Castillo J.R., Caruso J.A. (2003) Effect of Metal Ions on the Molecular Weight Distribution of Humic Substances Derived from Municipal Compost: Ultrafiltration and Size Exclusion Chromatography with Spectrophotometric and Inductively Coupled Plasma-MS Detection. Analytical Chemistry 75, 761-767.

Retardation of radionuclides relevant to waste disposal in clay stone and saline systems - sub-project 1

Rückhaltung endlagerrelevanter Radionuklide im natürlichen Tongestein und in salinaren Systemen – Teilprojekt 1

Final Report

Karlsruher Institut für Technologie, Institut für Nukleare Entsorgung

Förderkennzeichen 02E10961

Nidhu Banik, Muriel Bouby-Laliron, Nicolas Finck, Katja Hinz, Tom Kupcik, Rémi Marsac, Andreas Schnurr, Christian Marquardt, Thomas Rabung

Bundesministerium für Wirtschaft und Energie

Das diesem Bericht zugrundeliegende Vorhaben wurde mit Mitteln des Bundesministeriums für Wirtschaft und Technologie unter dem Förderkennzeichen 02E10961 gefördert. Die Verantwortung für den Inhalt dieser Veröffentlichung liegt bei den Autoren.

Zusammenfassung

Das hier beschriebene Vorhaben lief in den Jahren 2011 bis 2015 in Rahmen des BMWi Förderprogramm „Entsorgung gefährlicher Abfälle in tiefen geologischen Formationen: Verbesserung von Instrumentarien für die Sicherheitsbewertung von Endlagern und Untertagedeponien“. Die Untersuchungen umfassten Sorptions-, Diffusions-, Komplexierungs- und Löslichkeitsexperimente mit dem Schwerpunkt auf Tonstein- und Salzsteinsysteme. Durch das Vorhaben wurde eine große Anzahl neuer experimenteller Daten als Schlüssel-Eingangsgrößen für die Bewertung des Quellterms (maximal erwartete Löslichkeit) der Actiniden (III, IV, V, VI) in Tonstein/Salzstein gewonnen. Durch die Wahl der experimentellen Bedingungen wurde ein breites Spektrum von Endlagerkonzepten und -szenarien abgedeckt.

Die Sorptionsuntersuchungen wurden mit dreiwertigen, vierwertigen, fünfwertigen und sechswertigen Actiniden untersucht: Cm(III)/Eu(III), Np(IV/V)), Pu(IV/V) und U(VI); Eu(III) wurde als dreiwertiges chemisches Analogon für dreiwertige Actiniden eingesetzt. Die Sorption der Actiniden wurde untersucht an dem reinem Tonmineral Illit und an dem natürlichen Tonstein Opalinuston, bei variierenden Grundelektrolyt-Konzentrationen und –Gemischen unter Ausschluss von CO_2. Die Batch-Experimente wurden ergänzt durch Laserfluoreszenz-Untersuchungen, welche zwischen pH_c 3 und 12 (für $MgCl_2$-Lösungen wegen der Ausfällung von $Mg(OH)_2$ nur bis pH_c 9) durchgeführt wurden.

Die experimentellen Sorptionsdaten zeigen für Eu(III) einen nur kleinen Einfluss der Salinität auf den log K_D-Wert., speziell im neutralen bis basischen pH_c-Bereich. In saurem Medium wird die Sorption mit steigender NaCl-Konzentration verringert, da der Kationenaustausch-Prozess durch Erhöhung der Na^+-Konzentration unterdrückt wird. Der gleiche Effekt wird auch in $CaCl_2$ und $MgCl_2$-Lösungen beobachtet. Bei pH_c-Werten größer als 8 wird in allen untersuchten Systemen eine beinahe vollständige Sorption mit log $K_D \geq 4.5$ erhalten. Zeitaufgelöste Laserfluoreszenz-Spektroskopie (TRLFS)-Untersuchungen mit Cm(III) in salinen Lösungen zeigen, dass die erste Koordinations-Schicht von dem Metallion nicht signifikant verändert wird und damit die Cm(III)-Speziation durch die erhöhte Ionenstärke nicht beeinflusst wird. Für die Modellierung mit dem Oberflächenkomplexierungsmodell 2SPNE SC/CE wurden über den gesamten Ionenstärkebereich deshalb identische Spezies angenommen. Dieses Modell beschreibt die Eu(III)/Cm(III) Sorption über den gesamten pH- und Ionenstärkebereich recht gut. Die Aktivitätskoeffizienten und die Wasseraktivität wurden hierbei mit dem Pitzer-Modell angepasst.

Die Sorption der Aktinylionen Np(V) und U(VI) wird durch die Ionenstärke über den untersuchten pH_c-Bereich kaum beeinflusst. Wie erwartet ist die Sorption von Np(V) schwächer als für die anderen Kationen. Sie startet ab ca. pH_c 8 (>20 %) und erreicht bei $pH_c > 10$ eine quasi-quantitative Sorption. Die experimentellen Daten können mit

dem 2SPNE SC/CE-Sorptionsmodell gut beschrieben werden. Die Sorptionskanten der U(VI)-Sorption ähneln der Sorptionskanten von Eu(III). Allerdings ist die pH-Kante für U(VI) ein wenig zu kleineren pH-Werten verschoben, da das U(VI) leichter hydrolysiert. U(VI) zeigt kaum Kationenaustausch und die pH-abhängige Sorption beginnt bei etwa pH_c 4. Die Sorption ist zwischen pH 6 und 11 quasi quantitativ. Bei höheren pH-Werten nimmt die Sorption ab, weil als dominierende Spezies $UO_2(OH)_4^{2-}$ gebildet wird und die zweifach negative Ladung dieser Spezies die Uran-Sorption stark verringert. Die Modellierung mit dem 2SPNE SC/CE-Sorptionsmodell beschreibt die experimentellen Daten recht gut bis pH_c ~ 7. Bei höheren pH-Werten werden mit dem Modell niedrigere K_d-Werte als im Experiment erhalten und es wird eine Ionenstärke-Abhängigkeit vorhergesagt, die nicht im Experiment beobachtet wurde.

Die Sorption von Np(V) wurde auch über längere Reaktionszeiten von bis zu 2 Monaten als Funktion des pH-Wertes (pH 3-10) und in 0.1 M NaCl-Lösungen unter Argonatmosphäre untersucht. Ab einer Reaktionszeit von einer Woche wurde keine weitere Veränderung der Sorption von Np beobachtet und das Erreichen eines Gleichgewichtszustand konnte damit vermutet werden. Unter anaeroben Bedingungen sind die Fest-Flüssig-Verteilungskoeffizienten (K_d oder R_d) der Np(V)-Sorption an Illit allerdings größer als unter Luft. Die Beobachtung, dass R_d mit abnehmenden pe-Wert (pe = -log a_{e^-},negative dekadischer Logarithmus der Elektronenaktivität in Lösung) zunimmt, lässt auf eine Reduktion des fünfwertigen zu vierwertigem Np schließen. Über das in Lösung gemessene Redoxpotential wird auf einen ersten Blick das Np(V) als dominierende Redoxstufe vorhergesagt. Allerdings konnte eine Reduktion von Np(V) an der Illit-Oberfläche über XANES-Messungen (Röntgen-Nahkanten-Absorptionsspektroskopie) bestätigt werden. Die Np(IV/V)-Speziation in Gegenwart von Illit konnte konsistent mit dem 2SPNE SC/CE-Modell beschrieben werden. Die experimentell gemessenen pe-Werte wurden für die Berechnung des Np-Redoxzustands verwendet, wobei die notwendigen Oberflächenkomplexierungskonstanten für das vierwertige Np (Np(IV)) an die experimentellen Daten angefittet wurde. Die so erhaltenen Konstanten sind konsistent mit Konstanten, die über einen „linear free energy relationship“ (LFER) abgeleitet wurden. Die vorliegende Studie zeigt hiermit, dass die Reduktion von Np(V) in der Gegenwart von sorbierenden Mineral-Oberflächen im Vergleich zur wässrigen homogenen Lösung ohne Festkörper thermodynamisch bevorzugt ist.

Die Pu-Sorption an Illit wurde ebenfalls untersucht in 0.1 M NaCl-Lösung und unter anaeroben Bedingungen. Im pH-Bereich 3 bis 10 ist die Sorption von Pu sehr stark (log R_d > 4 L kg^{-1}). Ein Mischung von Pu(III) und Pu(IV) wird bei pH < 5 beobachtet. Eine solche starke, pH-unabhängige Sorption wird im Modell unter Berücksichtigung der gemessenen Redoxpotential und damit abgeleiteten individuellen Redoxverteilung von Pu erhalten, wenn man für die unbekannten Pu(III)-Daten Eu(III)-Illit-Sorptionsdaten verwendet (Eu(III) gilt als chemisches Analogon für Pu(III)). Wie schon mit Eu(III) gezeigt wurde, wird die Pu(III,IV)-Sorption durch die Anwesenheit von Calcit in Illit/Calcit-Suspensionen kaum beeinflusst. Die hier aus experimentellen Daten und Modellierungen erhaltenen Sorptions-Daten können gut verwendet werden um die Pu-Rückhaltung in reduzierenden calcit-haltigen Grundwässern, wie sie für nukleare Endlager durchaus zu erwarten sind, vorherzusagen.

Generell kann man als Ergebnis für die Sorptionsstudien hervorheben, dass die Vorhersagen mittels dem 2SPNE SC/CE-Modell ganz gut mit den experimentellen Daten übereinstimmen, wenn man Ionenstärke-Korrekturen für die Aktivitäten der gelösten Spezies mit dem Pitzer bzw. SIT-Modell vornimmt und dabei die Redoxgleichgewichte der Spezies in der Lösung berücksichtigt. Eine starke bis sehr starke Sorption der drei-, vier-, fünf- und sechswertigen Aktiniden an Tonmineralien wird erwartet unter salinen Bedingungen und Abwesenheit von Karbonat.

Im Rahmen der Arbeiten bezüglich der Rückhaltung von Radionukliden an Eisenkorrosionsprodukten wurde Grüner Rost-Chlorid und Magnetit, die dreiwertiges Neodym und Americium enthalten (Nd, Am), synthetisiert. Die Festkörper wurden charakterisiert mittels Röntgendiffraktometrie (XRD) und Raman-Spektroskopie. Zusätzlich wurden Informationen mittels Röntgen-Photoelektronen-Spektroskopie (XPS) bezüglich Speziation der Strukturelemente und den Dopant erhalten. Scanning-Elektronenmikroskopie (SEM) lieferte Informationen über die Größe und Form der Partikel. Grüner Rost (GR) wurde hergestellt, indem eine Mischung aus Fe(II) und Fe(III)-Ionen in Anwesenheit von Nd(III) direkt ausgefällt wurde. Der dotierte Nd(III)-GR wurde mit sauerstofffreien Wasser gewaschen, um die Umwandlung zu Magnetite zu starten und anschließend zu charakterisieren. Parallel dazu wurde Magnetit aus einer Fe(II)/Fe(III)-Lösung synthetisiert, die auch Tracer-Konzentrationen an Am(III) enthielt. Es ist schwierig die gesamten Ergebisse der Raman, XRD und SEM-Untersuchungen in Einklang zu bringen. Aber in keinen der Proben beeinflusste der Dopant die entstandene Mineralphase und weder Nd(III) noch Am(III) bildeten eine separate Phase durch Ausfällung.

Die Diffusion von HTO, Cl^-, Eu, Np(V) und Fulvinsäure in Illit wurde in „In“-Diffusions- oder „Through“-Diffusions-Versuchen untersucht. Hierzu wurden kompaktierte, zylindrische Na-Illit-Proben und NaCl als Grundelektrolyt verwendet. Die Diffusionsparameter von HTO und Cl^- wurden in 0.1 M und 0.5 M NaCl untersucht. Die Diffusions-Koeffizienten (D_e) und die Porosität (ε) für HTO sind für beide Ionenstärken sehr ähnlich und zeigen, dass die Erhöhung der Ionenstärke kaum einen Einfluss auf die geometrischen Eigenschaften (Tortuosität (α), Konstriktivität) des Illits hat. Für das Anion Chlorid ist D_e und α in 0.5 M NaCl größer als in 0.1 M. Im Vergleich zu HTO ist D_e kleiner und kann mit einem reduzierten zugänglichen Porenraum für anionische Tracer erklärt werden. Anionen werden durch die negativ geladenen Tonoberfläche in den Poren abgestoßen. Der Diffusionsversuch mit Eu(III) zeigte ein stetiges Abnehmen der Eu(III)-Konzentration im Reservoir bis fast auf null über eine Zeitdauer von 1500 h. Eu(III) wird damit vollständig im Ton aufgenommen. Eine Desorption des Eu(III) mit einem Wasser/Alkohol-Gemisch Eu(III) wurde nicht beobachtet. Np(V)-Diffusion wurde in zwei „Through“-Diffusions-Experimente mit PEEK/Membran bzw. Edelstahlfilter durchgeführt. Nach 100 Tagen Reaktionszeit wurde ein Durchbruch von Np(V) beobachtet, wobei ein Steady State nicht erreicht wurde. Der Kurven-Verlauf des Diffusionsflusses als Funktion der Zeit, als auch die zeitliche Abnahme der Np(V)-Konzentration im Reservoir war in beiden Experimenten signifikant unterschiedlich. Eine schlüssige Erklärung für diese Unterschiede konnte bisher nicht gefunden werden. Fulvinsäure zeigt ebenfalls eine Diffusion durch kompaktierten Illit. Aus den experimentellen Daten wurde ein Diffusionskoeffizient mit $D_e = 1.51 \times 10^{-11}$ m^2/s bzw. 1.70×10^{-11} m^2/s für 0.1 und

1.0 M NaCl ermittelt werden. Für α wurden Werte von -0.44 und 0.61 (0.1 und 1.0 M NaCl) abgeleitet. D_e für Fulvinsäure ist hierbei vergleichbar mit D_e-Werten für negativ geladene Tracer wie $^{36}Cl^-$. Auf der anderen Seite erscheint der negative Wert für α recht unrealistisch.

Die vorliegenden Untersuchungen der Np(V)-Komplexierung mit den niedermolekularen Tonorganika Propionat und Lactat zeigt, dass hauptsächlich jeweils ein 1:1-Komplex – Np(V)-Propionat- bzw. Np(V)-Lactat-Komplex gebildet wird. Die Komplexbildungskonstanten wurden zu log β_0 (25° C) = 1.32 ± 0.05 für Np (V) Propionat und log β_0 (25° C) = 2.07 ± 0.01 für Np (V) Lactat bestimmt. Beide Komplexbildungskonstanten nehmen mit der Ionenstärke (0.5 <NaCl <2.5 m) und der Temperatur (20 <T <60 ° C) zu. Die Komplexbildungsreaktion ist für die Propionat-Komplexierung endotherm und entropiegetrieben, gemäß der folgenden ermittelten Daten für $\Delta_r H^0_m$ = 16.3 ± 3.0 kJ mol^{-1} and $\Delta_r S^0_m$ = 77 ± 9 J mol^{-1} K^{-1}. Die Größe von $\Delta_r S^0_m$ ist konsistent mit einem zweizähnigen Koordinationsmodus, was auch durch spektroskopische Ergebnisse bestätigt wird. Die Laktatkomplexbildungsreaktion ist dagegen exotherm und entropiegetrieben, was durch $\Delta_r H^0_m$ = -5.4 ± 1.4 kJ mol^{-1} und $\Delta_r S^0_m$ = 19 ± 4 J mol^{-1} K^{-1} belegt wird. Dieses Verhalten wird vermutlich durch den Einfluss der α-Hydroxyl-Gruppe im Laktat verursacht.

Die Stabilität bei höheren Salinitäten von natürlichen kleinen organischen Komponenten (SSOM) und Fulvinsäure (FA) wurde in NaCl-, $MgCl_2$- und $CaCl_2$-Lösungen untersucht. Die ersten Ergebnisse zeigen eine hohe Stabilität des SSOM unter den vorliegenden Bedingungen: Der DOC variiert um weniger als 5-10%, und ein Einfluss ist bis zu 3 M NaCl nicht zubeobachten. Bei Ionenstärken (IS) von 5 M NaCl, sowie 3 M $CaCl_2$, $MgCl_2$ und HCl zeigen sich bei den Absorptionsspektren einige Veränderungen. Eine detailiertere Auswertung der Absorptionsspektren mittels „Differential Spectroscopy“ lässt vermuten, dass die Erhöhung der IS spezifisch bestimmte Gruppen beeinflusst (Aromaten mit oder ohne Substitution wie –OH oder –COOH subsitutierte Benzolringe oder Carboxylphenole). Eine Veränderung der Konformation bzw. Größe der Komponenten wurde durch eine Kombination von Größenausschlusschromatographie (SEC) und UV-Vis-Absorptions-Spektroskopie identifiziert. Natürliche und synthetische FA zeigen bei steigender Ionenstärke mit NaCl (> 3 M) eine Erhöhung des hydrodynamischen Radius (Molekulargewicht), während die Zugabe von $CaCl_2$ oder $MgCl_2$ eine Verkleinerung des Makromoleküls bewirkt. Der maximale hydrodynamische Radius wurde mittels SEC zu 2 nm, 1.7 nm und 3.8 nm für FA-573, FA-532 und SFA-1 bestimmt. Mit diesen Untersuchungen wurde gezeigt, dass die natürlichen Fulvinsäuren ihre Mobilität als Kolloide auch in natürlichen Grundwässern mit höheren Ionenstärken beibehalten.

Im Rahmen einer Promotion wurde der Einfluss von Borat auf die Komplexbildungsreaktionen, Löslichkeiten und Redoxreaktionen der Actiniden untersucht unter endlagerrelevanten Bedingungen. Die Untersuchungen erstreckten sich von verdünnten bis salinaren Lösungssysteme sowie von reduzierten (+III) bis zu oxidierten (+VI) Actinid-Redoxzuständen. Für die dreiwertigen Ln/An(III) und das fünwertige Np(V) wurde der

größte Einfluss von Borat auf die Löslichkeiten beobachtet. Löslichkeitsdaten in Verbindung mit Festkörper- und Lösungs-Charakterisierung wurden beschrieben mittels der Gleichgewichtsthermodynamik der aquatischen Systeme und dem SIT-Formalismus für Ionenstärkekorrekturen. Die Bildung von schwerlöslichen Ln/An(III)- und An(V)-Borat-Festphasen stellt einen bisher unbekannten Rückhaltemechanismus für dreiwertige und fünfwertige Actiniden dar. Diese Art von Rückhaltung ist besonders für das mobile Np(V) relevant. Die erhaltenen Ergebnisse verdeutlichen, dass die Borat-Wechselwirkung für die korrekte Abschätzung der Actinidenverhaltens unter Endlagerbedingungen berücksichtigt werden muss.

.

Summary

This project was performed from 2011 to 2015 within the frame of the BMWi R&D program “Entsorgung gefährlicher Abfälle in tiefen geologischen Formationen: Verbesserung von Instrumentarien für die Sicherheitsbewertung von Endlagern und Untertagedeponien“ The studies comprises sorption, diffusion, complexation and solubility experiments with focus on clay systems as well as salt rock systems. The investigations within the project generated new experimental data which provides key inputs for the assessment of the source term (maximum expected solubility) for actinides (III, IV, V, VI) covering a wide spectrum of waste disposal concepts and scenarios.

The sorption studies were performed with tri-, tetra-, penta-, and hexavalent actinides: Cm(III) and Eu(III) as trivalent analogon, respectively, Np(IV/V)), Pu(IV/V) and U(VI). The sorption was investigated on pure clay mineral illite and the natural claystone opalinus clay by varying the background electrolyte concentration and composition (($[NaCl]_{max}$ = 4.0 M, $[MgCl_2]_{max}$ = 2.0 M und $[CaCl_2]_{max}$ = 4.0 M) and with exclusion of CO_2. The batch experiments and the laser fluorescence investigations were performed at pH_c between 3 and 12 (for $MgCl_2$ up to pH_c 9).

The experimental sorption data shows for Eu(III) a small influence of the salinity on the log K_D values, especially in the neutral up to the alkaline pH_c range. In acidic media the sorption is significantly diminished with increasing NaCl concentration, because the cation exchange reaction is suppressed with increasing Na^+ concentration in solution. This effect is also observed for $CaCl_2$ and $MgCl_2$. Nevertheless, a almost quantitative sorption (log $K_D \geq 4.5$) occurs for all systems at $pH_c > 8$. TRLFS investigations with Cm(III) in saline systems hints to no significant change of the first coordination sphere of the metal ion, meaning that the surface speciation of Cm(III) is not influenced by elevated ionic strength. Identical surface species were also assumed for the modelling of the experimental data with the 2SPNE SC/CE sorption model. This model describes the Eu(III)/Cm(III) sorption over the total pH_c and ionic strength range. For the adjustment of the activity coefficients of the solution species and the water activity the Pitzer approach was used.

The actinyl cations Np(V) and U(VI) shows no significant ionic strength influence of the sorption over the total pH_c range. As expected, the sorption of Np(V) is weaker than the other cations and starts at pH_c ~ 8 (>20%), but reaches quasi quantitative sorption at $pH_c > 10$. The experimental data can be described with the 2SPNE SC/CE model quite well. The sorption edges of U(VI) systems are comparible with the Eu(III) systems. Because of the slightly stronger hydrolysis the U(VI) pH edge is slightly shifted to lower pH_c values. No significant cation exchange is observed at the experimental conditions and the pH dependent sorption starts (<20%) at about pH_c ~4. The sorption is quasi quantitative (> 99,5%) between pH_c 6 and 11. At higher pH_c values the sorption decreases, because the two-fold negative charged species $UO_2(OH)_4^{2-}$ dominates the aqueous speciation. The modeling with the 2SPNE SC/CE model describes quite well the experimenta data up to pH_c ~ 7. At higher pH_c values the model predicts a lower

sorption and an ionic strength influence of the sorption that is not observed in the experiment.

The sorption of Np(V) onto illite was also intensively investigated over reaction times until two months as a function of pH (3-10) in 0.1M NaCl under Ar atmosphere. After about one week reaction time under ambient atmosphere, only an insignificant variation of Np sorption is observed and the establishment of reaction equilibrium can be assumed. Surprisingly, solid-liquid distribution ratios (R_d) are clearly higher than those measured for Np(V) sorption onto illite under aerobic conditions. The observation that R_d increases with decreasing pe (pe = -log a_{e^-}, negative decadic logarithm of electron activity in solution) suggests partial reduction to Np(IV), although measured redox potentials (pe values) at a first glance suggest the predominance of Np(V). Reduction to Np(IV) at the illite surface could indeed be confirmed by X-ray absorption near-edge spectroscopy (XANES). Np speciation in presence of the purified Na-illite under given conditions is consistently described by applying the 2SPNE SC/CE model. Measured pe data are taken to calculate Np redox state; the necessary surface complexation constants for Np(IV) are derived by applying a data fitting procedure. These constants are very consistent with results obtained by applying an existing linear free energy relationship (LFER). The Np(V)/Np(IV) redox borderline of a Eh-pH diagram, calculated with the new Np(IV) surface complexation constants, is shifted in presence of illite surfaces by 3-5 pe units (0.2-0.3 V) towards redox neutral conditions. Our study suggests that Np(V) reduction in presence of a sorbing mineral phase is thermodynamically favored in contrast to the solution without the solid.

We also investigated Pu sorption onto illite under anaerobic conditions in 0.1 M NaCl. In the pH range 3 < pH < 10, Pu uptake is constantly high (log R_d > 4 L kg^{-1}). A mixture of Pu(III) and Pu(IV) occurs in solution for pH < 5. Using Eu(III)-illite uptake data (with Eu(III) as a chemical analogue of Pu(III)), adsorption models for the individual redox states and measured redox potentials, overall Pu uptake is accurately predicted for a mixture of redox states. As in previous sorption studies on Eu(III), results for Pu(IV) interaction with an illite:calcite mixture suggest that Pu(III,IV) uptake by illite is weakly affected by the presence of carbonate. Our experimental and modeling results can be used to predict Pu retention in the reducing, calcite saturated groundwaters expected for potential nuclear waste repository sites.

Generally, the model prediction with the 2SPNE SC/CE model agree quite well with the experimental values by using ionic strength corrections – Pitzer or SIT - for the activity of the aqueous species and including redox equilibria in solution. A strong sorption of trivalent, tetravlent, pentavalent and hexavalent actinides on clay minerals is expected under saline conditions and absence of carbonate.

Concerning the impact of iron corrosion products on radionuclide retention, the syntheses and characterization of green rust chloride and magnetite containing trivalent f-elements (Nd, Am) was performed. The bulk solids were characterized by X-ray diffraction (XRD) and Raman spectroscopy and X-ray photoelectron spectroscopy (XPS) was

used to obtain information on the speciation of the various structural elements and dopant. Finally, scanning electron microscopy (SEM) provided information on the size and shape of the particles. Green rust (GR) was synthesized by direct precipitation of a mixture of Fe(II) and Fe(III) ions in the presence of trace amounts of Nd(III) or Am (III). The doped GR were washed with deoxygenated water to initiate their transformation to magnetite, but only the Nd-containing sample was analyzed. Separately, magnetite was synthesized by direct precipitation from a solution containing Fe(II) and Fe(III) ions and trace amounts of Am(III). It is difficult to harmonise the results of Raman spectroscopy, XRD, and SEM data, but in none of the sample the dopant (Nd or Am) had an influence on the synthesis of iron phase and it does not precipitate as a separate phase.

The diffusion of HTO, Cl^-, Eu, Np(V), and fulvic acid in illite was investigated in in-diffusion or through-diffusion experiments. The diffusion ("in" or "through" diffusion) experiments were performed with compacted, cylindrical Na-illite samples and in NaCl as background electrolyte. The diffusion parameters of HTO and Cl^- were determined in 0.1 M and 0.5 M NaCl. HTO diffusion coefficients (D_e) and values for the porosity (ε) are similar in 0.1 and 0.5 M NaCl, indicating that an increase in background electrolyte concentrations has no effect on the geometrical properties (tortuosity (α) or constrictivity). For the anion Cl^-, D_e and α were deduced to be higher in 0.5 M NaCl. The lower D_e value for Cl^- compared to HTO can be related to a reduced accessible pore space for anionic tracers, as anions are repelled from the vicinity of the negatively charged clay surfaces. The diffusion experiment with Eu(III) showed a steadily decreasing Eu concentration in the reservoir for < 1500 h, and the Eu concentration dropped to almost zero. This result indicates a complete Eu uptake onto the Na-illite mineral. The Eu(III) was not released from the clay by replacing the reservoir solution with several water/alcohol mixtures. The Np(V) diffusion was investigated in two through-diffusion experiments with i) a PEEK/membrane set-up and ii) stainless steel filter set-up. A breakthrough of Np was observed after 100 days, but a steady state was not established. The time-dependent curves of the diffusion flux and the decrease of the Np concentration in the reservoir was different for both experimentals. These observations cannot be explained at the moment. Fulvic acid (FA) also shows diffusion in the compacted illite. The diffusion coefficients of $D_e = 1.51 \times 10^{-11}$ m^2/s and 1.70×10^{-11} m^2/s were deduced for 0.1 and 1.0 M NaCl, respectively. For α, the calculated values were -0.44 and 0.61 (0.1 and 1.0 M NaCl, respectively). The D_e for FA are comparable to D_e values determined for negatively charged traces (i.e. $^{36}Cl^-$). On the other hand, the value for the rock capacity factors seems to be unrealistic.

The present studies of the Np(V) complexation with low-molecular weight clay organics propionate and lactate show that the 1:1-complex – Np(V)-propionate or -lactate complex - is mainly formed. The complex formation constants were determined to be $\log \beta_0$ (25°C) = 1.32 ± 0.05 for Np(V) propionate and $\log \beta_0$ (25°C) = 2.07 ± 0.01 for Np(V) lactate. Both complex formation constants increase with ionic strength (0.5 < NaCl < 2.5 m) and temperature (20 < T < 60°C). The complex formation reaction is endothermic for propionate complexation and entropy driven, as evidenced in the present work with $\Delta_r H^0_m = 16.3 \pm 3.0$ kJ mol^{-1} and $\Delta_r S^0_m = 77 \pm 9$ J mol^{-1} K^{-1}. The magnitude of $\Delta_r S^0_m$ is consistent with a bidentate coordination mode, which is also confirmed by spectrocopic

results. However, the lactate complex formation reaction is exothermic and entropy driven, evidenced by $\Delta_r H^0_m$ = -5.4 ± 1.4 kJ mol^{-1} and $\Delta_r S^0_m$ = 19 ± 4 J mol^{-1} K^{-1}. This might be caused by the influence of the α-hydroxy group in the lactate molecules.

The stability of small sized organic matter (SSOM) and fulvic acid (FA) was studied in NaCl, $MgCl_2$, and $CaCl_2$ solutions. The first results indicate a high stability of the SSOM under the present conditions: the DOC varies by less than 5-10% and no effect is noticeable up to 3 M NaCl. At 5 M NaCl or ionic strength (IS) of 3 M for $CaCl_2$/$MgCl_2$ and HCl some variations are noticeable on the absorption spectra. A refined analysis of the absorption spectra by differential spectroscopy suggests, that an increase of the ionic strength affects more specifically some kind of groups (aromatic with or without substitution like –OH and –COOH-substituted benzene rings or carboxyphenols). Conformation (size) changes are qualitatively evidenced by a combination of size exclusion chromatography (SEC) and UV-Vis absorption spectroscopy. For the fulvic acids, natural or synthetic, the NaCl addition (> 3 M) results in an expansion of the hydrodynamic volume (molecular weight) while the addition of $CaCl_2$ or $MgCl_2$ results in a compaction of the macromolecule. The maximum hydrodynamic diameter values estimated from SEC data are respectively 2 nm, 1.7 nm and 3.8 nm for FA-573, FA-532 and SFA-1 respectively. The natural fulvic acids can thus certainly preserve their mobility in high ionic strength natural media

In the frame of a PhD thesis the impact of borate on the chemical behaviour of actinides has been studied under repository-relevant conditions, with special emphasis on complexation reactions, solubility phenomena and partly also on redox processes. The study extends from dilute to concentrated saline systems and from reduced (+III) to oxidized (+VI) actinide redox states. The strongest impact of borate on the solubility was observed ofr the trivalent Ln/An(III) and the pentavalent Np(V). Solubility data in combination with solid and aqueous phase characterization have been described and quantified in terms of equilibrium thermodynamics of aqueous systems using the SIT formalism for ionic strength corrections. The formation of sparingly soluble Ln/An(III)– and An(V)–borate solid phases represents a so-far unknown retention mechanism for these redox states, and it is especially relevant for the highly mobile Np(V). These results highlight the need of accounting for borate interactions for the correct assessment of actinide behaviour under repository conditions.

This work was performed at the Karlsruhe Institute of Technology, Institute for Nuclear Waste Disposal (KIT-INE) by several colleagues contributing to the experiments, data evaluation, implementation and writing of the present report:

Nidhu Lal Banik contributed to sorption studies of neptunium and plutonium on OPA and illite, complexation of Np(V) with lactate and propionate.

Muriel Bouby-Laliron contributed to studies of the stability of humic and fulvic acid at high ionic strengths.

Nicolas Finck contributed to interaction studies of actinides with iron phases

Katja Hinze contributed within the frame of her PhD thesis to the studies of borate impact on the actinide solubilities

Tom Kupcik contributed to diffusion studies of europium, neptunium and fulvic acid.

Christian Marquardt contributed to the sorption and complexation studies and was the editor of the final report.

Remi Marsac contributed to sorption studies of neptunium and plutonium on OPA and illite, modelling of sorption with PREEQC, complexation studies with humic and fulvic acids.

Thomas Rabung contributed to the sorption studies.

Andreas Schnurr contributed within the frame of his PhD thesis to sorption studies of curium, europium, uranium with OPA and illite, modelling of the experimental studies with PREEQC

In the studies are also involved some bachelor, master and DAAD students: Sarah Waltz, Alexandre Diascorn, Alesandre Vasiliev.

Table of Contents

1 Introduction

In the context of final disposal of radioactive waste in deep geological formations the sorption onto mineral phases and particularly onto surfaces of clay minerals represents an important retention mechanism for actinides. The sorption onto clay minerals was intensively investigated in the last decades. However, these investigations have mostly been performed at low back elektrolyte concentrations (I_{max} = 0.1 M). In Jurassic and Cretareceous clay deposits in Nothern Germany as well as in sediments in Canada, which are also discussed as host rocks for repositories, groundwaters with higher salt concentrations are expected. The geochemical modelling of radionuclide soption in saline solutions has not been developed so far. Therefore, the application of the widely used sorption model for low ionic strengths (2SPNE SC/CE) are to be tested for high ionic strength (I > 1 M) in the frame of this project. Relevant geochemical aspects were investigated regarding the retention of the actinides uranium, neptunium, plutonium, americium, curium as well as the lanthanide europium in clay stone. The lanthanide Eu represents a chemical anologon for trivalent actinides. The focuses in this project were on the sorption, diffusion, complexation and redox processes of the actinides at higher ionic strengths in clay systems. Some preliminary experiments were also performed at higher temperature, e.g. the complexation of Np(V) with clay organics propionate and lactate.

The opalinus clay (OPA) from the Mont Terri project (Switzerland) as a reference natural clay stone and, as one main component of the OPA, the pure clay mineral illite was taken for the studies. Additionally, aspects of the impact of corganic compounds found in the OPA, small molecules like propionate and polyelectrolytes like fulvic acids, are included in the investigations. The canister as an important component of the waste generates corrosion products in case of water intrusion into the repository that can have a positive influence on the retention of radionuclides. First experiments in this project have been performed to elucidate the role of these corrosion products on the retention. Another aspect has been studied: the interaction of borate with lanthanides (III) and actinides (III, IV, V, VI) in dilute to concentrated saline solutions. Boron can be present as component of the emplaced waste in a nuclear waste repository. In certain rock salt formations, high boron concentrations can also occur in the intruding brine solutions. In this framework, it is very relevant to understand the impact of borate in the chemical behaviour of actinides (e. g. complexation, solubility phenomena or redox processes) under repository relevant conditions.

The work within the project proceeded in close cooperation with the Helmholtz Center Dresden-Rossendorf, the Universities of Mainz, Potsdam, Heidelberg, Köln, the Saarland, as well as the Technical Universities Dresden and Munich.

2 Sorption of radionuclides on clay minerals and iron phases

Actinide retention at clay mineral surfaces is a well-established process, which has been intensely investigated in the context of nuclear waste disposal. Up to now, however, almost no experimental data for actinide sorption at elevated ionic strength is available in the literature. In addition, also no mechanistic sorption model exists that reliably describes actinide uptake at elevated ionic strength (I > 1 M). Such conditions are to be expected e. g. in the vicinity of a repository in rock salt formations, in the Jurassic and lower Cretaceous clay rock layers in Northern Germany and in sedimentary layers in Canada, which are identified as potential host rock for the disposal of high level nuclear waste. The results of these studies are presented in the first part of this chapter.

The clay barrier is not the only solid phase that can fix radionuclides. A second important retention phase in the near field is the iron from canister material that is converted into secondary iron phases during corrosion processes with ground water. These secondary phases might retain radionuclides by sorption and incorporation into the mineral structure. The relevance of such iron phases is elucidated in preliminary sorption experiments with the goal to help designing experiments for future projects. The second part of this chapter deals with the iron phases.

2.1 Sorption onto Clay minerals

Within the present study, the uptake of actinides (Cm(III) and the trivalent analogue lanthanide Eu(III), Np(V), Pu(IV/V) and U(VI)) onto illite and on an Opalinus clay sample was investigated in dilute to concentrated saline systems.

2.1.1 Trivalent actinides and lanthanides (Cm(III) and Eu(III))

The sorption of the trivalent actinide Cm(III) and the analogue element Eu(III) onto illite was investigated in NaCl, $CaCl_2$, and $MgCl_2$ solution. The investigated back electrolytes and their maximum concentrations were $[NaCl]_{max}$ = 4.0 M, $[MgCl_2]_{max}$ = 2.0 M and $[CaCl_2]_{max}$ = 4.0 M. To avoid carbonate complexation, the experiments were performed in the absence of CO_2 in a glovebox with argon atmosphere. Eu(III) batch sorption experiments and Cm(III) time-resolved laser fluorescence spectroscopy (TRLFS) studies were carried out in the pHc range 3 - 12 (for $MgCl_2$ solutions up to pHc = 9).

Clay materials were obtained as aqueous suspensions from the Laboratory for Waste Management (LES) of the Paul Scherrer Institute (PSI), Switzerland. The preparation and pretreatment (Bradbury and Baeyens, 2009a) of the Illite du Puy along with details of the experimental methodologies have been described in much detail in a number of previous publications (Baeyens and Bradbury, 2004; Bradbury and Baeyens, 2002, 2009a; Poinssot et al., 1999). Relevant information such as N2-BET surface area and

cation exchange capacity is available in these references and will not be repeated here. All suspensions were stored in the dark at 4 °C prior to use and utilized within one year after preparation.

All experiments were carried out under controlled argon atmosphere in glove boxes (O_2 ~ 2 ppm) at room temperature (25 ~ °C). Eu sorption measurements were carried out as a function of pH at constant ionic strength and solid to liquid ratio. Details of the experimental procedures, geochemical modelling and data evaluation are described in (Schnurr et al., 2015).

To simulate the clay/actinide/solution systems even at high ionic strengths, the computer program PHREEQC (Parkhurst and Appelo, 1999) was used, which has a built-in ability to handle both Pitzer equations and adsorption modeling. As we applied a non-electrostatic sorption model, there was no need to select a specific surface charge model to simulate surface This program also has a built-in SIT option, but the SIT formalism is restricted to I < 3–4 m. SIT coefficients for the Cm/Eu species were taken from (Neck et al., 2009).

We verified that the calculations involving the Pitzer formalism and an adsorption model gave consistent results. To this end a code comparison was carried out. One set of model calculations was performed using the program ECOSAT 4.8 (Keizer and van Riemsdijk, 1999). Because of the fact that to our knowledge no previously published surface complexation modeling that involves the Pitzer formalism, such a cross check was deemed to be useful. There are no fundamental differences between the two ways of calculations.

Table 1: Formation constants for hydrolysis and chloride complexation at infinite solution used for Eu in the sorption modeling. Data are from the NEA-TDB (Guillaumont et al., 2003)

Complexation reaction	log K°
$Eu^{3+} + H_2O = Eu(OH)^{2+} + H^+$	-7.2
$Eu^{3+} + 2\ H_2O = Eu(OH)_2^+ + 2\ H^+$	-15.1
$Eu^{3+} + 3\ H_2O = Eu(OH)_3 + 3\ H^+$	-26.2
$Eu^{3+} + 4\ H_2O = Eu(OH)_4^- + 4\ H^+$	-40.7
$Eu^{3+} + Cl^- = EuCl^{2+}$	0.24
$Eu^{3+} + 2\ Cl^- = EuCl_2^+$	-0.74

Eu sorption onto illite is modeled with the 2 site protolysis non-electrostatic surface complexation and cation exchange (2SPNE SC/CE) sorption model (Bradbury and Baeyens, 1997, 2002). The model considers two types of high surface density protolysable (W1 and W2) sites to simulate clay proton titration data. In the latest version of the model (Bradbury and Baeyens, 2009a), only strong sites, S, have been considered for modeling cation surface complexation data at trace metal ion concentrations.

Table 2: Cation exchange capacities (CEC) and surface hydroxyl group densities for SWy-2 and Illite du Puy (Bradbury and Baeyens, 2006, 2009a)

Site types	Na-SWy-2 Site capacity (mol/kg)	Na-illite Site capacity (mol/kg)
$\equiv S^{S}OH$	2.0×10^{-3}	2.0×10^{-3}
$\equiv S^{W1}OH$	4.0×10^{-2}	4.0×10^{-2}
$\equiv S^{S2}OH$	4.0×10^{-2}	4.0×10^{-2}
CEC (meq/100g)	87.7	22.5

Table 3: Protolysis of Eu(III) surface species to model Eu sorption on illite with the 2SPNE SC/CE model and SWy-2 for comparison reasons (Bradbury and Baeyens, 2006, 2009a)

Reactions	Na-SWy-2	Na-illite
Surface protolysis	Log $K_{protolysis}$	
$\equiv S^{S}OH + H^{+} = \equiv S^{S}OH_2^{+}$	4.5	4.0
$\equiv S^{S}OH = \equiv S^{S}O^{-} + H^{+}$	-7.9	-6.2
$\equiv S^{W1}OH + H^{+} = \equiv S^{W1}OH_2^{+}$	4.5	4.0
$\equiv S^{W1}OH = \equiv S^{W1}O^{-} + H^{+}$	-7.9	-6.2
$\equiv S^{W2}OH + H^{+} = \equiv S^{W2}OH_2^{+}$	6.0	8.5
$\equiv S^{W2}OH = \equiv S^{W2}O^{-} + H^{+}$	-10.5	-10.5

Table 4: Cation exchange reaction of illite (IdP) and SWy at infinite dilution to model Eu sorption on illite with the 2SPNE SC/CE model and SWy-2 for comparison reasons (Bradbury and Baeyens, 2006, 2009a), (Schnurr, 2015).

Cationic exchange reactions	Na-SWy-2	Na-illite
	Log $K_{protolysis}$	
$NaX + H^{+} \rightarrow HX + Na^{+}$	4.5	4.0
$2\ NaX + 2\ Ca^{2+} \rightarrow CaX_2 + 2\ Na^{+}$	-7.9	-6.2
$3\ NaX + Eu^{3+} \rightarrow EuX_3 + 3\ Na^{+}$	4.5	4.0
$3\ CaX_2 + 2\ Eu^{3+} \rightarrow 2\ EuX_3 + 3\ Ca^{2+}$	-7.9	-6.2

Table 5: Thermodynamic equilibrium parameters at infinite dilution to model Eu sorption on illite (IdP) with the 2SPNE SC/CE model (Bradbury and Baeyens, 2009b).

Surface complex[#] (log K_{SC})	Na-IdP	Na-IdP (p.w.)	Ca-IdP*	Ca-IdP (p.w.)
$\equiv S^SOEu^{2+}$	1.9	1.9	0.4 (Δ-1.5)	0.4
$\equiv S^SOEu(OH)^+$	-4.6	-4.1	-5.4 (Δ-0.8)	-4.9
$\equiv S^SOEu(OH)_2$	-12.8	-12.0	-13.1 (Δ-0.3)	-12.3
$\equiv S^SOEu(OH)_3^-$	-24.0	-23.2	-24.3 (Δ-0.3)	-23.7
$\equiv SSOCa_3Eu(OH)_6^{2+}$	-	-		-55.5

*: the values accord to the analog Δlog K_{SC} (values in parathesis) of Na-SWy to Ca-SWy in (Schnurr, 2015).

[#]: surface complex formation:

$\equiv S^SOH + Eu^{3+} = \equiv S^SOEu^{2+} + H^+$

$\equiv S^SOH + Eu^{3+} + H_2O = \equiv S^SOEu(OH)^+ + 2H^+$

$\equiv S^SOH + Eu^{3+} + 2H_2O = \equiv S^SOEu(OH)_2 + 3H^+$

$\equiv S^SOH + Eu^{3+} + 3H_2O = \equiv S^SOEu(OH)_3^- + 4H^+$

2.1.1.1 Sorption of Eu(III) on illite (IdP) in the NaCl system

Ionic strength has a small impact on log K_D values for Eu(III) in NaCl systems at near-neutral to alkaline pHc. Only under acidic pHc conditions where cation exchange is the dominating binding mechanism a significant decrease of Eu(III) sorption is observed with increasing NaCl concentration. Unlike to the NaCl system, a significant decrease in the uptake is observed in all solutions at elevated $MgCl_2$ and $CaCl_2$ concentrations. Nonetheless, log K_D values (K_D in $L \cdot kg^{-1}$) remain high (log $K_D \geq 4.5$) for all systems in the pHc range 8 - 11. TRLFS studies do not indicate any significant change in the first coordination sphere of Cm(III) at a given pHc if ionic strength is increased. As a consequence, we do not expect any change in the surface speciation of Cm(III) at elevated ionic strength compared to previous studies at low background electrolyte concentration. Identical surface species are assumed and Eu(III) uptake data are sufficiently well described using the 2SPNE SC/CE model calibrated at lower ionic strength. The impact of elevated ionic strength on the activities of solutes and of water is taken into account by applying the Pitzer approach.

The uptake of Eu onto illite is presented as percentage sorbed (Figure 1) and log K_D (Figure 2) versus pH_m. The sorption edges include replicate measurements from two years apart (2010 and 2012) with two different clay batches. The data points obtained with the two batches are plotted together in Figure 1 and 2. They do not differ significantly. The general pH_m dependent sorption of trivalent metal cations onto clay minerals shows the usual features. At low pH_m values and I = 0.09 m, Eu uptake is higher than 50% and reaches nearly 100% for pH > 5–6 (Figure 1). The uptake in the low pH region is reduced with increasing salt content. The amount of adsorbed Eu at pH_m = 3–

4 decreases from 50% to 70% for the lowest NaCl concentration (0.09 m) to nearly no sorption for higher NaCl concentrations (0.92 and 3.90 m). Also, a slight shift of the sorption edge to higher pH_m with increasing NaCl concentration is observed. Nevertheless, almost complete uptake of Eu (≥ 99.5%) is observed for all investigated NaCl concentrations at pH_m ≥ 6.5. The results for Eu sorption onto illite clearly show that for pH values relevant to nuclear waste disposal (pH_m~8) for typical clay porewater conditions and pHm > 10 in the presence of cementitious material), at least in pure NaCl solutions and in the absence of carbonate, no significant ionic strength effect is observed. Such a relationship might, however, simply be invisible due to large analytical uncertainties in this pH range. The shaded area in Figure 2 represents the region of very high log K_D values >6.2 corresponding to >99.97% sorption which corresponds to the calculated detection limit of our analytical method (based on the 3r standard deviation of the background criterion).

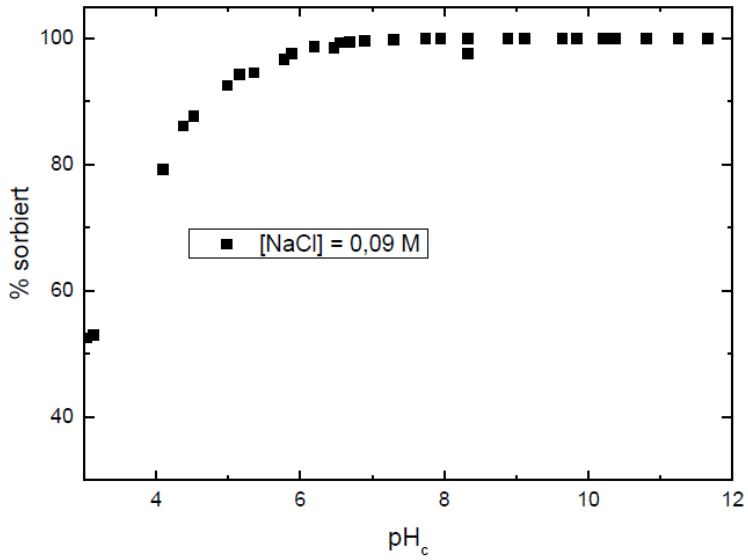

Figure 1: Eu(III) sorption on Illit du Puy (IdP) plotted as sorbed % against pH_c in NaCl (0.09 M) ; S :L = 2 g/L, $[Eu]_{total}$ = 2.0 x 10^{-7} M.

Additionally, the log K_d values for Cm(III) sorption on IdP, deduced from the fluorescence emission spectra discussed later on (s. next chapter), are also plotted in Figure 2. All own data are faced to the data from Bradbury and Baeyens (Bradbury and Baeyens, 2009a, 2015).

The dependence of the ionic strength on the Eu(III) sorption significantly occurs in the lower pH_c range until 6.5. The sorption decreases with increasing NaCl concentration; the main sorption mechanism of cation exchange is suppressed with increasing Na^+ concentration in solution. In the range of the main sorption mechanism of inner sphere complexation – pH_c > 6.5 – the ionic strength effect is very weak. Small deviations of the data are in the range of the experimental uncertainties. At pH_c ~ 8 and higher, the range of quasi quantitative sorption is observed. The experimental data at pH_c > 8.5 in

the present work are near the scope of the detection limit, which was estimated to be log K_d ≥ 6.25 (≥ 99.97 %) with 3σ standard deviation. The data within this range shows relatively large uncertainties.

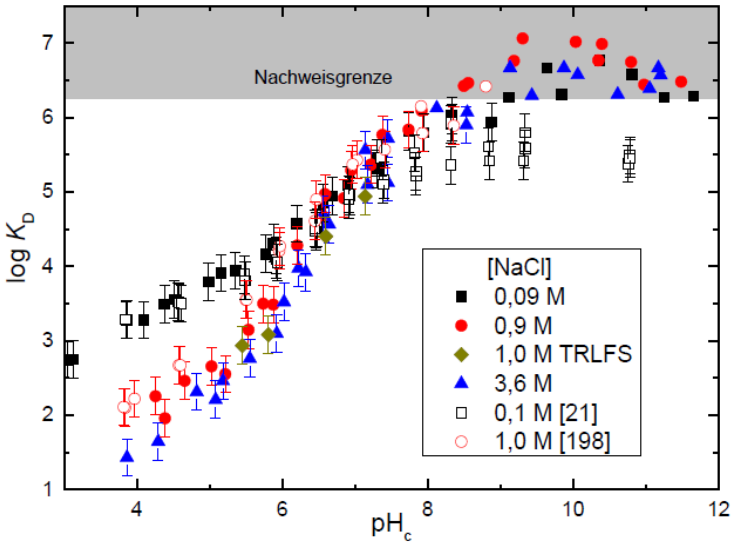

Figure 2: Eu(III) sorption on Illit du Puy (IdP) plotted as log KD against pHc at different NaCl concentrations (0.09, 0.90, 3.60 M) ; S :L = 2 g/L, [Eu]total = 2.0 x 10-7 M. The data from TRLFS measurments of Cm(III) sorption and data from literature (Bradbury and Baeyens, 2009a, 2015) are additionally shown.

By comparison of data in diluted NaCl solution from the present work with data from literature, both data set show almost identical trend of the sorption edge until pH_c of ~8. At pH_c > 8 the data of the present experimental work are about 0.5 – 0.8 log K_d units systematically larger than in previous work. The difference of about 0.5 log K_d units – this corresponce to a difference between 99.90 and 99.97 % sorption – occurs at very low Eu(III) concentration near the detection limit. The low metal concentration implies high requirements on the analytical methods for a reliable data evaluation. As a consequence, the difference among the individual data sets is not significant, equals the experimental uncertainties and is appraised as not relevant. Two possible reasons might explain the difference of the data sets, which only differ in the technique of the phase separation. Bradbury and Baeyens centrifuge the sample volumes at g_{max} = 105000 directly after reaching the equilibrium time and subsequently takes the supernatant for further investigations (Bradbury and Marques, 2013). In the present work the suspension was centrifuged after the equilibrium time with g_{max} = 694000 and finally the supernatant was conveyed by a syringe into a new vial. Either, the selection of the lower speed of centrifugation does not separate all particle sizes, especially nano-particles, and feigns lower sorption, or, an extra sorption of Eu(III) on the vial wall feigns higher sorption. The very small discrepancy of the results – percentual difference at the second decimal place - cannot be clarified because of the application of disparate tools.

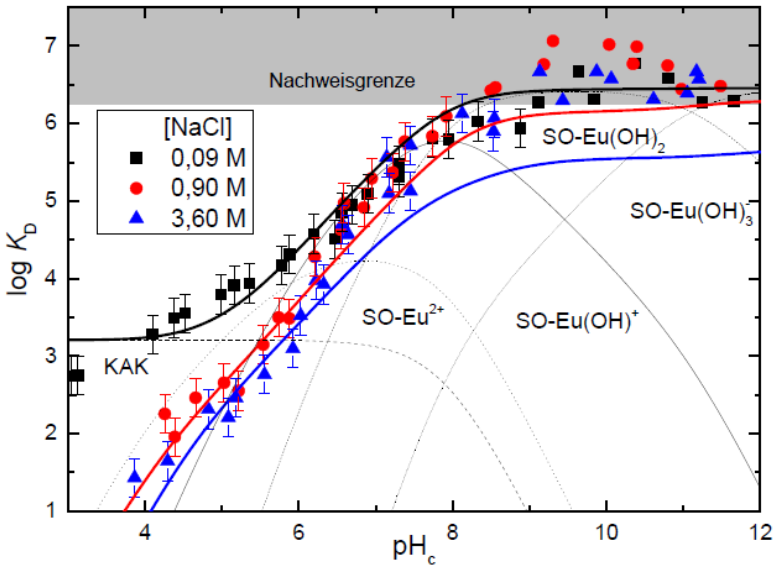

Figure 3: Modeling (solid lines) of the Eu(III) sorption data (symbols) plotted as log K_D against pH_c at different NaCl concentrations (0.09, 0.90, 3.60 M) ; S :L = 2 g/L, $[Eu]_{total}$ = 2.0 x 10^{-7} M. The 2SPNE SC/NE model with detailed sorption species distribution at I = 0.09 M was used.

To demonstrate the analogy of Eu(III) and Cm(III), the Cm(III) data at 1.0 M NaCl, deduced from TRLFS spectra, are also shown in Figure 2. TRLFS cannot differentiate between uncomplexed and free Cm(III) aqua ion in solution and outersphere sorbed Cm(III) spezies. But at high ionic strength the outersphere complexation is totally suppressed and the free Cm(III) aqua ion and the Cm(III) surface species can be discriminated spectroscopically and a log K_d can be determined. The Cm(III) data deduced from the spectra fits very well to the Eu(III) data from (Bradbury and Baeyens, 2015) and from this work.

The results of the modelling of the Eu(III) sorption data with the 2SPNE SC/CE approach are shown in Figure 3. The corresponding constants used for the calculation are listed in Table 2 Table 5. The constants of the surface complexes slightly differ from literature constants (Δlog K_{SC} ±0, +0.5, 0.8, 0.8 for the surface complexes SO-Eu^{2+} to SO-$Eu(OH)_3^-$), and they were adjusted to get the best fit to the latest data diluted NaCl solution. the curves. These adaptation was necessary to minimize the deviation of the experimental data from the modelling curve using literature data and to describe the data correctly. This correct data set at dilute ionic strength (I ≤ 0.1 M) for the modelling is a prerequisite to reliable describe the experimental data at saline conditions including the activity coefficients deduced by the Pitzer formalism. The modelling curve describes the experimental data at high ionic strengths quite well. The suppressed cation exchange at low pH values as well as the trend of the sorption edges is reflected correctly. Furthermore, the modelling of the probed systems specifies the quasi quantitative sorption (>99.5%; log K_d > 5.5) at pH_c > 8, according to the experimental data. However, the modelling also predicts a general ionic strength dependence of the sorption in the mid to high pH_c range, that is not observed in the experiments. Either, the relatively large uncertainties in the band of the detection limit because of the

analytical restrictions mask such a ionic strength dependence, or the model is inadequately parameterized. The approach of a non-electrostatic surface complexation model might also be inadequate for the application at very high ionic strengths. The implementation of an additional species like in the uranyl system (Schnurr, 2015), the mixed surface complex ΞSO-Eu-Cl-OH, could correct the deviation in the model. Such a species that occurs in only small concentrations could not be detected by spectroscopy and, hence, is not considered, here. Nonetheless, the modelling with the 2SPNE SC/CE model produces quite well results and can predict the Eu(III) sorption onto illite over a broad pH_c range at high saline NaCl solutions.

2.1.1.2 Sorption on Illit (IdP) in $CaCl_2$ and $MgCl_2$ systems

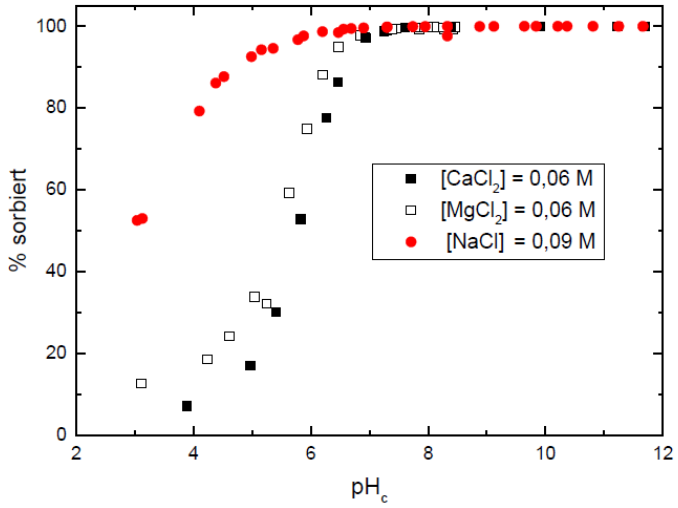

Figure 4: Comparison of Eu(III) sorption on Illite in NaCl (0.09 M), $CaCl_2$ (0.06 M) and $MgCl_2$ (0.06 M) solutions.

The results of Eu(III) sorption on illite in diluted $CaCl_2$ und $MgCl_2$ (0,06 M) solutions and for comparison reasons in NaCl (0.09 M) solution are shown in Figure 4. Because the $Mg(OH)_2$ precipitates at pHc > 9, the investigation stops for the Mg^{2+} system at pH_c 9 (Altmaier et al., 2003a). Figure 4 clearly demonstrates, that even in diluted solutions of $CaCl_2$ and $MgCl_2$ the cation exchange reaction is suppressed in contrast to NaCl solutions. At low pH_c values no significant sorption of Eu(III) is observed. The sorption edge is found in the pH_c range 5 – 7 and quasi full sorption is observed above pH_c ~7. There is no difference in the influence on the sorption between Mg^{2+} and Ca^{2+}. This behavior becomes clearer when the concentration of Ca and Mg is increased up to 2 M as shown in Figure 5. The sorption edges of each cation at the same concentration are almost superimposed. Differences in the sorption data between both cations are within the experimental error margin.

It stands out that the sorption edge shifts to higher pH_c values with increasing ionic strength at pH_c values below 9. At higher pH_c values no difference in the sorption is visuable, because the sorption is quasi quantitative, and it maintains independent of the ionic strength up to pH_c 12, the maximum pH value in the experiment.

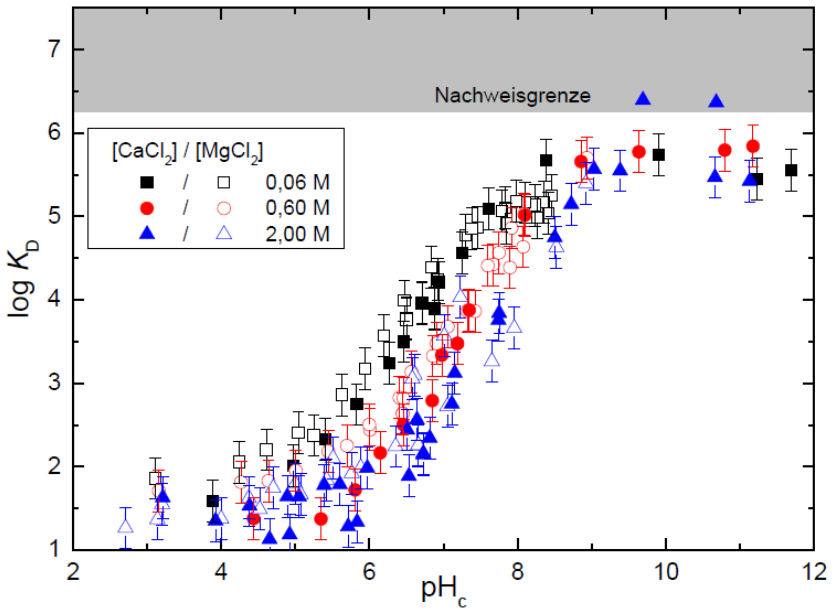

Figure 5: Distribution coefficients log K_d of Eu(III) sorption on illite ($[Eu]_{total}$ = 2,0 · 10^{-7} M, solid:liquid = 2 g/L) as a function of pH_c in $MgCl_2$ and $CaCl_2$ solutions with various concentrations (0.06, 0.60, 2.00 M).

Up to now, no surface complexation constants log K_{sc} are published for the Ca-Illite and Mg-illite surface complexes. As basis for an estimation of a parameter set for the illite sorption, the information from studies of the Eu(III) montmorillonite sorption has been taken. For montmorillonite, a parameter set of log K_{sc} values are given in the literature (Bradbury and Baeyens, 2006; Schnurr, 2015) for the Eu(III) sorption on Na-montmorillonite and Ca-montmorillonite (Na-SWy and Ca-SWy) at back ground electrolyte concentrations of [NaCl] = 0.1 M and [$CaCl_2$] = 0.06 M. For the illite only log K_{sc} values of the Na-illite are available. Analog to the montmorillonite system, the differences in the surface complexation constants between Eu(III) sorption on Na-SWy and Ca-SWy are taken to establish a new parameter set for Eu(III) sorption on Ca-illite (Ca-IdP). That means that the log K_{sc} values from the Eu(III)/illite/NaCl system were diminished by the same amount as found for the montmorillonite system (Δlog K_{SC} -1.5, -0.8, -0.3, -0.3 for the surface complex $\equiv$SO-Eu^{2+} to $\equiv$SO-$Eu(OH)_3^-$) (Table 5). The modelling of Eu(III) sorption on $CaCl_2$/$MgCl_2$ solution by the 2SPNE SC/CE including the new parameter set is shown in Figure 6.

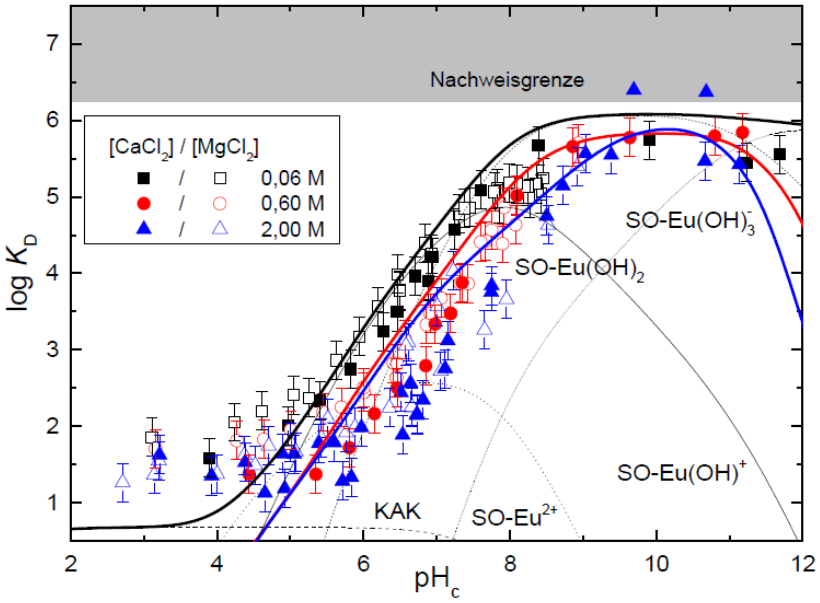

Figure 6: Eu(III) sorption ($[Eu]_{total}$ = 2.0 · 10^{-7} M) an IdP (S:L = 2 g/L) plotted as log K_D against pH_c values at various $MgCl_2$ und $CaCl_2$ concentrations (0.06, 0.60, 2.00 M). The lines are the modelled values by 2SPNE SC/CE modell including detailed sorption speciation at I = 0.18 M.

The experimental are described quite well with the modelled results for the diluted electrolyte solutions. The cation exchange reaction in the acidic pH_c range (< 5) is slightly underestimated, but has only minor relevance in the range of 10% total sorption. The increase of the sorption edge in the near neutral pH_c range (5 – 8) and the quasi quantitative sorption in the alkaline range (pH_c > 8) describes the observed behavior of the Eu sorption. The sorption edges in saline solution are also simulated quite well, but slightly overestimates the Eu(III) sorption in the middle pH_c range. But the deviation between modelled and experimental results is insignificant larger than the experimental error. At pH_c > 11, the simulated curves of log K_d abruptly drops down. This suppression of the sorption can be explained by the generation of a mixed Ca-Eu-OH species in solution, the dominant solution species at higher Ca concentrations and pH_c values Figure 7.

In summary we establish, that the pure NaCl system as well as the pure $CaCl_2$ ($MgCl_2$) system is described quite well from diluted to saline conditions by geochemical modelling with the certain parameter set. Consequently the question arises whether the sorption in mixed Na-Ca/Mg-Cl electrolyte systems, which is the general situation in natural ground waters, shows the same behavior and can also be described with the same quality.

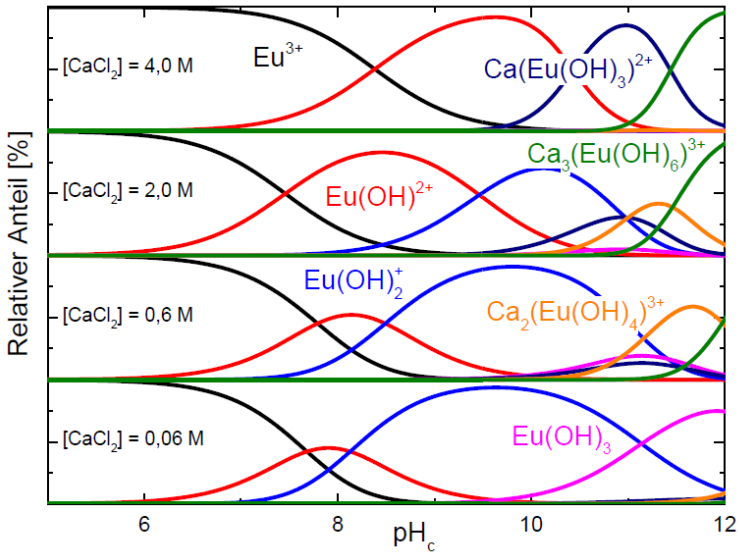

Figure 7: Speciation of Eu(III) in aqueous $CaCl_2$ solutions ($[Eu]_{total}$ = 2,0 · 10^{-7} M) in $CaCl_2$ ($[CaCl_2]$ = 0.06, 0.6, 2.0 and 4.0 M).

First investigations in a mixed electrolyte system are shown in Figure 8. Batch experiments of Eu(III) and Illite at two pH_c values (pH 6.1 and 7.3) were investigated at various concentration ratios of NaCl and $CaCl_2$. The ionic strength was kept constant at I = 1.0, to minimize the effect of the ionic strength. The choosen pH_c values correspond to conditions where inner-sphere complexation mainly occur. It is observed, that the Eu(III) sorption decreases with increasing $CaCl_2$ concentration at both pH_c values. However, the effect is quite small. The data are within the experimental error margin (max. Δ log K_D = 0.5) for pH_c 6.1. The effect is slightly larger at pH_c 7.3 with Δ log K_D = 0.8. The experimental uncertainty is certainly larger because of the stronger sorption. Still, a significant influence of the $CaCl_2$ on the Eu(III) sorption occurs, which is definitely not caused by an ionic strength effect.

For the modelling of mixed Na-Ca-Cl systems the relative portion of the ion exchange sites occupied by Na^+ and Ca^{2+} ions must be known. The fractions can be calculated by the selectivety coefficient based on the reaction 2 Na-X + Ca^{2+} = CaX_2 + 2 Na^+. The relative occupation of the sites by Na^+ and Ca^{2+} is listed in Table 6. The concentration of all available ionic exchange sites used in the modelling is divided into the clay fraction NaX and CaX_2. The Eu(III) sorption is described by surface complexation with the parameter set (log K_{sc}) for Na- and Ca-IdP. In a first approach, each of both clay mineral fractions are considered as single and independent illite fractions, the sodium form NaX and the calcium form CaX_2. The capacity of the available ion exchange sites is estimated from the cation exchange capacity. The sorption on both IdP fractions is estimated by the corresponding surface complexation constants of each surface species.

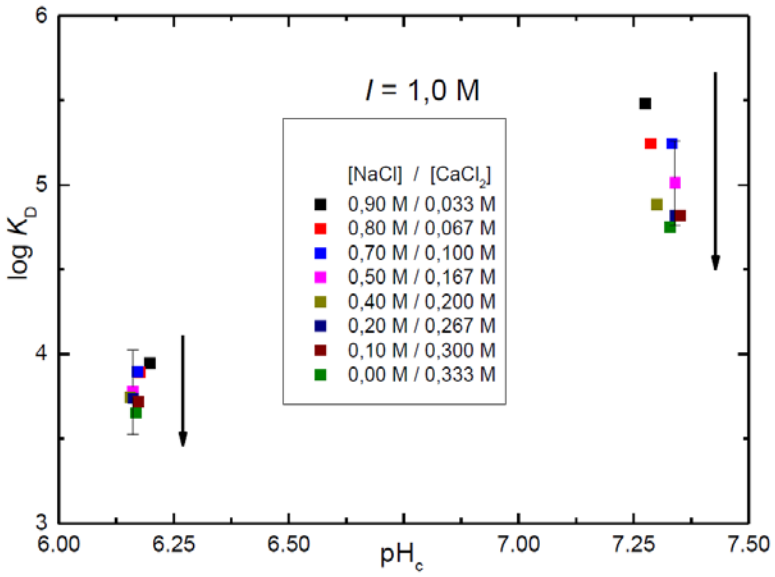

Figure 8: Eu(III) sorption ($[Eu]_{gesamt}$ = $2.0 \cdot 10^{-7}$ M) on IdP (S :L = 2 g/L) plotted as log K_d against the pH_c in different NaCl – $CaCl_2$ mixtures (I = 1 M).

Table 6: Calculation of the relative occupation of cation exchange sites ($[X_{gesamt}]$ = 4.5×10^{-4} M) in experiments with various NaCl/$CaCl_2$ ratios in solution (Bradbury and Baeyens, 2009a), (Schnurr, 2015).

[NaCl]	$[CaCl_2]$	[NaX]	$[CaX_2]$	NaX (%)	CaX_2 (%)
0.9	0.033	$3.80 \cdot 10^{-4}$	$3.50 \cdot 10^{-5}$	84.38	15.62
0.8	0.067	$3.21 \cdot 10^{-4}$	$6.41 \cdot 10^{-5}$	71.44	28.56
0.7	0.100	$2.72 \cdot 10^{-4}$	$8.89 \cdot 10^{-5}$	60.42	39.58
0.5	0.167	$1.85 \cdot 10^{-4}$	$1.33 \cdot 10^{-4}$	41.03	58.97
0.4	0.200	$1.45 \cdot 10^{-4}$	$1.52 \cdot 10^{-4}$	32.26	67.74
0.2	0.267	$7.06 \cdot 10^{-5}$	$1.90 \cdot 10^{-4}$	15.70	84.30
0.1	0.300	$3.50 \cdot 10^{-5}$	$2.07 \cdot 10^{-4}$	7.79	92.21
$1x10^{-5}$	0.333	$1.53 \cdot 10^{-7}$	$2.25 \cdot 10^{-4}$	0.03	99.97

The result of the modelling at conditions (Na^+ to Ca^{2+} ratios) depicted from Table 6 is shown in Figure 9. The simulation demonstrates a significant influence of the Ca^{2+} on the sorption. In the low pH_c range, the difference between low and high Ca^{2+} content is especially pronounced. In general, the difference increases with decreasing pH_c value. At pH_c values 8.5 and higher, the data between almost pure NaCl and $CaCl_2$ solutions differ only in ~0.3 log units; they can be regarded as constant considering the error margin. This observation follows the trend of the difference in the log K_{sc} values of both

clay fractions with 1.5 and 0.8 log units for surface species ≡SO-Eu^{2+} and ≡SO-$Eu(OH)^{+}$, respectively, in the acidic and neutral pH_c range. In the alkaline pH_c range the difference is only 0.3 log units between the log K_{sc} of ≡SO-$Eu(OH)_2$ und ≡SO-$Eu(OH)_3^-$.

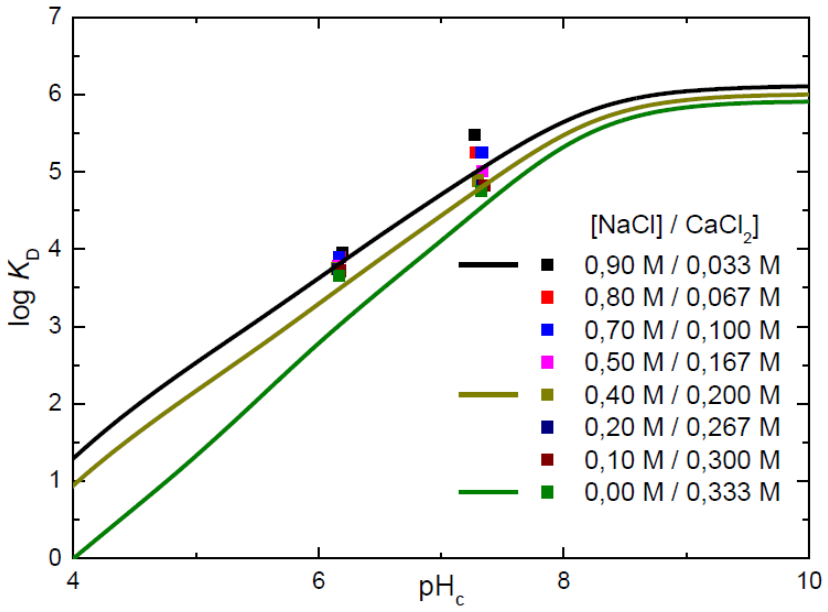

Figure 9: Eu(III) sorption ($[Eu]_{total}$ = 2,0 · 10^{-7} M) on illite (IdP) (S:L = 2 g/L) plotted as log K_D against the pH_c value in various NaCl - $CaCl_2$ mixtures (I = 1 M). The curves were generated by predictions with the 2SPNE SC/CE model.

Because of the limited number of data and relative high experimental error, the model approach could not completely be verified. This model approach needs to be proven by additional investigations. Nevertheless, the modelling reflects the general trend of the experimental data.

2.1.1.3 Curium (Cm(III)) sorption on illite (IdP)

TRLFS investigations of Cm(III) on SWy in NaCl and $CaCl_2$ electrolyte systems showed that the chloride as back electrolyte does not affect the innersphere surface species of Cm(III) (Schnurr et al., 2015; Schnurr, 2015). The spectroscopic investigations was performed to demonstrate whether the sorption of Cm(III) on illite differs from the sorption on montmorillonite. A comparison of the results of the batch sorption experiments between Eu(III) sorption on SWy and IdP showed very similar behavior (Schnurr et al., 2015). Figure 10 exhibits the fluorence emission spectra on the Cm-IdP system (m_{Cm} = 2 10^{-7} m, S:L ratio = 0.25 g/L) exemplary at ionic strength of 0.1 M NaCl. Parallel to this series, spectra were also recorded for ionic strengths of 1 and 4 M NaCl but they are not shown here. In comparison to the fully hydrated Cm^{3+}_{aquo} ion (pH_c = 1) the concentration of the aquatic Cm(III) species decreases with increasing pH_c value according to

increasing sorption. The band maxima simultaneously shifts to higher wavelengths. The emission spectra demonstrate that several species (surface and aqueous species) have to be considered and that the spectra are similar to the fluorescence spectra in the Cm(III)-SWy system (NaCl).

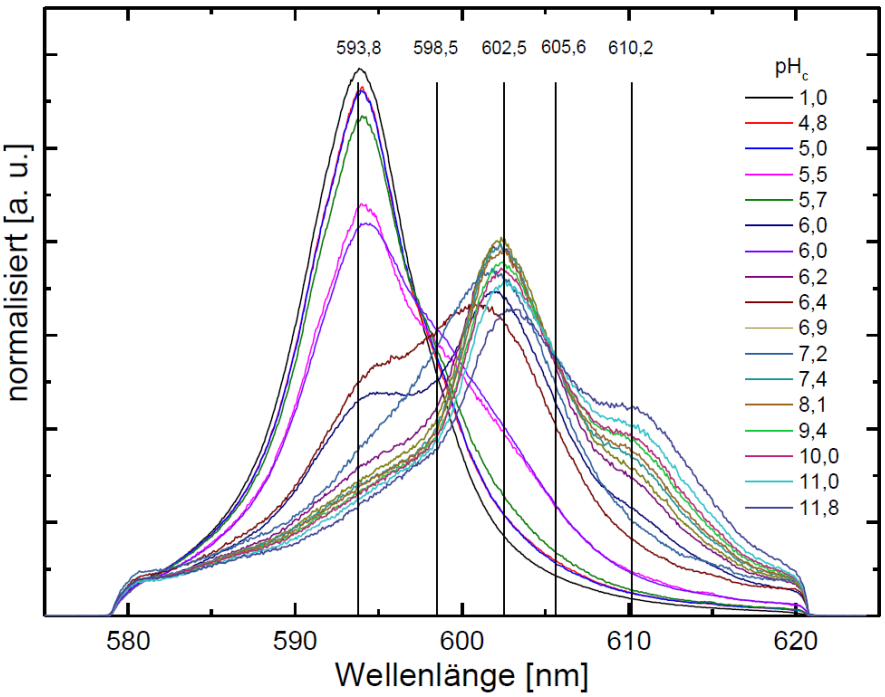

Figure 10: pH_c dependence of the TRLFS spectra (peak area normed) $[Cm]_{Total}$ = 2.0 · 10^{-7} M, [NaCl] = 0.1 M, IdP, S:L = 0.25 g/L.

Peak deconvolution of the spectra for each ionic strength results in a minimum of single compounds of four inner-sphere surface species. They exhibit emission band peak-maxima for illite (in brackets for montmorillonite) at approximate 598.5 (598.5), 602.5 (602.4), 605.6 (605.8) and 610.2 (610.4) nm (±0.2 nm) (Figure 10). The first three inner-sphere complexes can be assigned to the same surface species that had been previously reported for illite and montmorillonite (Rabung et al., 2005): >SOCm$(H_2O)_5^{2+}$, >SOCm(OH) $(H_2O)^{4+}$, >SOCm$(OH)_2(H_2O)_3$. An additional inner-sphere surface species with a higher peak shift was observed at high pH_m. From the compilation of all pure component spectra of the different electrolyte solutions (Figure 11) no significant influence of NaCl background electrolyte concentration on Cm surface speciation exists. Even at mNaCl = 4.37 m, peak deconvolution results in the four inner-sphere surface species with approximately the same emission band positions. This corroborates our modeling assumptions in having identical surface species independent of NaCl ionic strength.

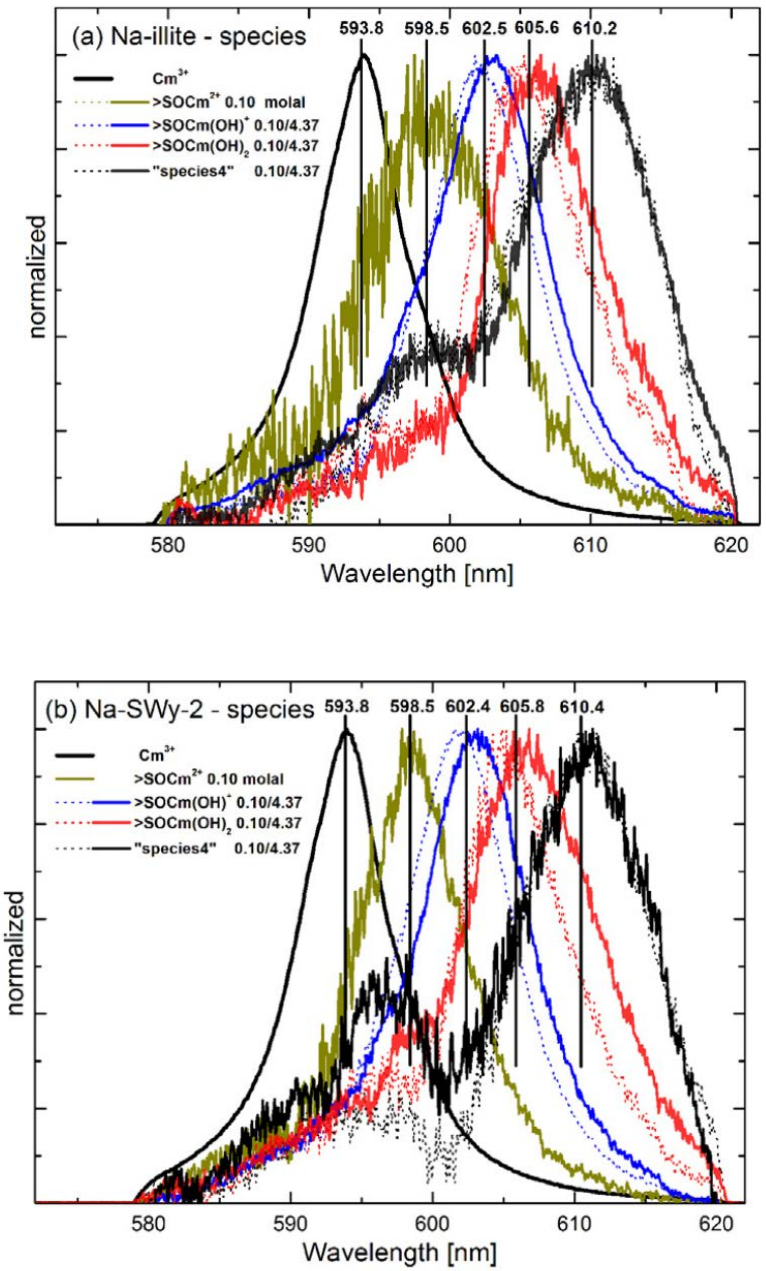

Figure 11: (a) Na-illite, (b) Na-SWy-2: Pure component spectra derived from peak deconvolution of measured fluorescence spectra obtained at each ionic strength (0.10, 4.0 M (0.10 and 4.37 m))

The measurements of fluorescence life times in the Cm(III)–IdP systems yield in τ_0 = 68±2 µs for Cm^{3+}_{aquo} ion and τ_1 = 113±10 µs, corresponding to a species with 4.8 ± 0.3 H_2O/OH^- units in the first coordination sphere of the Cm(III). The 4th sepcies at high pH_c values has a significant longer life time with τ_2 = 165±15 µs. These results agree quite well with earlier results in the montmorillonite system from (Rabung et al., 2005)

The lifetime measurements support the results and interpretations based on the fluorescence emission spectra that there is no ionic strength dependency for the different inner-sphere sorption species. Additional inner-sphere coordinated chloride would lead

to a further increase of the fluorescence lifetime. In view of the decreasing H_2O activity at high NaCl concentrations, the unchanged number of water molecules in the first Cm coordination sphere is certainly remarkable and points to a strong binding to the central metal ion.

The nature of the species causing the fluorescence band at 610 nm was examined in additional experiments concerning silicate in solution. Based on findings from (Huittinen et al., 2012), where a similar Cm species in their sorption studies with kaolinite was found from the fluorescence spectra, this species was assigned to a mixed clay mineral / curium / silicate surface complex. The occurrence of silicate in solution can be explained by dissolution of the clay material at alkaline conditions (pH_m > 10).

According to (Huittinen et al., 2012), Cm(III) illite samples were prepared at pH_c 9 and 0.1 M NaCl (TRIS buffer for pH fixation) and various amount of dissolved Si(IV) were added to the samples. The pH of 9 was chosen because no dissolution of the clay and, hence, no release of Si occurs and no absorption of any Si species is expected at 610 nm.

The spectra of the four samples with Si(IV) concentrations of 0, $1 \cdot 10^{-5}$, $1 \cdot 10^{-4}$, $1 \cdot 10^{-3}$ M are shown in Figure 12. Addition of small amount of Si(IV) has no effect on the Cm spectra. The shift of the maximum to 602.5 nm is not influenced by Si(IV) but is rather a consequence of the sorption to the illite resulting in the inner sphere species >SO-$Cm(OH)(H_2O)_4^+$. At Si)IV) concentrations of ≥ 10^{-3} M, which is below the solubility of amorphous silica, a change in the spectra accompanied by a significant peak shift (~604 nm) is observed. This supports the above mentioned hypothesis that with increasing silicate concentration in solution additional inner-sphere surface species involving silicate can be formed. A possible stoichiometry for the species at pH_m = 9 could be $>SOCm(OH)_x(SiO_4)_y\ (H_2O)_{4-x}$ (with x, y = 1, 2).

Based on this result, the 610 nm species in the illite sorption study might be assigned to a clay/curium/silicate/ hydroxo surface complex as the measured aqueous silica concentration is m_{Si} = 7 10^{-3} m at pHm > 11 (Bradbury and Baeyens, 2009a). The increased lifetime of τ = 165 ± 15 µs at higher pH values supports the hypothesis of a silicate containing Cm surface complex. Similar lifetime values have been reported by (Huittinen et al., 2012). The lifetime would be compatible with a $>SOCm(OH)_x(SiO_4)_y(H_2O)_{3-x}$ (with x, y = 1, 2) species with silicate binding in a bidentate mode. However, additional studies are required to obtain more information on the exact stoichiometry and structure of this surface complex.

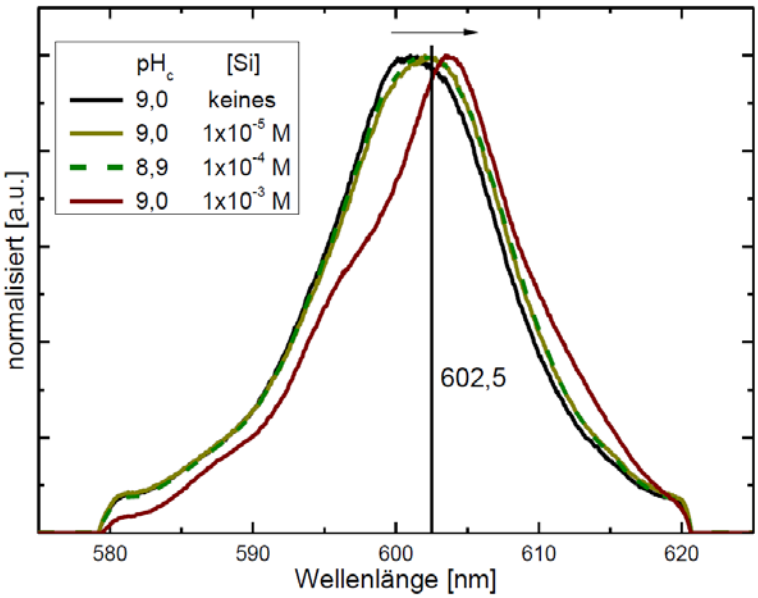

Figure 12: Cm(III) fluorescence spectra of solution containing IdP (0.25 g/L), different amounts of Si(IV) (0, $1 \cdot 10^{-5}$, $1 \cdot 10^{-4}$, $1 \cdot 10^{-3}$ M), and 0.1 M NaCl at $pH_c = 9$.

2.1.1.4 Sorption of Eu(III) on natural Opalinus clay mineral

Finally, the results of the sorption of the pure illite mineral have to be compared with a natural claystone. For that, the Opalinus clay (OPA) has been chosen, as one of the most investigated claystone originating from the Mont Terri underground facility. Because the OPA is a heterogenous compound containing many various minerals, we decide to use only the fraction of the clay minerals of the OPA. The Opalinus claystone was purified and minor components like organic compounds, calcite and quartz, were removed. The thus purified clay sample is named OPA-CF (OPA clay fraction) and consisted mainly of illite/smectite mixed phases, kaolinite and minor amounts of calcite. With OPA-CF batch sorption experiments similar to the former sorption experiments were performed. The experimental results are shown in Figure 13 together with data from the pure Eu-illite system in NaCl and $CaCl_2$ solutions. Following the “bottom up” approach from Bradbury and Baeyens, the mixed illite/smectide mix phases is handled like the pure illite mineral. That means that the sorption behavior of the OPA is governed by the illite, whereas minor components like kaolinite and chlorite are considered as not relevant. The results of the Eu(III) sorption experiments with OPA-CF are faced with those of the pure Eu(III) illite, without any corrections or assumptions.

Figure 13 (on the left, a, b, c) shows the comparison of both systems in NaCl solutions with various concentrations (0.09, 0.9, and 3.6 M). The Eu(III) sorption edge on illite and OPA-CF is for all NaCl concentrations quite similar and the increase of the sorption is nearly the same. The K_d values in the quasi quantitative sorption range with > 99.5 %

Eu(III) sorption (pH_c> 8) is for OPA somehow lower as the very high values for the pure illite system. But both systems show with log K_d values > 5 very strong sorption. In the pH_c range 9 – 10 the OPA-CF system shows a slightly diminished sorption at all ionic strengths. This is caused by a small amount of carbonate in solution released from the OPA-CF, because of dissolution of calcite as a component of OPA that could not be removed during the purification. Finally, we can state that the illite in the OPA-CF is the clay mineral fraction that dominates the sorption of Eu(III).

Figure 13 (on the right) shows also the comparison between Eu(III) sorption on OPA-CF and illite in $CaCl_2$ solutions. The sorption results show a slightly stronger sorption in the range of the sorption edge for OPA-CF at 0.06 M and partly at 0.6 M $CaCl_2$. However, this distinction is with < 0.5 log units within the margin of the experimental uncertainty. At pH_c and higher, both systems behave identically. The experimental data at 2.0 M $CaCl_2$ are also identical over the whole pH_c range, consistent with the Eu-Na-OPA system. The small difference in the Eu-Na-OPA system caused by the carbonat in solution at pH_c ~9 – 10, can not be observed in the Ca system. The reason could be the small carbonate concentration and the precipitation of calcite in the Ca containing solution. Analog to the NaCl system, the illite dominates the Eu(III) sorption in the OPA-CF and can be regarded as the main clay mineral fraction in the OPA responsible for the sorption of trivalent actinides.

2.1.2 Sorption of neptunium(V) onto illite in the NaCl system

Studies of the sorption of neptunium are somehow more complex than the trivalent lanthanides and actinides, because it is a redox sensitive element and can exist in two different oxidation states, the tetravalent and pentavalent oxidation state. Thus, the chemical behavior can change from weak to strong interactions and vice versa. The trivalent and the hexavalent neptunium has no relevance at environmental and reducing conditions like in a deep geologic formation. The studies were started with pentavalent neptunium (Np(V)) and the results of these sorption studies with illite are published in (Marsac et al., 2015a).

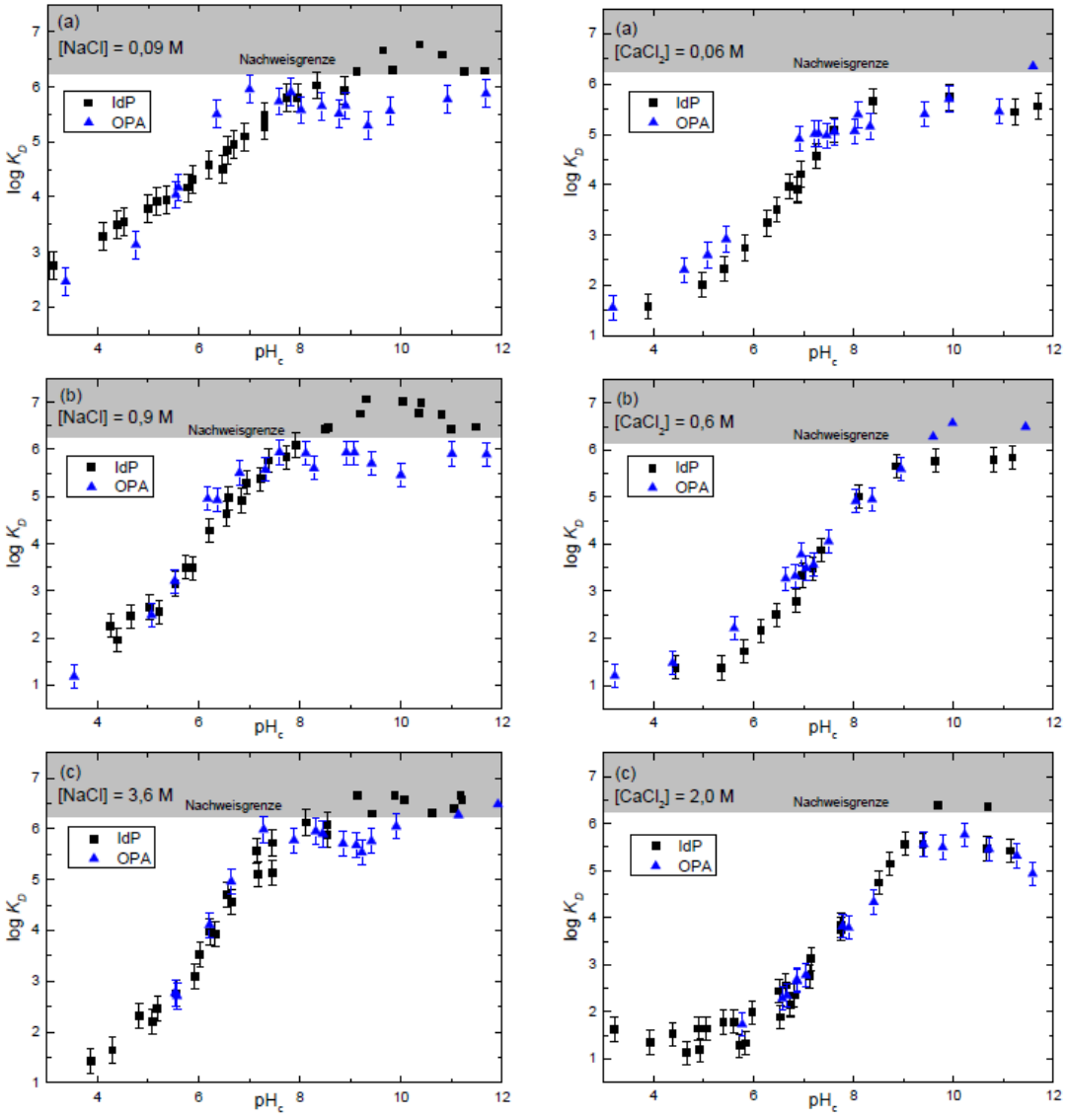

Figure 13: Eu(III) sorption on OPA clay fraction (OPA-CF) and IdP in NaCl (0.09, 0.90 und 3.60 M) and in $CaCl_2$ (0.06, 0.6, and 2.00 M) plotted as log Kd against pHc ([Eu]total = 2.0 · 10-7 M, S:L = 2 g/L).

2.1.2.1 Neptunium redox speciation on the illite surface

Purified Na-illite was used in this work and was provided within the EC project CP CatClay (www.catclay.org). The purification process is described in detail in (Marsac et al., 2015a). Despite intensive purification, the illite contains 7 wt.% Fe_2O_3.

All sorption experiments were performed as batch type experiments at initial Np(V) concentrations in the range of $3x10^{-8}$ to 10^{-4} M. Maximum Np concentration is below the solubility limit of relevant Np(V)-bearing solids (Guillaumont et al., 2003). The batch experiments were carried out at room temperature in an argon glove box (<1 ppm O2,

absence of CO2). At a solid to liquid ratio of 2 g/L, the suspensions were preconditioned in 0.1 M NaCl by shaking continuously for 4–5 days. To achieve a given target pH value 0.1 M HCl or 0.1 M NaOH were added. After 7, 21, 35 and 63 days, pH and Eh were measured in the suspension and an aliquot of each sample was centrifuged in a Ultracentrifuge at 90,000 rpm for 1 h. The supernatant and all other solutions were analyzed for Np by liquid scintillation counting (LSC). The oxidation state of Np in solution were determined by liquid-liquid extraction with HDEHP and PMBPA (Bertrand and Choppin, 1982; Nitsche et al., 1994).

Results obtained in batch experiments will be expressed throughout as distribution coefficients (Rd in L/kg), calculated by the following equation:

$R_d = ([Np]_{tot}/[Np]_{aq} - 1) \times V/m$

where $[Np]_{aq}$ and $[Np]_{tot}$ (mol/L) are the dissolved (final) equilibrium and total (initial) concentrations of Np in solution, respectively. The term V/m corresponds to the aqueous solution volume to illite mass ratio (L/kg). An uncertainty of ±0.3 is commonly associated with log R_d determination for radionuclide sorption to clay minerals (Bradbury and Baeyens, 2009a), although for low $[Np]_{tot}$ and high uptake, the uncertainty on log R_d might be higher.

Figure 14 presents the Np sorption to illite (Rd in L/kg) as a function of pH (i.e. pH-edge). Only the highest and the lowest Np total concentrations investigated in the present study at various pH are presented here: $[Np]_{tot} = 10^{-6}$ M (Figure 14a) and $3x10^{-8}$ M (Figure 14b). Results obtained for intermediate $[Np]_{tot}$ are consistent with those data. The complete dataset is provided within the supplementary file of (Marsac et al., 2015a). R_d values determined after different reaction times (7, 21, 35 and 63 days) are presented.

After about one week reaction time, only an insignificant variation of Np sorption is observed and the establishment of reaction equilibrium can be assumed. Surprisingly, solid–liquid distribution ratios (Rd) are clearly higher than those measured for Np(V) sorption onto illite under aerobic conditions.

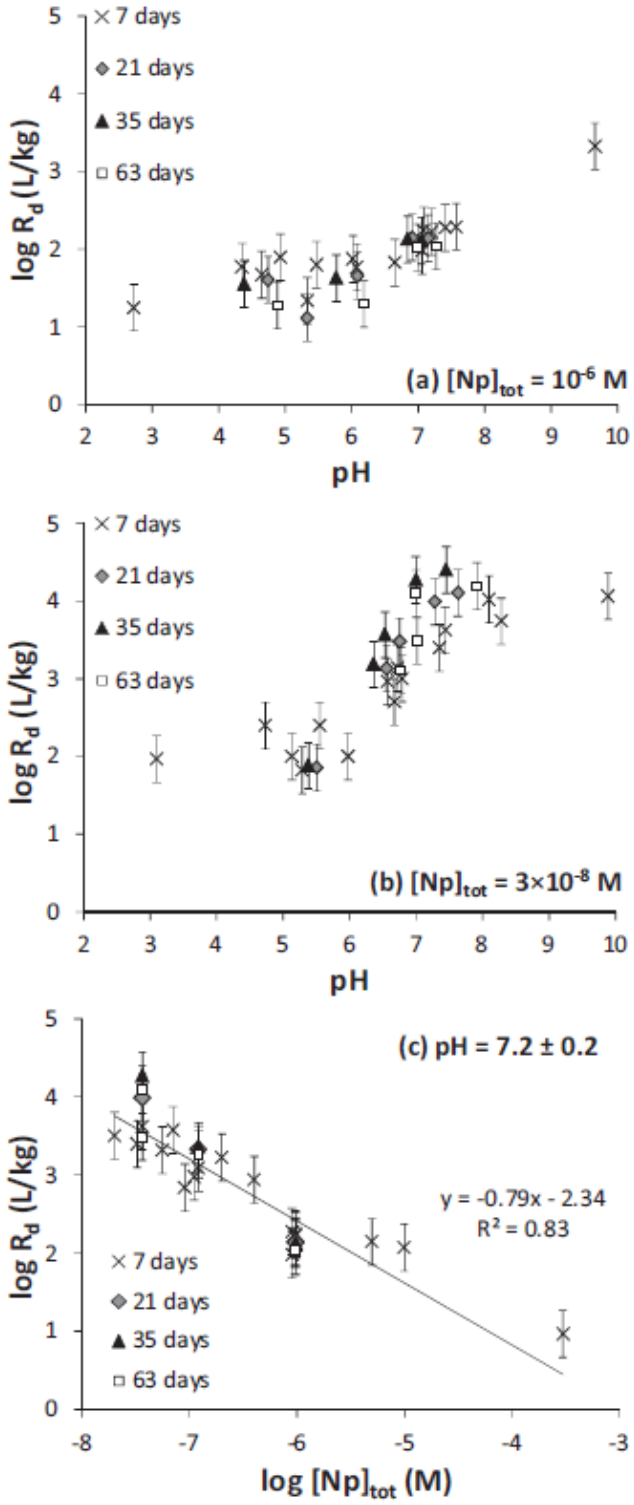

Figure 14: Np sorption to illite (R_d, in L/kg) versus pH measured for different reaction times (7, 21, 35, 63 days) and a Np total concentration of (a) 10^{-6} M and (b) $3x10^{-8}$ M. (c) Results obtained for pH = 7.2 ± 0.2 are plotted as log R_d versus $[Np]_{tot}$.

For $[Np]_{tot} = 10^{-6}$ M (Figure 14a), most of the data being recorded for pH < 8 show only a small increase of R_d with pH, which is consistent with the weak surface complexation

of Np(V) at the edges of clay particles. For $[Np]_{tot} = 3\times10^{-8}$ M (Figure 14b) and pH < 6, R_d values are relatively similar to those measured at higher metal ion concentration. However, a significant increase of R_d is observed for pH > 6 with values being 1 to 2 orders of magnitude higher than for experiments with $[Np]_{tot} = 10^{-6}$ M. Slightly more scattering R_d values are observed for $[Np]_{tot} = 3\times10^{-8}$ M but the sorption results are reproducible within an experimental uncertainty for log R_d of about ± 0.5. When increasing $[Np]_{tot}$, pH-edges are shifted to higher pH, i.e. a decrease of R_d with increasing $[Np]_{tot}$ is observed at a given pH. This is consistent with non-ideal sorption behavior of Np. Sorption data for pH = 7.2 ± 0.2 are plotted as log R_d versus log $[Np]_{tot}$ in Figure 14c, which further illustrates the non-ideal sorption behavior.

The observation that R_d increases with decreasing pe (pe = -log activity(e^-)) suggests partial reduction to Np(IV), although measured redox potentials (pe values) at a first glance suggest the predominance of Np(V). A redox state analysis applied to one of the samples (pH = 7.0; $[Np]_{tot} = 10^{-5}$ M; [NaCl] = 0.1 M; m/V = 2 g/L) also corroborates the partial reduction of Np(V) to Np(IV) on the illite surface. After one week contact time, only Np(V) is found in solution (93±10%). After re-suspending the illite in 1M HCl for 2 days, a significant amount of the desorbed Np is found to be Np(IV) (41±10%).

Np redox speciation at the illite surface is further investigated by XANES. The Np L_3-XANES measured at pH = 7.4 and 9.6, m/V = 20 g/L and 3×10^{-4} M of Np (initially introduced as NpO_2^+) is presented in Figure 15. These samples contain the highest $[Np]_{tot}$ and exhibits as well the highest pe (pe = 6.8 ± 0.8). At pH 7.4, 15 % of the total Np is sorbed onto illite (i.e. 2.3×10^{-3} mol/kg). XANES spectra of the NpO_2^+ and Np^{4+} aquo ions in 0.1 M $HClO_4$ from (Gaona et al., 2012) are used as references for Np(V) and Np(IV). The Np-illite XANES for pH = 7.4 shows significant differences compared to a Np(V) reference, especially an increase in WL intensity. Reduction to Np(IV) at the illite surface could indeed be confirmed by X-ray absorption near-edge spectroscopy (XANES). By fitting the Np-illite XANES with a linear combination of Np(V) and Np(IV) reference samples, 14 % of the adsorbed Np is determined to be Np(IV). In the sample at pH = 9.6, the measured pe does not significantly differ from that obtained at pH = 7.4 (pe = 6.8 ± 0.8), reflecting more oxidizing conditions. Due to the higher pH, 90 % of Np is sorbed to the illite surface (1.3×10^{-2} mol/kg). The Np L_3-XANES at pH 9.6 shows a less intense WL compared to pH 7.4. The LCF using the XANES spectra of NpO_2^+ and Np^{4+} aquo-ion shows that only 5 % of the adsorbed Np at the illite surface is Np(IV).

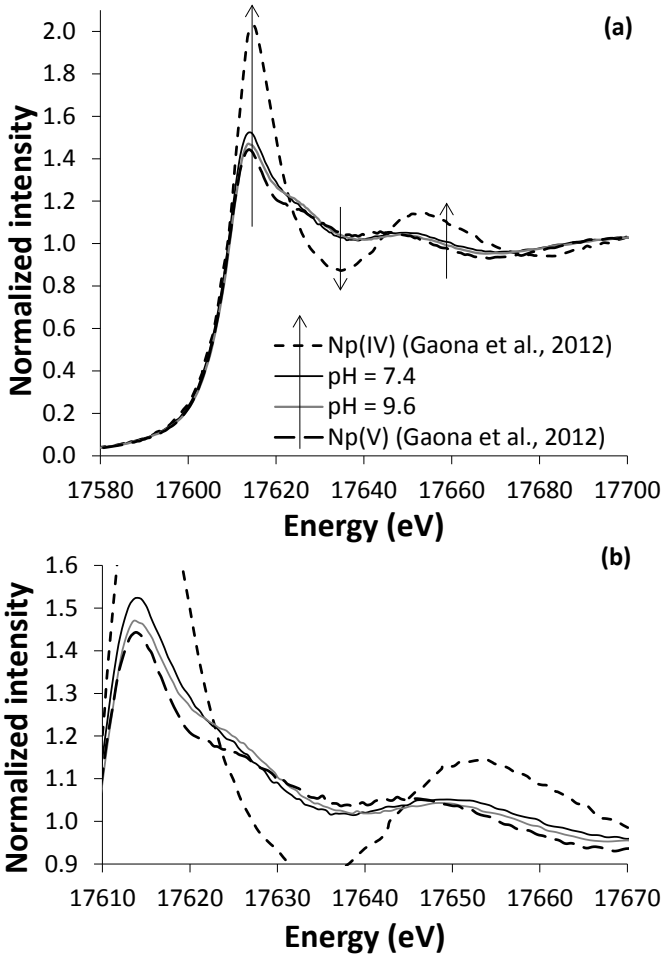

Figure 15: (a) Np L3-XANES measured for a Np-illite sample prepared at pH = 7.4 and 9.6 ($[Np]_{tot} = 3\times10^{-4}$ M, m/V = 20g/L, Eh = 0.40 ± 0.05 V). Reference XANES of aqueous Np(IV) and Np(V) in 1M $HClO_4$ from (Gaona et al., 2012) are shown for comparison. Arrows highlight a Np(V) reduction to Np(IV) process in the present study. The area between 17610 and 17670 eV is enlarged in (b).

Np speciation in presence of the purified Na-illite under given conditions is consistently described by applying the two sites protolysis non-electrostatic surface complexation and cation exchange model (2SPNE SC/CE). Only strong sites at the illite surface were considered and only sorption data with experimentally determined pe are considered. The last is necessary because pe is needed to calculate Np redox speciation according to the first equation in Table 7. The Np redox state and surface complexation constants for Np(IV) are derived by applying a data fitting procedure. Constants are very consistent with results obtained by applying an existing linear free energy relationship (LFER).

Table 7: Reactions and respective thermodynamic constants used in the present modeling section.

Reaction	log K (I = 0)
$NpO_2^+ + 4\ H^+ + e^- = Np^{4+} + 2\ H_2O$	10.21
$NpO_2^+ + H_2O = \equiv NpO_2OH + H^+$	-11.3
$NpO_2^+ + 2\ H_2O = \equiv NpO_2(OH)_2^- + 2\ H^+$	-23.6
$Np^{4+} + H_2O = NpOH^{3+} + H^+$	0.55
$Np^{4+} + 2\ H_2O = Np(OH)_2^{2+} + 2\ H^+$	0.35
$Np^{4+} + 3\ H_2O = Np(OH)_3^+ + 3\ H^+$	-2.3 (Pu)
$Np^{4+} + 4\ H_2O = Np(OH)_4 + 4\ H^+$	-8.3
$NpO_{2(am)} + 2\ H_2O = Np^{4+} + 4\ OH^-$	-56.7
$X\text{-}Na + NpO_2^+ = X\text{-}NpO_2$	0^f
$\equiv SOH + H^+ = \equiv SOH_2^+$	4^f
$\equiv SOH = \equiv SO^- + H^+$	-6.2^f
$\equiv SOH + NpO_2^+ = \equiv SO\text{-}NpO_2 + H^+$	-2.0^f
$\equiv SOH + NpO_2^+ + H_2O = \equiv SO\text{-}NpO_2OH^- + 2\ H^+$	-10.3^f
$\equiv SOH + Np^{4+} = \equiv SO\text{-}Np^{3+} + H^+$	nd (8.4 ± 0.6)
$\equiv SOH + Np^{4+} + H_2O = \equiv SO\text{-}NpOH^{2+} + 2\ H^+$	nd (8.2 ± 0.7)
$\equiv SOH + Np^{4+} + 2\ H_2O = \equiv SO\text{-}Np(OH)_2^+ + 3\ H^+$	6.4 ± 1.2 (6.0 ± 0.7)
$\equiv SOH + Np^{4+} + 3\ H_2O = \equiv SO\text{-}Np(OH)_3 + 4\ H^+$	0.7 ± 1.3 (1.0 ± 1.1)
$\equiv SOH + Np^{4+} + 4\ H_2O = \equiv SO\text{-}Np(OH)_4^- + 5\ H^+$	-5.7 ± 1.2 (nd)

Aqueous reaction constants and the solubility product of $NpO_{2(am)}$ are taken from (Guillaumont et al., 2003). The missing $Np(OH)_3^+$ formation constant is taken from the analogue $Pu(OH)_3^+$. "f" denotes fixed parameters during the fitting procedure, taken from (Bradbury and Baeyens, 2009b). Np(IV) surface complexation constants are fitted from the present experimental results associated with their uncertainty. Calculated values using a LFER are shown for comparison between parentheses. "nd" refers to values that could not be determined.

The results are presented in Figure 16 for the complete dataset used to fit the surface complexation constants for Np(IV).

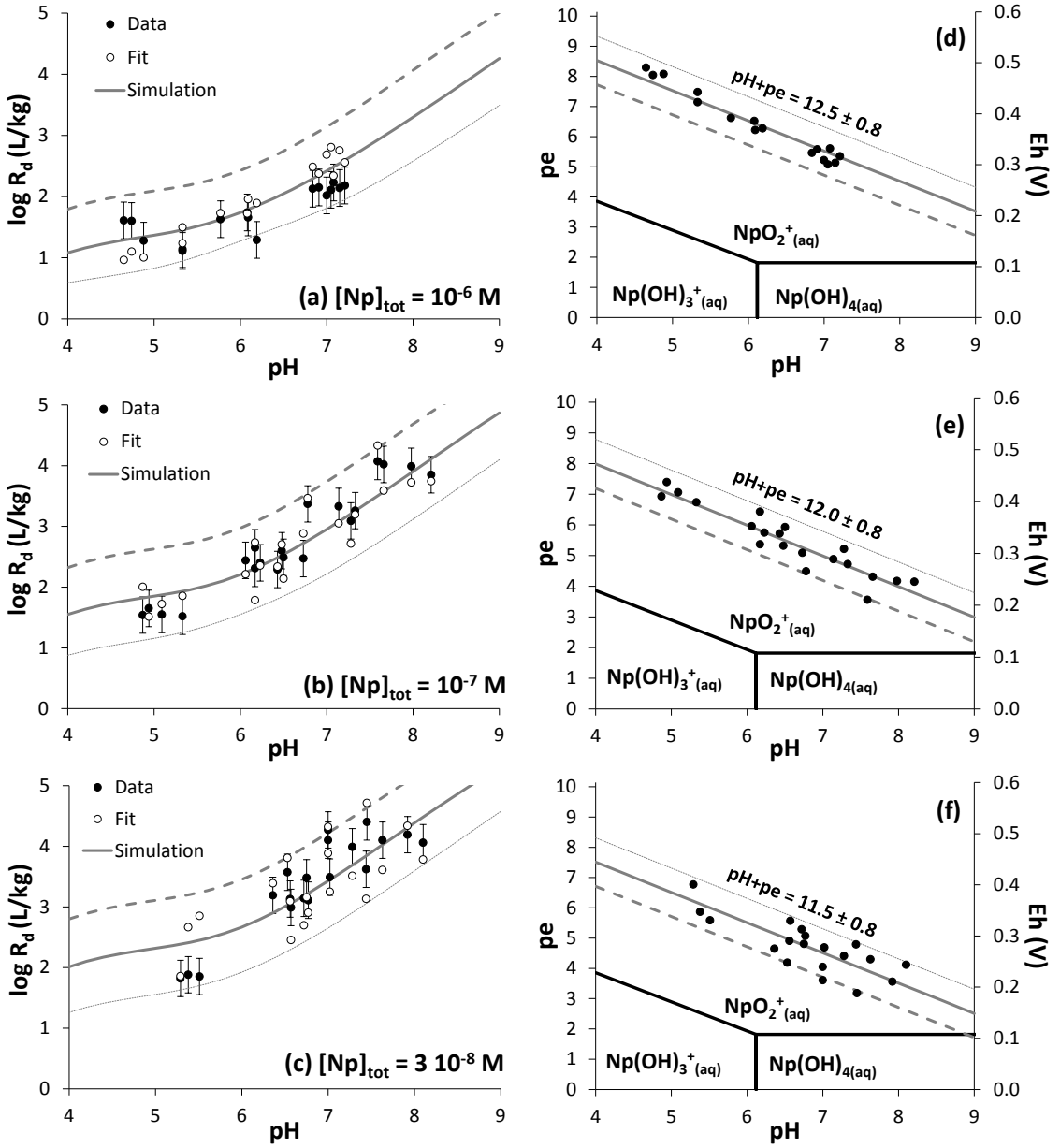

Figure 16: Experimental log R_d (black circles) and the corresponding calculated values (white circles) with the fitted surface complexation constants for Np(IV) with illite versus pH for $[Np]_{tot} = 10^{-6}$ (a), 10^{-7} (b) and 3×10^{-8} M (c). The corresponding redox (pH-pe/Eh plot) conditions are shown on the right side with the predominance diagram for aqueous Np species (d) (e) (f). Lines represent calculations made for constant pH+pe (bold line) ± 0.8 (lower limit: bold dashed line; upper limit: thin dashed line).

Figure 16 a, b, and c show log R_d versus pH for the three series of experiments with $[Np]_{tot} = 10^{-6}$, 10^{-7} and 3×10^{-8} M, respectively. Experimental log R_d and the corresponding calculated values with the fitted constants are shown, respectively, as black and white symbols. Figure 16 c, d, and e show the corresponding redox conditions for each series on a pH-pe(Eh) diagram. In addition, calculations with constant redox conditions

(i.e. constant pH+pe values) for each series in the range of the expected experimental uncertainty (i.e. ± 0.8 pe units / ± 50 mV) illustrate the coupled effect of pH and pe on Np sorption to illite. The increase of log R_d with decreasing $[Np]_{tot}$ is well described. More detailed explanation regarding simulation and the used data are given in (Marsac et al., 2015a).

Taking Np(IV) surface complexation constants into account, the calculated Np(V)/ Np(IV) redox borderline shifts in presence of illite surfaces by 3–5 pe units (0.2–0.3 V) towards redox neutral conditions. From this observation we suggest that Np(V) reduction in presence of a sorbing mineral phase is thermodynamically favored resulting in an Np(IV) surface species.

Based on constants given in Table 7: Reactions and respective thermodynamic constants used in the present modeling section., a predominance diagram for Np surface speciation are constructed for the pH range 4 < pH < 10 (Figure 17; grey lines). The pe-pH diagram is superimposed by the respective predominance diagram for aqueous species (Figure 17; black lines). When Np(V) sorption is weak (pH < 8) reduction to Np(IV) at the surface is thermodynamically highly favored due to the strong sorption of Np(IV) even at relatively high pe. The redox boundary for the Np(V)/Np(IV) couple for Np illite surface species is by approximately 4.6-5 pe units (0.27-0.30 V) higher than for the corresponding dissolved Np species at pH < 8. For pH > 8, Np(V) surface complexation to illite edge sites increases, via the formation of $\equiv SO\text{-}NpO_2OH^-$ species according to the 2SPNE SC/CE model. Consequently, reduction to Np(IV) at the illite surface becomes less favorable and the redox boundary surface species is only approximately 3 pe units (0.18 V) higher as compared to the respective solute species at pH = 10. Figure 17 clearly demonstrates that despite the fact that all data lie within the predominance field of aqueous Np(V) species (black lines), reduction to Np(IV) becomes thermodynamically favored in the presence of illite (grey lines). The high R_d values measured under the given experimental conditions can be explained by the strong sorption of Np(IV) species at the illite surface being in equilibrium with Np(V) species in solution.

Still the question arises, how the Np(V) is reduced to Np(IV). In absence of oxidizing or reducing agents experimentally determined pe-pH values should follow the “redox neutral” line with (pe + pH) =13.8 (dashed line in Figure 17, (Neck et al., 2007)). Apparently, our data lie below this line, i.e. a reductant is needed for the reduction. Fe(II) is known as an efficient redox partner (Marsac et al., 2015a). Although the illite sample investigated in our studies was purified under aerobic conditions, the presence of traces of structural Fe(II) or adsorbed Fe(II), possibly formed via partial dissolution of the clay under anaerobic conditions, cannot be ruled out. A spectroscopic identification of Fe(II) in our experimental system, however, appears to be hardly possible. A maximum of 6.8×10^{-4} mol Np/kg illite was found to be reduced Np(IV). The corresponding amount of Fe(II) required for Np(V) reduction then corresponds to about 0.08 % of the total amount of Fe contained in the illite (7wt.% as Fe_2O_3 gives 0.88 mol of Fe per kg of illite). Such small fractions are very likely below the detection limit of available experimental techniques. Presently, we are unable to determine precisely the nature of the

redox reaction on a molecular scale. Nevertheless, the fact that sorption data can be consistently described by using pe values as a relevant master parameter clearly demonstrates the applicability of the thermodynamic equilibrium approach to simulate coupled redox sorption processes in clay mineral systems.

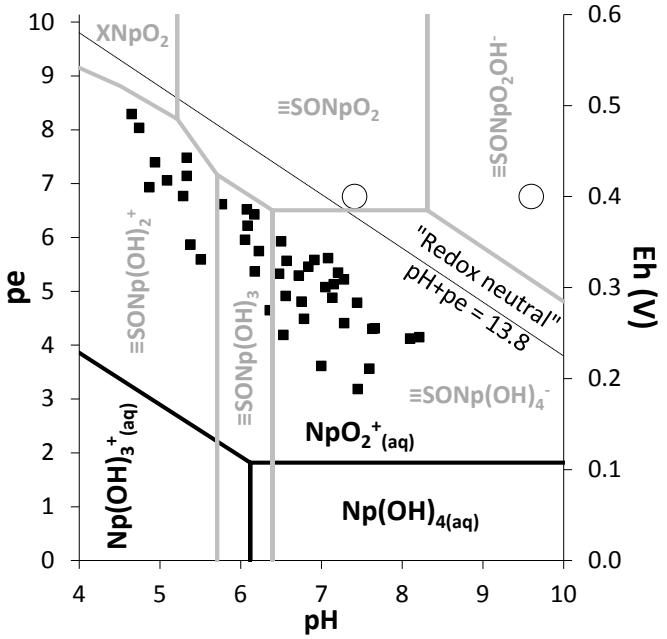

Figure 17: pH-pe (or Eh on the secondary scale) diagram of Neptunium in 0.1 M NaCl solution (black lines) and superimposed Np predominance diagram calculated at the illite surface (grey lines). It shows that the Np(V)/Np(IV) borderline at the illite surface is between 3 and 5 pe units (0.18-0.30 V), depending on the pH, higher than the corresponding one in solution. Experimental pH-pe values are also plotted (without error bars for clarity, s. also (Marsac et al., 2015a)), showing that in the present batch experiments, Np(V) prevails in solution whereas and Np(IV) prevails at the surface, explaining the stronger Np-illite sorption observed compared with literature, under aerobic condition.

Conclusions

The unusually high Np(V) sorption to illite observed in the present study can be explained by partial reduction and concurrent formation of stable Np(IV) surface species. We found a clear relationship of measured pe with Rd values: Np sorption increases with decreasing redox potential. Our combined batch sorption, spectroscopic and geochemical modeling study suggests that the predominance field of reduced Np(IV) species in a pe-pH diagram expands significantly due to the thermodynamically favored formation of Np(IV) surface complexes in a wide pH range. The retention of redox sensitive Np species is thus much more efficient under pe conditions only slightly below redox neutrality in presence of mineral surfaces than expected. Scoping geochemical

estimations of radionuclide redox states at given pe and pH values but neglecting surface complexation reactions can thus be misleading. The result that measured pe values can be taken as a master parameter to simulate complex redox processes including surface reactions is encouraging, even though the determination of redox potentials is flawed by relatively high analytical uncertainties. Nevertheless, by using the measured pe as an input parameter, Np(IV) surface complexation constants for the 2SPNE SC/CE model could be fitted to the experimental data which are very comparable to those values estimated by applying an established LFER approach. The complete sorption dataset can be numerically described assuming surface mediated reduction of Np(V) to Np(IV) based on the strong affinity of Np(IV) for the illite surface.

The exact mechanism of Np(V) reduction, however, could not be clarified within the present study due to the apparently limited concentration of reductant species. The fact that redox and sorption equilibria establish relatively fast, points to a surface mediated process. Electron transfer from adsorbed or structurally bound Fe(II) to surface bound Np(V) is considered as a plausible mechanism for the observed coupled redox/sorption reaction. The presented modeling approach, however, predicts reduction also in absence of an explicit reductant in the solid. The thermodynamical stability of Np(IV) surface species alone is sufficient to shift the redox borderline and to induce partial Np(V) reduction.

The presented modeling concept might be applicable as well to describe the behavior of other redox-sensitive elements in the geosphere.

2.1.3 Plutonium

2.1.3.1 Plutonium sorption at the kaolinite surface

Plutonium with its particularly complex redox chemistry may be thermodynamically stable in the states +III to+VI depending on the redox conditions in the environment. Mineral surfaces can also affect Pu redox speciation. Therefore, the interpretation of Pu sorption data becomes particularly challenging, even for simplified laboratory experiments with simple mineral phases.

The present study focuses on the Pu sorption to kaolinite. Am(III), Th(IV),Np(V) andU(VI) literature sorption data are used as analogues for the corresponding Pu redox states to calibrate a simple surface complexation model, and the Nernst formalism is applied. (Marsac et al., 2015b)

The data used for this work and the simulation curves are shown in Figure 18.

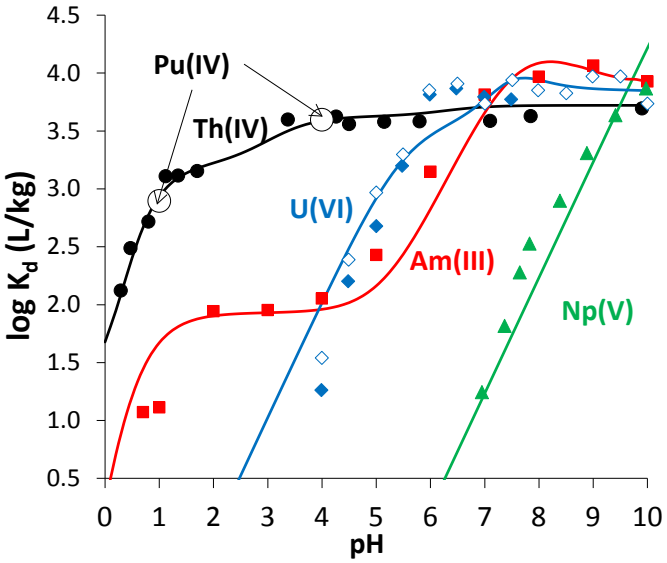

Figure 18: Experimental sorption data (K_d, in L/kg) on kaolinite versus pH for actinides with different redox states (Am(III)/Th(IV)/Np(V); data from (Amayri et al., 2011; Banik et al., 2007; Buda et al., 2008) for 0.1 M $NaClO_4$. Data for U(VI) are taken from (Křepelová, 2007) for 0.1 M $NaClO_4$ in the presence of CO_2 (closed diamonds; pH < 8) and 0.01 M $NaClO_4$ in the absence of CO_2 (open diamonds). The elements are considered as chemical analogues for Pu(III/IV/V/VI). Pu(IV) data are recalculated from the sorption data and Pu redox state analysis of (Banik, 2006) using eq. 17 (two large white circles). Curves represent the modeled result for each Pu redox state.

Two independent pH–pe diagrams, one for the kaolinite surface and another for the aqueous phase, are constructed and superimposed. This allows visualization of the prevalent Pu redox state in both phases. The model suggests that the stability field of the most strongly adsorbing redox state is larger at the surface than in solution. Because Pu(V) weakly sorbs to kaolinite, it never prevails at the surface.Within the stability field of Pu(V) in 0.1M $NaClO_4$ solution, Pu(VI) and Pu(IV) prevail at the kaolinite surface under oxidizing and slightly reducing conditions, respectively. By contrast, the Pu(III)/Pu(IV) boundary is hardly affected because both redox states strongly sorb to kaolinite, especially for pHN 6. The present method is applied to literature data for Pu sorption to kaolinite.

Our model is applied to the experimental data of (Banik et al., 2007) where 6.6×10^{-9} M of Pu(IV) was contacted with 4 g/L kaolinite in 0.1 M $NaClO_4$. The experimental percentage of Pu uptake reported by (Banik et al., 2007) in air (only for pH < 8) and in argon atmosphere are shown in Figure 19a together with Th(IV) data ($[^{234}Th]_{tot} = 6.6 \times10^{-13}$ M). Pu overall uptake is systematically lower than Th(IV). Overall Pu uptake increases from 10 to 80% for 0 < pH < 3, decreases down to ~60% for pH around 4 and reaches again ~80% above pH = 7. The dip at intermediate pH is unusual and cannot be explained by Pu(IV) alone, which becomes clear from a redox state analysis of Pu in the aqueous phase.

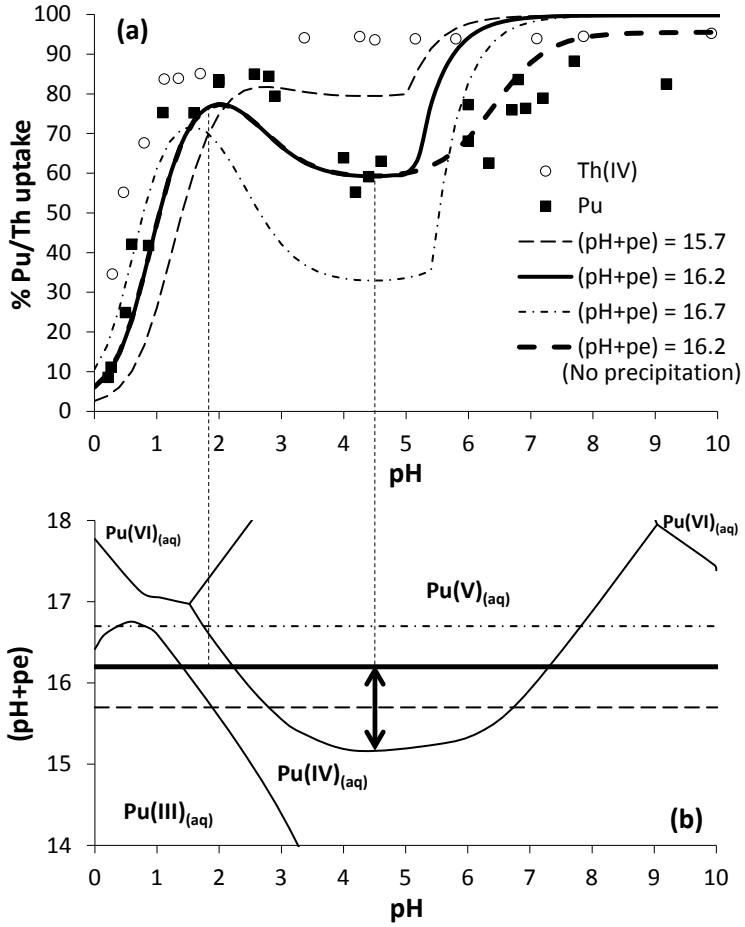

Figure 19: (a) Percentage uptake of Pu and Th by kaolinite ($[Pu]_{tot}$ = 6.6 ×10^{-9} M / $[Th]_{tot}$ = 6.6 ×10^{-13} M; 0.1 M $NaClO_4$; S/V = 4 g/L; either under ambient air below pH = 8 or argon atmosphere) experimentally obtained by (Banik et al., 2007) and calculated for pH+pe = 16.2, considering (bold line) or not (bold dashed line) the precipitated $PuO_{2(am)}$ to be removed from the aqueous phase with the kaolinite. The model sensitivity to pe is illustrated applying ±0.5 uncertainty on the pe: pH+pe = 15.7 (dashed line) and 16.7 (dashed-dotted line); precipitated $PuO_{2(am)}$ is considered to have been removed with kaolinite. (b) Predominance diagram for the aqueous solution plotting pH+pe versus pe to visualize constant redox conditions horizontally. The legend is valid for (a) and (b).

The present approach allows the description of overall Pu uptake on kaolinite, by applying thermodynamic concepts and by simultaneously taking into account the complete Pu redox chemistry and the respective sorption behavior. The calculations are very sensitive to pe, as illustrated in Figure 19 by considering pe ± 0.5 (corresponding to ± 0.03 V). This result clearly shows that without any information concerning the redox conditions in the experiment, it is almost impossible to predict Pu uptake by kaolinite.

Above pH = 5, information about pe is not available. Simulations are made assuming pH+pe = 16.2 as before. Because of the strong assumption, the simulations and discussions should be considered with caution. For pH = 9, Pu(IV) is the dominant redox

state in solution (see Figure 19b), consistent with redox state analysis. For pH > 5, the solution is oversaturated with respect to $PuO_{2(am,hyd)}$: total aqueous $[Pu(IV)]_{tot,aq}$ equals approximately 10^{-9} M for pH = 9, whereas the Pu(IV) solubility limit is $10^{-10.4\pm0.5}$ M (Neck et al., 2007). This circumstance implies a lot of problems like Pu-colloid formation that is discussed in (Marsac et al., 2015b). Unfortunately, the sorption of Pu-colloids to kaolinite cannot be simulated yet using a mechanistic model without making additional assumptions. However, the sorption of Pu(IV)-colloids to minerals needs to be studied in further experiments.

Table 8: Thermodynamic constants at zero ionic strength used in the present study (Guillaumont et al., 2003). The missing hydrolysis constants for Pu are taken from the corresponding analogues (in brackets). Surface complexation constants for Pu(III, IV, V, VI) are obtained assuming that the experimental uptake data of Am(III), Th(IV), Np(V) and U(VI) by kaolinite are representative for the uptake of the corresponding Pu redox states. (*) Exchange and surface complexation constants have been determined by (Tertre et al., 2008). Some constants could not be determined since no appropriate experimental data were available. According to (Tertre et al., 2006; Tertre et al., 2008), the surface area of kaolinite is 10 m²/g, site density for ≡SOH and exchange sites are 1.66 and 3.70 µmol/m², respectively.

	Reaction	Log K (I = 0)
Solubility	$PuO_{2(am,hyd)} + 2\ H_2O = Pu^{4+} + 4\ OH^-$	-58.33
Redox	$PuO_2^{2+} + e^- = PuO_2^+$	15.82
	$PuO_2^{2+} + 4\ H^+ + 2\ e^- = Pu^{4+} + 2\ H_2O$	33.27
	$PuO_2^+ + 4\ H^+ + e^- = Pu^{4+} + 2\ H_2O$	17.45
	$Pu^{4+} + e^- = Pu^{3+}$	17.69
Hydrolysis	$PuO_2^{2+} + H_2O = PuO_2OH^+ + H^+$	-5.50
	$PuO_2^{2+} + 2\ H_2O = PuO_2(OH)_2 + 2\ H^+$	-13.20
	$PuO_2^{2+} + 3\ H_2O = PuO_2(OH)_3^- + 3\ H^+$	-20.25 (U)
	$PuO_2^{2+} + 4\ H_2O = PuO_2(OH)_4^{2-} + 4\ H^+$	-32.40 (U)
	$PuO_2^+ + H_2O = PuO_2OH + H^+$	-11.30 (Np)
	$PuO_2^+ + 2\ H_2O = PuO_2(OH)_2^- + 2H^+$	-23.60 (Np)
	$Pu^{4+} + H_2O = PuOH^{3+} + H^+$	0.60
	$Pu^{4+} + 2\ H_2O = Pu(OH)_2^{2+} + 2\ H^+$	0.60
	Continuation Table 8	
	$Pu^{4+} + 3\ H_2O = Pu(OH)_3^+ + 3\ H^+$	-2.30
	$Pu^{4+} + 4\ H_2O = Pu(OH)_4 + 4\ H^+$	-8.50
	$Pu^{3+} + H_2O = PuOH^{2+} + H^+$	-6.90
	$Pu^{3+} + 2\ H_2O = Pu(OH)_2^+ + 2\ H^+$	-15.10 (Am)
	$Pu^{3+} + 3\ H_2O = Pu(OH)_3 + 3\ H^+$	-26.20 (Am)

Exchange	$2\ X\text{-}Na + PuO_2^{2+} = X_2\text{-}PuO_2 + Na^+$	nd
	$X\text{-}Na + PuO_2^{+} = X\text{-}PuO_2 + Na^+$	nd
	$3\ X\text{-}Na + Pu^{3+} = X_3\text{-}Pu + Na^+$	1
	$4\ X\text{-}Na + Pu^{4+} = X_4\text{-}Pu + Na^+$	nd
	$X\text{-}Na + H^+ = X\text{-}H + Na^+$	$-1^{(*)}$
Surface complexation	$\equiv SOH + PuO_2^{2+} = \equiv SO\text{-}PuO_2^{+} + H^+$	0.2
	$\equiv SOH + PuO_2^{2+} + H_2O = \equiv SO\text{-}PuO_2OH + H^+$	-6.9
	$\equiv SOH + PuO_2^{2+} + 2\ H_2O = \equiv SO\text{-}PuO_2(OH)_2^{-} + 3\ H^+$	-14.5
	$\equiv SOH + PuO_2^{+} = \equiv SO\text{-}PuO_2 + H^+$	-4.0
	$\equiv SOH + Pu^{4+} = \equiv SO\text{-}Pu^{3+} + H^+$	nd
	$\equiv SOH + Pu^{4+} + H_2O = \equiv SO\text{-}PuOH^{2+} + 2\ H^+$	6.0
	$\equiv SOH + Pu^{4+} + 2\ H_2O = \equiv SO\text{-}Pu(OH)_2^{+} + 3\ H^+$	3.2
	$\equiv SOH + Pu^{4+} + 3\ H_2O = \equiv SO\text{-}Pu(OH)_3 + 4\ H^+$	-3.0
	$\equiv SOH + Pu^{3+} = \equiv SO\text{-}Pu^{2+} + H^+$	$-0.5^{(*)}$ (Eu)
	$\equiv SOH + Pu^{3+} + H_2O = \equiv SO\text{-}PuOH^{+} + 2\ H^+$	-9.3

It is well known that Pu redox speciation has a strong impact on its mobility in the environment. Various experimental studies have shown that mineral surfaces affect Pu redox speciation. In the present study, Pu redox speciation at the kaolinite surface is interpreted based on the thermodynamic stability of the respective Pu redox state at the surface. To overcome difficulties in the interpretation of results related to the sensitivity of Pu to redox conditions, uptake data on kaolinite of the more redox-stable Am(III), Th(IV), Np(V) and U(VI) - chemical analogues for Pu(III,IV,V,VI) - are used to calibrate a surface complexation model. To fully understand Pu redox chemistry in the aqueous kaolinite suspension, the system is treated separately for the aqueous solution and the kaolinite surface, and the two resulting Pu predominance diagrams are superimposed. This method visualizes how the prevailing Pu redox states can differ between solution and surface for given pH/pe conditions. Notably, the kaolinite surface has no impact on the Pu(IV)/Pu(III) distribution in neutral to alkaline conditions, in the absence of aqueous ligands other than OH^-. Therefore, the study of Pu(III) sorption to minerals is relevant for the reducing conditions encountered in deep geological nuclear waste repository sites. Under slightly oxidizing conditions, Pu(IV) can be stabilized at the kaolinite surface within the stability field of Pu(V) in solution, which significantly increases overall Pu uptake. The present model predicts overall experimental Pu uptake when the Pu(V)/Pu(IV) redox couple is involved. This suggests that Pu-mineral interaction is strong, even under slightly oxidizing condition. Also Pu(VI) can be stabilized at the kaolinite surface within the stability field of Pu(V) in solution, under oxidizing conditions. Its impact on overall Pu uptake is limited to redox conditions in equilibrium with ambient air atmosphere (O_2), by the weak Pu(VI) sorption to kaolinite for pH < 5 and the strong Pu(VI)-carbonate (due to atmospheric CO_2) complexation in alkaline conditions. Inde-

pendent experimental data for other minerals with Pu and with Np corroborate our approach. The derived equations are of rather generic form making them easily applicable yet to other adsorbant/adsorbat systems.

Based on the thermodynamic stability of the sorbed Pu species, the exact redox mechanism does not need to be explicitly considered but the redox potential of the system must be known. Measurement of redox potential is rarely simple and often bears large uncertainties, but the pe (or Eh) strongly affects overall Pu uptake by kaolinite. A redox state analysis of aqueous Pu can provide information on pe, when a steady state is reached. The determination of pe from Pu redox state analysis heavily relies on the accuracy of the available thermodynamic database for aqueous complexes, i.e. their capability to describe the speciation of the different Pu redox states in presence of various ligands. This fact becomes more important for natural samples that are more complex than the systems considered in this work.

2.1.3.2 Plutonium sorption at the illite surface

As already shown before, the geochemical behavior of Pu strongly depends on its redox speciation. In this study we investigated Pu sorption onto Na-illite, a relevant component of potential host rocks for high-level nuclear waste repositories, under anaerobic conditions. More details about experimental conditions as well as about the methods used in this study are described in (Banik et al., 2016).

The purified Na-illite was provided within the EC project CP CatClay (www.catclay.org). The source material derives from lacustrine continental sediments deposited at the Upper Eocene (~ -35 Ma) in the basin of Le Puy en Velay (Massif Central, France). The purification procedures and the characterization of the purified illite were given in detail in (Marsac et al., 2015a) and will not be repeated here.

A ^{238}Pu stock solution was used. The concentration of the Pu stock solution was 3.9×10^{-5} M in 0.1M $HClO_4$. The ^{238}Pu stock solution contained 85% Pu(IV), 11% Pu(V) and 4% Pu(III). A diluted solution ([Pu] = 7.8×10^{-7} M) in 0.1 M $HClO_4$ was prepared from the main stock solution to perform experiments at low Pu(IV) concentration. The concentrations of ^{238}Pu in solution were determined by LSC. In addition, the stock solution of ^{238}Pu was checked by ICP-MS measurements and the results are in excellent agreement with LSC measurements. Pu redox state distribution in the stock solution was determined by liquid-liquid extraction with HDEHP and PMBP (Marquardt et al., 2004; Nitsche et al., 1994).

All sorption experiments were performed as batch type experiments. The effect of pH was investigated at an initial Pu concentration ($[Pu]_{tot}$) of 8×10^{-11} M. In addition the effect of $[Pu]_{tot}$ is investigated for $8\times10^{-11} < [Pu]_{tot} < 10^{-8}$ M and pH = 4.3, 6.2 and 9.3. A first series of batch experiments was carried out at room temperature in an argon glove box (< 1 ppm O_2, absence of CO_2). At a solid to liquid ratio of 2 g L^{-1}, the suspensions

were preconditioned in 0.1 M NaCl under continuous shaking for 4-5 days. pH was adjusted by adding 0.1 M HCl or 0.1 M NaOH. The samples were closed and shaken end-over-end. After one week, pH and Eh were measured in the suspension and an aliquot of each sample was centrifuged in a Beckman L7 Ultracentrifuge at 90000 rpm for 1 h. The supernatant was analyzed for dissolved Pu by LSC. The same procedure was repeated after one year contact time.

Eu(III) is investigated as a chemical analogue of Pu(III). A radiotracer solution from Amersham International was used with a total Eu concentration of 6.0×10^{-4} M. Batch Eu sorption experiments were performed with $[Eu]_{tot} = 3\times10^{-9}$ M applying the same protocol as for Pu except that, because no redox reaction is involved, (i) one week contact time was chosen and (ii) the Eh measurement was not recorded. After ultracentrifugation, the supernatant was analyzed for dissolved Eu by γ-spectrometry.

Batch Pu sorption experiments involving an illite/calcite mixture were also performed under same conditions mentioned before. The calcite was purchased from Merck, Germany. On the basis of a previous study on Eu(III) sorption to a smectite:calcite mixture (Hartmann et al., 2008) and to avoid the potential release of $CO_{2(g)}$ during long-term equilibration of the sample (e.g. one year), Pu uptake was measured one week after the addition of Pu. Two series of experiments were conducted at pH ≈ 8.5 and 10, respectively, with $[Pu]_{tot}$ = 0.5, 0.8 and 1×10^{-9} M. An additional ("control") series of experiments is performed in the absence of calcite for pH ≈ 10, the same range of $[Pu]_{tot}$ and one week equilibration time.

The modelling of the data was performed with the geochemical speciation program PHREEQC (Parkhurst and Appelo, 1999) and the results were visualized by PHREEPlot (Kinniburgh D. G. and Cooper D. M., 2009). Thermodynamic constants for Pu and Eu/Am aqueous speciation are taken from the NEA thermodynamic database (Guillaumont et al., 2003). The specific ion interaction theory (SIT) (Ciavatta, 1980) is used for the calculation of the activity coefficients of aqueous species. In case of gaps in the Pu database, data from analogue species are chosen (i.e. Eu/Am(III), Np(IV), Np(V) and U(VI) for the respective Pu redox states). The formation constant of $Pu(OH)_2(CO_3)_2^{2-}$ selected in THEREDA (Release 2013-08-02) is also used.

Auxiliary reactions and constants are taken from the SIT database provided by PHREEQC (sit.dat file). Again, the 2SPNE SC/CE model is used to simulate Pu and Eu sorption to illite. For the calculations in the presence of calcite, the total dissolved inorganic carbon concentration ([DIC]) is assumed to be in equilibrium with calcite in a closed system with no gas phase. A summary of the thermodynamic database, SIT coefficients and parameters for the 2SPNE SC/CE model is given in in Table 9, Table 10, and Table 11.

Table 9: Relevant aqueous reaction for the calculations of Pu sorption and speciation in the present study. Thermodynamic constants are taken from the NEA-TDB[1] and refer to the value at infinite dilution. Ternary Pu(IV)-hydroxo-carbonato complexes formation constants are taken for THEREDA[2]. In case of gaps in the available database for Pu, data for analogues are used (i.e. Eu/Am(III), Np(IV), Np(V) and U(VI) for the respective Pu redox states). Although available for Pu, the formation constants for $PuOH^{2+}$ and $Pu(OH)_{4(aq)}$ are taken from Eu/Am(III) and Np(IV) to ensure the consistency between aqueous speciation and surface complexation modeling, i.e. to avoid additional corrections of the literature parameters for the 2 SPNE SC/CE model.

	Reaction	Available for Pu	Value used	Analogue
Redox	$PuO_2^{2+} + e^- = PuO_2^+$	15.82		
	$PuO_2^{2+} + 4\ H^+ + 2\ e^- = Pu^{4+} + 2\ H_2O$	33.27		
	$PuO_2^{+} + 4\ H^+ + e^- = Pu^{4+} + 2\ H_2O$	17.45		
	$Pu^{4+} + e^- = Pu^{3+}$	17.69		
Hydrolysis	$AnO_2^{2+} + H_2O = AnO_2OH^+ + H^+$	-5.50	-5.50	
	$AnO_2^{2+} + 2\ H_2O = AnO_2(OH)_2 + 2\ H^+$	-13.20	-13.20	
	$AnO_2^{2+} + 3\ H_2O = AnO_2(OH)_3^- + 3\ H^+$		***-20.25***	U(VI)
	$AnO_2^{+} + H_2O = AnO_2OH + H^+$		***-11.30***	Np(V)
	$An^{4+} + H_2O = AnOH^{3+} + H^+$	0.60	0.60	
	$An^{4+} + 2\ H_2O = An(OH)_2^{2+} + 2\ H^+$	0.60	0.60	
	$An^{4+} + 3\ H_2O = An(OH)_3^{+} + 3\ H^+$	-2.30	-2.30	
	$An^{4+} + 4\ H_2O = An(OH)_4 + 4\ H^+$	-8.50	***-8.30***	Np(IV)
	$An^{3+} + H_2O = AnOH^{2+} + H^+$	-6.90	***-7.20***	Am/Eu(III)
	$An^{3+} + 2\ H_2O = An(OH)_2^{+} + 2\ H^+$		***-15.10***	Am/Eu(III)
	$An^{3+} + 3\ H_2O = An(OH)_3 + 3\ H^+$		***-26.20***	Am/Eu(III)
Chloride	$AnO_2^{2+} + Cl^- = AnO_2Cl^+$	0.23	0.23	
	$AnO_2^{2+} + 2\ Cl^- = AnO_2Cl_2$	-1.15	-1.15	
	$An^{4+} + Cl^- = AnCl^{3+}$	1.80	1.80	
	$An^{3+} + Cl^- = AnCl^{2+}$		***0.24***	Am/Eu(III)
	$An^{3+} + 2\ Cl^- = AnCl_2^{+}$		***-0.74***	Am/Eu(III)
Carbonate	$An^{4+} + 2\ H_2O + 2\ CO_3^{2-} =$ $An(OH)_2(CO_3)_2^{2-} + 2\ H^+$	18.24	18.24	

(1): Guillaumont, R.; Fanghänel, Th.; Fuger, J.; Grenthe, I.; Neck, V.; Palmer, D. A.; Rand, M. H. Update on the Chemical Thermodynamics of Uranium, Neptunium, Plutonium, Americium and Technetium; Elsevier: Amsterdam, 2003. (2): THEREDA, Thermodynamic Reference Database. Release 2013-08-02. www.thereda.de.

Table 10: Surface complexation and cation exchange parameters for the 2 SPNE SC/CE model are taken from the literature[3,4,5] and for Pu(IV) (determined in the present study). The surface complexing site density is $[\equiv S]_{tot} = 2 \times 10^{-3}$ mol/kg. The cation exchange capacity is $[X]_{tot} = 0.225$ eq/kg. "na" refers to non-available values. Only the relevant reactions and constants for the present calculations are tabulated.

	Reaction	Np	Pu	Am	Value used
Surface	$\equiv SOH + H^+ = \equiv SOH_2^+$				4.00
	$\equiv SOH = \equiv SO^- + H^+$				-6.20
	$\equiv SOH + An^{4+} = \equiv SO\text{-}An^{3+} + H^+$	na	na		
	$\equiv SOH + An^{4+} + H_2O = \equiv SO\text{-}AnOH^{2+} + 2\ H^+$	na	9.9 ± 0.5		9.9
	$\equiv SOH + An^{4+} + 2\ H_2O = \equiv SO\text{-}An(OH)_2^+ + 3\ H^+$	6.4 ± 1.2	5.9 ± 0.5		5.9
	$\equiv SOH + An^{4+} + 3\ H_2O = \equiv SO\text{-}An(OH)_3 + 4\ H^+$	0.7 ± 1.0	0.1 ± 0.5		0.1
	$\equiv SOH + An^{4+} + 4\ H_2O = \equiv SO\text{-}An(OH)_4^- + 5\ H^+$	-5.7 ± 1.2	-6.4 ± 0.5		-6.4
	$\equiv SOH + An^{3+} = \equiv SO\text{-}An^{2+} + H^+$			3.1	***3.1***
	$\equiv SOH + An^{3+} + H_2O = \equiv SO\text{-}AnOH^+ + 2\ H^+$			-4.4	***-4.4***
	$\equiv SOH + An^{3+} + 2\ H_2O = \equiv SO\text{-}An(OH)_2 + 3\ H^+$			-12.7	***-12.7***
	$\equiv SOH + An^{3+} + 3\ H_2O = \equiv SO\text{-}An(OH)_3^- + 4\ H^+$			-24.3	***-24.3***
Exchange	$2\ X\text{-}Na + Ca^{2+} = X_2\text{-}Ca + 2\ Na^+$				1.04
	$3\ X\text{-}Na + An^{3+} = X_3\text{-}An + 3\ Na^+$				1.9
	$4\ X\text{-}Na + An^{4+} = X_4\text{-}An + 4\ Na^+$				na

(3): Bradbury, M. H.; Baeyens, B. Sorption modelling on illite Part I: Titration measurements and the sorption of Ni, Co, Eu and Sn. *Geochim. Cosmochim. Acta* **2009**, *73*, 990-1003. (4): Bradbury, M. H.; Baeyens, B. Sorption modeling on illite Part II: actinide sorption and linear free energy relationships. *Geochim. Cosmochim. Acta* **2009**, *73*, 1004-1013. (5): Marsac, R.; Banik, N. L.; Diascorn, A.; Kupcik, T.; Lützenkirchen, J.; Marquardt, C. M.; Schäfer, T.; Schild, D.; Rothe, J.; Dardenne, K.; Geckeis, H. Neptunium redox speciation at the illite surface. *Geochim. Cosmochim. Acta* **2015**, *152*, 39-51.

Table 11: SIT parameters (ε(i,k)) used in the present study, taken from the NEA-TDB[1] for Pu or the corresponding analogue (as in Table S1). "na" refers to non-available values (set equal to 0).

i	k	ε(i,k)
H^+	Cl^-	0.12
Na^+	Cl^-	0.03
Na^+	OH^-	0.04
PuO_2^{2+}	Cl^-	0.22
PuO_2OH^+	Cl^-	na
$PuO_2(OH)_3^-$	Na^+	-0.09
PuO_2Cl^+	Cl^-	0.22
PuO_2^+	Cl^-	0.09
Pu^{4+}	Cl^-	0.4
$PuOH^{3+}$	Cl^-	0.2
$Pu(OH)_2^{2+}$	Cl^-	0.1
$Pu(OH)_3^+$	Cl^-	0.05
$Pu(OH)_2(CO_3)_2^{2-}$	Na^+	na
$PuCl^{3+}$	Cl^-	0.62
Pu^{+3}	Cl^-	0.23
$PuOH^{2+}$	Cl^-	-0.04
$Pu(OH)_2^+$	Cl^-	-0.06
$Pu(OH)_3$	Cl^-	0
$Pu(OH)_3$	Na^+	-0.17
$PuCl^{2+}$	Cl^-	0.191
$PuCl_2^+$	Cl^-	0.129

(1): Guillaumont, R.; Fanghänel, Th.; Fuger, J.; Grenthe, I.; Neck, V.; Palmer, D. A.; Rand, M. H. *Update on the Chemical Thermodynamics of Uranium, Neptunium, Plutonium, Americium and Technetium*; Elsevier: Amsterdam, 2003.

Results and Discussion

Figure 20 presents Pu sorption to illite (R_d in L/kg) as a function of the pH (i.e. pH-edge) after 1 week and 1 year contact time for $[Pu]_{tot} = 8\times10^{-11}$ M. While Pu uptake by illite is always high, R_d values are significantly lower after 1 week for 4 < pH < 7: about 5-10% of Pu remained in solution. For pH = 4, aqueous redox state analysis of Pu was performed on contact with illite after ultracentrifugation ($[Pu]_{tot} = 10^{-8}$ M). About 90% of

Pu in the aqueous phase was Pu(V), which weakly sorbs to clays, by analogy with Np(V) (Bradbury and Baeyens, 2006; Gorgeon, 1994). Because the Pu stock solution contains ~10% of Pu(V), the lower uptake after 1 week compared to 1 year contact time is attributed to slow reduction kinetics of Pu(V) to Pu(IV), in agreement with previous studies on montmorillonite (Begg et al., 2013; Zavarin et al., 2012) or other minerals (Hixon et al., 2013; Hixon and Powell, 2014; Powell et al., 2005). For pH > 7, log R_d values increase with the pH. For pH = 10, aqueous redox state analysis of Pu showed only the presence of Pu(IV) after 1 week. This might be attributed to an increasing reduction rate of Pu(V) to Pu(IV) with the pH, as observed for hematite and goethite (Powell et al., 2005). Between 1 week and 1 year, for pH < 7, Pu uptake by illite increases. However, for pH > 7, Pu uptake does not significantly evolve with time.

The log R_d slightly increases from approximately 4 to 5.3 L kg^{-1} with increasing pH from 3 to 5 and remain constant at log R_d = 5.3 ± 0.5 L kg^{-1} (2σ) for pH > 5. The Pu-illite sorption isotherms for pH = 4.3, 6.2 and 9.3 are shown on Figure 20b as log R_d versus log $[Pu]_{aq}$ (i.e. the final aqueous Pu concentration in solution after ultracentrifugation). Log R_d does not vary significantly with log $[Pu]_{aq}$ for the pH values investigated, with more scatter in the data for pH = 4.3. The measured log $[Pu]_{aq}$ values in the presence of illite are close or below to the solubility limit of Pu(IV), i.e. log $[Pu]_{aq}$ ≈ -9 (for pH = 4.3) and -10.4 M (for pH > 6) (Neck et al., 2007). No effect of $PuO_{2(am,hydr)}$ precipitation on Pu uptake is observed at the highest $[Pu]_{aq}$ investigated.

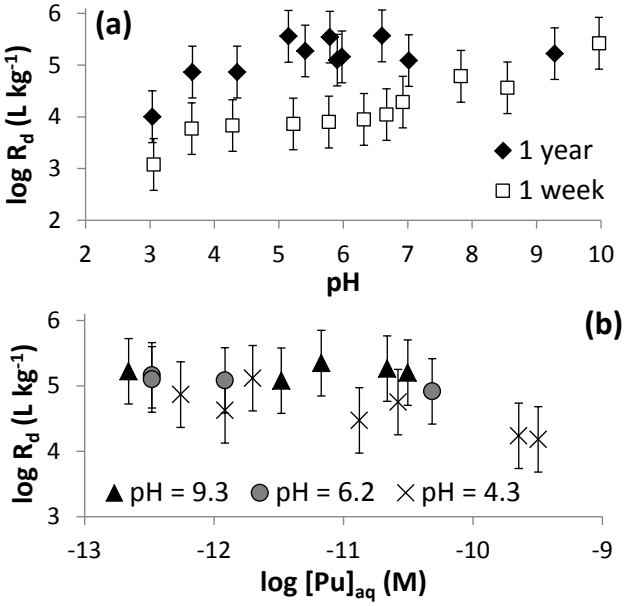

Figure 20: (a) Pu sorption to illite (R_d in L kg^{-1}) in 0.1 M NaCl as a function of the pH for $[Pu]_{tot}$ = 8×10^{-11} M after 1 week and 1 year contact time. (b) Pu-illite sorption isotherms for pH = 4.3, 6.2 and 9.3 after 1 year contact time.

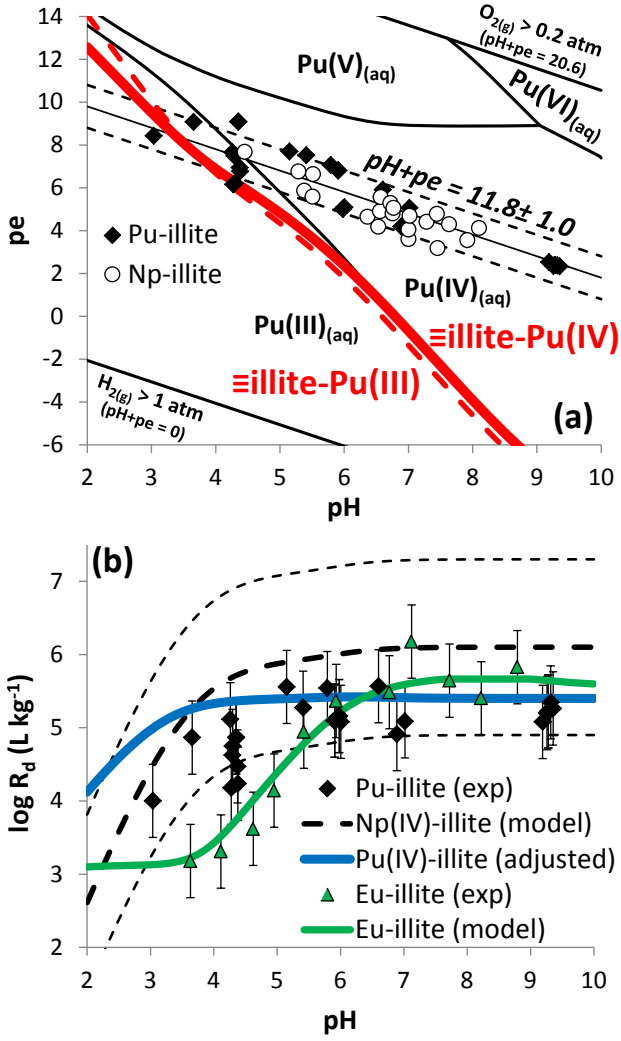

Figure 21 (a) Predominance pH-pe diagram for Pu in 0.1 M NaCl. Measured pH-pe values in the Pu-illite (present work) and Np-illite (Marsac et al., 2015a) suspensions in 0.1 M NaCl are shown as symbols. The bold red lines show the estimated (on the basis of chemical analogues; dashed line) and presently determined (solid line) Pu(IV)/Pu(III) borderline at the illite surface (see text for more details). (b) Pu and Eu(III) uptake data on illite (R_d in L kg^{-1}) as a function of pH compared with the predicted Eu/Am(III) (green bold line), Np(IV) (dashed black line) and the present model for Pu(IV) (blue bold line) based on the 2 SPNE SC/CE framework. Thin dashed lines correspond to the uncertainty associated to the surface complexation constants for Np(IV).

In Figure 21a, the experimental pH-pe values are compared to those reported for the Np-illite system (Marsac et al., 2015a) after contact times from 7 to 63 days. Only the data for the lowest $[Np(V)]_{tot}$ are shown (3×10^{-8} M) because higher $[Np(V)]_{tot}$ affected the pe. This is likely due to the limited redox capacity of the illite. Although the experimental pe involves large uncertainties, pH-pe measurements from both studies agree well, which suggests that the redox conditions of the 0.1 M NaCl illite suspension can be described relatively well by pH + pe = 11.8 ± 1.0. Figure 21 also includes the predominance pH-pe diagram for Pu in 0.1 M NaCl solution. According to the calculations and the uncertainty in pe, significant amounts of Pu(III) are expected in the aqueous

phase below pH ≈ 5. This is confirmed by aqueous Pu redox state analysis, i.e. after illite removal by ultracentrifugation ($[Pu]_{tot} = 10^{-8}$ M). For pH = 4.3, 22 ± 10% of Pu(III) and 85 ± 10% of Pu(IV) are detected. Pu(IV) is expected to prevail in solution above pH ≈ 5. For pH = 6.9, aqueous redox state analysis of Pu shows that the amount of Pu(III) is insignificant (5 ± 10%) and only Pu(IV) is found.

The redox speciation of actinides may differ between the aqueous and adsorbed states (Marsac et al., 2015b; Marsac et al., 2015a). With a simple equation the stability field of different Pu redox states at a mineral surface (Marsac et al., 2015b), regarding only the relevant oxidation states Pu(IV) and Pu(III):

$$\{Pu(IV)/Pu(III)\}_{surf} = \{Pu(IV)/Pu(III)\}_{aq} + (\log R_d(Pu(III)) - \log R_d(Pu(IV)))$$

where $\{Pu(IV)/Pu(III)\}_{aq}$ involves the Nernst equation and describes the Pu(IV)/Pu(III) borderline in the aqueous phase shown on Figure 21a, and $\{Pu(IV)/Pu(III)\}_{surf}$ relates to the illite surface. The log R_d(Pu(III)) and log R_d(Pu(IV)) values in the above equation represent the individual uptake of the two redox states under the same physico-chemical conditions. Because the individual R_d values are not currently available for the two redox states of Pu, Eu(III) and Np(IV) are taken as analogues of Pu(III) and Pu(IV), respectively.

In order to accurately estimate the sorption behavior of Pu(III) to our illite, Eu(III) sorption experiments in 0.1 M NaCl ($[Eu]_{tot} = 3\times10^{-9}$ M) are carried out for 3 < pH < 10 and the results are shown on Figure 21b. Predictions by the 2SPNE SC/CE model are in good agreement when using the set of surface complexation constants determined for Am(III) (Bradbury and Baeyens, 2009b). For pH < 4, Eu uptake is controlled by cation exchange. For pH > 4, Eu uptake increases with pH before reaching a plateau (ca. pH > 7) at nearly 100% uptake due to surface complexation. No experimental data for Np(IV) sorption to illite in the absence of Np(V) are available, but Figure 21b shows the pH-edge of Np(IV) in 0.1 M NaCl predicted with the 2 SPNE SC/CE model (Marsac et al., 2015a). The simulated log R_d values for Np(IV) are constant for pH > 4. The predicted decrease in log R_d with decreasing pH below pH 4 must be considered with caution, because the model for Np(IV) was only calibrated for 4 < pH < 10, as discussed later. Since experimental pe values were required to calibrate of the model for Np(IV), the predicted log R_d values for Np(IV) involve relatively large uncertainties (ca ± 1.1 log R_d units, dotted lines on Fig. 2b). Using the above equation, $\{Pu(IV)/Pu(III)\}_{surf}$ can now be calculated (Figure 21a, bold red dotted line). For pH < 7, Eu sorption to illite is weaker than Np(IV). The stability field of Pu(IV) is enlarged at the illite surface and overlaps with the stability field of Pu(III) in the aqueous phase. For pH > 7, Eu(III) and Np(IV) uptake are almost equal: the Pu(IV)/Pu(III) borderline at the illite surface coincides with the one in solution. Given the measured pH-pe values, Pu(IV) is expected to prevail (or, at least, to be present in significant amounts) at the illite surface in all samples. For pH > 5, Pu(III) is negligible and Pu uptake by illite is controlled by Pu(IV). For pH < 5, overall Pu uptake by illite is expected between Eu(III) and Np(IV).

At this point, it appears possible to provide a more accurate description of Np/Pu(IV) sorption to illite with the 2SPNE SC/CE model than previously possible (Marsac et al., 2015a). Given the similar chemical behavior of Np and Pu, their uptake on illite is not expected to differ by more than ±0.5 log R_d units. Because Pu(IV) prevails at the illite surface and in solution for pH > 6, the predicted overall Pu uptake is insensitive to small pe variations. Figure 21b shows that our Pu data are in the range of expected log R_d values but in the lower range defined by the confidence interval on complexation constants for Np(IV). Therefore, the surface complexation constants for Pu/Np(IV) in the 2SPNE SC/CE model can be slightly adjusted and the associated uncertainty confidently reduced to the experimental error on log R_d. For pH < 4, the predicted decrease in log R_d(Np(IV)) values are in contrast to the available Th(IV) and Sn(IV) data, where log R_d values remain constant down to pH < 3 (Bradbury and Baeyens, 2009a, 2009b). This follows from the fact that the formation constant for $\equiv SONpOH^{2+}$ is not known, because experimental data are not available at pH < 4 (Marsac et al., 2015a). The formation of $\equiv SOPuOH^{2+}$ is included in the present model and an adjusted thermodynamic constant extends the sorption plateau down to pH = 3. The predicted independent uptake of Pu(IV) is shown on Figure 21b. As shown in Figure 21a (bold grey line), $\{Pu(IV)/Pu(III)\}_{surf}$ is weakly affected by these adjustments and our previous conclusions remain valid.

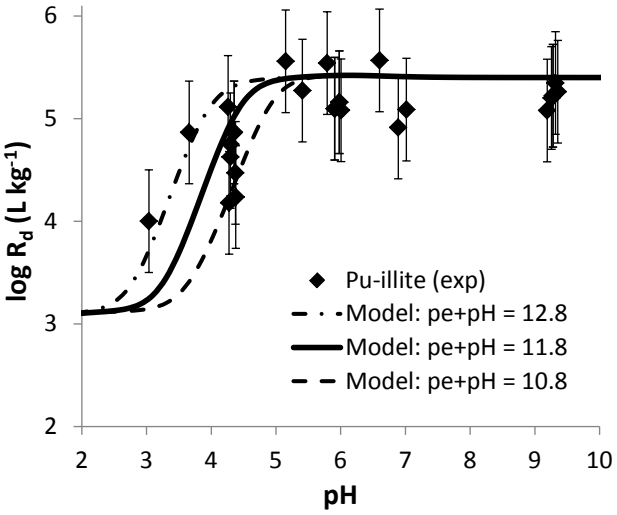

Figure 22: The experimental results for Pu sorption to illite (R_d in L kg^{-1}) as a function of pH are compared with overall log R_d calculated for pH+pe = 11.8 ± 1.0 (bold line; lower and upper values: dashed and dashed-dotted lines, respectively).

The surface complexation parameters for Am(III) are used for Pu(III) and the overall log R_d for Pu (i.e. accounting for the presence of both Pu(III) and Pu(IV) in the suspension) is calculated for pH+pe = 11.8±1.0 with the 2 SPNE SC/CE model. Experimental and model results are compared Figure 22. For pH > 5, Pu(IV) prevails both at the surface and in solution, and overall log R_d for Pu equals log R_d(Pu(IV)). For pH < 5, model and experiment are in agreement, and Figure 22 illustrates the effect of pe on the overall log R_d values. These results suggest that the modeling approach previously developed for Pu sorption to kaolinite (Marsac et al., 2015b), with focus on the Pu(V)/Pu(IV) cou-

ple, can be directly applied to illite even when the Pu(IV)/Pu(III) redox couple is involved. The model can be used to predict Pu uptake by illite in more reducing conditions than those investigated here.

Pu sorption to illite in the presence of calcite.

Natural clay rocks such as OPA and COx contain significant amounts of calcite and the effect of dissolved carbonate on Pu retention must be taken into account. Here, we report the first Pu(IV)-illite uptake data in the presence of carbonate from an illite-calcite mixture under inert atmosphere. In the absence of calcite, the experimental Pu uptake by illite for pH = 10 after only one week contact time agrees with the data obtained after one year, as shown on Figure 23. Therefore, Pu uptake data after 1 week contact time represents a steady-state, at least at alkaline pH. In the presence of calcite, pe = 4.4 and 0.8 is measured for pH = 8.5 and 9.8, which is within the stability field of aqueous Pu(IV). The experimental log R_d values in the presence of calcite are plotted in Figure 23, together with model predictions for Pu uptake on illite and for the total dissolved inorganic carbon concentration ([DIC]). The model predicts [DIC] = 1.2×10^{-3} and 4.3×10^{-4} M for pH = 8.5 and 9.8, respectively. For pH = 8.5, log R_d = 5.3 ± 0.5 L kg^{-1} is measured, suggesting that Pu sorption to illite is weakly affected by the presence of carbonates in our experimental conditions, in agreement with the model. The observation is consistent with Th uptake on MX-80 bentonite at pH = 7.6 and OPA at pH = 8, with and without carbonate ([DIC] = 4.2×10^{-4} M and 1.8×10^{-4} M) (Bradbury and Baeyens, 2005, 2009b, 2011). For pH = 9.8, Pu uptake (log R_d = 4.5 ± 0.5 L kg^{-1}) is slightly lower on average than in the absence of calcite, which might suggest a slight effect of carbonate, unlike what the model predicts. Pu uptake by calcite could not be modeled accurately above pH = 9 by others (Zavarin et al., 2005) and our modeling results also suggest that aqueous Pu-carbonate complexation is not accurately described with the current thermodynamic database for alkaline and low [DIC] conditions. However, this has little impact in the present study, which shows that Pu sorption to illite is only weakly affected by carbonate complexation in a calcite saturated solution. The model is used to predict Pu uptake by illite down to pH = 7, to mimic natural clay rock porewaters conditions such as in OPA or COx, which exhibit pH ≈ 7.5. The range of modeled [DIC] in equilibrium with calcite in the presence of Na-illite (i.e. accounting for the Ca^{2+}-Na^{+} exchange reaction) for 7 < pH < 8 (i.e. 1.5-5 mM) is similar to OPA porewater (≈ 3 mM) (e.g. (Pearson et al., 2011)). The model predicts minor decrease of log R_d down to 4 L kg^{-1} for pH = 7, where [DIC] = 5 mM. Because the formation of ternary Eu(III)- or U(VI)-carbonato surface complexes occurred in the case of smectite (Marques Fernandes et al., 2008; Marques Fernandes et al., 2012), a similar uptake mechanism cannot be excluded for Pu(IV) and illite. Further studies on tetravalent actinide sorption to clay minerals as a function of [DIC] are required to more accurately predict Pu(IV) sorption in natural clay rock-porewater systems.

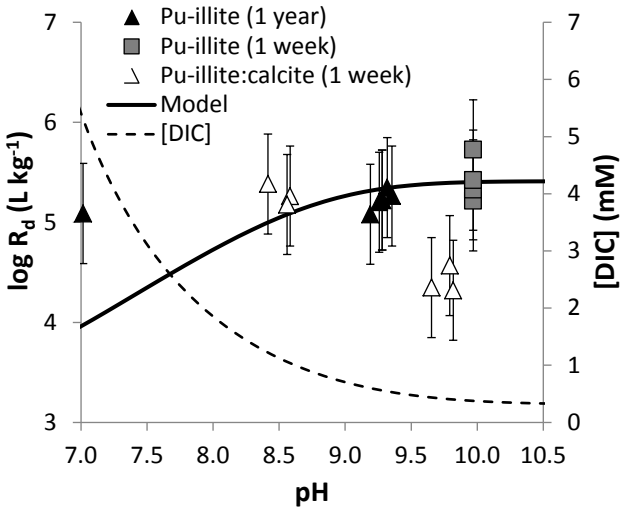

Figure 23: Experimental results for Pu sorption to illite (R_d in L kg^{-1}) versus pH after 1 year and 1 week (for pH = 10) in the absence of calcite, and after 1 week in the presence of calcite. The lines are model predictions of log R_d values for Pu (bold line) and the total inorganic carbon concentration ([DIC], in mM; dashed line) in the case of the Na-illite in contact equilibrium with calcite.

2.1.4 Conclusions

The results of our Np and Pu studies - Pu(IV)/Pu(III) transitions in presence of illite, the outcome of studies of the Pu(V)/Pu(IV) redox reactions in aqueous kaolinite suspensions, or the Np(V)/Np(IV) transitions in presence of illite - demonstrate the applicability of the approach to describe actinide redox reactions in presence of mineral surfaces over a wide range of possible redox conditions (i.e. when Pu(III), Pu(IV) and Pu(V) occur). A more accurate simulation of redox sensitive element behavior in near surface soil systems and deep geological formations becomes possible by implementing measured pe values of a given system into geochemical surface speciation calculations. Therefore, this study may allow more accurate prediction of Pu mobility in the geosphere. Because natural systems can be much more complex, containing e.g. carbonates and natural organic matter, further studies are required to verify the applicability of the present approach to a wider range of geochemical conditions and other redox sensitive elements (e.g. cerium, technetium, arsenic, chromium).

2.1.5 U(VI) sorption on Illite at high ionic strengths

The sorption of hexavalent uranium (U(VI), UO_2^{2+}) onto illite was investigate in the NaCl system as well as in the $CaCl_2$ and $MgCl_2$ system. In these experiments the Illite de

Puy (IdP) was used and its purification and characterization is described in detail in (Schnurr et al., 2015; Schnurr, 2015).

U(VI) sorption in the NaCl system

The sorption data (log K_D) of U(VI) sorbed onto IdP (Illite de Puy) are shown Figure 24 at different NaCl solutions. The sorption is quasi quantitative over a broad pH range. At a pH > 11, a significant decreasing of the sorption is observed. The experimental data agree well with data of U(VI) sorption on illite from the literature (Bradbury and Baeyens, 2009b). The differences at high log K_D values might be caused by different different phase separation as mentioned for the Eu(III) sorption studies onto illte. A slight portion of colloidal clay minerals remaining in solution after centrifugation or filtration can affect result at such low uranium concentration in solution. The ionic strength effect is not significant in NaCl solution with concentrations between 0.1 and 4.0 M. At pH values below pH_c, no difference is observed at the different ionic strengths. At pH_c> 7, the log K_D seemingly depends slightly on the ionic strength.

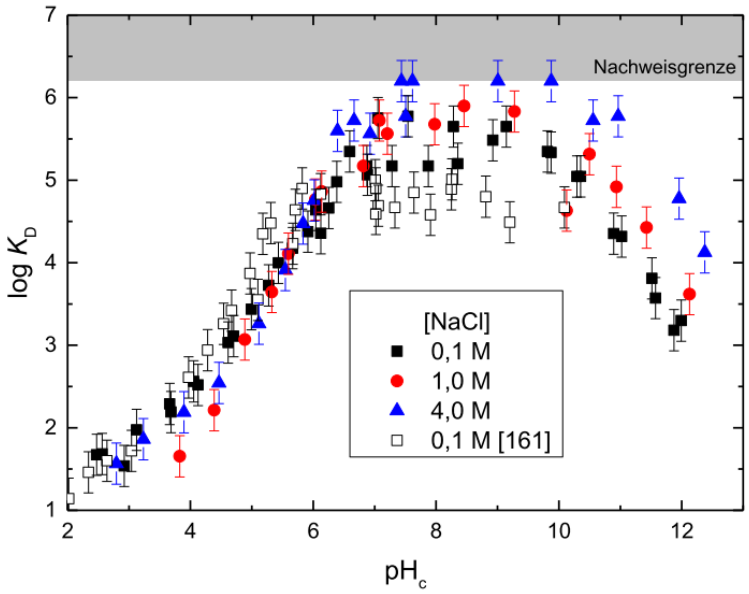

Figure 24: U(VI) sorption on IdP (S:L = 2 g/L) plotted as log K_d versus pH_c values at different NaCl concentrations. Opened quadratic symbols are data from (Bradbury and Baeyens, 2009b). $[U]_{total}$ = 4.0x 10^{-7} M.

Because of the fact that the uranium concentration in this pH range is near the detection limit of the ICP-MS and, hence, the experimental error is rather high, the observed ionic strength effect mustn't be over-interpreted. However, because of the rather low scattering of the data, the ionic strength dependence is obvious. At pH_c>10, the uranium concentration in solution becomes higher, the experimental error becomes smaller and these data might confirm a ionic strength effect at higher pH_c values.

For the modelling with the surface complexation model 2SPNE SC/CE the parameter set of (Bradbury and Baeyens, 2009b) was used. The experimental results from literature slightly differ from the present experimental data. Because of this observation, the inner-sphere complexation constants (log K_{SC}) were slightly modified and adapted to the new experimental data. The difference of the modified log K_{SC} values to the original ones is rather small (Δ log K_{SC} 0, 0.1, 0.4, 0.5 for the four surface species, Table 12) and lie within the uncertainty of the published constants as well as the experimental error margin. The modelling with the adapted parameter set is shown in Figure 25. The modelling results agree well with experimental data at all ionic strengths at lower pH_c values up to pH_c 7. At higher pH_c values a significant difference occurs and the trend between modelling and experiments exhibits an opposing trend. Especially at high ionic strength of [NaCl] = 4 M the modelling underestimates the experimental data.

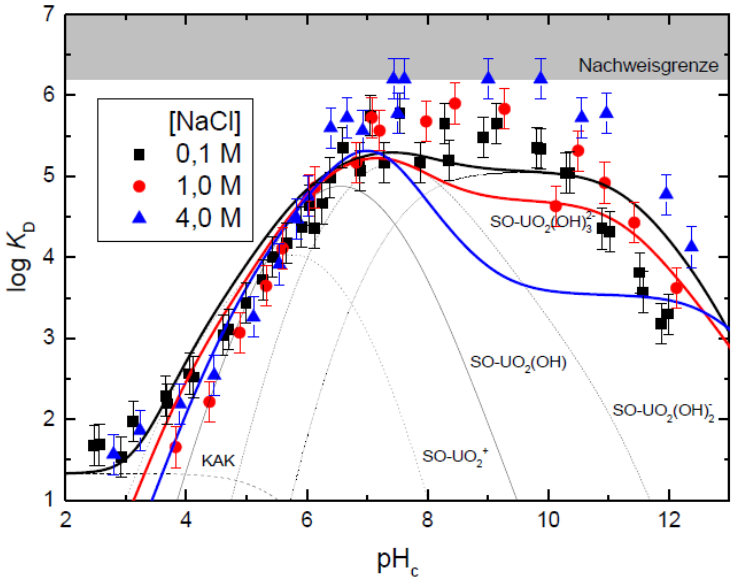

Figure 25: U(VI) sorption on IdP: Comparison between experimental data (symbols) and modelling by the 2SPNE SC/CE model (curves). The species distribution is exemplary shown for 0.1 M NaCl. $[U]_{total}$ = 4.0x 10^{-7} M; IdP: S/L = 2 g/L.

A second adjustment of the model is shown in Figure 26. An additional inner-sphere sorption species is included, which enhances the part of the sorbed uranium with increasing chloride concentration: SO-$UO_2Cl(OH)_2^{2-}$. Modelling with this species significantly improves the description of the experimental data at higher ionic strengths and higher pH_c values. Particularly, the ionic strength dependences at pH_c > 11 is satisfactorily reflected. The species SO-$UO_2Cl(OH)_2^{2-}$ is not mentioned in the literature and cannot definitiely be confirmed in this work. But several findings hint to the existence of such a species. Fuger could identifiy a mixed solid phase of uranium: $UO_2ClOH \cdot 2H_2O$ (Fuger et al., 1983). Additionally, spectroscopic investigations by Runde show that mixed U(VI) complexes with Cl-OH and Cl-CO_3 are possible (Runde, 2011).

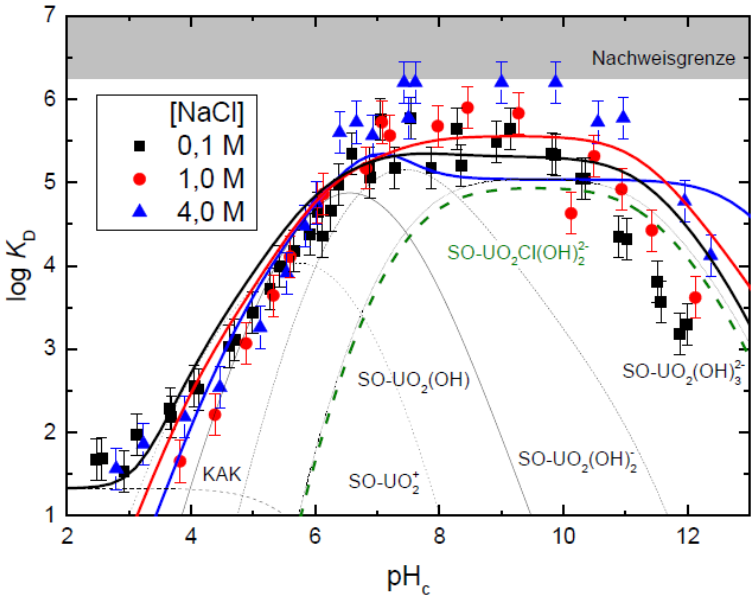

Figure 26: U(VI) sorption on IdP in NaCl solution: Comparison between experimental data (symbols) and modelling (lines) by the 2SPNE SC/CE model including the species SO-$UO_2Cl(OH)_2^{2-}$ (green dashed curve). The species distribution is exemplary shown for 0.1 M NaCl. $[U]_{total}$ = 4.0x 10^{-7} M; IdP: S/L = 2 g/L.

U(VI) sorption in the $MgCl_2$ and $CaCl_2$ system

Further investigations were performed to elucidate the influence of the background electrolyte on the U(VI) sorption on illite. For this sorption batch experiments in $MgCl_2$ and $CaCl_2$ were made. The sorption edges of both electrolytes are very similar at low ionic strengths (I = 0.18 M). For $MgCl_2$ the sorption experiment stops at pH_c ~9, because at higher pH_c the $Mg(OH)_2$ starts to precipitate. Comparison with the NaCl system at comparable ionic strength (I = 0.1 M) shows a very congruent sorption behavior. Only at very high pH_c values (pH_c > 11) the U(VI) sorption decreases stronger in the NaCl system. Nevertheless, the U(VI) is quasi quantitatively sorbed on the illite surface in the relevant pH_c range of 6 – 11.

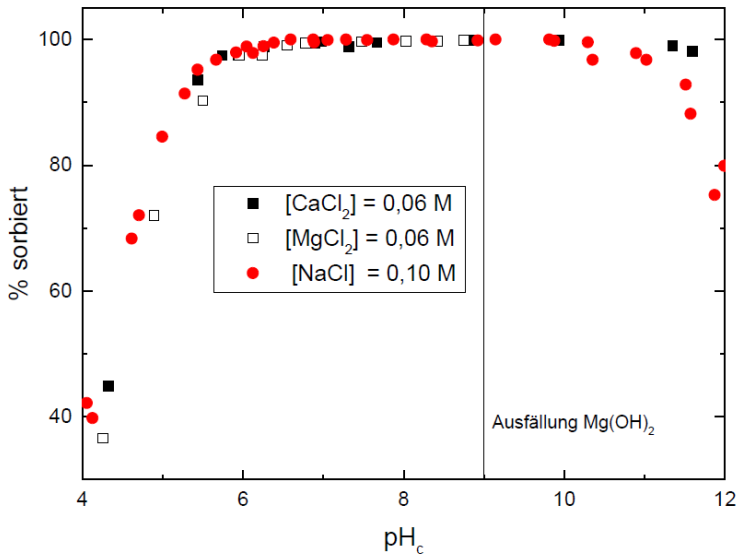

Figure 27: U(VI) sorption ([U]total = $4.0 \cdot 10^{-7}$ M) an IdP (S:L = 2 g/L) plotted as % sorbed against pHc value in $MgCl_2$ (black, open), $CaCl_2$ (black, closed, 0.06 M) and NaCl (red, 0.10 M) solutions.

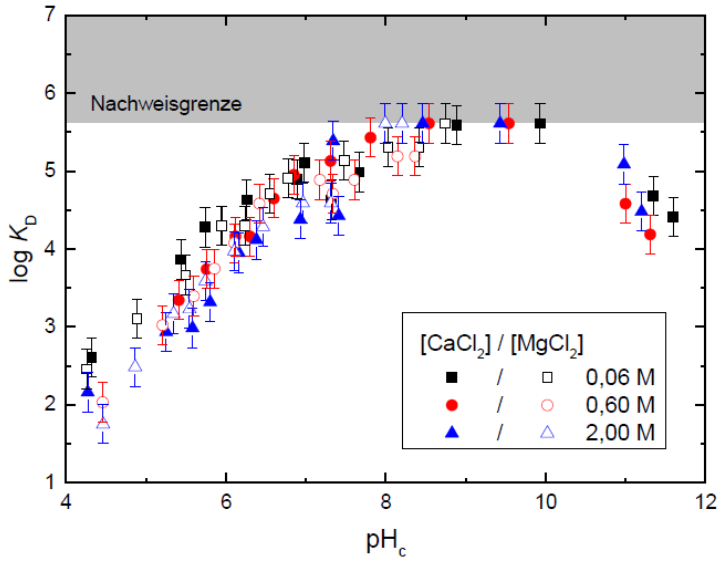

Figure 28: : U(VI) sorption on IdP (S:L = 2 g/L) in Ca/$MgCl_2$ solution plotted as log K_d versus pH_c values at different $MgCl_2$ (open symbols) and $CaCl_2$ (closed symbols) concentrations.

A very similar sorption behavior of U(VI) on illite is also observed at elevated ionic strength as it is demonstrated in Figure 28. In the pH_c range 4.5 – 7 only a small ionic strength dependence is observed; the pH_c sorption edge is slightly shifted to higher pH_c values with increasing ionic strength (< 0.5 log K_D units per 1 M electrolyte). At pH_c > 8 the sorption is quasi quantitive (log K_D > 5) and no significant change is obvious with increasing ionic strength. The radionuclide concentrations in solution of all systems reach the experimental detection limit and the sorption gains a maximum at log K_D =

5.5 (99.95% sorption). Only at very high pH_c values (>12) the log K_D lessens to log K_D > 4 (95%).

As mentioned before, different data set for modelling of the radionuclide sorption exist in the literature, especially for Eu(III) on Na- and Ca-clays. For the Ca-IdP no data sets of the inner sphere surface complexation constants for U(VI) are available in the literature. Therefore, the constants from the Na-IdP system were used to deduce the constants for the Ca-IdP system. The log K_{SC} of the U(VI) sorption on Na-IdP were corrected by the same difference values (Δ log K_{SC}) that were observed between the Eu(III) sorption on Na- and Ca-montmorillonite system (details see (Schnurr, 2015)). The result of the modelling by using the deduced log K_{SC} parameter set is shown in Figure 29 for 0.06 M $CaCl_2$. Neither the published log K_{SC} of the Na-IdP, nor the deduced log K_{SC} for the Ca-IdP can describe correctly the experimental data. It is obvious that the difference between the Na and Ca system is not so much pronounced for U(VI) such as for Eu(III). Therefore, it can be assumed that the difference in log K_{SC} of U(VI) sorption between the Na and Ca system is not as large as in case of Eu(III) and that a new dataset is required. For a new modelling the log K_{SC} parameter set for the Ca-IdP was slightly elevated (Table 12), to describe the experimental data at 0.06 M $CaCl_2$ correctly.

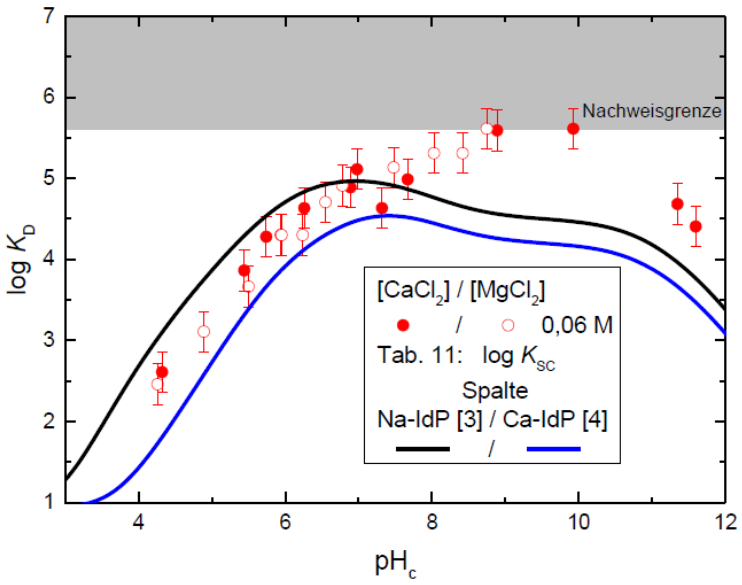

Figure 29: U(VI) sorption on IdP (S:L = 2 g/L) in 0.06 M Ca/$MgCl_2$ solution; comparison between experimental log K_D values (symbols) and calculation (curves) by the 2SPNE SC/CE model using the log K_{SC} for Na-IdP (black) and Ca-IdP (blue) from Table 12 (column 2 and 4).

Even at higher ionic strength the modified parameter set describes quite well the range around the edge. However, the decreasing sorption with increasing ionic strength at pH_c > 8 does not match with the experimental data, but not so distinct like in the Na system.

Table 12: Thermodynamic equilibrium parameters (log K_{SC}) at infinite dilution to model U(VI) sorption on illite (IdP) with the 2SPNE SC/CE model (Bradbury and Baeyens, 2009b)

Surface complex[#] (log K_{SC})	Na-IdP	Na-IdP (p.w.)	Ca-IdP*	Ca-IdP (p.w.)
$SSOUO_2^+$	2,0	2,0	0,5 (Δ -1,5)	0,7
$SSOUO_2(OH)$	-3,5	-3,4	-4,3 (Δ -0,8)	-4,0
$SSOUO_2(OH)_2^-$	-10,6	-10,2	-10,9 (Δ -0,3)	-10,3
$SSOUO_2(OH)_3^{2-}$	-19,0	-18,5	-19,3 (Δ -0,3)	-18,2
$SSOUO_2Cl(OH)_2^{2-}$	-	-17,5	-	-17,5

*: the values accord to the analog Δlog K_{SC} (values in parathesis) of Na-SWy to Ca-SWy in (Schnurr, 2015)

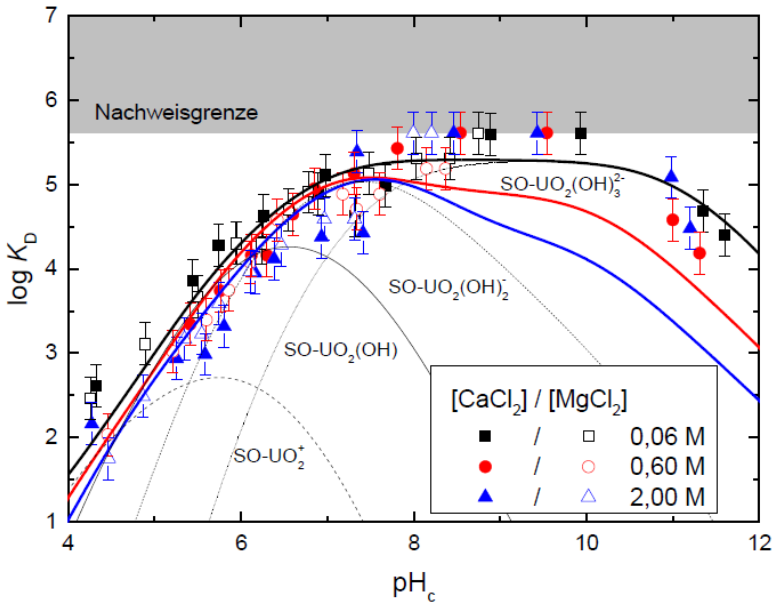

Figure 30: U(VI) sorption on IdP (S:L = 2 g/L) in Ca/$MgCl_2$ solution at various concentrations; comparison between experimental log K_D values (symbols) and calculation (curves) by the 2SPNE SC/CE model including sorption species distribution at 0.18 M salt concentration. The log K_{SC} used for the modelling is listed in Table 12 (column 5).

Figure 31 shows the modelling anolog to the NaCl system by introducing a further inner sphere sorption species ($SO\text{-}UO_2Cl(OH)_2^{2-}$). This species is regarded as one of several possible species in the $CaCl_2$ system. Especially in solutions with higher Ca^{2+} concentrations other species like $SO\text{-}UO_2\text{-}Ca_xCl_y(OH)_z$ are also feasible. Also in presence of carbonate very stable Ca complexe with UO_2 are described in the literature, like $Ca\text{-}(UO_2)_2\text{-}CO_3$-species (Dong and Brooks, 2006; Guillaumont et al., 2003). However, the addition of species that are definitely not characterized would over-parametrise the modelling and such species are neglected here. As shown in Figure 31, the experimental data are well described by regarding the new U(VI) surface species over the whole pH_c and ionic strength range.

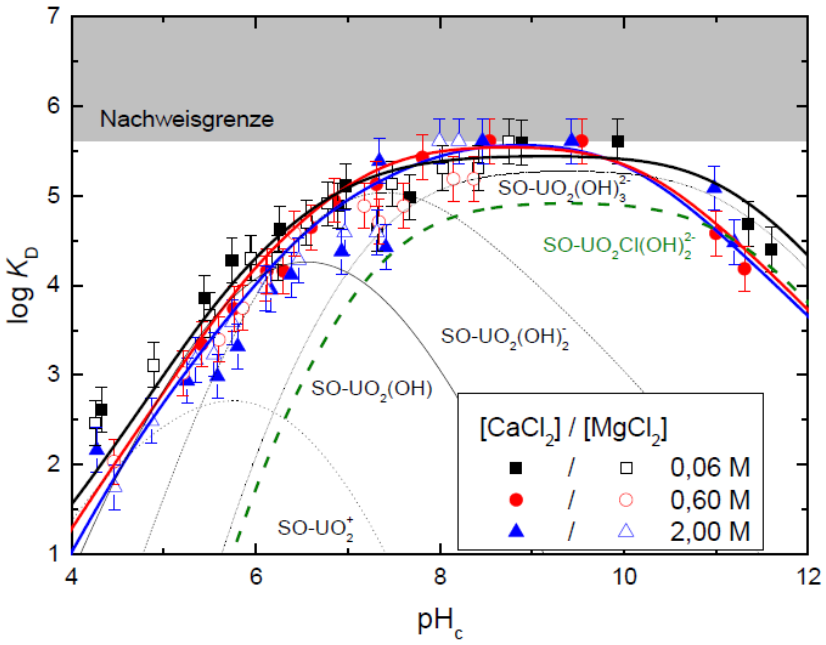

Figure 31: U(VI) sorption on IdP (S:L = 2 g/L) in Ca/$MgCl_2$ solution at various concentrations; Calculation of the sorption including the surface species SO-$UO_2Cl(OH)_2^{2-}$ (green dashed curve). Modelling with the 2SPNE SC/CE model and log K_{SC} listed in Table 12 (column 5).

2.1.6 Conclusions

The U(VI) shows only a minimal cation exchange at lower pH_c values, which is not observable at higher pH_c values and inner-sphere complexation takes place. The 2SPNE SC/CE model can describe the experimental data at $pH_c \leq 7$ for NaCl and $pH_c \leq 8$ for the Ca/$MgCl_2$ system. At higher pH_c values (>8), the modelling predicts for the sorption an influence of the ionic strength that is not observed in the experiment. By introducing a additional possible surface species (SO-$UO_2Cl(OH)_2^{2-}$), the experimental data are described quite well over the whole pH_c and ionic strength range. However, the existence of this species could definitely not confirmed in the present work and is one of the main task for future investigations.

2.2 Iron phases

Corrosion processes of final disposal container made of iron in contact with ground water transforms the iron into new iron phase. These secondary phases can interact with radionuclides and might immobilize them. In this work package first experiments with secondary products like Green Rust (GR) or magnetite (MAG) have been performed to get more insight into their behaviour with respect to the actinides. To keep the condi-

tions as simple as possible and to exclude redox reactions of the radionuclide of interest, the redox stable trivalent lanthanide neodymnium and the trivalent actinide americium were probed. The GR and the MAG were synthesized in presence of both metal ions and the state of them in the matrix were characterized by XRD, XPS and SEM.

The results obtained for the green rust (GR) chloride synthesized in the presence of Nd(III) are presented first. The results obtained for GR and magnetite (MAG) prepared by direct precipitation in the presence of Am(III) are presented in the second section.

2.2.1 Green rust synthesized in the presence of Nd(III)

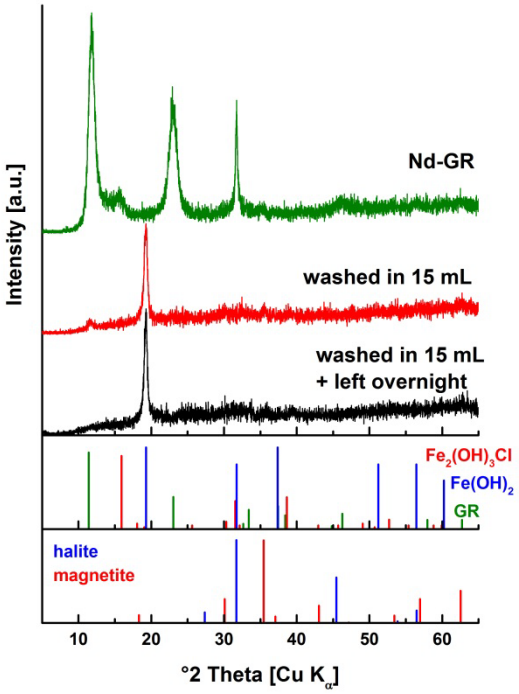

Figure 32: X-ray diffractogram of the sample Nd-GR and of the sample after different washing procedures, with comparison to the database.

Green rust was precipitated by addition of NaOH to a solution containing Fe(II), Fe(III) and trace amounts of Nd(III) ions (molar ratios Fe(II)/Fe(III) = 5/1 and Fe_{tot}/Nd = 3000/1, sample Nd-GR) under Ar (glove box). The pH (7.4(1)) and E_h (-535(20) mV *vs* Ag/AgCl) were recorded. The X-ray diffractogram indicated the formation of GR and minor amount of a by-product identified as $Fe_2(OH)_3Cl$, together with halite due to the high salt content (Figure 32). SEM micrographs revealed a layered structure, as expected for GR, and some aggregates that could possibly correspond to $Fe_2(OH)_3Cl$ (Figure 33). XPS was used to obtain information on the speciation of the elements. The position and the shape of the elemental line are governed by the immediate chemical environment. Data were collected at different positions on the sample: at the edge, at the center and at an intermediate position. The O 1s line indicated an increased oxide compo-

nent from the edge (~30 %) to the middle (~60 %) of the sample and at the same time, the proportion of Fe(III) increases concomitantly, based on the intensity of the Fe 2p satellite peak. This deprotonation of hydroxyl groups occurring simultaneously with an increase in ferric iron has already been reported (Mullet et al., 2008) and correspond to the ferrous iron oxidation within the GR structure. Obviously, the sample is not homogeneous, at least to a certain depth where information can be obtained by XPS (~3 nm). No Nd(III) could be detected. Finally, the sample was analyzed by Raman spectroscopy. Measurements were performed by placing the sample in a thin quartz cuvette closed with a septum screw cap. The detection of GR corroborates the XRD data, and magnetite was also detected by Raman but not by XRD. Magnetite is an oxidation product of GR: the best explanation is a diffusion of air into the cuvette followed by a wet oxidation. In contrast, XRD data were collected on dried sample where GR is less reactive toward oxygen.

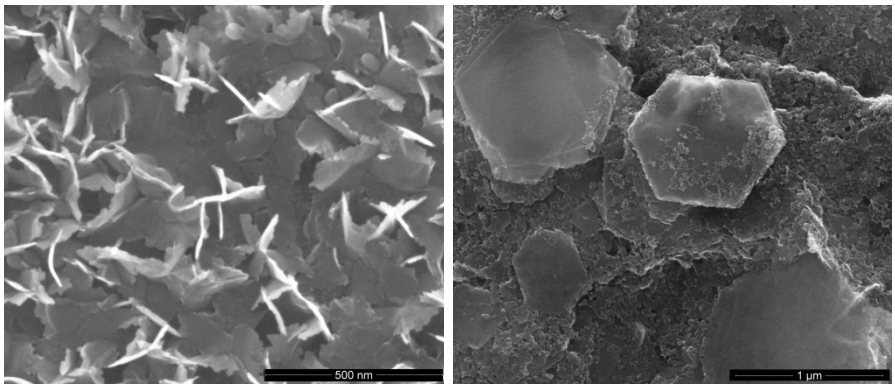

Figure 33: SEM micrographs of the sample Nd-GR before (left) and after (right) washing and aging overnight. Both samples exhibit a layered structure.

Part of this Nd-GR suspension (1.5 mL) was washed by centrifuging and replacing the supernatant by deoxygenated water (15 mL). The solid phase was analyzed by XRD shortly after this washing procedure and after additionally allowing to react overnight. No difference due to the longer reaction time could be detected. XRD data evidenced the formation of $Fe(OH)_2$ (Figure 32), but no Fe(III)-bearing phase could be detected. However, a substantial part of the small particles exhibited magnetic properties, suggesting the formation of small sized magnetite particles. SEM revealed the presence of large hexagonal platelets, as for Nd-GR, together with fine grained particles (Figure 33). These aggregates represent a small fraction of the sample, possibly magnetite, but could not be detected/identified by XRD.

2.2.2 Green rust and magnetite synthesized in the presence of Am(III)

Green rust was precipitated in the presence of Am(III) following a procedure identical to that for Nd(III) (molar ratios Fe(II)/Fe(III) = 5/1 and Fe_{tot}/Am = 1500/1, sample Am-GR). The final pH and E_h were, respectively, 7.3(1) and -486(20) mV *vs* Ag/AgCl. Separately, magnetite was precipitated in the presence of Am(III) by drop wise addition of a

Fe(II)/Fe(III) solution containing Am(III) (molar ratios Fe(II)/Fe(III) = 1/2 and Fe_{tot}/Am = 1500/1, sample Am-Magn) to a NaOH solution. Here, the final pH and E_h were, respectively, 12.3(1) and -685(20) mV *vs* Ag/AgCl. Only the sample Am-GR was analyzed by XRD: it contains green rust and the by-product $Fe_2(OH)_3Cl$, similarly to Nd-GR. SEM micrographs indicated that Am-GR exhibits a layered structure, as can be expected for GR compounds, and Am-Magn consists of aggregates of fine grained particles (10-20 nm).

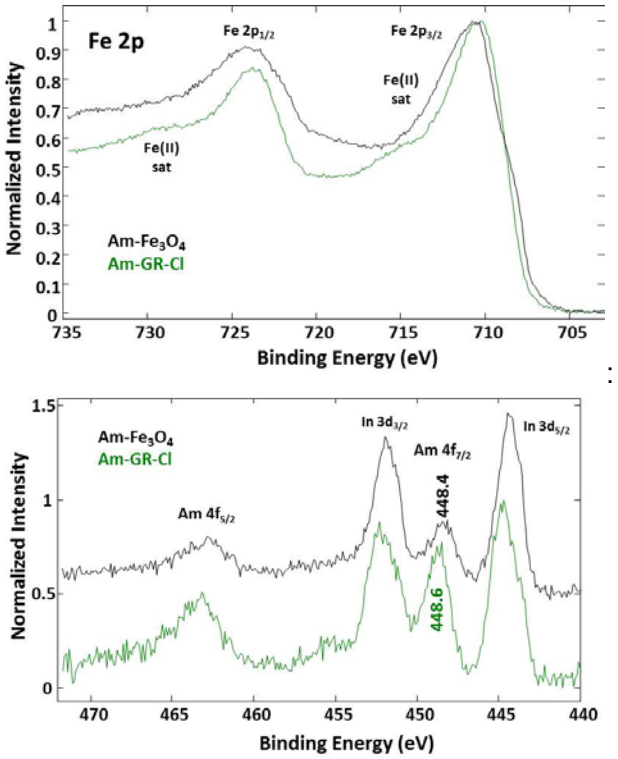

Figure 34: XPS Fe 2p (left) and Am 4f (right) spectra of the GR and magnetite containing Am(III). The indium line comes from the substrate

XPS data were collected for both samples. The Fe 2p narrow spectrum of Am-GR and Am-Magn (Figure 34) match with literature data (Huber et al., 2012; Mullet et al., 2008). The O 1s spectra indicate an equal proportion of oxide and hydroxide in Am-GR and a dominant oxide component in Am-Magn. Am-GR certainly underwent a partial oxidation similarly to Nd-GR. Despite the low content, Am(III) spectra could be recorded. The elemental line is within uncertainty located at similar energy in Am-GR and in Am-Magn, between that of the metal and that of the oxide (Gouder et al., 2005).

The samples were also analyzed by Raman spectroscopy: only magnetite could be detected in both samples. This is contradictory to the XRD and SEM data. No GR could be detected in Am-GR, meaning that the sample must have underwent a transformation. To prepare the Am-GR sample, part of the suspension was centrifuged and the supernatant removed. A small amount of water was used to dilute the wet paste and introduce the sample in the septum screw caped quartz cuvette. The sample Nd-GR was washed with a large amount of water and only $Fe(OH)_2$ could be detected by XRD: the

Am-GR sample preparation can thus not have led to the observed sample transformation. In contrast, it may rather be the diffusion of air in the cuvette followed by a wet oxidation. The same effect was observed for Nd-GR, but to a lesser extent. Part of the Am-GR suspension (1.5 mL) was washed with deoxygenated water (15 mL) similarly to Nd-GR and left in contact. This sample is not analyzed yet.

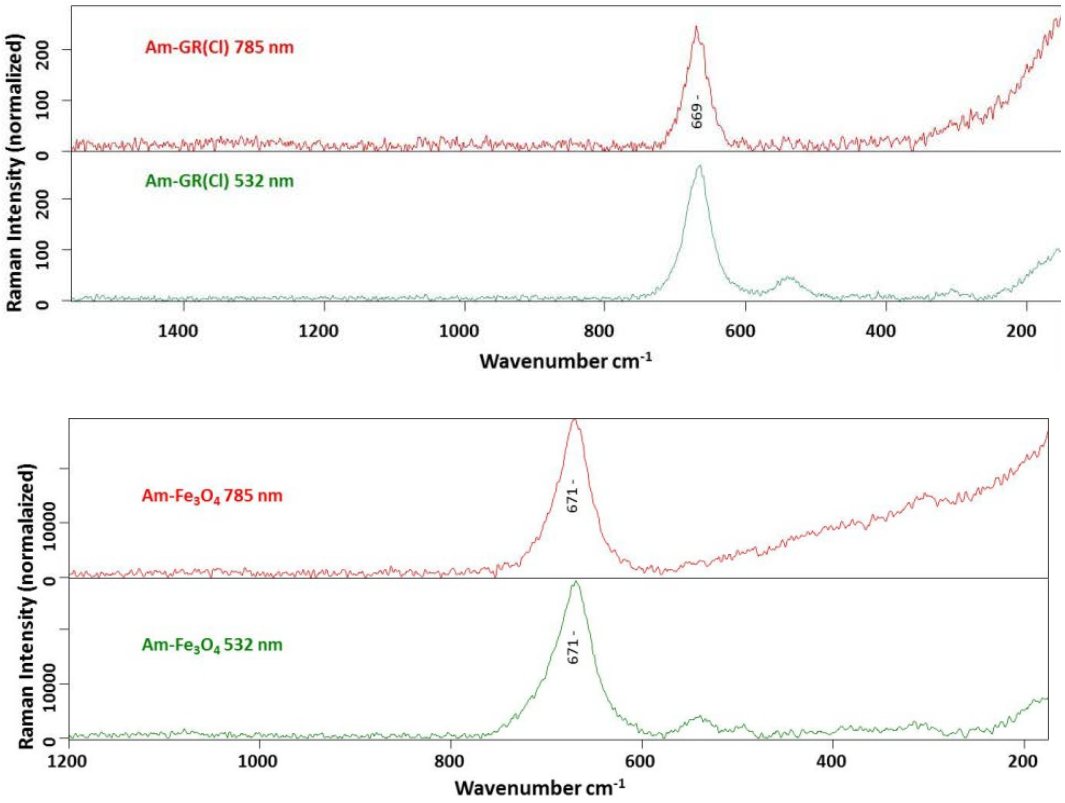

Figure 35: Raman spectra of Am-GR (top) and Am-Magn recorded at two wavelengths. Only magnetite is detected.

3 Diffusion of radionuclides in clay minerals

The main process responsible for possible transport of radionuclides in clay formations is molecular diffusion. Understanding the diffusion properties of radionuclides in clay formation is one key issue in performance assessment of repositories. Clay can be used as host rock or as buffer material to establish a repository. Natural clay rock possesses a heterogenous composition and therefore heterogeneous diffusion properties. To ease the experiment, the diffusion of radionuclides was investigated with a single clay mineral. The illite was chosen as a main component of opalinus clay, like described in the sorption section. The non-swelling illite should exhibt only interparticle porosity and no intraparticle porosity.

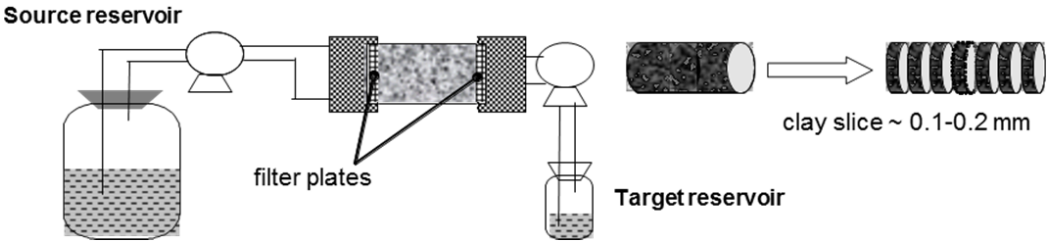

Schematic illustration of the through-diffusion method

Illite de Puy used in this study was purified according to a procedure agreed on within the EC project CP CatClay (www.catclay.org). The diffusion (“in” and “through” diffusion) experiments with a compacted, cylindrical Na-illite sample (8.18 – 8.72 g, diameter = 2.54 cm, thickness = 1 cm, compaction factor = 1.61 g/cm^3) were performed with

NaCl as background electrolyte. The experimental set-up (s. above) consists of a diffusion cell made of PEEK material or stainless steel.

3.1 Diffusion of Tritium and Chloride in Illite

Breakthrough curves for HTO and ^{36}Cl in 0.1 M NaCl, as well as the activity/concentration decrease in the source reservoir, are presented in Figure 36 a and b. The data are also representative for the higher ionic strength. For both tracers, a steady state (indicated by a constant flux) is achieved after ~3 days and remained more or less constant to the end of the experiment. In case of ^{36}Cl, the values for the diffusive flux are observed to scatter, which can be related to a low activity in the downstream solution. The results are presented in Table 13. It should be kept in mind, that the activity in the high-concentration reservoir decreased during the course of the experiment to ~91% of the initial concentration in case of HTO (the decrease in case of ^{36}Cl was only 2%). As constant boundary conditions were thus not fulfilled, the diffusion parameters calculated hereby may be inaccurate.

Table 13: Summary of D_e (m^2 s^{-1}) and α (-) values for HTO and ^{36}Cl in Na-illite at a bulk dry density (ρdb) of ~1700 kg m^{-3} together with literature data ((Glaus et al., 2010), unpublished data from SCK-CEN and PSI).

Tracer	NaCl (M)	D_e (x 10^{-10}) (m^2s^{-1})	α	Performed by
HTO	0.1	1.95 ± 0.04	0.53	This work
	0.5	1.97 ± 0.05	0.43	This work
^{36}Cl	0.1	0.67 ± 0.04	0.18	This work
	0.1	0.28 ± 0.03[a]	0.12 ± 0.03[a]	(Glaus et al., 2010)
	0.5	1.00 ± 0.05	0.25	This work
	0.5	0.53 ± 0.07[a]	0.18 ± 0.04[a]	(Glaus et al., 2010)

[a] ρ_{db} = 1900 kg m^{-3}

HTO diffusion coefficients and values for rock capacity factor α (Glaus et al., 2010) (or the porosity ε, respectively) are similar in 0.1 and 0.5 M NaCl, indicating that an increase in background electrolyte concentrations has no effect on the geometrical properties (tortuosity or constrictivity) on the compacted clay mineral. However, an increase in ionic strength affected the transport parameters in case of ^{36}Cl, where D_e and α are observed to be higher in 0.5 M NaCl. The lower D_e value for ^{36}Cl compared to HTO can be related to a reduced accessible pore space for anionic tracers (anion accessible porosity ε_{acc}), as anions are repelled from the vicinity of the negatively charged clay sur-

faces. On the other hand, the increase in D_e at higher ionic strength can be linked to an enhanced electrostatic shielding of this negative surface charge, increasing the fraction of anion accessible pore space (Glaus et al., 2010). In case of ^{36}Cl, available diffusion coefficients and ε values in the literature are only reported for a higher bulk dry density (ρ_{db}) of ~1900 kg m^{-3}

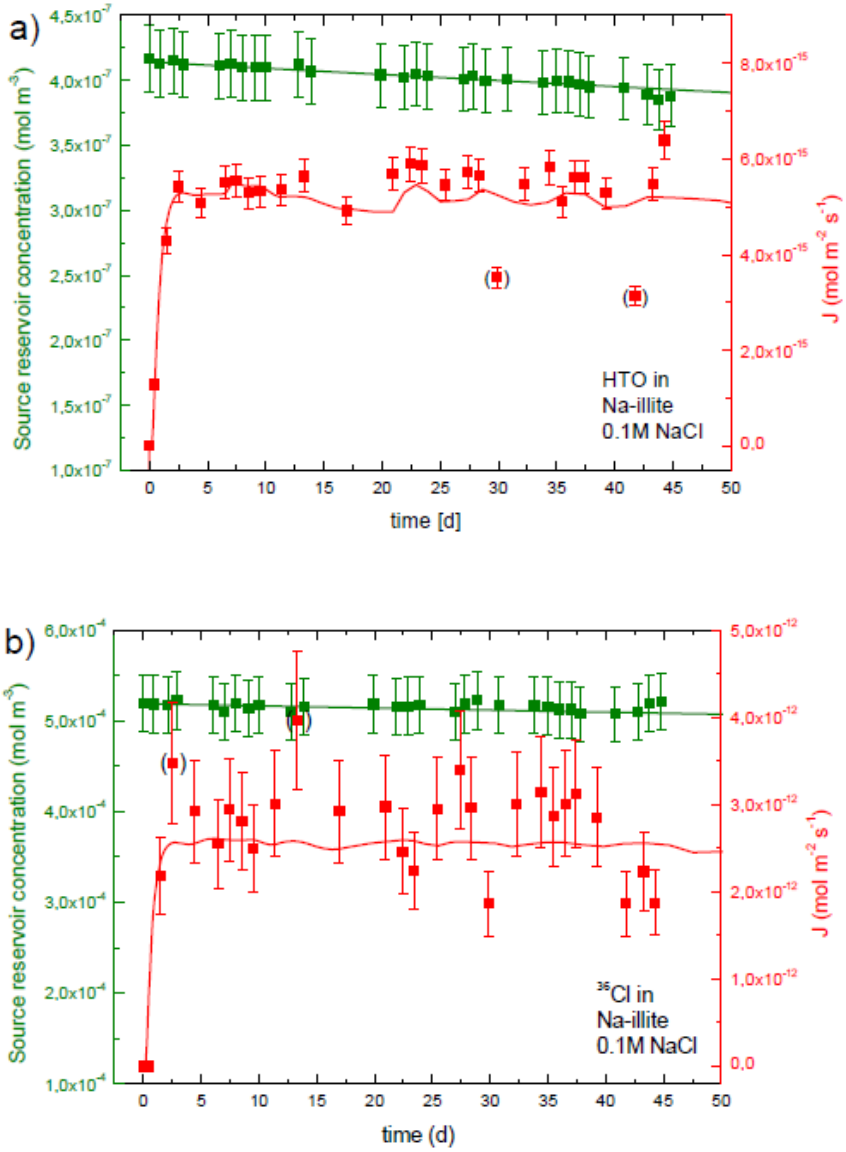

Figure 36: Diffusion of HTO (a) and $^{36}Cl^-$ (b) in compacted Na-illite (ρdb~1700 kg m^{-3}) at pH 5.5 and 0.1 M NaCl as mass flux in the low concentration reservoir (J) and evolution of the source reservoir concentration.

Consequently, D_e and α are lower compared to the present set of experiments at ρ_{db} ~1700 kg m_{-3}, but are also observed to increase with increasing background electrolyte concentration (Table 13).

3.2 Diffusion of Eu(III) in compacted illite

The experimental set-up comprises a diffusion cell made of PEEK material, a peristaltic pump and a reservoirs containing a Eu solution (Eu: $1E^{-6}$ M). The starting pH of the solutions was 5.3, but drifted to 6.4 during the experiment as no buffer was added. The solutions were circulated through the end plates with a total running time of 152 days (3650 hours).

The diffusion experiment result show a steadily decreasing Eu concentration for < 1500 h, reaching very low Eu(III) concentrations at the detection limit. This result indicates an almost complete Eu uptake onto the Na-illite mineral, which can be due to an increase of pH from 5.3 to 6.4. The Eu ions are not sorbed onto potential colloidal phases in the reservoirs, as the Eu concentration remained unchanged before and after phase separation by ultracentrifugation (90000 rpm for 1h).

After the in-diffusion experiment, the contact solution was exchanged by different methanol/water ratios followed by full methanol diffusion and consecutive LR white (epoxy resin) impregnation. As the analysis of the various alcohol/water mixtures and the epoxy resin revealed no mobilization of Eu during this preparation steps, this procedure opens a way for post-processing procedures (microstructure analysis including spatial resolved laser fluorescence studies).

The results of the in-diffusion experiments indicate a quantitative uptake of Eu onto Illite, which correlates with an increasing solution pH. In addition, an exchange of the electrolyte solution against an epoxy resin for impregnation purposes does not mobilize the tracer used, therefore being an appropriate way to preserve the illite microstructure, facilitating post-processing analysis.

3.3 Diffusion of Np(V)

The diffusion of Np(V) in compacted Na-illite at pCO_2 = -3.5 (atmospheric conditions) in 0.1 M NaCl is investigated by through-diffusion technique. Two experiments (NP1 and NP2) have been performed: 1. for the first experiment a diffusion cell with stainless steel filters at the in- and outlet was used; 2. for the second experiment a diffusion cell with PEEK supporting plates and filter membranes was applied instead of steal. A schematic illustration of the setup is given in Figure 37.

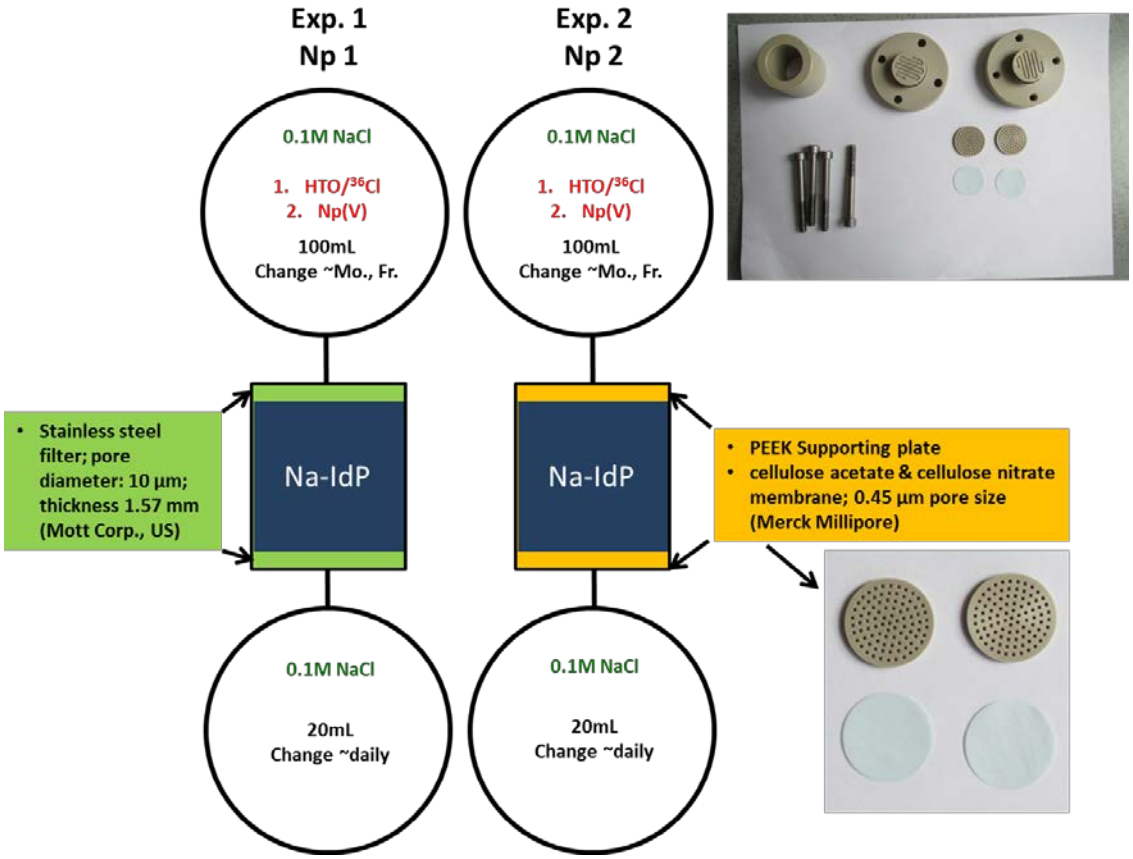

Figure 37: Schematic illustration of the two Np diffusion experiments NP1 and NP2.

The pH of the solution was pH 4.6 in experiment 1 (NP1) and pH 4.8 in experiment 2 (NP2). The Na-illite was compacted to an ilite core with a bulk dry density of ~1600 kg m^{-3}. In NP1, the core was sandwiched between stainless steel filters (Stainless steel: 316L, pore diameter: 10 mm, diameter = 0.0254 m, thickness = 0.0016 m; MOTT industrial division, Farmington, USA) and closed with two end-pieces. In NP2, a PEEK supporting plate with cellulose acetate and nitrate filters (0.45 µm pore size, Merck Millipore) was used. The samples were pre-equilibrated with 0.1 M NaCl solutions from both sides. After one month the solutions were replaced against new ones. The solution in one reservoir was spiked with $1.6x10^{-5}$ M ^{237}Np (~100 Bq cm^{-3} V = 100 mL), while the other one contained the background electrolyte solely (V = 20 mL), representing the high (HCR)- and low-concentration (LCR) reservoir, respectively. The solution in the LCR is replaced daily, in order to keep the concentration of the tracer in this reservoir as low as possible (Van Loon et al. 2003). Samples from the HCR are being taken periodically (every 2-3 days). The activities in both reservoirs are measured by liquid scintillation counting (TRICARB 3110TR, Perkin-Elmer).

The results of the diffusion experiments are shown in Figure 38. It is obvious, that a difference exist between experiment NP1 and NP2. A plausible explanation could not be found, but might be related to sorption phenomena and texture of the filter material.

A breakthrough was observed after 100 days. Unfortunately, both experiments have not achieved a steady state. After reaching a maximum, the diffusive flux decreased and this behavior cannot be explained at the moment. Maybe neptunium could not reach the low concentration reservoir because of blocked tubings. The Np(V) experiment could not completed within the project term, but it will be further examined in the frame of subsequent projects. As next steps, the clay cores must be characterized by HTO diffusion, and then, after stopping the experiment, post-mortem analysis of the cores must be performed by autoradiography, spectroscopic methods, and abrasive peeling. Additionally, modeling of the experiments can help to interpret the diffusion behavior of Np(V) in illite.

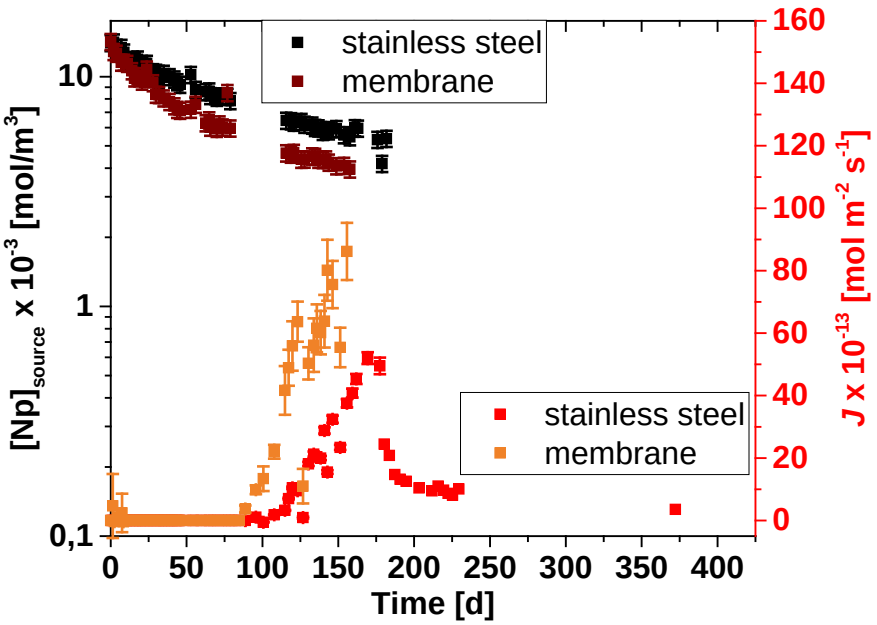

Figure 38: Np flux and break through cumulated activity of experiment Np1 (stainless steel filter, black and red points) and Np2 (peek supporting plate plus filter membrane, dark and light brown points) as a function of time.

3.4 Diffusion of fulvic acid in Illite

Natural clay stone very often contains organic fractions (dissolve organic matter, DOM) of various composition from small low molecular weight molecules up to large polyelectrolytes with colloidal behavior. The colloidal organics can complex radionuclides very strong and might facilitate radionuclide migration as DOM nanoparticle borne transport. Whether such colloid organics can migrate via diffusion processes through a compacted clay like illite is one key question for performance assessment. The diffusive transport in these systems was observed to be higher for cations and lower for anions, compared to neutral species. While the reduced mass transport for anionic tracers is generally explained by a reduced accessibility of the total pore space due to a repulsive interaction of the equally charged surfaces and solutes (anion exclusion effect), the reason for the enhanced transport of cationic species (surface diffusion) is under inten-

sive discussion. Here, the experiment should show, whether tritiated fulvic acid (^{3}T-FA), as an analogue for DOM, has diffusive properties in compacted Na-illite.

Na-illite with the same properties like in the Eu and Np experiment was used in this study. In contrast to the metal cation experiments, the volume on the low concentration side was increased to 500 mL and the container was not replaced regularly. The experiments were performed at two ionic strengths (0.1 and 1 M NaCl), while the pH was fixed at 5 with an organic buffer ($5x10^{-3}$ M MES). Samples were taken in regular intervals and the activities in both compartments were determined by liquid scintillation counting. The experimental results are illustrated in Figure 39.

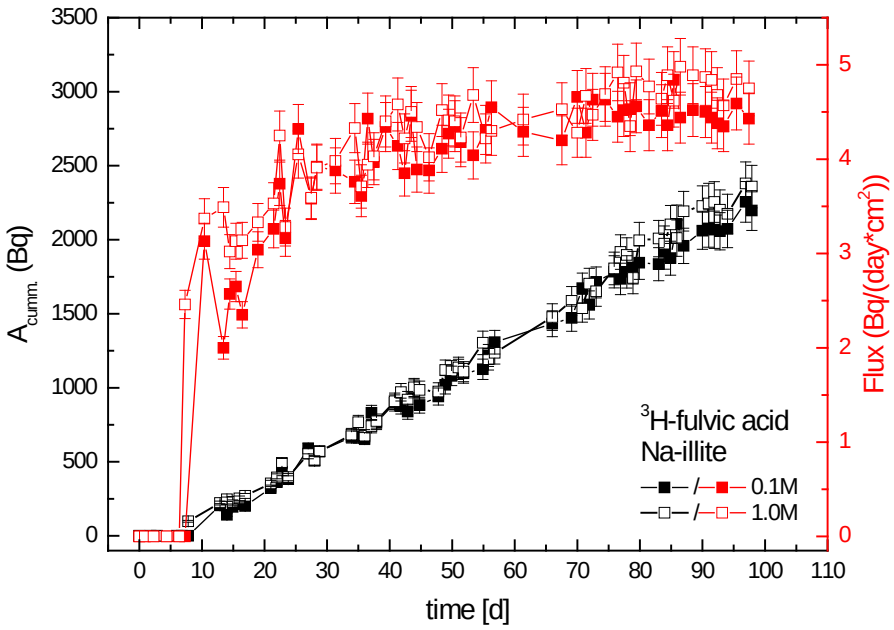

Figure 39: Diffusion of fulvic acid (FA) in compacted Na-illite at pH 5 and NaCl as back electrolyte: cumulated activity of ^{3}H-FA in LCR and flux of FA as a function of time.

During the experimental time the activity in the low concentration reservoir increased gradually, with a steady state (constant flux) observed after ~70 d. Due to the fact, that the decrease in activity in the high concentration compartment as well as the increase in the low concentration reservoir exceeded 1% of the initial concentration on the high concentration side, the boundary conditions used in the analytical solution are not fulfilled and the diffusion coefficient (D_e) as well as the rock capacity factor (α) can only be estimated by linear regression analysis. Taking these uncertainties into account, diffusion coefficients of D_e = $1.51x10^{-11}$ m^2/s and $1.70x10^{-11}$ m^2/s can be calculated for 0.1 and 1.0 M NaCl, respectively. For α, the calculated values were -0.44 and 0.61 (0.1 and 1.0 M NaCl, respectively). The diffusion coefficients for FA are comparable to D_e values determined for negatively charged traces (i.e. $^{36}Cl^-$). However, these values should be

taken with care (and seems to be unrealistic for the rock capacity factors). More reliable data for D_e and α can be obtained by fitting the data in numerical (2-D) simulations, which will be applied in the future.

3.5 Conclusions

The diffusion of non and weak absorbing ions can be described quite well and the results from different studies show a good match. However, the experiments with strong absorbing metal cations, fulvic acid, as well as with redox sensitive metal ions exhibits some experimental difficulties. The boundary conditions for an unambiguous evaluation are mostly not given. Hence, the results have large uncertainties und are sometimes inconsistent. On these grounds well designed experiments shall be performed in future projects to give more insight into the diffusion of strong absorbing ions.

4 Clay organic compounds, fulvic and humic acid: interactions with radionuclides

Natural clay rock formations, considered as a potential host rock for nuclear waste disposal, can contain a significant amount of organic matter. This organic matter can be low molecular organic (LMWO) (Courdouan et al., 2007a), as well as fulvic acid-like organic compounds (Schäfer et al., 2003). Additionally, humic acids were also included as a significant component of ground waters found in the cover deposits of salt rock formations and the Jurassic and lower Cretaceous clay rock layers in Northern Germany. To what extent these organic components might have an impact on the geochemical behavior of selected actinides is the aspect of the following chapter.

4.1 Investigation of the Np(V) propionate and lactate complex formation.

Low molecular weight organics (LMWO; e.g. acetate, propionate, lactate) might significantly impact the speciation and mobility of radionuclides in aqueous media. There are less thermodynamic data reported for the complexation of pentavalent actinides with LMWO, especially under elevated temperature conditions, relevant for assessing the long-term safety of disposal options for heat-producing high-level nuclear waste. The complexation of pentavalent neptunium aquo ion with propionate and lactate was studied by absorption spectroscopy, EXAFS, and with solvent extraction. The structural formula of propionic acid, lactic acid, and acetic acid for comparison reasons are given here:

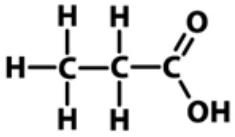

Propionic acid

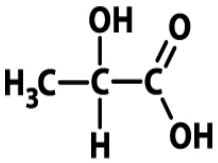

Lactic acid

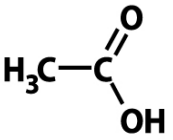

Acetic acid

The complexation of Np(V) with the propionate ligand has not been studied so far, and hence, neither complex formation constants are available. The lactate complexation of Np(V) were described in a few studies using extraction methods and absorption spectroscopy. Most of the works give only conditional complex formation constants at various ionic strengths and only at room temperatures. A complex formation constant at ionic strength zero is only given in one publication. The Pitzer formalism was used to extrapolate to I = 0. An overview of the available complex formation constants of Np(V) lactate complexation is given in Table 17.

4.1.1 Spectroscopic study of the Np(V) propionate complex formation

In the present chapter, the complexation of Np(V) with propionate by using absorption spectroscopic is described. In the experiments the impact of ionic strength, ligand concentration and temperature was probed. The results are published in (Vasiliev et al., 2015).

The concentration of Np(V) was held between 2×10^{-5} and 6×10^{-5} M for UV-Vis/NIR experiments. Samples were usually equilibrated for 1–2 days prior to the measurement. Complexation of Np(V) with propionate in NaCl solution was studied by two independent series of measurements. A first set of samples was prepared at different NaCl concentrations (I = 0.5–4.0 M) with total propionate concentration ($[Prop]_{tot}$) being varied from 0.03 to 0.1 M to determine the ionic strength dependence of Np(V)-propionate complexation at room temperature. The ionic strength was adjusted with solid NaCl and the pHc was adjusted to 5 with aliquots of 0.01 M HCl. A second set of samples was prepared at a constant I = 0.5 M, $[Prop]_{tot}$ varying from 0.03 to 0.1 M and T varying from 20 to 85 °C using a constant temperature circulator (Thermo Haake DL30-W45/BOpen-Bath, Germany) to determine the temperature dependence of Np(V)- propionate complexation. pHc was adjusted to 5 at room temperature, before raising T. In addition, two experimental series at various $[Prop]_{tot}$ with I = 0.5 M, T = 23 and 85 °C were prepared at pHc = 7 to confirm the results obtained at pH_c = 5. For pH measurements at I > 0.1 m, an empirical correction term was applied to correct the measured operational pH-values (pH_{exp}) to thermodynamically well-defined quantities (Vasiliev et al., 2015).

For EXAFS measurements, the samples were prepared at four different NaCl concentrations (from 0.5 to 4.37 m) with a constant propionate concentrations of 0.48 M and constant Np(V) concentration of $7.7\text{x}10^{-4}$ mol L^{-1} (pHc = 5.5–5.1).

<u>pH measurements</u>

The measurements of operational pH values were performed with an Orion 2 Star Benchtop pH meter using an Orion 8103SC combination pH electrode. Commercial pH Titrisol buffer concentrates (Merck p.a.) were used to calibrate the setup at room temperature. For pH measurements at I > 0.1 m NaCl, an empirical correction term was applied for the measured operational pH-values (pH_{exp}) to obtain thermodynamically well-defined quantities. An empirical correction coefficient (A) that depends on background electrolyte composition and concentration and that has been accurately determined in our laboratories for aqueous NaCl systems and at room temperature (Altmaier et al., 2003a) was used to correct the operational pH_{exp} values according to equations

$$pH_c = pH_{exp} + A_{NaCl}$$

and

$A_{NaCl} = 0.0013 (m_{NaCl})^2 + 0.1715 m_{NaCl} - 0.0988$

where m_{NaCl} is the molality of the background electrolyte. The pHc is a measurement of the molality of the proton (-log $[H^+]$) and is only made here at room temperature.

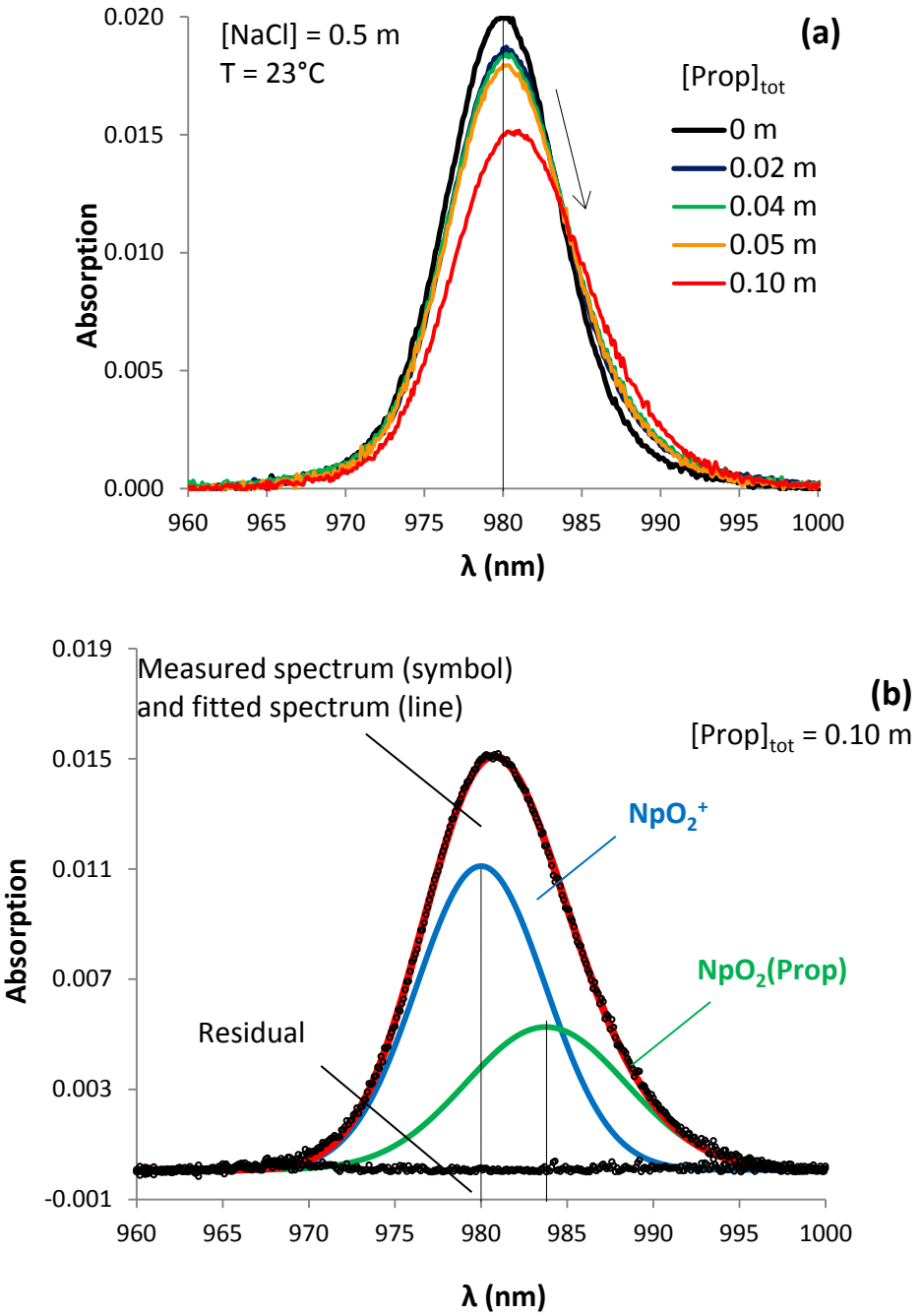

Figure 40: (a) Np(V) absorption spectra for various propionate concentrations (0–0.1 M) at [Np(V)]tot = 5.94 × 10−5 M, I = 0.51 m; T = 23 °C. (b) Example of a deconvoluted spectrum ([Prop] = 0.1 m; I = 0.51 m; pHc = 5.0, T = 23 °C.)

Results and Discussion

Figure 40a - the absorption spectra of Np(V) in the presence of propionate in [NaCl] = 0.51 m for T = 23 °C and pHc = 5 – exemplarily shows the spectrophotometric results of the Np(V)-propionate complex formation in [NaCl] solution and at T = 23 °C. Generally, as the concentration of propionate increases, the intensity of the absorption band of free NpO_2^+ at 980 nm decreases and the maximum of the absorption band is shifting to higher wavelengths. This is an indication that the NpO_2^+ ion is complexed by forming a new absorption band at higher wavelengths caused by the Np(V) propionate complex. Peak deconvolution of the spectra allows the determination of a single complex, as shown in Figure 40 for one spectrum. According to the peak deconvolution performed within the present study, the absorption band of the Np(V)-propionate complex has its maximum at ~984 nm, similar to the 1:1 Np(V) acetate complex (Pokrovsky and Choppin, 1997; Seibert et al., 2001). The absorption spectra shows very similar changes with increasing propionate concentration at different temperature while keeping I constant.

Effect of ligand concentration

The experimental data are plotted in Figure 41 according to the following equation for three different titration series:

$$\log \frac{[NpO_2(Prop)_n{}^{(1-n)}]}{[NpO_2{}^+]} = \log \beta + n \times \log[Prop^-]_{eq}$$

,

consistent with the following reaction reaction:

$NpO_2^+ + n\ Prop^- = NpO_2(Prop)_n^{(1-n)}$.

Results for T = 23 °C and 85 °C are faced (both in [NaCl] = 0.51 m solution) to show the effect of temperature on the complexation reaction. A comparison of the results at [NaCl] = 0.5 m and 3.20 m at T = 23 °C demonstrates the effect of ionic strength. The slopes (n = 1.05 ± 0.05 at 23 °C; 0.99 ± 0.11 at 85 °C; 1.04 ± 0.15 for I = 3.2 m) confirm the formation of an 1:1 NpO_2-propionate complex. The y-intercept, log β, is determined as 1.04 ± 0.06 at 23 °C and increases with temperature (1.36 ± 0.13 at 85 °C) and with ionic strength (1.34 ± 0.15 at 3.2 m). The same stoichiometry is found at ionic strengths varying from 0.51 to 3.2 m (constant T, pHc = 5 and 7) or varying T from 20 to 85 °C (constant I, pHc = 5 and 7).

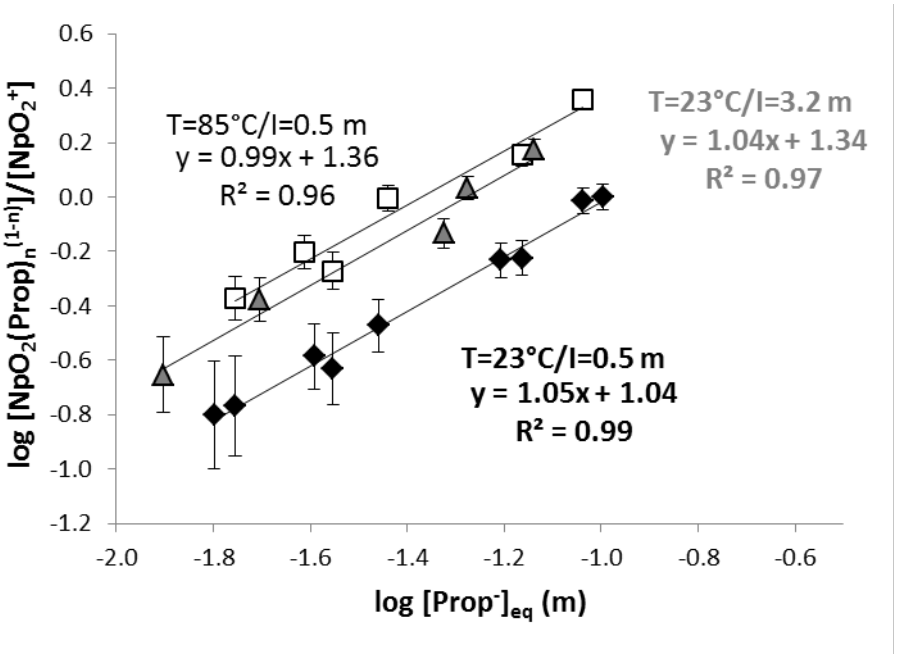

Figure 41: Slope analysis of the Np(V) propionate complex formed at 23 and 85 °C for [NaCl] = 0.51 m, and 23 °C for [NaCl] = 3.2 m. Slopes ≈ 1 (1.05 ± 0.05 and 0.99 ± 0.11 for both T, respectively, 1.04 ± 0.15 for I = 3.2 m) indicate the formation of the 1:1 complex. Log β (conditional) increases both with the temperature and the ionic strength (from 1.04 ± 0.06 to 1.36 ± 0.13).

Effect of ionic strength

This procedure allows evaluation of equilibrium constants (β_0) at infinite dilution:

$$\beta_0 = \beta \times \frac{\gamma(NpO_2L)}{\gamma(NpO_2^+)\cdot\gamma(L^-)}$$

In SIT, activity coefficients can be expressed as:

$$\log\gamma_i = -z^2\frac{A(T)\sqrt{I}}{1+1.5\sqrt{I}} + \sum_k \varepsilon(i,k)\cdot m_k$$
$$= -z^2 D + \sum_k \varepsilon(i,k)\cdot m_k$$

where m_k is the molality of the aqueous species *k*; $\varepsilon(i,k)$ is the specific ion interaction coefficient between species i and k; *D* is the Debye-Hückel term; *A(T)* is the limiting Debye-Hückel equation slope, that depends on temperature:

$$A(T) = e^3\sqrt{\frac{2\pi N\rho}{100(K\varepsilon_d T)^3}}$$

where *N* is the Avogadro number, *e* stands for absolute electronic charge, ε_d is here the dielectric constant of water at the given temperature, ρ is the pure water density, *k* is the Boltzman constant, and *T* is temperature (K).

By systematically varying the NaCl background electrolyte concentration at constant T and applying an appropriate model for activity coefficients (γ) it is possible to extrapolate the conditional equilibrium constants β to the standard equilibrium constant (β_0) at zero ionic strength.

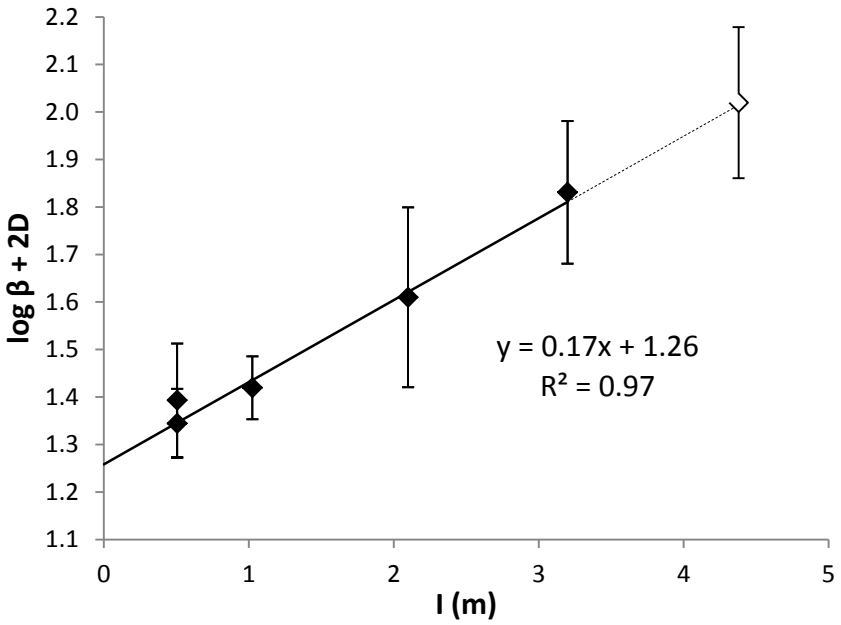

Figure 42: SIT plot of the equilibrium reaction $NpO_2^+ + Prop^- \rightleftharpoons NpO_2(Prop)$ in NaCl, yielding log β_0 = 1.26 ± 0.03. The white symbol ([NaCl] = 4.37 m) shows data outside the recommended applicability of the SIT (data not used in the regression). The dotted line shows the extrapolation of the results obtained for lower I to 4.37 m.

This was done with the equation

$$\text{Log } \beta - \Delta Z^2 \times D = \log \beta_0 - \Delta\varepsilon \times I$$

where $\Delta Z^2 = \sum Z^2(\text{products}) - \sum Z^2(\text{adducts}) = -2$ for the formation reaction above, and $\Delta\varepsilon = \varepsilon(Na^+ + Cl^-; NpO_2(Prop)) - \varepsilon(Na^+; Prop^-) - \varepsilon(Cl^-; NpO_2^+)$.

Experimental data are plotted according to the equation as log β + 2D versus I in Figure 42, resulting in a linear relationship as expected. From the slope, Δε is obtained as −0.17 ± 0.03 and the y-intercept (log β_0) equals to 1.26 ± 0.03. Log β_0 and Δε are in agreement with previously determined values for NpO_2-acetate complexation at 25 °C.25 Using ε(Cl–; NpO_2^+) = 0.09 ± 0.05 and assuming ε(Na+; Prop–) = 0.08 ± 0.01 by analogy with acetate, ε(Na+ + Cl–; NpO_2(Prop)) would not be significantly different from

zero, which is expected for a non-charged species in accordance with SIT. Note that we have investigated Np(V)-propionate complexation up to 4.37 m, which is outside the recommended validity range of SIT. Therefore, these data are not used for the regression as indicated by the dotted lines in Figure 42. However, in this case it is obvious that the SIT approach remains applicable even above its usually accepted applicability limit.

Effect of temperature

The temperature effect on the NpO2+ complexation by propionate was investigated between 20 and 85 °C, for [NaCl] = 0.51 m at pHc = 5 and 7. Log β(T) is corrected to I = 0 for each temperature by applying the SIT as described in the previous section to obtain log β_0(T). As a first approach, heat capacity was hypothesized to be zero as observed, for instance, in recent Cm(III) propionate/acetate and uranyl acetate complexation studies (Fröhlich et al., 2013; Fröhlich et al., 2014; Sladkov, 2014). I.e. the molal standard reaction enthalpy $\Delta_r H^0_m$ and entropy $\Delta_r S^0_m$ do not vary with temperature between 20 and 85 °C. Following this simplification, $\Delta_r H^0_m$ and $\Delta_r S^0_m$ can be obtained from an Arrhenius plot on the basis of the van't Hoff equation

$$\log \beta_0(T) = -\frac{\Delta_r H^0_m}{RT\ln(10)} + \frac{\Delta_r S^0_m}{R\ln(10)}$$

where R is the ideal gas constant. Figure 43 shows the plot of log β_0(T) versus 1/T.

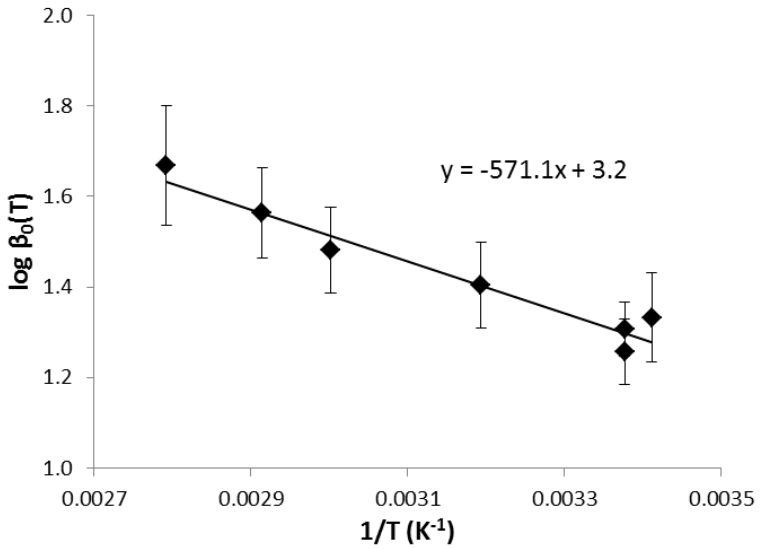

Figure 43: Np(V)-propionate complexation constant extrapolated to zero ionic strength (log β_0) versus the reciprocal of the temperature (K^{-1}).

The NpO_2(Prop) complex formation reaction significantly increases over about half an order of magnitude when increasing the temperature from 20 °C to 80 °C. A linear relationship is observed, confirming the initial hypothesis of zero heat capacity. $\Delta_r H^0_m$ and

$\Delta_r S^0_m$ are calculated as 10.9 ± 1.2 kJ mol^{-1} and 62 ± 4 J mol^{-1} K^{-1}, respectively. Both values are positive, showing that the formation of the NpO_2(Prop) complex is endothermic and entropy driven. Positive ΔrH^0_m and ΔrS^0_m are likely due to dehydration effects of NpO_2^+ and $Prop^-$ ions.

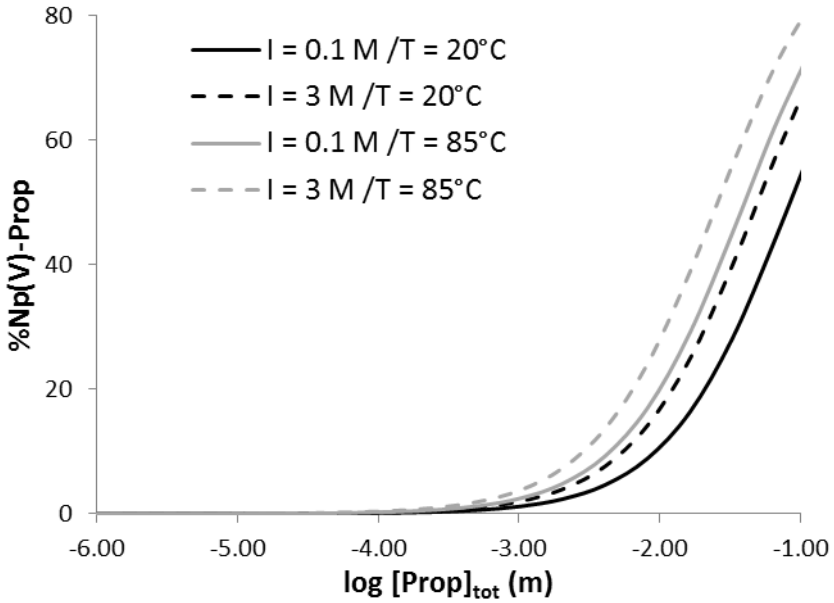

Figure 44: Calculated percentage of the Np(V)-propionate complex ($[Np(V)]_{tot}$ = 10^{-10} m) versus log[Prop]tot for pHc = 7 and I = 0.1 or 3 m and T = 20 or 85 °C using thermodynamic parameters determined in this study.

Np(V)-propionate complexation at environmentally relevant propionate concentrations Simulations are made for pHc = 7, with 0.1 and 3 m NaCl and T = 20 and 85 °C using the presently obtained Np(V)-propionate complexation parameters in order to test the impact of propionate on Np speciation under more environmentally relevant conditions than the present laboratory study. The percentage of Np(V), in aqueous solutions at pHc 7 present as the NpO2+ cation, complexed to propionate versus $log[Prop]_{tot}$ is shown in Figure 44 ([Np(V)]tot = 10^{-10} m). Although Np(V)-propionate complexation increases with I between 0.1 and 3 m for a given T, or with T between 20 and 85 °C for a given I, propionate remains a relatively weak ligand for Np(V) under these conditions: only 1–5% of Np(V) is bound to propionate for $[Prop]_{tot}$ = 10^{-3} m. In natural clay rocks porewater (e.g. OPA/COx), where propionate is present at lower concentration (127 µM, (Courdouan et al., 2007a; Courdouan et al., 2007b)) and where Np(V) is in competition with other cations, propionate complexation is expected to have a minor impact on Np(V) speciation.

The present study shows that the stability constant for the formation of the 1:1 NpO_2^+-propionate complex, with log β^0(25 °C) = 1.26 ± 0.03, increases both with the ionic strength (0.5 < NaCl < 4.37 m) and temperature (20 < T < 85 °C). The complex formation reaction is endothermic and entropy driven, as evidenced by $\Delta_r H^0_m$ = 10.9 ± 1.2 kJ mol^{-1} and $\Delta_r S^0_m$ = 62 ± 4 J mol^{-1} K^{-1}, determined in this work. The magnitude of $\Delta_r S^0_m$ is consistent with a bidentate coordination mode, which is also shown by EXAFS

analysis, leading to the replacement of two water molecules in the first coordination shell of NpO_2^+ by the propionate ligand (Vasiliev et al. 2015). The newly derived thermodynamic data ($\Delta_rH^0_m$, $\Delta_rS^0_m$, log β^0(T)) for the Np(V)-propionate complexation are a valuable contribution to the thermodynamic databases which are the basis of a reliable safety assessment for nuclear waste disposal scenarios. Using the comprehensive modeling tools and the thermodynamic data derived in this work, it becomes possible to predict the potential impact of the propionate (including respective ionic strength and temperature effects) on the geochemical behavior of Np(V). Our predictions indicate that propionate has a minor impact on Np(V) speciation in environmentally relevant propionate concentrations.

Table 14: Thermodynamic data and interaction parameters according SIT for Np(V) propionate complex formation in NaCl solution determined in the present study. Uncertainties are reported at ± 1σ confidence level. Individual ε(i,k) values are estimated based on ε(Na^+; acetate$^-$) value.

Parameter	$NpO_2^+ + Prop^- \rightleftharpoons NpO_2(Prop)$
$\log \beta_0(25\ °C)$	1.26 ± 0.03
$\Delta\varepsilon$ (in NaCl)	−0.17 ± 0.03
$\varepsilon(NpO_2^+; Cl^-)$[23]	0.09 ± 0.05
$\varepsilon(Na^+; Prop^-)$[23]	0.08 ± 0.01
$\varepsilon(Na^+ + Cl^-; NpO_2Prop)$	0.00 ± 0.06
$\Delta_rH^0_m$ (kJ M^{-1})	10.9 ± 1.2
$\Delta_rS^0_m$ (J K^{-1} M^{-1})	62 ± 4

4.1.2 Investigation of propionate and lactate complexation by Solvent extraction

In this work a solvent extraction technique was applied to determine the thermodynamic parameters of the Np(V) propionate and lactate complexation at varying NaCl concentration, ligand concentration, and temperature. The specific ion interaction theory (SIT) was used for correlation of ionic strength effects and the temperature dependent thermodynamic stability constants as well as $\Delta_rH^0_m$ and $\Delta_rS^0_m$ of the complexation reactions are determined.

Complexation experiment

All concentrations given in mol L^{-1} (molarity, M) were corrected to mol kg^{-1} H_2O (molality, m) for later calculations to avoid changes in the concentration because of changes

in solution density by temperature and ionic strength. The concentration of Np(V) was held at 3×10^{-6} M in all extraction experiments. A first set of samples was prepared at different NaCl concentrations (I = 0.5–2.5 M) with total propionate ($[Prop]_{tot}$) being varied from (0.005-0.15 M) and lactate concentration ($[Lac]_{tot}$) (0.01-0.13 M) to determined the ionic strength dependence of Np(V) propionate and lacate complexation at room temperature. Furthermore, additional series were prepared at a constant ionic strength of 0.5 m with varying the ligand concentration in the same ranges and different temperatures from 22°C up to 60 °C. For maintaining of a constant temperature a water thermostat was used. The ligand (Prop, Lac) concentrations were obtained by adding of aliquots of a 1.0 M solution of propionic acid, 0.5 M and solution of sodium lactate. The pH_c in each experimental batch was adjusted to a desired value of 7.0±0.1 at room temperature with 0.01 M HCl or NaOH and stabilized by introducing buffer of $5\cdot10^{-3}$ mol/L piperazine-N,N′-bis(2-ethanesulfonic acid) (PIPES). 2-thenoyltrifluoroacetone (TTA) and 1,10-phenanthroline were used without purification. A $1\cdot10^{-3}$ M TTA + $5\cdot10^{-4}$ M of 1,10-phenanthroline solution in isoamyl alcohol (Inoue and Tochiyama, 1982) was prepared and used as an organic phase for the extraction of NpO_2^+.

Solvent extraction

For the extraction 2 mL of $1\cdot10^{-3}$ M of TTA with $5\cdot10^{-4}$ M of 1,10-phenanthroline in isoamyl alcohol and 2 mL of the sample solution were mixed in tubes. The tubes were inserted into the holes of the temperature-controlled shaker for 3 hours at desired temperature. Afterwards the tubes were centrifuged at the same temperature and 0.5 ml aliquots were taken from both phases to measure ^{237}Np content using Beckman Liquid Scintillation Counter (LSC) by mixing aliquots of the samples with 10 ml Ecolite scintillator. No quenching effects were observed either in aqueous or organic phases under the experimental conditions. In the remaining aqueous phase pH_{exp} was determined and pHc was calculated as described below. The hydrolysis of NpO_2^+ is insignificant when pHc < 8 at the present temperature range of 20-60 °C (Rao et al., 2004). At room temperature Np(V)-carbonate complexation is negligible for pH < 7.5. To our knowledge, there is no study on Np(V) carbonate complexation at elevated temperature. Since this work was carried out at $pH_c = 7.0 \pm 0.3$, the hydrolysis and carbonate complexation reactions are not taken into account.

pH measurements

In the present study, measurements of operational pH values were performed with an Orion 2 Star Benchtop pH meter using an Orion 8103SC combination pH electrode. Commercial pH Titrisol buffer concentrates (Merck p.a.) were used to calibrate the set-up at room temperature. For pH measurements at I > 0.1 m NaCl, an empirical correction term was applied for the measured operational pH-values (pH_{exp}) as described in chapter 4.1.1. The pHc is a measurement of the molality of the proton (-log $[H^+]$) and is only made here at room temperature. The apparent proton dissociation constant of propionate/lactate (pK_a) remains below 5 within the range of [NaCl] and T investigated. For pHc = 7 (i.e. > pK_a + 2), both ligands can be considered as fully unprotonated.

PIPES was chosen as a buffer for its maximum water solubility, minimum solubility in all other solvents (i.e. during the extraction experiment), minimal salt effects and minimal change in pKa with temperature (Good et al., 1966). Hence, pHc is not expected to be significantly affected when varying the temperature and the total ligand concentration ($[Prop]_{tot}$ or $[Lac]_{tot}$) is considered equal to the free ligand concentration ($[prop^-]_{eq}$ of $[Lac^-]_{eq}$) for the calculations.

Determination of the distribution ratio(D_0) in absence of a ligand

The complexation reaction of Np(V) with ligand L^- can be expressed as:

$$NpO_2^+ + n \cdot L^- \leftrightarrow NpO_2L_n^{(1-n)}$$

with the conditional stability constant (β, in $kg \cdot mol^{-1}$) defined as:

$$\beta = \frac{[NpO_2L_n^{(1-n)}]}{[NpO_2^+] \times [L^-]^n}$$

We used Neptunium(V) extraction by synergetic extraction with the mixture of 2-thenoyltrifluoroacetone (TTA) and 1,10-phenanthroline (Phen). The method was successfully applied for complexation studies of Np(V) complexes with organic acids by Inoue and Tochiyama (Inoue and Tochiyama, 1982, 1983).

The extraction could be presented by the reaction:

$$NpO_{2\,(a)}^+ + HT_{(o)} + n \cdot B_{(o)} \leftrightarrow NpO_2T \cdot nB_{(o)} + H_{(a)}^+$$

where (o) and (a) refers to the species in the organic and aqueous phases, and HT and B represents TTA and Phen, respectively.

Extraction is characterized by a distribution ratio (D) that depends on the species of extracting ions, pH and other factors:

$$D(pH, T, I) = \frac{\Sigma[M]_o}{\Sigma[M]_a}$$

where $\Sigma[M]_o$ is the total concentration of metal ion in the organic phase and $\Sigma[M]_a$ is the total concentration of metal ion in the aqueous phase. Assuming the presence of various species in the aqueous phase and D_o as a distribution ratio in the absence of a ligand, it can be written:

$$D_0^k / D^k = 1 + \Sigma\beta_n \cdot [L_n]^n$$

where *k* is a serial number of a particular experiment.

In case of a 1:1 Np-ligand complexation - we have observed in our spectroscopical study of both propionate and lactate - the above equation can be simplified to:

$$D_0^k / D^k = 1 + \beta[L^-]$$

and the slope of the graph [L] versus D^k_0/D^k is equal to the conditional stability constant. For application of liquid-liquid extraction it is necessary to obtain D_0 (distribution ratio in the absence of a ligand) values for all changing conditions namely pH_c, ionic strength and temperature at fixed concentrations of extractants (TTA and 1,10-phenanthroline) and Np(V) ions.

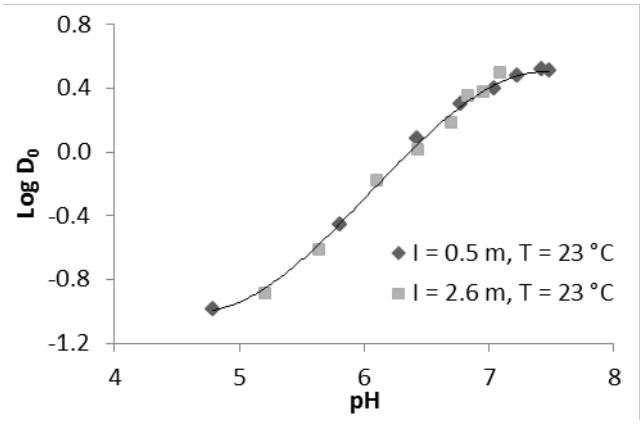

Figure 45: Distribution ratios of Np(V) upon extraction by $1 \cdot 10^{-3}$ M TTA and $5 \cdot 10^{-4}$ M 1,10-phenanthroline in the absence of complex forming ligands at 23 ^{0}C with two ionic strength 0.5 m and 2.6 m NaCl.

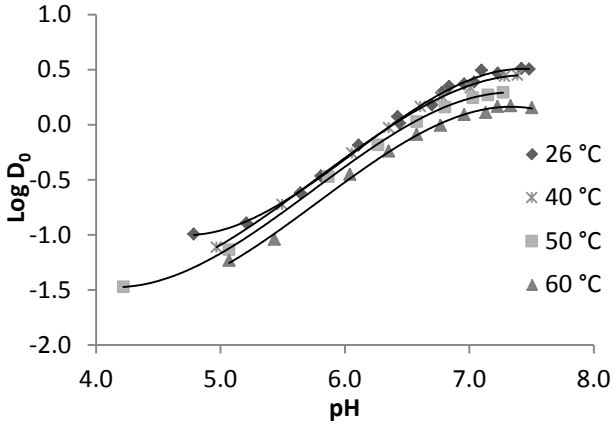

Figure 46: Distribution ratios of Np(V) upon extraction by $1 \cdot 10^{-3}$ M TTA and $5 \cdot 10^{-4}$ M 1,10-phenanthroline in the absence of complex forming ligands at varying temperature and at 0.5 m NaCl.

Figure 45 shows the results of synergistic extraction of Np(V) as a function of pH_c in the absence of complexation agents at two ionic strengths 0.5 m and 2.5 m. The slope of the linear part of this curve is equivalent to 0.74 that well fits to the literature data (In-

oue and Tochiyama, 1982). No significant influence of ionic strength on D_0 values was observed. Otherwise by increasing the temperature of the system distribution ratios slightly decrease as demonstrated in Figure 46. The data from Figure 45 and Figure 46 were used to determine D_0 at the measured pH_c values.

The effect of TTA complexation with Np(V) in the aqueous phase as well as Np(V)-Cl complex formation was found to be negligible under all presented conditions (Inoue and Tochiyama, 1982).

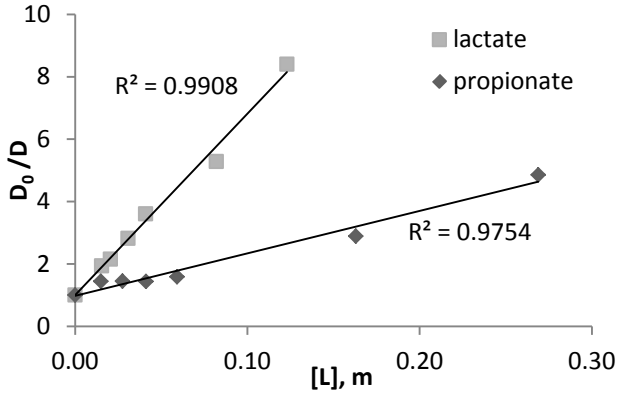

Figure 47: Representative plot of D_0/D versus free ligand concentration. Aqueous phase: 0.5 m NaCl. Organic phase: 0.001 m TTA + 0.0005 m 1,10-phenanthroline.

Figure 47 shows typical plots of the experimental values of D_o/D as a function of free propionate, lactate concentrations. Distribution ratios of Np(V) in organic and aqueous phases were found to decrease with increasing concentration of all investigated ligands. The decrease in D is caused by the increase in concentration of Np(V)-L complexes in the aqueous phase with increasing ligand concentration and pH that are not extracted into the organic phase by TTA+Phen. The linear dependences of D_o/D from the concentration of the ligands indicate the formation of only 1:1 complexes for Np-propionate and Np-lactate complexes. The slope of the straight lines (Figure 47) is equal to the conditional complex formation constants (β_c). Each value of β_c was calculated from six to eight experimental data points for each graph.

Table 15 summarizes the experimental results and published data for the conditional complex formation constants of Np(V) and the clay organics acetate, propionate, and lactate. No dependence of the conditional complex formation constants on pH_c in the 6-8 pH_c region is established indicative that only the unprotonated complexes NpO_2L are present. Therefore for simplification in this study the pH_c was chosen to be high enough

for complete dissociation of the propionic and lactic acids. The tendency in the variation of conditional complex formation constants with ionic strength is similar to the literature data obtained for the ionic strength from 0.3 m to 5.0 m (Table 15).

Effect of ionic strength

SIT is applied to extrapolate the complex formation constant at given ionic strength to zero ionic strength. As mentioned before the equation

$$\log \beta - \Delta z^2 \cdot D = \log \beta_0 - \Delta \varepsilon \cdot I$$

was used with $\Delta z^2 = -2$ to obtain the ions interaction coefficient Δε. Figure 48 presents the plot of log β + 2D on I (m). The intercept of the linear approximation equals to the stability constant at zero ionic strength and the slope to ions interaction coefficient (Δε). The conditional complex formation constants log β_c at given ionic strength used for the extrapolation are listed in Table 15. For all studied ligands we obtained a slight increase of log β_c with ionic strength. The complex formation constants for Np(V)-propionate at zero ionic strength log β_0 was obtained from intercept of the linear regression analysis: logβ_0 = 1.32 ± 0.03.

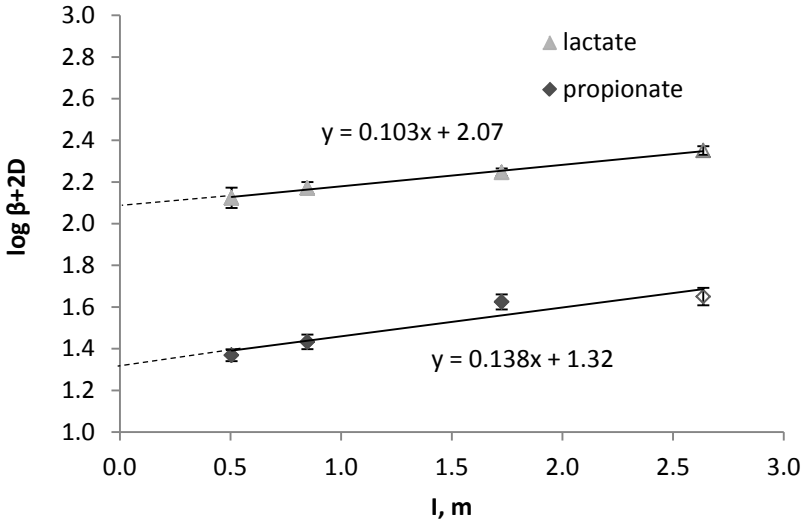

Figure 48: SIT plot of the equilibrium reaction $NpO_2^+ + L^- \rightleftharpoons NpO_2(L)$ in NaCl, yielding logβ_0 = 1.32 ± 0.03 for propionate and logβ_0 = 2.07 ± 0.03 for lactate. The white symbol ([NaCl] = 2.5 m) shows data outside the recommended applicability of the SIT (data not used in the regression). The dotted line shows the extrapolation of the results obtained for lower I to 2.5 m.

Table 15: Conditional complex formation constants of neptunium (V) acetate, propionate, and lactate formation at 25±1 °C.

Reaction	Medium	pH range	Method	log β_c	Reference
NpO_2^++$Acet^-$↔ NpO_2Acet	0.30 m NaCl	6.0-7.2	LLE	1.05±0.04	A
	1.00 m NaCl	6.0-7.2	LLE	1.13±0.05	A
	2.00 m NaCl	6.0-7.2	LLE	1.25±0.05	A
	3.00 m NaCl	6.0-7.2	LLE	1.55±0.05	A
	4.00 m NaCl	6.0-7.2	LLE	1.70±0.20	A
	5.00 m NaCl	6.0-7.2	LLE	1.80±0.02	A
	1.05 m $NaClO_4$	7.0	LLE, cal	0.74±0.04	B
NpO_2^++$Prop^-$↔ NpO_2Prop	0.51 m NaCl	7.0±0.5	LLE	0.99±0.03	present work
	0.83 m NaCl	7.0±0.5	LLE	1.01±0.03	present work
	1.67 m NaCl	7.0±0.5	LLE	1.14±0.03	present work
	2.50 m NaCl	7.0±0.5	LLE	1.14±0.04	present work
NpO_2^++$Lact^-$↔ NpO_2Lact	0.51 m NaCl	7.0±0.5	LLE	1.75±0.05	present work
	0.83 m NaCl	7.0±0.5	LLE	1.75±0.03	present work
	1.67 m NaCl	7.0±0.5	LLE	1.76±0.02	present work
	2.50 m NaCl	7.0±0.5	LLE	1.84±0.02	present work
	0.30 m NaCl	6.0-7.2	LLE	1.78±0.03	A
	1.00 m NaCl	6.0-7.2	LLE	1.43±0.04	A
	2.00 m NaCl	6.0-7.2	LLE	1.48±0.05	A
	3.00 m NaCl	6.0-7.2	LLE	1.76±0.02	A
	4.00 m NaCl	6.0-7.2	LLE	1.93±0.06	A
	5.00 m NaCl	6.0-7.2	LLE	1.95±0.04	A

*LLE – liquid-liquid extraction, spec – absorption spectroscopy, cal – calorimetry. A: (Moore et al., 1999); B: (Rao et al., 2010).

A further experimental problem arises in comparing complex formation constants obtained by different techniques (Choppin, 1997). Solvent extraction is a technique from which log β_0 is calculated by using the total complexed metal species, i.e. outer and inner sphere complexes. Spectroscopic technique takes into account only inner sphere species and that is expressed in a slightly lower value with log β_0 = 1.26 ± 0.03 (Vasiliev et al., 2015). It is noticeable that the log β_0 of Np(V)-acetate (literature date) and Np(V)-propionate are similar and equal to ca. 1.3. This could be explained by the fact that only the carboxyl group participates in complex formation. An increase of the chain length by one $–CH_2$ group has no significant impact on the complexation process and hence on log β_0.

Effect of temperature

Effect of the temperature on the complexation was investigated at T = 25, 40, 50 and 60 °C and c (NaCl) = 0.51 m (Table 16). The log β_c was corrected to complex formation constant log β(T) at infinite dilution for each temperature using SIT approach as described above. With the assumption that molal standard reactions enthalpy $\Delta_r H_m^0$ and entropy $\Delta_r S_m^0$ do not change with temperature – the heat capacity does not change

significantly with T - under the experimental conditions, it is possibly to estimate these thermodynamic parameters from an Arrhenius plot on the basis of the van't Hoff equation:

$$\log \beta(T) = \frac{\Delta_r H_m^0}{RT \ln 10} + \frac{\Delta_r S_m^0}{R \ln 10}$$

where *R* is the ideal gas constant. Figure 49 plots log β(T) versus the reciprocal temperature (°K) 1/T. The linear dependences of the complex formation constants as a function of temperature confirms the assumptions, that $\Delta_r H_m^0$ and $\Delta_r S_m^0$ do not significantly change with temperature.

Table 16: Conditional stability constants of neptunium (V) complex formation at different temperatures.

Reaction	Method	Medium	T, °C	log β_c	Reference
$NpO_2^+ + Acet^- \leftrightarrow$	spec, cal	1.04 m $NaClO_4$	25	1.05±0.04 (SIT) *	a
NpO_2Acet	spec, cal	1.04 m $NaClO_4$	40	1.11±0.03 (SIT)*	a
	spec, cal	1.04 m $NaClO_4$	55	1.19±0.03 (SIT)*	a
	spec, cal	1.04 m $NaClO_4$	70	1.34±0.05 (SIT)*	a
$NpO_2^+ + Prop^- \leftrightarrow$	LLE	0.51 m NaCl	25	0.99±0.03	p. work
NpO_2Prop	LLE	0.51 m NaCl	40	1.15±0.01	p. work
	LLE	0.51 m NaCl	50	1.29±0.10	p. work
	LLE	0.51 m NaCl	60	1.36±0.06	p. work
$NpO_2^+ + Lact^- \leftrightarrow$	LLE	0.51 m NaCl	25	1.75±0.05	p. work
NpO_2Lact	LLE	0.51 m NaCl	40	1.77±0.03	p. work
	LLE	0.51 m NaCl	50	1.71±0.02	p. work
	LLE	0.51 m NaCl	60	1.69±0.02	p. work

* In this work log β(T) at zero ionic strength was deduced with SIT approach.
References: a: (Rao et al., 2010).

It should be noted that in case of propionate complexation the log β significantly increases with temperature, whereas for lactate the log β slightly decreases. The values of $\Delta_r H_m^0$ and $\Delta_r S_m^0$ are listed in the Table 17 together with literature data for comparison reasons. The standard reaction enthalpy $\Delta_r H_m^0$ for propionate and acetate are positive indicaticating that complexation of Np(V) is an endothermic reaction. The dehydration energy of the metalion or ligand (positive enthalpy) preponderates the metal-ligand interaction (negative enthaply). The positive entropy of the reaction signals an entropy driven reaction where the degree of disorder is enhanced by removing a water molecule from the first hydration sphere of entropy. It was pointed out from Choppin (Choppin, 1997) that the 1:1 complexes of Ln(III) with monocarboxylate ligands are predominantly outer sphere in character if pKa of ligand acid is < 2 and predominantly inner sphere if the $pK_a > 3$. The $\Delta_r H_m^0 > 0$ indicates that dehydration energy is required for complexes formation and supports the model of inner-sphere binding of Np(V)-propionate complexes with only one carboxylate group. Relatively high value of entropy

factor could be connected with bidentate coordination mode of Np-OOC binding for acetate and propionate both 75±6 $J \cdot M^{-1}K^{-1}$ (Rao et al., 2010) and 77±9 $J \cdot M^{-1}K^{-1}$, respectively) with replacement of two water molecules from the inner sphere of Np.

For lactate $\Delta_r H_m^0$ is slightly negative and the value of -5.4±1.4 is comparable with literature data. In case of lactate no stability constants at elevated temperature is available for Np(V) in literature, only data for lactate complexation of Nd^{3+} was found (Tian et al., 2010). They explain the results in the way that the Ln(III) lactate complexation is more favored by enthalpy - less dehydration energy is required to form the coordination bond - probably because the R-hydroxyl group is less hydrated than the carboxylate group. Additionally, the Ln(III) lactate interaction is stronger than the Ln(III)-acetate or propionate interaction so that more energy is gained in the former. The same can be assumed for Np(V). Due to the participation of the hydroxyl groups there is a stronger Np-ligand interaction and ordering of the system which expressed in negative enthalpy and in 2 times lower entropy value than for propionate and acetate complexation.

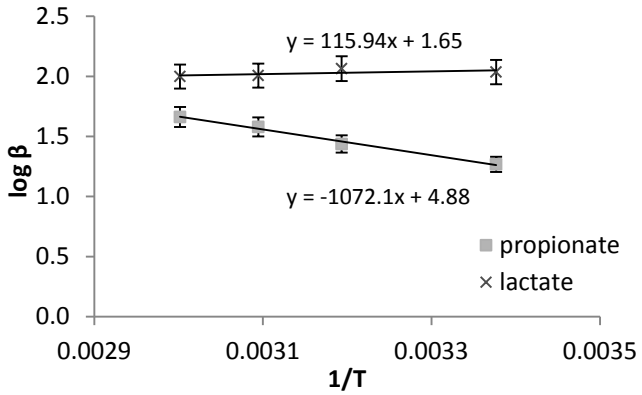

Figure 49: Np(V) complexation constants corrected to zero ionic strength (log β_0) versus the reciprocal of the temperature (K^{-1})

Comparison of thermodynamic data with literature data

The thermodynamic parameters of the complex formation reaction between Np(V) and ligands obtained in this study and comparison to literature data are summarized in Table 17.

Recently published data (Vasiliev et al., 2015) for the spectroscopic studies of Np(V)-propionate at elevated temperature and ionic strength are available and are faced to the present studies by the extraction method (see Table 17). Data available in literature for highly analog chemical systems were published by (Rao et al., 2010) for Np(V) complexation with acetate. They obtained a complexation constant at zero ionic strength log β_0 and $\Delta\varepsilon$ values for the 1:1 NpO_2^+-acetate complex similar to the values for propionate derived in this work, with NaCl (log β_0 = 1.28 ± 0.04 and $\Delta\varepsilon$ = -0.24 ±

0.02) and $NaClO_4$ (log β_0 = 1.27 ± 0.02 and $\Delta\varepsilon$ = -0.08 ± 0.01) used as background electrolyte. At 298.15 K and [$NaClO_4$] = 1.05 m, (Rao et al., 2010) determined Δ_rH_m = 18.1 ± 1.8 kJ mol^{-1} and Δ_rS_m = 75 ± 6 J mol^{-1} K^{-1}, which are comparable to our present results for the propionate system. In general, positive $\Delta_rH^0_m$ and $\Delta_rS^0_m$ are found for actinide complexes with monocaroboxylic ligands, for example, $Cm(III)(Prop)^{2+}$ ($\Delta_rH^0_m$ = 5.7 ± 1.8 kJ mol^{-1} and $\Delta_rS^0_m$ = 84 ± 5 J mol^{-1} K^{-1} (Fröhlich et al., 2013); ($\Delta_rH^0_m$ = 6 ± 2 kJ mol^{-1} and $\Delta_rS^0_m$ = 79 ± 8 J mol^{-1} K^{-1} (Fröhlich et al., 2014) or $U(VI)(Acetate)^+$ ($\Delta_rH^0_m$ = 14.5 ± 1.5 kJ mol^{-1} and $\Delta_rS^0_m$ = 104 ± 6 J mol^{-1} K^{-1} (Sladkov, 2014). For all these actinides, the magnitude of $\Delta_rS^0_m$ is comparable because both acetate and propionate coordinate mainly in a bidentate fashion, replacing two water molecules in the first coordination shell of the actinide.

Table 17: Thermodynamic parameters specific ion interaction coefficients ($\Delta\varepsilon$) of neptunium (V) complex formation with acetate, propionate and lactate (in NaCl solution), according to the reaction: $NpO_2^+ + L^- = NpO_2L$.

Complex	Method	log β_0 (25°C)	$\Delta_rH^0_m$ (kJ M^{-1})	$\Delta_rS^0_m$ (J K^{-1} M^{-1})	$\Delta\varepsilon$	
NpO_2Ac^-	spec, cal	1.28± 0.04	18.1±1.8*	75±6*	-0.24±0.02	a[§]
		1.27± 0.02			-0.08±0.01	a[$]
		1.46±0.22			Pitzer	f
NpO_2Prop	lle	1.32±0.05	16.3±3.0	77±9	-0.14±0.03	pw
	spec	1.26 ± 0.03	10.9 ± 1.2	62 ± 4	-0.17±0.03	b
NpO_2Lact	lle	2.07±0.01	-5.4±1.4	19±4	-0.10±0.01	pw
	lle	1.97			Pitzer	e
	lle	1.70			unknown	e
	lle	1.10±0.08[&]				c
	spec	1.75±0.02[#]				j
$NdLact^{2+}$	cal	2.57 ± 0.09*	-2.02±0.22	43±1	-	d
	spec	2.58 ± 0.05*				d
$CmAc^{2+}$	spec	3.18 ± 0.34	6 ± 2	79 ± 8	-0.17±0.01	h
$CmProp^{2+}$	spec	3.24 ± 0.17	5.7 ± 1.8	84 ± 5	-0.11±0.02	g
UO_2Ac^+	CE	2.94 ± 0.08	14.5 ± 1.5	104 ± 6	-0.14	i

a: (Rao et al., 2010); b: (Vasiliev et al., 2015); c: (Eberle and Schaefer, 1969); d: (Tian et al., 2010); e: (Moore et al., 1999); f: (Novak et al., 1996); g: (Fröhlich et al., 2013); h: (Fröhlich et al., 2014); i: (Sladkov, 2014); j: (Inoue and Tochiyama, 1983).
[#]: 0.01 M $NaClO_4$; *: 1.05 m $NaClO_4$; [§]: in NaCl solution; [$]: in $NaClO_4$ solution; [&]: 1 M $NaClO_4$
spec: spectroscopy, cal: calorimetry; lle: liquid-liquid extraction; CE : capillary electrophoresis

Np(V)-propionate/lactate complexation at environmentally relevant concentrations

Preliminary calculations are made for pH = 9, in 0.1 M NaCl and at T = 25° C using the presently obtained Np(V)-propionate complexation parameters to illustrate the impact of propionate on Np speciation in environmentally relevant conditions. The percentage of Np(V) complexed to propionate versus log $[Prop]_{tot}$ is shown in Figure 50 ($[Np(V)]_{tot}$ = 10^{-9} M). At ligand concentrations up to 0.01 M, less than 1% occurs as propionate complex, because propionate is a weak ligand for Np(V) at these conditions. In natural clay rocks porewater (e.g. OPA/COx), where propionate is present at lower concentration (≤ 27 µM (Courdouan et al., 2007a; Courdouan et al., 2007b)) and where Np(V) is in competition with other cations, propionate complexation is expected to have a minor impact on Np(V) speciation. The lactate complexation is more pronounced than the propionate, but reaches not more than 10% at 0.01 M lactate concentration. However, the lactate concentration in environmental pore waters is also very low compared to other inorganic and organic ligands and surface species. The concentration found in OPA pore waters is ≤ 9 µM (Courdouan et al., 2007a; Courdouan et al., 2007b). We conclude, that the lactate complexation is also expected to have a minor impact on the Np(V) speciation in clay formations comparable to OPA.

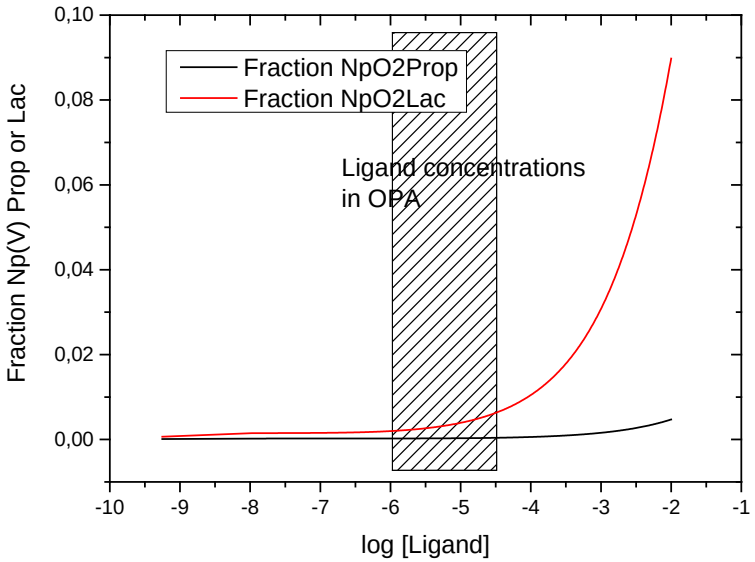

Figure 50: Chemical equilibrium diagram for Np(V) propionate and lactate complexation at pH 9 and 0.1 M NaCl (T= 25 °C). The box represents propionate and lactate concentrations found in OPA pore water and various extracts (Courdouan et al., 2007a; Courdouan et al., 2007b).

4.1.3 Conclusions

In present study, liquid-liquid extraction was succesfully applied and distribution ratio for Np(V)-propionate and Np(V)-lactate was calculated.

The present study shows that the stability constant for the formation of 1:1 NpO_2^+-propionate/lactate complex, clearly identified as the dominant species under the investigated conditions with log β_0 (25°C) = 1.32 ± 0.05 for Np(V) propionate and log β_0 (25°C) = 2.07 ± 0.01 for Np(V) lactate. Both complex formation constants increase with ionic strength (0.5 < NaCl < 2.5 m) and temperature (20 < T < 60°C). The complex formation reaction is endothermic for propionate complexation and entropy driven, as evidenced in the present work with $\Delta_r H^0_m$ = 16.3 ± 3.0 kJ mol^{-1} and $\Delta_r S^0_m$ = 77 ± 9 J mol^{-1} K^{-1}. The magnitude of $\Delta_r S^0_m$ is consistent with a bidentate coordination mode (Rao et al., 2010; Sladkov, 2014), which is also shown by spectrocopic results (Lucks et al., 2012). The results are in a good agreement with literature (Rao et al., 2010; Vasiliev et al., 2015). However, the lactate complex formation reaction is exothermic and entropy driven, evidenced by $\Delta_r H^0_m$ = -5.4 ± 1.4 kJ mol^{-1} and $\Delta_r S^0_m$ = 19 ± 4 J mol^{-1} K^{-1}. This could be caused by the influence of the α-hydroxy group in the lactate molecules. The role of the α-hydroxy group was also well reported in the literature for complexation of Nd(III) with lactate (Tian et al., 2010).

With the new set of thermodynamic data ($\Delta_r H^0$m, $\Delta_r S^0$m, logβ_0(T)) for the Np(V) propionate and lactate complexation, it becomes possible to predict the impact of small clay organics - including respective ionic strength and temperature effects - on the geochemical behavior of Np(V). Our predictions indicate that these small clay organic molecules has a minor impact on Np(V) speciation in environmentally relevant clay organic concentrations as found for OPA.

4.2 Humic acid complexes at high ionic strengths

4.2.1 Stabilization of polynuclear plutonium(IV) species by humic acid

Humic colloids such as humic acids (HA) are ubiquitous in natural waters and present a high binding capacity for dissolved metal ions. Although Pu(IV) was considered as rather immobile due to its low solubility, it shows a colloid-facilitated transport in presence of humic colloids (Artinger et al., 2003). Several studies have shown that the interaction of strongly hydrolysable elements with HA (e.g. Fe(III)) (Gustafsson et al., 2007; Karlsson and Persson, 2010) can lead to the stabilization of small polynuclear species, although the experiments were performed below the saturation index of relevant solid phases. Pu(IV) has an intrinsic tendency to form a great variety of dissolved polynuclear species (Walther et al., 2009). Furthermore, it was previously shown by spectroscopy (Dardenne et al., 2009) , at relatively high Pu concentration, that HA can inhibit its precipitation by forming small polynuclear species.

Although the formation of tetravalent plutonium (Pu(IV)) polymers with natural organic matter was previously observed by spectroscopy, there is no quantitative evidence of

such reaction in batch experiments. In the present study, published in (Marsac et al., 2014). Pu(IV) interaction with humic acid (HA) was investigated at pH 1.8, 2.5 and 3, as a function of HA concentration and for Pu total concentration equal to 6 x 10^{-8} M. The finally measured Pu(IV) concentrations ($[Pu(IV)]_{eq}$) are below Pu(IV) solubility limit.

Pu(IV)–HA interaction can be explained by the complexation of Pu(IV) monomers by HA up to $[Pu(IV)]_{eq}$ ~10^{-8} M. However, the slope of the log–log Pu(IV)–HA binding isotherm changes from ~0.7 to ~3.5 for higher $[Pu(IV)]_{eq}$ than ~10^{-8} M and at any pH. This result suggests the stabilization of hydrolyzed polymeric Pu(IV) species by HA, with a 4:1 Pu:HA stoichiometry. This confirms, for the first time, previous observations made by spectroscopy in concentrated systems. The humic ion binding model, Model VII, was introduced into the geochemical speciation program PHREEQC and was used to simulate Pu(IV) monomers binding to HA. The simulations are consistent with other tetravalent actinides–HA binding data from literature.

The stabilization of a Pu tetramer $[Pu_4(OH)_8]^{8+}$ by HA was proposed to illustrate the present experimental results for [Pu(IV)]eq > 10^{-8} M. Predictive simulations of Pu(IV) apparent solubility due to HA show that the chosen Pu(IV)-polymer has no impact for pH > 4. However, the comparison between these predictions and recent spectroscopic results suggest that more hydrolyzed polymeric Pu(IV) species can be stabilized by HA at pH > 4. Polymeric Pu(IV)–HA species might significantly enhance Pu(IV) apparent solubility due to humics, which support a colloid-facilitated transport of this low solubility element.

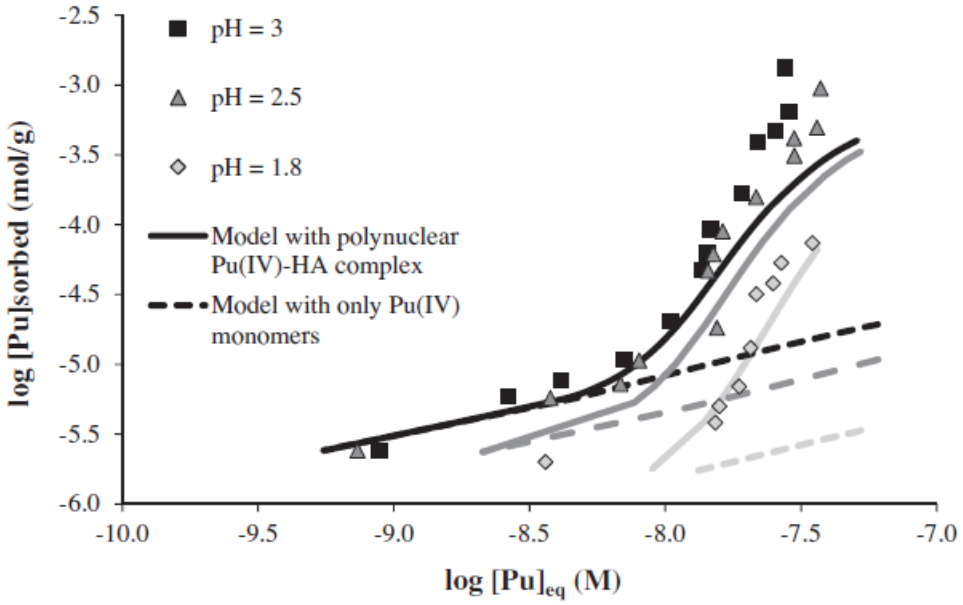

Figure 51: Comparison between experimental and modeling results of Pu(IV)–HA binding considering with or without stabilization of Pu(IV) tetramer by HA.

4.2.2 Conclusions

The present study on Pu(IV) humate complexation at pH < 3 yields evidence for the complexation of both mono and polynuclear Pu(IV) species to HA, at conditions where no Pu(IV) precipitation is expected. Model VII is used to simulate Pu(IV) monomers binding to HA. The simulations are consistent with other tetravalent actinides–HA binding data from literature (Reiller et al., 2008). The stabilization of a Pu tetramer [$Pu_4(OH)_8^{8+}$] by HA is proposed to illustrate Pu(IV)–HA interaction in conditions where polynuclear Pu(IV)–HA species are formed. Although a robust model considering both the formation of mono- and polynuclear Pu(IV) complexes with HA cannot be derived from the present and previous studies, such polynuclear species are expected to have an impact under relevant conditions in the environment. They significantly increase the Pu(IV) apparent solubility due to HA complexation, more than by humate complexation of monomeric Pu(IV) species. Due to their similar chemical properties, comparable mechanisms are also expected for other tetravalent actinides, such as U(IV) and Np(IV). Such a mechanism of humate or fulvate complexation strongly supports a transport of An(IV) as a humic colloid-borne species as observed in migration experiments (Artinger et al., 2003). Therefore, further studies should be dedicated to the colloidal stability of An(IV)–HA (i.e. mono- and polynuclear) complexes. More generally, the stabilization of polynuclear cations by HA seems to be a relevant mechanisms at least for cations presenting a high tendency for hydrolysis such as An(IV), Al(III) (Browne and Driscoll, 1993; Sutheimer and Cabaniss, 1997) or Fe(III) (Gustafsson et al., 2007; Karlsson and Persson, 2010). This might impact the fate of these elements in the environment but might also affect other elements through the competition for organic matter binding sites.

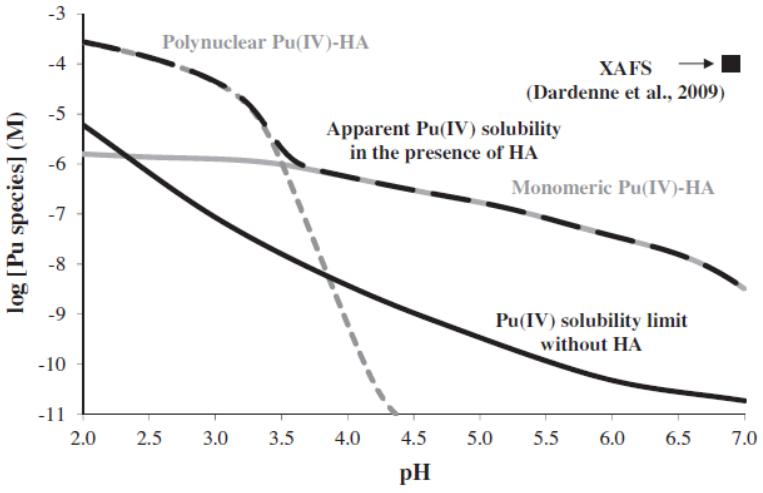

Figure 52: Simulated Pu(IV) solubility versus pH in a 0.1M of NaCl solution containing 140 mg L^{-1} of HA or no HA. The experimental condition studied by XAFS (Dardenne et al., 2009), where polynuclear Pu(IV)–HA species were evidenced, is also shown for comparison.

4.3 Investigations on the stability of humic substances at elevated ionic strengths

To predict the long term safety of a nuclear waste repository, the behaviour of the organic matter (OM), amongst with the humic substances, has to be examined under relevant and specific conditions. In case of regarding i) salt rock formation, ii) the Jurassic and lower Cretaceous clay rock layers in Northern Germany or iii) sedimentary layers like in Canada for a repository host rock, the potential impact of high ionic strength media have to be considered. A crucial point is to determine how it influences the stability of the colloidal organic matter and its metal ions binding properties. In recent investigations (Bouby and Buckau, 2012) in perchlorate media it was shown that even up to 3 M the destabilization of the humic acids (HAs) tested was not complete.

The aim of this work is to examine the stability of fulvic acids (FA) as representative of small size OM (smaller than humic acid) in chloride media of high ionic strengths (IS). The study uses two natural FAs extracted from two ground waters sampled in the Gorleben Site, Lower Saxony, Germany.

The results are completed with those obtained by using i) one synthetic fulvic acid (SFA), ii) one of the two groundwater as received and, iii) a lignin derivative. The OM colloidal suspensions are prepared in NaCl, $CaCl_2$, $MgCl_2$, $FeCl_3$ and HCl for ionic strengths varying from 10^{-2} M up to 6.5 M. Evolution of the suspensions is followed by UV-Visible spectrophotometry and TOC analysis before and after centrifugation. To complete the observation of an eventual flocculation, the size variations of the organic matter under those conditions are inspected by using the SEC/UV-Vis technique.

4.3.1 Material and methods

Gorleben groundwater Gohy-532

This natural groundwater is pumped from a bore-hole (number 532) which gives its name to the sample (Gohy-532). Characterization details can be found in previous works of Artinger, Buckau, Schäfer et al. (Artinger et al., 1996; Artinger et al., 1999; Artinger et al., 2000; Buckau et al., 2000b; Buckau et al., 2000d; Buckau et al., 2000c; Buckau et al., 2000a; Schafer et al., 2003; Schäfer et al., 2005).

Fulvic acids (FA): FA-573 & FA-532

These two fulvic acids are isolated, purified and characterized from the corresponding natural Gorleben ground waters pumped out from the bore – hole numbers 573 and 532. For more details on the isolation and purification processes see (Artinger et al., 2000; Wolf et al., 2004). To obtain a stock solution, a small amount of the final products

is dissolved in NaOH 0.1 mol.L^{-1} (ultrapure, Merck) and then diluted with ultrapure water. The dissolved organic carbon content is measured with a TOC analyzer (TOC-5000, Shimadzu). The FA concentrations are respectively 512 mg/L (FA-573) and 139 mg/L (FA-532). The FA stock solutions are stored at 4^{o}C in a fridge prior to use.

Synthetic (SFA-1)

The synthetic fulvic acid used (SFA-1) is kindly provided by A.K. Kiprop (present address Chemistry Department, Moi University, P.O Box 3900-30100, Eldoret, Kenya). The synthesis was done in the frame of his PhD work in the laboratory UMR 7566 G2R, Nancy Université CNRS, France. Briefly, it consists in an auto polymerisation reaction of cathecol at constant stirring (3000 rpm) and pH during 1 month followed by dialysis at various molecular weight cut-off (MWCO), deep frozing, lyophilization and grounding. More details can be found in (Kiprop, 2009; Kiprop et al., 2013). A stock solution is prepared following the protocol described in the paragraph just above. The SFA concentration is 214 mg/L (SFA-1).

Lignosulfonic acids sodium salt (LS-NA)

Lignosulfonic acid is a lignin-derived poly anionic macromolecule. The commercial product is provided by Sigma-Aldrich. The MWCO is 52 kDa. The salt is used as received. A small amount is dispersed in a mixture ultrapure water/NaOH at pH 10 to obtain a stock solution which is kept in the fridge prior to use. The concentration is 1264 mg/L.

Electrolytes

The NaCl (6.5 M), $CaCl_2$ (2.3 M) and $MgCl_2$ (2.1 M) electrolyte solutions are prepared from the salts (Merck. P.A.) dissolved in ultrapure water. A $FeCl_3$ electrolyte (0.43 M) is prepared in HCl (2M). A 4 M HCl solution is prepared by diluting a calibrated standard volume (Merck, ultrapure, p.a.) in 250 mL instead of 1 L. A 2-(N-morpholino)-ethanesulfonic acid (MES) buffer stock solution (1 M) is freshly prepared in ultrapure water.

OM suspension preparation and ionic strength effect study

The final suspensions (15 mL) are prepared by mixing the appropriate volumes of the different stock solutions together. The MES concentration is 10^{-3} M in all the samples. The final OM concentrations are 25 mg/L for FA-573, SFA-1 and LS-NA and 11.6 mg/L for FA-532 and Gohy-532. The final ionic strengths are 0.01 M, 3 M and 5 M in NaCl, 3 M in $CaCl_2$ and $MgCl_2$, 3 M in HCl and 4.58 M in $FeCl_3$/HCl.

The pH are only indicative as no correction is applied to take into account the salt effect. They are all adjusted after the mixing at 6.5 ± 0.2. They remain constant 24 h later. (Note: the pH are not measured for the electrolyte HCl 3M and $FeCl_3$/HCl).

The DOC concentration is checked in each sample before centrifugation and after (30 min at 4000 rpm, Megafuge 2.0 R, Thermo Scientific, Heraeus Instrument) for each supernatant. All the suspensions prepared in NaCl 0.01 M are measured by UV-Vis. spectrophotometry prior to and after the centrifugation. The supernatants of all the other samples are only measured after centrifugation by UV-Vis. spectrophotometry.

UV-Vis spectrophotometry

UV-Vis spectroscopy is commonly used for the characterization of humic substances (Artinger et al., 2000; MacCarthy, 1985; Schnitzer, 1978). The spectra are recorded on a UV-Visible spectrophotometer (Cary 50 Conc, Varian) over the range 900-199 nm after placing some mL of the solutions to be analyzed in quartz cuvettes (precision cells, quartz Suprasil® 300, QX 10.0 mm, HELLMA).

Size Exclusion Chromatography

The general principle of the Size Exclusion Chromatography has been described in details else-where, see e.g (Conte and Piccolo, 1999; Pelekani et al., 1999; Perminova, IV et al., 2003; Piccolo, 2001; Striegel et al., 2009). Very briefly, in SEC, the compounds are primarily separated on the basis of their hydrodynamic molecular size. Molecules that are larger than the pore size of the packing material are excluded and elute first at the exclusion/void volume. Smaller molecules can penetrate throughout the porous infrastructure and are then retarded leading to an elution at higher retention time.

In this study, we use a Bio-Silect® SEC250-5 (300*7.8 mm, 5 µm particle size, 250 A pore size, Bio-Rad Laboratories, California, USA) size exclusion column to perform the separation. A degasser (1100 series, model G1322A, Hewlett-Packard, Waldbronn, Germany) and an isocratic pump (model G1310A, Hewlett-Packard, Waldbronn, Germany) are used to deliver the eluent through the chromatographic column. The eluent consisted of ultra pure water with tris-buffer at 1.10^{-2} M and 5.10^{-3} M NaCl. The elution flow rate is fixed at 1 ml·min^{-1}. The injections are made via a 6-ports/2-channels injection valve (Knauer, Germany) and a PEEK sample loop of 100 µL (Rheodyne, USA). Connections and other tubing are made of PEEK as well. From the SEC column, the eluent solution is directed through an UV-Vis detector (Postnova analytics, Germany) recording the signal at 225 nm. An additional injection valve with a PEEK sample loop of 100 µL is added before the UV-Vis detector for direct injection and recovery measurement. SEC data handling are performed by using the ClarityTM GPC software (Data Apex, the Czech Republic). The calibration is performed with PSS reference standards (Polysciences, Eppelheim, Germany) of various molecular weight (0.891, 1.67, 3.42,

6.43, 15.8, 33.5 kDa). The main characteristics of the column are its total permeation volume and its exclusion volume determined from the total permeation time (498 s) and exclusion time (312 s) and are respectively: 8.27 mL and 5.35 mL, under the present experimental conditions.

4.3.2 Results and discussion

DOC

The DOC concentrations do not vary drastically (not more than 5-10 %) and without any trend. It is not associated to a specific electrolyte neither to an ionic strength value. It could thus be considered to be in the analytical error range. Nevertheless, this absence of significant variation is the first indication that the small organic matter (macro)molecules investigated present a high stability; i.e. it remains suspended even at high ionic strength.

Electrolytes absorption spectra.

The respective contributions of the electrolytes (see Figure 53) to the UV-Vis absorption spectra has been substracted. Actually, the absorption of the NaCl (5 M), $CaCl_2$ (3 M), and $MgCl_2$ (3 M) electrolytes is significant in the range 200-230 nm (Figure 53). The HCl (3 M) absorption is evident over a more extended range (200-300 nm). Note that the absorption of the $FeCl_3$ (0.4 M) / HCl (2 M) solution is above the limit of the detection and thus cannot be substracted properly. Accordingly, the nevertheless corrected UV-Vis spectra in that electrolyte cannot be considered. But, as said above, the DOC does not vary significantly in that electrolyte even if a flocculation is visible by eye. It suggests either a rather high stability of the OM at that IS (4.6 M) and in presence of iron and chloride ions.

FA-573 behavior in high ionic strength electrolytes: UV-Vis. absorption spectra variations and chromatograms

The FA-573-UV-Vis absorption spectra in the different electrolytes are presented Figure 54. The evolution of the UV-Vis absorption spectra are presented hereafter for all the suspensions after subtraction of the electrolyte contribution: FA-573 (Figure 54), FA-532 (Figure 56), Gohy-532 (Figure 57), SFA-1 (Figure 58), and LS-Na (Figure 59).

Humic compounds are complex macromolecular polymers consisting of 120 to 150 aliphatic and aromatic compounds intermingled in such a manner that they have lost their individual identities (Rashid, 1985). The resulting biopolymer is composed of an aromatic core (i.e. (poly-)phenols, (poly-) aromatics), linked with aliphatic side chains (i.e. carbohydrates, proteins, organic acids, fatty acids by-products of transformation), in various configurations and cross-linked in random fashions. Humic compounds contain

a variety of functional groups (constituting about 20 to 30 % of the molecule), such as aliphatic and aromatic carboxyls, phenolic hydroxyls, alcoholic hydroxyls, carbonyls, quinones, methoxyls and amino groups.

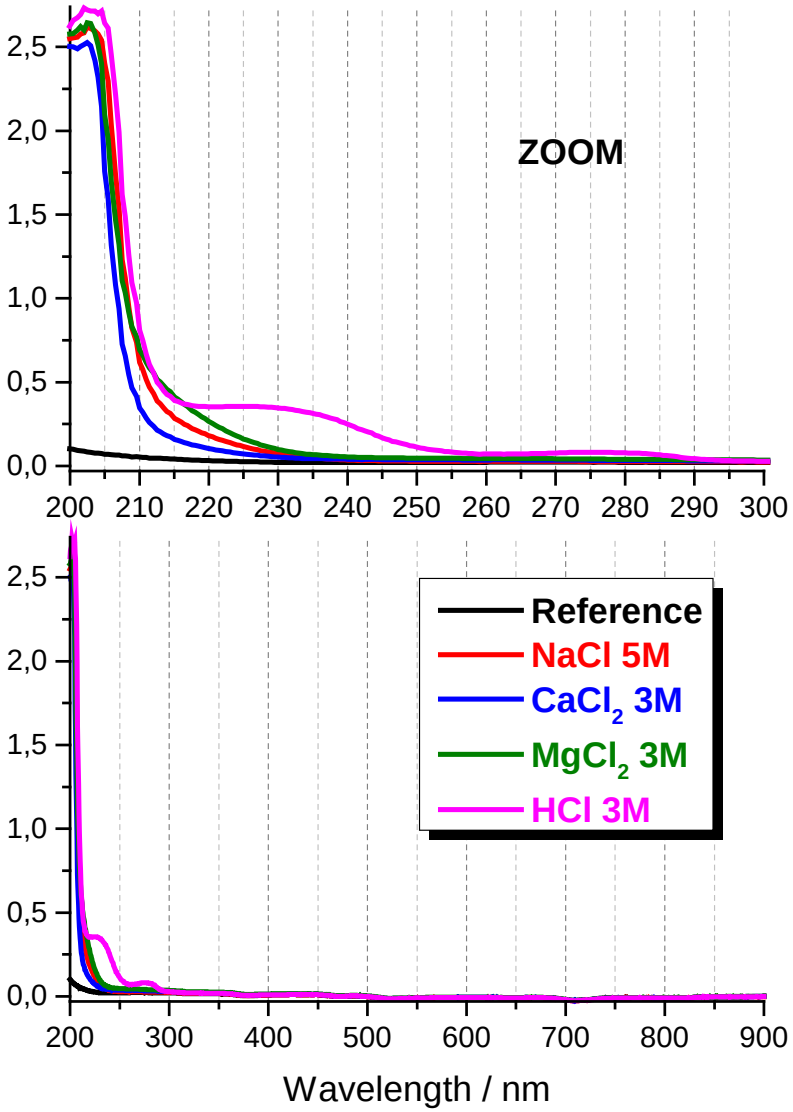

Figure 53: UV-Vis spectra of the electrolytes used to fix the ionic strength.

Humic compounds absorb light over a wide range of wavelength due to the presence of the vast majority of the chromophores that absorb in the UV region (< 400 nm) i.e. the aromatic groups with various degrees and types of substitution, including mono-and polysubstituted phenols and various aromatic acids (Korshin et al., 1997). The spectra of humic substances are frequently described in the literature by an increasing absorption with decreasing wavelength without characteristic feature. This is due to the high number of chromophore types without any possessing a unique and distinguishable absorption spectrum, combined with internal vibration and rotation of the molecules and inter-molecular interactions which broaden the absorption peaks in the UV-spectrum (Korshin et al., 1997).

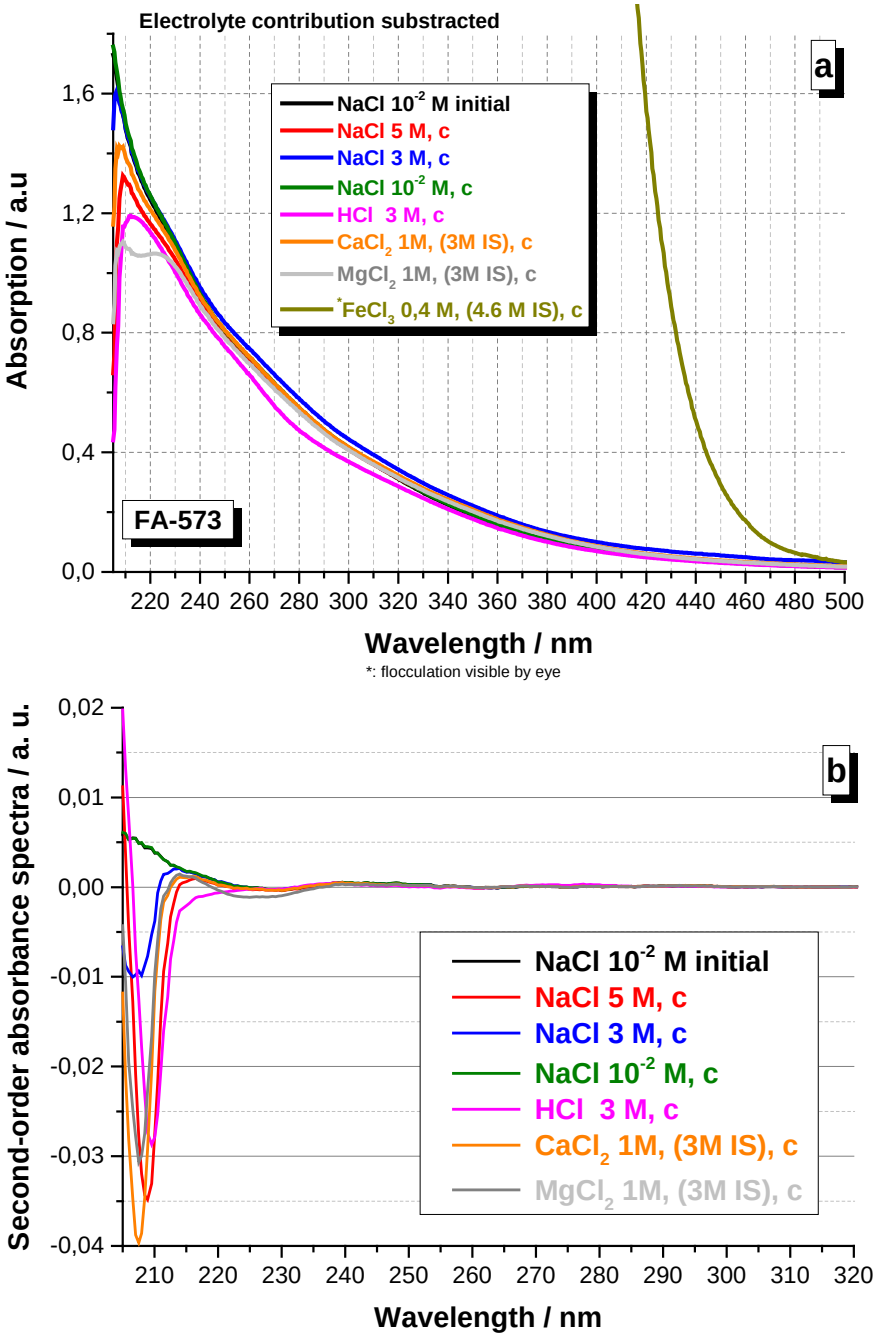

Figure 54: a) FA-573 UV-Vis spectra (range 210-500 nm) in different electrolytes and thus ionic strengths (IS) obtained after centrifugation. The electrolyte contributions have been substracted. [FA-573]= 25 mg.L-1. b) Second-order derivatives examplary shown in the range 205-320 nm.

Thus not surprisingly, the fulvic acid FA-573 (Figure 54a, black line – overlain by the green line!) UV-Vis absorption spectrum present the same pattern as that frequently reported in the literature (see (Baes and Bloom, 1990) for example and references cited) with an inflection point at ~ 230 nm. The centrifugation has no effect on this organic matter, as seen on the corresponding UV-Vis spectrum strictly identical (Figure 54a).

At 3 M NaCl (Figure 54a, blue line), the absorption spectrum differs from the one obtained in 10^{-2} M NaCl, an effect clearly accentuated at 5 M NaCl (Figure 54a, red line). A change is observed as well in $CaCl_2$ 1 M (i.e. 3 M IS). At a first look the absorption spectra pre-cited remain quasi featureless. Clear changes appear at the opposite at 1 M $MgCl_2$ (i.e. 3 M IS) and at 3 M HCl. The absence of significant DOC variations is a strong indication of the FA-573 stability in the different electrolytes and thus at these high ionic strengths but it does not say anything about the conformation of the organic molecule. To obtain more information the spectra variations are further examined based on data treatment proposed in the literature.

Unfortunately, the UV spectrum deconvolution into the constituent spectra of individual chromophore is impossible (Korshin et al., 1997). A more precise characterization is often made by considering the specific absorption at one wavelength or the absorption ratio at two wavelengths (i.e. for example the E4/E6 absorbance ratio at 465 nm and 665 nm) for a qualitative description of the curvature of the absorption continuum and mainly to determine the nature of the organic matter investigated. Actually, an increase in the specific absorption and a decrease in the absorption ratio are indicative of an increasing humification, aromaticity and molecular weight of humic substances (Chin et al., 1994).

Another characterization consists in modeling the UV spectra as a combination of three Gauss-shaped bands in analogy to benzene (Korshin et al., 1997) which presents three bands at 180 nm, 203 nm and 253 nm. It was proposed to attribute absorbance at wavelengths < ~ 190 nm to the local excitation (LE) band, absorbance between 190 nm and 240 nm to the benzenoid (Bz) band and absorbance at wavelength > 240 nm to the electron-transfer (ET) transition. Despite overlapping, it is thought that the composite LE, Bz and ET band in natural organic matter do not lose their identity and may be extracted from the UV spectra. Some authors have already applied this protocol successfully to describe the fractionation of humic substances in contact with mineral surface (Claret et al., 2008).

Presently, the same approach could be used in order to detect any specific subtle change induced by ionic strength on the different band constituents. The idea is, as proposed in (Korshin et al., 1997) and used by (Claret et al., 2008), to fit each absorption spectrum by a sum of three Gaussians using a nonlinear regression fitting procedure. Nevertheless, in a first approach, the convergence of the fits was difficult to obtain. Consequently, the next idea has been to use the derivative (differential) spectroscopy (Perkampus, 1992) to better isolate and thus determine the specific wavelength (band peak maximum) where any absorption spectra variation takes place and to see if there is an ionic strength influence (i.e. an eventual shift of this band peak maximum).

Table 18: Band peak maxima positions (± 0.5 nm) as obtained after differential spectroscopy (see text for details). a: initial, b: after centrifugation, c: not clearly determined.

	NaCl 0.01 M[a]	NaCl 0.01 M[b]	NaCl 5 M[b]	NaCl 3M[b]	HCl 3M[b]	$CaCl_2$ 3M[b]	$MgCl_2$ 3 M[b]
FA-573	-	-	208.7	207.4	209.7	207.6	207.8
	229.9	230.4	229.8	229.1	-	229.8	226.1
	261.6	261.7	261.5	262.1	261.9	261.1	261.0
	311.0	310.5	310.9	311.3	318.6	311.3	311.7
FA-532	-	-	208.4	204	208.9	207.1	207.4
	229.7	229.8	229.9	227.8	-	229.2	225.6
	264.4	266.3	263.7	264.8	260.6	262.3	262.8
	311.3	311.4	318.5	311.6	318.7	318.9	318.8
Gohy-532	-	-	208.1	204.7	208.9-	207.0	207.3
	-	-	-	-	216.8	-	-
	(231.3)[c]	(230.3)[c]	(230.5)[c]	-	229.9	230.5	229.8
	266.1	266.4	262.5	261.4	260.7	266.1	265.9
	311.1	311.0	318.6	311.9	318.8	318.9	318.8
SFA-1	-	-	208.9	204.5	209.5	207.1	206.7
	231.3	230.9	-	229.9	229.9	230.5	225.8
	287.6	286.4	287.7	287.6	283.7	285.3	285.5
	327.3	327.4	327.5	326.9	328.3	327.4	327.8
LS-Na	-	-	208.6	207.9	209.5	207.9	207.8
	236.6	233.7	234.0	235.0	234.7	232.5	232.2
	285.7	286.1	285.7	286.0	285.9	286.6	286.1
	(327.6)[c]	(327.9)[c]	(318.2)[c]	(326.6)[c]	(327.1)[c]	(318.4)[c]	(318.0)[c]

Derivative spectroscopy is the representation of the first- and second-derivative as well as higher-order derivatives of a normal (or zero-order) spectrum with respect to wavelength (or wavenumber). It emphasizes subtle spectral features. This enables better resolution of multicomponent samples to be obtained. Numerous examples of applications are reported nowadays as it has become a useful analytical/data processing technique to extract qualitative and quantitative information from spectra consisting of unresolved and/or greatly overlapping bands (see (Bosch Ojeda and Sanchez Rojas, 2013; Pavón et al., 2012) for details). Amongst the firsts (Cieslewicz and Gonet, 2004), Hur et al. (Hur et al., 2006) used this method to obtain valuable dissolved organic matter (DOM) discrimination indices. Similarly to (Hur et al., 2006), we used the method of Savitsky and Golay in the present study (Savitzky and Golay, 1964). The process involved a stepwise interval smoothing of the original zero-order spectra using a constrained second order polynomial function to obtain the second derivative (i.e. $d^2A(\square)/d^2$

Software (Microcal Software, Inc.). The results are exemplary shown Figure 54b for the range 205-320 nm. The minimum obtained are the band peak maxima of the UV-Vis. spectra. The results are summarized Table 18.

For FA-573, 3 band peak maxima can be isolated at ~ 230 nm, ~ 262 nm, ~ 311 nm and in addition one at ~207-209 nm for the highest ionic strength. No change occurs after the centrifugation (3 peaks detected), confirming the visual spectral observation. It is presently difficult to state on the significance of the slight peaks shifts observed for the bands located at ~ 230 nm, ~ 260 nm and ~ 311 nm for increasing ionic strength with maybe an exception in $MgCl_2$ (peak at ~226 nm instead of 230 nm initially) and in HCl 3M (peak at ~319 nm instead of 311 nm initially). Nevertheless, a clear effect of the ionic strength is detected with the appearance of an additional peak located at 207-210 nm in each electrolyte.

(Baes and Bloom, 1990) recorded the UV-Vis spectra of some fulvic acids and they noted shoulders in the 260-290 nm and 310-330 nm range. The pH-dependent behavior of these bands make them suggest that the relevant chromophoric systems are –OH and –COOH-substituted benzene rings. In addition, they attributed the very strong absorbance at very short wavelengths (e.g., 210 nm) to the benzonoid bands of the carboxyphenols. This opened somehow the way to the analogy with the benzene proposed later by (Korshin et al., 1997) as benzene presents 3 bands at 180 nm, 203 nm and 253 nm, or one may think eventually as well to an analogy with the benzoic acid, the simplest aromatic carboxylic acid which presents 3 bands centered near 190 nm, 230 nm and 280 nm (Baum and McClure, 1979)

In the present case, for the fulvic acid FA-573, one can attribute similarly the peaks located at ~ 207~209 nm and at ~ 230 nm to the Bz band, the peaks at ~ 262 nm and ~ 311 nm to the ET band. This kind of groups (aromatic with or without substitution like –OH and –COOH-substituted benzene rings or carboxyphenols) could thus be thought as the ones affected by an increase of the ionic strength. The variations observed would reflect a change in their environment. Nevertheless, many other functional groups (Liu and Ryan, 1997) could have been affected.

Maybe of interest is to remember few studies done in the 60's to correlate changes in protein structure from denaturation or proteolysis with alterations of their UV absorption spectra in the wavelength range 200 to 320 nm (Donovan, 1969; Glazer and Smith, 1960; Martin and Bhatnagar, 1966; Móra and Elöudi, 1968). It was first proposed that the spectral changes in the 220-250 nm region may be due to peptide chromophore undergoing an helix-coil transition (Glazer and Smith, 1960). Later, the absorption changes observed near 230 nm were attributed primarily to environmental effect on the aromatic chromophore (Martin and Bhatnagar, 1966; Móra and Elöudi, 1968) (e.g. indol and phenol for globular protein compared to the helix to coil transition of the amide group (Donovan, 1969)). According to these pioneer works and due to the presence of a band at 230 nm, it appeared interesting to follow the size evolution of the fulvic acids as a function of the ionic strength. This has been done by using the SEC-UV-Vis equipment. (Note: Due to the low pH of the suspension in HCl 3M, it was not analyzed by SEC).

The SEC chromatograms after injection of the FA-573 suspensions prepared in NaCl 10^{-2} M are similar before or after the centrifugation (see Figure 55). It confirms that the centrifugation has thus no effect. The UV-FA-573-chromatograms present peak maxima at ~6 min and a shoulder at ~7 min which, according to the calibration done with Na-PSS standards, indicate that the size of the main FA-573 fraction is comprised between 1.5 and 2 nm (hydrodynamic diameter) with a residual fraction below 1 nm (see Table 19). The chromatograms are drastically different for increasing ionic strengths with the appearance of an additional peak after the total permeation time (see Figure 55).

Table 19: SEC-hydrodynamic diameter values (in nm).

	FA-573	FA-532	SFA-1	LS-Na
1st (main) Fraction	1,5-2	< 1.5	< 1,5	3,0
2nd(minor) Fractions	< 1 nm	< 1 nm	< 1 nm	< 1 nm

In 5M NaCl, the FA-573 peak is broader and the elution peak maximum is detected at ~ 5.7 min. This is attributed to intramolecular electrostatic interactions. Adding NaCl to increase the ionic strength at 5 M may have shielded the internal electrostatic repulsive forces that act to expand the FA-573. The result is a more compact FA-573 shape with an outer layer of Na^+ ions. This finally increases the hydrodynamic volume occupied by the fulvic acids. This results in earlier elution volumes (times) with respect to those observed in the absence of high NaCl concentration. This has been already reported in the literature (Striegel et al., 2009). In $CaCl_2$ 3M (IS), the chromatograms are less reproducible. Nevertheless, it is clear that the FA-573 peak is shifted but this time towards later elution times (~ 6.2 min). This might be due to a Ca^{2+}-induced bridging effect on the FA-573 molecule resulting in a more compacted (and thus smaller) molecule. The same remarks can be done for the chromatograms obtained in $MgCl_2$ 3M (IS), which are very reproducible. In that electrolyte, the peak shift is even more pronounced (elution at ~ 7 min). This means that the compaction could be even more pronounced. This might be as well related to the more pronounced shift of the UV band initially measured at 230 nm which occurs at ~226 nm in $MgCl_2$ (see Table 18). Accordingly, a variation of this band peak maximum could be considered as a conformation change indicator as proposed in the past for the proteins (Donovan, 1969; Glazer and Smith, 1960; Martin and Bhatnagar, 1966; Móra and Elöudi, 1968).

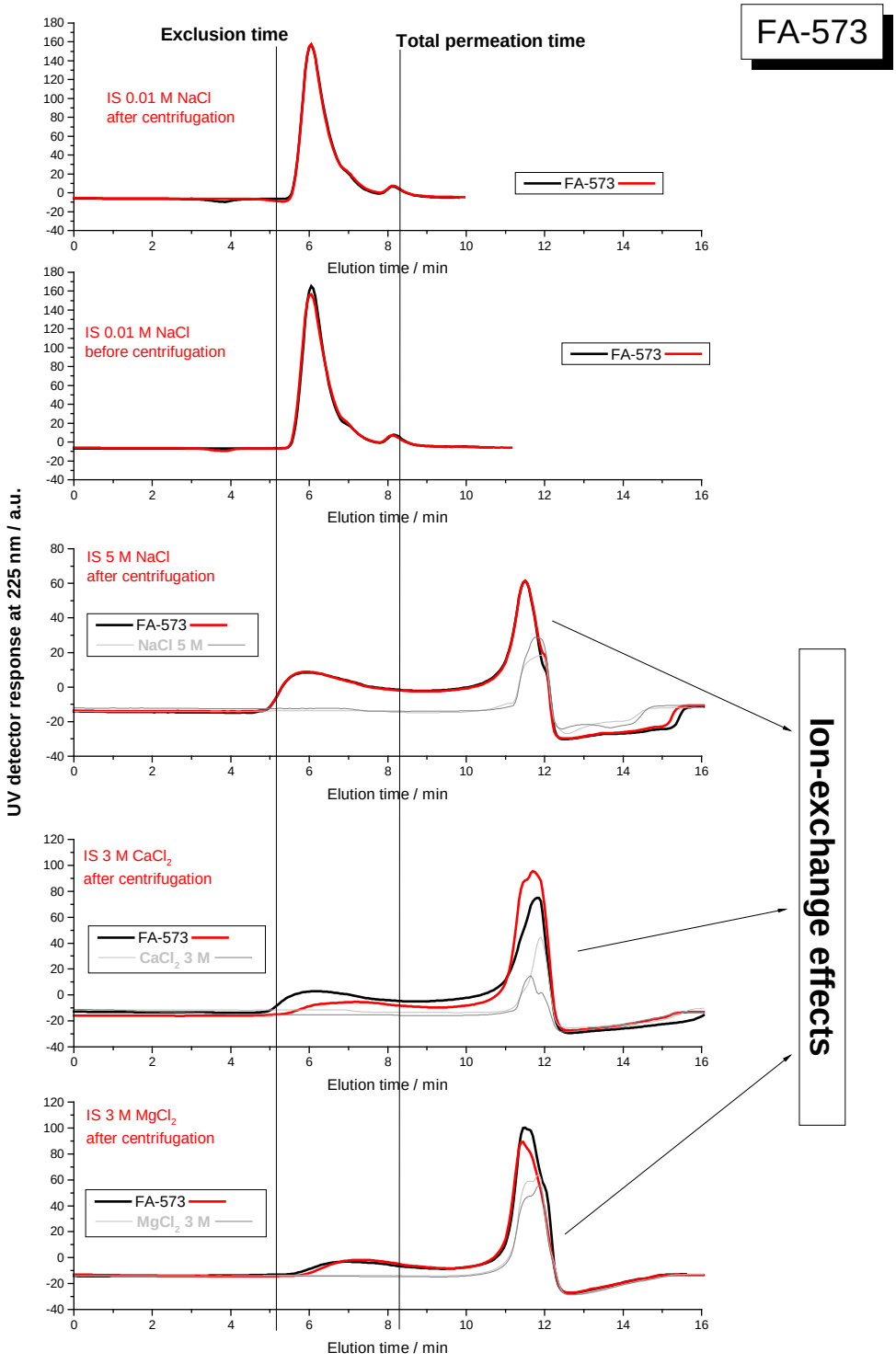

Figure 55: FA-573-UV-chromatograms obtained after injection of the FA-573 suspensions prepared in different electrolytes, 100 µL injected, 2 measurements.

The second peaks detected after the total permeation time (between 10.5-12.5 min) are attributed to ion-exchange effects (Striegel et al., 2009). This arises due to the pH-induced dissociation of the silanol groups of the column packing material. It acts as a cation-exchange sites onto which the cations can adsorb, resulting in elution after the total column volume (or in no elution). In addition to the sorption, the counterions (like

here Na^+, Ca^{2+}, Mg^{2+}) experience a preferential diffusion into the pores of the packing material to balance the difference between the stagnant and the flowing mobile phase. This so-called *ion inclusion effect* (Striegel et al., 2009) may result in later elution as those presently observed.

In conclusion, the FA-573 fulvic acids are stable in high ionic strength chloride electrolyte media nevertheless they experience variable conformation (size) changes as a function of the counterions (Na^+, Ca^{2+} or Mg^{2+}). The following ordering might be proposed concerning the hydrodynamic diameters: $MgCl_2$ (3M IS) < NaCl (10^{-2} M IS) < $MgCl_2$ (3M IS) < NaCl (5M IS) < 2 nm.

FA-532 and Gohy-532 behavior in high ionic strength electrolytes: UV-Vis absorption spectra variations and chromatograms

The UV-Vis. absorption spectra are presented Figure 56 (FA-532) and Figure 57 (Gohy-532). Note that the fulvic acids FA-532 are isolated, extracted and purified from the original Gohy-532 ground water sample. Accordingly, and in agreement with literature, the FA-573, FA-532 and Gohy 532 UV-Vis. absorption spectra present similar patterns in NaCl 10^{-2} M.

The variations observed in Figure 56 for the fulvic acids FA-532 are rather comparable to the ones described for the fulvic acids FA-573. On the opposite, the variations are more pronounced on the absorption spectra of the original Gohy-532 ground water. This might be due to the fact that the Gohy-532 ground water contains other constituents more affected by the ionic strength than its fulvic acids fraction. One can emit the hypothesis that this is mainly the fulvic acids fraction which remains rather unaffected and in suspension.

The same data treatment has been applied and the results are similar to those previously described. The same absorption bands can be isolated at ~ 230 nm, ~ 264 nm and 311 nm initially, with an additional one for increasing ionic strength at ~ 204-209 nm. The peak shifts of the band at 260 nm and 311 nm might be more significant than for the FA-573 (see Table 18).

Accordingly the same conclusion can be proposed: the ionic strength affects more specifically some kind of groups (aromatic with or without substitution like –OH and –COOH-substituted benzene rings or carboxyphenols), this is accompanied by conformation (size) changes as visible by SEC-UV-Vis. analysis (data not shown) leading to the following hydrodynamic diameter ordering for FA-532: $MgCl_2$ (3M IS) < NaCl (10^{-2} M IS) <= $CaCl_2$ (3M IS) < NaCl (5M IS) < 1,7 nm. The initial FA-532 hydrodynamic diameter of the main fraction in NaCl 10^{-2} M is estimated < 1.5 nm (see Table 19).

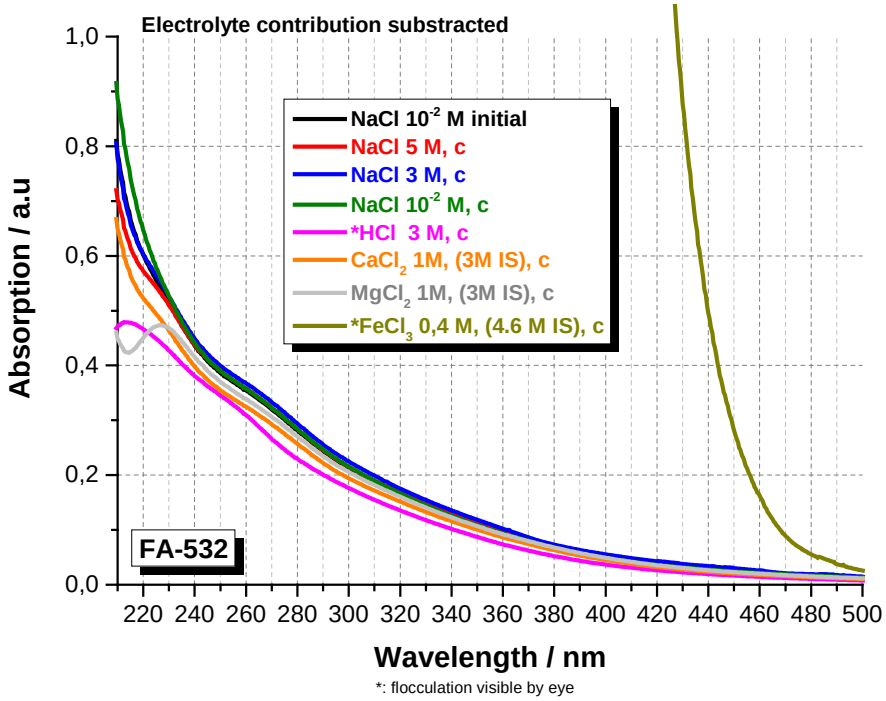

Figure 56: FA-532 UV-Vis spectra (range 210-500 nm) in different electrolytes and thus ionic strengths (IS) obtained after centrifugation. The electrolyte contributions have been substracted. [FA-532]= 12 mg.L^{-1}.

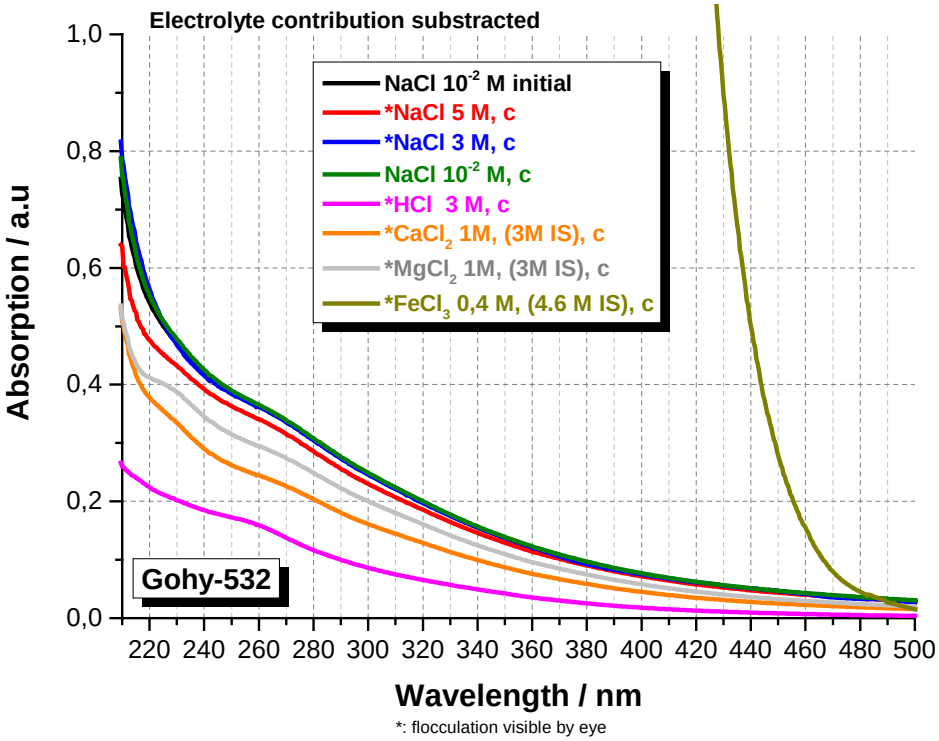

Figure 57: Gohy-532 UV-Vis. spectra (range 210-500 nm) in different electrolytes and thus ionic strengths (IS) obtained after centrifugation. The electrolyte contributions have been substracted. [Gohy-532]= 12 mg L^{-1}.

SFA-1 behavior in high ionic strength electrolytes: UV-Vis. absorption spectra variations and chromatograms

The absorption spectra of the synthetic fulvic acids SFA-1-UV-Vis in different electrolytes are presented Figure 58. The pattern in NaCl 10^{-2} M is similar to the one reported in literature for natural fulvic acids. It is consistent with the UV-Vis absorption spectra recorded after its synthesis (Kiprop, 2009) showing clearly three broad bands at ~ 228 nm, 278 nm and 362 nm. In the present work, the data analysis by differential spectroscopy indicate the presence of three bands as well but located at ~231 nm, ~ 288 nm and 327 nm. The last band is thus shifted compared to estimation done by the raw visual inspection of the UV-spectra (Kiprop, 2009). The results are nevertheless in good agreement. A last band at ~ 484 nm was proposed but not presently clearly detected.

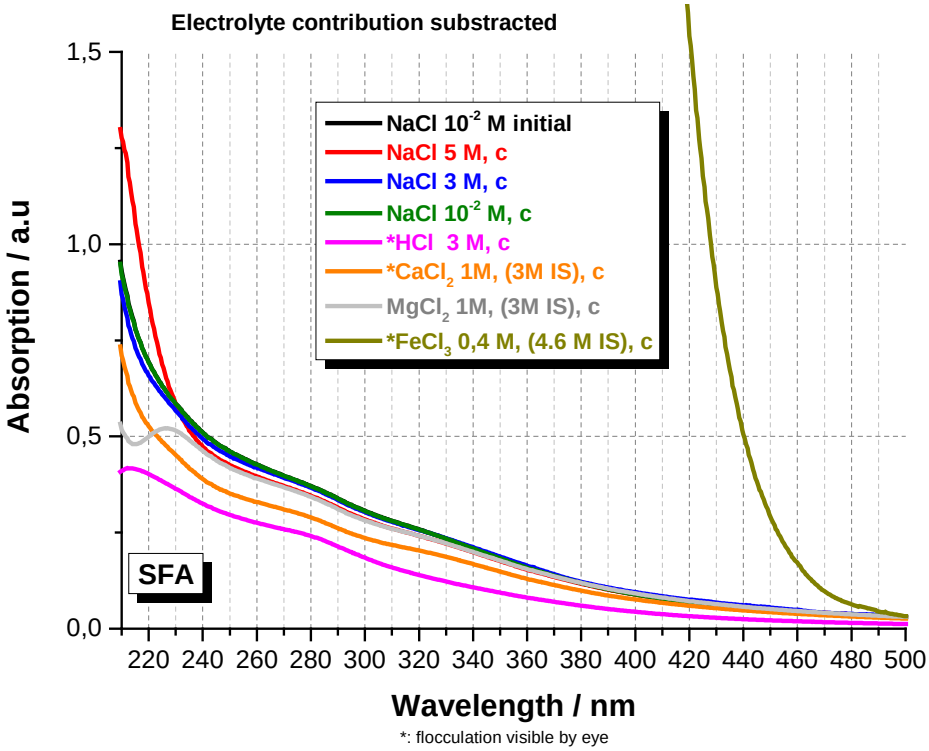

Figure 58: SFA-1 UV-Vis spectra (range 210-500 nm) in different electrolytes and thus ionic strengths (IS) obtained after centrifugation. The electrolyte contributions have been substracted. [SFA-1]= 25 mg L^{-1}.

A noticeable effect of the ionic strength is seen (Figure 58) especially above 3 M IS and in HCL electrolyte. At high ionic strength, a fourth band can be isolated from the data treatment (see Table 18) located at ~205-210 nm, similarly to the natural fulvic acids.

This synthetic fulvic acid is obtained from the polymerization of catechol. The molecular structure determined from ATR-FTIR spectroscopy (Kiprop, 2009) consists of several

aromatic rings linked to each other through aryl-aryl and ether bonds, each aromatic ring may bear up to to five substitutional groups. The first (~ 231 nm) and second band (~ 288 nm) are assigned to the aromatic bands. The slight variations of the peak maxima of these bands for increasing ionic strength may indicate its specific effect on these substituted (or not) aromatic groups.

SEC-UV-Vis analysis was performed (data not shown). The hydrodynamic diameter of the main size fractions are listed in Table 19. The variations of the SFA-1-chromatograms present great similarities with the chromatograms of the natural fulvic acids. The following size sequence effects can be proposed: $MgCl_2$ (3M IS) < NaCl (10^{-2} M IS) <= $CaCl_2$ (3M IS) < NaCl (5M IS) < 3.8 nm. Note that this is a much bigger size than observed for the natural fulvic acids.

LS-Na behavior in high ionic strength electrolytes: UV-Vis. absorption spectra variations and chromatograms

The LS-Na-UV-Vis absorption spectra of this lignin-derived poly anionic macromolecule in the different electrolytes are presented Figure 59. This compound was under investigation for its use as plasticizer in cement composition, reason for why its study could be of interest.

The UV-Vis spectra present a clear feature at 280 nm which is accordingly one of the band clearly detected by differential spectroscopy (see Table 18). The centrifugation has apparently an effect as noted by a decrease of the absorption at wave length below 230 nm. This leads to a shift in the peak maximum position detected by differential spectroscopy (see Table 18).

This organic macromolecule is affected by increasing ionic strength as seen by the variation of the absorption spectra, especially below 230 nm, and as reflected by the shift of this band peak maxima values and the detection of an additional band with a peak maxim value at ~ 208-209 nm. Again it might be seen as a specific IS effect on substituted (or not) aromatic groups.

Some conformation (size) changes have been seen by SEC-UV analysis (data not shown). The hydrodynamic diameter of the main size fractions are specified in Table 19. Nevertheless, in that case only a clear shift towards bigger size (elution at earlier retention time) is noticeable. The following size sequence effects can be proposed: NaCl (10^{-2} M IS) < $MgCl_2$ (3M IS) < 2.7 nm <$CaCl_2$ (3M IS) & NaCl (5M IS) much bigger as eluted at the exclusion time limit (i.e. the size cannot be estimated).

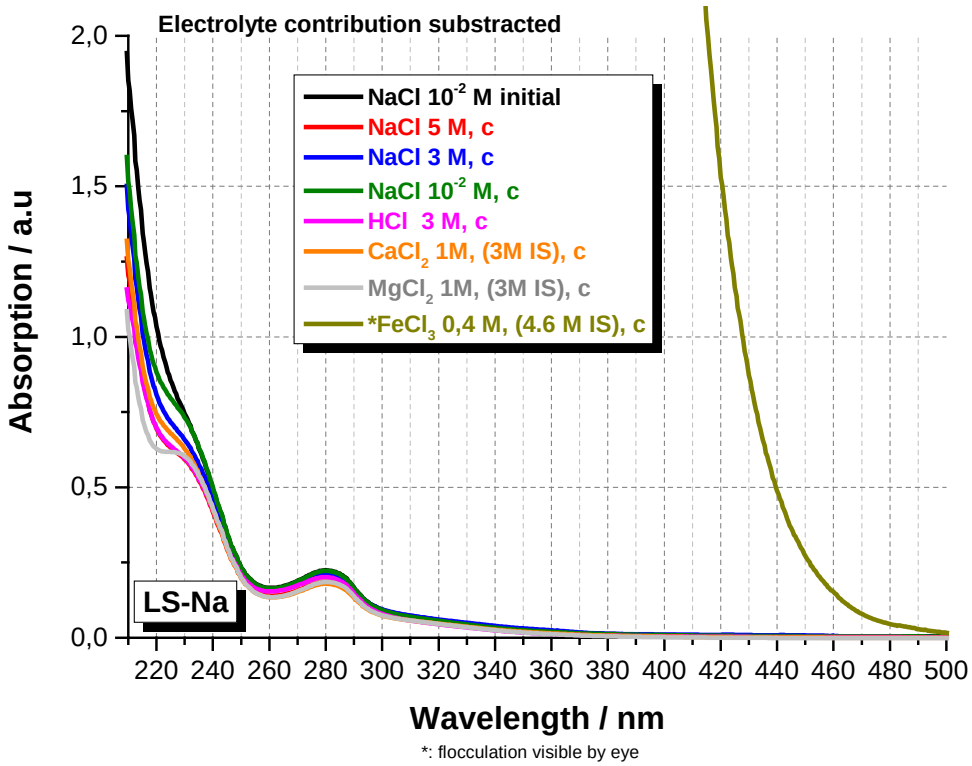

Figure 59: LS-Na UV-Vis. spectra (range 210-500 nm) in different electrolytes and thus ionic strengths (IS) obtained after centrifugation. The electrolyte contributions have been substracted. [LS-Na]= 25 mg L^{-1}.

4.3.3 Conclusions

The first results indicate a high stability of the small sized organic matter under the present conditions: the DOC varies by less than 5-10%. No effect is noticeable up to 3 M IS in NaCl. At 5 M IS NaCl or 3 M IS $CaCl_2$/$MgCl_2$ and HCl some variations are noticeable on the absorption spectra.

The fulvic acids (FA-573 and FA-532) isolated from the respective Gorleben ground waters (Gohy-573 and Gohy-532) behave similarly. The synthetic fulvic acids (SFA-1) react as the natural ones but its final conformation appears more expanded. This synthetic product might be a good analogue for natural fulvic acids with the advantage of a better known (controlled) composition;

A refined analysis of the absorption spectra by differential spectroscopy evidence various band which can be attributed to the local excitation band (LE), to the benzenoid band (Bz) and to the electron-transfer transition band (ET). The shifts of the corresponding band peak maxima (if considered significant enough) suggest that an increase of the ionic strength affects more specifically some kind of groups (aromatic with or without substitution like –OH and –COOH-substituted benzene rings or carboxyphenols). This would reflect a change in their close environment;

Conformation (size) changes are qualitatively evidenced by SEC-UV-Vis analysis. For the fulvic acids, natural or synthetic, the NaCl addition (> 3 M) results in an expansion of the hydrodynamic molecular volume due to intramolecular electrostatic interactions (even more pronounced for the synthetic FA), while the addition of $CaCl_2$ or $MgCl_2$ results in a compaction of the macromolecule certainly due to a divalent cation-induced bridging effect (the Mg^{2+} being more efficient). The maximum hydrodynamic diameter values estimated from SEC data are respectively 2 nm, 1.7 nm and 3.8 nm for FA-573, FA-532, and SFA-1, respectively. The natural fulvic acids can thus certainly preserve their mobility in natural media of high ionic strength. For the lignin-derived macromolecule, the ionic strength increase results in an expansion of the hydrodynamic molecular volume whatever the electrolytes up to ~ 2.7 nm ($MgCl_2$, 3M IS) and more (no quantification possible) for $CaCl_2$ (3M IS) and NaCl (5M). Here, the mobility cannot be guaranteed.

These conclusions are restricted to the experimental time frame of the present work, i.e. 24 hours. More work is necessary to state on their long term stability in high ionic strength electrolyte media. The fulvic acids seem to preserve their stability even in high ionic strength media even if they experience conformational change. This is certainly due to their low molecular weigth and density close to the one of the solvent. It does not mean that they preserve their complexation properties as the functional groups are affected in their environment, a point which call for further investigations.

5 Solubility of Actinides in presence of borate and at high ionic strengths

The interaction of borate with lanthanides (III) and actinides (III, IV, V, VI) is investigated in dilute to concentrated saline solutions. Boron can be present as component of the emplaced waste in a nuclear waste repository. In certain rock salt formations, high boron concentrations can also occur in the intruding brine solutions. In this framework, it is very relevant to understand the impact of borate in the chemical behaviour of actinides (e. g. complexation, solubility phenomena or redox processes) under repository relevant conditions. In spite of this, only a limited number of studies on the interaction of borate with lanthanides and actinides are reported in the literature. This is also reflected by the absence of any thermodynamic data selection for actinide–borate aqueous complexes or solid compounds in the current NEA–TDB reviews. In order to gain a better understanding of the processes taking place in the Ln(III)– and An(III, IV, V, VI)–borate systems, comprehensive solubility experiments in combination with spectroscopic studies and a detailed solid phase characterization were performed under repository-relevant conditions.

In the present work, the interaction of borate with actinide (III, IV, V, VI) is investigated in diluted to concentrated saline solutions with a combination of solubility experiments, spectroscopic methods (including TRLFS, EXAFS and UV–Vis/NIR) and comprehensive solid phase characterization (accomplished with XRD, XPS, SEM–EDS, XANES/EXAFS). The work comprises experimental conditions relevant for different concepts of radioactive waste disposal, and thus different background electrolytes (NaCl, $MgCl_2$ and $CaCl_2$) as well as a broad pH-range ($6 \leq pHm \leq 13$) are considered. The main objectives of this work are:

- The solubility of Nd(III) is studied in dilute to concentrated NaCl, $CaCl_2$ and $MgCl_2$ solutions with varying pH and boron concentration. Focus is given to the possible formation of Nd(III)–borate compounds and their eventual role on the immobilization of An(III). Thus a comprehensive solid phase characterization is performed using XRD, XPS and SEM–EDS. Additional TRLFS experiments with Cm(III) give information on the aqueous speciation of An(III)/Ln(III) in the presence of borate. With these data, a first thermodynamic description is proposed for the system Ln(III)/Cm(III)-Na^+-Mg^{2+}-Ca^{2+}-H+-Cl^--$B(OH)_4^-$ at 25°C.
- The solubility of Np(V) is studied in dilute to concentrated NaCl and $MgCl_2$ solutions with varying pH and boron concentration. Focus is given to the possible formation of Np(V)–borate compounds and their possible impact on the Np source term. Solid phase characterization is accomplished using XRD, SEM–EDS, XPS and EXAFS techniques. The aqueous speciation of Np under increasing concentrations of borate is investigated using UV–Vis/NIR. The combination of solubility data, spectroscopic results and solid phase characterization is aimed at deriving a first thermodynamic description for the system Np(V)- Na^+-Mg^{2+}-Ca^{2+}-H+-Cl^--$B(OH)_4^-$at 25°C.

- Because of their stronger hydrolysis and the expectedly weaker interaction with borate, the solubility of Th(IV) and U(VI) is exemplarily investigated in dilute to concentrated NaCl and $MgCl_2$ solutions and at various boron concentrations. Solubility measurements are complemented with solid phase characterization using XRD. The system Pu(III)–Pu(IV) is considered to gain insight on the effect of borate on the chemical behavior of redox sensitive actinides and allow a better assessment of the plutonium source term.

5.1 Experimental

Details of the experimental parameters and applied methods can be find in (Hinz, 2015; Hinz et al., 2015). This report contains only a brief summary.

5.1.1 Chemicals

All chemicals used in the experiments were obtained from Merck or specifically prepared at INE and were not further purified. All solutions were prepared with purified water from a Milli-Q-academic apparatus (Millipore, 18.2 MΩ) purged with Argon before use. The long-lived curium isotope ^{248}Cm ($t_{1/2}$ = 3.4×10^5 years) was used for the TRLFS measurements. The stock solution used in the experiments (2×10^{-5} M Cm(III) in 0.1 M $HClO_4$) had an isotopic composition of 89.7% ^{248}Cm, 9.4% ^{246}Cm, 0.4% ^{243}Cm, 0.3% ^{244}Cm and 0.1% ^{247}Cm. A ^{237}Np stock solution was previously prepared with 2.5 g of ^{237}Np ($t_{1/2}$ = 2.14·10^6 years), which was purified from trace impurities of Pu and Am using an ion exchange method. The resulting Np solution (0.32 M ^{237}Np in 0.01 M HCl) was characterized by gamma spectrometry, liquid scintillation counting (LSC), UV–Vis/NIR and alpha spectrometry, which confirmed both the chemical and radiochemical purity of the ^{237}Np stock solution. Pu solubility experiments were performed with ^{242}Pu with the exact isotopic composition of ^{242}Pu (99.4%), ^{239}Pu (0.58%), ^{238}Pu (0.005%) and ^{241}Pu (0.005%). Since the main isotope is ^{242}Pu (t1/2 = 375000 years), no radiolysis effects, occurring by the decay of short lived Pu isotopes in concentrated chloride solutions are expected.

5.1.2 pH measurement in saline solutions

In solutions with I ≥ 0.1 m, ion interaction processes affect the activity coefficient of H^+ (γ_{H+}) and the liquid junction potential. To determine pH in high salinity no longer the activity of H^+ but the concentration of H^+ are used (Knauss et al., 1990):

$$pH_m = -log(m_{H+}) \; and \; pHc = -log(c_{H+})$$

Where pH_m and pH_c are the negative logarithm of the molal and molar concentration of H^+, respectively.

The values pH_m and pH_c can be calculated from the operationally measured pH_{exp} and an empirical correction factor (A) where liquid junction potential and the activity coefficient of H^+ are included.

$$pH_m = pH_{exp} + A_m \qquad and \qquad pH_c = pH_{exp} + A_c$$

with

$$A_m = log\ {}^{m}\gamma_{H+} + \Delta E_j\, F/RTln(10)$$

and

$$A_c = log\ {}^{c}\gamma_{H+} + \Delta E_j\, F/RTln(10)$$

The correction factor A is experimentally determined for the respective salt system and concentration with a set of reference solutions with known proton concentration.

For pH measurements in this work, a combination glass pH electrode (type ROSS, Orion), freshly calibrated against dilute standard pH buffers (pH 7–13, Merck), was used to determine the molar or molal H_+ concentration, $[H^+]$ and m_{H+}, respectively. Whenever needed, pH adjustments were performed with HCl-NaCl-NaOH, HCl-$MgCl_2$ and HCl-$CaCl_2$ solutions of proper ionic strength. Alkaline solutions in $MgCl_2$ and $CaCl_2$ were adjusted with $Mg(OH)_2$(s) and $Ca(OH)_2$(s), respectively. All "A" factors used in this work for NaCl, $CaCl_2$ and $MgCl_2$ solutions were previously reported by Altmaier et al (Altmaier et al., 2003a; Altmaier et al., 2008) and are summarized in Table 20. The pH_m measurements performed following this approach are assigned with an uncertainty of ± 0.04 pH units. Note that the impact of borate on the background electrolyte is not corrected for the determination of pH. Nonetheless, it cannot be excluded that high boron concentrations ($[B]_{tot}$ = 0.4 M) might have impact on pH measurements in this work. The uncertainty of pH measurements in these specific cases is considered ± 0.1 pH units.

Table 20: A_c- and A_m values used in this work for the quantification of pH_c and pH_m, respectively.

Salt system	**Concentration**	**A_c**	**A_m**
NaCl	0.1 M	-0.08	-0.08
NaCl	1.0 M	0.09	0.08
NaCl	5.0 M	0.95	0.9
$CaCl_2$	0.25 M	0	-0.01
$CaCl_2$	1.0 M	0.34	0.33

$CaCl_2$	3.5 M	1.77	1.71
$MgCl_2$	0.25 M	0.03	0.03
$MgCl_2$	1.0 M	0.4	0.4
$MgCl_2$	3.5 M	1.98	1.93

5.1.3 Speciation of boron in aqueous saline solutions

^{11}B-NMR in NaCl, $CaCl_2$ and $MgCl_2$ solutions: ^{11}B-NMR spectra were recorded with a Bruker NMR-spectrometer (Avance III, 400 MHz) with a field strength of 9.4 T and a corresponding ^{11}B resonance frequency of 128.4 MHz with a broadband observe probe. The ^{11}B chemical shifts (δ) are referenced externally with respect to BF_3 etherate in $CDCl_3$. All spectra were evaluated with the software Top Spin (Bruker). For all spectra a pulse sequence with a very short delay time (100 µs) was used. The ^{11}B-NMR measurements were performed under atmospheric conditions in teflon liners (Rototec-Spintec, PTFE-FEB-NMR Tube Liner 8'', 5 mm) filled with 400 µL sample solution and mixed with 40 µL D_2O at 25°C. Table 21 summaries the samples prepared in dilute and concentrated NaCl, $MgCl_2$ and $CaCl_2$ with 0.04-0.4 M total boron concentration with varying pH_m .

Table 21: Experimental conditions in the system investigated by ^{11}B-NMR

System	**Concentration of background electrolyte**	**$[B]_{tot}$**	**pHm**
NaCl	0.1 M	0.04 M, 0.16 M	8; 12
NaCl	5.0 M	0.04 M, 0.16 M	2.6; 8; 12
$CaCl_2$	0.25 M	0.04 M	8; 12
$CaCl_2$	3.5 M	0.04 M	8; 12
$MgCl_2$	0.25 M	0.04 M, 0.16 M, 0.4 M	8
$MgCl_2$	3.5 M	0.04 M, 0.16 M, 0.4 M	8

5.1.4 Determination of total metal concentration and aqueous speciation techniques used for Ln(III) and An(III/IV/V/VI) in solution

The total aqueous concentration of Nd, Th and U was measured by ICP–MS after phase separation by 10 kD ultrafiltration (~1.5 nm, Pall Life Sciences) (Thermo scientific X-Series II for Nd(III) and Perkin Elmer Elan 6100 for Th(IV) and U(VI)).

LSC measurements were performed to determine concentrations of Np and Pu and the measurement has been done in PP vials (20 mL, Zinsser Analytic). After 10 kD ultrafiltration (~1.5 nm, Pall Life sciences), a small aliquot of the sample was mixed with 10 mL LSC cocktail (Ultima Gold XR, Fa. Perkin-Elmer). Samples were measured for 30 minutes with a Perkin Elmer 1220 Quantulus. The Quantulus apparatus used in this work provides a pulse shape analyzer (PSA) to perform a simultaneous alpha/beta gross counting, which allows the distinction between alpha and beta pulses, and hence, the distinction between ^{237}Np and its daughter ^{233}Pa.

In this work the Pu concentration in solution was determined using the low energetic β –emitter ^{241}Pu, because alpha peaks of ^{242}Pu, ^{239}Pu, ^{238}Pu, and ^{241}Am (daughter from the ^{241}Pu) cannot be separated by LSC.

Cm(III) concentrations and speciation was performed by time resolved laser fluorescence spectroscopy (TRLFS). Experiments were performed with $1 \cdot 10^{-7}$ M Cm(III) per sample in dilute to concentrated NaCl, $CaCl_2$ and $MgCl_2$ solution. Total boron concentrations ranged from 0.004 M to 0.4 M. Spectra in NaCl and $MgCl_2$ systems were collected at pH_m = 8.0 ± 0.1, whereas spectra in $CaCl_2$ were collected at pH_m = 8.0 ± 0.1 and 12.0 ± 0.1. Cm(III)–TRLFS spectra in NaCl an $CaCl_2$ solutions with freshly prepared borate solutions ($[B]_{tot} \geq 0.04$ M) showed very pronounced kinetic effects. Therefore, sufficiently long equilibration times (~ two weeks) were allowed for all matrix solutions used in the TRLFS experiments shown in this work. After this equilibration time, the Cm(III) was spiked to the matrix solutions. The samples were measured within 2 hours after the Cm(III) addition. Measurements with longer equilibration times (up to 2 days) did not show any relevant kinetic effect on the fluorescence spectra.

The speciation of Np(V) was done by absorption spectroscopy. Absorption spectra of Np(V) were collected with a Varian UV-Vis spectrometer (Cary 5E) against a reference solution with the same background electrolyte and borate concentration as the measured sample. Spectra were recorded in the range λ = 850 – 1250 nm with a step width of 0.2 nm. All measurements were performed with ~3 mL of sample solution in quartz cuvettes with d = 1 cm.

5.1.5 Solid phase characterization (XRD, XPS, SEM-EDS, EXAFS)

Solid phases from the Nd, Pu, Np and U solubility experiments were characterized by XRD, XPS and SEM-EDS after a given equilibrium time. Selected solid phases from the Np(V) solubility experiments were also investigated by EXAFS.

5.1.6 Ln(III)/An(III/IV/V/VI) solubility experiments

Nd(III) and An(III/IV/V/VI) solid phase preparation

Amorphous Nd(III) hydroxide used in the solubility experiments was prepared by hydration of crystalline neodymium hydroxide (Nd_2O_3(cr), Merck) in Milli-Q water under an argon atmosphere (Neck et al., 2009). The complete transformation of the oxide into the hydroxide phase was confirmed by XRD (JCPDF file No: 70-0214, JCPDS 2001). $Nd[B_9O_{13}(OH)_4]$(cr) was prepared by the group of Dr. Evgeny Alekseev at the research center Jülich (FZJ).

To prepare $Pu^{IV}O_2$(am,hyd), a purified ^{242}Pu(VI) stock solution was added to a pH-buffered (25 mM MES) and redox-buffered (1.5 mM hydroquinone) solution leading to an immediate formation of aqueous Pu(V) and a slow "reductive precipitation" of $Pu^{IV}O_2$(am,hyd). The mild in situ "reductive precipitation" leads to a microcrystalline solid phase which is less affected to aging effects than "fresh" $Pu^{IV}O_2$(am,hyd) prepared by addition of NaOH to an acidic Pu(IV) solution.

$Th(OH)_4$(am) was prepared under argon atmosphere by titration of thorium chloride stock solution with carbonate-free NaOH up to pH ~10. The precipitate was washed with Milli-Q water several times before further use in the solubility experiments.

NpO_2OH(am,fresh) was prepared under argon atmosphere by titration of a (radiochemically pure) acidic ^{237}Np(V) stock solution with carbonate-free NaOH. The resulting precipitate (NpO_2OH(am,fresh)) was separated from the solution by centrifugation and washed several times with water before use in the solubility experiments.

Metaschoepite $UO_3 \cdot 2H_2O$(cr) was prepared under argon atmosphere by a very slow titration of an acidic uranium(VI) chloride stock solution with carbonate-free NaOH. In the precipitation process, the pH was checked regularly and kept always below 5 to avoid the transformation of $UO_3 \cdot 2H_2O$(cr) into sodium uranate or other Na–U(IV)–OH ternary phases.

Sodium uranate, $Na_2UO_2O_7 \cdot H_2O$(cr), was prepared by transformation of initial metaschoepite in 2.5 M NaCl solution at pH_m ~12 for several months. The new formed solid was separated and washed before use in the solubility experiments.

Sample preparation

All experiments were prepared and carried out at 22±2 °C in Ar-gloveboxes under exclusion of O_2(g) and CO_2(g). Solubility samples in NaCl, $MgCl_2$ and $CaCl_2$ solutions were prepared from undersaturation conditions of the respective Ln/An hydroxide. A detailed list of all prepared samples for $Nd(OH)_3$(am), PuO_2(am,hyd), $Th(OH)_4$(am), NpO_2OH(am,fresh), $UO_3 \cdot 2H_2O$(cr) and $Na_2U_2O_7 \cdot H_2O$(cr) is given in Table 22 to Table

27. Boron concentrations ($[B]_{tot}$) in $MgCl_2$, NaCl and $CaCl_2$ solutions were restricted to 0.4 M, 0.16 M and 0.04 M, respectively. The limitations in solubility observed for these systems are likely related with the formation of stable Mg-, Na- and Ca-borate solid phases [85]. Preliminary spectroscopic experiments (Cm(III)–TRLFS) conducted with freshly prepared borate solutions showed Cm(III)-borate complex formation with pronounced kinetic effects, which decreased notably with the pre-equilibration of borate in the corresponding saline solution. Consequently, the boron containing saline solutions were equilibrated for at least 2 weeks before the addition of the Ln/An hydroxide phase. Solubility experiments with PuO_2(am,hyd) were performed in 0.1 M NaCl solution and $[B]_{tot}$ = 0.16 M in the present of 2 mM $Na_2S_2O_4$ and hydroquinone as reducing system. Ln/An concentrations, pH and Eh (Pu experiments) were determined at regular time intervals for up to 860 days. The concentration of Ln/An(III) was quantified after phase separation by 10 kD ultrafiltration (~ 1.5 nm, Pall Life Sciences) by ICP-MS and LSC.

Table 22: Experimental conditions in the solubility study with $Nd(OH)_3$(am).

System	Concentration of background electrolyte	$[B]_{tot}$	pHm	Equilibration time
NaCl	0.1 M	0.004 M; 0.04 M; 0.16 M	7-13	7-142 days
NaCl	5.0 M	0.004 M; 0.04 M; 0.16 M	8-13	7-142 days
$CaCl_2$	0.25 M	0.004 M; 0.04 M	8-12	7-142 days
$CaCl_2$	3.5 M	0.004 M; 0.04 M	8-12	7-142 days
$MgCl_2$	0.25 M	0.004 M; 0.04 M 0.16 M; 0,4 M	8-12	7-72 days
$MgCl_2$	3.5 M	0.004 M; 0.04 M; 0.16 M; 0.4 M	8-12	7-72 days

Table 23: Experimental conditions in the solubility study with $Nd[B_9O_{13}(OH)_4]$(cr).

System	Concentration of background electrolyte	$[B]_{tot}$	pHm	Equilibration time
NaCl	0.1 M; 5.0 M	0.16 M	6-9	7-48 days
$MgCl_2$	0.25 M; 3.5 M	0.16 M	6-9	7-48 days

Table 24: Experimental conditions in the solubility study with PuO_2(am,hyd).

System	Concentration of background electrolyte	$[B]_{tot}$	Reducing chemical	pHm	Equilibration time
NaCl	0.1 M	0.16 M	Na2S2O4	7.5; 9	14-300 days
NaCl	0.1 M	0.16 M	Hydroquinone	7.5; 9	14-300 days

Table 25: *Experimental conditions in the solubility study with $Th(OH)_4(am)$.*

System	Concentration of background electrolyte	$[B]_{tot}$	pHm	Equilibration time
NaCl	0.1 M	0 M; 0.16 M	7; 9; 11	14-860 days
NaCl	5.0 M	0 M; 0.16 M	8; 9; 11	14-860 days
$MgCl_2$	0.25 M	0 M; 0.16 M	7.5; 9	14-860 days
$MgCl_2$	3.5 M	0 M; 0.16 M	7.5; 9	14-860 days

Table 26: *Experimental conditions in the solubility study with $NpO_2OH(am,fresh)$.*

System	Concentration of background electrolyte	$[B]_{tot}$	pHm	Equilibration time
NaCl	0.1 M	0.04 M; 0.16 M	8-9	14-300 days
NaCl	5.0 M	0.04 M; 0.16 M	8-9	14-300 days
$MgCl_2$	0.25 M	0.04 M; 0.16 M	8-9	14-300 days
$MgCl_2$	3.5 M	0.04 M; 0.16 M	8-9	14-300 days

Table 27: *Experimental conditions in the solubility study with UO_3□2 $H_2O(cr)$ and $Na_2U_2O_7$□$H_2O(cr)$.*

System	Concentration of background electrolyte	$[B]_{tot}$	pHm	Equilibration time
NaCl	0.1 M	0 M; 0.04 M;0.16 M	*7; 9; 11*	14-138 days
NaCl	5.0 M	0 M; 0.04 M;0.16 M	*8; 9; 11*	14-138 days
$MgCl_2$	0.25 M	0 M; 0.04 M; 0.16 M	*7.5; 9*	14-138 days
$MgCl_2$	3.5 M	0 M; 0.04 M; 0.16 M	*7.5; 9*	14 138 days

5.2 ^{11}B-NMR in NaCl, CaCl2 and MgCl2 solutions

In this work, ^{11}B-NMR spectra were collected in dilute to concentrated NaCl and $MgCl_2$ solutions within $2.6 \leq pH_m \leq 12$ and $0.04\ M \leq [B]_{tot} \leq 0.4\ M$ with the aim of gaining further insight on the speciation of boron, especially under the poorly investigated highly

saline conditions. An introduction about the boron chemistry as well as interpretation of recorded NMR spectra can be found in (Hinz, 2015).

5.2.1 ^{11}B-NMR studies in NaCl solutions

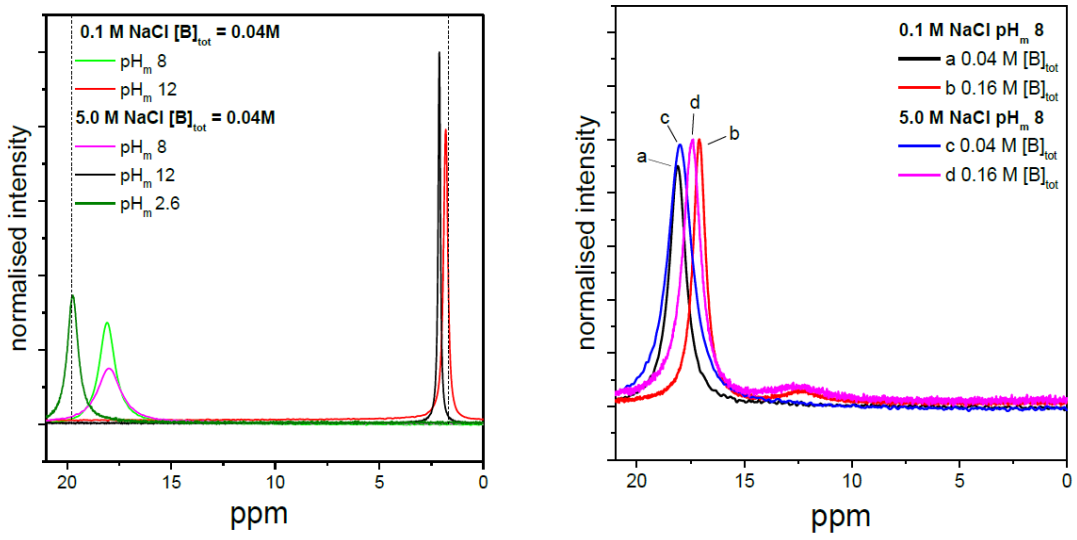

Figure 60: ^{11}B-NMR spectra collected in 0.1 M and 5.0 M NaCl solutions: (left) spectra with 2.6 ≤ pHm ≤ 12 and [B]tot = 0.04 M, (right) spectra with pHm = 8 and a) 0.04 M [B]tot b) 0.16 M [B]tot in 0.1 M NaCl and c) 0.04 M [B]tot d) 0.16 M [B]tot in 5.0 M NaCl.

^{11}B-NMR spectra were collected for 0.1 M and 5.0 M NaCl solutions with 0.04 M ≤ $[B]_{tot}$ ≤ 0.16 M at pH_m = 2.6, 8 and 12 are shown in Figure 60. A single reference signal corresponding to the exchange peak of the monomeric species $B(OH)_3(aq)$–$B(OH)_4^-$ is observed in all systems with $[B]_{tot}$ ≤ 0.04 M. At this $[B]_{tot}$ no (or very few) polyborates are present in solution. In the NaCl system at pH_m = 2.6, the peak at ~ 20 ppm can be unequivocally assigned to $B(OH)_3(aq)$. In dilute and concentrated NaCl systems and pH_m = 8, the peak observed 17-18 ppm indicates the predominance of $B(OH)_3(aq)$ in the solution. For the same pH a broad second peak can be observed at $[B]_{tot}$ = 0.16 M. According to studies in KCl, NaCl and LiCl solutions this broad peak at ~12–14 ppm can be assigned to the triborate species $B_3O_3(OH)_4^-$ (Hertam, 2011; Salentine, 1983). At pH_m = 12, the chemical shift observed at 0–3 ppm agrees very well with the expected predominance of $B(OH)_4^-$ in the solution at high pH_m. The results in NaCl solutions are in good agreement with data from Borkowski and co-workers measured in water at comparable $[B]_{tot}$ (Borkowski et al., 2011).

5.2.2 ^{11}B-NMR studies in $CaCl_2$ and $MgCl_2$ solutions

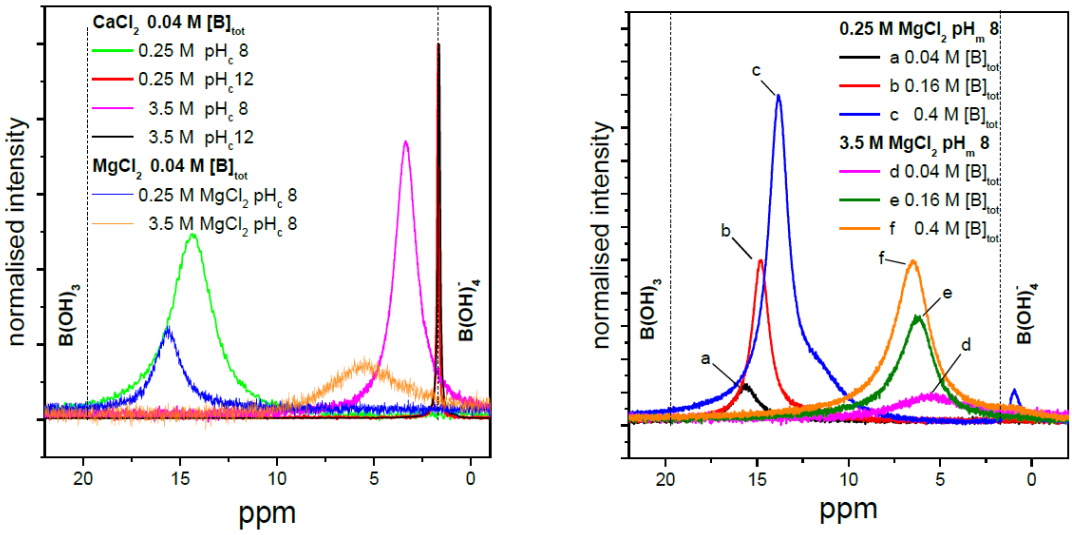

Figure 61: ^{11}B-NMR spectra collected in 0.25 M and 3.5 M $CaCl_2$ and $MgCl_2$ solutions: (left) spectra with $8 \leq pH_m \leq 12$ and $[B]_{tot} = 0.04$ M, (right) spectra with $pH_m =$ 8 and a) 0.04 M $[B]_{tot}$ b) 0.16 M c) 0.4 M $[B]_{tot}$ in 0.25 M $MgCl_2$ and d) 0.04 M $[B]_{tot}$ e) 0.16 M $[B]_{tot}$ f) 0.4 M $[B]_{tot}$ in 3.5 M $MgCl_2$.

^{11}B-NMR spectra were collected for 0.25 M and 3.5 M $CaCl_2$ with $[B]_{tot} = 0.4$ M at $pH_m =$ 8 and 12, and collected for 0.25 M and 3.5 M $MgCl_2$ with $0.04 \text{ M} \leq [B]_{tot} \leq 0.4$ M at $pH_m =$ 8 are shown in Figure 61. For comparison purposes, peak positions for $B(OH)_3(aq)$ and $B(OH)_{4^-}$ in NaCl solutions are shown as dashed lines. Analogously to the NaCl system, a single resonance peak is visible in the spectra collected for samples in $CaCl_2$ and $MgCl_2$ solutions with $[B]_{tot} = 0.04$ M. Nevertheless, significantly broader peaks are detected in these salt solutions compared to the NaCl system. At $pH_m = 8$, the peak at ~17–18 ppm observed in the NaCl system and indicating the predominance of $B(OH)_3(aq)$ is shifted to lower ppm in $CaCl_2$ and $MgCl_2$ solution. Note further that the peak broadening and peak shift are more pronounced in concentrated $MgCl_2$ and $CaCl_2$ solutions for the same pH ($pH_m = 8$) and boron concentration ($[B]_{tot} = 0.04$ M). This observation can be likely explained by the complexation of Mg/Ca with B, as presented in the thermodynamic calculations shown in Figure 62 conducted using the thermodynamic and activity models reported by Felmy and co-workers on the system Mg^{2+}-$B(OH)4^-$ - Cl^- - H_2O (Felmy and Weare, 1986).

In 0.25 M $MgCl_2$ solutions with $pH_m = 8$, the peak position is shifted from ~ 16 ppm to ~13 ppm when increasing $[B]_{tot}$ from 0.04 M to 0.4 M. The observed peak at $[B]_{tot} = 0.4$ M is very broad and shows a pronounced shoulder at ~12 ppm and a second small peak at 0.7 ppm. The shoulder and the additional peak indicate the presence of more than one boron species present in the investigated solution. A significant peak broadening is also observed in 3.5 M $MgCl_2$ solutions. The fraction diagram shown in Figure 62 shows the predominance of $B(OH)_3(aq)$ and $MgB(OH)_{4^+}$ species, and thus the observed peak broadening cannot be attributed to the presence of polyborate species. In

contrast to the NaCl system, no peak assignment is possible in $CaCl_2$ and $MgCl_2$ systems at pH_m 8 due to the lack of literature data.

At pH_m = 12 in $CaCl_2$ systems the peak position at ~ 2 ppm indicates $B(OH)_4^-$ as main borate species similar to observations made in NaCl systems. In contrast to systems at lower pH values, no broadening of this peak is observed at increased $CaCl_2$ concentration. No further information on aqueous boron speciation in saline solution can be drawn from the measured NMR spectra.

5.2.3 Conclusions

^{11}B-NMR studies conducted in NaCl, $CaCl_2$ and $MgCl_2$ solutions at pH_m = 2.6, 8 and 12 give insight in the complex borate speciation in saline solutions. Spectra measured in NaCl solutions are similar to spectra collected in water with the same pH_m and comparable $[B]_{tot}$. According to the collected spectra and consistently with literature data, the speciation of boron is only weakly influenced by the presence of monovalent cations like Na^+, K^+ and Li^+ (Hertam, 2011; Salentine, 1983). Based on the reported literature data, the detected peaks can be correctly assigned to the expected boron species, although no quantitative analysis of the spectra is possible.

In contrast to the NaCl systems, very broad peaks are observed in $CaCl_2$ and $MgCl_2$ solutions. At pH_m = 8 the peak position in both $CaCl_2$ and $MgCl_2$ systems is significantly shifted compared to peaks at same pH_m and $[B]_{tot}$ measured in NaCl solutions, indicating the formation of Ca/Mg–borate complex. This is in good agreement with thermodynamic calculations indicating the formation of the complex $MgB(OH)_4^+$. For more specific information on the boron speciation in presence of high NaCl, $CaCl_2$ and $MgCl_2$ concentrations, additional comprehensive experiments are needed.

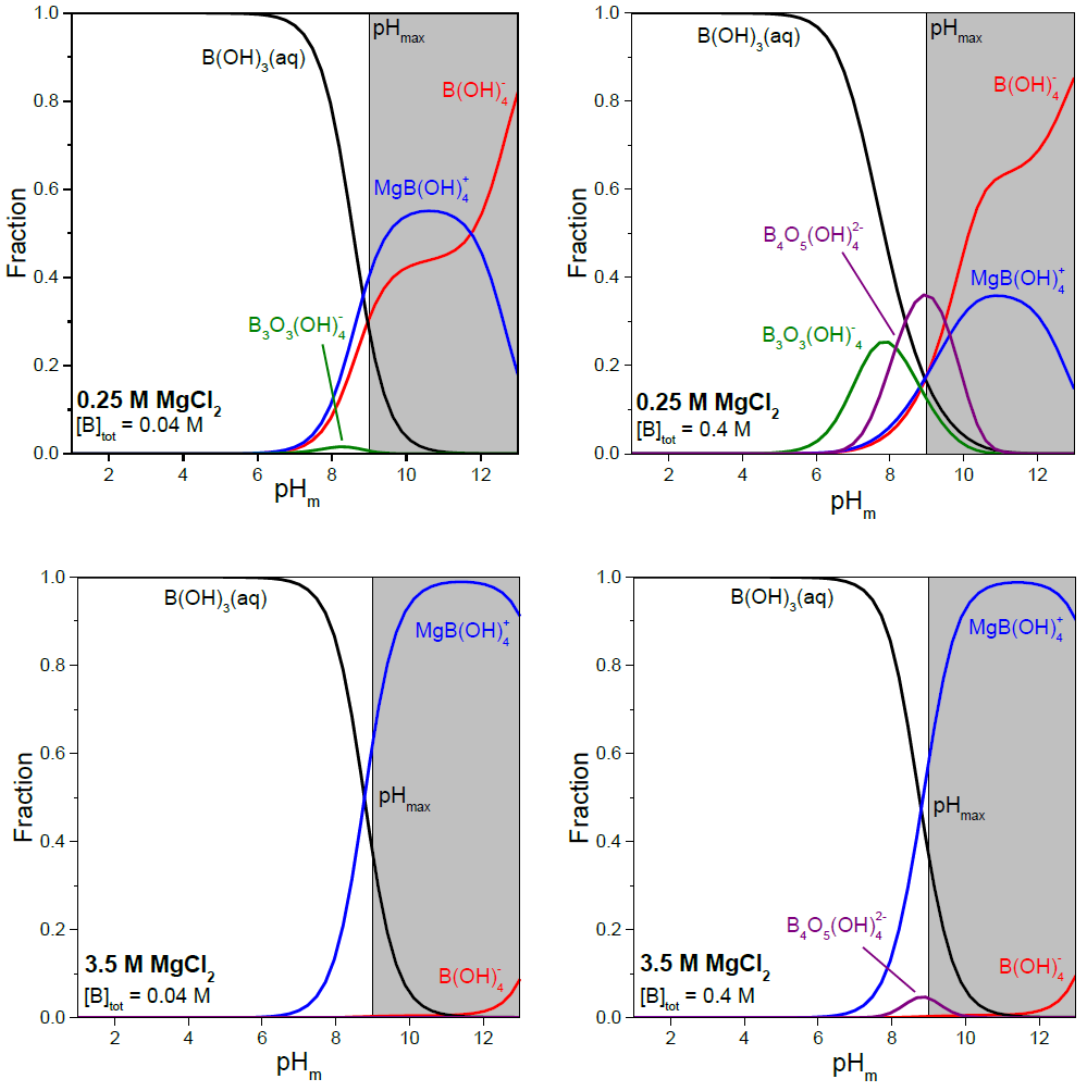

Figure 62: Fraction diagram of aqueous borate species in 0.25 M and 3.5 M $MgCl_2$ as calculated with the thermodynamic and activity models reported in (Felmy and Weare, 1986). The highest pH in dilute to concentrated $MgCl_2$ solutions is limited to pH_{max} ~9 by the precipitation of $Mg(OH)_2$(s) or Mg–OH– Cl phases, and thus calculations above this pH represent only a modelling exercise giving insight on the possible interaction Ca–borate in $CaCl_2$ systems (where pH_{max} ~12) under the assumption of a comparable complexation behavior of Ca^{2+} and Mg^{2+}.

5.3 Interaction of Ln(III)/An(III) with borate

The interaction of Ln(III)/An(III) with borate was investigated from undersaturation conditions with $Nd(OH)_3$(am) in dilute to concentrated NaCl, $CaCl_2$ and $MgCl_2$ solutions with 0.04 M ≤ [B]tot ≤ 0.4 M at 6 ≤ pH_m ≤ 13. Samples were equilibrated for up to 142 days, and pH_m and [Nd(III)] were monitored at regular time intervals. After attaining equilibrium conditions, selected solid phases were characterized by XPS, SEM-EDS and XRD. For comparison purposes, additional solubility experiments with a well-

defined Nd(III) borate solid phase, $Nd[B_9O_{13}(OH)_4](cr)$, were performed in NaCl and $MgCl_2$ solutions with $[B]_{tot}$ = 0.16 M. The aqueous phase was further investigated by TRLFS with 10-7 M Cm(III) in 0.1 – 5.0 M NaCl, 0.25 – 3.5 M $MgCl_2$ and 0.25 – 3.5 M $CaCl_2$ with 0.004 M ≤ [B]tot ≤ 0.4 M and pHm = 8. Additional Cm(III) TRLFS spectra were collected at pHm = 12 for $CaCl_2$ systems.

5.3.1 Solubility of Nd(III) in NaCl, $CaCl_2$ and $MgCl_2$ solutions

The experimental solubility data of Nd(III) determined in 0.1 M – 5.0 M NaCl and 0.25 M – 3.5 M $MgCl_2$ and $CaCl_2$ solutions in the presence of 0.004 M ≤ $[B]_{tot}$ ≤ 0.4 M are shown in Figure 63 to Figure 68. Note that only data corresponding to thermodynamic equilibrium (constant pH_m and [Nd(III)]) are presented in the figures. For comparison purposes, the figures also show the experimental solubility data and calculated solubility curves for $Nd(OH)_3(am)$ as reported by Neck et al. in the absence of borate under analogous pH_m and ionic strength conditions (Neck et al., 2009). In the figures of 0.1 M, 5.0 M NaCl and 0.25 M, 3.5 M $MgCl_2$ systems undersaturation solubility data obtained with $Nd[B_9O_{13}(OH)_4](cr)$ and $[B]_{tot}$ = 0.16 M are also provided.

No significant effect of borate on Nd(III) solubility is observed in near neutral to slightly alkaline pH_m values (7 ≤ pH_m ≤ 9) and $[B]_{tot}$ ≤ 0.04 M (dilute salt systems: 0.1 and 1.0 M NaCl; 0.25 M $MgCl_2$) or $[B]_{tot}$ ≤ 0.004 M (concentrated salt systems: 5.0 M NaCl; 1.0 and 3.5 M $MgCl_2$). Under these conditions, the concentration of Nd(III) is in good agreement with borate-free solubility data obtained under analogous pH_m and ionic strength conditions (Neck et al., 2009).

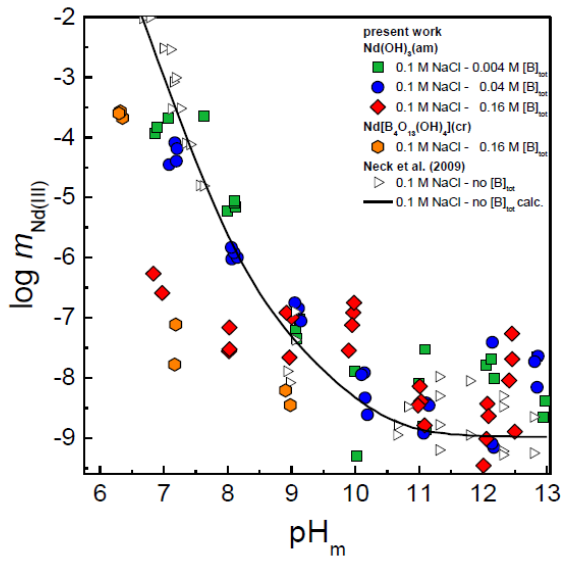

Figure 63: Solubility of $Nd(OH)_3(am)$ and $Nd[B_9O_{13}(OH)_4](cr)$ in the presence of 0.004 M ≤ $[B]_{tot}$ ≤ 0.16 M in 0.1 M NaCl solutions. Comparison with experimental (open symbols, black) and calculated (solid line) solubility data in the absence of borate as reported in (Neck et al., 2009).

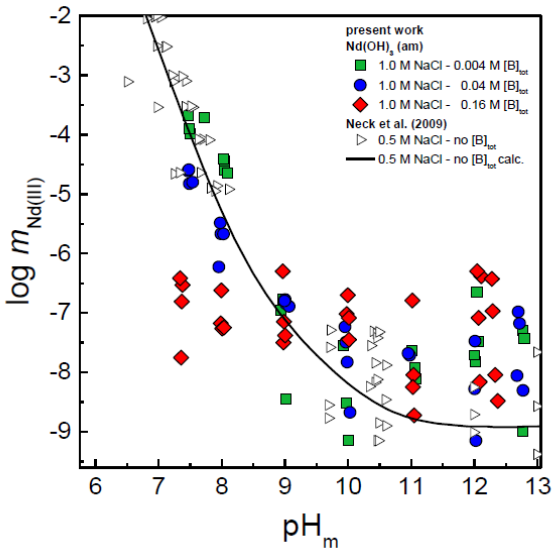

Figure 64: Solubility of $Nd(OH)_3(am)$ in the presence of 0.004 M ≤ $[B]_{tot}$ ≤ 0.16 M in 1.0 M NaCl solutions. Comparison with experimental (open symbols, black) and calculated (solid line) solubility data in the absence of borate as reported in (Neck et al., 2009).

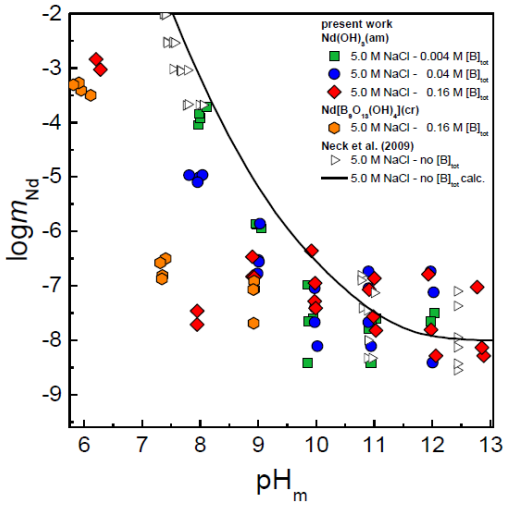

Figure 65: Solubility of $Nd(OH)_3(am)$ and $Nd[B_9O_{13}(OH)_4](cr)$ in the presence of 0.004 M ≤ $[B]_{tot}$ ≤ 0.16 M in 5.0 M NaCl solutions. Comparison with experimental (open symbols, black) and calculated (solid line) solubility data in the absence of borate as reported in (Neck et al., 2009).

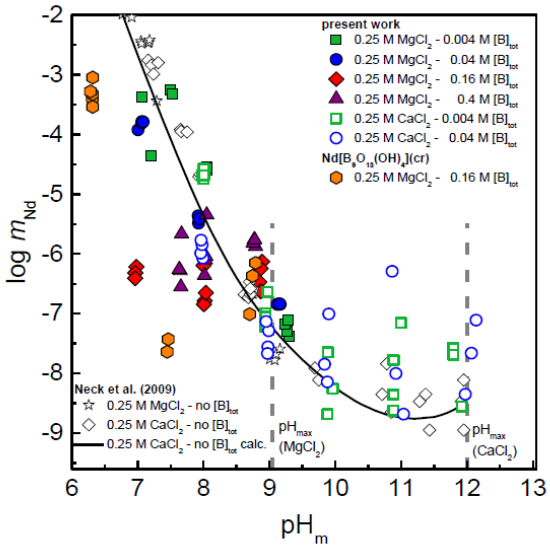

Figure 66: Solubility of $Nd(OH)_3(am)$ and $Nd[B_9O_{13}(OH)_4](cr)$ in the presence of 0.004 M ≤ $[B]_{tot}$ ≤ 0.4 M in 0.25 M $MgCl_2$ and $CaCl_2$ solutions. Comparison with experimental (open symbols, black) and calculated (solid line) solubility data in the absence of borate as reported in (Neck et al., 2009).

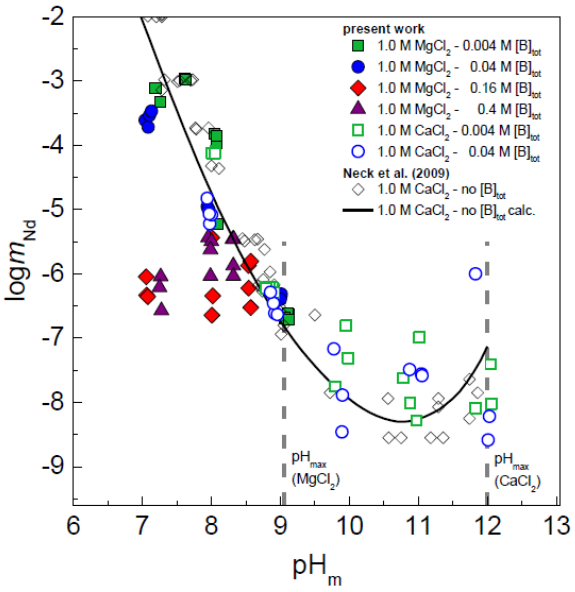

Figure 67: Solubility of $Nd(OH)_3(am)$ in the presence of 0.004 M ≤ $[B]_{tot}$ ≤ 0.4 M in 1.0 M $MgCl_2$ and $CaCl_2$ solutions. Comparison with experimental (open symbols, black) and calculated (solid line) solubility data in the absence of borate as reported in (Neck et al., 2009).

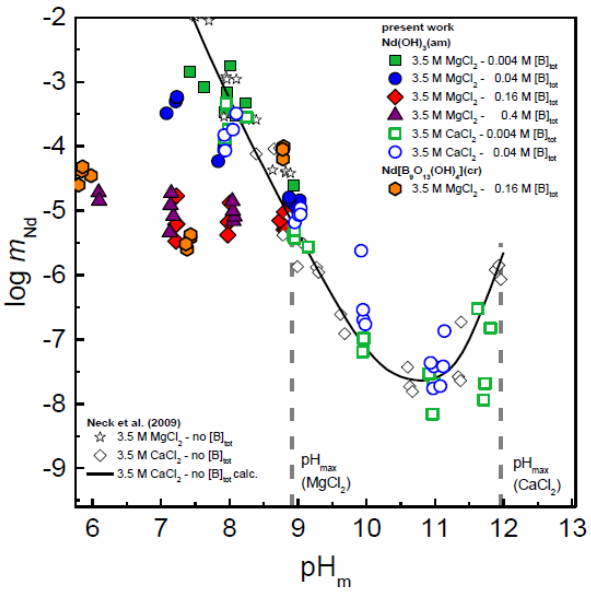

Figure 68: Solubility of $Nd(OH)_3$(am) and $Nd[B_9O_{13}(OH)_4]$(cr) in the presence of 0.004 M ≤ $[B]_{tot}$ ≤ 0.4 M in 3.5 M $MgCl_2$ and $CaCl_2$ solutions. Comparison with experimental (open symbols, black) and calculated (solid line) solubility data in the absence of borate as reported in (Neck et al., 2009).

At enhanced $[B]_{tot}$ ≥ 0.16 M, a significant decrease in the Nd(III) concentration occurs for all NaCl and $MgCl_2$ systems evaluated. The drop in solubility at $[B]_{tot}$ ~0.16–0.4 M is accompanied with a changed slope of the solubility curve from –2 to approximately 0. This observation clearly indicates the transformation of $Nd(OH)_3$(am) into a new solubility controlling borate-bearing solid phase. After an equilibration time of 72 to 142 days (depending upon salt system), the measured Nd(III) concentrations remain constant at □10–6.5 M (in 0.25 M $MgCl_2$) to 10–5 M (in 3.5 M $MgCl_2$). These solubility limits are more than three orders of magnitude lower than those observed in the absence of borate (Hinz, 2015). The decrease in Nd(III) solubility in NaCl solutions is similar, although the overall solubility is slightly lower indicating that increasing $MgCl_2$ concentrations and resulting high ionic strength enhances significantly the solubility of Nd(III) in the presence of borate as it is also the case in borate-free systems. No (or very limited) effect of borate on Nd(III) solubility is observed in $CaCl_2$ solutions in contrast to NaCl and $MgCl_2$ systems, very likely due to the lower boron solubility in this background electrolyte ($[B]_{tot}$ ≤ 0.04 M).

Solid phase characterization

Solid phases of selected solubility experiments were investigated after attaining equilibrium conditions by XRD, SEM–EDS and XPS. Very distinct XRD pattern are observed for this solid phase, confirming that none of the solubility experiments initiated with $Nd(OH)_3$(am) led to the formation of this solid phase (above the detection limit of XRD, □5%). In contrast to XRD, XPS analyses of the solid phases from solubility samples with $[B]_{tot}$ ≥ 0.16 M confirm the presence of a newly formed borate-bearing secondary

phase on the surface of $Nd(OH)_3(am)$ indicating the formation of a new solubility controlling borate-bearing solid phase. This mechanism is confirmed by SEM–EDS technique, which suggest that the formation of a Nd(III)-borate solid phase takes place as a coating on an unreacted $Nd(OH)_3(am)$ core (for details see in (Hinz, 2015).

5.3.2 Cm(III) aqueous speciation in the presence of borate: TRLFS

Fluorescence emission spectra of Cm(III) were measured with 0.004 M ≤ $[B]_{tot}$ ≤ 0.4 in 0.1 M–5.0 M NaCl and 0.25 M–3.5 M $CaCl_2$ and $MgCl_2$ solutions at pH_m = 8. The normalised spectra in 0.1 M and 5.0 M NaCl solution are presented in Figure 69. Spectra at pH_m = 8 in 0.25 M and 3.5 M $MgCl_2$ solutions are presented in Figure 70. In $CaCl_2$ solutions additional spectra with 0.004 ≤ $[B]_{tot}$ ≤ 0.04 M at pH_{max} ~12 were taken and are shown in Figure 71. Furthermore, fluorescence decay measurements were performed for Cm(III) in NaCl, $CaCl_2$ and $MgCl_2$ solutions with 0.004 M ≤ $[B]_{tot}$ ≤ 0.4 at pH_m = 8. Note that boron concentrations in NaCl and $CaCl_2$ solutions were restricted due to the precipitation of Na- and Ca-borate solid phases, to 0.16 M and 0.04 M, respectively. The resulting fluorescence lifetimes are presented in Table 28.

Cm(III) TRLFS studies in NaCl solutions

In the near neutral pH_m region (pH_m = 8) in the absence of borate, several Cm(III) species are expected to be present in solution simultaneously. Their relative contribution depends on the ionic strength and electrolyte composition of the respective solution. Besides the free Cm^{3+} aquo ion, also Cm(III) complexes such as $CmCl^{2+}$, $CmCl_2^{+}$, $Cm(OH)^{2+}$ and $Cm(OH)_2^{+}$ can be present in different proportions. At very low $[B]_{tot}$ = 0.004 M no significant influence of borate on Cm(III) aqueous speciation can be observed in all investigated samples (Figure 69). The peak maximum, located at ~603 nm of the scattered spectra in 0.1 M NaCl solution can be associated mainly with the $Cm(OH)_2^{+}$ complex.. In the absence of complexing ligands other than hydroxide, generally a strong decrease in aqueous Cm(III) concentration at higher pH_m (pH_m ≥ 8) is observed due to sorption on surfaces and precipitation as hydroxide. This explains the low intensities and spectral scattering observed for these measured spectra at very low $[B]_{tot}$.

In 5.0 M NaCl and $[B]_{tot}$ = 0.004 M two peaks with maxima at 594 nm and 604 nm can be found. The first peak can be attributed to the Cm(III) aquo ion (with small contributions of chloro complexes very likely present in higher NaCl concentrations), the second peak can be assigned to the second hydrolysis species $Cm(OH)_2^{+}$, as expected at pH_m = 8. The measured spectra with low $[B]_{tot}$ in NaCl solutions are in good agreement with the corresponding solubility data (Figure 63 and Figure 65).

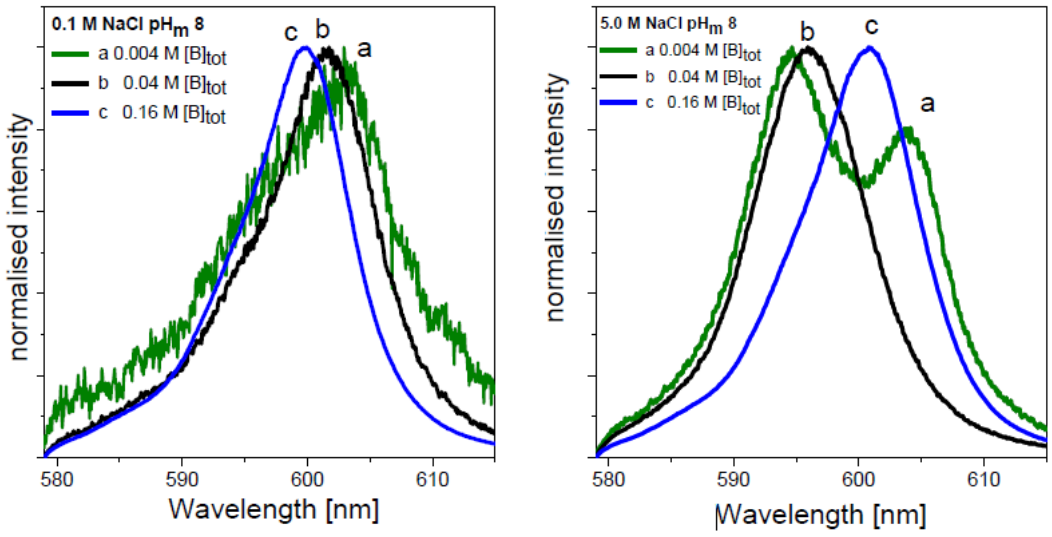

Figure 69: TRLFS emission spectra of Cm(III) in 0.1 M and 5.0 M NaCl solutions at pHm = 8 and various borate concentrations.

With increasing $[B]_{tot}$ ($[B]_{tot}$ > 0.004M), an effect of borate on the Cm(III) speciation is observed in 0.1 M NaCl solutions with a peak shift to shorter wavelengths in combination with an increased fluorescence intensity of the spectra. At $[B]_{tot}$ = 0.16 M the competition between borate complexation and hydrolysis leads to a suppression of the Cm(III) hydrolysis species and the formation of a borate containing Cm(III) complex with a peak maximum at ~ 600 nm. A very short fluorescence lifetime (τ = 59 µs) at $[B]_{tot}$ = 0.16 M is observed in 0.1 M NaCl solutions. This decrease in the fluorescence lifetime together with a clear shift in the emission spectra in comparison to the Cm(III) aquo ion cannot be explained at the moment. The presence of Cm(III) containing colloids by precipitation of a Cm(III) borate solid, in accordance to the analogue Nd(III)-solubility experiments (Figure 63), could lead to a decrease in the fluorescence lifetime.

The double peak observed in 5.0 M NaCl solution and at $[B]_{tot}$ = 0.004 M indicates that the Cm(III) hydrolysis at pHm = 8 is less pronounced compared to 0.1 M NaCl and considerable amounts of uncomplexed Cm^{3+} are still present. By increase of $[B]_{tot}$ to 0.04 M, the peak maximum assigned to the second hydrolysis species at ~ 604 nm disappears due to competition with borate and a broad peak with a peak maximum at ~ 596 nm can be detected consisting of contributions of Cm^{3+} and a new formed Cm(III) borate component. Further increase of $[B]_{tot}$ up to 0.16 M leads to a decrease of the Cm(III) aquo ion contribution, the fluorescence peak is shifted to ~ 601 nm which can be explained only by the formation of a Cm(III)–borate complex. At the same time an increase of the corresponding fluorescence lifetime from 77 µs at $[B]_{tot}$ = 0.04 M to 108 µs at $[B]_{tot}$ = 0.16 M is measured. The fluorescence decay curves in all investigated systems show a single averaged exponential decay for all spectra, caused by a faster ligand exchange than the lifetime of the excited state. According to the relation of (Kimura et al., 1996), 4 H_2O molecules are removed from the first hydration sphere of the Cm(III) complex at $[B]_{tot}$ = 0.16 M. Note that no influence of high ionic strength on this linear relation is considered. The peak positions (~ 600-601 nm) at $[B]_{tot}$ = 0.16 M for

both 0.1 M and 5.0 M NaCl solutions are very similar implying that similar Cm–borate species are formed.

Cm(III) TRLFS studies in $CaCl_2$ and $MgCl_2$ solutions

In contrast to NaCl systems, no Cm(III) hydroxide species are found in dilute to concentrated $MgCl_2$ solutions under near neutral pH_m conditions (pH_m = 8) and absence of borate (Herm, 2012). Note that these findings are in contrast to studies with $Nd(OH)_3$(am) in $MgCl_2$ solutions, where hydrolysis species of Nd(III) species are prevailing at this pH (Neck et al., 2009). In $MgCl_2$ solutions spectra with high boron concentrations up to 0.4 M $[B]_{tot}$ could be measured and allow a systematic investigation of the Cm(III) borate complexation.A broad emission peak at ~597 nm at $[B]_{tot}$ = 0.04 M can be observed for both investigated $MgCl_2$ concentrations. The shift of the peak maximum compared to the borate-free system indicates the complexation of Cm(III) with borate. The corresponding fluorescence lifetimes (77 µs – 87 µs, depending upon salt system and ionic strength) are significantly increased compared to the fluorescence lifetime of the Cm(III) aquo ion with 64 µs± 3 µs.

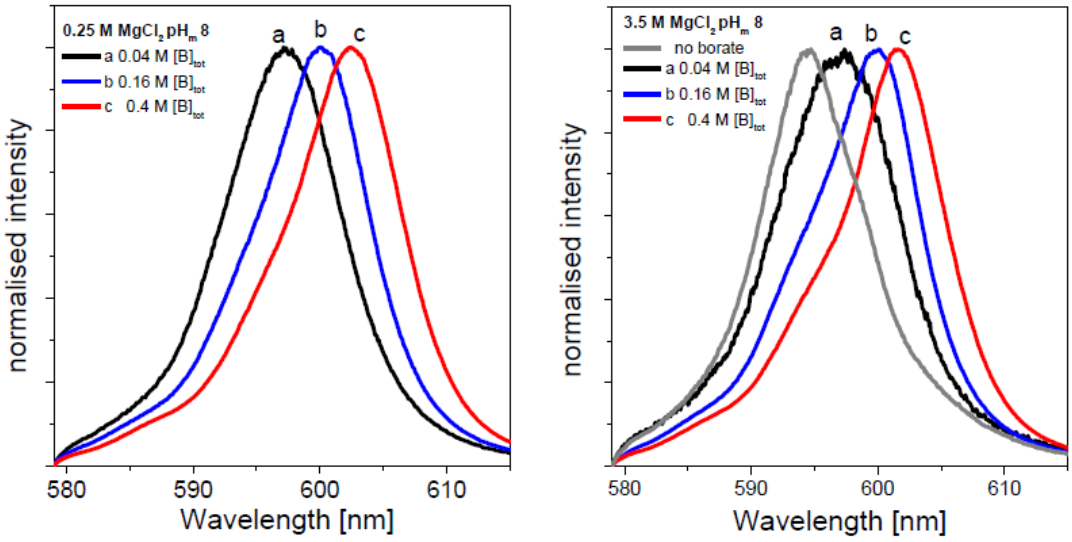

Figure 70: TRLFS emission spectra of Cm(III) in 0.25 M and 3.5 M MgCl2 solutions at pHm = 8 and various [B]tot. Comparison with a spectrum in the absence of borate.

With increasing $[B]_{tot}$, the peak maxima of the fluorescence emission bands are further shifted to higher wavelengths, clearly indicating the formation of Cm(III) complexes with borate. These pronounced bathochromic peak shifts support the assumption that more than one Cm(III)–borate complexes exist under these conditions, as also proposed for the NaCl system. The bathochromic peak shift of the Cm(III) emission with increasing $[B]_{tot}$ is accompanied with an increase of the fluorescence lifetimes up to 121 µs for 3.5 M $MgCl_2$ and $[B]_{tot}$ = 0.4 M (see Table 28).

Table 28: *Fluorescence lifetimes (τ) and peak maxima (**λmax**) in NaCl, $CaCl_2$ and $MgCl_2$ solutions at pH_m = 8 and various $[B]_{tot}$.*

Background electrolyte	**0.004 M $[B]_{tot}$**		**0.04 M $[B]_{tot}$**		**0.16 M $[B]_{tot}$**		**0.4 M $[B]_{tot}$**	
τ [µs]	**λ_{max} [nm]**	**τ [µs]**	**λ_{max} [nm]**	**τ [µs]**	**λ_{max} [nm]**	**τ [µs]**	**λ_{max} [nm]**	
0.1 M NaCl	–	603	77 ± 5	601	59 ± 5	600	–	–
5.0 M NaCl	85 ± 5	604	77 ± 5	596	108 ± 5	601	–	–
0.25 M CaCl2	72 ± 5	594	78 ± 5	597	–	–	–	
3.5 M CaCl2	73 ± 5	595	77 ± 5	596	–	–	–	
0.25 M $MgCl_2$	–	–	85 ± 5	597	96 ± 5	600	114 ± 7	603
3.5 M MgCl2	–	–	87 ± 5	597	95 ± 5	600	121 ± 7	602

According to the Kimura equation (Kimura et al., 1996), 3 H_2O molecules are removed in the Cm(III) complexes found in 0.25 M and 3.5 M $MgCl_2$ with [B]tot = 0.16 M, and 4 to 4.5 H_2O molecules for 0.25 M $MgCl_2$ and 3.5 M $MgCl_2$ with $[B]_{tot}$ = 0.4 M, respectively. The formation of Cm(III)–borate species in weakly alkaline $MgCl_2$ solutions shows no clear dependence on ionic strength of the solution within the uncertainty limits of the technique, as already observed in NaCl systems.

Under highly alkaline conditions (pH_m = 12), no influence of borate on the emission spectra can be observed in $CaCl_2$ solutions and $[B]_{tot} \leq 0.04$ M (Figure 71). The measured spectra and corresponding fluorescence lifetimes in presence of borate in both 0.25 M and 3.5 M $CaCl_2$ solutions are in good agreement with the borate-free system (Rabung et al., 2008). As already discussed for the Nd(III) solubility data, borate is a weak ligand that can only compete with hydrolysis under near-neutral pH conditions and relatively high $[B]_{tot}$, but cannot outcompete hydrolysis under hyperalkaline conditions.

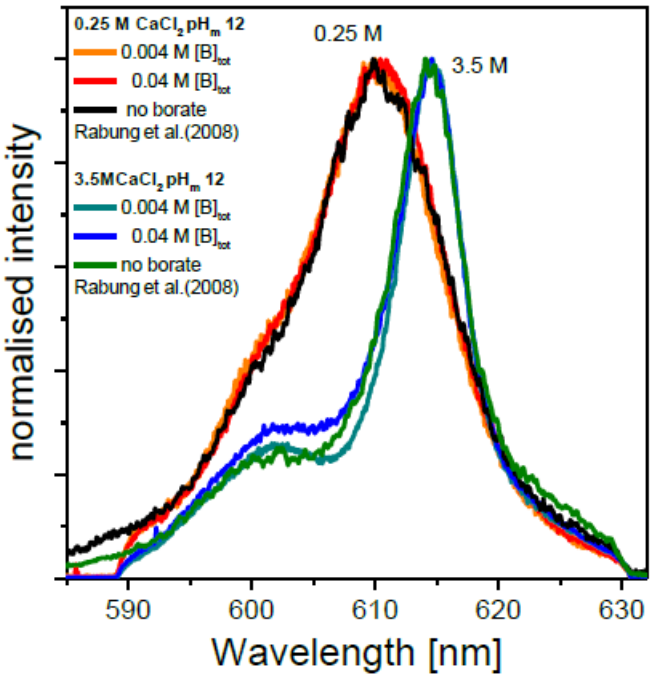

Figure 71: TRLFS emission spectra of Cm(III) in 0.25 M and 3.5 M CaCl2 at pHm = 12 and various borate concentrations in comparison with borate-free literature data.

5.3.3 Conclusions

Solubility studies with $Nd(OH)_3(am)$ and TRLFS investigations with Cm(III) confirm the formation of aqueous complexes of Ln(III) and An(III) with borate in dilute to concentrated NaCl, $MgCl_2$ and $CaCl_2$ solutions under near-neutral pHm conditions and [B]tot ≥ 0.04 M. At [B]tot ≥ 0.16 M and near-neutral pHm (pHm = 8), Cm(III)–borate aqueous species outcompete hydrolysis and become predominant. TRLFS indicates that (at least) two Cm(III)–borate species (maybe 1:1 and 1:2) form in NaCl and $MgCl_2$ solutions, although the exact stoichiometry of the complexation reaction remains unknown. A similar trend can be found in UV-Vis studies with Np(V) in $MgCl_2$ solutions with comparable $[B]_{tot}$. Despite the clear formation of LnIII/AnIII–borate aqueous species in near neutral pHm conditions, no significant increase in solubility is observed for $Nd(OH)_3(am)$ in the presence of $[B]_{tot} \leq 0.4$ M in all investigated systems.

Conversely, a clear drop in the Nd(III) solubility of 2–3 orders of magnitude occurs at 6 ≤ pHm ≤ 9, indicating the formation of a new solubility controlling borate-bearing solid phase. This mechanism is confirmed by XPS and SEM–EDS technique (Hinz, 2015), which suggest that the formation of a Nd(III)-borate solid phase takes place as a coating on an unreacted $Nd(OH)_3(am)$ core. Unlike solubility studies with $NpO_2(OH)(am)$, no complete transformation of the initial Nd(III) solid occurred in samples with $[B]_{tot} \geq 0.16$ M. The significant decrease observed in the Ln(III)/An(III) solubility at pHm < 9 related to the formation of secondary An(III)–borate alteration phases represents a hither-

to unknown actinide retention mechanism in repository systems. A thermodynamic evaluation and model of the Ln(III)/An(III) interactions in the presence of borate in NaCl, $CaCl_2$ and $MgCl_2$ systems is proposed in chapter **Fehler! Verweisquelle konnte nicht gefunden werden.**.

5.4 Solubility of Th(IV) in the presence of borate

Figure 72 and Figure 73 show the solubility of $Th(OH)_4(am)$ determined in 0.1 M – 5.0 M NaCl and 0.25 M – 3.5 M $MgCl_2$ solutions with $[B]_{tot}$ = 0 and 0.16 M and varying pH_m. Data points below the detection limit were set to log m_{Th} = –10 for dilute (0.1 M NaCl and 0.25 M $MgCl_2$) and -9 and -8.5 for concentrated (5.0 M NaCl and 3.5 M $MgCl_2$) solutions, respectively, due to the different dilution steps needed in each case for ICP–MS measurements. For comparison purposes, the figures also show the calculated solubility of $Th(OH)_4(am)$ (both for fresh and aged phases) in dilute NaCl and $MgCl_2$ systems in the absence of borate. Under these boundary conditions and provided the predominance of the neutral species $Th(OH)_4(aq)$ over the complete pH-range investigated in this work, no significant effect of ionic strength is foreseen according with thermodynamic calculations.

The solubility of $Th(OH)_4(am)$ remains largely unaffected by borate in dilute NaCl and $MgCl_2$ solutions over the entire pHm range considered in this work. However, a slight increase in the solubility of Th(IV) compared to borate-free systems can be claimed for samples with $[B]_{tot}$ = 0.16 M, both in concentrated NaCl and $MgCl_2$ solutions at pH_m ~8–9. Although Th(IV)–borate complexation appears unlikely considering the strong tendency of Th(IV) towards hydrolysis, this hypothesis cannot be completely ruled out in view of the experimental data gained in this work. Large scattering of the measured data is observed in all samples. A similar behavior in this pH_m region (pHm > 6) has been reported for Nd(III) and Th(IV) in the absence of boron. This observation can be likely explained by the tendency of neutral aqueous species to sorb (*i.e* $Th(OH)_4(aq)$), the presence of colloidal nanoparticles not removed from the solution by ultrafiltration and the very low concentrations of Th(IV) in solution (close to the detection limit of ICP–MS) (Altmaier et al., 2004; Neck et al., 2009). Note further that especially tetravalent actinides tend to form stable colloids in saline solution. In the case of thorium, these have been reported to increase the total concentration in solution 2–3 orders of magnitude (Altmaier et al., 2004).

The difficulties in evaluating the aquatic chemistry of Th(IV) within this pH region are also reflected on the quality (i.e. associated uncertainty) of the thermodynamic data available for this system in the absence of borate. This fact is discussed in more detail in (Hinz, 2015).

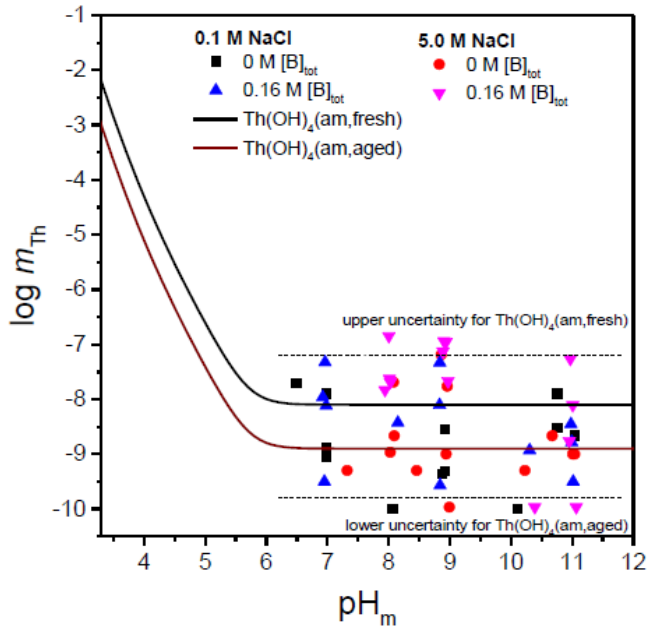

Figure 72: Solubility of $Th(OH)_4(am)$, experimentally determined in the presence of 0 M ≤ $[B]_{tot}$ ≤ 0.16 M in 0.1 M and 5.0 M NaCl solutions. Comparison with solubility of $Th(OH)_4(am,fresh)$ and $Th(OH)_4(am,aged)$, as calculated for 0.1 M NaCl using the NEA-TDB thermodynamic selection.

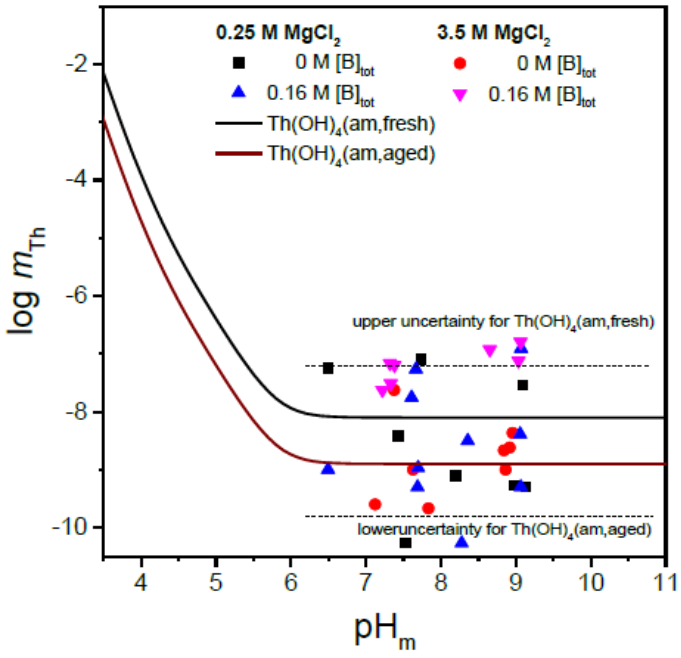

Figure 73: Solubility of $Th(OH)_4(am)$ experimentally determined in the presence of 0 M ≤ $[B]_{tot}$ ≤ 0.16 M in 0.25 M and 3.5 M $MgCl_2$ solutions. Comparison with solubility of $Th(OH)_4(am,fresh)$ and $Th(OH)_4(am,aged)$, as calculated for 0.25 M $MgCl_2$ using the NEA-TDB thermodynamic selection.

5.4.1 Conclusions

In contrast to Ln(III)/An(III), An(V) and An(VI) systems investigated in this work, no significant effect of borate on the Th(IV) solubility was observed in dilute NaCl and $MgCl_2$ systems within 6.5 ≤ pHm ≤ 11 and $[B]_{tot}$ = 0.16 M. A slight increase in the solubility of Th(IV) could be claimed for both concentrated NaCl and $MgCl_2$ systems at pHm = 7.5–9, which may hint towards a weak Th(IV)– borate complexation in this pHm region under these experimental conditions. Further experimental evidences would be needed to confirm this possibility. The weaker Th(IV)–borate interaction compared to Ln(III)/An(III), An(V) and An(VI) is in good agreement with the strong hydrolysis tendency of tetravalent actinides, which significantly outcompetes the formation of weaker complexes. The sparingly soluble Th(IV) oxy-hydroxide phase controlling the solubility in the conditions of this experiment retains very low Th(IV) concentrations in solution, and thus prevents the formation of any secondary phase in the presence of borate. The large scattering in the solubility data observed both in the absence and presence of borate is attributed to the predominance of the neutral aqueous species $Th(OH)_4(aq)$ and the possible formation of polymeric/colloidal Th(IV) species (Altmaier et al., 2004), and reflects also the large uncertainty associated to the thermodynamic data available for Th(IV) aqueous species and solid compounds forming in these conditions.

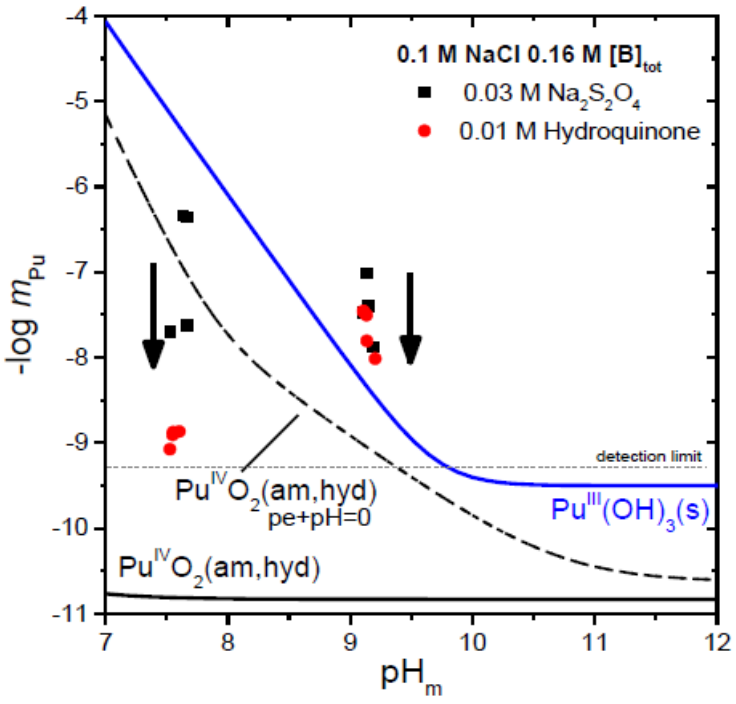

Figure 74: Solubility of $Pu^{IV}O_2$(am,hyd) in the presence of $[B]_{tot}$ = 0.16 M with 0.03 M $Na_2S_2O_4$ and 0.01 M hydroquinone in 0.1 M NaCl solutions. Comparison with calculated solubility data for $Pu^{IV}O_2$(am,hyd) (black solid line) and $Pu(OH)_3$(s) (blue solid line) and the calculated equilibrium of Pu(III)(aq) with $Pu^{IV}O_2$(am,hyd) with pe + pH = 0 (dashed line) in the absence of borate as reported in NEA-TDB.

5.5 Interaction of Pu(III/IV) with borate

The solubility of $Pu^{IV}O_2$(am,hyd) in 0.1 M NaCl solution with $[B]_{tot}$ = 0.16 M in the presence of $Na_2S_2O_4$ and hydroquinone at pH_m = 7.5 and 9.0 is presented in Figure 74. Experimental Eh and pH values of the samples are displayed in the Pu Pourbaix diagram (Figure 75).

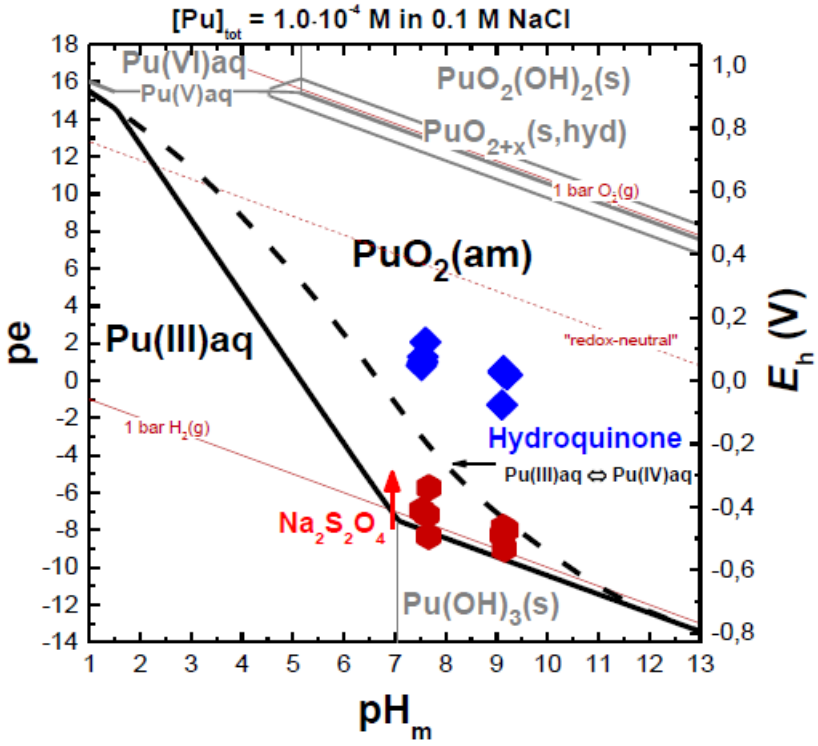

Figure 75: Pourbaix diagram calculated for [Pu]tot =10^{-4} M in 0.1 M NaCl and absence of borate. Dashed and solid lines represent the calculated borderlines for the individual Pu redox species (Guillaumont et al., 2003; Neck et al., 2007). pe and pHm values are shown for the solubility samples in the presence of hydroquinone (blue) and $Na_2S_2O_4$ (red).

Measured Eh values for the two samples with hydroquinone are in the stability field of $Pu^{IV}O_2$(am,hyd). The experimental Pu(IV) solubility at pH_m ~7.5 is at the detection limit for LSC, i.e. $1 \cdot 10^{-9}$ M. This upper limit value is consistent with the expected $Pu^{IV}O_2$(am,hyd) solubility. XPS analysis confirm $Pu^{IV}O_2$(am,hyd) as solubility controlling phase. In conclusion, no significant effect of borate on the Pu(IV) aqueous and solid phase speciation is observed at pH_m = 7.5 in slightly reducing solutions, which is consistent with the results obtained for Th(IV) (chapter 5.4). At pH_m = 9.0 the experimental $Pu^{IV}O_2$ (am,hyd) solubility is significantly enhanced compared to the Pu solubility expected for the measured (pe + pH) conditions (log [Pu(IV)] = -10.8) (Figure 74. In the first two measurements (t ≤ 14 d), [Pu] was at ~10^{-7} M and slowly decreased to ~10^{-8} M within 300 days. Thus, no stable conditions were reached indicating that strong kinetics affect the equilibration process. Note that no change in the oxidation state of Pu in the solid phase was detected by XPS (see (Hinz, 2015)), although the

low concentrations in solution prevent the accurate characterization of the redox state in the aqueous phase. Although the complexation of Pu(IV) with borate was considered unlikely due to the very strong tendency of An(IV) towards hydrolysis in alkaline solutions (Rai et al., 1999; Yamaguchi et al., 1994), the experimental observations gained in this work could be explained properly on the basis of this hypothesis. Note that a similar increase in solubility is found for $Th(OH)_4$(am) in concentrated NaCl and $MgCl_2$ solutions at pH_m = 9, thus indicating that the complexation of Pu(IV) and Th(IV) with borate cannot be completely ruled out (chapter 5.4). Note however that no Th(IV) solubility increase in these conditions was found for dilute NaCl solutions. The enhanced [Pu] can hardly be attributed to the initial presence of Pu(III) as the redox conditions (pe + pH) are clearly in the stability field of Pu(IV) (the hydroquinone sample at pH_m = 7.5 is even closer to the stability field of Pu(III), but does not show any indication for the presence of Pu(III)). More experimental data in the investigated conditions with longer equilibration times are needed to completely understand the observed processes.

Redox conditions in the two samples with $Na_2S_2O_4$ are very close to the borderline of $Pu^{IV}O_2$(am,hyd)/$Pu(OH)_3$(s). At pH_m = 7.5, fast transformation of the initial $Pu^{IV}O_2$(am,hyd) into a dark solid phase occurred within one week. The main oxidation state of the latter is Pu(III) as confirmed by XPS analysis after 300 days. The peak shape and position of the $4f_{3/2}$ and $4f_{7/2}$ transitions are in agreement with Pu(III) reference spectra (Larson and Haschke, 1981; Larson and Motyl, 1990). The experimental Pu solubility within the first two measurements (~ $5 \cdot 10^{-7}$ M) is clearly above the Pu(IV) solubility curve, but slightly lower than expected for $Pu(OH)_3$(s) according to the data from NEA. The solubility constant log $*K°_{s,0}${$Pu(OH)_3$(s)} = 15.8 ± 1.5 is reported with a large uncertainty of 1.5 log-units which can explain the deviations (Guillaumont et al., 2003). Recent results from Fellhauer further suggest a lower value for the solubility constant of ~ log $*K°_{s,0}${$Pu(OH)_3$(s)} = 14.35 (Fellhauer, 2013). Therefore it is likely that the solubility for t ≤ 14 d is controlled by $Pu(OH)_3$(s). For t > 14 d (i.e. in the last two measurements) pe-values are slightly increasing, and $[Pu]_{tot}$ decreasing to ~2 10^{-8} M. Note that $Na_2S_2O_4$ is only metastable in neutral pH conditions (Holman and Bennett, 1994; Munchow and Steudel, 1994). The slightly increasing pe values for the sample at pH_m = 7.5 points to slow decomposition of $Na_2S_2O_4$. While the measured (pe + pH) values suggest a solubility control by the reductive dissolution equilibrium (see below; implying a quantitative re-oxidation of $Pu(OH)_3$(s) to PuO_2(am,hyd)), XPS clearly revealed the presence of a rather oxidation state pure Pu(III) solid phase. Therefore, the decrease in $[Pu]_{tot}$ for t > 14 d is likely caused by the formation of a Pu(III) borate coating or borate containing Pu(III) solid phase similar to the findings in Nd(III) solubility studies.

For the sample at pH_m = 9 ($Na_2S_2O_4$), XPS analysis indicates the presence of both Pu(III) and Pu(IV) in the solid phase after t = 300 d (see (Hinz, 2015). The measured $[Pu]_{tot}$ at pH_m = 9 after short equilibration time is enhanced compared to the solubility expected under these pe + pH conditions, i.e. *the reductive dissolution equilibrium*:

$PuO_2(am,hyd) + 4\ H^+ + e^- \rightleftharpoons Pu^{3+} + 2\ H_2O$

As the experimental [Pu] is even higher than that of $Pu(OH)_3(s)$ in borate-free systems, the formation of Pu(III) borate complexes has to be considered, analogously to the Cm(III) borate complexes observed under comparable experimental conditions. In solubility studies with $Nd(OH)_3(am)$, the increase in [Nd(III)] in 0.1 M and 1.0 M NaCl at pH_m = 9 and 10 in presence of $[B]_{tot} \geq 0.16$ M is attributed to Nd(III)-borate complexes (see chapter 5.3). The initial [Pu] decreased with time (by ~ 1 order of magnitude after t = 300 d) indicates that no equilibrium has been attained. As for the sample at pH_m = 7.5 ($Na_2S_2O_4$), the decrease of initial [Pu] (i.e. [Pu(III)]) is consistent with the formation of a Pu(III) borate coating or borate containing Pu(III) solid phase as reported for Nd(III) in chapter 5.3.

5.5.1 Conclusions

Solubility studies with $Pu^{IV}O_2(am,hyd)$ under mildly reducing conditions controlled by hydroquinone and with $[B]_{tot}$ = 0.16 M show a differential behavior at pHm = 7.5 and pHm = 9.0. Hence, the very low solubility determined at pHm = 7.5 is in good agreement with the reported solubility of Pu(IV) in equilibrium with $u^{IV}O_2$ (am,hyd) in the absence of borate. The solubility increase observed at pHm = 9 could be explained by a possible Pu(IV)-borate interaction, similar to observations made with Th(IV) in concentrated NaCl and $MgCl_2$ solutions at same pH. Note however that a Pu(IV)-borate complexation leading to an increased Pu(IV) solubility was considered unlikely on the basis of the strong tendency of Pu(IV) towards hydrolysis, and thus additional experiments evidences are needed to clarify the influence of borate on the Pu(IV) solubility and speciation in this pHm region. The slow decrease of the measured Pu concentration at this pH_m with time clearly indicates that no equilibrium conditions are reached after 300 days. XPS analysis of the alteration phases in the presence of hydroquinone and $[B]_{tot}$ = 0.16 M showed no reduction of the initial Pu(IV) solid, as expected under the measured pe + pH conditions.

In the presence of $Na_2S_2O_4$, a complete (pH_m = 7.5) and partial (pH_m = 9) reduction of the initial $Pu^{IV}O_2(am,hyd)$ to a Pu(III) solid phase occurs according to XPS analyses. At pH_m = 7.5, the measured Pu solubility at short equilibration times (t ≤ 14 d) are in agreement with a solubility control by $Pu(OH)_3(s)$. The continuous decrease in $[Pu]_{tot}$ (i.e. [Pu(III)]) with time and the XPS results at the end of the solubility experiments are consistent with the formation of a Pu(III) borate coating or formation of a Pu(III)-borate solid phase similar to observations gained for Nd(III) under analogues experimental conditions. At pH_m = 9, the formation of Pu(III)-complexes likely occurs slightly enhancing the Pu(III) solubility compared to the borate-free system. The latter agrees with the findings for Cm(III) and Np(V) at this pH_m with comparable $[B]_{tot}$ in NaCl media. In most samples, no stable Pu(III/IV) concentrations are measured clearly indicating that longer equilibration times than 300 days are needed. Additional experimental efforts are

needed to gain a conclusive insight on the impact of borate on the Pu solubility and redox chemistry under weakly alkaline reducing conditions.

5.6 Solubility of Np(V) in the presence of borate

The system Np(V) – borate was intensively studied by Hinz and the results are described and discussed in detail in her Ph.D. thesis (Hinz, 2015). Here, only the most important findings of this study are summarized.

The solubility of Np(V) with borate was investigated from undersaturation conditions using $NpO_2OH(am)$ as starting material. Experiments were performed in NaCl and $MgCl_2$ solutions with 0.04 M ≤ $[B]_{tot}$ ≤ 0.16 M at 6 ≤ pH_m ≤ 9. [Np(V)] and pH_m were monitored at regular time intervals for up to 270 days. After reaching equilibrium conditions, solid phases from selected samples were characterized by XPS, SEM–EDS, XRD, XANES and EXAFS. The interaction of Np(V) with borate in the aqueous phase was further investigated in an independent batch series with ~10^{-4} M Np(V) in 0.25 M and 3.5 M $MgCl_2$ with 0.04 M ≤ $[B]_{tot}$ ≤ 0.16 M and pH_m = 8 and 9 by UV-VIS/NIR spectroscopy.

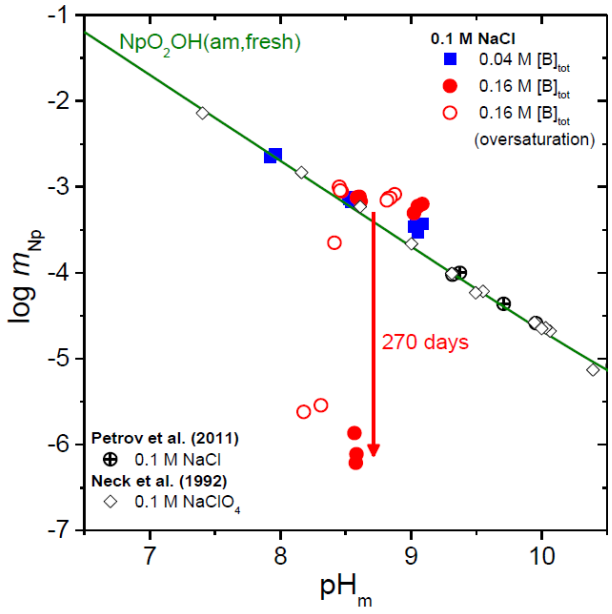

Figure 76: Solubility of Np(V) in the presence of 0.04 M ≤ $[B]_{tot}$ ≤ 0.16 M in 0.1 M NaCl solutions (blue and red symbols). Comparison with experimental (open symbols, black) solubility data in the absence of borate as reported by (Neck et al. 1992) and (Petrov et al. 2011). Solid line corresponding to the solubility of NpO_2OH(am,fresh) in 0.1 M NaCl calculated according to the NEA– TDB selection.

5.6.1 Solubility of Np(V) in NaCl and $MgCl_2$ solutions

The experimental solubility data of Np(V) in 0.1 M NaCl, 5.0 M NaCl, 0.25 M $MgCl_2$ and 3.5 M $MgCl_2$ solutions in the presence of 0.04 M ≤ $[B]_{tot}$ ≤ 0.16 M are shown in Figure 76 to Figure 79. The figures also show experimental and calculated solubility of Np(V) in the absence of borate as reported by Petrov et al., Neck et al. and the NEA-TDB (Guillaumont et al., 2003; Neck et al., 1992; Petrov et al., 2011).

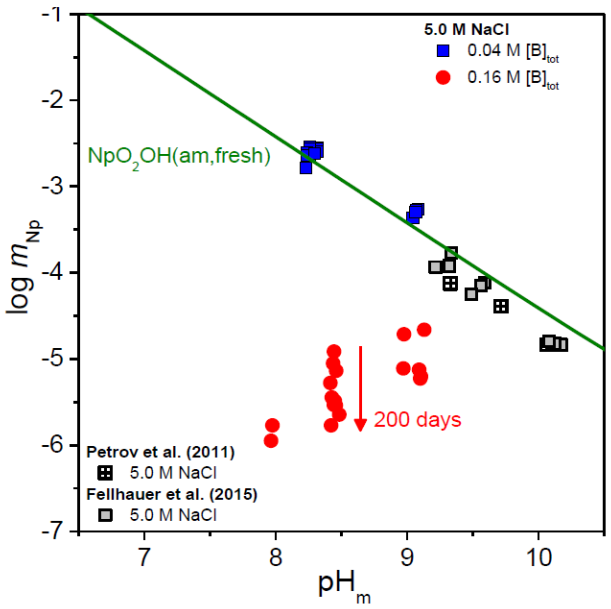

Figure 77: Solubility of Np(V) in the presence of 0.04 M ≤ $[B]_{tot}$ ≤ 0.16 M in 5.0 M NaCl solutions (blue and red symbols). Comparison with experimental (open symbols, black) solubility data in the absence of borate as (Fellhauer et al, 2015) and (Petrov et al., 2011). Solid line corresponding to the solubility of NpO_2OH(am, fresh) in 5.0 M NaCl calculated according to the NEA–TDB selection. Arrow indicates that the decrease in the concentration of Np for the same solubility sample was only completed after 270 days

Within the timeframe of this study, low boron concentrations ($[B]_{tot}$ = 0.04 M) show no significant effect on the solubility of Np(V) in 5.0 M NaCl and 0.25 M and 3.5 M $MgCl_2$ solutions with 8 ≤ pH_m ≤ 9.The experimentally measured Np(V) solubility in these systems is in good agreement with Np(V) solubility data in the absence of borate (Fellhauer, 2015; Neck et al., 1992; Petrov et al., 2011). A slight increase in the Np(V) solubility is observed in 0.1 M NaCl solutions with pH_m = 9 and $[B]_{tot}$ ≥ 0.04 M, indicating the possible formation of Np(V)–borate complexes in solution. Similar to observations made for Nd(III) (see chapter 5.3), a distinct decrease in solubility occurs in 0.1 M and 5.0 M NaCl solutions with higher boron concentration ($[B]_{tot}$ = 0.16 M) and pH_m ≤ 9 (Figure 76 and Figure 77). The drop in the solubility is accompanied by a transformation of the initial greenish NpO_2OH (am) into a white-grayish solid phase. The solid phase transformation was fast in 5.0 M NaCl (~2 weeks), but slower in 0.1 M NaCl where it occurred only for pH_m ≤ 8.5. Note that samples prepared from oversaturation conditions in 0.1 M NaCl and $[B]_{tot}$ = 0.16 M result in very similar experimental observations than samples

prepared from undersaturation conditions: a slight increase of Np(V) concentration at pH_m ~ 8.8 and a drop in the Np(V) solubility at $pH_m \leq 8.5$ together with a slow transformation of the solid phase. In both cases, the concentration of Np(V) in equilibrium with the newly formed solid phase is approximately three orders of magnitude lower than the solubility of NpO_2OH(am,fresh). The transformation is tentatively faster at lower pH_m values, see Figure 76 to Figure 79. It is therefore likely that the non-occurrence of a solid phase transformation in 0.1 M NaCl and $pH_m > 8.5$ is due to insufficient equilibration time.

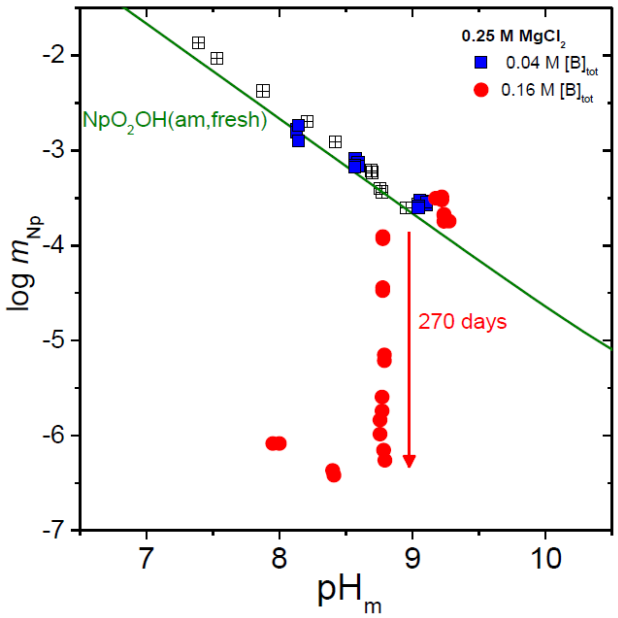

Figure 78: Solubility of Np(V) in the presence of 0.04 M ≤ $[B]_{tot}$ ≤ 0.16 M in 0.25 M $MgCl_2$ solutions (blue and red symbols). Comparison with experimental (open symbols, black) solubility data in the absence of borate as reported by (Petrov et al.,uhhuhj 2011). Solid line corresponding to the solubility of NpO_2OH(am,fresh) in 0.25 M $MgCl_2$ calculated according to the NEA–TDB selection.

A comparable decrease in Np(V) solubility accompanied by a transformation of the initial greenish NpO_2OH(am) into a newly formed white–gray solid phase occurs in dilute $MgCl_2$ systems at $pH_m < 9$ and $[B]_{tot} = 0.16$ M (Figure 78). Similarly to the dilute NaCl system the solubility of Np(V) decreased slowly and attained a constant value (~$10^{-6.5}$ M) only after 270 days. In 3.5 M $MgCl_2$ solutions with $[B]_{tot} = 0.16$ M only a minor decrease in Np(V) solubility is observed after 270 days. As observed in Nd(III), Cm(III) and U(VI) solubility studies (see chapters 5.3 and 5.7) actinide borate interactions in $MgCl_2$ solutions are less pronounced than in NaCl solutions at comparable pH_m and ionic strength conditions. As discussed in chapter 5.2 based on the ^{11}B-NMR data gained in this work in combination with the thermodynamic model reported by Felmy and co-workers (Felmy and Weare, 1986), the formation of Mg–borate complexes decreases the concentration of free borate and outcompetes the formation of An–borate aqueous complexes and solid phases.

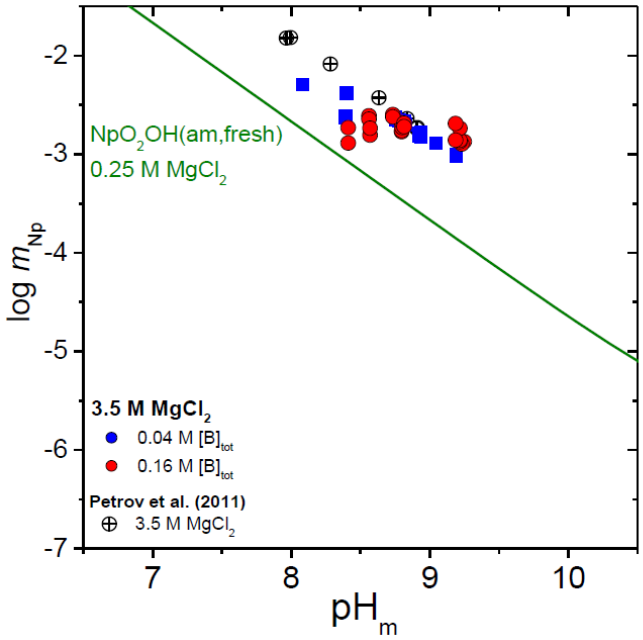

Figure 79: Solubility of Np(V) in the presence of 0.04 M ≤ $[B]_{tot}$ ≤ 0.16 M in 3.5 M $MgCl_2$ solutions (blue and red symbols). Comparison with experimental (open symbols, black) solubility data in the absence of borate as reported by (Petrov et al., 2011). Solid line corresponding to the solubility of NpO_2OH(am, fresh) in 0.25 M $MgCl_2$ calculated according to the NEA–TDB selection. Calculations were restricted to 0.25 M $MgCl_2$ due to a lack of ion interaction parameters for high concentrated $MgCl_2$ systems.

Solid phase characterization by XRD, XPS and SEM-EDS

Solid phases of selected solubility experiments in 0.1 M, 5.0 M NaCl and 0.25 M $MgCl_2$ with $[B]_{tot}$ = 0.16 M were investigated after attaining equilibrium conditions by XRD, SEM–EDS and XPS. Np-L_{III} XANES and EXAFS spectra were also acquired for the alteration phases formed in 0.25 M $MgCl_2$, 0.1 M NaCl and 5.0 M NaCl, all of them with $[B]_{tot}$ = 0.16 M and pH_m ~ 8.5. Spectra were collected at the INE-Beamline for Actinide Research at ANKA.

In contrast to the initial X-ray amorphous NpO_2OH(am,fresh), XRD diffractograms of the transformed solid phases show a series of sharp peaks, indicating the crystalline character of the newly formed solid phase (Figure 80). Although with certain similarities, the diffractograms obtained for the solid phases formed in NaCl and $MgCl_2$ solutions are markedly different, indicating that the cation of the background electrolyte participates (or at least influences) in the formation of the secondary solid phase. Note that the collected diffractograms gave no positive match with any of the existing borate entries in the JCPDS database. Note further that, in spite of the several washing steps

with ethanol, all diffractograms collected for Np(V) secondary phases formed in 5.0 M NaCl solutions showed only very strong reflexes corresponding to NaCl (data not shown in Figure 80).

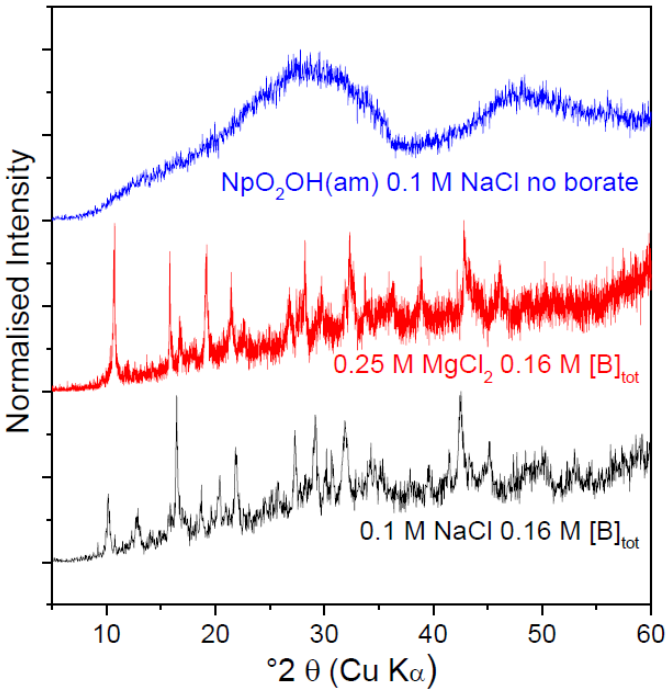

Figure 80: Diffractograms of the solubility-controlling Np(V) solid phases in the absence and presence of borate ($[B]_{tot}$ = 0.16 M) in 0.1 M NaCl and 0.25 M $MgCl_2$ solutions at pH_m ~8.5.

XPS analyses of the Np(V) secondary phases formed in dilute NaCl and $MgCl_2$ solutions confirm the stoichiometric presence of boron and Na^+/Mg^{2+}. The composition of the newly formed solid phases hint towards the formation of solid phases with stoichiometry $NpO_2[B_5O_6(OH)_4]\cdot 2NaOH$ and $(NpO_2)_2[B_5O_6(OH)_4]_2\cdot 3Mg(OH)_2(cr)$, respectively (Hinz, 2015).

SEM images of the surface of the Np(V)–borate solid phases formed in NaCl and $MgCl_2$ solutions are shown in Figure 81. Solid phases collected from samples in 0.1 M NaCl (Figure 81 a) and 0.25 M $MgCl_2$ solutions (Figure 81 b) show a homogeneous transformation and distribution of Np(V) in the entire investigated area. The sample equilibrated in 0.1 M NaCl contains very thin (~20 nm) hexagonal platelets with a diameter of ~ 500 nm. The structure of the sample equilibrated in 0.25 M $MgCl_2$ looks similar in shape but appears more amorphous. The investigation of the Np(V)–borate solid phase formed in 5.0 M NaCl (Figure 81 c and d) clearly shows the co-existence of two phases. Hence, massive, crystalline hexagonal blocks appear surrounded by an amorphous phase. EDS analyses indicated the predominance of Na and Cl in the block structures, whereas the amorphous phase would correspond to the newly formed Np(V)–borate phase. The identification of NaCl and presence of an amorphous Np(V) phase is consistent with the observations collected by XRD, where only the pattern of

NaCl could be identified and no additional peaks of a newly formed Np(V)–borate solid phase were observed.

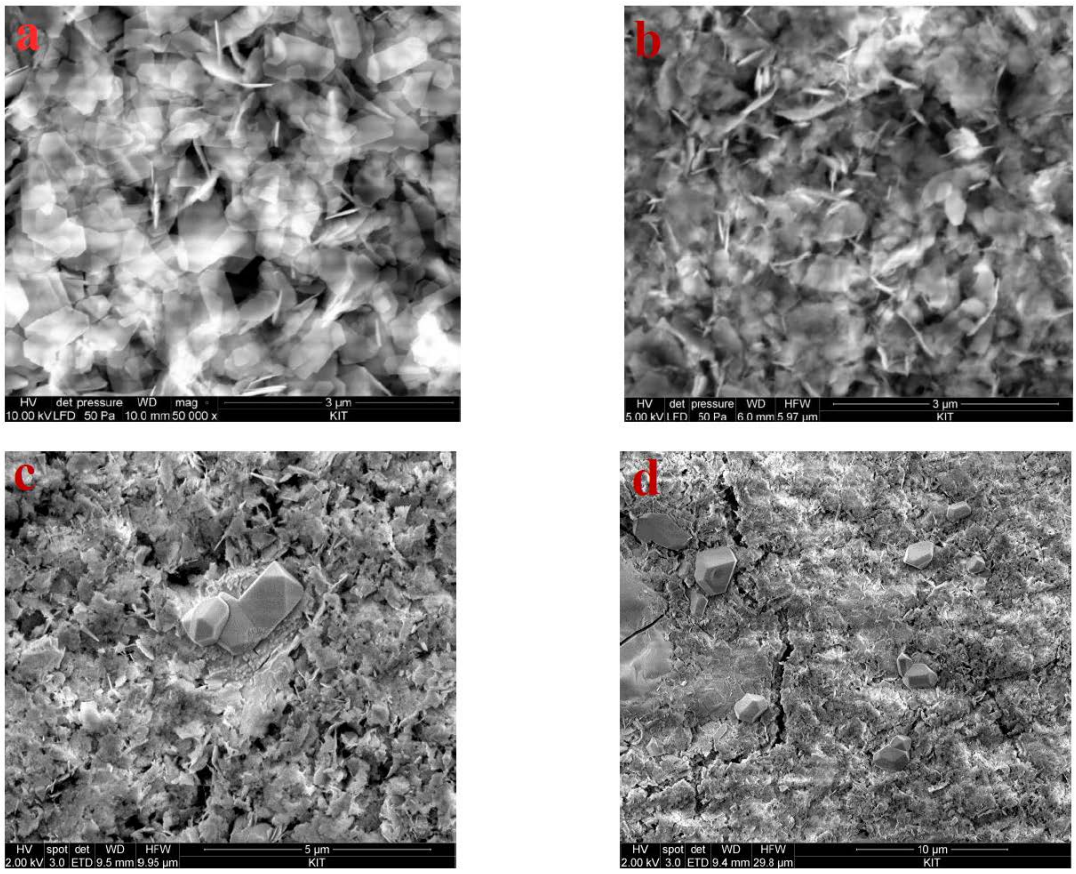

Figure 81: SEM-images of the new formed solubility-controlling Np(V) solid phases in the presence of borate ($[B]_{tot}$ = 0.16 M) in 0.1 M NaCl (a) and 0.25 M $MgCl_2$(b) and 5.0 M NaCl (c, d).

EXAFS investigations (Hinz, 2015) confirmed the Np(V)–borate compound formed in 0.1 M NaCl as the most stable and well crystallized structure, whereas the structures formed in 5 M NaCl and in 0.25 M $MgCl_2$ are less stable and undefined probably consisting of a mixture of different phases. Note that EXAFS analyses are in good agreement with the findings obtained by XRD and SEM–EDS techniques.

5.6.2 Conclusions

Solubility studies with $NpO_2OH(am)$ combined with accurate solid phase characterization and UV-Vis/NIR investigations (not shown here, see (Hinz, 2015)) confirm that the presence of borate strongly affects both the aqueous and solid speciation of Np(V)) in dilute to concentrated NaCl and $MgCl_2$ solutions at pHm = 8 and 9 and [B]tot ≥ 0.04 M. UV–Vis/NIR investigations confirm the formation of at least one Np(V)–borate complex in $MgCl_2$ solutions. A much weaker interaction is observed in concentrated $MgCl_2$ solu-

tions, as a result of the competition between Mg^{2+} and NpO_2^+ for borate complexation. The evaluation of the spectroscopic data collected suggests $B(OH)_4^-$ as most probable complexing borate species in the aqueous phase, although the exact stoichiometry of the complexation reaction and the determination of a formation constant was not feasible in this work. A similar trend in borate complexation was observed for Cm(III) in NaCl, $CaCl_2$ and $MgCl_2$ solutions with comparable $[B]_{tot}$ using TRLFS (see chapter 5.3).

In spite of the clear formation of Np(V)–borate aqueous species in solution at moderate pH_m, no significant increase in the solubility of NpO_2OH(am, fresh) is observed in the presence of $[B]_{tot} \leq 0.4$ M. On the contrary and similarly to Nd(III), a clear drop in the Np(V) solubility occurs in borate-bearing NaCl and $MgCl_2$ solutions with pHm ≤ 9. The drop in solubility is accompanied by a visible change of the initial solid (from green to white-gray), confirming the formation of a new solid phase. The formation of this previously unreported Np(V)–borate solid phase is further confirmed by XRD, XPS, SEM–EDS and EXAFS analysis (details are found in (Hinz, 2015)). This solid phase transformation constitutes a previously unreported retention mechanism for the highly mobile Np(V).

5.7 Solubility of U(VI) in the presence of borate

The system U(VI) – borate was studied by Hinz and the experiments and results are described and discussed in detail in her Ph.D. thesis (Hinz, 2015).

The solubility of U(VI) was studied from undersaturation conditions in the presence of 0 M ≤ $[B]_{tot}$ ≤ 0.16 M with 4.5 ≤ pH_m ≤ 9.3 in 0.1 M and 5.0 M NaCl and 0.25 and 3.5 M $MgCl_2$ solutions. Samples in 0.1 M and 5.0 M NaCl systems with $pH_m \geq 7.5$ were prepared with $Na_2U_2O_7 \cdot H_2O$(cr) as initial solid phase. In all samples in 0.25 and 3.5 M $MgCl_2$ systems and in 0.1 M and 5.0 M NaCl systems with $pH_m < 7.5$ freshly prepared meta-schoepite $UO_3 \cdot 2H_2O$(cr) was added as initial solid phase. For comparison purposes, samples with U(VI) in the same pH_m and ionic strength conditions but without borate were prepared and measured following the same experimental approach. The U(VI) concentration was regularly quantified in combination with the measurement of pH_m for up to 380 days. Solid samples from selected solubility experiments were characterized by XRD after attaining equilibrium conditions.

5.7.1 Solubility of U(VI) in NaCl and $MgCl_2$ solutions

The solubility of U(VI) in 0.1 M, 5.0 M NaCl, 0.25 M $MgCl_2$ and 3.5 M $MgCl_2$ solutions with 0 M ≤ $[B]_{tot}$ ≤ 0.16 M is shown in Figure 82 and Figure 83. The figures also show the solubility of $UO_3 \cdot 2H_2O$(cr) and $Na_2U_2O_7 \cdot H_2O$(cr) in NaCl and $MgCl_2$ solutions as calculated using the thermodynamic and (SIT) activity models.

No effect of borate on the solubility of U(VI) is observed in dilute to concentrated NaCl solutions at $pH_m \leq 6.5$ (solubility control by $UO_3 \cdot 2H_2O$(cr)). The weak complexation capacity of borate is not sufficient to outcompete the cationic hydrolysis species of U(VI) prevailing in this pH region. Note also that in this pH_m region the non-complexing $B(OH)_3$(aq) species is dominating the aqueous chemistry of boron. These data are also in excellent agreement with the solubility of $UO_3 \cdot 2H_2O$(cr) as calculated in the absence of borate. In 0.1 M and 5.0 M NaCl solutions at $pH_m \geq 7.5$, a solubility increase with increasing $[B]_{tot}$ is observed. This effect is more pronounced in 5.0 M NaCl solution with an increase in U(VI) solubility of about 1.5 orders of magnitude, rather than in 0.1 M NaCl solution where a slight increase of ~ ½ order of magnitude is seen. This solubility increase unequivocally hints towards the formation of U(VI)–borate aqueous complexes within the pH-range 7.5–9. Lucchini et al. investigated the solubility of U(VI) in a synthetic brine solution (2.2-4.2 M NaCl and ~ 0.01 M $[B]_{tot}$) and found no effect of borate on the U(V) solubility at pH_m ~8.9 but the used $[B]_{tot}$ are significantly lower compared to the present experiments (Lucchini et al., 2007).

In contrast to the observations made for Nd(III) and Np(V), no decrease in the solubility of U(VI) is observed in NaCl solutions within the timeframe of the experiment (380 days). Hence, in spite of the observed U(VI)–borate interaction in the aqueous phase, such interaction did not progress further towards the formation of a secondary U(VI)–borate solid phase. It is worth mentioning that [U(VI)] in equilibrium with $Na_2U_2O_7 \cdot H_2O$(cr) at pH_m = 7.5 is significantly lower than the solubility-limit set by $Nd(OH)_3$(am) and NpO_2OH(am), and thus that the solubility product of a potentially-forming U(VI)–borate solid phase is not exceeded. Although not evaluated in the present work, the formation of a U(VI)–borate solid phase at pH_m ~9 and absence of Na^+ ($I \rightarrow 0$) cannot be completely ruled out. In these conditions, $UO_3 \cdot 2H_2O$(cr) allows significantly higher [U(VI)] in solution compared to $Na_2U_2O_7 \cdot H_2O$(cr) (1 to 2 log-units difference, see dashed lines in Figure 82), which may lead to the formation of a secondary U(VI)–borate solid phase.

In contrast to the observations made for Nd(III) and Np(V), no decrease in the solubility of U(VI) is observed in NaCl solutions within the timeframe of the experiment (380 days). Hence, in spite of the observed U(VI)–borate interaction in the aqueous phase, such interaction did not progress further towards the formation of a secondary U(VI)–borate solid phase. It is worth mentioning that [U(VI)] in equilibrium with $Na_2U_2O_7 \cdot H_2O$(cr) at pH_m = 7.5 is significantly lower than the solubility-limit set by $Nd(OH)_3$(am) and NpO_2OH(am), and thus that the solubility product of a potentially-forming U(VI)–borate solid phase is not exceeded. Although not evaluated in the present work, the formation of a U(VI)–borate solid phase at pH_m ~9 and absence of Na^+ ($I \rightarrow 0$) cannot be completely ruled out. In these conditions, $UO_3 \cdot 2H_2O$(cr) allows significantly higher [U(VI)] in solution compared to $Na_2U_2O_7 \cdot H_2O$(cr) (1 to 2 log-units difference, see dashed lines in Figure 82), which may lead to the formation of a secondary U(VI)–borate solid phase.

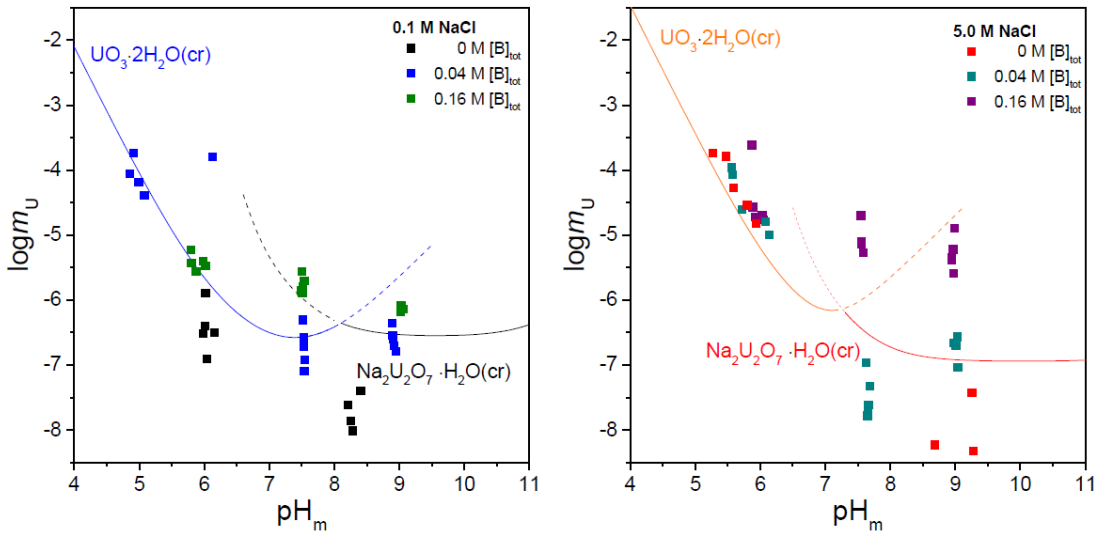

Figure 82: Solubility of $UO_3 \cdot 2H_2O$(cr) and $Na_2U_2O_7 \cdot H_2O$ (cr) in the presence of 0 M ≤ $[B]_{tot}$ ≤ 0.16 M in 0.1 M and 5.0 M NaCl solutions. Comparison with calculated solubility of $UO_3 \cdot 2H_2O$(cr) (blue line) and $Na_2U_2O_7 \cdot H_2O$ (cr) (black line) in the absence of borate as reported in Altmaier et al. (Altmaier et al., 2003b).

A weaker effect of borate (compared to the NaCl system) on the U(VI) solubility can be observed for dilute to concentrated $MgCl_2$ systems. This effect is especially visible at pH_m = 7.5 and $[B]_{tot}$ = 0.16 M. As already observed in the Np(V) solubility studies, actinide borate interactions in $MgCl_2$ solutions are less pronounced than in NaCl solutions at comparable pH_m and ionic strength conditions. This effect is likely caused by a changed boron speciation in $MgCl_2$ media due to an interaction of Mg^{2+} with borate species in solution. This effect was also hinted in ^{11}B-NMR experiments (see chapter 5.2).

In $MgCl_2$ systems, the solubility data in the borate-free systems is partly scattered and lower than the expected solubility reported in the literature (Altmaier et al., 2003b). The lower solubility is likely caused by differences in the crystallinity and particle size of the initial solid phase controlling the solubility of U(VI).

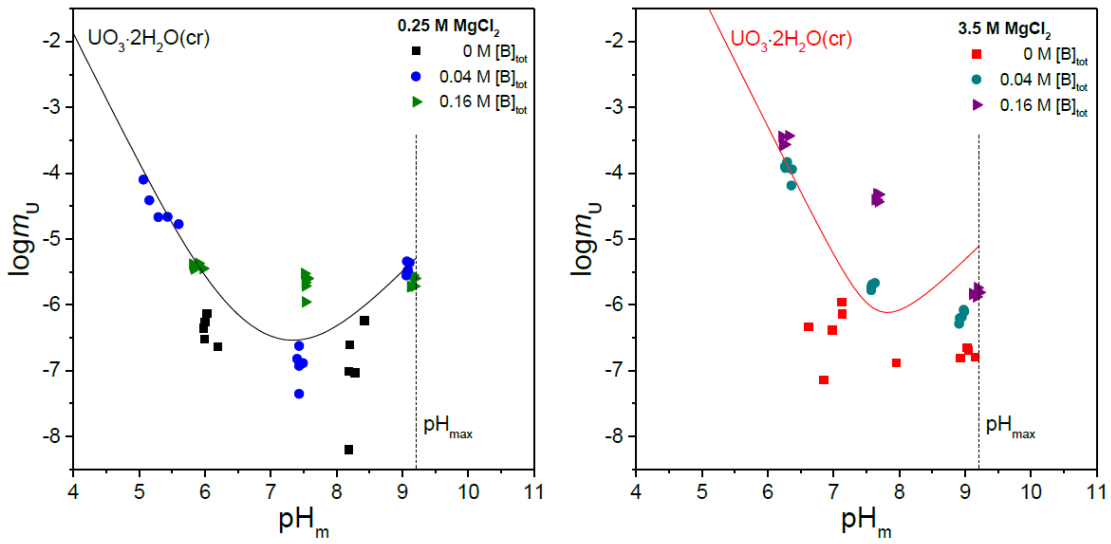

Figure 83: Solubility of $UO_3 \cdot 2H_2O$(cr) in the presence of 0 M ≤ $[B]_{tot}$ ≤ 0.16 M in 0.25 M and 3.5 M $MgCl_2$ solutions. Comparison with calculated solubility of $UO_3 \cdot 2H_2O$(cr) in the absence of borate (solid line) as reported in Altmaier et al. (Altmaier et al., 2003b).

5.7.2 Solid phase characterization

XRD diffractograms obtained for selected solid phases are shown in Figure 84. In all cases the measured patterns agree very well with those reported for UO3·2H2O (cr) JCPDF file No: 43-0364 and Na2U2O7·H2O(cr) (Altmaier et al., 2003b), indicating that the bulk U(VI) controlling solid phase in all investigated samples is not affected by the presence of borate.

5.7.3 Conclusions

Experimental data from U(VI) solubility studies in the presence of borate showed an increase in U(VI) solubility in NaCl systems at 7.5 ≤ pH_m ≤ 9 for $[B]_{tot}$ ≥ 0.04 M likely caused by the formation of aqueous U(VI)-borate complexes. A weaker effect of borate is observed in dilute to concentrated $MgCl_2$ solutions, where a slight solubility increase at pH_m = 7.5 and $[B]_{tot}$ = 0.16 M can be seen. No drop in U(VI) solubility caused by the transformation of the initial solid phase as observed in Nd(III) (see chapter 5.3) and Np(V) systems (see chapter 5.6) is found in NaCl and $MgCl_2$ solutions under the investigated conditions. This behavior is likely related with the very low uranium concentration imposed by $Na_2U_2O_7 \cdot H_2O$(cr) as solubility controlling-phase in NaCl media under weakly alkaline conditions, although it could also be due to slow kinetics. In very dilute systems (absence of Na^+), the higher uranium concentrations under weakly alkaline conditions set by $UO_3 \cdot 2H_2O$(cr) may lead to the formation of secondary U(VI)–borate

solid phases. The observations collected in this work allow neither confirming nor rejecting the latter hypothesis, and thus provide space for additional studies.

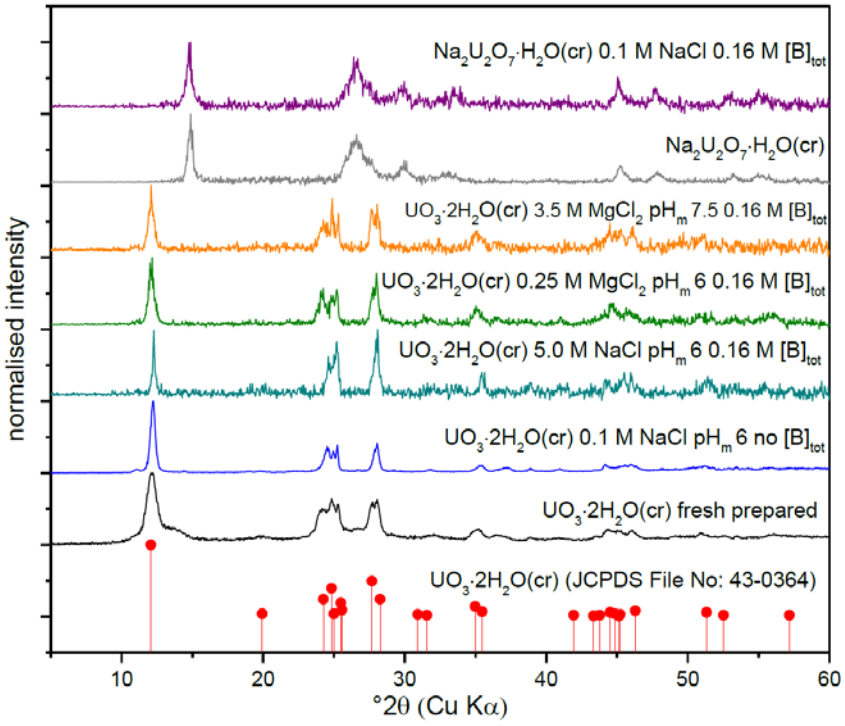

Figure 84: *XRD pattern of freshly prepared initial $UO_3 \cdot 2H_2O$(cr), $UO_3 \cdot 2H_2O$(cr) reference [137] and $UO_3 \cdot 2H_2O$(cr) alteration phases from solubility experiments in NaCl and $MgCl_2$ systems with 0 M ≤ $[B]_{tot}$ ≤ 0.16 M at pH_m 6–7.5 and initial $Na_2U_2O_2 \cdot H_2O$ (cr) and $Na_2U_2O_2 \cdot H_2O$ (cr) alteration phases from solubility experiment in 0.1 M NaCl and $[B]_{tot}$ = 0.16 M.*

List of Tables

List of Figures

6 References

Altmaier, M., Metz, V., Neck, V., Muller, R., Fanghanel, T., 2003a. Solid-liquid equilibria of Mg(OH)(2)(cr) and Mg-2(OH)(3)Cl center dot 4H(2)O(cr) in the system Mg-Na-H-OH-O-Cl-H2O at 25 degrees C. Geochimica et Cosmochimica Acta 67 (19), 3595–3601.

Altmaier, M., Neck, V., Fanghaenel, T., 2008. Solubility of Zr(IV), Th(IV) and Pu(IV) hydrous oxides in CaCl(2) solutions and the formation of ternary Ca-M(IV)-OH complexes. Radiochimica Acta 96 (9-11), 541–550.

Altmaier, M., Neck, V., Fanghanel, T., 2004. Solubility and colloid formation of Th(IV) in concentrated NaCl and MgCl2 solution. Radiochimica Acta 92 (9-11), 537–543.

Altmaier, M., Neck, V., Metz, V., Müller, R., Schlieker, M., Fanghänel, T., 2003b. The solubility of U(VI) in NaCl and MgCl2 solution, in: 9th International Conference on Chemsitry and Migration Behavior of Actinides and Fission Products in the Geosphere. Migration '03, Gyeongju, Korea. 21. - 26.09.2003, Yuseong, Daejeon, Korea, p. 46.

Amayri, S., Jermolajev, A., Reich, T., 2011. Neptunium(V) sorption on kaolinite. Radiochimica Acta 99 (6), 349–357.

Artinger, R., Buckau, G., Geyer, S., Fritz, P., Wolf, M., Kim, J.I., 2000. Characterization of groundwater humic substances: influence of sedimentary organic carbon. Applied Geochemistry 15 (1), 97–116.

Artinger, R., Buckau, G., Kim, J.I., 1996. Influence of sedimentary organic matter on dissolved fulvic acids in groundwater: Significance for groundwater dating with C-14 in dissolved organic matter, in: IAEA (Ed.), Isotopes in Water Resources Management. Proceedings of a Symposium on Isotopes in Water Resources Management organized in Co-Operation with the United Nations Educational, Scientific and Cultrural Organization and Held in Vienna, 20 - 24 March 1995, IAEA-SM-336/26.

Artinger, R., Buckau, G., Kim, J.I., Geyer, S., 1999. Characterization of groundwater humic and fulvic acids of different origin by GPC with UV/Vis and fluorescence detection. Fresenius' Journal of Analytical Chemistry 364 (8), 737–745.

Artinger, R., Buckau, G., Zeh, P., Geraedts, K., Vancluysen, J., Maes, A., Kim, J.I., 2003. Humic colloid mediated transport of tetravalent actinides and technetium. Radiochimica Acta 91 (12), 743–750.

Baes, A.U., Bloom, P.R., 1990. Fulvic acid ultraviolet-visible spectra. Influence of solvent and pH. Soil Science Society of America Journal 54 (5), 1248–1254.

Baeyens, B., Bradbury, M.H., 2004. Cation exchange capacity measurements on illite using the sodium and cesium isotope dilution technique: Effects of the index cation, electrolyte concentration and competition: modeling. Clays Clay Miner. 52 (4), 421–431.

Banik, N.l., Marsac, R., Luetzenkirchen, J., Diascorn, A., Bender, K., Marquardt, C.M., Geckeis, H., 2016. Sorption and Redox Speciation of Plutonium at the Illite Surface. Environmental Science & Technology 50 (4), 2092–2098.

Banik, N.L., 2006. Speciation of tetravalent plutonium in contact with humic substances and kaolinite under environmental conditions. PhD thesis, Mainz, Germany.

Banik, N.L., Buda, R.A., Buerger, S., Kratz, J.V., Trautmann, N., 2007. Sorption of tetravalent plutonium and humic substances onto kaolinite. Radiochimica Acta 95 (10), 569–575.

Baum, J.C., McClure, D.S., 1979. Ultraviolet transitions of benzoic acid - 1. Interpretation of the singlet absorption spectrum. J Am Chem Soc 101 (9), 2335–2339.

Begg, J.D., Zavarin, M., Zhao, P., Tumey, S.J., Powell, B., Kersting, A.B., 2013. Pu(V) and Pu(IV) sorption to montmorillonite. Environmental Science and Technology 47 (10), 5146–5153.

Bertrand, P.A., Choppin, G.R., 1982. Separation of actinides in different oxidation states by solvent extraction. Radiochimica Acta 31 (3-4), 135–138.

Borkowski, M., Richmann, M., Kalanke, S., Reed, D. T., 2011. Borate chemistry and interactions with Actinides in high ionic strength solutions at moderate pH.: Proceedings of the international workshop ABC-Salt in Karlsruhe (Germany), (2011). Karlsruher Institut für Technologie (KIT), Karlsruhe.

Bosch Ojeda, C., Sanchez Rojas, F., 2013. Recent applications in derivative ultraviolet/visible absorption spectrophotometry: 2009-2011. A review. Microchemical Journal 106, 1–16.

Bouby, M.G., Buckau, G., 2012. Ionic strength and complexation induced humic agglomeration study: Humic acid agglomeration study as a function of ionic strength and metal ion loading, in: Altmaier, M., Kienzler, B., Metz, V., Reed, D.T. (Eds.), Proceedings of the International Workshop ABC-Salt (II) and HiTAC 2011, Karlsruhe.

Bradbury, M.H., Baeyens, B., 1997. A mechanistic description of Ni and Zn sorption on Na-montmorillonite Part II: Modelling. Journal of Contaminant Hydrology 27 (3-4), 223–248.

Bradbury, M.H., Baeyens, B., 2002. Sorption of Eu on Na- and Ca-montmorillonites: Experimental investigations and modelling with cation exchange and surface complexation. Geochimica et Cosmochimica Acta 66 (13), 2325–2334.

Bradbury, M.H., Baeyens, B., 2005. Modelling the sorption of Mn(II), Co(II), Ni(II), Zn(II), Cd(II), Eu(III), Am(III), Sn(IV), Th(IV), Np(V) and U(VI) on montmorillonite: Linear free energy relationships and estimates of surface binding constants for some selected heavy metals and actinides. Geochimica et Cosmochimica Acta 69 (4), 875–892.

Bradbury, M.H., Baeyens, B., 2006. Modelling sorption data for the actinides Am(III), Np(V) and Pa(V) on montmorillonite. Radiochimica Acta 94 (9-11), 619–625.

Bradbury, M.H., Baeyens, B., 2009a. Sorption modelling on illite Part I: Titration measurements and the sorption of Ni, Co, Eu and Sn. Geochimica et Cosmochimica Acta 73 (4), 990–1003.

Bradbury, M.H., Baeyens, B., 2009b. Sorption modelling on illite. Part II: Actinide sorption and linear free energy relationships. Geochimica et Cosmochimica Acta 73 (4), 1004–1013.

Bradbury, M.H., Baeyens, B., 2011. Predictive sorption modelling of Ni(II), Co(II), Eu(IIII), Th(IV) and U(VI) on MX-80 bentonite and Opalinus Clay: A "bottom-up" approach. Applied Clay Science 52 (1-2), 27–33.

Bradbury, M.H., Baeyens, B., 2015. unpublished data, Sorption data of Eu(III) on Illite.

Bradbury, M.H., Marques, M.M., 2013. Private communication about Phase separation.

Browne, B.A., Driscoll, C.T., 1993. pH-dependent binding of aluminum by a fulvic acid. Environmental Science and Technology 27 (5), 915–922.

Buckau, G., Artinger, R., Fritz, P., Geyer, S., Kim, J.I., Wolf, M., 2000a. Origin and mobility of humic colloids in the Gorleben aquifer system. Applied Geochemistry 15 (2), 171–179.

Buckau, G., Artinger, R., Geyer, S., Wolf, M., Fritz, P., Kim, J.I., 2000b. C-14 dating of Gorleben groundwater. Applied Geochemistry 15 (5), 583–597.

Buckau, G., Artinger, R., Geyer, S., Wolf, M., Fritz, P., Kim, J.I., 2000c. Groundwater in-situ generation of aquatic humic and fulvic acids and the mineralization of sedimentary organic carbon. Applied Geochemistry 15 (6), 819–832.

Buckau, G., Artinger, R., Kim, J.I., Geyer, S., Fritz, P., Wolf, M., Frenzel, B., 2000d. Development of climatic and vegetation conditions and the geochemical and isotopic composition in the Franconian Albvorland aquifer system. Applied Geochemistry 15 (8), 1191–1201.

Buda, R.A., Banik, N.L., Kratz, J.V., Trautmann, N., 2008. Studies of the ternary systems humic substances - Kaolinite - Pu(III) and Pu(IV). Radiochimica Acta 96 (9-11), 657–665.

Chin, Y.P., Aiken, G., O'Loughlin, E., 1994. Molecular weight, polydispersity, and spectroscopic properties of aquatic humic substances. Environmental Science and Technology 28 (11), 1853–1858.

Choppin, G.R., 1997. Inner versus outer sphere complexation of f-elements. Journal of Alloys and Compounds 249 (1-2), 9–13.

Ciavatta, L., 1980. The Specific Interaction Theory in Evaluating Ionic Equilibria. Annali di Chimica 70 (11-1), 551–567.

Cieslewicz, J., Gonet, S.S., 2004. Properties of humic acids as biomarkers of lake catchment management. Aquatic Sciences 66 (2), 178–184.

Claret, F., Schaefer, T., Brevet, J., Reiller, P.E., 2008. Fractionation of Suwannee River Fulvic Acid and Aldrich Humic Acid on alpha-Al2O3: Spectroscopic Evidence. Environmental Science & Technology 42 (23), 8809–8815.

Conte, P., Piccolo, A., 1999. High pressure size exclusion chromatography (HPSEC) of humic substances: Molecular sizes, analytical parameters, and column performance. Chemosphere 38 (3), 517–528.

Courdouan, A., Christl, I., Meylan, S., Wersin, P., Kretzschmar, R., 2007a. Characterization of dissolved organic matter in anoxic rock extracts and in situ pore water of the Opalinus Clay. Applied Geochemistry 22 (12), 2926–2939.

Courdouan, A., Christl, I., Meylan, S., Wersin, P., Kretzschmar, R., 2007b. Isolation and characterization of dissolved organic matter from the Callovo-Oxfordian formation. Applied Geochemistry 22 (7), 1537–1548.

Dardenne, K., Seibert, A., Denecke, M.A., Marquardt, C.M., 2009. Plutonium(III,IV,VI) speciation in Gorleben groundwater using XAFS. Radiochimica Acta 97 (2), 91–97.

Dong, W., Brooks, S.C., 2006. Determination of the formation constants of ternary complexes of uranyl and carbonate with alkaline earth metals (Mg2+, Ca2+, Sr 2+,

and Ba2+) using anion exchange method. Environmental Science and Technology 40 (15), 4689–4695.

Donovan, J.W., 1969. Changes in ultraviolet absorption produced by alteration of protein conformation. Journal of Biological Chemistry 244 (8), 1961–1967.

Eberle, S.H., Schaefer, J.B., 1969. Stabilitätskonstanten der Komplexe des neptunyl(V)-ions mit α-hydroxykarbonsäuren. Journal of Inorganic and Nuclear Chemistry 31 (5), 1523–1527.

Fellhauer, D., 2013. Untersuchungen zur Redoxchemie und Löslichkeit von Neptunium und Plutonium. Ph.D. Thesis, Heidelberg.

Fellhauer, D., 2015. Solubility of Np(V) in 5 M NaCl. Private communication.

Felmy, A.R., Weare, J.H., 1986. The prediction of borate mineral equilibria in natural waters: Application to Searles Lake, California. Geochimica et Cosmochimica Acta 50 (12), 2771–2783.

Fröhlich, D.R., Skerencak-Frech, A., Morkos, M.L., Panak, P.J., 2013. A spectroscopic study of Cm(III) complexation with propionate in saline solutions at variable temperatures. New Journal of Chemistry 37 (5), 1520–1528.

Fröhlich, D.R., Skerencak-Frech, A., Panak, P.J., 2014. A spectroscopic study on the formation of Cm(iii) acetate complexes at elevated temperatures. Dalton Transactions 43 (10), 3958–3965.

Fuger, J., Parker, V.B., Hubbard, W., Oetting, F.L., 1983. The chemical thermodynamics of actinide elements and compounds: Part 8. The actinide halides, Vienna.

Gaona, X., Tits, J., Dardenne, K., Liu, X., Rothe, J., Denecke, M.A., Wieland, E., Altmaier, M., 2012. Spectroscopic investigations of Np(V/VI) redox speciation in hyperalkaline TMA-(OH, Cl) solutions. Radiochimica Acta 100 (10), 759–770.

Glaus, M.A., Frick, S., Rosse, R., van Loon, L.R., 2010. Comparative study of tracer diffusion of HTO, Na-22(+) and Cl-36(-) in compacted kaolinite, illite and montmorillonite. Geochimica et Cosmochimica Acta 74 (7), 1999–2010.

Glazer, A.N., Smith, E.L., 1960. Effect of Denaturation on the Ultraviolet Absorption Spectra of Proteins. Journal of Biological Chemistry 235 (10), PC43-PC44.

Gorgeon, L., 1994. Contribution à la modélisation physico-chimique de la rétention de radioéléments à vie longue par des matériaux argileux. Ph.D. thesis, Paris.

Gouder, T., Oppeneer, P.M., Huber, F., Wastin, F., Rebizant, J., 2005. Photoemission study of the electronic structure of Am, AmN, AmSb, and Am2O3 films. Physical Review B 72 (115122), 1–7.

Guillaumont, R., Fanghänel, T., Fuger, J., Grenthe, I., Neck, V., Palmer, D.A., Rand, M.H., 2003. Update on the Chemical Thermodynamics of Uranium, Neptunium, Plutonium, Americium and Technetium. Nuclear Energy Agency Organisation for Economic Co-Operation and Development, Issy-les-Moulineaux (France).

Gustafsson, J.P., Persson, I., Kleja, D.B., van Schaik, J.W.J., 2007. Binding of iron(III) to organic soils: EXAFS spectroscopy and chemical equilibrium modeling. Environmental Science & Technology 41 (4), 1232–1237.

Hartmann, E., Geckeis, H., Rabung, T., Luetzenkirchen, J., Fanghaenel, T., 2008. Sorption of radionuclides onto natural clay rocks. Radiochimica Acta 96 (9-11), 699–707.

Herm, M., 2012. Untersuchung der Löslichkeit und Speziation von drei- und sechswertigen Actiniden in nitrathaltigen salinaren Lösungen. Diploma Thesis, Karlsruhe.

Hertam, A., 2011. 11-B-NMR spektroskopische Untersuchungen zum Lösungszustand von Boraten in konzentrierten Salzlösungen. Diploma Thesis, Freiberg, Germany.

Hinz, K., 2015. Interaction of Ln(III) and An(III/IV/V/VI) with borate in dilute to concentrated NaCl, CaCl2 and MgCl2 solutions. Ph.D. Thesis, Karlsruhe, 157 pp.

Hinz, K., Altmaier, M., Gaona, X., Rabung, T., Schild, D., Richmann, M., Reed, D.T., Alekseev, E.V., Geckeis, H., 2015. Interaction of Nd(III) and Cm(III) with borate in dilute to concentrated alkaline NaCl, MgCl2 and CaCl2 solutions: solubility and TRLFS studies. New Journal of Chemistry 39 (2), 849–859.

Hixon, A.E., Arai, Y., Powell, B.A., 2013. Examination of the effect of alpha radiolysis on plutonium(V) sorption to quartz using multiple plutonium isotopes. Journal of Colloid and Interface Science 403, 105–112.

Hixon, A.E., Powell, B.A., 2014. Observed Changes in the Mechanism and Rates of Pu(V) Reduction on Hematite As a Function of Total Plutonium Concentration. Environmental Science & Technology 48 (16), 9255–9262.

Holman, D.A., Bennett, D.W., 1994. A multicomponent kinetics study of the anaerobic decomposition of aqueous sodium dithionite. Journal of Physical Chemistry 98 (50), 13300–13307.

Huber, F., Schild, D., Vitova, T., Rothe, J., Kirsch, R., Schaefer, T., 2012. U(VI) removal kinetics in presence of synthetic magnetite nanoparticles. Geochimica et Cosmochimica Acta 96, 154–173.

Huittinen, N., Rabung, T., Schnurr, A., Hakanen, M., Lehto, J., Geckeis, H., 2012. New insight into Cm(III) interaction with kaolinite - Influence of mineral dissolution. Geochimica et Cosmochimica Acta 99, 100–109.

Hur, J., Williams, M.A., Schlautman, M.A., 2006. Evaluating spectroscopic and chromatographic techniques to resolve dissolved organic matter via end member mixing analysis. Chemosphere 63 (3), 387–402.

Inoue, Y., Tochiyama, O., 1982. Solvent extraction of neptunium (v) by thenoyltrifluoroacetone and 1,10-phenanthroline or tri-n-octylphosphine oxide. Radiochimica Acta 31 (3-4), 193–196.

Inoue, Y., Tochiyama, O., 1983. Study of the complexes of Np(V) with organic ligands by solvent extraction with TTA and 1, 10-phenanthroline. Polyhedron 2 (7), 627–630.

Karlsson, T., Persson, P., 2010. Coordination chemistry and hydrolysis of Fe(III) in a peat humic acid studied by X-ray absorption spectroscopy. Geochimica et Cosmochimica Acta 74 (1), 30–40.

Keizer, M.G., van Riemsdijk, W.H., 1999. ECOSAT - A computer Program for the calculation of speciation and Transport in soil-water systems, Version 4.8. Wageningen University, Wageningen, Netherlands.

Kimura, T., Choppin, G.R., Kato, Y., Yoshida, Z., 1996. Determination of the hydration number of Cm(III) in various aqueous solutions. Radiochimica Acta 72 (2), 61–64.

Kinniburgh D. G., Cooper D. M., 2009. PhreePlot: Creating graphical output with PHREEQC.

Kiprop, A.K., 2009. Synthesis and characterization of fulvic acids in the C-H-O, C-H-O-N and C-H-O-N-S systems. UV-Visible spectroscopic investigations of uranyl(VI)-fulvate complexation as a function of pH at 25oC and 1 bar. Ph.D. Thesis, UMR 7566 G2R, Nancy (France).

Kiprop, A.K., Coumon, M.-C.J., Pourtier, E., Kimutai, S., Kirui, S., 2013. Synthesis of Humic and Fulvic Acids and their Characterization using Optical Spectroscopy (ATR-FTIR and UV-Visible). International J. Appl. Sci. Technol. Vol. 3 (No. 8).

Knauss, K.G., Wolery, T.J., Jackson, K.J., 1990. A new approach to measuring pH in brines and other concentrated electrolytes. Geochimica et Cosmochimica Acta 54 (5), 1519–1523.

Korshin, G.V., Li, C.W., Benjamin, M.M., 1997. Monitoring the properties of natural organic matter through UV spectroscopy: A consistent theory. Water Research 31 (7), 1787–1795.

Křepelová, A., 2007. Influence of humic acid on the sorption of uranium(VI) and americium(III) onto kalonite. Dissertation, Dresden, Germany.

Larson, D.T., Haschke, J.M., 1981. XPS-AES characterization of plutonium oxides and oxide carbide. The existence of plutonium monoxide. Inorganic Chemistry 20 (7), 1945–1950.

Larson, D.T., Motyl, K.M., 1990. Detection of plutonium hydride using X-ray photoelectron spectroscopy. Journal of Electron Spectroscopy and Related Phenomena 50 (1), 67–76.

Liu, X., Ryan, D.K., 1997. Analysis of fulvic acids using HPLC/UV coupled to FT-IR spectroscopy. Environmental Technology 18 (4), 417–423.

Lucchini, J.-F., Borkowski, M., Richmann, M.K., Ballard, S., Reed, D.T., 2007. Solubility of Nd3+ and UO22+ in WIPP brine as oxidation-state invariant analogs for plutonium. Journal of Alloys and Compounds 444, 506–511.

Lucks, C., Rossberg, A., Tsushima, S., Foerstendorf, H., Scheinost, A.C., Bernhard, G., 2012. Aqueous Uranium(VI) Complexes with Acetic and Succinic Acid: Speciation and Structure Revisited. Inorganic Chemistry 51 (22), 12288–12300.

MacCarthy, P., 1985. Spectroscopic methods (other than NMR) for determining functionality in humic substances, in: Aiken, R., McKnight, D.M., Wershaw, R.L., MacCarthy, P. (Eds.), Humic substances in soil, sediment and water: Geochemistry, isolation and characterization. Wiley - Interscience, New York, NY, pp. 527–559.

Marquardt, C.M., Seibert, A., Artinger, R., Denecke, M.A., Kuczewski, B., Schild, D., Fanghanel, T., 2004. The redox behaviour of plutonium in humic rich groundwater. Radiochimica Acta 92 (9-11), 617–623.

Marques Fernandes, M., Baeyens, B., Bradbury, M.H., 2008. The influence of carbonate complexation on lanthanide/actinide sorption on montmorillonite. Radiochimica Acta 96 (9-11), 691–697.

Marques Fernandes, M., Baeyens, B., Daehn, R., Scheinost, A.C., Bradbury, M.H., 2012. U(VI) sorption on montmorillonite in the absence and presence of carbonate: A macroscopic and microscopic study. Geochimica et Cosmochimica Acta 93, 262–277.

Marsac, R., Banik, N.l., Luetzenkirchen, J., Marquardt, C.M., Dardenne, K., Schild, D., Rothe, J., Diascorn, A., Kupcik, T., Schaefer, T., Geckeis, H., 2015a. Neptunium redox speciation at the illite surface. Geochimica et Cosmochimica Acta 152, 39–51.

Marsac, R., Banik, N.l., Marquardt, C.M., Kratz, J.V., 2014. Stabilization of polynuclear plutonium(IV) species by humic acid. Geochimica et Cosmochimica Acta 131, 290–300.

Marsac, R., Banik, N.L., Luetzenkirchen, J., Buda, R.A., Kratz, J.V., Marquardt, C.M., 2015b. Modeling plutonium sorption to kaolinite: Accounting for redox equilibria and the stability of surface species. Chemical Geology 400, 1–10.

Martin, C.J., Bhatnagar, G.M., 1966. Unfolding reactions of proteins. I. Kinetic and equilibrium measurements of diisopropylphosphorylchymotrypsin and chymotrypsinogen in urea. Biochemistry 5 (4), 1230–1241.

Moore, R.C., Borkowski, M., Bronikowski, M.G., Chen, J.F., Pokrovsky, O.S., Xia, Y.X., Choppin, G.R., 1999. Thermodynamic modeling of actinide complexation with acetate and lactate at high ionic strength. Journal of Solution Chemistry 28 (5), 521–531.

Móra, S., Elöudi, P., 1968. Investigation of the Near and Far Ultraviolet Denaturation Difference Spectra of Dehydrogenases. European Journal of Biochemistry 5 (4), 574–582.

Mullet, M., Guillemin, Y., Ruby, C., 2008. Oxidation and deprotonation of synthetic Fe-II-Fe-III (oxy)hydroxycarbonate Green Rust: An X-ray photoelectron study. Journal of Solid State Chemistry 181 (1), 81–89.

Munchow, V., Steudel, R., 1994. The Decomposition of Aqueous Dithionite and its Reactions with Polythionates SNO62- (N = 3-5) Studied by Ion-Pair Chromatography. Zeitschrift für Anorganische und Allgemeine Chemie 620 (1), 121–126.

Neck, V., Altmaier, M., Fanghänel, T., 2007. Solubility of plutonium hydroxides/hydrous oxides under reducing conditions and in the presence of oxygen. Comptes Rendus Chimie 10 (10-11), 959–977.

Neck, V., Altmaier, M., Rabung, T., Lützenkirchen, J., Fanghänel, T., 2009. Thermodynamics of trivalent actinides and neodymium in NaCl, MgCl2, and CaCl2 solutions:

Solubility, hydrolysis, and ternary Ca-M(III)-OH complexes. Pure and Applied Chemistry 81 (9), 1555–1568.

Neck, V., Kim, J.I., kanellakopulos, B., 1992. Solubility and Hydrolysis Behaviour of Neptunium(V). Radiochimica Acta 56 (1), 25–30.

Nitsche, H., Roberts, K., Xi, R.H., Prussin, T., Becraft, K., Almahamid, I., Silber, H.B., Carpenter, S.A., Gatti, R.C., Novak, C.F., 1994. Long-term Plutonium Solubility and Speciation Studies in a Synthetic Brine. Radiochimica Acta 66-7, 3–8.

Novak, C.F., Borkowski, M., Choppin, G.R., 1996. Thermodynamic Modeling of Neptunium(V)-Acetate Complexation in Concentrated NaCl Media. Radiochimica Acta 74, 111–116.

Parkhurst, D.L., Appelo, C., 1999. User's guide to PHREEQC (Version 2): A computer program for speciation, batch-reaction, one-dimensional transport, and inverse geochemical calculations. Water-Resources Investigations Report 99-4259.

Pavón, J.C., de Torres, A.G., Ojeda, C.B., Rojas, F.S., Alonso, E.I., 2012. Derivative Techniques in Molecular Absorption, Fluorimetry and Liquid Chromatography as Tools for Green Analytical Chemistry, in: , Handbook of Green Analytical Chemistry, pp. 245–259.

Pearson, F.J., Tournassat, C., Gaucher, E.C., 2011. Biogeochemical processes in a clay formation in situ experiment: Part E - Equilibrium controls on chemistry of pore water from the Opalinus Clay, Mont Terri Underground Research Laboratory, Switzerland. Applied Geochemistry 26 (6), 990–1008.

Pelekani, C., Newcombe, G., Snoeyink, V.L., Hepplewhite, C., Assemi, S., Beckett, R., 1999. Characterization of natural organic matter using high performance size exclusion chromatography. Environmental Science & Technology 33 (16), 2807–2813.

Perkampus, H.-H., 1992. UV-VIS Spectroscopy and Its Applications. Springer Berlin Heidelberg, Berlin, Heidelberg, 1 online resource.

Perminova, IV, Frimmel, F.H., Kudryavtsev, A.V., Kulikova, N.A., Abbt-Braun, G., Hesse, S., Petrosyan, V.S., 2003. Molecular weight characteristics of humic substances from different environments as determined by size exclusion chromatography and their statistical evaluation. Environmental Science & Technology 37 (11), 2477–2485.

Petrov, V.G., Kalmykov, S.N., Altmaier, M., 2011. Solubility and phase transformations of Np(V) hydroxide in solutions with different ionic strengths. Moscow University Chemsitry Bulletin 66 (2), 107–115.

Piccolo, A., 2001. The supramolecular structure of humic substances. SOIL SCIENCE 166 (11), 810–832.

Poinssot, C., Baeyens, B., Bradbury, M.H., 1999. Experimental and modelling studies of caesium sorption on illite. Geochimica et Cosmochimica Acta 63 (19-20), 3217–3227.

Pokrovsky, O.S., Choppin, G.R., 1997. Neptunium(V) Complexation by Acetate, Oxalate and Citrate in NaClO4 Media at 25°C. Radiochimica Acta 79 (3), 167–171.

Powell, B.A., Fjeld, R.A., Di Kaplan, Coates, J.T., Serkiz, S.M., 2005. PU(V)0(2)(+) adsorption and reduction by synthetic hematite and goethite. Environmental Science & Technology 39 (7), 2107–2114.

Rabung, T., Altmaier, M., Neck, V., Fanghänel, T., 2008. A TRLFS study of Cm(III) hydroxide complexes in alkaline CaCl<inf>2</inf> solutions. Radiochimica Acta 96 (9-11), 551–559.

Rabung, T., Pierret, M.C., Bauer, A., Geckeis, H., Bradbury, M.H., Baeyens, B., 2005. Sorption of Eu(III)/Cm(III) on Ca-montmorillonite and Na-illite. Part 1: Batch sorption and time-resolved laser fluorescence spectroscopy experiments. Geochimica et Cosmochimica Acta 69 (23), 5393–5402.

Rai, D., Hess, N.J., Felmy, A.R., Moore, D.A., Yui, M., Vitorge, P., 1999. A thermodynamic model for the solubility of PuO2(am) in the aqueous K+-HCO3--CO32--OH--H2O system. Radiochimica Acta 86 (3-4), 89–99.

Rao, L., Tian, G., Srinivasan, T.G., Zanonato, P., Di Bernardo, P., 2010. Spectrophotometric and calorimetric studies of Np(V) complexation with acetate at various temperatures from T=283 to 343 K. Journal of Solution Chemistry 39 (12), 1888–1897.

Rao, L.F., Srinivasan, T.G., Garnov, A.Y., Zanonato, P.L., Di Bernardo, P., Bismondo, A., 2004. Hydrolysis of neptunium(V) at variable temperatures (10-85 degrees C). Geochimica et Cosmochimica Acta 68 (23), 4821–4830.

Rashid, M.A., 1985. Geochemistry of Marine Humic Compounds. Springer New York, New York, NY, 300 pp.

Reiller, P.E., Evans, N.D.M., Szabo, G., 2008. Complexation parameters for the actinides(IV)-humic acid system: a search for consistency and application to laboratory and field observations. Radiochimica Acta 96 (6), 345–358.

Runde, W., 2011. Effect of chloride on actinyl(V) and (VI) speciation and solubility: the formation of ternary complexes.: Book of abstracts. 13th International Conference on the Chemistry and Migration Behaviour of Actinides and Fission Products in the Geosphere, Beijing, China, September, 18-23, 2011,, 2011, Beijing.

Salentine, C.G., 1983. High-field 11B NMR of alkali borates. Aqueous polyborate equilibria. Inorganic Chemistry 22 (26), 3920–3924.

Savitzky, A., Golay, M.J.E., 1964. Smoothing and Differentiation of Data by Simplified Least Squares Procedures. Anal. Chem. 36 (8), 1627–1639.

Schafer, T., Hertkorn, N., Artinger, R., Claret, F., Bauer, A., 2003. Functional group analysis of natural organic colloids and clay association kinetics using C(1s) spectromicroscopy. Journal de Physique IV 104, 409–412.

Schäfer, T., Buckau, G., Artinger, R., Kim, J.I., Geyer, S., Wolf, M., Bleam, W.F., Wirick, S., Jacobsen, C., 2005. Origin and mobility of fulvic acids in the Gorleben aquifer system: Implications from isotopic data and carbon/sulfur XANES. Organic Geochemistry 36 (4), 567–582.

Schäfer, T., Claret, F., Bauer, A., Griffault, L., Ferrage, E., Lanson, B., 2003. Natural organic matter (NOM)-clay association and impact on Callovo-Oxfordian clay stability in high alkaline solution: Spectromicroscopic evidence. Journal de Physique IV 104, 413–416.

Schnitzer, M., 1978. Humic substances chemistry and reactions, in: Schnitzer, M., Khan, S.U. (Eds.), Soil Organic of Soils. Elsevier, Amsterdam (The Netherlands), pp. 1–64.

Schnurr, A., 2015. Untersuchungen zur Radionuklidsorption an Tonmineraloberflächen bei hohen Ionenstärken. Dissertation, Karlsruhe, 161 pp.

Schnurr, A., Marsac, R., Rabung, T., Luetzenkirchen, J., Geckeis, H., 2015. Sorption of Cm(III) and Eu(III) onto clay minerals under saline conditions: Batch adsorption, laser-fluorescence spectroscopy and modeling. Geochimica et Cosmochimica Acta 151, 192–202.

Seibert, A., Mansel, A., Marquardt, C.M., Keller, H., Kratz, J.V., Trautmann, N., 2001. Complexation behaviour of neptunium with humic acid. Radiochimica Acta 89 (8), 505–510.

Sladkov, V., 2014. Interaction of uranyl with acetate in aqueous solutions at variable temperatures. Journal of Chemical Thermodynamics 71, 148–154.

Striegel, A.M., Yau, W.W., Kirkland, J.J., Bly, D.D., 2009. Modern Size-Exclusion Liquid Chromatography: Practice of Gel Permeation and Gel Filtration Chromatography: Second Edition, in: , Modern Size-Exclusion Liquid Chromatography: Practice of Gel Permeation and Gel Filtration Chromatography: Second Edition, pp. 1–494.

Sutheimer, S.H., Cabaniss, S.E., 1997. Aluminum binding to humic substances determined by high performance cation exchange chromatography. Geochimica et Cosmochimica Acta 61 (1), 1–9.

Tertre, E., Castet, S., Berger, G., Loubet, M., Giffaut, E., 2006. Surface chemistry of kaolinite and Na-montmorillonite in aqueous electrolyte solutions at 25 and 60 degrees C: Experimental and modeling study. Geochimica et Cosmochimica Acta 70 (18), 4579–4599.

Tertre, E., Hofmann, A., Berger, G., 2008. Rare earth element sorption by basaltic rock: Experimental data and modeling results using the "Generalised Composite approach". Geochimica et Cosmochimica Acta 72 (4), 1043–1056.

Tian, G., Martin, L.R., Rao, L., 2010. Complexation of lactate with neodymium(III) and europium(III) at variable Temperatures: Studies by potentiometry, microcalorimetry, optical absorption, and luminescence spectroscopy. Inorganic Chemistry 49 (22), 10598–10605.

Vasiliev, A.N., Banik, N.L., Marsac, R., Froehlich, D.R., Rothe, J., Kalmykov, S.N., Marquardt, C.M., 2015. Np(V) complexation with propionate in 0.5-4 M NaCl solutions at 20-85 degrees C. Dalton Transactions 44 (8), 3837–3844.

Walther, C., Rothe, J., Brendebach, B., Fuss, M., Altmaier, M., Marquardt, C.M., Buechner, S., Cho, H.-R., Yun, J.-I., Seibert, A., 2009. New insights in the formation processes of Pu(IV) colloids. Radiochimica Acta 97 (4-5), 199–207.

Wolf, M., Buckau, G., Geyer, S., 2004. Isolation and characterisation of new batches of GoHy-573 humic and fulvic acids, in: Buckau, G. (Ed.), Humic substances in performance assessment of nuclear waste disposal: Actinide and iodine migration in the far-field., pp. 111–124.

Yamaguchi, T., Sakamoto, Y., Ohnuki, T., 1994. Effect of the complexation on solubility of Pu(IV) in aqueous carbonate system. Radiochimica Acta 66-7, 9–14.

Zavarin, M., Powell, B.A., Bourbin, M., Zhao, P., Kersting, A.B., 2012. Np(V) and Pu(V) Ion Exchange and Surface-Mediated Reduction Mechanisms on Montmorillonite. Environmental Science & Technology 46 (5), 2692–2698.

Zavarin, M., Roberts, S.K., Hakem, N., Sawvel, A.M., Kersting, A.B., 2005. Eu(III), Sim(III), Np(V), Pu(V), and Pu(IV) sorption to calcite. Radiochimica Acta 93 (2), 93–102.

Final Report

Project[a]:

"Interaction and transport of Actinides in natural clay systems in the presence of humic substances and clay organic matter"

Subproject[b] 6:

"Molecular process understanding of interactions between Lanthanide ions and components of homogeneous and heterogeneous saline systems"

K. Brennenstuhl, K. Burek, S. Eidner, M.U. Kumke[#]

University of Potsdam, Institute of Chemistry, Physical Chemistry

Karl-Liebknecht-Str. 24-25, 14476 Potsdam-Golm

[#]kumke@uni-potsdam.de

[a]Deutscher Titel: Rückhaltung endlagerrelevanter Radionuklide im natürlichen Tongestein und in salinaren Systemen

[b]Deutscher Titel: Teilprojekt 6: Zum molekularen Prozessverständnis der Wechselwirkungen von Lanthanoidionen mit Komponenten homogener und heterogener salinarer Systeme

Das diesem Bericht zugrunde liegende Vorhaben wurde mit Mitteln des Bundesministeriums für Wirtschaft und Technologie und dem Förderkennzeichen 02E11011 gefördert. Die Verantwortung für den Inhalt dieser Veröffentlichung liegt bei den Autoren.

Das Forschungsvorhaben war ein Teilprojekt im Forschungsverbund „Rückhaltung endlagerrelevanter Radionuklide im natürlichen Tongestein und in salinaren Systemen“ und erfolgte in Kooperation mit folgenden Institutionen:

Helmholtz-Zentrum Dresden-Rossendorf, Institut für Ressourcenökologie

Karlsruher Institut für Technologie, Institute für Nukleare Entsorgung

Johannes Gutenberg-Universität Mainz, Institut für Kernchemie

Universität des Saarlandes, Institut für Anorganische und Analytische Chemie und Radiochemie

Technische Universität Dresden, Sachgebiet Strahlenschutz, Professur Radiochemie

Universität Heidelberg, Physikalisch Chemisches Institut

Technische Universität München, Fachgebiet Theoretische Chemie

Abstract

In the project processes related to the fate of radionuclides at high ionic strength *I* (0 mol·L^{-1} < *I* < 4 mol·L^{-1})[c] in clay and salt host rock formations, which are typical for the northern part of Germany, were investigated for temperatures *T* < 353 K using optical spectroscopic methods. The fundamental process understanding, which is necessary for the full exploitation of the analytical data, and the improvement as well as the development of analytical (spectroscopic) "tools" were key aspects of the work performed. In the experiments Lanthanide(III) (Ln(III)) ions were used as natural analogs and were investigated using laser-based spectroscopic techniques, especially time-resolved laser fluorescence spectroscopy (TRLFS) and Raman spectroscopy complemented with sum frequency generation (SFG) spectroscopy. Especially Raman and SFG spectroscopy were used to characterize clay mineral surfaces and interlayers of such for structural effects of Ln(III) ions and low molecular weight organic compounds. Potential organic ligands originating for the clay minerals were investigated. Here, naturally occurring polymers such as humic substances (HS) and low molecular weight organics (LMWO) were investigated. In order to bridge the gap between HS and LMWO also synthetic polymers of a known composition were included in order to consider effects that are related to the macromolecular character of HS. In this context in order to mimic certain properties, a novel polymer (polyvinyl benzoic acid) at two different molar weights was synthesized. In the experiments the influence of the temperature and of the overall background concentration (ionic strength) as well as chemical properties (Na vs. Ca, Mg) were elucidated. In addition to organic ligands also borate as a potential inorganic component in the repository was investigated. For the organic ligands on the one hand side the intrinsic fluorescence was evaluated to determine the complexation of different Ln(III) ions and on the other hand side the luminescence of the Ln(III) was analyzed. The sorption on clay mineral surfaces and the complexation with low molecular weight organic ligands and borate as well as model and natural polymers (e.g., HS) were investigated using different Ln(III) ions as luminescence probes. Especially Europium(III) (Eu(III)) was applied as a luminescence probe due to its outstanding sensing capabilities. The analysis of the spectral luminescence intensity distribution revealed difference in the binding by HS and was used in combination with site-selective excitation to identify the presence of different complexes in the sample. Here, especially measurements at ultra low temperatures proofed to be very valuable due to the outstanding spectral resolving power in the identification of different polyborate complexes. From the luminescence data conditional binding constants and their variation with temperature and ionic strength were determined. Moreover, using different excitation schemes for starting the luminescence mechanistic details on the complexation of Ln(III) by organic ligands and effects of different ions used as background electrolytes were evaluated. While under direct excitation conditions an overall luminescence signal was obtained containing possible contributions from non-complexed Ln(III) ions, a sensitized excitation using the ligand as "light collector" yielded only information on the bound part. The da-

[c] 0 mol·L^{-1} means no additional ion were added, ionic strength is determined by the concentration of the Ln(III)

ta were further evaluated for differences in binding sites using competition experiments with other ions such as Ca(II) and Mg(II) in combination with the NICA Donnan model. For the determination of the average distance between bound Ln(III) ions the inter-lanthanide energy transfer (ILET) was applied as a method of choice for distance determinations in the intermediate range of several nanometers. The ILET was applied to different organic polymer as well as to clay mineral samples. For the ILET a couple of Ln(III) ions, one acting as energy donor and the other as the acceptor, are bound in/on the sample. From the distance (= degree of loading) dependence of the donor luminescence, the average distance of bound metal ions was calculated. The interplay between different lanthanide- and ligand-related radiationless deactivation pathways was investigated using different combinations of Ln(III) ions and low molecular weight organic ligands. In the combinations the Lanthanide specific parameters of energy gap between ground and electronically excited states as well as the redox potential were considered. For the ligands the energy of the ligand's triplet state and the redox potential were taken into account. In a systematic evaluation the contribution of the different parameters was determined. The results underline that a thorough understanding of the complex interplay between the ligand- and lanthanide-related electronic (molecular) properties is indispensible for a correct determination of macroscopic parameters such as binding constants. The effect of low molecular organic compounds on the surface and interfacial properties of clay minerals was investigated using Raman- and SFG spectroscopy. The intercalation of small organics in the interlayer could be clearly identified. The intercalation was determined from the alteration in the vibrational frequencies of different hydroxyl groups. Here, the special sensitivity of SFG spectroscopy and Raman microscopy were used to investigate these effects.

1. Introduction

According to a recent study of the BGR[1] clay layers of the Early Cretaceous in Northern Germany are potentially suited to host a deep underground repository for high level nuclear waste. Compared to clay layers so far investigated in other countries the geochemical boundary conditions are special with respect to the ionic strength and the salt concentration of the pore waters present. In contrast to clays investigated in Switzerland, Belgium or France the intrinsic ionic strength *I* of pore waters in Northern Germany is distintly higher (up to $I = 4\ mol \cdot L^{-1}$). A similar situation would also be found in the near field of salt rock formations, which is an alternative option for an underground repository in Germany, in case of water intrusion. This could start corrosion processes of the metal containers and the specific redox chemistry at high ionic strength conditions need to be understood in order to perform reliable model calculations. So high ionic strength is a key parameter to be taken into account in the risk assessment of potential nuclear waste repositories in Germany. However, the speciation of radionuclides under such high ionic strength conditions is hampered by the fact that the data base is lacking respective thermodynamic core data. Moreover, in the early stages of a repository the temperature in the near field may be distinctly elevated by the heat production of the waste materials (depending on the host rock formation the initial temperatures present can be as high as $\sim 200°C$ for salt and $\sim 100°C$ for clay).[1] In contrast to this particular condition the majority of the investigations were performed and the subsequent thermodynamic data were collected for room temperature conditions.

Therefore, the collaborative project was focused on fundamental process understanding related to the fate of radionuclides at high ionic strength *I* ($0\ mol \cdot L^{-1} < I < 4\ mol \cdot L^{-1}$)[c] in clay and salt host rock formations, which are typical for the northern part of Germany. The sorption to clay minerals at high ionic strength and at elevated temperature ($T < 353$ K) as well as the influence of different components present is the system was of interest. The complexation of Actinides (and Lanthanides as natural analogs) with borate and low molecular weight organic compounds in the presence high salt concentrations (NaCl, KCl, $MgCl_2$, $CaCl_2$) and at elevated temperatures was monitored. In the experiments complementary analytical techniques were used to tackle the challenge related to investigations of diffusion of Actinides, the redox chemistry under high ionic strength conditions and the influence of elevated temperature.

The work carried out at the University of Potsdam focused on the interactions between Ln(III) ions (e.g., Eu(III)) as chemical homologue for trivalent actinide ions – like Americium(III) or Curium(III)) with repository relevant inorganic (Borate) and organic ligands. As organic ligands small molecules such as formiate, acetate, or lactate as well as aromatic carboxylic acids, oligomers, and polymers as models for naturally occurring organics in clay minerals were taken into account. In the project Ln(III) ions were used as natural analogs and were investigated using laser-based spectroscopic techniques, especially time-resolved laser

fluorescence spectroscopy (TRLFS) and Raman spectroscopy (complemented with sum frequency generation spectroscopy). Ln(III) were applied as a luminescence probes due to their outstanding sensing capabilities. The sorption on clay mineral surfaces and the complexation with low molecular weight organic ligands and borate as well as model and natural polymers (e.g., humic substances) was investigated. In addition also the interaction of organic compounds and clay minerals was monitored by Raman microscopy and SFG spectroscopy to monitor the interactions between both from the ligand's point of view.

2. Experimental details

2.1 General experimental details

Lanthanide(III) complexes with model ligands

As model compounds for binding sites in HS, different (hydroxy)benzoic acids were investigated. The relative positions of the hydroxyl- and/or carboxyl group were systematically varied, in order to study the effect of complex formation and of the ligand structure on the luminescence spectra of different Ln(III) ions (Eu(III), Terbium (Tb(III)), Samarium (Sm(III)) and Dysprosium(Dy(III)). All reagents were of analytical grade. All chemicals were ordered from Sigma-Aldrich with the highest purity available.

Ln(III)-complexes with salicylic acid or phthalic acid (see Figure 1S)were prepared from aqueous (using Milli-Q water (Milli-Q Advantage A10, Merck)) stock solution of Ln(III)-salts ($TbCl_3 \cdot xH_2O$, $SmNO_3 \cdot 6H_2O$, $DyNO_3 \cdot 5H_2O$, $EuCl_3 \cdot 6H_2O$) and model ligands with a concentration of $c = 10^{-2}$ mol·L^{-1}. The concentrations as well as the molar ratio of Ln(III) ions and model ligands investigated are summarized in Table 1.

Table 1: Concentrations and molar ratio of Tb(III) /Sm(III) / Dy(III) and ligands.

	Molar ratio	*c* (Ln(III)) / mol·L^{-1}	*c* (ligand) / mol·L^{-1}
Tb(III) salicylic acid	1:99	$1.0 \cdot 10^{-4}$	$9.9 \cdot 10^{-3}$
Tb(III) phthalic acid	1:5	$1.0 \cdot 10^{-4}$	$5.0 \cdot 10^{-4}$
Sm(III) salicylic acid	1:45	$1.0 \cdot 10^{-4}$	$4.5 \cdot 10^{-3}$
Sm(III) phthalic acid	1:3	$1.0 \cdot 10^{-4}$	$3.0 \cdot 10^{-4}$
Dy(III) salicylic acid	1:45	$1.0 \cdot 10^{-4}$	$4.5 \cdot 10^{-3}$
Dy(III) phthalic acid	1:6	$1.0 \cdot 10^{-4}$	$6.0 \cdot 10^{-4}$

From speciation analysis (based on stability constants taken from literature (see Table 1S)) the molar ratios of the prepared solutions were calculated to the point where the solution contains the highest possible amount of Ln(III) complexes with one ligand (see Figure 2S). In Table 2S the calculated species distributions are shown.

The p*H* value was adjusted to a point at which the model ligand was in the single deprotonated form to ensure complexation with the Ln(III) ion. Furthermore, acid conditions were chosen to avoid the formation of Ln(III) hydroxyl complexes as well as carbonates. Speciation diagrams of the model ligands were calculated from pK_a values taken from literature (see Table 2S and Figure 3S). The p*H* of salicylic acid containing solutions was adjusted to 5.0 and of phthalic acid containing solutions to 4.2 with sodium hydroxide and hydrochloric acid. All solutions were stored in the fridge and soonest measured after five days to ensure an adjusted complex equilibrium.

For the Eu(III) solutions containing salicylic acid or phthalic acid as background electrolyte 0.1 mol·L^{-1} sodium perchlorate solution was applied. The concentration of Eu(III) was in both cases $c_{Eu(III)}$ = 5.7·10^{-3} mol·L^{-1} and of the model ligands 3.4·10^{-2} mol·L^{-1}. From speciation analysis based on stability constants taken from literature (see Table 1S) it was calculated that only a very minor concentration of the "free" Eu(III) aquo complex was present (see Table 2S and Figure 4S). To avoid formation of hydroxyl and carbonate complexes the p*H* was adjusted to five with sodium hydroxide and hydrochloric acid. Each solution was equilibrated for approximately five days prior to the luminescence measurements. The samples were stored in the dark at room temperature (RT).

Influence of ionic strength

Aqueous Ln(III) samples were prepared by solving Ln(III) salts in Milli-Q water. The variation of the ionic strength *I* (0.1 mol·L^{-1}, 1 mol·L^{-1} and 4 mol·L^{-1}) was realised by the addition of sodium chloride. Sodium chloride purchased from Aldrich with the highest purity available.

Synthesis of polyvinyl benzoic acid

In a three-necked flask equipped with reflux condenser 1 g (6.7 mmol) 4-vinylbenzoic acid, 10 mL dimethylformamide, 0.189 g (0.67 mmol, short-chain) or 1.89 mg (0.067 mmol, long-chain) of the initiator 4,4'-Azobis(4-cyano pentanoic acid) was mixed together under nitrogen atmosphere. Afterwards the mixture was heated to 65 °C and stirred for 24 hours. The reaction solution was transferred over a syringe filter into 200 mL of diethyl ether. In the next step, the diethyl ether was decanted. The polymer was washed with 200 mL of Diethyl ether, sucked off via Glass frit and dried over three days under high vacuum.

Clay samples

Kaolinite samples were received from Clay Mineral Society. As samples kaolinite Kaolin KGa-1b (low-defect) and Kaolin KGa-2 (high-defect) were used in this study. KGa-2 is a less crystallized, whereas KGa-1b is a well crystallized kaolinite.[2]

Synthesis of intercalation compounds

The synthesis of intercalation compounds of potassium acetate and kaolinite followed a slightly modified instruction of Frost et al.[3] To acetic acid potassium hydroxide was added and subsequently diluted with deionized water to give a 60 % (for some experiments also 30 %) potassium acetate solution. For the intercalation to 1 mL of this solution 0.3 g kaolinite was added and for 72 hours put on an orbital shaker (compact shaker KS 15, Edmund Bühler GmbH, Hechingen, Germany) with a shaking speed of 350 rpm. The resulting suspension was centrifuged (Centrifuge 5804, Eppendorf Vertrieb Deutschland GmbH, Wesseling-Berzdorf, Germany) for 30 minutes at 8000 rpm. The supernatant was decanted and the remaining solid material dried in a desiccator for at least 48 hours over Sicapent®.

For the intercalation of potassium hexanoate, hexanoic acid and potassium hydroxide were neutralized. Afterwards the solution was evaporated to dryness, which gives potassium hexanoate. For the intercalation a dimethyl sulfoxide (DMSO) kaolinite (KGa-1b) intercalation

compound (rate of intercalation around 71 % from XRD measurements) was used as starting material. From this precursor 0.5 g were added to a solution of 13.5 g potassium hexanoate in 12.5 mL of water. The suspension was stirred for two hours at 50 °C and sucked off through a glass frit. The solid was washed three times with water. Afterwards it was vacuum dried overnight.

The synthesis of the DMSO-KGA-1b intercalation compound followed a synthesis publicized by Li et al., but without any precondition of the kaolinite.[4] In a 100 mL round bottom flask, 4 g KGa-1b, 64 mL DMSO and 15 mL Methanol were mixed. This suspension was heated to reflux at 85 °C for 96 hours. After cooling down to room temperature, the suspension was filtered through a glass frit. The solid material was washed three times with ethanol and dried overnight under vacuum.

Eu(III) LMWC complexes with Kaolin KGa-2

To a Eu(III) solution ($c_{Eu(III)} = 4 \cdot 10^{-4}$ mol·L^{-1}, background electrolyte 0.01 mol·L^{-1} $NaClO_4$)) a low molecular weight compounds (LMWC) (e. g., formic, acetic, propionic, or glycolic acid) with a concentrations between 0 mol·L^{-1} ≤ c_{LMWO} ≤ 10^{-1} mol·L^{-1} was added. Kaolin KGa-2 was added and the p*H* was adjusted to five. After stirring for one hour, the suspension was centrifuged for 30 minutes at 7000 rpm. Solid and supernatant were separated and the solid fraction was dried overnight at 35 °C. With the dried solids, time-resolved luminescence measurements were carried out.

2.2 Methods

Luminescence measurements of Lanthanide(III) complexes with model ligands

The luminescence decay times of Tb(III) complexes in the temperature range between 278 K < *T* < 353 K were recorded by using a Fluoromax 4 spectrofluorometer (*HoribaJobin-Yvon*) coupled to a single photon counting controller (*HORIBA Scientific*) in the multichannel scaling mode. Tb(III) was directly excited with λ_{ex} = 378 nm and the detected emission wavelength was λ_{em} = 542 nm. Luminescence decay time curves of Tb(III) complexes were also measured by indirect excitation of Tb(III) (Tb(III) salicylate: λ_{ex} = 325 nm, Tb(III) phthalate: λ_{ex} = 330 nm). In order to maintain the desired temperature, a thermostat system was used (*LAUDA, Proline RP 845 C*).

Time-resolved laser luminescence spectroscopy measurements of Sm(III), Dy(III) and Eu(III) complexes were performed using a pulsed Nd-YAG Laser (Spectra Physics) combined with an optical parametric oscillator (*GWU Lasertechnik*) for excitation. The luminescence was detected using an iCCD-camera coupled spectrograph (*Andor Technology*). For the Sm(III) and Dy(III) complexes the emission spectra were recorded in the spectral range of 457 nm ≤ λ_{em} ≤ 741 nm, the emission spectra of the Eu(III) complexes were recorded in the range of 575 nm < λ_{em} < 636 nm. For the measurements in the hole temperature range (77 K ≤ *T* ≤ 353 K) an excitation wavelength λ_{ex} = 477 nm was applied to excite the Sm(III) ion directly ($^4I_{11/2} \leftarrow {}^6H_{5/2}$-transition). For Dy(III) complexes λ_{ex} = 450 nm ($^4I_{15/2} \leftarrow {}^6H_{15/2}$-transition)

and for Eu(III) complexes λ_{ex} = 394 nm was chosen ($^5L_6 \leftarrow {}^7F_0$-transition). One complete luminescence decay was measured by collecting 100 to 130 luminescence spectra at increasing δt using a step width between 6 μs < Δt < 10 μs for Sm(III) or Dy(III) and of Δt = 50 μs for Eu(III). For one luminescence spectra five laser pulses were accumulated. For the Eu(III) measurements in the time-gated detection scheme, the initial delay time after the laser flash (δt) was varied between 0.4 μs < δt < 30.4 μs (depending on the temperature) in order to discriminate luminescence originating from the luminescence of the $^5D_1 \rightarrow {}^7F_0$ transition. In the case of Sm(III) and Dy(III) an initial delay time of δt = 152 μs was used. The time dependence of the Sm(III), Dy(III) and Eu(III) luminescence was analysed based on a box car technique. To adjust the temperature in the range 278 K < *T* < 353 K a thermostat was used (Lauda).

An Oxford Dewar was used for the luminescence decay time measurements of Sm(III), Dy(III) and Eu(III) as well as Tb(III) complexes in the lower temperature range (77 K ≤ *T* ≤ 275 K).

The time-resolved measurements of Tb(III) complexes in the lower temperature range (77 K ≤ *T* ≤ 275 K) were recorded as well with a pulsed Nd-YAG Laser (Spectra Physics) combined with an optical parametric oscillator (*GWU Lasertechnik*). The luminescence was detected with an iCCD-camera coupled spectrograph (*Andor Technology*). The excitation wavelength λ_{ex} = 378 nm (according to $^5G_5 \leftarrow {}^7F_6$-transition) was used to excite the Tb(III) ion directly and the emission spectra were recorded in the spectral range of 400 nm ≤ λ_{em} ≤ 739 nm. By collecting 120 luminescence spectra (100 accumulations for one luminescence spectra) at increasing δt while using a step width of Δt = 500 μs a complete luminescence decay was measured. The initial delay time after the laser flash was δt = 1 μs. The time dependence of the Tb(III) luminescence was analyzed by using the boxcar technique.

For luminescence spectroscopy at ultra low temperatures, sample solutions were transferred to quartz tubes (40 mm length x 4 mm o. d. x 2 mm i.d.; volume ca. 100 μL), and sealed with rubber septums. Samples were cooled to ~ 5 K in a lab-built sample holder, mounted on a closed-cycle helium refrigerator (SRDK-205 cryostat; Janis Research Company). The samples were excited using a dye laser (LPD 3002; Lambda Physics, Göttingen, Germany) pumped by a Nd:YAG laser (QuantaRay, Spectra Physics). Coumarin 153 (Radiant Laser Dyes & Accessories GmbH) was used as laser dye. The laser was operated at 20 Hz with a pulse width of 10 ns. The Eu(III) emission was collected at a 90 ^{O} angle relative to the excitation light by two 10 cm F/4 quartz lenses and focused on the entrance slit of a triple monochromator (Spex 1877). For detection an intensified charged-coupled device (iCCD) camera (iStar DH720-25U-03; Andor Technologies) was used in the gated mode. In order to obtain adequate stray light suppression, delay and gate width of the iCCD were set to 1 μs and 10 ms, respectively. The achieved spectral resolution in the emission dimension was 0.1 nm (3 cm^{-1}) in a total spectral detection window of 37 nm. Each emission spectrum was accumulated for 1 s to 5 s, comprising 20 to 100 laser pulses. The excitation wavelength was varied

with a scan rate ranging from 0.001 nm/s to 0.05 nm/s, yielding a resolution in the excitation dimension between 0.03 cm^{-1} and 1.5 cm^{-1}. The decay curves were extracted from time series of emission spectra (delay 1 µs, gate width 10 ms) of 200 spectra. For each sample several decay series were recorded, at each excitation wavelength λ_{exc} corresponding to a separate species in the TLS.

Data analysis

Luminescence decays: In case the luminescence decay curves were monoexponential, they were evaluated according to eq. (1)

$$y = y_0 + B \cdot exp\left(-\frac{t}{\tau}\right) \quad (1)$$

y is the measured luminescence intensity at time *t* after the laser flash, *B* is the luminescence intensity at *t* = 0, τ is the luminescence decay time, and y_0 accounts for residual background signal.

From the in-depth analysis of the Eu(III) luminescence, especially when recorded at cryogenic conditions, a wealth of information can be obtained:

$^5D_0 \rightarrow {}^7F_0$ transition energy: The $^5D_0 \leftarrow {}^7F_0$ transition is extremely weak because of parity forbiddance. It gains intensity in cases in which the symmetry of the Eu(III) complex is lowered, for instance due to the formation of non-centrosymmetric complexes or due to vibrational motion of the ligands. For being non-degenerate the $^5D_0 \leftarrow {}^7F_0$ transition is a powerful indicator for the presence of different coexisting complexes in a sample. Moreover, its energy is very sensitive to specific parameters characterizing the complex. Two partly contradicting effects determine the energy of the $^5D_0 \leftarrow {}^7F_0$ transition: i) the nephelauxetic effect and ii) the splitting of the $^7F_1$ transition, which is dependent on the crystal field exerted by the ligands.

Point symmetry group and asymmetry ratio r: Under site-selective excitation conditions the number of STARK levels in the $^5D_0 \rightarrow {}^7F_1$ and $^5D_0 \rightarrow {}^7F_2$ transitions can be used to determine the point symmetry group of the coordination polyhedron.

The integrated intensity of the $^5D_0 \rightarrow {}^7F_2$ transition is especially sensitive to the complex symmetry. The more the local complex symmetry deviates from inversion symmetry the more the parity forbiddance is relaxed. In contrast, the integrated $^5D_0 \rightarrow {}^7F_1$ emission is not affected and can therefore be used as an internal reference. A change of the "asymmetry ratio *r*" (Equation 2) indicates an alteration of the complex symmetry. In general, an increasing deformation of the coordination polyhedron following the exchange of water molecules by other ligands results in a larger *r* value according to:

$$r = \frac{I(\,^5D_0 \rightarrow {}^7F_2)}{I(\,^5D_0 \rightarrow {}^7F_1)} \quad (2)$$

The asymmetry ratio *r* depends on several other parameters, such as i) the polarizability of the ligands, ii) the complex-related concentration of the ligands, and iii) the dielectric constant of the solvent. Nonetheless, for samples containing the same or very similar ligands, investigated under identical experimental conditions, *r* may be used as a discriminator for different species present in the sample.

Number of water molecules in the first coordination sphere: A major radiationless deactivation pathway of Eu(III) is related to the OH groups present in the first, but also (to a minor extent) in the second coordination sphere of the complex. It has been established that the number of water molecules n_{H2O} in the first coordination sphere of Eu(III) can be determined from luminescence decay time measurements τ_{obs}. The well-known empirical equations of HORROCKS et al. and KIMURA et al. have been extended to account for additional quenching contributions from other ligands and from OH groups in the second coordination sphere with the terms 0.25 and 0.4 n_{OH}, respectively.

$$n_{H_2O} = 1.2\left(\frac{1ms}{\tau_{obs}} - 0.58 - 0.25 - n_{OH} \cdot 0.4\right) \tag{3}$$

This formula was derived at room temperature conditions. Since no influence of temperature on the fluorescence decay time was observed ($\tau_{Eu(H_2O)_{8-9}^{3+}}$ = 100 µs ± 10 µs at 298.15 K and 106 µs ± 10 µs at 4.7 K) it is concluded that the quenching efficiency of OH vibrations is not altered with temperature and thus eq. (3) can also be used at 4.7 K.

The equation takes only the effect of X-H vibrations as possible acceptors for a radiationless energy transfer into account. The presence of (organic) ligands can add additional options for a radiationless deactivation. Especially the triplet state and the redox properties of the ligand may have to be taken into account. In general, the experimental observed luminescence decay time is determined by the rate constants of the different deactivation processes. Here, the fastest process rules the observed decay kinetics. The nature of this process is strongly depending on the particular ligand. The general expression for the luminescence decay time of a Ln(III) complex is:

$$\tau_{Ln(III)\ complexes} = \frac{1}{k_r + k_{pet} + k_{ebt} + (n-x)\cdot k_{OH} + \sum_j k_j^{nr}} \tag{4}$$

Here, the rate constants k_x are related to the respective processes (r = radiative, pet = photo-induced (charge) electron transfer, ebt = energy back transfer, OH = OH quenching, nr = other non-radiative deactivation processes).

The contribution of the different ligand-related processes can extracted from luminescence decay time data of the respective Ln(III) complex and the Ln(III) aquo complex ($[Ln(H_2O)_n]^{3+}$):

$$\frac{1}{\tau_{Ln(III)\ complexes}} - \frac{1}{\tau_{[Ln(H_2O)_n]^{3+}}} = k_{pet} + k_{ebt} - x \cdot k_{OH} \tag{5}$$

In aqueous solution only Sm(III), Dy (III), Tb(III) and Eu(III) show luminescence. Some photophysical parameters of these ions are listed in Table 2.

Table 2: Luminescence deacy times τ of the Ln(III) ions in water (taken from [5]) and life time of the radiative deactivation τ_{rad} (taken from [6]) and the emitting state of selected Ln(III) ions.

Lanthanide(III) ion	τ / µs	τ_{rad} / µs	emitting state
Dy^{3+}	2.5	1850	$^4F_{9/2}$
Tb^{3+}	430	9020	$^5D_4$
Sm^{3+}	2.7	6260	$^4G_{5/2}$
Eu^{3+}	110	9670	$^5D_0$

Temperature dependence of τ - Arrhenius data evaluation

The luminescence decay times τ of the Ln(III) complexes were measured in the temperature range of 77 K < *T* < 353 K. The experimental rate constants $k = 1/\tau$ were evaluated by the Arrhenius equation to determine the activation energy E_a of the overall rate determining process:

$$\ln k = \ln A - \frac{E_a}{R \cdot T} \qquad (6)$$

In case of Ln(III) in complexes with organic ligands *k* was determined according to eq. (6) in order to analyse the temperature dependence of the ligand-related deactivation processes.

Energy transfer

The occurrence of the non-radiative transfer of energy is a well-known photophysical phenomenon. Depended on the mechanism it is differentiated between an exchange of electrons and a resonant energy transfer. The exchange (or Coulomb) interaction requires an overlap of the involved orbitals and happens on short distances, whereas the resonant mechanism is based on a dipole-dipole interaction between an electronically excited donor and acceptor in its ground state. The efficiency of the energy transfer η depends on the distance *R* between donor and acceptor

$$\eta = \frac{R_0^6}{R^6 + R_0^6}. \quad (7)$$

The distance R_0 is called the Förster distance, where the efficiency of the energy transfer is 0.50. The R_0 value is determined by the luminescence quantum efficiency of the donor, the overlap integral of donor's emission spectrum and acceptor's absorption spectrum as well as the refractive index of the surrounding medium, and by the orientation factor κ^2. Horrocks and coworkers calculated Förster distances for different donor/acceptor pairs.[7] They found a Förster distance of 8.53 Å (9.12 Å) for the pair Eu(III)/Nd(III) (Tb(III)/Nd(III)) in solution. The energy transfer efficiency can be calculated from luminescence decay time τ or luminescence intensity *I*.

$$\eta = 1 - \frac{I_{\mathrm{DA}}}{I_{\mathrm{D}}} = 1 - \frac{\tau_{\mathrm{DA}}}{\tau_{\mathrm{D}}} \quad (8)$$

Here, the index "DA" means donor's luminescence intensity *I* or luminescence decay time τ in presence of an acceptor and "D" reflects *I* or τ in absence of an acceptor. By knowing the Förster distance R_0 distances of suitable Ln(III) ions can be deduced from stationary or time-resolved luminescence measurements.

Complexation of Lanthanide(III) ions by humic substances

The complexation of Ln(III) ions by HS can be described by a simple 1:1 complex formation

$$\mathrm{Ln}^{3+} + \mathrm{HS}^{y-} \leftrightharpoons [\mathrm{LnHS}]^{3-y}.$$

For a reaction like this, a mass action law can be formulated

$$\beta = \frac{c([\mathrm{LnHS}]^{3-y})}{c(\mathrm{Ln}^{3+}) \cdot c(\mathrm{HS}^{y-})}. \quad (9)$$

In the equation above $c([\mathrm{LnHS}^{3-y}])$, $c(\mathrm{Ln}^{3+})$ and $c(\mathrm{HS}^{y-})$ are the concentrations of the complex formed, the concentration of the Ln(III) ions in solution and the concentration of free binding sites in the HS, respectively. Due to the formation of a complex between Ln(III) ions and HS, the intrinsic fluorescence of HS is quenched. The quenching of the intrinsic fluorescence can be used to derive conditional complexation constants β from titration experiments following an approach of Ryan and Weber.[8,9] In these experiments the concentration of the Ln(III) ion is subsequently increased and the fluorescence intensity is measured. The intrinsic fluorescence intensities at a certain Ln(III) concentration is given relative to the intrinsic HS fluorescence, when no Ln(III) ions are present. From these I_{rel} the conditional complexation constants β can be derived using applying following equation.

$$I_{\mathrm{rel}} = 1 + \frac{I_{\mathrm{ML,rel}} - 1}{2\beta c_{\mathrm{L}}} \left(\beta c_{\mathrm{L}} + \beta c_{\mathrm{M}} + 1 - \sqrt{(\beta c_{\mathrm{L}} + \beta c_{\mathrm{M}} + 1)^2 - 4\beta^2 c_{\mathrm{L}} c_{\mathrm{M}}} \right) \quad (10)$$

In this equation $I_{\mathrm{ML,rel}}$ is the relative remaining intrinsic HS fluorescence at high Ln(III) ion concentrations, c_{M} is the total Ln(III) ion concentration and c_{L} the total number of binding

sites, which is given by the third of the number of charges[d] in the HS at a given p*H* value. The charge density was calculated from a modified Henderson-Hasselbalch equation.[10]

$$Q_{\mathrm{tot}} = \frac{Q_1}{1+(K_1[H^+])^{1/n_1}} + \frac{Q_2}{1+(K_2[H^+])^{1/n_2}} \qquad (11)$$

The parameters K_1, K_2, n_1, n_2, Q_1 and Q_2 are available from the International Humic Substance Society (IHSS) and are listed in Table 3.

Table 3: p*H* titration and elemental composition parameters of some HS under investigation given by the IHSS [10]. Abbreviations: SR – Suwannee River, PP – Pahokee Peat, HA – humic acid, FA – fulvic acid.

	C content / %	Q_1 / meq/g·C	lg(K_1)	n_1	Q_2 / meq/g·C	lg(K_2)	n_2
SRHA	52.63	9.74	4.35	3.3	4.48	10.44	1.73
PPHA	56.37	9.64	4.22	3.2	0.94	9.86	1
SRFA	52.44	11.66	3.76	3.24	2.05	9.84	1.45
PPFA	50.45	14.22	3.99	3.33	0.76	9.57	1

Refractive index

The refractive index was measured using a multi-wavelength refractometer (DSR-λ, Schmidt+Haensch) in the wavelength range of 400 nm < λ < 1000 nm. The measurements were carried out at 20 °C as well as 35 °C and data points were taken at seven wavelength (403,3 nm; 495,9 nm; 598,7 nm; 669,9 nm; 742,3 nm; 842,8 nm; 945 nm). The experimental data were interpolated with the help of a Cauchy equation and evaluated by a self-written program in LabView[e].

Vibrational spectroscopy measurements

Theoretical background

Due to the interaction of an electromagnetic wave with matter, the electric field ***E*** can induce a dipole momentum μ in the matter.[11]

$$\boldsymbol{\mu} = \boldsymbol{\mu_0} + \boldsymbol{\alpha E} + \boldsymbol{\beta_{SFG} E^2} + \boldsymbol{\gamma E^3} + \cdots \qquad (12)$$

The strength of the induced dipole moment depends on the polarizability α, and the first and second order hyperpolarizabilities β_{SFG} and γ, respectively. A static dipole momentum is reflected by $\boldsymbol{\mu}_0$. In a bulk phase, the single induced dipole momenta give a macroscopic property, the polarization ***P***, which can be expressed by

$$\boldsymbol{P} = \boldsymbol{\varepsilon_0}\left(\boldsymbol{\chi^{(1)} E} + \boldsymbol{\chi^{(2)} E^2} + \boldsymbol{\chi^{(3)} E^3} + \cdots\right). \qquad (13)$$

[d] Due to coordination of one Ln(III) ion, its three positive charges have to be compensated.

[e] The programm in LabView was written by Marvin Münzberg

$$\boldsymbol{P} = \boldsymbol{P}^{(1)} + \boldsymbol{P}^{(2)} + \boldsymbol{P}^{(3)} + \cdots$$

Here, ε_0 is the vacuum permittivity, $\chi^{(1)}$ are the first order (linear) susceptibility as well as $\chi^{(2)}$ and $\chi^{(3)}$ the non-linear second and third order susceptibilities, respectively. Non-linear effects can only be observed, when strong electric fields are applied. For a sum-frequency generation (SFG) experiment, two electric fields resulting from visible and IR laser radiation have to overlap in space and time on the desired sample. The electric field felt by the matter is

$$\boldsymbol{E} = \boldsymbol{E}_{\mathrm{IR}} \cos(\omega_{\mathrm{IR}} t) + \boldsymbol{E}_{\mathrm{vis}} \cos(\omega_{\mathrm{vis}} t) \tag{14}$$

with $\boldsymbol{E}_{\mathrm{IR}}$ and $\boldsymbol{E}_{\mathrm{vis}}$ being the electric field of the IR light with a frequency ω_{IR} and the electric field of the vis light ω_{vis}, respectively. For SFG only the second term in eq. (13) has to be considered. By inserting the expression for $\boldsymbol{E}$ given in eq. (14) into $\boldsymbol{P}^{(2)}$ and solving the quadratic dependence of $\boldsymbol{E}$, gives four different electric fields. One of them is a static one, a second gives the doubled frequency, a third the difference frequency and the fourth the sum of both incident electric fields. For SFG, the fourth term is of importance.

The second order susceptibility $\chi^{(2)}$ is the macromolecular average of the molecular hyperpolarizability β_{SFG}, which is given by[11]

$$\chi^{(2)} \propto \beta_{\mathrm{SFG}} \propto \frac{A_{\mathrm{K}} M_{\mathrm{IJ}}}{\omega_{\nu} - \omega_{\mathrm{IR}} - \mathrm{i}\Gamma}. \tag{15}$$

In the above equation, A_{K} is the IR and M_{IJ} the Raman transition momentum, respectively. The molecular vibration frequency is denoted with ω_{ν} and the IR frequency with ω_{IR}. The value
Γ^{-1} is the relaxation time of the involved vibrational excited state. As closer ω_{IR} is to ω_{ν} the higher is the value of β_{SFG} and hence the SFG signal intensity I_{SFG} for a single transition

$$I_{\mathrm{SFG}} \propto I_{\mathrm{IR}} I_{\mathrm{vis}} \left| \chi^{(2)} \right|^2 \tag{16}$$

as it is proportional to the square of $\chi^{(2)}$ and direct to the intensities of the laser beams in the visible I_{vis} and infrared I_{IR} region of the spectrum.[12] For media with a center of inversion $\chi^{(2)}$ will vanish.[13] A disordered (bulk) phase has inversion symmetry and gives thereby no SFG signal. Only at surfaces and interfaces the symmetry is broken and SFG signals will appear. For that reason SFG spectroscopy is extremely interface sensitive. Another prerequisite arises from eq. (15). Only vibrational transitions, which are Raman and IR allowed, will give rise to a SFG signal.

Raman spectroscopy

Raman spectra were recorded using a confocal Raman microscope (alpha 300RA, WITec GmbH, Ulm, Germany). The excitation was achieved by fiber-coupled single mode laser operating at 532 nm. The excitation light was focused on the sample by a 100x objective. The

scattered light was collected through the same objective, guided through an optical fiber to the spectrograph and was measured with a CCD camera. The integration time was adjusted dependent on the signal level and lies typically between 0.5 s and 180 s. To increase the signal-to-noise ratio, the final spectrum results from the accumulation of 3 to 15 single spectra. The received spectra were processed (baseline correction, cosmic ray removal) with an instrument specific software, WITec Control.

SFG spectrometer

The SFG measurements were carried out on a commercial available SFG spectrometer (EKSPLA, Vilnius, Lithuania). The setup is based on the 1064 nm output of a Nd:YAG laser with a pulse duration ≤ 30 ps and a repetition rate of 10 Hz, which is directed into a harmonic unit. Here, part of the incident light is frequency doubled (second harmonic, 532 nm) and partly coupled out. The other part of the second harmonic and the remaining fundamental is guided into an optic-parametric oscillator and an optic-parametric amplifier, which convert the fundamental and second harmonic by non-linear processes to tunable infrared light (2.3 µm ≤ λ ≤ 10.0 µm).

In a typical experiment, the vibration of the OH region of the kaolinite was scanned from 3550 cm^{-1} to 3750 cm^{-1} with an increment of 1 cm^{-1}. To increase the signal-to-noise ratio of the SFG signal at each step, the signal was accumulated ten times.

XRD measurements

X-ray diffraction measurements (XRD) of the kaolinite samples were carried out at an X-Ray Powder Diffractometer D5005 with a Copper anode (Siemens/Bruker) by Dr. C. Günther, Institute of Earth- and Environmental Sciences at the University of Potsdam.

3. Results and discussion

3.1 Influence of temperature and ionic strength on the luminescence of Lanthanide(III) complexes

Due to the outstanding selectivity and sensitivity, luminescence techniques are powerful analytical tools in speciation analysis of Actinides (or Lanthanides as natural analogous). Based on spectroscopic data, especially kinetic data, complexation constants and stoichiometric information are determined. However, in the data evaluation care has to be taken that the fundamental photophysics underlying the observed luminescence signals is fully understood before conclusions on the complexes are drawn. Especially the interplay between the electronic systems of the Ln(III) and the ligands is important. Although the f-electrons of the Lanthanides do not (or only to a very small extend) contribute to the binding of ligands, the luminescence of the Lanthanides, which originated from transitions within the f-electron multiplet, can be distinctly influenced. In water the Ln(III) form aquo complexes (depending on the p*H* of the solutions other complexes may also be formed). Upon complexation of an organic (or inorganic) ligand, water is released from the first coordination sphere. Depending on the ligand and its complexation properties, one or two water molecules may be release. Because of the effective luminescence quenching by water molecules in the first (but also to a lesser extent by water molecules in higher) coordination spheres, it is expected that the Ln(III) luminescence quenching is decreased upon binding of an organic ligand resulting in higher luminescence efficiency and increased luminescence decay times. In addition to the reduced luminescence quenching the exchange of water molecules with organic ligand(s) is also altering the symmetry of the complexes which subsequently affects the spectral intensity distribution observed for Eu(III). Here, alteration of the ligand field is reflected in the intensity and spectral positions of the Stark levels. For a qualitative and especially for a quantitative evaluation of spectroscopic parameters in speciation analysis the electronic interplay between Ln(III) ion and ligand(s) needs to be taken into account.

Low molecular organic compounds such as glycolic acid and salicylic acid (see Figure 1S) were used as model compounds for i) low molecular organics found (released) in (from) clays and ii) building block of natural organic matter (e.g., HS). In the experiment the electronic (and redox) properties were varied by the change of the ligands as well as of the Ln(III) ion. The organic ligands investigated varied in their triplet energies and in their overall photochemistry. The Ln(III) ions were selected for the differences in the energy gap between the highest energy level of the electronic ground state and the lowest energy level of the first excited state (see Table 4).

Table 4: Energy values of the first excited electronic level and energy gap values for Ln(III) ions.[14–17]

	Sm(III)	Eu(III)	Tb(III)	Dy(III)
Energy of first excited electronic level / cm^{-1}	17924	17200	20500	21200
energy gap ΔE / cm^{-1}	7400	12300	14800	7850

Based on reported binding constants the speciation distributions for the different ligand-Ln(III) combinations were calculated. Based on the calculation the sample composition was adjusted. In order to minimize the complexity of the samples, compositions in which mainly the Ln(III) aquo complex and the 1:1 complex with the ligand was present were chosen. Ionic strength (0 mol·L^{-1} < *I* < 4 mol·L^{-1})[c] and temperatures (77 K < *T* < 353 K) were varied and the effect on the luminescence decay kinetic was monitored for Ln(III) = Eu(III), Tb(III), Sm(III) and Dy(III).

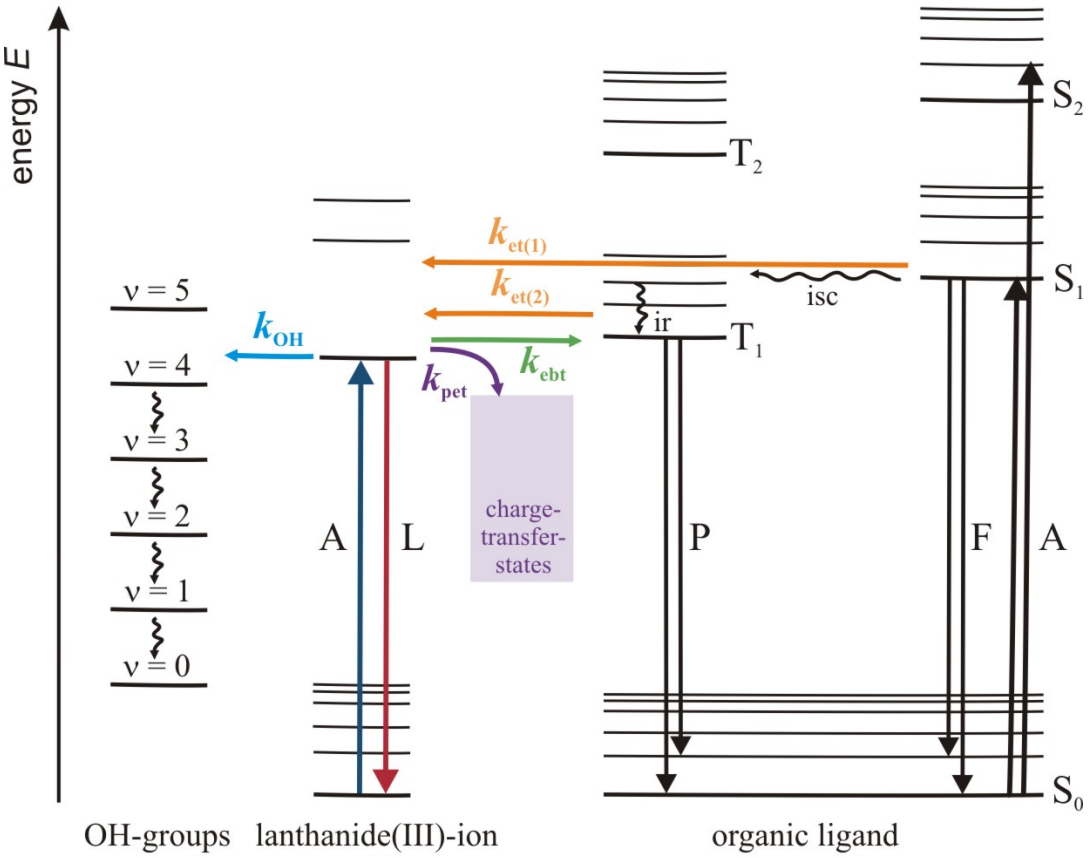

Figure 1: Summary of the possible intra-complex deactivation (quenching) processes for Ln(III) ions. Shown is the complex interplay between relative energy difference and quenching process determining the overall luminescence of the Ln(III) complex. Considered are the energy difference between i) Ln(III)-related energy levels, ii) ligand and Ln(III) levels, including water, and iii) the redox properties of the partners (A – absorption, L – luminescence, P – phosphorescence, F – fluorescence, S – singulet state, T – triplet state, ir – inner relaxation, isc – intersystem crossing, *k* – rate constant of: OH – quenching by OH-vibrations, ebt – energy back transfer and pet – photo induced electron transfer).

In Figure 1 an overview of the different intra-complex radiationless deactivation processes to be considered for Ln(III) complexes with organic ligands is shown. Three major additional pathways for radiationless deactivation need to be taken into account: i) deactivation by OH-vibrations (but also to other functional groups such as NH with suitable vibrational energies may be considered), ii) energy (back) transfer to the ligand (e.g., to ligand triplet state), and iii) photoinduced redox reaction between Ln(III) and ligand (e.g., photoinduced electron or

charge transfer between ligand and Ln(III)). Case i) and ii) are both radiationless energy transfer processes. The contribution of the different intra-Ln(III) and complex-related radiationless deactivation processes is determined by the corresponding rate constants and here the fastest process(es) will dictate the observed overall deactivation. Hence, the specific combination of Ln(III) and ligand each having specific intrinsic electronic properties has to be considered in the interpretation of the spectroscopic data during speciation analysis. In order to evaluate the different radiationless deactivation pathways and to show the consequences on the data interpretation, Ln(III) and ligands were combined to foreground specific deactivation processes.

Direct excitation conditions

Case i) deactivation via OH-vibrations in aqueous solution

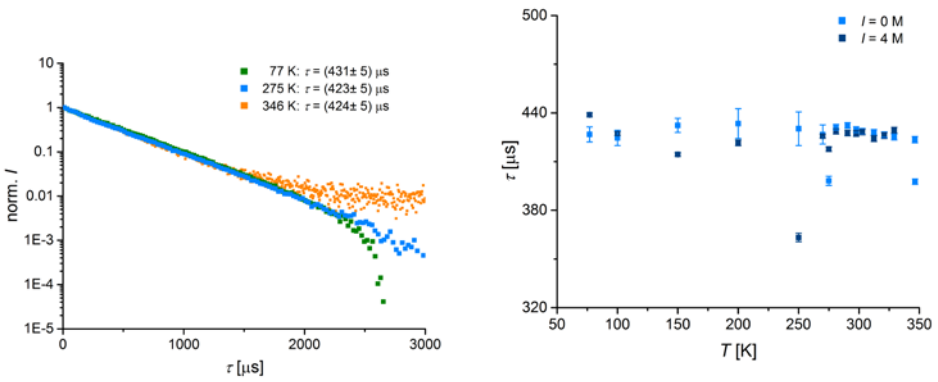

Figure 2: (left) Luminescence decay kinetics of $[Tb(H_2O)_8]^{3+}$ at different temperatures (λ_{ex} = 378 nm, λ_{em} = 542 nm). (right) Luminescence decay time of $[Tb(H_2O)_8]^{3+}$ at different temperature for low and high ionic strength conditions.

The influence of temperature and ionic strength on the luminescence decay time was investigate for Ln(III) = Eu(III), Tb(III), Dy(III), and Sm(III) aquo complexes. In Figure 2 the influence of temperature and of ionic strength on the luminescence decay kinetics (and decay time) of the Tb(III) aquo complex is shown. The luminescence decay time was determined for a temperature interval of around ΔT = 300 K and no systematic influence was found. The experiments was also carried out with samples at different ionic strength (0 mol·L^{-1} < I < 4 mol·L^{-1})[c]. From the results (see Figure 2 (right)) no temperature influence could be deduced. Moreover, the comparison between the luminescence decay times at the different ionic strength shows that it has also no influence on τ. Same results were obtained for the other Ln(III) ions investigated. From the luminescence measurements of the Ln(III) aquo complexes it can be concluded that the luminescence quenching efficiency of the water molecules in the first (and second) coordination sphere of the Ln(III) ions is not altered by the ionic strength. So additional Coulomb effects due to high concentration of ions in the water phase (e.g., change in the vibrational frequencies due to water cluster formation etc.) are not reflected in an altered luminescence behavior of the Ln(III) ions here. For the different Ln(III) the ex-

perimentally determined luminescence decay times of the corresponding aquo complexes are summarized in Table 5.

Table 5: Luminescence decay times of the different Ln(III) aquo complexes. Shown are the average values calculated based on the results obtained for measurements in the temperature range of 77 K < *T* < 353 K and for ionic strengths of 0 mol·L^{-1} [c] < *I* < 4 mol·L^{-1}.

Ln(III) aquo complex	Luminescence decay time τ / µs
Tb(III)	425 ± 5
Eu(III)	110 ± 3
Sm(III)	2.9 ± 0.3
Dy(III)	2.9 ± 0.3

The comparison of the luminescence decay times determined for the different Ln(III) aquo complexes showed that the fastest luminescence decay kinetics are observed for Sm(III) and Dy(III). Both Ln(III) are characterized by a small energy difference ΔE between the lowest energy level of the first excited state and the highest energy level of the ground state (see also Figure 8). For both Ln(III) ΔE is in the range around 7500 cm^{-1}. On the other hand Tb(III) is characterized by a $\Delta E \sim$ 14800 cm^{-1} and Eu(III) by a $\Delta E \sim$ 12300 cm^{-1}. As a consequence the related rate constants for the radiationless energy transfer to the OH-vibrations of water is very high in case of Sm(III) and Dy(III) compared to Tb(III) or Eu(III). Using Fermi`s golden rule for the estimation of the rate constants the Franck Condon factor and the density of states in the accepting electronic system are of relevance. For the system of Ln(III) (donor) and H_2O (acceptor) the decreasing Franck Condon factor may be considered as the major factor ruling the rate constant.

Case ii) deactivation via energy (back) transfer (ebt) to ligand

In the next step the luminescence kinetics of Ln(III) in complexes with different organic ligands were investigated. A spectrum of different low molecular weight carboxylic acid was applied in the experiments. Here, the electronic properties of the ligands were varied with respect to the presence of additional hydroxylic (or comparable functional groups like NH and SH) and of aromatic structure. Especially the latter parameter defines the relative position of the ligand-related triplet states, which may serve as a "sink" in case of an energy back transfer (ebt) for the Ln(III) to the ligand. In order to become effective the rate constant for the ebt has to compete with the other deactivation processes such as quenching by OH-vibrations (vide supra). In the experiments low molecular weight organic ligands with different triplet energies were selected to probe the contribution of this deactivation process.

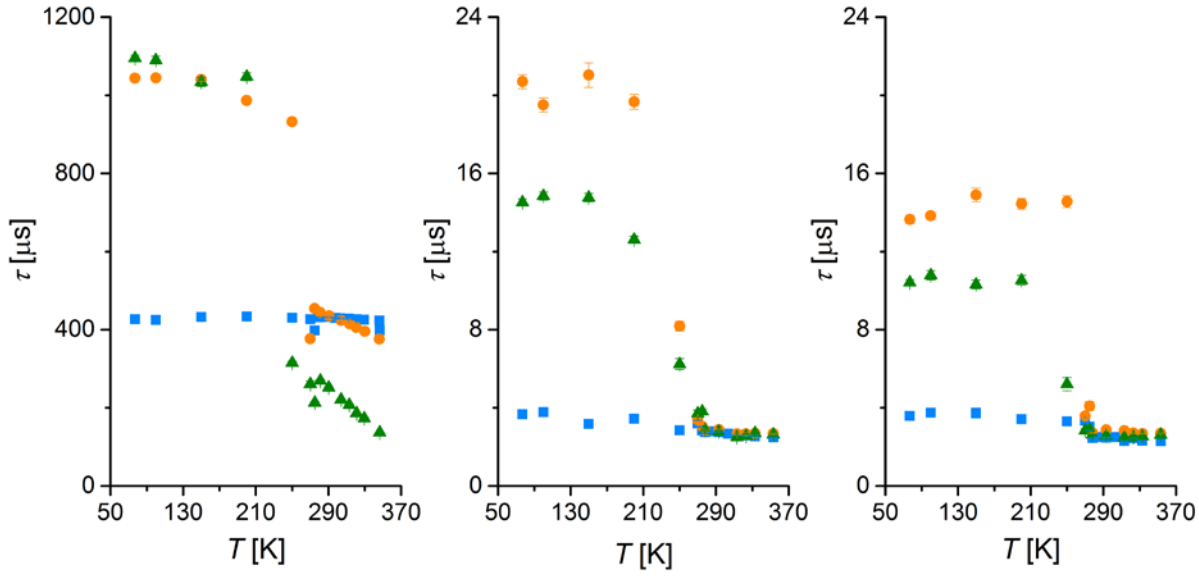

Figure 3: Luminescence decay times of Tb(III) (left, λ_{ex} = 378 nm , λ_{em} = 542 nm), Sm(III) (middle, λ_{ex} = 477 nm, λ_{em} = 592 nm), and Dy(III) (right, λ_{ex} = 450 nm, λ_{em} = 570 nm) in the temperature range 77 K < *T* < 353 K (orange circles: phthalate (p*H* = 4.2); green triangles: salicylate (p*H* = 5.0); blue squares: H_2O).

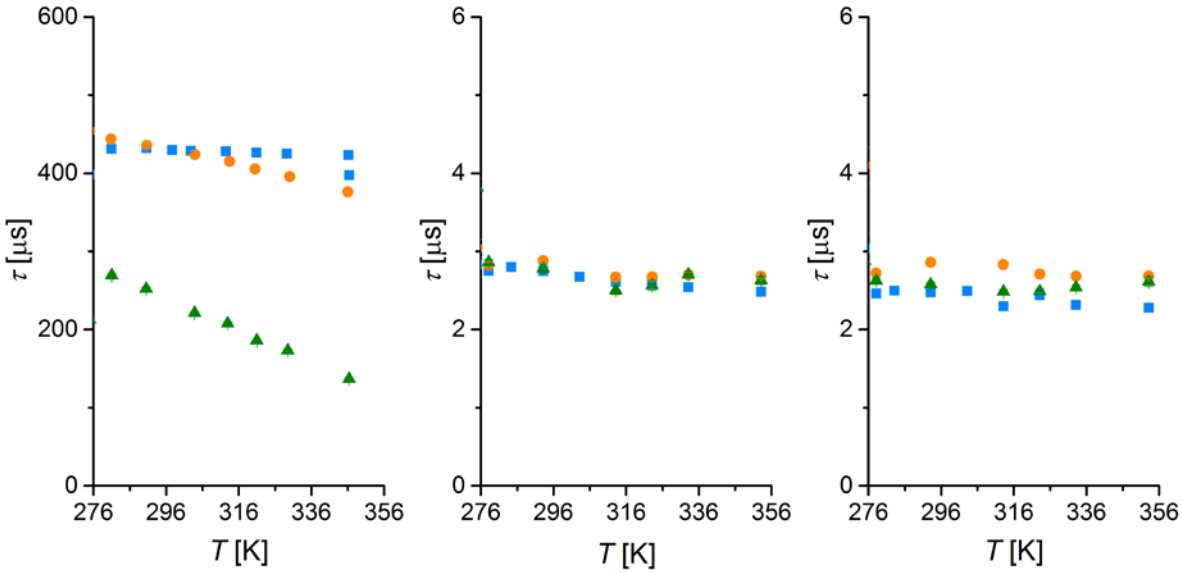

Figure 3a: Luminescence decay times of Tb(III) (left, λ_{ex} = 378 nm , λ_{em} = 542 nm), Sm(III) (middle, λ_{ex} = 477 nm, λ_{em} = 592 nm), and Dy(III) (right, λ_{ex} = 450 nm, λ_{em} = 570 nm) in the liquid phase (orange circles: phthalate (p*H* = 4.2); green triangles: salicylate (p*H* = 5.0); blue squares: H_2O) at temperatures between 276 K < *T* < 353 K.

In Figure 3 the luminescence decay times of the Ln(III) = Tb(III), Sm(III), and Dy(III) in complexes with salicylate and phthalate are shown determined in the temperature range of 77 K < *T* < 353 K. Depicted are also the τ values found for the respective Ln(III) aquo complexes. In contrast to the Ln(III) aquo complexes the phthalate and salicylate ligands have a dis-

tinct influence on the overall temperature dependence of τ and moreover, depending on the combination of Ln(III) and ligand the differential change with temperature is different. The most pronounced change was observed for salicylate in combination with Tb(III).

For Sm(III) and Dy(III) two clearly separated region can be identified in Figure 3. For temperatures below the freezing temperature of the solutions (around T = 270 K) the luminescence decay times were i) longer compared to the Ln(III) aquo complex and ii) for complexes with phthalate compared to salicylate longer τ were determined (Figure 3 (middle and right)). In the solid phase the luminescence decay times of the complexes were increased because water molecules are removed from the first coordination sphere and substituted by the coordinating group (e.g., carboxylic group) of the ligands. It can be assumed that one carboxylic group will replace two water molecules. Therefore, phthalate is potentially more effective because four water molecules are removed from the Ln(III) coordination, in case of salicylate only two water molecules (three if the hydroxylic group also contributes). This is reflected in the overall larger τ found for the Ln(III) complexes with phthalate (see Figure 3). For the liquid phase samples of Sm(III) and Dy(III) no differences to the corresponding Ln(III) aquo complexes were found (see Figure 3a). Here, the kinetic lability of Ln(III) complexes may determine the overall quenching. Due to a fast ligand exchange in combination with a very efficient OH-quenching (large Franck Condon factors, vide supra) the observable luminescence decay time is significantly reduced. Since Sm(III) as well as Dy(III) have an energy gap of 7000 $cm^{-1} < \Delta E <$ 8000 cm^{-1}, the energy difference to the ligand-related triplet state is large (several thousand cm^{-1}, see Figure 8 and Table 6) and subsequently a (thermally activated) energy transfer from the electronically excited Ln(III) (= Sm(III), Dy(III)) to the ligand triplet state is not operative.

Table 6: triplet energies E_T of the ligands.[18,19]

	E_T /cm^{-1}
salicylic acid	23800
phthalic acid	27400

Complexes of phthalate and salicylate with Tb(III) show divergent trends. For the solid phase i) only a weak temperature dependence at T < 270 K and ii) only minor differences between both ligands are found for the luminescence decay times. The quenching by water molecules is due to its unfavorable Franck Condon factor (vide supra) less efficient (compared to Dy(III) or Sm(III)). For the higher temperatures the differences between salicylic and phthalic acid again become evident (see Figure 3a). Since the triplet energy of the salicylic acid is smaller compared to phthalic acid, also the energy difference between Tb(III) excited states and triplet states in salicylic acid is smaller. This leads to a more efficient energy transfer and subsequently to a higher quenching influence. Because of the unfavorable coupling to OH-vibrations, the energy transfer to ligand triplet states comes into play for Tb(III) complexes.

For the temperature range of 278 K < *T* < 353 K the influence of the ionic strength (0 mol·L^{-1} < *I* < 4 mol·L^{-1})^{c} on the observed luminescence decay kinetics was investigated. In Figure 4 the luminescence decay times of Tb(III) and Dy(III) salicylate complexes are shown.

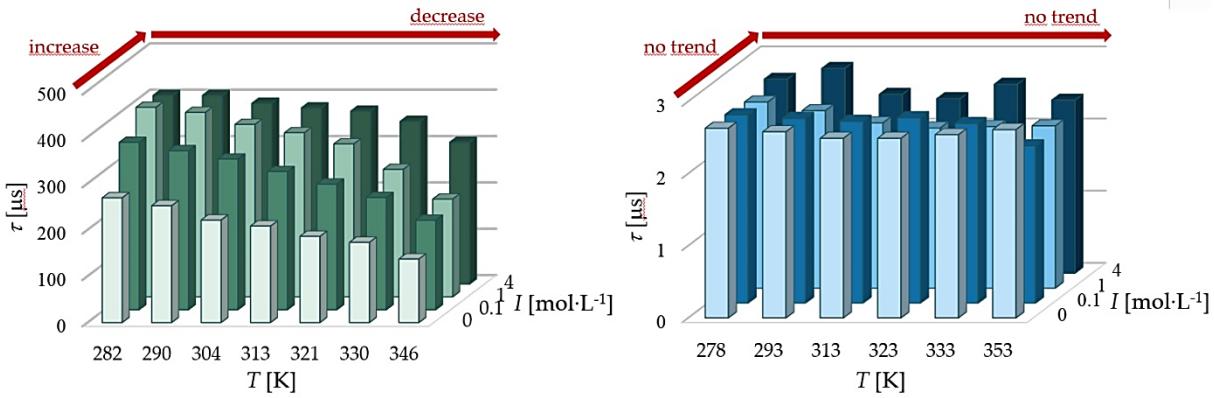

Figure 4: Luminescence decay times of salicylate complexes with Tb(III) (left) and Dy(III) (right) for the temperature range of 278 K < *T* < 353 K at different ionic strength (0 mol·L^{-1} < *I* < 4 mol·L^{-1})^{c}.

While for Dy(III) no further influence of the ionic strength was found, for the Tb(III) salicylate an increase in the luminescence decay time with increasing ionic strength was found. This increase could be caused by a shift of the Tb(III) complex equilibrium to a higher amount of Tb(III) aquo complexes, for what interactions between sodium ions and salicylate ligands are responsible and as a result less salicylate was coordinated by Tb(III). Because of the missing influence of salicylate on the luminescence decay time of Dy(III) in comparison to the Dy(III) aquo complexes this shift could not be observed.

An Arrhenius analysis of the luminescence decay times further underlines the differences in contributions of the radiationless energy transfer processes for Ln(III) aquo complexes and for Ln(III) complexed by organic ligands, respectively. While for Ln(III) aquo complexes the general high efficiency of the OH-quenching is reflected by a very low activation barrier, for Ln(III) complexed by organic ligands the contribution of an energy back transfer to the ligand may have to be considered (see Figure 5 (left)). In case of Tb(III) this deactivation process can compete with the OH related quenching. In this case the quenching is characterized by a different activation barrier. For Dy(III) and Sm(III) still the OH-related quenching is the major deactivation pathway and subsequently the determined activation energy is low (see Figure 5 (right)).

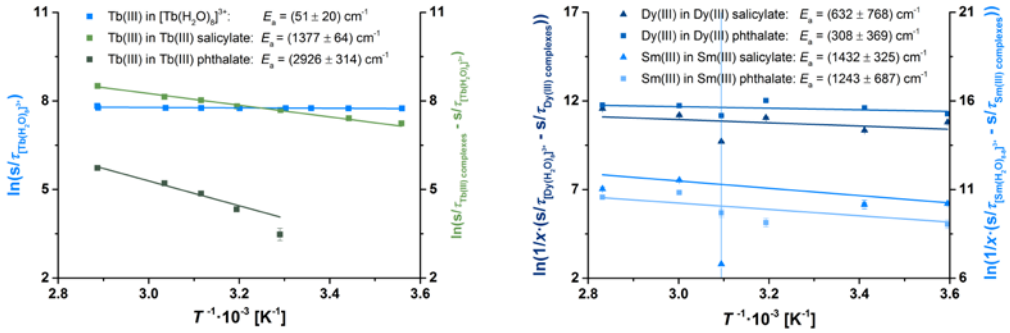

Figure 5: Arrhenius data evaluation for Tb(III) (left) as well as Sm(III) and Dy(III) (right) in aquo complexes as well as in complexes with organic ligands

Indirect excitation conditions

The experiments were performed under direct excitation of the Tb(III). In order to support the conclusions drawn with respect to the thermally activated energy back transfer via the ligands tiplet state (vide supra), additional experiments under indirect excitation conditions were carried out.

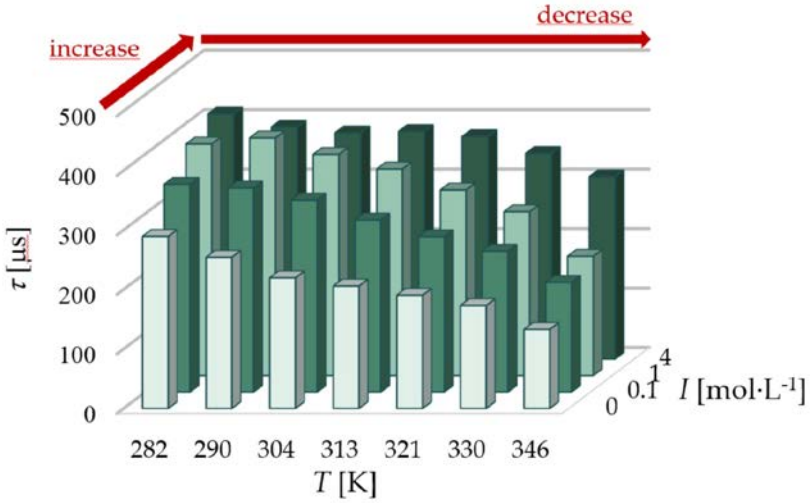

Figure 6: Dependence of the luminescence decay time of Tb(III) in complexes with salicylic acid in the temperture range 278 K < *T* < 353 K for different ionic strength *I*. The decay times were determined from luminescence kinetics measured under sensitized excitation conditions (λ_{ex} = 325 nm) (For comparison with direct excitation of Tb(III) at λ_{ex} = 378 nm see also Figure 4).

In Figure 6 luminescence decay times for Tb(III) in complexes with salicylic acid determined for indirect excitation (λ_{ex} = 325 nm) are summarized. Like in the case of direct excitation (see Figure 4) τ decreased with increasing temperature. Due to the reduced formation of complexes at higher ionic strength this effect was decreased and almost diminished at I = 4 mol·L^{-1}.

In Figure 7 (left) the luminescence decay times for Tb(III) in complexes with salicylate and phthalate under indirect excitation conditions are shown. In the experiment the ligands were used as sensitizers which transfer the energy in a subsequent step effectively to Tb(III). Be-

cause the absorption coefficients of the organic ligands are significantly higher compared to the intrinsic Tb(III) absorption coefficients, the sensitization in general is an excellent approach for sensitive luminescence detection of such complexes.

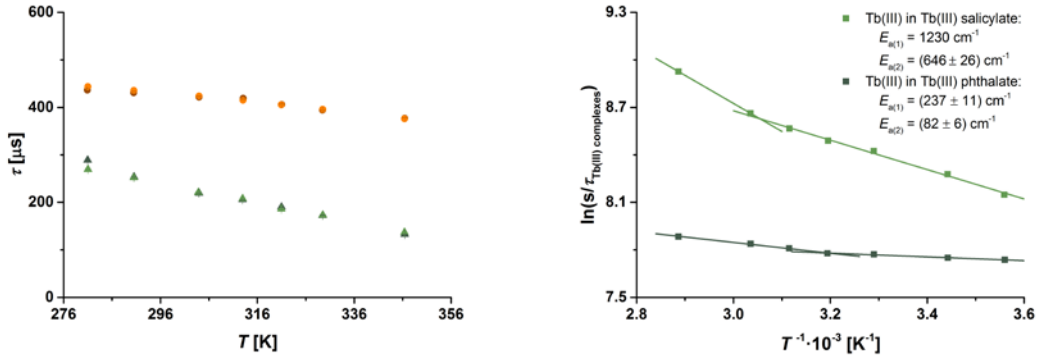

Figure 7: (left) Luminescence decay times of Tb(III) in complexes with salicylate (green triangles) and phthalate (orange circles) (λ_{em} = 545 nm). The decay kinetics were measured for direct (light symbols, λ_{ex} = 378 nm) and indirect (dark symbols, excitation of salicylate with λ_{ex} = 325 nm and of phthalate with λ_{ex} = 330 nm) excitation via the respective ligand for the temperature range of 276 K < T < 353 K. (right) Results of the Arrhenius data evaluation for indirect excitation conditions for salicylate and phthalate as ligands for Tb(III).

In Figure 7 the results obtained for direct and indirect excitation condition are compared and it can clearly be seen that there is no difference in the luminescence decay time. Consequently, also the respective Arrhenius data evaluation (Figure 7 (right)) yielded activation energies which were in excellent agreement with data obtained for direct excitation conditions (vide supra). This finding excludes an effective involvement of radiationless deactivation via a charge-transfer (metal-to-ligand or ligand-to-metal charge transfer) reaction, since in this case the direct excitation of the ligand would alter the respective ligand-related redox properties drastically and a different luminescence decay time could be expected. The fact that no difference is observe between both excitation schemes is a supporting evidence that the processes contributing to the depopulation of the Tb(III)-$^5D_4$ state are identical.

In Figure 8 the different radiationless energy transfer pathways (case i) and ii)) contributing to the observed overall reduction of the luminescence decay time of Ln(III) complexes are summarized. The interplay between the different deactivation processes is responsible for the effective overall luminescence decay kinetics and determined by the fastest of such (vide supra).

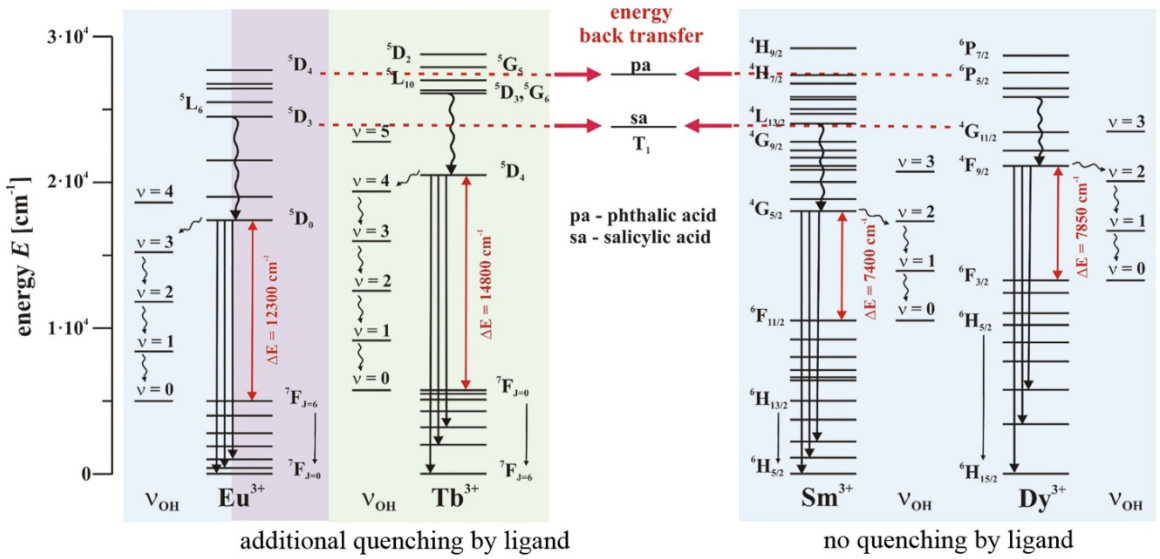

Figure 8: Schematic overview of the Ln(III) energy levels in relation to (overtone) water vibrations or the energy of triplet states of ligands used in the project (energy values taken from [16,17]).

Case iii) deactivation via an intra-complex photoinduced electron transfer (pet) reaction

In addition to radiationless energy transfer processes also the option of an electron transfer (or charge transfer) from ligand to the Ln(III) ion or vice versa should be taken into account. Among the investigated Lanthanides Europium can be found in the oxidation state +II and +III, although under normal conditions for the complexes investigated in aqueous solution only the +III form is observed. This is true for complexes formed and analysed in the electronic ground state. The situation if one of the components (Eu(III) or organic ligand) is in an electronically excited state could be different.

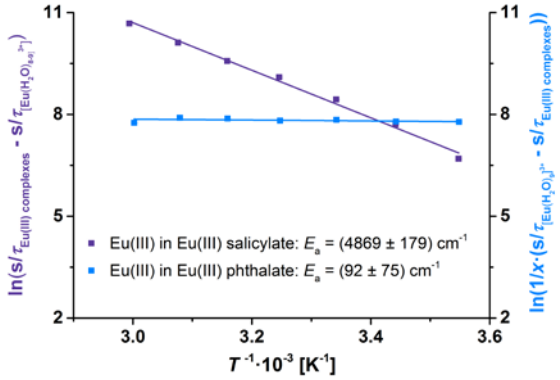

Figure 9: Arrhenius data evaluation of the corrected luminescence decay constants for Eu(III) complexed by salicylate (violett squares) and phthalate (blue squares) (λ_{ex} = 394 nm, λ_{em} = 618 nm).

In Figure 9 the Arrhenius data evaluation of the corrected luminescence decay times for Eu(III) in complexes with salicylate and phthalate is shown. It can be seen that for the two organic ligands a distinctly different temperature dependence was observed. While for the phthalate complexes (almost) a very small activation energy is calculated (resembling the case, in which the remaining water is involved like in the case of Sm(III) or Dy(III), vide

supra), for salicylate a much larger activation energy was determined. Based on transient absorption spectroscopy data for Eu(III) salicylate complexes it was shown that the solvate electron, which can be observed in aquous salicylate solutions upon pulsed laser excitation, is fully quenched.[20] In addition, the Eu(III) luminescence decay time of Eu(III) complexed by salicylate is reduced compared to the Eu(III) aquo complex.[21] Therefore, it is attractive to attribute the observed luminescence quenching by salicylate to an photoinduced electron transfer, in which the Eu(III) is reduced by the photoexcited salicylate to Eu(II). The obtained Eu(II) complex is not stable in aquous solution and decays radiationless further to the starting conditions (Eu(III) salicylate complex).

In summary, the luminescenece decay time is deterimined by a sum of different radiationless deactivaiton processes, of which the fastest determines the overall observed luminescence decay (see eq. (4)).

In order to evaluate luminescecence decay time data properly, the rate determining process needs to be identified. The rate-determining process is a consequence of the interplay between different factors defined by the ligand and the Ln(III) ion. In Figure 10 a summary of the rate-determining processes for the different Ln(III)-complexes investigated is given. In the evaluation of luminescence decay data the presence of rate determining processes has to be introduced. As an example, for Eu(III) the calculation of water molecules based on the empirical Horrocks equation should be modified according to:

$$n_{H_2O} = A \cdot \left(\frac{1}{\tau^{\#}_{H_2O}} - \frac{1}{\tau_{D_2O}} - X \right) \qquad (17) \qquad \text{with} \qquad \frac{1}{\tau^{\#}_{H_2O}} = \frac{1}{\tau_{D_2O}} - k_{pet} \qquad (18)$$

The parameter *X* contains additional contributions, e.g., of ligands in the second coordination sphere (see also eq. (4)).

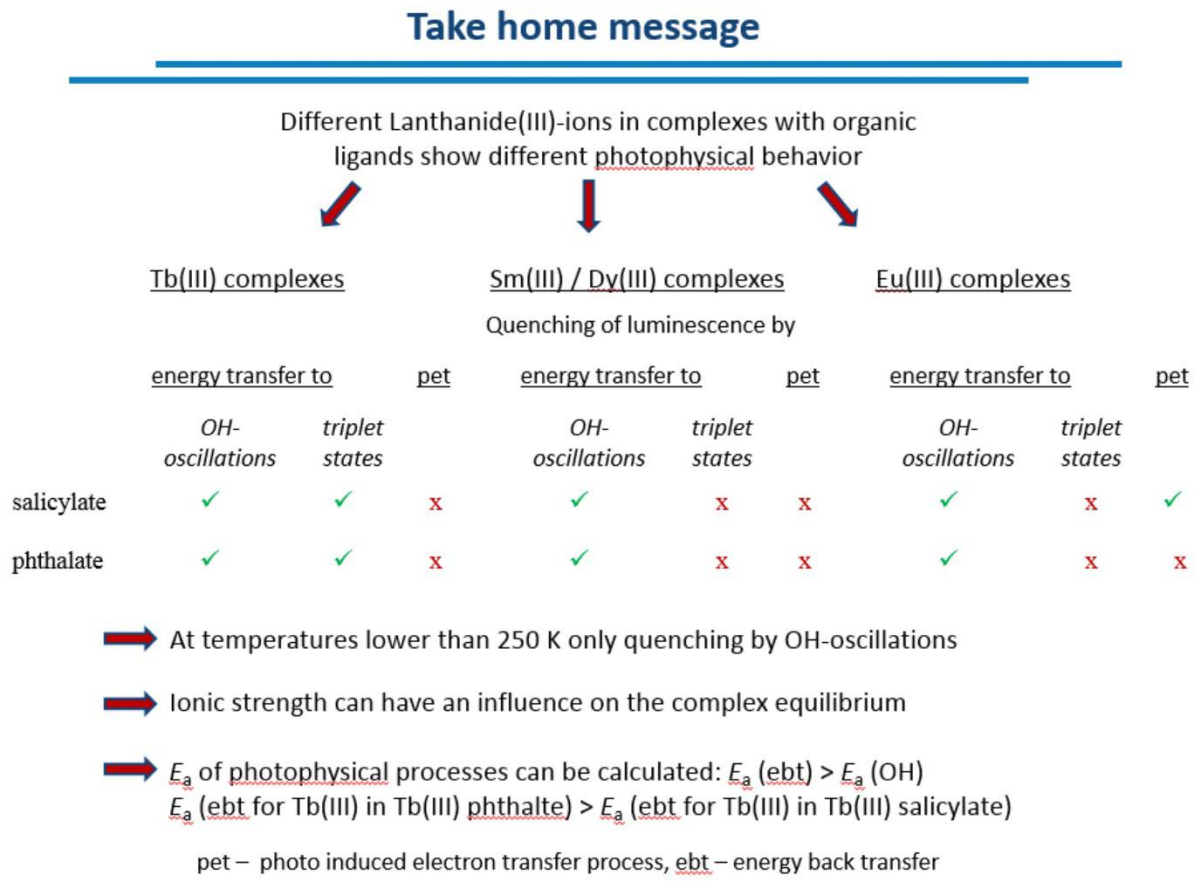

Figure 10: Summary of the contributions of the different radiationless deactivation processes operative in the investigated Ln(III) complexes.

3.2 Refactive index of salt solutions up to *I* = 4 mol·L^{-1}

The refractive index of water containing i) NaCl, ii) $NaClO_4$, and iii) $CaCl_2$ was determined for different ionic strength, different p*H*, and two different temperatures in the wavelength range of 400 nm < λ < 1000 nm (see Figure 11).

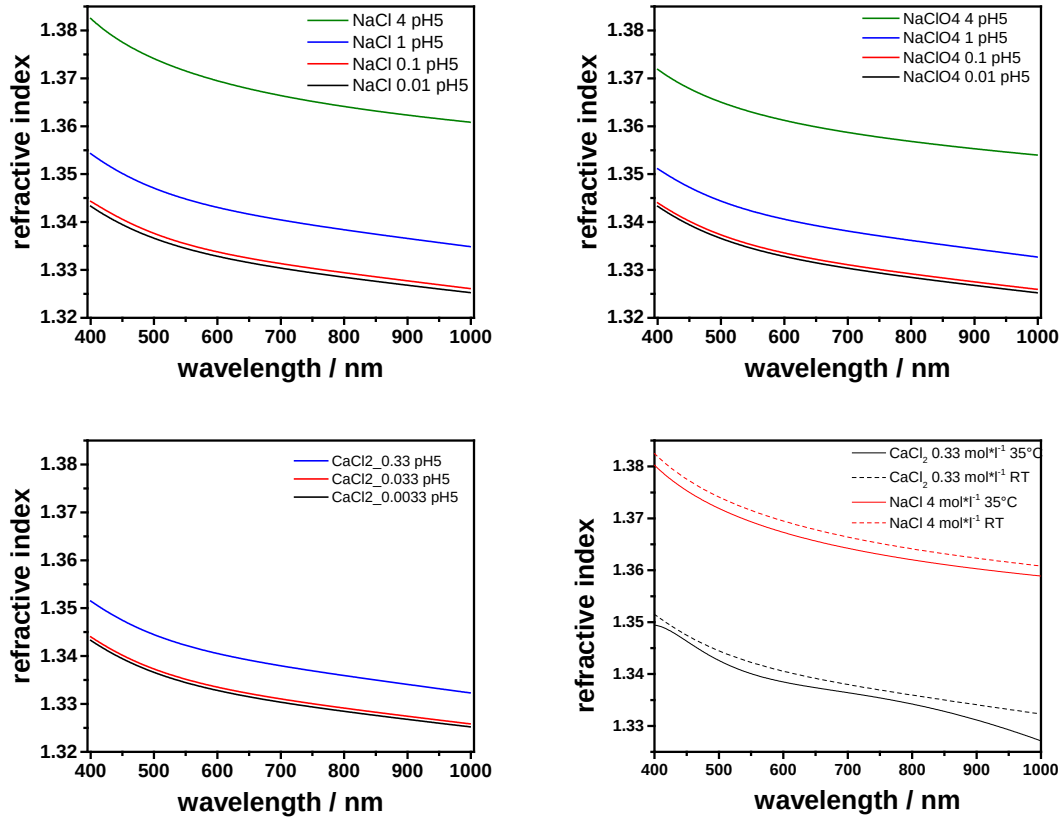

Figure 11: Refractive index of water containing different salts. (Bottom, right) Influence of temperature on the refractive index of solutions containing high concentrations of $CaCl_2$ or NaCl.

The comparison of the salts showed only minor differences in the absolute value for the same ionic strength. On the other hand, the overall ionic strength of the solution had a distinct influence on the refractive index. Especially for high ionic strength solutions the refractive index significantly increased in the monitored spectral range. Moreover, also the temperature of the solution is effecting the refractive index *n* of the solution, however only to a smaller extend comparing the influence of the ionic strength.

These findings have implications on luminescence parameters and subsequently on the quantitative evaluation of such when data of different ionic strength (or salt concentration) are compared quantitatively.

Two frequently used luminescence parameters in speciation analysis are luminescence quantum yield Φ_L (or for simplification often the luminescence intensity) and the luminescence decay time τ. Both parameters are connected by

$$\Phi_L = \frac{\tau}{\tau_0} \tag{19}$$

τ_0 (and τ) are defined by the Einstein coefficients A_{21} and B_{12}, respectively. Taking the theory into account the rate constant for the luminescence k_L can be written as

$$k_L = \frac{1}{\tau_L} = \frac{8000 \cdot \pi \cdot c_0 \cdot \ln 10}{N_A} \cdot \frac{n_L^3}{n_{abs}} \cdot \frac{g_{ex}}{g_L} \cdot \left\langle \nu^{-3} \right\rangle^{-1} \cdot \int \frac{\varepsilon(\nu)}{\nu} \cdot d\nu \tag{20}$$

Depending on the difference between excitation and emission wavelength the dispersion may be neglected. In that case a rough approximation according to Strickler and Berg for the luminescence decay time can be performed:

$$\frac{1}{\tau_L} = 2.88 \cdot 10^{-9} \cdot n^2 \cdot \int \frac{(2 \cdot \nu_c - \nu)^3}{\nu} \cdot \varepsilon(\nu) \cdot d\nu \tag{21}$$

From eq. (21) a quadratic dependence of the reversed luminescence decay time on the refactive index n is predicted. By looking at the extreme values for I = 0.1 mol·L^{-1}and 4 mol·L^{-1}, respectively, a change in τ of 5 - 10% can be expected due to the variation in the refractive index. So, for decay time based speciation this needs to be taken into account when results of different ionic strength samples are compared. Sine τ is correlated with the luminescence quantum efficiency (and therefore, also with intensity) via eq. (19) this affects also this luminescence parameter.

Based on the data acquired (see Figure 11) this correction can be easily carried out, which will help to further improve the precision of luminescence based speciation.

3.3 Complexation of Lanthanides by borate

Borates have been identified as a potential ligand in nuclear waste repositories. Especially in salt formations, which are one of the major geological formations evaluated. In addition to mineral as natural sources, boron is also a constituent of materials used in the nuclear technology process (e.g., borosilicate glass coquilles; boron as part of the cooling water becomes part of the spent nuclear fuel inventory to be stored). Therefore, the formation of boron complexes with Lanthanide complexes was investigated. In aqueous systems $B(OH)_3$ and polyborates are potential interaction partners for metal ions such as Ln(III). The aqueous chemistry of $B(OH)_3$ is complex, while at concentrations $c < 0.025$ mol·L^{-1} only boric acid and its different anions is found, at higher concentrations (and depending on the p*H* of the solution) a number of different polyborates are formed and dominantly found in the system (see Figure 12).

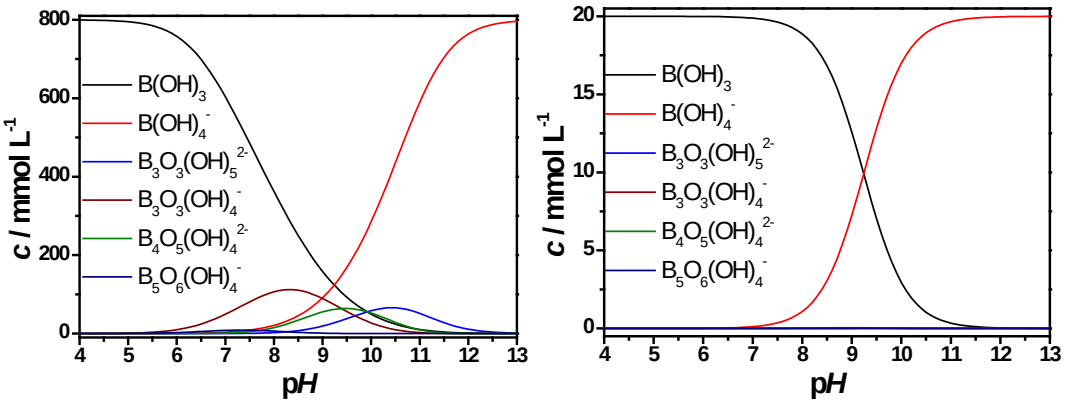

Figure 12: (left) speciation of borate for c = 0.8 mol·L^{-1} and (right) for c = 0.02 M based on data taken from [22] and calculated using ChemEQL 3.0[23].

In Figure 13 the luminescence spectra of Eu(III) at increasing borate concentrations (0 mol·L^{-1} < c(BS) < 0.02 mol·L^{-1}) are shown. In this concentration range (and p*H*) no formation of polyborate species is expected (s. also Figure 12 (left)). In the left part of Figure 13 the Eu(III) luminescence spectra are depicted. It can be seen that the spectral intensity distribution is not change by the presence of borate up to concentrations of 0.02 mol·L^{-1}. This was found for all samples investigated at p*H* < 7.

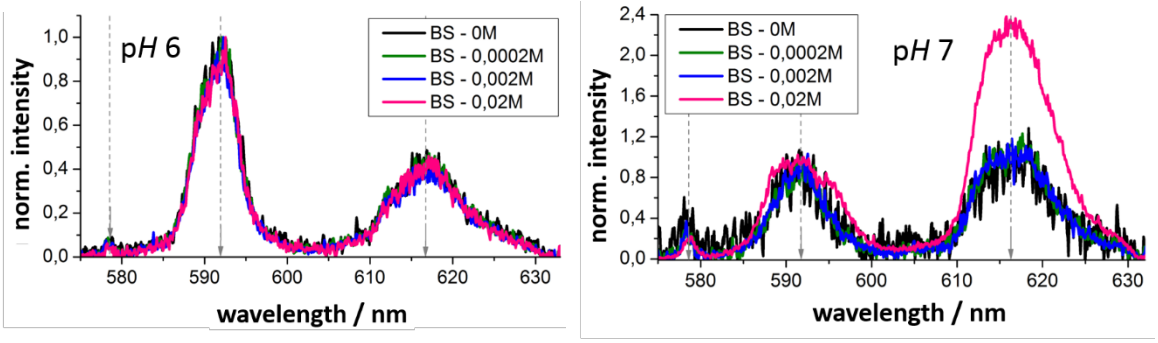

Figure 13: Luminescence spectra of Eu(III) (λ_{ex} = 394 nm, c(Eu(III) = 0.4 mmol·L^{-1}) in the presence of increasing borate (BS) concentration at two p*H* values.

At p*H* = 7 at the highest borate concentration investigated an alteration in the spectral intensity distribution was observed (see Figure 13 (right)), which indicates that the coordination sphere of Eu(III) is changed by the complexation of borate. Based on measurements of the luminescence decay kinetics the corresponding decay times were determined for different borate concentrations and p*H*.

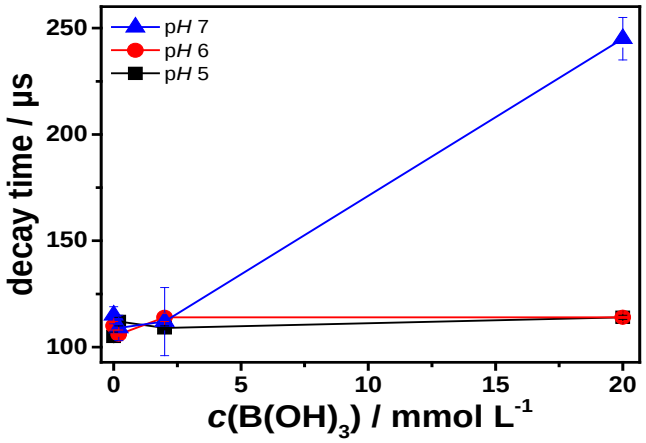

Figure 14: Luminescence decay time τ of Eu(III) (λ_{ex} = 394 nm, λ_{em} = 613 nm) in the presence of borate at three different p*H* (after three days of equilibration).

From Figure 14 can be concluded that also the luminescence decay kinetics of Eu(III) is not altered due the presence of borate in the investigated concentration range for p*H* < 7. Only at p*H* = 7 and high borate concentration a distinct alteration of τ was found, which perfectly corroborates the results of the spectra analysis. Based on the empirical relationship (see e.g., eq. (17)) the number of water molecules substituted by the borate in the first coordination sphere of Eu(III) was estimated to 2 - 3. However, the possible influence of the borate itself on the Eu(III) luminescence decay kinetics has to be kept in mind (vide supra for the detailed discussion of ligand-related radiationless deactivation). Here, further research is necessary.

For p*H* = 7 also the aging of the samples was investigated. In Figure 15 (left) the alterations observed in the spectral intensity distribution after five days are shown. Compared to Figure 13 (right) additional spectral features are observed. In addition the spectral intensity distribution changes also the luminescence decay kinetics were altered. Here, a further increase with longer contact time was found, e.g., for the sample containing 20 mmol·L^{-1} boric acid (p*H* = 7) the luminescence decay time increased to τ = 380 µs after one week equilibration time. These samples were stored under ambient conditions. In order to test the influence of CO_2 experiments with samples prepared with and without CO_2 were investigated.

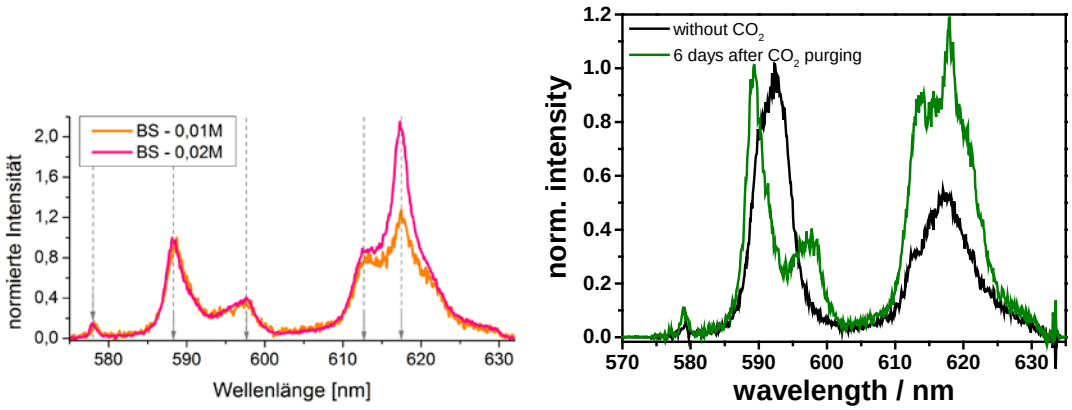

Figure 15: (left) Eu(III) luminescence spectra (λ_{ex} = 394 nm, p*H* = 7, RT) of Eu(III) borate solutions after five days of contact time under ambient conditions are shown. (right) Influence of CO_2 on the Eu(III) luminescence spectra in the presence of borate (c = 0.02 mol·L^{-1}, p*H* = 7).

In Figure 15 (right) the effect of CO_2 after six days of contact is shown. The comparison with the spectra on the left shows a strong resemblance and makes it tempting to attribute the observed spectral changes to the formation of mixed complexes between Eu(III), borate, and CO_2, respectively. For the aged samples also a slow precipitation of a white solid over weeks was observed indicating that a water insoluble complex is formed. At p*H* =7 (and below) at concentrations c < 0.02 mol·L^{-1} borate is a weak ligand and cannot compete with other ligands like low molecular weight organic acids. This has been shown in competition experiments with glycolic acid as a model ligand.

In collaboration with the Technical University of Dresden and the Helmholtz Center Dresden Rossendorf also the interaction of Eu(III) with polyborates at p*H* < 6 was investigated. Here, site-selective luminescence spectra recorded at T = 5 K proved to be especially valuable in the identification of different Eu(III) polyborate complexes formed in the investigated system. For a detailed description of experiments performed please referrer to the report of the Technical University of Dresden.[24] As an example in Figure 16 the different luminescence spectra (at room temperature and under site-selective excitation conditions at T = 5 K) of solid Eu(III) borate samples obtained from the solutions are shown.

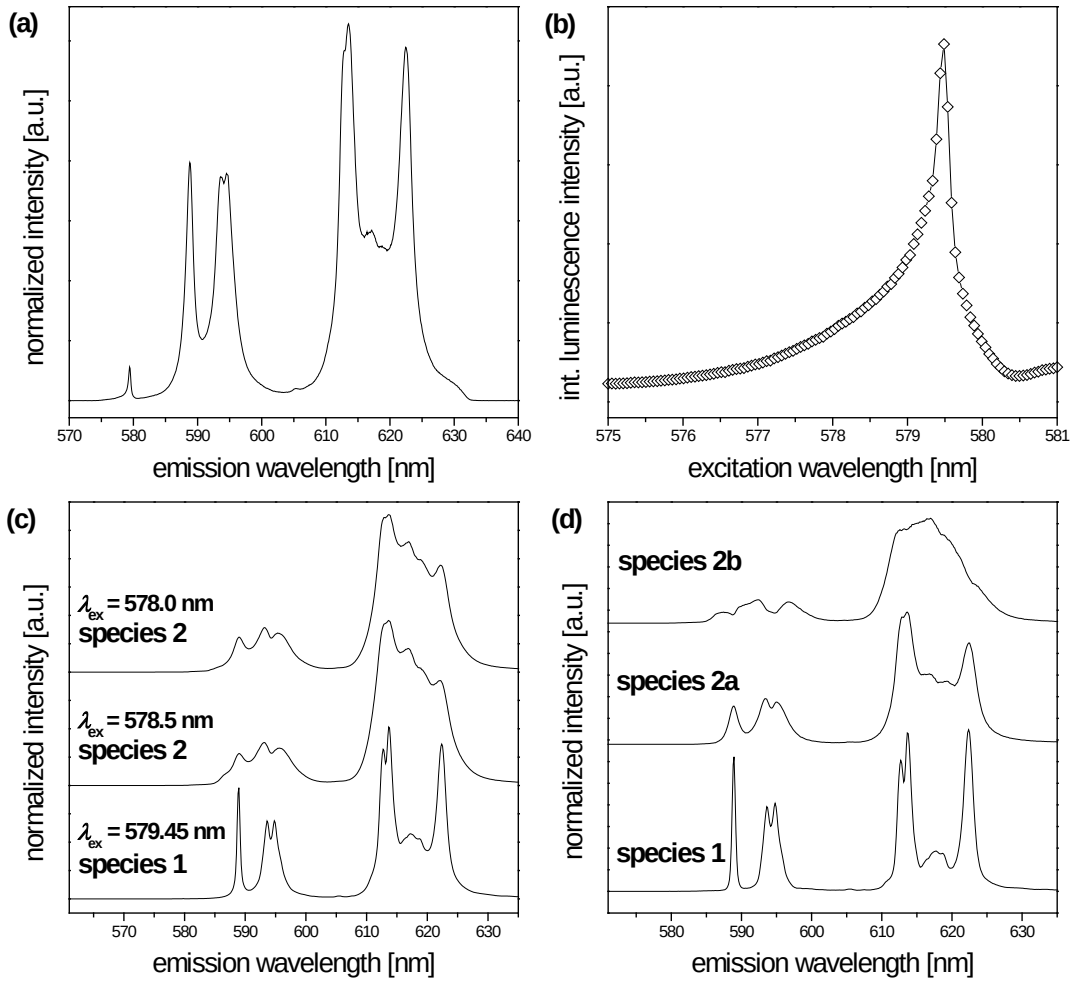

Figure 16: Solid-state luminescence spectra of the solid Eu(III) borate: (a) emission spectrum recorded at RT (λ_{ex} = 394 nm), (b) excitation spectrum at *T* = 5 K, (c) emission spectra (λ_{ex} = 578.0 nm, 578.50 nm and 579.45 nm, respectively, *T* = 5 K), (d) emission spectra determined from the PARAFAC analysis of the time-resolved spectra at *T* = 5 K (λ_{ex} = 578.50 nm and 579.45 nm, respectively).

In summary, the possible impact of borate on the mobilization of Actinide(III) ions in a nuclear waste repository is expected to be small. Based on the results, borates have only a minor mobilization potential for trivalent Actinides in the slight acidic to neutral p*H* range since the complexation is very weak - especially in comparison to other ligands, *e.g.*, carbonate, hydroxide and other organic compounds present in the system. Moreover, due to the formation of solid (poly)borate phases already at slight acidic p*H* the immobilization of trivalent Actinides will be supported. Future research is required to investigate the actinide-borate interactions in the alkaline p*H* range in detail.

3.4 Interactions of Europium(III) with natural occurring polymers

Organic material, especially polymeric organic material is an important complexing agent as natural organic polymers, like humic substances (HS), are ubiquitous in the environment. The ground and pore waters in North Germany lower cretaceous clays have relatively high salt concentrations.[25] In the following the complexation of Eu(III) as Ln(III) ion by different HS in solutions with different background electrolytes and different electrolyte concentration was investigated.

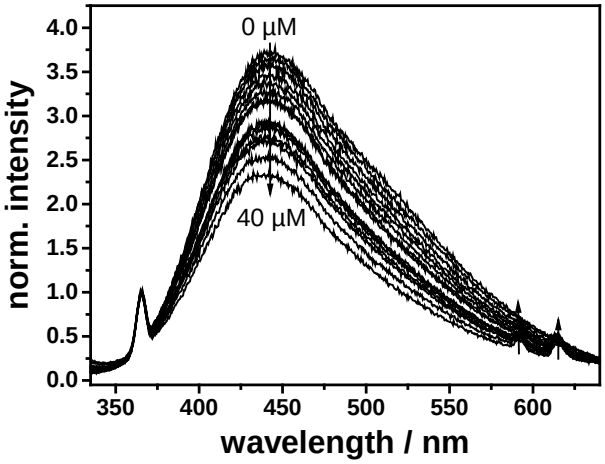

Figure 17: Typical fluorescence of a humic substance. Shown is a fluorescence spectrum of Pahokee Peat Fulvic Acid with a concentration of 10 mg·L^{-1} in 0.5 mol·L^{-1} NaCl solution at p*H* = 5. Excitation was at λ_{ex} = 325 nm. The arrows indicates the changes upon increasing Eu (III) concentration from 0 µmol·L^{-1} to 40 µmol·L^{-1}.

Figure 17 shows a typical fluorescence spectrum of HS. By increasing the Eu(III) concentration from 0 µmol·L^{-1} to 40 µmol·L^{-1} the intrinsic HS fluorescence intensity is quenched. Around 600 nm two peaks (located around 592 nm and 615 nm) show increasing intensity with increasing Eu(III) concentration. These two peaks arises from the luminescence of the Eu(III) ions, which is excited via HS molecules. From this measurement, the conditional complexation constant can be derived using eq. (10).

To calculate conditional binding constants by the use of eq. (10), the measured fluorescence intensity at every Eu(III) concentration is added up from 425 nm to 475 nm and divided by the integrated fluorescence intensity in absence of Eu(III). This approach gives plots as shown in Figure 18. By non-linear least square fitting of eq. (10) to the data, values for the conditional complexation constant and the remaining fluorescence $I_{ML,rel}$ could be derived. In Figure 18 experimental data (points) and the result of the fitting procedure (straight lines) for the complexation of Eu(III) ions by Pahokee Peat Fulvic Acid are shown.

These measurements were conducted for the humic acid (HA) and fulvic acid (FA) fraction of Pahokee Peat (PP) and Suwannee River (SR) humic substances. In the investigation mainly two different ionic strengths (0.5 mol·L^{-1} and 3.0 mol·L^{-1} NaCl) at different temperatures (room temperature, 35 °C and 50 °C) were considered.

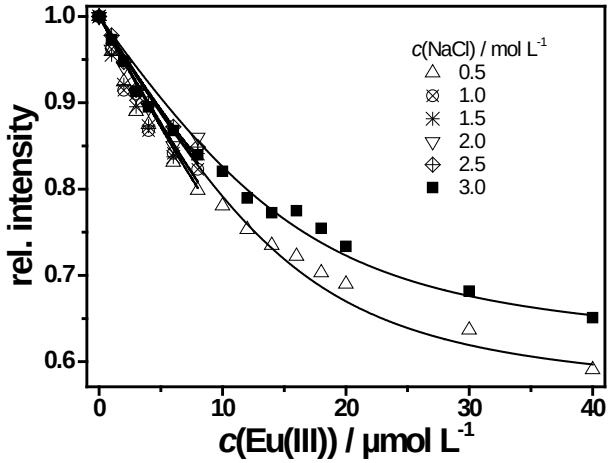

Figure 18: Plot of the relative intrinsic fluorescence intensity of Pahokee Peat Fulvic Acid at p*H* = 5 as function of the Eu(III) concentration and different concentrations of NaCl as background electrolyte as given in the legend. The straight lines are the results of a non-linear least square fitting of eq. (10) to the data.

The complexation of Eu(III) ions by SRFA and SRHA as well as PPFA and PPHA was investigated by stationary fluorescence measurements in dependence of ionic strength and temperature. From Figure 19 it clearly can be seen, that the complexation is stronger for PP than for SR as the lg β values are one unit higher for PP. For the effect of temperature and ionic strength no clear trends were found. Neither an increase of ionic strength from 0.5 mol·L^{-1} to 3.0 mol·L^{-1} nor of temperature from 22 °C to 50 °C gave a pronounced effect on the conditional complexation constants.

A crucial parameter is – besides the very fundamental assumption of a 1:1 complexation – the concentration of the ligand / binding sites in the HS. The approach was to calculate this concentration from the charge density of the HS at the given p*H*. But this charge density is known only at room temperature. The calculation of complexation constants requires in principle knowledge about the activities of ligands and metal ions. In this approach, concentration are used instead. Theories, like SIT[f] or Pitzer, allow to calculate activity coefficients for ions in solution. But these attempt will fail for HS as HS are complex mixtures of an unknown number of pieces.

In the following, the interaction of HS with Ln(III) ions will be investigated on a more mechanistic level. In addition to Eu(III) also Lanthanum(III) (La(III)) and Neodymium(III) (Nd(III)) were included in the study. The aim was to derive average distances between complexed Ln(III). Hereby, a more intrinsic parameter is at hand, which will help to describe the interaction on a molecular level.

[f] Specific Interacion Theory

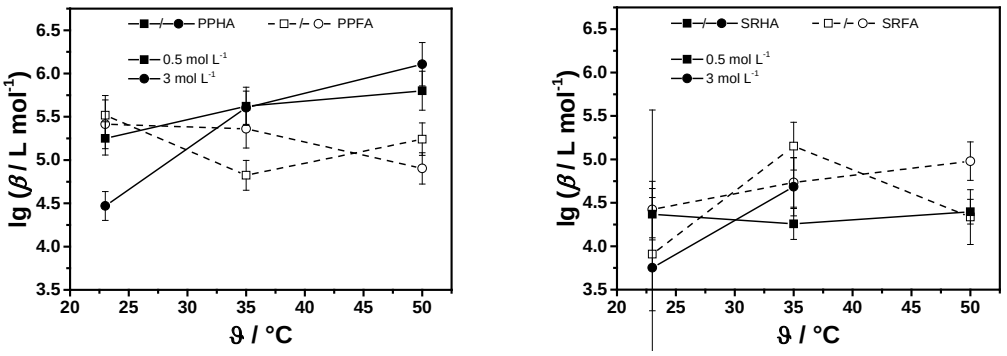

Figure 19. Conditional constants for the complexation of Eu(III) ions by the FA and HA fractions of PP (left) and SR (right). The concentration of the humic substance was 10 mg·L^{-1} at p*H* = 5.

As representative, HA from the Gorleben site – Gohy573 FA and Gohy573 HA – were chosen. The question was, how the composition of the background electrolyte influences the interaction of the Ln(III) ions with Gohy573 HA and Gohy573 FA, respectively. As background electrolyte NaCl and $MgCl_2$ were used. At the beginning of the investigations it was recognized, that the $MgCl_2$ influences the intrinsic fluorescence of the humic material. This also showed up by addition of Eu(III) ions to solutions containing Gohy573 FA or HA and $MgCl_2$ as background electrolyte. Contrary to the comparable measurements, as shown in Figure 17 and Figure 18, with NaCl as background electrolyte no pronounced decrease of the intrinsic fluorescence intensity could be observed upon addition of Eu(III) ions. As the intrinsic fluorescence of HS is very broad and featureless – a result of their complex and heterogeneous structure – it is not the best observable to study interactions between Ln(III) ions and HS in detail. In contrast, some Ln(III) ions have a distinct luminescence emission, which is altered due to changes in their chemical environment, for example due to complexation reactions.

Eu(III) was used as luminescence probe in the experiments and was excited indirectly via HS molecules. Consequently, only Eu(III) complexed to chromophors of the HS are monitored. Here, the humic substance molecules act as a so called antennae, which collect the excitation light and transfer it to the Eu(III) ion. The excitation of the Eu(III) via HS is more efficient than a direct excitation of the Eu(III) ions as the extinction coefficients of the latter are very low ($\varepsilon < 3$ L·mol^{-1}·cm^{-1})[6].

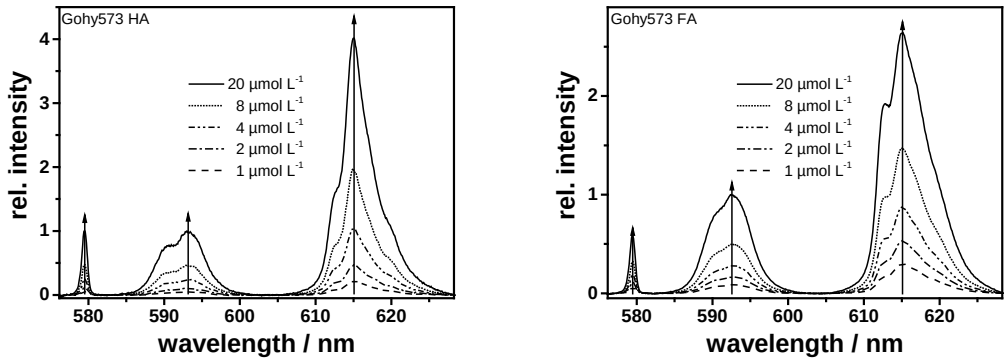

Figure 20: Luminescence spectra of Eu(III) at different Eu(III) concentrations in solution with 12.5 mg·L^{-1} HS and 0.1 mol·L^{-1} $MgCl_2$ at p*H* = 5, λ_{ex} = 356 nm.

In Figure 20 luminescence spectra of Eu(III) in solutions with Gohy573 HA and Gohy573 FA are shown after indirect (sensitized) excitation via HS at λ_{ex} = 356 nm. By increasing the Eu(III) concentration also the intensity of the Eu(III) luminescence increases. Due to the excitation scheme, only Eu(III) ions, which are complexed to humic substance molecules, will show luminescence. Therefore, an increase in luminescence intensity means also that more Eu(III) ions are complexed to the humic substance.

The Eu(III) luminescence spectra show differences for the complexation of Eu(III) by Gohy573 FA and Gohy573 HA. What clearly can be seen is that the intensity of the $^5D_0 \rightarrow {}^7F_2$ transition (around 615 nm) is higher relative to the intensity of the $^5D_0 \rightarrow {}^7F_1$ transition (around 592 nm) for Eu(III) complexed to Gohy573 HA. For the highest Eu(III) concentrations, the relative intensity of the $^5D_0 \rightarrow {}^7F_2$ transition increases up to four for Gohy573 HA and only to 2.6 for Gohy573 FA. Also the coordination geometry of the complexes formed must be different as the luminescence spectra looks different. In Eu(III) Gohy573 HA complexes, the $^5D_0 \rightarrow {}^7F_0$ transition has nearly the same intensity as the $^5D_0 \rightarrow {}^7F_1$ transition, whereas for Eu(III) Gohy573 FA complexes the $^5D_0 \rightarrow {}^7F_0$ transition has only half of the relative intensity compared to the $^5D_0 \rightarrow {}^7F_1$ transition. In addition, the splitting of the $^5D_0 \rightarrow {}^7F_1$ and $^5D_0 \rightarrow {}^7F_2$ transition show slightly differences for FA and HA as complexing ligands. For comparison both luminescence spectra at the highest Eu(III) concentration (20 µmol·L^{-1}) are plotted in one diagram (cf. Figure 21).

Each ^7F_J states split in a ligand field in up to *2J+1* energetically different sublevels, known as Stark levels. Depending on the energy differences of these Stark levels and the symmetry, in which the Eu(III) ion is embedded, the splitting can also be seen in the luminescence spectra. Görller-Wallrand and Binnemans summarized, how luminescence excitation or emission spectra can be used to derive the symmetry of the Eu(III)'s ligand field in single crystals.[26]

However, this approach to deduce the symmetry of Eu(III) species in the presence of HS will fail, as it cannot be expected that only one specific Eu(III) complex will be formed. Nevertheless, from the luminescence emission spectra shown in Figure 21 differences in the splitting

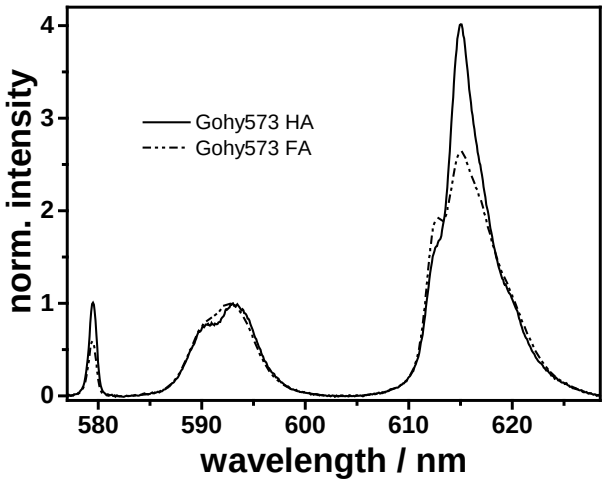

Figure 21: Comparison of the normalized luminescence spectra of Eu(III) complexed by Gohy573HA and Gohy573 FA, respectively, *c*(Eu(III) = 20 µmol·L^{-1}.

of the $^5D_0 \rightarrow {}^7F_1$ and $^5D_0 \rightarrow {}^7F_2$ transitions depicted. Interestingly enough, in the luminescence spectrum of Eu(III) Gohy573 HA complexes the splitting of the $^5D_0 \rightarrow {}^7F_1$ transition is better resolved (two local maxima) compared to Eu(III) complexes with Gohy573 FA (one maximum and a shoulder). The opposite trend is found for the luminescence transition $^5D_0 \rightarrow {}^7F_2$. Here, for Eu(III) Gohy573 HA complexes a maximum with two shoulders is found, whereas for Eu(III) Gohy573 FA complexes two local maxima can be seen and a shoulder on the bathochromic side of the peak can be anticipated.

A parameter easier accessible is the asymmetry ratio *r* (cf. eq. (2)), which is more straight forward to compare different Eu(III) luminescence spectra. For the luminescence spectra shown in Figure 20 this parameter was calculated and plotted in Figure 22. For both, complexation by Gohy573 HA or Gohy573 FA, the asymmetry ratio decreases slightly by background electrolyte ($MgCl_2$) concentration of 0.10 mol·L^{-1} with increasing Eu(III) concentration. When increasing the concentration of $MgCl_2$ to 0.85 mol·L^{-1}, the decrease of asymmetry

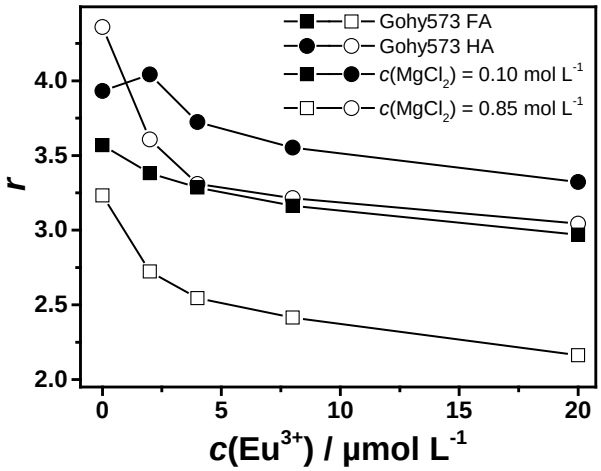

Figure 22: Asymmetry ratio *r* calculated with eq. (2) extracted from luminescence spectra of Eu(II) complexed to Gohy573 FA or Gohy573 HA at different concentration of $MgCl_2$ as background electrolyte. Excitation of the Eu(III) luminescence at 356 nm, p*H* = 5, *c*(HS) = 12.5 mg·L^{-1}.

ratio *r* is stronger.

By increasing the Eu(III) concentration, more and more binding sites of the HS are occupied. One approach to describe the interactions of HS with protons or metal ions is the NICA Donnan model.[27,28] In this model two kinds of binding sites – a stronger and a weaker one – are assumed, which allow specific interactions between humic substance molecules and metal ions. Non-specific interactions are also taken into account by including a Donnan sub-model in this approach. The decreasing trend of the asymmetry ratio can be interpreted in these terms. At low Eu(III) concentrations, most of the Ln(III) ions are expected to be coordinated by strong binding sites, which produce a stronger ligand field and hence a more intense $^5D_0 \rightarrow {}^7F_2$ transition – due to its hypersensitive character – will show up in the luminescence spectrum. With increasing Eu(III) concentration also weaker binding sites are involved in the

complexation. This reduces the intensity of the hypersensitive transition and hence the value of the asymmetry ratio *r*.

An increase of the background electrolyte concentration has at least two effects. On one hand, the number of competing metal ions for binding sites is increased. On the other hand, HS can also be understood as polyelectrolytes and consequently the increase in ionic strength will also affect the humic substance conformation. As can be seen in Figure 22 the increase of the background electrolyte concentration leads to a decrease of the asymmetry ratio *r*. At lower $MgCl_2$ concentrations (less than 10 mmol·L^{-1}) no influence on the asymmetry ratio *r* was observed. Both findings are in accordance with the general trends discusses so far. A similar behavior for the complexation of Eu(III) ions by Gohy573 HA in solutions containing Ca(II) was found.[29,30] In these experiments, KNO_3 was used to control the ionic strength and $Ca(NO_3)_2$ was added. At Ca(II) concentration below 1 mmol·L^{-1} the asymmetry ratio *r* remains constant as the amount of bound Eu(III) is not affected. At higher Ca(II) concentrations a decrease of *r* was observed and accounted to a replacement of Eu(III) ions by Ca(II). The changes in *r* was led back to changes in the humic substance conformation.

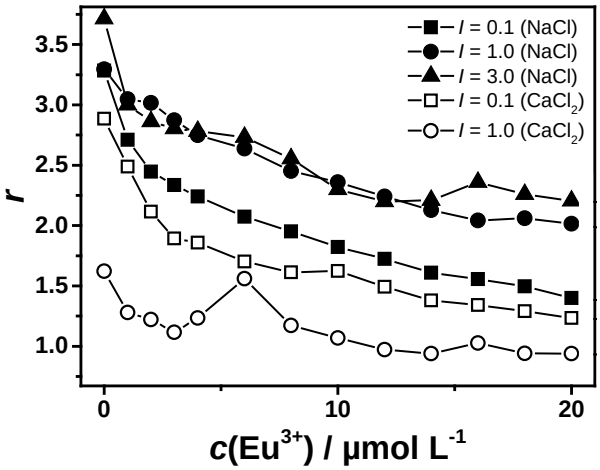

Figure 23: Asymmetry ratio *r* (left) of Eu(II) complexes with SRFA in aqueous solution containing different concentrations of background electrolyte (NaCl or $CaCl_2$) . The ionic strength of *I* = 0.1 mol·L^{-1} (1.0 mol·L^{-1}) for $CaCl_2$ corresponds to *c*($CaCl_2$) = 0.033 mol·L^{-1} (0.33 mol·L^{-1}). λ_{ex} = 325 nm, p*H* = 5.

The background electrolyte acts not only due to the number of ions in solution. In Figure 23 the effect of $CaCl_2$ and NaCl as background electrolytes on the luminescence asymmetry ratio *r* is compared. The ionic strength was chosen to lie within *I* = 0.1 mol·L^{-1} and *I* = 3.0 mol·L^{-1}. The increase of the NaCl concentration leads to a shift of *r* to greater values, whereas increasing of the $CaCl_2$ concentration showed the opposite trend. In this case *r* decreases. At comparable ionic strength for $CaCl_2$ and NaCl (*I* = 1.0 mol·L^{-1}) the value of the asymmetry ratio *r* was distinctly lower in Eu(III) luminescence spectra arising from complexes with SRFA in $CaCl_2$ containing solutions. The main difference in both electrolyte systems is the charge of the cation. A single positive charged ion like Na(I) has only one valency for interaction with opposite charged ions, whereas Ca(II) can interact with more than one opposite charge. It is conceivable that this opens the possibility to link humic substance molecules together, which will have significant effects on further interactions with metal ions like Ln(III) ions. As already

discussed, above a certain concentration the cations from the background electrolyte itself become strong competitors for binding sites, which leads to a displacement of the Eu(III) ions.

To account for macromolecular effects, such as changes in conformation, the measurement of distances between binding sites might be a good indicator. But these distances are hardly to measure. A way out is to measure them indirectly by the distances between bound Ln(III) ions. This can be achieved by applying the ILTE.

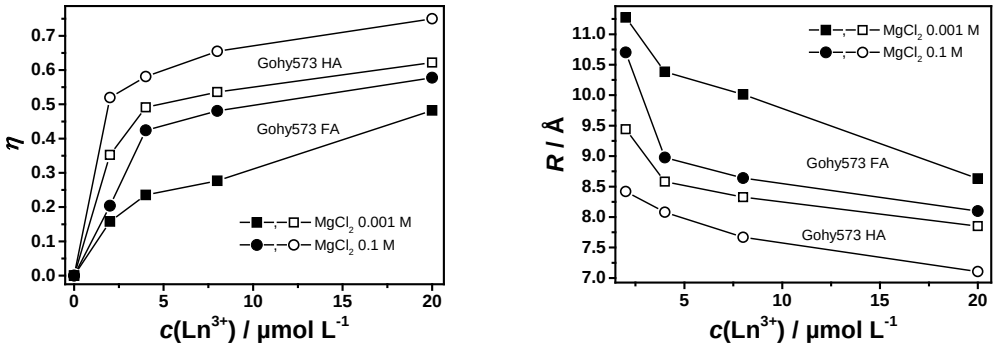

Figure 24: Energy transfer efficiencies (left) as calculated from steady state measurements according eq. (8) and resulting distances using eq. (7) with R_0 = 8.53 Å as published by Horrocks et al.[7]. See text for details of experimental procedure.

To solutions containing Eu(III) and Gohy573 HA or Gohy573 FA, respectively, La(III) or Nd(III) ions were added. It is known, that Nd(III) can quench the Eu(III) luminescence by an ILET based on an Förster resonance energy transfer mechanism depending on the distance between both ions.[7] La(III) itself will not quench Eu(III)'s luminescence as it is no suitable acceptor for such a transfer of energy. In the experiments 5 µmol·L^{-1} of Eu(III) and 12.5 mg·L^{-1} HS were mixed and allowed to form complexes. Subsequently, in two sets of experiments La(III) and Nd(III) ions, respectively, were added. In both cases, the Eu(III) luminescence intensity changes. In case of adding La(III) ions, the changes are due to effects of competition for binding sites and of alteration in the HS conformation, which could have an influence on the sensitization process as well as on the binding site of Eu(III). It is assumed, that the addition of Nd(III) ions has the same impact on the humic substance and on the bound Eu(III). But, additionally Nd(III) can quench the luminescence of Eu(III) due to an operative energy transfer between both ions. To evaluate the efficiency of the energy transfer carefully, measurements with La(III) and Nd(III) are necessary. The changes in luminescence intensity, when adding La(III) reflects the behavior of the Eu(III) luminescence without contribution of an acceptor and is in eq. (8) denoted as I_D. The experiment with adding Nd(III) to the solutions gives the values for I_{DA}. Based on these prerequisites the calculated energy transfer efficiency is shown in Figure 24 (left). With a Förster distance R_0 taken from the literature[7], the energy transfer efficiency could be transformed into distances between bound Eu(III) and Nd(III) as shown in Figure 24 (right). Independent of the HS or of the ionic strength, the addition of Ln(III) ions to the Eu(III) HS complexes results in a decrease of the inter-lanthanide distances. This is reasonable as more binding sites are occupied. Therefore, the mean dis-

tance between them has to decrease. An increase in ionic strength yields to an overall decrease of the distances. This could be a result from alterations in the conformation of the HS due to processes like coagulation or folding, both known macromolecular effects.

3.5 Interactions of Europium(III) with natural occurring polymers

One of the main challenge one has to deal with when working with HS is their chemical heterogeneity. A way to overcome this circumstance is to use model substances, which represents substructures of HS and address certain properties. One kind of model substances are low molecular weight compounds, such as substituted benzoic acids or substituted phenyl moieties, which are known as basic structures in HS (cf. Scheffer/Schachtschabel, page 57).[31] It is attractive to assume, that these type of substructures accounts for the photophysical behavior and primary complexation moieties in HS. By investigating complexes of Ln(III) ions with these compounds basic photophysics of Ln(III) HS complexes can be mimicked and studied. But low molecular weight compounds cannot model macromolecular effects involved in the complex formation. For this purpose, another type of model compounds has to be considered. In a first attempt, poly(acrylic acid) (PAA) was chosen.[32(Appendix B-7)] The complexation of Ln(III) ions by PAA was of interest. By making use of the ILET, distances between coordinated Ln(III) ions could be calculated. The calculated distances showed a dependence on p*H* as well as ionic strength. From this an influence due to conformation alterations upon Ln(III) complexation and hence macromolecular effects could be concluded. Although with PAA macromolecular effects could be addressed, effects like sensitization of Ln(III) luminescence could not be mimicked.

Therefore, an attempt to investigate both parameteres, a novel model polymer was utilized, in which macromolecular behavior and a substructure, which accounts for the photophysical behavior of HS, were combined. As monomer 4-vinylbenzoic acid was chosen. In a radical polymerization[g] with 4,4'-azobis(4-cyano-pentanoic acid) as initiator two polymers with different chain length were synthesized. Gel permeation chromatography gave peak molecular weights M_p of 5 200 g·mol^{-1} and 17 000 g·mol^{-1} for the short-chain (PVBA 52 00) and the long-chain (PVBA 17 000) polymer, respectively.

[g] see experimental part

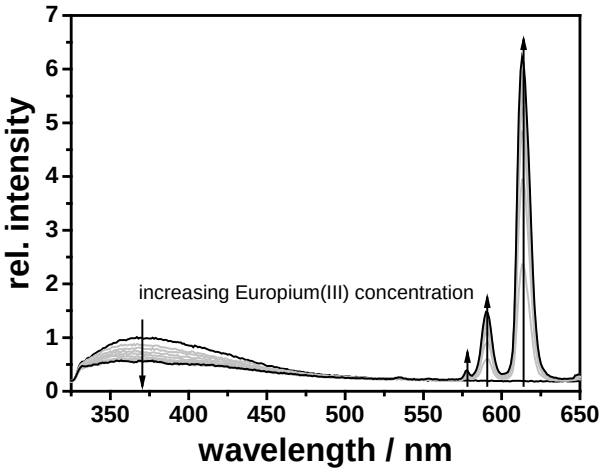

Figure 25: Stationary luminescence spectrum of PVBA 5200 upon addition of Eu(III). c(PVBA 5200) = 50 mg·L^{-1}, λ_{ex} = 288 nm, pH = 6.5, 1 mol·L^{-1} NaCl as background electrolyte. Eu(III) concentration was increased from 0 µmol·L^{-1} to 20 µmol·L^{-1}.

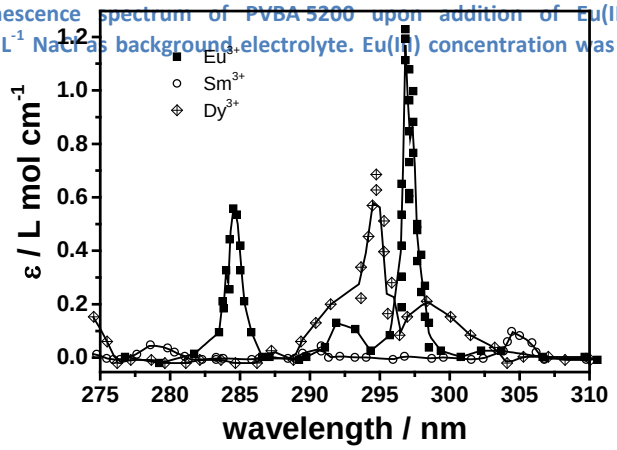

Figure 26: Part of the absorption spectra of Eu(III), Sm(III) and Dy(III) ions in aqueous solution. Data points were extracted from absorption spectra given in literature[6]. The straight lines are the result of a linear interpolation of these data points.

The fluorescence emission of the synthesized polymer – plotted in Figure 25 – shows similarities to the fluorescence emission of a humic substance upon addition of Eu(III) ions. A relatively broad fluorescence emitted between 330 nm < λ < 500 nm could be observed after excitation at 288 nm. Compared to HS (cf. Figure 17) the emitted fluorescence is higher in energy and not as broad compared the humic substance fluorescence. Interestingly, a sensitization of the Eu(III) luminescence was observed. Both, the broad fluorescence and sensitization abilities makes PVBA to an interesting polymeric model compound for HS.

In Figure 26 the absorption spectra between 275 nm < λ < 310 nm of Ln(III) ions used in this study are compared. As the extinction coefficients are very small at 288 nm, a direct excitation even at the highest used Ln(III) concentrations c(Ln(III)) = 20 µmol·L^{-1} is very unlikely.

The sensitization experiments were also carried out with Sm(III) and Dy(III). Both Ln(III) ions have much shorter decay times (cf. Table 2) due to a more effective quenching of their luminescence in aqueous solution. Comparable to the measurements with Eu(III) the luminescence of Sm(III) or Dy(III) could be sensitized via the PVBA as well. As an example, this is depicted for Dy(III) and PVBA 5 200 in Figure 27. The intrinsic PVBA fluorescence is quenched upon addition of Dy(III) ions. The excitation energy is transferred to the complexed Dy(III) ions, which thereupon show luminescence. In the shown spectral region, Dy(III) has two transitions from $^4F_{9/2} \rightarrow {}^6H_{15/2}$ and $^4F_{9/2} \rightarrow {}^6H_{13/2}$. The intrinsic PVBA fluorescence overlaps with the luminescence resulting from the higher energy transmission in Dy(III). For further evaluation the luminescence intensity arising from the $^4F_{9/2} \rightarrow {}^6H_{13/2}$ transition was used.

The dependence of the luminescence sensitization on the Ln(III) ion concentration was similar for the different Ln(III) ions used in this study as shown in Figure 28. Up to a concentration of 11 µmol·L^{-1} the luminescence intensity increases and at higher concentrations the

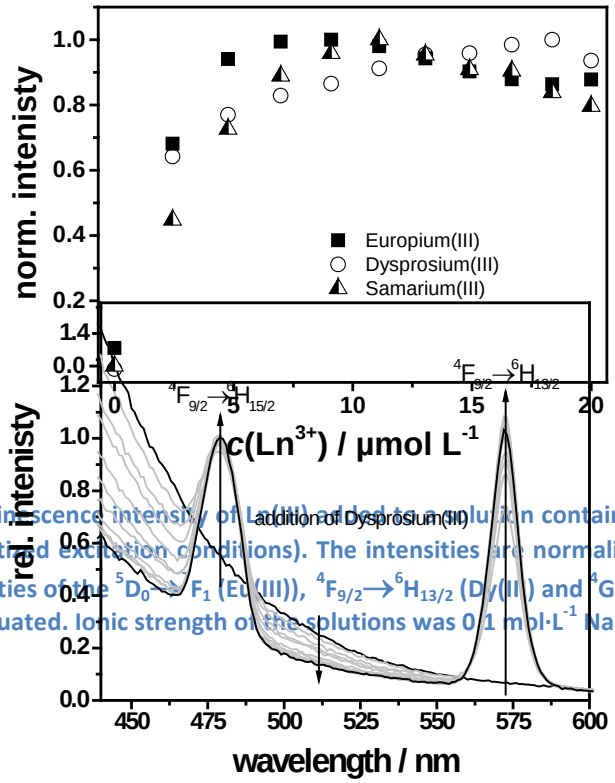

Figure 28: Normalized luminescence intensity of Ln(III) added to a solution containing 50 mg·L^{-1} upon excitation at λ_{ex} = 288 nm (sensitized excitation conditions). The intensities are normalized to their specific maximum intensity. The intensities of the $^5D_0 \rightarrow {}^7F_1$ (Eu(III)), $^4F_{9/2} \rightarrow {}^6H_{13/2}$ (Dy(III)) and $^4G_{5/2} \rightarrow {}^6H_{7/2}$ (Sm(III)), respectively, transition were evaluated. Ionic strength of the solutions was 0.1 mol·L^{-1} NaCl.

Figure 27: Stationary luminescence spectrum of PVBA 5 200 without and upon addition of Dy(III) ions. Dy(III) concentration was increased up to 20 µmol·L^{-1}. λ_{ex} = 288 nm, pH = 6.5, c(PVBA 5 200) = 50 mg·L^{-1}.

luminescence intensity stays constant (in case of Dy(III)) or slightly decreases (Eu(III) and Sm(III)).

The measurements shown in Figure 28 were needed to define the Ln(III) ion concentrations for the measurements making use of the ILET to evaluate distances of coordinated Ln(III) ions. To find a compromise between sufficient luminescence intensity and metal loading, which allows the coordination of further Ln(III) ions (e.g., acting a acceptor) 5 µmol·L^{-1} was chosen. The highest total Ln(III) ions concentration was 20 µmol·L^{-1}.

In Figure 29 the effect of the addition of La(III) ions to solutions containing PVBA 5 200 and Eu(III) on the luminescence asymmetry ratio *r* – calculated according to eq. (2) – is compared for different ionic strengths (NaCl: 0.1 mol·L^{-1}, 1.0 mol·L^{-1} and 3 mol·L^{-1}). For the lowest concentration of background electrolyte, no effect on *r* can be concluded. Obviously, the coordinated Eu(III) is not affected by the addition of further metal ions. For the higher ionic strengths, the values of the asymmetry ratio scatter a little, but in principle, it remains constant. Comparable results (0.1 mol·L^{-1} and 1.0 mol·L^{-1} NaCl, respectively) were found for the

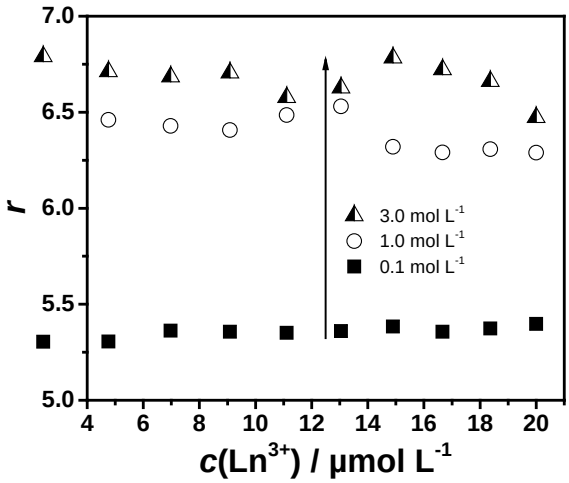

Figure 29: Asymmetry ratio *r* of the Eu(III) luminescence in complexes with PVBA 5 200 upon addition of La(III) ions. The Eu(III) concentration was 5 µmol·L^{-1}. Given is the total luminescence concentration. λ_{ex} = 288 nm, p*H* = 6.5.

higher molecular weight polymer PBVA 17 000.

If coordinated Eu(III) ions will be expelled from binding site due to competition, it will have no effect on the asymmetry ratio as only complexed Eu(III) ions can be excited via sensitization by the polymer. But to account for that, measurements with La(III) are indispensible, as they reflect influences only resulting from the increased Ln(III) ions concentration, which is shown in Figure 30. For the short-chain polymer PVBA 5 200 the Eu(III) luminescence intensity increases for ionic strength 1.0 mol·L^{-1} and 3.0 mol·L^{-1}, when La (III) ions are added. At lower ionic strength, an opposite trend was observable. For the long-chain polymer PVBA 17 000, the general dependency of the Eu(III) luminescence intensity upon addition of La(III) was the same for an ionic strength of 0.1 mol·L^{-1} and 1.0 mol·L^{-1}, respectively. The addition of Nd(III) quenches the Eu(III) luminescence intensity as a result of the aforemen-

tioned ILET. The luminescence intensities plotted in Figure 30 can be used, to calculate the energy transfer efficiency according to eq. (8) with I_{DA} as the luminescence intensity in presence of Nd(III) and I_D as the corresponding luminescence intensity in presence of La(III).

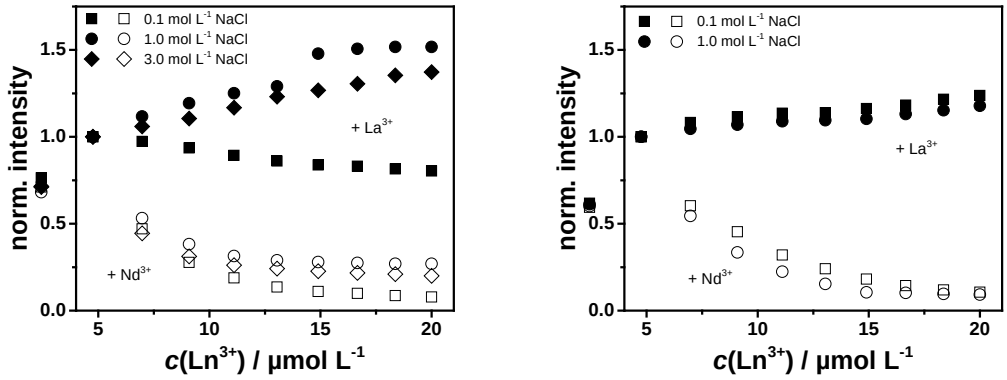

Figure 30: Change of Eu(III) intensity upon addition of La(III) and Nd(III), respectively. To a PVBA 5 200 (left) or a PVBA 17 000 (right) solution containing 5 µmol·L^{-1} of Eu(III). The concentration of the polymer was 50 mg·L^{-1} and p*H* = 6.5.

Besides Eu(III) also Dy(III) and Sm(III) were used as donors. In these experiments Nd(III) was used as an acceptor. For all chosen donor-acceptor-pairs a luminescence quenching of the donor was found. The measurements were carried out for PVBA 5 200 and PVBA 17 000 as polymers in 0.1 mol·L^{-1} NaCl solution. For the measurements with Eu(III) as donor, the I_D values results from titration with La(III) ions as shown in Figure 30. For measurements with Sm(III) or Dy(III) as donor, the I_D values were taken from their resulting luminescence intensity upon their increasing concentration.

Figure 31 gives the energy transfer efficiencies calculated according to eq. (8) for relevant donor-acceptor-pairs are shown. The highest transfer efficiencies from the above mentioned experiments can be found for Eu(III) as donor. Dy(III) shows smaller and Sm(III) the smallest η values. Eq. (7) tells, that the energy transfer efficiency depends on the distance between the involved donor and acceptor ion as well as on the Förster distance R_0. The distances of the complexed Ln(III) ions should be very similar independent from the donor ion. Therefore, the differences in energy transfer efficiency have to result from different Förster radii. This is the key issue of this analysis. If no Förster distances are available from literature, they have to be calculated for each donor-acceptor-pair from photophysical parameters

$$\boldsymbol{R_0} = \sqrt[6]{\frac{9\ln(10)\kappa^2\Phi_D J}{128\pi^5 N_A n^4}}. \qquad (22)$$

Necessary parameters are the luminescence quantum yield Φ_D, the overlap integral of donor emission and acceptor absorption *J*, refractive index *n* and the orientation factor κ^2. Whereas *J* can be derived from absorption and stationary luminescence measurements, the determination of Φ_D is crucial.

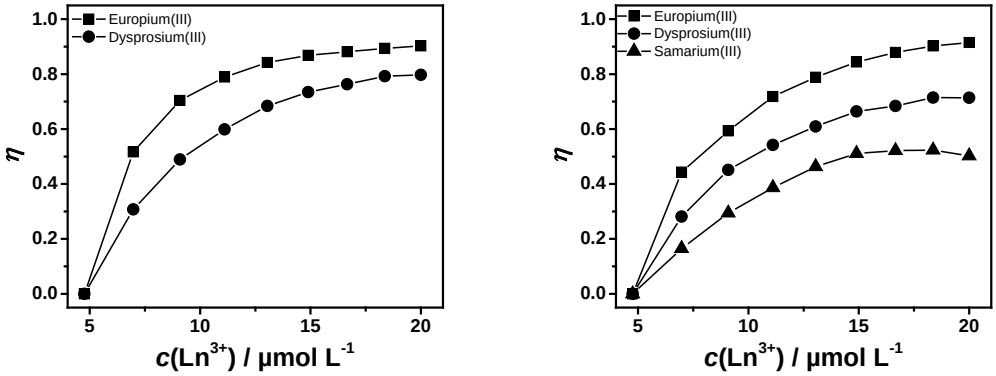

Figure 31: Energy transfer efficiencies η calculated according eq. (8) from stationary luminescence measurements for Ln(III)ions complexed to PVBA 5 200 (left) and PVBA 17 000 (right), respectively. The ionic strength was set to 0.1 mol·L^{-1} using NaCl. *c*(polymer) = 50 mg·L^{-1}, p*H* = 6.5. Details of the calculation are given in the text.

Dependent on how exact the energy transfer efficiency can be determined, a distance interval from $0.6 \cdot R_0 < R < 1.6 \cdot R_0$ corresponding to $0.95 < \eta < 0.05$ is accessible. By choosing a donor-acceptor-pair determinations of distances within a specific distance interval (governed by R_0) becomes possible.

So far, only results from stationary luminescence measurements were shown. The investigations dealing with the ILET were also performed by time-resolved measurements. Hereby, a second photophysical parameter – the luminescence decay time – is at hand, which is sensitive to energy transfer processes. In these experiments Eu(III) was mainly used as donor as changes in its luminescence decay time are easier to measure with a required accuracy compared to Dy(III) or Sm(III).

For both, the short-chain and the long-chain polymer, the addition of La(III) ions results in an increase of Eu(III) luminescence decay time. Upon addition of Nd(III) ions the luminescence decay time of Eu(III) decreases. In Figure 32 (a) – (c) the luminescence decays of Eu(III) in complexes with PVBA are shown. Figure 32 (d) summarizes the derived luminescence decay times of Eu(III). The luminescence decays were fitted to a stretched exponential equation to account for the restricted dimension of the energy transfer.[33]

$$I = I_0 + A_1 \exp\left(-\frac{t}{\tau} - C\left(\frac{t}{\tau}\right)^{\gamma}\right) + A_2 \exp\left(-\frac{t}{\tau}\right) \qquad (23)$$

In this equation, *I* is the measured luminescence intensity and τ the decay time of the donor (Eu(III)). *T*he time after laser flash is given by *t*. Background intensity resulting from noise of the detection system is reflected by I_0. The parameter *C* is proportional to the acceptor concentration and γ accounts for the local geometry. The third term was included to account for donor ions, which were not quenched by an acceptor. During the fitting procedure of the decays given in Figure 32 (a) – (c) comparable γ value arised (cf. Table 7). Independent of the

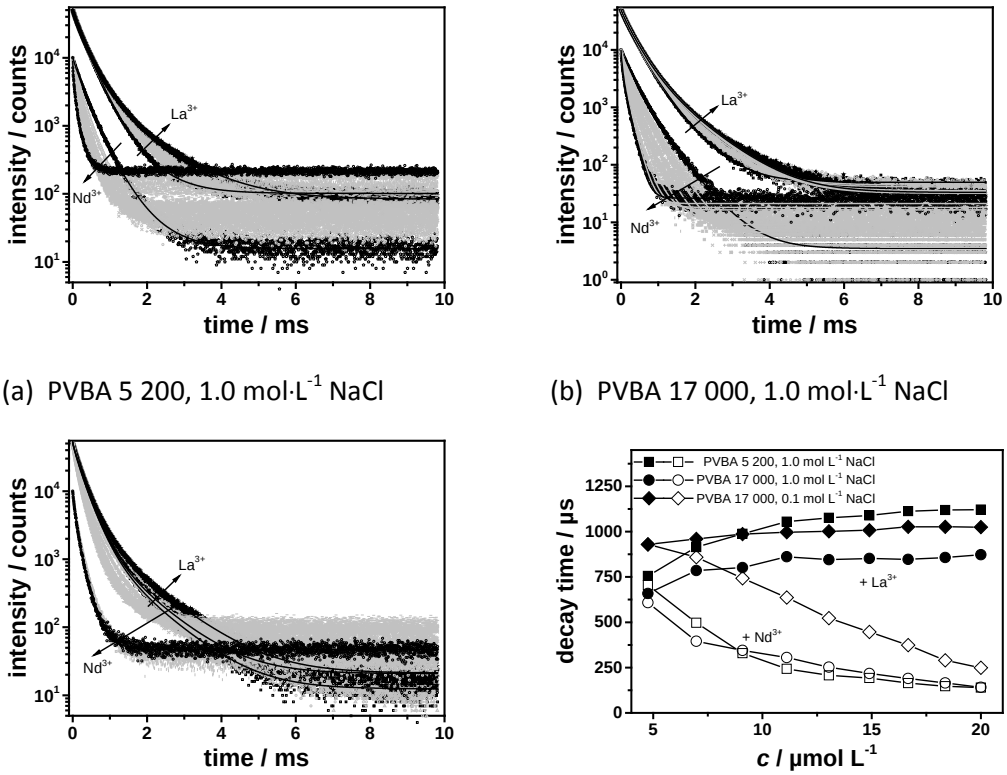

Figure 32: Luminescence decay kinetics and luminescence decay time of Eu(III) luminescence complexed to PVBA in presence of La(II) and Nd(III), respectively. *c*(Polymer) = 50 mg·L^{-1}, p*H* = 6.5, λ_{ex} = 288 nm, λ_{em} = 615 nm.

molecular weight of the polymer and the ionic strength, the measure of the local geometry γ is comparable.

By comparing Figure 32 (d) with Figure 30 the same trend can be concluded. For the short-chain polymer PVBA 5 200 and an ionic strength of 1.0 mol·L^{-1} NaCl, for the luminescence decay time as well as for the luminescence intensity of Eu(III) a pronounced increase by increasing La(III) concentration can be found. An increase of Eu(III)'s luminescence intensity and luminescence decay time, respectively, can also be found for the long-chain polymer PVBA 17 000 at ionic strength of 0.1 mol·L^{-1} or 1.0 mol·L^{-1} NaCl, but only to a lesser extent. The effect to the Eu(III) complexed to the lower molecular weight polymer is stronger.

Up to now, for the donor-acceptor pairs the results of stationary and time-resolved experiments were presented. In all cases a quenching of the donor luminescence either decay time

Table 7: Measure of local geometry parameter γ resulting from the fitting of the decay curves given in Figure 32 (a) – (c) to eq. (23).

c(NaCl) / mol·L^{-1}	PVBA 5 200	PVBA 17 000
0.1	—	0.85
1.0	0.83	0.88

or intensity, when increasing the acceptor concentration was found. For the donor-acceptor-pair Eu(III)-Nd(III) is a Förster distance known from literature.[7] The first step is to calculate the energy transfer efficiency η from the luminescence intensities plotted in Figure 30 or the luminescence decay time given in Figure 32. With eq. (7) and a Förster distance of R_0 = 8.53 Å from literature distances between the Ln(III) ions complexed to the polymer were derived.

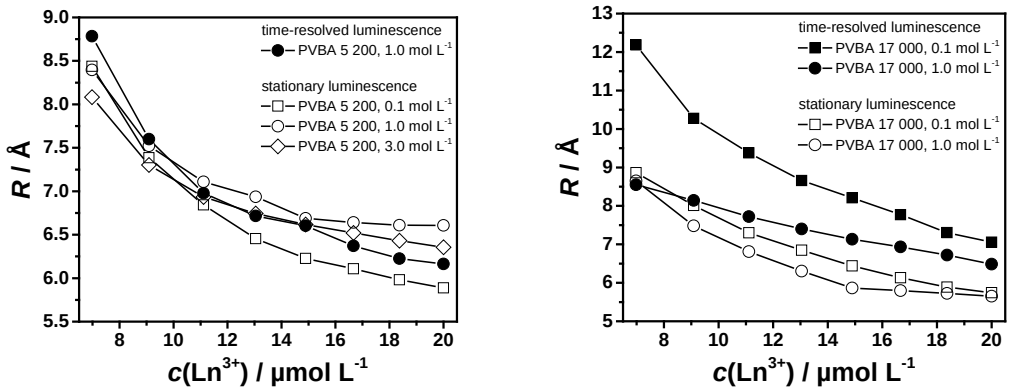

Figure 33: Derived distances *R* between Ln(III) ions coordinated by the short-chain polymer (left) and the long-chain polymer (right), respectively (c(Polymer) = 50 mg·L^{-1}, p*H* = 6.5).

In Figure 33 for both polymers (PVBA 5 200 and PVBA 17 000) distances *R* between coordinated Ln(III) ions are plotted. For the short-chain polymer (PVBA 5 200) no clear trend can be concluded. Independent on the ionic strength the distances decrease from (8.4 ± 0.3) Å down to (6.3 ± 0.3) Å. For PVBA 17 000, stationary and time-resolved luminescence measurements give different results. Whereas from stationary measurements, almost no effect from the ionic strength can be found, the time-resolved measurements show an effect of the ionic strength. Here, the distances decreases by increasing ionic strength. This can be explained, if the polymer is understood as a polyelectrolyte. An increase in ionic strength lead to a charge compensation along the polymer chain, what subsequently alters the confirmation of the polymer. A possible alteration can be the folding of the polymer, which is connected to a reduction in size and hence decrease of distances between coordinated Ln(III) ions.

3.6 Vibrational spectroscopy on mineral surfaces

Kaolin and intercalation of LMWC

Before the vibrational spectra of intercalation compounds can be discussed, the vibrational spectra of the source clays Kaolin KGa-1b and Kaolin KGa-2 have to be analysed. In this study Raman microscopy and SFG spectroscopy were combined to obtain complementary information for a chemical speciation at mineral interfaces.

From each Kaolin sample Raman spectra at three different points of the sample were measured. The spectra were background corrected. Averaging of the three spectra gave a mean Raman spectrum. The averaged Raman spectra for KGa-1b and KGa-2 are depicted in Figure 34.

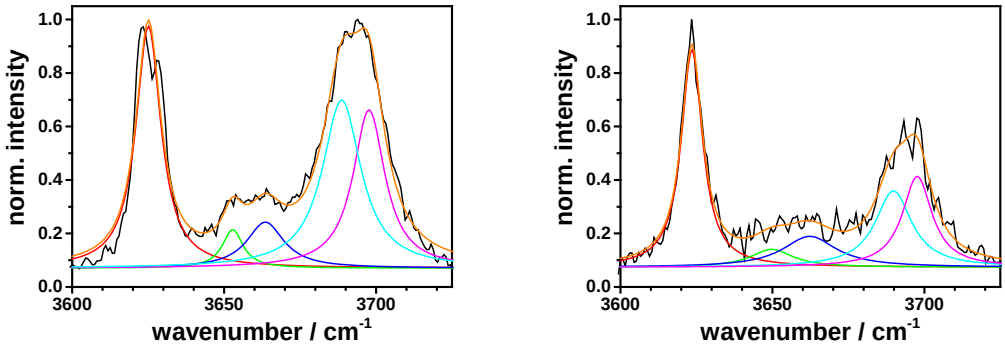

Figure 34: Averaged Raman spectra (black) of Kaolin KGa-1b (left) and KGa-2 (right). To each underlying vibration a Lorentzian function was fitted. Five vibration could be resolved: ν_1 (red), ν_2 (green), ν_3 (blue), ν_4 (cyan) and ν_5 (magenta). The sum of all single Lorentzian functions gives the cumulated fit (orange).

For both Kaolin samples five peaks could be observed. Fitting of the data to Lorentzian functions gave the peak positions and areas of the single vibrational transitions. The results are summarized in Table 8. For both samples the vibrational frequencies are slightly different, but an assignment to expected OH vibrations in kaolinite was possible.[34,35] The inner hydroxyl group originates the vibration around 3625 cm^{-1}. The inner surface hydroxyl groups have vibrations around 3650 cm^{-1}, 3665 cm^{-1}, 3689 cm^{-1} and 3698 cm^{-1}. The values found are in good agreement with the values reported by Frost et al.[34] The fitting of the peaks around 3650 cm^{-1} and 3665 cm^{-1}, especially for KGa-2, was challenging as the intensities of these vibrational transitions are rather low.

Table 8: Results of fitting the Raman spectra of both Kaolin samples to a sum of Lorentzian functions. Given are the peak positions and the relative peak areas (rel. area).

Vibration	KGa-1b		KGa-2	
	Peak position / cm^{-1}	rel. area / %	Peak position / cm^{-1}	rel. area / %
ν_1	3625 ± 1	30.1 ± 0.6	3623 ± 1	35.5 ± 0.8
ν_2	3653 ± 1	4.0 ± 1.7	3650 ± 3	11.7 ± 5.4
ν_3	3664 ± 1	8.5 ± 2.8	3666 ± 3	10.3 ± 5.9
ν_4	3689 ± 1	32.3 ± 5.8	3689 ± 1	14.9 ± 4.8
ν_5	3698 ± 1	25.2 ± 7.1	3697 ± 1	27.6 ± 4.3

The next step was to use SFG spectroscopy to monitor the OH vibration region of the same kaolinite samples. Following eq. (15) the intensity of a SFG signal depends as well on the probability for a Raman as for an IR transition. Additionally, SFG spectra stems from interfaces in the material, whereas Raman spectroscopy gives signals from a bulk phase. Therefore, some differences between Raman and SFG spectra are to be expected.

Comparable to the Raman spectra, also the SFG spectra (cf. Figure 35) show two strong peaks, one around 3620 cm^{-1} and the other one around 3700 cm^{-1}. These transitions can be assigned to the ν_1 and ν_5 transition, respectively. The exact values of the vibration frequencies, given by the peak positions resulting from fitting with a sum of Lorentzian functions, are listed in Table 9. In both kaolinites KGa-1b and KGa-2, the transitions ν_1 and ν_5 are slightly shifted < 5 cm^{-1} in the SFG compared to Raman spectra. Also at a frequency around 3688 cm^{-1} a transition, denoted with ν_4, was present, which is almost not shifted compared to the Raman spectra. At 3642 cm^{-1} a vibrational transition shows up, but its origin is not that clear. Possibly, this signal could be i) the vibration ν_2 shifted about 10 cm^{-1} or ii) a signal arising

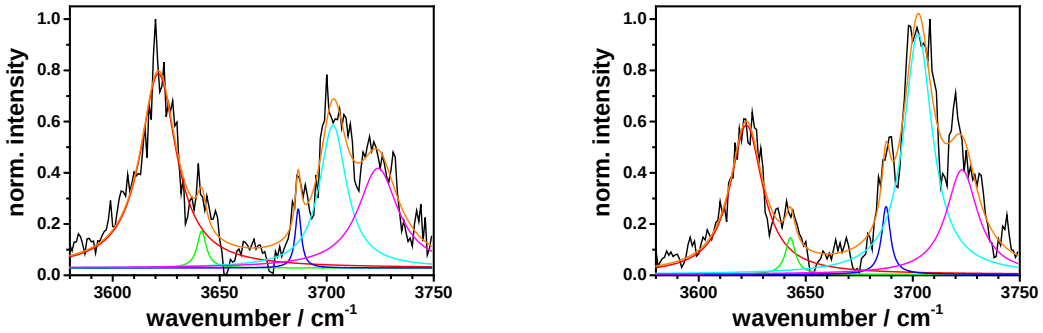

Figure 35: SFG spectra of Kaolin KGa-1b (left) and KGa-2 (right) corrected for intensity of vis (I_{vis}) and IR (I_{IR}) laser beam. The measured spectrum (black) was fitted to a sum of Lorentzian functions. As fitting result, the peak position and peak area of the vibrational transitions could be obtained. In the fitting five vibrational transitions were assumed, giving vibrations ν_1 (red), ν_4 (blue) and ν_5 (cyan). Deviating from the Raman spectra shown in Figure 35, vibrations at ν_x (magenta) and ν_z (green) were found.

from surface adsorbed water, condensed from air.

The intensity of SFG signals is direct proportional to the intensity of the IR light reaching the sample. The shown SFG spectra are corrected for both, I_{vis} and I_{IR}. For technical reasons, the intensity of the laser beams are measured in a given distance from the sample surface, what is no problem for the visible light as it does not interact with the air. In contrast, the IR light, needed to probe the range of OH vibrations, can be absorbed by present water vapor. This makes a correction for the intensity of the IR light challenging. Here, the SFG setup has to be improved. Therefore, the apparent transition at 3642 cm^{-1} could be an artefact, resulting from a dip in the higher energetic edge of the ν_1 transition due to an absorption of the corresponding IR light by ambient water vapor.

In the SFG spectra also a transition around 3665 cm^{-1} can be observed, but it was not possible to include it in the fitting procedure. This weak transition can be related to the vibration ν_3 known from Raman spectra. In the SFG spectra an additional peak around 3723 cm^{-1} could

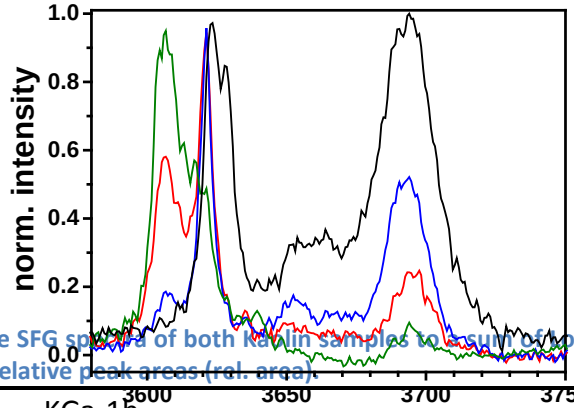

Figure 36: Raman microscopy spectra of three different spots (blue, red and green) of an intercalated KGa-1b sample. For comparison, also the Raman spectrum of an untreated KGa-1b sample (black) is plotted.

Table 9: Results of fitting the SFG spectra of both Kaolin samples to a sum of Lorentzian functions. Given are the peak positions and the relative peak areas (rel. area).

Vibration	KGa-1b		KGa-2	
	Peak position / cm^{-1}	rel. area / %	Peak position / cm^{-1}	rel. area / %
ν_1	3621 ± 1	45.1 ± 3.2	3622 ± 1	30.4 ± 2.7
ν_z	3642 ± 1	2.2 ± 1.0	3643 ± 1	2.3 ± 1.0
ν_4	3687 ± 1	2.3 ± 0.9	3688 ± 1	3.7 ± 1.3
ν_5	3703 ± 1	24.9 ± 3.6	3702 ± 1	43.1 ± 3.8
ν_x	3724 ± 1	25.6 ± 4.4	3723 ± 1	20.6 ± 3.4

be observed. The origin of this vibration is yet not clear. A quantitative analysis of SFG spectra is difficult, because of the aforementioned uncertainties in the determination of the actual IR intensity reaching the sample. The weak intensity of the vibration ν_4 is clear by comparing IR and Raman spectra. In IR spectra of kaolinites the transition at 3688 cm^{-1} is only weak.[36] As the probability of a SFG process is directly proportional to the IR transition momentum, also the intensity of this transition in a SFG spectrum is expected to be low.

Under some conditions, small organic material can intercalate into kaolinite lattice layers. The intercalation happens at the inner surface hydroxyl groups, which affects the vibrational spectrum.[37,38] Additionally, also the distance between layers in the kaolinite structure will increase upon intercalation.[37]

In Figure 36 the Raman spectra received at three different points of an intercalated Kaolin KGa-1b sample are plotted. For the intercalation potassium acetate was used. As can be seen, the spectra are different. Using the spatial resolution of the Raman microscope, a chemical imaging of the clay surfaces becomes possible. From the three spectra plotted in Figure 36 differences in the intercalation at the probed spots of the sample can be extracted.

The Raman spectrum plotted in green reflects the highest degree of intercalation. Due to the intercalation an additional band at ν_{Ac} = 3607 cm^{-1} in the Raman spectrum can be observed. This band arises from the interactions of the inner surface hydroxyl groups with acetate. During intercalation hydrogen bonds between layers of the kaolinite were broken and new hydrogen bonds to the acetate were formed.[37] As only the inner surface hydroxyl groups are affected by this interaction, the vibration frequency ν_1 of the inner hydroxyl group remained unchanged. From Figure 36 it is obvious, that with increasing intensity of ν_{Ac} the intensities of ν_2 to ν_5 decreased. For a complete intercalation, the intensities of these vibrations can become zero.[38]

The intercalation could also be shown with SFG spectroscopy. In Figure 37 a SFG spectrum of an intercalation formed between KGa-1b and potassium acetate is shown. The intensity of the vibrational transition at 3620 cm^{-1} is reduced compared to the SFG spectrum received for a pure KGa-1b sample (plotted in gray). Nonetheless, in the intercalated sample a transition around 3606 cm^{-1} can be seen. Compared to the pure KGa-1b samples, the intensity of the ν_3 vibration as well as the vibrations around 3700 cm^{-1} were almost not changed, which is a clear difference to the Raman measurements. After intercalation of potassium acetate a decrease in the intensities of these vibrations is expected. Contrary to Raman measurements, for the formation of a SFG signal, the probability for an IR transition plays a role, too. When water is adsorbed at the surface of the Kaolinite, this will influence the SFG signal, as the water itself has a strong IR absorption. Hence, the unchanged SFG signal at wavenumbers above 3650 cm^{-1} may be a result of adsorbed water.

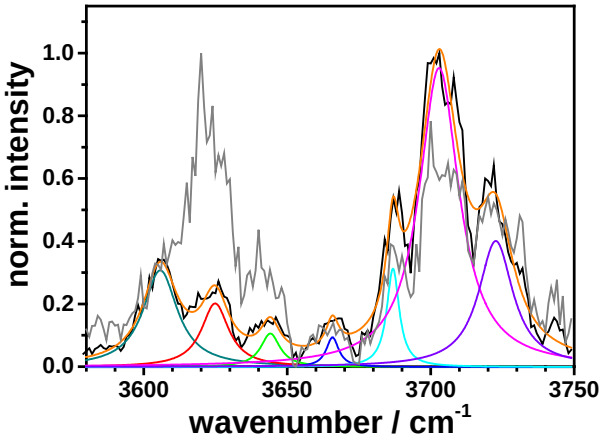

Figure 37: SFG spectra (black) of an intercalation complex of KGa-1b and potassium acetate. In addition to the vibrational bands ν_1 (red), ν_z (green), ν_5 (magenta) and ν_x (violet) fitting to a sum of Lorentzian functions gave ν_3 (blue) and ν_{Ac} (dark cyan). For comparison, the SFG spectrum of the pure KGa-1b (gray) is plotted.

A complementary approach to study the intercalation is the use of X-ray powder diffraction (XRD) measurements. An intercalation changes the distances of the lattice layers of the Kaolinite, which subsequently alters the positions of the reflexes in an XRD spectrum.

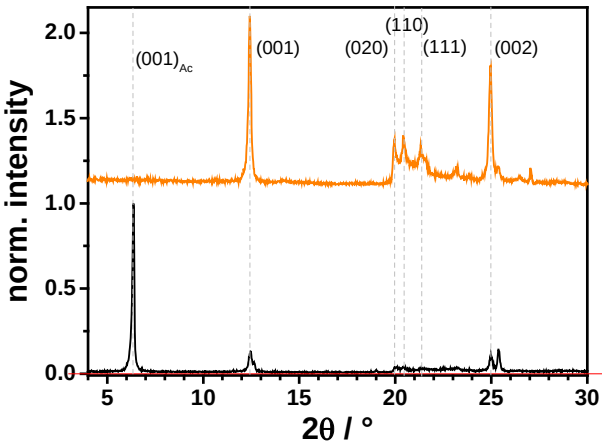

Figure 38: XRD spectra of potassium acetate intercalated KGa-1b (black) and pure KGa-1b (orange). For clarity, the XRD of the pure Kaolinite was shifted about one unity to higher intensities. The assignment of the reflexes to the lattice planes followed data from literature.[39]

In the pure Kaolinite KGa-1b, the reflex of the (001) plane is at $2\theta = 12.4$ °, shown in Figure 38. Applying the Bragg equation[h] and a wavelength of the copper anode of $\lambda_{Cu} = 1.5405$ Å gives a distance of 7.13 Å, which is very near to a literature known value of 7.14 Å.[3] The (001) basal reflex shifts to a lower value ($2\theta = 6.4$ °) upon intercalation (cf. Figure 38). This translates in a distance of 13.8 Å, which is a little bit shorter than reported values.[40] Intercalation happens within the kaolinite layers, which changes the position of the reflexes originated by (00*l*) planes. The lattice in *a* and *b* direction are not influenced by intercalation. In the XRD spectrum of the intercalated KGa-1b sample the reflex from the (001) plane of the non-intercalated KGa-1b can be observed. This shows that no completed intercalation occurred.

To figure out, how fast potassium acetate intercalates into kaolinite, the contact time of the potassium acetate solution and the kaolinite was varied. As parameter for the evaluation the degree of intercalation d*I* was chosen, which can be calculated by the relative appearance of the reflex originating from intercalated $I_{(001),\ \text{intercalated}}$ and non-intercalated $I_{(001),\ \text{non-intercalated}}$ kaolinite, respectively.[3]

$$\mathrm{d}I = \frac{I_{(001),\ \text{non-intercalated}}}{I_{(001),\ \text{non-intercalated}} + I_{(001),\ \text{intercalated}}} \qquad (24)$$

[h] $2d_{hkl}\sin\theta = n\lambda$

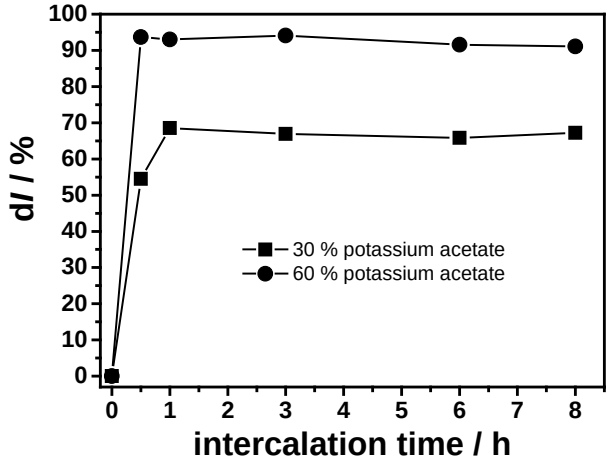

Figure 39: Degree of intercalation after certain impact times between potassium acetate and Kaolin KGa-1b. For analyzing the time dependence, a 60 weight percent (bullets) and a 30 weight percent (squares) potassium acetate solution was used.

In Figure 39 the degrees of intercalation for impact time between 30 minutes and 8 hours are compared. It turned out, that the degree of intercalation was almost independent of the contact time. Only for the 30 weight percent potassium acetate solution, an increase from d*I* = 55 % to d*I* = (67 ± 1) % was found. For the potassium acetate solution the degree of intercalation is (93 ± 2) % independent on contact time. Due to the sample preparation, contact times smaller than half an hour were hardly accessible as after stirring, the suspensions were centrifuged for 30 minutes. During the centrifugation process, ongoing intercalation might be possible. In additional experiments with 30 weight percent potassium acetate solutions and shorter contact times, with 10 minutes (20 minutes) of stirring and subsequently, 30 minutes centrifugation a d*I* of around 42 % (41 %) was found. That there is no difference in d*I* for both contact times, supported the mentioned imitation in time resolution. Above contact times of 40 minutes d*I* approaches a plateau. Obviously, the formation of the intercalation compound reaches an equilibrium.

Besides XRD also Raman microscopy and SFG spectroscopy were used to evaluate the time dependence of the intercalation process. The attempt was made to derive degrees of intercalation d*I* also from Raman and SFG measurements. In analogy to the XRD measurements (eq. (24)) also from vibrational spectroscopy a discrimination between intercalated and pure kaolinite is possible. As discussed earlier, the vibrations ν_2, ν_3, ν_4 and ν_5 can be assigned to the pure kaolinite, whereas ν_{Ac} reflects a vibration of the intercalated KGa-1b. The degree of intercalation d*I* can be calculated with

$$\mathrm{d}I = \frac{I(\upsilon_{Ac})}{I(\upsilon_{Ac})+I(\upsilon_2)+I(\upsilon_3)+I(\upsilon_4)+I(\upsilon_5)}, \tag{25}$$

where $I(\nu_i)$ is the intensity of the *i*th vibration. As can be seen in Figure 40 (left) for an impact time of 50 minutes between potassium acetate solution and kaolinite KGa-1b, Raman microscopy gives for certain sample spots different vibrational spectra. The high spatial resolution is an advantage for chemical imaging, but is an obstacle for comparing d*I* values de-

duced from XRD with them derived from Raman microscopy measurements. XRD reflects bulk information and Raman microscopy information from a very specific point at the sample surface. Therefore, Raman spectra were recorded at five different positions of the sample and the degree of intercalation was calculated from every measurement. Finally, from all five d*I* values a mean value and a standard deviation were computed. This approach was applied for all samples with different impact times. The results are plotted in Figure 40 (right). The values for d*I* are smaller than for the degree of intercalation calculated from XRD measurements (cf. Figure 39). Possibly, the differences originate from the measuring arrangement. It is known, that the crystallinity of kaolinite decreases upon intercalation.[3] For Raman microscopy, the scattered light is measured in reflection. The lower the crystallinity the higher the amount of diffuse reflection. Light, which is diffusely scattered from the surface will not be collected from the objective and will not contribute to the measured Raman spectrum. Therefore, in the Raman spectrum scattered light originating from crystalline regions will predominate. But, this might be regions, in which intercalation will take place to a lesser extent.

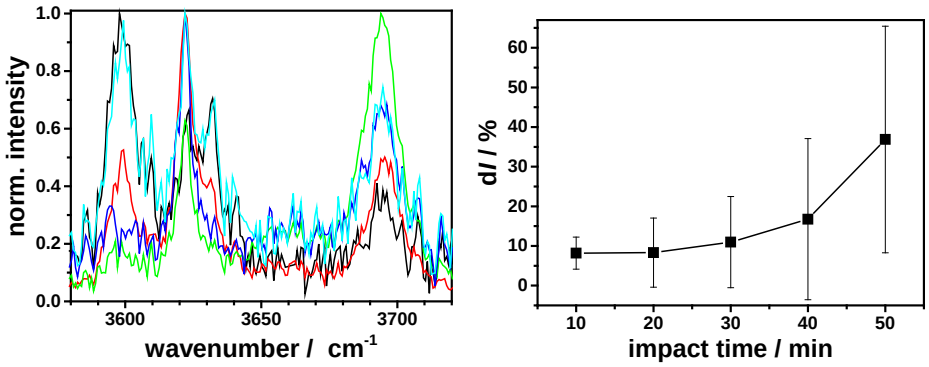

Figure 40: (left) Raman spectra of a sample with an impact time for intercalation of 50 minutes taken at different positions of the sample. (right) Degree of intercalation d*I* calculated from Raman measurements.

A direct intercalation of longer-chain molecule is not possible. A way out, is an indirect intercalation.[41,42] Here, an already intercalated kaolinite is necessary. During the indirect intercalation the guest molecule is expelled and replaced by the longer-chain molecule. A possible precursor for an indirect intercalation is a DMSO kaolinite intercalation complex.

An intercalation of KGa-1b with potassium hexanoate was studied as well. A DMSO KGa-1b intercalation compound was used as precursor. In Figure 41 and Table 10 the vibrational spectra and vibrational frequencies for both, Raman and SFG, of this compound are shown. In both spectra, the main OH vibration expected for kaolinite samples can be observed. The peak position of certain vibrations differ slightly in SFG and Raman spectra. For comparison, also the vibrational spectrum of the pure KGa-1b is plotted in Figure 41. In the SFG spectrum a pronounced vibration at ν_{DMSO} = 3667 cm^{-1} can be observed, which is also observable in the Raman spectrum at ν_{DMSO} = 3664 cm^{-1}. These vibration can be assigned in accordance with literature to the vibration of the intercalated DMSO.[43] In the Raman spectrum, the assignment is not as straightforward as ν_{DMSO} overlaps with the ν_3 vibration of the pure kaolinite,

which is only weak present in the SFG spectrum. In accordance with the published Raman spectra, the intensity of the vibration ν_4 and ν_5 also decreases upon intercalation of DMSO.[43]

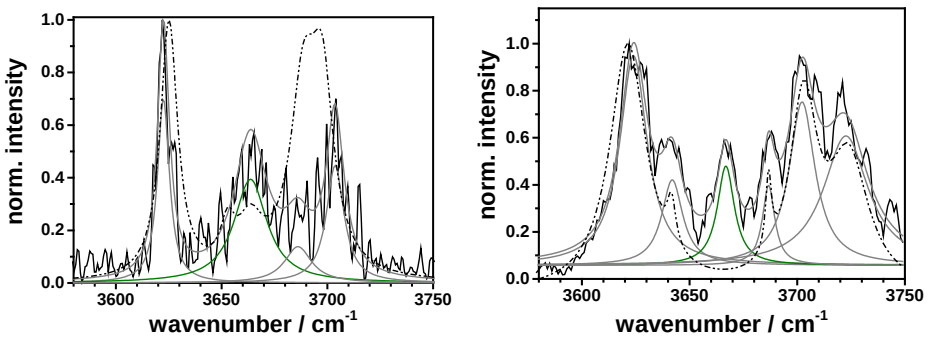

Figure 41: Vibrational spectra of the DMSO KGa-1b intercalation compound. The vibrational spectrum of pure KGa-1b is plotted with a dashed-dotted line. Due to intercalation a vibration (dark green) around 3664 cm^{-1} (Raman, left) and 3667 cm^{-1} (SFG, right) arising from the intercalated DMSO was detectable. To the measure data a sum of Lorentzian functions was fitted. The single Lorentzian as well as their sum are plotted with gray lines.

The intercalation could also be monitored by XRD measurements (cf. Figure 42). Here, the reflex from the (001) plane shifts to $2\theta = 8.0$ °, which corresponds to a layer distance of 11.04 Å – a value consistent with a published value of 11.21 Å.[42]

Table 10: Peak positions and relative peak intensities (rel. intensity) of the DMSO KGa-1b intercalation compound. The peak maxima and relative intensities were derived by fitting the measured data to a sum of Lorentzian functions.

	Raman		SFG	
	peak position / cm^{-1}	rel. Intensity / %	peak position / cm^{-1}	rel. intensity / %
ν_1	3622 ± 1	25.2 ± 2.0	3624 ± 1	28.3 ± 1.7
ν_2	—	—	3642 ± 1	8.8 ± 1.5
ν_{DMSO}	3664 ± 1	39.5 ± 6.2	3667 ± 1	8.4 ± 0.9
ν_4	3686 ± 3	11.3 ± 7.8	3687 ± 1	4.9 ± 1.1
ν_5	3704 ± 1	24.0 ± 4.2	3702 ± 1	21.0 ± 2.9
ν_X	—	—	3723 ± 1	28.6 ± 3.2

With the DMSO intercalated kaolinite precursor compound an indirect intercalation should be possible. In Figure 42 the XRD spectrum of the potassium hexanoate intercalated KGa-1b kaolinite and for comparison also the XRD spectrum of pure and DMSO intercalated KGa-1b are shown. The indirect intercalation results in the formation of the (001) reflex at $2\theta = 4.8$ °, which correlates with a layer distance of 18.4 Å. But, also the intensity of the reflex at $2\theta = 12.4$ ° increases. Obviously, a de-intercalation competes with the desired indirect intercalation. The reflex at 12.4 ° not only increases in intensity, but also is broadened to smaller reflection angles. This behavior is known from de-intercalation, when some layers do not shrink to their original distance.[44] As can be seen from Figure 42, the intensity of reflexes originated from de-intercalated KGa-1b are higher than the reflex from the potassium hexanoate intercalated KGa-1b, which indicates a low degree of intercalation. Applying eq. (24),

the degree of intercalation is about d*I* = 10 %. The low degree of intercalation is also reflected by SFG and Raman measurements as the received spectra looks like the vibrational spectra of the pure Kaolin KGa-1b.

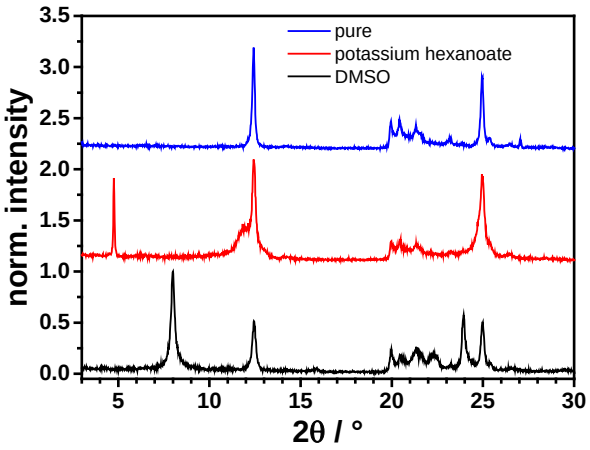

Figure 42: XRD spectra of the pure KGa-1b, DMSO intercalated and potassium hexanoate intercalated KGa-1b. For clarity, the XRD spectra are vertically shifted.

Lanthanide(III) complexes with LMWC

In addition to luminescence measurements also Raman spectroscopy was used to study the interaction between Ln(III) and LMWC. For these investigations glycolic acid was chosen. Because the luminescent Ln(III) ions interfered with the Raman measurements they were substituted by the (under the experimental conditions applied) non-luminescence Gadolinium(III) (Gd(III)). Due to the low Raman intensity, glycolic acid was used in a concentration of

Table 11: Complexation constants for Eu(III) LMWC complexes at an ionic strength of *I* = 0.1 mol·L^{-1}. Values are taken from literature.[22]

Ln(III):acid	lg *K*				
	formic acid	acetic acid	propionic acid[#]	glycolic acid	
1:1	1.44	2.13	2.23	2.93	2.54[##]
1:2	1.94	3.64	3.75	5.07	4.48[##]
1:3	–	4.24		6.52	5.85[##]

[#] *I* = 0.1

[##] *I* = 1, Ln(III) = Gd(III)

0.5 mol·L^{-1} to receive a decent Raman signal. To achieve a considerable complexation (cf. Table 11) Gd(III) concentrations from 0.01 mol·L^{-1} to 1.0 mol·L^{-1} were chosen.

With the literature values for the complexation constants given in Table 11 a speciation calculation was carried out. The result of this calculation is shown in Figure 43 left. At p*H* = 5 and a Gd(III) concentration of 0.01 mol·L^{-1} most of the glycolic acid is in its deprotonated form and the Gd(III) is almost completely complexed as [Gd(glycolate)$_3$]. With higher the Gd(III) concentration the amount of 1:3 Gd(III) glycolate complexes decreases and a 1:1 complex is favorable at *c*(Gd(III) = 1 mol·L^{-1}. Under this experimental conditions almost no free glycolate is expected.

This shift in the equilibrium concentrations can be monitored by Raman spectroscopy. Corresponding Raman spectra are plotted in Figure 43 right. At low Gd(III) concentration a peak around 915 cm^{-1} can be observed. This peak can be assigned to the C-C vibration.[45] With increasing Gd(III) concentration, a distinct shift of this vibration to higher wavenumbers is observed. Quantum mechanical calculations[i] showed, that the differences in the position of the C-C stretching vibration in the different Gd(III) glycolate complexes are relatively small and therefore hardly to resolve with Raman spectroscopy. The changes in the Raman spectrum are in good agreement with the speciation diagram.

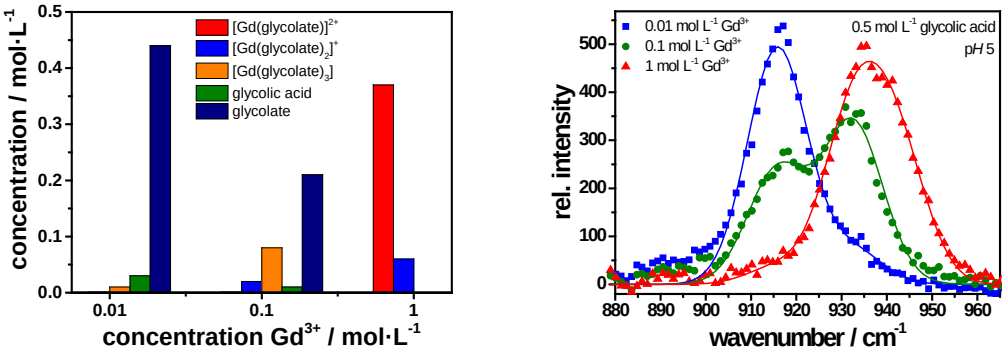

Figure 43: Left: Speciation diagram for the expected concentrations of the different Gd(III) glycolate complexes. The calculation of the speciation was done with the ChemEQL package[j] and based on the stability constants given in Table XX1.[23] Right: Raman spectra at different concentrations of Gd(III). *c*(glycolic acid) = 0.5 mol·L^{-1}, p*H* = 5.

[i] Calculations performed by Dr. Thomas Ritschel, now Gonotech GmbH. Calculations were carried out using Gaussian 09 program suite[48]. The geometries were fully optimized at the B3LYP level of theory using the polarized triple zeta split valence 6-311+G(d,p) basis set for the light atoms (C, O and H). For Gd(III) the MWB53 basis together with an effective core potential (ECP) for the inner shells (up to and including 4*f*) was utilized. The effect of the solvent was taken into account by the use of polarizable continuum model (PCM).

[j] An actual version of this software package can be found at http://www.eawag.ch/en/department/surf/projects/chemeql/.

3. 7 Europium(III) complexes with LMWC and Kaolinit

The interaction of Eu(III) with kaolinite Kaolin KGa-2 in the presence of different LMWC was investigated. LMWC used were formic, acetic, propionic, and glycolic acid, respectively. When taking a $4 \cdot 10^{-4}$ mol·L^{-1} Eu(III) solution with increasing concentration of LMWC at p*H* = 5 the luminescence decay time increases as can be seen in Figure 44 (left). Only at LMWC concentrations above 10^{-4} mol·L^{-1} a change of the luminescence decay time compared to Eu(III) in water can be noticed. This is due to the weak complexes, which are generally formed between Ln(III) and LMWC. In Table 11 the stability constants for Eu(III) (and Gd(III)) complexes with LMWC investigated are listed. By comparing the stability constants for the 1:1 complexes, the trend of the luminescence decay time upon increasing LMWC concentration can be understood.

Formic acid has the lowest stability constant and therefore forms the weakest complexes. By direct excitation of Eu(III) at λ_{ex} = 394 nm ($^5L_6 \leftarrow {}^7F_0$-transition), both, the complexed and the aqueous Eu(III) are excited and contribute to the observed luminescence. Therefore, the luminescence decay time is measured as a mean value of free and bound Eu(III). For acetic and propionic acid, the stability constants are nearly the same. A similar value for Eu(III) luminescence decay is found. The strongest complexes are formed with glycolic acid, which give raise to the highest luminescence decay time, reaching a value of τ = 218 µs ± 2 µs. The same conclusions can be drawn from the asymmetry ratios *r*, which are plotted in Figure 45. For the ligands investigated the complex formation will mainly occur via the carboxylic group. Therefore, a similar influence on the Eu(III) luminescence is expected.

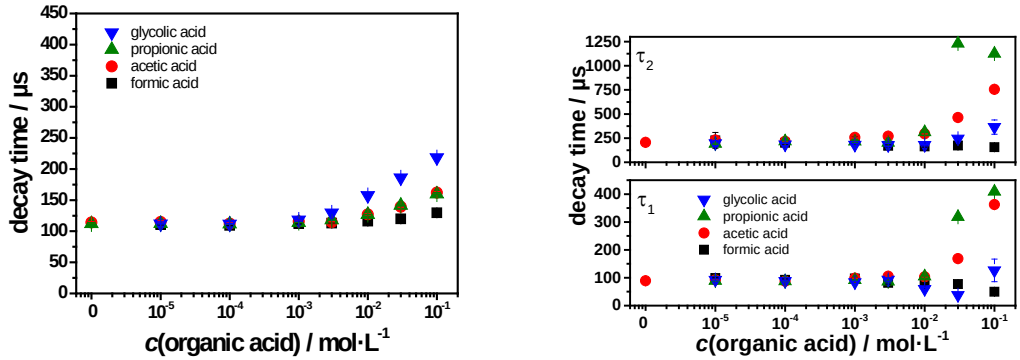

Figure 44: Decay time of Eu(III) derived from time-resolved measurements. Left: Resulting decay times of the Eu(III) in solutions with LMWC before mixing with Kaolin KGa-2, *c*(Eu(III)) = $4 \cdot 10^{-4}$ mol·L^{-1}, p*H* = 5, λ_{ex} = 394 nm. Right: Decay-times of Eu(III) in solutions with LMWC after sorption onto Kaolin KGa-2. Experimental details: p*H* = 5, background electrolyte 0.01 mol·L^{-1} $NaClO_4$.

For the dried Eu(III) LMWC complexes with Kaolin KGa-2 samples the kinetic of the Eu(III) luminescence was more complex compared to aqueous solutions (vide supra). The luminescence decays could be reasonably well fitted by a biexponential rate law and the extracted (operationally defined) luminescence decay times are shown in Figure 44 (right). Formic acid as well as glycolic acid has apparently no or only a minor impact on the luminescence decay times, whereas acetic and propionic acid have a distinct influence on the luminescence decay time.

A second parameter is the asymmetry ratio *r*. In Figure 45 left, the luminescence spectra for an adsorbed Eu(III) species after mixing of Kaolin KGa-2 and acetic acid at different concentrations is shown. At acetic acid concentration above 10^{-3} mol·L^{-1} the Eu(III) luminescence spectrum is altered and subsequently also the asymmetry ratio. These changes are a consequence of sorption of Eu(III) to the clay phase and are also observed for the other solids received from ternary solutions as can be seen in Figure 45. For all LMWC the asymmetry ratio increases from around $r = 1.3$ up to $r = 5$, depending on the LMWC. Comparable to the trends found with the binary mixtures, formic acid has the weakest effect on *r*. For the solids, separated from ternary mixture with one of the other three acids, respectively, the alteration of the asymmetry ratio with LMWC concentration is roughly the same.

Both, the multi-exponential luminescence decay as well as the changes in the asymmetry ratio point to a sorption of Eu(III) on the kaolinite. Due to adsorption the Eu(III) asymmetry ratio increases to about $r = 1.3$ compared to $r = 0.6$ for the Eu(III) aqueous species (cf. Figure 45 (right)). Also in the presence of LMWC Eu(III) is adsorbed to the mineral surface. Here, the asymmetry ratio points to adsorbed Eu(III) LMWC complexes. From both, luminescence decay times and asymmetry ratio, the adsorbed Eu(III) species in presence of acetic acid and propionic acid, respectively, is subjected to the strongest alteration.

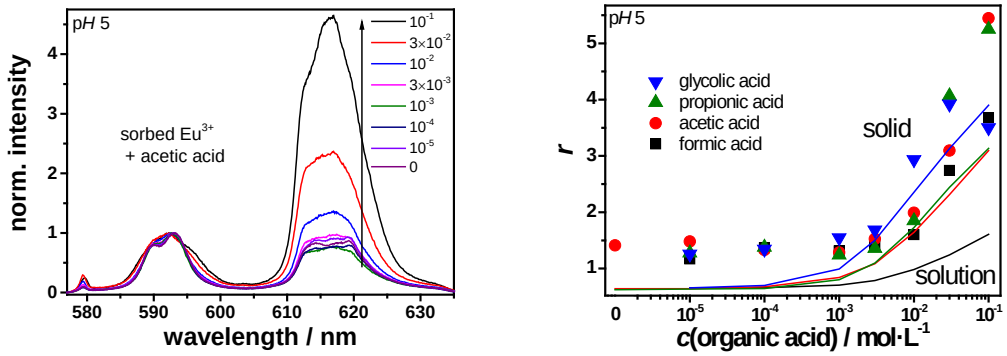

Figure 45: Left: Luminescence spectra of sorbed Eu(III) species after mixing with acetic acid at given concentration and Kaolin KGa-2. From these luminescence spectra the asymmetry ratio can be calculated from the intensities of the transitions around 592 nm ($^5D_0 \rightarrow {}^7F_1$) and around 615 nm ($^5D_0 \rightarrow {}^7F_2$) (cf. eq. (2)). Right: Asymmetry ratio *r* of the Eu(III) in presence of LMWC in solution (lines) and adsorbed to Kaolin KGa-2. *c*(Eu(III)) = $4 \cdot 10^{-4}$ mol·L^{-1}, p*H* = 5, λ_{ex} = 394 nm, background electrolyte 0.01 mol·L^{-1} $NaClO_4$.

4. Research achievements during the project period

Publications

- J. Schott, J. Kretzschmar, M. Acker, S. Eidner, M.U. Kumke, B. Drobot, A. Barkleit, S. Taut, V. Brendler, Th. Stumpf, "Formation of a Eu(III) borate solid species from a weak Eu(III) borate complex in aqueous solution", *Dalton Transactions* 43(30), 11516-11528 (2014).
- A. Demetriou , I. Pashalidis , A.V. Nicolaides, M.U. Kumke, "Surface mechanism of the boron adsorption on alumina in aqueous solutions", *Desalination and Water Treatment* 51(31-33), 6130-6136 (2013).
- H. Lippold, S. Eidner, M.U. Kumke, J. Lippmann-Pipke, "Diffusion, degradation or on-site stabilisation – Identifying causes of kinetic processes involved in metal-humate complexation", *Applied Geochemistry* 27, 250-256 (2012).
- P.-A. Primus, M.U. Kumke, "Flash Photolysis Study of Complexes between Salicylic Acid and Lanthanide Ions in Water", *Journal of Physical Chemistry A* 116(4), 1176-1182 (2012).
- Th. Schäfer, F. Huber, H. Seher, T. Missana, U. Alonso, M.U. Kumke, S. Eidner, F. Claret, F. Enzmann, "Nanoparticles and their influence on radionuclide mobility in deep geological formations", *Applied Geochemistry* 27, 390-403 (2012).
- S. Antoniou, I. Pashalidis, A. Gessner, M. U. Kumke, "The effect of humic acid on the formation and solubility of secondary solid phases ($Nd(OH)CO_3$ and $Sm(OH)CO_3$)", *Radiochimica Acta* 99(4), 217-223 (2011).
- S. Antoniou, I. Pashalidis, A. Gessner, M.U. Kumke, "Spectroscopic investigations on the effect of humic acid on the formation and solubility of secondary solid phases of $Ln_2(CO_3)_3$", *Journal of Rare Earth* 29, 516-521 (2011).

PhD Thesis

- Bettina Marmodée, "Fluorescence Line-Narrowing-Spektroskopie zur Charakterisierung von Eu(III) in Komplexen mit kleinen organischen Liganden", Dissertation, Universität Potsdam (2012).
- Stefanie Kuke, "Lanthanoide(III) in Komplexen mit niedermolekularen Säuren – Spektroskopische Betrachtung komplex-spezifischer Löschmechanismen in Eu(III)- und Tb(III)-Komplexen", Dissertation, Universität Potsdam (2013).

Bachelor, Diploma and Master Thesis

- Christina Schimmeck (2011, Bachelorarbeit) "Lumineszenzspektroskopische Charakterisierung von Tropolon und substituierten Benzoesäuren in Komplexen mit Europium.
- Marian Süßmann (2012, Bachelorarbeit) "Einfluss von Temperatur und Ionenstärke auf die Komplexierung von Europium(III) mit Huminstoffen."

- Melissa-Jane Monks (2012, Bachelorarbeit) „Lumineszenz-basierte Speziation von Europium(III)-Borat-Komplexen“
- Madlen Rühlmann (2013, Bachelorarbeit) "Einfluss der Ionenstärke und des pH-Wertes auf die Konformation von Polymeren."

- Max L. Schütte (2014, Bachelorarbeit) "Lumineszenzspektroskopische Untersuchung der Europium-Huminstoff-Wechselwirkung in Abhängigkeit der Elektrolytzusammensetzung."
- Michel Wehrhold (2014, Bachelorarbeit) "Lumineszenzuntersuchungen an Uranyl-Acetat-Proben."
- Manuela Haupt (2012, Diplomarbeit) "Speziation niedermolekularer Säuren in Gegenwart von Eu(III) und Mineralphasen mittels Raman-Spektroskopie."
- Julia Prinz (2013, Masterarbeit) "Untersuchung der Sorption von organischen Substanzen an Alumosilikat-Modelloberflächen mittels Schwingungsspektroskopie."
- Katja Burek (2014, Diplomarbeit) "Temperatur- und Ionenstärke-Einflüsse auf die Lumineszenz von Lanthanoiden in Komplexen mit niedermolekularen organischen Liganden."
- Tobias Garling (2015, Masterarbeit) "Untersuchung der Sorption von niedermolekularen organischen Stoffen an Mineraloberflächen mittels SFG-Spektroskopie."

References

1. BGR. *Endlagerung radioaktiver Abfälle in Deutschland - Untersuchung und Bewertung von Regionen mit potenziell geeigneten Wirtsgesteinsformationen*. (2007).
2. Clay Mineral Society. *http://www.clays.org/SOURCE%20CLAYS/SCdata.html* , last access on 5th December 2015
3. Cheng, H., Liu, Q., Yang, J., Du, X. & Frost, R. L. Influencing factors on kaolinite–potassium acetate intercalation complexes. *Appl. Clay Sci.* **50,** 476–480 (2010).
4. Li, Y., Sun, D., Pan, X. & Zhang, B. Kaolinite intercalation precursors. *Clays Clay Miner.* **57,** 779–786 (2009).
5. Kimura, T., Nagaishi, R., Kato, Y. & Yoshida, Z. Luminescence study on solvation of americium(III), curium(III) and several lanthanide(III) ions in nonaqueous and binary mixed solvents. *Radiochim. Acta* **89,** 125–130 (2001).
6. Carnall, W. T. in *Handbook on the Physics and Chemistry of Rare Earth* (1979).
7. Horrocks, W. D. & Sudnick, D. R. Lanthanide ion luminescence probes of the structure of biological macromolecules. *Acc. Chem. Res.* **14,** 384–392 (1981).
8. Ryan, D. K. & Weber, J. H. Copper(II) complexing capacities of natural waters by fluorescence quenching. *Environ. Sci. Technol.* **16,** 866–872 (1982).
9. Ryan, D. K. & Weber, J. H. Fluorescence quenching titration for determination of complexing capacities and stability constants of fulvic acid. *Anal. Chem.* **54,** 986–990 (1982).
10. IHSS. http://www.humicsubstances.org/acidity.html.
11. Lambert, A. G., Davies, P. B. & Neivandt, D. J. Implementing the Theory of Sum Frequency Generation Vibrational Spectroscopy: A Tutorial Review. *Appl. Spectrosc. Rev.* **40,** 103–145 (2005).
12. Richmond, G. L. Molecular bonding and interactions at aqueous surfaces as probed by vibrational sum frequency spectroscopy. *Chem. Rev.* **102,** 2693–2724 (2002).
13. Demtröder, W. *Laser Spectroscopy 1*. (2014). doi:10.1007/978-3-642-53859-9
14. D'Aléo, A., Pointillart, F., Ouahab, L., Andraud, C. & Maury, O. Charge transfer excited states sensitization of lanthanide emitting from the visible to the near-infra-red. *Coord. Chem. Rev.* **256,** 1604–1620 (2012).
15. Carnall, W. T. Spectral Intensities of the Trivalent Lanthanides and Actinides in Solution. II. Pm3+, Sm3+, Eu3+, Gd3+, Tb3+, Dy3+, and Ho3+. *J. Chem. Phys.* **49,** 4412 (1968).
16. W. T. Carnell, J. V. Beitz, H. Crosswhite, K. Rajnak, J. B. M. in *Systematics and the Properties of the Lanthanides* (ed. Sinha, S. P.) 389 – 450 (D. Reidel Publishing Company, 1983).
17. Stein, G. Energy gap law in the solvent isotope effect on radiationless transitions of rare earth ions. *J. Chem. Phys.* **62,** 208 (1975).
18. Arnaud, N. & Georges, J. Influence of pH, surfactant and synergic agent on the

luminescent properties of terbium chelated with benzoic acid derivatives in aqueous solutions. *Analyst* **125,** 1487–1490 (2000).

19. Panak, P., Klenze, R., Kim, J. I. & Wimmer, H. A study of intramolecular energy transfer in Cm(III) complexes with aromatic ligands by time-resolved laser fluorescence spectroscopy. *J. Alloys Compd.* **225,** 261–266 (1995).

20. Primus, P.-A. & Kumke, M. U. Flash Photolysis Study of Complexes between Salicylic Acid and Lanthanide Ions in Water. *J. Phys. Chem. A* **116,** 1176–1182 (2012).

21. Kuke, S., Marmodée, B., Eidner, S., Schilde, U. & Kumke, M. U. Intramolecular deactivation processes in complexes of salicylic acid or glycolic acid with Eu(III). *Spectrochim. Acta. A. Mol. Biomol. Spectrosc.* **75,** 1333–40 (2010).

22. Martell, A. E. & Smith, R. M. *Critical Stability Constants, Vol. 3: Other Organic Ligands*. (1989).

23. Müller, B. ChemEQL: http://www.eawag.ch/en/department/surf/projects/chemeql/.

24. Schott, J. *et al.* Formation of a Eu(III) borate solid species from a weak Eu(III) borate complex in aqueous solution. *Dalton Trans.* **43,** 11516–28 (2014).

25. Brasser, T. & Brewitz, W. Anwendbarkeit der Indikatoren 'teufenabhängige Mineralisation / Salzgehalt' für die Erfüllung der allgemeinen Anforderung 'keine oder langsame Grundwasserbewegung'. *Bericht an den AKEnd* **GRS-A-2956,** (2002).

26. Görller-Walrand, C. & Binnemans, K. in *Handbook on Physics and Chemistry of Rare Earth* (eds. K. A. Gschneidner, J. & Eyring, L.) **23,** (Elsevier Science B.V., 1996).

27. Milne, C. J., Kinniburgh, D. G., van Riemsdijk, W. H. & Tipping, E. Generic NICA-Donnan Model Parameters for Metal-Ion Binding by Humic Substances. *Environ. Sci. Technol.* **37,** 958–971 (2003).

28. Milne, C. J., Kinniburgh, D. G. & Tipping, E. Generic NICA-Donnan Model Parameters for Proton Binding by Humic Substances. *Environ. Sci. Technol.* **35,** 2049–2059 (2001).

29. Marang, L., Eidner, S., Kumke, M. U., Benedetti, M. F. & Reiller, P. E. Spectroscopic characterization of the competitive binding of Eu(III), Ca(II), and Cu(II) to a sedimentary originated humic acid. *Chem. Geol.* **264,** 154–161 (2009).

30. Marang, L., Reiller, P. E., Eidner, S., Kumke, M. U. & Benedetti, M. F. Combining Spectroscopic and Potentiometric Approaches to Characterize Competitive Binding to Humic Substances. *Environ. Sci. Technol.* **42,** 5094–5098 (2008).

31. Blume, H.-P. *et al. Scheffer/Schachtschabel: Lehrbuch der Bodenkunde*. (2010).

32. in *KIT Scientific Report 7633* (ed. Marquardt, C.) (2013).

33. Tcherkasskaya, O., Ni, S. & Winnik, M. A. Direct Energy Transfer Studies of the Domain-Boundary Interface in Polyisoprene-Poly(methyl methacrylate) Block Copolymer Films. *Macromolecules* **29,** 610–616 (1996).

34. Frost, R. L. & Kloprogge, J. T. Towards a single crystal Raman spectrum of kaolinite at 77 K. *Spectrochim. Acta Part A Mol. Biomol. Spectrosc.* **57,** 163–175 (2001).

35. Rouxhet, P. G., Samudacheata, N., Jacobs, H. & Anton, O. Attribution of the OH stretching bands of kaolinite. *Clay Miner.* **12,** 171–179 (1977).

36. Shoval, S. Hydroxyl-Stretching Bands 'A' and 'Z' in Raman and Infrared Spectra of Kaolinites. *Clay Miner.* **34,** 551–563 (1999).

37. Ledoux, R. . L. & White, J. L. Infrared study of the OH groups in expanded kaolinite. *Science* **143,** 244–5 (1964).

38. Frost, R. L., Kristof, J., Horváth, E. & Kloprogge, J. T. Raman spectroscopy of potassium acetate-intercalated kaolinites over the temperature range 25-300 °C. *J. Raman Spectrosc.* **32,** 271–277 (2001).

39. Wang, W.-M., Yeh, H.-W., Chen, P.-Y. & Wang, M.-K. Kaolin Mineralogy of Clays in Paleosol Profiles on the Late-Miocene Sediments in Penghu Islands (Pescadores), Taiwan. *Clays Clay Miner.* **46,** 1–9 (1998).

40. Cruz, M. D. R. & Duro, F. I. F. New data on the kaolinite-potassium acetate complex. *Clay Miner.* **34,** 565–577 (1999).

41. Sugahara, Y., Satokawa, S., Kuroda, K. & Kato, C. Kaolinite-Pyridine Intercalation Compound derived from Hydrated Kaolinite. *Clays Clay Miner.* **37,** 143–150 (1989).

42. Gardolinski, J., Peralta-Zamora, P. & Wypych, F. Preparation and Characterization of a Kaolinite-1-methyl-2-Pyrrolidone Intercalation Compound. *J. Colloid Interface Sci.* **211,** 137–141 (1999).

43. Frost, R. L., Kristof, J., Horvath, E. & Kloprogge, J. T. Deintercalation of dimethylsulphoxide intercalated kaolinites - a DTA/TGA and Raman spectroscopic study. *Thermochim. Acta* **327,** 155–166 (1999).

44. Frost, R. L., Kloprogge, J. T., Kristof, J. & Horvath, E. Deintercalation of Hydrazine-Intercalated Low-Defect Kaolinite. *Clays Clay Miner.* **47,** 732–741 (1999).

45. Cassanas, G., Morssli, M., Fabrègue, E. & Bardet, L. Etude Spectrale de l'Acide Glycolique, des Glycolates et du Processue de Polymérisation. *J. Raman Spectrosc.* **22,** 11–17 (1991).

46. Choppin, G. R. & Friedman, H. G. Complexes of Trivalent Lanthanide Ions. III. Bidentate Chelates. *Inorg. Chem.* **5,** 1599–1603 (1966).

47. Wood, S. A. The aqueous geochemistry of the rare-earth elements: Critical stability constants for complexes with simple carboxcylic acids at 25°C and 1 bar and their application to nuclear waste management. *Eng. Geol.* **34,** 229 – 259 (1993).

48. GAUSSIAN 09, Revision A.02, Gaussian Inc., Wallingford CT. (2009).

Supporting Information

Table 1S: Stability constants for Ln(III)-complexes with salicylic acid and Phthalic acid (RT, I = 0 mol·L^{-1}).[46,47]

Ligand	ML_1	ML_2
Tb(III) salicylic acid	2.38	4.75
Tb(III) phthalic acid	4.83	6.96
Sm(III) salicylic acid	2.49	4.71
Sm(III) phthalic acid	5.16	7.39
Dy(III) salicylic acid	2.13	4.65
Dy(III) phthalic acid	4.97	6.75
Eu(III) salicylic acid	2.45	4.73
Eu(III) phthalic acid	3.45	5.17

Table 2S: With ChemEQL 3.1[23] **calculated species distribution (RT, I = 0 mol·L^{-1}).**

	Ln(III) aquo complex / %	Ln(III)-L_1 / %	Ln(III)-L_2 / %
Tb(III) salicylic acid	36	41	23
Tb(III) phthalic acid	4	92	4
Sm(II) salicylic acid	30	41	29
Sm(II) phthalic acid	3	94	3
Dy(III) salicylic acid	41	24	35
Dy(III) phthalic acid	2	95	3
Eu(III) salicylic acid	3	17	80
Eu(III) phthalic acid	1	43	56

Table 3S: pK_a values of model ligands.[47]

Model ligand	p$K_{a\,(1)}$	p$K_{a\,(2)}$
Salicylic acid	2.97	13.74
Phthalic acid	2.89	4.68

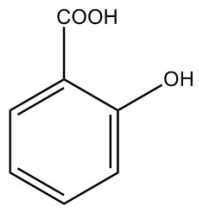

salicylic acid

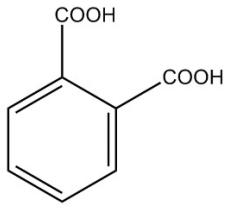

phthalic acid

Figure 1S: structure of model ligands investigated.

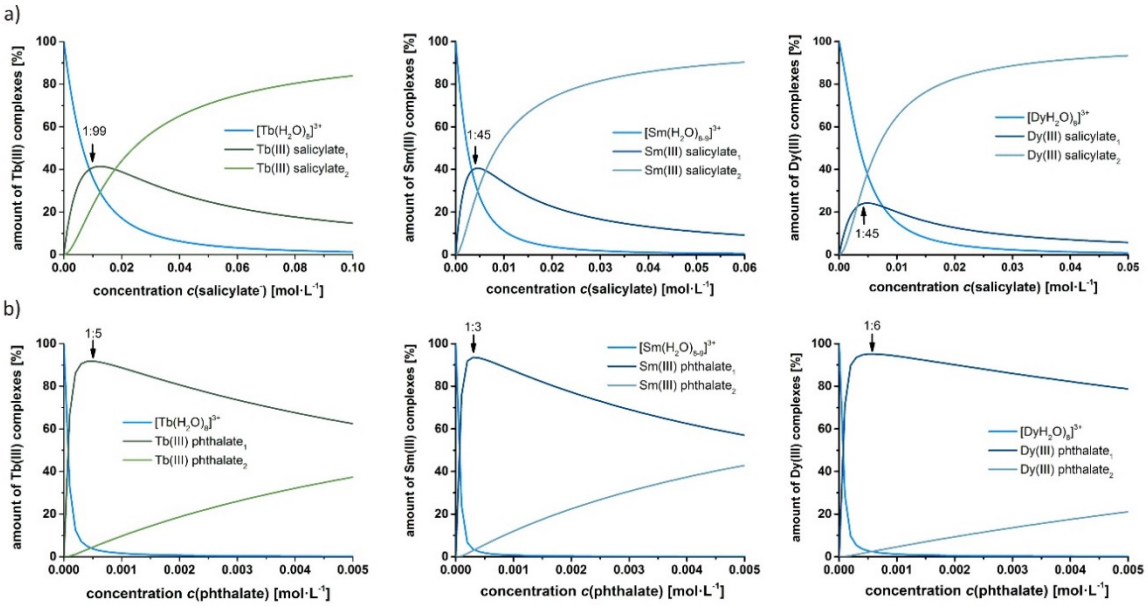

Figure 2S: speciation diagrams of Tb(III), Sm(III) and Dy(III) ($c_{Ln(III)}$ = 10^{-4} mol·L^{-1}) in complexes with a) salicylic acid (p*H* = 5.0) and b) phthalic acid (p*H* = 4.2) (RT, *I* = 0 mol·L^{-1}) (calculated with ChemEQL 3.1[23], stabilitiy constants taken from[47]).

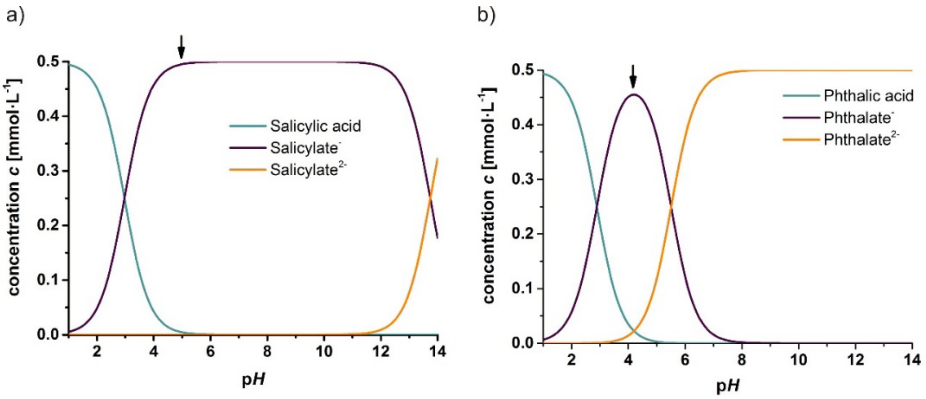

Figure 3S: speciation diagrams of a) salicylic acid and b) phthalic acid (calculaterd with ChemEQL 3.1[23], p*K*a values taken from[47]).

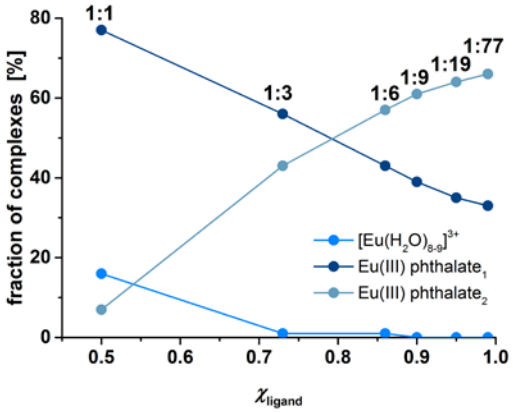

Figure 4S: speciation diagram of Eu(III) in complexes phthalic acid (p*H* = 5.0) (RT, *I* = 0 mol·L^{-1}) (calculated with ChemEGL 3.1[23], stability constants taken from[47]).

TECHNISCHE UNIVERSITÄT DRESDEN

Sachgebiet Strahlenschutz Professur für Radiochemie

Final Report of the BMWi Joint Research Project

RETENTION OF RADIONUCLIDES RELEVANT FOR FINAL DISPOSAL IN NATURAL CLAY ROCK AND SALINE SYSTEMS

Subproject:

SPECTROSCOPIC AND THERMODYNAMIC STUDIES ON THE INTERACTION OF AN(III) AND LN(III) WITH COMPLEXING LIGANDS IN SALINE MEDIA

Margret Acker, Juliane Schott, Franziska Taube, Astrid Barkleit, Melanie Müller, Steffen Taut, Thorsten Stumpf

BMWi Project No.: 02 E 11021

Technische Universität Dresden
Sachgebiet Strahlenschutz und Professur für Radiochemie
01062 Dresden
Germany
https://tu-dresden.de/die_tu_dresden/arb_umw_schutz/npzr_zentrales_radionuklidlabor

DRESDEN concept

Das diesem Bericht zugrundeliegende Vorhaben wurde mit Mitteln des Bundesministeriums für Wirtschaft und Energie unter dem Förderkennzeichen 02E11021 gefördert. Die Verantwortung für den Inhalt dieser Veröffentlichung liegt beim Autor

VERBUNDVORHABEN:

Rückhaltung endlagerrelevanter Radionuklide im natürlichen Tongestein und in salinaren Systemen

TEILPROJEKT

Spektroskopische und thermodynamische Untersuchungen zur Wechselwirkung von An(III) und Ln(III) mit endlagerrelevanten Komplexbildnern in salinaren Medien

Ausführende Institution: TU Dresden
Bereich für Mathematik und Naturwissenschaften
Fachbereich Chemie und Lebensmittelchemie
Professur für Radiochemie
01062 Dresden

TU Dresden
Sachgebiet Strahlenschutz
01062 Dresden

Dresden, den 18.01.2016

Abstract

The presented project deals with studies on basic interactions between trivalent actinides and lanthanides (represented by Am(III)/Cm(III) and Eu(III)/Nd(III)) with borate species and low molecular organic ligands in order to generate reliable thermodynamic data for long-term safety and risk assessment of nuclear waste repositories. The interaction with borate species, studied for the first time in this project, is of particular interest because of their presence in the salt deposits (a potential host rock) as well as in glass coquilles and concrete constructions in the near field to the radioactive waste. Low molecular organic ligands as dissolved organic matter are in the pore water of argillaceous rocks (also a potential host rock).

The complexation behaviour of two different Eu(III)-borate-systems, first the Eu(III)-polyborate and second the Eu(III)-organoborate system, was investigated by time-resolved laser fluorescence (TRLFS) and ^{11}B NMR spectroscopy in NaCl/$NaClO_4$ media at different ionic strengths mainly at pH $\leq$ 6. In both Eu(III)-borate systems a weak 1:1 complex with a complexation constant log β^0 in the range of 2.6 to 3.3 was identified.

At pH 6, only ~2 % of the total boron is present as different polyborate species (tri- and pentaborate species) as determined by ^{11}B NMR spectroscopy. In the complexation studies, these different polyborate species were considered as sum as one complexing so called "polyborate" species. Ionic strength dependent investigations in NaCl and $NaClO_4$ media and the subsequently applied SIT approach (specific ion interaction theory) led to the following complexation constants and specific interaction coefficients of the 1:1 Eu(III)polyborate complex: log $\beta^0_{(NaClO4)}$ = 3.17 ± 0.2 with $\varepsilon(EuB(OR)_4^{2+}, ClO_4^-)$ = 0.31 ± 0.05 kg·mol^{-1} and log $\beta^0_{(NaCl)}$ = 3.12 ± 0.21 with $\varepsilon(EuB(OR)_4^{2+}, Cl^-)$ = 0.025 ± 0.04 kg·mol^{-1}.

The formation of two organoborates, namely salicylatoborate BSal and lactatoborate BLac, were studied by ^{11}B NMR spectroscopy and their formation constants of log β^0_{BSal} = 1.10 ± 0.14 and log β^0_{BLac} = 0.57 ± 0.22, respectively, were determined as prerequisite requirement to study the Eu(III) complexation with organoborates. For the first time, a 1:1 Eu(III)-salicylatoborate and 1:1 Eu(III)-lactatoborate complex were identified. A complexation formation constant of log β^0_{EuBSal} = 2.69 ± 0.17 was determined for the Eu(III)salicylato-borate complex and a range of the complexation constant log β^0_{EuBLac} from 2.58 to 3.25 was

estimated for the Eu(III)-lactatoborate complex depending on the used complexation constants of the Eu(III)-lactate complexes (occurring as competitive reaction to the Eu(III)-organoborate complexation) in the analysis.

It was furthermore observed, that a solid Eu(III)-(poly)borate phase precipitates within days to weeks depending on the total boron concentration, medium and the ionic strength. This Eu(III)-borate solid was isolated and characterized by XRD, TRLFS, IR- und NMR spectroscopy. This phase turned out to be amorphous with a ratio of fourfold to threefold coordinated boron environment of 3:1. Solid-state site-selective TRLFS revealed three Eu(III) solid species of which two almost identical.

Isothermal micro-titration calorimetry (ITC) were performed for a simultaneous determination of complexation enthalpies and constant of the complexation of Eu(III)/Nd(III) with low molecular ligands as function of ionic strength. For the formation of 1:1 complexes of Eu(III)/Nd(III) with lactate, oxalate, and malonate a complete thermodynamic dataset consisting of log β_1^0, $\Delta_r G^0$, $\Delta_r H^0$, $\Delta_r S^0$, specific ion interaction coefficients ε(complex, Cl^-) was determined. Furthermore, for the first time the sum of specific enthalpic interaction coefficients $\Delta\varepsilon_L$ were derived from ionic strength dependent measurements. The ITC studies of lactate and oxalate were completed and supported by time resolved fluorescence spectroscopy with Eu(III)/Cm(III) and UV-vis absorption spectroscopy with Am(III), respectively, and the complex constants were determined thereof.

In summary, the here obtained thermodynamic data and their dependence on the ionic strength contribute to a more realistic assessment of long-term safety and risks in nuclear waste repositories located in salt rock or argillaceous rock formations.

Zusammenfassung

Das vorliegende Projekt befasst sich mit Untersuchungen zu Wechselwirkungen zwischen dreiwertigen Actiniden und Lanthaniden (repräsentiert durch Am(III)/Cm(III) und Eu(III)/Nd(III)) mit Boratspezies als auch niedermolekularen organischen Liganden für die Bereitstellung von gesicherten thermodynamischen Daten für eine Langzeitsicherheitsanalyse und Risikobewertung von Endlagern für hochradioaktive Abfälle.
Von besonderem Interesse ist hierbei die spektroskopische und thermodynamische Charakterisierung der Wechselwirkung mit Boratspezies, die in diesem Projekt zum ersten Mal durchgeführt wurde. Borate sind im Steinsalz (potentielles Wirtsgestein) natürlich enthalten und Boratverbindungen werden Bestandteil des Inventars eines nuklearen Endlagers sein, u.a. in Glaskokillen der hochradioaktiven Abfälle, im Zementausbau.
Niedermolekulare organische Liganden sind als lösliche natürliche organische Materie im Porenwasser von Tongesteinen (ebenfalls ein potentielles Wirtsgestein) enthalten.

Das Komplexverhalten von zwei unterschiedlichen Eu(III)-Boratsystemen, nämlich erstens von Eu(III)-Polyborat und zweitens von Eu(III)-Organoborat, wurden mittels zeitaufgelöster laserinduzierter Fluoreszenzspektroskopie (TRLFS) und ^{11}B-NMR Spektroskopie in NaCl/ $NaClO_4$ Medium in Abhängigkeit der Ionenstärke bei pH-Werten $\leq$ 6 untersucht. In beiden Eu(III)-Boratsystemen wurde ein schwacher 1:1 Komplex mit einer Komplexbildungs-konstante log β^0 im Bereich von 2.6 bis 3.3 identifiziert.

Mittels ^{11}B-NMR-Spektroskopie wurde bei pH 6 ein Anteil an Polyboratspezies (im Wesentlichen Tri-und Pentaboratspezies) von rund 2 % des Gesamtborgehaltes bestimmt.
Diese verschiedenen Polyborate wurden hinsichtlich ihrer komplexierenden Wirkung als ein Spezies betrachtet, wobei dessen Konzentration aus der Summe über alle einzelnen Polyboratspezies gebildet wurde. Ionenstärkeabhängige Untersuchungen in NaCl und $NaClO_4$ Medium und deren Auswertung mittels SIT (specific ion interaction Theorie) ergaben die folgenden Komplexierungskonstanten und spezifischen Wechselwirkungskoeffizienten des 1:1 Eu(III)-Polyboratkomplexes: log $\beta^0_{(NaClO4)}$ = 3.17 ± 0.2 mit $\varepsilon(EuB(OR)_4^{2+}, ClO_4^-)$ = 0.3 ± 0.05 kg·mol^{-1} und log $\beta^0_{(NaCl)}$ = 3.12 ± 0.21 mit $\varepsilon(EuB(OR)_4^{2+}, Cl^-)$ = 0.025 ± 0.04 kg·mol^{-1}.

Als Voraussetzung für die Untersuchung der Komplexierung von Eu(III) mit Organoboraten wurde die Bildung von zwei Organoboraten, nämlich Salicylatoborat and Lactatoborat charakterisiert und die jeweiligen Bildungskonstanten mittels ^{11}B-NMR Spektroskopie bestimmt (log β^0_{BSal} = 1.10 ± 0.14 und log β^0_{BLac} = 0.57 ± 0.22).
Zum ersten Mal konnte ein 1:1 Eu(III)-Salicylatoborat- und 1:1 Eu(III)-Lactatoboratkomplex identifiziert und die entsprechenden Komplexbildungskonstanten ermittelt werden. Die Komplexbildungkonstante für den Eu(III)-Salicylatoboratkomplex wurde mit log β^0_{EuBSal} = 2.69 ± 0.17 bestimmt. Für den Eu(III)-Lactatoborat kann nur ein Bereich von log β^0_{EuBLac} von 2.58 bis 3.25 angeben werden, abhängig von den in der Auswertung verwendeten Literaturdaten für die Komplexbildungskonstante für die Eu(III)-Lactatkomplexierung, die als Konkurrenzreaktion zu der Eu(III)-Organoboratkomplexierung auftritt.

Es wurde weiterhin festgestellt, dass eine Ausfällung einer festen Eu(III)-Polyboratphase innerhalb von einigen Tagen bis Wochen, abhängig von der eingesetzten Borkonzentration und der Ionenstärke, erfolgt. Dieser Eu(III)-Polyboratfeststoff wurde isoliert und mittels XRD, TRLFS, IR- und NMR-Spektroskopie charakterisiert. Der Feststoff ist amorph mit einem Verhältnis der vierfach zu dreifachkoordinierten Bor-Umgebung von 3:1 im Boratliganden. Aus Untersuchungen des Eu(III)-Polyboratfeststoffes mittels Festköper-TRLFS und selektiver Anregung einzelne Spezies konnten drei Eu(III)-Spezies identifiziert werden, von denen zwei nahezu identisch sind.

Für eine simultane Bestimmung von insbesondere Komplexierungsenthalpien und Komplexbildungskonstanten als Funktion der Ionenstärke der An(III)/Ln(III) Komplexierung mit niedermolekularen organischen Liganden wurde die isotherme Mikro-Titrationskalorimetrie (ITC) als neue Methode etabliert. Für die Bildung der 1:1 Komplexe von Eu(III)/Nd(III) mit Lactat, Oxalat und Malonat wurden vollständige thermodynamische Datensätze bestehend aus log β^0_1, $\Delta_r G^0$, $\Delta_r H^0$, $\Delta_r S^0$ und spezifischen Wechselwirkungs-koeffizienten ε(Komplex, Cl^-) bestimmt. Ferner wurde erstmals die Summe der spezifischen enthalpischen Wechselwirkungskoeffizienten $\Delta\varepsilon_L$ der Komplexierungsreaktion aus den ionenstärke-abhängigen Messungen ermittelt. Die ITC-Messungen im Eu(III)/Nd(III)-Lactat- und Oxalatsystem wurden durch TRLFS-Messungen mit Eu(III)/Cm(III) sowie UV-vis absorptionsspektroskopische Untersuchungen mit Am(III) ergänzt und die entsprechenden Komplexbildungskonstanten bestimmt.

Zusammenfassend kann festgehalten werden, dass die hier bestimmten thermodynamischen Daten und deren Abhängigkeit von der Ionenstärke zu einer realistischeren Einschätzung der Langzeitsicherheit und Risiken von potentiellen Endlagern im Salzgestein oder Tongesteinsformationen beitragen.

1 Introduction

It is widely accepted that the final disposal of high-level radioactive waste as result of the peaceful use of nuclear energy has to be performed in deep geological formations. Due to their long half-lives (over thousands of years), actinides make a significant contribution to the long-term heat generation and radiotoxicity of the nuclear waste. Therefore, the actinides (mainly with oxidation states +3 and +4 [GEC2013, GEC2012, MET2012) are the main focus of this repository research.

The final disposal of high-level radioactive waste requires a special concept to isolate the waste and to store it safely in a proper environment for a time period of 10^6 years. Therefore the operation of a nuclear waste repository requires a long-term safety and risk assessment.

Salt rocks, crystalline and argillaceous rock formations are currently under consideration for potential host rocks for the deep geological disposal of nuclear waste.

A typical accident scenario for a long-term safety analysis is water ingress into the repository, which accelerates corrosion and initiates dissolution processes of the stored inventory, host rock components, and backfill materials. The released radionuclides may be involved in a multitude of geochemical interaction processes in the near and far field of a repository, e.g. sorption on mineral surfaces and diffusion, complexation with (in)organic ligands, redox reactions, and precipitations leading to their mobilization or immobilization. Such geochemical reactions depend strongly on the specific parameters of the aquatic system, e.g. pH, Eh, ionic strength, temperature, presence and concentration of complexing ligands, sorbents and colloids.

In Germany salt and argillaceous formations are considered as the most promising geological formation for nuclear waste storage. Both have in common that in case of water ingress salt solutions can occur with high to very high ionic strengths.

Formation water (pore water) in the northern and northwestern German argillaceous rocks can have ionic strengths up to 3.5 to 5 M [Kie03]. Additional to inorganic solution components, argillaceous rocks contain soluble organic compounds (up to 4%) such as low molecular weight organic ligands (like formate, actetate, propionate, lactate) and humic substances, which are able to influence the migration of actinides by forming of soluble complexes [CLA2005, COU2007a, b, GLA2005, GRA2010].

In the case of salt rocks, the brine composition is determined by the phase equilibria between the present salt compounds and aqueous solution. These salt

solutions consist mainly of Na^+, Cl^+, Mg^{2+}, Ca^{2+}, K^+ and SO_4^{2-} (oceanic system) and can achieve ionic strengths up to 11 M (depending on the depth and rock salt). Important trace components could be the anions like bromid and borate [HER2006].

Furthermore, higher temperatures (e.g. up to 100 °C in clay formation) due to the radioactive decay in waste affects additional parameters which include, the complexation behavior of actinides, as well as the composition of pore waters and brines in the near field of the nuclear depository.

Therefore, the determination of thermodynamic data for complexation reactions of actinides with (in)organic ligands is a key for geochemical modeling and prediction of actinide mobilization processes. A wide range of such data as well as solubility data are summarized in several thermodynamic reference databases, e.g. Thermochemical Database (TDB) Project of NEA and OECD [HUM2005, GUI2003], Nagra/PSI Chemical Thermodynamic Data Base [HUM2002] and Thermodynamic Reference Database from Germany (THEREDA, [http://www.thereda.com]). In recent years, intensive efforts have been made to expand these thermodynamic databases with data for elevated temperatures and high ionic strengths (including the estimation and determination of corresponding specific ion interaction coefficients for Pitzer and/or SIT approach, e.g. THEREDA). Despite these efforts the current thermodynamic databases are still lacking in complete thermodynamic data ($\log \beta_n^0$, $\Delta_r G^0$, $\Delta_r H^0$, $\Delta_r S^0$, specific ion interaction coefficients ε(j,k) and specific enthalpic interaction coefficients ε_L(j,k)) for complexation reaction of trivalent actinides (Am^{3+}) with (in)organic ligands determined in salt media (NaCl, KCl, $CaCl_2$) at elevated ionic strengths and temperature.

The objective of this project is the determination of unknown thermodynamic data, and the validation of known data of complexation reactions of trivalent lanthanides (Eu^{3+}, Nd^{3+}) and actinides (Am^{3+}, Cm^{3+}), with selected in(organic) ligands which are assumed to play a vital role in actinide mobilization in a potential nuclear repository.

The project is divided into two parts: Part one deals with the determination of complexation constants for the interaction of Eu(III) (as inactive analogue for trivalent actinides) with borate compounds, which has not been studied to date, and for which thermodynamic data are unknown (see chapter 3).

In the second part, the complexation of trivalent lanthanides (Eu^{3+}, Nd^{3+}) with low molecular organic ligands had been performed by isothermal micro-titration calorimetry and additionally, spectroscopic methods (Eu(III) and actinides Am^{3+}, Cm^{3+}), in mainly aqueous

NaCl solution at different ionic strengths up to 3 molal. These complexation studies are focused on the determination of complexation enthalpies and in particular complexation enthalpies as a function of ionic strength for the SIT approach to extend the existing thermodynamic database (see chapter 4).
More detailed information about the motivation, scientific background, the importance of the chosen systems, and applied techniques are given in the respective chapters.

This work was part of the BMWi joint project „Retention of radionuclides relevant for final disposal in natural clay rock and saline systems", between the Karlsruher Institut für Technologie (Institut für Nukleare Entsorgung), Johannes Gutenberg-Universität Mainz (Institut für Kernchemie), Helmholtz-Zentrum Dresden-Rossendorf (Institut für Ressourcenökologie), Universität des Saarlandes (Institut für Anorganische Festkörperchemie), Technische Universität Dresden (Sachgebiet Strahlenschutz), Technische Universität München (Fachgebiet Theoretische Chemie), Universität Potsdam (Institut für Chemie-Physikalische Chemie) and Ruprecht-Karls-Universität Heidelberg (Physikalisch-chemisches Institut).

2 Basics to determination of thermodynamic standard data

In this chapter summarizes some basics about the determining of the thermodynamic data as they were used in this report.

2.1 Stability constants

A reaction between metal ion M or proton H and ligand L is an equilibrium reaction and can be expressed by using the law of mass action (charged and hydration shells were omitted for simplicity, Eq. 2.1 and 2.2).

$$M + L \leftrightarrow ML\ (complexation) \text{ or } H + L \leftrightarrow HL\ (protonation) \quad 2.1$$

$$with\ K = \left(\frac{a_{ML}}{a_M \cdot a_L}\right)_{eq}\ for\ complexation\ and\ with\ K^H = \left(\frac{a_{HL}}{a_H \cdot a_L}\right)_{eq}\ for\ for\ protonation \quad 2.2$$

a…activity
K…stability constant

The equilibrium constant K (K^H) gives information about the thermodynamically strength of the interaction between the reacting agents[1]. If the complexation reaction is carried out stepwise each equilibrium is characterized by an individual stability constant K_n that covers the involved species. The individual stability constants K_n are summarized to an overall or cumulative formation constant β_n of the respective complex ML_n.

$$M + L \leftrightarrow ML \qquad K_1 = \frac{a_{ML}}{a_M \cdot a_L} \quad 2.3$$

$$ML + L \leftrightarrow ML_2 \qquad K_2 = \frac{a_{ML_2}}{a_{ML} \cdot a_L} \quad 2.4$$

$$M + nL \leftrightarrow ML_n \qquad \beta_n = K_1 \cdot K_2 \cdot \ldots \cdot K_n = \frac{a_{ML_n}}{a_M \cdot a_L^n} \quad 2.5$$

The relation between activity a_j of the species j and concentration c_j of the species j is expressed by the activity coefficient γ_j:

$$a_i = \gamma_j \cdot c_j \quad 2.6$$

γ_j…activity coefficient of the species j
a…activity of the species j
c_j…concentration of the species j

[1] In the following only the complexation reaction is considered, the following remarks can also applied to the protonation reaction.

At infinite dilution the activity coefficient γ_j is equal to 1. Under real conditions γ_j is a function of ionic strength, temperature, and pressure. The activity coefficient describes any interactions between the species in the considered system as deviation of the real system to the ideal reference state at infinite dilution. Due to these dependencies, the stability constant always refers to conditions of ionic strength, temperature and pressure at which it was determined. Such conditional constants β' can be converted into constants β^0 which are referring to a standard state by using the activity coefficient γ_j (Eq. 2.7 and 2.8).

$$\beta^0 = \frac{a_{ML}}{a_M \cdot a_L} = \frac{c_{ML}}{c_M \cdot c_L} \cdot \frac{\gamma_{ML}}{\gamma_M \cdot \gamma_L} = \beta' \cdot \frac{\gamma_{ML}}{\gamma_M \cdot \gamma_L} \qquad 2.7$$

$$\text{or} \quad log\beta^0 = log\beta' + log\gamma_{ML} - log\gamma_M - log\gamma_L \qquad 2.8$$

2.2 Specific Ionic Interaction theory

In thermodynamic data bases thermodynamic data always refer to a standard state. According to IUPAC [LAF1982], the standard state for a solute j (m_j = 1 mol/kg) in a solution is given by its infinite dilution ($\lim_{m_j \to 0} m_j = 0\, mol \cdot kg^{-1}$) at T = 25 °C and at p^0 =1 atm, and represents an activity coefficient γ_j of unity [HUM2005]. However, in solutions with highly charged ions, the measurement at infinite dilution is not possible. Therefore, inert background electrolytes of sufficiently high concentration are used to ensure constant activity coefficients. The activity coefficients of all species present in a solution must be estimated which can be done by different approaches. The Debye-Hückel-Theory includes electrostatic, non-specific long-distance interactions between ions which are approximated as point charges. This theory is valid for very low ionic strengths I_m < 0.001 mol·kg^{-1} (molal = m). The extended Debye-Hückel-Theory considers the solvation shell and the specific, effective ionic radius which is expressed by the Debye-Hückel term D (Eq. 2.9-2.11). To include short-ranging, non-electrostatic interaction between the ions, the specific ion interaction (SIT) approach was developed. It bases on the Debye-Hückel theory but includes as additional term the interaction coefficient ε(j,k) between cation j and anion k including all ions are present in solution (Eq. 2.9). The theory was first outlines by Brønsted [BRÖ1922, BRÖ1922b] and refined by Scatchard [SCA1936] und Guggenheim [GUG1966]. The Debye-Hückel parameters A and B are pressure and temperature dependent and can be found in tables. At T = 25°C the constant A is (0.509 ± 0.001) kg$^{1/2}$·mol$^{-1/2}$ and B·a_j is 1.5 kg$^{1/2}$·mol$^{-1/2}$ (determined by [SCA1976], confirmed by [CIA1980]).

$$\log \gamma_j = -z_j^2 \cdot D + \sum_k \varepsilon\,(j,k,I_m) m_k \qquad 2.9$$

with $$D = \frac{A \cdot \sqrt{I_m}}{1 + B \cdot a_j \cdot \sqrt{I_m}} = \frac{0.509 \cdot \sqrt{I_m}}{1 + 1.5 \cdot \sqrt{I_m}} \qquad 2.10$$

and $$I_m = \frac{1}{2} \sum_i m_i {z_i}^2 \qquad 2.11$$

γ_j…activity coefficient of species j
z…charge of ions j
D…Debye-Hückel term
A and B…Debye-Hückel parameter
a_j…ion size parameter for the hydrated ion j
I_m… ionic strength, molal
m…molal, mol·kg^{-1}
ε_j…interaction coefficient between cation j and anion k

Due to the high concentration of the background electrolyte, for instance NaCl, which exceeds the concentrations of the reactants about a few orders of magnitude, the molalities m_{Na+} und m_{Cl-} (Eq. 2.12) become the most dominant contribution regarding to the interaction coefficients. After the substitution of γ_j in Eq. 2.7 through Eq. 2.9, the linear relation in Eq. 2.13 is derived.

$$m_{Na^+} = m_{Cl^-} \approx I_m \qquad 2.12$$

$$log\ \beta' - \Delta z^2 \cdot D = log\ \beta^0 - \Delta\varepsilon \cdot I_m \qquad 2.13$$

with $$\Delta z^2 = \sum z^2\,(products) - \sum z^2\,(educts) \qquad 2.14$$

and $$\Delta\varepsilon = \sum_j \nu_j \cdot \varepsilon\,(j,k) \qquad 2.15$$

β…stability constant
z… charge of ions j
D…Debye-Hückel term
ε … interaction coefficient between cation j and anion k
I_m… ionic strength, molal
m…molal, mol·kg^{-1}
v…stoichiometry coefficient (ν_j are positive for products and negative for reactants)

By plotting $\log \beta'$ - $\Delta z^2 \cdot D$ vs. I_m (Eq. 13) the stability constant $\log \beta^0$ at I = 0 and the difference in interaction coefficients of all involved species, $\Delta\varepsilon$, can be determined from the intercept and the slope, respectively.

According to Eq. 2.15, the difference in ion interaction coefficients $\Delta\varepsilon$ is equal to the sum of specific ion interaction coefficients ε(j,k) between the involved ion species and the ions of the background electrolyte. The individual ion interaction coefficients describe the specific short-

range interactions. For uncharged species and species of equal charge the ion interaction coefficient $\varepsilon(j,k)$ is zero. Since trivalent actinides and lanthanides have similar ionic radii, the single interaction coefficient of 0.23 ± 0.02 kg·mol^{-1} from the NEA-TDB [HUM2005] can be used for (Eu^{3+}, Cl^-), (Am^{3+}, Cl^-) and (Cm^{3+}, Cl^-) for interaction in NaCl medium. Using $\varepsilon(M^{3+}, Cl^-)$, $\varepsilon(L^{n-}, Na^+)$ for a ligand L and the respective $\Delta\varepsilon$ value as determined by linear regression of the SIT plot (Eq. 2.13), the individual ε-value for the complex species (1:1 complex) can be derived according to Eq. 2.16.

$$\varepsilon(ML^{3-n}, Cl^-/Na^+) = \Delta\varepsilon_1 + \varepsilon(M^{3+}, Cl^-) + \varepsilon(L^{n-}, Na^+) \qquad 2.16$$

The complexation enthalpy as function of ionic strength can be derived using the SIT approach too (Eq. 2.17, 2.18). This procedure is similar to that of the stability constant but the Debye-Hückel term D_L and $\Delta\varepsilon_L$ value represent enthalpic parameters [GRE1997, HUM2005].

$$\Delta_r H_m - \Delta z^2 \cdot D_L = \Delta_r H_m^0 - RT^2\, \Delta\varepsilon_L \cdot I_m \qquad 2.17$$

with $$D_L = \frac{3}{4} \cdot \frac{A_L \cdot \sqrt{I_m}}{1 + 1.5 \cdot \sqrt{I_m}} \qquad 2.18$$

$\Delta_r H_m$ ...molale reaction enthalpy
z... charge of ions j
D_L...enthalpic Debye-Hückel term
$\Delta\varepsilon_L$ ...difference in the enthalpy-interaction coefficients
R...universal gas constant
T...temperature
I_m... ionic strength, molal
A_L...enthalpic Debye constant

A_L is 1.986 kJ·kg$^{1/2}$·mol$^{-3/2}$ at 25°C [HUM2005]. The single enthalpic interaction coefficient ε_L represents the temperature dependency of the single interaction coefficient ε(j,k) and can be determined from the sum in enthalpy interaction coefficients using Eq. 2.19 and 2.20.

$$\varepsilon_L\,(j,k) = \left(\frac{\partial\varepsilon\,(j,k)}{\partial T}\right)_P \qquad 2.19$$

$$\Delta\varepsilon_L = \sum_j \nu_j \cdot \varepsilon_L\,(j,k) \qquad 2.20$$

ε_L ...relative partial molar enthalpy specific ion interaction coefficient between cation j and anion k
$\Delta\varepsilon_L$ ...difference of the enthalpy-interaction coefficients
ν...stoichiometry coefficient

2.3 Gibbs free energy and entropy

The Gibbs free energy $\Delta_r G$ and entropy $\Delta_r S$ can be derived from the stability constant and the enthalpy by using the Gibbs-Helmholtz-Equation:

$$\Delta_R G = -RT \cdot ln\, K = \Delta_R H - T \cdot \Delta_R S \qquad 2.21$$

$$\Delta_R S = R \cdot ln\, K + \frac{\Delta_R H}{T} \qquad 2.22$$

During complex formation mainly three processes determine the energetic distribution: (i) the partially dehydration of the reactants (which depends also on the solvent), (ii) the energy released when the metal ion and the ligand form the complex (bonding) and (iii) the energy released when the dehydrated water molecules form hydrogen bonding with the bulk water. Process (i) requires energy ($\Delta_r H$ is positive) and liberates water. A gain in $\Delta_r S$ (a gain in the degrees of freedom in solution) is obtained which is then stated positive. The dehydration of trivalent metal ions during complexation reactions plays an important role considering the energetics. Process (ii) releases energy ($\Delta_r H$ is negative). Process (iii) possesses a very small negative enthalpy. The dimension of the respective parts (especially process (i) and (ii)) determines if a reaction is exothermic or endothermic, or driven by entropy or enthalpy respectively. [CHR1972, HAN2001, KIT2006, MAR1991, RAO2007] That means, that the driving force of a reaction can be derived using the Gibbs-Helmholtz equation (Eq. 2.21). Fig. 2.1 shows three possible scenarios for thermodynamic energetics of a reaction. Reaction A is enthalpy-driven (T·$\Delta_r S$ and $\Delta_r H$ are negative). Reaction B is entropy-driven (T·$\Delta_r S$ and $\Delta_r H$ are positive) and reaction C is both enthalpically and entropically stabilized (T·$\Delta_r S$ and $\Delta_r H$ possess the same magnitudes).

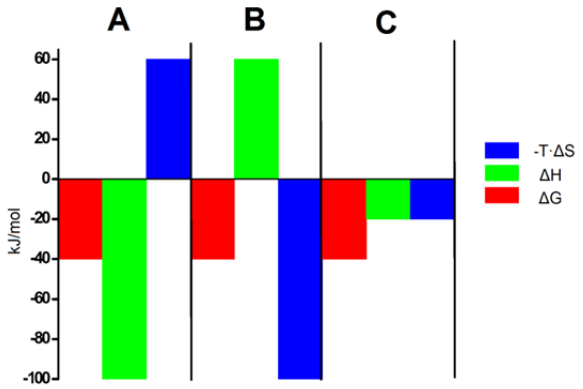

Fig. 2.1: Energetics of a chemical reaction ($-T\cdot\Delta_R S$ is shown)

2.4 Determination of the uncertainties of the thermodynamic data

In order to estimate the random experimental uncertainty of the thermodynamic parameters, a weighted average value $\bar{x}_w$ of n individual measurements of the quantity x_i was determined (Eq. 2.23). The weights w_i are the reciprocal squares of the corresponding standard deviation σ_i (95 % probability) of least-squares procedure of the data fitting in the used analysis programs (HYPΔH, LETAGROP, SPECFIT, HYPERQUAD)

$$\bar{x}_w = \frac{\sum w_i x_i}{\sum w_i} \quad with \quad w_i = \frac{1}{\sigma_i^2} \qquad i = 1, \ldots, n \qquad 2.23$$

The uncertainty σ_w of the weighted average value $\bar{x}_w$ is obtained from the sum over the weights w_i of all measurements according to Eq. 2.24.

$$\sigma_w = \frac{1}{\sqrt{\sum w_i}} \qquad 2.24$$

If no multiple individual measurements were available, then uncertainty σ_w was estimated. This was done, for instance, in the case of measurements with Am(III) and Cm(III).

The thermodynamic standard data are derived from the SIT plots of the weighted averages $\bar{x}_w$ of the conditional thermodynamic data by applying a weighted linear regression according to the procedure described in [TAY1982] and [HUM2005] by using fitting program OriginPro8.0.

2.5 Conversions and pH measurements

The most samples were prepared in the molal concentration scale (mol·kg^{-1} H_2O). For the data analysis with the analyzing programs HYPΔH, LETAGROP, SPECFIT, HYPERQUAD which used the molar scale the molality were converted into molarity scale using the conversion factors from the NEA-TDB [HUM2005]. For the determination of the stability constants at standard state ($\log \beta^0$) using the SIT, the conditional constants in molarity should be converted to constants in molality. According to the method in the literature [GRE1992], the equilibrium constant of a reaction in molality (K_m) is related to that in molarity (K_M) by Eq. 2.25:

$$log\ K_m = log\ K_M + \sum \nu_B \cdot log_{10} \varrho \qquad 2.25$$

ϱ...conversion factor defined as $\varrho = m_B/c_B$ [dm^3 of solution per kg H_2O] with molalität m_B as mole of substance B dissolved in 1 kg pure water, molarität c_B as mole of substance B dissolved in ($1000\rho - c_B M$), ρ... density, M...molar weight of the solute
$\sum \nu_B$...the sum of the stoichiometric coefficients of the reaction (ν_r is positive for products and negative for reactants)

The pH measurements were mostly carried out with a Ross-Electrode (Orion 8103SC) with an accuracy of 0.05 units. The electrode was calibrated using standard buffer solutions (pH 1-10, Merck). For pH measurements at $I > 0.1$ mol·kg^{-1} an empirical, ionic strength dependent correction factor A(I) has to be included. Eq. 2.26 shows the relation of the pH readings (pH_c) at the pH meter and the negative logarithm of the free proton concentration.

$$-\log[H^+] = pH_c + A(I) \qquad 2.26$$

A(I) was determined in separate calibration measurements according to the procedure of Altmaier et al. [ALT2003] by preparing solutions of known total proton concentration and known ionic strength. The ionic strength dependence of the pK_w value of water was taken into consideration [KRO1995, MAE1987]. The solutions with ionic strengths between 1 and 5 mol·kg^{-1} and pH 1, 3, 12 and 13 were measured. The shift of the calibration line along the pH axis with increasing ionic strength with respect to the reference calibration line at I = 0 corresponds to the A values. The correction factor A(I) was obtained by determination of the difference of the zero-crossing potential of the calibration line and reference calibration line. All calibrations were performed at 25°C.

3 Investigation of the interactions of Eu(III), Am(III) and Cm(III) with borate

3.1 Motivation

Borate compounds are identified as species in a nuclear waste repository system, particularly in rock salt, potentially interacting with actinides [BOR2010, ALT2013]. Their occurrence in a nuclear waste repository results from natural and technological sources:
(1) Salt deposits (as minerals, like borax, sassolite, ulexite, colemanite, boracite) and its brines. For instance at the WIPP site (Waste Isolation Pilot Plant, USA) borax deposits and boron containing seepage brine were found [SNI2003].
(2) Corroded glass coquilles made of borosilicate glass in which high-level radioactive waste is fused.
(3) Remains of boron containing water from the cooling circuit of (spent) nuclear fuels (boric acid as neutron absorber).
(4) Cement as waste form for LLW and MLW (borate in cement as retarding agent for its workability).
These borate compounds are considered as ligands influencing the actinide mobilization in the case of water ingress into a nuclear waste repository.

The interaction, particularly the complexation, of (poly)borates with actinides is not sufficiently investigated so far in order to estimate a possible actinide mobilization in a nuclear waste repository. Hence, it is necessary to study the relevance of borate species concerning their actinide mobilization potential.
In their pioneering work Borkowski et al. investigated the complexation of Nd(III) (as chemical analog for trivalent actinides, e.g., Am(III), Pu(III), Cm(III)) in borate solutions at high ionic strength (up to I = 5 M, NaCl) and alkaline conditions which are typical for the WIPP site. From solubility experiments they determined a 1:1 Nd(III)-(tetra)borate complexation constant log β_1^0 = 4.55 (extrapolated to zero ionic strength with SIT approach) [BOR2010]. This An(III)/Ln(III)-borate complex is interpreted to be a predominant species under the WIPP brine conditions (up to $[B]_{total}$ = 0.16 M , pH_c = 8-9) [BOR2010].
However, the results of Borkowski et al. could not be reproduced: Hinz et al. carried out Nd(III) solubility experiments under high ionic strength and alkaline conditions and observed a clear solubility decrease of Nd(III) in presence of (poly)borate species (up to 4.5 orders of magnitude depending on pH, ionic strength and electrolyte) [HIN2015]. The reason for this

solubility decrease is the transformation of the initial $Nd(OH)_3$ solid phase into a borate containing Nd(III) solid phase [HIN2015].
A further overview about existing monoborate complexes with alkaline metals, alkaline earth metals, Al(III), Fe(III), Co(III), Ni(II), Cu(II), Zn(II), Cd(II) and Pb(II) is given in [BOU1981] and [SCHO2015/2016].

The aim of the work presented in this chapter is to contribute to a better understanding of the An(III)/Ln(III)-(poly)borate system. Primarily, the complexation properties of (poly)borates with respect to An(III)/Ln(III) are in the focus of the investigations to derive fundamental thermodynamic data. For this purpose the complexation between borate species (polyborates, organoborates) and trivalent europium (chemical analog of trivalent actinides, e.g., Am(III), Pu(III), Cm(III)) was studied spectroscopically by means of time-resolved laser-induced fluorescence spectroscopy (TRLFS) and nuclear magnetic resonance spectroscopy (NMR), to begin with at I_m = 0.1 m ($NaCl/NaClO_4$). The investigations were extended by Am(III)/ Cm(III)-(poly)borate complexation studies in NaCl media, by Eu(III)-(poly)borate complexation studies under higher ionic strength conditions in different salt media (NaCl, $NaClO_4$, $CaCl_2$, $MgCl_2$, KCl) and by investigations of a solid europium borate phase which is formed under the studied conditions.
The basics, results and discussion presented in this chapter are already published in parts in two articles of Schott et al. [SCHO2014, SCHO2015] and in the thesis of J. Schott [SCHO2015/2016].

Working hypothesis and approaches

It should be noted that in the An(III)/Ln(III)-borate system a multitude of reactions occur in the alkaline pH range. These reactions, including the formation of a variety of (poly)borate species (cf. chapter 3.2) and the strong hydrolysis of trivalent f-elements, compete with the An(III)/Ln(III)-borate complexation and making their study impracticable. For a basic understanding of this system it is more reasonable to carry out complexation studies under acidic conditions which were applied in this work.
The Eu(III) speciation up to pH 6 under ambient conditions is exclusively dominated by the Eu(III) aqua ion. The formation of solid Eu(III)-hydroxides and -carbonates can be excluded. Unfortunately, no monoborate species exists up to pH 6 and $[B]_{total}$ = 0.7 M (solubility limit of boric acid as (poly)borate source), cf. chapter 3.2. Above $[B]_{total}$ = 0.025 M polyborate species occur (cf. chapter 3.2) which have an effect on the Eu(III) speciation due to a complex

formation with Eu(III) (cf. chapter 3.4.2). Thus, polyborates were used as borate ligands in the Eu(III) complexation studies. Certainly, the polyborate equilibrium is still complex in the acidic pH range, because several polyborates coexist, but much simpler than in the alkaline region. However, the mathematical deconvolution and separation of the individual polyborate complexes with Eu(III) is not feasible. Consequently, the approach in this work is to generalize all coexisting polyborate species to one model borate species "$B(OR)_4^-$" assuming that all borate species with the structural unit "$B(OR)_4^-$" show similar complexation properties with Eu(III).

In a second approach organoborates, also containing this structural unit "$B(OR)_4^-$", were applied for the complexation studies in the An(III)/Ln(III)-borate system. When using hydroxycarboxylate-based organoborates (cf. chapter 3.2) these studies also can be carried out in the acidic pH range (cf. chapter 3.5.2) with the same reason as for the polyborate approach (avoiding An(III)/Ln(III) hydrolysis). Both approaches shall provide consistent and assured thermodynamic complexation data for the An(III)/Ln(III)-borate system.

From recent DFT studies it is known that the Eu(III) complexation by the model borate species "$B(OR)_4^-$" is not significantly influenced by the nature of the moieties R (R = H, organic moieties (aliphatic, aromatic), other threefold coordinated boron center(s), including the simple monoborate species and inorganic polyborates with one binding site "$B(OR)_4^-$" unit) [SCHO2015].

3.2 Speciation of the borate system

This chapter gives only a short overview about the complex speciation in the borate system. For more details see the thesis of J. Schott [SCHO2015/2016].

$B(OH)_3$-(poly)borates

Boric acid, $B(OH)_3$, is a weak acid with a high dissociation constant ($pK_{a,BH}$ = - $\log K_{11}$ = 8.98, I = 0.1 M $NaClO_4$ [ING1962]) acting as a Lewis acid (hydroxide acceptor), Eq. 3.1:

$$B(OH)_3 + H_2O \leftrightarrow B(OH)_4^- + H^+ \qquad K_{11} = \frac{[B(OH)_4^-]\,[H^+]}{[B(OH)_3]} \qquad 3.1$$

The monoborate anion, $B(OH)_4^-$, is the simplest borate structure existing in a considerable amount in the alkaline pH range (pH > 9). Above a total boron concentration ($[B]_{total}$) of 0.025 M in the pH region from 4 to 13 a polymerization of boric acid or monoborate occurs

and polyborates are formed [ING1957]. These polyborates consist of trigonal planar [BO_3] units and tetrahedral [BO_4^-] units with a negative charge at the boron atom. The [BO_3] and [BO_4^-] units are multifariously connected and form different kinds of polyborates. Clearly identified polyborate species in solution are $B_3O_3(OH)_4^-$ (triborate I), $B_5O_6(OH)_4^-$ (pentaborate), $B_4O_5(OH)_4^{2-}$ (tetraborate) and $B_3O_3(OH)_5^{2-}$ (triborate II) [HIR1979, ING1963, ING1962, JAN1979a, JAN1979b, MAY1976, MOM1967, SAL1983, SPE1970] (Fig. 3.1). In this work the polyborate formation constants from Ingri et al. [ING1962, ING1963] determined by potentiometric titration were used (cf. Eq. 3.2 to Eq. 3.5). The polyborate equilibria are almost independent on the ionic strength [ING1962, ING1963, MES1972]. Hence, the polyborate formation constants were used up to I_m = 3 m (NaCl/$NaClO_4$).

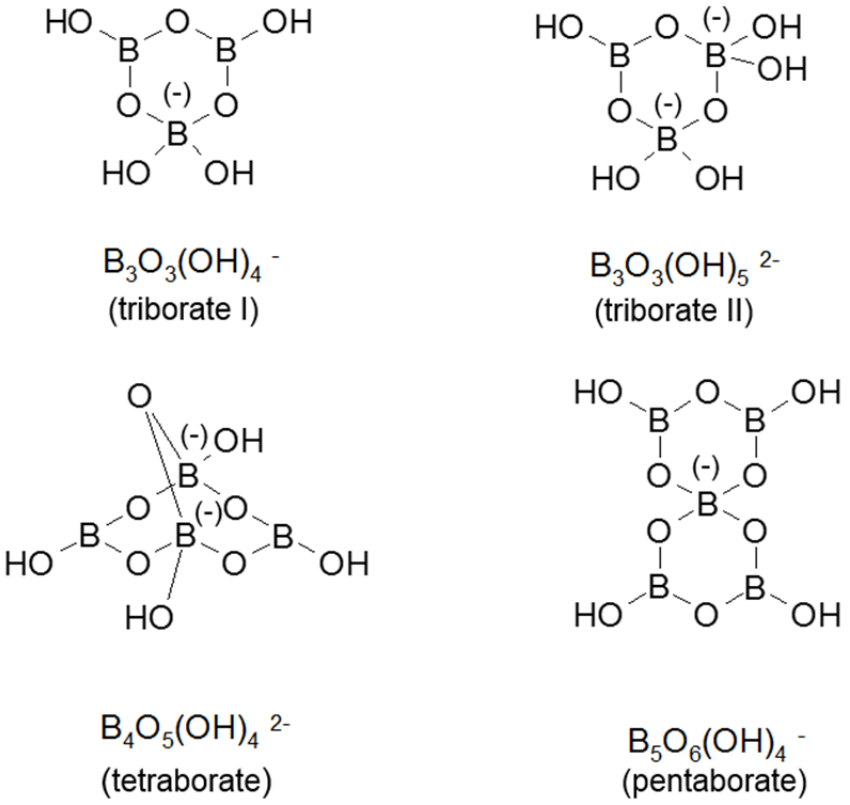

Fig. 3.1: Structure of the clearly identified polyborate species in solution

$$3\,B(OH)_3 \leftrightarrow B_3O_3(OH)_4^- + H^+ + 2\,H_2O$$

$$K_{13} = \frac{[B_3O_3(OH)_4^-]\,[H^+]}{[B(OH)_3]^3} \quad \text{with } \log K_{13} = -7.29 \text{ [ING1962]} \qquad 3.2$$

$$5\,B(OH)_3 \leftrightarrow B_5O_6(OH)_4^- + H^+ + 5\,H_2O$$

$$K_{15} = \frac{[B_5O_6(OH)_4^-]\,[H^+]}{[B(OH)_3]^5} \quad \text{with } \log K_{15} = -6.77 \text{ [ING1962]} \qquad 3.3$$

$$4\,B(OH)_3 \leftrightarrow B_4O_5(OH)_4^{2-} + 2\,H^+ + 3\,H_2O$$

$$K_{24} = \frac{[B_4O_5(OH)_4^{2-}]\,[H^+]^2}{[B(OH)_3]^4} \quad \text{with } \log K_{24} = -14.91 \text{ [ING1963]} \qquad 3.4$$

$$3\,B(OH)_3 \leftrightarrow B_3O_3(OH)_5^{2-} + 2\,H^+ + H_2O$$

$$K_{23} = \frac{[B_3O_3(OH)_5^{2-}]\,[H^+]^2}{[B(OH)_3]^3} \quad \text{with } \log K_{23} = -16.77 \text{ [ING1963]} \qquad 3.5$$

Fig. 3.2 illustrates a $B(OH)_3$-polyborate speciation in the pH range 3 to 14 for a solution containing $[B]_{total}$ = 0.025 M to 0.7 M (I = 0.1 M, NaCl/$NaClO_4$). Up to pH 6 (the highest investigated pH in this work) the species $B(OH)_3$, $B_3O_3(OH)_4^-$ (triborate I) and $B_5O_6(OH)_4^-$ (pentaborate) are present in solution. Between pH 4 and pH 5 the polyborate species $B_3O_3(OH)_4^-$ and $B_5O_6(OH)_4^-$ appear at $[B]_{total} > 0.4$ M. At pH 6 and $[B]_{total}$ = 0.7 M around 3.5 % of polyborates (almost equally distributed on both polyborate species) are present in solution. The remaining and largest part in solution under the considered conditions is represented by boric acid.

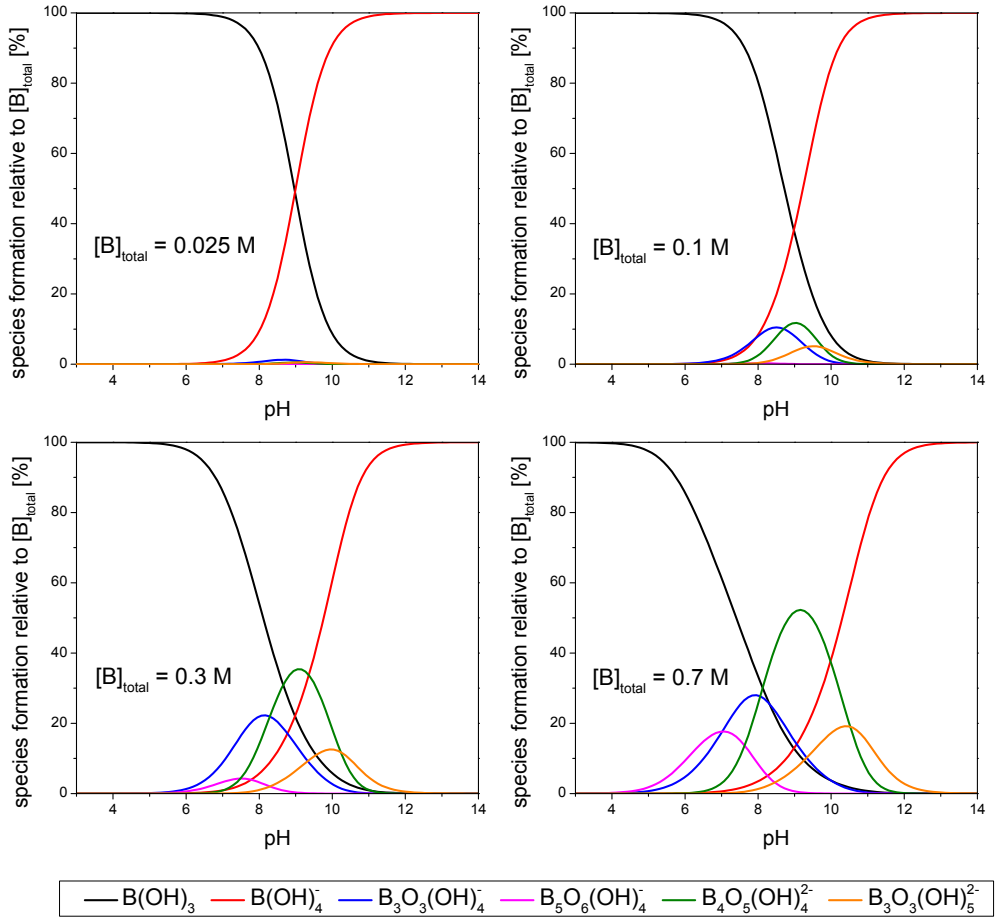

Fig. 3.2: *$B(OH)_3$-polyborate speciation relative to $[B]_{total}$ for different $[B]_{total}$ as a function of pH, I = 0.1 M ($NaCl/NaClO_4$). Calculation with Ingri´s formation constants [ING1962, ING1963] for different (poly)borates (*cf. *Eq. 3.1 to Eq. 3.5).*

Organoborates

Besides the inorganic (poly)borates a further group of borate structures, named organoborates, can be defined, e.g., [KÖS2010, OI1992, MIY2008, MIY2013]. Two possible ways for the organoborate formation are shown in Fig. 3.3. The reaction of boric acid with hydroxycarboxylates, Fig. 3.3a, and monoborate with polyols, Fig. 3.3b, leads to the formation of cyclic organic borate compounds (organoborates or borate esters) with a fourfold coordinated boron center. The ring size of the organoborates depends on the position of the functional groups in the organic molecule. In contrast to the polyol-based organoborates the ones based on hydroxycarboxylates are formed (and are stable) in the acidic pH range (see chapter 3.5.1). Here, metal complexation studies can be carried out with good chances. Hence, hydroxycarboxylate-based organoborates were used to study the complexation with Eu(III).

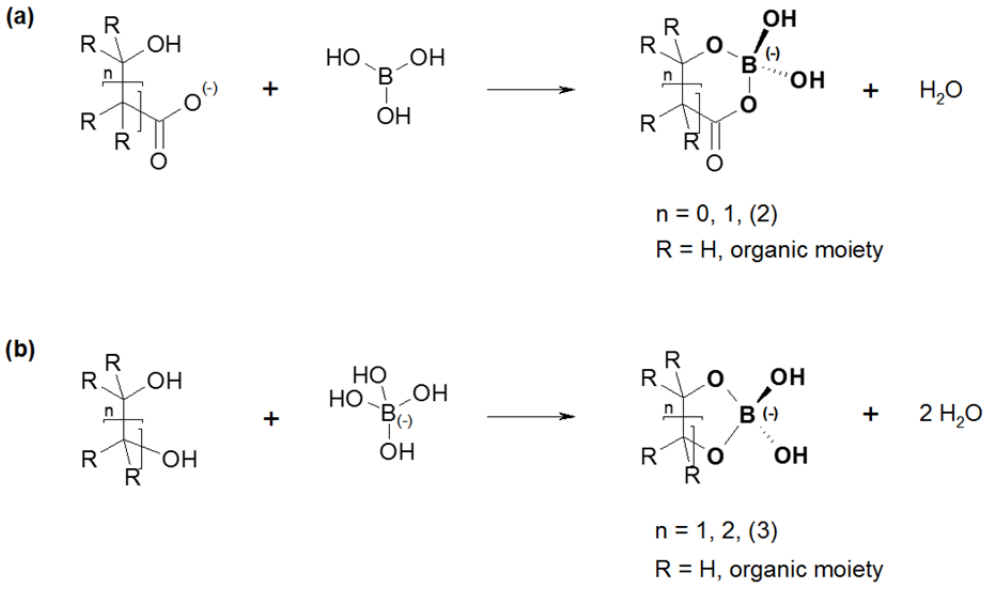

Fig. 3.3: General structures of organoborates resulting from reaction of (a) boric acid with hydroxycarboxylates and (b) monoborate with polyols

3.3 Methods and experimental

All methods that have been used, in particular ^{11}B NMR and time-resolved laser-induced fluorescence spectroscopy (TRLFS), and further experimental details are described in detail in the thesis of J. Schott [SCH2015/2016].

3.3.1 Chemicals and solutions

Chemicals of analytical grade and deionized water were used for the preparation of solutions. Europium oxide Eu_2O_3, europium chloride $EuCl_3 \cdot 6H_2O$, sodium salicylate, sodium L-lactate (all from Sigma-Aldrich), and boric acid $B(OH)_3$ (Merck) were used without further purification. The total boron concentration, $[B]_{total}$, was adjusted with boric acid. Solutions were prepared under ambient conditions (T = 22°C, $p_{CO_2} = 10^{-3.5}$ bar). The ionic strength of the solutions was adjusted with sodium perchlorate $NaClO_4 \cdot H_2O$ (Merck), sodium chloride NaCl (Roth), potassium chloride KCl (Merck), calcium chloride $CaCl_2 \cdot 2H_2O$ (Merck) or magnesium chloride $MgCl_2 \cdot 6H_2O$ (Merck). A 0.03 M (≈ 0.03 m) Eu(III) stock solution was prepared by dissolving Eu_2O_3 in 0.1 M $HClO_4$. Its concentration was verified with ICP-MS (Elan 9000, Perkin Elmer). The pH measurements (adjustment, potentiometric titration) were carried out with a glass electrode (SCHOTT), which was calibrated with buffer solutions (NIST/PTB standard buffers). The pH of the solutions was adjusted with NaOH or $HClO_4$ (both from Merck) of various concentration (0.1 M to 2 M).

3.3.2 Determination of pK_a of boric, salicylic and lactic acid

Potentiometric titrations of solutions containing varying concentrations of boric acid, sodium salicylate or sodium lactate were carried out. The solutions were prepared at around pH 2 and I = 0.1 M ($NaClO_4$) under ambient conditions. 20 mL of each solution were automatically titrated (736 GP Titrino/TiNet 2.50, Metrohm) up to pH 12 under N_2-atmosphere in a temperature adjustable titration vessel at 22 °C by adding 0.1 M NaOH (carbonate-free). The dynamic titration procedure was used. 60 seconds after adding of NaOH the pH measurements were initiated. The titration data were analyzed with the computer program Hyperquad2008 [HYP2008a] to determine the pK_a values of boric, salicylic and lactic acid.

3.3.3 $B(OH)_3$-polyborate speciation studies

Samples with variable $[B]_{total}$ (0.02 m to 0.7 m) were prepared under ambient conditions at pH_c 5 and pH_c 6, I_m = 0.1 m ($NaClO_4$, NaCl, $CaCl_2$, $MgCl_2$, KCl). High total boron concentrations (up to 0.7 m) were used to induce the formation of polyborate species. After the dissolution of boric acid the samples were stored at least for one week to allow adjusting the boric acid/polyborate equilibria. Then, appropriate amounts of $NaClO_4 \cdot H_2O$, NaCl, KCl, $CaCl_2 \cdot 2H_2O$ or $MgCl_2 \cdot 6H_2O$ were added to the $B(OH)_3$/polyborate solutions to adjust ionic strengths up to I_m = 3 m. These solutions were equilibrated at least one week again. Then, the samples were measured by means of ^{11}B NMR spectroscopy.

3.3.4 Studies on Ln(III)/An(III)-polyborate interactions

Eu(III)-(poly)borate complexation studies at I_m = 0.1 m

Samples with variable $[B]_{total}$ (up to 0.7 m) were prepared at around pH_c 6 and I_m = 0.1 m ($NaCl/NaClO_4$) as described for the solutions prepared for the $B(OH)_3$-polyborate speciation studies. 2 g of a polyborate containing solution were transferred into a quartz cuvette and the 0.03 m Eu(III) stock solution was added to adjust a total Eu(III) concentration of $3 \cdot 10^{-5}$ m. The samples were titrated at the same day (to exclude precipitation) from around pH_c 6 down to around pH_c 2 by adding appropriate amounts of $HClO_4$. After each titration step a stationary europium luminescence spectrum was measured. The complex formation constant of the Eu(III)-(poly)borate complex was determined from the stationary TRLFS data with the program HypSpec (version 1.1.18) [HYP2008b].

Eu(III)-(poly)borate complexation studies up to I_m = 3 m

Samples with variable $[B]_{total}$ (up to 0.7 m) were prepared at pH_c 6, and variable ionic strength (I_m = 0.1 m to 3 m, $NaClO_4$/NaCl/$CaCl_2$/$MgCl_2$/KCl) as described for the solutions prepared for the $B(OH)_3$-polyborate speciation studies. A total Eu(III) concentration of $3 \cdot 10^{-5}$ m was adjusted with the 0.03 m Eu(III) stock solution. The stationary and time-resolved europium luminescence spectra of each solution recorded after the Eu(III) addition (Eu(III)-borate solid formation can be excluded) were used for the determination of the complexation constant of the Eu(III)-(poly)borate complex in dependency on ionic strength with the program HypSpec (version 1.1.18) [HYP2008b], and to identify the amount of species with parallel factor analysis (PARAFAC). PARAFAC was carried out by Björn Drobot (Helmholtz-Zentrum Dresden-Rossendorf, Institute of Resource Ecology) using the N-way toolbox for Matlab [AND2000]. The applied settings for the analysis are described in Drobot et al. [DRO2015].

Cm(III)-(poly)borate complexation studies at I_m = 0.1 m

Samples with variable $[B]_{total}$ (up to 0.7 m) were prepared at around pH_c 6 and I_m = 0.1 m (NaCl) as described for the solutions prepared for the $B(OH)_3$-polyborate speciation studies. A total Cm(III) concentration of $2 \cdot 10^{-7}$ m was adjusted with a $2.4 \cdot 10^{-4}$ m ^{248}Cm(III) stock solution. The samples were titrated at the same day (to exclude precipitation) from around pH_c 6 down to around pH_c 2 by adding appropriate amounts of $HClO_4$. After each titration step a stationary curium luminescence spectrum was measured. The complex formation constant of the Cm(III)-(poly)borate complex were determined from the stationary TRLFS data with the program HypSpec (version 1.1.18) [HYP2008b].

Am(III)-(poly)borate complexation studies up to I_m = 3 m

Samples with $[B]_{total}$ = 0.7 m were prepared at around pH_c 6 and up to I_m = 3 m (NaCl) as described for the solutions prepared for the $B(OH)_3$-polyborate speciation studies. A total Am(III) concentration of around $6 \cdot 10^{-7}$ m was adjusted with a 10^{-5} m ^{243}Am(III) stock solution. The samples were titrated at the same day (to exclude precipitation) from around pH_c 6 down to around pH_c 2 by adding appropriate amounts of $HClO_4$. After each titration step a UV/Vis absorption spectrum was measured using a 1-meter long path flow cell (World Precisions Instruments) and fiber optic spectrometer (MCS601, Carl Zeiss). The complex formation constant of the Am(III)-(poly)borate complex in dependency on ionic strength was determined from UV/Vis data with the program HypSpec (version 1.1.18) [HYP2008b].

Eu(III)-borate solid formation studies in suspension

Samples with variable $[B]_{total}$ (0.2 m to 0.7 m) were prepared at pH_c 5 and pH_c 6, and variable ionic strength (I_m = 0.1 m to 3 m, $NaClO_4$/NaCl/$CaCl_2$/$MgCl_2$/KCl) as described for the solutions prepared for the $B(OH)_3$-polyborate speciation studies. A total Eu(III) concentration of $3 \cdot 10^{-5}$ m was adjusted with the 0.03 m Eu(III) stock solution. Directly after the Eu(III) addition a part of each solution was retained and stored. The remaining part of each solution was observed in increasing intervals (days, weeks, months) and at each investigation date stationary and time-resolved europium luminescence spectra were recorded. The retained samples were studied in a final analysis after ending the solid formation studies. They were filtered through different membranes (1.2 μμ and 0.2 μm pore size). The initial solution and its filtrates were studied with TRLFS (determination of europium species), DLS (confirmation of colloid-like particles) and ICP-MS (determination of europium content).

Synthesis and isolation of the Eu(III)-borate solid

A solution containing $[B]_{total}$ = 0.7 m was prepared at pH_c 6 and variable ionic strength (I_m = 0.1, 1 and 3 m, $NaClO_4$ or NaCl) as described for the solutions prepared for the $B(OH)_3$-polyborate speciation studies. Then, $EuCl_3 \cdot 6H_2O$ (solid) was added to adjust 0.01 m total Eu(III) concentration. The pH_c had to be re-adjusted after the Eu(III) addition. A white solid precipitated rapidly. The solid was stored in its solution for three weeks and then separated from the liquid phase by centrifugation. The solid was washed several times with deionized water, and then dried by lyophilization.

The Eu(III)-borate solid was studied with XRD, IR spectroscopy, solid-state ^{11}B NMR spectroscopy and solid-state site-selective TRLFS.

3.3.5 Studies on Eu(III)-organoborate interaction

Formation of organoborates

Solutions with varying $[B]_{total}$ and total salicylate/lactate content were prepared at pH 5 and I = 0.1 M ($NaClO_4$) under ambient conditions and equilibrated for one day. $[B]_{total}$ was in large excess so the 1:1 organoborate compound is formed exclusively. Then, ^{11}B NMR measurements of the solutions were carried out. The organoborate formation studies in dependency on ionic strength were carried out with solutions containing 0.01 m salicylate, $[B]_{total}$ = 0.2 m at pH_c 5 and variable ionic strength up to 3 m (NaCl). The organoborate

formation constants K_{BL} were calculated from the ^{11}B NMR data by means of the software HySS (version 4.0.31) [HYSS2009]. The equilibrium reactions Eq. 3.11 to Eq. 3.13 (see chapter 3.5.1) were considered for the analysis procedure. The formation constant K_{BL} was iteratively determined by varying the K_{BL} value until the calculated free boric acid and organoborate concentrations were equal to those determined by ^{11}B NMR spectroscopy (integration of the concentration proportional ^{11}B signal areas).

Eu(III)-salicylate complexation studies

Solutions with variable total salicylate concentration were prepared at pH 5.5 and I = 0.1 M ($NaClO_4$) under ambient conditions. A total Eu(III) concentration of $3 \cdot 10^{-5}$ M was adjusted with a 0.03 M Eu(III) stock solution. The samples were titrated from pH 5.5 down to around pH 2 by adding $HClO_4$. After each titration step a stationary europium luminescence spectrum was recorded. The data sets were analyzed with the software HypSpec (version 1.1.18) [HYP2008b] to determine the complexation constant of the 1:1 Eu(III)-salicylate complex and its single spectrum.

Eu(III)-organoborate complexation studies

For the TRLFS studies solutions with variable total salicylate or lactate concentration and $[B]_{total}$ were prepared at around pH 5 and I = 0.1 M ($NaClO_4$) under ambient conditions. $[B]_{total}$ was adjusted up to 0.4 M to provide high-level conversion of the organic compound into the respective organoborate. One day after the solution preparation, 2 mL of a solution with adjusted total organic content and $[B]_{total}$ were transferred into a quartz cuvette. A total Eu(III) concentration of $3 \cdot 10^{-5}$ M was adjusted with the 0.03 M Eu(III) stock solution. The samples were titrated from around pH 5 down to around pH 2 by adding $HClO_4$. After each titration step a stationary and, in some cases, also a time-resolved europium luminescence spectrum was recorded. The stationary TRLFS data from the pH titration series were analyzed with HypSpec (version 1.1.18) [HYP2008b] to determine the complexation constants of the EuBL complexes.

The time-resolved luminescence spectra of the Eu(III)-salicylate- or lactate-$B(OH)_3$ system were analyzed with PARAFAC (carried out by Björn Drobot, Helmholtz-Zentrum Dresden-Rossendorf, Institute of Resource Ecology, using the N-way toolbox for Matlab [AND2000]). The applied settings for the analysis are described in Drobot et al. [DRO2015]. From PARAFAC the luminescence lifetimes of pure Eu(III) species, individual luminescence spectra and Eu(III) species distributions were obtained. The Eu(III) species distributions serve as

basis to calculate the complexation constant for the Eu(III)-organoborate complexes. The complexation constant was determined by an iterative procedure using the program HySS (version 4.0.31) [HYSS2009]. The equilibrium reactions Eq. 3.11 to Eq. 3.16 (see chapter 3.5.1 and 3.5.2) were considered for the analysis procedure. The complexation constant was determined iteratively until the calculated concentrations of the Eu(III) species in the respective system were equal to those determined by PARAFAC.

For the ^{11}B NMR measurements solutions with constant total organic content (0.005 M or 0.01 M salicylate, 0.005 M lactate) and $[B]_{total}$ (0.2 M) were prepared at pH 5 under ambient conditions at I = 0.1 M ($NaClO_4$). One day after $EuCl_3 \cdot 6H_2O$ was added to adjust a total Eu(III) concentration up to 0.05 M. This ^{11}B NMR investigation series was extended with solutions of 0.01 m salicylate, $[B]_{total}$ = 0.2 m, variable total Eu(III) concentration up to 0.05 m, at pH_c 5 and up to I_m = 3 m (NaCl). The complexation constant of the Eu(III)-organoborate complex was calculated from ^{11}B NMR spectroscopic data by analyzing the Eu(III) concentration dependent chemical shift of the organoborate. A detailed description of this procedure is given in Schott et al. [SCHO2015]. Knowing the information of the fractions of free and Eu(III) bound organoborate the complexation constant was determined by an iterative procedure using the speciation program HySS (version 4.0.31) [HYS2009]. The complexation constant of the Eu(III)-organoborate in the speciation model was varied until the calculated free and Eu(III) bound organoborate concentrations are equal to those determined by ^{11}B NMR spectroscopy.

3.3.6 ^{11}B nuclear magnetic resonance spectroscopy (^{11}B NMR)

^{11}B NMR spectra of boron containing solutions were recorded on a Varian Unity Inova 400 spectrometer and an Agilent DD2-600 MHz NMR system with a field strength of 9.4 T (corresponding ^{11}B resonance frequency: 128.4 MHz) and 14.1 T (corresponding ^{11}B resonance frequency: 192.4 MHz), respectively. A 5 mm broadband probe was used. The ^{11}B chemical shifts (δ) are referenced externally with respect to BF_3 etherate in $CDCl_3$. A 5 mm NMR tube (quartz), containing the aqueous solution and a D_2O filled coaxial insert for deuterium lock, were used. As the investigations were performed in H_2O the ^{1}H water signal was suppressed. In presence of Eu(III) the observed ^{11}B chemical shift was corrected by subtraction of the bulk susceptibility contribution term ($\Delta\delta_{susc}$) [SCHO2015]. The NMR measurements were carried out in cooperation with Jérôme Kretzschmar (Helmholtz-Zentrum Dresden-Rossendorf, Institute of Resource Ecology).

Solid-state ^{11}B NMR experiments were carried out on a Bruker Ascend 800 spectrometer, operating at 17.6 T (corresponding ^{11}B resonance frequency: 256.8 MHz). A CP/MAS TriGamma probe and a 2.5 mm ZrO_2 rotor were used. The sample was rotated at a spinning frequency of 16 kHz. The solid-state NMR measurements were carried out in cooperation with Prof. Dr. Eike Brunner and Dr. Silvia Paasch at the Technische Universität Dresden, Institute of Bioanalytical Chemistry.

The NMR spectra were qualitatively and quantitatively analyzed (peak search and integration) with the computer program MestReNova (Version 6.0.2) [MES2009] by Jérôme Kretzschmar (Helmholtz-Zentrum Dresden-Rossendorf, Institute of Resource Ecology).

3.3.7 Time-resolved laser-induced fluorescence spectroscopy (TRLFS)

All measurements were carried out using a time gated detection mode to resolve the temporal characteristics of the europium luminescence.

Measurements of the europium containing solutions or suspensions were carried out with a Nd:YAG-OPO laser system (Continuum). Europium luminescence spectra of the stirred solutions/suspensions were recorded with a constant excitation wavelength of 394 nm, a time window of 1 ms, pulse energy of 2-3 mJ and an optical multichannel analyzer (monochromator and spectrograph MS 257 and iCCD camera Andor iStar, all LOT-Oriel). Recording conditions for stationary spectra: wavelength range 565 nm to 650 nm, 1200 line mm^{-1} grating, 0.2 nm resolution, 3000 accumulations. Recording conditions for time-resolved spectra: wavelength range 440 nm to 780 nm, 300 line mm^{-1} grating, 0.7 nm resolution, 100 accumulations, delay time steps 15 µs to 90 µs.

The solid-state TRLFS measurements at room temperature (22 °C) were performed using a Nd:YAG-OPO laser system (Nd:YAG: Quanta Ray, Spectra Physics; OPO: Flexi Scan, GWU-Lasertechnik). A Eu(III)-borate solid sample was placed into a self-made sample holder. The europium luminescence was detected with a spectrograph (MS 257, LOT-Oriel) equipped with an iCCD camera (iStar DH720, Andor Technology).

For the solid-state TRLFS measurements at low temperature (T < 5 K) a Eu(III)-borate solid sample was placed in a copper sample holder on top of a cooling head. The low temperature was generated using a closed cycle helium cryostate (Helium compressor unit CKW-21, Sumitomi Heavy Industries Ltd.; Turbolab 80, Oerlikon Leybod Vacuum; Model 331 Temperature Controller, Lakeshore). As excitation source a dye laser (Cobra Stretch, Sirah Laser- und Plasmatechnik) and as laser dye Pyrromethen 597 (Sirah Laser- und

Plasamatechnik) were used. The laser dye was excited by the second harmonic output of a Nd:YAG laser (Quanta Ray, Spectra Physics). The excitation light was guided through an optical fiber to the Eu(III) sample. The emitted luminescence light was transferred through the same optical fiber to a spectrograph (Shamrock SR-303i, Andor Technology) equipped with an iCCD camera (iStar DH 720, Andor Technology).

The solid-state TRLFS measurements were carried out at the University of Potsdam, Institute of Chemistry (Physical Chemistry), in cooperation with Prof. Dr. Michael U. Kumke and Dr. Sascha Eidner.

TRLFS data analysis

Different luminescence transition bands characterize the europium luminescence spectrum. In particular the $^5D_0 \rightarrow {}^7F_0$ (at around 578 nm; forbidden for the Eu(III) aquo ion), $^5D_0 \rightarrow {}^7F_1$ (at around 592 nm) and $^5D_0 \rightarrow {}^7F_2$ (at around 616 nm) transition bands are analyzed. TRLFS spectra were analyzed with the software Origin™ (version 7.5G, OriginLab Corporation). Stationary and time-resolved raw spectra were baseline corrected. Stationary luminescence spectra were normalized to the $^5D_0 \rightarrow {}^7F_1$ transition band, because the luminescence intensity of this transition is independent from the chemical environment of Eu(III) [BÜN1989]. Furthermore, the F_1/F_2 ratio can be calculated.

The luminescence lifetimes were determined according to the exponential decay equation, Eq. 3.6:

$$I(t) = \sum_{i=1}^{n} I_{0,i} \cdot e^{-t/\tau_i} \qquad 3.6$$

I(t)...total luminescence intensity at time t
$I_{0,i}$...starting intensity of the species i at time t = 0
τ_i...lifetime of the species i

Depending on the characteristic of the luminescence decay, monoexponential or biexponential decay equations were used to fit the luminescence decay curves.

A correlation between the luminescence lifetime and the amount of water molecules n_{H_2O} in the first hydration shell of Eu(III) was observed [HOR1979]. A respective empirical equation was derived, Eq. 3.7:

$$n_{H_2O} \pm 0.5 = 1.07 \cdot \tau_{H_2O}^{-1}(ms) - 0.62 \qquad 3.7$$

Hence, from n_{H_2O}, i.e., hydration state of Eu(III), further information about the chemical environment of europium are deducible, e.g., connection to the complexing ligand/surfaces (sorption) or incorporation into a solid phase. Applying Eq. 3.7, the luminescence lifetime of

the Eu(III)aquo ion (around 110 µs) corresponds to 9 water molecules in the first hydration shell of Eu(III).

Series of time-resolved europium luminescence spectra and excitation spectra were analyzed with PARAFAC. The PARAFAC was carried out by Björn Drobot (Helmholtz-Zentrum Dresden-Rossendorf, Institute of Resource Ecology) using the N-way toolbox for Matlab [AND2000]. The applied settings for the analysis are described in Drobot et al. [DRO2015].

3.3.8 Miscellaneous methods

Infrared spectroscopy (IR)

FT-IR spectra were recorded on a Bruker Vertex 70v Fourier transform infrared spectrometer in the range 7500 cm^{-1}- 370 cm^{-1} with a resolution of 4 cm^{-1}. The samples were prepared as KBr pellets. The IR measurements were carried out by Karsten Heim (Helmholtz-Zentrum Dresden-Rossendorf, Institute of Resource Ecology).

Powder X-ray diffraction (powder XRD)

The experiments (under proposal I-20130337) were performed at the PETRA III synchrotron radiation source at DESY Hamburg, Germany (High Resolution Powder Diffraction, P02.1) [STR2014]. Synchrotron radiation with an energy of 60 keV (corresponding to λ = 0.207 Å) was used. Diffraction patterns were collected in Debye-Scherrer-geometry with a PerkinElmer XRD 1621 area detector. The diffraction patterns were processed with the software FIT2D [HAM1996] employing a CeO_2 standard for calibration. The measurement and spectrum analysis were initiated and carried out by Dr. Christoph Hennig (Helmholtz-Zentrum Dresden-Rossendorf, Institute of Resource Ecology) and Dr. Sabrina Labs (Forschungszentrum Jülich, Insitute of Energy and Climate Research (IEK-6), Nuclear Waste Management).

Scanning electron microscopy (SEM)

The sample was prepared on a membrane filter (50 nm pore size) by filtrating a Eu(III)-borate solid suspension ($[B]_{total}$ = 0.7 m, $[Eu]_{total}$ = $3 \cdot 10^{-5}$ m, pH_c 6, I_m = 0.1 m ($NaClO_4$)). The sample preparation was carried out by Stephan Weiss (Helmholtz-Zentrum Dresden-Rossendorf, Institute of Resource Ecology). Scanning electron microscopy was carried out with a Hitachi S-4800 operating at an accelerating voltage of 0.5 kV and a magnification of

50000. The SEM measurements were performed by Elfi Christalle (Helmholtz-Zentrum Dresden-Rossendorf, Institute of Ion Beam Physics and Material Research).

Dynamic Light Scattering (DLS)

The scattered light intensity of Eu(III)-borate solid suspensions and its filtrates ($[B]_{total}$ = 0.2 m to 0.7 m, $[Eu]_{total} = 3 \cdot 10^{-5}$ m, pH_c 6) was detected with a photon correlation spectrometer (Brookhaven Instruments) equipped with a laser source (argon ion laser from LEXEL Laser) or with the Zetasizer Nano ZS (Malvern Instruments). The latter device was used to determine particle size distributions. The DLS investigations were supervised by Stephan Weiss (Helmholtz-Zentrum Dresden-Rossendorf, Institute of Resource Ecology).

Inductively Coupled Plasma Mass Spectrometry (ICP-MS)

The determination of the europium and boron content in a sample were performed with ICP-MS (Elan 9000, Perkin Elmer). The measurements were carried out by the analytic department at the Institute of Resource Ecology, Helmholtz-Zentrum Dresden-Rossendorf.

Miscellaneous

The determined values of equilibrium constants were extrapolated to infinite dilution, following the extended Debye-Hückel approach as published by Davies [DAV1962] or SIT. The specified uncertainties given in this chapter 3 correspond to 2σ, i.e., 95% confidence level.

Acknowledgment

The authors would like thank all colleagues as mentioned by name in this experimental section for their contribution and support.

3.4 Interaction of Eu(III), Am(III) and Cm(III) with polyborate

3.4.1 ^{11}B NMR spectroscopy of polyborate containing solutions

NaCl and $NaClO_4$ medium

The aqueous $B(OH)_3$-(poly)borate speciation is an essential prerequisite to interpret the observed complexation and solid formation when Eu(III) is present in the $B(OH)_3$-polyborate system. ^{11}B NMR is well applicable to identify (poly)borate species in aqueous solution. The assignment of ^{11}B NMR signals to respective polyborate species is taken from literature [JAN1979b, SAL1983, HER2011]. The polyborate speciation studies at pH_c 5 and pH_c 6, at low ionic strength ([NaCl/$NaClO_4$] = const. = 0.1 m, $I_m \approx 0.1$ m[1]) were complemented with studies at higher ionic strengths up to I_m = 3 m (NaCl/$NaClO_4$).

At pH_c 5 and up to $[B]_{total}$ = 0.5 m, I_m = 0.1 m (NaCl/$NaClO_4$), no polyborate species were detected by ^{11}B NMR (Fig. 3.4a). The only boron species found was the undissociated boric acid at δ = 19.4 ppm. Above $[B]_{total}$ = 0.5 m a small ^{11}B NMR signal at 1.2 ppm, displaying a further boron species, occurs. At pH_c 6 and $[B]_{total}$ > 0.4 m, I_m = 0.1 m (NaCl/$NaClO_4$), three boron species at δ = 19.4 ppm, 13.3 ppm and 1.2 ppm can be observed (Fig. 3.4b).

The signals at δ = 19.4 ppm, 13.3 ppm and 1.2 ppm are assigned to boric acid $B(OH)_3$, the triborate I species $B_3O_3(OH)_4^-$ and the pentaborate species $B_5O_6(OH)_4^-$, respectively. With increasing $[B]_{total}$ the amount of the polyborate species increases.

A sample with $[B]_{total}$ = 0.7 m (pH_c 6, I_m = 0.1 m ($NaClO_4$)) aged for six months showed no differences in the ^{11}B NMR spectrum compared to a freshly prepared one (Fig. 3.4b). Thus, the $B(OH)_3$-(poly)borate speciation remains stable.

The polyborate speciation (determined at pH_c 6) is not significantly influenced by ionic strength in NaCl/$NaClO_4$ medium. This ionic strength independency is in accordance with literature [ING1962, MES1972]. At pH_c 6 and $[B]_{total}$ = 0.7 m around 2 % of the total boron speciation are represented by the polyborate species. This is in good agreement with the calculated polyborate amount of ~ 3.5 % under the same conditions. Thus, the formation constants of polyborates from literature [ING1962, 1963] will be applied in Eu(III) complexation studies for ionic strength up to I_m = 3 m.

[1] maximum ionic strength, if $[B]_{total}$ = 0.7 m: $I_m = 0.5 \cdot ([Na^+] \cdot 1^2 + [Cl^-/ClO_4^-] \cdot (-1)^2 + [Na^+] \cdot 1^2 + [B(OR)_4^-] \cdot (-1)^2) = 0.5 \cdot (0.1\text{ m} + 0.1\text{ m} + 0.025\text{ m} + 0.025\text{ m}) = 0.125\text{ m} = I_{m,max}$

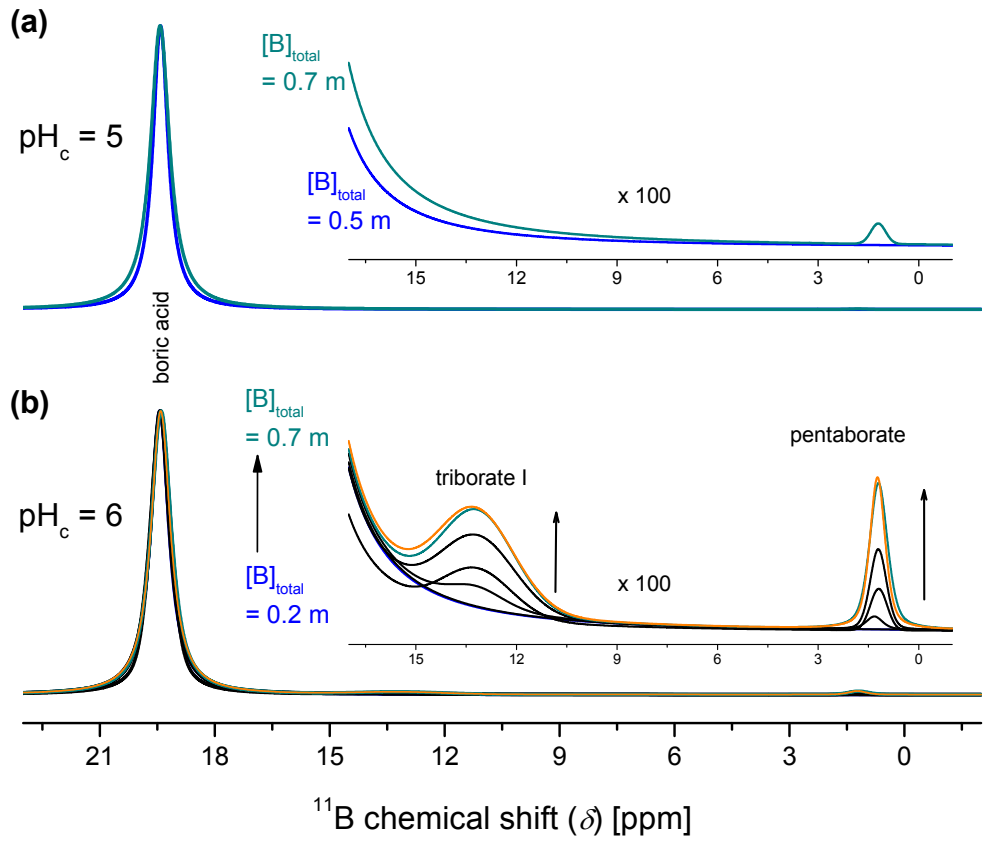

Fig. 3.4: *^{11}B NMR spectra (normalized) of solutions containing variable amounts of $[B]_{total}$ (0.2 m to 0.7 m, step size 0.1 m) at (a) pH_c 5 and (b) pH_c 6; in each case I_m = 0.1 m ($NaClO_4$), (orange curve spectrum after six months). The insets show expansion of the polyborate region.*

$CaCl_2$ and $MgCl_2$ medium

Obviously, divalent earth alkaline metal ions influence the polyborate speciation. From ^{11}B NMR studies of polyborate containing solutions in $CaCl_2$ medium an interaction of Ca^{2+} with polyborate species is observed, Fig. 3.5. For the same studies in $MgCl_2$ medium this conclusion is not unambiguously, but the comparable complexation constants[2] for $CaB(OH)_4^+$ and $MgB(OH)_4^+$ allow the assumption that also Mg^{2+} interacts with (poly)borates. Hence, the polyborate speciation in solution is significantly changed in comparison to that in NaCl/$NaClO_4$ medium.

[2] log $\beta(CaB(OH)_4^+, I < 0.16$ M) = 1.80 [REA1976], log $\beta(MgB(OH)_4^+, I < 0.16$ M) = 1.63 [REA1976],

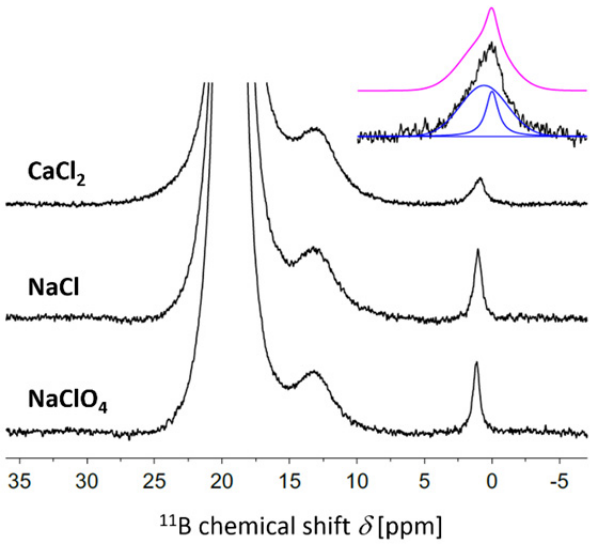

Fig. 3.5: *^{11}B NMR spectra of a polyborate containing solution in $CaCl_2$ medium, and for comparison in NaCl and $NaClO_4$ medium, solution: $[B]_{total}$ = 0.7 m, pH_c 6, I_m = 3 m*

KCl medium

Polyborate speciation studies at higher ionic strength conditions adjusted with KCl at pH_c 6 were not realizable. A solid (presumably a potassium containing (poly)borate phase) precipitated already at moderate KCl concentrations (> 0.5 m).

3.4.2 Complex formation of Eu(III) with (poly)borates

The complex formation in the Eu(III)-$B(OH)_3$-polyborate system was studied with time-resolved laser-induced fluorescence spectroscopy (TRLFS). This method allows the detection of Eu(III) species with high sensitivity at low metal concentrations ($\approx 10^{-5}$ M).

NaCl and $NaClO_4$ medium up to I_m = 0.1 m

Up to $[B]_{total}$ = 0.7 m, and at I_m = 0.1 m, pH_c = 5 or pH_c = 6, stationary and time-resolved luminescence spectra of Eu(III) were measured. With increasing $[B]_{total}$ the europium luminescence spectra and lifetimes change. The intensities of the $^5D_0 \rightarrow {}^7F_0$ and $^5D_0 \rightarrow {}^7F_2$ luminescence bands increase (Fig. 3.6a) indicating a Eu(III) complexation. This intensity increase with rising $[B]_{total}$ is less pronounced at pH_c 5 (Fig. 3.6 b). At pH_c 6, I_m = 0.1 m, and $[B]_{total}$ = 0.7 m (highest investigated total boron concentration, solubility limit of $B(OH)_3$) the luminescence lifetime of europium rises up to 149-150 µs, which corresponds to a removal of 2-3 water molecules from the first hydration shell of europium.

These findings clearly show a Eu(III) complexation by the present polyborate species. At pH_c 6 and up to $[B]_{total} \approx 0.1$ m, where no or almost none polyborates and exclusively $B(OH)_3$ exist, no changes in the Eu(III) luminescence spectra (Fig. 3.6b) compared to those of the Eu(III) aquo ion occur. Hence, boric acid forms no complexes with Eu(III). At higher $[B]_{total}$ polyborates occur and concurrently changes in the Eu(III) luminescence spectra (Fig. 3.6b) are observed. Obviously, there is an interaction between Eu(III) and polyborates, and the Eu(III) speciation then includes respective Eu(III)-(poly)borate species.

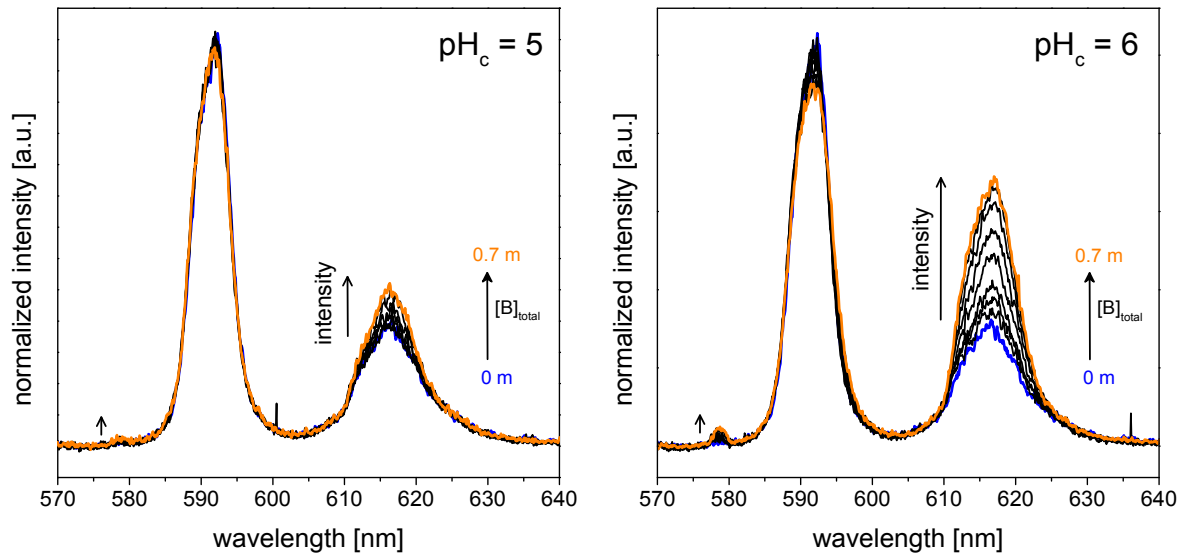

Fig. 3.6: Europium luminescence spectra left at pH_c = 5 and right at pH_c = 6 as a function of $[B]_{total}$ (step size 0.1 m), $3 \cdot 10^{-5}$ m Eu(III), I_m = 0.1 m ($NaClO_4$)

Additionally, the influence of polyborates on the Eu(III) speciation was investigated for different $[B]_{total}$ as a function of pH. For illustration the F_1/F_2 ratio (area ratio of the $^5D_0 \rightarrow {}^7F_1$ and $^5D_0 \rightarrow {}^7F_2$ luminescence bands) is plotted against pH (Fig. 3.7). Coming from the acidic pH range the effect of polyborates on the Eu(III) speciation starts at pH_c 4.0 to 4.5. Below $pH_c \approx$ 4.0 to 4.5, the polyborate concentration is too low to influence the europium speciation. This is in good agreement with the calculated $B(OH)_3$-polyborate speciation (see Fig. 3.2).

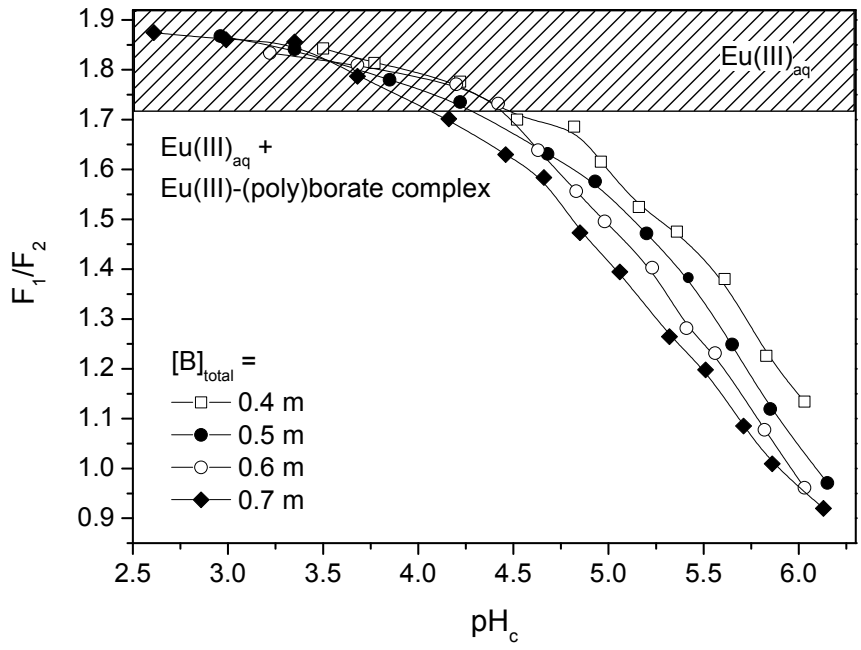

Fig. 3.7: F_1/F_2 as a function of pH_c, pH titration of solutions containing $3 \cdot 10^{-5}$ m Eu(III) and $[B]_{total}$ = constant, I_m = 0.1 m ($NaClO_4$)

The data sets of the series with variable $[B]_{total}$ (pH_c = constant) and pH titration series ($[B]_{total}$ = constant) were used to determine a complexation constant, at least its order of magnitude, of the Eu(III)-(poly)borate species. This, however, proved to be difficult, because all polyborate equilibria (also those beyond pH_c 6) intertwine and several polyborates coexist. The mathematical deconvolution and separation of single Eu(III)-polyborate complexes were not possible.

The polyborates existing up to pH_c 6, i.e., triborate $B_3O_3(OH)_4^-$ and pentaborate $B_5O_6(OH)_4^-$, are summarized to one model borate species "$B(OR)_4^-$" (see chapter 3.2). Its concentration is the sum of the concentrations of all the (poly)borate species under the respective conditions. Depending on pH and $[B]_{total}$ this sum was calculated from the speciation data of Ingri et al. [ING1962, ING1963]. This approach is warrantable, because DFT calculations confirm a comparable behavior of various borate species regarding the Eu(III) complexation [SCHO2015]. Furthermore, the PARAFAC of the europium TRLFS data as a function of $[B]_{total}$ showed that until $[B]_{total}$ = 0.7 m only the Eu(III) aquo ion and one europium complex exist. This means: (1) The model borate species "$B(OR)_4^-$" as sum of several polyborate species is verified, and (2) only the formation of the 1:1 Eu(III)-borate complex, $EuB(OR)_4^{2+}$ (borate ligand with one binding site), has to be considered, Eq. 3.8

$$Eu^3 + B(OR)_4^- \leftrightarrow EuB(OR)_4^{2+} \qquad 3.8$$

According to Eq. 3.8, the complexation constant β_1 for the $EuB(OR)_4^{2+}$ complex is expressed in Eq. 3.9

$$\beta_1 = \frac{[\mathrm{EuB(OR)_4^{2+}}]}{[\mathrm{Eu^{3+}}][\mathrm{B(OR)_4^-}]} \qquad 3.9$$

The analysis of the spectroscopic data yielded the average complex formation constants for the Eu(III)-borate complex, $EuB(OR)_4^{2+}$, at I_m = 0.1 m (NaCl/$NaClO_4$), Tab. 3.1

Tab. 3.1: *Average log β_1 (I_m = 0.1 m ($NaClO_4$/NaCl)) and corresponding log β_1^0 (extrapolation to infinite dilution according to Davies approach [DAV1962]) of the Eu(III)-borate complex, $EuB(OR)_4^{2+}$ (borate ligand with one binding site). T = 22 °C, uncertainty: 2σ [SCHO2015/2016]*

$\log \beta_1$	$\log \beta_1^0$	
2.02 ± 0.30	2.66 ± 0.30	from pH titration data sets
2.58 ± 0.05	3.22 ± 0.05	from data sets with variable $[B]_{total}$

Single values for log β_1 from different data sets are given in [SCHO2015/2016].

From the pH titration data sets an averaged value of log β_1^0 = 2.66 ± 0.30 (2σ) and from the data sets with variable $[B]_{total}$ an averaged value of log β_1^0 = 3.22 ± 0.05 (2σ) were determined. Both values differ slightly. It might be assumed, that kinetic effects on the polyborate formation (pH titration series carried out with acid) play a role. However, to illustrate the order of magnitude of the Eu(III)-borate complexation constant these values are combined to yield log β_1^0 = 2.7 to 3.2. It demonstrates that this complex is quite weak. The Eu(III)-(poly)borate complexation constant of this work seems to be reliable for different reasons:

(1) The used TRLFS is a species sensitive method (in comparison to solubility experiments) that allows to observe the Eu(III)-(poly)borate species directly even in the presence of only small amounts of complexing (poly)borates in the investigated pH region.

(2) The order of magnitude of the Eu(III)-borate complexation constant fits well in a relationship to estimate metal-borate complexation constants according to Bousher [BOU1995], Fig. 3.8.

(3) The complexation studies were carried out under less difficult conditions (avoiding of the strong Eu(III) hydrolysis, simplification of the polyborate speciation).

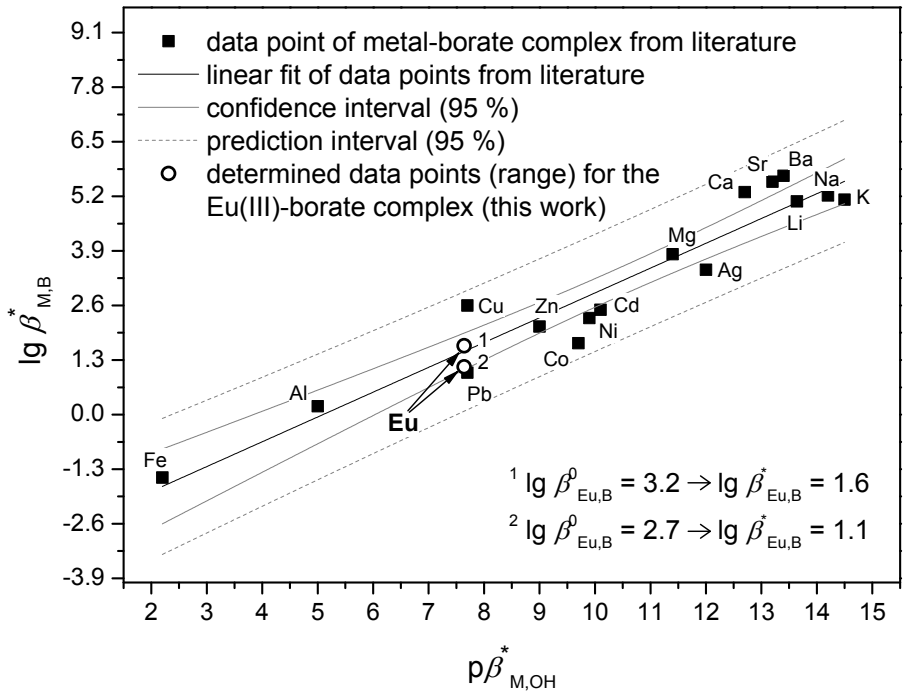

Fig. 3.8: Linear relationship (according to Bousher [BOU1995]) between complexation constants of metal-borate complexes and first metal hydrolysis constants. The determined data points for Eu(III) (this work) integrate well into this relationship

Speciation distributions for the Eu(III)-(poly)borate system were calculated as a function of pH and $[B]_{total}$, Fig. 3.9. With increasing $[B]_{total}$ the Eu(III)-(poly)borate complexation expands into the acidic pH range and into the moderate alkaline pH range supressing the Eu(III) hydrolysis (primarily the first hydrolysis step).

Remark: Although, there are some similarities between the borate and silicate system (e.g., comparable pK_a of boric acid and silicic acid, formation of "poly" species) the Eu(III) complexation with these ligands is not similar and the complex formation with silicate is five to six orders of magnitude more stable (log β_1^0 ($EuSiO(OH)_3^{2+}$) = 8.6[3] [THA2007]) than with borate.

[3] data available for I = 0.2 M $NaClO_4$, extrapolation to infinite dilution with Davies approach [DAV1962]

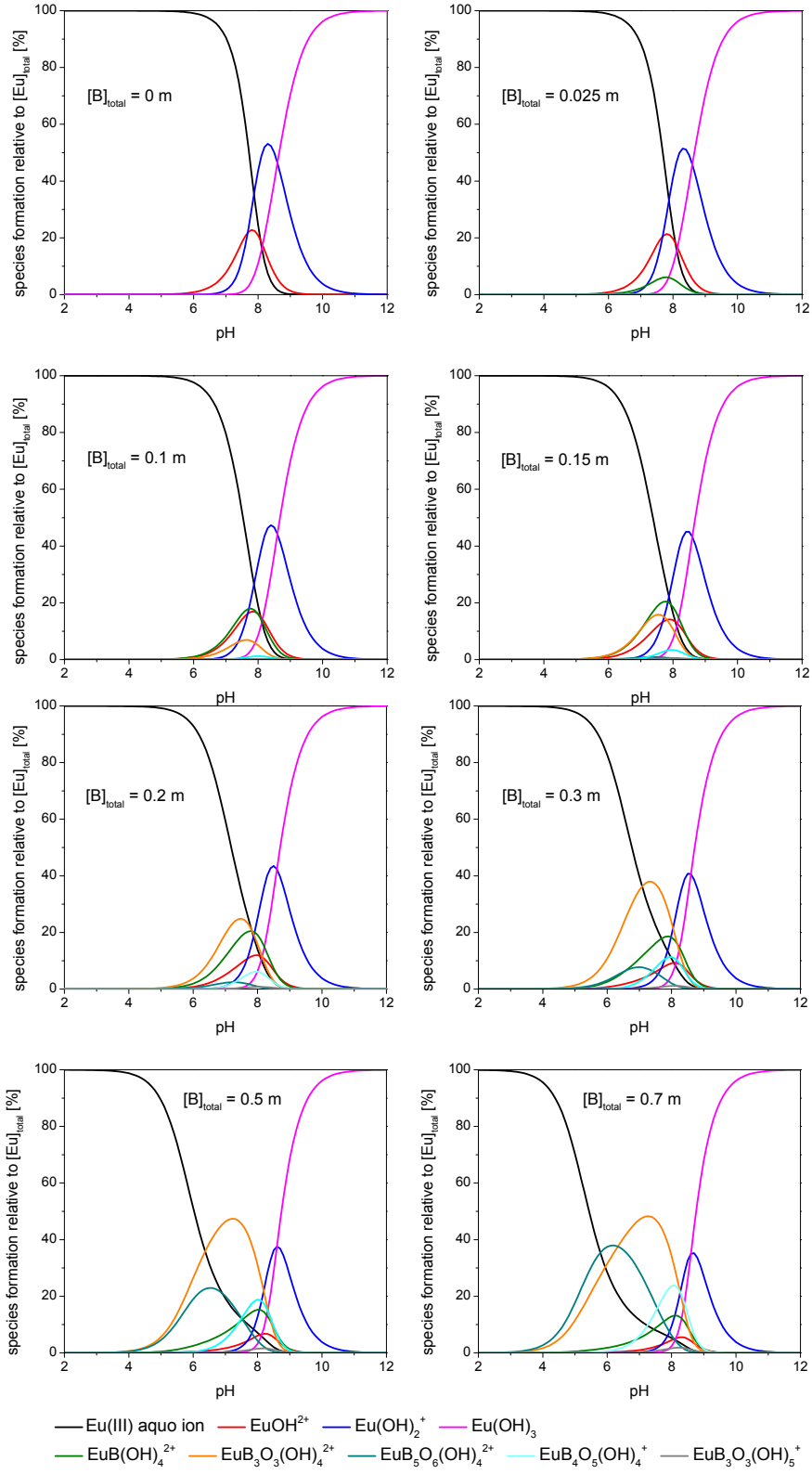

Fig. 3.9: *Eu(III)-(poly)borate speciation as a function of $[B]_{total}$ and pH (carbonate-free system), $[Eu(III)]_{total} = 3 \cdot 10^{-5}$ M, $I_m = 0.1$ m ($NaClO_4$). Application of log β_1 ($EuB(OR)_4^-$) = 2.0 (primarily valid for Eu(III) complexes with borate ligands having one binding site) for all the Eu(III)-(poly)borate complexes, although there are Eu(III) complexes with borate ligands having two binding sites*

NaCl and $NaClO_4$ medium up to I_m = 3 m

The complexation studies in the Eu(III)-(poly)borate system at higher ionic strengths were carried out at constant pH_c 6 and variable $[B]_{total}$. A Eu(III) complexation by polyborates is observed for all ionic strengths up to I_m = 3 m ($NaClO_4$/NaCl). An increase of the F_1/F_2 ratio (Fig. 3.10) and, thus, a decrease of complexation were observed for samples of same composition, but varying ionic strength ($NaClO_4$/NaCl).

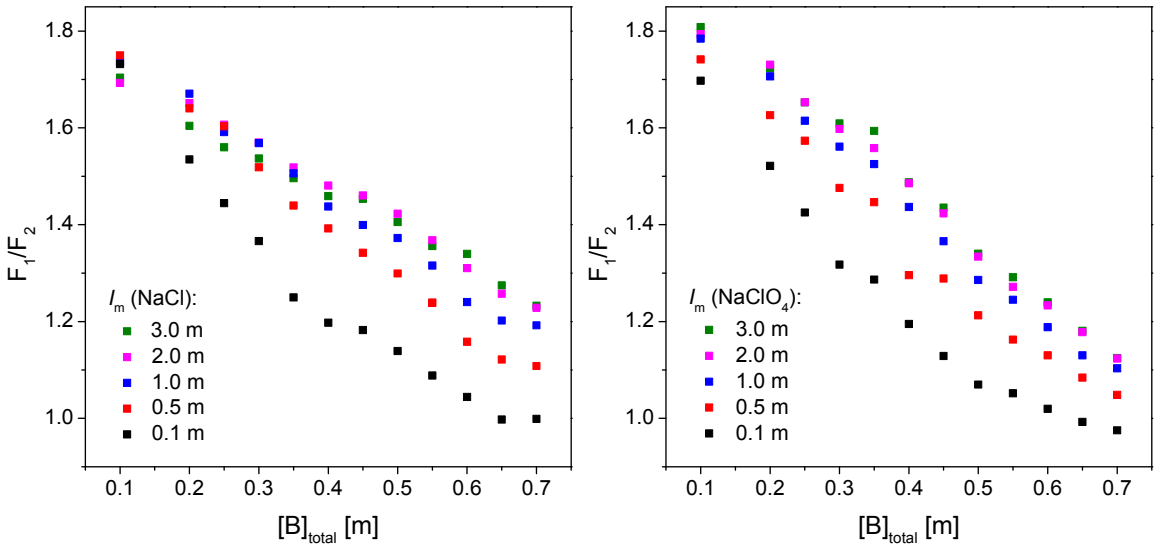

Fig. 3.10: F_1/F_2 ratio as a function of $[B]_{total}$ and ionic strength, left: NaCl medium, right: $NaClO_4$ medium

The analysis of the spectroscopic data yielded the complex formation constants for the Eu(III)-borate complex, $EuB(OR)_4^{2+}$, for different ionic strengths adjusted with $NaClO_4$ and NaCl (Tab. 3.2).

Tab. 3.2: Log β_1 values of the Eu(III)-borate complex, $EuB(OR)_4^{2+}$ (borate ligand with one binding site), as a function of ionic strength (in $NaClO_4$ or NaCl), $[Eu(III)]_{total} = 3 \cdot 10^{-5}$ m, $[B]_{total}$ variable, pH_c = 6, T = 22 °C; averaged uncertainty for log β_1 (estimated): 0.2 (2σ)

I_m [m] $NaClO_4$	log β_1 (series 1)	log β_1 (series 2)	log β_1 (series 3)	I_m [m] NaCl	log β_1 (series 1)	log β_1 (series 2)
0.1	2.56	2.60	2.40	0.1	2.54	2.38
0.5		2.31		0.5	2.20	
0.7	1.94	2.23		0.7	2.15	
1	2.02	2.14	2.08	1	2.15	2.01
2	2.06	2.14		2	2.06	
3	1.89	2.09	2.01	3	2.09	2.00

The analysis of the ionic strength dependency of the Eu(III)-(poly)borate complexation in the NaCl and $NaClO_4$ medium was carried out with SIT approach (cf. chapter 2.2, an example of

SIT plots is shown in Fig. 3.11). From $\Delta\varepsilon$ the individual ion interaction coefficients $\varepsilon(\mathrm{EuB(OR)_4^{2+}},\mathrm{Cl^-})$ and $\varepsilon(\mathrm{EuB(OR)_4^{2+}},\mathrm{ClO_4^-})$ were calculated (Eq. 3.10).

$$\Delta\varepsilon = \sum \varepsilon(\mathrm{EuB(OR)_4^{2+}},\mathrm{Cl^-/ClO_4^-}) - \sum \varepsilon(\mathrm{Eu^{3+}},\mathrm{Cl^-/ClO_4^-}) - \sum \varepsilon(\mathrm{Na^+},\mathrm{B(OR)_4^-}) \qquad 3.10$$

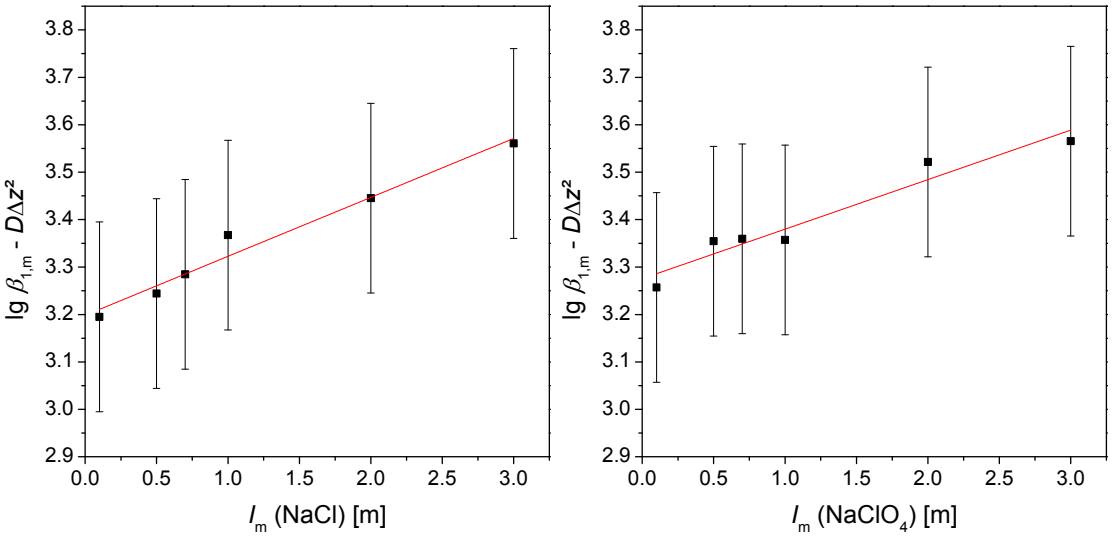

Fig. 3.11: SIT plots for the Eu(III)-(poly)borate-NaCl system (left) and Eu(III)-(poly)borate-$NaClO_4$ system (right), Error bars: 2σ from estimation

The data for $\log \beta_1^0$ and $\Delta\varepsilon$ derived from SIT plots for several series of the Eu(III)-(poly)borate-NaCl system and Eu(III)-(poly)borate-$NaClO_4$ system are summarized in Tab. 3.3 and Tab. 3.4, respectively.

Tab. 3.3: Summarized values for $\log \beta_1^0$, $\Delta\varepsilon$ and $\varepsilon(EuB(OR)_4^{2+}, Cl^-)$ for the Eu(III)-(poly)borate-NaCl system, uncertainty: 2σ

series	$\log \beta_1^0$	$\Delta\varepsilon$ [kg·mol^{-1}]	$\varepsilon(EuB(OR)_4^{2+}, Cl^-)$ [kg·mol^{-1}]
1	3.20	-0.12	0.04*
2	3.05	-0.15	0.01*
average	3.12 ± 0.21	-0.13 ± 0.04	0.025 ± 0.04

*calculated with values of $\varepsilon(Na^+, B(OH)_4^-)$ = -0.07 kg·mol^{-1}and $\varepsilon(Am^{3+}, Cl^-)$ = 0.23 kg·mol^{-1}, from [HUM2005]

Tab. 3.4: Summarized values for $\log \beta_1^0$, $\Delta\varepsilon$ and $\varepsilon(EuB(OR)_4^{2+}, ClO_4^-)$ for the Eu(III)-(poly)borate-$NaClO_4$- system, error: 2σ

series	$\log \beta_1^0$	$\Delta\varepsilon$ [kg·mol^{-1}]	$\varepsilon(EuB(OR)_4^{2+}, ClO_4^-)$ [kg·mol^{-1}]
1	3.14	-0.09	0.33*
2	3.28	-0.10	0.32*
3	3.09	-0.14	0.28*
average	3.17 ± 0.20	-0.11 ± 0.05	0.31 ± 0.05

*calculated with values of $\varepsilon(Na^+, B(OH)_4^-)$ = -0.07 kg·mol^{-1} and $\varepsilon(Am^{3+}, ClO_4^-)$ = 0.49 kg·mol^{-1}, from [HUM2005]

$CaCl_2$ and $MgCl_2$ medium

A Eu(III) complexation by polyborate species at pH_c 6 is observed in the $CaCl_2/MgCl_2$ medium. However, the decrease of the Eu(III)-(poly)borate complexation in the $CaCl_2/MgCl_2$ medium with increasing ionic strength is significantly stronger than in the $NaCl/NaClO_4$ medium, Fig. 3.12. This more pronounced decrease cannot be exclusively attributed to its ionic strength dependency, but rather to a competitive complexation of the polyborate species by Ca^{2+} and Mg^{2+} (see chapter 3.4.1). Due to this competition, the ionic strength dependency study of the Eu(III)-(poly)borate complexation in $CaCl_2/MgCl_2$ medium cannot be analyzed.

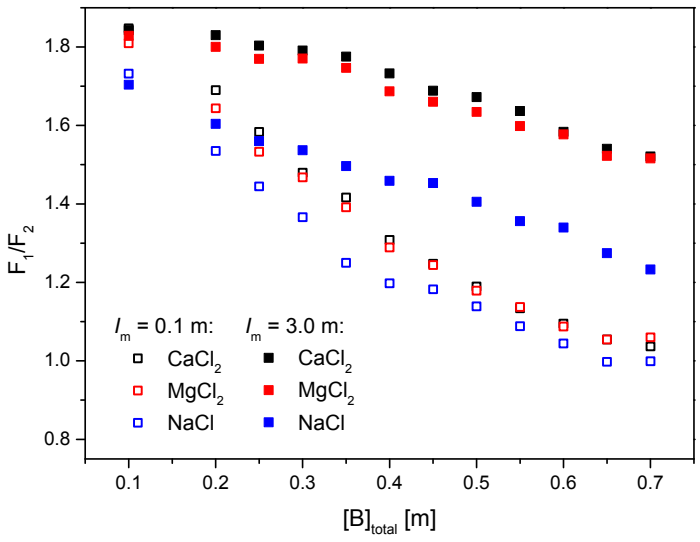

Fig. 3.12: F_1/F_2 ratio as a function of $[B]_{total}$ and ionic strength, pH_c 6, comparison of MCl_2 (M = Ca, Mg) with NaCl medium

KCl medium

Eu(III)-(poly)borate complexation studies at higher ionic strength conditions adjusted with KCl at pH_c 6 were not realizable. A solid (presumably a potassium containing (poly)borate phase) precipitated already at moderate KCl concentrations (> 0.5 m).

3.4.3 Formation and structural characterization of a solid Eu(III)-borate phase

Investigation of the formation of the Eu(III)-borate solid phase in NaCl and $NaClO_4$ medium

Some days after the preparation of sample solutions containing Eu(III) and (poly)borate at pH_c 6 ($[Eu]_{total} = 3 \cdot 10^{-5}$ m, up to $[B]_{total} = 0.7$ m), I_m = 0.1 m to 3 m ($NaClO_4$/NaCl), remarkable changes in europium luminescence spectra and lifetimes were observed. These changes firstly occur in the samples with the highest total boron concentration ($[B]_{total} = 0.7$ m), later also in samples with lower $[B]_{total}$. In these spectra the luminescence bands are characteristically split corresponding to the $^5D_0 \rightarrow {}^7F_1$ and $^5D_0 \rightarrow {}^7F_2$ transitions and the luminescence lifetimes distinctly increase (up to around 700 µs corresponding to 0-1 remaining water molecules in the first hydration shell of Eu(III)) in comparison to the luminescence spectra and lifetimes measured for the samples directly after their preparation, Fig. 3.13. These changes indicate the formation of another europium species. In contrast, in similarly prepared Eu(III) and (poly)borate containing samples at pH_c 5 no significant changes in the europium luminescence spectra and lifetimes were observed. The luminescence spectra and lifetimes remained constant throughout the investigation period (71 days) [SCHO2015/2016].

The Eu(III) and (poly)borate containing solutions which show the characteristically split europium luminescence spectra were membrane filtrated (pore size 0.2 µm). The ICP-MS analysis of the filtrates confirmed a removal of Eu(III) due to the filtration. No other known europium solids (hydroxides, carbonates) are thermodynamically stable under the used experimental conditions. Hence, a solid Eu(III)-borate phase is formed. The described Eu(III)-(poly)borate complex (cf. chapter 3.4.2) is supposed to be the precursor of this solid. A hypothesis for the structure of this solid Eu(III)-borate is shown in Fig. 3.14.

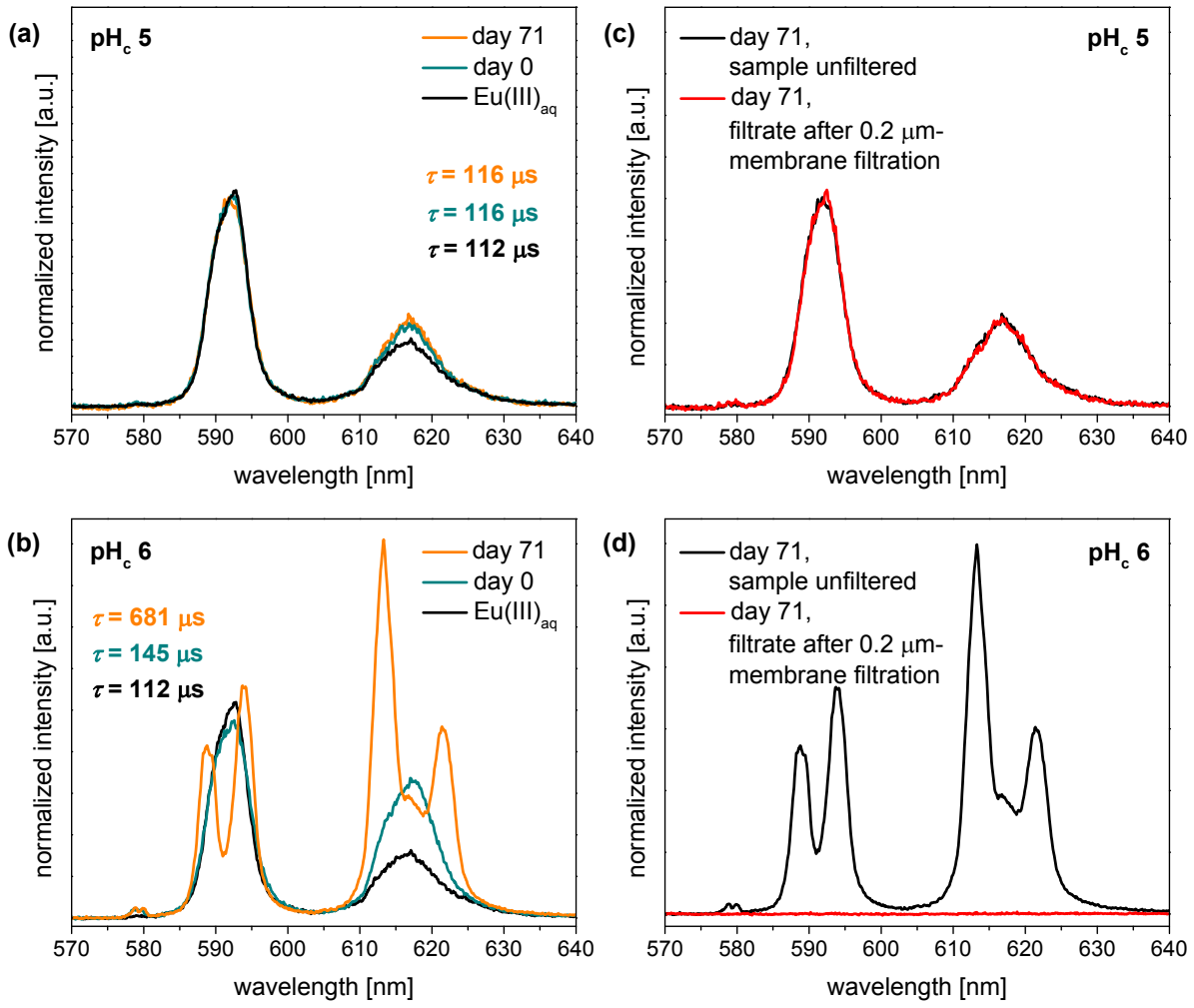

Fig. 3.13: *Left: development of Eu(III) luminescence spectra and lifetimes after different times at (a) pH_c = 5 and (b) pH_c = 6; right: Eu(III) luminescence spectra of unfiltered and filtered solutions at (c) pH_c = 5 and (d) pH_c = 6, filtration after 71 days; solution: $[B]_{total}$ = 0.6 m, $[Eu(III)]_{total} = 3 \cdot 10^{-5}$ m, I_m = 0.1 m ($NaClO_4$)*

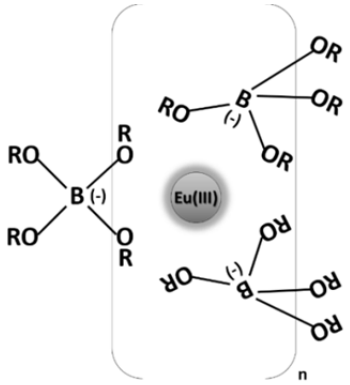

Fig. 3.14: *Possible Eu(III) environment in the Eu(III)-borate solid; R = H, other threefold coordinated boron centers, condensed borate structures*

The progress of the Eu(III)-borate solid formation was systematically investigated by TRLFS in Eu(III) and (poly)borate containing solutions ($[Eu]_{total} = 3 \cdot 10^{-5}$ m, $[B]_{total}$ = 0.2 m to 0.7 m) at pH_c 6 and different ionic strengths up to I_m = 3 m in $NaClO_4$ and NaCl medium.

With progressing precipitation the splitting of the luminescence bands increases and yields finally to a spectrum characteristic for the solid Eu(III)-borate at the end of the precipitation (Fig. 3.15, left). During the precipitation a biexponential europium luminescence decay curve was observed. The short luminescence lifetime (< 150 µs, depending on solution composition) is attributed to the dissolved Eu(III) species (Eu(III) aquo ion and Eu(III)-(poly)borate complex) and the long luminescence lifetime (> 600 µs) is attributed to the precipitated Eu(III)-borate, Fig. 3.15, right. After a certain time, depending on $[B]_{total}$, only the longer luminescence lifetime was found (Fig. 3.15, right). The solid Eu(III)-borate is stable over a long time, because its corresponding luminescence lifetime was reproduced even after 1.5 years (maximum observation time), independent from ionic strength and electrolyte ($NaClO_4$ or NaCl).

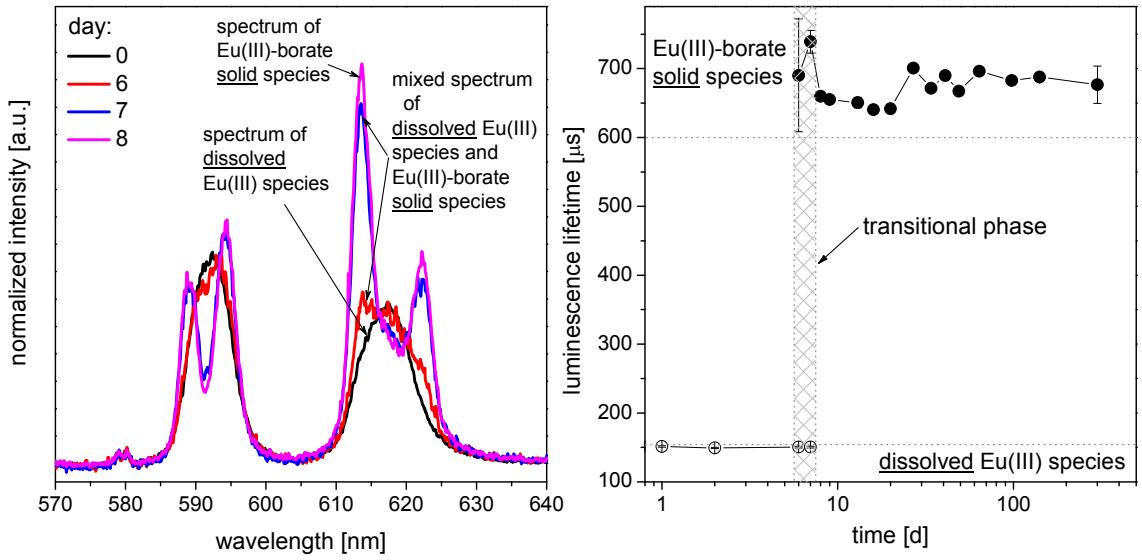

Fig. 3.15: Left: formation progress of the Eu(III)-borate solid species for a solution containing $[Eu(III)]_{total} = 3 \cdot 10^{-5}$ m, $[B]_{total} = 0.7$ m, $I_m = 0.1$ m ($NaClO_4$) at $pH_c = 6$, right: Eu(III) luminescence lifetime observed with observation time

Generally, for all investigated ionic strengths ($NaCl/NaClO_4$), except some outlier, it is found that the lower $[B]_{total}$ (smaller the polyborate concentration) the slower is the formation of the solid species (Tab. 3.5, Tab. 3.6). For instance, at $[B]_{total}$ = 0.7 m, I_m = 0.1 m ($NaClO_4$), the precipitation starts much earlier (between 2 to 6 days) than at $[B]_{total}$ = 0.4 m, I_m = 0.1 m ($NaClO_4$), (between 98 and 141 days). The precipitation was detected from $[B]_{total}$ = 0.3 m. This indicates that the concentration of the polyborates below this concentration and, hence, the amount of the Eu(III)-(poly)borate complex (the precursor of the solid) is too low to

induce the Eu(III)-borate precipitation, at least within the investigated time period of 1.5 years. This explanation also can be applied for solutions at pH_c 5 with variable $[B]_{total}$ up to 0.7 m ($NaClO_4$), where no precipitations were observed.

Table 3.5 and Table 3.6 summarizes the period for the first indication of the Eu(III)-borate precipitation in solution. Even though there are some outliers (precipitation early than expected) a tendency in the precipitation as function of ionic strength and electrolyte ($NaClO_4$ or NaCl) can be described. In the NaCl medium the Eu(III)-borate precipitation is delayed with increasing ionic strength. In comparison to that, precipitation in the $NaClO_4$ medium seems to be accelerated in general with increasing ionic strength.

Tab. 3.5: Time period of the first indication of the Eu(III)-borate precipitation as a function of $[B]_{total}$ and ionic strength, medium: NaCl;bracketed : outlier, values in days (d).

I_m [m], NaCl	$[B]_{total}$ [m]					
	0.2	**0.3**	**0.4**	**0.5**	**0.6**	**0.7**
0.1	n.p.	‡	49-64 d	20-27 d	6-7 d	2-6 d
0.4	n.p.	n.p.	64-120 d	20-27 d	6-7 d	2-6 d
1	n.p.	n.p.	64-120 d	20-27 d	(2-6 d)	6-7 d
2	n.p.	n.p.	‡	41-49 d	16-20 d	9-13 d
3	n.p.	n.p.	‡	41-49 d	16-20 d	9-13 d

n.p.: no precipitation observed, ‡: precipitation observed, beginning of precipitation undefined, (>> 120 d)

Tab. 3.6: Time period of the first indication of the Eu(III)-borate precipitation as a function of $[B]_{total}$ and ionic strength, medium: $NaClO_4$;bracketed: outlier, values in days (d).

I_m [m], $NaClO_4$	$[B]_{total}$ [m]								
	0.2	**0.3**	**0.4**	**0.45**	**0.5**	**0.55**	**0.6**	**0.65**	**0.7**
0.1	n.p.	‡	49-64 d	41-49 d	27-34 d	9-13 d	6-7 d	2-6 d	2-6 d
0.4	n.p.	‡	‡	·/·	(2-6 d)	13-34 d	8-13 d	7-8 d	2-6 d
0.7	n.p.	‡	‡	34-64 d	13-34 d	13-34 d	8-13 d	7-8 d	2-6 d
1	n.p.	‡	98-141 d	64-98 d	20-27 d	13-16 d	8-9 d	7-8 d	2-6 d
2	n.p.	‡	‡	34-64 d	13-34 d	13-34 d	(2-6 d)	6-7 d	2-6 d
3	n.p.	‡	49-64 d	27-34 d	16-20 d	2-6 d	2-6	2-6 d	2-6 d

n.p.: no precipitation observed, ‡: precipitation observed, beginning of precipitation undefined (>> 141 d),
·/·: no adequate sample, precipitation possible

Investigation of the formation of the Eu(III)-borate solid phase in $CaCl_2$ and $MgCl_2$ medium

Obviously, the Eu(III)-borate solid formation is increasingly suppressed with increasing Ca^{2+}/Mg^{2+} concentration. No Eu(III)-borate precipitation was observed after 140 days at I_m = 3 m and up to $[B]_{total}$ = 0.7 m. For comparison at $[B]_{total}$ = 0.7 m in 3 m NaCl medium already after 9-13 days a Eu(III)-borate precipitation started (see Table 3.6).

From ^{11}B NMR spectroscopic study of the polyborate speciation and Eu(III)-(poly)borate complexation studies in $CaCl_2$/$MgCl_2$ medium (cf. chapter 3.4.1 and 3.4.2) it is known that Ca^{2+} and Mg^{2+} are competition ions to Eu(III) concerning the complexation with polyborate species. Obviously, these alkaline earth metal ions (ubiquitious ions in natural waters and brines) are able to suppress the An(III)/Ln(III)-borate precipitation.

Eu(III)-borate species of colloidal character

The long term samples ($[Eu]_{total} = 3 \cdot 10^{-5}$ m, $[B]_{total}$ = 0.2 m to 0.7 m, $NaClO_4$/NaCl medium) for the filtration experiments were not only filtered through a membrane filter with 0.2 µm pores. In a previous filtration step a membrane filter with 1.2 µm pores was applied.

The luminescence spectrum of the Eu(III)-borate solid species was still detectable for the filtrates after the 1.2 µm-membrane filtration of the samples prepared in 0.1 m electrolyte medium ($NaClO_4$/NaCl). Furthermore, a raised scattered light intensity was observed in these filtrates. After the 0.2 µm-membrane filtration step these particles were not detected anymore. Hence, the size for the most part of the particles is between 0.2 µm and 1.2 µm.

The particle size determination with dynamic light scattering (DLS) was difficult, because the particle amount was low. With this method the particle size distribution is in the range 100-1000 nm.

Thus, from the results of DLS and filtration the detected particles can be classified as colloids (by definition colloids are particles smaller than 1 µm (IUPAC definition [IUP1972]), albeit they are quite large. A further indication for the formation of a colloidal species is that at higher ionic strengths (already at I = 0.4 m in the studied system) this species cannot be detected (except an outlier). It is known that colloids are destabilized in presence of higher salt concentrations/ionic strengths [HOF2004].

SEM images show small particles < 1 µm on the 50 nm-membrane filter surface. Agglomerate like structures of the particles and isolated particles can be identified. An EDX

analysis to determine the particle composition was not possible, because the particle amount was too low.

However, the possibility of the colloid formation in the Eu(III)-(poly)borate system opens further An(III)-mobilization pathways, to be considered in safety and risk assessments.

Structural characterization of the Eu(III)-borate solid species

The solid Eu(III)-borate was characterized by powder X-ray diffraction (XRD), infrared spectroscopy (IR), solid-state ^{11}B NMR, and solid-state site-selective TRLFS. XRD indicates that the precipitated Eu(III)-borate is almost an amorphous phase. There are weak reflexes, but they do not coincidence with the diffraction pattern of known solid europium borates. The observed reflexes might be attributed to a poorly crystallized sodium pentaborate phase ($Na_2[B_5O_8(OH)]\cdot H_2O$) [MEN1983] which might be co-precipitated with the Eu(III)-borate.

By IR spectroscopy the borate structure in the isolated solid can be clearly confirmed. The ionic strength and background electrolyte ($NaClO_4$ or NaCl) have no effect on the borate structure (cf. [SCH2015/2016])

in the Eu(III)-borate solids that precipitated from the corresponding sample solutions. The IR spectrum is different from that of boric acid (Fig. 3.16a) characterized by its B(3)-O vibration modes (Fig. 3.16, Tab. 3.7) [JUN1995, PAR1960, BET1955]. Besides the vibration modes of B(3)-O the Eu(III)-borate shows vibration modes of B(4)-O. The assignment of these modes (Tab. 3.7) is based on literature data [BEL2004, HUA2010, JAN1980, JUN1995, LEM1999, LIX2007]. Furthermore, in the literature so called pulse vibrations are described being typical for different polyborate structures [JUN1995]. Characteristic pulse vibrations of tri-, tetra-, penta- and hexaborates occur in the wavenumber range from 650 cm^{-1} to 530 cm^{-1} [JUN1995]. In this range one vibration band at 550 cm^{-1} is observed in the measured IR spectrum of the Eu(III)-borate (Fig. 3.16). This band might be an indication for a pentaborate structure, an assignment to the bending mode of B(3)-O and B(4)-O is also possible (Tab. 3.7). The vibration band at 1631 cm^{-1} observed in all IR spectra is assigned to structural water, which obviously exists in the solid Eu(III)-borate. There is no hint from IR spectroscopy for another major solid phase, e.g., co-precipitation of a carbonate.

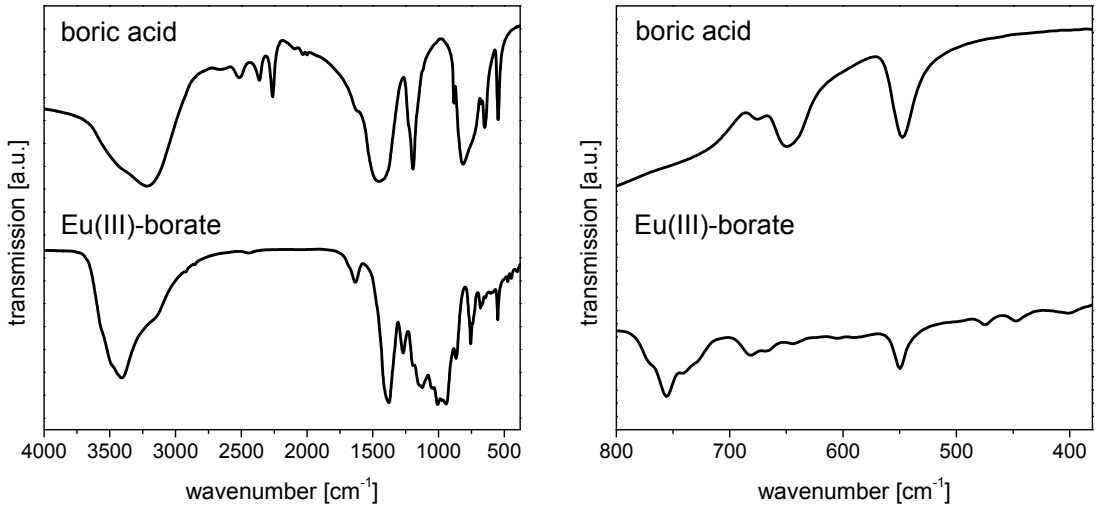

Fig. 3.16: IR spectrum of the isolated Eu(III)-borate solid and for comparison of boric acid in the range of 4000-380 cm^{-1} (left) and 800-380 cm^{-1} (right)

Tab. 3.7: Observed vibration frequencies in the IR spectra of boric acid and the isolated Eu(III)-borate solid

boric acid, solid	**assignment**	**Eu(III)-borate, solid**	**assignment**
548 (s)	δ(B(3)-O) [JUN1995], δ(B-O), in-plane O-B-O angle deformation mode [BET1955, PAR1960]	450 (w)	δ(B(4)-O) [JAN1980, JUN1995, LIX2007]
645 (m)	γ(B(3)-O) [PAR1960], γ(O-H), out-of-plane OH deformation mode [BET1955], δ(B-O) [PAR1960]	550 (w)	δ(B(3)-O)/δ(B(4)-O) [JUN1995], potentially ν_p(pentaborate) [HUA2010, JUN1995, LIX2007]
806 (m)	γ(B(3)-O), out-of-plane angle deformation mode [BET1955, JUN1995] γ(O-H), twisting [PAR1960]	680 (w)	γ(B(3)-O) [HUA2010, JAN1980, LIX2007]
883 (s, b)	ν_s(B-O) [BET1955, JUN1995, PAR1960]	756 (m)	γ(B(3)-O) [HUA2010, JAN1980, JUN1995, LIX2007]
1196 (m)	ν_{as}(B(3)-O) [JUN1995], δ(O-H), in-plane B-O-H angle deformation mode [BET1955, PAR1960]	800-1200 (s)	ν_s(B(3)-O), ν_s(B(4)-O), ν_{as}(B(4)-O) [HUA2010, JAN1980, JUN1995, LIX2007]
1450 (s)	ν_{as}(B-O) [BET 1955, JUN1995, PAR1960]	1269 (m)	δ(B-O-H) [BEL2004, HUA2010, JUN1995, LIX2007]
2262 (m), 2363 (m), 2517 (m)	no B-O modes (adsorbed gaseous CO_2) or B_2O_3 impurities [MED2007], combination frequencies of ν(O-H), ν(B-O), δ(O-H), δ(B-O) [BET1955, PAR1960]	1379 (s)	ν_{as}(B(3)-O) [HUA2010, JUN1995, LIX2007]
3217 (s, b)	ν(O-H) [BET1955, JUN1995, PAR1960]	1631 (w)	δ(H-O-H), structural water [JUN1995, LIX2007]
		3400 (s, b)	ν(O-H) [JUN1995, LIX2007]

b = broad, m = middle, s = strong, w = weak, B(3) = trigonal planar (threefold coordinated) boron center, B(4) = tetrahedral (fourfold coordinated) boron center, ν = stretching vibration, δ = in-plane bending, γ = out-of-plane bending

For the solid-state ^{11}B NMR investigation La(III) instead of Eu(III) was used in order to avoid the interference of the paramagnetic Eu(III) with the NMR signals. IR spectroscopy confirmed a similar structure of the precipitated La(III)-borate as for Eu(III)-borate. The solid-state ^{11}B NMR spectrum of La(III)-borate, Fig. 3.17 shows two typical signals which are very well separated due to the setting of a high magnetic field, frequently high sample rotation, and ^{1}H decoupling. The signal at around 2 ppm, which has a Gaussian line shape, is assigned to the fourfold coordinated boron center(s) and the signal at around 18 ppm to the threefold coordinated boron center(s). The latter signal shows the typical line shape for second order quadrupolar interactions. The fit of the ^{11}B NMR spectrum of the La(III)-borate solid confirms one major solid phase.

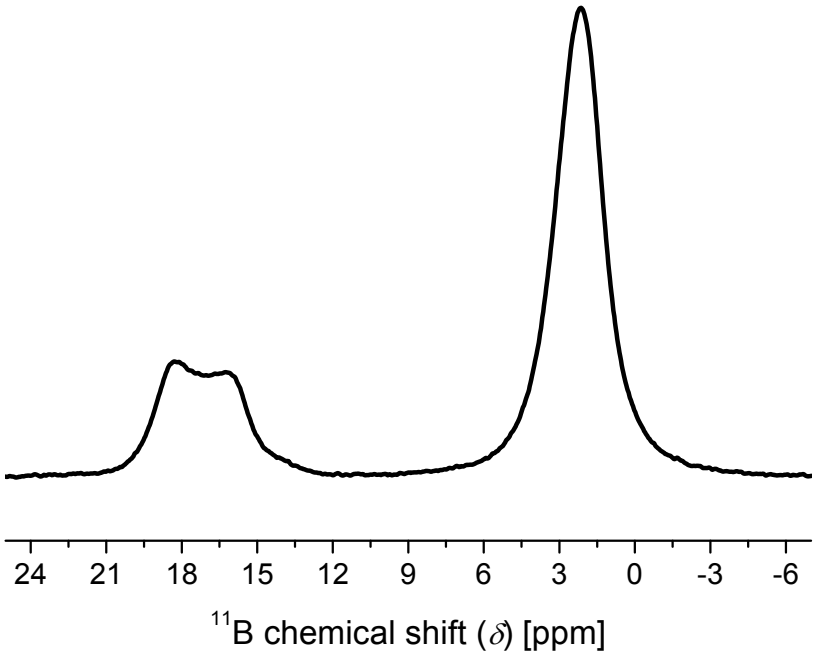

Fig. 3.17: Solid-state ^{11}B NMR (B_0 = 800 MHz) spectrum of the La(III)-borate solid as representative for the Eu(III)-borate solid

Usually, the ratio of the fourfold coordinated to threefold coordinated boron centers from the relative intensities of the two types of boron signals gives access to structural information of a borate solid [MÜL1993, TUR1986], even if its amorphous. The analysis of the solid-state ^{11}B NMR spectrum of La(III)-borate reveals a ratio of 3:1. Unfortunately, the structure of the borate ligand cannot be deduced. The high amount of fourfold coordinated boron environments (i.e., negative charges), probably neutralizes the high charge (+3) of the lanthanide ion, suggesting a high(er) degree of condensation of the borate ligand. Probably, polyborate species (tri-/pentaborate) isolated in solution assemble as higher condensated borate ligands.

To get more information about the precipitated Eu(III)-borate site-selective TRLFS of the solid Eu(III)-borate precipitated at different ionic strengths (0.1, 1, 3 m $NaClO_4$/NaCl) was performed at low temperature (T < 5 K). The excitation spectra of the six different Eu(III)-borate samples in Fig. 3.18 show asymmetric shapes. This asymmetry points to the presence of more than one Eu(III) species in the respective solid phase. It has to be noted that these luminescence measurements are much more sensitive than solid-state ^{11}B NMR (detecting only one major species).

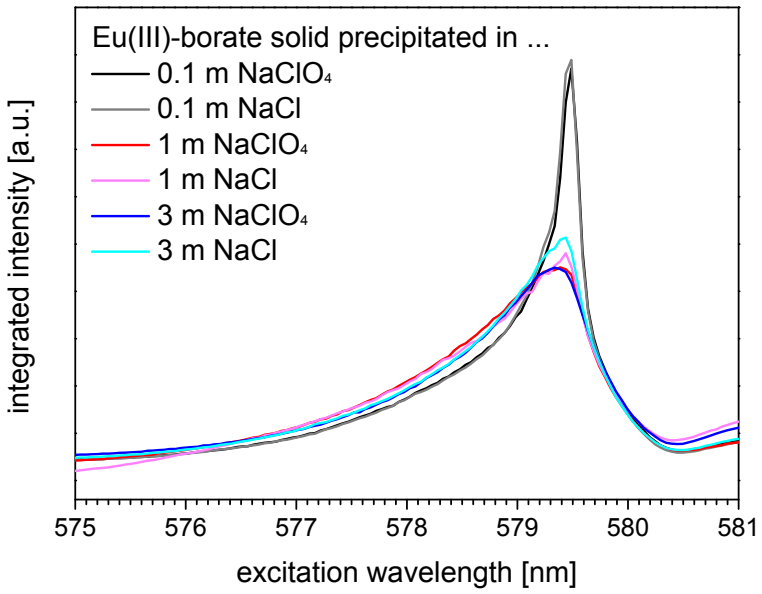

Fig. 3.18: Excitation spectra at low temperature (T < 5 K) of the Eu(III)-borate solid precipitated at different ionic strengths and media ($NaClO_4$/NaCl)

Based on the excitation spectra (Fig. 3.18) the samples were excited at λ_{ex} = 579.45 nm (peak maximum in all excitation spectra) and at lower wavelengths (λ_{ex} = 578.50 and 578.0 nm). The lower wavelengths were chosen to detect further possible europium species and to minimize the contribution of the strongly luminescent species excited with λ_{ex} = 579.45 nm.
Depending on the excitation wavelength at least two different europium species were identified in each sample (Fig. 3.19). The spectra recorded at λ_{ex} = 578.0 nm and 578.50 nm are nearly identical. It is interpreted that both spectra describes one and the same species. Independent from the medium in which the Eu(III)-borate solid was precipitated, the luminescence spectra obtained at λ_{ex} = 579.45 nm can be assigned to the Eu(III)-borate, because the spectrum is comparable to the spectrum of the suspended Eu(III)-borate (comparison Fig. 3.15 left with Fig. 3.19). In contrast, more different luminescence spectra were recorded at λ_{ex} = 578.50 nm (Fig. 3.19). However, these spectra are comparable to the spectra of the Eu(III)-borate precipitated at higher ionic strengths and recorded at λ_{ex} =

579.45 nm. Hence, they are assigned to at least one further (a third), most likely, Eu(III)-borate solid species.

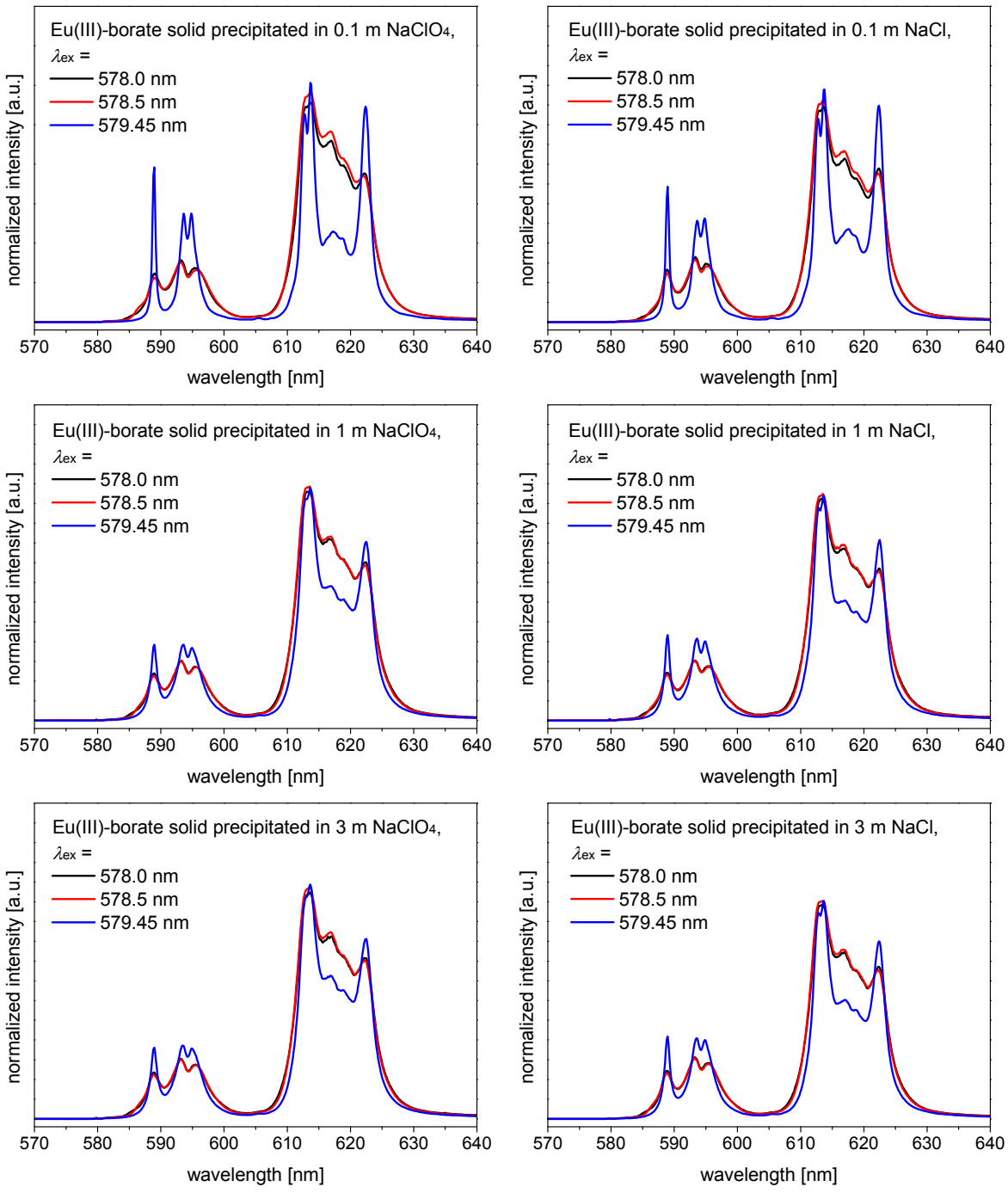

Fig. 3.19: Comparison of the Eu(III) luminescence spectra at low temperature (T < 5 K) of the Eu(III)-borate solid excited at different λ_{ex}; Eu(III)-borate solid precipitated at different ionic strengths and media ($NaCl/NaClO_4$)

In addition to the stationary luminescence spectra, the luminescence decay curves of the Eu(III)-borate precipitates produced at different ionic strengths were measured at different excitation wavelengths and at low temperature (T < 5 K) (Tab. 3.8).

Clearly two luminescence lifetimes were found for each precipitation system for λ_{ex} = 578.5 nm. A short lifetime (average 260 μs) and a longer lifetime (average 600 μs) were extracted. In contrast, only one luminescence lifetime was found at λ_{ex} = 579.45 nm. The luminescence lifetime is somewhat higher (average around 770 μs) at low ionic strength than for that at higher ionic strengths (average around 600 μs). The latter luminescence lifetime is quite similar to longer lifetime determined at λ_{ex} = 578.50 nm. Again, no clear electrolyte effect is detectable.

PARAFAC analysis of the time-resolved as well as of the excitation based data (from low temperature measurements) of the Eu(III)-borate (precipitated at different ionic strengths in $NaClO_4$ medium[4]) provided emission spectra (Fig. 3.20) and lifetimes (Table 3.8) of three europium species (named species A, B and C) as well as a species distribution as a function of the precipitation conditions (Fig. 3.21).

Tab. 3.8: Luminescence lifetimes of the Eu(III)-borate solid for excitations at different λ_{ex}.

	solid precipitated in	excitation wavelength λ_{ex}	
		578.50 nm	**579.45 nm**
luminescence lifetime, obtained from low temperature (< 5 K) measurements	0.1 m $NaClO_4$	263 μs 619 μs	771 μs
	1 m $NaClO_4$	360 μs 654 μs	600 μs
	3 m $NaClO_4$	208 μs 558 μs	566 μs
	0.1 m NaCl	218 μs 601 μs	759 μs
	1 m NaCl	285 μs 597 μs	635 μs
	3 m NaCl	228 μs 573 μs	620 μs
luminescence lifetime, obtained from PARAFAC of low temperature (< 5 K) luminescence data	882 μs (species A) → 0-1 remaining H_2O*		
	717 μs (species B) → 0-1 remaining H_2O*		
	335 μs (species C) → 2-3 remaining H_2O*		

* … in the first hydration shell of Eu(III)

[4] Spectra of the Eu(III)-borate precipitated at different ionic strengths in NaCl medium were not analyzed, because no electrolyte effect on the solid formation was observed.

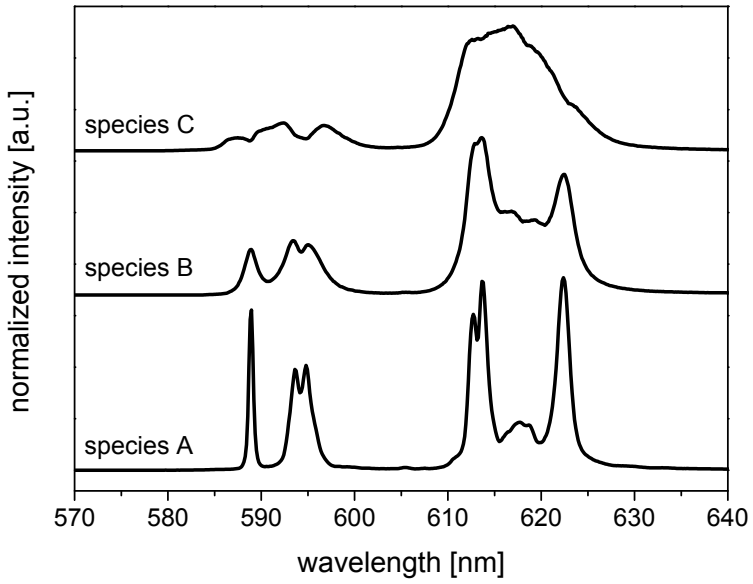

Fig. 3.20: Luminescence spectra of single Eu(III) species determined with PARAFAC from low temperature (< 5 K) luminescence data

Comparing Fig. 3.19 and Fig. 3.20 one species (named species A) is quite similar to the measured spectrum at λ_{ex} = 579.45 nm of the Eu(III)-borate precipitated at low ionic strength. A second species (named species B) is similar to the measured spectrum at λ_{ex} = 579.45 nm of the Eu(III)-borate solid precipitated at higher ionic strengths. The third species (named species C) shows less similarity to the two other species. It is a species with a quite short luminescence lifetime (335 µs) in comparison to species A (882 µs) and species B (717 µs). From this qualitatively discussion of species assignment a species distribution (result from PARAFAC) as a function of ionic strength at which the Eu(III)-borate was precipitated (Fig. 3.21) clarifies the relative composition of the borate species in the precipitated Eu(III)-borates. Under low ionic strength precipitation conditions (0.1 m $NaClO_4$) species A, species B and species C occur in the Eu(III)-borate solid in equal parts. Under high ionic strength precipitation conditions only species B and species C exist in the Eu(III)-borate solid.

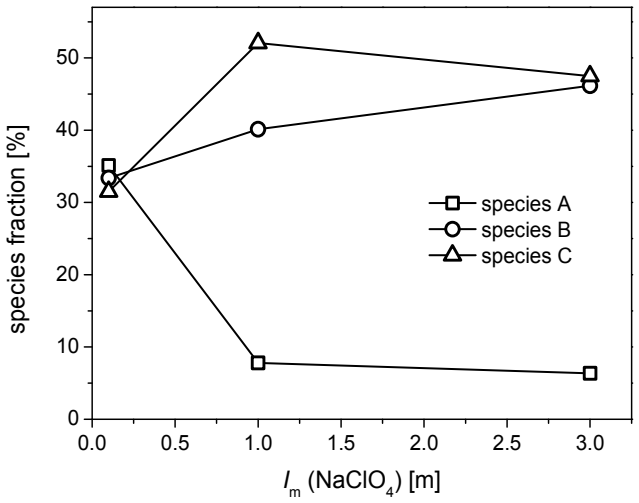

Fig. 3.21: Fraction of different solid species in the Eu(III)-borate solid precipitated at different ionic strengths

Species B resembles species A, however, species A has a somewhat longer luminescence lifetime (Table 3.8). Both species are Eu(III)-borate species, probably, with a similar basic structure and short-range order (see results from IR spectroscopy), but presumably with different water contents (hence, somewhat different luminescence lifetimes), different degree of condensation of the borate ligand, and different long-range order. Because of its less structured spectrum, its short lifetime and its occurrence under any precipitation condition it is assumed that species C is a fundamental constituent of the precipitated Eu(III)-borate solids.

From the splitting pattern of the Eu(III) luminescence bands structural information of the local europium environment can be obtained [BIN2015, BÜN1989]. The spectrum of species A shows that the $^5D_0 \rightarrow {}^7F_1$ luminescence band split into three peaks and the $^5D_0 \rightarrow {}^7F_2$ luminescence band split into five peaks. The $^5D_0 \rightarrow {}^7F_1$ and $^5D_0 \rightarrow {}^7F_2$ luminescence bands in the spectrum of species B show similar splitting patterns as described for species A. For both species A and B this indicates a local europium environment with low symmetry (triclinic, monoclinic or orthorhombic) [BIN2015, BÜN1989]. However, there is another interpretation of the splitting pattern of the $^5D_0 \rightarrow {}^7F_1$ luminescence band and, hence, the local symmetry of europium, given by Bünzli et al. [BÜN2011]: A low symmetry is existent if the $^5D_0 \rightarrow {}^7F_1$ luminescence band is equally split into three components and these peaks have similar intensities. If this splitting pattern is unsymmetrical, as it is the case for species A and species B, then a higher symmetry (*e.g.*, tetragonal or trigonal/hexagonal) has to be expected. With this declaration the $^5D_0 \rightarrow {}^7F_1$ luminescence band of species A and species B is only split into two components and the slight splitting of the second component indicates a slightly

distortion of the existent symmetry. As for the $^5D_0 \rightarrow {}^7F_1$ luminescence band a similar conclusion could be drawn for the splitting pattern of the $^5D_0 \rightarrow {}^7F_2$ luminescence band of species A and species B. The $^5D_0 \rightarrow {}^7F_2$ luminescence band also could consist of only three or four components (sub-splitting as indication for symmetry distortion) instead of five peaks, pointing to a higher symmetry (tetragonal or trigonal/hexagonal). Fortunately, the $^5D_0 \rightarrow {}^7F_3$ transition was recorded (occurrence at around 653 nm) during the low temperature solid-state site-selective TRLFS measurements. For species A the $^5D_0 \rightarrow {}^7F_3$ luminescence band is split into five main peaks. Summarizing the splitting patterns of all luminescence bands for species a tetragonal or trigonal/hexagonal symmetry (more likely in consideration of the results from solid-state ^{11}B NMR, see above) around Eu(III) can be deduced [BIN2015, BÜN1989]. For species B the $^5D_0 \rightarrow {}^7F_3$ luminescence band exhibits no distinct splitting pattern. Presumably, this species also has a tetragonal or trigonal/hexagonal symmetry around Eu(III). The luminescence bands of species C do not show a distinct splitting pattern. Hence, it is not possible to deduce the symmetry of the local europium environment in species C.

3.4.4 First results for the interaction of Cm(III) and Am(III) with polyborates

Cm(III)-(poly)borate complexation

The interaction of Cm(III) with polyborates was studied by TRLFS as function of the borate concentration (Fig. 3.22, left) and pH (Fig. 3.22, right). In presence of polyborates a red shift of the luminescence band of Cm(III) is observed and a complexation can be assumed. A preliminary complexation constant of log β_1^0 ($CmB(OR)_4^{2+}$) = 3.0 (single value) was estimated. This value fits well into the range of complexation constant determined for the Eu(III)-(poly)borate complex (cf. chapter 3.4.2, log β_1^0 ($EuB(OR)_4^{2+}$) = 2.7 to 3.2).

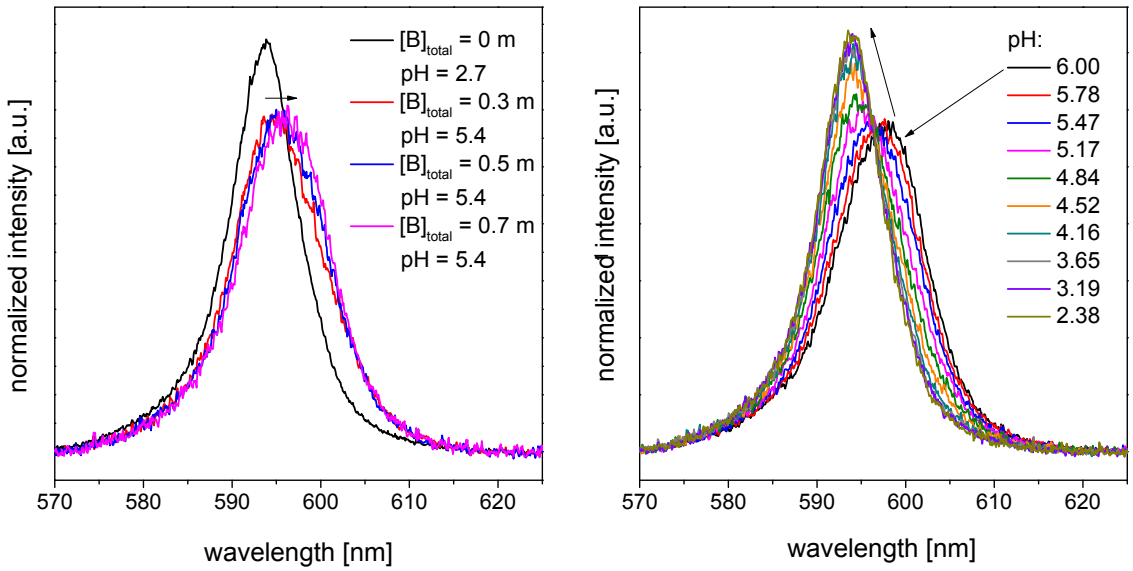

Fig. 3.22: Left: Cm(III) luminescence spectra as a function of $[B]_{total}$, $[Cm(III)]_{total} = 2 \cdot 10^{-7}$ M, $I_m = 0.1$ m (NaCl), right: pH titration series of a solution containing $[Cm(III)]_{total} = 2 \cdot 10^{-7}$ M and $[B]_{total} = 0.7$ m, $I_m = 0.1$ m (NaCl) by means of TRLFS (data analysis with spectra from pH 2.38 up to pH 5.17 to avoid Cm(III) hydrolysis)

Am(III)-(poly)borate complexation

Several pH titration series of solutions containing $[Am(III)]_{total} = 6 \cdot 10^{-7}$ M, $[B]_{total} = 0.7$ m, and different ionic strengths were carried out by UV/Vis spectroscopy using a long path flow cell (1 meter). A red shift of the Am(III) absorption band from 503 nm to 505 nm and an increase of the absorption intensity with decreasing pH was observed (Fig. 3.23).

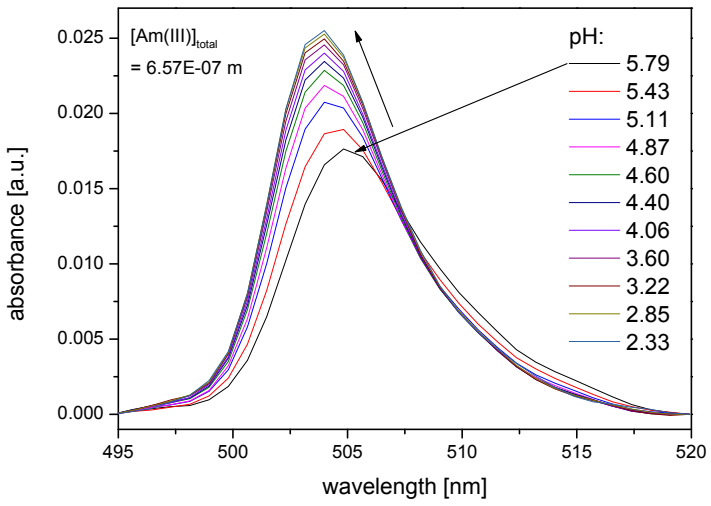

Fig. 3.23: pH titration series of a solution containing $[Am(III)]_{total} = 6 \cdot 10^{-7}$ m and $[B]_{total} = 0.7$ m, $I_m = 0.1$ m (NaCl) by means of UV/Vis spectroscopy with a long path flow cell (1 meter) (data analysis with spectra from pH 2.33 up to pH 5.43 to avoid Am(III) hydrolysis)

Tab. 3.9: *Log β_1 values of the Am(III)-borate complex, $AmB(OR)_4^{2+}$ (borate ligand with one binding site), as a function of ionic strength (NaCl), $[Am(III)]_{total} = 6 \cdot 10^{-7}$ M, $[B]_{total} = 0.7$ m, pH_c variable, T = 22 °C; error for log β_1 (estimated): 0.2 (2σ).*

I_m [mol/kg] NaCl	log β_1
0.1	2.06
0.5	1.79
1	1.77
2	n.d.
3	n.d.
0	2.68*

n.d.: not determinable (spectrum variation too small),
*from SIT calculation (cf. Fig. 3.24)

The SIT plot shows a good linear relation (Fig. 3.24). The derived thermodynamic values are log β_1^0 = 2.68 ± 0.2 and $\Delta\varepsilon_1$ = - 0.31 ± 0.04 kg·mol^{-1} (errors were not taken from SIT plot, uncertainties were estimated, in analogy to Eu(III)-polyborate system, cf. chapter 3.4.2)

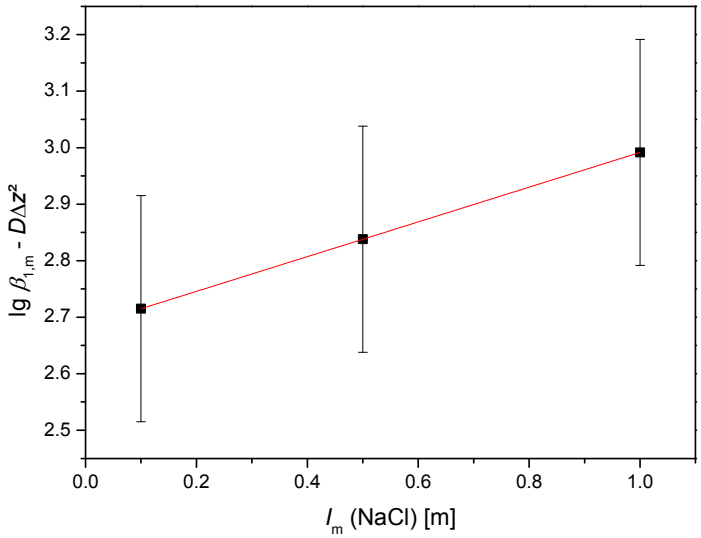

Fig. 3.24: *SIT plot for the Am(III)-(poly)borate-NaCl system (error bars: 2σ from estimation)*

The log β_1^0 for the Am(III)-(poly)borate complex fits well into the range of complexation constant determined for the Eu(III)-(poly)borate complex. However, the $\Delta\varepsilon_1$ value for the Am(III)-(poly)borate-NaCl system is quite low in comparison to the well determined value of the Eu(III)-(poly)borate-NaCl system (see chapter 3.4.2, Tab. 3.4). The $\Delta\varepsilon_1$ value for the Am(III)-(poly)borate-NaCl system was determined with only few data points without repetition and, hence, should be seen as a first estimation only.

3.5 Interaction of Eu(III) with organoborates

The Eu(III)-organoborate complexation was studied in comparison to the Eu(III)-(poly)borate system and to confirm the hypothesis that all borate compounds with the "$B(OR)_4^-$" unit exhibit a comparable complexation behavior regarding An(III)/Ln(III) independent from R (see chapter 3.1). This study is particular addressed to the question to what extent the ring size (five-or six-membered) of the organoborate and the nature of the organic moiety R (aromatic or aliphatic) influence the Eu(III) complexation.

As organoborate ligands were chosen (Fig. 3.25):

- salicylatoborate (six-membered ring, aromatic moiety), and
- lactatoborate (five-membered ring, aliphatic moiety):

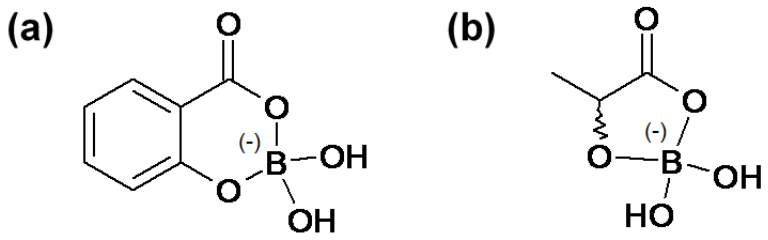

Fig. 3.25: Investigated organoborates: a) salicylatoborate, b) lactatoborate

3.5.1 Formation of organoborates

All studied organoborates were formed by the reaction of boric acid and the respective carboxylate (salicylate/lactate, cf. chapter 3.2, Fig. 3.3). The existence of organoborates can be clearly verified by specific ^{11}B NMR signals. For each organic-boron system two characteristic signals in the ^{11}B NMR spectrum are found. In each ^{11}B NMR spectrum a signal at 19.3 ppm appears (Fig. 3.26) which is assigned to boric acid (see chapter 3.4.1). Further ^{11}B chemical shifts at 2.9 ppm and 6.3 ppm for the salicylate-boron and lactate-boron system, respectively, are observed (Fig. 3.26). The ^{11}B chemical shift at 2.9 ppm is assigned to the salicylatoborate and that at 6.3 ppm to the lactatoborate. The ^{11}B chemical shift of salicylatoborate is in full agreement with literature (δ_{BSal} = 2.9 [MIY2008]). The formation of lactatoborate is less pronounced than that of salicylatoborate. The ^{11}B signal intensity of lactatoborate is weaker than that of salicylatoborate for the same solution composition.

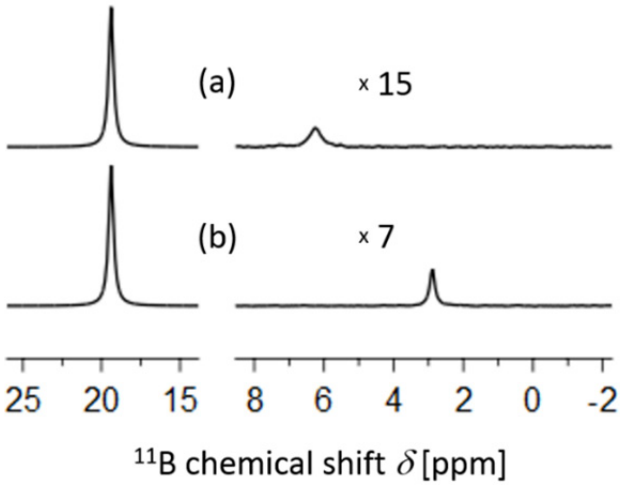

Fig. 3.26: *^{11}B NMR spectra of aqueous solutions (pH 5, I = 0.1 M ($NaClO_4$)) with (a) $[B]_{total}$ = 0.2 M and $[lactate]_{total}$ = 0.005 M , lactate, (b) $[B]_{total}$ = 0.2 M and $[salicylate]_{total}$ = 0.005 M; scaling factors of the organoborate signals are given*

Obviously, the ring size of the organoborate has a stronger influence on the ^{11}B chemical shift of the respective organoborate than the nature of the organic moiety (e.g., inductive effect) bound to the "$B(OR)_4^-$" unit. The ^{11}B chemical shift of salicylatoborate (2.9 ppm), possessing a six-membered ring, is remarkably more upfield shifted than that of lactatoborate (6.3 ppm), where a five-membered ring is formed. The ring size effect on the ^{11}B chemical shift of organoborates and, therefore, the differentiation of five-membered and six-membered organoborates is also known from literature [MIY2003, MIY2013, VAN1985]. Additionally, the carbonyl group typically induces only downfield shifts of about 1-2 ppm regardless of the ring size [MIY2013].

In order to calculate the species distribution in the studied systems, the following chemical equilibria were considered, Eq. 3.11-3.13.

$$LH \leftrightarrow L^- + H^+ \qquad K_{a,LH} = \frac{[L^-][H^+]}{[LH]} \qquad (3.11)$$

$$BH + H_2O \leftrightarrow B^- + H^+ \qquad K_{a,BH} = \frac{[B^-][H^+]}{[BH]} \qquad (3.12)$$

$$BH + L^- \leftrightarrow BL^- + H_2O \qquad K_{BL} = \frac{[BL^-]}{[BH][L^-]} \qquad (3.13)$$

LH…organic acid (salicylic or lactic acid), L^-…deprotonated organic acid (salicylate (Sal), lactate (Lac)), BH…boric acid, B^-…deprotonated boric acid (monoborate), BL^-…organoborate (salicylatoborate (BSal), lactatoborate (BLac))

The equilibrium constants $K_{a,LH}$ for lactic and salicylic acid as well $K_{a,BH}$ for boric acid were determined by potentiometric titration (Tab. 3.10) The values are in good agreement with literature data [ING1962, POR2003, LAJ1997].

Tab. 3.10: pK_a values of the used organic acids and boric acid determined within this work, uncertainty: 2σ, (T = 22 °C)

acid	pK_a (I = 0.1 M)	pK_a (I = 0)*
salicylic acid	2.83 ± 0.04	3.04 ± 0.04
lactic acid	3.73 ± 0.01	3.94 ± 0.01
boric acid	9.13 ± 0.04	9.34 ± 0.04

* Extrapolation to infinite dilution according to Davies approach [DAV1962]

The evaluation of the ^{11}B NMR spectra led to the average formation constants K_{BL} of salicylatoborate and lactatoborate (Tab. 3.11) according to Eq. 3.13. These values are in accordance with literature data. The reaction (Eq. 3.13) is isocoulombic. Hence, the extrapolation to infinite dilution by the Davies approach [DAV1962] does not change the value of log K_{BL} determined at I = 0.1 M.

Tab. 3.11: Average formation constants K_{BL} of salicylatoborate and lactatoborate determined within this work compared to literature values, pH = 5, I = 0.1 M, T = 22 °C, uncertainty: 2σ.

organoborate	log K_{BL}	log K^0_{BL}, a
salicylatoborate	1.10 ± 0.14, p.w., b 1.04 [LUK1988], c; 1.23 [MIK1978], d; 1.28 [PAA1985], c	1.10 ± 0.14, p.w.
lactatoborate	0.57 ± 0.22, p.w., b 0.60 [PAA1988], d; 0.96 [PIZ1984], d; 0.52 [PIZ1994], b	0.57 ± 0.22, p.w.

a…extrapolation to infinite dilution according to Davies approach [DAV1962], b…NMR spectroscopy, c… photometry, d… potentiometry, p.w…present work

A speciation calculation for the salicylate-boron and lactate-boron systems is shown in Fig. 3.27. In each case the fraction of the respective organoborate reaches its maximum at pH 5-6. At pH > 8 the organoborate fraction distinctly decreases, because the concentration of available boric acid decreases. Thus, the optimum pH for the existence of organoborates is in the range pK_a (organic acid) < pH < pK_a(boric acid). This correlation is described in detail by Van Duin et al. [VAN1984].

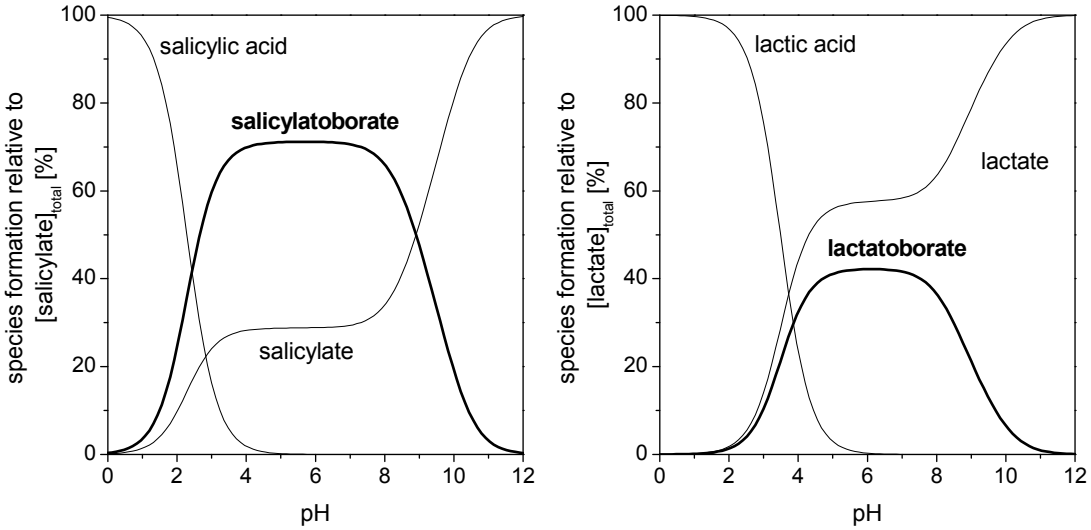

Fig. 3.27: Speciation of different organic-boron systems for solutions with $[organics]_{total}$ = 0.005 M and $[B]_{total}$ = 0.2 M, I = 0.1 M, T = 22 °C (pK_a and log K_{BL} taken from Tab. 3.10 and 3.11), left: salicylate-$B(OH)_3$ system, right: lactate-$B(OH)_3$ system

The salicylatoborate formation is less influenced by ionic strength (NaCl). The analysis of the ionic strength dependency of the salicylatoborate formation in the NaCl medium by SIT (Fig. 3.28), yielded a linear relation with following values for log K^0_{BL} = 1.02 ± 0.2 and $\Delta\varepsilon$ = - 0.06 ± 0.02 kg·mol^{-1}.

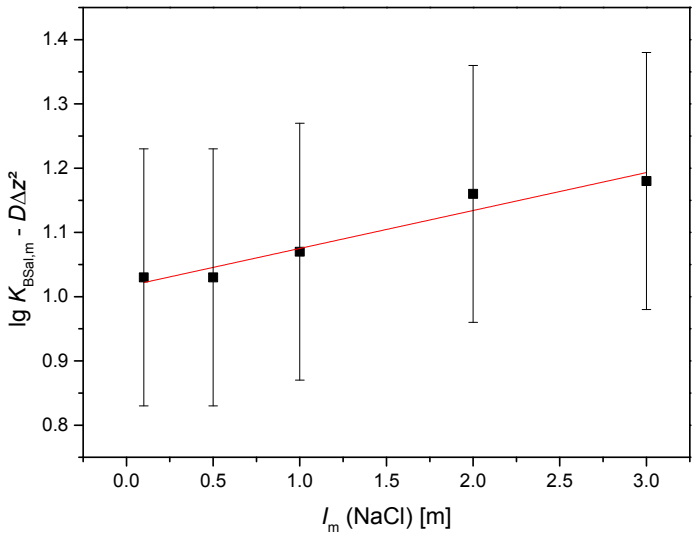

Fig.3.28: SIT plot for the salicylatoborate-NaCl system (uncertainty: 0.2 (2σ))

3.5.2 Complex formation of Eu(III) with organoborates

Additional to the above described equilibria for the formation of the organoborates (Eq. 3.11 to 3.13) the following equilibria (Eq. 3.14-3.16) have to be considered for the determination of the Eu(III)-organoborate complexation.

$$Eu^{3+} + L^{-} \leftrightarrow EuL^{2+} \qquad \beta_{11} = \frac{[EuL^{2+}]}{[Eu^{3+}][L^{-}]} \qquad 3.14$$

$$Eu^{3+} + 2\,L^{-} \leftrightarrow EuL_2^{+} \qquad \beta_{12} = \frac{[EuL_2^{+}]}{[Eu^{3+}][L^{-}]^2} \qquad 3.15$$

$$Eu^{3+} + BL^{-} \leftrightarrow EuBL^{2+} \qquad \beta_{EuBL} = \frac{[EuBL^{2+}]}{[Eu^{3+}][BL^{-}]} \qquad 3.16$$

LH…organic acid (salicylic or lactic acid), L^-…deprotonated organic acid (Sal, Lac), BH…boric acid, B^-…deprotonated boric acid (monoborate), BL^-…organoborate (BSal, BLac), EuL^{2+}…1:1 Eu(III)-organic complex (Eu(III)-salicylate (EuSal), Eu(III)-lactate (EuLac)), EuL_2^+… 1:2 Eu(III)-organic complex ($EuSal_2$, $EuLac_2$), $EuBL^{2+}$…1:1 Eu(III)-organoborate complex: (Eu(III)-salicylatoborate (EuBSal) or Eu(III)-lactatoborate (EuBLac))

The Eu(III)-salicylate and Eu(III)-lactate complexation constants according to Eq. 3.14 and 3.15 were determined with TRLFS or obtained from literature. Values for log β_{1n} for EuL_n complexes (with n = 1, 2 and L = lactate or salicylate) are summarized in Tab. 3.13. Our values show a good agreement with literature data. These Eu(III)-organic complexation constants and spectroscopic data are involved in the determination of log β_{EuBL} of the Eu(III)-organoborate complexes. Particularly for the lactate system, the 1:2 Eu(III)-lactate complex is required, because this species (in contrast to the $EuSal_2$ species) is a dominant species under the used conditions.

Tab. 3.13: Eu(III) complexation constants (according to Eq. 3.14 and Eq. 3.15), I = 0.1 M, T = 22-25 °C, error: 2σ.

L	log β_{11}	log β_{11}^0	log β_{12}
salicylate	2.10 ± 0.26, b, p.w. 1.84 [BAR2013], b 2.02 [HAS1989], c	2.74 ± 0.26 a, b, p.w.	 3.56 [BAR2013], b 3.84 [HAS1989], c
lactate	2.51 [BAR2014], b 3.09 [GOU1966], c, d		4.45 [BAR2014], b 5.38 [GOU1966] c, d

*a…*extrapolation to infinite dilution according to Davies approach [DAV1962], *b…* TRLFS, c… potentiometry, *d…* Dy(III) instead of Eu(III), *p.w*…present work

Obviously, the log β_{11} and log β_{12} values for the Eu(III)-lactate complexes deviate significantly in literature. Therefore, upper and lower limits for β_{11} and β_{12} were used to calculate upper and lower limits of log β_{EuBL} for the Eu(III)-lactatoborate complex.

The presence of boric acid influences the Eu(III)-salicylate as well the Eu(III)-lactate system. The luminescence spectrum of the Eu(III)-ligand solution (cf. Fig. 3.29 I) clearly differs from the spectrum in presence of boric acid under the same conditions (Fig. 3.29, II). An intensity decrease of the $^5D_0 \rightarrow {}^7F_0$ transition (at around 578 nm) and $^5D_0 \rightarrow {}^7F_2$ transition (at around 616 nm) is observed. There are two qualitative explanations for that:

(1) Free ligand is removed due to the formation of the respective organoborate and, hence, the Eu(III)-ligand complexation is repressed.

(2) A formation of an Eu(III)-organoborate complex occurs, which has different luminescence properties compared to the Eu(III)-salicylate or Eu(III)-lactate complex.

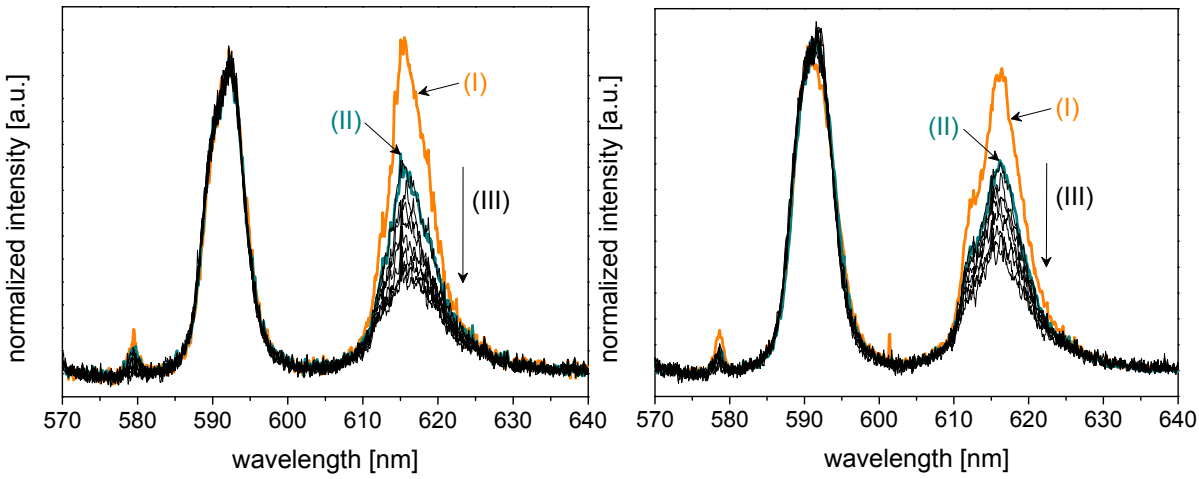

Fig. 3.29: Influence of boric acid on left: Eu(III)-salicylate system and right: the Eu(III)-lactate system. Eu(III) luminescence spectra of solutions at pH ≈ 4.4 and $[Eu(III)]_{total} = 3 \cdot 10^{-5}$ M, I = 0.1 M ($NaClO_4$) with (I) $[lactate]_{total} = 0.002$ M or $[salicylate]_{total} = 0.01$ M, (II) $[lactate]_{total} = 0.002$ M + $[B]_{total} = 0.4$ M or $[salicylate]_{total} = 0.01$ M + $[B]_{total} = 0.2$ M, (III) pH titration of a solution containing $[Eu(III)]_{total} = 3 \cdot 10^{-5}$ M, $[lactate]_{total} = 0.002$ M + $[B]_{total} = 0.4$ M or $[salicylate]_{total} = 0.01$ M + $[B]_{total} = 0.2$ M from pH ≈ 4.4 down to pH ≈ 2

Time-resolved luminescence data from a series of solutions which contained varying $[B]_{total}$, constant Eu(III) concentration of $3 \cdot 10^{-5}$ M and 0.01 M salicylate or lactate were analyzed with PARAFAC. Three Eu(III) species were identified in each system: Eu(III) aquo ion, 1:1 Eu(III)-salicylate and Eu(III)-salicylatoborate for the Eu(III)-salicylate-boron system, and 1:1 Eu(III)-lactate, 1:2 Eu(III)-lactate and Eu(III)-lactatoborate for the Eu(III)-lactate-boron system. From this analysis the speciation for the Eu(III)-$B(OH)_3$-salicylate and Eu(III)-$B(OH)_3$-lactate system were obtained (Fig. 3.30). Due to the increasing formation of the organoborate with increasing $[B]_{total}$ the fraction of the Eu(III)-organoborate complex increases. Concurrently, a decrease in the fraction of the Eu(III)-ligand complex(es) can be observed due to the removal of free ligand by the organoborate formation.

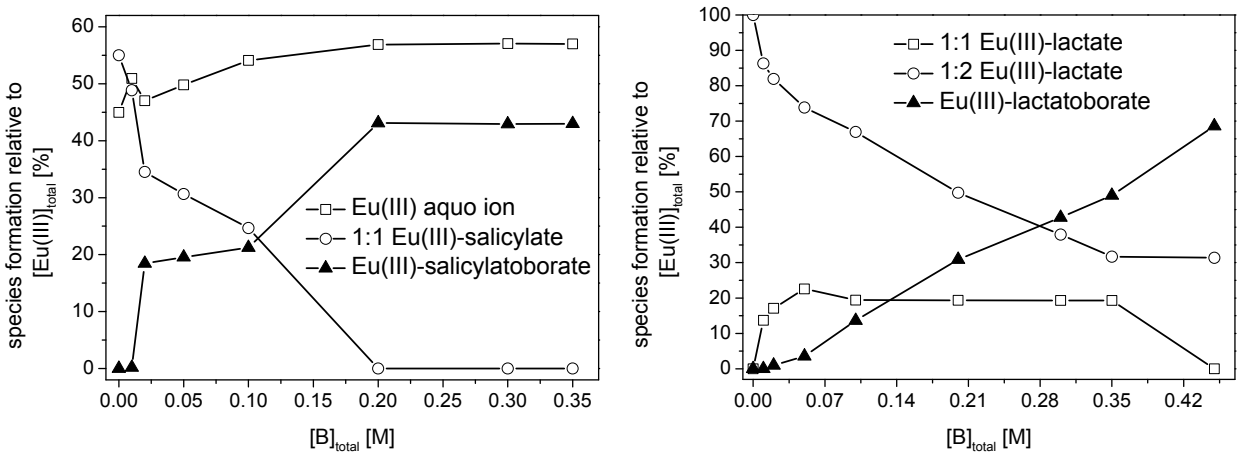

Fig. 3.30: Europium(III) speciation obtained from PARAFAC, left: Eu(III)-boron-salicylate system, right: Eu(III)-boron-lactate system, solutions: $[Eu(III)]_{total} = 3 \cdot 10^{-5}$ M, $[ligand]_{total} = 0.01$ M and varying $[B]_{total}$, pH 5, I = 0.1 M ($NaClO_4$)

Furthermore, different TRLFS pH titration series of solutions with $3 \cdot 10^{-5}$ M Eu(III) and variable $[B]_{total}$ and salicylate or lactate concentration were carried out at $I = 0.1$ M in $NaClO_4$ medium. For each titration step a stationary luminescence spectrum was measured (cf. Fig. 3.29 III).

The complexation constants for the Eu(III)-organoborate complexes according to Eq. 3.16 obtained by the analysis of time-resolved luminescence data (PARAFAC analysis) and stationary luminescence spectra (pH-titration) are summarized in Tab. 3.13. Unfortunately, the Eu(III)-lactatoborate TRLFS pH titration series were very difficult to analyze so that the result is omitted here. A separation of the Eu(III)-lactatoborate complex from the stationary TRLFS titration data was not possible. This is a result of the relatively strong Eu(III)-lactate complexation and the formation of the also relatively strong 1:2 complex already at low lactate concentrations. However, the PARAFAC of time-resolved luminescence spectra and analysis of the obtained Eu(III) speciation (Fig. 3.30, right) gave a hint for the order of magnitude of the Eu(III)-lactatoborate complexation constant (Table 3.13).

Additionally, the complex formation constants for the Eu(III)-organoborates were derived from ^{11}B NMR measurements. In both Eu(III)-organoborate systems Eu(III) induces a shift of the ^{11}B NMR signal of the organoborates (Fig. 3.31). This Eu(III) induced NMR signal shift is used to determine the complex formation constant. The procedure is described in our publication from Schott et al. [SCHO2015].

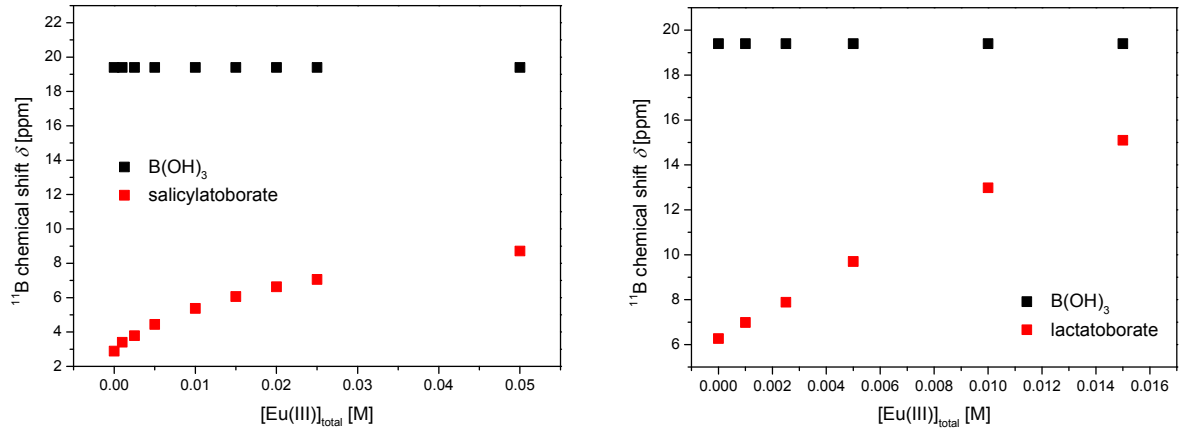

Fig. 3.31: *^{11}B chemical shift of left: salicylatoborate and right: lactatoborate as a function of $[Eu(III)]_{total}$; solutions: $[ligand]_{total}$ = 0.005 M, $[B]_{total}$ = 0.2 M, $[Eu(III)]_{total}$ = variable, pH 5, ^{11}B chemical shift corrected according to [SCHO2015]*

In the Eu(III)-lactatoborate system the uncertainty of the ^{11}B NMR data analysis is much higher than that of salicylatoborate. This uncertainty comes from the overlapping of the ^{11}B NMR signals of lactatoborate and $B(OH)_3$ with increasing Eu(III) concentration. The separation of the signals of lactatoborate and $B(OH)_3$ is possible only up to $[Eu(III)]_{total}$ = 0.015 M. In the frame of the described uncertainties (overlapping of NMR signals, deviation in literature data for β_{1n} for EuLac and $EuLac_2$, Tab. 3.12) a log β_{EuBL} range for the Eu(III)-lactatoborate complex is derived (Table 3.13). Assuming the lower limits of the Eu(III)-lactate complexation constants are valid (e.g., log β_{EuLac}= 2.51 and log β_{EuLac2}= 4.45 from [BAR2014]) log β^0_{EuBL} for the Eu(III)-lactatoborate complex ranges from 2.58 ± 0.22 to 2.82 ± 0.26. In contrast, assuming the upper limits of the Eu(III)-lactate complexation constants are to be valid (log β_{DyLac} and log β_{DyLac_2} from [GOU1966] for Dy(III), cf. Tab. 3.12) log β^0_{EuBL} for the Eu(III)-lactatoborate complex ranges from 3.01 ± 0.26 to 3.25 ± 0.15. All results are summarized in Table 3.13.

Tab. 3.13: *Eu(III)-salicylatoborate and Eu(III)-lactatoborate complexation constants, I = 0.1 M, T = 22 °C; uncertainty: 2σ.*

log β_{EuBL}	log β^0_{EuBL} [a]	used method and parameters for data analysis
Eu(III)-salicylatoborate		
1.93 ± 0.48	2.57 ± 0.48	TRLFS (pH titration series, $[salicylate]_{total}$ = variable, $[B]_{total}$ = variable) [b]
2.11 ± 0.32	2.75 ± 0.32	PARAFAC ($[salicylate]_{total}$ = 0.01 M, $[B]_{total}$ = variable) [b]
1.95 ± 0.32	2.59 ± 0.32	^{11}B NMR ($[salicylate]_{total}$ = 0.005 M, $[B]_{total}$ = 0.2 M) [b]
2.12 ± 0.28	2.76 ± 0.28	^{11}B NMR ($[salicylate]_{total}$ = 0.01 M, $[B]_{total}$ = 0.2 M) [b]
2.05 ± 0.17	**2.69 ± 0.17**	**average of log β_{EuBL} from all methods**

Eu(III)-lactatoborate		
2.50 ± 0.69	3.14 ± 0.69	PARAFAC ($[lactate]_{total}$ = 0.01 M, $[B]_{total}$ = variable) [c]
3.06 ± 0.45	3.70 ± 0.45	PARAFAC ($[lactate]_{total}$ = 0.01 M, $[B]_{total}$ = variable) [d]
1.94 ± 0.22 to 2.18 ± 0.26	2.58 ± 0.22 to 2.82 ± 0.26	^{11}B NMR ($[lactate]_{total}$ = 0.005 M, $[B]_{total}$ = 0.2 M) [c]
2.37 ± 0.26 to 2.61 ± 0.15	3.01 ± 0.26 to 3.25 ± 0.15	^{11}B NMR ($[lactate]_{total}$ = 0.005 M, $[B]_{total}$ = 0.2 M) [d]

[a] extrapolation to infinite dilution according to Davies approach [DAV1962]; [b] fixed parameters for data analysis: $pK_{a,Sal}$= 2.83, log K_{BSal} = 1.10, log β_{EuSal} = 2.10; [c] fixed parameters for data analysis: $pK_{a,Lac}$ = 3.73, log K_{BLac} = 0.57, log β_{EuLac} = 2.51 [BAR2014], log β_{EuLac2} = 4.45 [BAR2014]; [d] fixed parameters for data analysis: p$K_{a,Lac}$ = 3.73, log K_{BLac} = 0.57, log β_{DyLac} = 3.09 [GOU1966], log β_{DyLac2} = 5.38 [GOU1966]

Obviously, the Eu(III) complexation with lactatoborate seems to be somewhat stronger than with salicylatoborate. Taking into account the uncertainties, the complexation constants of both EuBSal and EuBLac are in the range log β^0_{EuBL} = 2.6 to 3.3. Higher deviations are a result from the high complexity of the systems combined with the uncertainties of the equilibrium constants. The ring size of the organoborate and the organic moieties bound to the "$B(OR)_4^-$" unit seem to have only a small influence.

The complexation constants of the studied Eu(III)-organoborate complexes are well comparable to those of the Eu(III)-(poly)borate complex (see chapter 3.4.2). This confirms the initial hypothesis (see chapter 3.1): Borates with the "$B(OR)_4^-$" unit (one binding site) exhibit a similar complexation behavior with respect to trivalent lanthanides (and actinides) regardless if R is an organic or inorganic function.

The Eu(III)-salicylatoborate complexation decreases with increasing ionic strength up to I_m = 3 m (NaCl), Fig. 3.32. This is in agreement with the results from the Eu(III)-(poly)borate complexation system (see chapter 3.4.2).

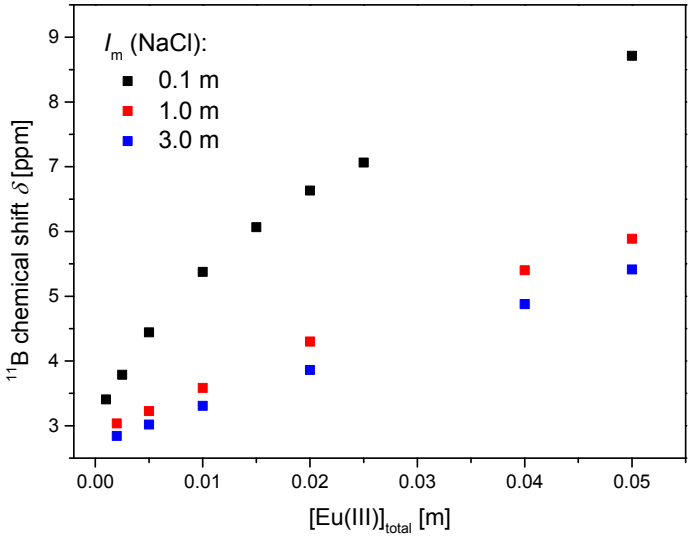

Fig. 3.32: *^{11}B chemical shift of salicylatoborate as a function of $[Eu(III)]_{total}$; solutions: $[salicylate]_{total}$ = 0.01 m, $[B]_{total}$ = 0.2 m, $[Eu(III)]_{total}$ = variable, I_m = variable, pH_c = 5, ^{11}B chemical shift corrected according to [SCH2015].*

3.5.3 Speciation calculations in the Eu(III)-salicylate/lactate-B(OH)$_3$ system

Speciation distributions for the Eu(III)-salicylate/lactate-B(OH)$_3$ system are calculated as a function of pH and [organics]$_{total}$, Fig. 3.33 and Fig. 3.34. With increasing [ligand]$_{total}$ the Eu(III)-(poly)borate complexation is consequently supressed by the Eu(III)-salicylatoborate /Eu(III)-lactatoborate and Eu(III)-salicylate or Eu(III)-lactate complexation.

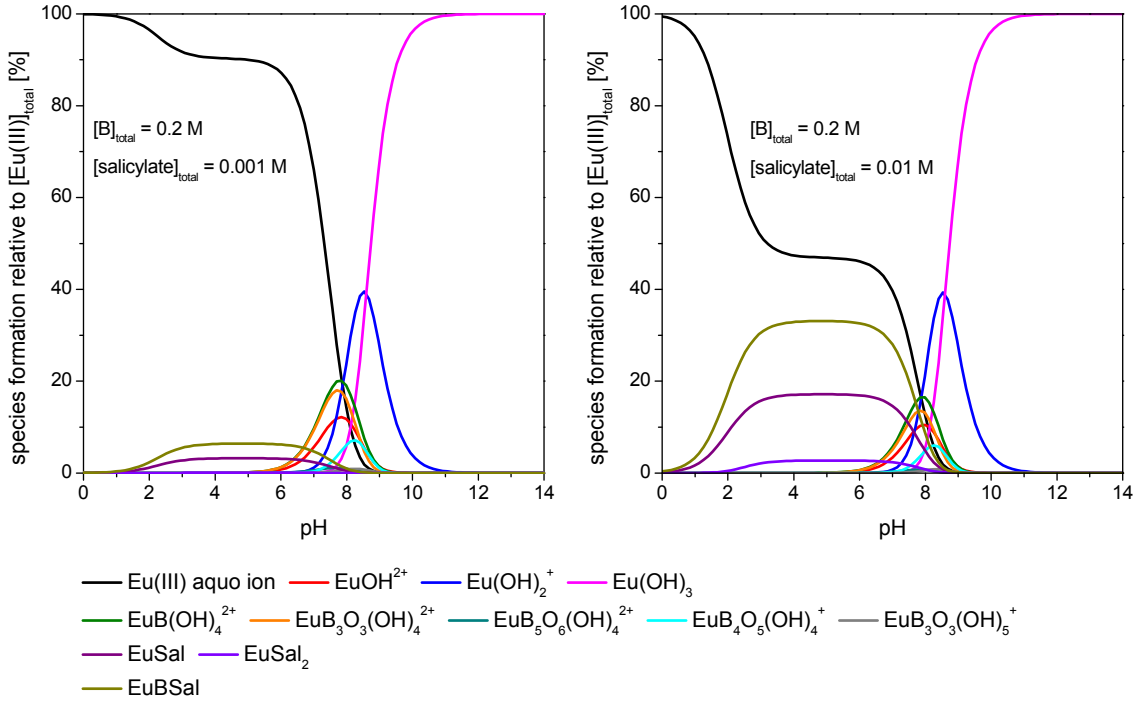

Fig. 3.33: Speciation for the Eu(III)-salicylate-$B(OH)_3$ system as a function of $[salicylate]_{total}$ and pH (carbonate-free system), $[Eu(III)]_{total} = 3 \cdot 10^{-5}$ M, I = 0.1 M ($NaClO_4$). Application of log β_{EuBSal} = 2.0, and log β_{EuB} = 2.0 (primarily valid for Eu(III) complexes with borate ligands having one binding site) for all the Eu(III)-(poly)borate complexes, although there are Eu(III) complexes with borate ligands having two binding sites

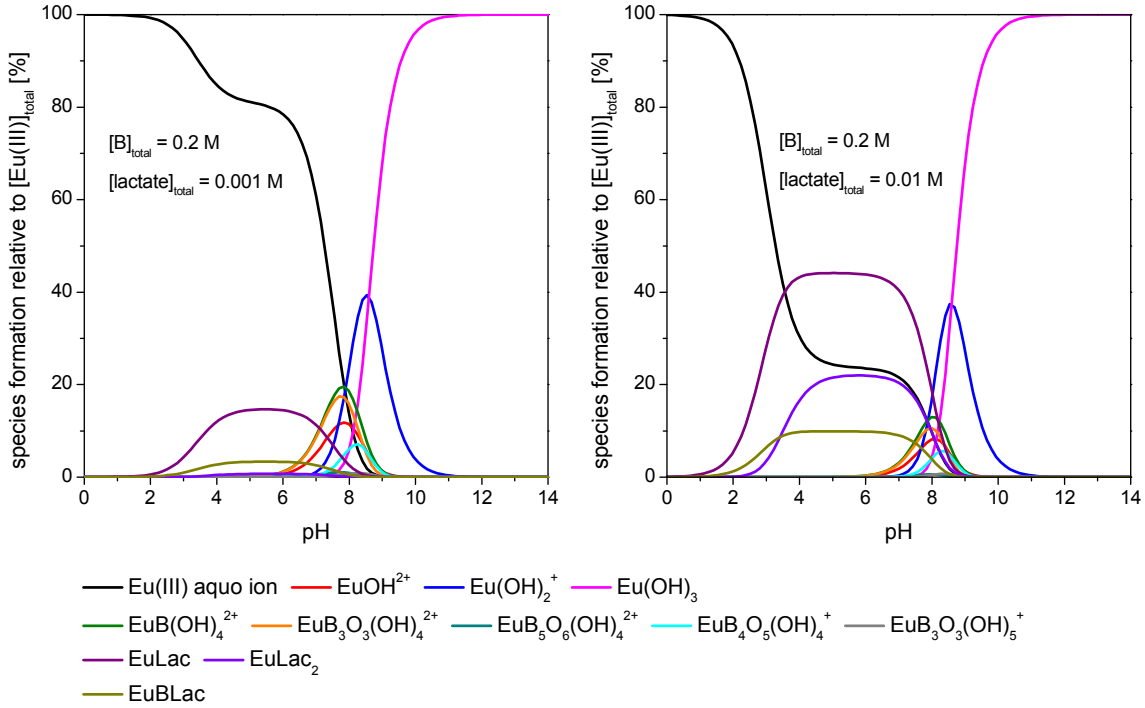

Fig. 3.34: Speciation for the Eu(III)-lactate-$B(OH)_3$ system as a function of $[lactate]_{total}$ and pH (carbonate-free system), $[Eu(III)]_{total} = 3 \cdot 10^{-5}$ M, I = 0.1 M ($NaClO_4$). Application of log β_{EuBLAc} = 2.0, and log β_{EuB} = 2.0 (primarily valid for Eu(III) complexes with borate ligands having one binding site) for all the Eu(III)-(poly)borate complexes, although there are Eu(III) complexes with borate ligands having two binding sites

3.5.4 Influence of organics on the Eu(III)-borate precipitation

The precipitation of the Eu(III)-borate occurs even in presence of salicylate (Fig. 3.35a) and lactate (Fig. 3.35b). Obviously, up to $[ligand]_{total}$ = 0.002 M in both systems the presence of salicylate and lactate has no influence on the progress of the precipitation; it is as fast as in absence of the organic ligands. Only in presence of $[lactate]_{total}$ = 0.02 M the Eu(III)-borate precipitation is somewhat retarded.

There is a hint that the dissolved Eu(III) in the Eu(III)-salicylate-$B(OH)_3$ system is not completely converted into the Eu(III)-borate precipitate: For $[salicylate]_{total}$ = 0.02 M a second presumably dissolved Eu(III) species is detected besides the Eu(III) bound in the Eu(III)-borate precipitation. Remarkably, a dissolved species was not identified for the lactate system. It is yet unclear, whether the salicylatoborate and lactatoborate species can be incorporated as ligands (i.e., to substitute borate ligands) in the Eu(III)-borate precipitation. It might be assumed that the "$B(OR)_4^-$" unit is blocked by the organic moiety so that an incorporation is less likely.

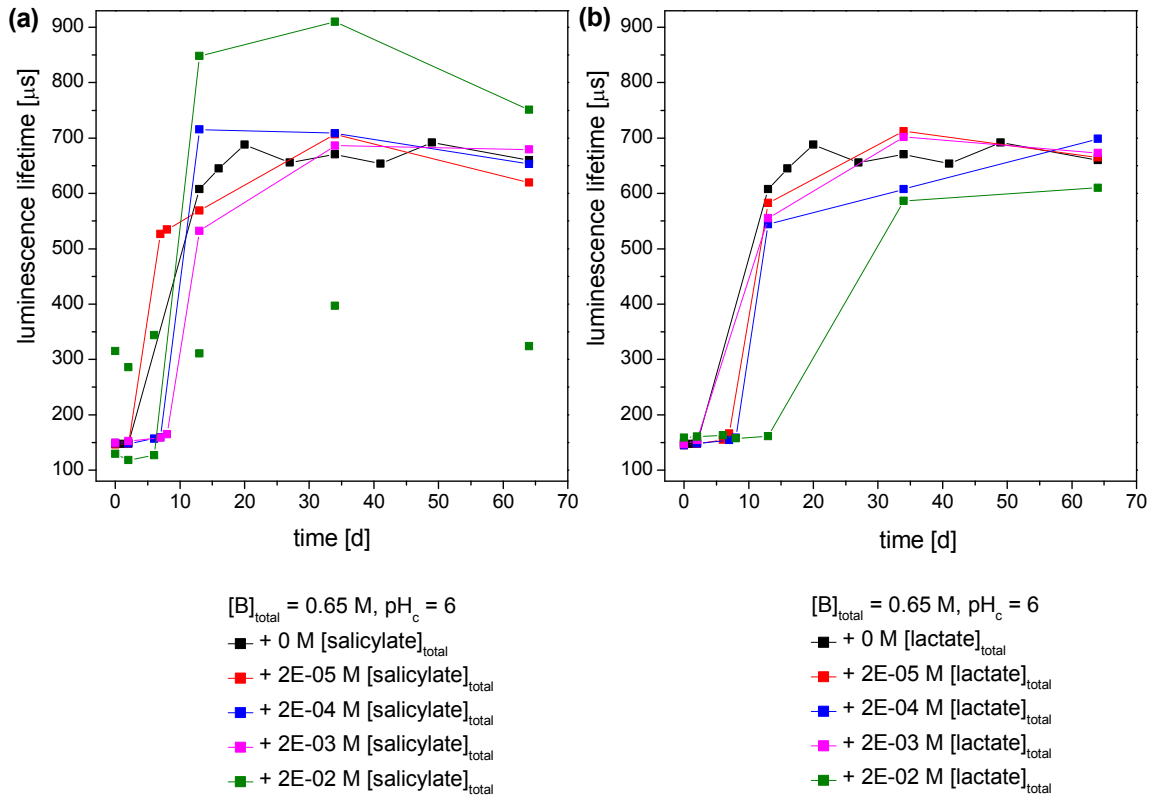

Fig. 3.35: Eu(III)-borate precipitation progress as a function of $[ligand]_{total}$, solution: $[Eu(III)]_{total} = 3 \cdot 10^{-5}$ M, $[B]_{total}$ = 0.65 M, $[ligand]_{total}$ = variable, pH = 6, I = 0.1 M ($NaClO_4$)

3.6 Summary

Borate compounds will be a part of the inventory of a nuclear waste repository. Borate sources are, for instance, glass coquilles for high-level radioactive waste, cementitious waste packages or naturally borate compounds in rock salt. Thus, the interactions of borate compounds with actinides are of general interest in the identification and characterization of mobilization pathways of radionuclides in the context of the safety and risk assessment for a future nuclear waste repository.

Until now, the interaction between actinides and borate species is investigated insufficiently. In the present work the interaction of Eu(III) as inactive analogue for trivalent actinides with borate species was thoroughly investigated for the first time. In addition, first spectroscopic studies were performed with the actinides Am(III) and Cm(III).

Starting from the assumption that all borate species with a „$B(OR)_4^-$“ unit have a similar and comparable complexation behavior towards Eu(III) two different approaches were chosen to study this Ln(III)/An(III)-borate system. For the first approach inorganic polyborate species and for the second approach organoborates (salicylatoborate and lactatoborate) were used. Both methods allowed the investigations in the weakly acidic pH range. Competing reactions, such as the strong hydrolysis of the An(III)/Ln(III), were avoided.

As a prerequisite for the complexation investigations the borate speciation and the formation of polyborate species in solution were studied with ^{11}B NMR spectroscopy at pH_c 5 and pH_c 6. The experimental determined amount of polyborate species (~ 2 %) agrees well with the calculated amount using polyborate formation constants from literature. Furthermore the formation of organoborates (salicylatoborate and lactatoborate) were studied by ^{11}B NMR spectroscopy and their formation constants were determined ($\log \beta^0_{BSal}$ = 1.10 ± 0.14, $\log \beta^0_{BLac}$ = 0.57 ± 0.22).

For the complexation studies different spectroscopic techniques were applied, mostly time-resolved laser-induced fluorescence spectroscopy (TRLFS) and ^{11}B NMR spectroscopy.

Generally, a 1:1 Eu(III)-borate complex ($EuB(OR)_4^{2+}$) with a complexation constant in the range of $\log \beta^0$ = 2.6 to 3.3 was determined (independent from the borate species). This range is also applicable for the complexation constant for a 1:1 An(III)-(poly)borate complex (An(III) = Am(III), Cm(III)). That means, the Ln(III)/An(III)-borate complexation is weak compared, for instance, to the strong hydrolysis reaction.

From complexation studies as function of ionic strength the specific interaction coefficients of the Eu(III)-polyborate complex species in NaCl and $NaClO_4$ medium were derived from SIT approach with $\varepsilon(EuB(OR)_4^{2+}, ClO_4^-)$ = 0.31 ± 0.05 kg·mol^{-1} (with corresponding log $\beta^0_{(NaClO4)}$ = 3.17 ± 0.2 and $\Delta\varepsilon$ = -0.11 ± 0.05 kg·mol^{-1}) and $\varepsilon(EuB(OR)_4^{2+}, Cl^-)$ = 0.025 ± 0.04 kg/mol (with corresponding $\beta^0_{(NaCl)}$ = 3.12 ± 0.21 and $\Delta\varepsilon$ = -0.13 ± 0.05 kg·mol^{-1}).

A complexation constant of log β^0_{EuBSal} = 2.69 ± 0.17 was determined for the Eu(III)-salicylatoborate complex and a range of the complexation constant log β^0_{EuBLac} from 2.58 to 3.25 was estimated for the Eu(III)-lactatoborate complex depending on the used complexation constants of the Eu(III)-lactate complexes in the analysis.

In the Eu(III)-polyborate system a Eu(III) precipitation was observed at pH_c 6 and studied by means of (solid-state site-selective) TRLFS, IR- and solid-state ^{11}B NMR spectroscopy. At low Eu(III) concentrations ($3\cdot10^{-5}$ m) this Eu(III)-borate precipitate forms within days to weeks depending on $[B]_{total}$ and the medium (background electrolyte, ionic strength). The higher $[B]_{total}$ and the Eu(III) concentration the faster is the precipitation. An effect of the presence of organics (salicylate, lactate) on the precipitation progress was not detected up to $[organics]_{total}$ = $2\cdot10^{-3}$ M. For $[lactate]_{total}$ = $2\cdot10^{-2}$ M a delay of the Eu(III)-borate precipitation progress and for $[salicylate]_{total}$ = $2\cdot10^{-2}$ M an incomplete conversion of the dissolved Eu(III) into the solid were observed. The Eu(III)-borate solid phase is long-term stable at pH_c 6, but dissolves increasingly with decreasing pH.

The isolated Eu(III)-borate solid was amorphous. Hence, structural information from X-ray diffraction was not obtainable. The analysis of the solid-state ^{11}B NMR spectrum of a La(III)-borate solid (structural similarity to the Eu(III)-borate solid confirmed with IR spectroscopy) reveals a ratio of the fourfold coordinated to the threefold coordinated boron environments of 3:1 in the borate ligand. Unfortunately, from this information no concrete structure of the borate ligand around La(III) was deducible. However, the high amount of fourfold coordinated boron environments suggests a high(er) grade of condensation of the borate structure.

More detailed investigations of the Eu(III)-borate solid by using solid-state site-selective TRLFS revealed three Eu(III) solid species. Luminescence spectrum and luminescence lifetime of two species are quite similar. They are assigned to the Eu(III)-borate species. Both species occur in equal parts if the Eu(III)-borate solid is precipitated at low ionic strength (0.1 m $NaClO_4$/NaCl), whereas high(er) ionic strengths (1 m or 3 m $NaClO_4$/NaCl) favors the

formation of only one of these species. The IR spectra of the Eu(III)-borate solids precipitated at different ionic strengths and electrolytes are almost identical. Hence, a high structural similarity of these two species can be expected. Differences are possible in the content of structural water, grade of condensation of the borate ligand or long-range order in the solid. The luminescence spectrum and luminescence lifetime of the third species differ significantly from that of the other species. Possibly, the third species is a primary stage of the completely formed Eu(III)-borate solid.

4 Thermodynamic studies on complexation of trivalent lanthanides and actinides with low molecular ligands

4.1 Motivation

In the far field of a nuclear waste disposal in deep geological formations the migration of actinides may be affected by natural organic matter (NOM). In salt formations as potential host rock humic substances (and their low molecular degradation products) originating from the overlying rock must be considered as strong complexing and mobilizing dissolved organic ligands [ART2000, SCHÄ2005]. In Clay formations that are also considered as host rocks (for instance Opalinus Clay, Callovo Oxfordian) dissolved organic matter has been detected in considerable amounts in the pore water. This organic matter shows a very heterogeneous composition - large and complex molecules such as humic and fulvic acids or kerogens as well as low molecular ligands like formate, acetate, propionate or lactate. All these compounds represent a large fraction of the dissolved organic carbon (DOC) in Clay formations (Opalinus Clay: 36%, Callovo Oxfordian: 88%) [COU2007 a, b].

The understanding of the binary system actinide-organic ligand and the thermodynamic quantification of the complex formation is of great importance to simulate and predict the mobilization of actinides by dissolved organic matter. Reliable enthalpy values in dependence of ionic strength are very important for modelling of the temperature influence of actinide/lanthanide speciation and thus their migration, because in the near field of nuclear waste disposal higher temperatures are predicted, for instance, in Clay formation up to 100°C [JOH2002].

Thus far, existing thermodynamic data for the binary system trivalent actinide/lanthanide-organic ligand exhibit large discrepancies are incomplete, or even completely missing. Furthermore, available data were obtained for restricted conditions only, e.g. for one temperature or one ionic strength. Systematic studies under variations of the ionic strength and temperature are still missing particularly for complex formation enthalpies, for which results are found only sparsely in the literature (cf. literature review in chapters 4.3.1, 4.4.1 and 4.5.1 for the selected ligands).

In the last two decades significant efforts were made and a considerable amount of thermodynamic data for the interaction of actinides with small organic ligand have been published [HUM2005, HUM2007, examples for trivalent actinides: CER2005, CHO1996, MAT2007, MOO1999, THA2009]. However, there was still a lack of systematic studies

concerning these interactions at function of ionic strength and temperature which is now being closed by the activities in this BMWi Joint Project particularly for Cm(III)/Am(III) systems: see [BAR2014, FRÖ2013, FRÖ2014, FRÖ2015a, SKE2014]. Due to the similarity of their chemical properties several studies with non-radioactive trivalent lanthanides were published. [BAR2013, TIA2010, XIO2011, see also ref. in chapters 4.3.1, 4.4.1 and 4.5.1]

One reason for discrepancies in published thermodynamic data might be the use of different experimental methods. Indirect methods like potentiometric measurements, solvent extraction, or solubility studies are methods that influence the chemical equilibrium while direct spectroscopic methods, such as fluorescence or absorption spectroscopy allows the study of an equilibrium without disturbance. A second reason for possible discrepancies is, that it is difficult to determine enthalpies of acceptable uncertainties from the temperature dependency of the complexation constants for systems with weak complex formation and/or weak heat evolution. The temperature dependent constants results in large scatter in the van't Hoff plot and produce inconsistent data.

More reliable data are obtained by direct measurements of the reaction enthalpy by micro-(titration) calorimetry. [RAO2007] Thus, the primary goal of this work was to establish the isothermal micro-titration calorimetry to study lanthanide/actinide-ligand interactions. This work was focused on fundamental micro-titration calorimetric investigations of the complexation reactions of the inactive trivalent analogs Nd(III) and Eu(III) with i) relevant small organic ligands that serve as model ligands for dissolved low molecular clay organics and ii) more complex ligands, like humic substances. The selected ligands are shown in Fig. 4.1.

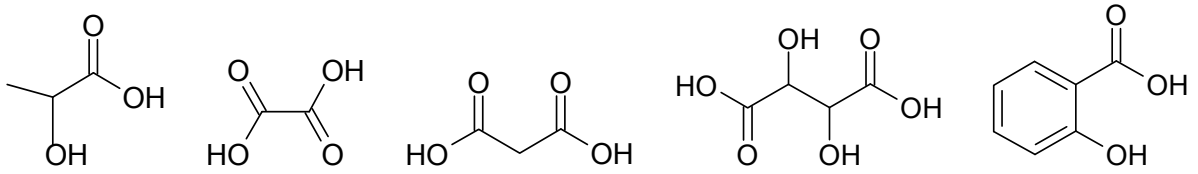

Lactic acid Oxalic acid Malonic acid Tartaric Acid Salicylic acid

Fig. 4.1: Selected ligands

Lactic, oxalic, malonic and tartaric acid serve as ligands for low molecular organics in clay rocks. Oxalic, malonic and tartaric acid are dicarboxylic acid and differ by their carbon chain length. Tartaric acid, like lactic and salicylic acid have an additional hydroxyl group in the α-

position which can be involved in complexation. The salicylic acid stands for a typical model ligand for humic acids.

Due to limitations of the isothermal micro-titration calorimeter used (see chapter 4.2.1) the studies were limited to ligands that have complex stability constants with trivalent actinides/lanthanides larger than log $K_1^0 \sim 2.8$. The calorimetric studies were completed by spectroscopic investigations using mainly fluorescence and absorption spectroscopy for selected ligands. Eu(III) is suitable for fluorescence investigations due to its very good luminescence properties, whereas for Nd(III) the absorption spectroscopy is more common [TIA2010].

The objective of our studies was the generation of a complete set of thermodynamic standard data ($\log K_n^0$, $\Delta_r G^0$, $\Delta_r H^0$, $\Delta_r S^0$) including the sum of interaction coefficients ($\Delta\varepsilon$) and the resultant specific ion interaction coefficients ε(j,k) of the individual species in the complexation of Nd(III) and/or Eu(III) with the selected organic ligands. Conditional stability constants and formation enthalpies were determined over a wide range of ionic strength (up to 3 molal) to generate a consistent data set that was used for SIT approach (specific ionic interaction theory, cf. chapter 2.2) to extrapolate the thermodynamic data at infinite dilution.

In the following chapters we present the results in detail for lactic, oxalic, and malonic acid. Unfortunately, micro-titration calorimetric measurements were not feasible with tartaric and salicylic acid. In the case of tartaric acid no measurable evolution of heat during complexation reaction was observable at all investigated ionic strengths and concentrations. For salicylic acid the complexation constants with Eu(III)/Nd(III) were too small to be measured. In spite of that, the complexation behavior of these both ligands were spectroscopically determined [BAR2013 for salicylic acid, MÜL2016 for tartaric acid], however, these results are not presented in detail in this report.

4.2 Methods

4.2.1 Isothermal micro-titration calorimetry

Introduction

During the late 1980s, isothermal micro-titration calorimetry (ITC) was developed and first introduced to biochemistry as a new method [FRE1990]. Since then, the method is widely used in various research areas, including radiochemistry.

Isothermal titration calorimetry is a method that provides a direct access to enthalpy values and equilibrium constants in one experiment which is an advantage compared to other methods like potentiometry, distribution methods, or spectroscopy. Nevertheless, the complexation constants determined by other methods are often used as fixed values in the evaluation of the calorimetric heat curve with respect to the enthalpy. This leads a more stable curve fitting and to a minimization of the uncertainty of the derived thermodynamic parameter. In the last few years, the titration calorimetry has been applied successfully to complexation reactions of actinides and lanthanides in aqueous solutions for the direct determination of reaction enthalpies [ZAN2001, RAO2002+2005+2007, JEN2001, JIA2002, and KIT2006]. Most of the publications are carried out at elevated temperatures to model the high temperatures in a nuclear waste repository [JIA2002, RAO2002+2007, ZAN2004]. Ionic strength dependencies of complexation reactions (of stability constants and enthalpies) have also been investigated to a lesser extent.

Theory

An isothermal calorimeter measures the heat flow as a function of time at a fixed temperature. Each titrant addition is observed as a heat pulse in the thermogram (in $\mu cal \cdot s^{-1}$ or $\mu J \cdot s^{-1}$) (Fig. 4.2). The integration of the signals gives the heat released or absorbed ($Q_{r,p}$) by the stepwise addition of a ligand molecule to a solution containing the metal ion under study.

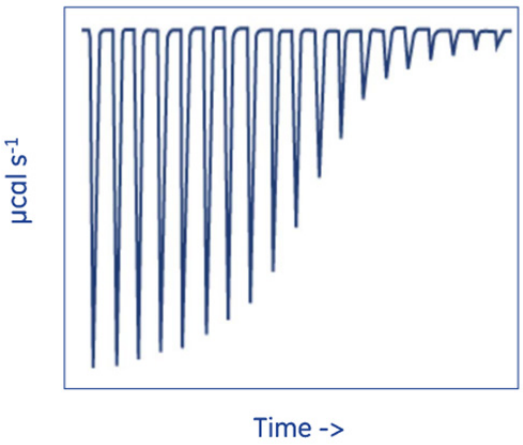

Fig. 4.2: Thermogram of a simulated reaction

The model that describes the ongoing reactions in the considered system is composed of the individual chemical reactions, the associated equilibrium constants as well as the mass and heat balance equations [EAT1985]. Equations 4.1 to 4.4 reflect the basis for titration calorimetry [FRE1990, RAO2006, HAN2011]. The net reaction heat $Q_{r,p}$ is a function of the enthalpy of the reaction and the number of moles $\Delta n_{p,j}$ of the *j*th reaction product at point p, $\Delta n_{p,j}$ is again a function of the cell volume, the concentrations of the components and the equilibrium constants of all reactions taking place in the reaction vessel (Eq. 4.2 and 4.3). If the stability constant(s) of the reaction(s) is (are) known, Eq. 4.4 is linear and the calculation of the complexation enthalpy is obtained by fitting the experimental to calculated heat curve using the least square method.

$$Q_{r,p} = \sum_j (\Delta_r H_j \cdot n_{p,j}) \qquad 4.1$$

$$Q_{r,p} = V \cdot \sum_j \Delta_r H_j \cdot [L_{B,j}] \qquad 4.2$$

$$[L_{B,j}] = [\mathrm{M}] \cdot \frac{\mathrm{n}_j K_j [L]}{1 + K_j [L]} \qquad 4.3$$

$$U(K_j, \Delta_r H_j) = \sum_{p=1}^{m} (Q_{r,p} - \sum (\Delta n_{p,j} \cdot \Delta_r H_j))^2 \qquad 4.4$$

$Q_{r,p}$ *...reaction heat at titration step p*
$n_{p,j}$ *...number of moles of the species j at the titration step p*
$\Delta_r H_j$ *...molar reaction enthalpy of the species j*
$L_{B,j}$ *...concentration of bound ligand to binding sites of set/species j*
V *...reaction volume*
M *...total concentration of macromolecule*
K_j *...assoziation constant for binding sites of set j*
n_j *...number of binding sites of set j*
U *...least squares, should be minimized*

If the complex formation constants are unknown, Eq. 4.4 becomes nonlinear expression and must be solved by an iterative technique [CHR1972, HAN2011].

Setup and principle of our isothermal titration calorimeter

The calorimetric titration experiments were performed with an isothermal titration calorimeter iTC_{200} from Malvern Instruments, Worcestershire, UK. The calorimeter is equipped with a sample cell containing the analyte solution and a reference cell that is filled with a reference solution (usually water). Both cells have a very small volume of 200 µl. The titrant is injected automatically in the sample cell via a syringe that is also used to stir the sample solution continuously. Throughout each measurement a total volume of 40 µL of the titrant solution can be added, mostly in steps of 1-2 µL. Both, the sample and reference cells are tempered to the preset temperature (2-80°C) and the differential power (DP, $\mu cal \cdot s^{-1}$ or $\mu J \cdot s^{-1}$) that is expended to maintain temperature equilibrium between the cells is recorded continuously throughout the calorimetric titration. The injection of the ligand leads to a rapid increase or decrease of the differential power signal due to the release or uptake of heat by the chemical reaction. The DP signal subsequently returns to the ground level as soon as the temperature difference between sample and reference cell is compensated. The next injection can be done if the DP signal is at a constant level. The time interval between the injections is adjustable (usually between 120-300 s). Thus, the result of a calorimetric titration is a thermogram displaying the DP signal versus time (cf. Fig. 4.2), which is characterized by either positive or negative heat pulses accompanying the injections. The integration of the heat pulses over time results in the overall experimental heats Q_{exp} for each titration step, which is composed of the reaction heats $Q_{r,p}$ and the heats of dilution of the titrant and mechanical effects, designated as Q_{dil}.

The dilution heat is determined separately by titration of the titrant into the background medium. The calorimeter is calibrated at least once a week by measuring the enthalpy of a water-water-titration and once a month by performing a Ca^{2+}-EDTA-titration, a widely used reference calibration system.

Data analysis

The thermograms are integrated using the MicroCal Origin Package (Vers. 7.2, *OriginLab*, Northhampton, MA, USA). The integrated heat curves are corrected for the dilution heat

($Q_{dil,p}$). The net reaction heat at the point p ($Q_{r,p}$) is obtained from the difference $Q_{r,p} = Q_{exp} - Q_{dil,p}$.

For the analysis and the determination of thermodynamic parameters from the calorimetric titration curves two programs were used: LETAGROP [ARN1970] and HypΔH. LETAGROP was used for the lactate protonation and Eu-lactate complexation reactions and HypΔH [GAN2008] was applied for the malonate and oxalate reactions. The programs allow the set-up of a chemical model with either unknown or known stability constants. The formation enthalpies are determined non-iteratively from the heat curves by least-squares fitting. In the case where stability constants are estimated, they were fitted iteratively by a non-linear least-squares regression. A detailed description of the simultaneous calculation of $\Delta_r H$ and $\log K$ is published in [CHR1972 and GAN2008].

For the protonation reactions of the ligands, the thermodynamic values of the autoprotolysis of water were fixed and in some cases the equilibrium constants for the protonation were fixed as well (for instance in case of lactate) in the chemical model of the fitting program.
For the complexation reaction, the thermodynamic values of the autoprotolysis water and the ligand protonation were fixed as known values.

Limitations of ITC experiments

The magnitude of the enthalpy and the stability constant as well as the number of reactions that can be determined within an ITC experiment is set by the calorimeters design (that basically means volume of the vessel and limit of the dynamic range of the DP signal).
The shape of the heat curve is a function of the equilibrium constants and can be very different depending on the number of the occurring equilibrium reactions. In Fig. 4.3 a calorimetric titration of pyromellitate (1, 2, 4, 5 benzenetetracarboxylate) with HCl is shown. The enthalpy values of three protonation steps could be determined from these curves.
It is important for the analysis of the heat curves that at the end of the calorimetric experiment the heat evolution of the reaction tends to zero.

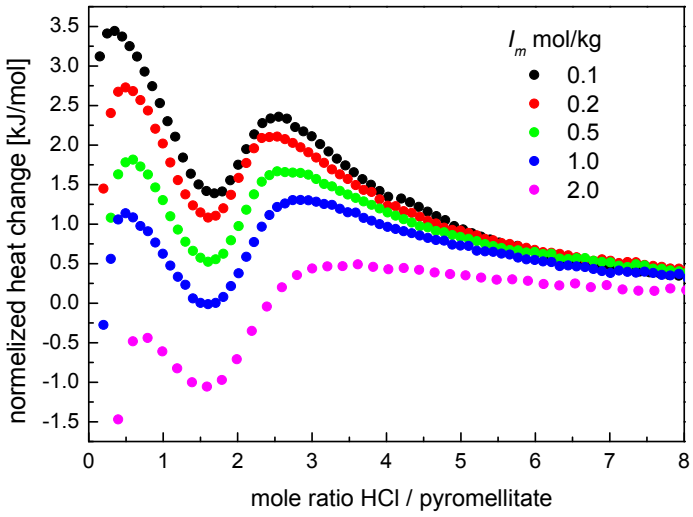

Fig. 4.3: Normalized heat change for titration of 4 mM Na-pyromellitate with 0.2 M HCl at different ionic strength in NaCl medium (T = 25°C, pH_{start} = 6, carried out with iTC_{200})

Generally, for a 1:1 complex or single protonation reaction a S-shaped curve is expected. This S-shaped curve can be described by the so called C-value (Eq. 4.5). The derivation of the C-value is given in [HAN2011].

$$C = K_{11} \cdot [M]_0 \qquad 4.5$$

The stability constant depends only on the curvature and is extracted from the slope of the S-shaped heat curve. The heat change is equal to the difference of magnitude of the heat curve at the beginning and the end of the titration, and the stoichiometry of the reaction is equal to the turning point.

In Fig. 4.4 simulated heat curves with different C-values, i.e. different metal concentrations and fixed stability constant are shown. The heat curves with C-values between 5 and 500 possess an ideal S-shape which is very important for the analysis. Heat curves around 1 and 1000 are still acceptable for a good analyzation. If the C-value is too low (C < 1), the curves don't show a S-shape, i.e. a pronounced slope which can be fitted properly and if the C-value is too high (C > 1000) the slope of the curve is too steep to fit the curves properly. That's why for complexation reactions which show $\log K$ values between ~3 and ~7, the initial metal concentration in a titration experiment with the iTC_{200} (V_0 = 200 µl) should be between 0.1 and 10 mM/l to derive reliable thermodynamic data from heat curves.

Generally one can deduce that, the lower $\log K$ values, the higher the $\Delta_r H$ values must be in order to calculate $\log K$ and $\Delta_r H$ with a given reliability.

The above remarks illustrate the limitation of the iTC_{200} and therefore often just the 1:1 complex of a reaction could be determined.

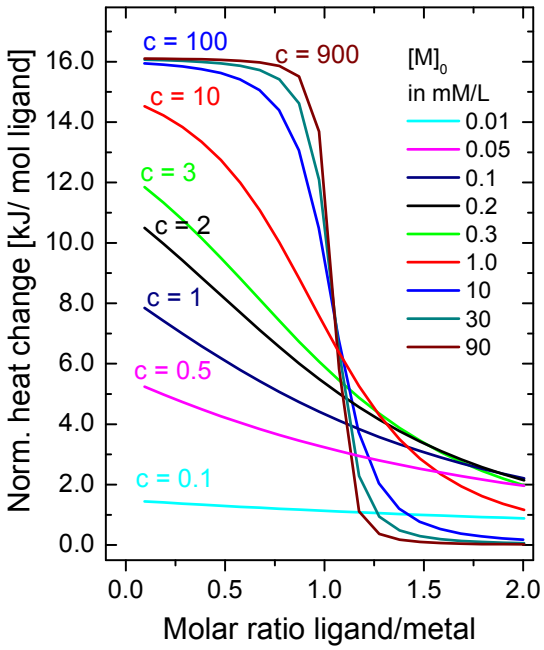

Fig. 4.4: *Simulated heat curves for our ITC_{200} with different C-values determined with log K_{11} = 4 and $\Delta_r H$ = 15 kJ·mol^{-1}, $[M]_0$ = 0.01- 90 mM/l, $[M]_0$:$[L]_0$=1:10, V_0 = 200 µl (iTC_{200})*

4.2.2 Additional spectroscopic methods

Time-resolved laser-induced fluorescence spectroscopy with Eu(III) and Cm(III)

The excitation wavelength of 394 nm (Eu(III)) or 396 nm (Cm(III)) was generated by a pulsed Nd:YAG-OPO laser system (Powerlite Precision II 9020 Laser, equipped with a Green PANTHER EX OPO from *Continuum*, Santa Clara, CA, USA). The luminescence is focused in a 90° angle into a glass fiber and detected through a multi-channel-analyzer (MCA). The MCA consists of an *Oriel MS 257* monochromator, a spectrograph with different grids and an *Andor iStar* ICCD-camera (*Lot-Oriel Group Europe*, Darmstadt). A constant time window was set to 1 ms. More details about the OPO system are described in [MOL2008]. The single parameters for europium and curium (stationary and dynamic measurements) are listed in Tab. 4.1.

Tab. 4.1: Parameter for stationary and dynamic fluorescence measurements (T = 25°C)

parameter	**Eu(III)**	**Cm(III)**
excitation-λ	394 nm	396 nm
pulse energy	2.8-3.1 mJ	2.8-3.1 mJ
grating	300/1200 mm^{-1}	300/1200 mm^{-1}
accumulation	300/2000	300/2000
λ-range	440-780 nm (dyn) 565-650 nm (stat.)	475-750 nm 567-640 nm

The **stationary luminescence spectra** were wavelength and baseline corrected with *OriginPro 8.6.0G* (*OriginLab*, Northhampton, MA, USA). The Eu(III) spectra were normalized to the peak area of the $^5D_0 \rightarrow {}^7F_1$ transition, which is not influenced by complexation due to its magnetic character. The Cm(III) spectra were normalized to the peak area. The stability constants were determined using the factor analysis program SPECFIT. Input parameters consisted of the total molar concentration of metal and ligand and the pK_a values of oxalate/lactate from literature. More information about the fitting algorithm and settings in SPECFIT are given in [GÜN2011 and BAR2013].

To validate the chemical model in SPECFIT, the standard deviation s_x (Eq. 4.6), the χ^2 value (Eq. 4.7), the Durbin-Watson-factor (DW factor, Eq. 4.8) and the relative fitting error (RE, Eq. 4.9) were used. The χ^2 value has an expected value of unity for random noise of a data series. The Durbin-Watson-factor gives hints about the autocorrelation of the residuals. The DW factor should lie between 1.6 and 2.4. A DW factor under 1.6 indicates self-correlation of the residuals which means that the chemical model has to be changed. The relative error (RE) should be less than 1 %.

$$s_x = \sqrt{\frac{\sum_{i=1}^{n}(x_i - \bar{x})^2}{(n-1)}} \qquad 4.6$$

s_x... estimated standard deviation
$\bar{x}$...average value
n...number of single values xi

$$\chi^2 = \sum_{i=1}^{N}\left[\frac{\{y_i - Y(x_i)\}^2}{\sigma_i^2}\right] \qquad 4.7$$

N...number of data points
Y_I...experimental values at the i-th abscissa point
$Y(x_i)$...calculated function at i-th abscissa point
σ_i^2...weighted average of the residuals of exp. data

$$DW = \frac{\sum_{t=2}^{N}(r_t - r_{t-1})^2}{\sum_{t=1}^{N}(r^2)} \qquad 4.8$$

DW…Durbin-Watson-factor
r…(Y_T-Y_t) residual
Y_T…experimental data point
Y_t…calculated data point
t…index of the data serie

$$RE = \sqrt{\frac{\sum_{i=1}^{N}(y_i - Y_i)^2}{\sum_{i=1}^{N} y_i^2}} \cdot 100\ \% \qquad 4.9$$

RE… relative fitting error
N…number of data points
γ_i…experimental value at i-th abscissa point
Y_i… calculated function at i-th abscissa point

Furthermore, a slope analysis according to the logarithmic mass action law (Eq. 4.10) was performed to validate the deconvoluted single spectra of the pure components from SPECFIT.

$$\log \beta_n + n \cdot \log c_{L(free)} = log\left(\frac{c_{ML_n}}{c_{M(free)}}\right), \qquad n = 1{,}2 \qquad 4.10$$

β_n…molar complex stability constant
n…stoichiometry coefficient
c_L…molar concentration of the free ligand
c_{MLn}…molar concentration of the complex
c_M…molar concentration of the free metal

The **time-resolved spectra** were measured in $10 - 20$ µs steps, and the lifetime was determined by fitting the integrated decay curves mono-exponentially according to equation 4.11 using OriginPro 8.6.0G (see also chapter 3.3.7).

$$I(t) = \sum_{i=1}^{n} I_{0,i} \cdot e^{-t/\tau_i} \qquad 4.11$$

I(t)…total luminescence at time t
$I_{0,i}$…starting intensity of the species I at time t=0
τ_i…lifetime of the species i

The number of water molecules in the first coordination shell of Eu(III) and Cm(III) were then calculated using the equation determined by [HOR1979] and [KIM1996] (Eq. 4.12).

$$n_{H_2O} \pm 0.5 = 1.07 \cdot \tau_{H_2O}^{-1}(ms) - 0.62 \text{ for Eu(III)} \qquad 4.12$$

and $$n_{H_2O} \pm 0.5 = 0.65 \cdot \tau_{H_2O}^{-1}(ms) - 0.88 \text{ for Cm(III)}$$

Using a few datasets of time-resolved spectra of Eu(III), a PARAFAC analysis was performed. This is a generalization of principal component analysis to higher orders [CAR1970,

HAR1970]. By including a 3rd dimension (e.g. time, wavelength and pH) and using constraints (unimodal and nonnegative constraints) a unique result can be derived characterizing individual species. Thereby the distribution of the species, the single luminescence spectra and the individual luminescence decays can be extracted for an estimated number of species in the sample. With the core consistency tool (included in the used N-way toolbox for Matlab [AND2000]) the number of species can be validated. A core consistency close to 100 % implies an accurate model [BRO2003]. Comparing PARAFAC to SPECFIT, PARAFAC is more accurate due to the inclusion of a 3rd dimension. The PARAFAC analysis was applied successfully to other systems before [DRO2015, SCHO2014, SAI2010,].

UV-vis measurements

Am(III) absorption spectra were recorded between 350 and 750 nm with 1000 accumulations using a Multi-channel spectrometer (Carl Zeiss MCS601, Jena, Germany) with a resolution of 0.8 nm/pixel. A Deuterium-Halogen-Light source DH-2000 (Avantes, Eerbeek, Netherlands) and 10 mm cuvette were used. Both were connected by fiber optics with the spectrometer. The Am(III) absorption spectra were analyzed using OriginPro 8.6.0G (OriginLab, Northhampton, MA, USA), baseline corrected and normalized to the peak area. The stability constants were determined using SPECFIT (see above)

4.3 Complexation with lactate

4.3.1 Literature study

Lactate is present as metabolite in all organisms and as decomposition product of humic substances in the pore water of clay layers [COU2007b]. Furthermore, lactic acid is used as a complexing agent in the separation process called TALSPEAK (Trivalent Actinide Lanthanide Separations by Phosphorus-reagent Extraction from Aqueous Complexes) [WEA1964, WEA1968] which is the first step in the partitioning and transmutation strategy of spent fuel.

Several publications have been published about the protonation of lactate (a selection is shown in Tab. 4.2). The protonation constants K_1^H were mostly determined in sodium perchlorate at different ionic strengths and temperatures. Interaction coefficients ($\Delta\varepsilon$ and ε(j,k)) have not been reported at all. It is obviously from Tab. 4.2 that the protonation

enthalpy decreases with increasing ionic strength. Furthermore, the few entropy data are always positive.

Tab. 4.2: Conditional stability constants, enthalpy and entropy values of lactate protonation in different media at 25°C

I_m / medium [mol·kg^{-1}]	log K_1^H	$\Delta_r H_1^H$ [kJ·mol^{-1}]	$\Delta_r S_1^H$ [J·mol^{-1}·K^{-1}]	Ref./ method
0	3.86 ± 0.2	0.43		MAR1937, a
0	3.86 ± 0.05			HOI1975, a
0.10 KNO_3	3.64 ± 0.05	2.9 ±0.2	79 ± 1	PIZ1994, b
0.10 $NaClO_4$*	3.69 ± 0.01			GAJ2001, b
0.10 $NaClO_4$	3.73 ± 0.01			SCHO2015, b
0.10 $NaClO_4$	3.62			PAA1988, b
0.10 $NaClO_4$	3.77			EBE1969, b
0.15 NaCl	3.50 ± 0.2			GLA1993, e
0.51 NaCl	3.48 ± 0.2			ASC1970, b
0.61 NaCl	3.55 ± 0.2			MAR1986, b
1.05 $NaClO_4$		-0.56 ± 0.02		Zal2010, c
1.00 NaTf*	3.65 ± 0.02	-1.48 ± 0.04	65 ± 1	Zal2010, c
1.02 NaCl	3.53			KOS1978, e
1.05 $NaClO_4$	3.57 ± 0.02			LUN84, d
1.05 $NaClO_4$	3.59 ± 0.03	-0.55 ± 0.22	68 ± 1	TIA2010, b,c
2.21 $NaClO_4$		-0.98 ± 0.02		ZAL2010, c
2.21 $NaClO_4$	3.65 ± 0.05			KRU76, b

a…conductivity, b…potentiometry, c…titration microcalorimetry, d…solvent extraction, e…coulometry, *…in molar scale (no conversion factors available)

Several stability constants have been published for the Eu(III)- and Am(III)-lactate complexation at different ionic strengths, determined by potentiometry and solvent extraction methods (cf. Tab. 4.3). Only very few publications report values for Cm(III)-lactate. The available literature values of Ln(III)/An(III)-lactate complexation enthalpies shows a weak exothermic reaction at higher ionic strength (> 1 mol·kg^{-1}) and a weak endothermic reaction at low ionic strength (cf. Tab. 4.4). Systematic investigations of the complexation constants and enthalpies as function of the ionic strength have not been reported until now. The background electrolyte sodium chloride which is the main constituent in clay formation waters [KIE2003, BGR2007, and HER2006] had been considered very scarcely.

Tab. 4.3: Selected stability constants for the complexation of lactate with An(III)/Ln(III) in different media at 25°C

Ln(III)/ An(III)	I_m / medium [mol·kg^{-1}]	log β_{11}	log β_{12}	log β_{13}	Ref./ method
Eu	0.10	2.51 ± 0.13	4.45 ± 0.12	5.83 ± 0.18	BAR2014, a, p.w.
Eu	0.20	2.55 ± 0.05	4.67 ± 0.06	5.55 ± 0.18	DEE1964, b
Eu	1.02 NaCl	2.94	4.38	5.44	DAN1982, b
Eu	1.05 $NaClO_4$	2.44 ± 0.09	4.24 ± 0.25	5.80 ± 0.10	LUN1984, b
Eu	1.05 $NaClO_4$	2.78 ± 0.02	4.72 ± 0.02	6.27 ± 0.02	TIA2010, a,c
Eu	2.21 $NaClO_4$	2.48 ± 0.2	4.50 ± 0.2	5.73 ± 0.2	CHO1961, c
Eu	2.21 $NaClO_4$	2.43 ± 0.2	4.46 ± 0.2	5.67 ± 0.2	AZI1971, b
Nd	1.00 NaTf*	2.63 ± 0.06	4.44 ± 0.05		ZAL2010, c
Nd	1.05 $NaClO_4$	2.60 ± 0.06	4.52 ± 0.05	6.02 ± 0.06	TIA2010, a,c
Nd	2.21 $NaClO_4$	2.40 ± 0.2	4.29 ± 0.2	5.29 ± 0.2	BUK1981, a
Am	0.10 $NaClO_4$	2.27 ± 0.05	4.50 ± 0.30	6.30 ± 0.30	BAR2014, a
Am	1 M NaTf*	2.68 ± 0.04	4.93 ± 0.06		ZAL2010, c
Am	1.05 $NaClO_4$	2.41 ± 0.2	4.19 ± 0.2	5.58 ± 0.2	LUN1984, b
Am	2.21 $NaClO_4$	2.47 ± 0.2	4.67 ± 0.2	5.83 ± 0.2	AZI1971, b
Cm	1.05 $NaClO_4$	2.96			KOS1980, b
Cm	1.5 M KCl	2.59 ± 0.2	4.29 ± 0.2		SAK1972, d [#]

a…spectroscopy, b…solvent extraction, c…potentiometry, d…electrophoresis, [#]…at 10°C, *…in molar scale (no conversion factors available), p.w…present work

Tab. 4.4: Selected reaction enthalpy and entropy values for the 1:1 complexation of lactate with An(III)/Ln(III) in different media at 25°C

Ln(III)/ An(III)	I_m / medium [mol·kg^{-1}]	$\Delta_r H_1$ [kJ·mol^{-1}]	$\Delta_r S_1$ [J·mol^{-1}·K^{-1}]	Ref. / method
Eu	0.10 $NaClO_4$	6.7 ± 6.2	71 ± 29	BAR2014, a, p.w.
Eu	1.05 $NaClO_4$	-2.14 ±0.77	46 ± 3	TIA2010, c, d
Eu	1.05 $NaClO_4$	-19 ± 2	-16 ± 6	LUN1984, b
Eu	2.21 $NaClO_4$	-8.17 ± 1.05	21 ± 3	CHO1966, d
Eu	2.21 $NaClO_4$	-4.3 ± 0.8	33 ± 3	AZI1971, b
Am	0.10 $NaClO_4$	3.7 ± 4.6	55 ± 15	BAR2014, a
Am	1.05 $NaClO_4$	-16 ± 3	-6 ± 9	LUN1984, b
Am	1.00 NaTf*	-5.38 ± 0.07	32 ± 2	ZAL2010, b
Nd	1.05 $NaClO_4$	-2.04 ± 0.22	43 ± 1	TIA2010, c, d

a…spectroscopy, b…solvent extraction (distribution), c…potentiometry, d…calorimetry, *…in molar (no conversion factors available), p.w…present work

In our recent publication [BAR2014] we studied the temperature dependent Am(III)- and Eu(III)-lactate complexation constants using TRLFS- and UV/Vis spectroscopy. The enthalpies were obtained from van't Hoff plots. By means of ATR FT-IR and NMR spectroscopy in combination with density functional theory (DFT) calculations, we found a side-on coordination of the Eu(III)-lactate complex with the hydroxyl group being

deprotonated (at pH = 6) which contradicts structure suggestions from earlier publications [TIA2010, DIC2002, KIE1977, CHE2012]. The most recent study about lactate from Fröhlich et al. [FRÖ2015b] confirms the side-on coordination to Am(III) through both the carboxylic and the α-hydroxy group using EXAFS.
In this chapter, micro-titration calorimetry was applied to obtain both the reaction enthalpies and formation constants of Eu(III) lactate complexation as function of ionic strength. For comparison, Cm(III)-lactate complexation was examined using TRLFS.

4.3.2 Experimental

Solutions

The reactants $EuCl_3 \cdot 6\ H2O$ (Sigma-Aldrich), Na-L-lactate (Sigma-Aldrich) and lactic acid (AppliChem) were analytical grade and were used without further purification. For experiments, solutions were prepared with deionized water; the ionic strength was adjusted with analytical grade sodium chloride (AnanlaR Normapur) to 0.5-3 m. Necessary pH adjustments were done with small amounts of NaOH and HCl by using a Ross-Electrode (type Ross, Orion, Thermo Scientific).

Isothermal micro-titration calorimetry

These experiments were performed in NaCl media at constant ionic strength between 0.1 and 3 m. For the lactate protonation, sodium lactate solutions (10 or 20 $mmol \cdot kg^{-1}$, pH ~ 6-7) at a defined ionic strength were titrated with a 0.1 M and a 0.2 M HCl with the same ionic strength like the sample, respectively. For the complexation solutions of 14 $mmol \cdot kg^{-1}$ Eu(III) and 38 $mmol \cdot kg^{-1}$ lactate (lactic acid) were prepared with pH = 3 and defined ionic strength. These samples were titrated with HCl with concentration between 0.1 and 0.25 M. Multiple titrations with different Eu(III) concentrations but same Eu(III)/lactate ratio were performed to reduce uncertainty.

TRLFS

A stock solution of the long-lived curium isotope ^{248}Cm ($t_{1/2} = 3.4 \cdot 10^5$ years) was used. This solution had the following composition: 97.3% ^{248}Cm, 2.6% 246-Cm, 0.04% 245-Cm, 0.02% 247-Cm, and 0.009% 244-Cm in 1.0 M $HClO_4$. The sample solutions with a Cm(III) concentration were titrated with aliquots (10-50 µl) of 0.05 and 0.5 M sodium lactate solution,

resulting in total lactate concentrations of $1 \cdot 10^{-4}$ – $5 \cdot 10^{-2}$ M. The total proton concentration in all solutions was fixed to $[H^+]_{total} = 1.86 \cdot 10^{-3}$ M. Every mixture was allowed to equilibrate for at least 5 min bevor the next titration step.

4.3.3 Results and discussion

Lactate protonation

The protonation constants and enthalpies for the lactate protonation were determined both potentiometrically and calorimetrically as function of the ionic strength by A. Skerencak-Frech from the Universität Heidelberg (see final report BMWi project, FZK 02E11031) [SKE2015/16]. Typical calorimetric titration curves of lactate protonation are shown in Fig. 4.5

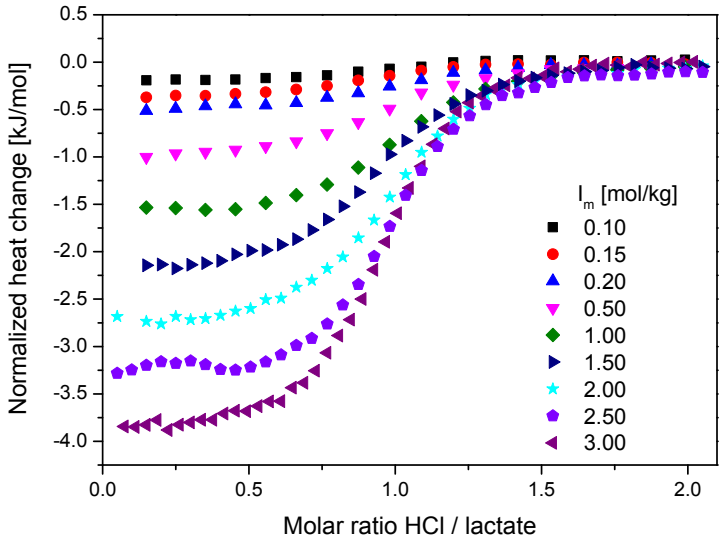

Fig. 4.5: Normalized heat change for titration of 10 mmol·kg^{-1} Na-lactate with 0.1 M HCl at various ionic strengths in NaCl medium (T = 25°C, pH_{start} = 6.6)

The heat curves for the lactate protonation show a decrease of enthalpy with increasing ionic strength. At low ionic strength (0.1- 0.2 m NaCl) the heat curves are without any pronounced sigmoidal shape and the heat exchange during protonation is very low. In this specific case, dehydration- and proton binding enthalpy compensate each other yielding to a very low enthalpy effect. This results to only slightly exothermic protonation enthalpies. The analysis of such heat curves regarding to both values K_1^H and H_1^H leads to values with large uncertainties. Therefore, the protonation constants determined by potentiometry

[SKE2015/16] were used as fixed values in the curve fitting procedure as initial parameters to increase the reliability of the fit and to reduce the uncertainty of the enthalpy that is derived from the calorimetric titration curves. The curves at higher ionic strengths (I_m > 1 m) possess a more pronounced S-shape and yield therefore to values of lower uncertainty.

The derived conditional protonation constants K_1^H are plotted as function of the ionic strength in Fig. 4.6 (left). Log K_1^0 and $\Delta\varepsilon_1$ calculated from the corresponding SIT plot in Fig. 4.6 (right) are in good accordance with values from [SKE2015/16] and other literature values (see Tab. 4.5).

For the first time, the individual interaction coefficient ε for (Na^+, Lac^-) was obtained (Tab. 4.5) by using the experimental $\Delta\varepsilon_1$ and literature value for $\varepsilon(H^+, Cl^-)$ = 0.12 ± 0.01 kg·mol^{-1} and ε(HLac, Na^+/Cl^-) = 0 kg·mol^{-1} [HUM2005]. Up to now in literature the acetate value $\varepsilon(Ac^-, Na^+)$ = 0.08 ± 0.01 kg·mol$^-$1 was used as analogue for lactate, because it is often assumed that small organic ions with the same charge have similar ε-values [CIA88], [HUM2005]. Our results show now, that this approximation is not valid since the $\varepsilon(Na^+, L^-)$ -values of these two small organic molecules differ by 50%. It has to be concluded that the OH group in lactate ion contributes to a significant extent to the complexation.

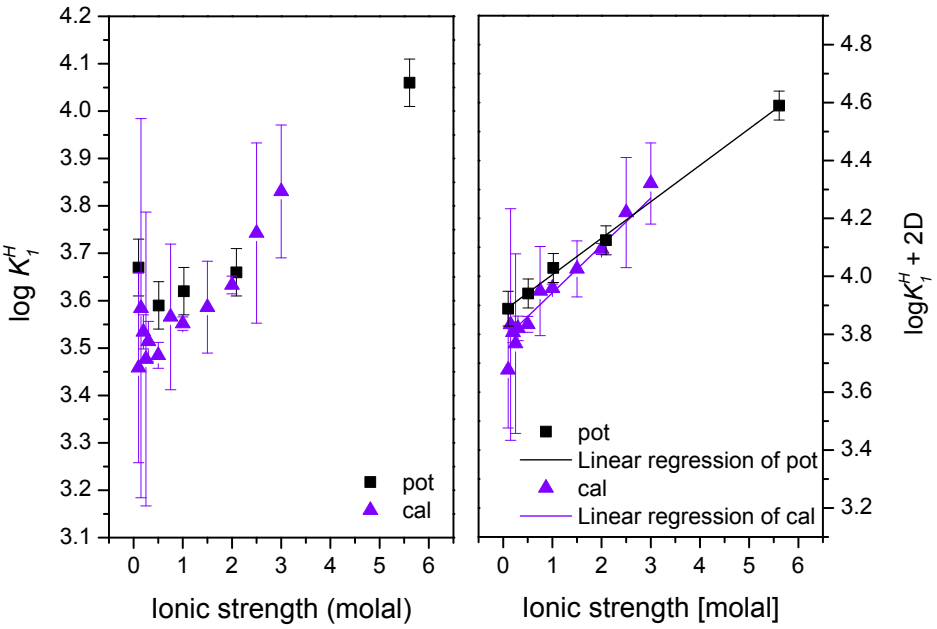

Fig. 4.6: Left: conditional protonation constants log K_1^H of lactate protonation at various ionic strengths in NaCl determined by potentiometry (pot) [SK2015/16] and calorimetry (cal), right: SIT plots

Tab. 4.5: Thermodynamic standard data for the lactate protonation compared to literature data

medium	log K_1^{H0} ± 2σ	$\Delta\varepsilon_1$ ± 2σ [kg·mol^{-1}]	ε(j,k) [kg·mol^{-1}]	$\Delta_r H_1^{H0}$ ± 2σ [kJ·mol^{-1}]	$\Delta\varepsilon_L$ ± 2σ (10^{-3} [kg· (mol·K)$^{-1}$]	$\Delta_r G_1^{H0}$ [kJ·mol^{-1}]	$\Delta_r S_1^{H0}$ [J·mol^{-1}·K^{-1}]	Ref./ method
$Lac^- + H^+ \rightleftharpoons HLac$								
NaCl	3.78 ± 0.04	-0.16 ± 0.02	ε(Na^+, Lac^-) = 0.04 ± 0.04	0.57 ± 0.02[#]	1.29 ± 0.02	-21.6 ± 0.2	74.3 ± 0.8	p.w., c
	3.88 ± 0.02	-0.13 ± 0.01	ε(Na^+, Lac^-) = 0.01 ± 0.03	0.68 ± 0.07	1.67 ± 0.11	-22.15	76.56 ± 0.40	SKE2015/16, b, c
	3.94 ± 0.01							SCHO2015, b
k.A.	3.86 ± 0.20			0.43				MAR1937, a, d
	3.90 ± 0.01							GAJ2001, b
$NaClO_4$	3.93 ± 0.03			1.65 ± 0.66[*]		-22.15 ± 0.16	74.28 ± 1.09	TIA2010, b
				1.64 ± 0.06[*]				ZAL2010, c

a…conductivity, b…potentiometry, c calorimetry, d…temperature variation (van't Hoff) from conductance measurements; [#]by analysis of the calorimetric heat curves by using log K^0 from [SKE2015/16], *literature values extrapolated using $\Delta\varepsilon_L$ from p.w., p.w…present work

Tab. 4.6: Thermodynamic standard data for complexation of An(III)/Ln(III) with lactate compared to relevant literature data

medium	Ln(III)/ An(III)	log $\beta_{1n}^0 \pm 2\sigma$	$\Delta\varepsilon_n \pm 2\sigma$ [kg·mol^{-1}]	$\Delta_r H_{1n}^0 \pm 2\sigma$ [kJ·mol^{-1}]	$\Delta\varepsilon_L \pm 2\sigma$ (10^{-3} [kg·(mol·K)$^{-1}$]	$\Delta_r G_{1n}^0$ [kJ·mol^{-1}]	$\Delta_r S_{1n}^0$ [J·mol^{-1}·K^{-1}]	Ref./ method
$Me^{3+} + Lac^- \rightleftharpoons MeLac^{2+}$, β_{11}^0								
NaCl	Eu	3.48 ± 0.05	-0.13 ± 0.01	0.51 ± 0.08	0.58 ± 0.09	-19.86	68.33	SKE2015/16, b, c
	Eu			2.29 ± 0.15[#]	1.33 ± 0.1	-19.9 ± 0.3	74.3 ± 1.5	p.w., c
$NaClO_4$	Eu	3.14 ± 0.28		9.3 ± 6.2		-18.2 ± 6.2	92 ± 29	BAR2014, p.w., d
	Eu	3.88 ± 0.03		2.50 ± 0.90*				TIA2010, b, e
	Am	2.87 ± 0.26		6.2 ± 4.6		-16.2 ± 4.6	75 ± 15	BAR2014, p.w., d
	Cm	3.64 ± 0.09	-0.23 ± 0.06			-20.8 ± 0,5		p.w., d
$Me^{3+} + 2\,Lac^- \rightleftharpoons MeLac_2^+$, β_{12}^0								
NaCl	Eu	6.16 ± 0.09	-0.19 ± 0.02					SKE2015/16, b, c
$NaClO_4$	Eu	5.49 ± 0.28		8.0 ± 6.6		-31.7 ± 6.6	133 ± 31	BAR2014, p.w., d
	Eu	6.58 ± 0.03						TIA2010, b, d
NaCl	Cm	7.16 ± 0.18	-0.27± 0.12			-40.8 ± 1.0		p.w., d
$Me^{3+} + 3\,Lac^- \rightleftharpoons MeLac_3$, β_{13}^0								
NaCl	Eu	7.76 ± 0.20	-0.23 ± 0.06					SKE2015/16, b, c
$NaClO_4$	Eu	7.07 ± 0.31		3.1 ± 6.9		-41.62 ± 6.9	150 ± 39	BAR2014, p.w., d
	Eu	8.49 ± 0.03						TIA2010, b, d

a…solvent extraction, b…potentiometry, c… calorimetry, d… spectroscopy, [#]by analysis of the calorimetric heat curves by using log K^0 from [SKE2015/16], *literature values extrapolated using $\Delta\varepsilon_L$ from p.w., p.w… present work

A short excursus in the thermodynamics of protonation and complexation

In this section a brief explanation about the influence of the ionic strength on thermodynamic quantities of protonation (Gibbs free energies, enthalpies and entropies) is given using the lactate protonation as example. This general description can be applied to the other described ligands and An(III)/Ln(III) ligand complex systems in this report.

With increasing ionic strength, the protonation enthalpy becomes more exothermic (up to ~ -4 $kJ \cdot mol^{-1}$ at I_m = 3 m NaCl) and the entropy decreases (Fig. 4.7). This trend was observed previously and can be explained by an agglomeration of sodium ions in the second coordination sphere around the lactate anion. The agglomeration of the sodium ions decreases the enthalpy that is necessary to dehydrate the ligand, so that the binding enthalpy becomes more dominant [BAR14]. It can be assumed that next to the inner sphere complex with the proton an outer sphere complex with the background electrolyte becomes more dominant if the ionic strength increases.

Inner sphere complexes are formed directly between complexing ion (metal ion or proton) and ligand without intervening water molecules. The formation of inner sphere complexes has mostly positive enthalpy and positive entropy values due to the relatively large dehydration enthalpy of the ions. Their formation is entropy-driven. Outer sphere complexes are considered as ion pairs where the metal ion and the ligand ion are separated by at least one water molecule so that the primary hydration sphere of the ions is minimally perturbed. Therefore outer sphere complexation shows mostly small enthalpies and negative entropy: their formation is enthalpy-driven. [CHO1997, CHO1994] Consequently, at high ionic strengths lower enthalpy and entropy values are expected compared to lower ionic strengths. This is the result of an increasing of outer sphere complexation because the dehydration of the ligand does not occur to the same extent at low ionic strength.

Since sodium is a very weak complexing agent it is assumed that only outer sphere complexation will take place here [CHO1997]. Fig. 4.7 shows the changes the thermodynamic parameters Gibbs energy, enthalpy, and entropy caused by such increasing of outer sphere complexation of Na^+ with lactate. The fraction of the entropy term relative to the *Gibbs* free energy decreases with increasing ionic strength while the enthalpy behaves vice versa. Up to 3 m NaCl the entropy decreased about 20 % relative to 0.1 m NaCl.

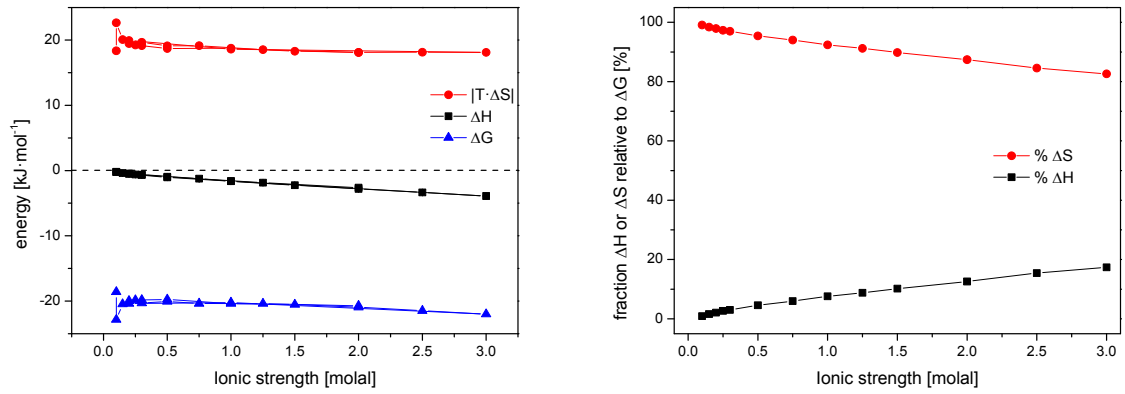

Fig. 4.7: Enthalpy, entropy and free Gibbs energy trend for the lactate protonation as f(I_m)

The enthalpy $\Delta_r H_1^{H0}$ (at I_m = 0) derived from the SIT plot (here not shown, cf. Tab. 4.5) shows that the protonation reaction is slightly endothermic as expected for small organic molecules. Generally speaking, for hard Lewis bases like carboxylates the dehydration and proton binding enthalpies compensate each other resulting in overall enthalpies of just a few kJ, making the protonation driven by entropy, because it is $|-T\cdot\Delta_r S| > |\Delta_r G| >> |\Delta_r H|$ (inner sphere complexation). This reflects a gain in the degrees of freedom (DF) in solution. The loss of the DF of the attached proton is compensated through the gain in DF of the water molecules which are released from the hydration shell of the ligand. That is why $\Delta_r S_1^{H0}$ shows a positive value (cf. Tab. 4.5).

There are very few enthalpy values for lactate protonation in literature. The $\Delta_r H_1^{H0}$ values from [ZAL2010] and [TIA2010] have been extrapolated using the enthalpic interaction coefficient $\Delta\varepsilon_L$ from the present work. The $\Delta_r H_1^{H0}$ value determined by [SKE2015/16] agrees very well with our data. The $\Delta\varepsilon_L$ value for lactate is not stated in any reference until now but can be now used for the extrapolation of the enthalpy to any ionic strength. The single enthalpic ε_L-value for (Lac^-, Na^+) cannot be calculated due to missing a recommend ε_L(H^+, Cl^-)-value in relevant thermodynamic databases.

Eu(III), Cm(III) and Am(III) complexation reaction with lactate

Fluorescence and absorption spectroscopy were used for the determination of the complex formation constants for the Eu-lactate in $NaClO_4$, Cm-lactate in NaCl, and Am-lactate in $NaClO_4$. Furthermore temperature dependent spectroscopic measurements with Eu(III) and Am(III) as well as micro-titration calorimetric measurements with Eu(III) were carried out for the determination of the formation enthalpies. The results for Eu(III)-lactate and Am(III)-lactate obtained by spectroscopy were already published in [BAR2014] (cf. Tab. 4.3 and 4.4).

Instead of them here we like to present the results for Cm(III)-lactate complexation from fluorescence measurements. The luminescence spectra of the Cm(III)- lactate titration show a red shift of the $^6D_{7/2} \rightarrow {}^8S_{7/2}$ transition of Cm(III) from 594 nm to about 600 nm with increasing lactate concentration (Fig. 4.8, left). Using SPECFIT, it was possible to extract two complex species next to the Cm(III) aqua ion (Fig. 4.8, right).

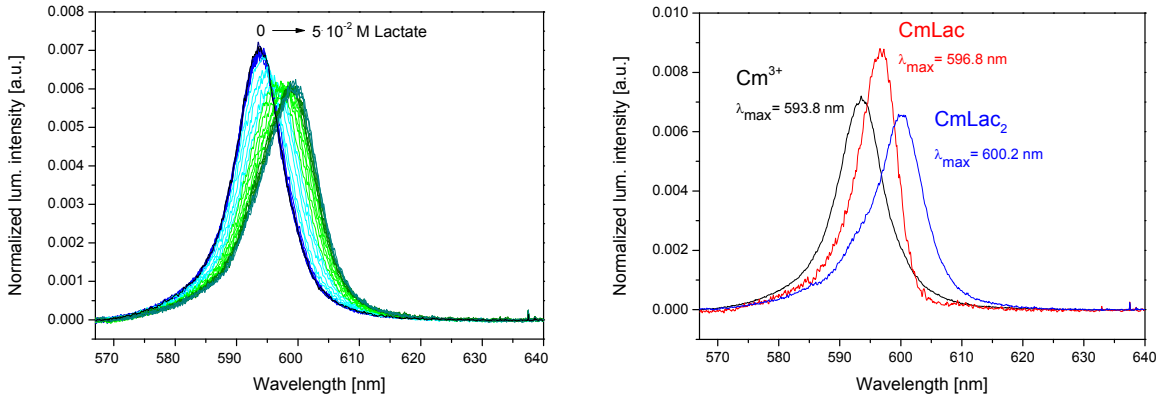

Fig. 4.8: Luminescence spectra of titration of Cm(III) with lactate, [Cm(III)]= $2.4 \cdot 10^{-7}$ M, [Lactate] = $5 \cdot 10^{-2}$ M, I_m = 2 m NaCl (left) and the single components extracted from SPECFIT (right)

Up to I_m = 5 m no significant formation of inner sphere Cm(III) chlorid complex is indicated [FAN1995+1998]. The averaged lifetime of the Cm(III) aqua ion determined at different ionic strengths as 69 ± 4µs (n_{H2O} = 8.4 ± 0.5) agrees well with values from literature [MOL2008, KIM2001, FAN1998, TIA2015]. The luminescence lifetime reaches its maximum of 104 ± 2 µs (n_{H2O} = 5.4 ± 0.5) at $5 \cdot 10^{-2}$ M lactate (Fig. 4.9). This lifetime corresponds to around 5 water molecules in the first hydration shell of the Cm(III) aqua ion which means that 4 water molecules were replaced by the ligand. This results to the formation of complexes with metal-to-ligand ratios of 1:1 and 1:2, namely $CmLac^{2+}$ and $CmLac_2^+$, which again correlates well with the findings from SPECFIT. The slope analysis confirmed the stoichiometry of the both complex species with having slopes of one and two, respectively. The SIT plots are again in a very good correlation with both complex stoichiometries as shown in Fig. 4.10.

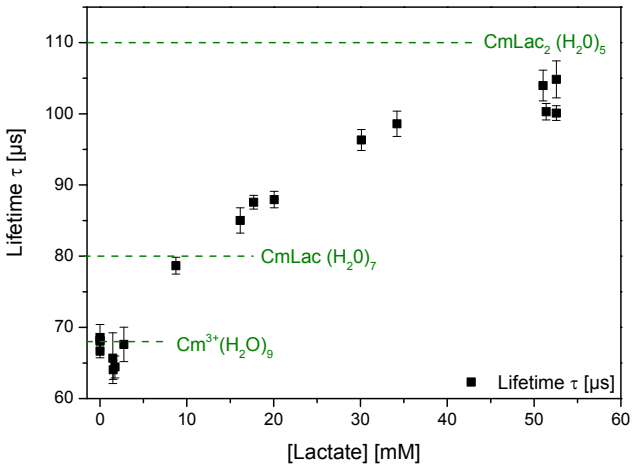

Fig. 4.9: Luminescence lifetimes of Cm(III) in dependency of lactate concentration

For these two species the ionic strength dependent complex stability constants were determined using SPECFIT. There are very few literature data for the Cm-lactate system (see Tab. 4.4 in chapter 4.3.1). The authors in [KOS1980] did not state any uncertainty of the thermodynamic formation constant of $CmLac^{2+}$. The formation constant log β_{11}^0 for $EuLac^{2+}$ is smaller than for the same Cm(III) complex. For the first time the sum of interaction coefficients $\Delta\varepsilon_n$ was determined for the formation of $CmLac^{2+}$ and $CmLac_2^{+}$ (Tab. 4.7). The specific interaction coefficients $\varepsilon(CmLac^{2+}, Cl^-) = 0.01 \pm 0.07$ kg·mol^{-1} and $\varepsilon(CmLac_2^{+}, Cl^-) = -0.02 \pm 0.13$ kg·mol^{-1} were derived by using the respective $\Delta\varepsilon_n$ values and the literature values for $\varepsilon(Lac^-, Na^+) = 0.01 \pm 0.03$ kg·mol^{-1} and $(Cm^{3+}, Cl^-) = 0.23 \pm 0.02$ kg·mol^{-1} [HUM2005].

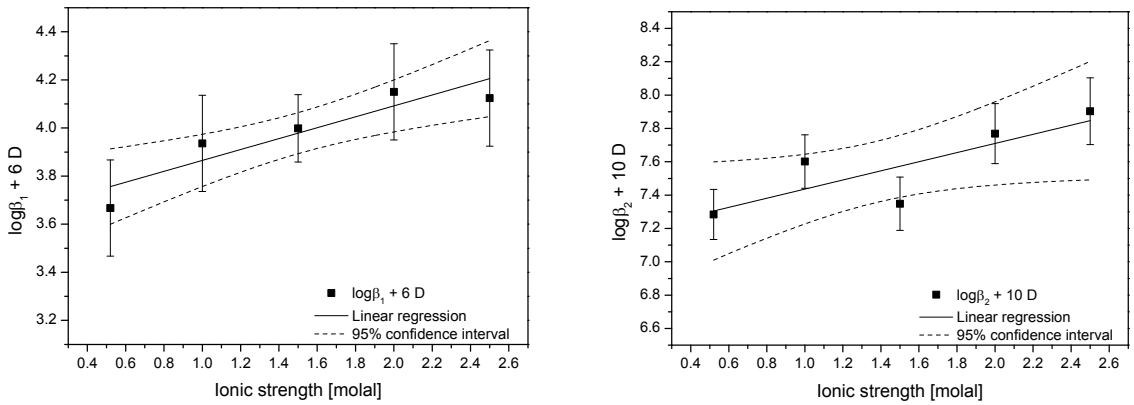

Fig. 4.10: SIT plots of the complex formation constant of the 1:1 (right) and 1:2 Cm(III)-lactate complex (left)

Tab. 4.7: Individual interaction coefficients of lactate complex species compared to literature values

species	ε(j,k) [mol·kg^{-1}]	medium	Ref.
($EuLac^{2-}$, Cl^-)	0.11 ± 0.03	NaCl	SKE2015/16
($CmLac^{2-}$, Cl^-)	0.01 ± 0.07	NaCl	p.w.
($EuLac_2^-$, Cl^-)	0.06 ± 0.05	NaCl	SKE2015/16
($CmLac_2^-$, Cl^-)	-0.02 ± 0.13	NaCl	p.w.

The enthalpy of the 1:1 Eu(III)-lactate complexation shows a similar behavior like the protonation enthalpy: it decreases (becomes more negative) with increasing ionic strength as shown in Fig. 4.11 (left).

The integrated heat curves were fitted with a high accuracy using the program LETAGROP including the thermodynamic data of protonation obtain by potentiometry (log K_1^H) and calorimetry ($\Delta_r H_1^H$) and three complexation species in the chemical model (Fig. 4.11 right).

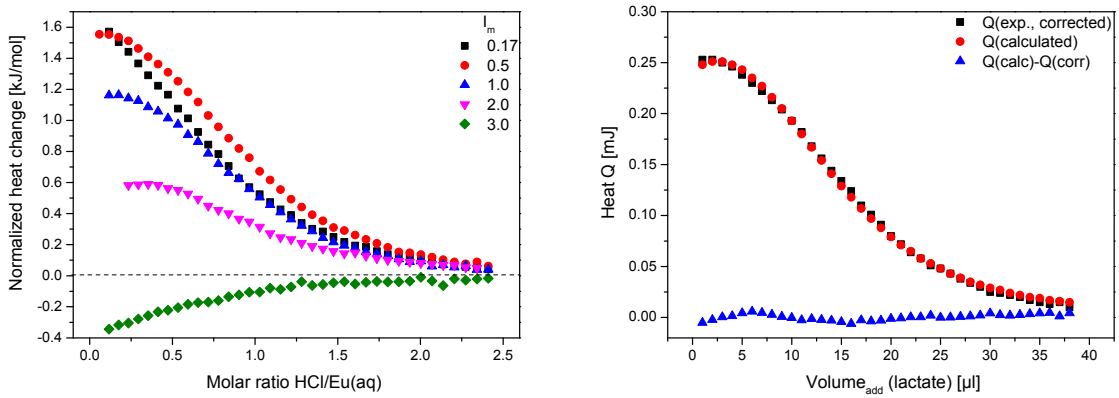

Fig. 4.11: Left: normalized heat curves of the Eu(III)-lactate complexation, [Eu(III)] = 14 mM and [Lac] = 38 mM titrated with 0.1 – 0.25 M HCl as f(I_m); (left); example of curve fitting with LETAGROP at I_m = 0.5 m including protonation species and three complex species (right)

The extrapolated enthalpy $\Delta_r H_{11}^0$ (cf. Fig. 4.12, SIT plot) of the 1:1 Eu(III) lactate complex is slightly endothermic, as expected from the literature (cf. Tab. 4.4). The enthalpy value from [SKE2015/16] and selected values from literature extrapolated by SIT by using the enthalpic interaction coefficient $\Delta\varepsilon_L$ derived for the first time in this work, (cf. Tab. 4.6) are in good agreement with the here determined value. The extrapolated complexation entropy $\Delta_r S_{11}^0$ is positive, thus the complexation is entropy-driven (see explanation above). This correlates with a gain in the degrees of freedom in solution like already stated out for the lactate protonation reaction.

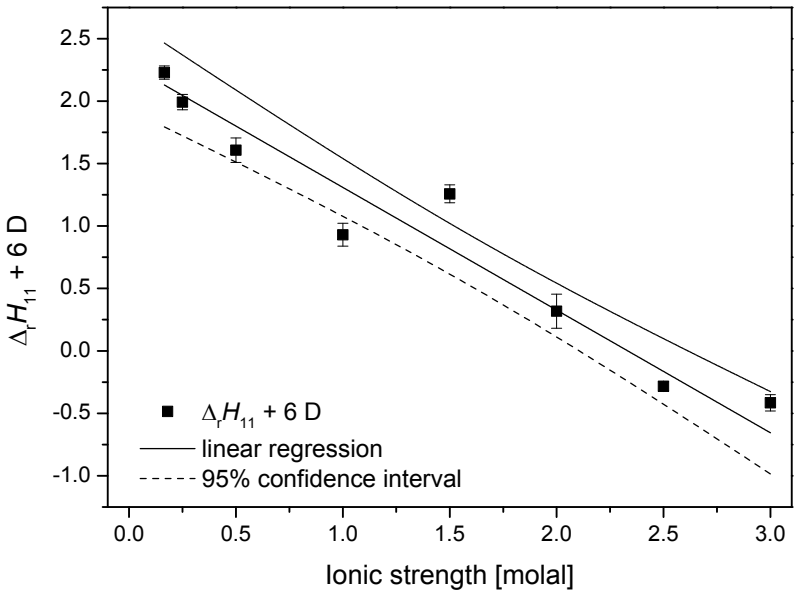

Fig. 4.12: SIT plot for the enthalpy values of the 1:1 Eu(III)-lactate complex formation

4.4 Complexation with oxalate

4.4.1 Literature study

Oxalate is a widespread metabolite of a variety of decomposition processes occurring in soil or in surface waters in the mM range [GAM2000]. Oxalate salts and complexes are relatively insoluble [GAM2000, HUM2005]. Therefore, oxalic acid is widely used as precipitation and separation agent of rare earth elements (REE) and actinides, an example is the "oxalic conversion" process to convert elemental plutonium in its oxide (e.g. in AREVAs spent nuclear fuel recycling plant in La Hague) [ALM2012, HUM2005].

Although oxalic acid is a diprotic acid we focus on the first protonation step in this report. A large number of references (~ 150) were found for the oxalate protonation in [HUM2005]. From the selected literature data in Tab. 4.8, it is seen that log K_1^H decreases with increasing ionic strength up to I_m = 2 m and then increases at ionic strengths above 2 m. The enthalpy generally decreases with increasing ionic strength.

Tab. 4.8: Conditional stability constants, enthalpy and entropy values of the first oxalate protonation step in different media at 25°C

I_m / medium [mol·kg^{-1}]	log K_1^H	$\Delta_r H_1^H$ [kJ·mol^{-1}]	$\Delta_r S_1^H$ [kg·mol^{-1}K^{-1}]	Ref./ method
0.04 NaCl	3.95 ± 0.02	6.0 ± 0.9	96 ± 3	ROB1992, a
0.10 NaCl	3.80 ± 0.02	5.1 ± 0.8	90 ± 3	KET1998, a
0.10 $NaClO_4$	3.82 ± 0.04	6.28 ± 0.21	94 ± 1	CHO1986, b
0.40 NaCl	3.65 ± 0.02	4.6 ± 0.9	85 ± 3	ROB1992, a
1.00 NaCl	3.54 ± 0.03	1.3 ± 1.0	72 ± 4	KET1998, a
1.00 NaCl	3.51 ± 0.04			MIZ1999, a
1.00 NaCl	3.50 ± 0.02	4.3 ± 0.7	82 ± 2	KET1991, a
1.02 NaCl	3.52 ± 0.01			CRE2004, a
1.00 $NaClO_4$	3.57 ± 0.02			BOT1965, a
1.00 $NaClO_4$	3.52 ± 0.01	4.13 ± 0.02	81 ± 1	BER2009, b
1.05 $NaClO_4$	3.58 ± 0.01			CHO1996, a
1.00 M KNO_3		2.71 ± 0.02		LIN1987, b, *
1.23 NaCl	3.54 ± 0.02	4.4 ± 0.9	83 ± 3	ROB1992, a
2.00 NaCl	3.47 ± 0.03	0.8 ± 0.8	69 ± 3	KET1998, a
3.15 NaCl	3.52 ± 0.03	-0.6 ± 0.3	65 ± 2	KET1998, a
3.20 NaCl	3.59 ± 0.02			CRE2004, a
3.51 $NaClO_4$	3.77 ± 0.01			CHO1996, a
4.00 NaCl	3.70 ± 0.04			MIZ1999, a
5.00 NaCl	3.73 ± 0.03	-2.4 ± 3.3	63 ± 11	KET1998, a
6.60 $NaClO_4$	3.99 ± 0.03	-6.20 ± 1.5	62 ± 8	THA2007, a

a...potentiometry, b...calorimetry, *… in molar scale (no conversion factor available)

It should be noted that sodium oxalate complexes are also reported in literature. The reported log K_1^{Na} values vary from 0.02 ± 0.02 to 1.12 ± 0.01 [HUM2005]. However, it turned out that the existence of such complexes can be neglected in our studies.

For the aqueous Am(III)-oxalate complexes $Am(Ox)_n^{3-2n}$, with n = 1 and 2, several data have been published (Tab. 4.9). The existence of complexes with higher n-values is fairly probable; however, their experimental study is limited due to their low solubility and the resulting very low complex concentration in solution. In the most recent publication about oxalate [SKE2015], the authors determined log β_n^0(T) values and the ion-ion interaction coefficients for four species $[Cm(Ox)_n]^{3-2n}$ (n = 1, 2, 3, 4) using temperature dependent TRLFS measurements, whereas the forth species only appeared at high temperatures (T > 60°C).
A complexation of Am(III) with HOx^- is possibly in principle, however, the stability constant is expected to be very small [HUM2005]. Several groups [MAI2014, CHO1996, VAL2003] confirmed that the fully deprotonated oxalate anion represents the main complexing species.

Mainly liquid-liquid-distribution experiments were carried out to examine An(III)/Ln(III)-oxalate complexation [CHO1996, BOR2001, SEK1965], furthermore solubility experiments [LEB1960, GRE1969, PAZ1987] and in recent years spectroscopic measurements [THA2006+2009; SKE2015] were applied. Calorimetric studies of An(III)/Ln(III)-oxalates are very scarce [CHO1986].

Tab. 4.9: Selected stability constants, enthalpy and entropy values for the 1:1 complexation of oxalate with An(III)/Ln(III) in different media at 25°C

An(III) Ln(III)	I_m/ medium [mol·kg^{-1}]	log β_{11}	log β_{12}	$\Delta_r H_1$ [kJ·mol^{-1}]	$\Delta_r S_1$ [kg·mol^{-1}K^{-1}]	Ref./ method
Cm	→ 0	6.86 ± 0.03	11.54 ± 0.09	-2.7 ± 0.8	121.8 ± 2.9	SKE15, a*
Nd	→ 0	7.21	11.51			CRO1951, b
Eu	→ 0	6.72	11.22			WOO93, c
Am	→ 0	6.51 ± 0.15	10.72 ± 0.20			HUM05
Am	→ 0	6.89				PAZ1987, d
Eu	0.05 M NH_4NO_3	5.60 ± 0.02	9.90 ± 0.03			SCHI2001, e
	0.05 $NaClO_4$	5.46				MAN66, b
	0.10 $NaClO_4$	5.30 ± 0.03		13.6 ± 2.5	147 ± 8	CHO1986, f, g
	0.51 $NaClO_4$	4.85	8.65			LYL1966, e
	0.68 $NaClO_4$	4.89 ± 0.22	8.68 ± 0.58			CAN1987, b
	1.00 $NaClO_4$	4.86	7.60			MAN66, b
	1.05 $NaClO_4$	5.02	8.66			GRE1969, d
	1.05 $NaClO_4$	4.85 ± 0.10	8.78 ± 0.09			SEK1965, b$^+$
	6.60 $NaClO_4$	5.03 ± 0.08	8.93 ± 0.09	22.5 ± 4.5	171 ± 11	THA2006, b
Am	0.30 NaCl	4.55 ± 0.10	8.24 ± 0.20			BOR2001, b
	0.70 NaCl	4.61 ± 0.10	7.93 ± 0.15			CAC1983, b
	1.00 NaCl	4.21 ± 0.10	7.81 ± 0.20			BOR2001, b
	1.05 $NaClO_4$	4.61 ± 0.20	8.31 ± 0.20			SEK1965, b
	1.05 $NaClO_4$	4.64 ± 0.10	8.30 ± 0.20			CHO1996, b
	2.00 NaCl	4.44 ± 0.15	8.26 ± 0.30			BOR2001, b
	3.00 NaCl	4.61 ± 0.20	8.47 ± 0.30			BOR2001, b
	3.50 $NaClO_4$	4.57 ± 0.10	8.42 ± 0.20			CHO1996, b
	6.60 $NaClO_4$	4.71 ± 0.20	9.00 ± 0.30			CHO1996, b
	6.60 $NaClO_4$	5.37 ± 0.09	9.04 ± 0.09	19.3 ± 4.7	167 ± 12	THA2006, b

a...TRLFS, b…distribution , c…exp. data taken from [CAN1987] and extrapolated using Pitzer parameter for maleate ion and its complexes, d…solubility, e…ion-exchange, f…potentiometry, g…calorimetry, *…at 20°C, +… values of log β ($EuOx^+$) and log β ($EuOx^{2-}$) reported by [SEK1965] were increased by 0.1 as suggested by Grenthe et al. [GRE1969].

Oxalate is known to be a strong chelating ligand because it consists of two carboxylic functions which can form a very stable 5-membered chelating ring. The chelate complexation (side-on coordination) with trivalent actinides in solution was already described by [DAN1981] (alkali metal complexes) using Raman spectroscopy, by [THA2006] using EXAFS measurements, and by [SKE2015] using quantum chemical calculations. This side-on

coordination was already expected due to existing crystal structures of Ln(III)/An(III)-oxalate complexes [ZHA2009 and WAN2013].

However, lacks in thermodynamic data of trivalent An(III)/Ln(III)-oxalate complexation still exist like complexation enthalpies and stability constants both as function of the ionic strength. Nd(III) as trivalent analogue to An(III) has not been investigated with oxalate in solution yet.

In the present work two different concentration ranges were examined. TRLFS and UV-Vis absorption measurements were done with Eu(III) and Am(III), respectively, at trace concentrations from 10^{-6} to $5 \cdot 10^{-5}$ M. Nd(III) was analyzed by titration calorimetry at mM concentrations. The purpose of these experiments was to complete the thermodynamic data set of the Ln(III)/An(III)-oxalate system in solution (and solid state) to get an overall understanding of the system.

4.4.2 Experimental

Solution

The reactants $EuCl_3 \cdot 6\ H_2O$ (*Aldrich*, p.a.), $NdCl_3\ 6\ H_2O$ (Alfa Aesar, p.a.), disodium oxalate (Aldrich, p.a.) and oxalic acid (Aldrich, p.a.) were used without further purification. For experiments, solutions were prepared with deionized water; the ionic strength was adjusted with sodium chloride (AnalaR Normapur, p.a.) to 0.5-3 m. Necessary pH adjustments were done with NaOH and HCl on a Ross-Electrode (Orion 8103SC) with an accuracy of 0.05 units and the pH was corrected like explained in chapter 2.5.

Isothermal micro-titration calorimetry

For the oxalate protonation, disodium oxalate solutions (5 or 10 mM, pH ~ 6) were titrated with 0.05 M and 0.075 M HCl solutions (at same ionic strengths), respectively. For the complexation, solutions of 0.75 to 1 mM Nd(III) (pH = 2.5) were prepared and titrated with aliquots of a 10 – 12 mM oxalic acid solution. The ionic strength of each solution was adjusted with NaCl. Multiple titrations at different Nd(III)-concentrations were performed to reduce uncertainty.

Time-resolved laser-induced fluorescence spectroscopy

For TRLFS, stock solutions of 0.05 m oxalic acid and 5 µmolal $EuCl_3 \cdot 6\ H_2O$ were prepared at pH ~ 1.95 and different ionic strengths. Aliquots of the oxalate solution (10 – 50 µl) were titrated into 2.5 ml of the Eu-solution having the same ionic strength. The maximal total oxalate concentration reached ≈ 9 mmolal. The temperature was fixed to 25 ± 1°C and the solutions were stirred throughout the measurements.

The single parameters for stationary and dynamic measurements are listed in Tab. 4.10

Tab. 4.10: Parameter for stationary and dynamic fluorescence measurements (T = 25°C)

parameter	**stationary measurement**	**dynamic measurement**
excitation-λ	394 nm ($^7F_0 \rightarrow {}^5L_6$)	394 nm
pulse energy	2.8-3.1 mJ	2.8-3.1 mJ
grating	1200 mm^{-1}	300 mm^{-1}
resolution	0.2 nm	0.7 nm
accumulation	2000	200-300
λ-range	565-650 nm	440-780 nm

UV-vis spectroscopy

Am-243 was supplied by the *Oak Ridge National Laboratory* as AmO_2. The oxide was dissolved in 30 % HNO_3 and aliquoted for experiments. The Am-stock solution has a concentration of $4.5 \cdot 10^{-3}$ $mol \cdot l^{-1}$. For UV-vis a 13 µM Am-243 solution was prepared in HCl and NaCl (total proton concentration equals the oxalate solution). 1 – 2 µl aliquots of 0.05 M oxalic acid were added (pH = 1.98 ± 0.05, at the same ionic strength), stirred for 5 min and the single spectra recorded on a spectrometer. A maximal oxalic acid concentration of ~ 9 mM was reached in every experiment.

The concentration of the Am(III) solution was determined by LSC (Liquid-Scintillation-Counting LSC6000 *Beckman*). After multiple measurements an average concentration of $1.3 \cdot 10^{-5} \pm 7.8 \cdot 10^{-7}$ $mol \cdot l^{-1}$ was determined.

The used UV/Vis system and evaluation of the spectra is described in chapter 4.2.2.

Solid characterization

The solid Ln(III)-oxalates were precipitated using 1 mM $EuCl_3 \cdot 6\ H_2O$ or 1 mM $NdCl_3 \cdot 6\ H_2O$ solutions and 12 mM oxalic acid solution (pH = 2.5, I_m = 0.5 m). The reagents were mixed in

a ratio of 1:5, one hour stirred at 70°C and overnight stirred at RT. The slightly violet solid (Nd) or the white solid (Eu), respectively were washed with water and ethanol and dried at 80°C.

DLS measurements were performed on a *Zetasizer Nano* (Malvern Instruments Ltd., UK, 2007). The light scattering which is caused by the backscattering by the particles in solution was measured for 10 sec for at least ten times. This was repeated 5 times to imitate 10-30 min spacing of the ITC measurements.

For the **fluorescence** measurements of the Eu-oxalate-suspension, 25 mg of the Eu-solid were suspended in 2.5 ml dest. H_2O and stirred during measurement. The time-resolved spectra were recorded in 20 µs steps (81 spectra) under the conditions described in Tab. 4.10.

Site-selective **TRLFS** measurements of the Eu-solid were performed at a temperature of about 40 K (10 K on the cryostat with helium cooling). The Nd:YAG-MOPO laser system from *Spectra Physics* (USA) generated the excitation wavelength of 580 nm. The optical multi-channel-analyzer consists of the spectrograph *SpectraPro 300i* from *Acton* (Germany), an ICCD camera from *Princeton Instruments* (USA) and the Delay-Generator DG535 from *Stanford Research Systems* (USA). The F_0-D_0-excitation spectra were recorded by screening (and summation of the F_4-peak intensity) of the absorption band between 575-581 nm.

With **elementary analysis** the carbon-hydrogen-ratio of the Eu-solid was determined. The measurement was performed at the institute of radio pharmacy of the HZDR on a *Euro Vector* CHNS-O elementary analyzer (*EuroEA* 3000; *HEKAtech* GmbH, Wegberg, Germany). A carbon-hydrogen-content of C = 11.06 % and H = 1.47 % was found. The theoretical carbon-hydrogen-content for $Eu_2Ox_3 \cdot 5\ H_2O$ ($C_6H_{20}O_{17}Eu_2$ MW = 657.92 $g \cdot mol^{-1}$) is C = 10.94 % and H = 1.52%

IR spectra were recorded of the solids Nd- and Eu-oxalate as well as of disodium oxalate and oxalic acid as reference substances (as KBr pellet) using a *Bruker* Vertex Fourier-Transform Infrared spectrometer (*Bruker* Instruments, Ettlingen) screening between 7500-370 cm^{-1} with a resolution of 4 cm^{-1} at room temperature.

4.4.3 Results and discussion

Oxalate protonation

The protonation constants for oxalate were determined thoroughly using calorimetry and temperature dependent potentiometric measurements (cf. chapter 4.4.1, Tab. 4.8). The second

protonation step can just be determined only in the highly acidic pH range (log $K_2^{H0} = 1.40$ [HUM2005]). Due to experimental restriction of our micro-titration calorimeter ITC_{200} (pH values smaller than 1.5 are not possible) only the first protonation step was considered. Nevertheless, the micro-titration calorimetric investigation of oxalate protonation is another example to proof the suitability of our micro-tiration calorimeter and our data handling routines.

The integrated heat curves (Fig. 4.13) show an endothermic protonation reaction at low ionic strengths as known for small organic ligands. As already explained in chapter 4.3.3 protonation reactions of mono- and dicarboxylates are often endothermic with very small enthalpy values because the breaking of the ligands hydration shell requires more energy than it is gained during bond formation between ligand and proton. The endothermic protonation reaction at small ionic strength changes to an exothermic reaction at higher ionic strength. The S-shape of the curve is not very pronounced at high ionic strength. That is why the values extracted by curve fitting must be treated with care (see explanation in chapter 4.2.1)

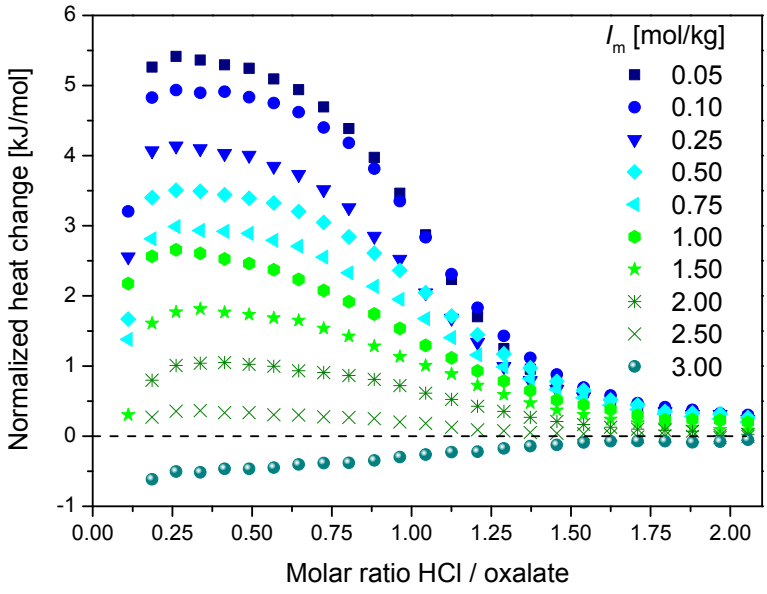

Fig. 4.13: Normalized heat change for titration of 5 mmol·kg^{-1} oxalate with 0.1 M HCl at various ionic strength in NaCl medium(T = 25°C, pH_{Start} = 5.6)

The SIT plots for the protonation reaction (Fig. 4.14) were generated using the extracted stability constant and the enthalpy, respectively. As already mentioned the large uncertainty in the stability constant in the SIT plot at I_m = 3 m results from the non-ideal shape of the heat

curves. The log K_1^H and $\Delta_r H_1^H$ values as well as the extrapolated log K_1^{H0}, $\Delta_r H_1^{H0}$ and $\Delta\varepsilon_1$ value correspond very well with literature data (cf. Tab. 4.11). The reference data given in [HUM2005] are derived from measurements in a variety of background electrolytes which could explain the slight difference to our $\Delta_r H_1^{H0}$ value.

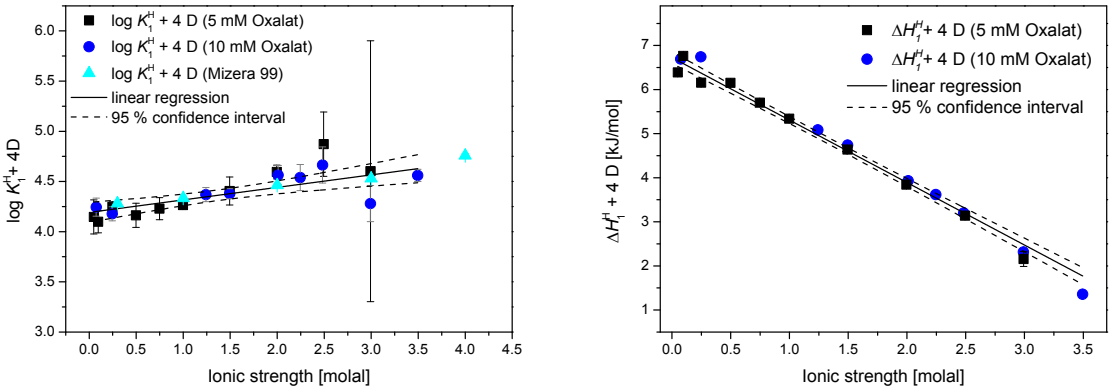

Fig. 4.14: SIT plots of oxalate protonation in NaCl, left: protonation constant, right: protonation enthalpy

Using $\varepsilon(H^+, Cl^-)$ = 0.12 ± 0.01 kg·mol^{-1} and $\varepsilon(Ox^{2-}, Na^+)$ = -0.08 ± 0.01 kg·mol^{-1} from the NEA-database [HUM2005] the calculated specific ε(j,k) for (Na^+, HOx^-) is -0.09 ± 0.02 kg·mol^{-1}. The derived $\varepsilon(Na^+, HOx^-)$ value is almost identical to the literature value of -0.07 ± 0.01 kg·mol^{-1} [HUM2005]. However, this $\varepsilon(Na^+, HOx^-)$ value is also similar to that of the completely deprotonated oxalate species with $\varepsilon(Na^+, Ox^{2-})$ = -0.08 ± 0.01 kg·mol^{-1} [HUM2005]. This shows that these species are very similar in their interactions with the surrounding in spite of different charges. The ε-values for oxalate recommended in [XIO2009] with $\varepsilon(Na^+, HOx^-)$ = -0.03 ± 0.02 kg·mol^{-1} and $\varepsilon(Na^+, Ox^{2-})$ = -0.02 ± 0.04 kg·mol^{-1} show slightly differences to the values mentioned above.

For the first time the difference of the enthalpic interaction coefficients $\Delta\varepsilon_L$ of (1.92 ± 0.05)·10^{-3} kg·mol^{-1}K^{-1} was determined in NaCl. In [HUM2005] the $\Delta\varepsilon_L$ value was extracted from $\Delta_r H_1^H$ values of different media ($\Delta\varepsilon_L$ = 2.26 ± 0.08 kg·mol^{-1}·K^{-1}).

Unfortunately, the single individual enthalpic interaction coefficients cannot be determined due to missing individual ε_L values of (H^+, Cl^-) and (Ox^{2-}, Na^+) species.

From extrapolated log K_1^{H0} and $\Delta_r H_1^{H0}$, the entropy $\Delta_r S_1^{H0}$ = 102.79 ± 0.96 J·mol^{-1}·K^{-1} ($T\cdot\Delta_r S_1^{H0}$ = 30.63 ± 0.29 kJ·mol^{-1}) and the free Gibbs energy $\Delta_r G_1^{H0}$= -23.90 ± 0.28 kJ·mol^{-1} were calculated. The entropy is positive and $T\cdot\Delta_r S_1^{H0} > -\Delta_r G_1^{H0} >> -\Delta_r H_1^{H0}$, i.e., that the protonation is entropy-driven. As already observed and discussed in the chapter about the lactate protonation (see chapter 4.3.3), the entropy ($T\cdot\Delta_r S_1^{H0}$) and the enthalpy $\Delta_r H_1^{H0}$ are decreasing with increasing ionic strength and even change their sign (Fig. 4.15).

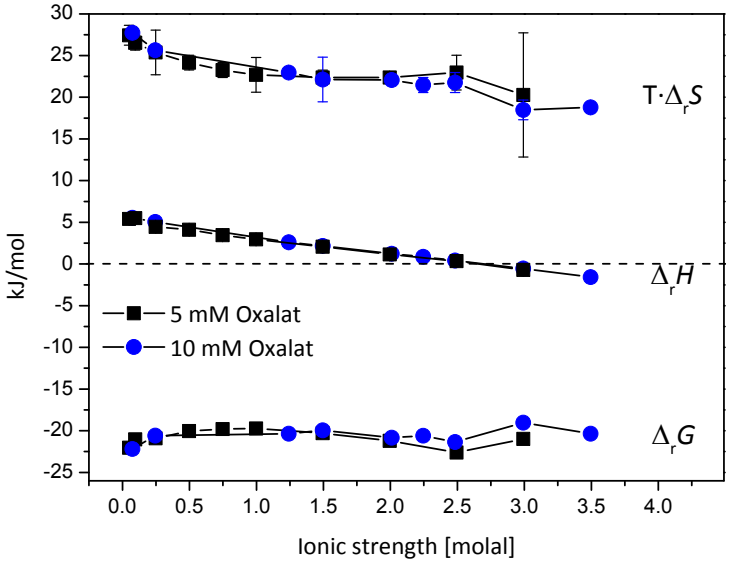

Fig. 4.15: Entropy, enthalpy and free Gibbs energy of the first protonation step of oxalate as f(I_m)

Tab. 4.11: Thermodynamic standard data for the first oxalate protonation step compared to literature data

medium	log K_1^{H0}	$\Delta\varepsilon_1$ [kg·mol^{-1}]	$\Delta_r H_1^{H0} \pm 2\sigma$ [kJ·mol^{-1}]	$\Delta\varepsilon_L \cdot 10^{-3}$ [kg·mol^{-1}K^{-1}]	$\Delta_r G_1^{H0}$ [kJ·mol^{-1}]	$\Delta_r S_1^{H0}$ [J·mol^{-1}·K^{-1}]	Ref./ method
NaCl	4.19 ± 0.05	-0.13 ± 0.03	6.73 ± 0.06	1.92 ± 0.05	-23.9 ± 0.3	102.8 ± 1.2	p.w., a
ClO_4^-	4.27		6.28 ± 0.21		-24.36	103.00	CHR1967, a
NaCl	4.29		6.49		-24.47	103.91	HAR1939, b
NaCl	4.24 ± 0.02	-0.12 ± 0.01			-24.19		MIZ1999, b
NaCl	4.28 ± 0.01	-0.11 ± 0.01	6.80 ± 0.50		-24.42 ± 0.06	105 ± 2	KET1991, b
NaOTf/NaCl	4.26 ± 0.01		7.3 ± 0.5		-24.30 ± 0.06	106 ± 2	KET1998, c
$NaClO_4$/NaCl	4.24 ± 0.01	-0.11 ± 0.01	7.30 ± 0.10	2.26 ± 0.08	-24.19 ± 0.06	105 ± 0.5	HUM2005*
$NaClO_4$	4.21 ± 0.04	-0.13 ± 0.04	9.10 ± 0.02		-24.02 ± 0.23	50.0 ± 0.8	BER2009, a

a...microcalorimetry, b...potentiometry, c… regressing the measurements made in Na-triflate media simultaneously with the recalculated measurements made in NaCl media, * mixed methods and media

Nd(III) complexation reaction with oxalate studied by ITC

The Nd(III) complexation reaction with oxalate was performed in our micro-titration calorimetry the typical mM range. The calorimetric titration curves (Fig. 4.16) show two different heat effects: first a fast exothermic reaction and second a slow, slightly exothermic reaction which takes about 20 min until the heat flow reaches the baseline again. A saturation of the reaction occurs at the end of the titration.

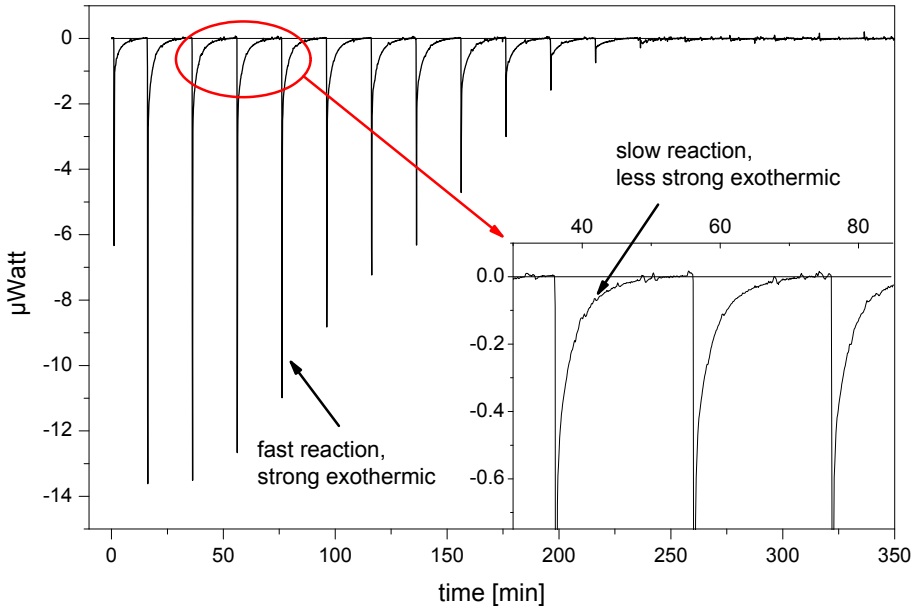

Fig. 4.16: Thermogram of the titration of 0.75 mM Nd(III) with 12 mM oxalic acid, pH = 2.5, I_m = 2.5 m in NaCl media, T = 25°C

We assume that the first reaction can be assigned to the complexation and the second process is the precipitation of the 2:3 solid according to the following mechanism:

$$Nd^{3+} + Ox^{2-} \rightleftarrows NdOx^{+}$$

$$2\,NdOx^{+} + Ox^{2-} \rightleftarrows Nd_2Ox_3$$

In the literature [HUM2005] it is stated that the 2:3 oxalate complex precipitates in weakly acidic or neutral solutions. The solubility products of $Am_2Ox_3 \cdot nH_2O$ and Nd_2Ox_3 are very low having a log K_{sp}= -30.66 [LEB60] and a log K_{sp}^0 = -31.57 ± 0.62 [XIO2011], respectively.

With the help of dynamic light scattering experiments (DLS) a precipitation at the mM concentration range during the calorimetric titration was proved. Even at very small oxalic acid concentrations the light scattering increases rapidly (beginning at a molar ratio of oxalate

to Nd(III) = 0.7, Fig. 4.17). Most of the heat curves also show an inflection point at the molar ratio Nd to Oxalate of 1.5 which could be assigned to the neutral 2:3 (or 1:1.5) complex.

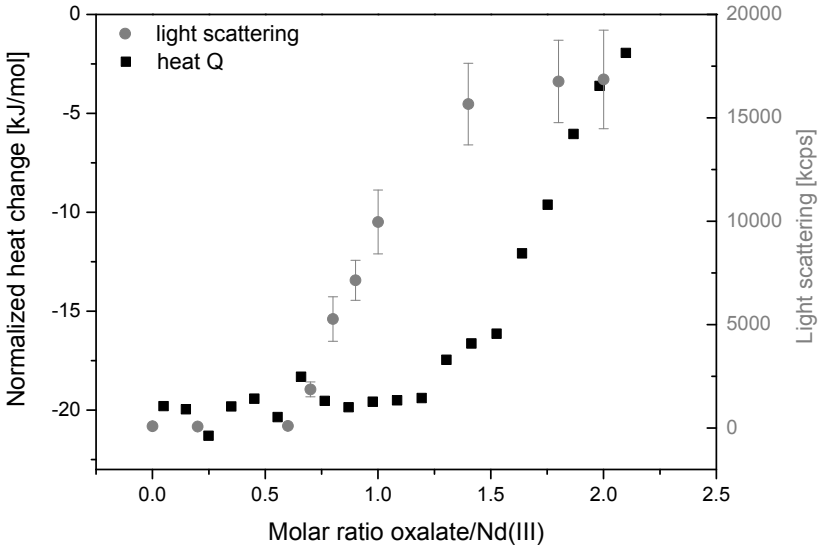

Fig. 4.17: Integrated heat curve and light scattering measurement at [Nd(III)] = 0.25 mM und [Oxalate] = 2.5 mM, I_m= 0.5 m, pH = 3

Thus, for the analysis of the calorimetric titration curves we included the 1:1 complex $Nd(Ox)^+$ and the 2:3 species Nd_2Ox_3, which is modelled as solution species with a stability constant that equals the solubility constant of Nd_2Ox_3 in order to include its stoichiometry in the data analysis. However, the heat curves analyzed in *HypΔH* with this simplification show a good approximation including these two "complexes" in the chemical model (Fig. 4.18).

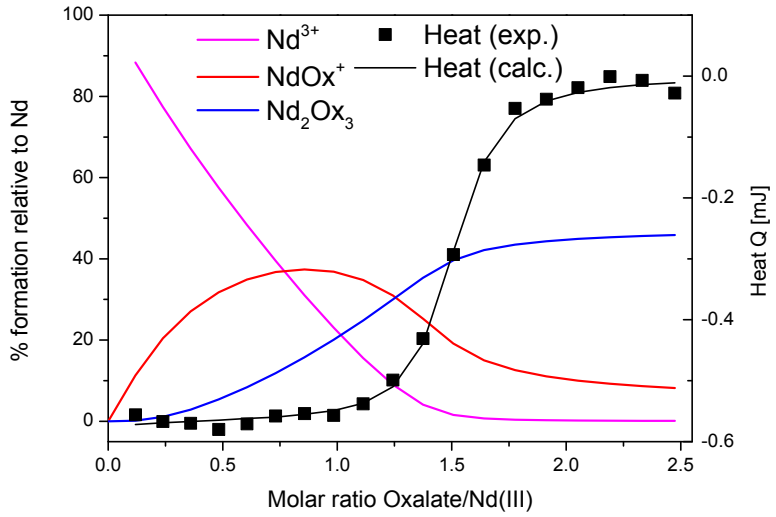

Fig. 4.18: Fit of the heat curve with HypΔH and respective speciation from HySS2006, I_m=1 m, [Nd(III)] = 1 mM, [oxalate] = 12mM, pH=2.5

Therefore, the thermodynamic data and the SIT plots are shown for the 1:1 complex only (Tab. 4.12, Fig. 4.19) and the averaged log β_{11} values for the first complex have considerable uncertainties (cf. SIT plot in Fig. 4.19). Nevertheless, the derived log β_{11}^0 agrees moderately well with literature values. There is no $\Delta\varepsilon_1$ reference value for Nd-oxalate complexation known so far. However, the $\Delta\varepsilon_1$ value of the analogous 1:1 Am-oxalate complex system is much lower than our value for Nd-oxalate. It is assumed this deviations result from the precipitations during the experiments and their treatment in the data analysis.

The extrapolated enthalpy $\Delta_r H_{11}^0$ shows an unusual strong exothermic value. An exothermic standard reaction enthalpy of the oxalate complexation can be attributed to the strong 5-membered chelating ring formed during complexation, however, the here determined reaction enthalpy appears too low. The entropy is positive. Thus, the 1:1 complex is both enthalpy and entropy driven ($T \cdot \Delta_r S_{11}^0 \approx |\Delta_r H_{11}^0|$) as stated already in [SKE2015] for $Cm(Ox)^+$. There are no enthalpy values available for the reaction of Nd-oxalate. The enthalpy-SIT plot in Fig. 4.19 shows that the enthalpies of the 1:1 complexes of Ln(III)/An(III) with oxalate become less exothermic with increasing ionic strength. This is the contrary to the ionic strength dependency of the lactate and malonate system (cf. chapter 4.3.3 and 4.5.3 respectively).

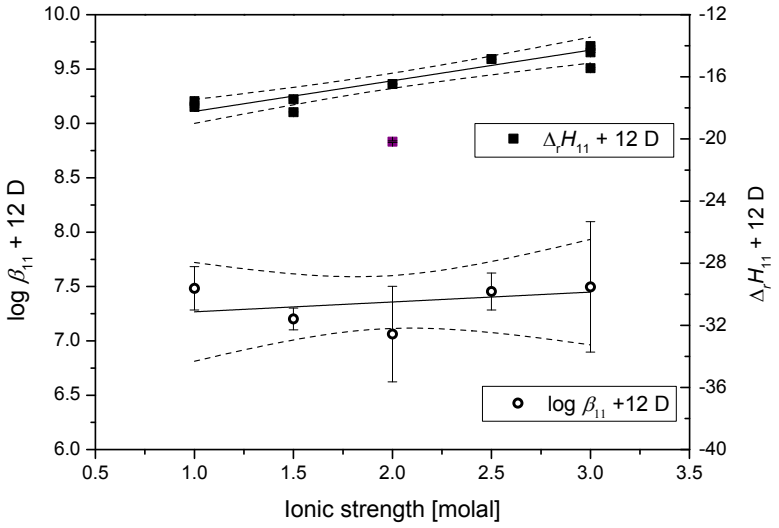

Fig. 4.19: SIT plots for the 1:1 Nd-oxalate complexation (complexation constant and complexation enthalpy) derived from micro-titration calorimetric measurements

Tab. 4.12: Thermodynamic standard data of 1:1 complexation of Ln(III)/An(III) with oxalate derived with different methods and compared to literature values

Ln(III) An(III)	medium	log $\beta_{11}^0 \pm 2\sigma$	$\Delta\varepsilon_1 \pm 2\sigma$ [kg·mol^{-1}]	log $\beta_{12}^0 \pm 2\sigma$	$\Delta\varepsilon_2 \pm 2\sigma$ [kg·mol^{-1}]	$\Delta_r H_{11}^0 \pm 2\sigma$ [kJ·mol^{-1}]	$\Delta\varepsilon_L \pm 2\sigma \cdot 10^{-3}$ [kg· (mol·K)$^{-1}$]	$\Delta_r G_{11}^0$ [kJ·mol^{-1}]	$\Delta_r S_{11}^0$ [J·mol^{-1}·K^{-1}]	Ref./ method
Nd	NaCl	7.18 ± 0.26	-0.09 ± 0.13			-20.20 ± 0.54	-2.67 ± 0.35	-41.0 ± 1.4	69.7 ± 6.8	**p.w., a**
Eu	NaCl	6.77 ± 0.09	-0.28 ± 0.09	10.23 ± 0.39	-0.65 ± 0.47			-38.6 ± 0.5		**p.w., b**
Am	NaCl	6.67 ± 0.04	-0.25 ± 0.05					-38.1 ± 0.2		**p.w., c**
literature values (extraploted to $I_m = 0$)										
Nd	$NaClO_4$	7.21								CRO1950, d
	NaCl/ $NaClO_4$	6.59 ± 0.40								XIO2011, $
	NaCl/ $NaClO_4$	6.30								LIU1997, e
	$NaClO_4$	7.21		11.51						MAN1966, d, #
Eu	$NaClO_4$	6.63	-0.69	10.87	-1.19					CET2008, §
	NaCl/ $NaClO_4$	6.91 ± 0.40								XIO2011, $
	$NaClO_4$	6.52 ± 0.98								MAN1966, d, #
	NaCl/ $NaClO_4$	6.72		11.22						WOO1993,
	NH_4NO_3	6.52		11.09						SCHI2001, f
	$NaClO_4$	6.97 ± 0.14		11.60 ± 0.10						SEK1964, d, +,++
	NaCl/ $NaClO_4$	6.53		10.62						LIU1997, e
Am	NaCl/ $NaClO_4$	6.51 ± 0.33	-0.33 ± 0.10							HUM2005*
	NaCl	6.28 ± 0.08		10.49 ± 0.08						BOR2001, d, +
	NaCl	6.74 ± 0.12								SEK1964,g, +
	NaCl	6.65								PAZ1987,g, +
Cm	NaCl	6.86 ± 0.03	-0.21 ± 0.01			-2.7 ± 0.8		-39.14 ±0.17	122.3 ± 3	SKE2015, b, **

a...micro-titration calorimetry, b... TRLFS, c…UV-Vis spectroscopy, d…distribution, e…coprecipitation, f…cation-exchange resin and ICP-MS, g…solubility

$… using $\Delta\varepsilon_1 = 0.69 \pm 0.06$ and log β_{11} ($LaOx^+$) = 6.00 ± 0.40, §… extrapolated using SIT based on exp. data from [SEK1965, LYL1966, MAN1966, CAC1983, CAN1987], *... derived from different methods and media, #... thermodyn. K_1 -value (average) extrapolated using Davies equation, ##... exp. data taken from [CAN1987] and extrapolated using Pitzer parameters for maleate ion and its complexes, +…extrapolated using SIT with $\Delta\varepsilon_1 = -0.33 \pm 0.10$ kg/mol, ++…values of log β($EuOx^+$) and log β_{11} ($EuOx^{2-}$) reported in [SEK1965) were increased by 0.1 as suggested by Grenthe et al. [GRE1969], **…at 20°C

For completeness, log K^0_{prec} and $\Delta_r H^0_{prec}$ for the precipitation reaction are given in Tab. 4.13. The thermodynamic stability constant of the Nd_2Ox_3 precipitation does not agree with log K^0_{prec} (Nd_2Ox_3) given in [XIO2011] or [GAM2000]. Under consideration that the solvents/ionic media are different in these references log K^0_{prec} (p.w.) is still satisfying. The enthalpy $\Delta_r H^0_{prec}$ of -67.59 ± 1.79 kJ·mol^{-1} seems very strong exothermic even for such oxalate precipitation reaction; for comparison $\Delta_r H^0_{prec}$ for the Ca-oxalate precipitation is -21.5 ± 0.5 kJ·mol^{-1}. Recently results respective $\Delta_r H^0_{prec}$ Nd_2Ox_3 precipitation determined by the calorimeter TAM III (TA instruments)[1] yielded to $\Delta_r H^0_{prec}$ = -19.33 ± 3.0 kJ·mol^{-1} at I = 0.5 m. ,

Tab. 4.13: Thermodynamic standard data for formation of the solid $Nd_2Ox_3 \cdot x\ H_2O$ derived from micro-titration calorimetric measurements compared to literature values (T = 25°C)

Ln(III) An(III)	medium	logK^0_{prec}	$\Delta\varepsilon_{1,prec}$ [kg·mol^{-1}]	$\Delta_r H^0_{prec}$ [kJ·mol^{-1}]	$\Delta\varepsilon_{L,prec} \cdot 10^{-3}$ [kg·mol^{-1}·K^{-1}]	Ref./ method
Nd	NaCl	22.1 ± 0.5	-0.80 ± 0.21	-67.59 ± 1.79	-13.33 ± 1.08	p.w., a
Nd	HCl	31.1 ± 0.9				XIO2011
Nd	HCl	15.7 ± 0.9				SAR1927
Nd	NaCl	15.6*				GAM2000, b
Am	$HClO_4$	30.66				LEB1960, b
Eu	$NaClO_4$	13.0*#				GRE1969, b

a…micro(titration)calorimetry, b…solubility, *…regarding the reaction: Nd^{3+} + 3/2 Ox^{2-} → ½ Nd_2Ox_3, #...at 20 °C, p.w…present work

Eu(III) complexation reaction with oxalate studied by TRLFS

The Eu(III) luminescence spectra show typical intensity changes with varying oxalate concentrations: The strong intensity increase of the hypersensitive $^5D_0$ → $^7F_2$ transition at about 615 nm and the appearance of the magnetic $^5D_0$ → $^7F_0$ transition at about 578 nm (Fig. 4.20, left). The splitting of the $^7F_1$ and the $^7F_2$ peak indicates the presence of a strong complex with low symmetry. The asymmetry ratio (r = I($^7F_2$)/I($^7F_1$)) used to show the ligands influence on the $^7F_2$ peak more clearly, increases from 0.5 to 0.6 for the Eu^{3+} aqua ion (literature value for Eu^{3+} aqua ion is r = 0.5 ± 0.1 [KUK2010, MOU1999, DEN2005]) up to 2.5 at higher oxalate concentrations Eu-salicylate complexes show an r-value of 2.4 for the 1:1 complex $EuSal^{2+}$ (monodentate) and r = 2.6 for the 1:2 complex $EuSal_2^+$ (chelat complex) [BAR2013].

[1] These experiments were performed after completion of this project.

Heller et al. [HEL2012] determined an r-value of 2.4 for the 1:2 Eu-citrate complex $Eu(Hcit)_2^{3-}$. Compared to these r-values of other chelate complexes, the r-value of Eu-oxalate points to the presence of a 1:1 and most probably to a 1:2 complex. In Fig. 4.20, right it is obviously that with increasing ionic strength the $^7F_2/^7F_1$-intensity ratio decreases (at the same oxalate concentration) which means a reduction of the complex strength until 2-3 m NaCl. This trend was already observed in [BOR2001, CHO1996].

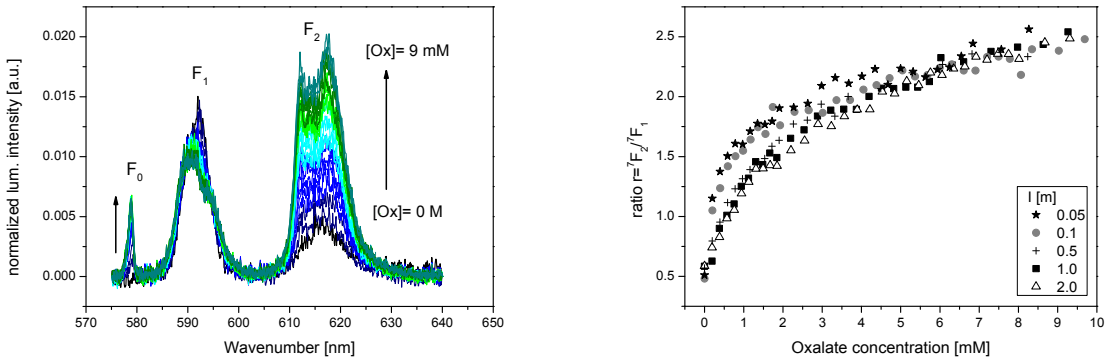

Fig. 4.20: Normalized luminescence spectra of the Eu(III)-oxalate titration at I=1 (left) and calculated r-values at different ionic strength (right), T = 25°C

The fluorescence lifetime of the Eu(III) aqua ion is independent from the ionic strength (Fig. 4.21, left) and has an average value of 112 ± 5 µs (n_{H2O} = 9.0 ± 0.5) which agrees very well with literature data [HOR1979, KIM2001, HEL2011]. During the titration with oxalate, the fluorescence lifetime prolongs to 149 ± 8 µs (n_{H2O} = 6.6 ± 0.5) (Fig. 4.21, right). The decay curve is fitted mono-exponentially independent of ionic strength or oxalate concentration. This is due to the fast ligand exchange of Eu(III) which results in a mixed lifetime of uncomplexed and complexed Eu(III) species [FAN1998]. Thakur et al. [THA2006] determined a lifetime for the 1:1 complex Eu(III)oxalate of 139 ± 3 µs (n_{H2O} = 6.8 ± 0.5) at I = 6.6 m. Eu(III)-BTC (pyromellitic acid) as well as Eu(III)-malonate complexes show similar lifetimes of τ = 135 ± 3 µs (n_{H2O} = 7.3 ± 0.5) or 148 µs (n_{H2O} = 6.6 ± 0.5), respectively [BAR2011, KIT2006]. In our case, 2-3 water molecules were replaced in the first coordination sphere of Eu(III), thus a 1:1 and a 1:2 Eu-oxalate complex could be present in solution.

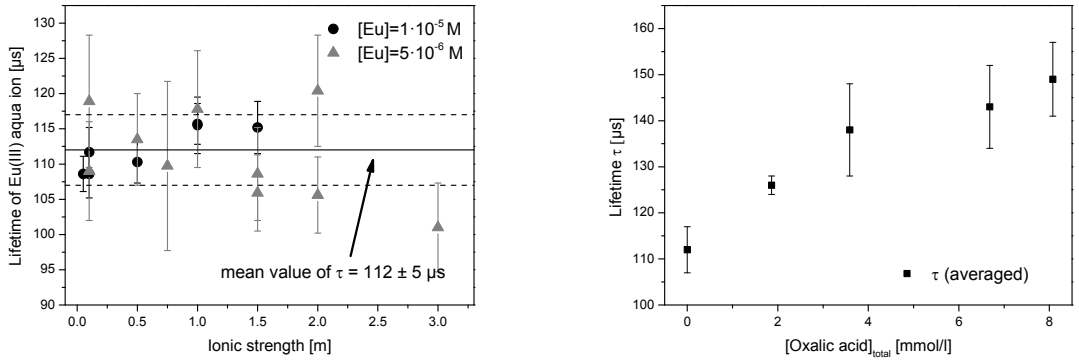

Fig. 4.21: Left: fluorescence lifetime of the Eu(III) aqua ion as f(I_m), right: averaged over all ionic strengths as f(oxalate concentration), T = 25°C

A parallel factor analysis (PARAFAC) of the time-resolved spectra at different ionic strengths was performed (Fig. 4.22). The spectra at I_m = 0.05 m were analyzed using a two component analysis including the Eu(III) aqua ion and the 1:1 complex (core consistency at 100 %). From I_m = 1 until 2 m, the Eu-oxalate system could be analyzed using three components resulting in appropriate lifetimes. Two component analyses (at I_m = 1 m and 2 m) would result in the known Eu(III) aqua ion lifetime and in a mixed lifetime of 1:1 and 1:2 complex. The lifetimes for the Eu(III) aqua ion and the 1:1 complex agree well with the lifetimes reported above. The lifetime for the 1:2 Eu-oxalate complexes was not reported in literature until now. Thus, by using the multidimensional analysis of PARAFAC, it was possible to determine the lifetime of the complex $Eu(Ox)_2^-$ in solution which is favored at higher ionic strengths due to the dehydration effect of the salt medium. All lifetimes of two- and three component analysis are averaged and collected in Tab. 4.14.

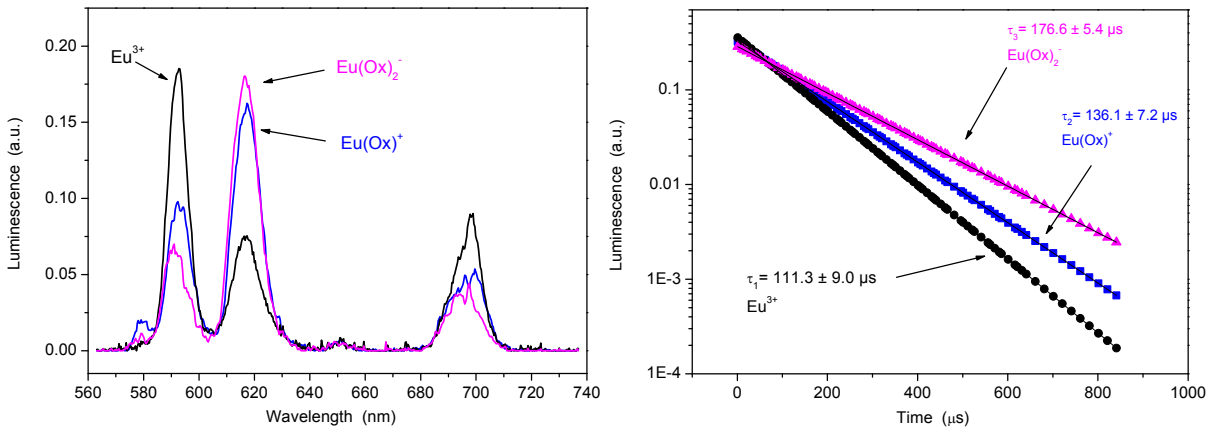

Fig. 4.22: Single luminescence spectra and mono-exponentially fitted decay curves of each species at I_m=1 m (NaCl), derived by PARAFAC

Tab. 4.14: Average lifetimes resulting from two (I_m= 0.05m) and three component analysis (I_m = 1 and 2 m) using PARAFAC

species	τ(µs)	n(H_2O)
Eu^{3+} (aq)	114 ± 0.8	8.8
$Eu(Ox)^{+}$	141 ± 0.4	7.0
$Eu(Ox)_2^{-}$	188 ± 0.9	5.1

Consequently, the 1:2 complex could be included in the analysis with SPECFIT at higher ionic strengths. The first complex showed good consistency in SPECFIT and also good linearity in the slope analysis with slopes around one (Fig. 4.23). The stability constant of the 1:2 Eu-oxalate complex had to be fixed within a certain range in the analysis in SPECFIT (values for $AmOx_2^-$ from [HUM2005]) and the resulting pure spectra were averaged. The overestimation of the second complex might be attributed to either a low or to the 1:1 complex equal luminescence of the 1:2 complex or low percentage of the complex in solution.

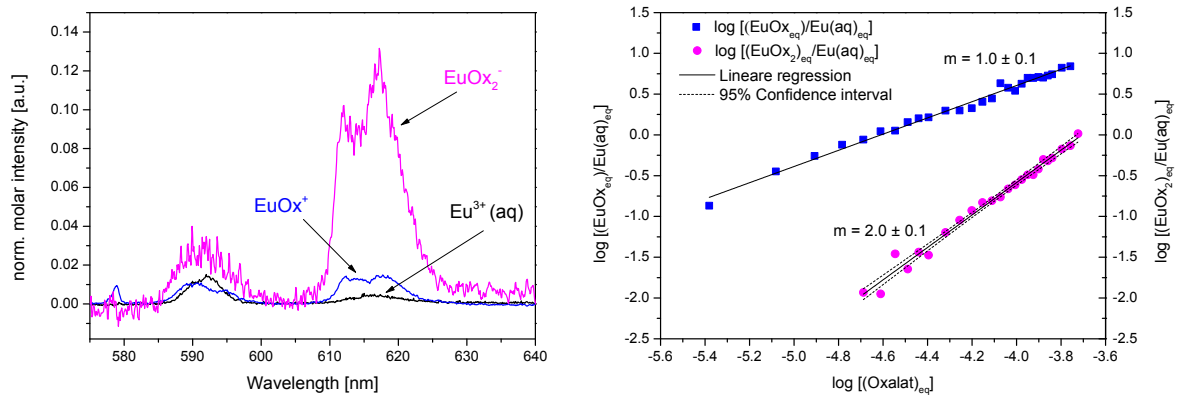

Fig. 4.23: Single luminescence spectra of Eu(III) species (left) and slope analysis (right) at I_m = 1 m (NaCl)

The SIT plot (Fig. 4.24) for the 1:1 Eu-oxalate complex shows good linearity and the extrapolated stability constant log β_{11}^0 are in good agreement with the literature values (cf. Tab. 4.12) The SIT plot for the 1:2 complex shows a slightly higher deviation from linearity than the 1:1 complex but the stability constant extrapolated to infinite dilution still lies within the range of literature values. For the Eu(III)-oxlate system, $\Delta\varepsilon_1$ shows similar values to related systems like Am(III)- and Cm(III)-oxalate. The value for $\Delta\varepsilon_2$ shows a high uncertainty.

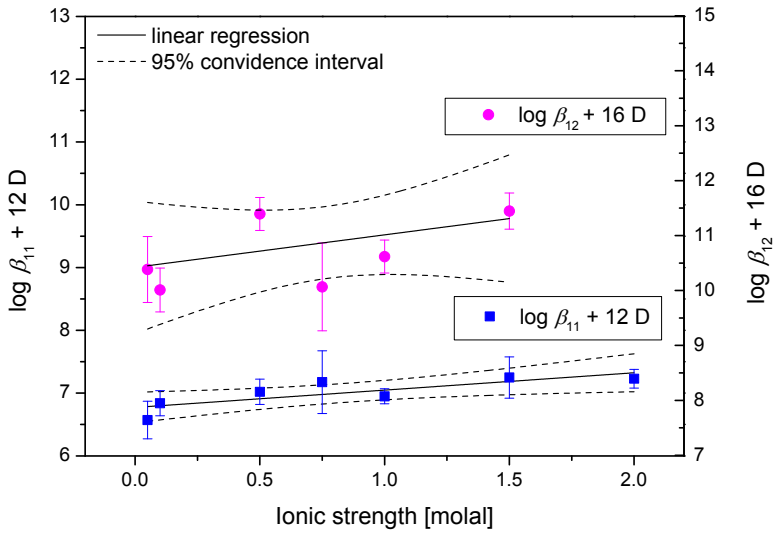

Fig. 4.24: *SIT plot for log β_{1n} for the formation of 1:1 and 1:2 Eu(III)-oxalate complexes (in NaCl)*

Am(III) complexation reaction with oxalate studied by UV-vis spectroscopy

The absorption maxima of Am(III) is between 503 nm and 504 nm which corresponds to the $^7F_0 \rightarrow {}^5L_6$ transition [KIM2001, BAR2014, EBE1972]. The UV-vis spectra of the titration of Am(III) with oxalate shows a red-shift of the Am(III) transition from 504 nm to 506 nm with rising oxalate concentration (Fig. 4.25). The red-shift of Am-lactate has the same magnitude and is described in [BAR2014]. Next to the red-shift, the intensity of the band decreases at higher oxalate concentrations, shown in Fig. 4.25, left. The absorption maximum is here at 507-508 nm. The intensity decrease and the increase of the baseline near the UV range (not shown) could be caused by precipitation processes.

At I_m = 1 m two complexes (3 components) were fitted using the SPECFIT (with Durbin Watson factor of 1.5 and error ≈ 1%, see chapter 4.2.2). The spectra with intensity decrease could not be fitted with two complexes because the second complex showed no consistency.

Therefore the data analysis was limited to the determination of log β_{11} for the $AmOx^+$ complex and the stability constant for the second complex included in the chemical model was taken from [HUM2005]. The slope analysis of the single component spectra of $Am(Ox)^+$ always resulted in slopes around unity (Fig. 4.26).

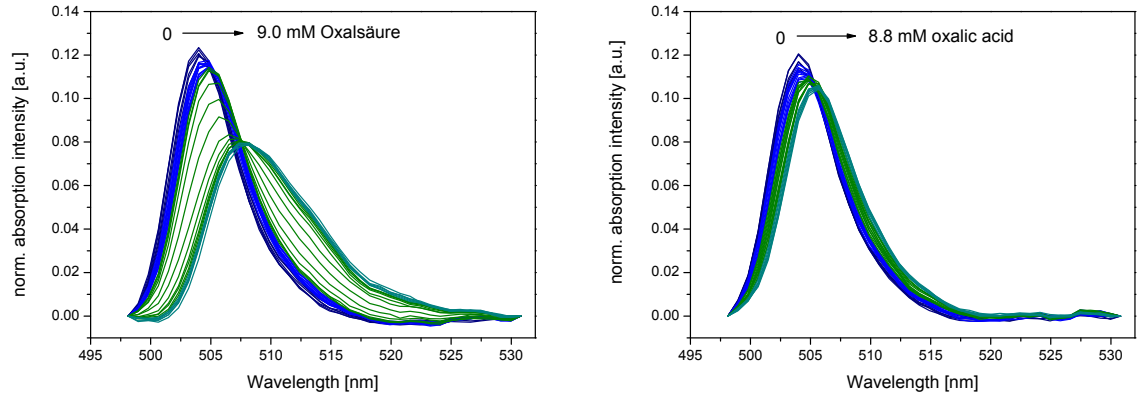

Fig. 4.25: UV/Vis spectra of the Am(III)-oxalate titration with $[Am^{3+}] = 1.3 \cdot 10^{-5}$ M at $I_m = 0.1$ m (left) und $I_m = 1$ m (right), pH = 2

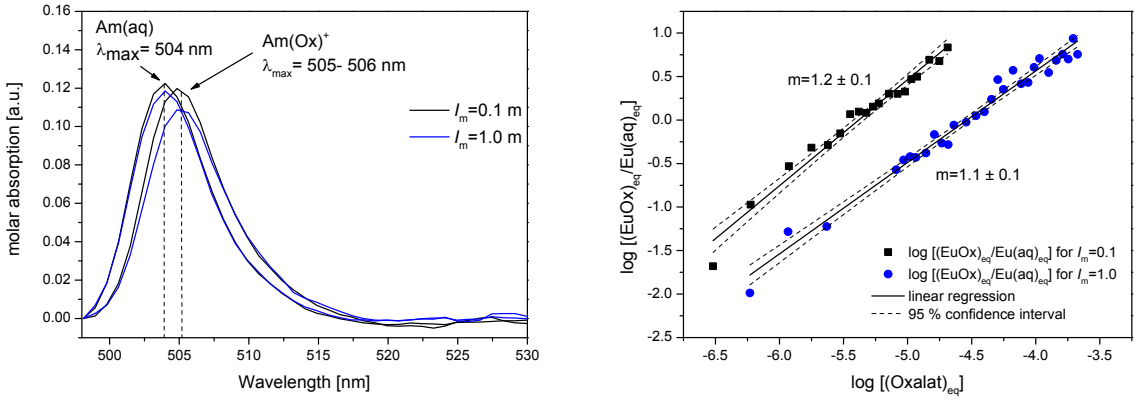

Fig. 4.26: Right: Single component absorption spectra, left: slope analysis

The SIT plot for the first Am-Ox complex shows good linearity (Fig. 4.27). The stability constant at I_m = 0.05 m was not included in the analysis due to strong deviation. In the SIT-theory the short range interactions between metal or/and ligand and background electrolyte have to be predominant. The deviation in the SIT plot at small concentrations of the background electrolyte (I < 0.25 m) might be attributed to the stronger influence of the interaction between ligand and metal ion instead of the above mentioned short range interactions between ligand or metal ion with the background electrolyte.

The extrapolated stability constant log β_{11}^0 as well as the $\Delta\varepsilon_1$ value is in good agreement with literature data. For the first time, $\Delta\varepsilon_1$ and the single interaction coefficient $\varepsilon(AmOx^+, Cl^-)$ with ε = -0.10 ± 0.05 kg·mol^{-1} were determined (mixed media were used in [HUM2005], ε = 0.08 ± 0.05 kg·mol^{-1}). However, all values listed in Tab. 3.12 do not differ very much from each other, so the medium effect between sodium chloride and sodium perchlorate is very little.

The log β_{11}^0 value from [BOR2001] was extrapolated to zero ionic strength by using one ionic strength only and $\Delta\varepsilon_1$ from [HUM2005] which could explain the deviation from our value.

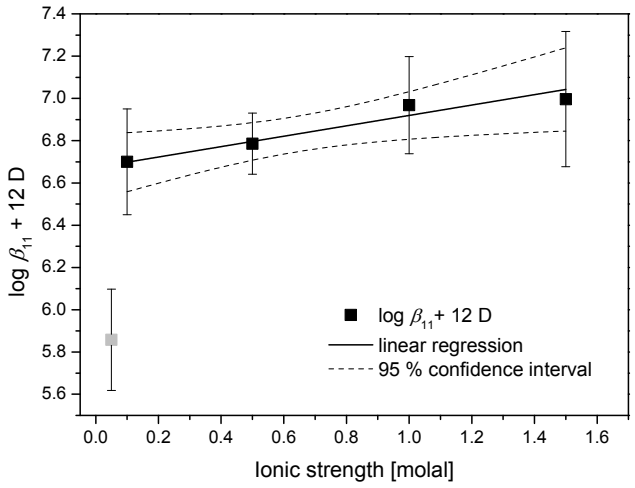

Fig. 4.27: SIT plot for the complexation constant of the 1:1 Am(III) oxalate complex, grey…not included in analysis

Characterization of the solid Eu(III)-oxalate

Luminescence measurements of the suspension

The fluorescence spectrum of the suspension of solid Eu-oxalate differs from the single spectra of the Eu-oxalate complexes (Fig. 4.28). The spectrum of the suspension has a $^7F_0$ peak at 579.7 nm with very low intensity (in contrary to 578.9 nm of the calculated 1:1 complex spectrum), a threefold splitting of the $^7F_1$ band and a relative small peak with a shoulder of the $^5D_0 \rightarrow {}^7F_2$ transition.

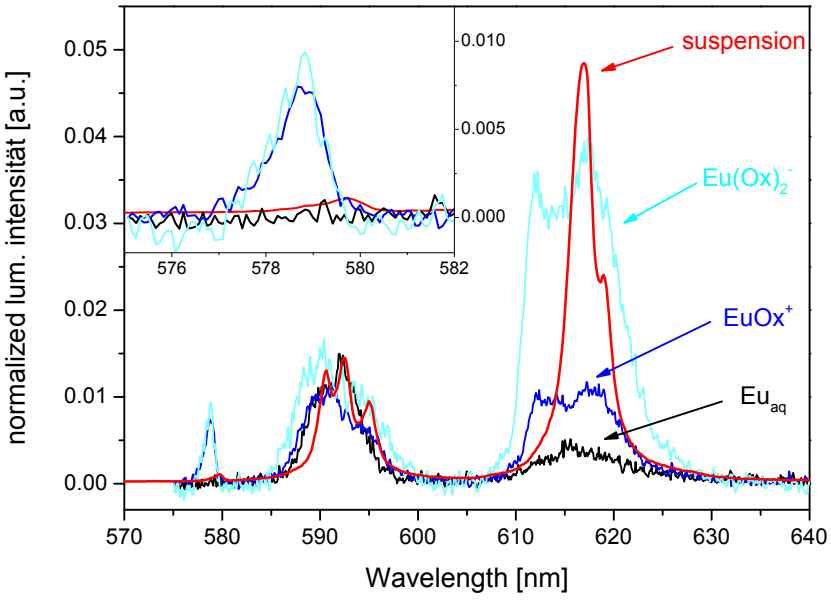

Fig. 4.28: Luminescence spectrum of the suspension (Eu(III)/Oxalate = 1:12) measured in comparison to the single component spectra of the Eu-oxalate complexes ([Eu] = $5 \cdot 10^{-6}$ M), I_m = 0.5 m, pH = 2 .5, T = 25°C

In the investigated Eu-oxalate suspensions there are one main species with a lifetime of 267 ± 1 µs (n_{H2O} = 3.4 ± 0.5). Due to the chelating character of oxalate, 6 water molecules were replaced by three bidentate oxalate molecules. This points to the presence of a 2:3 solid (or 1:1.5 solid) which is already known in literature [ZHA2009, WAN2013] and shown in Fig. 4.29 for Nd-oxalate. Horrocks et al. [HOR1969] found a similar lifetime of τ = 283 µs (n_{H2O} = 3.2 ± 0.5) and determined a composition of the crystalline solid of $\{Eu_2(H_2O)_6(Ox)_3\} \cdot 4\ H_2O$.

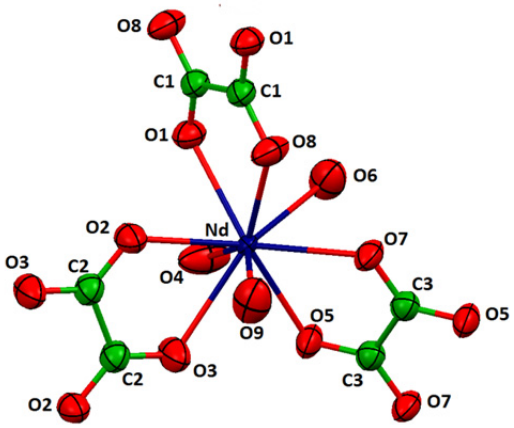

Fig. 4.29: Crystal structure of $[Nd(Ox)_{1.5}(H_2O)_3] \cdot 2H_2O$ [ZHA2009]

Site-selective TRLFS with Eu(III)

A direct excitation of Eu(III) within the $^5D_0 \rightarrow {}^7F_0$ transition which is non-degenerated shows one transition for each Eu(III)species. The excitation spectrum of the solid Eu-oxalate phase shows a main transition at 579.74 nm and small side peaks at 579.30 nm and 578.95 nm (Fig. 4.30). Thus, one main species and one or two side species can be expected.

The lifetime of the main species (λ_{ex} = 579.74 nm) is τ = 300 ± 3 µs (n_{H2O} = 2.9 ± 0.5) which points to the exchange of six water molecules in the first coordination shell of Eu replaced by three oxalate molecules acting as a chelating agent. This lifetime is very similar to the lifetime determined in the suspension mixture (267 ± 1 µs with n_{H2O} = 3.4 ± 0.5) and to the lifetime determined in [HOR1969], thus it can be attributed to the solid $\{Eu_2(H_2O)_6(Ox)_3\}\cdot 4\ H_2O$. The lifetime of the suspension measured at room temperature is smaller than this one obtained at low temperatures. This can be contributed to the reduction of the radiationless deactivation processes at low temperatures [KUK2010].

The minor species whose existence was also supposed can be seen in the site-selective spectrum as well, namely in the side peaks. The lifetime of the second highest peak in the excitation spectrum is τ = 423 ± 3 µs (n_{H2O} = 1.9 ± 0.5) which corresponds to an exchange of seven water molecules around Eu(III). Since now, this solid phase is not described in the literature. A possible composition could contain a protonated oxalate species which leads to a monodentate coordination: $\{Eu_2(Ox)_3(HOx)\}Na\cdot x\ H_2O$.

The emission spectra of both phases are demonstrated in Fig. 4.31. They are comparable to the emission spectrum of the Eu(III)-oxalate suspension which was recorded at room temperature. The maximum splitting of the $^7F_1$ peak (and hence also the maximum splitting of the $^7F_2$ peak which is not resolved due to the technical measurements reasons) indicates the presents of low symmetry phases. The known solid possesses a monoclinic crystal structure with a space group of $P2_1/c$ [ZHA2009]. According to the 'International Tables for Crystallography', this corresponds to a C_{2h}-symmetry. Hence, the second not identified species must also possess a low symmetry like S_1, C_S, C_1, C_2, C_{2v}, C_{2h}, D_2, D_{2h}. [BRU1989]

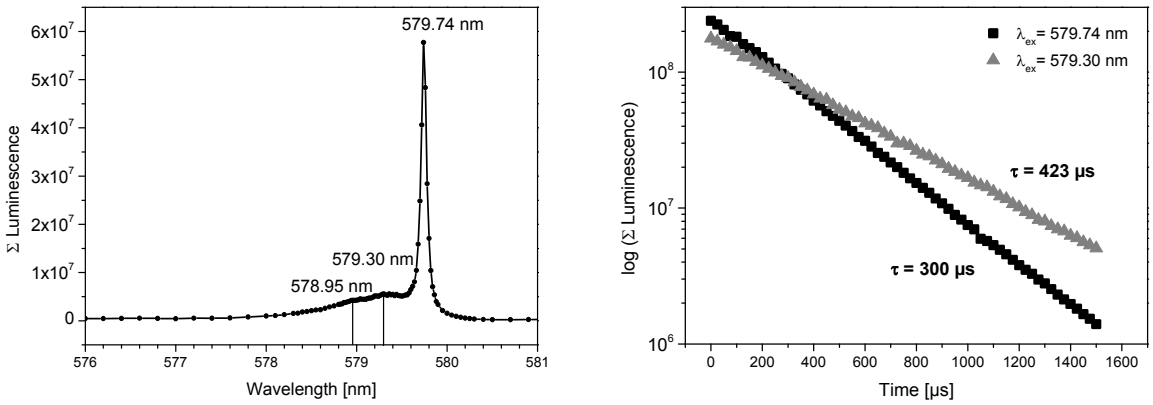

Fig. 4.30: Left: excitation spectrum of the Eu(III)-oxalate solid, right: the luminescence decay curves at different excitation wavelengths

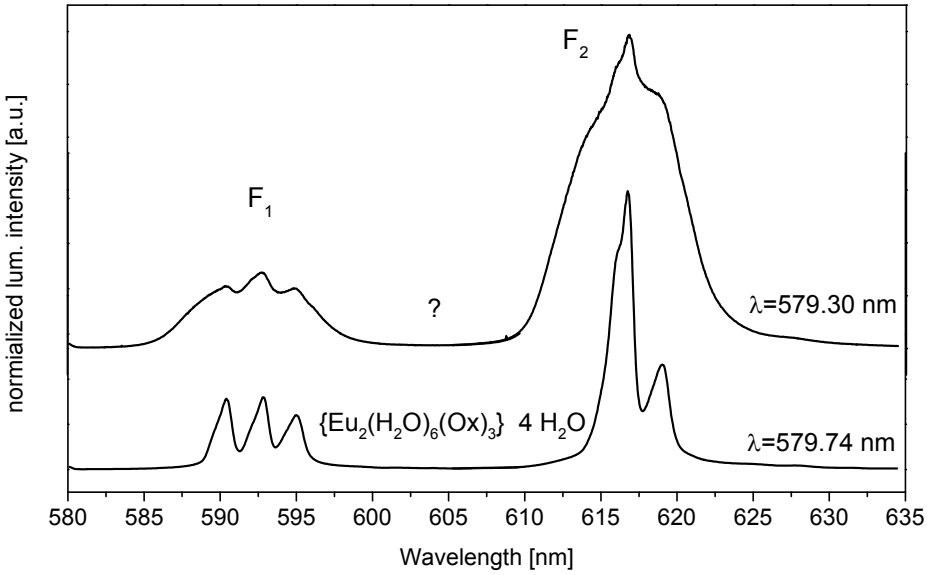

Fig. 4.31: Emission spectra of two solid Eu(III)-oxalate species

IR spectroscopy

In the IR spectra of both the Nd-oxalate and Eu-oxalate solid compared to disodium oxalate Na_2Ox and oxalic acid, it is visible that both phases are very similar (cf. Fig. 4.32). The asymmetric oscillation ν_{3as} ($\nu \sim 1640$ cm^{-1}) and the symmetric oscillation ν_{3s} ($\nu \sim 1300$ cm^{-1}) of the O-C-O group and the deformation oscillation δ (OCO$\cdots$M) at about 800 cm^{-1} are at the same wavenumbers like the oscillation of the sodium oxalate solid. The difference of the asymmetric and symmetric oscillation $\nu_{3s/as}$ (COO) ($\Delta\nu$) can give information about the

coordination geometry of the carboxylic groups. A relatively large difference, in our case 320 cm^{-1}, corresponds to a monodentate coordination of the carboxylic groups of the oxalate also called side-on coordination. This was already proved in crystal structures [ZHA2009, WAN2013]. The bidentate or chelating coordination of the carboxylic groups is negligible because this coordination would result in a smaller difference in the Δν value [BAR2014, DEA1980, KAK1987]. The additional sharp bands in the Eu(III)-oxalate spectrum (indicated with an arrow) are probably caused by coordinated crystal water. The most important oscillations of all four substances are summarized in Tab. 4.15

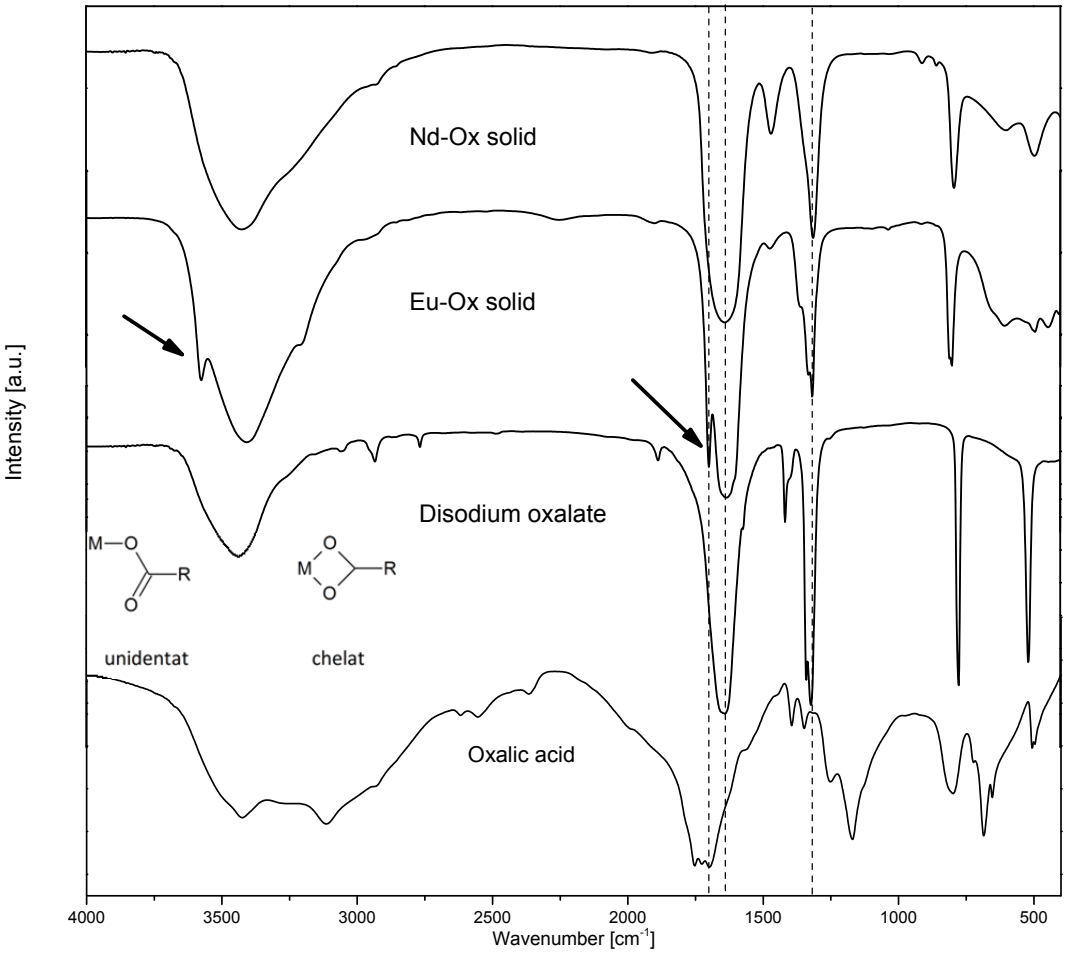

Fig. 4.32: IR spectra of the Nd(III)-oxalate and Eu(III)-oxalate solid and of oxalate reference substances

Tab. 4.15: Summary of most important oscillations of the IR spectra of the oxalate compound

wavenumber [cm^{-1}]	oscillation	functional group
3350- 3400	ν_s OH (wide)	H_2O
3200- 2500	ν OH (overtone)	H_2O/OH
1700-1750	ν_{3as} COO (s)	COOH (as dimer)→oxalic acid
~1640	ν_{3as} COO (s)	$C_2O_4^{2-}$
~1400	ν C-C	$C_2O_4^{2-}$, COOH
~1300	ν_{3s} COO (s)	$C_2O_4^{2-}$
1250	ν_{3s} COO (s) δ C-O-H	COOH→ oxalic acid
1170	γ (OH···O)	COOH→ oxalic acid
~800	δ (OCO···M) (s) δ C-O-H (wide)	$C_2O_4^{2-}$···M COOH→ oxalic acid

Furthermore, a XRD spectrum of the Nd-oxalate solid was recorded. The main species was determined to be $Nd_2Ox_3 \cdot 4.5\ H_2O$ which corresponds almost exactly to the identified fluorescence species $\{Eu_2(H_2O)_6(Ox)_3\} \cdot 4\ H_2O$ from [HOR1969].

4.5 Complexation with malonate

4.5.1 Literature study

Malonic acid (propandioic acid) is taken as a model ligand reflecting both the functional units of humic substances as well of a low molecular organic compound. Due to its ability to form moderately strong complexes with di- and trivalent metal cations and its implied significance for metal transport in the environment, the protonation of malonate and its complexation with trivalent ions has already been studied by many authors and some thermodynamic data are available for different media and ionic strengths. In Tab. 4.16 to 4.19 the essential literature values are summarized for the malonate protonation and complexation reaction, taken from [CHO1986, CHR1967, DEG1972, GEL1956, KIT2006, KET1992, KIR2008, POW1968, ROB1999, STE2001, SMI1987, THA2009, WAN2000, and WOO1993].

The most references describe the 1:1 and the 1:2 An(III)/Ln(III) complexes with the fully deprotonated malonate species Ma^{2-} but there is also one publication, in which the 1:3 complex was observed [KIT2006]. No literature data were found for complexes between lanthanides and the single protonated species HMa^-, but those complexes are known for monovalent and divalent metal cations [CAM1964, CAN1938, DAN1984, DAN1985].

General ion strength dependent enthalpy values are very scarce, as well as the interaction coefficients $\Delta\varepsilon_n$ and ε(Ln(III), malonate).

Tab. 4.16: Conditional stability constants for the protonation of malonate in different media at 25°C

I_m / medium [mol·kg^{-1}]	log K_1^H	log K_2^H	Ref/ method
0.1 NaCl	5.290 ± 0.002	2.635 ± 0.003	ROB1999, a
0.5 NaCl	5.071 ± 0.002	2.544 ± 0.003	
1 NaCl	5.009 ± 0.002	2.538 ± 0.003	
2 NaCl	5.014 ± 0.002	2.595 ± 0.003	
3 NaCl	5.080 ± 0.002	2.690 ± 0.003	
5 NaCl	5.293 ± 0.002	2.942 ± 0.003	
1 NaCl	4.99 ± 0.02	2.58 ± 0.02	STE2001, a,b
2 NaCl	4.98 ± 0.02	2.60 ± 0.02	
3.05 NaCl	5.09 ± 0.02	2.67 ± 0.04	
5.19 NaCl	5.39 ± 0.02	2.99 ± 0.03	
1 NaCl	5.253 ± 0.004	2.631 ± 0.005	KET1992, a
0 NaCl	5,697 ± 0,001	2.852 ± 0.003	
0.1 NaCl	5.253 ± 0.004	2.631 ± 0.005	
0.5 NaCl	5.016 ± 0.009	2.527 ± 0.01	
1 NaCl	4.946 ± 0.01	2.517 ± 0.012	
3 NaCl	5.056 ± 0.014	2.693 ± 0.012	
1.05 $NaClO_4$	5.0682 ± 0.01	2.59 ± 0.01	KIT2006, a, b
0.105 $NaClO_4$	5.2767	2.6467	DEG1972, a, b
2.204 $NaClO_4$	5.0679	2.5578	DEG1972, a, b
6.6 $NaClO_4$	5.72 ± 0.03	2.95 ± 0.04	THA2009, a
1.05 $NaClO_4$	5.08 ± 0.01	2.57 ± 0.01	RAO2002, a, b
0.105 $NaClO_4$	5.2982	2.6382	CAM1964, a

a…potentiometric, b…calorimetric

Tab. 4.17: Selected reaction enthalpies for the protonation of malonate in different media at 25°C

I_m / medium [mol·kg^{-1}]	$\Delta_r H_1^H$ [kJ·mol^{-1}]	$\Delta_r H_2^H$ [kJ·mol^{-1}]	Ref/ method
0.1 NaCl	4.9 ± 0.5		STE2001, a, b
1 NaCl	3.4 ± 0.5	-0.4 ± 0.05	
1,54 NaCl		-1.6 ± 0.05	
2 NaCl	1.5 ± 0.5	-2.73 ± 0.05	
3.05 NaCl	-0.8 ± 0.5	-3.1 ± 0.05	
5.19 NaCl	-6.5 ± 0.5	-6.93 ± 0.05	
1.03 NaCl	3.42 ± 0.3	-0.40 ± 0.3	
1.54 NaCl	2.38 ± 0.3	-1.60 ± 0.3	
2.09 NaCl	0.61 ± 0.3	-2.73 ± 0.3	
3.26 NaCl	-1.3 ± 0.3	-3.1 ± 0.3	

Tab. 4.17: Continuation

1 NaCl	-4.43 ± 0.11	0.9 ± 0.3	KET1992, a
0 NaCl	-5.13 ± 0.11	0.1 ± 0.3	
0.1 NaCl	4.43 ± 0.11	-0.9 ± 0.3	
0.5 NaCl	3.74 ± 0.18	-1.8 ± 0.3	
1 NaCl	3.04 ± 0.25	-2.5 ± 0.3	
3 NaCl	0.15 ± 0.44	-4.5 ± 0.7	
1.05 $NaClO_4$	1.81± 0.05	-1.6 ± 0.1	KIT2006, a, b
1.05 $NaClO_4$	2.07 ± 0.03	-1.64 ± 0.03	RAO2002, a, b
0.105 $NaClO_4$	3.85 ± 0.13	-1.21 ± 0.4	CHR1967, b

a…potentiometric, b…calorimetric

Tab. 4.18: Selected conditional stability constants for the complexation of malonate with trivalent lanthanides and actinides in different media at 25°

An(III)/ Ln(III)	**I_m / medium [mol·kg^{-1}]**	**log K_1**	**log K_2**	**Ref / method**
Nd	0.105 $NaClO_4$	4.3182 ± 0.07		DEG1972, a, b
Sm	2.204 $NaClO_4$	3.2279 ± 0.05		DEG1972, a, b
Sm	0.105 $NaClO_4$			DEG1972, a, b
Sm	0.105 $NaClO_4$	4.5082 ± 0.03		ANS1985, a, b
Eu	0.105 $NaClO_4$	4.1582 ± 0.01	2.455 ± 0.004	WAN2000, c, d
Eu	1.05 $NaClO_4$	3.6082 ± 0.03	2.4056 ± 0.014	KIT2006, a, b
Eu	0.105 $NaClO_4$	4.7082 ± 0.07	3.105 ± 0.04	DEG1972, a, b
Eu	6.6 $NaClO_4$	4.28 ± 0.06		THA2009, a
Am	6.6 $NaClO_4$	4.37 ± 0.05		THA2009, a
Cm	6.6 $NaClO_4$	4.42 ± 0.06		THA2009, a
Nd	0 $NaClO_4$	5.41	3.63	WOO1993, e
Sm	0 $NaClO_4$	5.68	3.50	WOO1993, e
Eu	0 $NaClO_4$	5.78	3.51	WOO1993, e
Nd	0.105 KNO_3	4.06	1.52	POW1968, a
Sm	0.105 KNO_3	3.81	1.23	POW1968, a
Eu	0.105 KNO_3	3.69	1.31	POW1968, a
Nd	0.105 (k.A)	4.0	2.39	SMI1987, e
Sm	0.105 (k.A)	4.2	2.59	SMI1987, a
Eu	0.105 (k.A)	4.3	2.69	SMI1987, a
Eu	0 NaCl	5.49 ± 0.07		XIO2011, §

a…potentiometry, b…calorimetry, c…fluorescence spectroscopy, d…absorption spectroscopy, §… extrapolated using SIT based on experimental data

Tab. 4.19: Selected reaction enthalpies for the complexation of malonate with trivalent lanthanides and actinides in different media at 25°C

Ln(III)/ An(III)	I_m / medium [mol·kg^{-1}]	$\Delta_r H_1$ [kJ·mol^{-1}]	$\Delta_r H_2$ [kJ·mol^{-1}]	Ref / method
Nd	0.105 $NaClO_4$	16.538 ± 0.293		DEG1972, a, b
Sm	2.204 $NaClO_4$	14.528 ± 0.167		DEG1972, a, b
Sm	0.105 $NaClO_4$	13.7746 ± 0.251		DEG1972, a, b
Sm	0.105 $NaClO_4$	13.77 ± 0.3		ANS1985, a, b
Eu	1.05 $NaClO_4$	14.00 ± 0.1	6.3 ± 0.4	KIT2006, a, b
Eu	0.105 $NaClO_4$	13.523 ± 0.377	7.827 ± 0.29	DEG1972, a, b
Eu	6.6 $NaClO_4$	16.3 ± 3.5		THA2009, a
Am	6.6 $NaClO_4$	15.7 ± 3.6		THA2009, a
Cm	6.6 $NaClO_4$	15.4 ± 3.4		THA2009, a
Sm	0.105 (k.A)	12.56	8.79	SMI1987, a

a…potentiometry, b…calorimetry

4.5.2 Experimental

Solutions

All chemicals were of analytical grade and used without further purification. The aqueous solutions of malonate were prepared freshly for each experiment by diluting the appropriate amount of solid disodiummalonate (Fluka) or malonic acid (AppliChem) in deionized water, respectively. Nd(III) stock solutions of 0.1 mol·kg^{-1} were prepared by dissolving solid $NdCl_3 \cdot 6H_2O$ (Alfa Aesar) or Nd_2O_3 (Merck). The exact Nd(III) concentration of the stock solutions were determined by ICP-MS (Elan9000, Perkin Elmer). The ionic strength of each sample solution was adjusted by adding NaCl, $NaClO_4$ or $CaCl_2$ (Merck, AppliChem, Fluka), respectively. The pH measurements were carried out with a combination pH electrode (type Ross, Orion, Thermo Scientific). The electrode was calibrated using standard buffer solutions of low ionic strength (I < 0.1 m, Merck) and for higher ionic strengths like procedure described in chapter 2.5

Isothermal micro-titration calorimetry

The experiments were performed in NaCl, $NaClO_4$ and $CaCl_2$ media, each at constant ionic strength (0.1-3 m). For the investigation of malonate protonation sample solutions with constant malonate concentration (2.5-15 mmol·kg^{-1}) and defined ionic strength were prepared and titrated with solutions of 25-50 mmol·kg^{-1} HCl or $HClO_4$ with the same ionic strength, respectively. The protonation of malonate in NaCl media was studied by three individual

series of measurement at different proton to malonate ratios varying between 2.7 and 10. One series of measurement at a proton to malonate ratio of 10 was performed in each $NaClO_4$ and $CaCl_2$ medium. The complex formation between Nd(III) and malonate was investigated in two modalities. In NaCl medium solutions with constant total Nd(III) concentration (2-5 mmol·kg^{-1}) and a defined ionic strength were prepared and titrated with a malonate stock solution (25-100 mmol·kg^{-1}) with the same ionic strength. Three individual series at different ligand to metal ratios between 9 and 20 were measured. In $NaClO_4$ and $CaCl_2$ media solutions of 1.5 mmol·kg^{-1} Nd(III) and 15 mmol·kg^{-1} malonate (metal to ligand ratio is 1:10) and certain ionic strengths were prepared and titrated with either $HClO_4$ or HCl (50 mmol·kg^{-1}). The experimental details of the calorimetric titrations are shown in Tab. 4.20

Tab. 4.20: Selected experimental series for isothermal micro-titration calorimetry of malonate protonation and Nd(III)-malonate complex formation

reactants		**medium**	I_m	$c_{analyte}$	$c_{titrant}$	$V_{titrant}$	$[H+]_{free}$
analyte	**titrant**		**[mol·kg^{-1}]**	**[mmol·kg^{-1}]**	**[mmol·kg^{-1}]**	**[mL]**	**[mol·kg^{-1}]**
Ma	HCl	NaCl	0.5-3	5	27	0.12	$1.6\cdot10^{-7}$-$3.8\cdot10^{-3}$
Ma	HCl	NaCl	0.25-0.75	10	27	0.08	$2.6\cdot10^{-7}$-0.01
Ma	HCl	NaCl	0.25-2	2.5	25	0.08	$5.7\cdot10^{-7}$-$2.7\cdot10^{-3}$
Ma	$HClO_4$	$NaClO_4$	0.1-1	15	50	0.08	$3\cdot10^{-5}$-$2.5\cdot10^{-3}$
Ma	HCl	$CaCl_2$	0.5-2	15	50	0.08	$1.3\cdot10^{-4}$-$2.4\cdot10^{-3}$
Nd	Ma	NaCl	0.25-3	2	25	0.04	$2.2\cdot10^{-6}$
Nd	Ma	NaCl	0.25-3	3	26,7	0.08	$2.2\cdot10^{-6}$
Nd	Ma	NaCl	0.5-3	5	100	0.04	$2.2\cdot10^{-6}$
Nd/Ma	$HClO_4$	$NaClO_4$	0.1-1	1.5/15	50	0.08	$3.6\cdot10^{-5}$-$2.4\cdot10^{-3}$
Nd/Ma	HCl	$CaCl_2$	0.5-2	1.5/15	50	0.08	$1.4\cdot10^{-4}$-$2.3\cdot10^{-3}$

Ma…malonate

4.5.3 Results and discussion

Malonate protonation

The protonation of malonate was studied in NaCl, NaCl and $CaCl_2$ in dependence of ionic strength. The thermogram of the titration of an almost neutral malonate solution with HCl or HClO4 shows clearly two steps (Fig. 4.33, left). The first step is an endothermic reaction that is characterized by a heat uptake upon ligand addition. In the second step the differential power decreases after ligand addition, typical for an exothermic reaction. Figure 4.33, right, shows the integrated heat curves at different ionic strengths in NaCl medium. The conditional constants and enthalpies for the protonation obtained from the evaluation of integrated calorimetric heat curves like described in chapter 4.2.1 are given in Tab.4.21

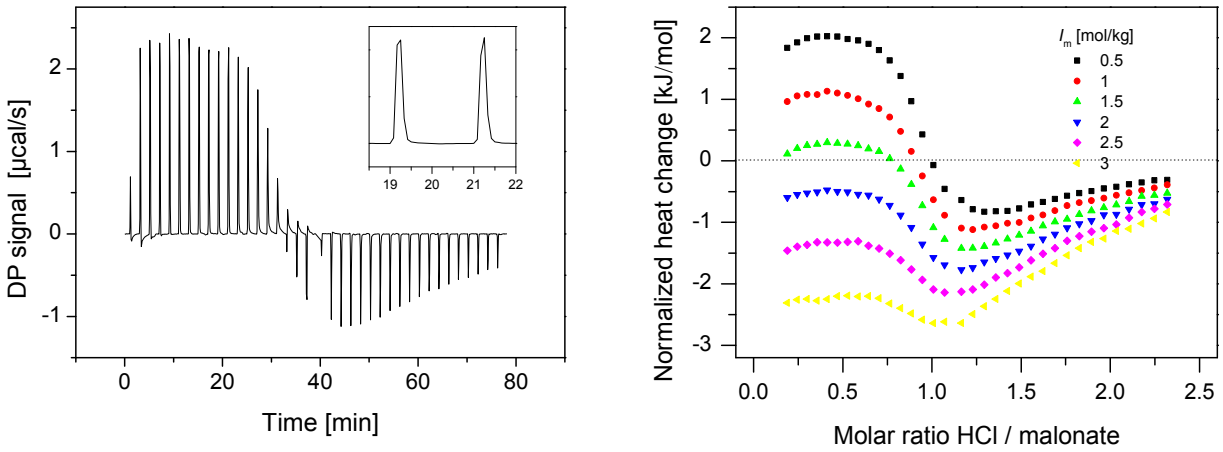

Fig. 4.33: *Left: Thermogram of titration of 5 mmol·kg^{-1} malonate with 0.1 m HCl (I = 0.5 m, T = 25°C). Within less than 1 min temperature equilibrium is reached (inset), right: normalized heat change for titration of 5 mmol·kg^{-1} malonate with HCl at various ionic strengths in NaCl medium (T = 25°C)*

Tab. 4.21: Conditional stability constants and formation enthalpies for malonate protonation at various ionic strengths in NaCl, $NaClO_4$ and $CaCl_2$ media (T = 25°C)

medium	I_m [mol·kg^{-1}]	$\log K_1^H \pm 2\sigma$	$\Delta_r H_1^H \pm 2\sigma$ [kJ·mol^{-1}]	$\log K_2^H \pm 2\sigma$	$\Delta_r H_2^H \pm 2\sigma$ [kJ·mol^{-1}]
NaCl	0.25	5.15 ± 0.08	3.12 ± 0.01	2.86 ± 0,20	-1.95 ± 0.06
	0.5	4.99 ± 0.03	2.10 ± 0.01	2.74 ± 0,17	-2.04 ± 0.08
	0.75	4.93 ± 0.08	1.67 ± 0.01	2.87 ± 0.14	-2.28 ± 0.12
	1	4.93 ± 0.07	1.13 ± 0.002	2.75 ± 0.13	-2.48 ± 0.04
	1.5	4.97 ± 0.16	0.28 ± 0.6	2.76 ± 0.14	-2.96 ± 0.02
	2	4.99 ± 0.09	-0.47 ± 0.03	2.79 ± 0.16	-3.31 ± 0.01
	2.5	5.00 ± 0.1	-1.25 ± 0.02	2.87 ± 0.12	-3.56 ± 0.02
	3	5.13 ± 0.34	-2.25 ± 0.02	2.86 ± 0.34	-4.18 ± 0.02
$NaClO_4$	0.1	5.35 ± 0.08	3.58 ± 0.04	2.61* [a]	-2.40 ± 0.04
	0.3	5.20 ± 0.06	2.99 ± 0.02	2.58*	-2.59 ± 0.04
	0.5	5.09 ± 0.02	2.51 ± 0.02	2.56*	-2.67 ± 0.04
	0.7	5.05 ± 0.01	2.32 ± 0.02	2.55*	-2.65 ± 0.02
	1.0	5.06 ± 0.08	1.89 ± 0.02	2.59*[b],[c]	-2.56 ± 0.22
$CaCl_2$	0.5	5.03*	2.5*	2.78 ± 0.12	-0.8 ± 4
	1	4.94*	1.12*	2.72 ± 0.04	1.1 ± 0.4
	1.5	4.97*	0.28*	2.64 ± 0.36	-0.86 ± 0.14
	2	5.00*	-0.47*	2.57 ± 0.9	-0.07 ± 0.34

* Treated as fixed values in analyses of the integrated heat curve, values from a) [DEG1972], b) [KIT2006], c) [KIR2008]

In Fig. 4.34, left, the determined values for the first protonation step are plotted together with literature values for NaCl and $NaClO_4$ media. Our values of the protonation constants and their ionic strength dependency show a good agreement with the literature value.

In the case of NaCl and $NaClO_4$ media it can be found that for the formation of the fully protonated acid H_2Ma the medium effects on log K_2^H are less pronounced than for the formation of single protonated species. The observed changes of log K_2^H with increasing ionic strength are smaller than the experimental uncertainty of the herewith determined values. In contrast, DeRobertis et al. [ROB199] observed a decline of log K_2^H of approximately 0.1 log units until an ionic strength of 1 mol·kg^{-1} within a steep increase between ionic strength from 2 to 5 mol·kg^{-1} NaCl. It should be noted that it was difficult to fit the stability of H_2Ma species from the heat curves in case of $NaClO_4$ medium. Therefore log K_2^H were treated as fixed values for the analysis of the heat curves in the program HypΔH. The ionic strength dependent values were estimated from literature [KIT2006], [KIR2008] and [DEG1972] and from the ionic strength dependence of K_2^H in NaCl medium.

A special case is the $CaCl_2$ media. Compared to NaCl/$NaClO_4$ a distinct decrease of log K_2^H is observable, but it was not possible to extract the thermodynamic data for the first protonation reaction from the heat curves. This is caused by the fact that under the given conditions the lowest adjustable pH was 3.6 so the formation of the single protonated species could not be observed to a sufficient extend. Therefore, stability constants and reaction enthalpies for this species were taken from the NaCl experiment and fixed throughout the fitting. Furthermore it is known that Ca^{2+} form quite strong complexes with both deprotonated forms Ma^{2-} and HMa^- [DAN1985], [DEE1991], [FEI1995]. Hence, the reactions 4.13 and 4.14 have also to be taken into heat curve analysis.

$$Ca^{2+} + Ma^{2-} \rightleftharpoons CaMa \qquad K_1^{Ca},\ \Delta_r H_1^{Ca} \qquad 4.13$$

$$Ca^{2+} + HMa^{-} \rightleftharpoons CaHMa^{+} \qquad \beta_{CaHMa},\ \Delta_r H_{CaHMa} \qquad 4.14$$

Stability constants and formation enthalpies of calcium malonate complexes are reported to be log K_1^{Ca} = 2.39 and $\Delta_r H_1^{Ca}$ = 7 kJ·mol^{-1} for CaMa and log β_{111}^0 = 6.59 and $\Delta_r H_{111}^0$ = 5 kJ·mol^{-1} for $CaHMa^+$, respectively [DAN1985]. The conditional thermodynamic data provided by Daniele et al. [DAN1984] were used to include both calcium malonate complexes in the chemical model for the least squares regression analysis.

With increasing ionic strength there is a decrease of the formation enthalpies for both protonation steps. The reactions proceed more exothermic at higher ionic strength. This is the same observation like for the lactate and oxalate system and an explanation are already given there (see chapter 4.3.3). At ionic strength larger than 1 m the reaction enthalpy for the first protonation step changes from endothermic to exothermic. The same effect was observed in [STE2001] too, who also studied the ionic strength dependency of malonate protonation in NaCl calorimetrically. But they used a calorimeter with a sample volume of 50 ml (250 times larger than our sample volume). Generally our enthalpy values shows the same trend like the literature values from [STE2001] and [ROB1999] but the values are somewhat lower (see Fig. 4.34 right for the first protonation reaction)

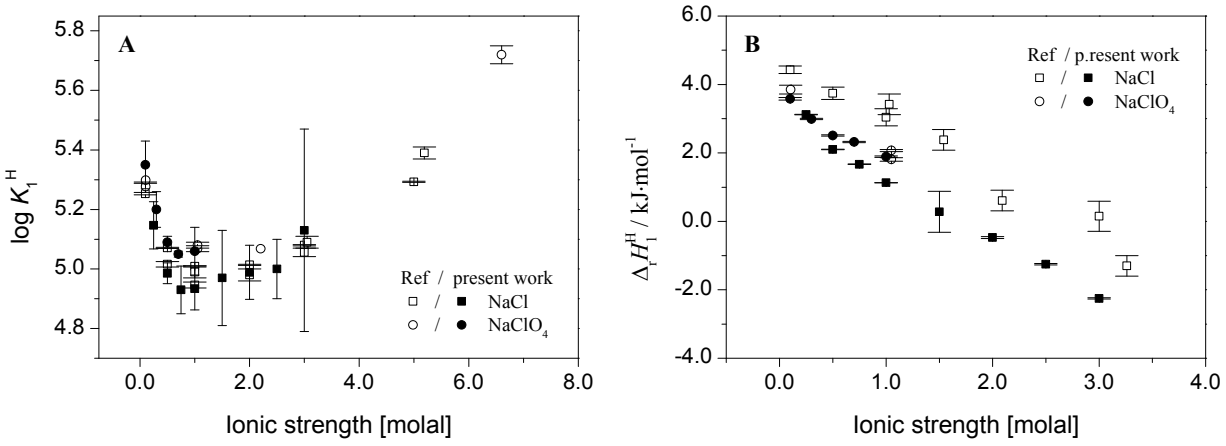

Fig. 4.34: Conditional thermodynamic data for malonate protonation as function of ionic strengths in NaCl and $NaClO_4$ media, left: protonation constant, right: protonation enthalpy The values presented with solid interior were determined in the present work. Literature data for NaCl were taken from the references [KET1992], [ROB1999], [STE2001], for $NaClO_4$ from [KIT2006], [DEG1972], [CHR1967], [THA2009], [RAO2002], [CAM1964]

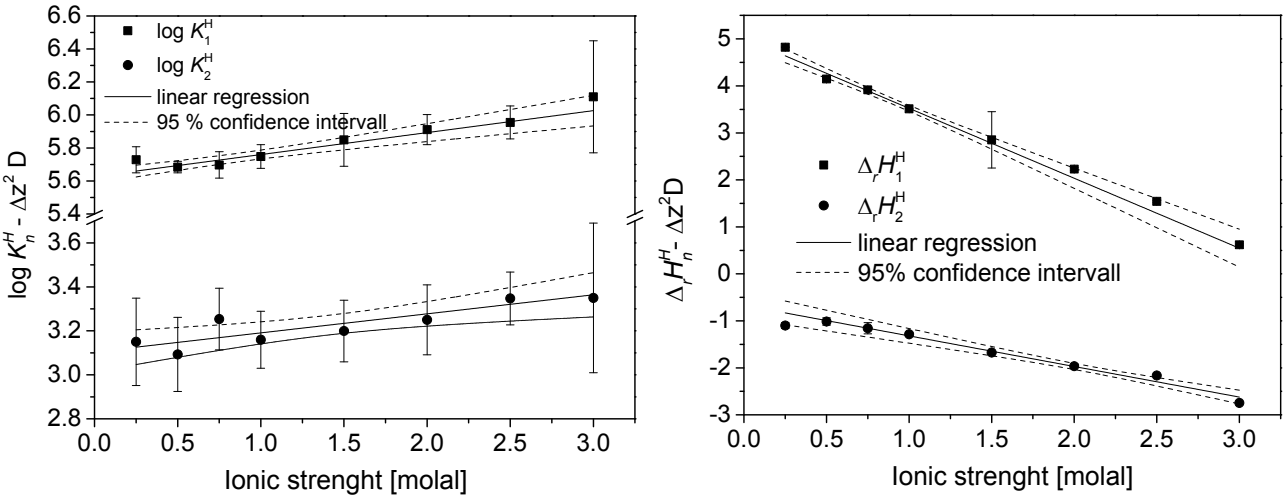

Fig. 4.35: SIT plots of malonate protonation, left: protonation constant, right: protonation enthalpy

The SIT-plots of the conditional stability constants and formation enthalpies of malonate protonation in NaCl/$NaClO_4$ media show a good linear relationship against the ionic strength (Fig. 4.35 for NaCl). The estimated standard values and for comparison the major literature values are depicted in Tab. 4.22.

Tab. 4.22: Thermodynamic standard data for the malonate protonation and 1:1 complexation of Nd(III) with malonate compared to literature data

medium	log $K_n^0 \pm 2\sigma$	$\Delta\varepsilon \pm 2\sigma$ [kg·mol^{-1}]	$\Delta_r H^0 \pm 2\sigma$ [kJ·mol^{-1}]	$\Delta\varepsilon_L \pm 2\sigma$ (10^{-3} [kg· (mol·K)$^{-1}$]	$\Delta_r G^0$ [kJ·mol^{-1}]	$\Delta_r S^0$ [J·mol^{-1}·K^{-1}]	Ref./ method
$Ma^{2-} + H^+ \rightleftharpoons HMa^-$							
NaCl	5.63 ± 0.08	-0.13 ± 0.08	5.01 ± 0.01	2.01 ± 0.01	-32.1 ± 0.5	124.6 ± 1.6	p. w., a
$NaClO_4$	5.76 ± 0.1	-0.06 ± 0.14	4.95 ± 0.04	0.90 ± 0.1	-32.9 ± 0.6	126.9 ± 2.0	p. w., a
	5.70		5.00		-32.5	126	DAN1985, c
NaCl	5.697 ± 0.001	-0.11 ± 0.02$^+$	5.13 ± 0.11	1.44 ± 0.3$^+$	-32.5	126.3 ± 0.4	KET1992, c
$NaClO_4$	5.62 ± 0.07	-0.21 ± 0.01			-32.1		XIO2011, §, c
NaCl	5.71 ± 0.006$^+$	-0.11 ± 0.004$^+$			-32.6		ROB1999, c
NaCl	5.66 ± 0.08[1,2]	-0.13 ± 0.04[1]	5.0	2.61 ± 0.52$^+$	-32.5	125.8	STE2001, b, c
$HMa^- + H^+ \rightleftharpoons H_2Ma$							
NaCl	3.10 ± 0.22	-0.09 ± 0.14	-0.67 ± 0.06	0.88 ± 0.04	-17.7 ± 1.3	57.1 ± 4.4	p. w., a
$NaClO_4$			-1.81 ± 0.08 *	-0.50 ± 0.18 *			p. w., a
$CaCl_2$	3.15 ± 0.44	0.02 ± 0.46	1.70 ± 1.6	0.88 ± 1.4	-18.0 ± 2.5	66.0 ± 13.8	p. w., a
	2.86		-1.00		-16.4	51	DAN1985, c
NaCl	2.852 ± 0.003	-0.11 ± 0.02[1]	0.1 ± 0.3	1.34 ± 0.22$^+$	-16.3	54.4 ± 1.0	KET1992, b, c
$NaClO_4$	2.90 ± 0.05	-0.1 ± 0.02			-16.6		XIO2011, §
NaCl	2.84 ± 0.008$^+$	-0.11 ± 0.006$^+$			-16.2		ROB1999, c
NaCl	2.90 ± 0.02$^{+,\#}$	-0.08 ± 0.01$^+$	-0.1	1.42 ± 0.96$^+$	-16.5	51.7	STE2001, b, c
$Nd^{3+} + Ma^{2-} \rightleftharpoons NdMa^+$							
NaCl	5.34 ± 0.14	-0.24 ± 0.08	17.2 ± 0.02	0.79 ± 0.02	-30,5 ± 0.8	159,9 ± 2.7	p.w., a
$NaClO_4$	6.16 ± 0.1	0.34 ± 0.3	19.44 ± 0.14	2.89 ± 0.28	-35,1 ± 0.6	183,2 ± 2.4	p.w., a
$NaClO_4$	5.41						WOO1993, §
NaCl (for Eu)	5.49 ± 0.11	-0.62 ± 0.11					XIO2011, §

a… micro-titration calorimetry, b… calorimetry, c… potentiometry, §… extrapolated using SIT based on experimental data, $^+$ values from SIT regression from conditionally constants, T = 25°C, #... T = 15°C, *… calculated from the micro-titration calorimetric with fixed K_2^0 values from KIT2006, KIR2008, DEG1972

Looking at the stability constant of single protonated malonate a good consistency between the datasets obtained in NaCl/$NaClO_4$ media and a good agreement with literature data is found. The same is true for the sum of the ion-ion interaction coefficients.

Some deviations exist in between the formation enthalpies, which are somewhat lower than the literature values. Kettler et al. [KET1992] determined the formation enthalpies from temperature dependence of stability constants between 25°C and 100°C. The determined standard state formation enthalpy bears a quite large uncertainty and the uncertainty range overlaps with our value. However, they fitted their temperature dependent stability constants together with literature values at additional temperatures and reported the standard state formation enthalpy to 5.13 ± 0.11 $kJ \cdot mol^{-1}$, which is in good agreement with the formation enthalpy obtained in this work. De Stefano et al. [STE2001] determined the enthalpies directly by calorimetric titration and fitting their results for ionic strengths between 0.1 and 5 $mol \cdot kg^{-1}$ also results in a quite large uncertainty, which is overlapping with the uncertainty determined in this work.

In case of the second malonate protonation step the standard state stability constants determined in this work are of about 0.2 log units higher than the literature values, but the uncertainty of the values overlap with the literature data. Among the formation enthalpies there is no consistency between the datasets. This is primary caused by the limitation of our micro-titration calorimeter (see chapter 4.2.1) with respect to the practically available concentration ranges, so that the second protonation step was incomplete recorded.

The both protonation enthalpies are too low to affect $\Delta_r G_n^0$ (n = 1, 2), thus the entropy change is the dominant driving force in the protonation of malonate (like lactate and oxalate protonation, cf. Chapters 4.3.3, 4.4.3).

For the first time values for the individual interaction coefficients $\varepsilon(Na^+, HMa^-)$, and $\varepsilon(Ca^{2+}, HMa^-)$ were determined using experimental $\Delta\varepsilon$ values and values for $\varepsilon(H^+, Cl^-) = 0.12 \pm 0.01$ $mol \cdot kg^{-1}$ and $\varepsilon(H^+, ClO_4^-) = 0.14 \pm 0.01$ $mol \cdot kg^{-1}$ taken from [HUM2005] and [CIA1980], respectively. The value for $\varepsilon(Na^+, Ma^{2-})$ were derived on the one hand by using $\varepsilon(Na^+, HMa^-)$ value determined in this work and on the other hand by using the literature value $\varepsilon(Na^+, HMa^-) = 0.03 \pm 0.04$ $mol \cdot kg^{-1}$ from [XIO2011]. The latter value was derived by SIT plot from values of the second dissociation constants of malonic acid in $NaClO_4$ taken from [SMI2004]. In Tab. 4.23 the individual interaction coefficients are summarized. There is a good agreement with literature values.

Tab. 4.23: Specific ion interaction coefficients of malonate species compared to literature values

species	ε(i,k) [mol·kg^{-1}]	medium	Ref.
$\varepsilon(Na^+, HMa^-)$	-0.03 ± 0.14	NaCl	p.w.
	0.11 ± 0.15	$NaClO_4$	p.w.
	-0.04 ± 0.03	$NaClO_4$	[XIO2011]
$\varepsilon(Ca^{2+}, HMa^-)$	-0.14 ± 0.46	$CaCl_2$	p.w.
$\varepsilon(Na^+, Ma^{2-})$	-0.02 ± 0.16	NaCl,	p.w.
	-0.03 ± 0.09	NaCl	calc. with value from [XIO2011]
	0.03 ± 0.21	$NaClO_4$	p.w.
	- 0.10 ± 0.14	$NaClO_4$	calc. with value from [XIO2011]
	0.03 ± 0.04	NaClO4	[XIO2011]

Nd(III) and Eu(III) complexation with malonate studied by ITC

The calorimetric titration studies of the complex formation of Nd(III) (or Eu(III)) were performed at two different modalities. In NaCl medium the complex formation was studied by titration of Nd(III) solutions with malonate solutions at the same pH and ionic strength. In $NaClO_4$ and $CaCl_2$ medium a solution containing both the lanthanide and malonate (mostly with a ratio of 1:10) with a defined proton concentration and ionic strength was titrated with either $HClO_4$ or HCl with the same ionic strength (examples of the thermograms are shown in Fig. 4.36 a, b).

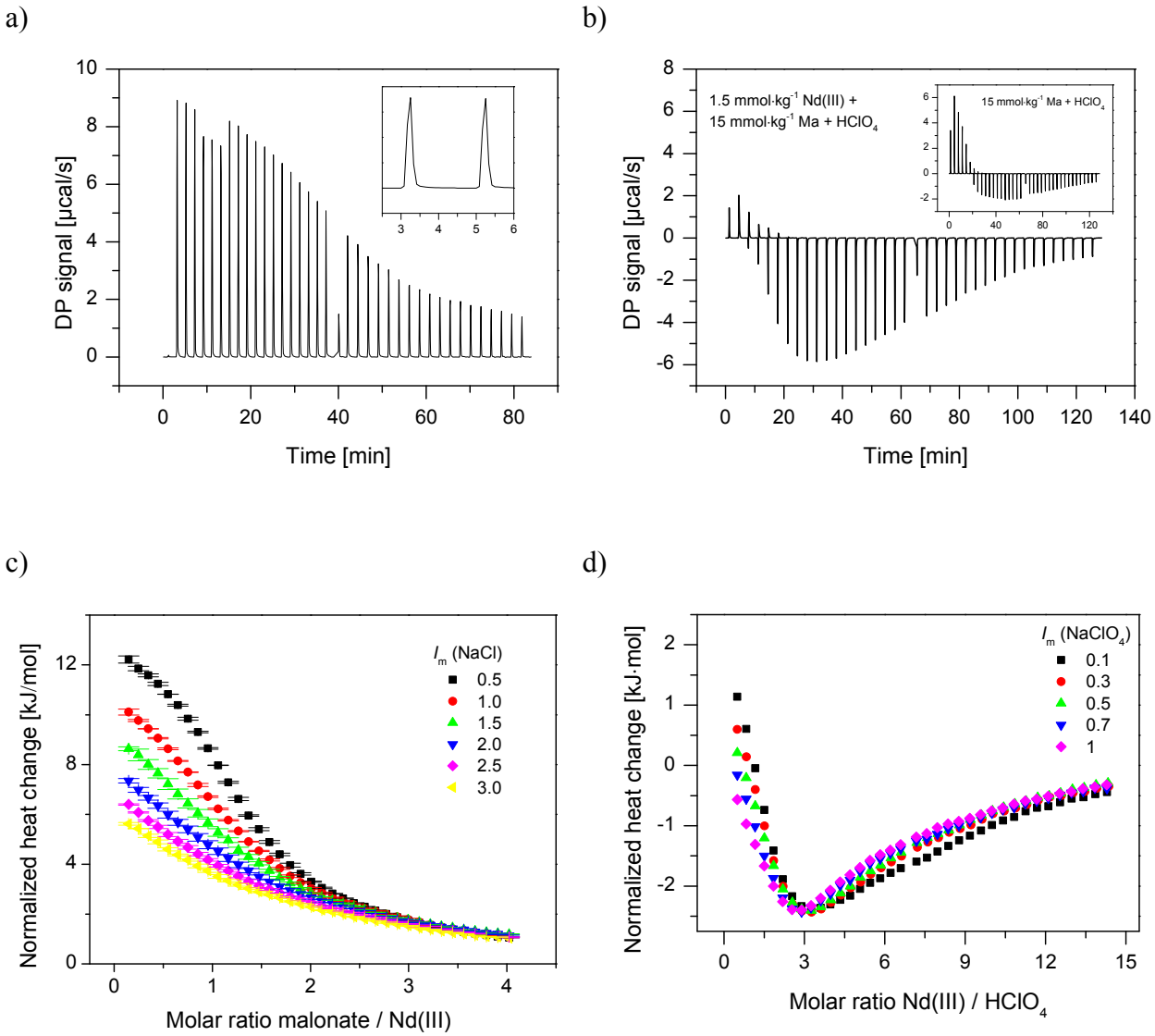

Fig. 4.36: *a) Thermogram of a calorimetric titration of 3 mmol·kg^{-1} Nd(III) with 26.7 mmol·kg^{-1} malonate I_m = 0.25 m, T = 25°C. The temperature equilibrium is regained within 1 min (inset)*

b) Thermogram of a calorimetric titration of a solution containing 1.5 mmol·kg^{-1} Nd(III) and 15 mmol·kg^{-1} malonate, which was titrated with 50 mmol·kg^{-1} $HClO_4$ (I_m = 0.1 m NaClO4, T = 25°C. The inset depicts the titration of malonate without of Nd(III)

c) Integrated heat curves for titration of 5 mmol·kg^{-1} Nd(III) with malonate at different ionic strengths in NaCl medium (T = 25°C). The curves were corrected for the heats of dilution

d) Integrated heat curves for titration of a solution containing 1.5 mmol·kg^{-1} Nd(III) and 15 mmol·kg^{-1} malonate with a 50 mmol·kg^{-1} $HClO_4$ solution at different ionic strengths (T = 25°C), corrected for the heats of dilution

The conditional stability constants and formation enthalpies for the Nd(III)-malonate complexes, that have been derived from the least-squares analysis of the integrated heat curves (examples in Fig. 4.36 c, d) are summarized in Fig. 4.37 together with literature data.

In the analysis of the curves the protonation constants and enthalpies determined in this work (see above) were taken as fixed values.

For both background electrolytes, NaCl and $NaClO_4$, the stability constant of the 1:1 Nd(III)-malonate complex is decreasing with increasing ionic strength. From an ionic strength of approximately 2.5 $mol \cdot kg^{-1}$ the complex stability slightly increases with increasing ionic strength. The reaction enthalpy continuously decreases with increasing ionic strength. Until now, there are no systematic studies on the ionic strength dependence of Nd(III)-malonate complex formation. Therefore, the ionic strength dependence of the herewith determined thermodynamic data is shown in Tab. 4.22 in comparison to those of analogue complexes with other trivalent lanthanides found in the literature.

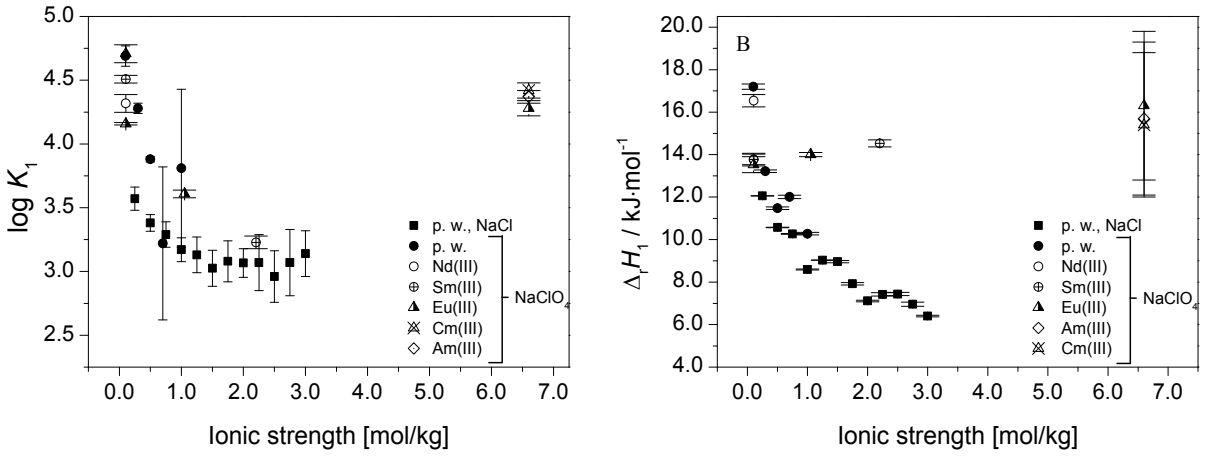

Fig. 4.37: *Conditional stability constants $\log K_1$ and reaction enthalpies $\Delta_r H_1$ for the formation of the 1:1 Nd(III)-malonate complex at different ionic strengths in NaCl and $NaClO_4$ (T = 25°C) in comparison to the data determined for other trivalent lanthanides and actinides. literature data were taken from [KIT2006], [DEG1972], [THA2009], [ANS1985], [WAN2000]*

The literature data for the analogue complexes of malonate with other lanthanides all come from two different working groups and all studies were performed using $NaClO_4$ as the background electrolyte (see Tab. 4.22). The $\log K_1$ values were determined by potentiometric measurements [KIT2006, DEG1972, THA2009, ANS1985] except of the values for the Am(III), Cm(III) and Eu(III) malonate complex at I_m = 6.6 m, which were determined by Wang et al. (2000) [WAN200] by spectrophotometry. In general the trend of our $\log K_1$ with the ionic strength is in good agreement with the literature values.

The reaction enthalpies were to a large extend determined by calorimetry [KIT2006, DEG1997, ANS1985], but there is also a study in which the enthalpy was calculated from

temperature dependent $\log K_1$ using the Van`t Hoff equation [THA2009]. The reaction enthalpies reported in the literature show an essentially different trend with the ionic strength than it is observed in this work. In this work the formation enthalpies $\Delta_r H_1$ strongly decrease with increasing ionic strength, while the variation of the literature values with ionic strength is less pronounced and can thus be interpreted to be increasing with increasing ionic strength. The only value that is available for the Nd(III)-malonate complex accounts for an ionic strength of 0.1 m ($NaClO_4$) [DEG1972] and is in the same order of magnitude as our determined value for the same ionic medium.

Like previously explained in [BAR2014] and chapter 4.3.3 the decreasing of the formation enthalpies indicates that less energies are needed to remove hydration waters of the reactants, the formation energies released by the complex formation becomes more dominant. The complex formation is driven by entropy, term $|-T\Delta_r S| >> |\Delta_r H|$ has been valid.

The SIT plots using the extracted stability constants and enthalpy values for the 1:1 Nd-malonate complex are shown in Fig. 3.38. The extrapolated thermodynamic values are summarized in Tab. 4.22 together with selected literature values.

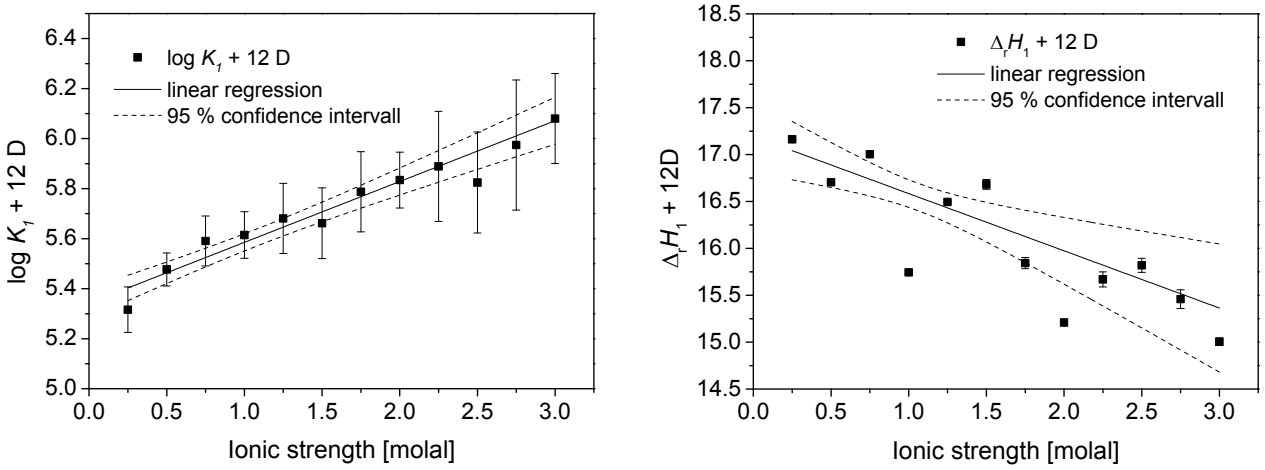

Fig. 4.38: SIT plots of 1:1 complexation of Nd(III) with malonate in NaCl , left: complexation constant, right: complexation enthalpy

From the determined $\Delta\varepsilon_1$ values the specific ion interaction coefficient ε_1 of 1:1 Nd(III) malonate complex were derived for the first time by using the following specific ion interaction coefficients from literature: $\varepsilon(Nd^{3+}, Cl^-)$ = 0.23 ± 0.02 mol·kg^{-1} [XIO2011] respectively $\varepsilon(Am^{3+}, ClO_4^-)$ = 0.49 ± 0.03 mol·kg^{-1} [HUM2005] and $\varepsilon(Na^+, Ma^{2-})$ = 0.03 ± 0.04 mol·kg^{-1} [XIO2011] (cf. Tab. 4.24).

Tab. 4.24: Specific ion interaction coefficients of 1:1 Nd(III) malonate complex species compared to literature values

species	ε(i,k) [mol·kg^{-1}]	medium	Ref.
ε(NdMa$^+$, Cl$^-$)	-0.04 ± 0.12	NaCl	p.w.
	0.02 ± 0.09	NaCl	calc. with value from [XIO2011]
ε(NdMa$^+$, ClO$_4^-$)	0.73 ± 0.33	NaClO$_4$	p.w.
	0.86 ± 0.30	NaClO$_4$	calc. with value from [XIO2011]

4.6 Summary

In the present study the complexation of trivalent lanthanides Eu/Nd and actinides Am/Cm with selected low molecular organic ligands was studied as function of ionic strength by means of isothermal micro-titration calorimetry (ITC) in combination with additionally spectroscopic methods. The investigated ligands lactate, oxalate, malonate and the here not presented tartrate and salicylate were chosen as typical representatives of low molecular weight organic matter in clay formation, metabolisms and model ligands for natural organic matter.

For the first time the ITC was used to determination of complete thermodynamic dataset (log K_n^0, $\Delta_r G^0$, $\Delta_r H^0$, $\Delta_r S^0$) of complexation reaction of trivalent lanthanides with the selected ligands. The aim was to establish this method for use with actinides; hence the very small sample volume of 200 µl of our micro-titration calorimetry device (ITC_{200}, Malvern Instruments). During the work it became clear that preferably 1:1 and (under favorable prerequisites) 1:2 complexes with complexation constants of log K_n^0 above approximately 2.8 can be examined by ITC. Furthermore, relatively high concentrations in sub- to mmol range of the reactants and multiple titrations are required, so that a routine application for actinides like Am(III) is not given at the present time. Nevertheless, it could be shown in the results discussed here, that the ITC is a powerful method for the determination of complexation enthalpies and complexation constants too as function of ionic strength up to approximately 4 m.

The case of lactate and oxalate the ITC studies were completed and supported by time resolved fluorescence spectroscopy with Eu(III)/Cm(III) and absorption spectroscopy with Am(III), respectively. It had been shown that thermodynamic data obtained by micro-titration calorimetric measurements and the data obtained by spectroscopic methods are comparable

within their errors. Generally our results are in good agreement with available literature values, occurring differences were discussed.

The great advantage of the ITC, namely the direct determination of the enthalpy, made it possible for both the protonation of the ligand as well as for the 1:1 complex reaction to evaluate the sum of enthalpic interaction coefficients $\Delta\varepsilon_L$ mainly in NaCl medium. These enthalpic interaction coefficients described the ionic strength dependency of the reaction enthalpies and can be used for extrapolation of enthalpy values at different ionic strength (NaCl) to standard value for $I_m = 0$ by using SIT approach. For the first time the sum of such enthalpic interaction coefficients $\Delta\varepsilon_L$ were derived for lactate, oxalate and malonate protonation and their 1:1 complexes with Eu(III) and/or Nd(III). Specific ε_L (j,k) values for the considered complex species cannot derived since no further values for ε_L (j,k) are available in the thermodynamic databases.

Oxalates of trivalent lanthanides and actinides have very low solubilities, thus a precipitation of a solid oxalates occurs just in the mM concentration ranges in which the micro-titration calorimeter operates. It is very challenging to separate mathematically the heat curve of the complexation from the heat curve of the precipitation. Therefore the here listed thermodynamic values for the Nd-oxalate system, especially the enthalpy can be seen only as first estimation.
The precipitated oxalate phase was analyzed, too. The main species has a composition of $\{Eu_2(H_2O)_6(Ox)_3\}\cdot 4\ H_2O$ which was solved by site-selective TRLFS.

Both the ligand protonation and the 1:1 complexation reaction are entropy driven. The only exception is the 1:1 complexation reaction with oxalate; here it is not clear whether the reaction is enthalpy or entropy driven.

5 References

ALM2012 L. De Almeida, S. Grandjean, N. Vigier, and F. Patisson: *Insights into the Thermal Decomposition of Lanthanide(III) and Actinide(III) Oxalates - from Neodymium and Cerium to Plutonium*. Eur. J. Inorg. Chem. 31, 4986–4999, (2012)

ALT2003 M. Altmaier, V. Metz, V. Neck, R. Müller, and T. Fanghänel: *Solid-liquid equilibria of $Mg(OH)_2$(cr) and $Mg_2(OH)_3Cl_4H_2O$(cr) in the system Mg-Na-H-OH-Cl-H_2O at 25°C*. Geochim. Cosmochim. Acta 67, 19, 3595–3601, (2003)

ALT2013 M. Altmaier, X. Gaona, and T. Fanghänel: *Recent Advances in Aqueous Actinide Chemistry and Thermodynamics*. Chem. Rev. 113, 901–943, (2013)

AND2000 C. A. Andersson and R. Bro: *The N-way Toolbox for MATLAB*. Chemom. Intell. Lab. Syst. 52, 1–4, (2000)

ANS1985 T. Y. Al-Ansi. PhD thesis, Florida State University, (1985)

ARN1970 R. Arnek: *High-speed computers as a supplement to graphical methods. II. Application of LETAGROP to calorimetric titrations.* Ark. Kemi 32, 81 (1970)

ART2000 R. Artinger, G. Buckau, S. Geyer, P. Fritz, M. Wolf, and J. I. Kim: *Characterization of groundwater humic substances: influence of sedimentary organic carbon.* Applied Geochemistry 15, 97–116, (2000)

ASC1970 J. Ascanio and F. Brito: *Hydrazonium ion as a depolarizer*. An. Quim. 66, 617, (1970)

AZI1971 A. Aziz, S. J. Lyle, J. E. Newbery: *Eurpium(III) complexes with propionate, lactate, pyruvate and α-alaninate in aqueous solution.* J. Inorg. Nucl. Chem. 33, 1757 -1764, (1971)

BAR2011 A. Barkleit, S. Tsushima, O. Savchuk, J. Philipp, K. Heim, M. Acker, S. Taut, and K. Fahmy: *Eu^{3+} Mediated Polymerization of Benzenetetracarboxylic Acid Studied by Spectroscopy, Temperature-Dependent Calorimetry, and Density Functional Theory*. Inorg. Chem. 50, 5451–5459, (2011)

BAR2013 A. Barkleit, M. Acker, and G. Bernhard: *Europium(III) complexation with salicylic acid at elevated temperatures*. Inorganica Chim. Acta 394, 535–541, (2013)

BAR2014 A. Barkleit, J. Kretzschmar, S. Tsushima, M. Acker: *Americium(III) and europium(III) complex formation with lactate at elevated temperature studies by spectroscopy and quantum chemical calculations.* Dalton Trans. 43, 11221-11232, (2014)

BEL2004 E. L. Belokoneva, A. G. Ivanova, S. Y. Stefanovich, O. V. Dimitrova, and V. S. Kurazhkovskaya: *New Ln[B6O9(OH)3] borates (Ln = Sm-Lu): Structure, properties, and structural relation to cationic Li4[B7O12]Cl conductors (Li-boracites).* Crystallogr. Rep. 49, 603–613, (2004)

BER2009 P. Di Bernardo, P. L. Zanonato, G. Tian, M. Tolazzi, and L. Rao: *Thermodynamics of the complexation of uranium(VI) with oxalate in aqueous solution at 10–70 °C.* Dalton Trans. 23, 4450, (2009)

BET1955 D. E. Bethell and N. Sheppard: *The infra-red spectrum and structure of boric acid*. Trans. Faraday Soc. 51, 9–15, (1955)

BIN2015 K. Binnemans: *Interpretation of europium(III) spectra*. Coord. Chem. Rev. 295, 1–45, 2015

BOR2001 Borkowski, M.: *Thermodynamic modeling of actinide complexation with oxalate at high ionic strength.* Journal of Radioanalytical and Nuclear Chemistry 248, 467-471, (2001)

BOR2010 M. Borkowski, M. Richmann, D. T. Reed, and Y. Xiong: *Complexation of Nd(III) with tetraborate ion and its effect on actinide(III) solubility in WIPP brine*. Radiochim. Acta 98, 577–582, (2010)

BOT1965 E. Bottari, L. Ciavatta: *Potentiometric study of iron(II) oxalate complexes*. Gazz. Chim. Ital. 95, (8-9), 908-20, (1965)

BOU1995 A. Bousher: *Review: Unidentate complexes involving borate*. J. Coord. Chem. 34, 1–11, (1995)

BRÖ1922 J. N. Brönsted: *Studies on solubility. IV. The principle of the specific interaction of ions*. J. Am. Chem. Soc. 44, 5, 877–898, (1922)

BRÖ1922b J. N. Brønsted: *Calculation of the osmotic and activity functions in solutions of uni-univalent salts*. J. Am. Chem. Soc. 44, 5, 938–948, (1922)

BRO2003 Bro, R. and. Kiers, H. A. L: *A new efficient method for determining the number of components in Parafac models*. J. Chemometrics 17, 274-286, (2003)

BÜN1989 J.-C. G. Bünzli: - *Luminescent Probes - in: Lanthanide Probes in Life, Chemical and Earth Sciences: Theory and Practice.* Amsterdam: Elsevier Science Publishers B. V., Eds. J.-C. G. Bünzli and G. R. Choppin, (1989)

BÜN1989 J.-C. G. Bünzli and G. R. Choppin: *Lanthanide Probes in Life, Chemical and Earth Sciences-Theory and Practice*. Amsterdam, Elsevier, (1989)

BÜN2011 J.-C. G. Bünzli and S. V. Eliseeva in: - *Basics of Lanthanide Photophysics - in: Lanthanide Luminescence. Photophysical, Analytical and Biological Aspects*. *Springer Series on Fluorescence, 7*. Berlin, Heidelberg: Springer-Verlag, Eds. P. Hänninen and H. Härmä, (2011)

CAC1983 M. S. Caceci, G. R. Choppin: *The determination of the first hydrolysis constant of Eu(III) and Am(III)*. Radiochim. Acta 33, 101-104, (1983)

CAM1964 E. Campi, G. Ostacoli, M. Meirone, and G. Saini: *Stability of the complexes of tricarballylic and citric acids with bivalent metal ions in aqueous solution.* Journal of Inorganic and Nuclear Chemistry 26, 553–564, (1964)

CAN1938 K. Cannan and A. Kibrick*: Complex formation between carboxylic acids and divalent metal cations.* Journal of the American Chemical Society 60, 2314–2320, (1938)

CAN1987 Cantrell K. J. and Byrne R. H.: *Rare earth element complexation by carbonate and oxalate ions.* Geochim. Cosmochim. Acta 51, 597–605 (1987)

CER2005 K. Cernochova, J. N. Mathur, G. R. Choppin: *Chemical speciation of Am, Cm and Eu with EDTA at high ionic strength: thermodynamics and laser fluorescence spectroscopy studies*. Radiochim. Acta 93, 733-739, (2005)

CET2008 Z. Cetiner, Y.-L. Xiong: *Chemical controls on the solubility, speciation, and mobility of lanthanum at near surface conditions: a geochemical modeling study*. Appl. Geochem. 23, 2301–2315 (2008)

CHE2012 X. Y. Chen, G. S. Go, W. C. Ewing, B. L. Scott and W. Runde: *Solid-State and Solution-State Coordination Chemistry of Lanthanide(III) Complexes with a- Hydroxyisobutyric Acid.* Inorg. Chem. 51, 13254 – 13263, (2012)

CHO1961 G. R. Choppin and J. A. Chopoorian: *Complexes of the lanthanide elements with α-hydroxy carboxylate ligands.* J. Inorg. Nucl. Chem. 22, 97-113, (1961)

CHO1966 G.R. Choppin and H. G. Friedman, Jr.: *Complexes of Trivalent Lanthanide Ions. III. Bidentate Chelates*. Inorg.Chem. 5, 1599-1603 (1966)

CHO1986 G. R. Choppin, A. Dadgar, and E. N. Rizkalla: *Thermodynamics of complexation of lanthanides by dicarboxylate ligands.* Inorg. Chem. 25, 3581–3584, (1986)

CHO1994 G. R. Choppin, E. N. Rizkalla, K. A. Gschneider (Ed.), and L. Eyring (Ed.): *Solution Chemistry of Actinides and Lanthanides*. Handbook Phys. Chem. Rare Earths Amsterdam, Elsevier Sci. BV, 18, 559–590, (1994)

CHO1996 G. R. Choppin, J. F. Chen: *Complexation of Am(III) by oxalate in $NaClO_4$ media*. Radiochim. Acta 74, 105-110, (1996)

CHO1997 G. R. Choppin: *Inner versus outer sphere complexation of f-elements*. J. Alloys Compd. 249, 9–13, (1997)

CHR1967 J. J. Christensen, R. M. Izatt, and L. D. Hansen: *Thermodynamics of Proton Ionization in Dilute Aqueous Solution. VII. dH° and dS° Values for Proton Ionization from Carboxylic Acids at 25°C*. J. Am. Chem. Soc., 89 213–222, (1967)

CHR1972 J. J. Christensen, J. Ruckman, D. J. Eatough, and R. M. Izatt: *Determination of equilibrium constants by titration calorimetry: Part I. Introduction to titration calorimetry*. Thermochim. Acta 3, 3, 203–218 (1972)

CIA1980 L. Ciavatta: *The specific interaction theory in evaluating ionic equilibria*. Annali di Chimica 70, 551–567 (1980)

CIA1988 L. Ciavatta: *The specific interaction theory in equilibrium analysis. Some empirical rules for estimating interaction coefficients of metal ion complexes.* Annali di Chimica 80, 255-262, (1990)

CLA2005 F. Claret, T. Schaefer, T. Rabung, M. Wolf, A. Bauer, G. Buckau: *Differences in properties and Cm(III) complexation modelling of isolated humic and fulvic acid derived from Opalinus clay and Callovo-Oxfordian argillite*. Applied Geochemistry 20, 1158-1168, (2005)

COU2007a A. Courdouan, I. Christl, S. Meylan, P. Wersin, R. Kretzschmar: *Isolation and characterization of dissolved organic matter from the Callovo-Oxfordian formation.* Applied Geochemistry 22, 1537-1548, (2007)

COU2007b A. Courdouan, I. Christl, S. Meylan, P. Wersin, R. Kretzschmar: *Characterization of dissolved organic matter in anoxic rock extracts and in situ pore water of the Opalinus Clay*. Applied Geochemistry 22, 2926-2939, (2007)

CRE2004 F. Crea, A. de Robertis, S. Sammartano: *Medium and alkyl chain effects on the protonation of dicarboxylates in $NaCl_{aq}$ and Et_4NI_{aq} at 25°C*, J. Solution Chem. 33, 499-528 (2004)

CRO1951 C. E. Crouthamel and D. S. Martin: *Solubility of the rare earth oxalates and complex ion formation in oxalate solution. II. Neodymium and cerium (III)*. J. Am. Chem. Soc. 73, 569, (1951)

DAN1981 P. G. Daniele: *The formation of proton and alkali-metal complexes with ligands of biological interest in aqueous solution. Thermodynamics of H^+, Na^+ and K^+-Oxalate complexes*, Thermochim. Acta 46, 103–116, (1981)

DAN1984 P. G. Daniele, A. De Robertis, S. Sammartano, and C. Rigano: *Calcium-malonate complexes in aqueous solution. Thermodynamic parameters and their ionic strength dependence.* Thermochim. Acta 72, 305–322, (1984)

DAN1985 P. G. Daniele, A. De Robertis, C. De Stefano, S. Sammartano, and C. Rigano: *On the possibility of determining the thermodynamic parameters for the formation of weak complexes using a simple model for the dependence on ionic strength of activity coefficients: Na^+, K^+, and Ca^{2+} complexes of low molecular weight ligands in aqueous solution*. J. Chem. Soc., Dalton Trans. 11, 2353–2361, (1985)

DAV1962 C. W. Davies, *Ion Association*. London: Butterworths, (1962)

DEA1980 G. B. Deacon and R. J. Phillips: *Relationships between the carbon-oxygen stretching frequencies of 3arboxylate complexes and the type of carboxylate coordination*. Coord. Chem. Rev. 33, 227–250, (1980)

DEE1964 Deelstra, H. and F. Verbeel: *The determination of the stability* constants *of the lanthanide α-hydroxybutyrate and lactate complexes by potentiometric titration.* Anal. Chim. Acta 31, 251-157, (1964)

DEE1991 D. W. Deerfield, D. J. Fox, M. Head-Gordon, R. G. Hiskey, and L. G. Pederseng: *Interaction of calcium and magnesium ions with malonate and the role of the waters of hydration: A quantum mechanical study*. J. Am. Chem. Soc. 113, 1892–1899, (1991)

DEG1972 G. Degischer and G. R. Choppin: *Malonate complexing of lanthanide ions.* J. Inorg. Nucl. Chem. 34, 2823–2830, (1972)

DEN2005 M.A. Denecke, A. Rossberg, P.J. Panak, M. Weigl, B. Schimmelpfennig, A. Geist: *Characterization and Comparison of Cm(III) and Eu(III) Complexed with 2,6-Di(5,6-dipropyl-1,2,4-triazin-3-yl)pyridine Using EXAFS, TRFLS, and Quantum-Chemical Methods.* Inorg. Chem. 44, 8418, (2005)

DIC2002 R.S. Dickens et al.: *Structural, Luminescence, and NMR Studies of the Reversible Binding of Acetate, Lactate, Citrate, and Selected Amino Acids to Chiral Diaqua Ytterbium, Gadolinium, and Europium Complexes*. J. Am. Chem. Soc. 124 (43), 12697–12705, (2002)

DRO2015 B. Drobot, R. Steudtner, J. Raff , G. Geipel, V. Brendler and S. Tsushima: *Combining luminescence spectroscopy, parallel factor analysis and quantum chemistry to reveal metal speciation – a case study of uranyl(VI) hydrolysis.* Chem. Sci. 6, 964–972, 2015

EAT1985 D.J. Eatough, E.A. Lewis, L.D. Hansen: *Instrumentation and data reduction*. in: J.K. Grime (Ed.), Analytical Solution Calorimetry, John Wiley, New York, 137–161 (1985)

EBE1969 S. H. Eberle and J. B. Schaefer: *Stabilitatskonstanten der Komplexe des Neptunyl(V)-lons mit α-Hydroxykarbonsäuren.* J. Inorg. Nucl. Chem. 31, 1523–1527, (1969)

EBE1972 Eberle, S. H. ; Moattar, F.: *Die Komplexe des Am(III) mit Zitronensaeure*. Inorg. Nucl. Chem. Letters 8, 265–270, (1972)

FAN1995 Th. Fanghänel, J.I. Kim, R. Klenze, Y. Kato: *Formation of Cm(III)chloride complexes in $CaCI_2$ solutions*. Journal of Alloys and Compounds 225, 308-311, (1995)

FAN1998 Th. Fanghanel, J.-I. Kim: *Spectroscopic evaluation of thermodynamics of trivalent actinides in brines*. Journal of Alloys and Compounds 271–273, 728–737, (1998)

FEI1995 J. B. Fein, L. Yane, A. Jyoti, and T. Handa: *"Experimental study of aluminum and calcium malonate complexation at 25, 35, and 80°C*. Geochimica et Cosmochimica Acta 59, 1053–1062, (1995)

FRE1990 E. Freire, O. L. Mayorga, M. Straume: *Isothermal Titration calorimetry*. Anal. Chem. 62 (18), 950A–959A (1990)

FRÖ2013 D. R. Fröhlich, A. Skerencak-Frech, M.-L. K. Morkosa and P. J. Panak: *A spectroscopic study of Cm(III) complexation with propionate in saline solutions at variable temperatures.* New J. Chem. 37, 1520-1528, (2013)

FRÖ2014 D. R. Fröhlich, A. Skerencak-Frech and P. Panak: *A spectroscopic study on the formation of Cm(III) acetate complexes at elevated temperatures.* Dalton Trans. 43, 3958-3965, (2014)

FRÖ2015a D. R. Fröhlich, A. Skerencak-Frech and P. Panak: *Complex formation of Cm(III) with formate studied by time-resolved laser fluorescence spectroscopy*. Applied Geochmistry 61, 312-317, (2015)

FRÖ2015b D. R. Fröhlich, A. Skerencak-Frech, U. Kaplan, C. Koke, A. Rossberg and Petra J. Panak: *An EXAFS spectroscopic study of Am(III) complexation with lactate.* J. Synchrotron Rad. 22, http://dx.doi.org/10.1107/S1600577515017853, (2015)

GAM2000 Gammons, C. H. and Wood, S. A.: *The aqueous geochemistry of REE. Part 8: Solubility of ytterbium oxalate and the stability of Yb(III)-oxalate complexes in water at 25°C to 80°C.* Chem. Geol. 166, 103–124, (2000)

GAN2008 P. Gans, A. Sabatini, and A. Vacca: *Simultaneous Calculation of Equilibrium Constants and Standard Formation Enthalpies from Calorimetric Data for Systems with Multiple Equilibria in Solution*. J. Solut. Chem. 37, 467–476 (2008)

GEC2012 H. Geckeis, K.-J. Röhlig, and K. Mengel: *Endlagerung radioaktiver Abfälle, Chemie im Endlagersystem*. Chem. Unserer Zeit, 46, 282–293, (2012)

GEC2013 H. Geckeis, J. Lützenkirchen, R. Polly, T. Rabung, and M. Schmidt*: Mineral-Water Interface Reactions of Actinides.* Chem. Rev. 113, 1016–1062, (2013)

GEL956 E. Gelles and G. H. Nancollas: *Electrochemical studies in the rare earth series part 2. Rare earth malonates.* Transact. of the Faraday Society 52, 680–685, (1956)

GLA1993 S. Glab, M. Maj-Zurawska, P. Lukomski, A. Hulanicki: *Ion-selective electrode control based on coulometrically determined stability constants of biologically important calcium and magnesium complexes*. Anal. Chim. Acta 273, 493, (1993)

GLA2005 M. A. Glaus, B. Baeyens, M. Lauber, T. Rabung, L. R. Van Loon: *Water-extractable organic matter from opalinus clay: Effect on sorption and speciation of Ni(III), Eu(III) and Th(IV)*. Applied Geochemistry 20, 443-451, (2005)

GOU1966 M. A. Gouveia and R. Guedes de Carvalho: *Formation constants of lanthanide lactate complexes*. J. Inorg. Nucl. Chem. 28, 1683–1688, (1966)

GRA2010 L. Grasset, J. Brevet, T. Schäfer, F. Claret, E. C. Gaucher, A. Albrecht, A. Ambles*: Sequential extraction and spectroscopic characterisation of organic matter from the Callovo-Oxfordian formation*. Organic Geochemistry 41, 221-233, (2010)

GRE1969 I. Grenthe, G. Gardhammar, and E. Rundcrantz: *Thermodynamic properties of rare earth complexes: VI. Stability constants for the oxalate complexes of Ce III , Eu III , Tb III and Lu III.* Acta Chem Scand. 23, 93–108, (1969)

GRE1972 I. Grenthe and H. Ots: *Thermodynamic properties of rare earth complexes*. Acta Chem. Scand. 26, 1229-1242 (1972)

GRE1992 I. Grenthe, J. Fuger, R. J. M. Konings, R. J. Lemire, A. B. Muller, C. Nguyen-Trung and H. Wanner: *Chemical Thermodynamics of Uranium*. ed. H. Wanner and I. Forest, Elsevier Science Publishers B.V., Amsterdam (1992)

GRE1997 I. Grenthe, I. Puigdomenech: *Modelling in aquatic chemistry*. Royal Institute of Technology, Stockholm, Sweden, OECD publications (1997)

GUG1966 E. A. Guggenheim: *Applications of Statistical Mechanics*. Clarendon Press, Oxford, (1966)

GUI2003 R. Guillaumont, T. Fanghänel, J. Fuger, I. Grenthe, V. Neck, D. A. Palmer and M. H. Rand: *Update on the Chemical Thermodynamics of Uranium, Neptunium, Plutonium, Americium and Technetium.* Elsevier, Amsterdam, (2003)

GÜN2011 A. Günther, R. Steudtner, K. Schmeide and G. Bernhard: *Luminescence properties of uranium(VI) citrate and uranium(VI) oxalate species and their application in the determination of complex formation constants*. Radiochim. Acta 99, 535 – 541 (2011)

HAM1996 A. P. Hammersley, S. O. Svensson, M. Hanfland, A. N. Fitch, and D. Häusermann: *Two-Dimensional Detector Software: From Real Detector to Idealised Image or Two-Theta Scan*. High Press. Res. 14, 235–248, (1996)

HAN2011 L. D. Hansen, G. W. Fellingham, and D. J. Russell: *Simultaneous determination of equilibrium constants and enthalpy changes by titration calorimetry: Methods, instruments, and uncertainties*. Anal. Biochem. 409, 2, 220–229, (2011)

HAR1939 H. S. Harned, L. D. Fallon: *The second ionization constant of oxalic acid from 0 to 50 °C.* J. Am. Chem. Soc. 61, 3111–3113, (1939)

HAS1989 Y. Hasegawa, Y. Morita, M. Hase, and M. Nagata: *Complexation of lanthanoid(III) with substituted benzoic or phenylacetic acids and extraction of these acids*. Bull. Chem. Soc. Jpn., 62, 1486–1491, (1989)

HEL2011 A. Heller, A. Barkleit, G. Bernhard: *Chemical speciation of trivalent actinides and lanthanides in biological fluids: the dominant in vitro binding form of curium(III) and europium(III) in human urine*. Chem. Res. Toxicol. 24, 193, (2011)

HEL2012 A. Heller, A. Barkleit, H. Foerstendorf, S. Tsushima, K. Heim, and G. Bernhard*: Curium(III) citrate speciation in biological systems: a europium(III) assisted spectroscopic and quantum chemical study*. Dalton Trans., 41, 13969, (2012)

HER2006 H.-J. Herbert, A. Schwandt: *Salzlösungszuflüsse im Salzbergbau Mitteldeutschlands.* GRS-226, (2006)

HER2011 A. Hertam: *^{11}B-NMR spektroskopische Untersuchungen zum Lösungszustand von Boraten in konzentrierten Salzlösungen*. Diploma thesis, Freiberg University of Mining and Technology, (2011)

HIN2015 K. Hinz, M. Altmaier, X. Gaona, T. Rabung, D. Schild, M. Richmann, D. T. Reed, E. V. Alekseev, and H. Geckeis: *Interaction of Nd(III) and Cm(III) with borate in dilute to concentrated alkaline NaCl, $MgCl_2$ and $CaCl_2$ solutions: solubility and TRLFS studies*. New J. Chem. 39, 849–859, (2015)

HIR1979 T. Hirao, M. Kotaka, and H. Kakihana: *Raman spectra of polyborate ions in aqueous solution*. J. Inorg. Nucl. Chem. 41, 1217–1220, (1979)

HOF2004 T. Hofmann: *Die Welt der vernachlässigten Dimensionen / Kolloide*. Chem. Unserer Zeit 38, 24–35, (2004)

HOI1975 H. Hoiland and E. Vikingstad: *Partial molal volumes and volumes of ionization of hydroxycarboxylic acids in aqueous solution at 25, 30, and 35.deg.* J. Chem. Soc., Faraday I 71, 2007, (1975)

HOR1979 W. Horrocks and D. R. Sudnick: *Lanthanide Ion Probes of Structure in Biology. Laser-Induced Luminescence Decay Constants Provide a Direct Measure of the Number of Metal-Coordinated Water Molecules*. J. Am. Chem. Soc. 101, 2, 333–340, (1979)

HUA2010 Sun Hua-Yu, Zhou Yan, Huang Ya-Xi, Sun Wei, and Mi Jin-Xiao*: Synthesis, Crystal Structure, Vibrational Spectroscopy, and Thermal Behavior of $Y[B_2O_3(OH)]_3$*. Chin. J. Struct. Chem., 29, 1387–1393, (2010)

HUM2002 W. Hummel, U. Berner, E. Curti, F. J. Pearson: *Nagra/PSI Chemical Thermodynamic Data Base 01/01*, Universal Publisher, Florida, (2002)

HUM2005 W. Hummel, G. Anderegg, L. Rao, I. Puigdomenech, and O. Tochiyama (OECD, NEA-TDB): *Chemical Thermodynamics of Compounds and Complexes of U, Np, Pu, Am, Tc, Se, Ni and Zr with Selected Organic Ligands, vol. 9*. Elsevier, Amsterdam, (2005)

HUM2007 W. Hummel, I. Puigdomenech, L. Rao, O. Tochiyama: *Thermodynamic data of compounds and complexes of U, Np, Pu and Am with selected organic ligands*. C. R. Chimie 10, 948-958, (2007)

HYP2008a P. Gans, A. Sabatini, and A. Vacca: *Hyperquad2008, Hyperquad suite of programs, Protonic Software*. Leeds, (2008)

HYP2008b P. Gans, A. Sabatini, and A. Vacca: *HypSpec, Hyperquad suite of programs, Protonic Software*. Leeds, (2008)

HYSS2009 P. Gans, A. Sabatini, and A. Vacca: *Hyperquad Simulation and Speciation (HySS), Hyperquad suite of programs, Protonic Software*. Leeds, (2009)

ING1957 N. Ingri, G. Lagerström, M. Frydman, and L. G. Sillén: *Equilibrium Studies of Polyanions, II Polyborates in $NaClO_4$ Medium*. Acta Chem. Scand. 11, 1034–1058, (1957)

ING1962 N. Ingri: *Equilibrium Studies of Polyanions, 8. On the First Equilibrium Steps in the Hydrolysis of Boric Acid, a Comparison between Equilibria in 0.1 M and 3.0 M $NaClO_4$.* Acta Chem. Scand. 16, 439–448, (1962)

ING1963 N. Ingri: *Equilibrium Studies of Polyanions, 11. Polyborates in 3.0 M Na(Br), 3.0 M Li(Br) and 3.0 M K(Br), a Comparison with Data Obtained in 3.0 M Na(ClO_4).* Acta Chem. Scand. 17, 581–589, (1963)

IUP1972 D. H. Everett: *Manual of Symbols and Terminology for Physicochemical Quantities and Units, Appendix II, Definitions, Terminology and Symbols in Colloid and Surface Chemistry*, Part I, Pure Appl. Chem. 31, 577–638, (1972)

JAN1979a R. Janda and G. Heller: *Ramanspektroskopische Untersuchungen an festen und in Wasser gelösten Polyboraten.* Z. Naturforschung 34b, 585–590, (1979)

JAN1979b R. Janda and G. Heller: *^{11}B-NMR-spektroskopische Untersuchungen an wäßrigen Polyboratlösungen.* Z. Naturforschung 34b, 1078–1083, (1979)

JAN1980 R. Janda and G. Heller: *IR- und Ramanspektren isotop markierter Tetra- und Pentaborate.* Spectrochim. Acta Part A 36, 997–1001, (1980)

JEN2001 Jensen, M. P., Nash, K.: *Thermodynamics of dioxoneptunium(V) complexation by dicarboxylic acids.* Radiochim. Acta 89, 557 (2001)

JIA2002 J. Jiang, L. Rao, P. Di Bernardo, P. L. Zanonato, A. Bismondo: *Complexation of uranium(VI) with acetate at variable temperatures.* Radiochim. Acta 90, 581, (2002)

JOH2002 L. H. Johnson, M. Niemeyer, G. Klubertanz, P. Siegel, and P. Gribi: *Calculations of the temperature evolution of a repository for spent fuel, vitrified high-level waste and intermediate level waste in opalinus clay*. tech. Rep., NAGRA, (2002)

JOH2002 L. H. Johnson, M. Niemeyer, G. Klubertanz, P. Siegel, and P. Gribi, *Calculations of the temperature evolution of a repository for spent fuel, vitrified high-level waste and intermediate level waste in opalinus clay*. tech. Rep., NAGRA, (2002)

JUN1995 Li Jun, X. Shuping, and G. Shiyang: *FT-IR and Raman spectroscopic study of hydrated borates.* Spectrochim. Acta Part A 51, 519–532, (1995)

KAK1987 M. Kakihana, T. Nagumo, M. Okamoto, and H. Kakihana: *Coordination structures for uranyl carboxylate complexes in aqueous solution studied by IR and carbon-13 NMR spectra*. J. Phys. Chem. 91, 6128–6136, (1987)

KET1991 R. M. Kettler, D. A. Palmer, and D. J. Wesolowski: *Dissociation Quotients of Oxalic Acid in Aqueous Sodium Chloride Media to 175°C.* Journal Solut. Chem. 20, 9, 905–927 (1991)

KET1992 R. M. Kettler, D. J. Wesolowski, and D. A. Palmer: *Dissociation quotients of malonic acid in aqueous sodium chloride media to 100°C.* J. Solution Chem. 21, 883–900, (1992)

KET1998 R. M. Kettler, D. J. Wesolowski, and D. A. Palmer: *Dissociation constants of oxalic acid in aqueous sodium chloride and sodium trifluoromethanesulfonate media to 175 °C.* J. Chem. Eng. Data 43, 337–350, 1998

KIE1977 A. P. G. Kieboom, C. A. M. Vijverberg, J. A. Peters and H. Vanbekkum: *Complexation of acetate, glycolate, lactate, malate and citrate anions with lanthanide(III) cations in aqueous solution as studied by NMR spectroscopy.* Recl. Trav. Chim. Pays-Bas-J. Roy. Neth. Chem. Soc. 96, 315 – 316, (1977)

KIE2003 B. Kienzler: *Geochemische begründete Eingangsparameter für Kritikalitätsuntersuchungen.* Karlsruhe, FZK-INE 002/03, (2003)

KIM1994 T. Kimura, G.R. Choppin: *Luminescence study on determination of the hydration number of Cm(III).* J. Alloys Compd. 313, 213–214, (1994)

KIM2001 T. Kimura, R. Nagaishi, Y. Kato, and Z. Yoshida: *Luminescence study on solvation of americium(III), curium(III) and several lanthanide(III) ions in nonaqueous and binary mixed solvents*. Radiochim. Acta 89, 125–130 (2001)

KIR2008 E. Kirishima, Y. Onishi, N. Sato, and O. Tochiyama: *Thermodynamic study on the U(VI) complexation with dicarboxylates by calorimetry.* Radiochim. Acta 96, 581–589, (2008)

KIT2006 H. Kitano, Y. Onishi, A. Kirishima, N. Sato and O. Tochiyama: *Determination of the thermodynamic quantities of complexation between Eu(III) and carboxylic acids by microcalorimetry*. Radiochim. Acta 94, 541-547, (2006)

KOS1980 V. N. Kosyakov, E. A. Yerin: *On the mechanism of trivalent actinide extraction in the system HDEHP – Lactic Acid with DTPA*. J. of Radioanalytical Chem. 56, 1-2 93-104, (1980)

KÖS2010 D. A. Köse, B. Zümreoglu-Karan, T. Hökelek, and E. Sahin: *Boric acid complexes with organic biomolecules: Mono-chelate complexes with salicylic and glucuronic acids*. Inorganica Chim. Acta 363, 4031–4037, (2010)

KRO1995 I. Kron, S. Marshall, P. May, G. Hefter, E. Königsberger: *The ionic product of water in highly concd. aqueous electrolyte solutions.* Monatshefte Chemie 126, 819–837, (1995)

KRU1976 I. Kruhak, B. Grabaric, I. Filipovic, I. Piljac: *Potentiometric determination of stability constants of cobalt(II), nickel(II), zinc(II), cadmium(II), and lead(II) complexes in buffer solutions of 2- and 3-hydroxypropanoic acids*. Croat. Chem. Acta 48, 119, (1976)

KUK1999 S. Kuke, B. Marmodee, S. Eidner, U. Schilde, M.U. Kumke: *Intramolecular deactivation processes in complexes of salicylic acid or glycolic acid with Eu(III).* Spectrochim. Acta, Part A 75, 1333, (2010)

LAF1982 M. Laffitte: *A report of IUPAC commission I.2 on thermodynamics: Notation for states and processes, significance of the word "standard" in chemical thermodynamics, and remarks on commonly tabulated forms of thermodynamic functions*. J. Chem. Thermodyn. 14, 805-815 (1982)

LAJ1997 L. H. J. Lajunen, R. Portanova, J. Piispanen, and M. Tolazzi: *Stability Constants for alpha-Hydroxycarboxylic Acid Complexes with Protons and Metal Ions and the Accompanying Enthalpy Changes - Part I: Aromatic ortho-Hydroxycarboxylic Acids*. Pure Appl. Chem. 69, 329–381, (1997)

LEB1960 I. A. Lebedev, S. V. Pirozhkov, and V. M. Razbitnoi: *Studies on complex formation between Am(III) and oxalate ions*. Sov. Radiochem. 2, 89–94, (1960)

LEM1999 S. Lemanceau, G. Bertrand-Chadeyron, R. Mahiou, M. El-Ghozzi, J. C. Cousseins, P. Conflant, and R. N. Vannier: *Synthesis and Characterization of H-$LnBO_3$ Orthoborates (Ln = La, Nd, Sm, and Eu).* J. Solid State Chem. 148, 229–235, (1999)

LIN1987 H. K. Lin, Z. Gu, Y. Chen: *Calorimetric measurement of the heat of formation of competitive mixed-ligand complexes. The Cu(II)-oxalate-ethylenediamine system*. Gazz. Chim. Ital. 117, (1), 23-6, (1987)

LIU1997 X. Liu, R. H. Byrne, and J. Schijf: *Comparative coprecipitation of phosphate and arsenate with yttrium and the rare earths: The influence of solution complexation*. J. Sol. Chem. 26, 1187–1198, (1997)

LIX2007 Zhu Lixia, Yue Tao, Wang Jiang, and Gao Shiyang: *FT-IR and Raman Spectroscopic Study of Hydrated Rubidium (Cesium) Borates and Alkali Double Borates*. Russ. J. Inorg. Chem. 52, 1786–1792, (2007)

LUK1988 O. Lukkari and J. Tamminen: *Equilibria of nitrosalicylic acids. Complex formation between boric acid and salicylic acid and nitrosalicylic acids*. Finn. Chem. Lett. 15, 13–17, (1988)

LUN1984 R. Lundqvist, J. F. Lu and I. Svantesson: *Hydrophilic complexes of the actinides. III. Lactate of Am^{3+}, Eu^{3+}, U^{4+} and UO_2^{2+}*. Acta Chem. Scand. Ser. A 38, 501 – 512, (1984)

LYL1966 Lyle S. J. and Naqvi S. J.: *A study of the distribution of series of positively charged europium complexes between a cation-exchanger and an external aqueous phase.* J. Inorg. Nucl. Chem. 28, 2993–3004 (1966)

MAE1987 M. Maeda, O. Hisada, Y. Kinjo, K. Ito: *Estimation of salt and temperature effects on ion product of water in aqueous solution*. Bull Chem. Soc. Jpn. 60, 3233–3239, (1987)

MAI2013 M. Maiwald: *Spektroskopische Untersuchungen zum Komplexierungsverhalten von Cm(III) mit Oxalat.* Universität Heidelberg, Bachelorarbeit, (2013)

MAN1966 P. G. Manning: *Europium oxalate ion association in water*. Can. J. Chem. 44, 3057–3062, (1966)

MAR1937 A. W. Martin and H. V. Tartar: *The Ionization Constant of Lactic Acid, 0-50°C from Conductance Measurements*. J. Am. Chem. Soc. 59, 2672, (1937)

MAR1986 E. Marklund, S. Sjoberg, L.-O. Öhman: *Equilibrium and structural studies of silicon(IV) and aluminium(III) in aqueous solution. 14. Speciation and equilibria in the aluminium(III)-lactic acid-hydroxide system*. Acta Chem. Scand. 40A, 367, (1986)

MAR1991 D. De Marco: *Thermodynamic relationships of complex formation. Part II. Enthalpy-entropy interdependence in hard-hard interactions in aqueous solution*, Thermochim. Acta 189, 213-222 (1991)

MAT2007 J. N. Mathur, K. Cernochova, G. R. Choppin: *Thermodynamics and laser luminescence spectroscopy of binary and ternary complexation of Am^{3+}, Cm^{3+} and Eu^{3+} with citric acid, and citric acid + EDTA at high ionic strength*. Inorganica Chimica Acta 360, 1785-1791, (2007)

MAY1976 L. Maya: *Identification of Polyborate and Fluoropolyborate Ions in Solution by Raman Spectroscopy*. Inorg. Chem. 15, 2179–2184, (1976)

MED2007 E. F. Medvedev and A. S. Komarevskaya: *IR spectroscopic study of the phase composition of boric acid as a component of glass batch*. Glass Ceram. 64, 42–46, (2007)

MEN1983 S. Menchetti, C. Sabelli, A. Stoppioni, and R. Trosti-Ferroni: *Hydrothermal synthesis at 250°C and X-ray study of resulting products in the $NaOH$-B_2O_3-H_2O system*. Neues Jahrb. Mineral. Abh. 148, 163–180, (1983)

MES1972 R. E. Mesmer, C. F. Baes, and F. H. Sweeton: *Acidity measurements at elevated temperatures. VI. Boric acid equilibria.* Inorg. Chem. 11, 537–543, (1972)

MES2009 *MestReNova, version 6.0.2,* Mestrelab Research S.L., (2009)

MET2012 V. Metz, H. Geckeis, E. Gonzalez-Robles, A. Loida, C. Bube, and B. Kienzler*: Radionuclide behaviour in the near-field of a geological repository for spent nuclear fuel.* Radiochim. Acta, 100, 699–713, (2012)

MIK1978 M. Mikesova and M. Bartusek: *Reaction of boric acid with salicylic and chromotropic acids and with their derivates.* Chem. Zvesti 32, 472–477, (1978)

MIY2003 Y. Miyazaki, K. Yoshimura, Y. Miura, H. Sakashita, and K. Ishimaru: *^{11}B NMR investigation of the complexation behavior of borate with polysaccharides in aqueous solution.* Polyhedron 22, 909–916, (2003)

MIY2008 Y. Miyazaki, H. Matsuo, T. Fujimori, H. Takemura, S. Matsuoka, T. Okobira, K. Uezu, and K. Yoshimura: *Interaction of boric acid with salicyl derivatives as an anchor group of boron-selective adsorbents*. Polyhedron 27, 2785–2790, (2008)

MIY2013 Y. Miyazaki, T. Fujimori, H. Okita, T. Hirano, and K. Yoshimura: *Thermodynamics of complexation reactions of borate and phenylboronate with diol, triol and tetritol*. Dalton Trans. 42, 10473–10486, (2013)

MIZ1999 J. Mizera , A. H. Bond, G. R. Choppin, R. C. Moore: *Dissociation constant of carboxylic acids at high ionic strengths*, in: *Actinide speciation in high ionic strength media*, Reed, D. T., Clark, and Rao, L., Eds., 113-124, Kluwer Academic/ Plenum Publ., New York, USA, (1999)

MOL2008 H. Moll, A. Johnsson, M. Schäfer, K. Pedersen, H. Budzikiewicz, and G. Bernhard: *Curium(III) complexation with pyoverdins secreted by a groundwater strain of Pseudomonas fluorescens*. BioMetals 21, 219–228, (2008)

MOM1967 R. K. Momii and N. H. Nachtrieb: *Nuclear Magnetic Resonance Study of Borate-Polyborate Equilibria in Aqueous Solution.* Inorg. Chem. 6, 1189–1192, (1967)

MOO1999 R. C. Moore, M. Borkowski, M. G. Bronikowski, J. Cheng, O. S. Pokrovsky, Y. Xia, G. R. Choppin: *Thermodynamik Modeling of Actinide Complexation with Acetate and Lactate at High Ionic Strength.* Journal of Solution Chemistry 28, 521-531, (1999)

MOU1999 C. Moulin, J. Wei, P. Van Iseghem, I. Laszak, G. Plancque, V. Moulin: *Europium complexes investigations in natural waters by time-resolved laser-induced fluorescence*. Anal. Chim. Acta 396, 253, (1999)

MÜL1993 D. Müller, A.-R. Grimmer, U. Timper, G. Heller, and M. Shakibaie-Moghadam: *^{11}B-MAS-NMR-Untersuchungen zur Anionenstruktur von Boraten.* Z. für Anorg. Allg. Chem. 619, 1262–1268, (1993)

MÜL2016 M. Müller: unpublished results, PhD thesis, will be submitted in 2016, Technische Universität Dresden

OI1992 T. Oi, T. Takeda, and H. Kakihana: *Esterification of Boric Acid with 1,2-Propanediol, 3-Amino-1,2-propanediol, and (+/-)-3-Dimethylamino-1,2-propandiol as Studied by ^{11}B NMR Spectroscopy.* Bull. Chem. Soc. Jpn., 65, 1903–1909, (1992)

PAA1985 T. Paal and M. Mate: *Stability of the salicylic acid-borate complex*. Magy. Kem. Folyoirat 91, 569–570, (1985)

PAA1988 T. Paal and M. Mate: *Stability of lactic acid-borate complexes*. Magy. Kem. Folyoirat 94, 143–144, (1988)

PAR1960 J. L. Parsons and M. E. Milberg: *Vibrational Spectra of Vitreous B_2O_3*xH_2O*. J. Am. Ceram. Soc. 43, 326–330, (1960)

PAZ1987 E. M. Pazukhin, A. S. Krivokhatskii, and A. S. Kochergin: *Complex formation of americium(III) in oxalate solutions*. Sov Radiochem. 29, 9–13, (1987)

PIZ1984 R. Pizer and R. Selzer: *The Boric Acid/Lactic Acid System. Equilibria and Reaction Mechanism*. Inorg. Chem., 23, 3023–3026, (1984)

PIZ1994 R. Pizer and P. J. Ricatto: *Thermodynamics of Several 1:l and 1:2 Complexation Reactions of the Borate Ion with Bidentate Ligands. B-NMR Spectroscopic Studies*. Inorg. Chem. 33, 2402, (1994)

POR2003 R. Portanova, L. H. J. Lajunen, M. Tolazzi, and J. Piispanen*: Critical evaluation of stability constants for alpha-hydroxycarboxylic acid complexes with protons and metal ions and the accompanying enthalpy changes*, *Part II. Aliphatic 2-hydroxycarboxylic acids.* Pure Appl. Chem. 75, 495–540, (2003)

POW1968 J. E. Powell, J. L. Farrell, W. F. S. Neillie, and R. Russell: *Stability trends of 1: 1 and 2: 1 dialkylmalonato rare-earth chelates.* Journal of Inorganic and Nuclear Chemistry 30, 2223–2231, (1968)

RAO2000 L. Rao, P. L. Zanonato, P. Di Bernardo, A. Bismondo: *Calorimetric and spectroscopic studies of Eu(III) complexation with tetramethylmalonamide and tetramethylsuccinamide in acetonitrile and dimethylsulfoxide*. Inorg. Chim. Acta 306, 49–64 (2000)

RAO2002 L. Rao, J. Jiang, P. Zanonato, P. Di Bernardo, A. Bismondo, and A. Y. Garnov: *Complexation of uranium (VI) with malonate at variable temperatures*. Radiochim. Acta 90, 581–588, (2002)

RAO2003 L. Rao, A. Y. Garnov, J. Jiang, P. Di Bernardo, P. Zanonato and A. Bismondo: *Complexation of Uranium(VI) and Samarium(III) with Oxydiacetic Acid: Temperature Effect and Coordination Modes*. Inorg. Chem. 42, 3685 (2003)

RAO2005 L. Rao, P. L. Zanonato, and P. Di Bernardo: *Interaction of Actinides with Carboxylates in Solution: Complexation of U(VI), Th(IV), and Nd(III) with Acetate at Variable Temperatures*. J. Nucl. Radiochem. Sci. 6, 1 (2005)

RAO2007 L. Rao: *Thermodynamics of actinide complexation in solution at elevated temperatures: application of variable-temperature titration calorimetry.* Chem. Soc. Rev. 36, 881-892, (2007)

RAO2008 L. Rao, G. Tian: *Thermodynamic study of the complexation of uranium(VI) with nitrate at variable temperatures.* J. Chem. Thermodynamics 40, 1001–1006 (2008)

REA1976 E. J. Reardon: *Dissociation Constants for Alkali Earth and Sodium Borate Ion Pairs from 10 to 50°C*. Chemical Geology 18, 309–325, (1976)

ROB1992 A. de Robertis, C. de Stefano, C. Rigano, S. Sammartano: *Salt effects on the protonation of oxalate in aqueous NaCl, KCl and tetraethylammonium iodide solution at 5≤ T ≤50°C and 0≤ I ≤1 mol·dm $^{-3}$.* Thermochim. Acta 202, 133-149, (1992)

ROB1999 E. De Robertis, C. De Stefano, and C. Foti: *Medium effects on the protonation of carboxylic acids at different temperatures.* J. Chem. Eng. Data 44, 262–270, (1999)

SAI2010 T. Saito, H. Sao, K. Ishida, N. Aoyagi, T. Kimura, S. Nagasaki, and S. Tanaka: *Application of Parallel Factor Analysis for Time-Resolved Laser Fluorescence Spectroscopy: Implication for Metal Speciation Study*. Environ. Sci. Technol. 44, 13, 5055–5060, (2010)

SAK1972 M. Sakanoue and M. Nakatani: *Determination of the formation constants of actinoid and lanthanoid lactate complexes by means of electrophoresis*. Bull. Chem. Soc. Jpn. 45, 3429, (1972)

SAL1983 C. G. Salentine: *High-Field 11B NMR of Alkali Borates. Aqueous Polyborate Equilibria*. Inorg. Chem. 22, 3920–3924, (1983)

SAR1927 L.A. Sarver, P.H.M.-P Brinton: *The solubilties of some rare-earth oxalates*. J. Am. Chem. Soc. 40, 943–958 (1927)

SCA1936 G. Scatchard: *Concentrated Solutions of Strong Electrolytes*. Chem. Rev.19, 3, 309–327 (1936)

SCA1976 G. Scatchard: *Equilibrium in solution: Surface and colloid chemistry*. Cambridge: Harvard University Press (1976)

SCHÄ2005 T. Schäfer, G. Buckau, R. Artinger, J.I. Kim, S. Geyer, M. Wolf, W.F. Bleam, S. Wirick and C. Jacobsen: *Origin and mobility of fulvic acids in the Gorleben aquifer system: implications from isotopic data and carbon/sulfur XANES.* Organic Geochemistry 36, 567-582, (2005)

SCHI2001 Schijf, J., Byrne, R.H.: *Stability constants for mono- and dioxalato-complexes of Y and the REE, potentially important species in groundwaters and surface freshwaters.* Geochim. Cosmochim. Acta 65, 1037–1046 (2001)

SCHO2014 J. Schott, J. Kretzschmar, M. Acker, S. Eidner, M. U. Kumke, B. Drobot, A. Barkleit, S. Taut, V. Brendler, and T. Stumpf: *Formation of a Eu(III) borate solid species from a weak Eu(III) borate complex in aqueous solution.* Dalton Trans. 43, 11516–11528, (2014)

SCHO2015 J. Schott, J. Kretzschmar, S. Tsushima, B. Drobot, M. Acker, A. Barkleit, S. Taut, V. Brendler, and T. Stumpf: *The interaction of Eu(III) with organoborates – a further approach to understand the complexation in the An/Ln(III)-borate system*. Dalton Trans. 44, 11095–11108, (2015)

SCHO2015/ 2016 J. Schott: *Investigation of the Interactions in the Eu(III)-borate System*. PhD thesis, Technische Universität Dresden, submitted at 19. December 2015

SEK1965 Sekine T.: *Solvent extraction study of trivalent actinide and lanthanide complexes in aqueous solutions. III. Oxalate complexes of La(III), Eu(III), Lu(III), and Am(III) in 1 M Na(ClO_4)*. Acta Chem. Scand. 19, 1476–1482 (1965)

SHI1969 M. Shiloh, M. Givon, Y. Marcus: *A spectrophotometric study of trivalent actinide complexes in solutions — III: Americium with bromide, iodide, nitrate and carbonate ligands*. J. Inorg. Nucl. Chem. 31, 1807–1814, (1969)

SKE2014 A. Skerencak-Frech, M. Maiwald, M. Trumm, D. R. Froehlich, J. Panak: *The Complexation of Cm(III) with Oxalate in Aqueous Solution at T = 20−90 °C: A Combined TRLFS and Quantum Chemical Study*. Inorg. Chem. 54, 1860-1868, (2014)

SKE2015 A. Skerencak-Frech, M. Maiwald, M. Trumm, D. R. Froehlich and P. J. Panak: *The Complexation of Cm(III) with Oxalate in Aqueous Solution at T =20 – 90°C: A Combined TRLFS and Quantum Chemical Study*. Inorg. Chem. 54, 1860−1868, (2015)

SKE2015/2016 A. Skerencak-Frech, D. R. Froehlich and P. J. Panak: *Retention of radionuclides relevant for final disposal in natural clay rock and saline systems.* Ruprecht-Karls-Universität Heidelberg (Physikalisch-chemisches Institut), Final Report BMWi joint project FZK 02E11031, (2015, 2016)

SMI1987 R. M. Smith and A. E. Martell: *Critical stability constants, enthalpies and entropies for the formation of the metal complexes of amiopolycarboxylic acids and carboxylic acids*. The Science of the Total Environment 64, 125–147, (1987)

SMI2004 R. M. Smith and A. E. Martell: *NIST Critical Selected Stability Constants of Metal Complexes Database Version 8.0. for Windows. NIST Standard Reference Database46*. National Institute of Standards and Technology, US Department of Commerce; Gaithersburg, MD 20899, (2004)

SNI2003 A. C. Snider: *Verification of the Definition of Generic Weep Brine and the Development of a Recipe for this Brine*. Sandia National Laboratories, Carlsbad, NM, Report ERMS 527505, (2003)

SPE1970 J. E. Spessard: *Investigations of borate equilibria in neutral salt solutions*. J. Inorg. Nucl. Chem. 32, 2607–2613, (1970)

STE2001 C. De Stefano, C. Foti, O. Giuffre, and S. Sammartano: *Dependence on ionic strength of protonation enthalpies of polycarboxylate anions in nacl aqueous solution.* J. Chem. Eng. Data 46, 1417–1424, (2001)

STR2014 T. Straaso, A.-C. Dippel, J. Becker, and J. Als-Nielsen: *Model-independent structure factors from powder X-ray diffraction: a novel approach*. J. Synchrotron Radiat. 21, 119–126, (2014)

TAY1985 J. R. Taylor: *An Introduction to Error Analysis: The Study of Uncertainties in Physical Measurements*. University Science Books, Sausalito, California, 2nd ed. (1982)

THA2006 P. Thakur, J. N. Mathur, C. J. Dodge, A. J. Francis, and G. R. Choppin: "*Thermodynamics and the structural aspects of the ternary complexes of Am(III), Cm(III) and Eu(III) with Ox and EDTA + Ox*. Dalton Trans. 40, 4829–4837, (2006)

THA2007 P. Thakur, D. K. Singh, and G. R. Choppin: *Polymerization study of o-Si(OH)$_4$ and complexation with Am(III), Eu(III) and Cm(III*). Inorganica Chim. Acta 360, 3705–3711, (2007)

THA2009 P. Thakur, P. N. Pathak, T. Gedris, G. R. Choppin: *Complexation of Eu(III), Am(III) and Cm(III) with Dicarboxylates: Thermodynamics and Structural Aspects of the Binary and Ternary Complexes.* Journal of Solution Chemistry 38, 265-287, (2009)

TIA2010 G. Tian, L. R. Martin, L. Rao: *Complexation of lactate with neodymium(III) and europium (III) at variable temperatures: studies by potentiometry, microcalorimetry, optical absorption and luminescence spectroscopy*. Inorg. Chem. 49, 10598-10605, (2010)

TIA2010 G. Tian, L.R. Martin and L. Rao: *Complexation of Lactate with Neodymium(III) and Europium(III) at Variable Temperatures: Studies by Potentiometry, Microcalorimetry, Optical Absorption, and Luminescence Spectroscopy*. Inorg.Chem. 49, 10598-10605, (2010)

TIA2015 G. Tian, Z. Zhang, L. R. Martin and L. Rao: *Complexation of Curium(III) with DTPA at 10 – 70 ° C: Comparison with Eu(III) – DTPA in Thermodynamics, Luminescence, and Coordination Modes*. Inorg. Chem. 54, 1232−1239, (2015)

TUR1986 G. L. Turner, K. A. Smith, R. J. Kirkpatrick, and E. Oldfield: *Boron-11 Nuclear Magnetic Resonance Spectroscopic Study of Borate and Borosilicate Minerals and a Borosilicate Glass*. J. Magn. Reson. 67, 544–550, (1986)

VAL2003 V. Vallet, H. Moll, U. Wahlgren, Z. Szabó, and I. Grenthe: *Structure and Bonding in Solution of Dioxouranium(VI) Oxalate Complexes: Isomers and Intramolecular Ligand Exchange.* Inorg. Chem., 42, 1982–1993, (2003)

VAN1984 M. Van Duin, J. A. Peters, A. P. G. Kieboom, and H. Van Bekkum: *Studies on borate esters I: The pH dependence of the stability of esters of boric acid and borate in aqueous medium as studied by ^{11}B NMR*. Tetrahedron 40, 2901–2911, (1984)

VAN1985 M. Van Duin, J. A. Peters, A. P. G. Kieboom, and H. Van Bekkum: *Studies on borate esters II: Structure and stability of borate esters of polyhydroxycarboxylates and related polyols in aqueous alkaline media as studied by ^{11}B NMR*. Tetrahedron 41, 3411–3421, (1985)

WAN2000 Z. M. Wang, L. J. van de Burgt, and G. R. Choppin: *Spectroscopic study of lanthanide(III) complexes with aliphatic dicarboxylic acids*. Inorg. Chim. Acta 310, 248–256, (2000)

WAN2013 Ping Wang, Rui-Qing Fan, Xin-Rong Liu, Li-Yuan Wang, Yu-Lin Yang, Wen-Wu Cao, Bin Yang, WuLiJi Hasi, Qing Su and Ying Mu: *Two-/three-dimensional open lanthanide–organic frameworks containing rigid/flexible dicarboxylate ligands: synthesis, crystal structure and photoluminescent properties*. Cryst.Eng.Comm. 15, 1931–1949, (2015)

WEA1964 B. Weaver, F. A. Kappelman: *TALSPEAK, A new method of separating americium and curium from the lanthanides by extraction from an aqueous solution of an aminopolyacetic acid complex with a monoacidic organophosphate or phosphonate*. ORNL-3559, (1964)

WEA1968 B. Weaver, F. A. Kappelman: *Preferential extraction of lanthanides over trivalent actinides by monacidic organophosphates from carboxylic acids and from mixtures of carboxylic and aminopolyacetic acids.* J. Inorg. Nucl. Chem. 30, 263, (1968)

WOO1993 S. A. Wood: *The aqueous geochemistry of the rare-earth elements: Critical stability constants for complexes with simple carboxylic acids at 25°c and 1 bar and their application to nuclear waste management*, Engineering Geology 34, 229–259, (1993)

XIO2009 Y.-L. Xiong: *The aqueous geochemistry of thallium: speciation and solubility of thallium in low temperature systems*. Environ. Chem. 6, 441–451, (2009)

XIO2011 Y. Xiong: *Organic species of lanthanum in natural environments: Implications to mobility of rare earth elements in low temperature environments*. Applied Geochemistry 26, 1130–1137, (2011)

ZAL2010 P. R. Zalupski, K. L. Nash and L. R. Martin: *Toward understanding the thermodynamics of TALSPEAK process. Medium effects on actinide complexation.* J. Solution Chem. 39, 1213–1229, (2010)

ZAN2001 P. L. Zanonato, P. Di Bernardo, A. Bismondo, L. Rao, G. R. Choppin: *Thermodynamic studies of the complexation between neodymium and acetate at elevated temperatures*. J. Solution Chem. 30, 1, (2001)

ZAN2004 P. Zanonato, P. Di Bernardo, A. Bismondo, G. Liu, X. Chen, L. Rao: *Hydrolysis of Uranium(VI) at Variable Temperatures (10 - 85 °C),* J. Solution Chem. 30, 1, (2001)

ZHA2009 X. Zhang, Y. Xing, C. Wang, J. Han, J. Li, M. Ge, X. Zeng, and S. Niu: *Lanthanide–alkali metals–oxalates coordination polymers: Synthesis and structures of* $[Nd(C_2O_4)1.5(H_2O)_3]\cdot 2H_2O$, $Nd(C_2O_4)(CH_3COO)(H_2O)$, $KLn(C_2O_4)_2(H_2O)_4$ *(Ln=Y, Tb).* Inorg. Chim. Acta 362, 1058–1064, (2009)

Physikalisch-Chemisches Institut, Universität Heidelberg

Spectroscopic investigations on the interaction of trivalent actinides/lanthanides with clay organic ligands

Daniel R. Fröhlich, Andrej Skerencak-Frech, Petra J. Panak

Final Report

Support Contract Number

02E11031

Physikalisch Chemisches Institut
Ruprecht-Karls Universität Heidelberg
Im Neuenheimer Feld 253
69120 Heidelberg
Germany

Content

1. Introduction

The final storage of high-level nuclear waste will be performed in deep geological formations. Besides other possible host rock formations (i.e. salt rocks and crystalline formations), natural clay rocks are investigated extensively in several European countries (e.g. Belgium [1], France [2], Germany [3], and Switzerland [4]). The main research focuses on the geochemical behavior of radionuclides contained in the spent fuel, including the long-lived transuranium elements (Np, Pu, and Am) which will determine the long-term radiotoxicity of high-level nuclear waste materials. Due to their long half-life, the geochemical properties of these elements are of particular interest. Thus, a comprehensive safety assessment has to include long-term predictions of the migration of the transuranium elements in the near- and far-field of a repository. Due to reducing conditions (e.g. due to corrosion of the steel canisters) expected in the near-field of the repository, +3 will be the predominant oxidation state of Pu, Am, and Cm. Therefore, the geochemistry of the trivalent actinides is of major concern for the long-term safety assessment. Their migration behavior is determined by different geochemical interaction mechanisms, including sorption, diffusion processes, and complexation reactions with (in)organic ligands in aqueous solution. The pore waters of natural clays contain a broad variety of organic and inorganic ligands which may affect the aqueous speciation and, therefore, the migration behavior of the actinides. The interactions strongly depend on the characteristics of the natural waters including pH, ionic strength, and redox potential. This clearly points out the complexity and extent of the required investigations.

Literature studies on the characterization of dissolved organic compounds in pore waters of different natural clays (i.e. Opalinus Clay and Callovo Oxfordian) showed that, besides macromolecular organics (e.g. kerogene, humic substances), low molecular weight organic compounds (LMWOC; e.g. formate, acetate, propionate, lactate, etc.) represent a large fraction of the total dissolved organic content (Opalinus Clay: 36%; Callovo Oxfordian: 88%) [5,6]. Furthermore, LMWOC may also be formed due to radiolytic degradation of organic macromolecules. Thus, the focus of this project was to investigate the interaction of trivalent actinides with various LMWOC. For comparison, the complexation with different fulvic acids as representative humic substances was investigated too.

Due to its excellent spectroscopic properties, Cm(III) was used as a representative trivalent actinide to thermodynamically characterize and quantify complexation reactions using time-resolved laser fluorescence spectroscopy, the specific ion interaction theory (SIT) and the integrated Van't Hoff equation. These thermodynamic studies were complemented by synchrotron based measurements (extended x-ray absorption fine structure (EXAFS) spectroscopy) using Am(III) to resolve the molecular structure of the formed complexes.

2. Materials and methods

2.1. Chemicals

All chemicals were purchased from Merck or Sigma/Aldrich. Three different fulvic acids (FAs) were used in this project. The FA from the Gorleben aquifer system (Gohy-573) was provided by the Institute of Nuclear Waste Disposal (KIT, Karlsruhe, Germany). This FA has a proton exchange capacity of 5.70 ± 0.09 meq/g. [7] To compare the complexation properties of FAs of different origin, two additional FAs, Suwannee River I (SR, 1S101F) and Nordic Lake (NL, 1R105F), were purchased from the International Humic Substance Society (IHSS). The proton exchange capacities (with respect to the carboxylic groups) of these FAs equal 11.44 (SR) and 11.16 meq/g (NL), respectively. Detailed information on the chemical properties of these two humic substances can be found on the IHSS website (www.humicsubstances.org).

2.2. Analytical methods

2.2.1. Time resolved laser fluorescence spectroscopy

TRLFS measurements are performed with a pulsed Nd:YAG (Surelite II, Continuum, USA) pumped dye laser system (NarrowScan, Radiant Dyes Laser & Acessoires

GmbH, Germany) with a pulse energy of 2-6 mJ at a repetition rate of 10 Hz using the dye Exalite 398. Eu(III) (used for experiments with fulvic acids) and Cm(III) are excited at 394.0 nm and 396.6 nm, respectively. Sample solutions are measured in quartz cuvettes embedded in a copper block. The temperature of the block is regulated by a thermostat (K6-mpc-NR, Peter Huber Kältemaschinen GmbH, Germany). The detector system consists of an iStar Gen II ICCD camera and a Shamrock SR-303i imaging spectrograph (both ANDOR Technology PLC, Northern Ireland). Fluorescence emission spectra are recorded using the 900 (Eu(III)) or the 1200 lines/mm grating (Cm(III)) of the spectrograph.

TRLFS samples are prepared from a 2×10^{-2} mol/kg Eu(III) and a 1×10^{-7} mol/kg Cm(III) stock solution in diluted $HClO_4$, respectively. The isotopic composition of the Cm(III) solution is: 89.7% Cm-248, 9.4% Cm-246, 0.3% Cm-244 and 0.6% Cm-243/245/247. The total metal ion concentrations are held constant at 1×10^{-6} mol/kg (Eu(III)) and 5×10^{-9} mol/kg or 1×10^{-8} mol/kg (Cm(III)), respectively.

Details on the sample composition used for complexation studies with the different ligand systems are given in the respective chapters (3.1. and 3.2.).

2.2.2. Extended X-ray absorption fine structure spectroscopy

EXAFS measurements were carried out at BM20 (Rossendorf Beamline (ROBL)) at the European Synchrotron radiation facility (ESRF, Grenoble, France) and at the INE beamline at the Angströmquelle Karlsruhe (ANKA, Karlsruhe, Germany). All samples were prepared from an Am(III) stock solution containing 30 MBq/l Am-243 and 17 MBq/l Am-241.

At BM20 we investigated the complexation of Am(III) with formate, acetate and lactate as a function of the pH value. Am L_{III}-edge EXAFS spectra of all samples were measured in fluorescence mode using a 13-element Ge-detector. The detector was positioned at an angle of 90 ° relative to the incoming beam. For energy calibration, a zirconium foil was measured simultaneously in transmission mode.

At the INE beamline we implemented a new high temperature cell to enable the measurement of EXAFS spectra at temperatures up to 200 °C and pressures up to 25 bar (Figure 1). The applicability of the high temperature cell was proven by

measuring the complexation of Am(III) with chloride at 25, 90, and 200 °C. The beamlime is equipped with a double-crystal monochromator (Si(111), Si(311), InSb(111), and Ge(422) crystal pairs available) and a mirror focusing system (Rh coated silicon mirrors). For our measurements, the Ge(422) crystal pair is used. The detuning in the middle of the scan range equales 70%. The spectra are collected in fluorescence mode at an angle of 90° using a 5 pixel Ge detector (Canberra Ultra-LEGe). The incident X-ray intensity I_0 is measured with an Ar filled ionization chamber at ambient pressure.

Except for the high temperature data, the whole data processing, including dead-time correction, energy calibration, averaging, extraction of the EXAFS signal and fitting, was performed using the EXAFSPAK software package [8]. EXAFS data at high temperatures were evaluated with Athena 0.8.061 and Artemis 0.8.012. [9] In all cases, the ionization energy (E_0) was set to 18515 eV. Theoretical scattering phases and amplitudes were calculated with FEFF8.20 or FEFF8.40 [10]. In all cases, the best theoretical model was fit to the raw k^3-weighted EXAFS spectra. The amplitude reduction factor S_0^2 was held constant at 0.9.

Details on the composition of the Am(III) samples with the different ligand systems are given in the respective chapters (4.1.-4.4.).

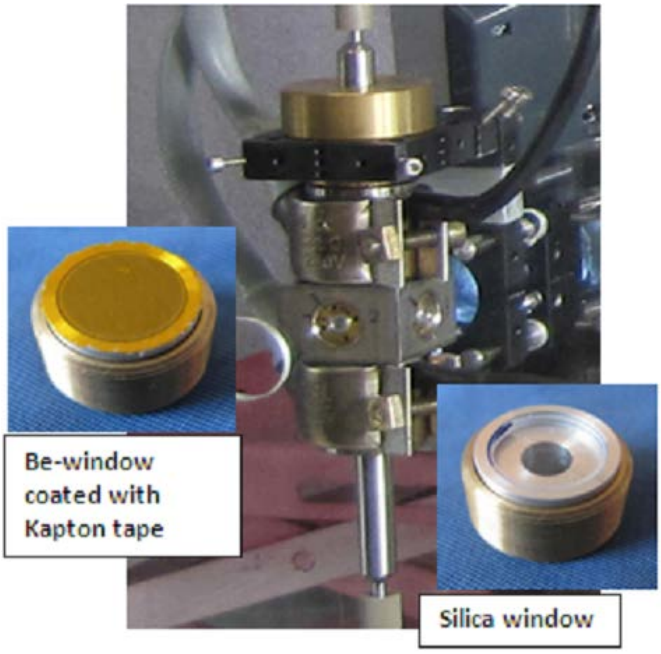

Figure 1: High temperature EXAFS cell with Be- and Si-windows.

2.3. Determination of thermodynamic data

The underlying purpose of this project is to thermodynamically characterize various complexation reactions of trivalent actinides with clay organic compounds. In this context, the following thermodynamic constants are determined: temperature dependent stability constants at zero ionic strength ($\log K^0_n(T)$), standard reaction enthalpies ($\Delta_r H^0_m$) and entropies ($\Delta_r S^0_m$).

At a first stage, the pure component spectra of the different Cm(III) species formed at various experimental conditions (the Cm(III) aquo ion and different complex species) are extracted from the experimental emission spectra. Using the pure component spectra, all experimental spectra (recorded as a function of temperature, ligand concentration and ionic strength) are deconvoluted. From the resulting Cm(III) speciation in combination with the free ligand concentration at given experimental conditions the conditional stability constants at a particular ionic strength and temperature are determined:

$$K_n^{'}(T) = \frac{[Cm(Lig)_n^{3-m\cdot n}]_{eq}}{[Cm(Lig)_{n-1}^{3-m\cdot n+m}]_{eq} \cdot [Lig^{m-}]_{eq}} \qquad (1)$$

In this equation, Lig refers to an arbitrary ligand with the charge –m. The free ligand concentration at equilibrium $[Lig^{m-}]_{eq}$ is calculated taking into account its dissociation constant as a function of temperature and possible complexation reactions with counter ions of the background electrolyte. Details on the calculation are described elsewhere [11].

Applying the specific ion interaction theory (SIT) theory, the thermodynamic stability constants ($K^0_n(T)$) at zero ionic strength are derived from equation (2):

$$\log K_n^0(T) = \log K_n^{'}(T) - \Delta z^2 \cdot D(T) + \Delta\varepsilon_n(T) \cdot I_m \qquad (2)$$

I_m is the ionic strength, $\Delta z^2 = \sum z^2(\text{products}) - \sum z^2(\text{educts})$ (z = ion charge,), D(T) is the temperature dependent Debye-Hückel term ($D(T) = A(T)\cdot I_m^{0.5}/(1+1.5 I_m^{0.5})$ with the Deby-Hückel parameters A(T) and $Ba_j(T)$ taken from the NEA TDB [12]. Δε(T) is the

difference between the binary interaction coefficients of the products and reactants ($\Delta\varepsilon(T) = \sum\varepsilon_i(T)_{prod} - \sum \varepsilon_i(T)_{ed}$).

By plotting $\log K'_n(T) - \Delta z^2 \cdot D(T)$ vs. I_m, the slope equals $-\Delta\varepsilon_n(T)$ and $\log K^0_n$ is derived from the y-intercept.

Standard reaction enthalpies and entropies of the respective complexation reactions are determined from the temperature dependency of $\log K^0_n$ according to the following equation:

$$\log K^0(T) = -\frac{\Delta_r H^0_m}{R \cdot T \cdot \ln(10)} + \frac{\Delta_r S^0_m}{R \cdot \ln(10)} \qquad (3)$$

There, R is the ideal gas constant (8.314 J/(K·mol)). By plotting $\log K^0_n(T)$ vs. T^{-1}, $\Delta_r H^0_m$ and $\Delta_r S^0_m$ are obtained from the slope and y-intercept of the linear regression, respectively.

In the case of humic substances (e.g. fulvic acids), the SIT cannot be applied due to the unknown molecular weight of the ligands. In this case we use the charge neutralization model implemented by Kim and Czerwinski [13] to determine thermodynamic data for the complexation of Cm(III) and Eu(III) with different fulvic acids (FAs). Again, peak deconvolution using the pure component spectra is applied to determine the speciation of Cm(III) or Eu(III) as a function of the FA concentration at different temperatures. The conditional stability constants as a function of temperature are determined from the speciation. According to the charge neutralization model, it is assumed that each Cm(III) or Eu(III) ion occupies three proton exchange sites of the fulvic acid which leads to a charge neutralization. The stability constant is given by equation (4):

$$\beta = \frac{[Me(III)FA]_{eq}}{[Me(III)]_{eq} \cdot [FA]_{eq}} \qquad (4)$$

There $[Me(III)FA]_{eq}$ and $[Me(III)]_{eq}$ are the concentrations of free and complexed Cm(III) or Eu(III) and $[FA]_{eq}$ is the concentration of the free FA in solution. The complexation properties of FA depend on the pH, ionic strength, nature of humic substance, etc. This is considered by introducing the loading capacity (LC) which is defined by equation (5):

$$LC = \frac{[Me(III)]_{\max}}{[FA]_{total}} \quad (5)$$

with $[Me(III)]_{max}$ being the maximum concentration of Cm(III) or Eu(III) that can be bound to the fulvic acid and $[FA]_{total}$ the total concentration of FA which is defined by equation (6):

$$[FA]_{total} = \frac{(FA) \cdot PEC}{Z} \quad (6)$$

(FA) is the fulvic acid concentration in g/kg H_2O, PEC the proton exchange capacity and Z the ionic charge of the metal ion. By using equations (5) and (6), the LC equals:

$$LC = \frac{Z \cdot [Me(III)]_{\max}}{PEC \cdot (FA)} \quad (7)$$

and the free FA concentration is calculated according to equation (8):

$$[FA]_{eq} = [FA]_{total} \cdot LC - [Me(III)FA]_{eq} \quad (8)$$

The combination of equations (4) and (8) results in:

$$[Me(III)]_{eq} = LC \cdot \frac{[Me(III)]_{eq} \cdot [FA]_{total}}{[Me(III)FA]_{eq}} - \frac{1}{\beta} \quad (9)$$

$[Me(III)]_{eq}$ and $[Me(III)FA]_{eq}$ are determined experimentally and $[FA]_{total}$ is calculated using PEC, (FA) and Z. The LC is determined by linear regression plotting $[Me(III)]_{eq} \times [FA]_{total}/[Me(III)FA]_{eq}$ vs. $[Me(III)]_{eq}$.

3. Time resolved laser fluorescence spectroscopy

3.1. Small organic ligands

3.1.1. Formate

Details on the application of this ligand system is described in [14]. To investigate the complexation of Cm(III) with formate, two series of samples were used. One series of samples was prepared by varying the ionic strength (I = 0.5-3.0 mol/kg) at a constant formate concentration of 0.05 mol/kg. The ionic strength was adjusted by adding solid NaCl. The second batch of samples was prepared at constant ionic strength (I = 1 mol/kg) varying the ligand concentration from 0 to 0.2 mol/kg. The formate concentrations were adjusted by adding either solid sodium formate or aliquots of a 0.5 mol/kg solution. The total proton concentration (adjusted with 0.01 mol/kg HCl) and the total Cm(III) concentration are held constant ($[H^+]_{total}$ = 8.5 × 10^{-5} mol/kg; $[Cm]_{total}$ = 5 × 10^{-9} mol/kg) in all samples. Each sample was measured at various temperatures in the range of 20 – 90 °C.

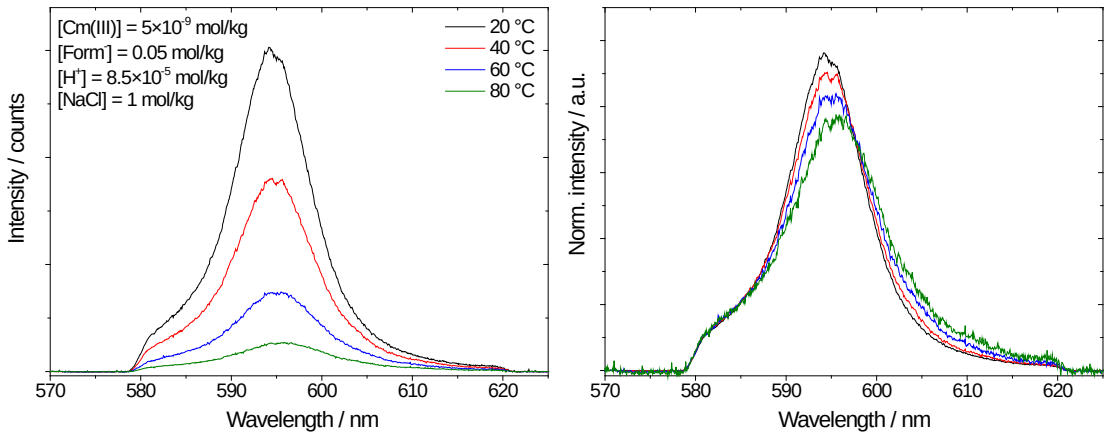

Figure 2: Emission spectra of 5 × 10^{-9} mol/kg Cm(III) in the presence of 0.05 mol/kg formate in 1 mol/kg NaCl solution as a function of temperature ($[H^+]_{total}$ = 8.5 × 10^{-5} mol/kg) without (left) and with (right) normalization with respect to the total peak area.

As an example, Figure 2 shows the emission spectra of 5×10^{-9} mol/kg Cm(III) in the presence of 0.05 mol/kg formate in 1 mol/kg NaCl solution as a function of temperature with and without normalization with respect to the total peak area. With increasing temperature the total peak area decreases due to the successive thermal population of higher energetic states of the Cm(III) ion [15]. For a better comparability all spectra are normalized with respect to the total peak area (Figure 2, right). It is clearly visible that the position of the emission band shifts towards higher wavelength with increasing temperature. This effect is attributed to the successive shift of the Cm(III) speciation towards complexed species. The evaluation revealed four Cm(III) species: the Cm(III) aquo ion and the complexed species $[Cm(Form)_n]^{3-n}$ (n = 1, 2, 3). The emission bands are located at 593.5 nm, 596.6 nm, 599.8 nm, and 604.1 nm.

The experimental spectra are deconvoluted using the pure component spectra. As an example, the resulting Cm(III) speciation as a function of the ligand concentration in 1 mol/kg NaCl solution at 20 and 70 °C is presented in Figure 3.

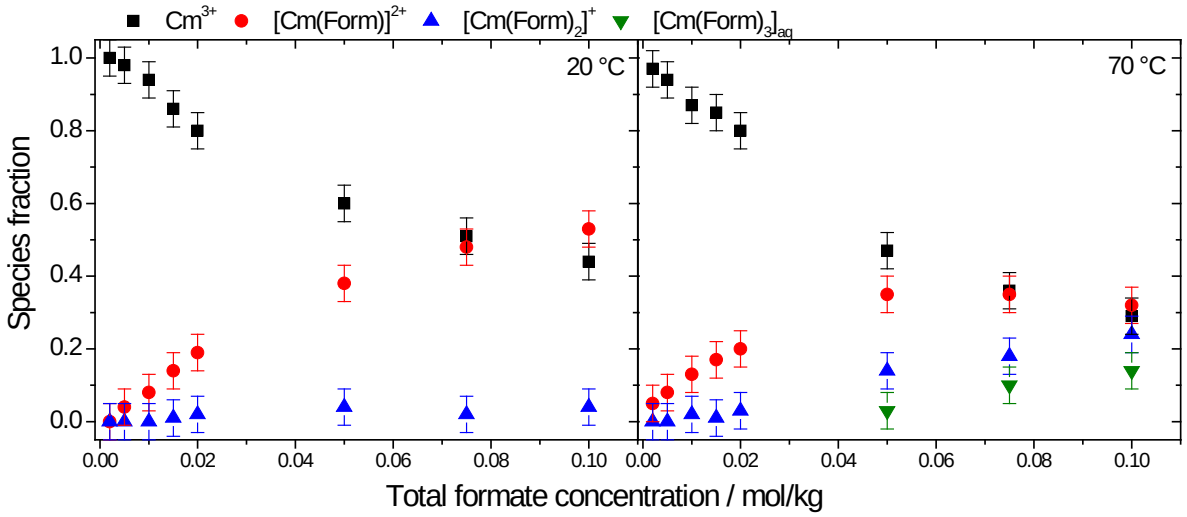

Figure 3: Speciation of Cm(III) as a function of the total formate concentration in 1 mol/kg NaCl solution at 20 (left) and 70 °C (right).

It is clearly visible that the Cm(III) speciation shifts towards complexed species with increasing ligand concentration. At higher temperature, the impact of formate on the

aqueous Cm(III) speciation increases and $[Cm(Form)_n]^{3-n}$ (n = 2,3) are present at higher fractions.

From the experimental speciation and the ligand concentration at equilibrium (calculated with $\log K^0_{HForm}(25\ °C) = -3.744$ and $\Delta_r H^0_m = 0.16$ kJ/mol (both values given in the NIST database 46.6 [16])) the thermodynamic stability constants are determined using the SIT.

The obtained $\Delta\varepsilon_n$ (n = 1,2) values do not show a significant temperature dependency. Therefore, average values were determined (shown in Table 1). In addition, the interaction coefficients for the interaction of $[Cm(Form)]^{2+}$ and $[Cm(Form)_2]^{+}$ with chloride ($\varepsilon(Cm(Form)^{2+},Cl^-)$ and $\varepsilon(Cm(Form)_2^{+},Cl^-)$) are calculated.

Table 1: $\Delta\varepsilon_n$ (n = 1-2) and $\varepsilon(Cm(Form)_n^{3-n},Cl^-)$ (n = 1, 2) values

$\Delta\varepsilon_1$	-0.13 ± 0.04
$\Delta\varepsilon_2$	-0.06 ± 0.02
$\varepsilon(Cm(Form)^{2+},Cl^-)$	0.13 ± 0.05
$\varepsilon(Cm(Form)_2^{+},Cl^-)$	0.10 ± 0.06

The temperature dependent stability constants are given in Table 2. Both $\log K^0_1(T)$ and $\log K^0_2(T)$ increase with increasing temperature by ≈ 0.4 and ≈ 0.8 log units, respectively. Therefore, both complexation reactions are endothermic. The Arhenius plot is shown in Figure 4. The linear fit yields $\Delta_r H^0_m$ values of 11.4 and 30.5 kJ/mol and $\Delta_r S^0_m$ values of 78.7 and 122.1 J/(K·mol) for the first and second complexation step, respectively (see also Table 3).

The $\log K^0_n$ (n = 1,2) values at room temperature are compared to the corresponding values of different lanthanide complexes which are tabulated in the NIST database 46.6: $\log K^0_1$: $Ln(Form)^{2+}$: 1.64-2.05; $\log K^0_2$: $Ln(Form)_2^{+}$: 0.63-1.54 [16]. In particular for $\log K^0_2$, the tabulated values show significant deviations when comparing different lanthanides. However, most of the literature data are comparable to the values of Cm(III) and the differences between $\log K^0_1$ and $\log K^0_2$ are in the same range.

Table 2: Temperature dependent thermodynamic stability constants log $K^0_n(T)$ for the stepwise formation of $[Cm(Form)_n]^{3-n}$ (n = 1,2).

T / °C	log K^0_1			log K^0_2		
	I_m = var.	[$Form^-$] = var.	Mean	I_m = var.	[$Form^-$] = var.	Mean
20	2.12 ± 0.06	2.10 ± 0.07	2.11 ± 0.01	-	-	-
30	2.13 ± 0.06	2.14 ± 0.06	2.13 ± 0.01	1.23 ± 0.46	1.10 ± 0.15	1.17 ± 0.09
40	2.21 ± 0.06	2.19 ± 0.05	2.20 ± 0.02	1.30 ± 0.40	1.26 ± 0.15	1.28 ± 0.03
50	2.27 ± 0.07	2.26 ± 0.09	2.26 ± 0.01	1.63 ± 0.21	1.40 ± 0.08	1.51 ± 0.16
60	2.30 ± 0.07	2.33 ± 0.12	2.32 ± 0.02	1.71 ± 0.17	1.51 ± 0.10	1.61 ± 0.14
70	2.32 ± 0.07	2.36 ± 0.11	2.34 ± 0.03	1.77 ± 0.15	1.64 ± 0.12	1.71 ± 0.09
80	2.39 ± 0.08	2.43 ± 0.18	2.41 ± 0.03	2.00 ± 0.11	1.81 ± 0.08	1.90 ± 0.14
90	2.49 ± 0.09	2.49 ± 0.19	2.49 ± 0.01	2.12 ± 0.11	1.90 ± 0.17	2.01 ± 0.15

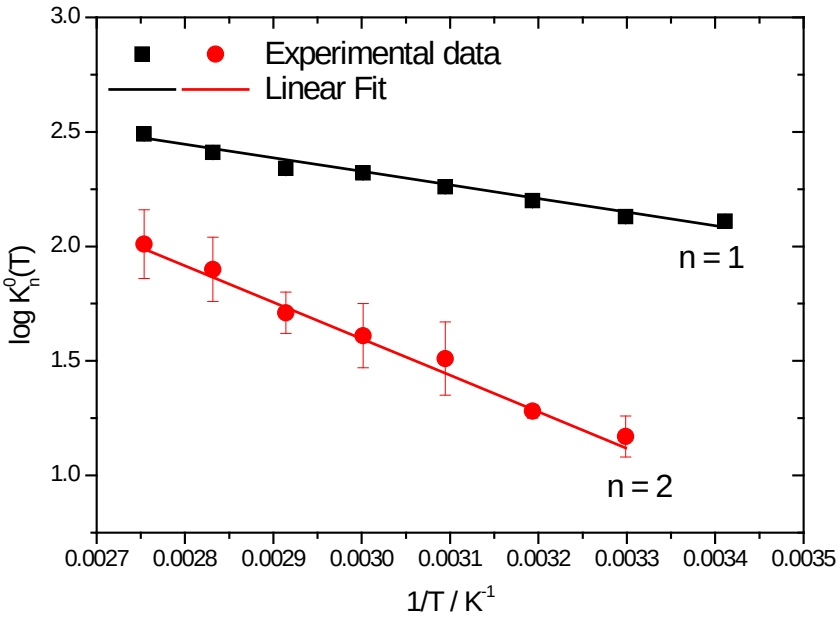

Figure 4: Arrhenius plot of log $K^0_n(T)$ for the formation of $[Cm(Form)_n]^{3-n}$ (n = 1,2) vs. 1/T.

Table 3: $\Delta_r H^0_m$ and $\Delta_r S^0_m$ values for the stepwise formation of $[Cm(Form)_n]^{3-n}$ (n = 1,2).

$Cm^{3+} + Form^- \rightleftharpoons Cm(Form)^{2+}$		$Cm(Form)^{2+} + Form^- \rightleftharpoons Cm(Form)_2^+$	
$\Delta_r H^0_m$ / kJ/mol	$\Delta_r S^0_m$ / J/K·mol	$\Delta_r H^0_m$ / kJ/mol	$\Delta_r S^0_m$ / J/K·mol
11.4 ± 0.7	78.7 ± 2.3	30.5 ± 7.6	122.1 ± 24.1

For a detailed description of the above mentioned results see:

D. R. Fröhlich, A. Skerencak-Frech, P. J. Panak, Complex formation of Cm(III) with formate studied by time-resolved laser fluorescence spectroscopy, Applied Geochemistry, *2015, **61**, 312-317.*

3.1.2. Acetate

The complexation of Cm(III) with acetate was studied following the same procedure as described above. In the case of acetate different background electrolytes ($NaClO_4$, NaCl, $CaCl_2$) were investigated. For NaCl and $NaClO_4$, two series of samples were prepared varying the ionic strength between 0.5 and 3.0 mol/kg at constant acetate concentrations of 0.005 and 0.02 mol/kg. For $CaCl_2$ only one ionic strength dependent series (I = 0.5-3.0 mol/kg) was investigated at a fixed acetate concentration of 0.05 mol/kg. In addition, one series at I = 1.0 mol/kg was prepared for each electrolyte varying the initial ligand concentration between 0.003 and 0.3 mol/kg. The ionic strength was adjusted by adding solid $NaClO_4 \cdot H_2O$, NaCl, or $CaCl_2 \cdot 4\ H_2O$.

The total proton concentration was adjusted with 0.01 mol/kg HCl or $HClO_4$ and held constant in all samples ($[H^+]_{total} = 9 \times 10^{-5}$ mol/kg). Also, the total Cm(III) concentration was fixed at 5×10^{-9} mol/kg or 1×10^{-8} mol/kg. Each sample was measured at various temperatures in the range of 20 – 90 °C.

The emission bands of the pure component spectra of the different Cm(III) acetate complexes are located at 596.5 ($[Cm(Ac)]^{2+}$), 599.3 ($[Cm(Ac)_2]^+$), and 602.0 nm ($[Cm(Ac)_3]$). In general, the complexation of Cm(III) with acetate shows that the speciation is shifted toward the complexed species with increasing temperature at a fixed ligand concentration. In solutions containing $CaCl_2$, however, this effect is less pronounced due to the complexation of Ca^{2+} with acetate which reduces the amount of acetate available for the complexation reaction with Cm(III).

The application of the SIT yields $\Delta\varepsilon_n$ (n = 1-3), $\varepsilon(Cm(Ac)_n^{3-n}, Cl^-)$ (n = 1,2), and $\varepsilon(Cm(Ac)_n^{3-n}, ClO_4^-)$ (n = 1,2) values summarized in Table 4. Again no visible temperature dependency of $\Delta\varepsilon_n$ (n = 1-3) is observed.

Table 4: $\Delta\varepsilon_n$ (n = 1-3), $\varepsilon(Cm(Ac)_n^{3-n}, Cl^-)$ (n = 1,2), and $\varepsilon(Cm(Ac)_n^{3-n}, ClO_4^-)$ (n = 1,2) values.

	$\Delta\varepsilon_1$	$\Delta\varepsilon_2$	$\Delta\varepsilon_3$	$\varepsilon(CmAc^{2+},ClO_4^-)$	$\varepsilon(CmAc_2^+,ClO_4^-)$
$NaClO_4$	-0.15 ± 0.02	-0.25 ± 0.09	-0.33 ± 0.10	0.42 ± 0.05	0.25 ± 0.09
	$\Delta\varepsilon_1$	$\Delta\varepsilon_2$	$\Delta\varepsilon_3$	$\varepsilon(CmAc^{2+},Cl^-)$	$\varepsilon(CmAc_2^+,Cl^-)$
NaCl	-0.17 ± 0.01	-0.13 ± 0.04	-0.17 ± 0.07	0.14 ± 0.04	0.09 ± 0.06
$CaCl_2$	-0.24 ± 0.03	-0.23 ± 0.04	-0.57 ± 0.35	0.26 ± 0.20	0.30 ± 0.29

The temperature dependent thermodynamic stability constants for the stepwise formation of $[Cm(Ac)_n]^{3-n}$ (n = 1-3) are given in Table 5. Similar results are obtained for all electrolyte systems. Log K^0_1 increases by 0.1-0.3 log units from 3.1-3.4 to 3.2-3.7 in the investigated temperature range. The temperature dependency is more pronounced for the second and third complexation step. Here, the increase of log K^0_n (n = 2,3) is in the range of about 1 log unit. Log K^0_2 increases from 1.5-1.7 to 2.6-2.7, whereas log K^0_3 increases from 0.4 to 1.1-1.3. In general, the thermodynamic stability constants are by about one log unit higher for the first and 0.5 log units higher for the second complexation step compared to the corresponding formate complexes. The same trend is also found for room temperature data of lanthanide complexes with acetate tabulated in the NIST database 46.6: log K^0_1: $Ln(Ac)^+$: 2.43-2.84; log K^0_2: $Ln(Ac)_2^+$: 1.57-1.96 [15] compared to the respective formate complexes (see chapter 3.1.1.).

Table 5: Temperature dependent thermodynamic stability constants log $K^0_n(T)$ for the stepwise formation of $[Cm(Ac)_n]^{3-n}$ (n = 1-3).

	T / °C	log K^0_1			log K^0_2			log K^0_3
		I_m = var.	$[Ac^-]_{total}$ = var.	Average ± 2σ	I_m = var.	$[Ac^-]_{total}$ = var.	Average ± 2σ	$[Ac^-]_{total}$ = var.
$NaClO_4$	20	3.23 ± 0.12	3.00 ± 0.12	3.12 ± 0.32	1.49 ± 0.56	1.47 ± 0.16	1.48 ± 0.02	-
	30	3.27 ± 0.12	3.06 ± 0.14	3.16 ± 0.30	1.74 ± 0.40	1.65 ± 0.19	1.69 ± 0.14	-
	40	3.28 ± 0.14	3.09 ± 0.16	3.19 ± 0.26	2.00 ± 0.50	1.77 ± 0.17	1.89 ± 0.32	0.40 ± 0.39
	50	3.27 ± 0.14	3.11 ± 0.15	3.19 ± 0.24	2.22 ± 0.28	1.88 ± 0.18	2.05 ± 0.48	0.60 ± 0.35
	60	3.27 ± 0.16	3.17 ± 0.16	3.22 ± 0.14	2.31 ± 0.30	2.03 ± 0.20	2.17 ± 0.40	0.73 ± 0.36
	70	3.27 ± 0.16	3.18 ± 0.22	3.22 ± 0.14	2.47 ± 0.32	2.11 ± 0.20	2.29 ± 0.52	0.87 ± 0.31
	80	3.26 ± 0.20	3.17 ± 0.28	3.21 ± 0.14	2.66 ± 0.48	2.24 ± 0.23	2.45 ± 0.60	0.97 ± 0.29
	90	3.29 ± 0.24	3.22 ± 0.32	3.25 ± 0.10	2.72 ± 0.24	2.38 ± 0.21	2.55 ± 0.48	1.08 ± 0.32

NaCl	20	3.06 ± 0.08	3.30 ± 0.11	3.18 ± 0.34	1.59 ± 1.02	1.64 ± 0.32	1.62 ± 0.08	0.39 ± 0.12
	30	3.09 ± 0.08	3.08 ± 0.12	3.09 ± 0.02	1.63 ± 0.30	1.73 ± 0.34	1.68 ± 0.14	0.46 ± 0.11
	40	3.14 ± 0.08	3.12 ± 0.12	3.13 ± 0.02	1.96 ± 0.12	1.76 ± 0.33	1.86 ± 0.28	0.55 ± 0.15
	50	3.17 ± 0.08	3.16 ± 0.13	3.16 ± 0.02	2.03 ± 0.24	1.84 ± 0.27	1.93 ± 0.28	0.69 ± 0.22
	60	3.19 ± 0.08	3.21 ± 0.13	3.20 ± 0.02	2.21 ± 0.18	2.00 ± 0.19	2.10 ± 0.30	0.92 ± 0.14
	70	3.20 ± 0.08	3.22 ± 0.15	3.21 ± 0.02	2.43 ± 0.26	2.23 ± 0.30	2.33 ± 0.28	0.99 ± 0.13
	80	3.19 ± 0.10	3.24 ± 0.17	3.22 ± 0.08	2.69 ± 0.34	2.40 ± 0.27	2.54 ± 0.42	1.07 ± 0.15
	90	3.18 ± 0.04	3.28 ± 0.18	3.23 ± 0.14	2.81 ± 0.52	2.58 ± 0.35	2.69 ± 0.32	1.26 ± 0.28
$CaCl_2$	20	3.35 ± 0.20	3.45 ± 0.17	3.40 ± 0.14	1.89 ± 0.32	1.48 ± 0.47	1.68 ± 0.58	-
	30	3.46 ± 0.20	3.50 ± 0.15	3.48 ± 0.06	1.91 ± 0.24	1.64 ± 0.34	1.77 ± 0.38	-
	40	3.55 ± 0.24	3.56 ± 0.14	3.56 ± 0.02	2.04 ± 0.20	1.84 ± 0.23	1.94 ± 0.28	-
	50	3.61 ± 0.26	3.61 ± 0.14	3.61 ± 0.02	2.20 ± 0.16	2.00 ± 0.21	2.10 ± 0.28	0.56 ± 0.44
	60	3.63 ± 0.26	3.65 ± 0.15	3.64 ± 0.02	2.29 ± 0.14	2.21 ± 0.17	2.25 ± 0.12	0.72 ± 0.40
	70	3.63 ± 0.26	3.65 ± 0.15	3.64 ± 0.02	2.37 ± 0.16	2.36 ± 0.21	2.36 ± 0.02	0.96 ± 0.44
	80	3.63 ± 0.28	3.68 ± 0.15	3.66 ± 0.08	2.52 ± 0.14	2.53 ± 0.17	2.53 ± 0.02	1.16 ± 0.43
	90	3.64 ± 0.30	3.72 ± 0.13	3.68 ± 0.10	2.62 ± 0.16	2.66 ± 0.14	2.64 ± 0.06	1.28 ± 0.40

$\Delta_rH^0_m$ and $\Delta_rS^0_m$ of the complexation reactions with acetate are positive for all complexation steps (see Table 6). For all background electrolytes, the thermodynamic data are in very good agreement. For the formation of $[CmAc]^{2+}$, $\Delta_rH^0_m$ is visibly smaller (3-6 kJ/mol) compared to the second (28-35 kJ/mol) and third (25-42 kJ/mol) complexation step. $\Delta_rS^0_m$ shows the same trend and increases from 70-88 J/(K·mol) for the first complexation step to 125-146 J/(K·mol) and 92-141 J/(K·mol) for the formation of $[CmAc_2]^+$ and $[CmAc_3]$, respectively. The comparison with the Cm formate complexes shows that the values for the first and second complexation step with acetate are in the same range as for the complexation with formate (see Table 3).

Table 6: $\Delta_rH^0_m$ and $\Delta_rS^0_m$ values for the stepwise formation of $[Cm(Ac)_n]^{3-n}$ (n = 1-3) in $NaClO_4$, NaCl and $CaCl_2$.

	$Cm^{3+} + Ac^- \rightleftharpoons Cm(Ac)^{2+}$		$Cm(Ac)^{2+} + Ac^- \rightleftharpoons Cm(Ac)_2^+$		$Cm(Ac)_2^+ + Ac^- \rightleftharpoons Cm(Ac)_3$	
	$\Delta_rH^0_m$ / kJ/mol	$\Delta_rS^0_m$ / J/K·mol	$\Delta_rH^0_m$ / kJ/mol	$\Delta_rS^0_m$ / J/K·mol	$\Delta_rH^0_m$ / kJ/mol	$\Delta_rS^0_m$ / J/K·mol
$NaClO_4$	3 ± 13	70 ± 37	33 ± 15	139 ± 52	29 ± 36	100 ± 106
NaCl	6 ± 2	79 ± 8	28 ± 12	125 ± 41	25 ± 9	92 ± 29
$CaCl_2$	6 ± 3	88 ± 10	35 ± 9	146 ± 26	42 ± 60	141 ± 174

More details are given in :

*D. R. Fröhlich, A. Skerencak-Frech, P. J. Panak, A spectroscopic study on the formation of Cm(III) acetate complexes at elevated temperatures, Dalton Transactions, 2014, **43**, 3958-3965.*

3.1.3. Propionate

According to the same procedure as for acetate, the complexation of Cm(III) with propionate was investigated in $NaClO_4$, NaCl, and $CaCl_2$ solution. In all samples $[H^+]_{total}$ (adjusted with HCl or $HClO_4$) was held constant at 1.3×10^{-4} mol/kg. The total concentration of Cm(III) either equaled 1×10^{-8} mol/kg (NaCl, $CaCl_2$) or 2×10^{-7} mol/kg ($NaClO_4$). For each background electrolyte, two separate sets of samples were prepared. In the first set of samples, the ionic strength was held constant at 1 mol/kg varying the ligand concentration between 0.001 and 0.03 mol/kg ($NaClO_4$, NaCl) or 0.001 and 0.04 mol/kg ($CaCl_2$). In the second set of samples, the ionic strength was varied ($NaClO_4$: 0.5-4.0 mol/kg; NaCl: 0.5-3.0 mol/kg; $CaCl_2$: 0.5-3.5 mol/kg) while fixing the ligand concentration at 0.005 mol/kg ($NaClO_4$, NaCl) or 0.05 mol/kg ($CaCl_2$). The ionic strength was adjusted by adding solid $NaClO_4 \cdot H_2O$, NaCl, or $CaCl_2 \cdot 4\ H_2O$. Each sample was measured at various temperatures between 20 °C and 90 °C.

Besides the Cm(III) aquo ion, two complex species ($[Cm(Prop)]^{2+}$ and $[Cm(Prop)_2]^+$) are observed at the given experimental conditions. The emission bands of the Cm(III) complexes are located at 596.5 and 598.9 - 599.9 nm, respectively.

$\Delta\varepsilon_n$ (n = 1,), $\varepsilon(Cm(Prop)_n^{3-n}, Cl^-)$ (n = 1,2), and $\varepsilon(Cm(Prop)_n^{3-n}, ClO_4^-)$ (n = 1,2) values, summarized in Table 7, are obtained using the SIT. The thermodynamic stability constants for the complex formation of Cm(III) with propionate at T = 20-90 °C obtained in the different background electrolytes are given in Table 8.

Table 7: $\Delta\varepsilon_n$ (n = 1,2), $\varepsilon(Cm(Prop)_n^{3-n}, Cl^-)$ (n = 1,2), and $\varepsilon(Cm(Prop)_n^{3-n}, ClO_4^-)$ (n = 1,2) values.

	$\Delta\varepsilon_1$	**$\Delta\varepsilon_2$**	**$\varepsilon(Cm(Prop)^{2+},ClO_4^-)$**	$\varepsilon(Cm(Prop)_2^{+},ClO_4^-)$
$NaClO_4$	**-0.13 ± 0.04**	**-0.14 ± 0.08**	**0.44 ± 0.05**	0.38 ± 0.10
	$\Delta\varepsilon_1$	$\Delta\varepsilon_2$	$\varepsilon(Cm(Prop)^{2+},Cl^-)$	$\varepsilon(Cm(Prop)_2^{+},Cl^-)$
NaCl	-0.11 ± 0.02	-0.14 ± 0.05	0.20 ± 0.03	0.14 ± 0.06
$CaCl_2$	-0.21 ± 0.02	-0.21 ± 0.02	0.29 ± 0.21	0.36 ± 0.29

Table 8: Temperature dependent thermodynamic stability constants log $K^0_n(T)$ for the stepwise formation of $[Cm(Prop)_n]^{3-n}$ (n = 1,2).

	T / °C	log K^0_1			log K^0_2		
		I_m = var.	$[Prop^-]_{total}$ = var.	Average	I_m = var.	$[Prop^-]_{total}$ = var.	Average
$NaClO_4$	20	3.34 ± 0.06	3.34 ± 0.07	3.34 ± 0.07	1.88 ± 0.06	1.65 ± 0.27	1.77 ± 0.28
	30	3.36 ± 0.07	3.34 ± 0.07	3.35 ± 0.08	1.93 ± 0.06	1.88 ± 0.17	1.90 ± 0.14
	40	3.37 ± 0.06	3.38 ± 0.07	3.37 ± 0.08	2.13 ± 0.06	2.01 ± 0.23	2.07 ± 0.21
	50	3.40 ± 0.06	3.39 ± 0.06	3.39 ± 0.07	2.34 ± 0.06	2.20 ± 0.19	2.27 ± 0.20
	60	3.44 ± 0.06	3.40 ± 0.06	3.42 ± 0.04	2.48 ± 0.06	2.36 ± 0.21	2.39 ± 0.20
	70	3.46 ± 0.06	3.44 ± 0.06	3.45 ± 0.05	2.54 ± 0.06	2.48 ± 0.20	2.51 ± 0.16
	80	3.50 ± 0.07	3.46 ± 0.06	3.48 ± 0.07	2.74 ± 0.06	2.64 ± 0.19	2.69 ± 0.18
	90	3.53 ± 0.08	3.46 ± 0.07	3.49 ± 0.11	2.93 ± 0.06	2.81 ± 0.15	2.87 ± 0.17
NaCl	25	3.36 ± 0.04	3.12 ± 0.09	3.24 ± 0.17	-	1.39 ± 0.24	-
	30	-	3.20 ± 0.09	-	-	1.41 ± 0.24	-
	40	3.55 ± 0.03	3.26 ± 0.07	3.41 ± 0.21	1.87 ± 0.19	1.53 ± 0.16	1.70 ± 0.24
	50	3.58 ± 0.04	3.32 ± 0.10	3.45 ± 0.18	2.00 ± 0.06	1.71 ± 0.23	1.86 ± 0.21
	60	3.62 ± 0.04	3.38 ± 0.10	3.50 ± 0.17	2.30 ± 0.08	1.93 ± 0.12	2.12 ± 0.26
	70	3.57 ± 0.05	3.42 ± 0.11	3.50 ± 0.11	2.59 ± 0.06	2.05 ± 0.14	2.32 ± 0.38
	80	3.58 ± 0.05	3.45 ± 0.10	3.52 ± 0.09	2.79 ± 0.05	2.30 ± 0.12	2.55 ± 0.35
	90	3.70 ± 0.05	3.43 ± 0.09	3.57 ± 0.19	2.87 ± 0.11	2.47 ± 0.09	2.67 ± 0.28
$CaCl_2$	20	3.45 ± 0.08	3.38 ± 0.11	3.42 ± 0.05	1.52 ± 0.10	1.38 ± 0.08	1.45 ± 0.10
	30	3.50 ± 0.08	3.44 ± 0.11	3.47 ± 0.04	1.66 ± 0.09	1.59 ± 0.19	1.63 ± 0.05
	40	3.55 ± 0.11	3.49 ± 0.10	3.52 ± 0.04	1.83 ± 0.07	1.75 ± 0.06	1.79 ± 0.06
	50	3.56 ± 0.12	3.54 ± 0.09	3.55 ± 0.01	2.02 ± 0.06	1.94 ± 0.07	1.98 ± 0.06
	60	3.60 ± 0.13	3.58 ± 0.07	3.59 ± 0.01	2.14 ± 0.06	2.15 ± 0.05	2.15 ± 0.01
	70	3.63 ± 0.14	3.62 ± 0.05	3.63 ± 0.01	2.25 ± 0.07	2.31 ± 0.05	2.28 ± 0.04
	80	3.65 ± 0.14	3.65 ± 0.06	3.65 ± 0.01	2.37 ± 0.07	2.46 ± 0.07	2.42 ± 0.06
	90	3.71 ± 0.15	3.69 ± 0.11	3.70 ± 0.01	2.54 ± 0.07	2.62 ± 0.06	2.58 ± 0.06

Similar results are obtained for all background electrolytes. Log K^0_1 and log K^0_2 increase by 0.2-0.3 and about 1.1 log units with increasing temperature. As expected, the determined stability constants are very similar to the results obtained for the complexation with acetate. Again, both complexation steps are endothermic and entropy driven. The related $\Delta_r H^0_m$ and $\Delta_r S^0_m$ values of the complexation reactions are presented in Table 9. Comparable results are obtained for all background electrolytes which are again in the same range as the thermodynamic data for the complexation with formate and acetate (see chapter 3.1.1. and 3.1.2.).

Table 9: $\Delta_r H^0_m$ and $\Delta_r S^0_m$ for the stepwise formation of $[Cm(Prop)_n]^{3-n}$ (n = 1,2) in $NaClO_4$, NaCl and $CaCl_2$ solution.

	$Cm^{3+} + Prop^- \rightleftharpoons Cm(Prop)^{2+}$		$Cm(Prop)^{2+} + Prop^- \rightleftharpoons Cm(Prop)_2^+$	
	$\Delta_r H^0_m$ / kJ/mol	$\Delta_r S^0_m$ / J/K·mol	$\Delta_r H^0_m$ / kJ/mol	$\Delta_r S^0_m$ / J/K·mol
$NaClO_4$	4.8 ± 1.0	79.8 ± 4.1	32.8 ± 4.1	144.5 ± 8.2
NaCl	5.7 ± 1.8	83.6 ± 5.2	44.2 ± 3.6	173.1 ± 11.0
$CaCl_2$	8.0 ± 1.4	92.7 ± 4.6	33.1 ± 1.7	140.4 ± 7.0

The results are described in detail in:

*A. Skerencak, S. Höhne, S. Hofman, C. Marquardt, P. J. Panak, Spectroscopic studies on the thermodynamics of the complexation of trivalent curium with propionate in the temperature range from 20 to 90°C, Journal of Solution Chemistry, 2013, **42**, 1-17.*

*D. R. Fröhlich, A. Skerencak, M. L. K. Morkos, P. J. Panak, A spectroscopic study of Cm(III) complexation with propionate in saline solutions at variable temperatures, New Journal of Chemistry, 2013, **37**, 1520-1528.*

3.1.4. Oxalate

In addition to complexation studies with monocarboxylic acids, the complexation of Cm(III) with oxalate was investigated in NaCl solution. The total concentrations of Cm(III) and H^+ were held constant at 5×10^{-9} and 9×10^{-3} mol/kg, respectively. Temperature (20 - 90 °C) and ionic strength (1.0 - 4.0 mol/kg) were varied for different total oxalate concentrations in the range of $0.47 - 7.55 \times 10^{-3}$ mol/kg. The ionic strength was adjusted by addition of solid NaCl.

At the given experimental conditions, four different Cm(III)-oxalate species are observed ($[Cm(Ox)_n]^{3-2n}$ (n = 1-4). The emission bands of these complex species are located 596.6 ($[Cm(Ox)]^+$), 599.1 ($[Cm(Ox)_2]^-$), 601.3 ($[Cm(Ox)_3]^{3-}$), and 604.6 nm ($[Cm(Ox)_4]^{5-}$. These shifts are comparable to those observed for the complexation with monocarboxylic acids (formate, acetate, propionate).

In accordance to the other ligand systems investigated, no temperature dependency of $\Delta\varepsilon_n$ (n = 1-4) is observed. Table 10 summarizes the average $\Delta\varepsilon_n$ and ε(i,k) values obtained for the Cm(III)-oxalate system in NaCl solution.

Table 10: $\Delta\varepsilon_n$ (n = 1-4), $\varepsilon(Cm(Ox)^+, Cl^-)$ (n = 1-3), and $\varepsilon(Cm(Ox)_n^{3-2n}, Na^+)$ (n = 2-4) values.

$\Delta\varepsilon_1$	-0.21 ± 0.03
$\Delta\varepsilon_2$	-0.12 ± 0.05
$\Delta\varepsilon_3$	-0.06 ± 0.04
$\Delta\varepsilon_4$	0.16 ± 0.20
$\varepsilon(Cm(Ox)^+, Cl^-)$	-0.06 ± 0.04
$\varepsilon(Cm(Ox)_2^-, Na^+)$	-0.26 ± 0.06
$\varepsilon(Cm(Ox)_3^{3-}, Na^+)$	-0.40 ± 0.10
$\varepsilon(Cm(Ox)_4^{5-}, Na^+)$	-0.32 ± 0.30

The thermodynamic stability constants for the stepwise formation of $[Cm(Ox)_n]^{3-2n}$ (n = 1-4) are presented in Table 11. Compared to the complexes with monocarboxylic acids (chapter 3.1.1.-3.1.3.), significant differences are observed for oxalate. Log $K^0_1(T)$ remains constant in the investigated temperature range, fluctuating between 6.73 and 6.86. Log $K^0_2(T)$ and log $K^0_3(T)$ also show only a slight temperature dependence increasing from 4.68 to 5.03 and from 2.11 to 2.40, respectively. As $[Cm(Ox)_4]^{5-}$ is only formed to a very small extent even at high temperatures, log $K^0_4(T)$ is determined at T ≥ 60 °C.

Table 11: Temperature dependent thermodynamic stability constants log $K^0_n(T)$ for the stepwise formation of $[Cm(Ox)_n]^{3-2n}$ (n = 1-4).

T / °C	Log K^0_1	Log K^0_2	Log K^0_3	Log K^0_4
20	6.86 ± 0.03	4.68 ± 0.09	2.11 ± 0.05	-
30	6.86 ± 0.06	4.71 ± 0.08	2.20 ± 0.10	-
40	6.80 ± 0.14	4.71 ± 0.11	2.24 ± 0.07	-
50	6.80 ± 0.18	4.78 ± 0.09	2.41 ± 0.10	-
60	6.75 ± 0.07	5.01 ± 0.09	2.38 ± 0.10	1.08 ± 0.22
70	6.73 ± 0.09	5.00 ± 0.11	2.40 ± 0.07	0.71 ± 0.12
80	6.86 ± 0.06	4.96 ± 0.05	2.48 ± 0.06	0.73 ± 0.07
90	6.76 ± 0.04	5.03 ± 0.12	2.40 ± 0.07	0.72 ± 0.06

Using the Van't Hoff equation, $\Delta_r H^0_m$ and $\Delta_r S^0_m$ of the related complexation reactions are obtained from the thermodynamic stability constants. The $\Delta_r H^0_m$ and $\Delta_r S^0_m$ values are shown in Table 12. It is obvious, that the standard reaction enthalpies and entropies are completely different compared to the results of the monocarboxylic acids (chapter 3.1.1.-3.1.3.). All complexation reactions are less endothermic (the formation of $[Cm(Ox)]^+$ is even exothermic). For the formation of $[Cm(Ox)]^+$, the gain in entropy is significantly higher compared to formate, acetate, and propionate. These findings are explained by the different binding mode of

oxalate towards Cm(III). Whereas monocarboxylic acids bind in an end-on fashion to the actinide ion, oxalate can bind through both carboxylic groups in a side-on coordination forming a 5-membered chelate ring. The formation of such a chelate complex results in a higher binding energy which is reflected by a lower standard reaction enthalpy.

Table 12: $\Delta_r H^0_m$ and $\Delta_r S^0_m$ values for the stepwise formation of $[Cm(Ox)_n]^{3-2n}$ (n = 1-3) in NaCl solution.

$Cm^{3+} + Ox^{2-} \rightleftharpoons Cm(Ox)^+$		$Cm(Ox)^+ + Ox^{2-} \rightleftharpoons Cm(Ox)_2^-$		$Cm(Ox)_2^- + Ox^{2-} \rightleftharpoons Cm(Ox)_3^{3-}$	
$\Delta_r H^0_m$ / kJ/mol	$\Delta_r S^0_m$ / J/K·mol	$\Delta_r H^0_m$ / kJ/mol	$\Delta_r S^0_m$ / J/K·mol	$\Delta_r H^0_m$ / kJ/mol	$\Delta_r S^0_m$ / J/K·mol
-2.7 ± 0.8	121.8 ± 2.9	10.8 ± 1.8	126.0 ± 3.2	10.3 ± 1.5	76.0 ± 3.1

The spectroscopic results are confirmed by quantum chemical calculations. For more details see:

A. Skerencak-Frech, M. Maiwald, D. R. Fröhlich, P. J. Panak, The thermodynamics of the complexation of Cm(III) with oxalate at increased temperatures: A spectroscopic study in the nanomolal concentration range, Inorganic Chemistry, 2015, ***54****, 1860-1868.*

3.2. Macromolecular organic ligands

In addition to investigations on the interaction of trivalent actinides with various LMWOC, complexation studies with different fulvic acids as representative humic substances were performed. Stock solutions of the different fulvic acids (Gohy-573, SR and NL) with concentrations of 0.8 to 1.0 g/kg H_2O were prepared by dissolution of the solid FAs in deionized water. The pH of the solutions was adjusted to 4 by

addition of a dilute NaOH solution. The total H^+ concentration was fixed at 10^{-4} mol/kg and 0.1 mol/kg NaCl was used as background electrolyte for all samples. The interaction of Eu(III) and Cm(III) with different FAs was investigated as a function of the temperature (20, 40, 60 and 80 °C) by varying the FA concentration between 0 and 20 mg/kg H_2O. The metal concentrations of Eu(III) and Cm(III) were held constant at 1×10^{-6} and 5×10^{-9} mol/kg, respectively.

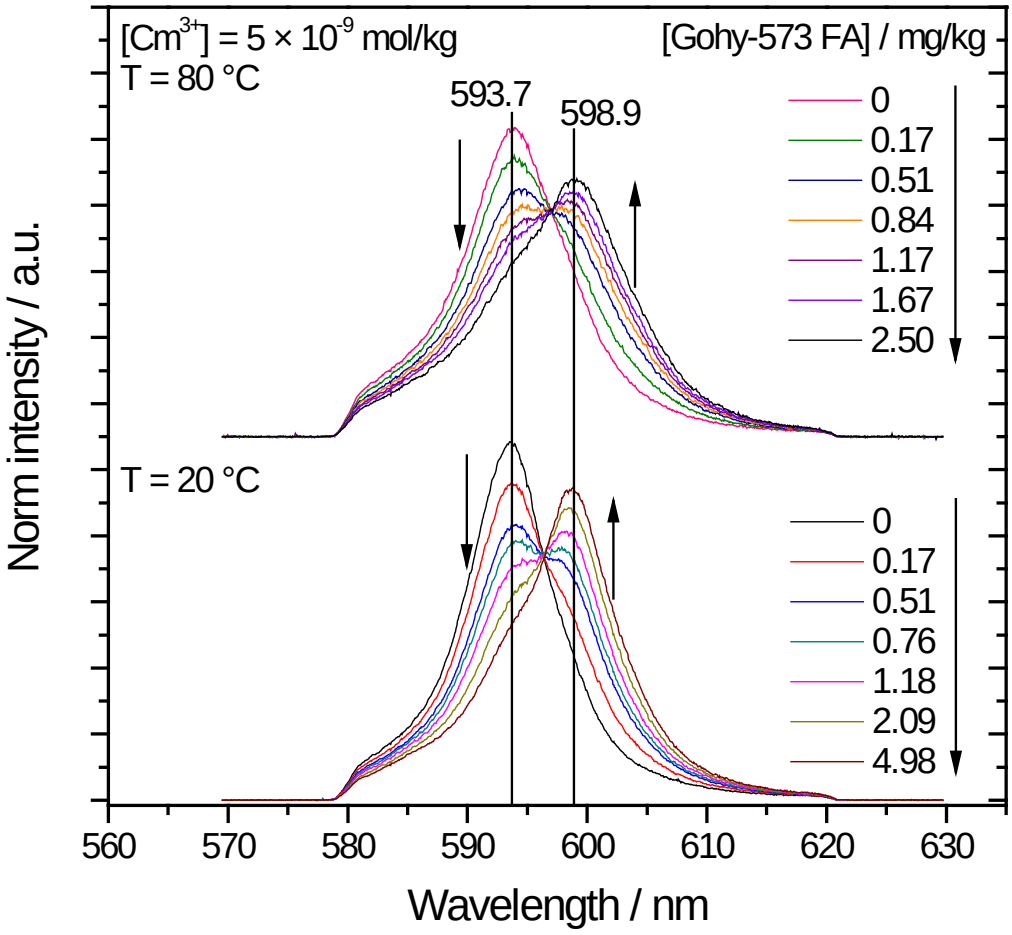

Figure 5: Emission spectra of 1×10^{-9} mol/kg Cm(III) in the presence of the FA Gohy-573 normalized to the total peak area at 20 and 80 °C.

As an example, the normalized emission spectra of Cm(III) in the presence of Gohy-573 at 20 and 80 °C as a function of the ligand concentration are presented in Figure 5. It is clearly visible that only two species are formed at the given

experimental conditions, the Cm(III) aquo ion at 593.7 nm and a complexed Cm(III) species at 598.9 nm. The same behavior is observed for the other investigated FAs and when using Eu(III) as metal ion. Figure 6 shows the normalized pure component spectra of the different Cm(III)- and Eu(III)-FA complexes at room temperature in comparison to the spectra of the related aquo ions. The emission spectra of the different FA complexes are almost identical indicating a congruent binding mechanism for all investigated ligand systems.

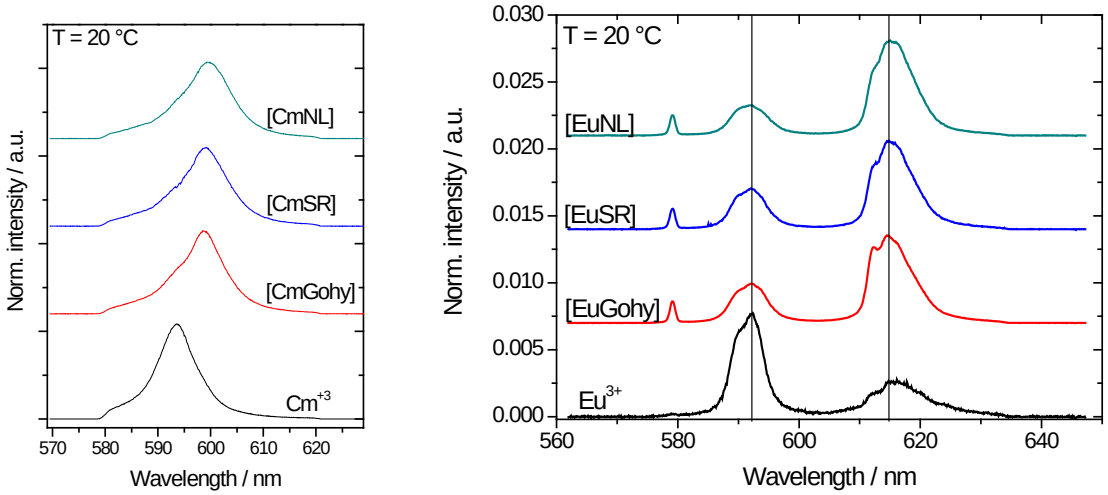

Figure 6: Normalized spectra of the different Cm(III)- (left) and Eu(III)-FA complexes (right) at room temperature in comparison to the spectra of the related aquo ions.

The pure component spectra are used to determine the Cm(III) and Eu(III) speciation. Using the charge neutralization model (see chapter 2.3.), the temperature dependent conditional stability constants (log β'(T)) at I = 0.1 mol/kg for the formation of the different Cm(III)- and Eu(III)-FA complexes are determined (see Table 13). For both trivalent metals ions an increase of log β'(T) with increasing temperature is found for the complexation with the different FAs. Also, the absolute values of log β'(T) are similar for each combination of FA and trivalent metal ion. The reaction enthalpies and entropies are summarized in Table 14. All complexation reactions are endothermic and entropy driven. In the case of Eu(III) the $\Delta_r H_m$ (23-34 kJ/mol) and

Table 13: Conditional stability constants (log β') at I = 0.1 mol/kg for the formation of different Cm(III)- and Eu(III)-FA complexes at T = 20, 40, 60, and 80 °C.

FA	T / °C	Log β'(T)	
		Cm(III)	Eu(III)
Gohy-573	20	6.29 ± 0.16	5.60 ± 0.23
	40	6.41 ± 0.24	6.00 ± 0.22
	60	6.68 ± 0.18	6.16 ± 0.09
	80	6.62 ± 0.26	6.64 ± 0.16
SR	20	6.05 ± 0.20	6.21 ± 0.28
	40	6.46 ± 0.28	6.45 ± 0.14
	60	6.66 ± 0.20	6.59 ± 0.16
	80	6.65 ± 0.36	6.94 ± 0.18
NL	20	6.05 ± 0.26	6.02 ± 0.25
	40	6.58 ± 0.10	6.17 ± 0.22
	60	6.64 ± 0.20	6.36 ± 0.17
	80	6.66 ± 0.24	7.00 ± 0.15

Table 14: Thermodynamic constants ($\Delta_r H_m$, $\Delta_r S_m$) for the formation of different Cm(III)- and Eu(III)-FA complexes at I = 0.1 mol/kg.

FA	$\Delta_r H_m$ / kJ/mol	$\Delta_r S_m$ / J/(K·mol)
	Cm(III)	
Gohy-573	14.1 ± 8.7	169 ± 28
SR	24.1 ± 11.0	199 ± 35
NL	15.0 ± 10.2	173 ± 32
	Eu(III)	
Gohy-573	32.1 ± 8.6	216 ± 26
SR	23.3 ± 9.3	198 ± 29
NL	34.2 ± 8.9	228 ± 27

$\Delta_r S_m$ (198-228 J/(K·mol)) values are slightly higher compared to the Cm(III) data ($\Delta_r H_m$: 14-24 kJ/mol, $\Delta_r S_m$: 169-199 J/(K·mol)). However, $\Delta_r H_m$ and $\Delta_r S_m$ for both metal ions are in good agreement regarding the relatively broad error range. The fact that the reactions are endothermic indicates that the investigated FAs predominantly form non-chelate complexes with Cm(III) and Eu(III). A more detailed description of the work can be found in:

*D. R. Fröhlich, A. Skerencak-Frech, M. Gast, P. J. Panak, Fulvic acid complexation of Eu(III) and Cm(III) at elevated temperatures studied by time-resolved laser fluorescence spectroscopy, Dalton Transactions, 2014, **43**, 15593-15601.*

4. Extended X-ray absorption fine structure spectroscopy

EXAFS spectroscopy has been used to complement the thermodynamic studies obtained by time resolved laser fluorescence spectroscopy. Am(III) has been chosen as a representative trivalent actinide to resolve the molecular structure of An(III) complexes with selected organic ligands.

4.1. Acetate

To resolve the molecular structure of the different acetate species, six samples were prepared. The Am(III) and acetate concentration were held constant at 10^{-3} and 0.2 mol/L, respectively. The pH of the samples was varied between 1 and 6 (see pH values given in Table 15).

The experimental k^3-weighted Am-L_3-edge EXAFS spectra together with the Fourier Transforms are presented in Figure 7. Only slight differences are visible, e.g. the small peak in the FT at $R+\Delta R \approx 3.75$ Å at high pH which is attributed to the non-coordinating distal carbon atom of acetate. The extracted structural data are summarized in Table 15. In all cases, approximately 10 oxygen neighbors at 2.48 ± 0.01 Å are observed in the first coordination sphere which is in agreement with literature data on Am(III) in aqueous solution studied by EXAFS [17]. Whereas the low pH samples mainly exhibit the Am(III) aquo ion, carbon neighbors are found at pH ≥ 3.4. The coordination number with respect to carbon increases from 0.4 at pH 3.4 to 2.0 at pH 5.9. Furthermore, the significance of the carbon shells is verified by comparing the reduced errors of the fits with and without carbon shells (see Table 15). For all samples with pH ≥ 3.4 an improvement of the fits is observed when taking into account the carbon shells, thus confirming the presence of acetate in the coordination sphere of Am(III). The coordinating and distal carbon neighbors are located at 2.78-2.84 and 4.39-4.41 Å, respectively. The interatomic distances clearly

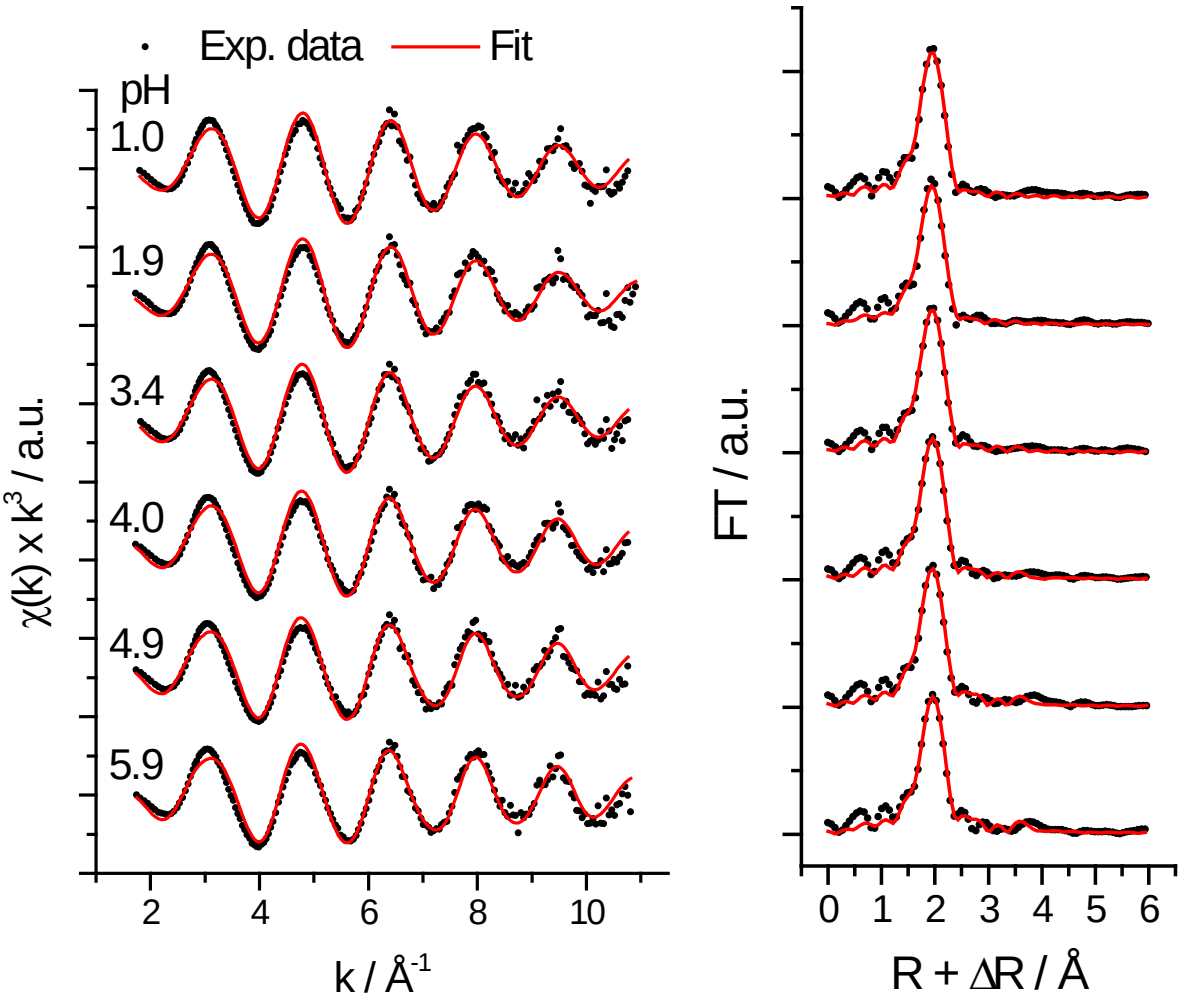

Figure 7: k^3-weighted EXAFS spectra (left) and Fourier Transforms (right) of 1 mM Am(III) in the presence of 0.2 M acetate as a function of the pH value.

Table 15: Structural data obtained from the EXAFS spectra shown in Figure 7.

Sample		1	2	3	4	5	6
pH		1.0	1.9	3.4	4.0	4.9	5.9
O	N	10.1 (3)	10.1 (4)	10.4 (5)	10.2 (4)	10.7 (5)	10.4 (5)
	R / Å	2.47 (1)	2.47 (1)	2.48 (1)	2.49 (1)	2.49 (1)	2.49 (1)
	σ^2 / Å²	0.009 (1)	0.009 (1)	0.009 (1)	0.009 (1)	0.010 (1)	0.009 (1)
$C_{carboxyl}$*	N	-	-	0.4 (4)	1.0 (3)	1.6 (0.4)	2.0 (4)
	R / Å	-	-	2.78 (7)	2.81 (3)	2.83 (2)	2.84 (1)

C_{distal}**	R / Å	-	-	4.39 (9)	4.41 (4)	4.41 (3)	4.41 (2)
ΔE_0 / eV			-2.0 (3)	-2.1 (3)	-1.6 (4)	-1.0 (3)	-1.0 (4)
Reduced error without C shells		0.192	0.217	0.185	0.177	0.219	0.234
Reduced error with C shells		-	-	0.183	0.174	0.213	0.214
k-range / $Å^{-1}$		1.8-10.8	1.8-10.8	1.8-10.8	1.7-10.8	1.7-10.8	1.8-10.8

point out that binding between Am(III) and acetate is bidentate as monodentate binding would result in significantly longer Am-C distances. In addition, the EXAFS data are analyzed by iterative transformation factor analysis to verify the chemical speciation, which is calculated on the basis of thermodynamic constants, and the used structural model. The experimental results are in very good agreement with the thermodynamic model. More details on the pH dependence of Am(III) complexation with acetate are given in:

D. R. Fröhlich, A. Skerencak-Frech, N. Bauer, A. Rossberg, P. J. Panak, The pH dependence of Am(III) complexation with acetate: an EXAFS study, Journal of Synchrotron Radiation, 2015, ***22****, 99-104*.

4.2. Lactate

Following the same procedure as described in the previous chapter, the complexation of Am(III) with lactate was investigated. Again six samples were prepared. The Am(III) concentration ranged between 0.13 and 0.27 mmol/L, the lactate concentration was in the range of 3.9 to 8.5 mmol/L. The pH was varied from 0.9 to 6.4 to track a continuous shift of Am(III) speciation with increasing pH. Figure 8 presents the k^3-weighted Am-L_3-edge EXAFS spectra and the Fourier Transforms.

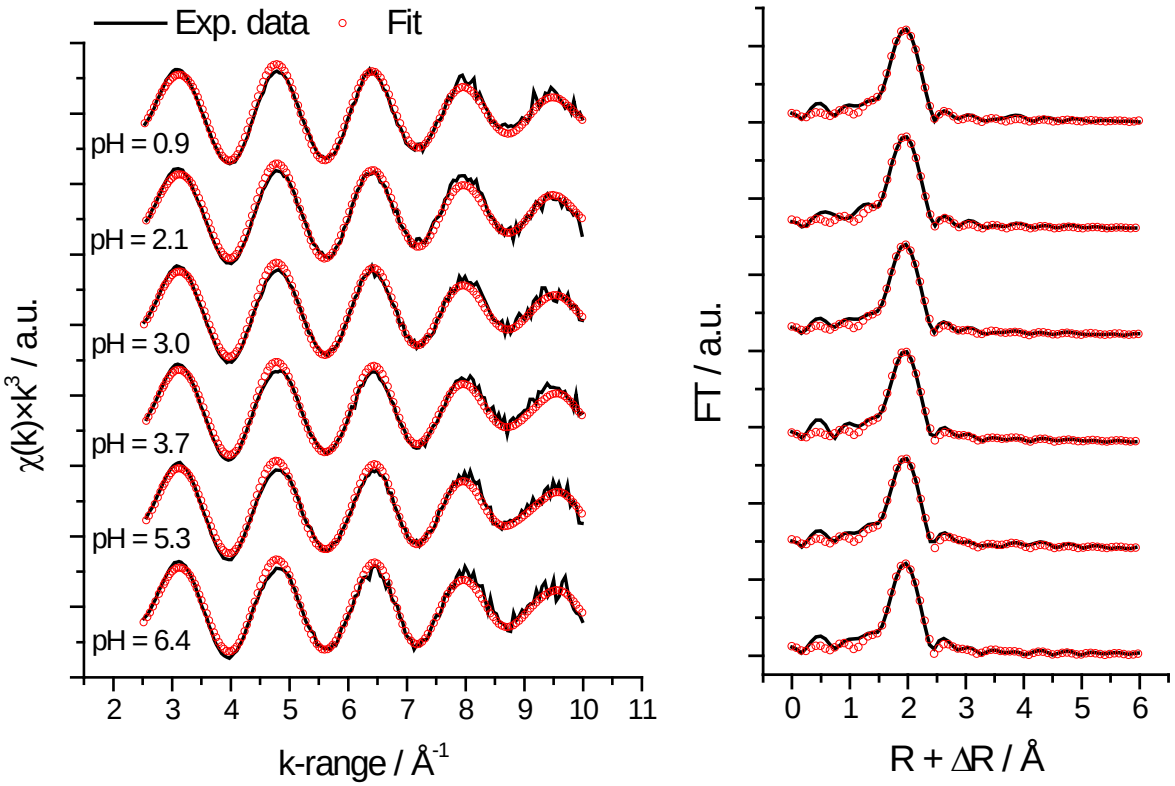

Figure 8: k^3-weighted EXAFS spectra (left) and Fourier Transforms (right) of 0.13-0.27 mM Am(III) in the presence of 3.9-8.5 mM lactate as a function of the pH value.

The structural data are summarized in Table 16. Again, the samples prepared at low pH (0.9 and 2.1) are dominated by the Am(III) aquo ion. At pH ≥ 3, the coordination number with respect to carbon increases continuously with increasing pH from 1.0 (pH 3.0) to 1.7 (pH 6.4). In the case of lactate an important question is whether the ligand binds through the carboxylic function only or through both the carboxylic and the α-hydroxy function. The coordinating carbon and distal carbon/oxygen neighbors are located at 3.41-3.43 and 4.32-4.36 Å, respectively. The interatomic distance between Am(III) and the coordinating carbon atoms is significantly longer compared to the acetate system (see chapter 4.1), thus pointing out a different binding mechanism. In fact, lactate forms a chelate complex through

Table 16: Structural data obtained from the EXAFS spectra shown in Figure 8.

Sample		1	2	3	4	5	6
pH		0.9	2.1	3.0	3.7	5.3	6.4
O	N	10.9 (3)	10.4 (3)	10.6 (3)	10.4 (4)	10.2 (3)	10.0 (4)
	R / Å	2.47 (1)	2.47 (1)	2.47 (1)	2.47 (1)	2.47 (1)	2.47 (1)
	σ^2 / Å²	0.0104 (4)	0.0099 (4)	0.0103 (4)	0.0103 (4)	0.0100 (5)	0.0094 (5)
C_{coord}*	N	-	-	1.0 (4)	1.6 (4)	2.2 (4)	1.7 (5)
	R / Å	-	-	3.43 (4)	3.43 (3)	3.41 (2)	3.42 (2)
C/O_{distal}**	R / Å	-	-	4.34 (5)	4.36 (4)	4.36 (3)	4.32 (4)
ΔE_0 / eV		-1.7 (3)	-1.5 (3)	-1.4 (2)	-1.4 (3)	-1.4 (3)	-1.3 (3)
Reduced error without C shells		0.1357	0.1460	0.1282	0.1678	0.1671	0.1978
Reduced error with C shells		-	-	0.1266	0.1578	0.1430	0.1843
k-range / $Å^{-1}$		2.54-9.99	2.56-9.98	2.53-9.99	2.56-9.98	2.56-9.98	2.52-9.99

* Debye Waller factor (σ^2) held constant at 0.005 Å², ** coordination number (N) of C/O_{distal} linked to N of the C_{coord}, σ^2 held constant at 0.005 Å², amplitude reduction factor (S_0^2) was set to 0.9 in all cases, uncertainties of each value obtained from the EXAFSPAK fit are given in parentheses. The absolute errors in N and the radial distances (R) are: N ± 20%, R ± 0.02 Å (Li *et al.*, 1995).

both functional groups. This has also been verified by comparison with thermodynamic speciation calculations as the two possible conformations result in different numbers of backscattering carbon neighbors (compare [18]). Regarding the coordination numbers, the experimental data are in excellent agreement with the thermodynamic modelling based on tabulated stability constants. The EXAFS spectra are also analyzed by iterative transformation factor analysis to further verify the determined Am(III) speciation and the used structural model. More details are given in:

*D. R. Fröhlich, A. Skerencak-Frech, U. Kaplan, C. Koke, A. Rossberg, P. J. Panak, An EXAFS spectroscopic study of Am(III) complexation with lactate, Journal of Synchrotron Radiation, 2015, **22**, 1469-1474.*

5. Development of new speciation methods

5.1. pH measurements at elevated temperatures

Previous experiments have shown that commercial sensors (Tophit CPS471D (Endress + Hauser)) did not provide accurate and stable pH values at elevated temperatures, even not after elongated measuring times. This was addressed to an insufficient flow around the probe head. The application of an additional circulating pump did not improve the result either.

Therefore, it was an important aim of the project to develop an alternative method to determine the pH and pK_S-values of small organic molecules (e.g. propionate, lactate, etc.) at elevated temperatures. Therefore, we used the indicator method combined with UV-Vis-spectroscopy utilizing the temperature dependency of the absoption spectra of selected dyes. As part of this work package we investigated the dyes acridine, bromophenol blue, bromothymol blue, and bromocresol green.

Measurements show that this method is applicable in the temperature range up to 100 °C, at higher temperatures the dyes start to degenerate irreversibly.

Bromocresol green was used successfully for the determination of the temperature dependent pK_S-values of propionate in the temperature range of 25 – 90 °C. After calibration of the temperature dependent pK_S-value of the dye versus standard pH buffer solutions, it was possible to determine the proton concentration at equilibrium for a given temperature using the SIT. With this information we were able to calculate the thermodynamic dissociation constant of propionic acid as a function of the temperature. Figure 9 shows the experimentally determined values for T = 25-90 °C compared to literature data [19]. In the low temperature range, excellent agreement is obtained for the experimental and the tabulated data. At higher temperatures a minor differences are observed (maximum ≈ 0.1 log units).

Analogous measurements were performed to determine the temperature dependency of the pK_S-value of lactic acid.

Thus, a new method for the determination of temperature dependent dissociation constants of small carboxylic ligand was implemented within this project.

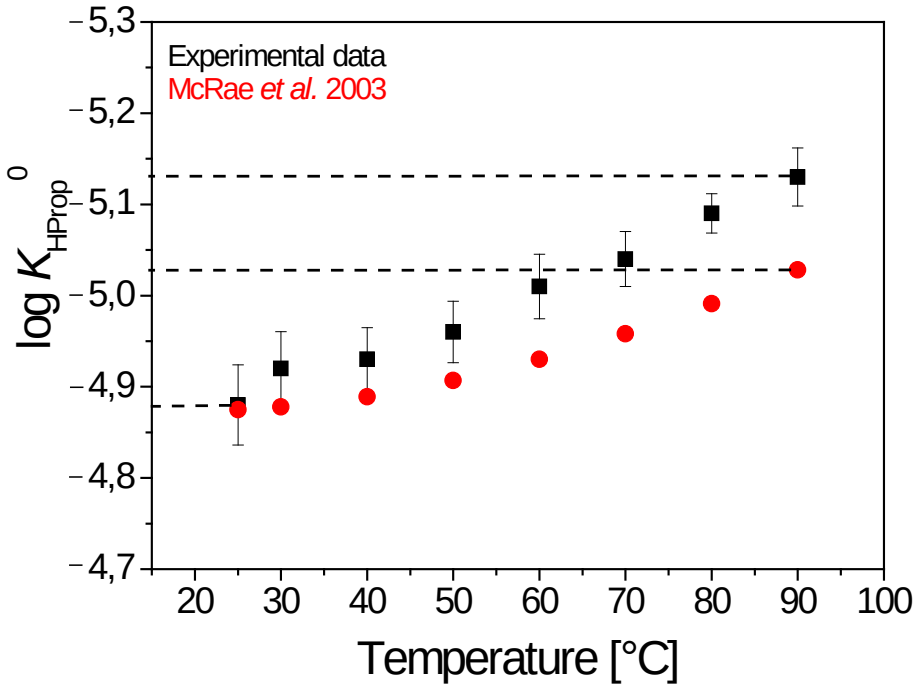

Figure 9 Experimental data of log $K^0_{HProp}(T)$ (black squares) in comparison to literature data (red circles [19]).

More details are presented in:

*A. Skerencak, S. Höhne, S. Hofman, C. Marquardt, P. J. Panak, Spectroscopic studies on the thermodynamics of the complexation of trivalent curium with propionate in the temperature range from 20 to 90°C, Journal of Solution Chemistry, 2013, **42**, 1-17.*

5.2. High-temperature EXAFS spectroscopy

A new device for EXAFS spectroscopic measurements at high temperatures has been developed (see Fig. 10). To implement and prove the functionality of this high-temperature cell, the complexation of Am(III) with chloride was investigated at T = 25,

90, and 200 °C. A sample solution with Am(III) and chloride concentrations of 1×10^{-3} and 3.0 mol/kg, respectively, was inserted into the cell. After the measurement at room temperature, the temperature was raised to 90 and 200 °C. The total proton concentration equaled 9×10^{-2} mol/kg.

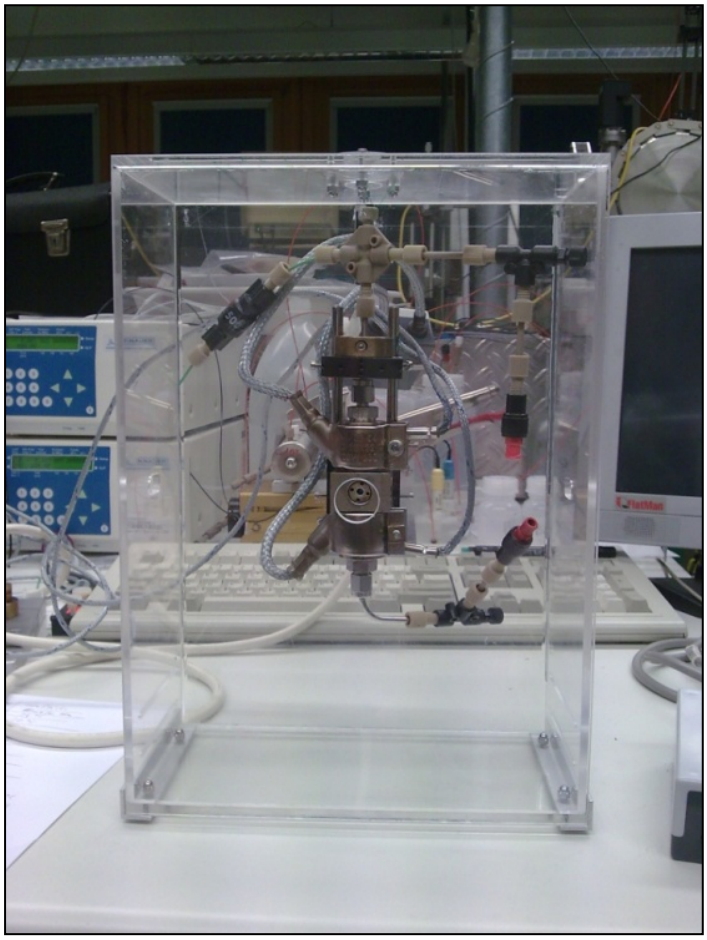

Figure 10 High-temperatur cell for EXAFS spectroscopic measurements.

The structural data are presented in Table 17. At T = 25 and 90 °C the Am(III) aquo ion is observed exclusively with 9-10 oxygen neighbors at 2.45-2.48 Å. At 200 °C, a second coordination sphere of 2.4 chloride atoms at 2.78 Å has to be added to accurately fit the experimental data. As a result, the coordination number with respect to oxygen decreases to 6.3. The results are compared to literature data [17] obtained at room temperature, where chloride concentrations > 10 M had to be applied to

observe an Am(III)-chloride interaction. As an important result, the present study points out that the impact of chloride on the speciation of Am(III) increases significantly with increasing temperature. At 200 °C the formation of Am(III)-chloride complexes is observed at significantly lower chloride concentration of ≥ 3 mol/kg. These results are confirmed by TRLFS studies proving that the log $\beta^\circ_2(T)$ value of $CmCl_2^+$ increases by more than 3 orders of magnitude in the studied temperature range.

Table 17: Structural data obtained from the EXAFS spectra of 1 mM Am(III) in the presence of 3 M Cl^- measured at various temperatures.

T / °C		25	90	200
O	N	9.6 (1.3)	9.0 (1.2)	6.3 (1.0)
	R / Å	2.45 (1)	2.48 (1)	2.44 (5)
	σ^2 / Å²	0.007 (2)	0.009 (2)	0.015*
Cl**	N	-	-	2.4 (0.5)
	R / Å	-	-	2.78 (5)
ΔE_0 / eV		-4.9 (1.3)	-5.0 (1.3)	-5.0 (2.0)

S_0^2 = 0.9; *fixed during fit; **third cumulant set to 0.003 (Am-O), 0.002 (Am-Cl)

The results show that the high-temperature cell, implemented within this project, is well suited for investigations of complexation reactions in aqueous solution in the temperature range up to 200 °C and will be applied successfully in future studies on the complexation of actinides with selected (in)organic ligands. More details on the high-temperature-high-pressure cell designed for TRLFS and EXAFS measurements are given in:

A. Skerencak-Frech, D. R. Fröhlich, J. Rothe, K. Dardenne, P. J. Panak, A combined TRLFS and EXAFS study on the complexation of trivalent actinides with chloride at T = 25 - 200°C, Inorganic Chemistry, 2014, 53, 1062-1069.

6. Summary

Aim of this work was the determination of thermodynamic data of complexation reactions of trivalent actinides with organic ligands in the temperature range up to 100 °C which is relevant for the final disposal of high-level nuclear waste in clay formations. The thermodynamic data were complemented by structural data of the complex species obtained by X-ray absorption spectroscopy.

Time-resolved laser fluorescence spectroscopy has been used to study the complexation of Cm(III) with formate, acetate, propionate, oxalate, and different fulvic acids. The interaction with small organic ligands was investigated in the temperature range of 20 - 90 °C. In case of monocarboxylic ligands (formate, acetate, propionate) endothermic reactions were observed for all complexation steps. The $\log K^0_n(T)$ values for the first and second complexation step with acetate and propionate range between 3.1-3.7 (n = 1) and 1.5-2.7 (n = 2) in the investigated temperature range. For formate, $\log K^0_1(T)$ and $\log K^0_2(T)$ are lower by about 1 and 0.5 log units, respectively, which is in accordance with literature data for trivalent lanthanides. In contrast to these findings, the first complexation step of Cm(III) with oxalate is exothermic, whereas the following complexation steps are less endothermic compared to monocarboxylic ligands. This is attributed to the different coordination mode as oxalate binds through both carboxylic groups forming a five-membered chelate ring.

The complexation of Cm(III) with different fulvic acids as representative macromolecular natural organic matter was investigated at 20, 40, 60, and 80 °C. In all cases, only one defined complex species was observed for each fulvic acid. The $\log \beta(T)$ values at I = 0.1 mol/kg increased with increasing temperature from 6.1-6.3 to 6.6-6.7 depending on the fulvic acid used. The endothermic complexation behavior suggests a binding mechanism through carboxylic functions of the macromolecules without forming chelate complexes. Investigations on the complexation of Eu(III) with the same fulvic acids provided similar results.

EXAFS spectroscopy has been used to resolve the molecular structure of acetate and lactate complexes as a function of the pH using Am(III) as representative trivalent actinide. As expected, both ligands exhibited different binding modes towards Am(III). Whereas acetate undergoes end-on coordination through the carboxylic function, lactate binds through both functional groups, the carboxylic and the α-hydroxy function, forming a five-membered chelate complex like oxalate. These different binding modes are distinguished easily due to the differences regarding the interatomic distances.

A well-funded understanding of the solution chemistry of actinides is of major importance for the long-term safety assessment of a nuclear waste repository in deep geological formations. The interaction of actinides with natural clay is determined by different geochemical processes including complex formation with various (clay)organic ligands which may influence the migration behavior of the actinides. The Nuclear Energy Agency – Thermodynamic Database (NEA-TDB) provides a large number of thermodynamic data for the interaction of actinide with various inorganic and organic ligands, but most data are limited to room temperature. As the near-field of a repository will heat up significantly due to the radioactive decay of the high-level nuclear waste, it is of high importance to determine thermodynamic constants at increased temperatures and to quantify the effect of temperature on the chemical properties of the actinides.

The present work clearly improves the general understanding of actinide complexation with macromolecular and low molecular weight (clay)organic compounds in the temperature range of 20 – 90 °C. The impact of monocarboxylic ligands which are present in natural pore waters of clays on the aqueous speciation of trivalent actinides is largely insignificant at room temperature which is reflected by the low stability constant determined for Cm(III), but increases continuously with increasing temperature. However, in comparison to other complexation reaction relevant at natural conditions, such as carbonate complexation and/or hydrolysis, the interaction with monocarboxylic ligands is negligible and will not have a significant impact on the migration behavior of actinide. In contrast, the complexation properties of α-hydroxy-carboxylic and dicarboxylic ligands as well as macromolecular organics

(e.g. fulvic acids) is more pronounced, but the temperature dependency of the complexation reactions is significantly lower compared to the monocarboxylic acids.

Lastly, the implementation of a new device for TRLSF and EXAFS measurement at high temperatures provides a powerful tool for future studies on complexation reactions and molecular structures of aqueous actinide complexes at elevated temperatures.

7. References

[1] ONDRAF/NIRAS, *SAFIR 2: Safety assessment and feasibility interim repor*,. NIROND-2001-06 E, ONDRAF/NIRAS, Brussels/Belgium, 2001.

[2] OECD, *Safety of geological disposal of high-level and long-lived radioactive waste in France - An international peer review of the "Dossier 2005 Argile" concerning disposal in the Callovo-Oxfordian formation*, NEA No. 6178, OECD Organisation for economic co-operation and development, 2006.

[3] P. Hoth, H. Wirth, K. Reinhold, V. Bräuer, P. Krull, H. Feldrappe, *Endlagerung radioaktiver Abfälle in tiefen geologischen Formationen Deutschlands – Untersuchung und Bewertung von Tongesteinsformationen*, BGR Bundesanstalt für Geowissenschaften und Rohstoffe, Hannover/Germany, 2007.

[4] NAGRA, *Projekt Opalinuston – Synthese der geowissenschaftlichen Untersuchungsergebnisse, Entsorgungsnachweis für abgebrannte Brennelemente, verglaste hochaktive sowie langlebige mittelaktive Abfälle*, Technical Report NTB 02-03, NAGRA Nationale Genossenschaft für die Lagerung radioaktiver Abfälle, Wettingen/Switzerland, 2002.

[5] A. Courdouan, I. Christl, S. Meylan, P. Wersin, R. Kretzschmar, *Applied Geochemistry*, 2007, **22**, 1537-1548.

[6] A. Courdouan, I. Christl, S. Meylan, P. Wersin, R. Kretzschmar, *Applied Geochemistry*, 2007, **22**, 2926-2939.

[7] J. I. Kim, G. Buckau, G. H. Li, H. Duschner, N. Psarros, *Fresenius Journal of Analytical Chemistry*, 1990, **338**, 245-252.

[8] G. N. George, I. J. Pickering, *EXAFSPAK: A suite of computer programs for analysis of X-ray absorption spectra.* Stanford Synchrotron Radiation Laboratory, Stanford/USA, 2000.

[9] B. Ravel, M. Newville, *Journal of Synchrotron Radiation*, 2005, **12**, 537-541.

[10] A. L. Ankudinov, C. E. Bouldin, J. J. Rehr, J. Sims, H. Hung, *Physical Review B*, 2002, **65**, 104107 1-11.

[11] D. R. Fröhlich, A. Skerencak-Frech, M. L. K. Morkos, P. J. Panak, *New Journal of Chemistry*, 2013, **37**, 1520-1528.

[12] R. J. Silva, G. Bidoglio, M. H. Rand, P. Robouch, H. Wanner, I. Puigdomenech, *Chemical thermodynamics Vol. 2. Chemical thermodynamics of americium*, OECD, NEA-TDB, North Holland, Amsterdam, 1995.

[13] J. I. Kim, K. R. Czerwinski, *Radiochimica Acta*, 1996, **73**, 5-10.

[14] D. R. Fröhlich, A. Skerencak-Frech, P. J. Panak, *Applied Geochemistry*, 2015, **61**, 312-317.

[15] G. Tian, N. M. Edelstein, L. Rao, *Journal of Physical Chemistry A*, 2011, **115**, 1933-1938.

[16] R. J. Motekaitis, *NIST Standard Reference Database 46 ver.6. – NIST critically selected stability constants of metal complexes (Martell, A.E., Smith, R.M., Eds)*, 2001.

[17] P. G. Allen, J. J. Bucher, D. K. Shuh, N. M. Edelstein, I. Craig, *Inorganic Chemistry*, 2000, **39**, 595-601.

[18] D. R. Fröhlich, A. Skerencak-Frech, U. Kaplan, C. Koke, A. Rossberg, P. J. Panak, *Journal of Synchrotron Radiation*, 2015, **22**, 1469-1474.

[19] B. R. McRae, B. A. Patterson, M. L. Origlia-Luster, E. C. Sorenson, E. M. Woolley, *The Journal of Chemical Thermodynamics*, 2003, **35**, 301-329.

8. Publications

Peer reviewed Journals:

D. R. Fröhlich, A. Skerencak, M. L. K. Morkos, P. J. Panak, A spectroscopic study of Cm(III) complexation with propionate in saline solutions at variable temperatures, *New Journal of Chemistry,* 2013, **37**, 1520-1528.

A. Skerencak, S. Höhne, S. Hofman, C. Marquardt, P. J. Panak, Spectroscopic studies on the thermodynamics of the complexation of trivalent curium with propionate in the temperature range from 20 to 90°C, *Journal of Solution Chemistry,* 2013, **42**, 1-17.

D. R. Fröhlich, A. Skerencak-Frech, P. J. Panak, A spectroscopic study on the formation of Cm(III) acetate complexes at elevated temperatures, *Dalton Transactions,* 2014, **43**, 3958-3965.

D. R. Fröhlich, A. Skerencak-Frech, M. Gast, P. J. Panak, Fulvic acid complexation of Eu(III) and Cm(III) at elevated temperatures studied by time-resolved laser fluorescence spectroscopy, *Dalton Transactions,* 2014, **43**, 15593-15601.

A. Skerencak-Frech, D. R. Fröhlich, J. Rothe, K. Dardenne, P. J. Panak, A combined TRLFS and EXAFS study on the complexation of trivalent actinides with chloride at T = 25 - 200°C, *Inorganic Chemistry,* 2014, **53**, 1062-1069.

D. R. Fröhlich, A. Skerencak-Frech, N. Bauer, A. Rossberg, P. J. Panak, The pH dependence of Am(III) complexation with acetate: an EXAFS study, *Journal of Synchrotron Radiation,* 2015, **22**, 99-104.

D. R. Fröhlich, A. Skerencak-Frech, P. J. Panak, Complex formation of Cm(III) with formate studied by time-resolved laser fluorescence spectroscopy, *Applied Geochemistry,* 2015, **61**, 312-317.

D. R. Fröhlich, A. Skerencak-Frech, U. Kaplan, C. Koke, A. Rossberg, P. J. Panak, An EXAFS spectroscopic study of Am(III) complexation with lactate, *Journal of Synchrotron Radiation,* 2015, **22**, 1469-1474.

A. Skerencak-Frech, M. Maiwald, D. R. Fröhlich, P. J. Panak, The thermodynamics of the complexation of Cm(III) with oxalate at increased temperatures: A spectroscopic study in the nanomolal concentration range, *Inorganic Chemistry,* 2015, **54**, 1860-1868.

Conference contributions:

Oral presentations:

A. Skerencak, S. Höhne, S. Hofmann, C. Marquardt, P. J. Panak, Complexation of Cm(III) with propionate in the temperature range from 20 to 90°C, GDCh Wissenschaftsforum, September 4 – 7, Bremen, Germany (2011).

A. Skerencak, P. J. Panak, T. Fanghänel, TRLFS studies of actinide complexation at elevated temperatures, HiTAC Workshop, November 9th, Karlsruhe, Germany (2011). **(invited)**

P. J. Panak, Time-resolved Laser Fluorescence Spectroscopy – A Valuable Tool for Actinide Speciation, Seminarvortrag Tschechische Technische Universität, May 5, Prag, Czech Republic (2013) **(invited)**.

Panak, P. J., Spectroscopic characterization of actinides, 2013 Summer School on Actinide Science & Applications, July 17, Karlsruhe, Germany (2013) **(invited).**

D. R. Fröhlich, A. Skerencak-Frech, P. J. Panak, A Combined EXAFS and TRLFS Spectroscopic Study to Determine the Thermodynamic and Structural Properties of Trivalent Actinide Complexes with Organic and Inorganic Ligands at Elevated Temperatures, 14th International Conference on the Chemistry and Migration Behaviour of Actinides and Fission Products in the Geosphere, Migration 2013, September, 8 – 13, Brighton, UK (2013).

A. Skerencak-Frech, D. R. Fröhlich, J. Rothe, K. Dardenne, P. J. Panak, A combined TRLFS and EXAFS study on the complexation of Cm(III) and Am(III) with chloride at T = 25 – 200°C, 16th International Symposium on Solubility Phenomena and Related Equilibrium Processes, July 21 – 25, Karlsruhe, Germany (2014).

P. J. Panak, Time-resolved Laser Fluorescence Spectroscopy – a Valuable Tool for Actinide Speciation, 16th International Symposium on Solubility Phenomena and Related Equilibrium Processes, July 21 - 25, Karlsruhe, Germany (2014) **(invited).**

A. Skerencak-Frech, C. Koke, D. R. Fröhlich, J. Rothe, K. Dardenne, P. J. Panak, A combined TRLFS and EXAFS study on the complexation of Cm(III) and Am(III) with chloride at T = 25 – 200°C, HiTAC II Workshop, April 14 – 16, Heidelberg, Germany (2015).

D. R. Fröhlich, A. Skerencak-Frech, A. Rossberg, P. J. Panak, Complexation of trivalent actinides with acetate studied by TRLFS and EXAFS spectroscopy, 45èmes Journées des Actinides, April 15 – 19, Prague Pruhonice, Czech Republic (2015).

P. J. Panak, Spectroscopic Characterization of actinides, 8th Summer School on Actinide Science & Applications 2015, June 15-19, Karlsruhe, Germany **(invited).**

D. R. Fröhlich, A. Skerencak-Frech, A. Rossberg, P. J. Panak, Spektroskopische Untersuchungen zur Komplexierung dreiwertiger Actiniden mit Acetat, GDCh Wissenschaftsforum, August 30 – September 2, Dresden, Germany (2015)

A. Skerencak-Frech, M. M. Maiwald, M. Trumm, D. R. Fröhlich, P. J. Panak, Komplexierung von Cm(III) mit Oxalat in wässriger Lösung bei T = 20 – 90°C: Eine kombinierte TRLFS und quantenchemische Studie, GDCh Wissenschaftsforum, August 30 – September 2, Dresden, Germany (2015).

A. Skerencak-Frech, M. M. Maiwald, M. Trumm, D. R. Fröhlich, P. J. Panak, Complexation of trivalent actinides with clay-organic ligands at T = 20 – 90°C, 15th International Conference on the Chemistry and Migration Behaviour of Actinides and Fission Products in the Geosphere "Migration '15", September 13 – 18, Santa Fe, USA, (2015).

Poster presentations:

A. Skerencak, P. J. Panak, W. Hauser, R. Götz, R., Klenze, T. Fanghänel, Spectroscopic and thermodynamic studies on the complexation of Cm(III) with SO_4^{2-} in the temperature range from 25 to 200°C, 13th International Conference on the Chemistry and Migration Behaviour of Actinides and Fission Products in the Geosphere, Migration 2011, September 18 – 23, Bejing, China (2011).

D. R. Fröhlich, A. Skerencak, J. Rothe, K. Dardenne, W. Hauser, R. Götz, R., Panak, P. J., A new experimental setup to study the complexation behaviour of actinides in aqueous solution by EXAFS spectroscopy up to 200 °C. 4th ANKA/KNMF User Meeting, October 10 – 11, Ettlingen, Germany (2012).

A. Skerencak, P. J. Panak, T. Fanghänel, Complexation and thermodynamics of trivalent actinides under near-field conditions of a nuclear waste repository, Workshop AG Chemie und Energie Energietransformationen - Die Rolle der Chemie, November 15, Karlsruhe, Germany (2012).

D. R. Fröhlich, A. Skerencak-Frech, P. J. Panak, Spektroskopische Untersuchungen zur Komplexbildung von Am(III)/Cm(III) mit einfachen organischen Liganden bei erhöhten Temperaturen, GDCh Wissenschaftsforum, September, 1 – 4, Darmstadt, Germany (2013).

A. Skerencak-Frech, D. R. Fröhlich, P. J. Panak, The Thermodynamics of the Complexation of Cm(III) with Small Organic Ligands under Saline Conditions and Increased Temperatures, 14th International Conference on the Chemistry and Migration Behaviour of Actinides and Fission Products in the Geosphere, Migration 2013, September, 8 – 13, Brighton, UK (2013).

A. Skerencak-Frech, D. R. Fröhlich, P. J. Panak, The Thermodynamics of the complexation of Cm(III) with small organic ligands under saline conditions and increased temperatures, Joint ITU-INE Research Fellows` Day, February, 6, Karlsruhe, Germany (2014).

D. R. Fröhlich, A. Skerencak-Frech, J. Rothe, K. Dardenne, P. J. Panak, Complexation of Americium(III) with chloride – A high-temperature EXAFS study, 7th Workshop on Speciation, Techniques, and Facilities for Radioactive Matertials at Synchrotron Light Sources, AnXAS 2014, May 20-22, Böttstein, Switzerland (2014).

KIT Scientific Working Papers
ISSN 2194-1629

www.kit.edu